ECCM

20

26-30 JUNE

2022

LAUSANNE

SWITZERLAND

Proceedings of the 20th European Conference on Composite Materials

COMPOSITES MEET SUSTAINABILITY

Vol 5 – Applications and Structures

Editors : Anastasios P. Vassilopoulos, Véronique Michaud

Organized by :

EPFL

Under the patronage of :

CCLAB Composite Construction Laboratory

LPAC Laboratory for Processing of Advanced Composites

ESCM EUROPEAN SOCIETY FOR COMPOSITE MATERIALS

ECCM 20
26-30 JUNE 2022
LAUSANNE SWITZERLAND

EPFL CCLAB Composite Construction Laboratory LPAC Laboratory for Processing of Advanced Composites

Proceedings of the 20th European Conference on Composite Materials ECCM20 26-30 June 2022, EPFL Lausanne Switzerland

Edited By :

Prof. Anastasios P. Vassilopoulos, CCLab/EPFL
Prof. Véronique Michaud, LPAC/EPFL

Oragnized by:

Composite Construction Laboratory (CCLab)
Laboratory for Processing of Advanced Composites (LPAC)
Ecole Polytechnique Fédérale de Lausanne (EPFL)

ISBN: 978-2-9701614-0-0
DOI: http://dx.doi.org/10.5075/epfl-298799_978-2-9701614-0-0

Published by :

Composite Construction Laboratory (CCLab)
Ecole Polytechnique Fédérale de Lausanne (EPFL)
BP 2225 (Bâtiment BP), Station 16
1015, Lausanne, Switzerland

https://cclab.epfl.ch

Laboratory for Processing of Advanced Composites (LPAC)
Ecole Polytechnique Fédérale de Lausanne (EPFL)
MXG 139 (Bâtiment MXG), Station 12
1015, Lausanne, Switzerland

https://lpac.epfl.ch

Cover:

Swiss Tech Convention Center
© Edouard Venceslau - CompuWeb SA

Cover Design:

Composite Construction Laboratory (CCLab)
Ecole Polytechnique Fédérale de Lausanne (EPFL)
Lausanne, Switzerland

©2022 ECCM20/The publishers

Disclaimer:

The ECCM20 organizing committee and the Editors of these proceedings assume no responsibility or liability for the content, statements and opinions expressed by the authors in their corresponding publication.

Editorial

This collection gathers all the articles that were submitted and presented at the 20th European Conference on Composite Materials (ECCM20) which took place in Lausanne, Switzerland, June 26-30, 2022.

ECCM20 is the 20th edition of a conference series having its roots back in time, organized each two years by members of the European Society of Composite Materials (ESCM).

The ECCM20 event was organized by the Composite Construction laboratory (CCLab) and the Laboratory for Processing of Advanced Composites (LPAC) of the Ecole Polytechnique Fédérale de Lausanne (EPFL).

The Conference Theme this year was “Composites meet Sustainability”. As a result, even if all topics related to composite processing, properties and applications have been covered, sustainability aspects were highlighted with specific lectures, roundtables and sessions on a range of topics, from bio-based composites to energy efficiency in materials production and use phases, as well as end-of-life scenarios and recycling.

More than 1000 participants shared their recent research results and participated to fruitful discussions during the five conference days, while they contributed more than 850 papers which form the six volumes of the conference proceedings. Each volume gathers contributions on specific topics:

Vol 1 – Materials

Vol 2 – Manufacturing

Vol 3 – Characterization

Vol 4 – Modeling and Prediction

Vol 5 – Applications and Structures

Vol 6 – Life Cycle Assessment

We enjoyed the event; we had the chance to meet each other in person again, shake hands, hold friendly talks and maintain our long-lasting collaborations. We appreciated the high level of the research presented at the conference and the quality of the submissions that are now collected in these six volumes. We hope that everyone interested in the status of the European Composites’ research in 2022 will be fascinated by this publication.

The Conference Chairs

Anastasios P. Vassilopoulos, Véronique Michaud

ECCM 20
26-30 JUNE 2022
LAUSANNE SWITZERLAND

Hosting Organizations

Composite Construction Laboratory (CCLab)
Laboratory for Processing of Advanced Composites (LPAC)
Ecole Polytechnique Fédérale de Lausanne (EPFL)

Venue

Swiss Tech Convention Center (https://www.stcc.ch)

Conference Chairs

Chair : Prof. Anastasios P. Vassilopoulos, EPFL, Switzerland
Co-Chair: Prof Véronique Michaud, EPFL, Switzerland

International Scientific Committee

Prof. Malin Åkermo SE
Dr. Emmanuel Baranger FR
Prof. Christophe Binetruy FR
Prof. Pedro Camanho PT
Prof. Konstantinos Dassios GR
Prof. Brian Falzon UK
Prof. Kristofer Gamstedt SE
Prof. Sotiris Grammatikos NO
Prof. Christian Hochard FR
Prof. Marcin Kozlowski PL
Prof. Stepan Lomov BE
Dr. David May DE
Prof. Stephen Ogin UK
Prof. Gerald Pinter AT
Prof. Silvestre Pinho UK
Prof. Yentl Swolfs BE
Dr. Julie Teuwen NL
Dr. Panayota Tsotra CH
Prof. Wim van Paepegem BE
Prof. Dimitrios Zarouchas NL
Dr. Andrey Aniskevich LV
Prof. Christian Berggreen DK
Dr. Nicolas Boyard FR
Prof. Valter Carvelli IT
Prof. Klaus Drechsler DE
Prof. Bodo Fiedler DE
Dr. Nathalie Godin FR
Prof. Roland Hinterholzl AT
Prof. Ian Kinloch UK
Dr. Thomas Kruse DE
Prof. Theodoros Loutas GR
Prof. Veronique Michaud CH
Prof. Alessandro Pegoretti IT
Prof. Joao Ramoa Correia PT
Prof. Jose Sena-Cruz PT
Prof. Antonio T. Marques PT
Prof. Thanasis Triantafillou GR
Prof. Albert Turon ES
Prof. Anastasios P. Vassilopoulos CH
Prof. Martin Fagerström SE
Dr. Alexandros Antoniou DE
Prof. Lars Berglund SE
Prof. Michal Budzik DK
Prof. Lucas Da Silva PT
Dr. Andreas Endruweit UK
Prof. Mariaenrica Frigione IT
Dr. Larissa Gorbatikh BE
Dr. Martin Hirsekorn FR
Prof. Vassilis Kostopoulos GR
Prof. Jacques Lamon FR
Prof. Staffan Lundstrom SE
Prof. Peter Mitschang DE
Dr. Soraia Pimenta UK
Prof. Paul Robinson UK
Dr. Olesja Starkova LT
Prof. Sofia Teixeira de Freitas NL
Dr. Stavros Tsantzalis GR
Prof. Danny van Hemelrijck BE
Prof. Michele Zappalorto IT
Dr. Miroslav Cerny CZ

Local Organizing Committee

Prof. Anastasios P. Vassilopoulos, EPFL
Prof. Véronique Michaud, EPFL
Angélique Crettenand and Mirjam Kiener, Lausanne Tourisme
And all those who helped, colleagues who reviewed abstracts and chaired sessions, and CCLab and LPAC students and collaborators who worked hard to make this conference a success.

ECCM 20
26-30 JUNE 2022
LAUSANNE SWITZERLAND

Sponsors

SHIMADZU
Excellence in Science

Bristol Composites Institute

JEC GROUP

suprem

Surface Measurement Systems
World Leader in Sorption Science

INSTRON

9T LABS

Anton Paar

DIA-STRON
DELIVERING MEASUREMENT SOLUTIONS

AELER

HRC

ICCM 23
BELFAST 2023
30 JULY – 4 AUGUST

TEIJIN

Functional Composite Materials

materials
an Open Access Journal by MDPI

ELSEVIER

Supporting partners

JEC

CertBond
COST Action CA18120

EsSENce

Switzerland Tourism.

SWISS

SBB CFF FFS

sampe
Switzerland

COMPOSITES UNITED | SWITZERLAND

canton de vaud

Lausanne

Contents

MULTIFUNCTIONAL FIBRE-REINFORCED COMPOSITE SANDWICHES FOR ECO-FRIENDLY BUILDINGS

Susana, P.B. Sousa[a,b], Andreia, Araújo[a,b], Luís, Amorim[a,b], Ricardo, Rocha[a], Helena, Teixeira[c], Raquel M., Santos[a,b]

a: Institute of Science and Innovation in Mechanical and Industrial Engineering, Rua Dr. Roberto Frias, 4200-465 Porto, Portugal – ssousa@inegi.up.pt
b: Associated Laboratory for Energy, Transports and Aeronautics, Porto, 4200-265, Portugal
c: Faculty of Engineering of the University of Porto, s/n, R. Dr. Roberto Frias, 4200-465 Porto, Portugal

Abstract: *The construction sector is an intensive resource-consumer and a source of pollution worldwide. In this context, innovation in this field provides the opportunity to achieve environmental sustainability through the development and use of new construction technologies and materials, such as sandwich panels. To further increase the eco-sustainability of buildings in future cities, synthetic raw-materials should be replaced by natural or recycled ones. In the present work, a multifunctional composite sandwich panel was developed using bio-based materials, which was compared to the traditional counterparts. After production, the most important properties of both panels were investigated, including thermal, mechanical and sustainability performance. The results revealed that it is feasible to use eco-friendlier materials for developing multifunctional sandwich panels for the construction sector. Additional studies are anticipated to optimize the developed solution without significantly compromising other relevant properties.*

Keywords: modular construction, sustainability, eco-composites, prefabrication, energy savings.

1. Introduction

It is expected that 66 % of the global population will be living in urban areas by 2050. This growth can have negative impacts on the sustainable development of the cities if no changes are foreseen, since nowadays they consume about 75 % of global resources and contribute for 80 % of greenhouse emissions (1). Thus, the construction industry has the potential to be one of the most dynamic sectors in the global sustainable economic development of the cities. Nevertheless, relevant technological developments and introduction of novel materials must be attained aiming at reducing the carbon footprint of this sector. Nowadays, the buildings in the EU-28 are responsible for approximately 42 % of the total energy consumption and 36 % of the total gas emissions (2, 3).
There are several concerns regarding current buildings, such as the fact that they are made with complex and different materials (i.e., concrete, steel, aluminium, and others); need of substantial amounts of energy (heating, cooling, ventilation, and power) throughout their use, construction/renovation, and demolition processes; and generation of enormous amounts of leftovers that are deposited in landfills, increasing energy costs and environmental impacts. The European Commission (EC) is looking forward to promoting circular economy principles for buildings' design and construction. However, this is challenging, and until now there are no established policies within most of European countries (2-5). To achieve the desired sustainability, it is necessary to develop and use new construction policies and technologies with smaller amounts of material and preferably from bio-based sources (2, 4-6).

  doi:10.5075/epfl-298799_978-2-9701614-0-0

Among the several constructive solutions for new structures, expansion of existing ones, and in structural rehabilitation, the application of advanced composite materials is potentially beneficial to the sector´s sustainability (6-9). However, there are some reservations about their use due to their fire behaviour. The main advantages of these materials are lightness, possibility of prefabrication, high strength to weight ratio, durability, thermal and acoustic insulation, fast curing time, ability to form complex shape, excellent finishing, and ease repair/maintenance. These are some of the enhanced features of the advanced composite materials over the conventional ones, which are significant assets in the production of construction elements (6, 9-11).

Sandwich panels are multifunctional composite elements that allow to address several requirements, including structural, thermal, and acoustic performance. To produce these panels, an insulation foam is combined with exterior layers based on Fibre Reinforced Polymer (FRP) laminates (6, 7, 10, 12).

Although this technical solution leads to less material quantities to produce a building, it is commonly made with materials from fossil and scarce resources (6, 10). Despite all the predictable advantages, the use of natural based-materials in sandwich composite systems suffered from some inherent drawbacks, i.e., strength, thermal and ultraviolet (UV) radiation resistance, and fire resistance (13-15). Bio-based matrix materials have received considerable attention lately, since they are obtained from sustainable sources. Nevertheless, bio-based thermoset resins normally have expressively lower properties than the petroleum-based counterparts, which can be overcome through a compromise strategy (combination of materials with partially from plant origin), allowing to achieve a superior material from a sustainable-performance perspective (16, 17).

Recently, basalt fibres (BFs) have been studied as sustainable alternatives for some fibre reinforcements since they are produced from basalt rock (biologically inert), not requiring any precursor or additives for their production. Besides, BFs have higher mechanical, chemical, thermal and electrical properties than glass fibres (16-18). Moreover, cork oak instead of traditional foams is a promising eco-friendly solution that has been widely investigated to develop sandwich panels (15, 18). The combination of distinct materials can offer balanced solutions to the broaden applications of multifunctional composite sandwiches (MCS) by developing synergetic effects (16-18).

Despite the large amount of research work carried out on advanced composite sandwich panels, only few studies were published regarding the effective impacts of this specific bio-based solution for the construction sector. Under this framework, the present work aims to develop new bio-based MCS with enhanced multifunctionalities, by using laminates made with basalt fibre and bio-epoxy resin, combined with cork instead of foam as core material for manufacturing structural lightweight modular panels aligned with a “nearly zero-energy and-emission” vision.

2. Materials and Methods

2.1. Raw-materials and manufacturing procedures

2.1.1. Raw-materials

To produce the standard and bio-based composite sandwich panels, it was used commercially available two-component epoxy (Biresin® CR83/CH 83-6, SIKA) and bio-epoxy (SR InfuGreen 810/SD 8824®, SICOMIN) resins, plain glass (200 g/m^2 E ®, Castro Composites) and basalt (220 g/m^2®, Castro Composites) woven fabrics, 80 mm thick extruded polystyrene (XPS) (Soprema®) and cork (Amorim Cork Insulation®) cores. The main properties of the raw-materials, as supplied by the manufacturer, are displayed in

  doi:10.5075/epfl-298799_978-2-9701614-0-0

Table *1*.

Table 1: Main properties of the raw-materials.

Property	Standard composite sandwich panel			Bio-based composite sandwich panel		
	Epoxy	Glass-fibre	XPS	Bio-epoxy	Basalt fibre	Cork
Tensile strength (MPa)	91.0	2 400	-	65.0	3 000	-
Tensile modulus (MPa)	3 200	73 000	-	2 790	89 000	-
Elongation at break (%)	8.4	-	-	5.9	-	-
Flexural strength (MPa)	134.0	-	-	107.0	-	-
Flexural modulus (MPa)	3 360	-	-	2 780	-	-
Compressive strength (MPa)	111.0	-	0.3	87.0	-	0.1
Density (g/cm³)	1.15	2.55	0.03	1.15	2.67	0.11
Glass transition temperature (°C)	80.0	-	-	85.0	-	-
Thermal conductivity (W/m.°C)	-	-	0.035	-	-	0.039

2.1.2. Manufacturing Procedures

Prior to sample manufacturing, fibres were conditioned in an oven at 100 °C to ensure moisture reduction and a better compatibility with epoxy-based resins. Composite laminates, were produced by vacuum infusion using 14 layers of 320 x 400 mm glass or basalt fabric, to achieve a thickness of around 2 mm. The epoxy resin system was mixed at room temperature (RT) and degassed for 15 minutes prior to use. Vacuum pressure was set at 500 mbar for filling, 800 mbar after filling for compaction and the laminates were cured for 16 h at RT. After demoulding, the laminates were subject to an additional thermal treatment (post-cure) for 16h at 60 °C. The MCS were prepared using the same conditions, with 4 layers of fibre fabric both on top and at the bottom of the core material (laminate with thickness of approximately 0.6 mm).

2.2. Test procedures

After post-curing stage, they were machined into different specimens to be further tested. The physical, thermal, and mechanical properties were assessed by several characterization techniques, including differential scanning calorimetry (DSC), dynamic mechanical analysis (DMA), in-plane shear stress, flexural and compression tests. The sustainability of developed solutions was also characterized by using CES EduPack eco audit toll.

2.2.1. Composite Laminates Characterization Methods

The standard ASTM D 792 (Method A) with an analytical scale (Radwag AS 220.R2) was used to determinate the laminates density. The fibre volume fraction was measured by burning the matrix at 625 °C in a muffle furnace (SNOL 3/1100) over 90 minutes, in accordance with ASTM D 3171- G. The DSC tests were performed to determine the thermal behaviour of the laminates and it were carried out following ISO 11357, using a TA Instruments (model Q20) with cooling system coupling RCS90. All experiments were conducted under an inert atmosphere (nitrogen at flow rate of 50 mL/min), to prevent oxidative degradation. The samples were heated from 50 to 150 °C, cooled down to 50 °C and heated again to 150 °C at 10 °C/min. The DMA tests were carried out through ISO 6721 by using Q800 manufactured from TA Instruments. The specimens were tested using a single cantilever fixture at 10 °C/min heating rate, from 35 to 150 °C, with an amplitude of 10 µm and frequency of 1 Hz. To determine the in-plane shear stress, the specimens were characterized based on ISO 14129. Before mechanical testing, the specimens were painted to measure the full-field strain over their surface using digital image correlation

  doi:10.5075/epfl-298799_978-2-9701614-0-0

(DIC). A universal testing machine (Instron 5900R) with hydraulic clamps and a 200 kN load cell were used. The samples were tested under tensile mode at a speed of 2 mm/min, and a distance between grips of 136 mm. DIC was used to record all experiments, allowing the visualization of cracks formation and propagation during mechanical solicitation.

2.2.2. Composite Sandwich Panels Characterization Methods

Edgewise compression test was performed in a Instron 5900R Universal Testing Machine, according to ASTM C 364/C 364-M, with a 100 kN load cell and at a speed of 2 mm/min. To analyse the sustainability of the two different developed sandwich panel solutions, it was used the CES EduPack eco audit tool (at material level, since the process to manufacture the sandwich panels is the same). This software allows the analysis of the energy consumption and carbon footprint of each sandwich panel for the whole life cycle, without exploring every parameter (19).

3. Results and Discussion

3.1. Composite Laminates

Data test results of the laminates corresponding to material volume fraction, DSC, DMA and in-plane shear stress tests are summarized in Table 2. The presented values represent the average results and correspondent standard deviations.

Table 2: Data test results of the developed laminates.

Test	Property	Standard	Bio-based
Density	**Composite density (g/cm³)**	1.71 ± 0.01	1.86 ± 0.01
Constituent Content	**Fibre volume (%)**	40.6 ± 0.4	47.6 ± 0.3
	Void volume (%)	0.5 ± 0.1	1.5 ± 0.6
DSC	**Glass transition temperature- 2nd heating ramp (°C)**	85.6 ± 1.1	97.9 ± 0.7
DMA	**Glass transition temperature (°C)**	90.7 ± 0.6	95.3 ± 0.1
	Storage modulus (GPa)	6.3 ± 0.2	8.5 ± 0.2
In-plane shear	**Maximum load (KN)**	6.3 ± 0.4	12.2 ± 0.6
	In-plane shear strength (MPa)	47.7 ± 2.3	108.4 ± 5.6
	Shear modulus (GPa)	1.74 ± 0.08	1.66 ± 0.07

The morphology of the developed composite solutions, evaluated using a stereo microscope, are depicted in Figure 1. The density of the bio-based laminate is slightly higher (+9 %) than the standard one, since BFs are denser than the glass fibres (Figure 1a and 1d) and considering that the produced basalt composite (BC) presented higher fibre volume fraction (20). Despite the slightly higher void content of the tested BC, the material showed superior in-plane shear strength and storage modulus behaviour (+126 % and +33 %, respectively), promoted by the intrinsic higher properties of basalt fabrics. Additional details presented Figure 1c denote that GC exhibited a local failure in the direction of the fibres (45°)(21). On the contrary, in the BC, the progression of loading leads to the matrix failure and the fibres rotates in a “scissoring” way (Figure 1f). In Figure 1g), it is visible the strong delamination that occurs in the BC, which was not so evidently observed in the GC. These results point out that if a better basalt fibre-matrix adhesion, through the surface modification of fibres using epoxysilane, and a lower void content is ensured, it would be possible to produce BC having even higher mechanical performance (20, 22).

  doi:10.5075/epfl-298799_978-2-9701614-0-0

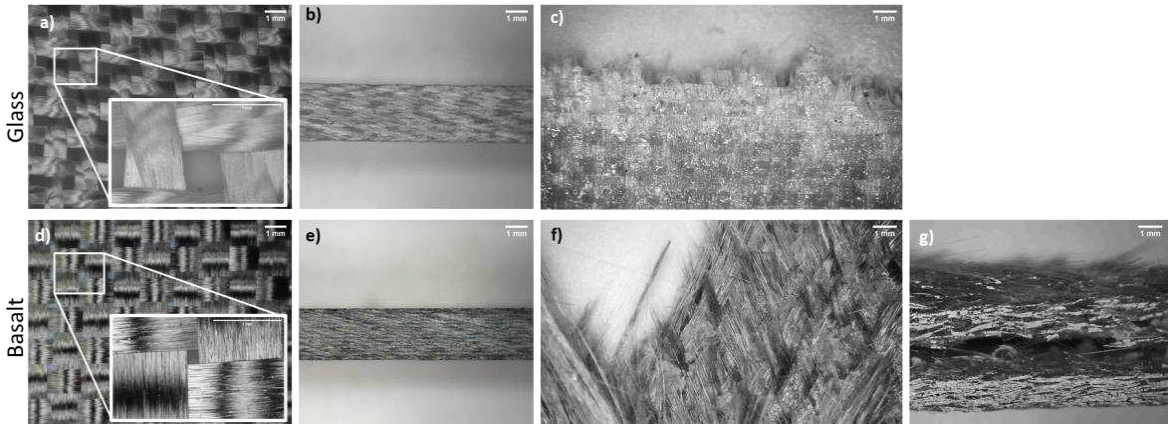

Figure 1: Fabrics and produced laminates details acquired using a stereo microscope: a) glass fabric, b) lateral view of the standard composite, c) fracture area of the in-plane shear strength of the standard composite, d) basalt fabric, e) lateral view of bio-based composite laminate, f) and g) fracture areas of the basalt laminate after in-plane shear strength test.

The viscoelastic properties of the developed composite laminate solutions were evaluated by DMA and the results are displayed in Figure 2 a).

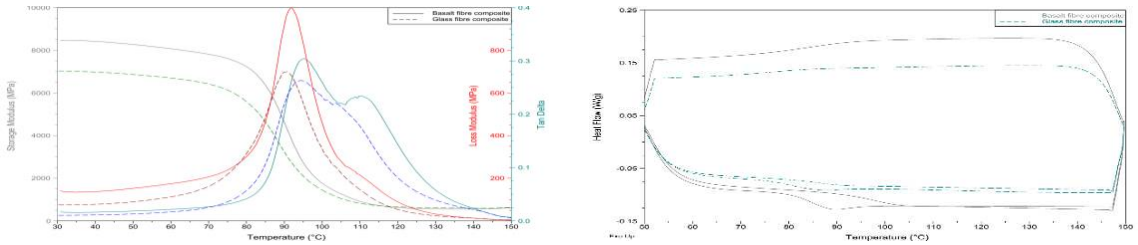

Figure 2: a) DMA and b) DSC test average results.

It is observed that BC solution present a slightly higher dynamic storage modulus (E') in comparison with glass composite (+ 35%), which is an important property to assess the load-bearing capacity. This result suggests that the eco-sustainable composite present an enhanced stiffness owing to the reinforcement effect imparted by basalt fibres. At temperatures higher than 70 °C, a steep drop in the E' value is observed, which is usually correlated to the maximum working temperature of the materials, and it is ascribed to the glass transition dynamics (T_g). The high values of loss modulus (E''), a measure of the energy dissipated as heat per deformation cycle, point out viscous behaviour, therefore remarkable damping properties, especially for the BC (23). The tan δ curve of the BC achieves a peak value of 95 °C, which corresponds to the T_g. However, it is also possible to observe a second peak value centred at 110 °C, which is an indicator that the curing reactions were not completed. A similar behaviour was observed in the GC, reaching a peak value of 91 °C (T_g), but the second peak was less pronounced than the bio-based composite, demonstrating that the cure was almost totally completed. The DSC experiments, showed in Figure 2 b), corroborate the findings attained by DMA. Laminates are not fully cured since in the second heating ramp in the DSC test these materials achieve higher T_g (up to 12 %). Although the procedure described in the supplier datasheet has been followed for the curing stage of composites, these results showed that is of paramount importance to control the material design and development, since the mechanical performance of GC and BC can be further improved.

3.2. Composite Sandwich Panels

Data test results of the sandwich panels corresponding to the compression test results and sustainability analysis are presented in Table 3. The presented values represent the average results and correspondent standard deviations.

Table 3: Data test results of the developed sandwich panels.

Test	Property	Standard	Bio-based
Compression	**Maximum load (KN)**	0.75 ± 0.13	0.7 ± 0.2
	Ultimate edgewise compressive strength (MPa)	5.77 ± 1.87	4.24 ± 1.5
	Detachment (%)	59.27 ± 22.82	53.21 ± 29.65
Sustainability (material)	**Energy (MJ)**	323	169
	CO_2 Footprint (kg)	15.3	8.69
	Cost (€)	11.4	26.7

It must be stand out that the manufacturing technology has a major influence on the properties of MCS, and in the scope of this research work it was used vacuum infusion process with success, allowing the reduction of operator work when compared with the other must common sandwich panels production processes, such as hand lamination (24). Since buckling behaviour of sandwich structures can be strongly affected by any imperfection, the edgewise compression tests in buckling mode were, therefore, considered to evaluate the adequacy of the manufacturing process for the used materials (25). In general, the behaviour of the specimens with facings was linear elastic until failure, which occurred by buckling of the facing because of local or complete debonding. Even though the developed bio-based MCS showed lower edgewise compressive performance, it also presented lower delamination (-10 %) than the standard one. The observed debonding in the standard panel was propagated along the laminate-core interface, while in the bio-based MCS occurred partial debonding and accompanied with some core cracking/failure, because the core surface was uneven, providing potentially a higher adhesion between the laminate and the core and making the debonding started at different points along the specimens (16, 17). This is possible to verify in the Figure 3, where the failure had developed at the interface in the standard MCS and in the core in the bio-based one.

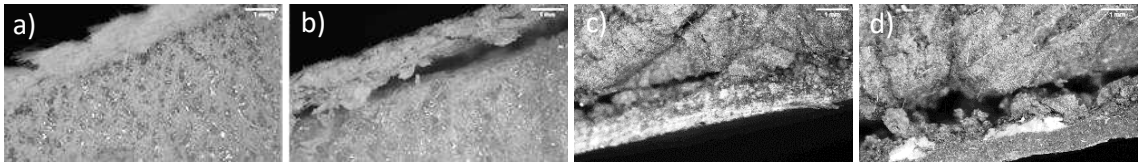

Figure 3: Interface areas of the MCS before and after the compression test: a) and b) standard MCS, and c) and d) bio-based MCS.

Since CES Edupack 2021 software does not consider XPS neither bio-epoxy matrices, it was considered similar materials, EPS (expanded polystyrene) and an epoxy matrix (the same of the standard solution), respectively. It is possible to observe that the highest impacts are found for the standard MCS because of its high-energy consumption and carbon dioxide (CO_2) footprint (-48 % and -43 %, respectively). Since bio-based MCS associated cost is significantly higher, its usage and spread in a wide range of construction applications may be not guaranteed.

  doi:10.5075/epfl-298799_978-2-9701614-0-0

4. Conclusions

In the search for a sustainable and alternative material to be used as a MCS for modular construction, tests and analyses were performed to study the behaviour of a bio-based solution. The following conclusions can be drawn from the investigation:

- BC with high fibre volume fraction (~50%) and improved mechanical properties were produced, but with greater void volume content than the standard one. The combination of the fibres with the matrix had led to slightly higher T_g (compared to the resin datasheets), yet the cure was not totally achieved in the two laminates.
- The results showed that the overall mechanical response of the sandwich panel strictly depend on the synergistic collaboration of the skins and core itself. Special attention should be paid in the use of basalt skins with cork core since the failure it is associated with cork shear rupture and not in the interface, leading to lower mechanical response.
- This research was limited to the utilization of the library on the CES Edupack 2021 software, which has a particularly important collection of materials information, but does not consider XPS neither bio epoxy matrices. In this sense, for future research, it is recommended to use a similar methodology or adapt this methodology to expand the spectrum of knowledge on sustainable solutions analysis.

Further research is still required to improve the BC to lower the void content and to enhance the cure through an improved manufacturing technique. This could increase the mechanical and thermal properties of the BC and allow the full exploitation of the promising properties of this bio-based laminate in the design of MCS. Due to the BFs mechanical properties, it is possible to reduce the quantity of this fabric to develop a composite with lower weight, which is an especially important characteristic for MCS. There for, additional studies are thus foreseen to explore and optimize bio-based MCS, so that they achieve higher performance without significant costs increase, to ensure widespread use of this developed sustainable solution.

Acknowledgements

This work was developed in the scope of “iclimabuilt” project, supported by the European Union under the HORIZON2020 Framework Programme for Research and Innovation under grant agreement no 952886. Acknowledgements are also due to Amorim Cork Insulation, for providing the cork foam.

5. References

1. De Marco A, Mangano G. Evolutionary trends in smart city initiatives. Sustainable Futures. 2021;3:100052.
2. Attia S, Al-Obaidy M, Baskar MJCB. Leadership of EU member States in building carbon footprint regulations and their role in promoting circular building design. 2021.
3. Dascalaki EG, Argiropoulou P, Balaras CA, Droutsa KG, Kontoyiannidis S. Analysis of the embodied energy of construction materials in the life cycle assessment of Hellenic residential buildings. Energy and Buildings. 2021;232:110651.
4. Häfliger I-F, John V, Passer A, Lasvaux S, Hoxha E, Saade MRM, et al. Buildings environmental impacts' sensitivity related to LCA modelling choices of construction materials. Journal of Cleaner Production. 2017;156:805-16.

  doi:10.5075/epfl-298799_978-2-9701614-0-0

5. Krasny E, Klarić S, Korjenić A. Analysis and comparison of environmental impacts and cost of bio-based house versus concrete house. Journal of Cleaner Production. 2017;161:968-76.
6. Samani P, Mendes A, Leal V, Miranda Guedes J, Correia N. A sustainability assessment of advanced materials for novel housing solutions. Building and Environment. 2015;92:182-91.
7. Samani P, Mendes A, Leal V, Correia N. Pre-fabricated, environmentally friendly and energy self-sufficient single-family house in Kenya. Journal of Cleaner Production. 2017;142:2100-13.
8. Ferdous W, Bai Y, Ngo TD, Manalo A, Mendis P. New advancements, challenges and opportunities of multi-storey modular buildings – A state-of-the-art review. Engineering Structures. 2019;183:883-93.
9. Lacey AW, Chen W, Hao H, Bi K. Structural response of modular buildings – An overview. Journal of Building Engineering. 2018;16:45-56.
10.Samani P, Gregory J, Leal V, Mendes A, Correia N. Lifecycle Cost Analysis of Prefabricated Composite and Masonry Buildings: Comparative Study. Journal of Architectural Engineering. 2018;24(1):05017012.
11.Smits J. Fiber-Reinforced Polymer Bridge Design in the Netherlands: Architectural Challenges toward Innovative, Sustainable, and Durable Bridges. Engineering. 2016;2(4):518-27.
12.Khan T, Acar V, Aydin MR, Hulagu B, Akbulut H, Seydibeyoglu MO. A review on recent advances in sandwich structures based on polyurethane foam cores. Polymer Composites. 2020;41(6):2355-61.
13.Manalo A, Aravinthan T, Fam A, Benmokrane B. State-of-the-art review on FRP sandwich systems for lightweight civil infrastructure. Journal of Composites for Construction. 2017;21(1):04016068.
14.Mohammadabadi M, Yadama V, Dolan JD. Evaluation of Wood Composite Sandwich Panels as a Promising Renewable Building Material. Materials (Basel). 2021;14(8):2083.
15.Jones D, Brischke C. Performance of bio-based building materials: Woodhead Publishing; 2017.
16.Torres JP, Hoto R, Andrés J, García-Manrique JA. Manufacture of Green-Composite Sandwich Structures with Basalt Fiber and Bioepoxy Resin. Advances in Materials Science and Engineering. 2013;2013:214506.
17.Scalici T, Fiore V, Valenza A. Experimental assessment of the shield-to-salt-fog properties of basalt and glass fiber reinforced composites in cork core sandwich panels applications. Composites Part B: Engineering. 2018;144:29-36.
18.Kamarian S, Song JI. Review of literature on eco-friendly sandwich structures made of non-wood cellulose fibers. Journal of Sandwich Structures & Materials. 2022:10996362211062372.
19.CES_Edupack. CES EduPack eco audit tool Granta Design Limited; 2021.
20.Elmahdy A, Verleysen P. Mechanical behavior of basalt and glass textile composites at high strain rates: A comparison. Polymer Testing. 2020;81:106224.
21.Liang Y, Wang H, Gu X. In-plane shear response of unidirectional fiber reinforced and fabric reinforced carbon/epoxy composites. Polymer Testing. 2013;32(3):594-601.
22.Plappert D, Ganzenmüller GC, May M, Beisel S. Mechanical Properties of a Unidirectional Basalt-Fiber/Epoxy Composite. Journal of Composites Science. 2020;4(3):101.
23.Karvanis K, Rusnáková S, Krejčí O, Žaludek M. Preparation, Thermal Analysis, and Mechanical Properties of Basalt Fiber/Epoxy Composites. Polymers. 2020;12(8):1785.
24.Kulpa M, Siwowski T. Stiffness and strength evaluation of a novel FRP sandwich panel for bridge redecking. Composites Part B: Engineering. 2019;167:207-20.
25.Najafi M, Darvizeh A, Ansari R. Characterization of moisture effects on novel agglomerated cork core sandwich composites with fiber metal laminate facesheets. Journal of Sandwich Structures & Materials. 2020;22(6):1709-42.

BUCKLING DRIVEN DISBOND GROWTH IN SANDWICH STRUCTURES EXPOSED TO CYCLIC LOADING

Christian Berggreen, Ignacio Vidal Pérez, Mehrtash Manouchehr

Department of Civil and Mechanical Engineering, Technical University of Denmark, Nils Koppels Allé, Building 404, DK-2800 Kongens Lyngby, Denmark, cbe@mek.dtu.dk

Abstract: *Composite sandwich structures in the aerospace and wind energy sectors are subjected to cyclic loading which can foster propagation of pre-existing defects or service induced damages such as face/core disbonds. These disbonds may end up reaching critical sizes, where local buckling of the face sheet is triggered, endangering the structure and deteriorating its aerodynamic efficiency. This work presents a numerical model combining finite element analysis and linear elastic fracture mechanics, aimed at predicting the propagation of face/core disbonds under fatigue loading. The model is compared with experiments performed on GFRP/PVC foam sandwich beams and panels with a pre-existing mid-span disbond exposed to four-point bending. A sensitivity study of the accuracy of the face/core interface fatigue fracture characterization parameters is also presented in order to assess the suitability of the linear elastic fracture mechanics approach in combination with experimental fracture mechanical input data generated using the DCB-UBM experimental fixture. The need for a standardized testing methodology for the fracture characterization of interface fatigue properties for sandwich composites is also discussed.*

Keywords: Sandwich; disbond/debond; PVC foam; LEFM; mixed-mode.

1. Introduction

The sandwich technology applied over the last decades has shown very good in-service behaviour in general and have accumulated millions of operation hours. In particular, good detectability of accidental impact damages was possible due to thin face sheet damage already visible at small impact energy levels. A considerable amount of sandwich construction is present throughout the world's commercial and military aviation fleet, in wind turbine blades, as well as in naval vessels, both in the form of primary and secondary structures. However, this type of composite structure is well known to exhibit several damage mechanisms that may potentially lead to component failure. There are many ways in which a sandwich structure can fail, e.g. core shear and compression, shear crimping, face sheet buckling, wrinkling and face/core disbonding. The disbond led separation of the face sheet from the core is one of the most severe damage modes, and it requires fracture mechanics based tools to assess as well as to predict the failure load or residual component fatigue life. Moreover, some in-service failures of several flight components have been attributed to disbond failure. An example includes the loss of an Airbus A310 rudder at altitude and many wind turbine blade failures, which can be traced back to disbond propagation in the trailing edge panels of the blade. Disbond growth can therefore lead to significant reduction in structural integrity and can have an influence on the operational safety of the aircraft or ship or the operational reliability of a wind turbine.

  doi:10.5075/epfl-298799_978-2-9701614-0-0

Numerical studies on fatigue crack propagation in sandwich composites are scarce in the open Literature. Moslemian *et al.* [1] - [2] introduced a numerical method, where several consecutive load cycles are modelled using the Finite Element Method along with a Linear Elastic Fracture Mechanics (LEFM) approach for predicting the crack propagation: the Crack Surface Displacement Extrapolation Method (CSDE) [3]. It is established that the crack propagation rate da/dN follows the Paris-Erdogan law $da/dN = C \cdot (\Delta G_{I/II})^m$ where $\Delta G_{I/II}$ is the variation of Strain Energy Release Rate (SERR) $G_{I/II}$ within the fatigue cycle. C and m are experimentally derived parameters that are known to be mode-mixity, $\psi_{I/II}$, dependent [4] - [5], i.e. $C = C(\psi_{I/II})$ and $m = m(\psi_{I/II})$. The SERR $G_{I/II}$ and the mode-mixity angle $\psi_{I/II}$ are considered as the couple of state variables that fully characterize the interface in terms of crack growth.

This makes Moslemian's method very dependent on how the fatigue characterization of the interface has been carried out. Both $G_{I/II}$ and $\psi_{I/II}$ must be kept constant during the fatigue characterization tests as the crack progresses in order to measure consistent crack propagation rates da/dN. At the time of writing this paper, no standard exists for the characterization of fatigue fracture properties in sandwich composites.

The Double Cantilever Beam with Uneven Bending Moments (DCB-UBM) was introduced for laminates by Sørensen *et al.* [9] and extended to sandwich composites by Lundsgaard-Larsen *et al.* [10] and has the advantage of keeping both the SERR and the mode-mixity phase angle constant as the crack propagates. The DCB-UBM has been used to characterize sandwich face/core interfaces under quasi-static loading for honeycomb cores, Saseendran *et al.* [11] [12] and foam cores, Berggreen *et al.* [13]. Successful benchmarks have been established with respect to analytical formulations [14]. Even though the experimental rig presented by Saseendran *et al.* is fatigue rated, experimental data using the rig to characterize sandwich interfaces under fatigue loading has not yet been presented.

The work presented at the conference utilizes the numeric method introduced by Moslemian *et al.* [2] in conjunction with fatigue experimental data generated using the DCB-UBM characterization test rig. The numerical method has been coded from the ground up using the commercial solver Abaqus and is applied to the case of a face/core disbond in GFRP/PVC foam sandwich beams and plates loaded in fatigue under four point bending, where the disbond propagation is buckling driven. The numerical results are compared to experiments and the suitability of the numerical approach in conjunction with DCB-UBM fatigue experimental data is discussed.

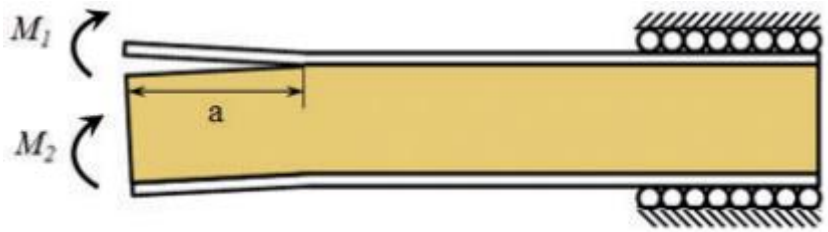

Figure 1. DCB-UBM specimen geometry, loads and boundary conditions. Source: [12]

2. Content

Numerical models combining finite element modelling and a state-of-the-art linear elastic fracture mechanics method was implemented and applied to predict the buckling driven fatigue propagation of a bi-material interface crack in both sandwich beams and panels under mixed-mode conditions at the disbond front. Both beams and panels were exposed to four-point bending loading with the disbond located between the inner loading points. The disbonds had a square through-width shape in the beams and a circular shape in the panels.

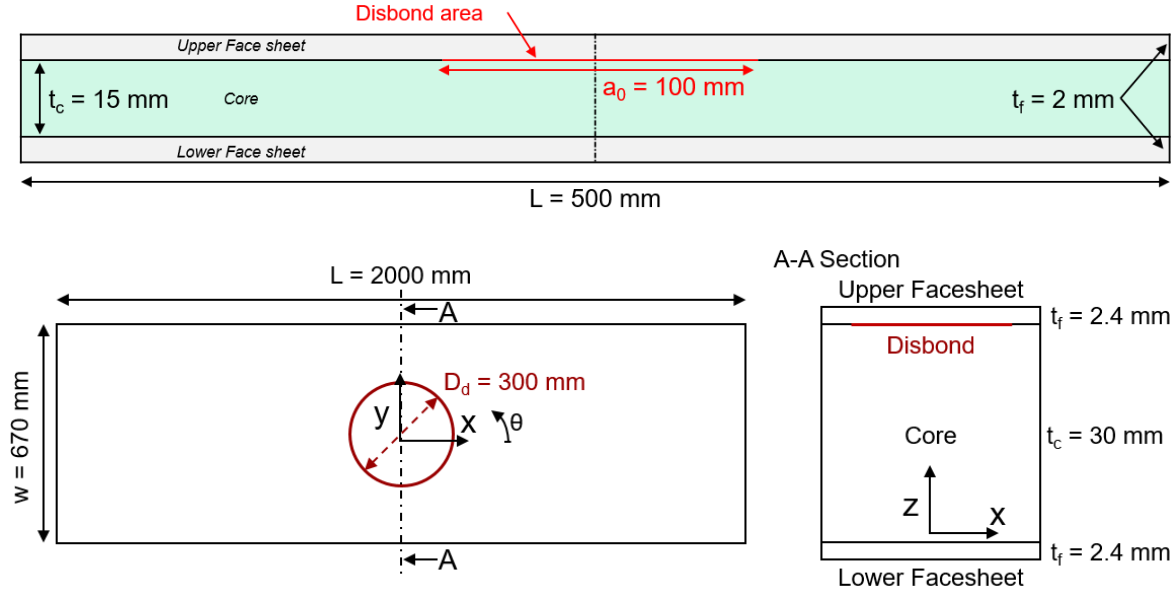

Figure 2. Beam (upper) and panel (lower) specimens containing disbonds between the upper face sheet and core.

The face/core interface fracture toughness and fatigue crack propagation rate were characterized experimentally using the Double Cantilever Beam with Unequal Bending Moments (DCB-UBM) test method. Fatigue propagation experiments were also carried out on sandwich beam and panel specimens with GFRP face sheets and PVC foam cores under four point bending in order to serve as reference for comparison with the numerical models. Correlation showed excellent results in the static realm and an overall over-prediction of the fatigue propagation rate for high levels of applied load, see Figure 2. The propagation trends were predicted fairly accurately. Some energy consumption phenomena, i.e. permanent deformation of the upper face sheet, were observed in the beam specimens which were not accounted for in the simulations.

A sensitivity study was presented to assess the accuracy of the fracture mechanics method. It was shown that the results are highly dependent on an accurate characterization of the fatigue fracture properties, primarily because of the mathematical form of the Paris-Erdogan law itself.

  doi:10.5075/epfl-298799_978-2-9701614-0-0

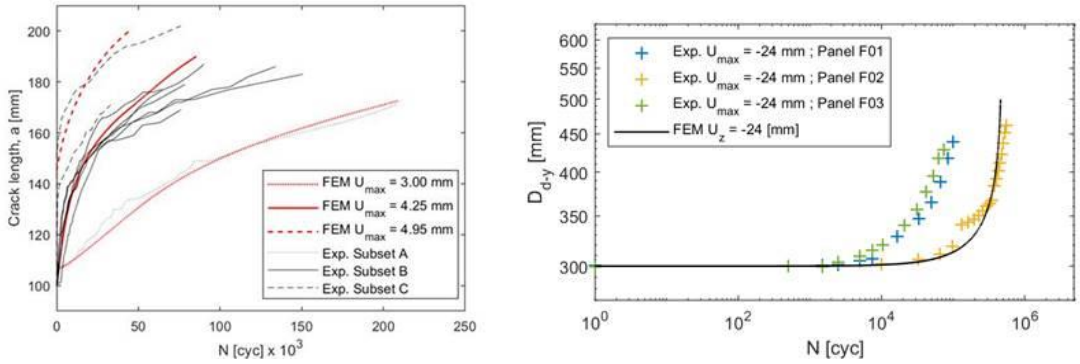

Figure 3. Crack length a vs number of cycles N: numerical vs experimental results for beam (left) and panel (right) specimens.

Acknowledgements

Support from both the Federal Aviation Administration (FAA), USA, and the Danish Ministry of Energy is gratefully acknowledged.

3. References

[1] R. Moslemian and C. Berggreen, “Interface fatigue crack propagation in sandwich X-joints-Part I: Experiments,” *J. Sandw. Struct. Mater.*, vol. 15, no. 4, pp. 429–450, 2013, doi: 10.1177/1099636213493372.

[2] R. Moslemian and C. Berggreen, “Interface fatigue crack propagation in sandwich X-joints-Part II: Finite element modeling,” 2013, doi: 10.1177/1099636213478289.

[3] C. Berggreen, B. C. Simonsen, and K. K. Borum, “Experimental and Numerical Study of Interface Crack Propagation in Foam-cored Sandwich Beams,” *J. Compos. Mater.*, vol. 41, no. 4, 2007, doi: 10.1177/0021998306065285.

[4] M. Manca, A. Quispitupa, C. Berggreen, and L. A. Carlsson, “Face/core debond fatigue crack growth characterization using the sandwich mixed mode bending specimen,” *Compos. Part A Appl. Sci. Manuf.*, vol. 43, no. 11, pp. 2120–2127, 2012, doi: 10.1016/j.compositesa.2012.07.001.

[5] L. A. Carlsson, “Face/core interface fracture characterization of mixed mode bending sandwich specimens,” doi: 10.1111/j.1460-2695.2011.01551.x.

[6] B. F. Sørensen *et al.*, “DCB-specimen loaded with uneven bending moments,” *Int J Fract*, vol. 141, pp. 163–176, 2006, doi: 10.1007/s10704-006-0071-x.

[7] C. Lundsgaard-Larsen, B. F. Sørensen, C. Berggreen, and R. C. Østergaard, “A modified DCB sandwich specimen for measuring mixed-mode cohesive laws,” *Eng. Fract. Mech.*, vol. 75, no. 8, pp. 2514–2530, 2008, doi: 10.1016/j.engfracmech.2007.07.020.

[8] V. Saseendran, C. Berggreen, and L. A. Carlsson, “Fracture Testing of Honeycomb Core Sandwich Composites Using the DCB-UBM Test,” in *Proceedings of the 20th*

International Conference on Composite Materials (ICCM20) Publication, 2015, Accessed: Jun. 09, 2020. [Online]. Available: http://www.mek.dtu.dk.

[9] V. Saseendran and C. Berggreen, "Mixed-mode fracture evaluation of aerospace grade honeycomb core sandwich specimens using the Double Cantilever Beam-Uneven Bending Moment test method," *J. Sandw. Struct. Mater.*, vol. 22, no. 4, pp. 991–1018, 2020, doi: 10.1177/1099636218777964.

[10] C. Berggreen, V. Saseendran, and L. A. Carlsson, "A modified DCB-UBM test method for interfacial fracture toughness characterization of sandwich composites," *Eng. Fract. Mech.*, vol. 203, pp. 208–223, Nov. 2018, doi: 10.1016/j.engfracmech.2018.06.036.

[11] G. A. Kardomateas, C. Berggreen, and L. A. Carlsson, "Energy-Release Rate and Mode Mixity of Face/Core Debonds in Sandwich Beams," *AIAA*, 2013, doi: 10.2514/1.J051765.

A MODIFIED SHEAR TORSION BENDING TEST FOR MODE-III FRACTURE TOUGHNESS MEASUREMENTS OF FACE/CORE INTERFACES IN SANDWICH COMPOSITES

Lujin Lin, Christian Berggreen, Brian Nyvang Legarth, Pietro Sabbadin

Department of Civil and Mechanical Engineering, Technical University of Denmark, Nils Koppels Allé, Building 404, Kongens Lyngby, Denmark – lujli@dtu.dk

Abstract: *This work presents mode-III fracture toughness measurement of sandwich composites by implementing the modified Shear-Torsion-Bending (STB) test fixture and method. Fracture mechanical analysis shows that the modified test fixture increases the mode-III distribution along the crack front. The specimens were made from GFRP face sheets and PVC foam core materials. The effect of the core density and core thickness was studied. The test results show that stable crack growth was observed using the modified STB method. The critical fracture loads were identified as input to a FE model with fracture mechanical analysis routines, to calculate the mode-III dominated fracture toughness along the crack front.*

Keywords: Mode-III fracture toughness; sandwich structures; modified STB; CSDE method.

1. Introduction

Mode-III fracture toughness measurements have been widely studied [1-4]. However, the literature contains little information on mode-III fracture characterization testing for sandwich composites. In the Cracked Sandwich Plate Twist (CSPT) [5] and Sandwich Tearing Beam (TB) [6] specimens, the mode-III loading was applied to the face sheet reinforced by a steel plate. However, the above methods failed to achieve stable crack propagation. Most recently, the Shear-Torsion-Bending (STB) [7][8] test fixture and method have been successfully employed for interlaminar mode-III fracture characterization of the laminated composites. Closed-form data reduction expressions have also been derived and applied with success. However, the original STB test method initially proved insufficient to measure the mode-III fracture toughnesses for the face sheet and core interface in a sandwich specimen as crack kinking and shear cracks in the core (see Fig. 1) made measurements of the mode-III face/core interface fracture toughness impossible. However, if modified, the STB method is still promising for mode III fracture toughness measurement for sandwich composites.

2. Content

This work presents a modified version of the STB test fixture, specially developed for testing sandwich specimens. Compared to the traditional STB test fixture, the free end of the specimen is now restrained between two support rollers, restraining the twisting deformation of the specimen, due to the torsional moments described above, see Fig. 2. The modified STB test

  doi:10.5075/epfl-298799_978-2-9701614-0-0

fixture was applied for mode-III characterization of sandwich specimens with E-glass/epoxy face sheets and a Divinycell H45, H100, and H160 PVC foam core respectively from DIAB. Two core thicknesses were considered as well. Moreover, to obtain the crack propagation, a 3D DIC system was used to monitor the out-of-plane displacement field near the crack tip. Additionally, two cameras were implemented to study the uneven crack front [9]. Experimental results show that a stable crack growth along the face/core interface was observed without kinking or shear cracking in the core, facilitating a reliable measurement of the mode-III fracture toughness in sandwich specimens. The reduction of the measured data was performed using a numerically computed fracture toughness based on a three-dimensional finite element model in conjunction with the Crack Surface Displacement Extrapolation (CSDE) mode-mixity method [10][11].

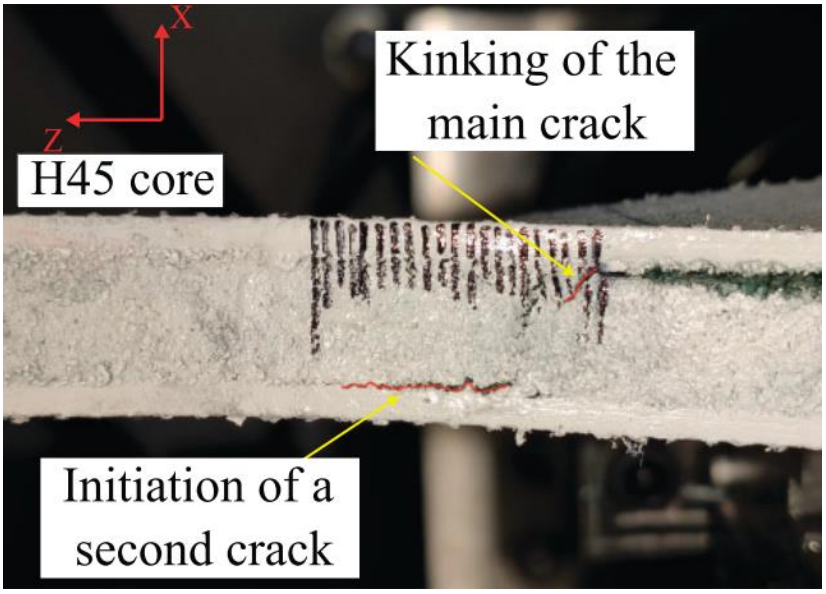

Figure 1. Crack kinking into the core [8].

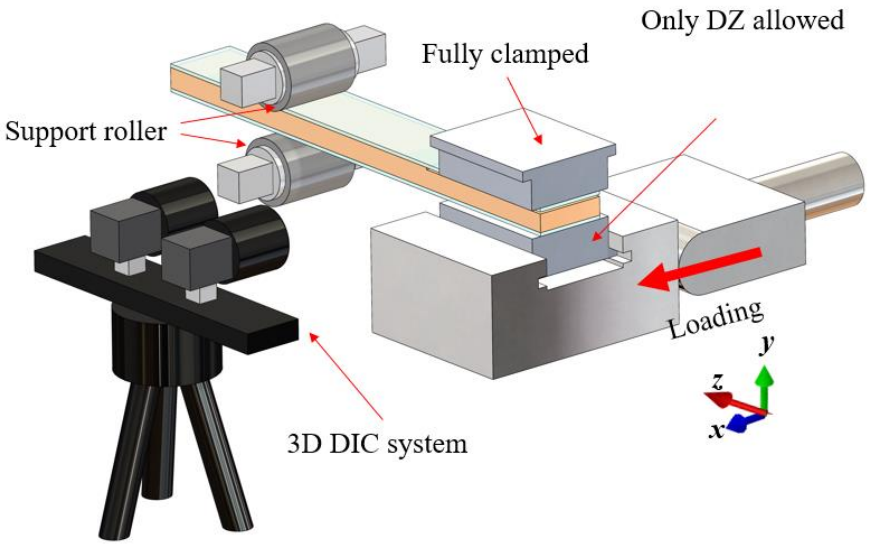

Figure 2. Modified STB test fixture with support rollers and setup.

  doi:10.5075/epfl-298799_978-2-9701614-0-0

Acknowledgements

Support from the US Navy – Office of Naval Research (ONR) grants N00014-16-1-2977 and N62909-21-1-2048 supporting Pietro Sabbadin, and the China Scholarship Council (CSC) grant 202006020039 supporting Lijin Lin, are gratefully acknowledged.

References

1. Donaldson, S. L. (1988). Mode III interlaminar fracture characterization of composite materials. Composites Science and Technology, 32(3), 225–249.
2. Lee, S. M. (1993). Edge crack torsion method for mode III delamination fracture testing. Journal of Composites Technology and Research, 15(3), 193–201.
3. Ratcliffe, J. G. (2004). Characterization of the Edge Crack Torsion (ECT) Test for Mode III Fracture Toughness Measurement of Laminated Composites. Nasa Technical Memorandum, (September).
4. Pereira, A. B., De Morais, A. B., & De Moura, M. F. S. F. (2011). Design and analysis of a new six-point edge crack torsion (6ECT) specimen for mode III interlaminar fracture characterisation. Composites Part A: Applied Science and Manufacturing, 42(2), 131–139.
5. Hernández-Pérez, A., Avilés, F., & Carlsson, L. A. (2013). Evaluation of the plate twist test to characterize mode III fracture of sandwich panels with a face/core interface crack. Engineering Fracture Mechanics, 104, 41–55.
6. Rodríguez-González, J. A., May-Pat, A., & Avilés, F. (2014). A beam specimen to measure the face/core fracture toughness of sandwich materials under a tearing loading mode. International Journal of Mechanical Sciences, 79, 84–94.
7. Sabbadin, P., Massabó, R., & Berggreen, C. (2020). An improved analysis of a STB specimen for fracture characterization of laminates and foam-cored sandwich composites under mode III loads. Engineering Fracture Mechanics, 236(June), 107198.
8. Sabbadin, P., Berggreen, C., Legarth, B. N., & Lin, L. (2021). A novel test fixture for mode III fracture characterization of monolithic laminates and composite sandwich specimens. Journal of Composite Materials.
9. Guillén-Rujano, R., Ku-Herrera, J. J., & Hernández-Pérez, A. (2021). Mode III Fracture Toughness Measurement Using the Transverse Shear Cracked Plate Specimen. Experimental Mechanics, (0123456789).
10. Suo, Z., & Hutchinson, J. W. (1990). Interface crack between two elastic layers. International Journal of Fracture, 43(1), 1–18.
11. Berggreen, C., Simonsen, B. C., & Borum, K. K. (2007). Experimental and numerical study of interface crack propagation in foam-cored sandwich beams. Journal of Composite Materials, 41(4), 493–520.

  doi:10.5075/epfl-298799_978-2-9701614-0-0

SHAPE AND SIZE OPTIMIZATION OF ADDITIVE MANUFACTURED LATTICE CORES WITH AN EVOLUTIONARY-BASED APPROACH FOR HIGH-PERFORMANCE SANDWICH PANELS

Athina, Kontopoulou[a], Riccardo, Manno[a], Bing, Zhang[a], Fabrizio, Scarpa[a], Giuliano, Allegri[a]*

a: Bristol Composites Institute (BCI), University of Bristol, Queens Building, BS8 1TR - athina.kontopoulou@bristol.ac.uk

Abstract: *The evolution of additive manufacturing techniques has vastly increased the design space of lattice structures, making it possible to create stiffer and lighter ones. This work deals with the evolutionary shape and size optimization of lattice structures, using a genetic algorithm (GA). A modelling framework involving finite element (FE) homogenization of representative volume elements (RVE) under strain-controlled Periodic Boundary Conditions (PBCs) is employed. Several designs of lattice structures were optimized with this approach. These designs were obtained superimposing basic lattice unit cells, such as body-centred cubic (BCC), face-centred cubic (FCC), simple cubic (SC) and octahedral, considering additive manufacturing constraints. The optimization objective was the maximisation of the specific compressive stiffness of the lattices, limiting the maximum relative density to 0.30. The optimized led to a five-fold increase of the specific compressive stiffness.*

Keywords: Lattice structures; Homogenization; Finite Element Method; Evolutionary Optimization.

1. Introduction

Replacing monolithic structural components with sandwich constructions reduces mass. Hence, the adoption of lightweight sandwich structures represents a primary means for cutting fossil fuel consumption in a wide range of engineering sectors. The core of sandwich structures plays a crucial role in determining the resulting mechanical performance, since the flexural stiffness can be increased with a minimum weight penalty [1]. In recent years, lattice structures have been extensively studied for application in sandwich panel cores in the transportation industry, but also in biomedical engineering [2]. This is because lattice cores offer unique specific mechanical properties, especially under compression. Lattice cores are periodic structures, characterized by the regular repetition of a minimum unit cell (or representative volume element - RVE). Thus, the ensuing mechanical properties primarily depend on the configuration and connectivity of the strut elements inside the RVE.

Nowadays, the development of additive manufacturing techniques has widened the design space and made the construction of lattice structures more time- and cost-efficient compared to the traditional methods, i.e. investment casting. Several studies have explored the influence of RVE node connectivity and geometry on the mechanical properties of lattice structures, especially those having BCC geometry. Abdulhadi et al. [3] investigated the effect of the angle between BCC struts and found that increasing it to 50° resulted in the highest specific compressive stiffness. Osman et al. [4] demonstrated that a higher angle in the RVE of octet-truss lattices significantly enhanced the specific energy absorption and the dimensional accuracy of the 3d assemblies printed via selective laser melting (SLM). Zhou et al. [5] also highlighted the

  doi:10.5075/epfl-298799_978-2-9701614-0-0 published under CC BY-NC 4.0 license

importance of self-supporting lattice structures with overhang angle larger than 35° angle, thus lattices with unit cell of larger height, lacking horizontal struts to improve manufacturability based on 3D printing capabilities. They also showed that bending-dominated behaviour could be changed to stretching-dominated by increasing the rotational symmetry and hierarchical level, and hence, the node connectivity of a lattice structure. Similarly, Chang et al. [6] enhanced the compressive properties of basic lattice structures, i.e. SC, BCC and regular tetrahedron cubic (RTC), by Boolean merging those into combined lattice designs with increased connectivity. However, in the literature systematic approach to optimise lattice designs with respect to their 3d printing manufacturability is lacking.

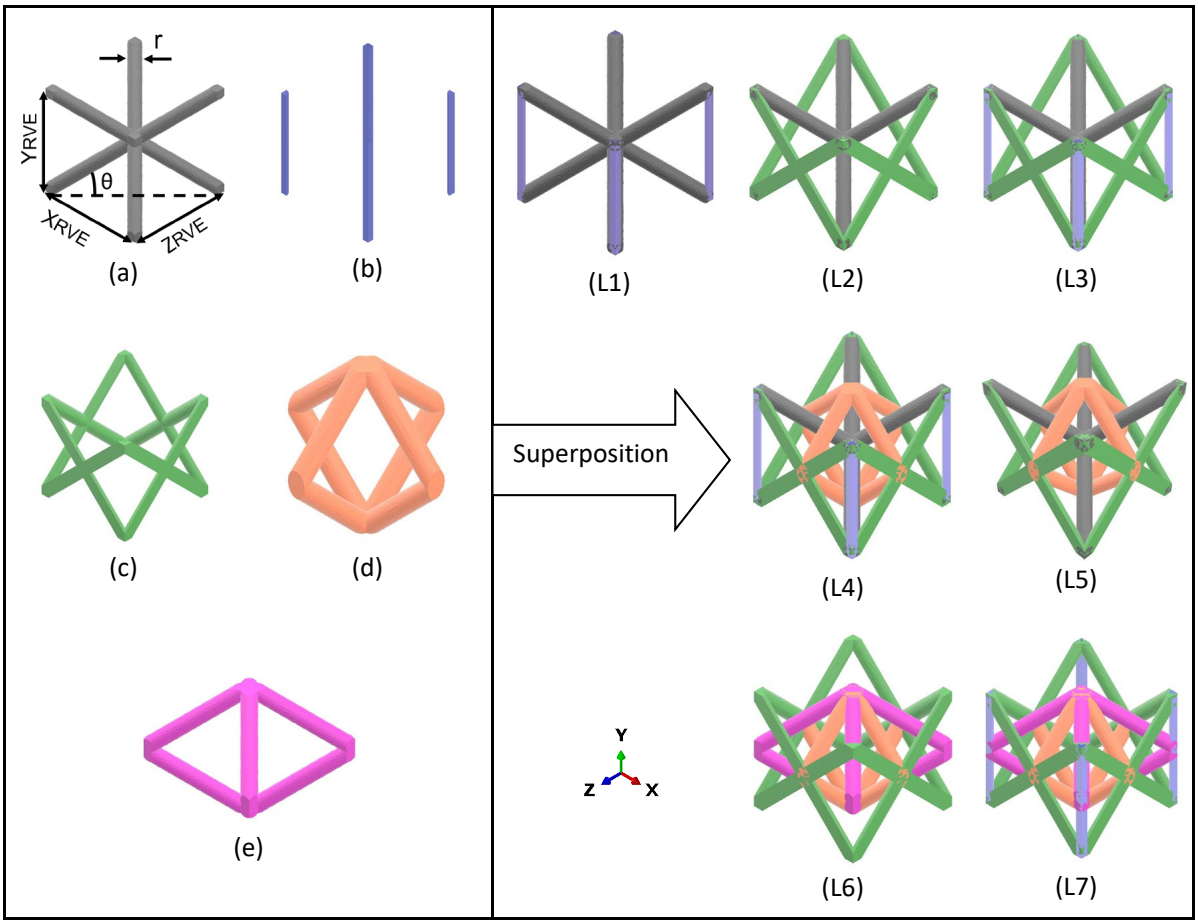

Figure 1. Basic (a-e) and superimposed (L1-L7) lattice designs.

In this work, we investigate an evolutionary finite element (FE) based optimization approach for the specific compressive stiffness of superimposed lattice designs. More in detail, a genetic algorithm is used to create random combinations of geometric variables describing lattice core RVEs, which are then virtually tested via FE simulation. This approach allows a thorough investigation of the design space by adjusting the RVE topology and geometrical configuration in an automated fashion. Specifically, here, we explore the effect of the angle and the radius of the lattice struts, as well as the RVE topology (i.e. the connectivity of the struts). We investigate seven superimposed lattice designs (L1-L7 in Figure 1) which have resulted by the merging of five basic lattice geometries. The basic configurations which were considered here, include: BCC (a), cubic lattice lacking horizontal bars (b), FCC (c), octahedron (d), and octahedron rotated by 45° (e) as shown in Figure 1. As can be seen in the figure, the superimposed lattice designs are illustrated by different colours according to the basic designs involved, specifically: (L1):(a)+(b),

  doi:10.5075/epfl-298799_978-2-9701614-0-0

(L2):(a)+(c), (L3):(a)+(b)+(c), (L4):(a)+(b)+(c)+(d), (L5):(a)+(c)+(d), (L6):(c)+(d)+(e), (L7):(b)+(c)+(d)+(e).

2. Materials and methods

2.1 Modelling framework

Periodic materials and structures can be modelled employing only one RVE to reduce significantly the computational time. To accurately compute the effective elastic properties of the RVE lattice designs, a FE-based volumetric homogenization technique is used together with the application of strain-controlled Periodic Boundary Conditions (PBCs). PBCs provide equal strain field to the RVE boundaries ($\partial\Omega_{\mathrm{RVE}}$), as required for the computation of the homogenised elastic properties, pairing the mesh nodes of the opposite boundaries through linear constrain equations as defined in Eq.(1), i.e.[7]:

$$u_x^+ - u_x^- = \varepsilon_{ij}^0 (x^+ - x^-) \; \forall \; x \in \; \partial\Omega_{RVE} \tag{1}$$

where x^+, x^- are the coordinates of opposite paired nodes, ε_{ij}^0 is the applied strain and u is the resulting displacement on $\partial\Omega_{RVE}$. In order to populate the stiffness matrix and calculate the elastic moduli through the homogenization process of each RVE design, six static analyses are imposed to the model. Each of these static analyses corresponds to one column of the stiffness matrix, including three uniaxial tensile strains and three simple shear strains, as described in the Eq.(2) in ref. [8]:

$$\mathrm{C}_{\alpha\beta} = \overline{\sigma}_{\alpha} = \frac{1}{\mathrm{V}_{\mathrm{RVE}}} \int_{\mathrm{V}_{\mathrm{EFF}}} \sigma_{\alpha} \; \mathrm{dV} \approx \; \frac{1}{\mathrm{V}_{\mathrm{RVE}}} \sum_{\mathrm{el}=1}^{\mathrm{N}} \sigma_{\alpha}^{el} V^{el} \; \text{when} \; \overline{\varepsilon}_{\beta} \; = \; 1. \tag{2}$$

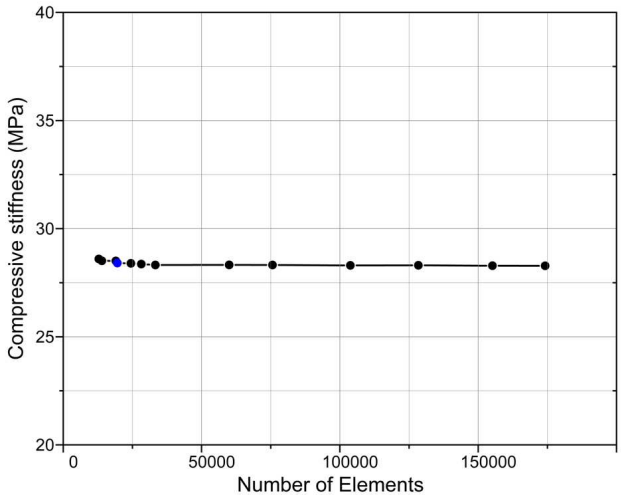

Figure 2. Mesh convergence study of L4 model.

3D solid FE models of several lattice topologies are created using the ABAQUS© software via a dedicated pre-processor written in Python, which translates the genomes generated by the genetic algorithm into solid FE models. For these models, solid quadratic tetrahedral (C3D10) elements were utilised with a meshing size of 0.25 mm. This mesh size was determined after observing less than 1% variation of the compressive stiffness with a total number of elements of 19,568 and compressive stiffness of 28.4 MPa for the L4 configuration with all radii equal to 0.3 mm and an RVE height of 8.0 mm (see the blue point in Figure 2). The material properties

  doi:10.5075/epfl-298799_978-2-9701614-0-0

used in all FE models were those of polylactic acid (PLA) 3d printing filament, i.e. Young's modulus of 1001 MPa, Poisson's ratio of 0.30 [9], and density of 1.24 g/cm^3 [10].

2.2 Evolutionary optimization algorithm

For the optimization of the RVE models, the genetic algorithm implementation available in MATLAB was employed, with the objective to maximise the compressive specific stiffness of the lattice designs. The lower and upper bounds of the design variables are given in Table 1. The height of the RVE (Y_{RVE}) was determined in order for the angle θ to range between 35° and 50°, in order to ensure a sufficient dimensional accuracy during 3D printing, as it is shown in Figure 1(a). The lower bound of the RVE height (Y_{RVE}) corresponds to angle θ=35° and the upper bound to θ=51.8°. All the struts radii for basic geometries can be optimised independently in each superimposed lattice, considering a range of 0.3mm-0.7mm. Moreover, the optimized lattice designs are required to not exceed the maximum relative density (ρ_{rel}) constraint, which was set to 0.3, otherwise the resulting genomes are assigned a low fitness value. The relative density of the lattice structures is defined as the ratio of lattice volume (V_{lat}) by the volume of the RVE (V_{RVE}):

$$\rho_{rel} = \frac{\rho^*}{\rho_s} = \frac{V_{lat}}{V_{RVE}} \quad (3)$$

Table 1: Lower and upper bounds of all design variables.

Design variables	Type	Lower bound	Upper bound
Y_{RVE}	Continuous	5.0	9.0
r_a	Continuous	0.3	0.7
r_b	Continuous	0.3	0.7
r_c	Continuous	0.3	0.7
r_d	Continuous	0.3	0.7
r_e	Continuous	0.3	0.7

2.3 Analytical validation of the modelling framework

To validate our homogenization FE modelling framework explained above, a BCC lattice structure with a constant RVE length and height of 5mm is considered. The analytical prediction of BCC stiffness based on the Euler-Bernoulli assumptions is given by solving Eq.(4) below from ref. [11]:

$$E^*_{BCC_{Euler}} = \rho_{rel} \frac{E_s}{1+2(l/2r)^2} = \sqrt{3}\,\pi \left(\frac{2r}{l}\right)^2 \times \frac{E_s}{1+2(l/2r)^2} \quad (4)$$

where E_s is the stiffness of the solid material and r is the radius of the BCC struts and l is the length of the RVE when considering an isotropic unit cell with $X_{RVE} = Y_{RVE} = Z_{RVE}$.

The theoretical approach of BCC stiffness according to Timoshenko beam theory is predicted by Eq.(5) in ref. [12]:

$$E^*_{BCC_{Timoshenko}} = \frac{4\sqrt{3}E_S}{\left[\frac{l^2}{\pi r^2}+\frac{l^4}{2\pi r^4}+\frac{1.000352l^2(1+\nu_S)\sqrt{2}}{r^2}\right]} \quad (5)$$

where ν_S is the material's Poisson's ratio.

The length of the struts, which is necessary for the calculation of the aspect ratio (r/L) of a lattice structure is given by solving Eq.(6).

$$L = \sqrt{X^2_{RVE} + Y^2_{RVE} + Z^2_{RVE}} \quad (6)$$

In Figure 3, the analytical predictions of the elastic modulus are compared against the finite element analysis results. The numerical results are in good agreement with the theoretical predictions for an aspect ratio smaller than 0.1. As the aspect ratio of the struts is increased, beam theories become less accurate, as it should be expected. Moreover, the beam-based analytical stiffness values in Eq.(4) and Eq.(5) cannot take into account the effect of the finite compliance at vertices.

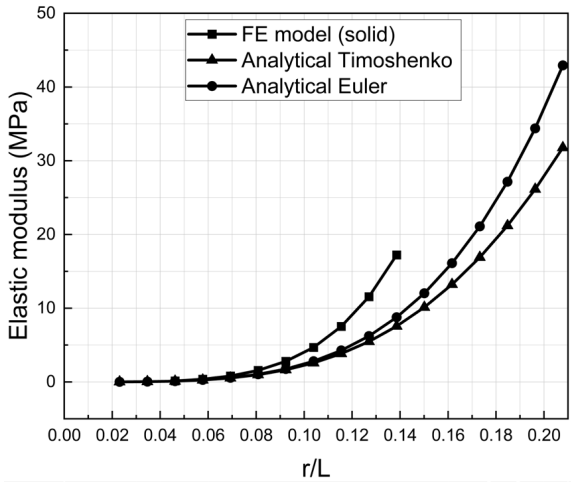

Figure 3. Comparison of theoretical and numerical results of elastic modulus for a wide range of aspect ratios r/L.

3. Results and Discussion

The optimized geometric variables for the seven superpositioned lattice structures (L1-L7) that resulted from the optimization procedure discussed above are presented in Table 2. The RVE height (Y_{RVE}) reached the specified upper bound in all lattice designs following the optimization. This is because the increased Y_{RVE} offers higher compressive stiffness, and in parallel increases the total volume of the RVE, thus enhancing the specific compressive stiffness of the overall lattice structure. Moreover, the higher height of the RVE makes the manufacturing of the lattice structures via additive techniques easier, increasing the overhang angle. Table 2 shows that the orientations of some struts have a stronger effect on the specific stiffness, thus their optimized radius is consistently larger than for others. For instance, the optimized radius of cubic struts (r_b) is found very close to the assigned upper bound (see Table 1), since the reinforcement parallel to the loading direction provides the greatest support to the structure. The radii of the FCC inclined struts (r_c) are the second most consistently increased. This is likely due to the increased connectivity that they offer to the overall super-positioned structure. The rest of the inclined

struts orientations (r_a, r_d, r_e) used in this work seem to provide negligible support to the overall lattice structure, hence their optimized radii resulted to be lower than the prescribed mid-range value between the bounds, as can be seen in Table 2.

All optimized lattice designs have a relative density lower than 0.3, satisfying the genetic algorithm constraint. The optimized lattice meshed RVE designs (L1 opt-L7 opt) are illustrated in Figure 4. It is evident the difference between the radii of the super-imposed basic structures, resulting in very distinct shapes and sizes compared to the initial super-imposed lattice structures in Figure 4.

Table 2: The optimized geometric variables.

Lattice Designs	Y_{RVE} (mm)	r_a (mm)	r_b (mm)	r_c (mm)	r_d (mm)	r_e (mm)	$\boldsymbol{\rho_{rel}}$
L1 opt	8.97	0.32	0.67	-	-	-	0.110
L2 opt	8.86	0.48	-	0.66	-	-	0.290
L3 opt	8.86	0.35	0.70	0.66	-	-	0.280
L4 opt	8.83	0.32	0.67	0.50	0.35	-	0.260
L5 opt	8.88	0.41	-	0.58	0.41	-	0.297
L6 opt	8.88	-	-	0.63	0.36	0.35	0.298
L7 opt	8.86	-	0.68	0.30	0.50	0.44	0.280

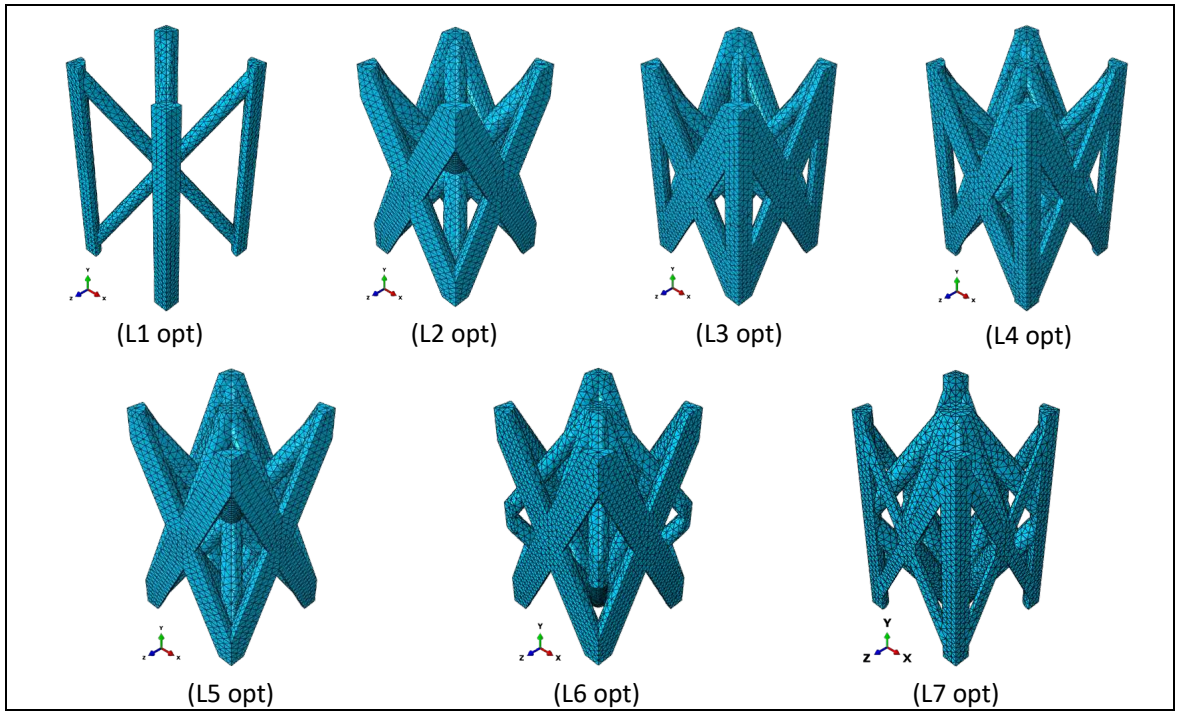

Figure 4. The lattice design models based on the optimized geometric variables.

In Figure 5 the specific compressive stiffnesses of the super-positioned lattice designs before optimization (L1-L7, in Figure 1) are compared against the ones after the evolutionary optimization (L1 opt-L7 opt, in Figure 4). All optimized lattice structures have increased specific

compressive stiffness, up to five times compared to the values before the optimization. The enhancements of specific compressive stiffness are: 226.7% for L1 opt, 534.6% for L2 opt, 241.4% for L3 opt, 227.9% for L4 opt, 374.0% for L5 opt, 389.6% for L6 opt and 219.8% for L7 opt. As mentioned before, the reinforcement parallel to the loading direction clearly dominates the specific stiffness, thus the lattice designs (L1 opt, L3 opt, L4 opt, L7 opt) which include cubic struts result in having the highest specific compressive stiffnesses compared to the other architectures.

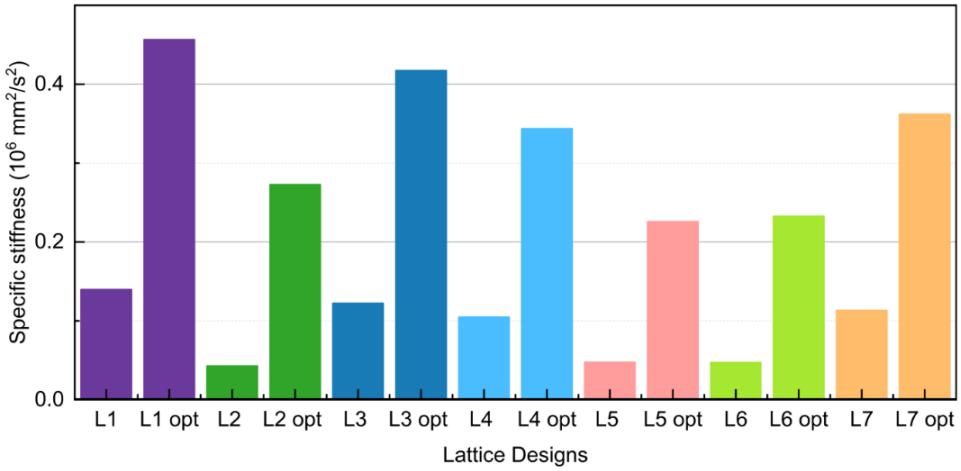

Figure 5. The specific compressive stiffness of lattice designs compared before (L1-L7) and after (L1 opt-L7 opt) the optimization.

4. Conclusions

Seven superimposed lattice unit cell designs have been optimized by considering the manufacturing constraints. The effect of different struts orientation was investigated on the specific compressive stiffness by optimising them individually. The following conclusions have been identified from this work:

- The increased height (Y_{RVE}) of the RVE results in a larger specific compressive stiffness and improves the dimensional accuracy of layer-by-layer additive manufacturing.
- All optimized lattice designs demonstrated enhanced compressive specific stiffness (up to five times compared to the baseline).
- The Cubic (b) and FCC (c) struts in the superimposed designs provide better specific stiffness to BCC (a) and octahedron (d) struts. Hence, Cubic and FCC struts typically have larger radii.

Acknowledgements

This work was supported by the Engineering and Physical Sciences Research Council through the Centre for Doctoral Training in Composites Science, Engineering and Manufacturing (Grant number EP/S021728/1).

5. References

1. Gibson LJ, Ashby MF. Cellular Solids. Cambridge University Press; 1997.

2. Mines R. Metallic Microlattice Structures. Springer International Publishing; 2019.
3. Abdulhadi HS, Mian A. Effect of strut length and orientation on elastic mechanical response of modified body-centered cubic lattice structures. Proc Inst Mech Eng Part L J Mater Des Appl. 2019;233(11):2219–33.
4. Osman MM, Shazly M, El-Danaf EA, Jamshidi P, Attallah MM. Compressive behavior of stretched and composite microlattice metamaterial for energy absorption applications. Compos Part B Eng. 2020;184(December 2019):107715.
5. Zhou H, Cao X, Li C, Zhang X, Fan H, Lei H, et al. Design of self-supporting lattices for additive manufacturing. J Mech Phys Solids. 2021;148:104298.
6. Feng J, Liu B, Lin Z, Fu J. Isotropic octet-truss lattice structure design and anisotropy control strategies for implant application. Mater Des. 2021;203.
7. Melro AR, Manno R. Microscale representative volume element: generation and statistical characterization. Multi-Scale Contin Mech Model Fibre-Reinforced Polym Compos. 2021;31–54.
8. Barbero EJ. Finite Element Analysis of Composite Materials Using Abaqus. 2013. 444 p.
9. Ye G, Bi H, Li Z, Hu Y. Compression performances and failure modes of 3D printed pyramidal lattice truss composite structures. Compos Commun. 2021;24:100615.
10. Verbatim. PLA Filament. 2018;335.
11. Ushijima K, Cantwell WJ, Mines RAW, Tsopanos S, Smith M. An investigation into the compressive properties of stainless steel micro-lattice structures. J Sandw Struct Mater. 2011;13:303–29.
12. Ptochos E, Labeas G. Elastic modulus and Poisson's ratio determination of micro-lattice cellular structures by analytical, numerical and homogenisation methods. J Sandw Struct Mater. 2012;14(5):597–626.

  doi:10.5075/epfl-298799_978-2-9701614-0-0

CLASSIFICATION AND DEVELOPMENT OF NEW COMPONENT TESTS FOR AIRCRAFT CABIN INTERIOR

Tobias S. Hartwich[a], Johann Schwenke[a], Lukas Schwan[a], Dieter Krause[a]

a: Institute of Product Development and Mechanical Engineering Design, Hamburg University of Technology – tobias.hartwich@tuhh.de

Abstract: *Honeycomb sandwich structures are widely used for cabin interior components in passenger aircrafts. The load introduction into the sandwich structure proves to be particularly critical. However, the verification takes place based on non-standardized tests abstracted from the application so that influences caused by boundary conditions and multiple load introduction points cannot be investigated. Moreover, these tests also do not allow comparisons of different designs. The variety of different test setups on component level has made the comparability of published results more difficult. This paper summarizes the state of the art of existing component tests. Based on that and using the example of an aircraft cabin partition, the existing test set-ups are checked for their suitability to cover all given load cases. New test setups with extended boundary conditions and several load introduction points are developed. For one test setup, test results are shown and compared to a conventional component test.*

Keywords: Sandwich; Component Test; Insert; Test Design; Cabin Interior

1. Introduction

Due to their good weight-specific material properties, honeycomb sandwich structures are widely used for cabin interior parts in commercial passenger aircrafts [1]. However, the load introduction into these sandwich structures often proves to be critical. The precise design of the load introduction points, which are conventionally realized by inserts for sandwich structures, is crucial for the safety of aircraft cabin components. Nevertheless, the verification takes place based on non-standardized tests abstracted from the application. Although various quasi-static component tests are suggested in the Insert Design Handbook [2], in the literature these tests have been performed differently and additionally, new component test setups have been developed [3–5]. In recent years this variety of different test setups on component level has made the comparability of published results more difficult. As shown in [6, 7] the consideration of the existing boundary conditions of the application has fundamental relevance for the quality of a design. This is usually not the case for the abstracted tests.

For the design of aircraft cabin monuments the Building Block Approach is mostly utilized [8]. Over different levels of complexity of a product, tests and analyses are carried out, starting from the material level via the component level to the complete product, in order to provide verification. However, many of the available test setups do not allow the evaluation of the performance of other designs at the component level. At the moment, only full-size tests are suitable for comparing new designs, such as additive manufactured designs using the direct energy deposition process [9], with conventional sandwich designs. Therefore, there is a need for design independent component tests.

  doi:10.5075/epfl-298799_978-2-9701614-0-0

In this paper, the differences between the individual component tests are shown and compared. Based on that, the suitability of the individual tests is evaluated using the application example of an aircraft cabin partition. Concepts for more application-oriented and independent component tests are then developed. Finally, one of these developed tests is conducted and the results are compared with those of a conventional component test.

2. Analyses of the existing component tests

The Insert Design Handbook [2] suggests a number of different tests for component verification. A selection of the common tests is shown in Figure 1. These are supplemented by bending and shear tests, which do not investigate the strength of an insert joint. These various test setups are typically used to conduct the component-level verification of aircraft cabin monuments.

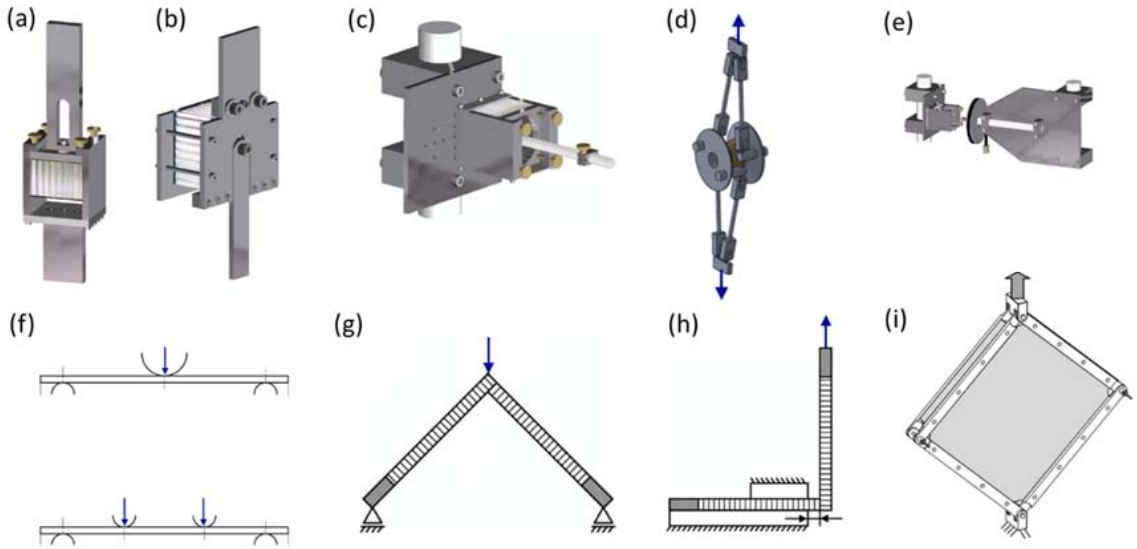

Figure 1. Variety of component tests: (a) pull-out test [2], (b) shear test [2], (c) insert bending test [2], (d) torsion test [10], (e) insert torsion test [2], (f) 3 and 4 point bending test [11], (g) bending test for corner joints [3], (h) shear test for corner joints [3], (i) frame shear test [12]

Usually, several load introduction points are located in the application near each other. Interactions between the individual points cannot be investigated in one of the test setups shown in Figure 1. For this, several inserts must be involved in the specimen. A selection of test setups with multiple load introduction points is shown in Figure 2.

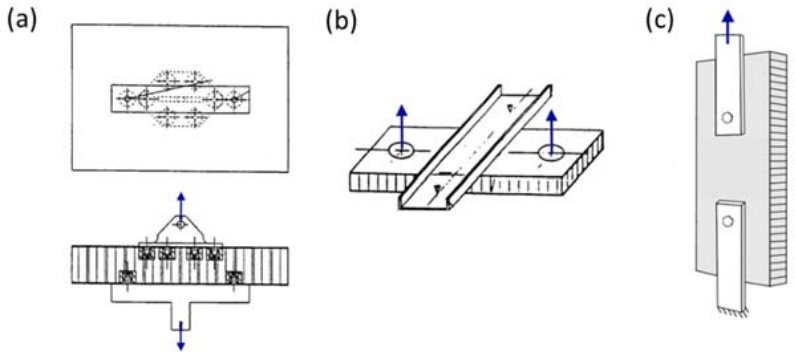

Figure 2. Component tests with multiple load introduction points: (a) and (b) ARIANE 4 tensile (pull-out) test methods [2], (c) insert shear test based on ASTM F606-95b [12]

  doi:10.5075/epfl-298799_978-2-9701614-0-0

Thus, these test designs are closer to an application than those shown in Figure 1. However, a test setup with several load introduction points for pull-out tests as shown in (a) and (b) has not been established so far. In contrast, the shear test with the two inserts, as shown in (c), has already become accepted in the application.

Furthermore, there are many different variations of a test type, which make it difficult to compare them with each other. Table 1 shows the variance of different pull-out tests conducted in the literature. For example, the cutout diameter, the loading rate and the specimen size vary. Therefore, a good comparability of the results of different test setups is not given. A defined standard would lead to better comparability of results.

Table 1: Variations of pull-out tests

Reference	Specimen size [mm]	Shape of the cutout [mm]	Loading rate [mm/min]	Number of inserts
[13]	80 x 80	⌀ 70 circular	1	1
[14, 15]	100 x 100	⌀ 70 circular	1	1
[12]	100 x 100	⌀ 80 circular	10	1
[16]	100 x 100	⌀ not given, circular	1	1
[17]	120 x 120	⌀ 80 circular	1	1
[18]	120 x 120	⌀ 80 circular	1.27	1
[3]	127 x 127	⌀ 100 circular	1, 500	1
[19]	140 x 140	⌀ 60 circular	0,5	1

3. Component tests for an aircraft cabin partition

3.1 Existing load cases in the example of an aircraft cabin partition

The application example considered in this paper is an aircraft cabin partition wall as used in entrance areas of commercial aircrafts. The requirements of such a partition are specified in CS-25.561 and CS 25.562 [20]. Figure 3 shows possible loads on the cabin partition.

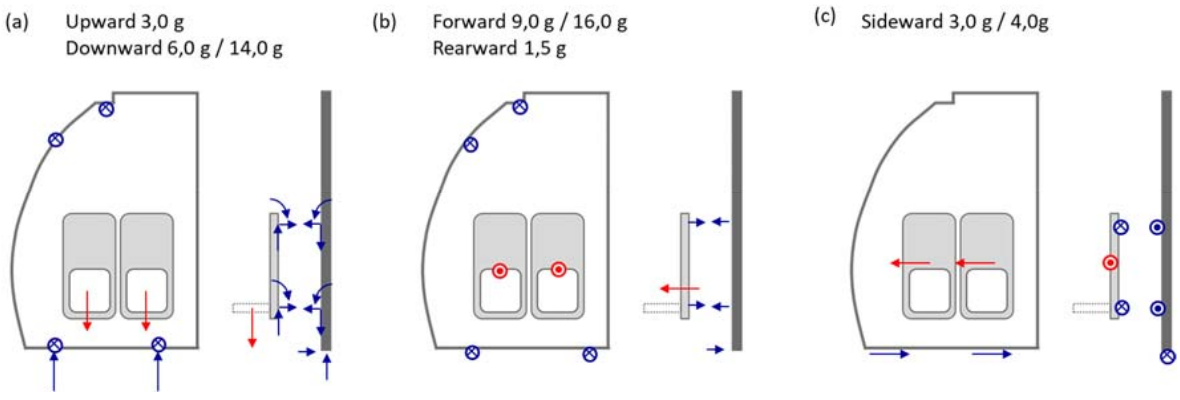

Figure 3. Load cases on an aircraft cabin partition according to EASA CS-25 [20]

This design regulation specifies accelerations for the various three-dimensional directions, which are used to calculate static design forces. For load introduction points of cabin attendant seats, even higher loads must be withstood during forward and downward loading. These are also indicated. The masses of the individual attachments are considered as they are in the application. The weight of a flight attendant is assumed to be 77 kg according to CS-25 [20].

As shown in the free-body diagrams in Figure 3, tensile, compressive and shear forces essentially act at the interfaces or at the load introduction points from the attachment parts into the partition. Thus, the partition itself is exposed to a global bending load in the critical load case of the forward direction.

3.2 Suitability of the current component test setups

Therefore, a pull-out test and a shear test, as shown in Figure 1 (a) and (b), are suitable for the strength verification of the individual load introduction points. In order to investigate the bending behavior of the materials used, bending tests such as those shown in Figure 1 (f) are recommended. Thus, the strength of individual joints as well as the material behavior can be verified with the present test setups.

However, if individual load introduction points are close together, there may be interactions between them. These cannot be detected and analyzed in the existing test setups. Furthermore, the boundary conditions of the bearing are abstracted from the application in a way that their influence on the structure cannot be investigated. Moreover, most established tests only consider the strength verification of insert connections. They are usually located at such a low level of structural complexity that they are not suitable as a component test for evaluating the performance of other designs. Additively manufactured structures, for instance, do not require inserts. Therefore, it makes sense to develop test setups that use larger components with more load introduction points and bearing points which are more oriented to the real application. The influence of various variables, such as the distance between the load introduction points or the influence of the shape between the bearing and load introduction points, can then also be investigated on test setups that are much closer to the application.

4. Development of new component tests

The development of the new component tests is done by combining a bottom-up with a top-down approach following the Wishbone approach from Ostergaard et al. [21]. The analysis from chapter 3.1 has shown that tensile and shear loads are the most relevant loads in the design of load introduction elements. For this reason, the shear as well as the pull-out test are used as a starting point and are successively extended to the new component tests (bottom-up). In chapter 3.2, it was further shown that the real bearing situation corresponds more to a bearing over load introduction elements than to a bearing over a fixation. Such a bearing situation realized by four joint connections is abstracted from the application (top-down) in the newly developed component tests, which are shown in Figure 4. Here, the load introduction in the test setups (a) and (b) is done via one load introduction point and in the test setups (c) and (d) via two load introduction points. In addition to the more realistic boundary conditions in the new component tests, the test setups are characterized by the fact that the same specimens can be used for both tensile and shear loading. This allows easy validation of virtual models, since only one type of specimen has to be manufactured and modelled for physical testing and numerical simulation and only the load direction in the numerical simulation has to be changed.

  doi:10.5075/epfl-298799_978-2-9701614-0-0

Furthermore, reductions of the loadbearing capacity of the individual load introduction elements due to a superposition of their stress fields can be taken into account.

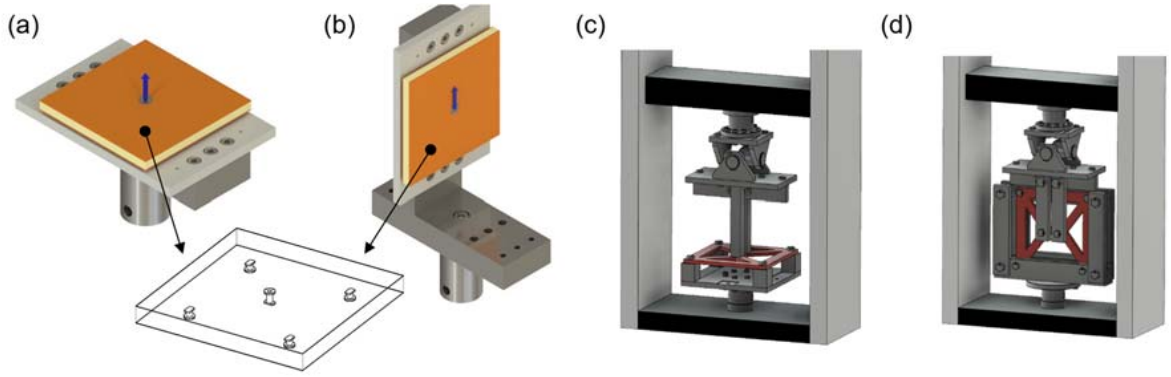

Figure 4. Concepts for pull-out test and shear test with extended boundary conditions (a), (b) and multiple load introduction points (c), (d)

By transferring the analytical formulas from the Insert Design Handbook [2] into a graphical representation, corresponding reduction areas were identified, which is shown in Figure 5 (a). Building on this, the mounting plate for fixing the specimen in the experimental setups (a) and (b) was designed in such a way that different effects can be investigated, which is shown in Figure 5 (b). Furthermore, an extension to a test setup with two load application points is also possible, as shown in the test setups (c) and (d). In these test setups, an additional universal joint is used for load application to avoid the introduction of transverse forces into the structure.

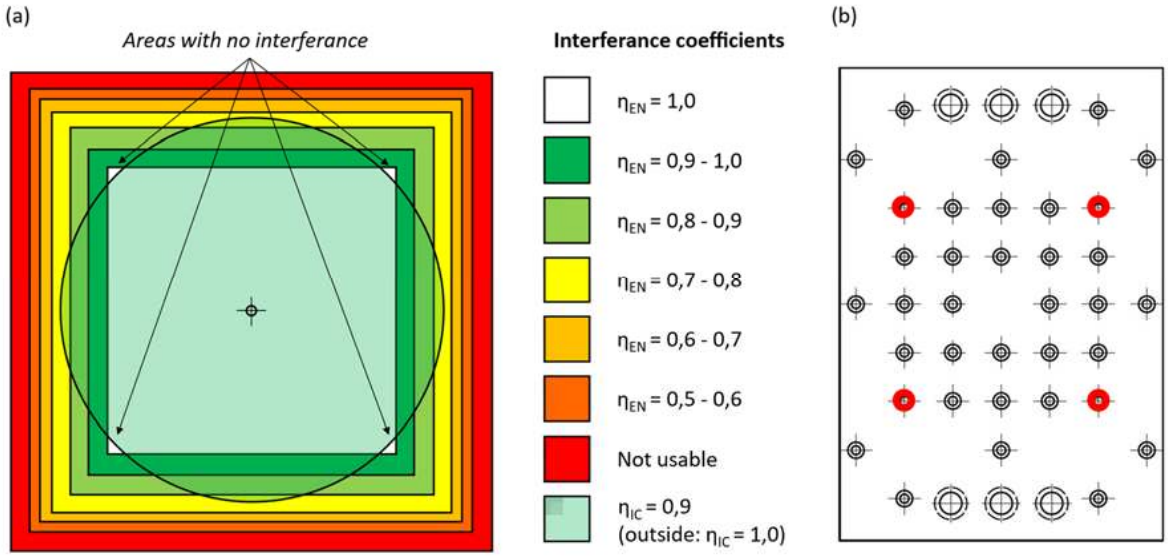

Figure 5. Graphical representation of interference areas for a 200 x 200 specimen (a) and mounting plate with red colored drill holes for configuration without loss of load bearing capacity of inserts (b)

5. Results

Figure 6 shows the test results of a sandwich structure with Nomex honeycomb core and face sheets of phenolic resin impregnated glass fiber fabric in the conventional pull-out test (red curve, test setup on the left) and in the new component test (blue curve, test setup on the right) according to Figure 4 (a). Both tests were performed on the same Galdabini Quasar 100 universal

  doi:10.5075/epfl-298799_978-2-9701614-0-0

testing machine with a loading rate of 2 mm/min. Furthermore, the optical 3D measuring system ARAMIS Adjustable from GOM was used in each case for displacement measurement as well as a HBM S9M-10 kN load cell is utilized for force measurement. For the pull-out test, a cutout diameter of 70 mm was selected, as recommended in the Insert Design Handbook [2]. In addition, the mounting of the inserts in the new component test was selected that, according to the analytical formulas from the Insert Design Handbook [2], no reduction in the load-carrying capacity of the individual inserts occurs.

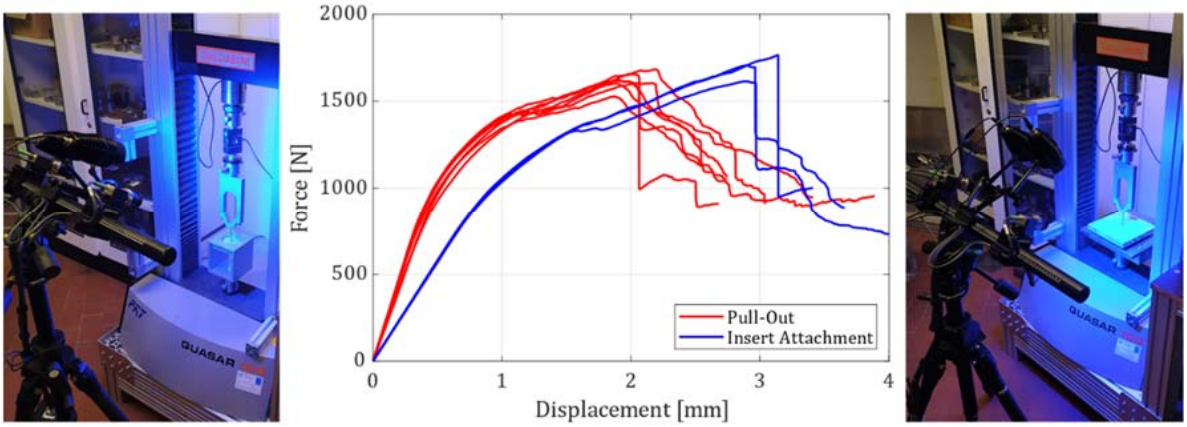

Figure 6. Comparison of a normal pull-out test with one with extended boundary conditions (insert attachment)

In the tests, deviations in the stiffnesses can be seen which, in addition to the changed bearing situation, can also be attributed to the larger specimen dimensions and the reduced stiffness of the sandwich specimen compared to the bearing. Furthermore, deviations in the strengths are evident. This can be explained by the changed load and the differentiated damage mechanisms occurring in the new component test compared to the conventional pull-out test. Due to this superimposed and more realistic loading, the new component test is well suited to validate virtual models also at structural complexity levels above the pull-out test. Furthermore, the new punctual bearing situation makes it possible to optimize the structure to the occurring load under the more realistic boundary conditions in a test setup that is less complex and less expensive than tests at the product level. With regard to the sandwich design, this optimization can be realized, for example, in the form of an optimization of the inserts and core filler or a reinforcement of the face sheets. Innovative designs, such as rod structures or additively manufactured structures, can also be compared with each other, since the advantages resulting from topology optimization, for example, are taken into account in the new component test.

6. Conclusion and Outlook

For the design of aircraft cabin components, there are a variety of different component tests for verification. Many of them are based on the specifications of the Insert Design Handbook [2], but still vary in test dimensions and execution. Test setups that consider multiple load introduction points are mostly unestablished. The same is also the case for the consideration of realistic boundary conditions. This is also illustrated by the example of an aircraft cabin partition considered in this paper. Furthermore, most of the test setups are only suitable for testing sandwich insert joints, so they are not suitable for a component-level design comparison.

  doi:10.5075/epfl-298799_978-2-9701614-0-0

Therefore, based on the identified gap, a number of more application-oriented component tests are developed. These investigate both tensile and shear loads. In a first step, the boundary conditions are extended and one load introduction point is considered. In the next step, the number of considered load introduction points is increased to two. Finally, the first developed test setup is implemented and used. Compared to a conventional pull-out test, a lower stiffness is determined. However, slightly higher loads are obtained under the more application-oriented boundary conditions, since the failure behaviour changes.

In the future, the other test setups will be implemented and their influence on structural performance will be determined. In a next step, other designs such as additively manufactured load path optimized structures will be tested and their performance compared to the conventional sandwich design.

Acknowledgements

The acknowledgements being relevant for this contribution are based on the research projects *DEPOSE – Additive Fertigung von Kabinenmonumenten mittels Direct Energy Deposition (20Q1905), CabinJoint - Ganzheitliche Betrachtung und Optimierung von Verbindungselementen für die Flugzeugkabine (20Q1904B) and EFFEKT - Effiziente Kabine durch digitale Vernetzung von Technologien und Systemen (20D1927D)* supported by the Federal Ministry for economic Affairs and Climate Actions (BMWK) on the basis of a decision by the German Bundestag.

7. References

[1] Zenkert D. Handbook of Sandwich Construction. 1997.
[2] European Cooperation for Space Standardization - ECCS. ECSS-E-HB-32-22A: Space Engineering Insert Design Handbook. 2011.
[3] Heimbs S, Pein M. Failure behaviour of honeycomb sandwich corner joints and inserts. Composite Structures 2009; 89(4): 575–88.
[4] Rodriguez-Ramirez JdD, Castanié B, Bouvet C. On the potting failure of inserts for sandwich panels: Review of defects and experimental analysis. Mechanics of Advanced Materials and Structures 2021; 28(21): 2210–2228.
[5] Seemann R, Krause D. Experimental and numerical analysis of nomex honeycomb sandwich panel inserts parallel to the face sheets. In: ECCM 17. Proceedings of the 17th European Conference on Composite Materials; 2016 June 26-30; Munich, Germany; 2016.
[6] Heyden E, Hartwich TS, Schwenke J, Krause D. Transferability of Boundary Conditions in Testing and Validation of Lightweight Structures. In: Krause D, Paetzold K, Wartzack S, editors. DFX 2019. Proceedings of the 30th Symposium Design for X; 2019 September 18-19; Jesteburg, Germany; 2019.
[7] Schwan L, Hüttich P, Wegner M, Krause D. Procedure for the transferability of application specific boundary conditions for the testing of components and products. In: Krause D, Paetzold K, Wartzack S, editors. DFX 2021. Proceedings of the 32nd Symposium Design for X; 2021 September 27-28; Tutzing, Germany; 2021.
[8] Department of Defense. Composite Material Handbook - Volume 3 Polymer matrix composites materials usage, design and analysis. 1997.
[9] Dambietz FM, Hartwich TS, Scholl-Corrêa J, Hoffmann P, Krause D. Influence analysis of the layer orientation on mechanical and metallurgic characteristics of DED manufactured

  doi:10.5075/epfl-298799_978-2-9701614-0-0

parts. In: LiM 2021. Proceeding of Lasers in Manufacturing Conference 2021; 2021 June 21-24; Munich, Germany; 2021.
[10] Mharsi K, Casari P, Sellami A, Fajoui J, Kchaou M. Mechanical Characterization of a Composite Sandwich Core Under Shear Stress Based on a Torsion Test. In: Kharrat M, Baccar M, Dammak F, editors. Advances in Mechanical Engineering, Materials and Mechanics. Springer International Publishing. 2021; 299–305.
[11] DIN Deutsches Institut für Normung e. V.. DIN 53293 - Prüfung von Kernverbunden, Biegeversuch. Beuth Verlag GmbH. 1982.
[12] Seemann R. A Virtual Testing Approach for Honeycomb Sandwich Panel Joints in Aircraft Interior. Springer Berlin Heidelberg. 2020.
[13] Bianchi G, Aglietti GS, Richardson G. Static Performance of Hot Bonded and Cold Bonded Inserts in Honeycomb Panels. Journal of Sandwich Structures & Materials 2011; 13(1): 59–82.
[14] Schwenke J, Krause D. Optimization of load introduction points in sandwich structures with additively manufactured cores. Design Science 2020; 6.
[15] Schwenke J, Hartwich T, Krause D. Optimierung von Inserts in Sandwichstrukturen durch additive Fertigung. In: Lachmayer R, Lippert RB, Kaierle S, editors. Konstruktion für die Additive Fertigung 2018. Springer Berlin Heidelberg. 2020; 243–259.
[16] Park H-S, Hwang D-H, Han J-H, Yang J. Development of shock-absorbing insert for honeycomb sandwich panel. Aerospace Science and Technology 2020; 104: 105930.
[17] Roy R, Nguyen KH, Park YB, Kweon JH, Choi JH. Testing and modeling of Nomex™ honeycomb sandwich Panels with bolt insert. Composites Part B: Engineering 2014; 56: 762–769.
[18] Nguyen K-H, Park Y-B, Kweon J-H, Choi J-H. Failure behaviour of foam-based sandwich joints under pull-out testing. Composite Structures 2012; 94(2): 617–624.
[19] Bunyawanichakul P, Castanié B, Barrau J-J. Non-linear finite element analysis of inserts in composite sandwich structures. Composites Part B: Engineering 2008; 39(7-8): 1077–1092.
[20] European Union Aviation Safety Agency EASA. Certification Specifications and Acceptable Means of Compliance for Large Aeroplanes - CS-25 Amendment 26. 2020.
[21] Ostergaard MG, Ibbotson AR, Le Roux O, Prior AM. Virtual testing of aircraft structures. CEAS Aeronaut Journal 2011; 1(1-4): 83–103.

  doi:10.5075/epfl-298799_978-2-9701614-0-0

STATIC AND DYNAMIC CRUSHING OF SANDWICH TUBES WITH A BIRCH CORE AND CARBON SKINS

Romain Guélou[a], Florent Eyma[a], Arthur Cantarel[a], Samuel Rivallant[a], Bruno Castanié[a]

a: Institut Clément Ader, Université de Toulouse, INSA – ISAE-SUPAERO – UPS – IMT Mines Albi, 3 rue Caroline Aigle, Toulouse 31400, France – bruno.castanie@insa-toulouse.fr

Abstract: This paper presents the results of static and dynamic crushing of wood sandwich tubes made with a birch core and carbon woven skins. 3 tubes (external diameter 64 mm, length 120 mm) were crushed in static and 3 others in dynamic under a drop tower. The results reveal very interesting energy absorption performance of such structures. The Specific Energy Absorption is 50.4 J/g in static and 66.6 J/g in dynamic, the energy absorbed is 5427 J in static and 7045 J in dynamic (170 kg launched at 4.2 m). These characteristics, which are quite comparable with those of tubes made of composite materials or aluminum alloys, show that these sandwiches with birch core are serious candidates for energy absorption with renewable materials.

Keywords: Wood; birch; sandwich tubes; crushing; energy absorption.

1. Introduction

Wood is a serious candidate for a sustainable transportation industry because of its light weight, its low embodied energy, its availability and its ability to store carbon. It was used extensively in the aeronautical industry during the Second World War with, in particular, the De Havilland Mosquito, one of the most famous planes of this war. Its fuselage and its wings were designed with a sandwich structure made with birch or Douglas fir skin and a Balsa core. It could reach 612 km/h and was manufactured in 7,781 units [1]. There is now renewed interest in these materials. Therefore, the authors have analysed statically many sandwich configurations whether with metallic or composite skins and a plywood core [2]. The behaviour of sandwiches with plywood core under low speed, low energy impact has also been the subject of recent studies [3]. It has been shown that wood-based sandwich structures also have very good residual compressive strength after impact [4], which prompted the authors to look more closely into the crash behaviour of these structures. Note that, despite the success of the WoodC.A.R program [5], the static and dynamic fracture modelling of wood structures remains an issue [6], therefore the studies on static and dynamic behavior of wood are mainly experimental.

The crushing response of wood was first studied by the authors on poplar tubes with different stackings [7]. The best configuration with horizontal layers on the inner and outer surfaces (belt effect) generates a SEA up to 30 J/g for a material 40 times less expensive than CFRP, and renewable. In addition, the authors also worked on sandwich tubes with a poplar core and skins either in carbon fabrics or in glass fabrics. Compression tests were performed statically [8] and dynamically [9] on a drop-weight crash test machine. It is remarkable that, in these two types of tests, the fact of passing from 2 to 6 internal poplar plies allowed the absorbed energy to be

  doi:10.5075/epfl-298799_978-2-9701614-0-0

doubled for a practically constant SEA. These results show the significant contribution of poplar in terms of energy absorption.

In this communication, the crushing tests of sandwich tubes with a core made with birch veneers and carbon skins will be presented.

2. Materials and Methods

The tubes were manufactured with carbon (M79 / 42% / 200 T2 / CHR-3 K, Hexcel) with an area weight of 345 g/m^2. The orientation of the fabrics, balanced 2–2 twill, was always [0/90] to achieve a hoop effect due to the 90° fibers. The core was stacked with 12 plies of 0.5 mm thick birch veneers supplied by Garnica. Veneers density is 0,504 g/cm^3, and veneers are bonded together between 8.8% and 9.8% HR. The tubes have an external diameter of 64 mm for a length of 120 mm. The manufacturing method will not be recalled here and readers can refer to previous papers of the authors [7, 8, 9]. After curing, a trigger is machined on the tubes. A picture of a typical tube is showed on Figure 1 (a). The static tests were carried out at a speed of 5 mm/min on an MTS system tension machine equipped with a 100 kN load cell and a displacement sensor. The tubes were crushed over ¾ of their length, i.e. 90 mm, which was long enough for a stable crushing mechanism to be observed when it existed.

(a) 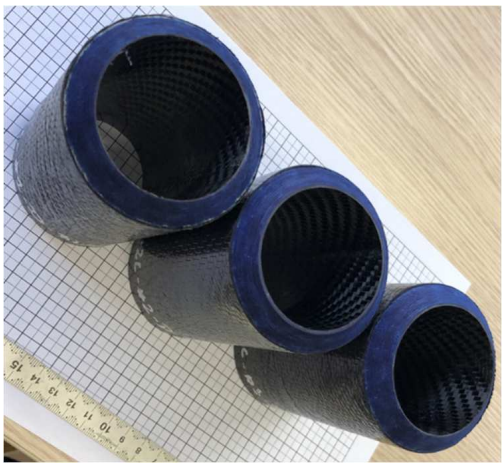 (b) 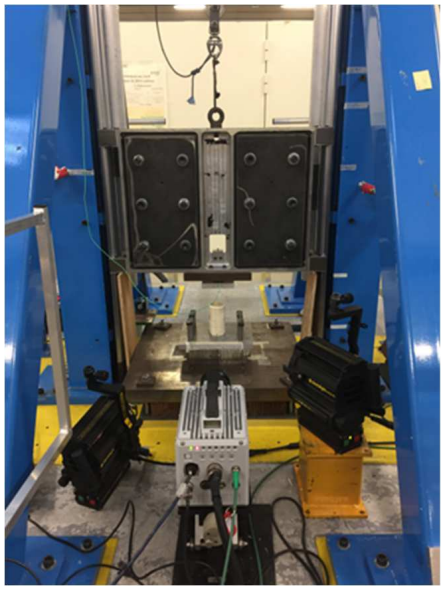

Figure 1. (a) Typical wood based carbon tubes (the trigger are paint in blue for post-mortem analysis), (b) Overview of the dynamic testing test rig with the high speed camera

The dynamic tests were carried out using a drop weight tower (Figure 1 (b)). These tests were interrupted after 80 mm of crushing for post-mortem observations on the samples. They were also filmed using a high-speed camera during the entire crash. A force sensor located between the mass and the upper crushing plate made it possible to obtain the crushing force with an acquisition frequency of 1 MHz. The displacement was calculated by double integration of the force from knowledge of the initial speed given by an optical sensor. No filtering was performed for data extraction. The high speed camera and the force signal were synchronized in order to

be able to link the images of the crushing front with the force-displacement curve. A redundant calculation of displacement was also carried out using the camera images for a few samples to verify the accuracy of the double integration method. More information on the tests and their analysis can also be found in [7, 8, 9]. Three tubes were crushed in static and three others in dynamics under a drop tower.

3. Static results

The force/displacement curves obtained experimentally for a static crushing length of 90 mm are shown Figure 2. The classical steps for crushing (initiation, transition and plateau) are found and the plateau is generally stable. The peak force (≈96,000 N) is relatively close to the plateau force (≈65,000 N) allowing a fairly good CFE (Crush Force Efficiency i.e ratio between the average effort and the maximum effort $F_{plateau}/F_{max}$) of around 0.68 to be obtained. The plateau of tube #2 being slightly lower than the other two, the $SEA_{plateau}$ (Specific Energy Absorption calculated in the plateau area, see [7, 8, 9]) of this tube is the lowest obtained (45.6 J/g). The $SEA_{plateau}$ of the other two tubes is around 50 to 52 J/g. The total energy absorbed is in average 5427 J

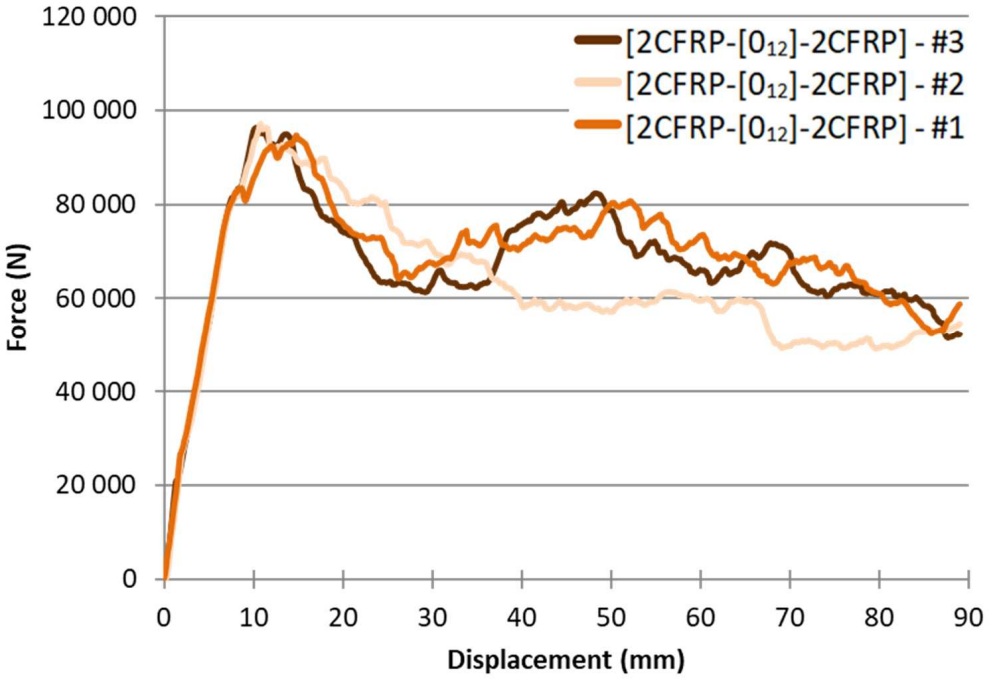

Figure 2. Force displacement curves for the 3 tubes under static crushing (the tubes are named from their stacking and their number).

The failure of these sandwich tubes is similar to that obtained with an I214 poplar core [8]. The initiation begins with the flattening of the chamfer that causes the fibers to break at 90°, dissociates the tube into a bundle allowing them to splay via bending (Figure 3). The main failure mode of this configuration seems to be splaying with the formation of petals.

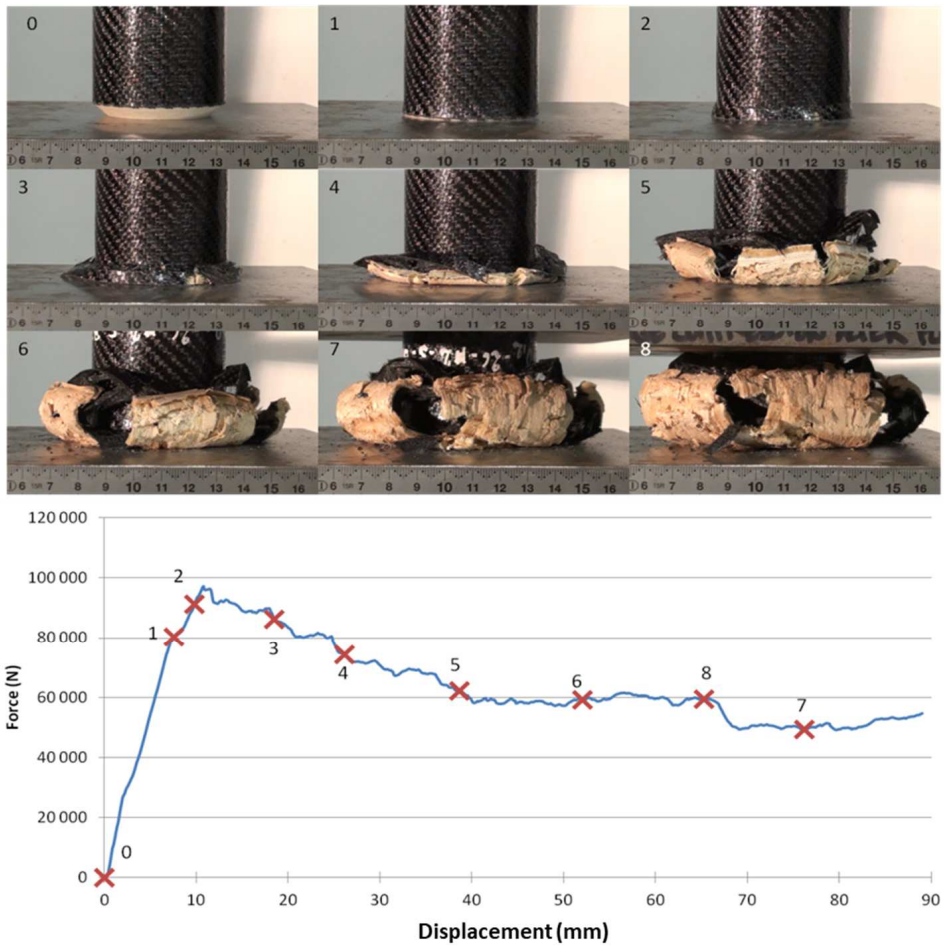

Figure 3. Static failure of specimen [2CFRP-[0_{12}]-2CFRP] - #2, association image and point on the force-displacement curve.

4. Dynamic results

The force/displacement curves obtained experimentally for a dynamic crushing length of 90 mm are shown Figure 4. A mass of 170 kg was launched at 4.2 m. The classical steps (initiation, transition and plateau) are found again but also much greater oscillations are observed on the plateau. This can be explained by the vibration of the experimental support due to the high energy absorbed. The averaged peak force is significantly higher than in static (≈121,590 N) and the plateau force reach ≈92300 N for a CFE of around 0.76. The plateau seems to be constant firstly and then increases at the end of the crushing (around 60 – 70 mm). A SEA of the order of 66.6 to 69.5 kJ/kg is reached. The total energy absorbed is in average 7025 J. In the same way as observed under static loadings, the failure begins with the crushing of the chamfer, leading to the failure of the carbon fibers at 90°, allowing the tube to dissociate into bundles. The latter then bend and then splay, then creating petals.

Post-mortem observation by cutting the specimens in half tubes shows the presence of unbroken petals over the entire periphery of the tube (Figure 5). An interior containment of debris generated by the fairly large interior splaying is also present. The blue color present at the failure front where the walls divide is due to the coloring of the chamfer (see Figure 1). If at the end of the crushing, the blue color is still present, it suggests that the chamfer is responsible for it, otherwise the blue color would have disappeared (the chamfer and its debris would have

been "ejected" from the front of the ruin, and an absence of color blue would have been noted). The blue coloring of the chamfer thus indicates that it contributes since the start of the crushing and allow the establishment of the splaying.

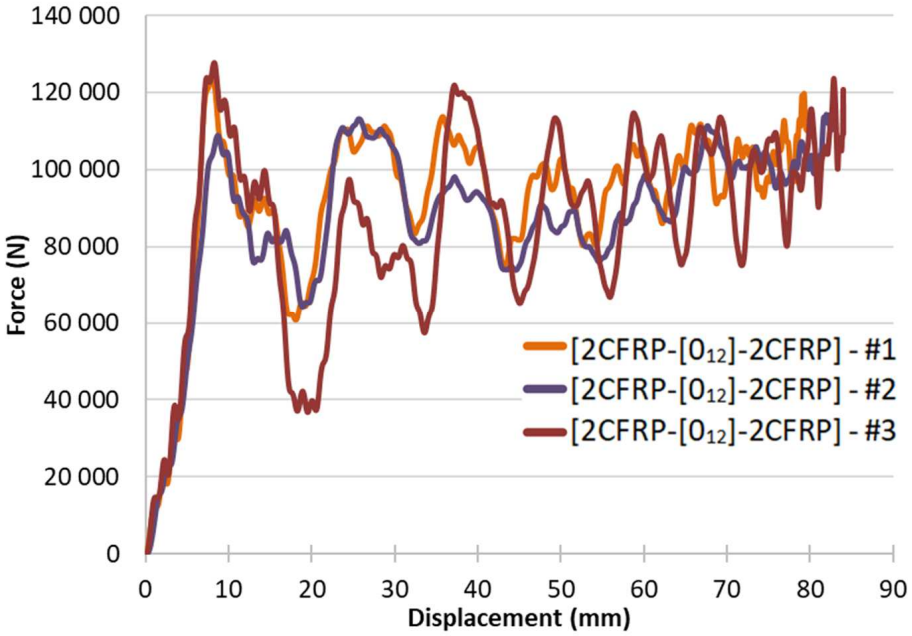

Figure 4. Force displacement curves for the 3 tubes under dynamic crushing (the tubes are named from their stacking and their number).

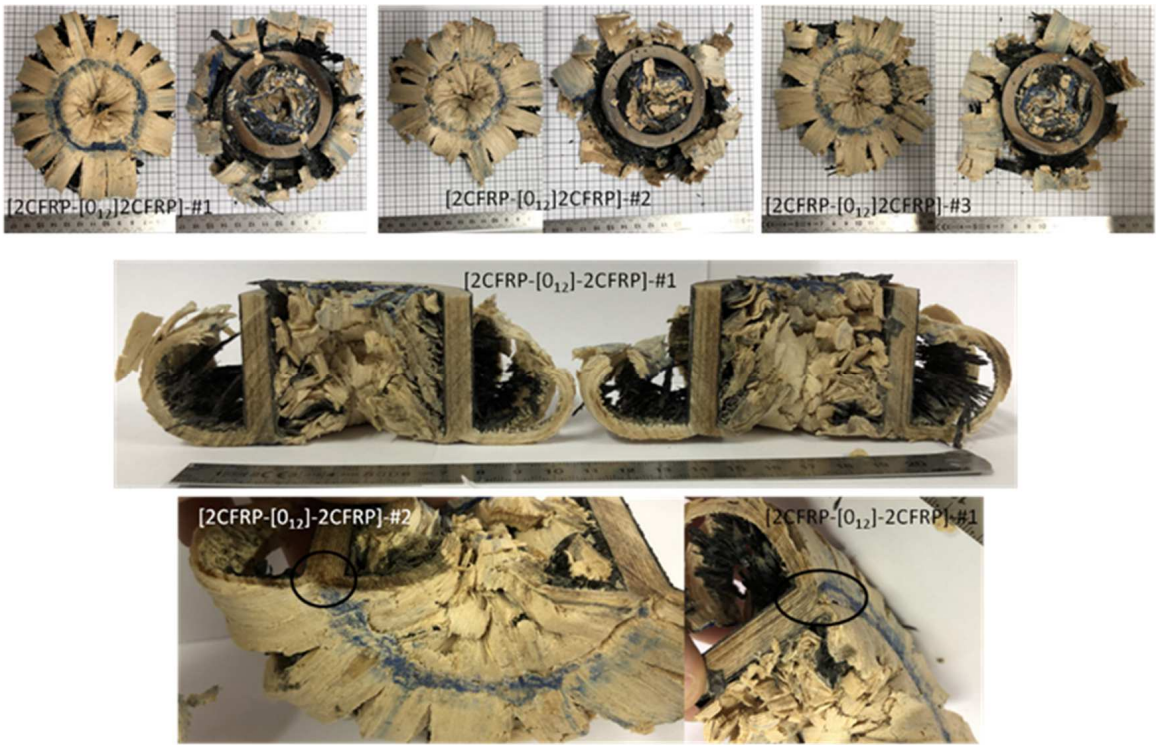

Figure 5. Post-mortem failure analysis of birch and carbon fiber sandwich tubes (a) overview (b) half-tubes.

5. Conclusions

The sandwich tubes with carbon skins and birch core have shown particularly interesting energy absorption performance. Whether static or dynamic, the overall failure mode of these tubes is splaying. However, in dynamics there is a compaction of internal debris absent in statics. The SEA is around 50 J/g in static and 65 – 70 J/g in dynamic. These values are of the same magnitude as for aluminum tubes or composite tubes. In comparison with a single carbon tubes made of four plies (See [8,9]), the coupling of birch to composite fibers is beneficial and allows additional energy absorption (7,300 J absorbed with the carbon fiber skins, 82% gain on absorbed energy) compared to the equivalence of independently crushed tubes. However, although the performances obtained with birch are superior to those obtained with poplar I214, CFRP tubes still work better on their own and have a higher SEA than sandwich tubes (81.3 J/g dynamic). A study in the process of being published shows that birch has very good characteristics in terms of energy absorption compared to oak and poplar. In general, this study shows that the composite skin/wood core coupling is a very good economic option for energy absorbers.

6. References

1. Castanié B, Bouvet C, Ginot M. Review of composite sandwich structure in aeronautic applications. Composites Part C: Open Access, 2020;1:100004.
2. Susainathan J, Eyma F, De Luycker E, Cantarel A, Castanié B. Manufacturing and quasi-static bending behavior of wood-based sandwich structures. Composite Structures 2017;182:487-504.
3. Susainathan J, Eyma F, De Luycker E, Cantarel A, Castanié B. Experimental investigation of impact behavior of wood-based sandwich structures. Composites Part A: Applied Science and Manufacturing 2018;109:10–19.
4. Susainathan J, Eyma F, De Luycker E, Cantarel A, Bouvet C, Castanié B. Experimental investigation of compression and compression after impact of wood-based sandwich structures. Composite Structures 2019;220:236–249.
5. Müller U, Jost T, Kurzböck C, Stadlmann A, Wagner W, Kirschbichler S, Baumann G, Pramreite M, Feist F. Crash simulation of wood and composite wood for future automotive engineering. Wood Material Science and Engineering 2020;15(5):312-324
6. Susainathan J, Eyma F, De Luycker E, Cantarel A, Castanié B. Numerical modeling of impact on wood-based sandwich structures. Mechanics of Advanced Materials and Structures 2020; 27(18):1583–1598.
7. Guélou R, Eyma F, Cantarel A, Rivallant S, Castanié B. Crashworthiness of poplar wood veneer tubes. International Journal of Impact Engineering 2021;147:103738.
8. Guélou R, Eyma F, Cantarel A, Rivallant S, Castanié B. Static crushing of wood based sandwich composite tubes. Composite Structures 2021;273:114317.
9. Guélou R, Eyma F, Cantarel A, Rivallant S, Castanié B. Dynamic crushing of wood-based sandwich composite tubes. Mechanics of Advanced Materials and Structures 2021, on line, https://doi.org/10.1080/15376494.2021.1991533.

Dimensional stability of paper-based sandwich panels during the quasi-static pressing process

Yuting, Wei[a], Franz Hirsch[a], Dietmar Süße[a], Birgit Lutsch[b], Markus Kästner[a]

a: Institute of Solid Mechanics, TU Dresden, 01062, Dresden, Germany
Email: markus.kaestner@tu-dresden.de
b: Papiertechnische Stiftung, Pirnaer Straße 37, 01809 Heidenau, Germany.

Abstract: *This study intends to understand and reduce the undesired unevenness on exterior surfaces of a paper-based sandwich structure with a corrugated core during the pressing process. Therefore, a finite element model using the commercial software ABAQUS is presented to quantify the formation of the surface unevenness. The sandwich structure adopted in the model consists of a decorative layer, an intermediate layer, a corrugated core, and a bottom layer. The simulation results with four different types of paper as the intermediate layer are compared and are consistent with the experimental results. Finally, the numerical model has been confirmed for analyzing the causes of the unevenness of the top surface and for reducing them by identifying the optimized design of the manufacturing process.*

Keywords: corrugated core; surface unevenness; pressing process; sandwich composite; finite element methods

1. Introduction

In recent years, the demand for lightweight structures in the automotive industry has increased significantly to develop economic and energy sustainability. Paper-based sandwich structures with a corrugated core can achieve these needs. They are utility in automotive manufacturing, e.g., for sunroof panels, floor luggage compartments, rear parcel shelves, and spare wheel covers. Generally, these sandwich panels consist of glass fiber or natural fiber intermediate layer with a PU matrix that foams significantly into the core [1]. Furthermore, there is a trend towards sandwich composites with natural fiber reinforcements to improve the recyclability of automobile components. However, there are still limitations due to the formation of undesired waviness structures on exterior surfaces during the manufacturing process. This includes pressing steps necessary to join the outer layer and core, resulting in uneven surfaces and lack of dimensional accuracy.

Since sandwich panels with a corrugated core are widely applied in the aerospace and automotive industry, a considerable amount of literature has been published [2–4]. While many of the previous studies are particularly focused on the compressive resistance and peak stress under the impact of corrugated cores [5–7], there have been few empirical investigations into waviness imperfections on exterior surfaces of the panel related to core fracture. This paper presents a sandwich architecture, where the existing glass fiber material was replaced with a paper-based material as an intermediate layer. A finite element model is developed to explore the relationship between the manufacturing process and the resulting shape deviations.

2. Modeling approach

2.1 Characterization of surface quality

  doi:10.5075/epfl-298799_978-2-9701614-0-0

Automotive manufacturers demand a high standard in controlling the appearance of vehicle exteriors [8, 9]. To accomplish these demands, plenty of instruments provide possibilities to measure the roughness and waviness for surface characterization. Two of these instruments are the micro-wave-scan by BYK-Gardner in Germany and the 3D Optical Profilometer by Keyence in Japan [10, 11]. BYK's micro-wave-scan identifies several waviness parameters on different wavelengths, where the shortwave (SW: 0.3 – 1.2 mm) and longwave (LW: 1.2 - 12 mm) parameters are of particular interest. The 3D Optical Profilometer VR 3200 by Keyence captures the entire surface so that even small features can be evaluated with the highest reliability. The waviness parameter *Wa* is specified in the wavelength range of 0.8 to 8 mm, whereas the roughness parameter *Ra* is specified in the range of 0 to 0.8 mm (both calculated using ISO 4288 [12]).

2.2 General sandwich composition and material modeling

The adopted sandwich structure consists of a top layer, an intermediate layer, a corrugated core, and a bottom layer, see Figure 1. The top layer corresponds to a high-gloss polymer-based material, which was determined from experimental data and modeled as an isotropic elastic-plastic material. The intermediate layer, the corrugated core and the bottom layer are all composed of different paper materials. The four distinct paper materials T1, P15, MB and EC are chosen for the intermediate and bottom layer, whereas the paper material WS90 is used for the corrugated core. The effects of the paper material WS90 are not investigated in this paper.

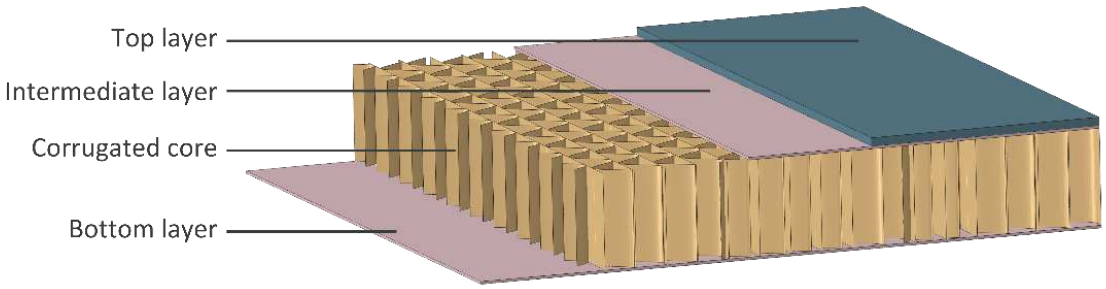

Figure 1. Sandwich structure with corrugated core

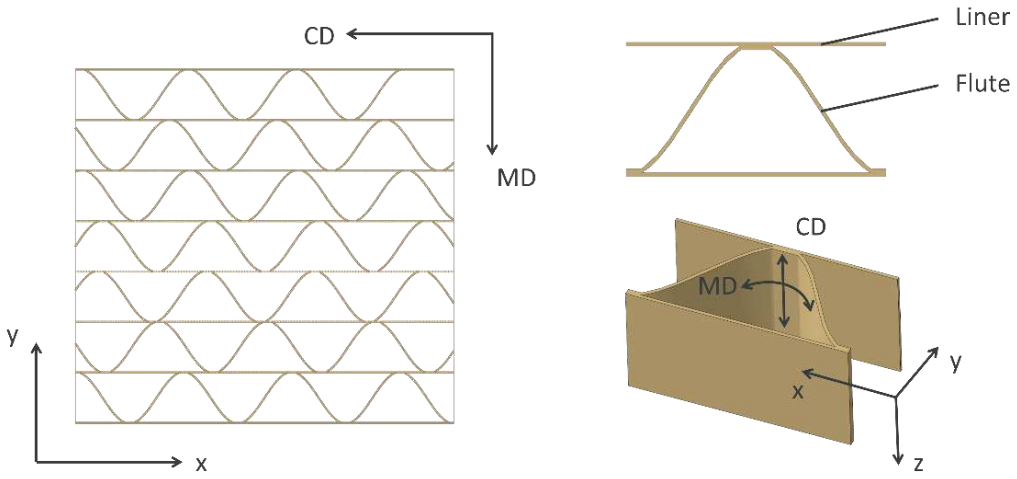

Figure 2. The principal direction MD and CD of the intermediate and bottom layer in the panel (left) and the sinusoidal geometry superimposed on one corrugation (right)

The in-plane properties of the paper materials were determined from experimental tensile and short-crush tests (SCT), while the elastic out-of-plane (ZD) properties are calculated based on the properties in the machine direction (MD) and the cross direction (CD) according to the estimation proposed by Persson et al [13–17], see Table 1.

Table 1: Elastic constants and thickness for the intermediate layer

Material	E_{MD} [MPa]	E_{CD} [MPa]	E_{ZD} [MPa]	$G_{MD\text{-}CD}$ [MPa]	$G_{MD\text{-}ZD}$ [MPa]	$G_{CD\text{-}ZD}$ [MPa]	$\nu_{MD\text{-}CD}$	$\nu_{MD\text{-}ZD}$	$\nu_{CD\text{-}ZD}$	t_{Thick} [mm]
T1 (1)	5181	2622	26	1426	94	75	0.37	0.01	0.01	0.42
P15 (2)	2416	1112	12	634	44	32	0.37	0.01	0.01	0.76
MB (3)	2877	1630	14	838	52	47	0.68	0.01	0.01	0.45
EC (4)	5832	2616	29	1511	106	75	0.47	0.01	0.01	0.43

(1)(2): Paper of Deep drawing

(3)(4): Paper of folding boxboard

The orthogonal elasticity with Hill plasticity of the immediate layer and the bottom layer was modeled using data in the table above.

2.3 Model definition in Abaqus

The manufacturing process is modeled simplistically as a pressing process as shown in Figure 3. The total height h_{total} of the panel in the initial configuration is defined by

$$h_{total} = h_{top} + h_{intermediate} + h_{core} + h_{bottom}, \quad (1)$$

with the layer tickness h_{top}, $h_{intermediate} = h_{bottom}$ and h_{core}.

The upper mold is moved vertically at 0.5 mm/s, while the lower mold remains fixed. This results in a compression of the panel to a residual height h_d. Different residual heights $h_{d\text{-}10}$, $h_{d\text{-}20}$, $h_{d\text{-}40}$ are analyzed corresponding to 10%, 20% and 40% of the total height h_{total}.

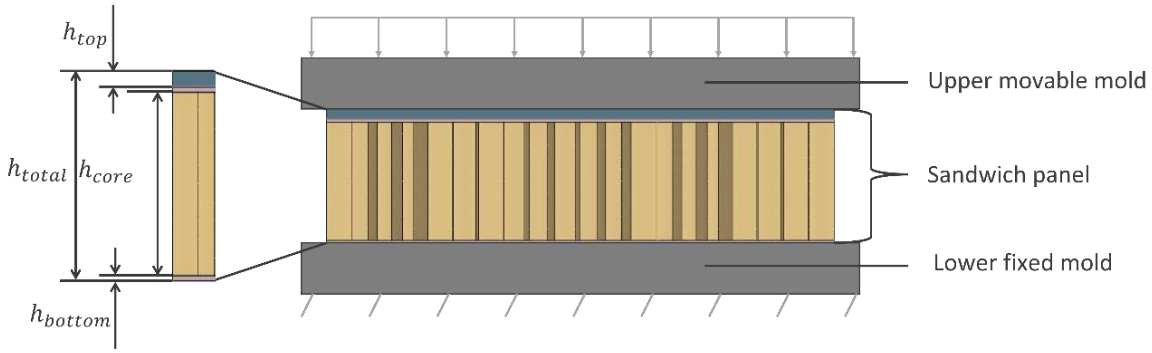

Figure 3. Schematic finite element model of the pressing process

All experiments were completed under the same conditions and the laboratory setting was with a room temperature of 23°C and relative humidity of 55%. The influence of moisture content and temperature on the material parameters were not considered in this investigation. The specific height values for the studied panels are listed in Table 2.

Table 2: Initial height h_{total} and resulting height h_d for the different panel configurations.

Intermediate layer	h_{total} [mm]	$h_{d\text{-}10}$ [mm]	$h_{d\text{-}20}$ [mm]	$h_{d\text{-}40}$ [mm]
		10% of h_{total}	20% of h_{total}	40% of h_{total}
T1	17.14	1.71	3.42	6.86
P15	18.52	1.85	3.70	7.40
MB	17.20	1.72	3.44	6.88
EC	17.16	1.72	3.44	6.86

The thickness of all layers in the panel are significantly smaller compared to the other dimensions, which is why shell elements are chosen in this contribution. Depending on the application Abaqus provides various types of shell elements. Due to the considerable deformation of the corrugated core in the height direction during the pressing process, a conventional shell element (S4R) is applied. Since the top layer (h_{top} = 1.3 mm), intermediate layer ($h_{intermediate}$ = 0.4 - 0.8 mm), and bottom layer (h_{bottom} = 0.4 – 0.8 mm) are all thicker than the corrugated paper (0.15 mm), the continuum shell element has advantages over conventional shell elements, e.g. allowing two-sided contacts and changes of shell thickness [18]. Hence, these three layers are discretized with continuum shell elements (SC8R).

The simulations are performed in Abaqus using the explicit solver for the quasi-static pressing process. The ratio of kinetic energy to internal energy is not surpassed 5% throughout the time, which ensure that the simulation generate a quasi-static model response [18]. Nonetheless, the numerical modeling of this process remains challenging because of the complicated contact interactions, the irregular shape of the corrugated core, and the non-linear characteristics of the paper materials.

3. Results

The manufactured exterior surfaces of the different panels were measured by the Keyence VR 3200 instrument. Figure 4 illustrates the topography of the external surface of $h_{d\text{-}10}$ for the sandwich panel with T1 paper, which is obtained numerically (left) and experimentally (right). It indicates that a typical waviness appears on the external surface in both simulation and manufacturing process, along with a high degree of resemblance in the topographic appearance.

  doi:10.5075/epfl-298799_978-2-9701614-0-0

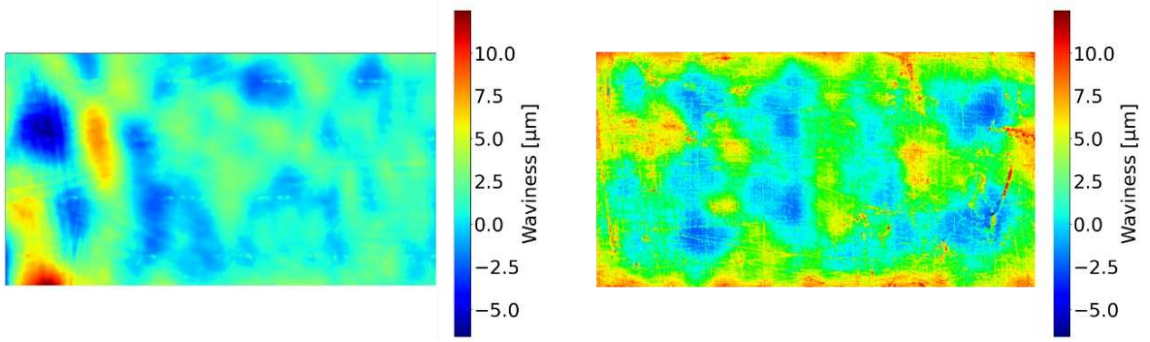

Figure 4. Exterior surface of the panel with T1 paper and residual height $h_{d\text{-}10}$ from simulation (left) and from the manufactured part (right)

To quantify the unevenness by characteristic parameters, the waviness parameter *Wa* and the roughness parameter *Ra* are calculated for all simulated surfaces. Thus the height profile of the surfaces were extracted from the simulation results and then assessed by a Gaussian filter (ISO 13565 [19]). High-pass filters and low-pass filters are used to separate the midline, the waviness parameter *Wa* and the roughness parameter *Ra* [20].

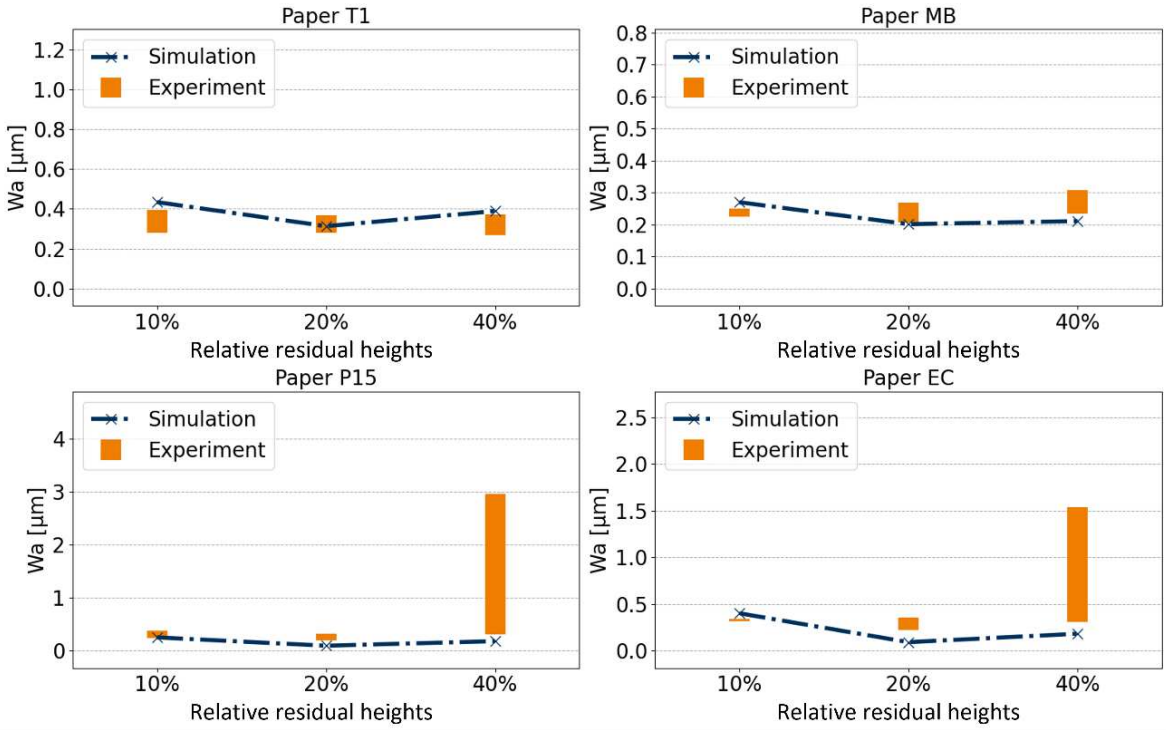

Figure 5. Comparison of waviness parameter Wa of the exterior surface with different paper materials as the intermediate layer from simulation and experiment.

The waviness parameter *Wa* and roughness parameter *Ra* were evaluated for the x- and y-directions respectively, see Figure 5. The parameters for the panels with paper T1, paper P15, paper MB and paper EC, correspond to Table 2. A good agreement between simulation and experiment in terms of the magnitude of *Wa* is achieved. In the case of $h_{d\text{-}40}$, the manufactured panels with paper P15 and paper EC seem to have higher waviness and scatter. A possible explanation is due to the difficulty of the experiment, which leads to insufficient data to obtain more accurate experimental results.

  doi:10.5075/epfl-298799_978-2-9701614-0-0

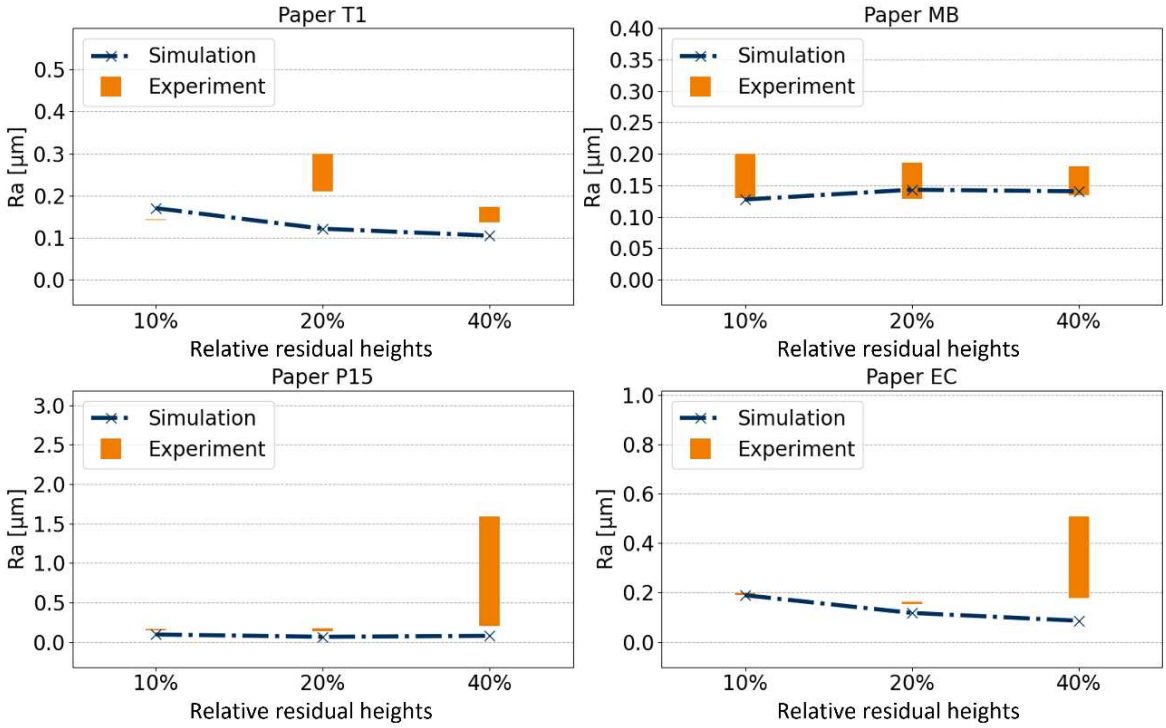

Figure 6. Comparison of roughness parameter Ra of the exterior surface with different paper materials as the intermediate layer from simulation and experiment

Similarly, Figure 6 reveals the roughness parameter *Ra* of the exterior surface from manufactured parts and simulations. The roughness parameter *Ra* on the manufactured panel with paper P15 and paper EC shows a similar trend with a large scatter at residual height $h_{d\text{-}40}$. In contrast to the waviness in Figure 5, the reliability of the simulated roughness of panels using paper T1 in Figure 6 is slightly lower. A possible explanation for these results may be the adhesive materials, which are not considered in the model because of their Temperature-dependent material characteristics and complicated contact interactions with other layers.

In summary, the present model can be used to analyze the surface roughness parameter *Ra* or waviness parameter *Wa.* Not every measured waviness of the manufactured part can be predicted, but the magnitude and trends agree well, even with this rather simple process model. The corrugated core in the finite element model is generated with a random arrangement of the adjacent flutes and held fixed. Due to computational costs the simulated panel size differs from the manufactured part. The fluting and the liner are bonded randomly to manufacture the corrugated cores based on sinusoidal geometry, which leads to the impossibility of obtaining the sinusoidal geometry-based corrugations with the same geometry for experiments [4]. The observed differences of the results between the simulation and the experiment could be due to the fact that the adhesive materials were not taken into account in the model. The geometric differences and the effects of adhesive materials need to be further investigated, as no such experimental data are available in the present study.

4. Conclusions and outlook

In order to analyze the causes of the unevenness of the outer surface of paper-based sandwich panels, this paper presented a numerical model to describe the pressing process. The height

  doi:10.5075/epfl-298799_978-2-9701614-0-0

profile of the top layer of manufactured parts was measured with the Keyence VR 3200 Profilometer, whereas the simulated height profile could be extracted directly from the simulation results. Then, the profiles were filtered with a Gaussian filter [19] and characterized by a roughness and waviness value. The model can predict the trends of roughness and waviness for different residual heights. To further improve the accuracy of this model and reduce the difference between experiment and simulation, more details need to be investigated. This includes the influence of the random arrangement of flutes within the core and the explicit modeling of adhesives between layers.

Acknowledgments

The research project was carried out in the framework of the industrial collective research programme (IGF no. 20956 N). It was supported by the German Federal Ministry for Economic Affairs and Climate Action (BMWK) through the AiF (German Federation of Industrial Research Associations eV) based on a decision taken by the German Bundestag. The work was supported the GWK by providing computing time through the Center for Information Services and HPC (ZIH) at TU Dresden on the HRSK-II. The authors would like to express their gratitude to industrial companies SWAP(Sachsen) GmbH and Frank-PTI GmbH for their guidance and support.

References

[1] Paul R, Klusmeier W. A Composite with a Composite with a Future. Status Report. Status Report, Bayer AG, Leverkusen 1997.
[2] S.Heimbs, P.Middendorf, M.Maier, editor. Sandwichstrukturen in der Flugzeugkabine: Materialmodellierung und dynamische Simulation; 2006.
[3] Dayyani I, Shaw AD, Saavedra Flores EI, Friswell MI. The mechanics of composite corrugated structures: A review with applications in morphing aircraft. Composite Structures 2015; 133: 358–80
[4] Britzke M. Verfahren zur automatisierten Fertigung rahmenloser Sandwichplatten mit Papierwabenkern; 2009.
[5] E Y-P, Wang Z-W. Stress Plateau of Multilayered Corrugated Paperboard in Various Ambient Humidities. Packag. Technol. Sci. 2012; 25(4): 187–202
[6] Gu X, Wang J, Lu G, Pan L, Lu L. Modelling for the in-plane plateau stress of honeycomb paperboard based on the induce effect of face paper with honeycomb core. International Journal of Mechanical Sciences 2020; 168: 105289
[7] Xue Li, Jun Wang, Chongxing Huang*, et al.* Mathematical models for predicting the quasi-static stress characteristics of corrugated paperboard with sinusoidal core along the longitudinal compression. International Journal of Mechanical Sciences 2018; 149: 136–49]
[8] Hai-zhuang Kang. Assessment of Paint Appearance Quality in the Automotive Industry. Degree of Doctor, Department of Systems Engineering, Brunel University 2000.
[9] Wolfram Reuter. Hochleistungs-Faser-Kunststoff-Verbunde mit Class-A-Oberflächenqualität für den Einsatz in der Fahrzeugaußenhaut 2001; (ISBN 3-934930-15-8).
[10] BYK-Gardner Digital Catalog 2018: Appearance introduction; 2018. Available from: URL: https://www.eurotom.pl/wp-content/uploads/2019/03/BYK-Gardner_Digital_Catalog_2018_E.pdf.

  doi:10.5075/epfl-298799_978-2-9701614-0-0

[11] Keyence O. 3D Measuring Macroscope, VR-3100.
[12] Geometrische Produktspezifikationen. ISO 4288: Oberflächenbeschaffenheit: Tastschnittverfahren Regeln und Verfahren für die Beurteilung der Oberflächenbeschaffenheit; 1996 1996.
[13] Sirkett DM, Hicks BJ, Berry C, Mullineux G, Medland AJ. Finite element simulation of folding carton erection failure. Proceedings of the Institution of Mechanical Engineers, Part C: Journal of Mechanical Engineering Science 2007; 221(7): 753–67
[14] Persson K. Material Model for Paper: Experimental and Theoretical Aspects. Diploma ReportLund University 1991.
[15] Baum GA, Habeger Jr CC, Fleischman Jr EH. Measurement of the orthotropic elastic constants of paper 1982.
[16] Beldie L. Mechanics of Paperboard Packages—Performance at Short Term Static Loading. Licentiate DissertationLund University 2001.
[17] T.M. Nordstrand. Parametric study of the post-buckling strength of structural core sandwich panels. Composite Structures 1995; 30(4): 441–51
[18] Michael Smith. ABAQUS/Standard User's Manual, Version 2020. United States: Dassault Systèmes Simulia Corp 2020.
[19] ISO 13565: Surface texture: Profile method; Surfaces having stratified functional properties. 1997.
[20] Deutsches Institut für Normung. Geometrische Produktspezifikation (GPS) – Filterung – Teil 61: Lineare Flächenfilter: Gauß-Filter. 4. Aufl., korr. Fassung 2012. Berlin: Beuth.

  doi:10.5075/epfl-298799_978-2-9701614-0-0

MECHANICAL BEHAVIOR OF INNOVATIVE SANDWICH MATERIALS

Joulia, Salloum[a], Romain, Léger[a], Loïc, Daridon[b], Patrick, Ienny[a]

a: LMGC, IMT Mines Alès, Univ. Montpellier, CNRS, Alès, France – joulia.salloum@mines-ales.fr
b: LMGC, Univ. Montpellier, CNRS, Montpellier, France

Abstract: *Foams are an important element in the dimensioning calculations of sandwich composite structures for nautical applications. Their standardized tests don't lead to establishing an intrinsic mechanical behavior. The aim of this paper is to study and characterize the elastic mechanical behavior of a reference foam of polyvinyl chloride (PVC) and those of recycled polyethylene terephthalate (PETr) substitute foams. Compression and shear tests, instrumented by a Digital Image Correlation method, were conducted on different shapes and dimensions of PVC and PETr foams in order to identify the mechanical parameters and thus, lead to measurements of apparent properties. Following the compression tests, PVC and PETr foams are found to be transversely isotropic. Using these experimental results, the elastic mechanical behavior of PVC and PETr foams is identified based on a finite element model updating method, using Abaqus and Matlab, by minimizing the difference between the simulated modulus, and the experimental apparent elastic one.*

Keywords: Sandwich materials; PVC; PETr; FEMU method.

1. Introduction

The use of fiber reinforced composites has increased in naval construction due to their favorable physical properties in particular their specific modulus, ease of fabrication and excellent mechanical behavior in the marine environment. As such, sandwich materials, composed of two laminated facings and a polymer foam core, are the first-choice materials for the design of light and rigid superstructures for the vessels. The mechanical behavior of sandwich materials made of recycled and bio-based materials (biopolymers reinforced by low environmental impact fibers) seems suitable for the nautical construction since these materials can offer equivalent specific mechanical properties compared with traditional composites, however, while having better environmental credentials [1][2][3][4]. The purpose of the study is to establish a homogenized behavior of a sandwich material. In order to do so, the work is divided into two parts: the characterization of the foam and then of the bio-based composite. The first part consists of studying the mechanical behavior of a reference foam of polyvinyl chloride (PVC) and those of recycled polyethylene terephthalate (PETr) substitute foams. The evaluation of the behavior of a foam-model is complicated as a result of the anisotropy induced by the process and the structural heterogeneity at the scale of laboratory tests [5][6][7][8]. This work is devoted to studying the elastic mechanical behavior of polymer foams subject to compression and shear tests. PVC and PETr foams were chosen as materials for this study. Unlike the shear tests, the standardized compression tests carried out are structural tests, hence the use of a numerical interpretation of the tests associated with a Finite Element Model Updating method of the test. Based on the experimental results of compression tests and on the mechanical behavior of the PVC and PETr foams, a three-dimensional finite element model has been implemented in a user-

  doi:10.5075/epfl-298799_978-2-9701614-0-0

defined material subroutine built on ABAQUS/Explicit linked to an optimization method on Matlab to predict the intrinsic elastic behavior of these polymer foams.

2. Materials and methods

In order to predict a material substitution by materials related to sustainable development, two different types of foam were used as materials for this work:

- PVC foam which is the reference material, has a density of 80 kg/m^3 and a commercial reference “AIREX C70”.
- PETr foam which is the substitute material, has a technical commercial reference "ArmaForm Core", and where two different densities were used (80 kg/m^3 and 115 kg/m^3). Recycled PET, which is more sustainable than the reference PVC foam, aims to replace this last in terms of performance.

The information in the table 1 below is taken from the datasheets of these foams.

Table 1: Mechanical properties of PVC and PETr foams

Foam type	Density [kg/m^3]		Compressive modulus [N/mm^2]		Shear modulus [N/mm^2]
PVC	80	DIN 53421	Average: 104 Minimum: 80	ASTM C393	Average: 30 Minimum: 24
PETr	80	ISO 844	57	ISO 1922	16
PETr	115	ISO 844	90	ISO 1922	26

Using the mechanical saw, the samples were cut from large sheets of rigid closed-cell foams with a thickness of 15mm.

Compression and shear tests were performed using an MTS testing machine in order to characterize the apparent physical properties of these polymer foams. These different tests are instrumented by a digital image correlation (DIC) technique [9]. Moreover, the implementation of the camera allows the visualization of real-time compression, shear progression, and the measurement of full-field displacement of specimens during the compression and shear tests.

PVC foam was assumed to be transversely isotropic, in-line with many preliminary experimental results and information from the literature on foam manufacturing processes [10] as well as the work of [5]. For the compression tests, the guidelines within the ISO 844 standard were followed. Consequently, the test specimens in this standardized test cannot be considered in the context of uniaxial compression which is a theory requiring a ratio of 2 at least, between the height and the width of the sample to be considered in uniaxial compression. Therefore, these compression tests are structural tests since the size of the sample would remain limited and not representative of its microstructure. And that is why a Finite Element model is needed to identify the intrinsic elastic parameters**.**

Compression tests on 15x15x15mm^3 cubic specimens were conducted along with two directions, longitudinal ($\vec{z}$ axis) and transversal (axis $\vec{x}$ or $\vec{y}$). Hence, these tests do not lead to

  doi:10.5075/epfl-298799_978-2-9701614-0-0

the determination of the intrinsic elastic parameters of the foam, and therefore, these tests have the sole purpose of confirming the transverse isotropy assumption.

Afterward, the intrinsic elastic behavior is identified by recalibrating a FE model of the tests, i.e., the need to carry out compression tests on larger specimens in order to experimentally determine the apparent properties of the material which will be considered as initialization parameters to apply the FE recalibration method. Compression tests along the $\vec{z}$ axis direction were then carried out on specimens of dimensions 30x30x15mm^3 and 60x60x15mm^3 respectively. On the other hand, a series of shear tests following the ISO 1922 were carried out on the foams in subject with the aim of determining the shear coefficients.

3. Experimental tests

3.1 Compression tests

According to ISO 844 standard (Rigid cellular plastics - Determination of compression properties), three sets of specimen's dimensions were tested in order to obtain the apparent elastic properties of the foams in compression. As shown in Figure 1, the cubic specimens compressed along two directions ($\vec{z}$ and $\vec{y}$ axis) are intended to validate the theory of transverse isotropy by calculating the ratio between the apparent stiffness modulus and the apparent transverse contraction coefficient corresponding to each test.

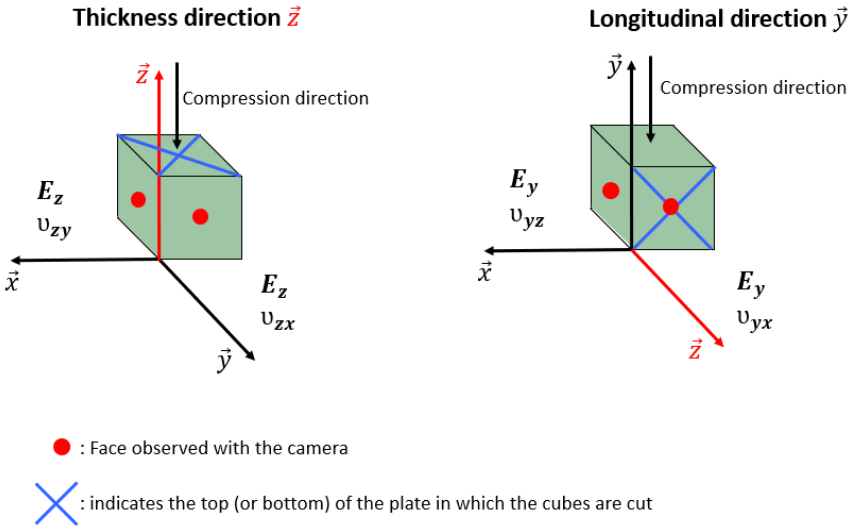

Figure 1: Compression tests in two directions

For each type of foam and for each set of dimensions 10 specimens were tested. Figures 2 and 3 show the apparent stiffness modulus $E_z$and the apparent transverse contraction coefficient υ_{zx} for the 10 cubic specimens of PVC80 as well as their average value.

Knowing that the equation that verifies transverse isotropy is:

$$-\frac{\upsilon_{zx}}{E_z} = -\frac{\upsilon_{xz}}{E_x} = -\frac{\upsilon_{yz}}{E_y} \quad (1)$$

Based on the experimental results obtained and using Eq. (1) which can let us validate the transverse isotropy theory, the ratio found is equal in the two directions ($\vec{z}$ and $\vec{y}$ axis).

  doi:10.5075/epfl-298799_978-2-9701614-0-0

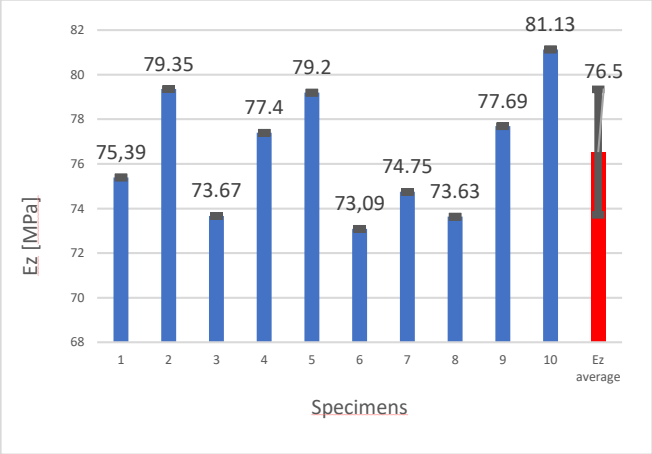

Figure 2: Apparent stiffness modulus E_z

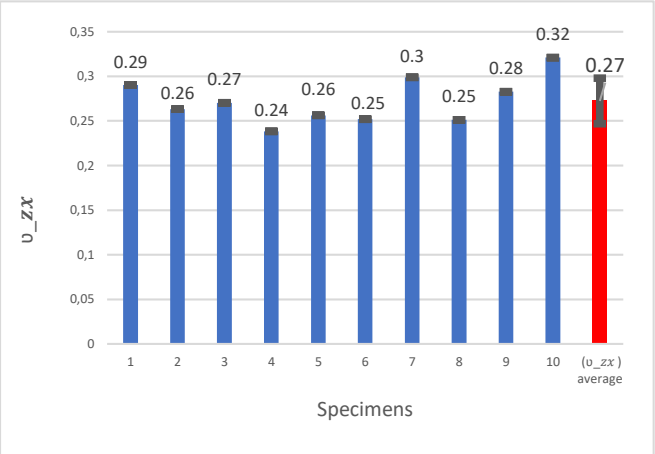

Figure 3: Apparent transverse contraction coefficient υ_{zx}

Results for the PVC80:

$\overline{E_z}$ = 76.5 MPa and $\overline{\upsilon_{zx}}$ = 0,272 => Ratio $= -\frac{\overline{\upsilon_{zx}}}{\overline{E_z}} = -\frac{0,27}{76,5} = -0,0035$

$\overline{E_y}$ = 50.05 MPa and $\overline{\upsilon_{yz}}$ = 0,188 => Ratio $= -\frac{\overline{\upsilon_{yz}}}{\overline{E_y}} = -\frac{0,19}{50.05} = -0,0038$

Using the same approach for the recycled PET80, this foam is also found to be transversely isotropic.

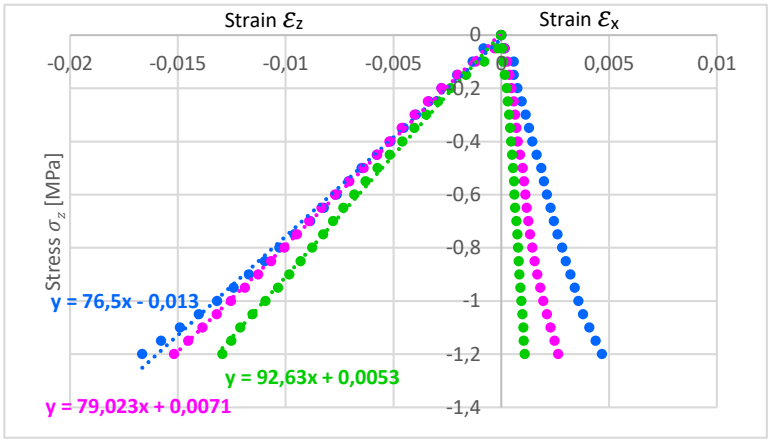

Figure 4: Experimental results PVC80 - Compression tests (3 specimen's dimensions)

Figure 4 shows the envelope of stress-strain curves obtained from the average of 10 different samples for each set of dimensions investigated (15x15x15 mm³, 30x30x15 mm³, 60x60x15 mm³) for the thickness direction. Accordingly, for the same material, PVC80 in this case, we have different apparent modulus for each set of dimensions (76.5 MPa, 79.023 MPa, and 92.63 MPa) which is proof that we are not in the case of uniaxial compression. And that is why a Finite Element model is needed to identify the intrinsic elastic parameters.

3.2 Shear tests

According to ISO 1922 standard (Rigid cellular plastics - Determination of shear properties) shear tests were conducted on the different types of foams in the $(\vec{x}, \vec{z})$ plane as in Figure 4 below in order to identify the last elastic parameter G_{xz} using the Digital Images Correlation (DIC method) [9].

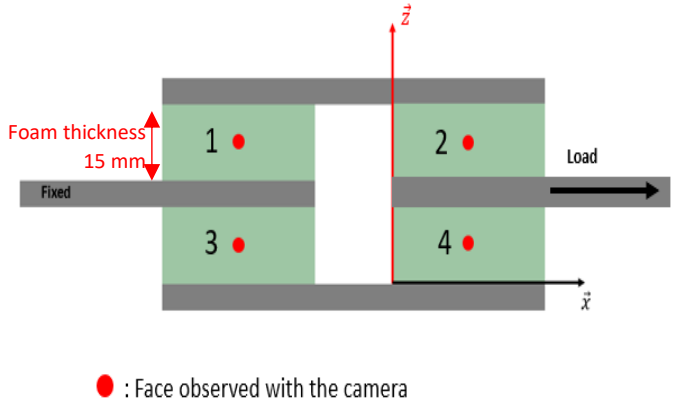

Figure 5: Shear test : $(\vec{x}, \vec{z})$ plane

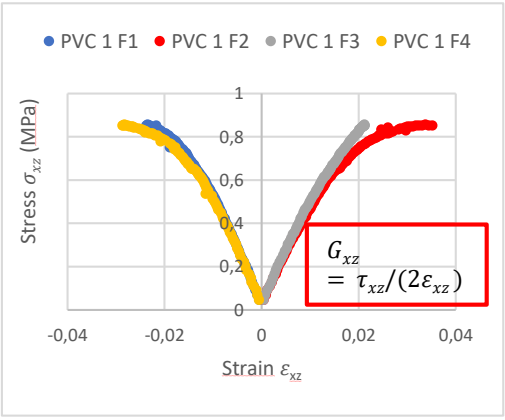

Figure 6: Experimental results PVC80 Shear tests (4 faces) - specimen 1

Based on the stress-strain experimental graphs shown in Figure 6, we determined the shear modulus G_{xz} for the different faces observed for each specimen. They are almost equal with an average of 24.35 MPa as shown in Table 2.

Table 2: Experimental results -Shear modulus G_{xz} (specimen 1)

Face	1	2	3	4
G_{xz} [N/mm^2]	24.71	23.09	24.02	25.56

Table 3 shows the different experimental results of the Shear modulus G_{xz} for the three types of foams. These results are similar to those shown in the datasheets for each foam (Table 1).

Table 3: Experimental results - Shear modulus [N/mm^2] Gxz for the different types of foams

Specimen	PVC 80	PETr 80	PETr 115
G_{xz} [N/mm^2] (Average)	27.04 (SD = 2.33)	12.19 (SD = 1.69)	21.89 (SD = 0.67)

Unlike the compression tests, the modulus G_{xz} calculated is an intrinsic parameter. The proof is shown on the graph below (Figure 7). The strain evolution profile is continuous all over the specimen. Accordingly, there is no need for a Finite Element model for this test.

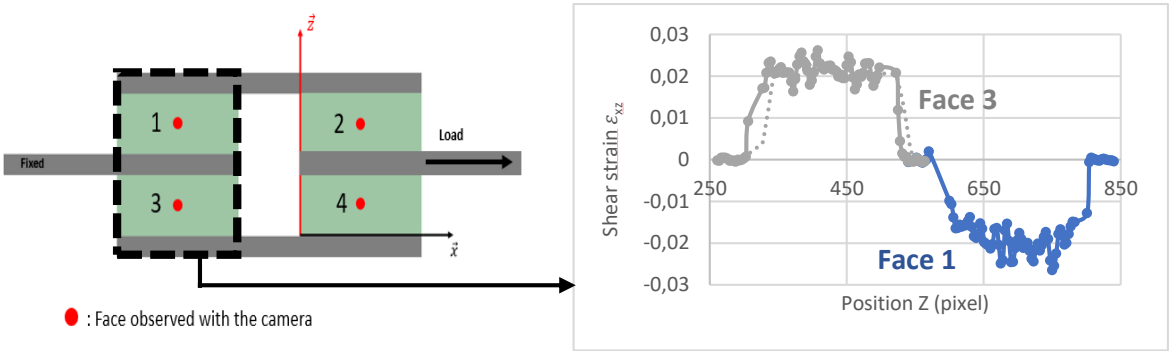

Figure 7: Strain evolution profile - specimen 1

4. Numerical simulations

4.1 Boundary conditions

As previously mentioned, we are not in the conditions of uniaxial compression. Therefore, in order to create a model which is as close as possible to the experimental test we imposed the following boundary conditions for the compression test in the thickness direction (Figure 8):

- Displacement Uz on the top face
- Displacement Ux = Uy on the sides
- Blocking the z displacement on the bottom face
- Applying two symmetries (along $\vec{x}$ and $\vec{y}$ axis)

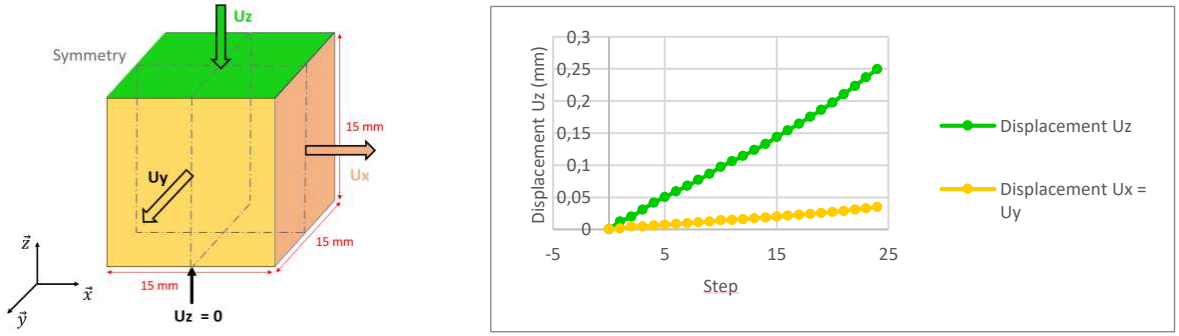

Figure 8: Boundary conditions for PVC80 - 15x15

Following the same concept, we imposed the boundary conditions for the compression test in the longitudinal direction ($\vec{y}$ axis).

4.2. Minimization

The method used to identify the intrinsic elastic behavior of the foam is based on a Finite Element Model Updating Method. An interface on Matlab linked to Python is created to link between the Finite Element model on Abaqus and the adjusting method on Matlab (Figure 9). This adjusting method, which already exists in Matlab's library, consists in minimizing the error between the experimental results and the simulated ones. As such, this error minimized is the average of the errors of the different compression tests in both the thickness and the longitudinal direction. Accordingly, the optimized elastic parameters (intrinsic) are those corresponding to the smallest error.

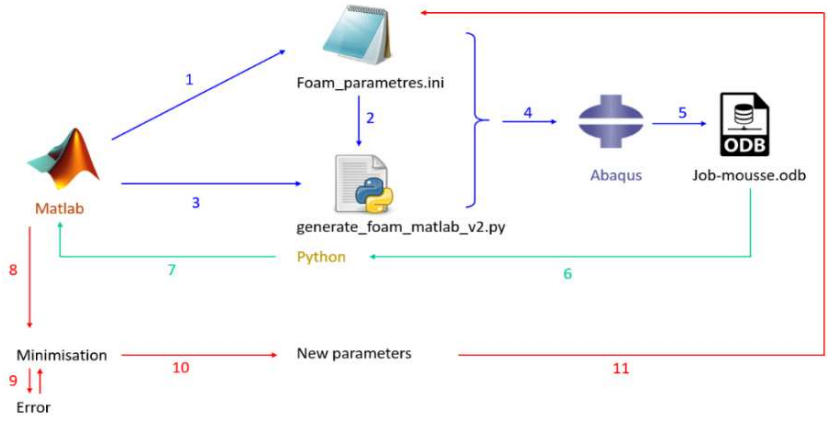

Figure 9: Interface Abaqus-Matlab-Python

  doi:10.5075/epfl-298799_978-2-9701614-0-0

5. Results and discussions

Figure 10 shows the different results of compressions tests conducted on 30x30x15 mm^3 specimens. The blue, green, and red graphs indicate the experimental, numerical before minimization (apparent), and numerical after minimization data respectively (optimized).

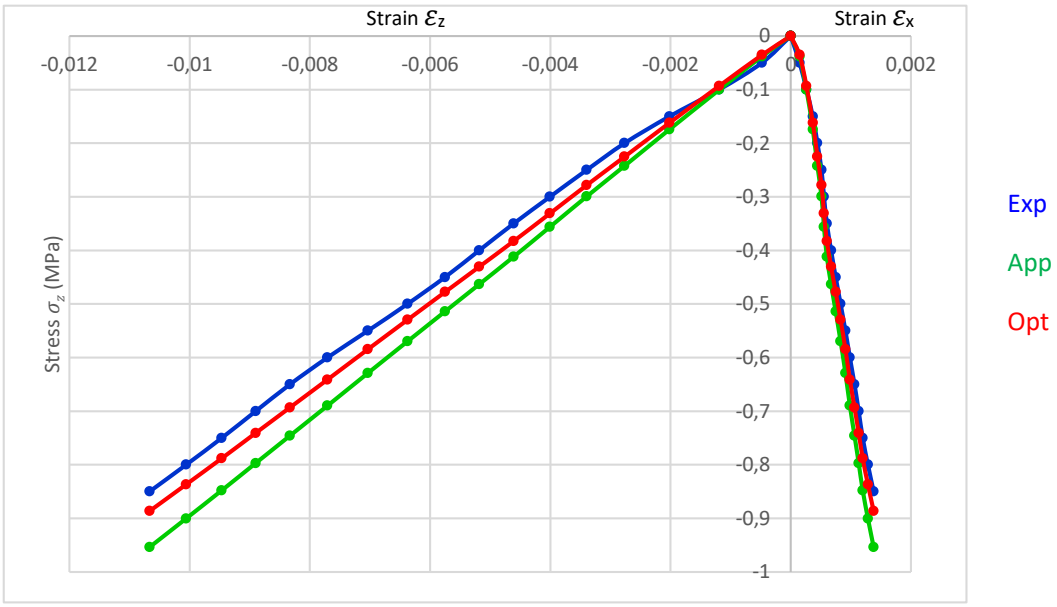

Figure 10: Numerical results - PVC80 (dimension specimen 30x30x15 mm^3)

The table 4 below shows the adjusted parameters obtained for the PVC80 and the PETr80 foams by minimizing the total error between the experimental and the numerical results for the different compression tests in parallel. By looking at the datasheets and the adjusted parameters, the datasheet Ez values are higher than the adjusted ones for both foams and the PETr80 always has a smaller Ez modulus than PVC80. Thus, as mentioned earlier, the values in the datasheets are based on standardized tests which are not following the theory of uniaxial compression, therefore, this FEMU method allows the determination of the intrinsic elastic parameters of the foams.

Table 4: Adjusted elastic parameters (compression tests)

Foam	Ey [N/mm^2]	Ez [N/mm^2]	υ_{xy}	υ_{yz}
PVC80	48.12	74.45	0.36	0.18
PETr80	19.14	42.95	0.32	0.15

6. Conclusions and perspectives

In this paper, an original method combining compression and shear tests, Digital Image Correlation (DIC) technique, and a Finite Element Model Updating Method (FEMU) was developed to characterize and predict the mechanical elastic behavior of PVC and PETr foams. The results analysis of the conducted compression tests showed that the PVC80 and the PETr80 foams represent a transversely isotropic behavior and the material parameters calculated are

considered apparent properties. DIC technique was successfully used to detect the surface strain for each compression and shear tests. Based on these experimental results, it has been confirmed that the conducted compression tests don't respect the theory of uniaxial compression. Therefore, a numerical model (on Abaqus) is developed by linking it to an optimization interface on Matlab which allowed us to adjust the material parameters by comparing the experimental and numerical properties in order to evaluate the real intrinsic elastic parameters of the foams (Young Modulus, Poisson's ratio …). This study will be complemented by establishing a statistical morphological model of the foam through a morphological analysis.

Acknowledgements

I would like to thank the Occitanie region for the funding of this thesis.

7. References

[1] P. Davies, D. CHOQUEUSE, P. CASARI, and H. DEVAUX, "Applications marines des matériaux composites - Cas des voiliers de compétition," *Tech. l'Ingénieur*, vol. 33, no. 0, pp. 1–16, 2014.

[2] Christophe BINÉTRUY, "Structures sandwiches," *Techcniques de l'ingénieur*, vol. 33, no. 0, 2012.

[3] A. T. Michael, "Characterization and modeling of biobased composites and structural insulated panels," no. June, p. 314, 2013.

[4] R. Burgueño, M. J. Quagliata, G. M. Mehta, A. K. Mohanty, M. Misra, and L. T. Drzal, "Sustainable cellular biocomposites from natural fibers and unsaturated polyester resin for housing panel applications," *J. Polym. Environ.*, vol. 13, no. 2, pp. 139–149, 2005.

[5] V. Tita, M. F. Caliri, R. A. Angélico, and R. B. Canto, "Experimental analyses of the poly(vinyl chloride) foams' mechanical anisotropic behavior," *Polym. Eng. Sci.*, vol. 52, no. 12, pp. 2654–2663, Dec. 2012.

[6] M. Francesco, S. Spadea, F. Fabbrocino, and P. Lonetti, "ScienceDirect ScienceDirect On the elastic properties of PVC foam," *Procedia Struct. Integr.*, vol. 28, no. 2019, pp. 1503–1510, 2020.

[7] Y. Wang and A. M. Cuitio, "Full-field measurements of heterogeneous deformation patterns on polymeric foams using digital image correlation," *Int. J. Solids Struct.*, vol. 39, no. 13–14, pp. 3777–3796, Jun. 2002.

[8] J. J. Feng and C. A. Bertelo, "Prediction of bubble growth and size distribution in polymer foaming based on a new heterogeneous nucleation model," 2004.

[9] S. Heinz and J. Wiggins, "Uniaxial Compression Analysis of Glassy Polymer Networks Using Digital Image Correlation," *Polym. Test.*, vol. 29, no. 8, Dec. 2010.

[10] D. Klempner, K. C. Frisch, and J. H. Saunders, "Handbook of Polymeric Foams and Foam Technology ".

  doi:10.5075/epfl-298799_978-2-9701614-0-0

TRANSPARENT ARMOUR REINFROCED BY BACTERIAL NANOCELLULOSE

Daniela, Wloch[a], Natalia, Herrera[a], Koon-Yang, Lee[ab]

a: d.wloch19@imperial.ac.uk, Department of Aeronautics, Imperial College London, South Kensington Campus, London SW7 2AZ, United Kingdom
b: Institute for Molecular Science and Engineering, Imperial College London, SW7 2AZ, United Kingdom

Abstract: *Bacterial nanocellulose (BC) is used to create highly transparent impact resistant composites with a total light transmittance of 89 %. The composites are produced by a fast and scalable UV-polymerization-based manufacturing process. BC nanopaper is an inherently strong and fracture resistant material and is used here as reinforcement for lightweight composites aiming for ballistic protection. It is shown that creating laminated composites with alternating layers of impact-modified acrylic sheets and bacterial cellulose nanopapers can increase the impact strength by 130 % compared to the pristine impact-modified acrylic sheet. It is further noteworthy that the stacking sequence influences the impact strength strongly where a sandwich-type layup is favoured over a block-type at the same amount of cellulose nanopapers used.*

Keywords: Bacterial cellulose, Nanopaper, Impact resistance, Transparency

1. Introduction

Bacterial nanocellulose (BC) is synthesized by bacteria such as *Komagateibacter* which results in an ultrapure and highly crystalline form of cellulose. The bacteria grow the cellulose directly into a network of intertwined cellulose fibres and ribbons, creating an intricate three-dimensional structure (1). The obtained membrane, which is also known as pellicle is white and jelly-like in appearance. Upon drying the pellicle, a nanopaper is formed with irreversible intra- and intermolecular hydrogen bonds forming in between the cellulose fibres. A single BC fibre has been estimated to have a bending modulus of 78 GPa (2) and a Young's modulus of up to 114 GPa (3), which surpasses the moduli of both Kevlar and Aramid fibres, some of the strongest industrially made fibres on the market today. The high stiffness and strength of the cellulose nanofibers is translated into the nanopaper which can reach a tensile modulus and strength of up to 17 GPa and 200 MPa respectively (4). These high tensile properties, beside the biodegradability and sustainability of the BC fibres have made it an attractive material for reinforcing especially biopolymeric matrices such as poly(lactic acid). Various researchers have poured their efforts into researching polymers reinforced by BC prepared by a variety of manufacturing methods, for applications such as packaging materials or as substrates for optoelectronic devices (5)(6)(7). It has however been shown that in general more than 30 wt.% of BC needs to be included into the polymer matrix to create composites with tensile properties exceeding those of a pristine poly(lactic acid) matrix (4). Since similar effects can be achieved with cheaper and more abundant natural fibres as filler materials, this work aims at exploring a different mechanical property of the BC network, namely its high fracture toughness. A BC nanopaper has a fracture toughness of 6.6 MPa $m^{1/2}$, which matches the one of a single Aramid fibre (8). The strong network forming capabilities of the BC combined with the hydrogen bonds in between the cellulose fibres create a highly fracture resistant material. In this work BC

  doi:10.5075/epfl-298799_978-2-9701614-0-0

nanopaper will be explored as a reinforcing material to bridge the current gap in impact strength between polymeric and silica-glass-based materials when it comes to impact resistance of transparent materials. Impact strength combined with a high level of transparency in materials becomes relevant in applications such as windshields, protective glazing, or transparent armour. Silica-glass-based composites are chosen today where high levels of impact resistance are required, with the disadvantage of a high weight, which is a major drawback in applications that require mobility. Therefore, this work explores to increase the impact resistance of impact-modified acrylic sheets through lamination with BC nanopaper. Different types of layups produced by a simple and scalable manufacturing process are explored in terms of impact strength and transparency.

2. Experimental

2.1 Materials

Impact-modified acrylic sheet (Plexiglas® Resist Clear 0RA65, 3 mm thick, light transmittance > 89 %) was purchased from Röhm GmbH (Darmstadt, Germany). BC in the form of pellicle containing 7 wt.-% solid content (dry grammage = 20 g m^{-2}) was purchased from Guilin Qihong Technology Co. Ltd. (Guilin City, China) and used as received. UV curable liquid adhesive (Dymax Ultra-Light Weld® 3069) was purchased from Intertronics (Oxfordshire, UK) and used as the adhesive to bond BC nanopaper to the impact-modified acrylic sheets. This adhesive belongs to the chemical class of acrylated urethanes and contains c.a. 25 - 39 wt.-% isobornyl acrylate and c.a. 10 - 24 wt.-% N,N-dimethylacrylamide and will further be referred to as acrylated urethane.

2.1.1 Preparation of BC nanopaper

BC nanopaper was prepared through a press-drying process. The as-received BC pellicle was cut into dimensions of 70 × 70 mm and directly press-dried between filter paper and several layers of blotting paper for 30 min at 120 °C under a weight of 1 tonne using a heated hydraulic press (Model 4122CE, Carver Inc., Wabach, IN, USA). The thickness of the resulting BC nanopaper, see Figure 1a, is ∼25 µm. All prepared BC nanopapers were stored in zip-lock sample bags containing silica gels to reduce ingress of moisture prior to subsequent use.

2.1.2 Preparation of BC nanopaper-reinforced impact-modified acrylic laminated composites

Prior to laminating the BC nanopaper with impact-modified (IM) acrylic, the BC nanopaper was vacuum impregnated with the UV curable acrylated urethane at a reduced pressure of 200 mbar and room temperature overnight. Concurrently, the as-received impact-modified acrylic sheet was compression moulded into a 70 × 70 sheet to the desired thickness using a heated hydraulic press (Model 4122CE, Carver Inc., Wabach, IN, USA) at 180 °C. The IM-acrylic composites reinforced with BC nanopaper were produced by sandwiching the impregnated BC nanopaper in between sheets of IM-acrylic and cured in a UV-light curing flood lamp system (Dymax ECE 5000, Intertronics, Oxfordshire, UK) for 6 min. The intensity of the flood lamp used was 225 mW cm^{-2}. Different setups of laminated composites were created, containing one, three or five layers of BC nanopaper in either a block or sandwich layup. Reference composites were created without the nanopaper by adhering sheets of IM-acrylic together with the acrylated urethane adhesive. All created composites have a final thickness of 3.5 mm. The samples are named showing their BC nanopaper content and layup, e.g., IM-acrylic+3SBC, contains three layers of BC nanopapers in a sandwich-type layup, see Figure 1c. To study the properties of the

thin layer in between the IM-acrylic sheets, thin film samples were prepared by polymerising films of the acrylated urethane adhesive and the impregnated BC nanopaper. These were polymerised for 1 minute in the aforementioned UV-light flood lamp system. The thin films have a thickness of 100 µm.

2.2 Characterisation

2.2.1 Optical light transmittance and haze

The total light transmittance of all specimens was measured using a UV-vis spectrophotometer (LAMBDA 365, PerkinElmer, Beaconsfield, UK) fitted with a 50 mm integrating sphere. The scanning wavelength was 200 – 700 nm at a scan speed of 240 nm/min. The haze was determined based on ASTM D1003 with the following equation

$$Haze = \left(\frac{T_4}{T_2} - \frac{T_3}{T_1}\right) * 100\% \quad (1)$$

where T_1 to T_4 describe different measurement setups. T_1 and T_3 are the background measurements without samples, one with the white standard for total transmittance, one with an open port for diffuse transmittance respectively. T_2 and T_4 are the equivalent total and diffuse measurements with the samples.

2.2.2 Charpy impact strength

Charpy impact strength was measured in accordance with ISO 179-1:2010 using a Charpy impact tester (Model 5102.100, Zwick Roell Ltd., Herefordshire, UK). A 2 J pendulum was used, and the impact velocity was estimated to be 2.97 m s^{-1}. Rectangular test specimen with dimensions of 40 mm × 10 mm × 3.5 mm were cut using a CO_2 laser cutter (Model VLS3.60, Universal Laser Systems GmbH, Vienna, AT) and used in this test. All samples were tested flatwise with a span length of 25 mm. Average results of five specimens were reported for each sample.

3. Results and Discussion

3.1 Optical properties

Figure 1 shows the difference between the BC nanopaper and the prepared composites, with the nanopaper being white, whereas all composites exhibit high levels of transparency and clarity.

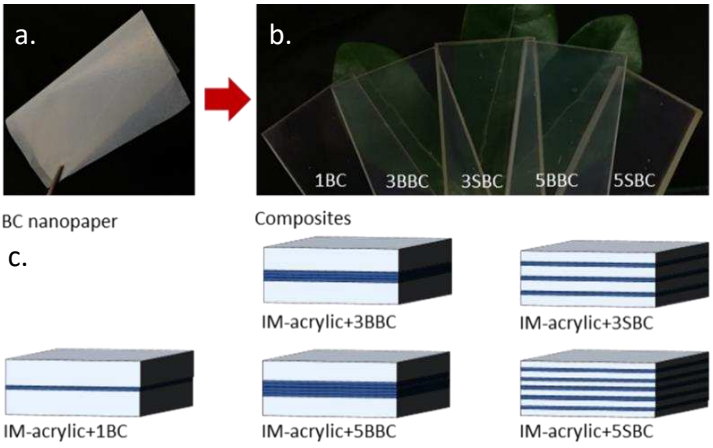

Figure 1. a. BC nanopaper, b. Block and sandwich composites, c. Schematic layup of composites

More precise details of light transmittance can be found in Figure 2, showing the measured UV-vis spectra. The light transmittance of the BC nanopaper is 60 % at 550 nm whereas the acrylated urethane and the thin film sample both exhibit higher transparency with 89 % and 85 % respectively. Light transmittance can be reduced by various phenomena occurring in the material such as absorption, reflection, scattering and refraction of the incident light. Scattering is due to local inhomogeneities of the optical properties in the material, as would be found in a composite whereas the other properties are defined by the average optical properties of the material (9). All three phenomenon occur due to differences in refractive index between the materials involved. In a composite the optical properties and light transmittance are governed by the amount of filler material, the diameter of the filler fibres and the difference in refractive index between the matrix and the filler material (10). The bigger the difference in refractive index, the more prominent become the influences of fibre volume fraction and size. The more filler material and the larger the fibre diameter, the lower the light transmittance. To minimize the effects of the cellulose nanofibers on the optical properties of the composites, the acrylated urethane resin was chosen to match the refractive index of the cellulose fibres, which is 1.618 in longitudinal and 1.543 in transverse fibre direction (11). The effect of the similar refractive indices can be seen in the increased total light transmittance of the thin film compared to the pristine nanopaper. The same is valid further in the laminated composites, which all exhibit high levels of light transmittance as seen in Figure 1b. A slight downward trend is observed though, accompanying the increasing amount of cellulose nanopaper in the specimens. Notable here is the difference between the block and sandwich composites, with the block composites reaching higher levels of transmittance. At 550 nm the IM-acrylic+3BBC and the IM-acrylic+3SBC have a total light transmittance of 82 % and 79 % respectively. A similar difference of 2 % in total light transmittance is found between the IM-acrylic+5BBC and the IM-acrylic+5SBC. The additional layers and interfaces created in the sandwiched composites lead to further light scattering and reflection, compared to the block samples, with the transmittance decreasing proportionally with the increase in layers of material in the composite. As a reference a laminated composite with six layers of IM-acrylic without the BC nanopaper was prepared, with a light transmittance of 86 %. The lowered transmittance compared to the IM-acrylic+Acrylated urethane with only two layers of IM-acrylic shows that the reduction in light transmittance is an effect of the increase in material layers as well as the addition of BC nanopapers.

  doi:10.5075/epfl-298799_978-2-9701614-0-0

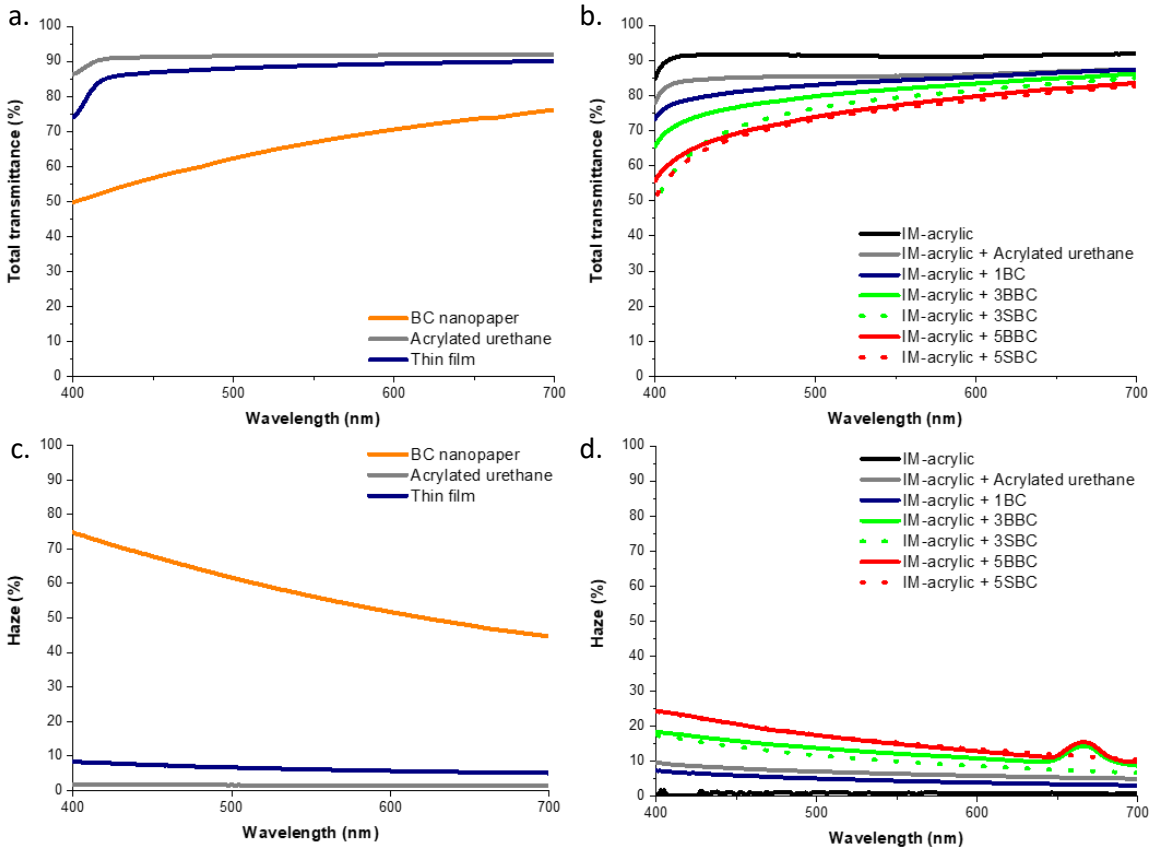

Figure 2. a+b. Total light transmittance of BC nanopaper, thin film and IM-acrylic composites, c+d. Haze of BC nanopaper, thin film and IM-acrylic composites

The haze values of the BC nanopaper and thin film are shown in Figure 2c. Compared to the nanopaper, the haze in the thin film is drastically decreased from 56 % to 6 % at 550 nm. Since the porosity is high in the nanopaper, being 35 %, the incident light is scattered at all air-fibre interfaces. Filling the pores with the acrylated urethane resin decreases the amount of scattering in the sample and therefore the total haze. This is therefore also a good indication for the successful impregnation of the BC nanopaper with the resin. Looking at the haze values of the laminated composites, the haze is generally low for all samples, at 4 % for IM-acrylic+1BC increasing to 15 % for IM-acrylic+5SBC. The increase is explained by the introduction of additional layers of BC nanopaper, which is a light dispersing material. Even though the haze is reduced in the thin film through the impregnation with the acrylated urethane, the addition of in total five layers of BC in the IM-acrylic+5SBC increases the probability of light scattering through the increased volume fraction of fibres in the composite. There is about a 2 % difference in haze between the block and sandwich samples of each set of either three or five layers of BC nanopaper in the sample, showing that there is a slight influence of the stacking sequence of the composite on the haze of the final material.

3.2 Impact strength

The Charpy impact strength of all composite samples and the pristine IM-acrylic sheets were measured in the flatwise direction, which most closely relates to an impact in a real-life setting of the material as a windshield or protective glazing. The results of the impact testing can be found in Figure 3. It is noted that there is no difference in impact strength between the pristine

IM-acrylic and the IM-acrylic+Acrylated urethane. Both are of the same thickness, which shows that the manufacturing process and the addition of the soft resin and the chosen manufacturing process does not influence the impact strength of the composites. Upon addition of one layer of BC nanopaper however, the impact strength increases from 11.6 kJ m^{-2} to 17.2 kJ m^{-2} compared to the pristine IM-acrylic sheet. A clear upward trend is observed the more layers of BC nanopaper are added, resulting in an impact strength of 26.7 kJ m^{-2} for the IM-acrylic+5SBC, an increase of 130 % compared to the IM-acrylic sheet. Interestingly, there is a clear difference between the block and sandwich samples in terms of impact resistance. Since the BC nanopaper content is 1 – 3wt.% for all laminated composites, the lamination sequence must have an influence on the impact behaviour. In both cases it is clear, that an added amount of BC nanopaper is favourable for an increase in impact strength, due to the high fracture toughness and strength of the BC itself. In the sandwich-layup the crack has to propagate over several material interfaces, from tough to weak and weak to tough material. It easily propagates from the tough IM-acrylic outer layer into the weak resin, but from the resin into the BC or the IM-acrylic layers, the driving force for the crack to propagate becomes very low (12,13). Every additional transition through a weak to tough interface reduces the driving force which increases the composites impact strength. This mechanism of crack growth inhibition even increases the impact strength without the need for delamination (14). In the sandwich-layup far more of these interfaces are present than in the block layup, even at the same amount of BC nanopapers, leading to a difference in impact strength. To show that the BC nanopaper plays a vital role in the composite, the reference laminated composite with six layers of IM-acrylic without BC nanopaper was measured and its impact strength is 20 J m^{-2}, which admittedly is higher than for the pristine IM-acrylic sheet and the IM-acrylic+1BC but 33 % lower than the same composite with BC nanopapers. The toughening effect of thin interlayers in a structure with varying Young's moduli between the laminated materials can be found in nature in materials such as nacre, bone or biosilica, leading to both a high stiffness and toughness in these materials (15). It has been shown that a difference in Young's modulus greater than five can lead to significant crack deflection and stopping, as is the case in the composites produced here, with the Young's moduli of the IM-acrylic, the BC nanopaper and the acylated urethan resin are 2 GPa, 10 GPa and 0.11 MPa respectively. This structure is wider known as a brick-and-mortar structure and has been found to increase the composites toughness without compromising their mechanical strength (16).

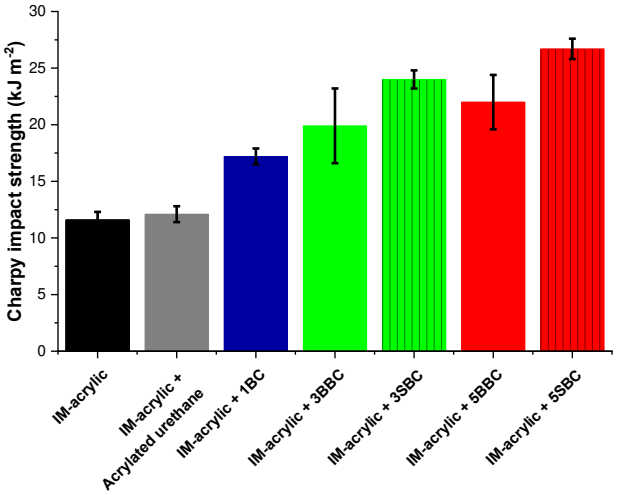

Figure 3: Flatwise Charpy impact strength of IM-acrylic composites

4. Conclusion

Highly transparent laminated composites of BC nanopaper and IM-acrylic were created with a fast and scalable UV-polymerisation based manufacturing process. It was shown that through matching of refractive indices and good impregnation of the BC nanopaper with the acrylated urethane resin composites with a total transmittance of 76 – 89 % at 550 nm could be prepared. The haze was highest for the IM-acrylic+5SBC composite, but with 15 % at 550 nm it still showed high optical clarity. The impact strength of the composites was evaluated through Charpy impact strength measurements, and the impact resistance was increased by up to 130 % in the IM-acrylic + 5SBC composite compared to the IM-acrylic sheet.

5. References

1. Mühlenthaler K. The structure of bacterial cellulose. In: Biochimica et biophysica acta 1949. 527–35.

2. Guhados G, Wan W, Hutter JL. Measurement of the Elastic Modulus of Single Bacterial Cellulose Fibers Using Atomic Force Microscopy. Langmuir 2005; 21(14):6642–6.

3. Hsieh YC, Yano H, Nogi M, Eichhorn SJ. An estimation of the Young's modulus of bacterial cellulose filaments. Cellulose 2008; 15(4):507–13.

4. Lee KY, Aitomäki Y, Berglund LA, Oksman K, Bismarck A. On the use of nanocellulose as reinforcement in polymer matrix composites. Compos Sci Technol 2014; 105:15–27.

5. Gindl W, Keckes J. Tensile properties of cellulose acetate butyrate composites reinforced with bacterial cellulose. Compos Sci Technol 2004; 64:2407–13.

6. Barud HS, Ribeiro SJL, Carone CLP, Ligabue R, Einloft S, Queiroz PVS, et al. Optically transparent membrane based on bacterial cellulose/ polycaprolactone. Polimeros 2013; 23(1):135–8.

7. Ummartyotin S, Juntaro J, Sain M, Manuspiya H. Development of transparent bacterial cellulose nanocomposite film as substrate for flexible organic light emitting diode (OLED) display. Ind Crops Prod 2012; 35(1):92–7.

8. Hervy M, Santmarti A, Lahtinen P, Tammelin T, Lee K. Sample geometry dependency on the measured tensile properties of cellulose nanopapers. Mater Des 2017; 121:421–9.

9. van Krevelen DW, te Nijenhuis K. Optical properties. In: Properties of Polymers. Elsevier B.V.; 2009. 287–318.

10. Iba H, Kagawa Y. Light transmittance of continuous fibre-reinforced composites: Analysis, model experiment and parametric study. Philos Mag B 1998; 78(1):37–52.

11. Brandrup J, Immergut EH, Grulke EA. Polymer Handbook. 4th ed. New York: Wiley; 1999.

12. Kolednik O, Predan J, Fischer FD, Fratzl P. Bioinspired Design Criteria for Damage-Resistant Materials with Periodically Varying Microstructure. Adv Funct Mater 2011; 21(19):3634–41.

13. Kolednik O. The yield stress gradient effect in inhomogeneous materials. Int J Solids Struct 2000; 37(5):781–808.

  doi:10.5075/epfl-298799_978-2-9701614-0-0

14. Zechner J, Kolednik O. Fracture resistance of aluminum multilayer composites. Eng Fract Mech 2013; 110:489–500.

15. Fratzl P, Gupta HS, Fischer FD, Kolednik O. Hindered crack propagation in materials with periodically varying young's modulus - Lessons from biological materials. Adv Mater 2007; 19(18):2657–61.

16. Magrini T, Bouville F, Lauria A, Le Ferrand H, Niebel TP, Studart AR. Transparent and tough bulk composites inspired by nacre. Nat Commun 2019;10:1–10.

ENHANCED ANTI-IMPACT PERFORMANCE OF COMPOSITE SANDWICH PANELS WITH MODIFIED POLYURETHANE FOAM CORES, EXPLOITING PHASE TRANSITION OCCURRENCE OF NON-NEWTONIAN POLYMER.

Konstantinos Myronidis[a], Michele Meo[a], Fulvio Pinto[a]

[a]: Department of Mechanical Engineering, University of Bath, Bath BA2 7AY, UK

km515@bath.ac.uk

Abstract: *Lightweight, flexible and low-cost materials which possess great energy absorption properties are in great demand in composite sandwich panels, and in body protective equipment used in sports and military. One of the most widely used materials in these applications is polyurethane foam (PUF), showing good energy absorption and shape restorability under low-rate dynamic loading conditions. However, their response to high-rate dynamic loading conditions can lead to cell wall damage significantly hindering their performance. In this work, a non-Newtonian polymer with high energy dissipation efficiency was selected as an excellent candidate for the enhancement of the mechanical properties of PUFs. Low Velocity Impact tests were employed directly on foams, composite sandwich panels and post-impact for the evaluation of their residual properties. Results indicated that the presence of the non-Newtonian polymer led to an improvement of the energy dissipation of the modified foams, averting cell wall damage, constituting these as ideal core structure candidates.*

Keywords: Sandwich panels, CFRP, Polyurethane foams, SSG.

1. Introduction

Polyurethane foams (PUFs) have been employed extensively in composite sandwich panels and protective applications where a combination of good impact energy absorption characteristics, low-weight and low-cost solutions is required, with industries ranging from sports protective equipment to body armours for military and law enforcement agents, to guarding devices for elderly people and automotive trim (1). These attractive attributes in combination with a relatively simple manufacturing process and flexibility offered to the end user, position PUFs among the first-choice materials in these sectors. One of the main disadvantages of PUFs though is their poor resistance to high-rate compressive loads, which results in permanent damage in the cell walls of their polymeric network (2) diminishing their mechanical properties.

In order to address this issue and to further improve the protective performance of PUFs, this work suggests the incorporation of an impact resistant, non-linear polymer, that belongs to particular non-linear polymers often referred as Shear Stiffening Gels (SSGs). SSGs belong to a broader family of materials which show a divergent behaviour from Newtonian fluids, namely Shear Thickening Fluids (STFs), and display rate-dependant, shear thickening characteristics. Although the underlying mechanism between STFs (3) and SSGs is significantly dissimilar, macroscopically these materials behave in a very similar way, displaying a rapid rise in stiffness in response to increasing applied shear rates. In particular for SSGs, a phase transition between viscous and rubbery state occurs under increasing shear frequencies, with this occurrence

  doi:10.5075/epfl-298799_978-2-9701614-0-0

regulated by the constituents in the formulation of the gel, resulting in the exemplary energy absorption characteristics of the material (4).

The implementation of SSG into PUFs has attracted considerable attention recently with two manufacturing processes emerging, a dip-coating and an one-step foaming process. Wang et al. (5) synthesised an SSG which was firstly dissolved in alcohol and acetone, and at a second stage immersed and dried into a PUF, which enabled the creation of a knee pad with safeguarding performance. The modified PUF showed great flexibility and enhanced impact characteristics in comparison to neat PUFs, by approximately two orders of magnitude. Fan et al. (6) selected a similar manufacturing method, introducing carbon nanotubes into the SSG, with the implementation to PUF conducted by spray-coating; in addition to the conductivity introduced to the new PUF/SSG structure, the attenuation of impact force achieved measured during a ball-drop experiment reached up to 71%, compared to 21% achieved by PUF only structures. A one-step foaming process of PUF incorporating SSG was investigated by Xiaoke et al. (7), with the modified structure showing improved strain rate sensitivity and superior specific strength and energy absorption characteristics compared to neat PUF. In subsequent studies on the same manufacturing process (8, 9), it was demonstrated that there was no chemical reaction between PU and SSG during this process, with the modified PUFs demonstrating enhanced energy absorption characteristics during impact events and additional desirable characteristics such as shape memory performance.

Based on these premises, it is evident that the introduction of SSG into PUFs can enhance the energy absorption characteristics of these and improve their impact resistance; based on these considerations, in this work both manufacturing processes of modified PUFs utilising SSG are investigated, with resulting structures employed as cores for CFRP sandwich panels. The constituents of the foam structures and the final products were thoroughly investigated via means of chemical and mechanical characterisation and a series of low velocity impact events on various configurations were used to assess their energy absorption characteristics.

2. Synthesis and Manufacturing

The manufacturing of the sandwich panels commenced with the synthesis of the polyborosiloxanes for the SSG, in a process as previously reported by our group (10). Polydimethylsiloxane (PDMS) and boric acid with a stoichiometric ratio of boron-to-silicon of 0.15 were homogenised in the presence of ethanol and reacted at 180 °C for 72 hours. The solution was left to cool at room temperature and then collected from the reacting container. The ratio of the constituents was carefully selected, in order to result into a rather viscous SSG which would promote its successful incorporation to the PUFs.

The second step of the manufacturing involved the incorporation of the SSG into PUF structures; two different methods were investigated, a one-step foaming process and a “Dip’n’Dry” method, as illustrated in Figure 1 below.

  doi:10.5075/epfl-298799_978-2-9701614-0-0

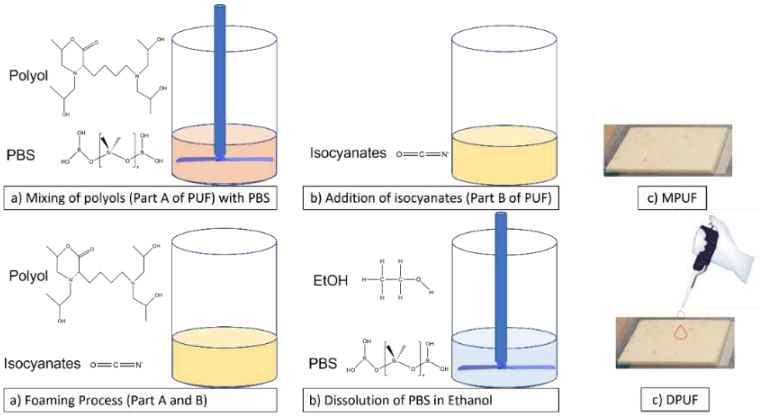

Figure 1 Manufacturing processes of modified PUFs. Top row, one-step foaming process (MPUF), bottom row "Dip'n'Dry" process (DPUF).

In the first method (top row Figure 1), the SSG and the polyols from the PUF were mechanically mixed with a stirrer at 1000 RPM for 1 Hour. Subsequently and upon careful examination of the homogenisation of the mixture, the isocyanates of the PUF were added to the solution, thoroughly mixed, and poured into a closed mould where the foaming process eventuated. In the second process, polyol and isocyanates (bottom row Figure 1) were firstly thoroughly mixed and poured into a closed mould for the foaming process; in a separate reacting container, the same amount of SSG was dissolved into ethanol and then immersed into the PUF. The modified PUF was then heated at 100 °C for 1 hour to allow for the evaporation of the solvent. For both manufacturing methods the amount of SSG employed to the modified PUFs was kept constant at 15% of the weight of the polyols. In addition to the modified PUFs, control PUFs were also manufactured to allow for evaluation of the performance of the modified PUFs. The resulting foam structures were labelled as MPUFs for the one-step foaming process, DPUFs for the "Dip'n'Dry" process and PUFs for the control samples.

The final steps of the manufacturing process entailed the preparation of the facesheets of the sandwich panels and their final assembly. Four layers of 2x2 twill carbon fibre prepreg were utilised per facesheet (XPREG® XC110 by Easycomposites) with a 3K filament count and areal weight of 210 gm^{-2}. Finally, all PUF cores were adhered to the facesheets using a prepreg adhesive film (XA120 by Easycomposites).

3. Results and discussion

Prior to the evaluation of the impact resistance of the sandwich panels via means of low velocity impact (LVI), mechanical and chemical characterisation of the constituents of the core structures was performed, in an attempt to investigate the effect of SSG into the foam structures.

3.1 Dynamic Measurements

In order to demonstrate the ability of the proposed SSG to store energy under increasing applied shear rates, oscillatory rheological measurements were employed. The rheometer in situ was a DHR-2 from TA instruments with a 25 mm parallel plate configuration. The frequency ranges investigated were between 0.01 and 100 Hz, in room temperature. The resultant storage (G') and loss (G'') moduli over the examined frequencies were drawn in logarithmic scales and depicted in Figure 2a. In addition to the rheological measurements of the SSG, Dynamic Mechanical Analysis was performed on all foam structures (Figure 2b), to evaluate their properties under dynamic loading conditions and to investigate the effect of the presence of

SSG to the PUF's ability to absorb energy. The instrument employed in these measurements was a Mettler Toledo DMA. The range frequencies investigated were between 0.1 and 20 Hz, carefully selected as to contain the range where the phase transition of the SSG eventuates and to eliminate the non-linearities of PUFs occurring towards higher spectra.

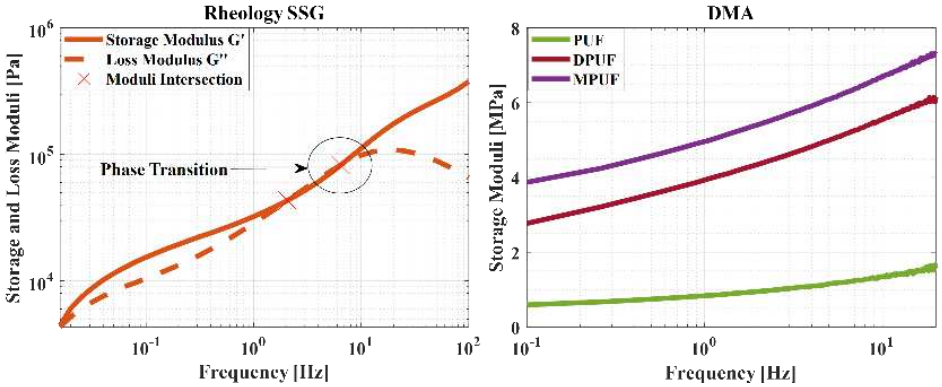

Figure 2 Dynamic measurements via a) Oscillatory rheological measurements of SSG, where Storage modulus (G') in continuous orange line, Loss modulus (G'') in dashed orange line with moduli intersections marked with red markers, and b) DMA on neat PUF (green line), DPUF (magenta line) and MPUF (purple line).

The examination of the progression of the curves for both moduli of the SSG indicates a non-linear material with frequency dependant properties. The values of G' at the start of the measurements remain at very low levels which can attributed to the viscous nature of the gel. Increasing the frequency of the oscillations during the measurements reflects to a rise in the values for both moduli, with the rather low ratio of dynamic boron oxygen bonds resulting in the intertwining of the moduli at a first stage (11). As the frequency range is increased and at approximately 6.46 Hz, a clear increase in the values recorded for G' appears and thereafter those for G'' follow a regressive trend. At this stage, a phase transition occurs in the material, from viscous to rubbery stage, which macroscopically gives rise to the stiffness of the SSG. In a microscopic level, a dynamic breaking and reformation of the boron oxygen covalent bonds occurs, with this restricting the disentanglement of the Si polymeric backbone of the SSG, resulting in energy consumed into this event and a solid-like behaviour of the material (12). The difference between G' minimum at 0.01 Hz and G' maximum at 100 Hz was approximately 371 KPa, a clear demonstration of the proposed SSG's energy absorption capabilities as a response to an external stimulus.

The results from DMA further corroborated the findings from the rheological measurements; the neat PUF sample (green line) displayed a typical behaviour of PUFs, with a maximum value of storage modulus of 1.66 MPa and an overall change of 1.07 MPa, in good agreement with literature (13). At the same time, both samples containing SSG clearly demonstrated a frequency dependant behaviour. The DPUF sample recorded a maximum storage modulus value of 6.15 MPa, whereas the MPUF 7.31 MPa. Although the minimum values for these samples were considerably higher compared to the PUF sample, the overall change was approximately 3.4 MPa on both occasions, ought to the presence of SSG; under increasing rates of deformation, the phase transition of the SSG observed in the rheological measurements is initiated, which is translated into a clear frequency-dependant response of the modified foam structures and an ability to store greater amounts of energy as opposed to neat PUF.

  doi:10.5075/epfl-298799_978-2-9701614-0-0

3.2 Fourier Transform Infrared Spectroscopy

The chemical characterisation of the SSG and PUFs was conducted via means of Fourier transform infrared spectroscopy (FT-IR), with the instrument employed for these being a Perkin Frontier Elmer FT-IR spectrometer. The measurements, depicted in Figure 3, included direct comparisons between the PDMS precursor (cyan line) used for the synthesis of the SSG, and the final SSG product (orange line) at a first stage, and at a second stage a direct comparison between a neat PUF (green line) and a MPUF (purple line), measured over a wavenumber frequency between 4000 cm^{-1} and 600 cm^{-1} which provided the required spectra.

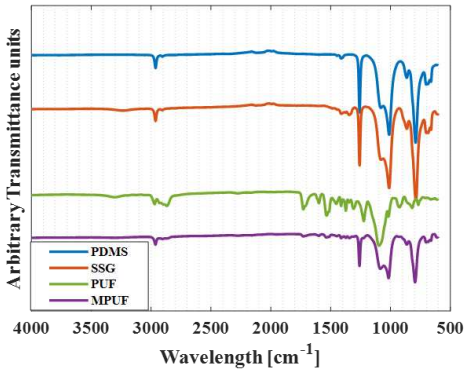

Figure 3 FTIR spectra obtained from PDMS precursor (cyan line), SSG (orange line) neat PUF (green line) and modified PUF with SSG (purple line).

In a direct comparison between the PDMS precursor and the SSG, two significant peaks can be identified which significantly differentiate the latter from its precursor, with the first found at 3200 cm^{-1} (O–H, broad peak) stretch and the second at 1300 cm^{-1} (B–O, s) stretch (14). The first stretch peak at 3200 cm^{-1} in comparison to the neighbouring signal of 2900 cm^{-1} can be attributed to methyl groups (CH_3) in the Si. The two peaks in conjunction indicate that a conversion of boric acid into the SSG backbone eventuated, leading to a formation of a dynamic network (15). The spectra obtained from neat PUF came in good agreement with literature (16), with the presence of a peak at 1379 cm^{-1} and the absence of one at 2269 cm^{-1}, indicating full reaction for the neat PUF. Evaluating the spectra obtained from the MPUF, absorption peaks eventuating at 1260 cm^{-1} and 790 cm^{-1}, due to the presence of Si-C bonds of the SSG, suggest that a masking effect takes place during the acquisition of the spectra which cannot be attributed to chemical crosslinking (9), leading to the creation of a double polymeric network with only physical changes.

3.3 Low Velocity Impact

The LVI tests were performed according to the ASTM 7136 standard (17), with three samples tested per typology of samples at an energy level of 8.5 J. The dimensions of the facesheets were 150x100 mm and the core thickness 15 mm for all typologies. The drop-weight tower employed in the tests consisted of a shuttle of 4.66 kg in weight, equipped with a hemispherical tip of 15mm. The acquisition of the impact data was achieved via a load cell and an oscilloscope connected to a PC. The impact energy level was achieved by adjusting the height from which the shuttle was released, and via Eq.(1).

$$E=mgh \quad (1)$$

In Eq.(1), E is the impact energy in J, m the mass of the shuttle in kg, g the gravitational acceleration taken as 9.806 ms^{-2} and h the height from which the shuttle was released in m. The

force-time data were integrated twice in respect to time via MatLab, and force-displacement curves of the impacted sandwich panels were drawn, which allowed for the evaluation of the energy absorbed by these. The LVI events were conducted at three stages; at first, impacts were conducted on the core structures directly, which were positioned on a CFRP facesheet utilised as a substrate (Figure 4a). The next set of impacts were conducted on sandwich panel configurations (Figure 4b), whereas for the last set of tests, the impacted sandwich panels had their undamaged bottom facesheets removed, and the impact events took place directly on the foam structures with the damaged top facesheets acting as substrates (Figure 4c), which allowed for the evaluation of the residual strength properties of all foam structures and whether the presence of SSG in the modified structures led to their improvement.

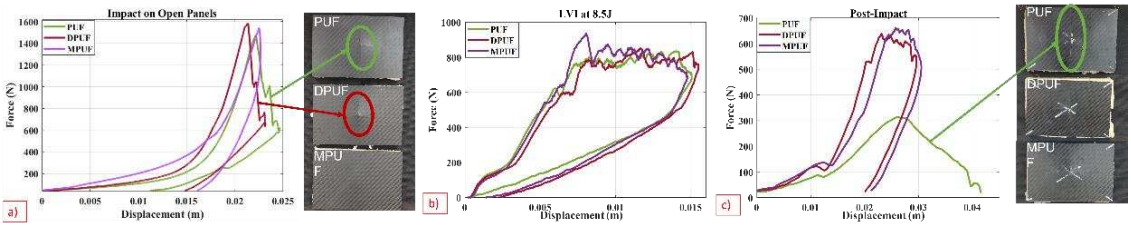

Figure 4 Force-displacement curves obtained from an impact energy level of 8.5 J, a) LVI on open foam structures, b) LVI on sandwich panels and c) LVI on previously impacted samples. PUF in green line, DPUF in magenta line and MPUF in purple line.

In the first set of impact events, that directly on the cores (Figure 4a), both PUF and DPUF samples appeared with similar responses, with the DPUF sample reaching maximum forces (Fmax) at lower displacements (-9%), a behaviour that can be attributed to the presence and underlying mechanism of the SSG. The oscillations in the curves appearing past Fmax designate damage occurring at the substrate (insert Figure 4a). The MPUF samples revealed a different response with an almost purely elastic behaviour and no obvious signs of damage to the substrate, as it is possible to appreciate from the evolution of the closed curve, with no oscillations appearing past Fmax.

The next set of impacts was conducted on composite sandwich panels. As it is possible to evaluate from the progression of the curve for the PUF sample (green line) in the LVI events of the sandwich panels (Figure 4b), the failure of the top skin occurred at approximately 600 N and thereafter a prolonged damage plateau appears resulting to a closed curved, suggesting that the there was no perforation of the bottom skin of these samples, with some core crushing. The maximum force values recorded were 833 N, at close proximity to the maximum displacement recorded at 15 m^{-3}. The energy absorbed by this typology of samples was approximately 4.84 J. The DPUF sample (magenta line) also avoided perforation of the bottom skin; the curve progression though in this case indicates a more ductile response from the target, in comparison to the PUF one, with a smoother first drop in the force values further corroborating this occurrence. The maximum forces and displacement recorded for this typology were at approximately the same levels as the neat PUF samples, with an increase in the energy absorbed by the sample at approximately 5.17 J. The MPUF sample (purple line) appeared to have sustained top skin failure at approximately 35% increased force value compared to the PUF sample, which was the maximum force at the same time. The maximum displacement was evaluated at similar levels to the other samples (15 m^{-3}) and an increase in the amount of absorbed energy was achieved, at approximately 5.37 J. All values of interest have been tabulated in Table 1 below.

Table 1 Average values of interest obtained during LVI events

Sample	Max Force [N]	Max Displacement [m^{-3}]	Top Skin Force failure [N]	Absorbed Energy [J]
PUF	833	15	610	4.84
DPUF	830	15.5	600	5.17
MPUF	933	14.8	933	5.37

In the impacts events for the evaluation of the residual properties of the sandwich panels (Figure 4c), the PUF samples displayed an open curve, an indication of perforation to the substrate and an inability of the PUF to offer any further protection. On the contrary, both DPUF and MPUF panels displayed closed curves and attained higher forces, as the presence of SSG increases the impact resistance of the structures averting catastrophic failure of the substrate. The inability of PUF to resist permanent deformation at higher dynamic loading conditions resulting in cell wall damage is evident in these tests; the poor residual properties of PUFs can only be attributed to permanent damage in the cells of the polymeric network, whereas at the same time both typologies incorporating SSG improved the residual strength of the structures. The avoidance of catastrophic failure of the substrates suggests that the damage of the sandwich panels was superficial and concentrated on the face sheets due to the presence of SSG. Indeed, during impact on the modified foams, the phase transition from viscous to rubbery state of the SSG occurs, with impact energy absorbed in its dynamic network rather than in opening of new surfaces, i.e. damaged in the polymeric cells.

3.4 Non-Destructive Evaluation

Post-impact, a three-dimensional reconstruction of the damage sustained by the sandwich panels was performed via means of computed tomography (CT) scanning. The equipment employed was a Nikon XT H 255 for the image acquisition and Avizo software for the post-processing of these.

In Figure 5 an estimation of the damaged areas of the top facesheets is illustrated with the use of the post-processing software.

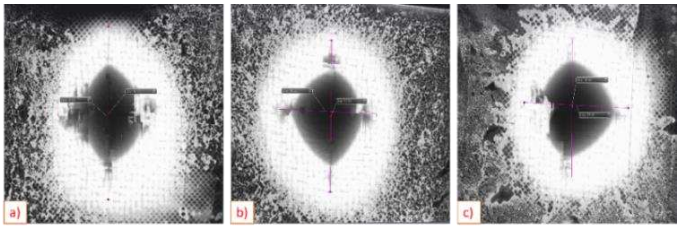

Figure 5 Estimation of damaged area of the top facesheet via means of CT-Scan, a) PUF, b) DPUF and c) MPUF sandwich panels

The damaged area for the neat PUF samples (Figure 5a) was estimated as 1661 mm^2, whereas the one for the DPUF ones as 1538 mm^2, a reduction of approximately 8%. The analogous area for the MPUF typology was evaluated as 1437.5 mm^2, 16% and 7% less in regard to the two other typologies. In order to further appreciate the impact resistance of the different samples, cross-sectional images were obtained as seen in Figure 6 below.

  doi:10.5075/epfl-298799_978-2-9701614-0-0

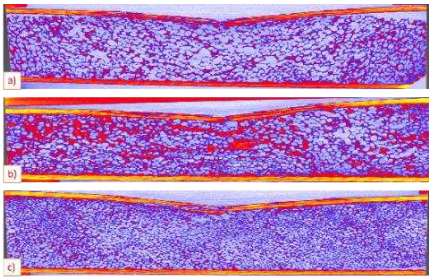

Figure 6 Cross-sectional images obtained via means of CT-Scan across different typologies, a)PUF, b)DPUF and c)MPUF.

The porosity between the PUF and DPUF samples in Figure 6a and Figure 6b appeared consistent, with the darker areas of the latter indicating the presence of the SSG. The MPUF typology appeared with cells of smaller size, which could be attributed to the presence of Si in the foaming process and its role as a nucleating agent. The depth of the damage for all typologies remained at similar levels at approximately 4.3 mm.

3.5 Discussion

A deeper analysis of the results obtained across all testing methods could reveal some further insights in regard to the performance of the proposed SSG and consecutively of the modified foams. The rheological measurements conducted on the SSG indicated a material with frequency dependant properties and with the ability to store greater amounts of energy as the shear rates applied onto this were increased, which was reflected in the overall difference in values of G'. The DM analysis on all foam structures clearly demonstrated that the modified foam structures displayed a frequency dependant behaviour as well, which was not held true for the neat PUF. The spectra obtained from FTIR confirmed the successful synthesis of the SSG and PUF, whereas at the same time eliminated the probability of a chemical bond between the PUF and the SSG. The implementation of SSG into the PUFs, irrespectively of the manufacturing method, clearly resulted in an improvement of the impact resistance of the composite sandwich panels and enhanced energy absorption characteristics. The impacts on the pristine samples (Figure 4a) revealed improved absorption characteristics by the modified PUFs, as despite all typologies absorbing similar amounts of energy, for the PUF typology this was consumed in the opening of new surfaces in the form of damage on the substrate. In the LVI events on the sandwich panels (Figure 4b), the amounts of absorbed energy achieved saw an increase of approximately 6% for the DPUF typology and 10% for the MPUF one, in comparison to the PUF. As observed in similar experiments (18), high strength face sheet properties can constrain the utilisation of core structures during LVI events, which could justify the similitude of the progression on the force-displacement curves. Nevertheless, the corresponding estimated damaged areas for the DPUF and MPUF typologies revealed a reduction of 8% and 16% respectively. These results further demonstrate that the modified cores offered enhanced overall performance with greater impact resistance, with the presence of SSG in the modified PUFs resulting in energy consumed in the polymeric network and in the breaking and reformation of the dynamic BO bonds (10). The residual properties of the sandwich panels (Figure 4c) offered a complete evaluation on the performance of all typologies. The neat PUF cores were unable to offer any protection to the impacted substrate which resulted in catastrophic failure, whereas the modified cores prevented this incident. In conjunction to the results from NDE and the similar depths of damage estimated in all cores, it can be speculated that the cell walls in the neat PUF cores sustained permanent damage, whereas the modified

cores displayed increased flexibility, as a result of the protection offered to these through the presence of the SSG in the double polymeric network. Finally, in regard to the evaluation of the manufacturing processes, although both appear to improve the impact resistance of the PUF cores, the MPUF emerged as more successful.

4. Conclusions

In this work, a novel, lightweight and low-cost core material for composite sandwich panels with excellent energy absorption properties is proposed. Two manufacturing processes for the implementation of the polyborosiloxane-based material into PUFs were evaluated, with both leading to enhanced energy impact resistance properties of the sandwich structures. The constituents of the foam structures were chemically and mechanically characterised, with the analyses demonstrating the frequency dependant characteristics of the SSG and the emerging modified core structures. The impact events revealed the superior performance of both DPFU and MPFU typologies, with enhanced energy absorption offered to the substrates (8% increased on average) and also demonstrated in the post LVI events on the sandwich panels that the significant improvement of their residual properties can only be attributed to the presence of SSG. The overall results of the experimental campaign clearly constitute the proposed modified PUFs as a low-cost solution which can further improve the performance of CFRP sandwich composite panels under dynamic, out-of-plane impact loading conditions.

Acknowledgements-Funding

The authors would like to thank Mr Edward Waggott for his assistance in this work.

The work in this publication was conducted under the project with title “Aegis, Advanced Energy-Absorption Polymer for Impact-Resistant Smart Composites” funded by the Engineering and Physical Sciences Research Council (EPSRC) [EP/T000074/1].

5. References

1. Murakami S, Saiki K, Hayashi M, Satou T, Fukami T. A Newly Developed MDI-Based Polyurethane Flexible Foam for Automotive Seat Cushion Having Both Superior Static and Dynamic Properties. Journal of Cellular Plastics. 2001;37(3):249-61.
2. Yang X, Xia Y, Zhou Q. Influence of stress softening on energy-absorption capability of polymeric foams. Materials & Design. 2011;32(3):1167-76.
3. Pinto F, Meo M. Design and Manufacturing of a Novel Shear Thickening Fluid Composite (STFC) with Enhanced out-of-Plane Properties and Damage Suppression. Applied Composite Materials. 2017;24(3):643-60.
4. Zhao C, Gong X, Wang S, Jiang W, Xuan S. Shear Stiffening Gels for Intelligent Anti-impact Applications. Cell Reports Physical Science. 2020;1(12):100266.
5. Wang S, Xuan S, Wang Y, Xu C, Mao Y, Liu M, et al. Stretchable Polyurethane Sponge Scaffold Strengthened Shear Stiffening Polymer and Its Enhanced Safeguarding Performance. ACS Applied Materials & Interfaces. 2016;8(7):4946-54.
6. Fan T, Xue S-S, Zhu W-B, Zhang Y-Y, Li Y-Q, Chen Z-K, et al. Multifunctional Polyurethane Composite Foam with Outstanding Anti-impact Capacity for Soft Body Armors. ACS Applied Materials & Interfaces. 2022;14(11):13778-89.
7. Xiaoke L, Kejing Y, Qianqian F, Kun Q. Shear thickening gel reinforced flexible polyurethane foam and its enhanced properties. Smart Materials and Structures. 2019;28(5):055017.

  doi:10.5075/epfl-298799_978-2-9701614-0-0

8. Liu X, Qian C, Yu K, Jiang Y, Fu Q, Qian K. Energy absorption and low-velocity impact response of shear thickening gel reinforced polyurethane foam. Smart Materials and Structures. 2020;29(4):045018.
9. Liu X, Yu K, Sun J, Guo W, Qian K. Effect of shear thickening gel on structure and properties of flexible polyurethane foam. Smart Materials and Structures. 2021;30(12):125008.
10. Myronidis K, Thielke M, Kopeć M, Meo M, Pinto F. Polyborosiloxane-based, dynamic shear stiffening multilayer coating for the protection of composite laminates under Low Velocity Impact. Composites Science and Technology. 2022;222:109395.
11. Martin JE, Adolf D, Wilcoxon JP. Viscoelasticity near the sol-gel transition. Physical Review A. 1989;39(3):1325.
12. Zhang S, Wang S, Hu T, Xuan S, Jiang H, Gong X. Study the safeguarding performance of shear thickening gel by the mechanoluminescence method. Composites Part B: Engineering. 2020;180:107564.
13. Razmara M, Saidpour S, Arunchalam S, editors. DMA investigation on polyurethane (PUR). International Conference on Fascinating Advancement in Mechanical Engineering (FAME2008); 2008: Citeseer.
14. Zinchenko G, Mileshkevich V, Kozlova N. Investigation of the synthesis and hydrolytic degradation of polyborodimethylsiloxanes. Polymer Science USSR. 1981;23(6):1421-9.
15. Li X, Zhang D, Xiang K, Huang G. Synthesis of polyborosiloxane and its reversible physical crosslinks. Rsc Advances. 2014;4(62):32894-901.
16. Hatchett DW, Kodippili G, Kinyanjui JM, Benincasa F, Sapochak L. FTIR analysis of thermally processed PU foam. Polymer Degradation and Stability. 2005;87(3):555-61.
17. ASTM D. 7136/D 7136M. Standard test method for measuring the damage resistance of a fibre-reinforced polymer matrix composite to a drop-weight impact event. 2007.
18. Vaidya UK, Pillay S, Bartus S, Ulven CA, Grow DT, Mathew B. Impact and post-impact vibration response of protective metal foam composite sandwich plates. Materials Science and Engineering: A. 2006;428(1):59-66.

INVESTIGATION OF RECYCLED POLYVINYL CHLORIDE REINFORCEMENT FOR PROPERTY ENHANCEMENT OF POLYURETHANE FOAM CORE FIBER REINFORCED POLYMER SANDWICH COMPOSITES

Haroon Mahmood[a], Marco Renon[b], Alessandro Pegoretti[a]

a: Department of Industrial Engineering, University of Trento, via Sommarive 9 – 38121, Trento - Italy (haroon.mahmood@unitn.it)
b: Diab S.p.A, via Alemagna, 29 – 32013, Longarone - Italy

Abstract: *End-of-life recycled polyvinyl chloride (rPVC) particulates were used as a filler to improve the mechanical performance of polyurethane (PU) based fiber reinforced polymer sandwich composites. rPVC particles were added from 2.5 wt% till 20 wt% in PU foam. Optical microscopy images revealed the variation of cell size of PU foam with respect to rPVC inclusion, i.e., progressive addition of rPVC particles decreased the cell size of PU foam. Using various density calculations, it was found that the added rPVC particles resulted in the opening of cellular structure of PU foams. Facesheet – core combination sandwiched composite specimens was fabricated using a woven fabric basalt fiber reinforced polymer (BFRP) face sheet with rPVC reinforced PU foam as core. A bicomponent epoxy resin was used as a matrix in the facesheet composite. The tensile and composite strengths were assessed through the flatwise tensile and compressive tests to evaluate the effect of PVC particles in the core of the sandwich composites.*

Keywords: sandwich composites; recycling; polyvinyl chloride; polyurethane; basalt fiber.

1. Introduction

With the rising levels of global warming and pollution in the world, there has been a lot of interest in the economic and strategic recycling of waste materials in recent years. Among the various challenges in this industry, separating and reutilizing polyvinyl chloride (PVC) from post-consumer waste such as insulated wires and cables, window profiles, and foams remains a difficult task for the global community. PVC is the world's second most manufactured thermoplastic in terms of volume out of which approximately 8% is utilized in the fabrication of wires and cables. [1,2] Due to its non-recyclable nature, PVC is either burnt or landfilled, posing a significant risk owing to the chlorine concentration in the polymer. In fact, the widely used burning process produces deadly dioxins, which can cause cancer and harm to the nervous system. [3,4] Rigid cross-linked interpenetrated network PVC foams, in particular, are widely used as the light core for composite sandwiches used in a variety of applications, ranging from wind blades to marine structures. When these artifacts approach the end of their useful lives, the PVC foams are currently disposed of in landfills, with the resulting waste of resources and environmental load. [5] Hence the need of the hour is to uncover the usefulness of such End-of-life PVC material in order to avoid further wastage of nonrecyclable material.

Polyurethanes (PUs) are a broad category of materials that come in a wide range of characteristics and formulations. Polyurethanes are widely used in a variety of industries, including shipbuilding, sports and footwear, construction, and the automotive industry [6-8]. PUs can be thermoplastic or thermosetting depending on their chemical composition. They are

  doi:10.5075/epfl-298799_978-2-9701614-0-0

made up of urethane linkages formed by reacting diisocyanates with polyols in the presence of catalysts. Polyol is a low molecular weight polymer with hydroxyl end groups that are commonly a polyether or polyester. Isocyanates are bifunctional or polyfunctional precursors that might be aromatic or aliphatic. Toluene diisocyanate (TDI) and diisocyanato-diphenylmethylene are the most frequently distributed isocyanates from a commercial standpoint (MDI). [9]

In this work, recycled PVC particles (rPVC) were added in different weight percentages into the rigid PU matrix with the aim to explore new thermomechanical properties of the produced composite panels. Particular attention was given to the investigation of the physical and morphological properties of the produced foams, which dictate the final mechanical properties of the samples. The properties of the resulting compounds were compared with the corresponding unmodified PU foam. These composite foams were used as core in sandwich composites having facesheets made by basalt fiber reinforced epoxy composites. The produced sandwich composites were mechanically tested to evaluate the effect of added PVC particles on the mechanical properties of the PU/rPVC sandwich composites.

2. Experimental

2.1 Materials and Methods

The cross-linked PVC foams were provided by Diab SpA (Longarone, BL, Italy). Divinycell was received in the form of powder which were a waste of the cutting process involved in the production of PVC-foamed panels. According to the technical data sheet of the company, the composition of the foam includes PVC (30%–75%), aromatic polyurea (15%–50%), and polyamide (3%–10%). The glass transition temperature (T_g) and apparent density of the PVC powder are 78.7 °C and 1.08 g/cm^3. The powder was sifted using a sieve having openings of 800 micron. Plain weave basalt fiber fabric (bi-axial) (Aerial density = 220 g/m^2) provided by Basaltex (Wevelgem, Belgium) was used as a reinforcement for facesheets. Three layers of the fabric was used to create the laminates. A bicomponent epoxy was used as a polymer matrix in the facesheets. The epoxy system consisted of an epoxy base (EC157.1) and an aminic hardener (W342), both provided by Elantas Italia S.r.l. (Collecchio, Italy). These two components were mixed at a ratio of 100:30 and cured for 8 h at 100 °C, as indicated by the producer's data sheet.

A rigid polyurethane foam was produced by combining an HDR R 150 polyol (density = 1.1 g/cm^3, viscosity at 23 °C = 1050 cP) with an ISN 1 isocyanate (density = 1.23 g/cm^3, viscosity at 23 °C = 200 cP) at a relative mass ratio of 100/130. The reagents were provided by Kairos Srl (Verona, Italy). The mixing step was carried out at room temperature with a cream time of 12–16 seconds, according to the datasheet.

In a beaker, the liquid precursors (isocyanate and polyol) and the appropriate amount of dried PVC particles were combined for 15 seconds at 500 rpm. The resultant combinations were then put into a 200 x 200 x 25 mm^3 wood mold and the mixture was made to expand for 20 minutes in an oven at 40 °C. In this method, clean PU foam and PU foams loaded with various quantities of PVC particles (ranging from 2.5 % to 20 % by weight) were created. Table 1 reports the list of the prepared samples, together with the adopted nomenclature and the relative concentration of the constituents.

Table 1: List of the prepared samples.

Sample	PVC (wt.%)	Polyol-POL (wt.%)	Isocyanate-ISCN (wt.%)
PU	0	43.5	56.5
PU-2.5PVC	2.5	42.4	55.1
PU-5PVC	5	41.3	53.7
PU-7.5PVC	7.5	40.2	52.3
PU-10PVC	10	39.1	50.9
PU-15PVC	15	37.0	48.0
PU-20PVC	20	34.8	45.2

The sandwich composites were produced by hand lay-up method. The basalt fiber fabric along with the PU foam were manually impregnated with epoxy resin and consolidated in a vacuum bagging technique setup as shown in Figure 1. The whole setup was placed under a hot-press at 100 °C for 8 hours under a compressive load of 0.05 MPa.

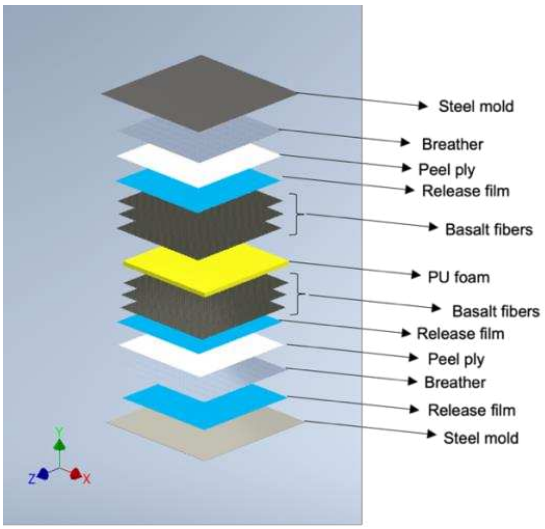

Figure 1. Schematic of vacuum bagging technique setup

2.2 Characterization and Testing

Optical microscope images of the foams were taken at different magnification levels by using a Nikon SMZ25 optical microscope equipped with a Nikon DS-Fi2 digital camera microscope. The mean cell size and the cell size distribution were evaluated on the obtained micrographs by using the software Image J®.

Degree of porosity of the produced foams was calculated by applying density measurements. For this reason, geometrical density (ρ_{geo}) was calculated by diving the mass of the foam for their volume. In this way, a density value that considers both the open and close pores could be obtained. On the other hand, theoretical density (ρ_{theo}) was calculated by the rule of mixture, knowing the density of the PVC particles (1.08 g/cm^3) and the bulk density of the neat PU matrix

(1.17 g/cm^3). Pycnometric density (ρ_{pyc}) refers to the density determined without considering the open pores, and it was determined by using a Micromeritics AccuPyc 1330TC (Micromeritics Instrument Corp., Norcross, USA) helium pycnometer operating at room temperature, by using a testing chamber of 1 cm^3. In this way, it was possible to determine the volume fraction of the open (ϕ_{OP}) and of the closed (ϕ_{CP}) pores along with the total porosity volume fraction (ϕ_{Ptot}), according to the expression reported in Eq. (1–3):

$$\phi_{OP} = 100 \cdot \left(1 - \frac{\rho_{geo}}{\rho_{pyc}}\right) \quad (1)$$

$$\phi_{CP} = 100 \cdot \rho_{geo} \cdot \left(\frac{1}{\rho_{pyc}} - \frac{1}{\rho_{theo}}\right) \quad (2)$$

$$\phi_{Ptot} = 100 \cdot \left(1 - \frac{\rho_{geo}}{\rho_{theo}}\right) \quad (3)$$

The cell wall fraction (ϕ_{CW}) was determined according to the expression reported in Eq. (4):

$$\phi_{CW} = 100 \cdot \frac{\rho_{geo}}{\rho_{theo}} \quad (4)$$

Uniaxial tensile and compressive tests were carried out based on ASTM-C297 (Standard test method for the flatwise tensile strength of sandwich constructions) and ASTM-C365 (Standard test method for the flatwise compressive strength of sandwich constructions) regulations respectively. For both tests, the cross-section of the PU/rPVC foam was chosen as 25 × 25 mm. The specimens were bonded to the jig using superfast glue.

3. Results and Discussion

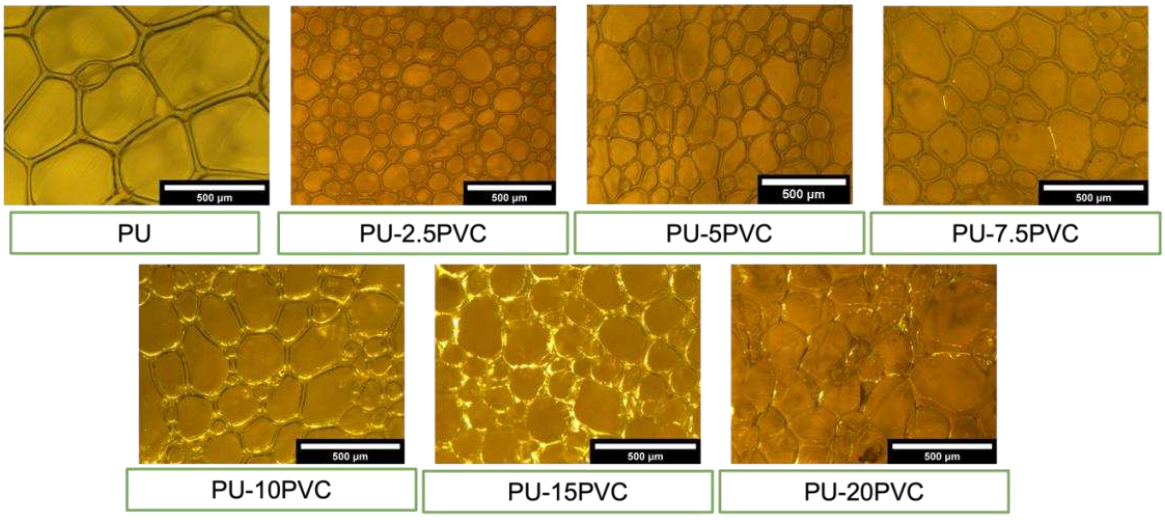

Figure 2. Optical images of PU/rPVC foams

Figure 2 compares the optical images of PU/rPVC foams with the neat PU foam. It can be seen that the cell size of the PU foam reduces dramatically with the addition of just 2.5 wt.% of PVC in PU foam. This indicates that the particle addition in the polyol/isocyanate mixture results a hinderance in the foaming process which inhibits the expansion of the produced cells. However, even with the increased addition of the PVC particulate (up to 20 wt.%) in the mixture, the formation of cell occurs with dimensions more or less the same.

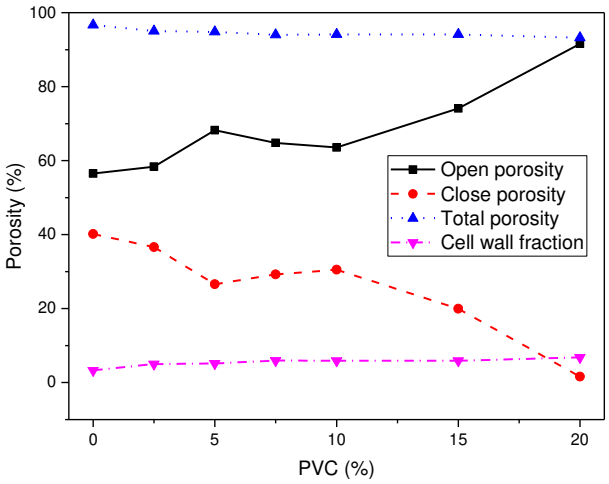

Figure 3. Evaluation of the porosity degree of the prepared foams.

Density measurements were done using various methodologies to gain a better understanding of the cell architecture of the foams, and the trends of open (OP), close (CP), and total porosity (P_{tot}) as a function of PVC particulate quantity are shown in Figure 3. The introduction of PVC particles into PU foams results in a substantial increase in open pores, a consequence of which the close porosity decreased. For a neat PU foam, the OP value observed was 56% while increasing the PVC content to 20 wt.% results in OP value of around 90%. This indicates that at high PVC concentrations, the microstructure of the foams is dominated by an open-pore morphology. This change in pore structure could affect the mechanical and thermal conductivity properties of the resultant foams. The existence of open porosity inside the foam, allows the interior air to travel within the pores, hence increasing the thermal conductivity values. An open-cell structure, on the other hand, improves sound insulation characteristics. [10] As a result, it is evident that assessing the effect of PVC addition in these foams is particularly linked to their intended application. Interestingly, both the total porosity (ϕP_{tot}) and the cell wall concentration (ϕ_{CW}) are not strongly influenced by the PVC addition.

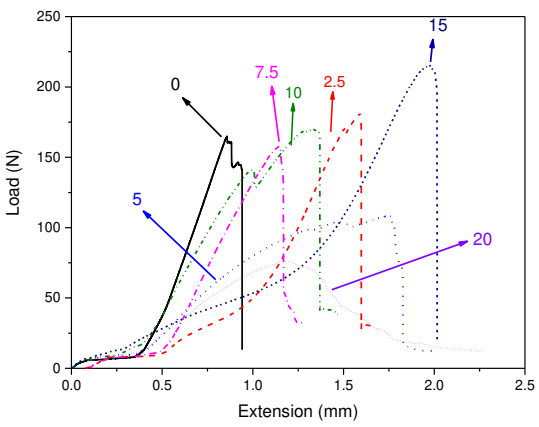

a)

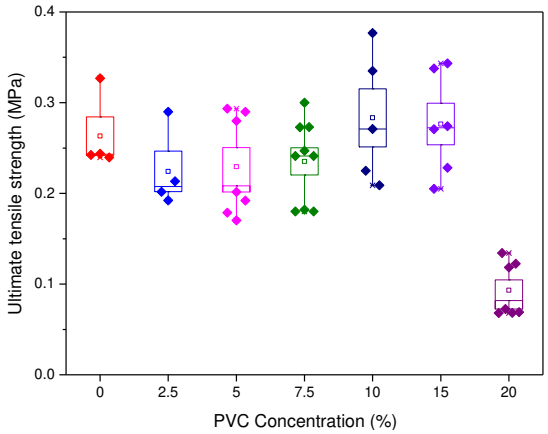

b)

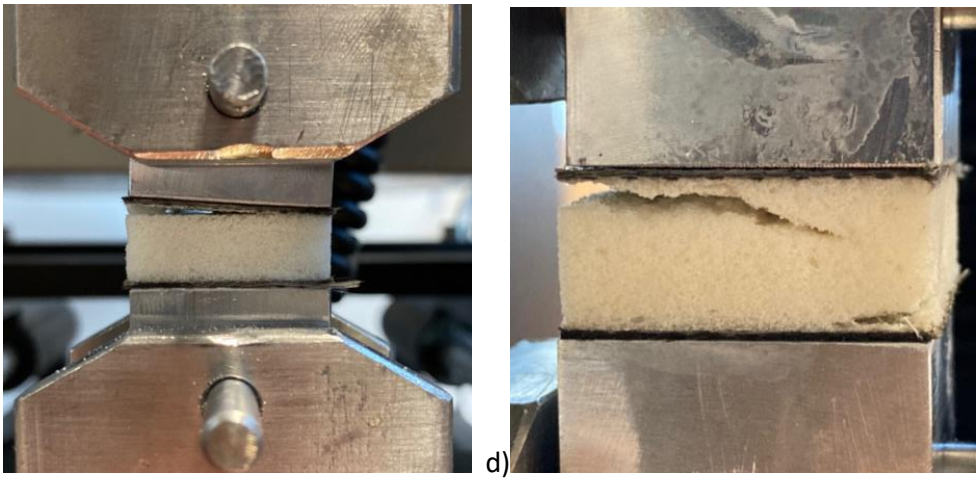

c) d)

Figure 4. Flatwise tensile strength results of sandwich composites where a) show the representative load-extension curves and b) ultimate tensile strength of the sandwich composites, c) and d) show the failure of the PU-2.5PVC and PU-20PVC specimens.

The flatwise tensile strength of bonded sandwich panels is primarily used as a quality control metric. The quality and strength of the core-to-facing adhesive connection are determined by this test. The results of such tests are shown and compared in Figure 4. Looking at the representative load-extension curves (Figure 4a), it can be observed that the gradual addition of PVC particles in PU foam results in an increased extension levels required to achieve failure in the specimen. However, the ultimate tensile strength values remained unvaried (Figure 4b) until a PVC content of 15 wt.%. Increasing further to 20 wt.% results in a drastic decrease in the strength values indicating a catastrophic failure of the specimen. This can be verified by comparing the failure of PU-2.5PVC and PU-20PVC specimens (Figure 4c and Figure 4d). The failure of former specimen took place at the interface of the facesheet and the core of the composite while for PU-20PVC, the failure was a mixture of the interface and the core suggesting that the increased content of PVC at a certain point renders the foam prone to premature failure under tensile loading.

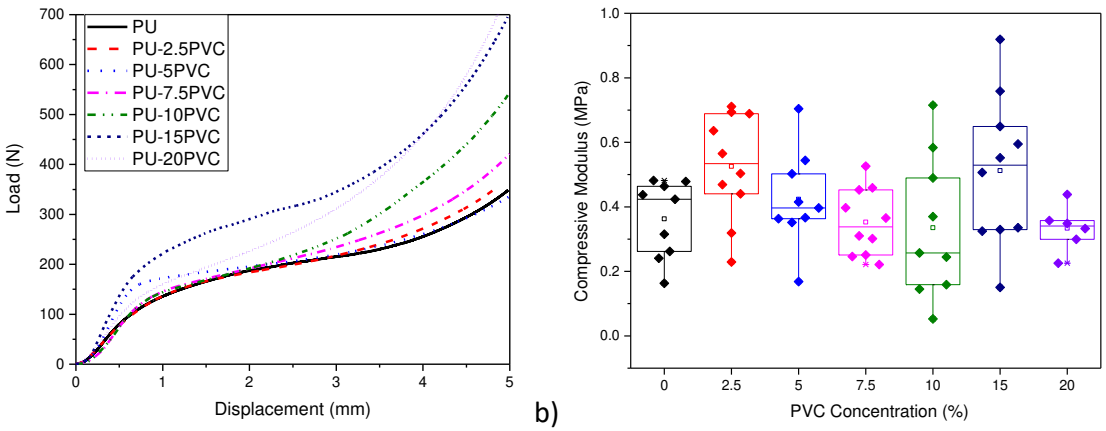

a) b)

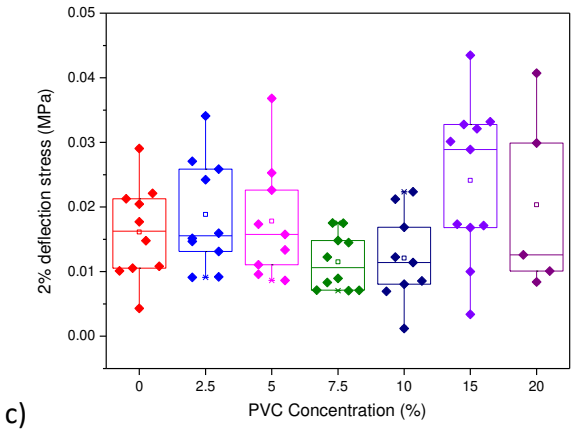

c)

Figure 5. Flatwise compressive test results of sandwich composites where a) show the representative load-displacement curves and b) compressive modulus of the sandwich composites and c) stress at 2% deflection.

Flatwise compressive tests were conducted on sandwich specimens to examine the compressive properties of the PU/rPVC cores. Figure 5a displays the typical compressive load–displacement responses of all the samples. The elastic section of the curve was linear, followed by a plateau zone where the stress remained nearly constant as deformation increased. The flat plateau was produced by the development of localized buckling within the cell walls. As the deformation increased, the cell walls stacked on top of each other resulting in the closure of most of the voids. Therefore, the foam became densified and displayed higher strength. As evident in Figure 5b, the modulus values slightly increased with high data distribution for samples containing higher concentration of PVC e.g., PU-10PVC and PU-15PVC sandwich composites. In other words, the modulus values of the foam would be different at different locations of the same panel which indicates an inhomogeneous distribution PVC particles distribution in PU foam and hence resulting in mechanical properties with high statistical error. The same can be said for the stress at 2% deflection for all composites (Figure 5c). Overall, the stress values obtained do not vary significantly for the produced sandwich composites, yet for higher PVC loading in PU results slightly higher stress levels obtained probably due to the rigid nature of PVC particles added.

4. Conclusions

In this work, recycled polyvinyl chloride (rPVC) particulates were added in the polyurethane foam (PU). Such PU/rPVC foam composites were used a core in a sandwich composite where the facesheets were fabricated by basalt fiber reinforced polymer composites. Optical microscopy analysis of the PU/rPVC foam showed a reduction of cell size of PU foam due to the progressive addition of the rPVC particles. Through various density calculations, it was found that the cellular structure of the PU foam shifted from closed porosity to open porosity with the addition of the rPVC particles. The flatwise tensile strength tests of the sandwich composites revealed unvaried tensile strength values until 15 wt.% PVC content whereas compressive properties slightly increased with the addition of rigid PVC particles. Overall, it can be concluded that the rPVC particles addition in the PU foam do not bring drastic deterioration of the physical and mechanical properties of the latter hence providing with cost and raw material saving measures.

  doi:10.5075/epfl-298799_978-2-9701614-0-0

Acknowledgements

This research activity has been financed by the Fondazione Cassa di Risparmio di Verona (Cariverona, Grant number 50428) within the project "Sviluppo di un processo per il riciclo di schiume rigide a base PVC provenienti da scarti di produzione e da manufatti (RE-FOAMS)".

5. References

1. Gohatre, O.K.; Biswal, M.; Mohanty, S.; Nayak, S.K. Effect of silane treated fly ash on physico-mechanical, morphological, and thermal properties of recycled poly(vinyl chloride) composites. *Journal of Applied Polymer Science* **2020**, *138*, 50387, doi:10.1002/app.50387.
2. Hakkarainen, M. New PVC materials for medical applications—the release profile of PVC/polycaprolactone–polycarbonate aged in aqueous environments. *Polymer Degradation and Stability* **2003**, *80*, 451-458, doi:https://doi.org/10.1016/S0141-3910(03)00029-6.
3. Robinson, B.H. E-waste: an assessment of global production and environmental impacts. *Sci Total Environ* **2009**, *408*, 183-191, doi:10.1016/j.scitotenv.2009.09.044.
4. Arya, S.; Gupta, A.; Bhardwaj, A. Economic analysis of electronics waste materials: A region based study. *Materials Today: Proceedings* **2021**, *46*, 10239-10243, doi:10.1016/j.matpr.2020.11.750.
5. Mahmood, H.; Nart, F.; Pegoretti, A. Effective recycling of end-of-life polyvinyl chloride foams in ethylene–propylene diene monomers rubber. *n/a*, doi:https://doi.org/10.1002/vnl.21896.
6. Pegoretti, A.; Dorigato, A.; Brugnara, M.; Penati, A. Contact angle measurements as a tool to investigate the filler–matrix interactions in polyurethane–clay nanocomposites from blocked prepolymer. *European Polymer Journal* **2008**, *44*, 1662-1672, doi:https://doi.org/10.1016/j.eurpolymj.2008.04.011.
7. Dorigato, A.; Pegoretti, A.; Penati, A. Effect of the polymer—filler interaction on the thermo-mechanical response of polyurethane-clay nanocomposites from blocked prepolymer. **2011**, *30*, 325-335, doi:10.1177/0731684410396599.
8. Kausar, A. Polyurethane Composite Foams in High-Performance Applications: A Review. *Polymer-Plastics Technology and Engineering* **2018**, *57*, 346-369, doi:10.1080/03602559.2017.1329433.
9. Galvagnini, F.; Dorigato, A.; Valentini, F.; Fiore, V.; La Gennusa, M.; Pegoretti, A. Multifunctional polyurethane foams with thermal energy storage/release capability. *Journal of Thermal Analysis and Calorimetry* **2022**, *147*, 297-313, doi:10.1007/s10973-020-10367-w.
10. Schiavoni, S.; D'Alessandro, F.; Bianchi, F.; Asdrubali, F. Insulation materials for the building sector: A review and comparative analysis. *Renewable and Sustainable Energy Reviews* **2016**, *62*, 988-1011, doi:https://doi.org/10.1016/j.rser.2016.05.045.

VIRTUAL TESTING OF HONEYCOMB SANDWICH STRUCTURES WITH MULTIPLE LOAD INTRODUCTION POINTS

Lukas Schwan[a], Johann Schwenke[a], Tobias S. Hartwich[a], Dieter Krause[a]

a: Institute of Product Development and Mechanical Engineering Design, Hamburg University of Technology (TUHH) – lukas.schwan@tuhh.de

Abstract: *In Nomex honeycomb sandwich structures, inserts are often used for local load introduction. In the surroundings of the inserts, complicated stress conditions occur, which can often lead to local failure of the structure. Due to design measures, several inserts often have to be positioned next to each other, which can lead to interferences of the stress fields, reducing the load-bearing capacity of the individual inserts. For such cases, only rough reduction factors are specified in the ESA insert design handbook, which can lead to large safety factors. To predict the influence of the positioning of two inserts and to minimize oversizing, pull-out tests as well insert proximity tests are carried out. Respective virtual models are build-up for further numerical investigations.*

Keywords: virtual testing; Nomex honeycomb; insert proximity test; multiple load introduction points

1. Introduction

In aircraft cabins, sandwich structures with Nomex honeycomb core are frequently used due to their very good weight-specific properties [1]. Since the core is not suitable for local load transfer, local stiffeners in the form of inserts are introduced into the structure with an adhesive compound, so-called potting [1–3]. In addition to the layered structure of the sandwich composite and the anisotropic material behavior of the constituents, complicated stress states arise due to large stiffness changes in the area of the load introduction elements [1]. For design reasons, often multiple inserts must be used to introduce loads into the structure, which can lead to an overlapping of their stress fields [3]. This can result in a reduction of the load-bearing capacity of the individual inserts. In the Insert Design Handbook (IDH) [3], analytical equations are given to determine not only the load-bearing capacity of individual inserts but also interference coefficients, which indicate reductions in the load-bearing capacity of the inserts. In the case of two inserts loaded in the same direction, a distinction between *close* and *distant* inserts according to Eq. (1) is made, where *a* denotes the distance between the insert centers and b_{p1}, b_{p2} describe the respective potting radii. If the inequation is fulfilled, the inserts are classified as *close* and the interference coefficient η_{IS1} for insert 1 can be calculated according to Eq. (2). If the same inserts are used, the interference coefficients are the same ($\eta_{IS1} = \eta_{IS2}$), otherwise the IDH [3] gives further equations for the determination of η_{IS2}. If the insert distance *a* is greater than the term given in Eq. (1), the inserts are classified as *distant* and there is no reduction in the load-bearing capacity ($\eta_{IS1} = \eta_{IS2} = 1$).

$$a \leq 5(b_{p1} + b_{p2}) \tag{1}$$

$$\eta_{IS1} = \frac{{b_{p1}}/{b_{p2}}}{1+{b_{p1}}/{b_{p2}}} \left(1 + \frac{a}{5 \cdot b_{p1}} \cdot \frac{1}{{b_{p1}}/{b_{p2}}}\right) \tag{2}$$

  doi:10.5075/epfl-298799_978-2-9701614-0-0

However, these are approximate and conservative equations [4, 5] that do not fully exploit the lightweight design potential and lead to over-dimensioning. Detailed numerical meso-models based on the finite element method (FEM), which are hierarchically structured, have been established in research as an alternative to the analytical equations [6–8]. With such FEM-models, for example, it is possible to predict the structural behavior of Nomex honeycomb sandwich structures in the pull-out test [4, 9, 10]. Corresponding numerical and experimental results for multiple inserts, like the insert proximity test proposed in the IDH [3], could not be found in the state of the art. Only Schwenke and Krause [11] have numerically shown an optimization for multiple load introduction points.

In this paper, a realization of a test setup for the insert proximity test as well as corresponding test results are shown for the first time. Based on the pull-out test, detailed numerical models are further implemented and extended to the insert proximity test. The experimental results are complemented by numerical studies to generate knowledge about the load introduction across multiple inserts and to minimize over-dimensioning in the design of insert groups.

2. Materials

The presented materials are used for the pull-out tests as well as the insert proximity tests. The partially potted insert configuration used is shown in *Figure 1* and is typically used in aircraft cabins. The total panel thickness is 20 mm and a Nomex honeycomb core from the manufacturer Euro-Composites with a cell size of 3.2 mm and a density of 48 kg/mm² according to the Airbus standard ABS5035-A4 is used. Two layers of glass fiber fabric reinforced phenolic resin prepreg to Airbus standard ABS5047-07 are placed on each side of the core. The SL607-3-6S inserts are cold-bonded into the structure with Scotch-Weld 9323 adhesive. The potting height is 17 mm.

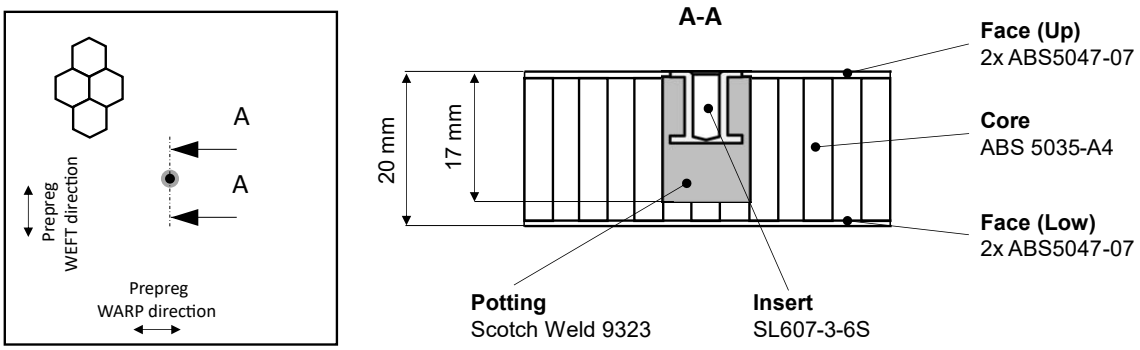

Figure 1. Used materials for the pull-out tests and the insert proximity tests.

3. Pull-out test

First, pull-out tests are performed to implement a numerical model, which will be extended to the insert proximity test.

3.1 Experimental study

The tests are performed following the recommendations from the IDH [3] and three specimens with a specimen size of 100 x 100 mm are tested. The cutout diameter is 70 mm and a loading rate of 2 mm/min is used. The tests are carried out on a Galdabini Quasar 100 universal testing machine, while the force is measured using an HBM S9M-10 kN load cell and the displacement is measured via machine crosshead. The experimental setup is shown in *Figure 2*.

  doi:10.5075/epfl-298799_978-2-9701614-0-0

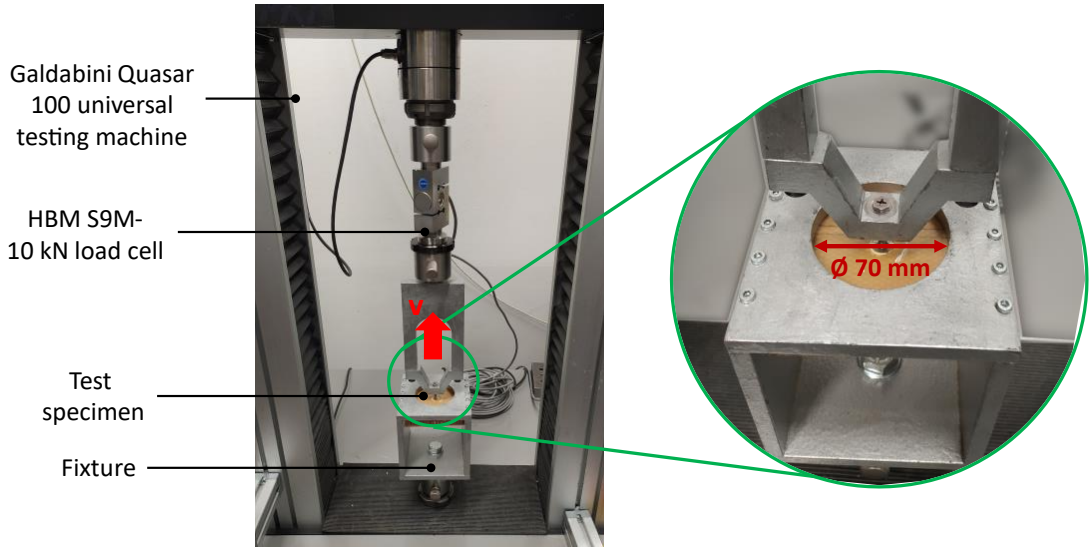

Figure 2. Experimental setup for the pull-out test.

3.2 Numerical study

The FEM-model of the pull-out test is implemented as a quarter model with a meso-core and the FEM solver Abaqus/Explicit is used. The meshed model is shown in *Figure 3*, using the modeling approaches and material models of Seemann [12].

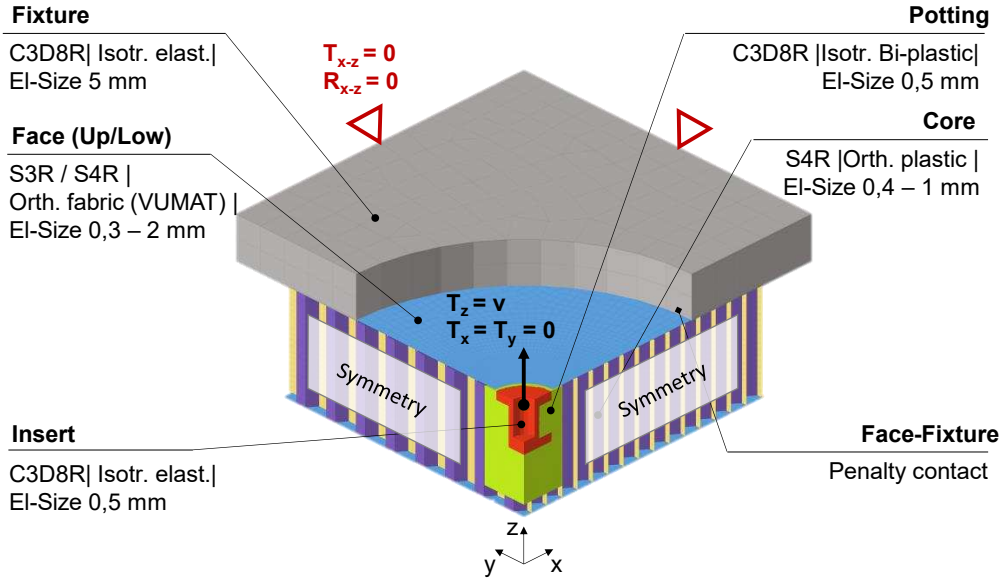

Figure 3. Meso model of the pull-out test modeled according to Seemann and Krause [9].

In particular, to predict the nonlinear behavior of the sandwich structure in the pull-out test, the shear buckling of the core as initial damage mechanism must be adequately modeled [3, 13]. To implement this with meso-models, the material properties of the phenolic resin impregnated Nomex paper type 412 are of great importance [14]. Following Seemann and Krause [14], an orthotropic plastic material model with Hashin failure criterion is used for modeling. While the elastic material parameters as well as the compressive and shear strengths are kept according to Seemann and Krause [14], the tensile strength in M- and X-direction is reduced as part of the model calibration in order to reduce the deviation from the tensile strengths reported in the

literature [15, 16]. Furthermore, various parameter and sensitivity analyses are performed to calibrate the fracture energies of the phenolic resin impregnated Nomex paper. The calibrated material parameters of the core are summarized in *Table 1*.

Table 1: Calibrated material parameters for the phenolic resin impregnated Nomex paper.

E_1	5.000 MPa	Longitudinal tensile strength, δ_{1t}	75 MPa	Longitudinal tensile fracture energy, G_{1t}	30 N/mm
E_2	4.000 MPa	Longitudinal compression strength, δ_{1c}	105 MPa	Longitudinal compression fracture energy, G_{1c}	10 kN/mm
G_{12}	1.450 MPa	Transverse tensile strength, δ_{2t}	30 MPa	Transverse tensile fracture energy, G_{2t}	20 N/mm
υ_{12}	0,2	Transverse compression strength, δ_{2c}	90 MPa	Transverse compression fracture energy, G_{2c}	10 kN/mm
		Shear strength, δ_{12}	44 MPa		

3.3 Results

Figure 4 (a) shows the results of the experimental study and the numerical simulation, with the test stiffness extracted from the test data. Initially, the sandwich structure exhibits linear elastic behavior, whereupon shear buckling of the core occurs, giving the force-displacement curve its characteristic progressive course until total failure of the structure occurs. Further, partial delamination and failure of the face sheets occur, which can also be detected in the tested specimens in *Figure 4 (b).* The results of the numerical simulation agree well with those of the physical tests, although the initial shear buckling is slightly overestimated in the virtual model.

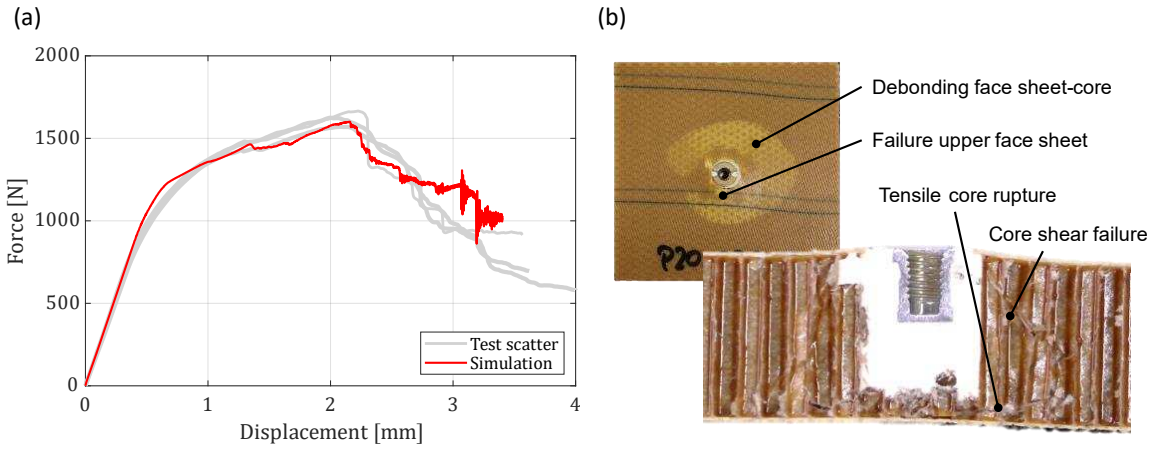

Figure 4: Results of the experimental study and numerical simulation (a); Damage mechanisms occurring in the physical test (b).

4. Insert proximity test

After the pull-out test has been successfully modeled numerically, experimental tests as well as numerical studies on the insert proximity test are performed.

4.1 Experimental study

The insert proximity tests are performed on the same universal testing machine with the same traverse speed as the pull-out tests. The optical 3D measuring system ARAMIS Adjustable from GOM is used for displacement measurement. The test setup is shown in *Figure 5*. A cutout

diameter of 140 mm and a specimen size of 200 x 200 mm are selected. Also, a universal joint is used for force application to prevent the introduction of transverse forces into the specimen. A steel plate with drilling holes is utilized for the testing of the different insert configurations. Furthermore, 14 mm, 50 mm and 80 mm are chosen as insert distances in W-Direction (cf. *Figure 5*). For the three chosen distances according to the analytical equations from the IDH [3] there is a slight, a moderate and no influence on the load-bearing capacity as a result of the superposition of the insert stress fields. Three specimens of each configuration are tested.

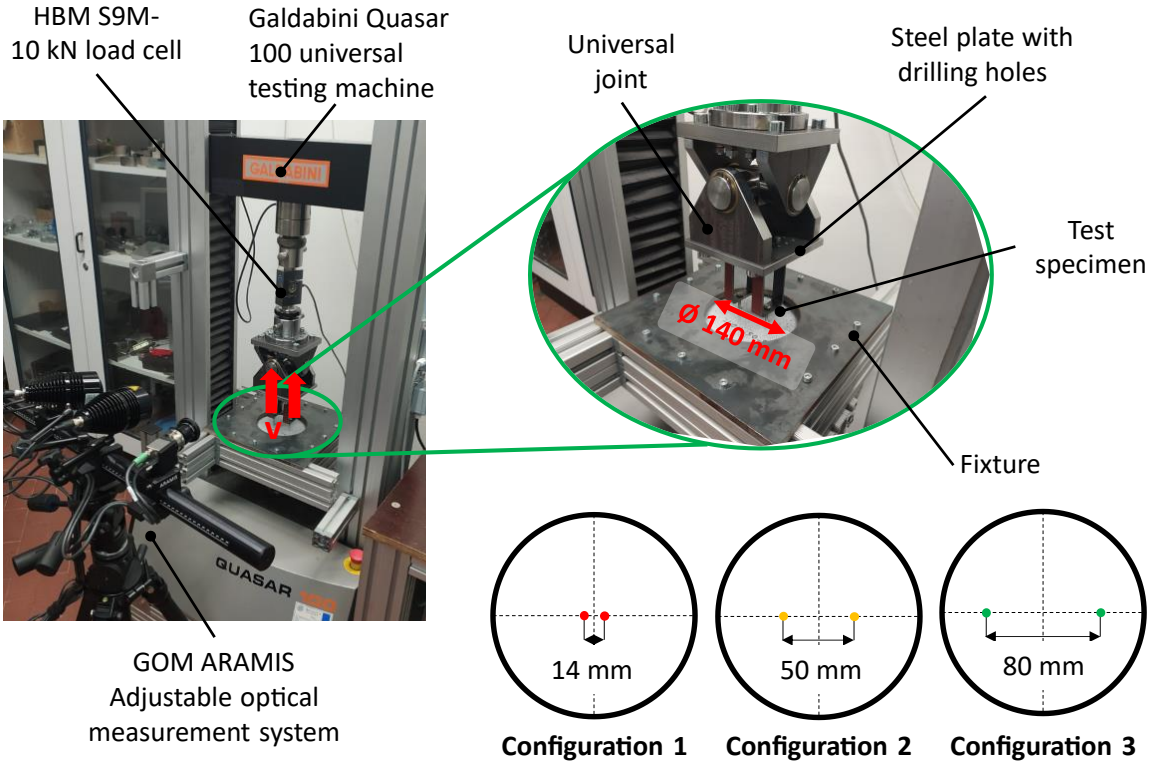

Figure 5. Test setup for the insert proximity test and different test configurations.

4.2 Numerical study

Two different models are implemented as part of the numerical study. In addition to a hybrid model, which is set up for the prediction of the progressive damage behavior, a solid model is also set up in order to be able to calculate different insert positions in a computationally efficient manner. With the exception of the solid core, both models are implemented as a quarter model with the same element sizes and material models as the pull-out model from chapter 3.2. To save computation time due to the larger sample size, the core in the hybrid model is modeled at a radius of 20 mm around the insert using a meso core in order to be able to represent the shear buckling. At a further distance, a solid core with an element size of 5 mm and an orthotropic plastic material model according to Seemann [12] is used, which is able to reproduce the elastic behavior of the core. The two cores were connected by a tied contact. When exploiting the symmetry in the quarter model using a meso or hybrid modeling approach, in which the geometry of the honeycomb core is represented, the resulting potting geometry has an effect on the shear stresses that occur in the individual honeycomb cell walls and thus on the resulting pull-out force [17]. Thus, the influence of the positioning of the inserts cannot be

  doi:10.5075/epfl-298799_978-2-9701614-0-0

studied in isolation due to its correlation with the resulting potting geometry. For this purpose, a solid model is implemented in which the honeycomb is not geometrically represented. Although the progressive damage behavior cannot be adequately represented by this, the solid models are suitable for determining the pull-out forces. The solid model is used to simulate insert distances between 14-120 mm in 10 mm increments in the L- and W-direction.

4.3 Results

Figure 6 (a-c) shows the results of the experimental tests for the different insert distances and the results of the corresponding numerical simulation with the hybrid model. In addition, in *Figure 6 (d)* a 50 mm specimen is shown, in which similar failure mechanisms as in the pull-out test can be identified. Overall, the results of the hybrid models are within the scatter of the tests and represent the progressive damage behavior of the structure well. While the maximum force for the 14 mm configuration is lower than the maximum forces of the 50 mm and the 80 mm configurations, a reduced strength for the 80 mm configuration compared to the 50 mm configuration can be observed.

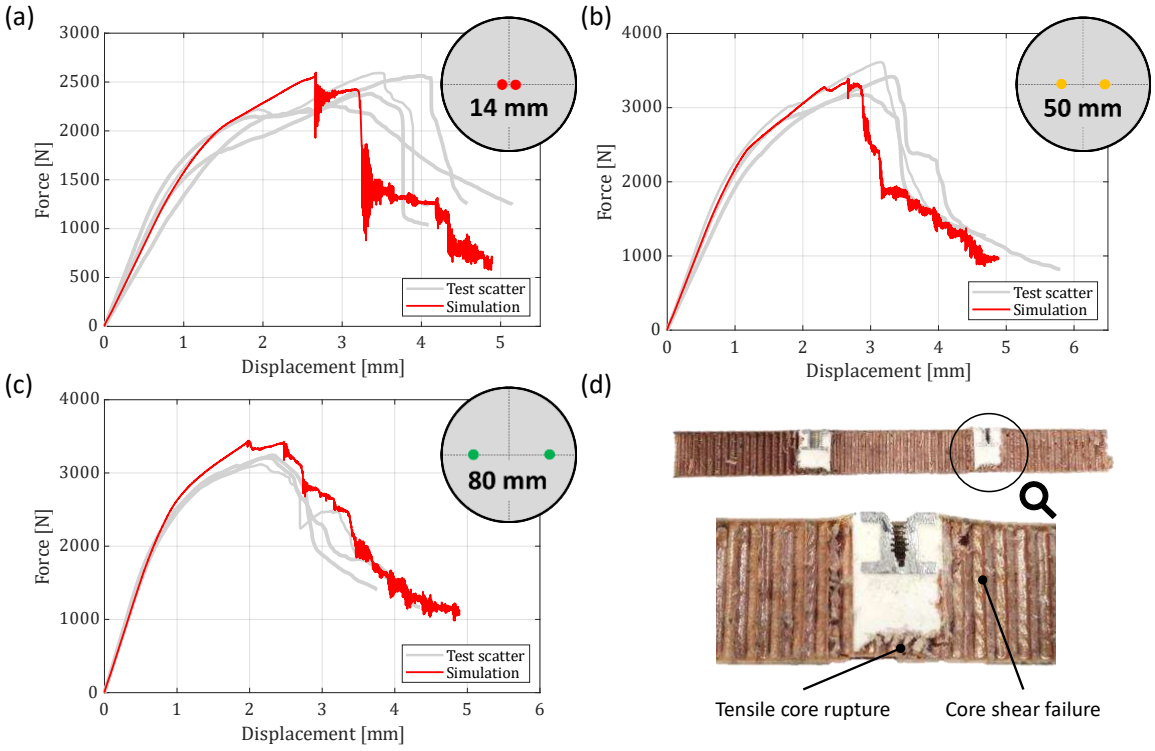

Figure 6. Results of the experiments and numerical simulations for different insert distances (a-c); Damage mechanisms occurring in the core in physical test of the 50 mm configuration (d).

The evaluation of the results of the solid model in smaller distance increments supports these findings from the physical tests and the numerical investigations with the hybrid model. *Figure 7 (a)* shows the simulatively determined as well as the analytically determined interference coefficients over the insert distance. While the analytic interference coefficients have been calculated according to Eq. (1) and Eq. (2), for the simulatively calculation the Equation from *Figure 7 (a)* is applied assuming an even load distribution in the insert proximity test. As reference, a solid model with a single insert is implemented for a pull-out test with a cutout diameter of 140 mm. The corresponding pull-out forces are afterward determined in the

  doi:10.5075/epfl-298799_978-2-9701614-0-0

force-displacement diagram by intersection of the simulation from the 5 %-regression line in the tests. In addition to the fact that no distinction is made between the L- and W- directions in the IDH [3], it is apparent that the analytical equations from the IDH [3] are conservative for insert distances until 40 mm compared to the simulatively determined interference coefficients. In the simulation, there is also a clear difference in the L- and W- directions which is due to the fact that the stress distribution in the core assumes an oval shape because of the stronger double walls (exemplarily shown in *Figure 7* (b)). As a consequence, the overlapping area of the stress fields with an insert positioning along the W-direction is smaller than in the L-direction. After a plateau is reached, the interference coefficients in the simulation reduce again. This can be attributed to restraint effects since parts of the stress fields of the inserts are now placed under the clamping. Such effects are not considered in the analytical equations in the IDH [3].

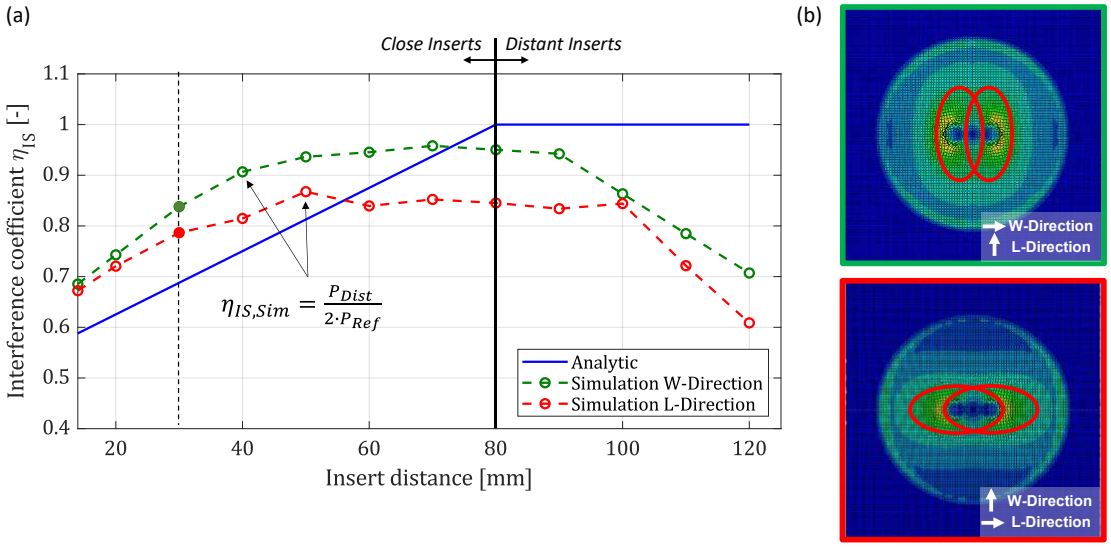

Figure 7. Interference coefficients over different insert distances (a); Stress fields for Insert distance of 30 mm in W-direction (green) and L-direction (red) (b).

5. Conclusion and outlook

If several inserts are loaded in the same direction, their stress fields can overlap, which leads to a reduction of their load-bearing capacities. In this paper, a detailed numerical model was implemented based on the pull-out test and was subsequently extended to the insert proximity test. Furthermore, test results of the insert proximity test for three different insert distances were shown. Using a hybrid modeling approach consisting of a meso and a solid core, the progressive damage behavior of the sandwich structure from the experiments could be accurately reproduced. Numerical studies of different insert distances with simplified solid models further show that the core orientation has a large influence on the resulting interference coefficients. Overall, the virtual models developed lead to an improvement in the design with multiple load introduction elements and result in a more accurate prediction compared to the analytical equations in the IDH. In further research, additional simulations for insert groups with asymmetric load introduction can be investigated. In order to ensure a successive transferability to the product level and to improve the numerical design, it is further planned to increase the structural complexity and to investigate larger structures.

  doi:10.5075/epfl-298799_978-2-9701614-0-0

Acknowledgements

The acknowledgements being relevant for this contribution are based on the research projects *EFFEKT (20D1927D); DEPOSE (20Q1905)* and *CabinJoint (20Q1904B)* supported by the Federal Ministry for economic Affairs and Climate Actions (BMWK) on the basis of a decision by the German Bundestag.

6. References

[1] Zenkert D. *Handbook of Sandwich Construction*. Cradley Heath: EMAS; 1997.
[2] Bitzer T. *Honeycomb Technology*. Dordrecht: Springer; 1997.
[3] European Cooperation for Space Standardization - ECCS. ECSS-E-HB-32-22A: *Space Engineering Insert Design Handbook*. 2011.
[4] Heimbs S, Pein M. Failure behaviour of honeycomb sandwich corner joints and inserts. *Composite Structures*. 2009; 89(4): 575–88.
[5] Dios Rodríguez-Ramírez J de, Castanié B, Bouvet C. Insert of sandwich panels sizing through a failure mode map. *Composite Structures*. 2020; 234: 111724.
[6] Department of Defense. *Composite Material Handbook - Volume 3 Polymer matrix composites materials usage, design and analysis*. 1997.
[7] Schwan L, Hüttich P, Wegner M, Krause D. Procedure for the transferability of application specific boundary conditions for the testing of components and products. In: Krause D, Paetzold K, Wartzack S. (eds.) *Proceedings of the 32nd Symposium Design for X, DfX 2021, 27-28 September 2021, Tutzing, Germany.*
[8] Heyden E, Hartwich TS, Schwenke J, Krause D. Transferability of Boundary Conditions in Testing and Validation of Lightweight Structures. In: Krause D, Paetzold K, Wartzack S. (eds.) *Proceedings of the 30th Symposium Design for X, DfX 2019, 18-19 September 2019, Jesteburg, Germany.*
[9] Seemann R, Krause D. Numerical modelling of partially potted inserts in honeycomb sandwich panels under pull-out loading. *Composite Structures.* 2018; 203: 101–9.
[10] Roy R, Nguyen KH, Park YB, Kweon JH, Choi JH. Testing and modeling of Nomex™ honeycomb sandwich Panels with bolt insert. *Composites Part B: Engineering*. 2014; 56: 762–9.
[11] Schwenke J, Krause D. Optimization of load introduction points in sandwich structures with additively manufactured cores. *Design Science*. 2020; 6.
[12] Seemann R. *A Virtual Testing Approach for Honeycomb Sandwich Panel Joints in Aircraft Interior*. Berlin: Springer Berlin Heidelberg; 2020.
[13] Rodriguez-Ramirez JdD, Castanie B, Bouvet C. Experimental and numerical analysis of the shear nonlinear behaviour of Nomex honeycomb core: Application to insert sizing. *Composite Structures.* 2018; 193: 121–39.
[14] Seemann R, Krause D. Numerical modelling of Nomex honeycomb sandwich cores at meso-scale level. *Composite Structures.* 2017; 159: 702–18.
[15] Tsujii. Analysis of Mechanical Properties of Aramid Honeycomb Core. *Transactions of the Japan Society of Mechanical Engineers Series A*. 1995; 61(587): 1608-14.
[16] Roy R, Park S-J, Kweon J-H, Choi J-H. Characterization of Nomex honeycomb core constituent material mechanical properties. *Composite Structures.* 2014; 117: 255–66.
[17] Slimane S, Kebdani S, Boudjemai A, Slimane A. Effect of position of tension-loaded inserts on honeycomb panels used for space applications. *Int J Interact Des Manuf*. 2018; 12(2): 393–408.

  doi:10.5075/epfl-298799_978-2-9701614-0-0

DESIGN AND FABRICATION OF MULTI-FUNCTIONAL ENERGY STORAGE COMPOSITES INTEGRATING ULTRATHIN LITHIUM-ION BATTERY WITH ENHANCED ELECTRO-MECHANICAL PERFORMANCE

Pias Kumar Biswas[a], Mayur Jadhav[a], Asel Ananda Habarakada Liyanage[b], Hamid Dalir[a,], Mangilal Agarwal[a,*]*

a: Integrated Nanosystems Development Institute, Purdue School of Engineering and Technology, Indiana University–Purdue University Indianapolis, Indianapolis, IN, 46202, USA
b: Multiscale Integrated Technology Solutions LLC, Indianapolis, IN, 46202, USA
Presenting author: piasbisw@iu.edu, *Corresponding author

Abstract: *Exponential advancement in the automotive and aerospace industry promotes the need for Multifunctional Energy Storage Composites (MESCs) to minimize the dependence on fossil fuels and reduce structural weight. This study proposes and evaluates a multi-functional carbon fiber reinforced polymer (CFRP) composite with an embedded lithium-ion polymer battery, demonstrating a structural integrity concept. Here electrospun epoxy-multiwalled carbon nanotubes (epoxy-MWCNT) nanofibers were incorporated precisely on the uncured CFRP surface to enhance adequate interfacial bonding and adhesion between the layers after curing. The mechanical and physical properties of modified CFRP have been evidenced to possess higher mechanical strength than the traditional CFRP composite. Commercial ultra-thin lithium-ion battery with higher energy density has been uniquely integrated into the core of the CFRP composite structure. Comparison with conventional CFRP composite and electro-mechanical testing ensured that the electrochemical property of the embedded battery was preserved in loading/unloading conditions, and the mechanical strength of the composite structure was not compromised.*

Keywords: Multi-functional Composites; Li-ion Battery, Electrospinning, Nanofibers, CFRPS

1. Introduction

Recently, structural batteries have emerged as a trendy concept for overcoming functional restrictions in load-bearing to achieve weight and volume savings in many structural domains such as airplanes, spacecraft, and commercial vehicles (1-3). These structural batteries provide energy storage capabilities. Rather than the energy storage elements themselves, the packaging material is critical for load-carrying capacity in these existing batteries. Numerous commercial sectors are attempting to lower the structural weight of their key products in order to mitigate global warming. Carbon fiber composites are increasingly being employed in structural components of motor vehicles, such as the body panels and chassis, to accomplish this goal. With the advancement of electric propulsion and the increasing demand for hybrid and electric vehicles on the market, issues for energy storage in these vehicles arise in terms of vehicle space. This also influences the vehicle's empty weight, as the battery system accounts for up to 25% of the vehicle's total body weight (4, 5). This creates relatively large storage space in the volume. In order to increase the vehicle's total storage, structural, and space economy, it is required to incorporate multi-functional composites into vehicle components. There are a number of methods for integrating electrical storage devices into composite structures. The first is the fabrication of the composite into a structural dielectric capacitor (SDCs) (6-8).

  doi:10.5075/epfl-298799_978-2-9701614-0-0

Contemporary Li-ion batteries are primarily designed for maximum energy storage performance at the expense of mechanical load carrying capacity and robustness. Li-ion pouch cells are constructed by stacking alternating anode and cathode layers separated by thin microporous polymer separator membranes (9). The advanced thin electrode films are made of copper and aluminum, which have a high structural composition. When these pouch cells are bent, applying the least mechanical load results in unjustified deformation and layer slippage. Due to the vacuum-sealed aluminum-polymer-laminate packing material, the structure has negligible strength. This study aims to synergistically syndicate the load-bearing capabilities of present battery elements to incorporate mechanical robustness into cells, resulting in significant volume and weight savings in the packaging. This work aims to fabricate structural load-bearing batteries using multi-functional energy storage composites (MESC) as an alternative technique. MESCs are a revolutionary energy storage device because they combine high mechanical strength with low weight and superior energy storage capabilities. MESCs are constructed by embedding Li-ion battery electrode materials in high-strength CFRP composites (10). This technique does not require altering Li-ion batteries' electrochemistry and can be included in standard industry designs, which are critical for engineering implementation. Due to the sandwich-style construction, the laminate's moment of inertia increases significantly, resulting in increased flexural rigidity. This mechanical robustness of the proposed CFRP composite structures enables them to be manufactured as multi-functional energy-storage devices for electric vehicles and other structural applications.

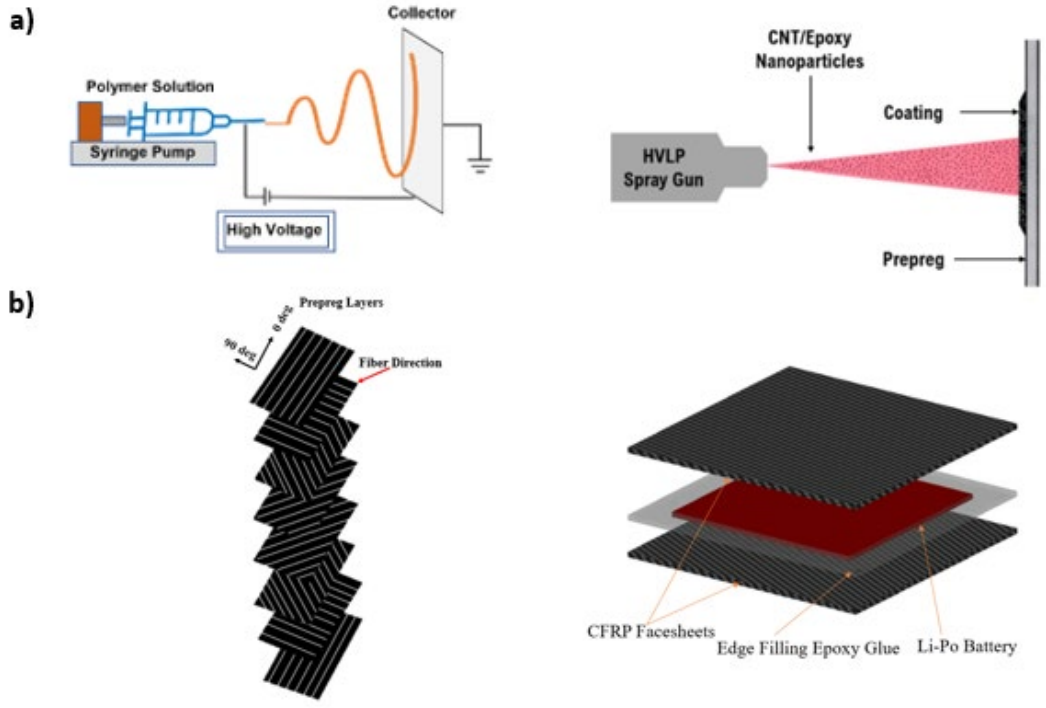

Figure 1: a) Electrospinning and air-spraying setup, b) stacking the prepreg layer (0°/90°/+-45°)2s., and integration of Li-ion battery in the core of the structure.

  doi:10.5075/epfl-298799_978-2-9701614-0-0

2. Methodology

2.1 Material Preparation

Masterbatch of MWCNTs/epoxy was synthesized using a previously published method by our group (10-12). Bisphenol A (50 - 99 pbw.%) and carbon nanotubes (5 wt.%) were mixed together, followed by the addition of Dimethylformamide (DMF) (1:4 volume ratio) and Triton X- 100 (20:1 volume ratio). Then the resulting mixture was sonicated for 10 mins in intervals of 45s and 30s rest between cycles. The same weight of more epoxy was added to the mixtures, and 15 mins stirring was done, followed by sonication. Finally, to have a uniform viscous mixture, the curing agent was mixed at a ratio of 15:1 and stirred at 50°C for 2 hours to obtain a homogeneous solution. The uniform mixture was then degassed and rested for 16 hrs prior to electrospinning. A syringe with a needle gauge of 26 G was filled with MWCNTs/epoxy mixture for electrospinning onto the CFRP layer. The Epoxy-MWCNT solution was air-sprayed onto the CFRP layers as an alternative method.

2.2 Electrospun CFRP Facesheets Sample Preparation

Electrospun and air sprayed Epoxy-MWCNT nanofibers were deposited onto (10 x 10 cm) precut prepreg layer with a plain weave pattern (SE70 Gurit Holding AG, Wattwil/ Switzerland). To decrease the void ratio, a hand layup process was used, followed by vacuum bagging. The stacking sequence on one side of the cell is $[0/90/\pm45]_{2s,}$ as reported in our previous work (13, 14). Square slots were cut before laying up in the stacking. A total of twenty layers were employed to create a single sample. Before curing, the samples were vacuum bagged for 60 minutes to ensure optimal adhesion between the layers. The sample was completely cured by placing it in a programmable oven (Easy Composite, UK) set to 120^{o}C for 25 minutes and vacuuming to a pressure of less than 1 bar. While maintaining the pressure, the samples were cooled to room temperature. The samples were given a smooth finishing at the edges for appearance. After curing, the sample had a final thickness of 0.52 cm.

2.3 Assembly of the Batteries Inside the CFRP Samples

The fabrication method of the MESC cell was operated sequentially. Two CFRP facesheets with the rectangular slot in the middle are placed flat on the surface. A prepreg sheet of the exact dimensions with a slot space is employed as the adhesion between the two surfaces. The edges of the two surfaces are heated at a temperature of 70^{o}C by means of a heat gun. The prepreg sheet is placed on one side of the CFRP face sheet, and the pouch cell battery is placed at the center of the surface. Due to the heated surface, the epoxy in the uncured prepreg sheet enables it to act as an epoxy adhesive, and both the surfaces are then joined together. The sample is then compressed in a heated hydraulic press to melt further the epoxy resin in the middle layer of the sample and helps to fuse both the surfaces of the facesheets together securely (100^{o}C, 0.5 MPa pressure). The sample remained to cool down to room temperature under the same temperature. During this phase, the epoxy solidified and thus equilibrated the stack mechanically. Edges of the sample were then sealed off with additional epoxy adhesive for a tidier appearance and homogeneity of the two surfaces. This method produced six samples with electrospun, air sprayed enhanced CFRP, and control CFRP sheets.

  doi:10.5075/epfl-298799_978-2-9701614-0-0

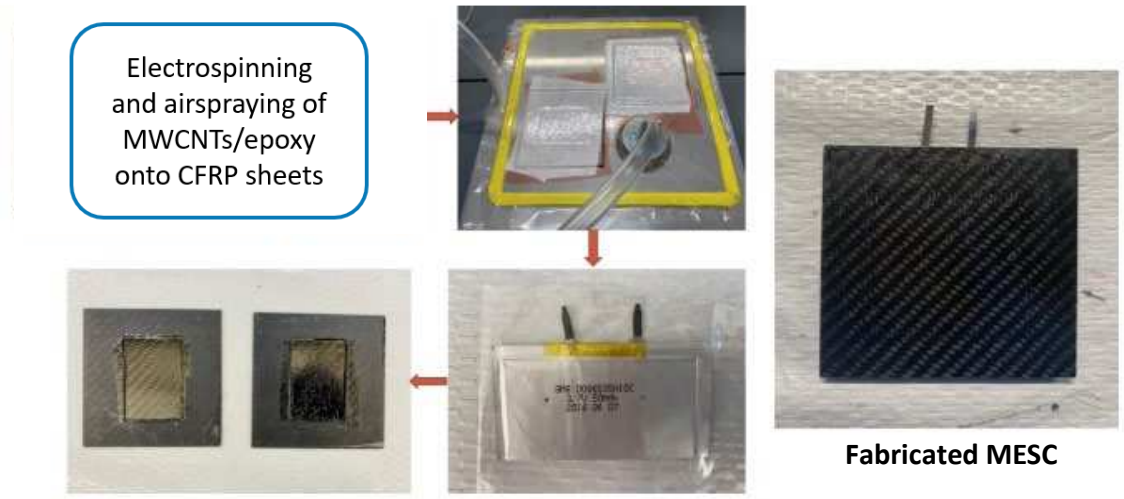

Figure 2: Hand layup method to fabricate MESC by enhanced CFRP facesheets.

3. Test Methods

3.1 Quasi-static Three-Point Bending

Three-point bending is performed to define the inter-laminar bond strength characteristics of the various types of CFRP-based MESC samples. For mechanical testing, a cylindrical roller is used as an applicator on the fixture for three-point bending (2 kN servo-hydraulic load frame, Integrated Resources Inc. MTS machine). This testing procedure followed the ASTM C393 standard technique. Flexure testing generates tensile stress on the convex side and compression stress along the midline, resulting in a shear stress area. The force required to bend the beam is measured under three-point loading circumstances. The cylindrical load applicator is positioned with its axes parallel to the load applicator axis and parallel to the specimen axis. At the mid-span of the sample, the cylindrical load applicator applied a vertical downward force along the line. The evaluation of adequate flexural rigidity of the sample is validated through the reinforcement of the inter-layer-shear inhibition capabilities. The load on the sample was applied at 3.33 mm/min. A linear variable differential transducer was employed throughout the experiment to measure the vertical displacement at the mid-span. The initial loading results were recorded, and the sample was subjected to continuous loading on the mid-span for 12 hours. This testing aims to analyze the battery characteristics for a period of time of continuous bending.

3.2 Electrochemical Characterization

The MESC samples were initially subjected to a continuous maximum bending load for 12 hours. The sample pouch cell battery was subjected to a bending load until deformation and when it was not under any loading and then tested. The initial purpose was to conduct an in-situ testing environment wherein the samples were subjected to bending loading and, at the same time, evaluated for electrochemical performance. However, due to the logistical constraints, the samples were subjected to the above specific bending cycle and then tested later. The samples were initially exposed to a slow calibration cycle between 3.0 V and 4.2 V to define the C rate. It is also the current at which the battery is discharged in 1 h. The initial discharge capacity of each sample at the beginning of life (BoL) was measured under constant current (CC) cycling at C/10.

The pouch cell battery is used for this testing to record the base performance. This testing calculates the expected capacity on the amounts of active materials added. The depth of discharge (DoD) is measured from the voltage difference while the current is interrupted. This charge-discharge cycle was repeated to measure the cell life performance by increasing the cycles of different sample types to compare the discharge capacity retention properties.

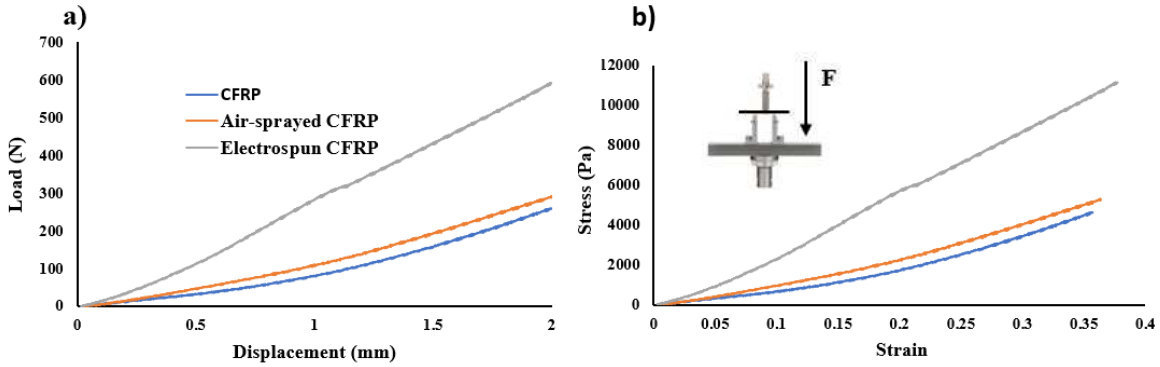

Figure 3: a) Load vs. displacement and b) strain vs. stress curves for different types of MESCs.

4. Results and Analysis

4.1 Quasi-static three-point bending test

The three-point bending for eight cell samples was performed to evaluate the mechanical performance of the MESC within themselves and the control pouch cell battery. The Interlaminar Shear Strength (ILSS) test sampling is much more insistent than the other shear tests. The values for flexural stress, elasticity in bending, and flexural strain are observed. The results are sensitive to the testing method based on the specimen, loading geometry, and strain rate. The stress required to fracture the samples yields a stress-deflection curve slope in this testing. The bending moment varies from zero at the support and maximum at the center. The electrospun CFRP sample has shown the highest load of 695.47 N, as shown in figure 3(a). The displacement had a limit of 2 mm as it is assumed to be the ideal state where the battery can take the maximum load without affecting its electrochemical characteristics. There is also an observation here that deformation of layers in the top did not occur and this maximum load could be further extended given there were no constraints on the displacement side. On the other hand, the control sample fabricated as a conventional CFRP sample shows the lowest peak load of 289.38 N with subsequent deformation in its top layers. The air sprayed CFRP sample displays a peak load of 365.25 N and lesser damage in the top layers than the conventional CFRP sample. The pouch cell battery could not register a peak load of more than 6 N before being completely deformed.

4.2 Flexural Rigidity

Flexural testing is the most practical method for gauging fiber-resin interface and matrices to assess the improvements in interlaminar properties. The electrospun CFRP sample demonstrated high flexural strength and strain compared with the control CFRP, and the air sprayed CFRP samples. The primary considerations in this sample were previous research experimentation revealed nano reinforcements integration causes a considerable increase in

the flexural properties. The packaging of the lithium-polymer battery shows a flexural strength of 410.27 psi and goes onto total deformation, while the control and the air-sprayed samples show a flexural strength of 230.15 psi 390.31 psi, respectively.

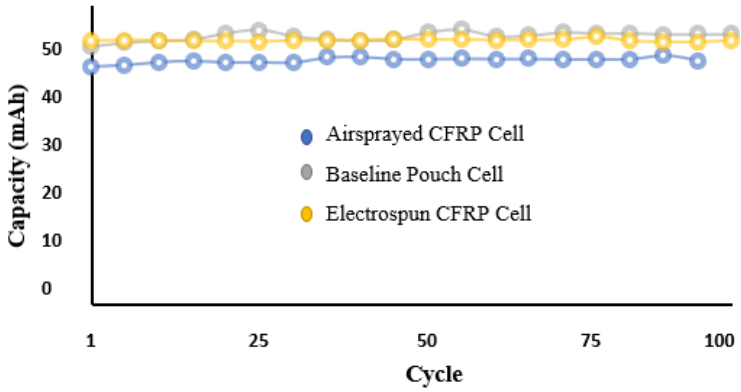

Figure 4: Battery performance inside different MESCs under loading conditions.

4.3 Electrochemical Analysis

The batteries were cycled using Landt battery analyzers (Landt Instruments), and all the electrochemical testing was performed at a temperature of 30° C. Each MESC was cycled 100 times at a rate of 1C. After each cycle, the charge-discharge rate and battery capacity were determined. Additionally, the baseline pouch cell battery was cycled before and after applying bending pressures. It demonstrated that the battery integrated into the electrospun CFRP enhanced MESC performs identically to a conventional pouch cell, as shown in figure 4. Similarly, the controlled and air played CFRP enhanced MESC significantly decreased battery performance under loading conditions. This demonstrates that electrospun CFRP cells are the optimal construction for the MESC in terms of overall testing properties.

5. CONCLUSION

The embedding of LiPo batteries within the sandwich CFRP surfaces' core in different orientations and characteristics presents a novel form of structurally integrated batteries in a distinctive material with a vertical integration process. In this process, the fundamental mechanical properties of the CFRP materials make the industry-standard Li-ion battery much more robust in a structural applications environment under the architecture of MESC. The highest strength in electrospun CFRP sandwich structures did not affect the batteries when the possibility of the malfunction was localized metal gouge to the structure's core. There was a significant increase in the mass of the sandwich composite with the inclusion of the LiPo batteries since they are much denser and can increase the self-weight of the structure and also can reduce the stiffness and strength at the same time. The design consideration, in this case, can be an equilibrium of particular properties and aim at increasing the energy storage density for obtaining lightweight structures. This was proven correct by the electrospun CFRP samples, which were comparatively lighter in weight than the air-sprayed and conventional samples and thinner in construction, resulting in maximum mechanical strength. The process of electrospinning the conventional CFRP facesheets is also economical and can open a versatile range for this kind of device in automotive structural applications and areas where flexibility can be a challenge.

  doi:10.5075/epfl-298799_978-2-9701614-0-0

Acknowledgements

The authors would like to express their gratitude to the National Science Foundation Major Research Instrumentation Program for supporting this research (#1229514) for FESEM. The authors declare a potential financial conflict of interest. Multiscale Integrated Technology Solutions LLC (MITS), which has been awarded the National Science Foundation (NSF) Small Business Technology Transfer (STTR) (#2036490) grant to conduct research and development (R&D) work on enhancing the strength of carbon fiber reinforced polymer composites, has potential commercial interest in the research presented in this paper.

6. References

1. Asp LE, Johansson M, Lindbergh G, Xu J, Zenkert D. Structural battery composites: a review. Functional Composites and Structures. 2019;1(4):042001.
2. Kalnaus S, Asp LE, Li J, Veith GM, Nanda J, Daniel C, et al. Multi-functional approaches for safe structural batteries. Journal of Energy Storage. 2021;40:102747.
3. Danzi F, Salgado RM, Oliveira JE, Arteiro A, Camanho PP, Braga MH. Structural Batteries: A Review. Molecules. 2021;26(8).
4. König A, Nicoletti L, Schröder D, Wolff S, Waclaw A, Lienkamp M. An Overview of Parameter and Cost for Battery Electric Vehicles. World Electric Vehicle Journal. 2021;12(1).
5. De Gennaro M, Paffumi E, Martini G, Giallonardo A, Pedroso S, Loiselle-Lapointe A. A case study to predict the capacity fade of the battery of electrified vehicles in real-world use conditions. Case Studies on Transport Policy. 2020;8(2):517-34.
6. Chan K-Y, Jia B, Lin H, Hameed N, Lee J-H, Lau K-T. A critical review on multi-functional composites as structural capacitors for energy storage. Composite Structures. 2018;188:126-42.
7. Chung DDL. Development, design and applications of structural capacitors. Applied Energy. 2018;231:89-101.
8. Chan K-Y, Lin H, Qiao K, Jia B, Lau K-T. Multi-functional graphene oxide paper embodied structural dielectric capacitor based on carbon fibre reinforced composites. Composites Science and Technology. 2018;163:180-90.
9. Aliahmad N, Biswas PK, Dalir H, Agarwal M. Synthesis of V2O5/Single-Walled Carbon Nanotubes Integrated into Nanostructured Composites as Cathode Materials in High Performance Lithium-Ion Batteries. Energies. 2022;15(2).
10. Biswas PK, Liyanage AAH, Jadhav M, Agarwal M, Dalir H. Higher strength carbon fiber lithium-ion polymer battery embedded multi-functional composites for structural applications. Polymer Composites. 2022;n/a(n/a).
11. Biswas PK, Aliahmad N, Dalir H, Agarwal M. Nanostructured V2O5-SWCNTs based lithium ion battery for multi-functional energy storage composites: materials synthesis and fabrication. AIAA Scitech 2021 Forum. AIAA SciTech Forum: American Institute of Aeronautics and Astronautics; 2021.
12. Aliahmad N, Wable V, Biswas PK, Hernandez I, Dalir H, Agarwal M. Carbon nanotube/epoxy submicron filaments for composite reinforcement applications. AIAA Scitech 2021 Forum. AIAA SciTech Forum: American Institute of Aeronautics and Astronautics; 2021.

13. Wable V, Biswas PK, Moheimani R, Aliahmad N, Omole P, Siegel AP, et al. Engineering the electrospinning of MWCNTs/epoxy nanofiber scaffolds to enhance physical and mechanical properties of CFRPs. Composites Science and Technology. 2021;213:108941.
14. Aliahmad N, Biswas PK, Wable V, Hernandez I, Siegel A, Dalir H, et al. Electrospun Thermosetting Carbon Nanotube–Epoxy Nanofibers. ACS Applied Polymer Materials. 2021;3(2):610-9.

  doi:10.5075/epfl-298799_978-2-9701614-0-0

MULTILAYER LEADING EDGE PROTECTION SYSTEMS OF WIND TURBINE BLADES: A REVIEW OF MATERIAL TECHNOLOGY AND DAMAGE MODELLING

Alexandros Antoniou[a], Kirsten Dyer[b], William Finnegan[c], Robbie Herring[b], Bodil Holst[d], Jakob Ilsted Bech[e], Ioannis Katsivalis[f], Tazefidan Kutlualp[a], Leon Mishnaevsky Jr.[e], Asta Šakalytė[g], Fernando Sánchez [h], Julie Teuwen[i], Trevor Young[f]*

a: Fraunhofer Institute for Wind Energy Systems, 27572 Bremerhaven, Germany
b: Offshore Renewable Energy Catapult, Offshore House, Albert Street, Blyth, NE24 1LZ, UK
c: MaREI Research Centre, School of Engineering, National University of Ireland Galway, University Road, Galway, Ireland, H91 TK33
d: University of Bergen, Department of Physics and Technology, 5007 Bergen, Norway
e: Department of Wind Energy, Technical University of Denmark, Roskilde, Denmark
f: University of Limerick, Limerick, Ireland, V94 T9PX
g: AEROX Advanced Polymers, 46185 Pobla Vallbona-Valencia, Spain
h: Research Institute of Design, Innovation and Technology, University CEU Cardenal Herrera, CEU Universities, Avda. Seminario S/N, 46115 Moncada-Valencia, Spain,
*Corresponding author (fernando.sanchez@uchceu.es)
i: Aerospace Manufacturing Technologies, Faculty of Aerospace Engineering, Delft University of Technology, Kluyverweg 1, Delft 2629HS, the Netherlands

Abstract: *The use of composites opens great prospects in the design and manufacture of the wind turbine blades due to their optimization versatility. Blade manufacturers employ polymeric surface materials to protect the composite structure from exposure to repeated impact of rain droplets which are mostly contributing to the leading edge erosion of wind turbine blades. Modelling tools considering multicomplex stress states and the material degradation are required for design purposes toward protection performance. This investigation summarizes a initial review based on two main issues: firstly, the LEP material configuration used in industry as a multilayer system considering the blade integration technology and, secondly, the modelling techniques and numerical procedures currently used to predict both wear surface erosion and interface delamination failure. The work is conducted in the framework of the IEA Wind TCP (International Energy Agency Wind Technology Collaboration Programme) - Task 46 Erosion of wind turbine blades.*

Keywords: Wind turbine blades; leading edge protection; droplet impact computational modelling; multilayer systems

1. Introduction

In the immediate future, wind power will provide more electricity than any other technology based on renewable and low-emission energy sources. As a result, the size of offshore wind turbines has increased to harvest more wind energy in order to achieve the 2050 EU carbon neutral targets. The use of composites opens great prospects due to their optimization versatility. However, composites perform poorly under rain droplet impact, perpendicular to the reinforcement direction and are sensitive to environmental factors such as heat, moisture, icing, salinity and UV.

  doi:10.5075/epfl-298799_978-2-9701614-0-0

The hindering of leading-edge erosion could be obtained through its polymer-based multilayer material optimization i.e. Leading Edge Protection LEP [2]. Both the surface erosion and the material intra-layer adhesion are affected by the shock wave produced from the collapsing water droplet after impact, see Figure 1. The propagating stress waves are reflected and transmitted to the composite laminate substrate through the thickness of the LEP system [3] .It is necessary to increase the interfacial mechanical resistance of the multi-layered system from the surface to the interface boundaries to damp the surface damage and avoid subsurface delamination [4].

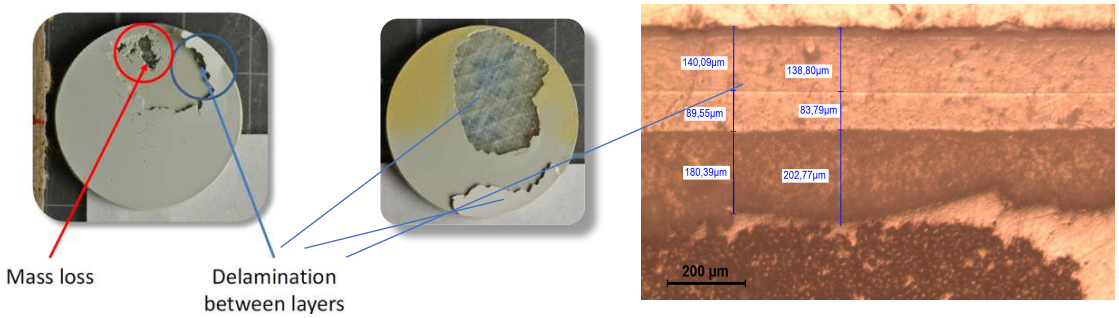

(a) (b)

Figure 1. (a) Rain erosion testing specimens. Erosion failure due to mass loss on surface and interface delamination. (b) Multilayer system microscopy. Two coating layers define an interface that tend to delaminate upon impingement, from [6].

Therefore, validated models considering the developed multicomplex stress states and the material degradation due to the environmental loads are required for design purposes toward anti-erosion protection performance. This investigation summarizes the initial review of the current literature conducted in the framework of the IEA Wind TCP (International Energy Agency Wind Technology Collaboration Programme) - Task 46 Erosion of wind turbine blades [5]. This review will allow for the identification of gaps within the research that can be explored during IEA Wind Task 46 on the Erosion of Wind Turbine Blades.

2. LEP material configuration and blade integration technology

2.1 LEP solutions used by industry

There are a variety of protection systems used by industry to mitigate the negative effects of erosion and extend the lifetime of the blades, including coatings, tapes, and soft shells. These are applied along the leading edge at the vulnerable portion of the blade. As shown in Figure 2, the application of coating systems is multi-layered with a filler layer used to smooth the surface before coating application. Some manufacturers include a primer layer to aid adhesion in the system. Tapes and thicker softshells are applied with adhesives directly to the blade in a single piece. Despite the different approaches, there is currently no solution that can protect blade edges for the entire lifetime of the blade. However, challenges and limitations exist with each of the current solutions, with regard to their level of rain erosion protection, challenges during manufacturing or application, failures in the adhesive used, and reduction in the aerodynamic performance of the blade due to the addition of the protection system along the leading edge.

  doi:10.5075/epfl-298799_978-2-9701614-0-0

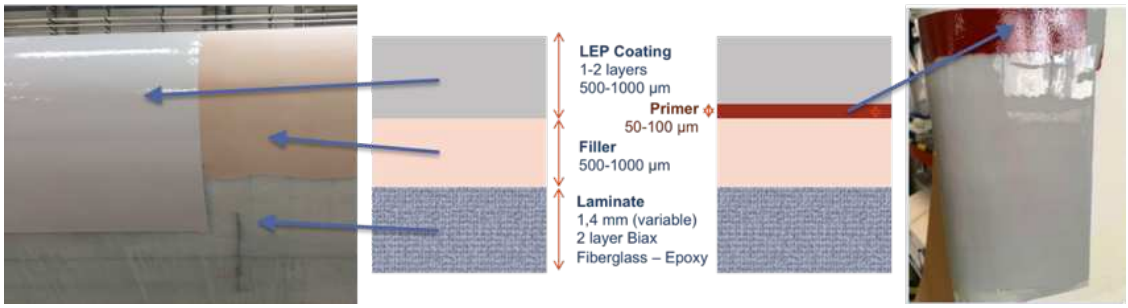

Figure 2. Leading Edge Protection (LEP) system configuration on the blade surface as a post-mould coating application multilayer system [6]

Protection systems either fail by surface erosion or delamination, with the quality of manufacture and application determining which failure mode occurs. Coatings rely on intensive manual techniques to be mixed and applied to the blade and as such can be vulnerable to defects. The defects then act as erosion initiators and encourage the development of erosion. Tapes and soft shells are manufactured away from site in controlled environments and are less prone to defects than coatings. However, if they are not effectively applied to the blade surface, wrinkles and air pockets can be introduced, reducing the adhesion of the bond. Consequently, further development in protection systems and their application is required.

The influence on the anti-erosion performance of the protection systems materials can be determined experimentally by testing, or by conducting analytical or numerical studies. The analysis (or design) of Leading-Edge Protection systems depends on the material properties in the configuration and the operational load to which it is designed during its realistic life, that is, it must be able to withstand accelerated loads and also fatigue field regimes. To make a selection or design of a specific protection system, appropriate modelling must be defined. Numerical and analytical models can be constructed with their own capabilities and limitations and, in all cases, appropriate material characterization for modelling input parameters identification is required.

3. Computational modelling techniques to predict erosion damage considering LEP multilayer protection systems

3.1 Modelling based on material fundamental properties

Several computational studies have been used to understand the mechanisms leading to damage initiation during liquid impingement. Previously, Keegan at al. [7] compiled a comprehensive review, which details modelling methods along with a number of other techniques for preventing erosion on the leading-edge erosion of wind turbine blades. Additionally, Dashtkar et al. [8] reviewed the liquid erosion mechanism, water erosion testing procedures and the contributing factors to the erosion of the leading edge of wind turbine blades, including a brief discussion on the use of carbon nanotubes and graphene nano-additives for improving the erosion resistance of the leading edge. Several reviews have been developed to contribute towards identifying the physical process of erosion and key failure mechanisms behind rain erosion, along with estimation of fatigue life of the coating material [9], [10].

Single droplet models are used to investigate the fluid-structure interaction and the stress/strain behaviour over time in multilayer systems. In most cases, these models analyse single droplet impacts and have been achieved using a variety of methods, including, a) the Lagrangian method [11], b) the Coupled Eulerian and Lagrangian (CEL) method [11, 12] and c) the smoothed particle

hydrodynamics (SPH) method [13,3]. A coupled Eulerian and Langrangian (CEL) method was used by Keegan et al. [14] to model rain droplet impact on wind turbine coating materials (epoxy based gelcoat) where the materials were modelled with ANSYS-predefined epoxy resin properties. The impact pressure due to the droplet from the simulations closely correlated with the analytical water hammer pressure. Keegan et al. [15] also used smooth particle hydrodynamics (SPH) to simulate rain and hail impact resulting in high correlations with the experiments, where multimaterial systems for gelcoated substrates were explored. The contact between the material interfaces were defined as fully fixed. Verma et al. [3] used the SPH method to perform a parametric study on the effect of different environmental conditions, such as droplet sizes, impact angles and velocities, on the rain erosion performance of wind turbine blades. The authors developed a coupled fluid structure interaction (FSI) model where the numerical model consists of structure domain modelled using traditional finite element method (FEM), and the fluid domain modelled using meshless SPH. The interfaces in the materials (gelcoat-CSM (chopped strand mat), CSM/GFRP (glass fibre reinforced plastic), between GFRP layers) were modelled through cohesive interactions. For the gelcoated substrates, most of the stresses are developed on the coating surface while the substrates (consisting of CSM and GFRP experience less stress development due to single droplet impact. In addition, they studied the effect of repetitive rain droplet impacts and managed to numerically correlate the erosion damage to the number of impacts. The authors used cohesive interfaces to introduce interfacial damage in the substrate/LEP interface but did not consider the effects of viscoelastic recovery of the polymer coatings. SPH modelling has also been investigated by Astrid et al. [16] where coatings were modelled using Finite Element methods (FEM). Doagou-Rad and Mishnaevsky [17] conducted a comparison between the CEL and SPH methods, which also compared to the analytical solution of the Modified Waterhammer Equation. The two numerical methods were in good agreement, but both were found to underestimate the impact stresses compared to the analytical solution. In addition, the authors performed a parametric study in which they considered environmental (impact angle and velocity, droplet shape), manufacturing (surface characteristics) and design (density, stiffness and Poisson's ratio) aspects of the LEP systems. Finally, they showed that considering the viscoelastic effects of the polymer materials could lead to a change in the damage pattern.

An alternative method, Discrete Element method (DEM), also based on meshless formulations, was investigated by Castorrini et al. [18]. A Streamline-Upwind/Petrov-Galerkin (SUPG) and Pressure-Stabilizing/Petrov-Galerkin (PSPG) stabilisation method were used together with particle-cloud tracking approach to estimate the key regions along the blade that are critical for erosion. Isotropic materials were used in the model, where the material properties needed as input were the fracture toughness of the material, as well as Rayleigh wave velocity, density, E-modulus, and poisson ratio.

A Cohesive zone modelling approach between layers was proposed also by Cortes et al. [4] to model the interfaces between coating and composite laminate. It is therefore necessary to understand and characterise the failure behaviour of the interface boundaries in multi-layer systems. To investigate the adhesion between coating and substrate pull-off tests, peeling–adhesion tests and nanoindentation testing where performed. Fraisse et al. [19] developed a coupled Eulerian-Lagrangian symmetric model to study impact of water droplet on coated laminate of the blade. The gel-coated multilayer material was modelled in Eulerian domain, where perfect contact was assumed and the water droplet was modelled in Lagrangian domain.

  doi:10.5075/epfl-298799_978-2-9701614-0-0

Fatigue analysis based on semi-empirical analytical modelling was proposed by Springer [20]. It considers a model that relates material fundamental properties to predict the time to failure in a rain erosion test. The stress history in the coating and in the substrate has to be identified analytically. It is affected by the shockwave progression due to the vibro-acoustic properties of each layer, and by the time interval of the repeated water droplet impacts. The fatigue life of the material is then calculated, and the model can be applied to estimate the stress at different locations through the thickness, i.e., the coating surface or at the coating–substrate interface, etc. It has been applied considering in-field conditions in [21]. It is based on numerical parameters defined with specific experimental observations. Herring et al. [22] analysed how variations on material or Rain Erosion Testing configurations may include important differences and uncertainties when applied in the performance analysis. However, the experimental data used to develop the model is unrepresentative of the testing and materials currently used within the wind industry. The Springer model also ignores the multilayer configuration. Fatigue analysis of the coated substrates subjected to stochastic rain field simulation was proposed by Hu et al. [23] using the coupled SPH and FEA approach. The gel-coated samples were modelled with perfect contact between the different layers in the FEA. Other computational studies were developed for the multi-impact fatigue analysis [24]. Pugh et. al. [25] did a comprehensive review of various analytical techniques to inspect and characterize the materials used in rain erosion to evaluate the performance.

Modelling tools provide a guidance in the selection and modulation of material protection properties and should reduce the scope of testing to verify the rain erosion resistance of LEP systems. The novelty and differentiation will likewise be based on an approach to the erosion problem including the material fundamental properties and establishment of the way the erosion occurs such as progressive failure mode or interface delamination. It is required additionally to include the influence of factors which had not been entirely or accurately covered in the treated modelling when evaluating a multilayer LEP system instead of a simplified coating-substrate approach.

3.2 Material characterization required as modelling input parameters

The previously referenced models aim to quantitatively predict the erosion damage of coated materials under the previously untested conditions. In this section the review is focused on studies of the mechanical parameters that may be included in such analysis.

Modelling damage and failure in a multilayer system can be achieved with two different approaches. The first approach is by introducing damage parameters (based on continuum or fracture mechanics) for each material separately which would require an extensive material characterisation at different strain rates. The second approach would be to consider the whole multilayer system as an interface and introduce an interfacial damage law. Such an approach could for example be, Cohesive Zone Modelling (CZM) which requires as an input the fracture energy of the interface. However, once again, the main challenge is related to the fact that such a characterisation would need to take place at very high strain rates to be representative of a water droplet impact event. In both cases, rain erosion is expected to contribute to property degradation and, therefore, a fatigue law would also need to be established which takes into consideration the gradual degradation of those parameters. Other factors that are expected to contribute to property degradation are high/low temperature cycles, moisture absorption and UV radiation. In such cases, characterisation tests should be repeated in both virgin state and

  doi:10.5075/epfl-298799_978-2-9701614-0-0

after environmental exposure to accurately capture accurate numerical modelling inputs. Table 1 provides an overview of the input parameters and the tests required to establish a single droplet impact model which takes material degradation, damage and failure into consideration.

Table 1: Summary of the needed material properties and required tests for the numerical modelling of water droplet impacts and progressive damage and failure

Input parameter	Test details	Test standard
Density	Water displacement testing	ASTM D792-00
Elastic modulus, Poisson's ratio, Yield stress, Failure stress, Failure strain, Complete stress-strain curve	Tensile testing	ASTM D882-18
	Compressive testing	ASTM D695-15
	Shear testing (Punch tool testing)	ASTM D732-17
Fracture toughness	Mode I: CT,SENB specimen	ISO 13586
	Mode II: TAST specimen	ASTM D5656-10
Interfacial fracture toughness	Mode I: Peel test	ASTM D1876-01
	Mode II: TAST specimen	ASTM D5656-10
	Mixed mode: Dolly test	
Fatigue crack growth rate	CT specimen	ASTM E647-15e1
Viscoelastic properties	DMTA	ASTM D5026-15
High-strain rate testing	Certain tests to be repeated at higher strain rates	Various
Degradation laws for environmental exposure	Certain tests to be repeated after environmental exposure	Various
Coefficient of linear thermal expansion	With a Vitreous Silica Dilatometer between−30°C and 30°C	ASTM D696-16
Diffusion coefficient	Gravimetric measurements	ISO 62:2008

The material properties need to be characterised at several temperatures and strain rates. Hoksbergen et al.[26] studied the sensitivity of the Springer model and stating that the Poisson ratio, strength values and fitted constants have the greatest impact on the model. They suggested utilizing numerical tools and using high-strain rate material properties to improve the accuracy of the Springer model. Domenech et. al.[27] proposed a modelling methodology to evaluate the viscoelastic behaviour of a multilayer coating system. They analysed with a simplied 1D analytical model the limits of the working frequency during a water droplet impact in a range of 0.5-7Mhz considering a multilayer configuration. Field et al. [28] did a review of well-established experimental techniques for high-rate deformation and shock studies. Poloscoser et. al.[29] subdivided dynamic range in low and high range, and drop weight principle, the split Hopkinson pressure bar test is recommended. The strain range between 10^4 – 10^8 1/s and is described with “impact” loading or “high speed velocity impact”, where plate impact test is used to acquire the desired high strain rate properties. Dynamic mechanical analysis (DMA) can be used to determine viscoelastic temperature and time (frequency) dependent behaviour. Based on this correlation the time temperature superposition principle (TTS) can be applied to determine the complex modulus and loss angle at high strain rates [30].

  doi:10.5075/epfl-298799_978-2-9701614-0-0

4. Conclusions and future work

This review will allow for the identification of gaps within the research that can be explored during IEA Wind Task 46. We aim initially to develop three main detected open issues: an interface characterisation methodology which will take into account the effect of the different layers of each LEP configuration, the strain rate sensitivity of the interface mechanical bahaviour and the analysis of the gradual property degradation due to rain erosion.

Acknowledgements

The third, seventh and last authors would like to acknowledge financial support from the Sustainable Energy Authority of Ireland (SEAI) (Awards: 19/RDD/430; 21/RDD/671; and IEA TCP Wind 46). The third author from Science Foundation Ireland (Grant no. 12/RC/2302_2), the eleventh author from the Agencia Valenciana de la Innovación (BEETool / INNVA1/2021/57).

5. References

1. R. Herring, K. Dyer, F. Martin and C. Ward, “The increasing importance of leading edge erosion and a review of existing protection solutions”, Renewable and Sustainable Energy Reviews, Volume 115, November 2019, 109382.
2. Leon Mishnaevsky. Toolbox for optimizing anti-erosion protective coatings of wind turbine blades: Overview of mechanisms and technical solutions. Wind Energy 22:11, 1636-1653.
3. Amrit Shankar Verma, Saullo G.P. Castro, Zhiyu Jiang, Julie J.E. Teuwen, Numerical investigation of rain droplet impact on offshore wind turbine blades under different rainfall conditions: A parametric study, Comp.Struc., Volume 241, 2020, 112096, ISSN 0263-8223
4. E. Cortés, F. Sánchez, L. Domenech, A. Olivares, T. M. Young, A. O’Carroll, F. Chinesta, Manufacturing issues which affect coating erosion performance in wind turbine blades, AIP Conference Proceedings 1896, 030023 (2017); https://doi.org/10.1063/1.5008010
5. https://iea-wind.org/task46/
6. Cortés E, Sánchez F, O’Carroll A, Madramany B, Hardiman M, Young T. On the material characterisation of wind turbine blade coatings: the effect of interphase coating–laminate adhesion on rain erosion performance. Materials 2017;10(10):1146.
7. Keegan, M.H., Nash, D.H., and Stack, M.M., "On erosion issues associated with the leading edge of wind turbine blades", Journal of Physics D: Applied Physics. vol. 46, pp. 383001, 2013
8. Dashtkar, A., Hadavinia, H., Sahinkaya, M.N., Williams, N.A., Vahid, S., Ismail, F., and Turner, M., "Rain erosion-resistant coatings for wind turbine blades: A review", Polymers and Polymer Composites. vol. 27, pp. 443-475, 2019
9. Chen J, Wang J, Ni A. A review on rain erosion protection of wind turbine blades. J Coatings Technol Res 2019;16(1):15–24.
10. H. M. Slot, E. R. M. Gelinck, C. Rentrop, and E. Van Der Heide. Leading edge erosion of coated wind turbine blades: Review of coating life models. Renewable Energy, 80:837–848, 2015.
11. Amirzadeh B., Louhghalam A., Raessi M., Tootkaboni M., A computational framework for the analysis of rain-induced erosion in wind turbine blades, part II: Drop impact-induced stresses and blade coating fatigue life, Journal of Wind Eng. and Ind. Aerodynamics, 163 (2017) 44-54
12. Doagou-Rad S., Mishnaevsky L., Bech J.I., Leading edge erosion of wind turbine blades: Multiaxial critical plane fatigue model of coating degradation under random liquid impacts, Wind Energy, 23 (2020) 1752-66

  doi:10.5075/epfl-298799_978-2-9701614-0-0

13. Hu W., Wang X., Chen W., Wang Y., Liu Z., Tan J., et al., A computational model of wind turbine blade erosion induced by raindrop impact, J.of Physics, 1452 (2020) 012048
14. Keegan MH, Nash D, Stack M, Modelling rain drop impact on offshore wind turbine blades, ASME Turbo Expo 2012; 2012. Article-GT.
15. Keegan MH, Nash D, Stack M. Wind turbine blade leading edge erosion: An investigation of rain droplet and hailstone impact induced damage mechanisms Ph.D. U.Strathclyde; 2014.
16. Astrid B. Investigation of droplet erosion for offshore wind turbine blades. Ann Acad Med Stetin 2014;59(1):170–1.
17. Doagou-Rad S., Mishnaevsky L., Rain erosion of wind turbine blades: computational analysis of parameters controlling the surface degradation, Meccanica, 55 (2019) 725-43
18. Castorrini A, Corsini A, Rispoli F, Venturini P, Takizawa K, Tezduyar TE. Computational analysis of wind-turbine blade rain erosion. Computers Fluids 2016;141:175–83.
19. Fraisse A, Bech JI, Borum KK, Fedorov V, Johansen NF-J, McGugan M, Mishnaevsky Jr L, Kusano Y. Impact fatigue damage of coated glass fibre reinforced polymer laminate. Renewable Energy 2018;126:1102–12.
20. Springer, G.S. *Erosion by Liquid Impact*; John Wiley and Sons: New York, NY, USA, 1976
21. Eisenberg, D.; Laustsen, S.; Stege, J. Wind turbine blade coating leading edge rain erosion model: Development and validation. *Wind. Energy* **2018**, *21*, 942–951, doi:10.1002/we.2200
22. Herring, R.; Domenech, L.; Renau, J.; Šakalytė, A.; Ward, C.; Dyer, K.; Sánchez, F. Assessment of a Wind Turbine Blade Erosion Lifetime Prediction Model with Industrial Protection Materials and Testing Methods. Coatings 2021, 11, 767.
23. W. Hu, W. Chen, X. Wang, Z. Jiang, Y. Wang, A.S. Verma, J.J.E Teuwen. Computational Framework for Coating Fatigue Analysis of Wind Turbine Blades Due to Rain Erosion, Applied Energy, 2021.
24. Doagou-Rad S., Mishnaevsky L., Bech J.I., Leading edge erosion of wind turbine blades: Multiaxial critical plane fatigue model of coating degradation under random liquid impacts, Wind Energy, 23 (2020) 1752-66
25. Pugh, K. and Nash, J. and Reaburn, G. and Stack, M.M. (2021) On analytical tools for assessing the raindrop erosion of wind turbine blades. Renew.Sust. Energy Reviews, 137. 110611.
26. Hoksbergen, N.; Akkerman, R.; Baran, I. The Springer Model for Lifetime Prediction of Wind Turbine Blade Leading Edge Protection Systems: A Review and Sensitivity Study. Materials 2022, 15, 1170. https://doi.org/10.3390/ma15031170
27. Domenech, L.; Renau, J.; Šakalytė, A.; Sánchez, F. Top Coating Anti-Erosion Performance Analysis in Wind Turbine Blades Depending on Relative Acoustic Impedance. Part 1: Modelling Approach. Coatings 2020, 10, 685. https://doi.org/10.3390/coatings10070685
28. Field, J. & Walley, S.M. & Proud, W. & Goldrein, H. & Siviour, Clive. (2004). Review of experimental techniques for high rate deformation and shock studies. International Journal of Impact Engineering - INT J IMPACT ENG. 30. 725-775. 10.1016/j.ijimpeng.2004.03.005.
29. Polocoser, Toby & Kasal, Bohumil & Stöckel, Frank. (2017). State-of-the-art: intermediate and high strain rate testing of solid wood. Wood Science and Technology. 51. 1-56. 10.1007/s00226-017-0925-6.
30. Vincent Dorléans, Rémi Delille, Delphine Notta-Cuvier, Franck Lauro, Eric Michau, Time-temperature superposition in viscoelasticity and viscoplasticity for thermoplastics, Polymer Testing, Volume 101, 2021, 107287, ISSN 0142-9418, https://doi.org/10.1016/j.polymertesting.2021.107287.

  doi:10.5075/epfl-298799_978-2-9701614-0-0

EFFECT OF MECHANICAL PROPERTIES AND INTERFACIAL CHARACTERISTICS ON THE DURABILITY OF LEADING-EDGE PROTECTION (LEP) MATERIALS FOR WIND TURBINE BLADES

Ioannis, Katsivalis[a], Angeliki, Chanteli[a], William, Finnegan[b], Trevor, Young[a]

a: Bernal Institute, University of Limerick, Limerick, V94 T9PX, Ireland – Ioannis.katsivalis@ul.ie
b: MaREI Research Centre, School of Engineering, National University of Ireland Galway,
Galway, H91 TK33, Ireland

Abstract: *Modern wind turbine blades experience tip speeds which can exceed 110 m/s. At such speeds, rain erosion of the Leading-Edge (LE) can have a significant impact on the performance of the blades, leading to reduced efficiency and increased need for repairs. To optimize the performance of the blades and reduce the effects of rain erosion, polymeric coatings, also known as Leading-Edge Protection (LEP) materials, are employed by the wind energy sector. In this work, the viscoelastic properties of two LEP materials are characterized using DMTA testing, while Rain Erosion Testing (RET) is also performed utilizing a whirling arm testing rig. The damage and failure of the LEP materials are characterized by analyzing the mass loss/exposure time relationships, photographic evidence, and CT-scanning. It is shown that porosity in the critical GFRP/LEP interface leads to stress concentrations and triggers an interfacial failure mode.*

Keywords: Wind energy; Rain Erosion Testing; Leading-Edge Protection materials; Viscoelastic properties; CT scanning

1. Introduction

The EU target for 2030 is to fulfil 32% of its total energy needs from renewables, while a long-term goal for carbon neutrality is set for 2050 [1]. To achieve these aims the existing technologies producing renewable energy, such as wind turbines, need to be improved in terms of producing more electricity at a lower cost. Technological advancements and better understanding of the performance of composite materials drives a continuous increase in the size of wind turbine blades. However, increasing the size of the blades also leads to increased tip speeds, which in cases can exceed 110 m/s [2]. At such speeds, rain erosion of the leading edge can have a significant impact on the performance of the blades, leading to reduced aerodynamic performance, increased need for repairs, reduced efficiency and ultimately, reduced energy production. To optimize the performance of the blades and reduce the effects of rain erosion, polymeric coatings, applied in-mold or post-mold, are being employed by the industry. However, these solutions can start to show signs of degradation after 2-5 years of usage, as opposed to the lifetime of wind turbines which is expected to be at least 25 years [3]. Therefore, it becomes essential to understand the damage mechanisms of the coating systems and develop methodologies to extend their service life. Figure 1 shows two characteristic cases of rain erosion damage on the leading-edge of a wind turbine blade.

Experimental studies have been used to explain the damage mechanisms taking place in the polymeric coatings during rain erosion. One of the most effective ways to study the effects of rain erosion experimentally is by creating an artificial rain-field and subjecting coating materials to simulated environmental conditions. Traditionally, the two most common methods to

  doi:10.5075/epfl-298799_978-2-9701614-0-0

simulate the rain-field is by using whirling arm test facilities [3] and jet erosion testing facilities [4]. Tobin et al. [5] compared the whirling arm facilities of the University of Limerick and SAAB aeronautics with the jet erosion testing facilities of the Airbus Group Innovations and have found relatively good agreement between the three testing facilities.

Figure 1: Examples of rain erosion damage on leading edges of wind turbine blades [6].

In addition to RET, mechanical characterization studies have been performed attempting to create correlations between the RET performance and key mechanical properties (e.g., stiffness or strength) of the LEP systems. For instance, O'Carroll et al. [3] used nano-indentation measurements on various plastics which were also exposed to RET and concluded that a reduction of the storage modulus and the hardness of plastics has an advantageous effect on their rain erosion performance.

A critical parameter in the performance of the LEP systems is related to the interfacial bonding between the blade substrate and the coating and the subsequent degradation of the interface following RET [2]. The quality of the adhesion depends on the application type and the different material layers used in each configuration, for instance the use of a filler or a primer before the LEP [7]. The bonding between the LEP and the substrate is affected by the presence of voids and defects which can have a significant effect on the stress propagation, and as a result, the durability of the coating. X-ray computed tomography (CT) has been used to identify such defects and explain damage and failure in LEP systems [8].

In this paper, two LEP material systems are subjected to RET utilizing the Whirling Arm Rain Erosion Rig (WARER) of the University of Limerick [9] and the damage initiation and propagation is evaluated using photographic evidence and mass loss measurements. In addition, the mechanical properties of the LEP materials are characterized utilizing DMTA testing, and an interface evaluation methodology is also used by means of CT-scanning. The differences in the performance of the two materials are highlighted and the experimental methodology is assessed on its suitability to explain different damage and failure mechanisms due to RET.

2. Methodology

2.1 Materials

Two LEP material systems, representative of systems employed in industry, were selected for investigation in this study based on a screening of the LEP market and recommendations of industrial partners. Both are polyurethane based materials and are identified as LEP 1 and LEP 2 throughout this study. The LEP materials were applied to Glass Fiber Reinforced Polymer (GFRP)

  doi:10.5075/epfl-298799_978-2-9701614-0-0

panels (TUFNOL Grade 10G/40) for rain erosion testing, while free film (bulk) material was used for experimental characterization. The coating of the panels and the curing of each LEP material took place according to their respective manufacturers' recommendations.

2.2 Experimental methodology

Dynamic Mechanical Thermal Analysis (DMTA) testing

DMTA testing was carried out aiming to characterize the viscoelastic properties of the LEP materials tested. Due to the flexible and soft nature of the tested LEP materials, the tensile mode of DMTA was used. Temperature sweep tests (temperature range: -80°C to 80°C) were performed for different frequencies (1, 10, 45, 100 Hz) aiming to identify the variations of storage and loss moduli, and also, the energy dissipation potential of each material by identifying the value of tanδ. Rectangular thin specimens, with dimensions 20 x 5 x 1 mm, were cut from the LEP material sheets and were used for the DMTA testing which was conducted according to [10]. The amplitude of the applied extension was 10 μm which resulted to a strain of about 0.05% and thus ensuring no plastic deformations were introduced to the specimens. During DMTA, the load and extension are recorded and are converted to stress and strain; thus, allowing to calculate the elastic and damping components of the stiffness response of the specimens. The Time Temperature Superposition (TTS) [11] principle was used to adjust the DMTA data to the high strain rates experienced during RET by creating master curves for the storage/loss moduli and tanδ over a range of frequencies.

Rain Erosion Testing (RET)

The rain erosion testing of the LEP materials was performed using the Whirling Arm Rain Erosion Rig (WARER), which was developed and built in the University of Limerick. More information on the facility and the testing protocol can be found in [3]. The guidelines of the G73-10 ASTM [12] standard are followed for the testing methodology. A typical cross section of the specimens tested is shown in Figure 2a. The test is interrupted in regular intervals so that the appropriate measurements can be made. More specifically, the exposure time is recorded along with mass loss measurements and photographic evidence of the damage initiation and propagation. The test is stopped when the rain droplets penetrate through the thickness of the LEP material. Figure 2b shows the typical wear scar developed in the WARER for substrate/LEP system tested. Most of the damage concentrates at the line between the 12 and 6 o'clock positions which is justified by the design of the WARER and the way the droplets impact the specimen. Similar damage patterns were observed for all tested specimens.

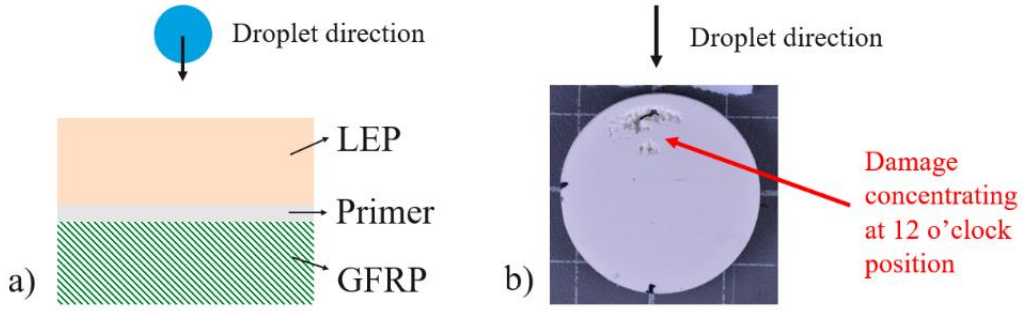

Figure 2: a) Typical cross section of the specimens exposed to RET and b) typical wear scar in an LEP configuration during testing

3. Results

3.1 DMTA testing

Figure 3 shows the variation of the storage/loss moduli and tanδ for the highest frequency examined (100 Hz) for both materials. A similar material behavior was observed; at lower temperatures, the polymers are at their glassy state with very high values for the storage modulus. As temperature increases, the polymers enter the glass transition region, they become softer, and the loss modulus and tanδ reach their peak. After the glass transition, with increasing temperature, the rubbery region follows and both storage and loss modulus decrease significantly. Increasing the testing frequency leads to a shift of the glass transition and the peak of the tanδ at higher temperatures.

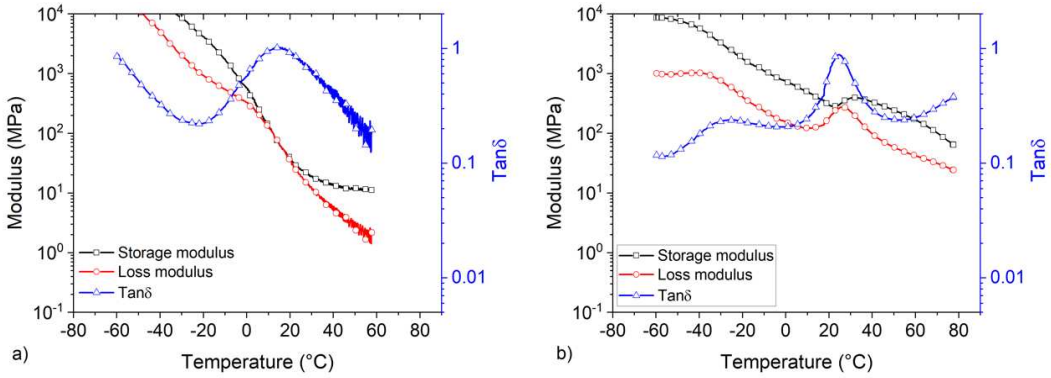

Figure 3: Variation of storage/loss moduli and tanδ over temperature for the highest examined frequency (100 Hz) for a) LEP 1 and b) LEP 2

TTS suggests that there is an analogy in the strain rate and temperature response of viscoelastic materials. More specifically, polymer materials are stiffer in lower temperature and higher strain rates and softer at higher temperatures and lower strain rates. Considering that the strain rates generated during droplet impacts are in the region of 10^6 Hz [13], it was considered beneficial to utilize TTS to estimate the stiffness response of the LEP materials at such strain rates. The data extracted from the different frequencies were used to create master curves for the storage/loss moduli taking as a reference point the data at 17°C. Figure 4a shows a characteristic master curve for the storage modulus of LEP 1 while Figure 4b shows the tanδ as a function of strain rate for both examined LEP systems. Table 1 summarizes the storage and loss moduli along with the tanδ at 17°C (temperature inside the WARER chamber during testing) for the highest examined frequency (100 Hz) and for a frequency representative of the droplet impacts (10^6 Hz).

Table 1: Summary table of viscoelastic properties at 10^2 and 10^6 Hz

Frequency	10^2 Hz			10^6 Hz		
Material	Storage modulus (MPa)	Loss modulus (MPa)	tanδ	Storage modulus (MPa)	Loss modulus (MPa)	tanδ
LEP 1	38.00	32.17	0.85	664.78	323.3	0.49
LEP 2	299.41	112.08	0.37	401.59	91.56	0.29

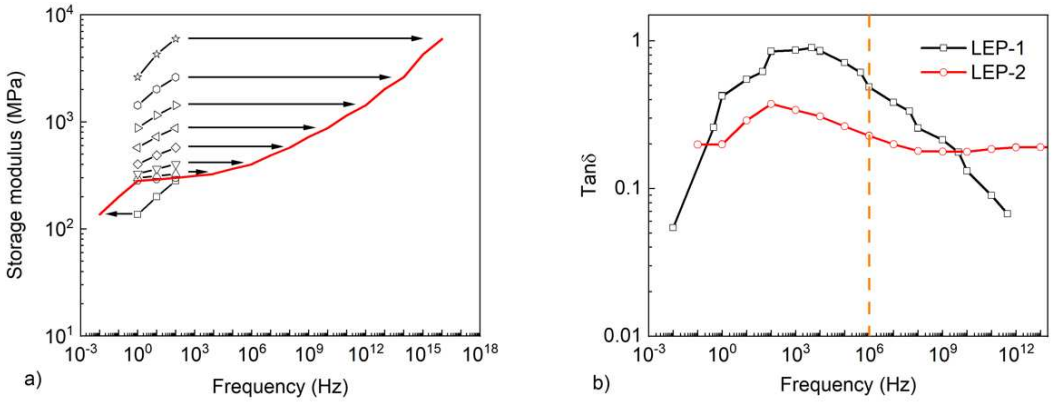

Figure 4: a) Storage modulus master curve for LEP 1 and b) tanδ variation over a range of frequencies utilizing TTS for LEP 1 and 2

3.2 Rain Erosion Testing

Figure 5 shows the mass loss/exposure time plots for the two LEP materials tested. The LEP materials displayed similar behavior in terms of mass loss. LEP 1 had a more significant initial mass loss which stabilized after about 15 minutes and displayed a mass loss plateau where no significant damage was recorded. After about 90 minutes the first specimen of LEP 1 failed, followed by the other two specimens (at 105 and 150 minutes). In the case of LEP 2, there was no significant initial mass loss but instead there is an accelerating mass removal rate, which eventually leads to failure at 150 mins for all tested specimens.

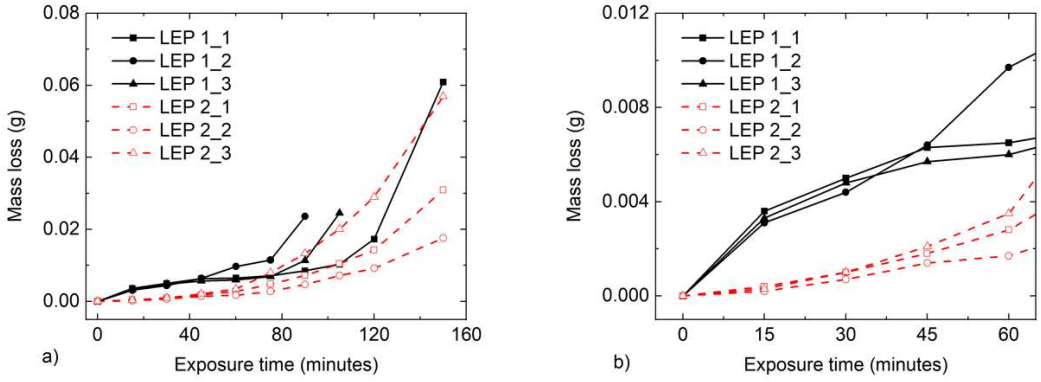

Figure 5: a) Mass loss/exposure time plot for LEP 1 and 2, b) detail of the initial part of the plot

Figure 6 shows characteristic specimens after failure for the two LEP materials. For all specimens the damage initiates at the 12 o'clock position and accumulates there until complete failure. For LEP 2, the damage expands from the 12 o'clock to the 6 o'clock position. Also, the damage is progressive and there is some warning (in the form of steady mass removal and roughening of the LEP surface) before complete failure. For LEP 1, there is not much warning before complete damage and failure occurs when large pieces of the LEP material are being removed due to delamination between the LEP and the composite GFRP substrate. It is speculated that delamination occurs due to voids in the LEP/substrate interface and imperfect bonding. These voids lead to stress concentrations and reflect the stress waves generated upon impact reducing the service life of LEP materials. In addition, it is speculated that the thickness of the LEP systems also plays a role. LEP 2 is significantly thicker, and the stress waves are mostly absorbed by the LEP material before they can reach the interface.

  doi:10.5075/epfl-298799_978-2-9701614-0-0

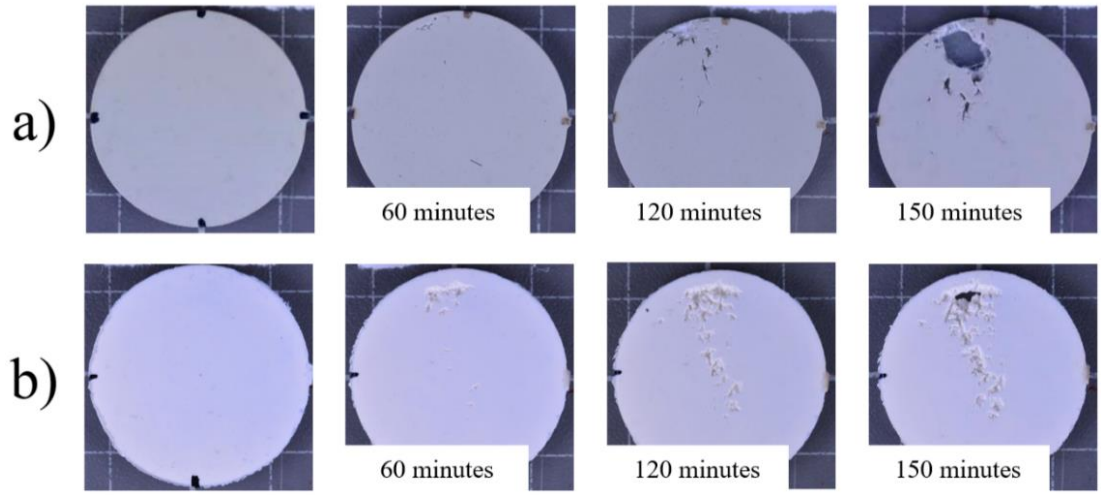

Figure 6: Damage progression with increasing exposure time for a) LEP 1 and b) LEP 2

3.3 CT scan

CT scanning was performed on both materials to identify porosity and defects which could contribute to the damage and failure mechanisms observed for the two LEP materials. X-ray micro-computed tomography (XMT) datasets were acquired using a Waygate Technologies V|TOMEX|L300 (Waygate Technologies, Germany) using a microfocus x-ray source capable of up to 300 kV of acceleration energy and a DXR-250 digital detector array (DDA) for image acquisition. The X-ray tube voltage of 120 kV and the current intensity of 70 µA was selected for data acquisition. Finally, the XMT data was acquired over 3000 projections captured across the rotation of 360° at a voxel resolution of 20.52 µm and a magnification of 10x.

Figure 7a shows the CT scan at the interface between the LEP and the substrate (for LEP 1) while Figures 7b and 7c show two perpendicular cross sections at the location of failure. It is worth noting that a thin filler layer exists between the LEP and the substrate. The scan shows that the filler layer has significant porosity compared to the LEP, which is mostly clear of defects. Cracks are seen to extend at the critical interface between the filler and the LEP leading to delamination between these two layers, which contributes to the failure of the specimen. The crack propagation between the two layers highlights the presence of stress concentrations and shows the critical role of the voids in the rain erosion performance of LEP material systems. These scans also emphasize the need for a careful design and application of the multilayer configuration.

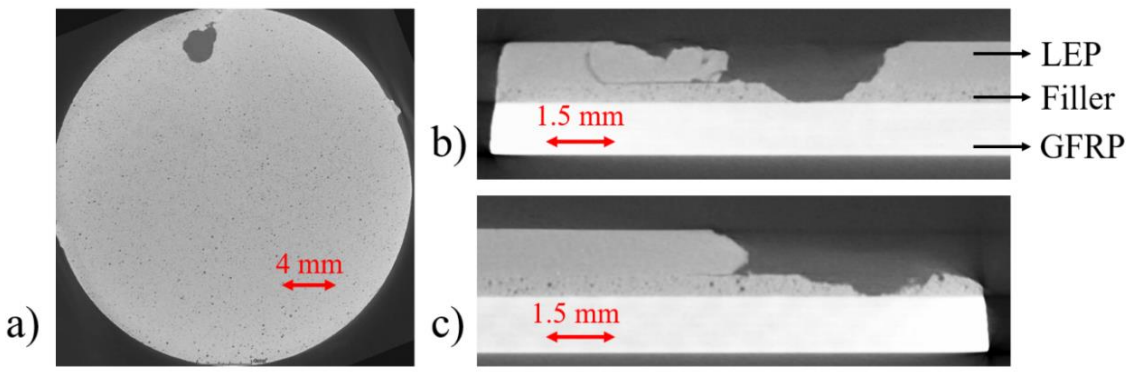

Figure 7: CT scan of LEP 1 after failure; 7a) cut between the LEP/GFRP interface, 7b, 7c) perpendicular cross sections at the failure location

Figure 8a shows the CT scan at the interface between the LEP and the substrate (for LEP 2) while Figures 8b and 8c show two perpendicular cross sections at the location of failure. No filler or primer is used between the substrate and the LEP. The LEP is mostly free of voids except a straight line far from the damage location which is assumed to be connected to the LEP application during the manufacturing stage. The LEP is free of voids even close to the damage location which is in line with the very gradual damage propagation that was observed experimentally. It is also speculated that the thick LEP layer (LEP 2 is about 40% thicker than LEP 1) partially absorbs and dissipates the stress waves before they reach the interface.

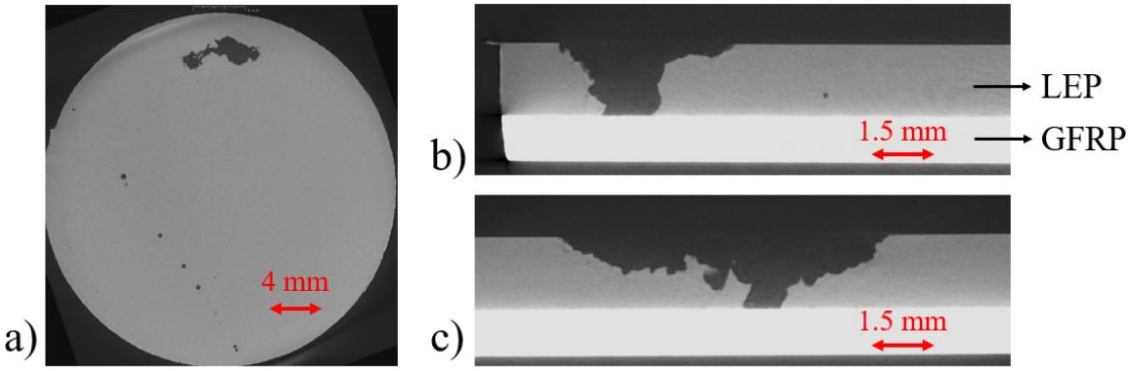

Figure 8: CT scan of LEP 2 after failure; 8a) cut between the LEP/GFRP interface, 8b, 8c) perpendicular cross sections at the failure location

4. Conclusions

DMTA testing is a common method for characterizing LEP materials. However, DMTA equipment have frequency limitations and cannot test at strain rates which are typically encountered in rain droplet impacts. It was shown that LEP 1 was softer at 100 Hz (at room temperature) but became significantly stiffer at strain rates representative (10^6 Hz) of rain droplet impacts. Therefore, it becomes critical to test in a range of temperatures and frequencies and then apply the TTS principle which allows to estimate the viscoelastic properties at higher/lower strain rates.

The two materials displayed a similar mass loss/exposure time behavior, but the damage and failure mechanism observed had distinct differences. LEP 1 did not suffer significant surface damage and thus did not provide much warning before failure. LEP 2 started showing signs of surface damage early on, with surface roughening and material removal. LEP 1 failed by the removal of a large part of the LEP material from the interface possibly due to delamination. LEP 2 failed more gradually as the damage progressed through the thickness.

The CT scanning showed that LEP 1 displayed a layer of porosity in the filler between the LEP and GFRP substrate which contributed to the damage and failure of the specimen. Stresses concentrated around the voids and led to the formation and propagation of cracks parallel to the filler/LEP interface. On the other hand, LEP 2 did not show any signs of porosity which is in line with the gradual surface failure which is not controlled by the interface. It is also speculated that correlations exist between the durability to rain erosion testing and the mechanical properties (and especially the viscoelastic properties) and thickness of the LEP systems. Therefore, future work includes evaluating a larger number of LEP systems, characterizing their mechanical properties with more methods before and after RET and also performing CT scans before and after RET.

  doi:10.5075/epfl-298799_978-2-9701614-0-0

Acknowledgements

The authors would like to acknowledge financial support from the Sustainable Energy Authority of Ireland (SEAI) (Award numbers: 19/RDD/430 and 21/RDD/671). The authors would also like to thank IEA Wind TCP Task 46 for supporting this research. The third author would like to acknowledge the support from Science Foundation Ireland (SFI), through the MaREI Research Centre for Energy, Climate and Marine (Grant no. 12/RC/2302_2). Finally, the authors would like to thank IT Waterford for assisting with the CT scanning testing and analysis.

5. References

1. Directive (EU) 2018/2001 of the European Parliament and of the Council of 11 December 2018 on the promotion of the use of energy from renewable sources, (2018).
2. Cortes E, Sanchez F, O'Carroll A, Madramany B, Hardiman M, Young TM. On the Material Characterisation of Wind Turbine Blade Coatings: The Effect of Interphase Coating-Laminate Adhesion on Rain Erosion Performance. Materials (Basel). 2017;10(10).
3. O'Carroll A, Hardiman M, Tobin EF, Young TM. Correlation of the rain erosion performance of polymers to mechanical and surface properties measured using nanoindentation. Wear. 2018;412-413:38-48.
4. Briscoe BJ, Pickles MJ, Julian KS, Adams MJ. Erosion of polymer-particle composite coatings by liquid water jets. Wear. 1997;203-204:88-97.
5. Tobin EF, Rohr O, Raps D, Willemse W, Norman P, Young TM. Surface topography parameters as a correlation factor for liquid droplet erosion test facilities. Wear. 2015;328-329:318-28.
6. Bartolomé L, Teuwen J. Prospective challenges in the experimentation of the rain erosion on the leading edge of wind turbine blades. Wind Energy. 2019;22(1):140-51.
7. Domenech L, Renau J, Šakalytė A, Sánchez F. Top Coating Anti-Erosion Performance Analysis in Wind Turbine Blades Depending on Relative Acoustic Impedance. Part 1: Modelling Approach. Coatings. 2020;10(7).
8. Mishnaevsky L, Fæster S, Mikkelsen LP, Kusano Y, Bech JI. Micromechanisms of leading edge erosion of wind turbine blades: X-ray tomography analysis and computational studies. Wind Energy. 2019;23(3):547-62.
9. Tobin EF, Young TM. Analysis of Incubation Period Versus Surface Topographical Parameters in Liquid Droplet Erosion Tests. Materials Performance and Characterization. 2017;6(2).
10. ASTM. D5026-15, Standard Test Method for Plastics: Dynamic Mechanical Properties: In Tension. West Conshohocken, PA: ASTM International; 2015.
11. Siviour CR, Jordan JL. High Strain Rate Mechanics of Polymers: A Review. Journal of Dynamic Behavior of Materials. 2016;2(1):15-32.
12. ASTM. ASTM G73-10 Standard Test Method for Liquid Impingement Erosion Using Rotating Apparatus. 2017.
13. Herring R, Dyer K, Martin F, Ward C. The increasing importance of leading edge erosion and a review of existing protection solutions. Renewable and Sustainable Energy Reviews. 2019;115.

  doi:10.5075/epfl-298799_978-2-9701614-0-0

COATING STRESS ANALYSIS FOR LEADING EDGE PROTECTION SYSTEMS FOR WIND TURBINE BLADES

Nick Hoksbergen[a], Remko Akkerman[a], Ismet Baran[a]

a: Faculty of Engineering Technology, University of Twente
Drienerlolaan 5, 7522NB Enschede, the Netherlands
Email: t.h.hoksbergen@utwente.nl

Abstract: *Offshore wind energy has high potential to generate clean energy. Wind turbine sizes are increasing and reaching above 200 m in diameter. The high velocity blade tips interact with rain droplets which cause erosion damage over time. To mitigate erosion damage, protective materials are applied to the leading edge. In order to effectively design these protection systems, the stress state in the layered material system has to be understood. The current work discusses a numerical model to predict the stress field in a co-bonded hybrid thermoplastic/thermoset layered composite system. It studies the influence of layer thickness, interphase thickness, droplet diameter and LEP material properties on the stress state in the hybrid composite coating system. It was found that the design of the system significantly influences the dynamic stress state in the layered system and as a result, the performance of these systems as protection layers for wind turbine blades gets diminished.*

Keywords: Wind energy; Leading edge protection; Numerical modeling; coating stress.

1. Introduction

Global climate accords demand lower CO_2-emissions and renewable energy is one way to achieve this. Offshore wind energy shows high potential to meet the increasing demand. Wind turbines are increasing in size, currently exceeding 200 m in diameter with corresponding tip velocities of over 100 ms^{-1}. The wind turbine blade leading edges interact with rain droplets and other airborne particles at high velocity causing erosion damage over time [1]. This leading edge erosion (LEE) is causing lower aerodynamic efficiency and hence lower annual energy production (AEP) while increasing the maintenance cost and therefore the levelized cost of energy (LCoE). In order to mitigate the erosion behavior, leading edge protection (LEP) systems are being developed in the form of liquid coatings and elastomeric tapes or shells. Since damage occurs over long periods of time, modeling is essential in order to effectively improve the performance of these LEP systems.

Liquid droplet impact causes different stress waves in an elastic solid [2]. It was shown that Rayleigh waves originate when the area under the applied load increases with the Rayleigh wave velocity. It was also shown that deformations in the solid are downward at the center of the applied load but are upward at the contact edge which ultimately causes the Rayleigh wave to exist. As contact pressure load, the Waterhammer pressure is generally used. A coating lifetime model was developed based on a 1D stress analysis through thickness of a coated substrate in [3]. It was shown that most materials fit a power law based on the ratio between the stress in the coating and the erosion strength of the material. Another method based on the Palmgren-Miner rule for fatigue analysis of the coating material has been proposed in [4]. It was shown

  doi:10.5075/epfl-298799_978-2-9701614-0-0

that reduction of liquid impact pressures or an increased safe operation zone by developing coatings with adjustable compressive stresses would lead to a longer material lifetime. Recently, it has been shown that a one dimensional analysis based on the Waterhammer pressure lacks physical representativity and causes issues for materials with similar strength values or Poisson ratios close to 0.5 [5]. This is especially the case for modern, tailored elastomeric coatings that are being used in the wind turbine sector. An alternative approach to modeling that is more physically representative is aimed for [5].

The stress state in the coating system was shown to be dependent on the impedance ratio of the coating material to the substrate [6]. The transmission and reflection of waves at the interface is related to the bonding of the two materials. It was shown that for co-bonded polymeric materials, the bonding properties are determined by the processing conditions and a co-continuous zone is generated that results in a good bonding between the two components [7–9].

A numerical modelling framework for lifetime analysis of wind turbine blades was introduced in [10,11]. It was shown that the contact pressure is dynamic and non-uniform since high pressures are present at the contact edge. The dynamic contact pressure was defined based on impacts on a rigid surface without considering the surrounding air. An axisymmetric finite element method (FEM) model was employed to determine the stress state in the coating-substrate system. The results were interpolated to determine fatigue life of a coated-substrate based on a distributed field of droplet impacts. Similar frameworks using smoothed particle hydrodynamics (SPH) and FEM as well as coupled Eulerian Lagrangian (CEL) methods in a single fluid-structure interaction simulation, including target elasticity, were proposed in [12,13]. It was later shown that the CEL and SPH approaches give similar results and that the SPH method is generally less computationally expensive [14]. These models enable to study the influence of impact parameters, material parameters and manufacturing defects on the predicted lifetimes and damage patterns. It was shown in [15] that the damage can be accelerated by heterogeneities in the coating system. For ABS based coating systems, the damage initiates at the surface in the form of pitting and extends by a cracking mechanism to cratering which ultimately causes material loss [16].

It was shown that impact pressures significantly change when taking into account the elasticity of the target as well as the presence of surrounding air [17]. This has not been taken into account in numerical frameworks so far. The current paper discusses a FEM based coating-stress analysis that utilizes a contact pressure profile for (visco-) elastic targets including surrounding air and focuses on the effect of LEP layer thickness, interphase properties and impact parameters on the resulting stress field. This approach allows for a more physically representative stress prediction and hence a more accurate lifetime prediction.

2. Methods

For the purpose of studying the stress in the coating system, the dynamic contact pressure for liquid droplet impact on elastic targets was used. These were solved by a multiphysics model in COMSOL consisting of a fluid-structure interaction simulation for a two-phase flow based on the level-set method using the incompressible Navier-Stokes equations. The resulting dynamic pressure profiles were extracted and used in ABAQUS as pressure load input on a two dimensional (2D) axisymmetric model that includes multilayer materials and was solved using an explicit time integration scheme. A functionally graded material was used in the interphase

region where the material properties were defined as a function of the thickness coordinate. The results of the simulations were the individual stress components for each time step. The initialization of the parameters and the execution of the simulations was automated using MATLAB. The materials used in the current modeling case studies are given in Table 1. Here, the epoxy material was used as backbone and the other materials were defined as the coating materials. The simulations include the variables and ranges given in

Table *2*. The current work focuses mainly on the effect of droplet diameter, LEP thickness, interphase thickness and material properties. These effects were studied independently with the exception of material parameters and LEP thickness which were analyzed simultaneously. The modeling framework returns the individual stress components which can be combined to equivalent stresses. Since the studied materials for the coating and backbone were isotropic, the Von Mises equivalent stress was considered in the analysis of the numerical modelling results.

Table 1: Material parameters used in the simulations.

Material	E [GPa]	ν [-]	ρ [kgm^{-3}]
Epoxy (backbone)	2.41	0.399	1255
TPU D60 (coating)	0.25	0.458	1100
ABS (coating)	2.45	0.408	1050
PAI (coating)	4.9	0.45	1425

Table 2: Variables and ranges considered in the simulations.

Impact velocity V [ms^{-1}]	Droplet diameter d [mm]	LEP thickness h_L [µm]	Interphase thickness h_I [µm]
100	1	250	0
110	2	500	50
120	3	750	100

The dynamic contact pressure profiles obtained from the simulation developed in COMSOL are depicted in Figure 1. It can be seen that initially, the central pressure is high but when the impact proceeds, the central pressure decreases and the contact edge pressure has a higher value. At the point where lateral jetting occurs, the pressure is released and decreases over the whole contact area, which indicates that mainly initial contact determines the pressures. Small droplets cause a narrower area with high pressure and the pressure decays earlier due to an earlier onset of lateral jetting.

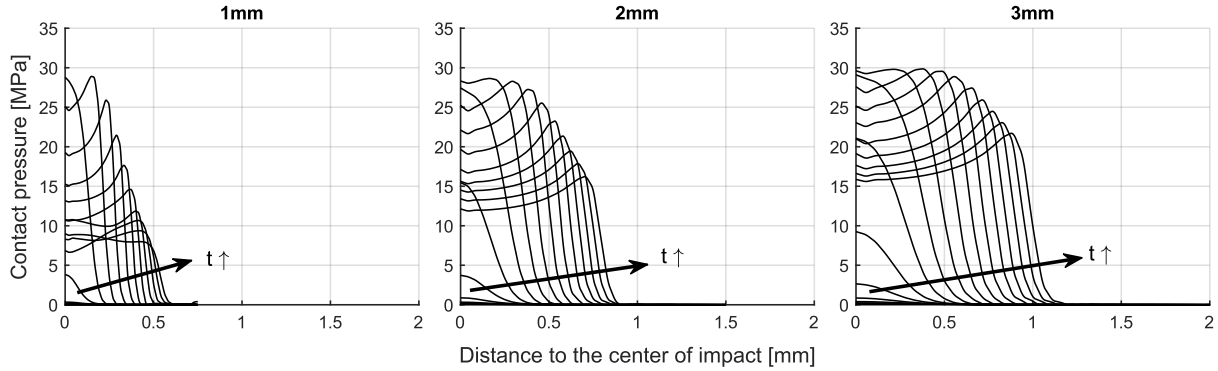

Figure 1: Dynamic contact pressure profiles for ABS coating material obtined from COMSOL and used as input for the FEM simulations in ABAQUS.

3. Results

The figures in this section show the stress field at the time frame in which the highest stress in the LEP was observed. It was found that impact velocity does not influence the shape of the stress fields but merely the magnitudes of the observed stresses.

The effect of droplet size on the stress field in the TPUD60 coating system with 500 µm LEP thickness and 0 µm interphase thickness is shown in Figure 2. It can be clearly seen that the highest stress occurs in the coating material close to the surface for small droplet diameters. For larger droplets, the interface plays an important role since reflections and transmission occur. In these cases, the highest stress was observed at a later time. This indicates that when designing LEP systems, the droplet size on site should be considered when determining the LEP thickness to apply.

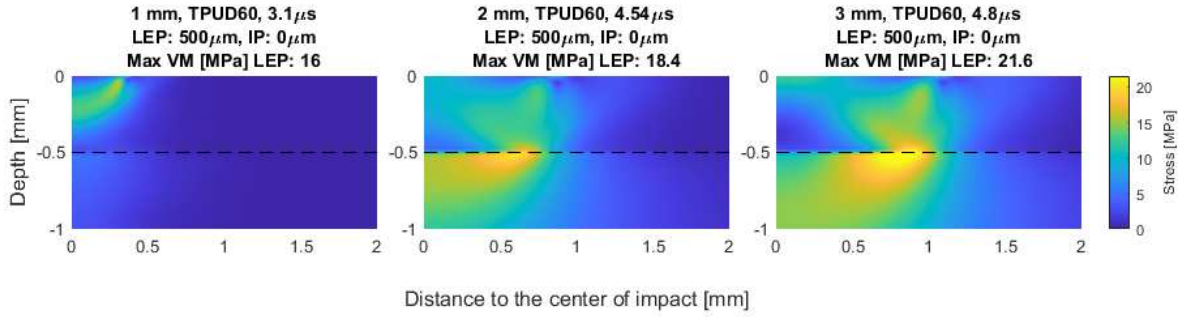

Figure 2: Effect of droplet size on the stress field in TPUD60 based coating systems.

The effect of the material properties on the stress field is shown for 250 µm, 500 µm and 750 µm LEP thicknesses and 0 µm interphases thickness in Figure 3. It can be seen that for materials where the coating properties are similar to that of the substrate (ABS), reflections at the interface only play a very minor role in the stress state. For coating materials where the properties differ from the substrate, more reflections occur that cause stress concentrations around the interface and in the LEP. This can lead to early failure, especially for small LEP thicknesses. There is a difference in time instance and location where these stress concentrations occur that seems to be related to whether the coating material is more compliant (TPUD60) or stiffer (PAI) than the substrate. Where more compliant coating materials lead to stress concentrations along the interface and stiffer coating materials lead to internal stress concentrations in the LEP caused by reflected waves.

Figure 3 also shows the effect of LEP layer thickness on the stress field. It can be seen that for ABS, LEP layer thickness does not play an important role due to the properties being similar to those of the substrate and therefore the impedance ratio being close to one. For TPUD60 and PAI however, it can be seen that the stress in the LEP is higher for lower LEP thicknesses. This is due to reflections occurring earlier in time. For small LEP thicknesses, the highest stress is driven by the reflections from the interface. For the larger LEP thicknesses, the stress is high at the surface and reflections do not seem to play a role any longer since the magnitude of the stress waves has enough time to decay due to dispersion. From this point on, the maximum stress does not change, and increasing LEP thickness further is not beneficial to have an elongated lifetime.

  doi:10.5075/epfl-298799_978-2-9701614-0-0

This suggest that there is an optimal LEP thickness that has to be designed based on the type of coating and substrate materials. It should be noted that the optimal LEP thickness is also related to the diameter of the impacting droplets as was shown in Figure 2.

Since reflections do not seem to play a role for higher LEP thicknesses, it can be argued that interphase properties do not change the maximum stress state in the system for higher LEP thicknesses. Because of this, the interphase thickness was studied only for the LEP thickness of 250 µm for both the TPUD60 and PAI materials.

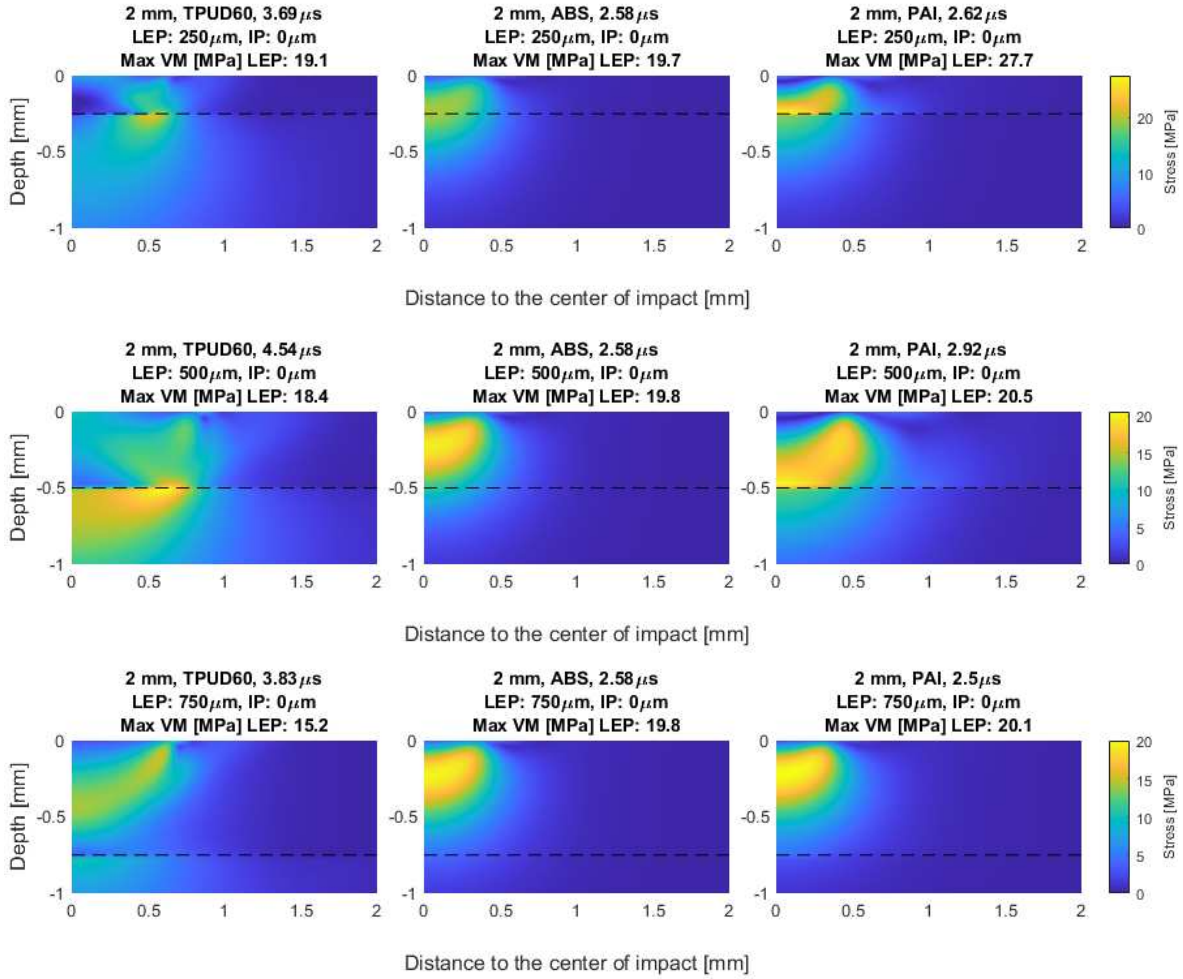

Figure 3: Effect of material properties and LEP thickness on the stress field in coated substrates.

The effect of interphase thickness on the stress field in TPUD60 based coating systems is shown in Figure 4. It can be seen that increasing interphase thickness causes the stress in the interphase to increase as well. This is likely to be caused by the interphase region beginning at a lower depth for thicker interphases. Although the stress field is spread more widely, a higher interphase thickness is not beneficial for the stress state. It should be noted that perfect bonding is assumed in the simulation and that in practical applications, the quality of the bond determines to a higher extend the effects occurring at the interphase. Also, the effect of interphase properties is less prominent than the effect of material properties as well as LEP thickness.

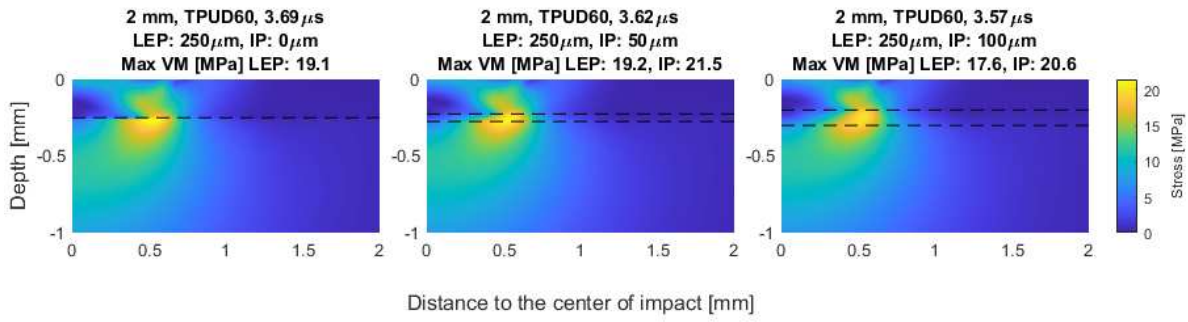

Figure 4: Effect of interphase thickness on the stress field of TPUD60 based coating systems.

A similar analysis was performed for PAI based coating systems in Figure 5. This figure clearly shows a decreasing stress with increasing interphase thickness. It is also observed that the stress field is more spread out due to the gradual transition of properties in the interphase layer. For PAI (which is stiffer than the substrate), the gradual transition results in a lower magnitude of the reflected wave leading to a lower concentration of stress in the LEP layer. This indicates that a thick interphase is desired when the LEP material is stiffer than the substrate and the highest stress in the system is caused by reflections. It should however be noted that the interphase properties might not follow a linear transition and that strength properties in the interphase region might differ from the properties of the pure polymeric materials. Experimental work is therefore required to investigate to what extend this observation can be utilized in practical applications.

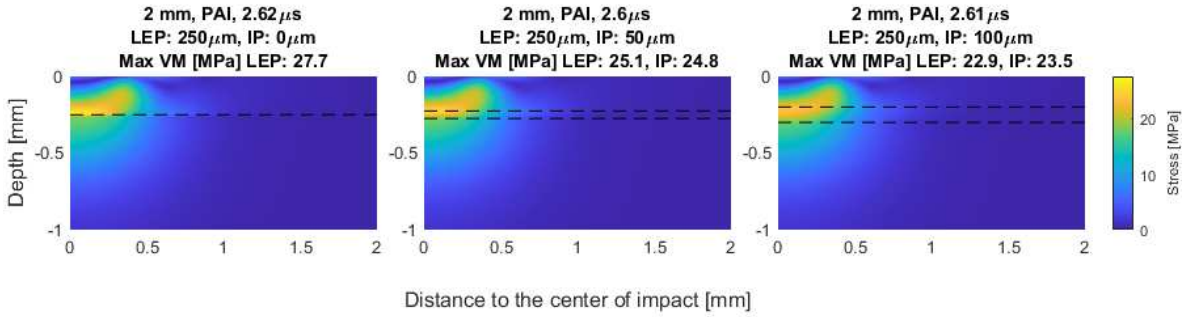

Figure 5: Effect of interphase thickness on the stress field of PAI based coating systems.

4. Conclusions

The results presented in this paper provided insight in the stress state in LEP systems for wind turbine blade protection against rain erosion. The pressure load used for the FEM simulations was based on sophisticated liquid droplet impact models and allowed for accurate prediction of stress fields. The effect of several impact, geometric and material parameters on the resulting stress field was analyzed and the following conclusions were drawn:

1. The LEP thickness is an important parameter in the lifetime of the system, an optimal thickness that induces lower stress state can be determined from the method proposed in this paper.

For thin LEP thicknesses, the maximum stress is determined by an interaction of the incoming wave and the reflected wave from the interface. There is a transition point in applied LEP thickness where this maximum stress is no longer caused by the reflection since the reflection occurs at a later point in time and the wave has a lower magnitude. Increasing the LEP thickness

  doi:10.5075/epfl-298799_978-2-9701614-0-0

further has no effect on the maximum stress observed in the LEP system and therefore this analysis provides a LEP thickness design limit.

2. Droplet size affects the width and duration of the contact pressure profile resulting in through thickness changes in the stress field.

Smaller droplets result in narrower contact pressure profiles and faster decay of the pressure. Larger droplets have longer duration and broader profiles. This means that the stress propagates further through thickness before the maximum is reached and reflections play a more dominant role for larger droplets. From this it can be concluded that thicker LEP layers are required for larger droplet impact cases.

3. Interphase thickness spreads the stress waves and has an effect on the stress state in the system based on the mechanism that causes the maximum stress.

The presence of an interphase leads to a gradual transition in properties across this interphase. In cases where the maximum stress is present in the LEP and driven by reflections caused by the interphase, a gradual transition of properties lowers the magnitude of the reflected wave and therefore decreases the maximum stress. In cases where the highest stresses are observed along the interphase region, the effect of a gradual transition is not beneficial for the stress state in the system. These mechanisms seem to be related with the compliance of the LEP material in relation to that of the substrate.

There is a delicate balance between material, impact and geometrical parameters and the performance of the LEP system that should be considered when designing LEP systems. The current work numerically analyzed these relations which resulted in more insight in the origins of stress in the materials that could lead to design guidelines for LEP systems in terms of LEP layer thickness, interphase thickness and materials to be used. Generally, it can be argued that interphase regions should not contribute to dispersion of wave energy and that a thick LEP leads to more reliable results. A material with high resistance to droplet impact loading should be applied with sufficient thickness to obtain LEP systems with extended lifetimes.

Future work includes experimental validation, 3D simulations and lifetime estimations using a lifetime prediction method based on the Palmgren-Miner rule.

Acknowledgements

This project is financed by TKI-Wind op Zee Topsector Energy subsidy from the Ministry of Economic Affairs of the Netherlands with the reference number TEWZ118008. The authors would like to thank Gautam Geeta Janardhan for the conclusions obtained in the context of his master thesis that have contributed to this paper.

5. References

[1] M.H. Keegan, D.H. Nash, M.M. Stack, On erosion issues associated with the leading edge of wind turbine blades, J. Phys. D. Appl. Phys. 46 (2013) 383001. https://doi.org/10.1088/0022-3727/46/38/383001.

[2] R.M. Blowers, On the Response of an Elastic Solid to Droplet Impact, IMA J. Appl. Math. 5 (1969) 167–193. https://doi.org/10.1093/imamat/5.2.167.

[3] G.S. Springer, Erosion by liquid impact, John Wiley and Sons, New York, NY, 1976.

[4] H.M. Slot, E.R.M.M. Gelinck, C. Rentrop, E. Van der Heide, Leading edge erosion of coated wind turbine blades: Review of coating life models, Renew. Energy. 80 (2015) 837–848.

https://doi.org/10.1016/j.renene.2015.02.036.

[5] N. Hoksbergen, R. Akkerman, I. Baran, The Springer Model for Lifetime Prediction of Wind Turbine Blade Leading Edge Protection Systems: A Review and Sensitivity Study, Materials (Basel). 15 (2022) 1170. https://doi.org/10.3390/ma15031170.

[6] E. Cortés, F. Sánchez, A. O'Carroll, B. Madramany, M. Hardiman, T.M. Young, On the material characterisation of wind turbine blade coatings: The effect of interphase coating-laminate adhesion on rain erosion performance, Materials (Basel). 10 (2017) 1146. https://doi.org/10.3390/ma10101146.

[7] J.S.M. Zanjani, I. Baran, R. Akkerman, Characterization of interdiffusion mechanisms during co-bonding of unsaturated polyester resin to thermoplastics with different thermodynamic affinities, Polymer (Guildf). 209 (2020) 122991. https://doi.org/10.1016/j.polymer.2020.122991.

[8] J.S.M. Zanjani, I. Baran, Co-bonded hybrid thermoplastic-thermoset composite interphase: Process-microstructure-property correlation, Materials (Basel). 14 (2021) 1–17. https://doi.org/10.3390/ma14020291.

[9] J.S.M. Zanjani, I. Baran, R. Akkerman, Combatting rain erosion of offshore wind turbine blades by co-bonded thermoplastic-thermoset hybrid composites, IOP Conf. Ser. Mater. Sci. Eng. 942 (2020) 012024. https://doi.org/10.1088/1757-899x/942/1/012024.

[10] B. Amirzadeh, A. Louhghalam, M. Raessi, M. Tootkaboni, A computational framework for the analysis of rain-induced erosion in wind turbine blades, part I: Stochastic rain texture model and drop impact simulations, J. Wind Eng. Ind. Aerodyn. 163 (2017) 33–43. https://doi.org/10.1016/j.jweia.2016.12.006.

[11] B. Amirzadeh, A. Louhghalam, M. Raessi, M. Tootkaboni, A computational framework for the analysis of rain-induced erosion in wind turbine blades, part II: Drop impact-induced stresses and blade coating fatigue life, J. Wind Eng. Ind. Aerodyn. 163 (2017) 44–54. https://doi.org/10.1016/j.jweia.2016.12.007.

[12] W. Hu, W. Chen, X. Wang, Z. Jiang, Y. Wang, A.S. Verma, J.J.E. Teuwen, A computational framework for coating fatigue analysis of wind turbine blades due to rain erosion, Renew. Energy. 170 (2021) 236–250. https://doi.org/10.1016/j.renene.2021.01.094.

[13] S. Doagou-Rad, L. Mishnaevsky, J.I. Bech, Leading edge erosion of wind turbine blades: Multiaxial critical plane fatigue model of coating degradation under random liquid impacts, Wind Energy. 23 (2020) 1752–1766. https://doi.org/10.1002/we.2515.

[14] S. Doagou-Rad, L. Mishnaevsky, Rain erosion of wind turbine blades: computational analysis of parameters controlling the surface degradation, Meccanica. 55 (2020) 725–743. https://doi.org/10.1007/s11012-019-01089-x.

[15] L. Mishnaevsky, S. Fæster, L.P. Mikkelsen, Y. Kusano, J.I. Bech, Micromechanisms of leading edge erosion of wind turbine blades: X-ray tomography analysis and computational studies, Wind Energy. 23 (2020) 547–562. https://doi.org/10.1002/we.2441.

[16] T.H. Hoksbergen, I. Baran, R. Akkerman, Rain droplet erosion behavior of a thermoplastic based leading edge protection system for wind turbine blades, IOP Conf. Ser. Mater. Sci. Eng. 942 (2020) 012023. https://doi.org/10.1088/1757-899X/942/1/012023.

[17] N.I.J. Henman, F.T. Smith, M.K. Tiwari, Pre-impact dynamics of a droplet impinging on a deformable surface, Phys. Fluids. 33 (2021) 092119. https://doi.org/10.1063/5.0064626.

THICKNESS VARIATION EFFECT ON COMPOSITES SURFACE LAYER PROTECTION SYSTEM DUE TO RAIN EROSION DAMAGE IN WIND TURBINE BLADES

Luis Domenech[a], Jorge Muñoz[b], Asta Šakalytė[c], Alberto Giménez[a], Jordi Renau[a], Víctor García-Peñas[a], Juan A. García[b], Fernando Sánchez[a]*

a: Research Institute of Design, Innovation and Technology, University CEU Cardenal Herrera, CEU Universities, Avda. Seminario S/N, 46115 Moncada-Valencia, Spain;
Email: *Corresponding author: luis.domenech@uchceu.es
b: Departamento de Ingeniería Mecánica y de Materiales, Universidad Politécnica de Valencia, 46022 Valencia, Spain
c: AEROX Advanced Polymers, 46185 Pobla Vallbona-Valencia, Spain

Abstract: *When considering the repeated impact of rain droplets, the high required tip speed is a key contributor to surface erosion damage on the leading edges of wind turbine blades. In this work, erosion lifetime prediction model developed by Springer has been computationally evaluated and implemented as a modelling approach to enable studies into the optimization of the surface protection coating mechanical properties. The resulting methodology allows the modulation of a coating's properties through analysis based on the uncertainties and induced effects of variation (density, impedance, endurance limit, coating thickness etc.). A complete map of the test conditions and material property input parameters required for the model is also presented. In this research the analysis is developed in terms of evaluating the effect of a coating thickness layer variation on the erosion performance. The computational framework was then used to calculate a range in the lifetime of the coating based on the layer thickness input and to scrutinize the Springer model.*

Keywords: wind turbine blades; rain erosion; leading edge protection; computational modelling;

1. Introduction

Leading edge protection (LEP) coating systems are applied to protect blade edges from rain erosion. The rain droplet impacts and the high required tip speed are key contributors to surface erosion damage on the leading edges of wind turbine blades, see Figure 1.

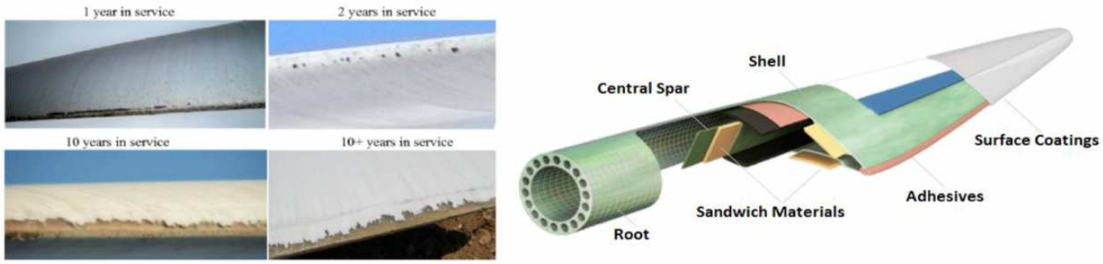

Figure 1. Examples of leading edge erosion over a range of years of service; Blade section with leading edge location where protection against erosion by rain is critical, from [1]

The Springer analytical model [2] has been widely referenced and validated to predict the erosion of coated materials under the previously untested material and operational conditions.

  doi:10.5075/epfl-298799_978-2-9701614-0-0

The erosion lifetime prediction model has been computationally evaluated and implemented as a modelling approach to enable studies into the optimization of the coating mechanical properties. The methodology presented in this work links the Springer model's lifetime prediction to the modulation of a coating's properties through analysis based on the uncertainties and induced effects of variation for a given material property (density, impedance, endurance limit, etc.). A complete map of the test conditions and material property input parameters required for the model [3] is presented, Figure 2.

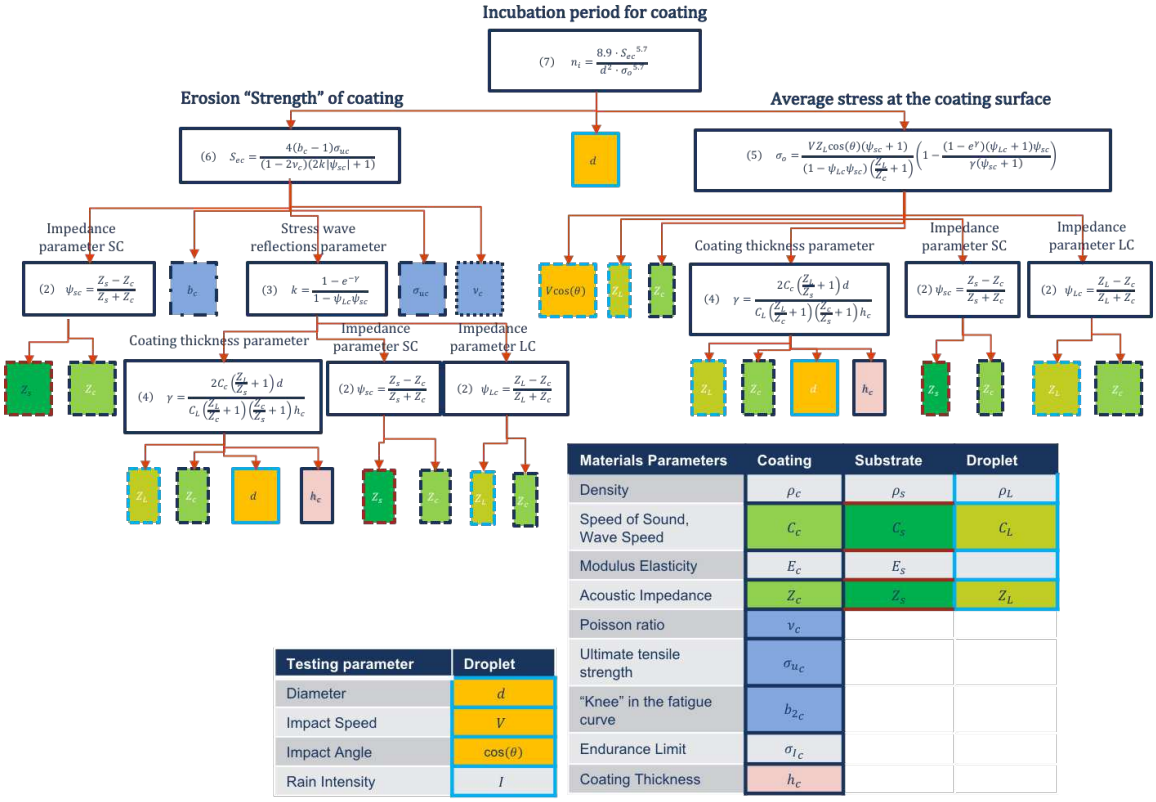

Figure 2. Diagram of material and testing parameters affecting rain erosion performance for used Springer [2] modelling, from [4]

2. Technological framework

The main contribution and achievement of the research is to define an industrial technological framework to assess and develop wind turbine blade leading edge protection material technologies, see Figure 3. The project BEETool will also make it possible to offer an advanced tool for the characterization and quantification of erosion caused by rain in reference materials and, therefore, will make it possible to adequately define their possible use, repair or replacement. The tools developed will form an integrated and versatile procedure for characterization, selection, evaluation and design by combining experimental and computational techniques of the different protection systems of any material configuration depending on the technology available by the blade manufacturer, environmental location, service conditions, operational conditions, etc. The material erosion performance depends on the interaction of the coating layers of the system and the impact / load conditions, as such, a parametric analysis was performed in this work to examine the influence of the selected coating thicknesses on the erosion performance, see Figure 4.

  doi:10.5075/epfl-298799_978-2-9701614-0-0

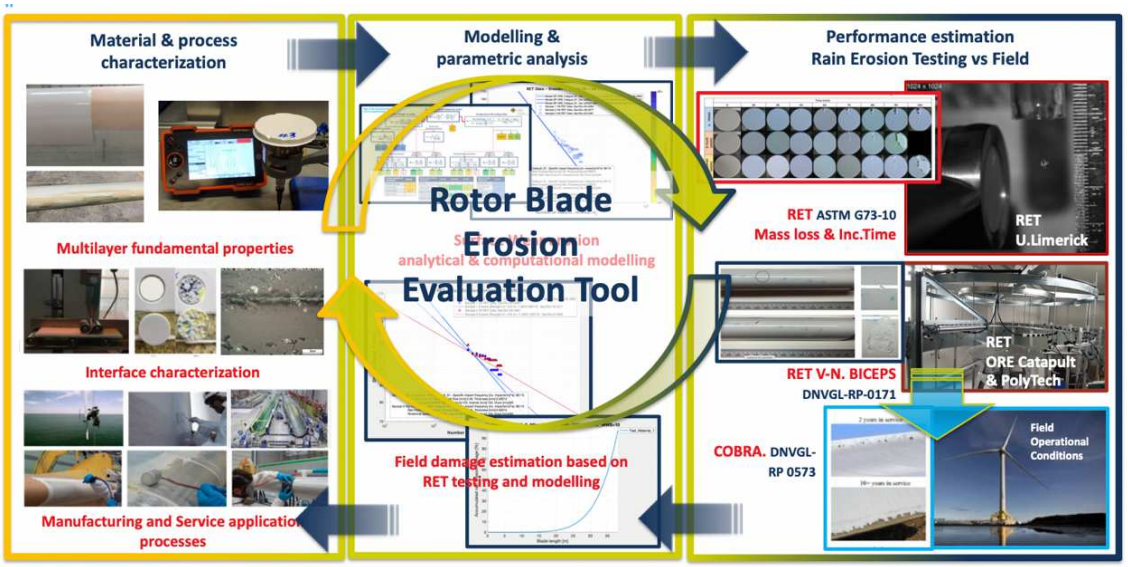

Figure 3. Technological framework proposed in the BEETool project to evaluate and develop technologies for materials to protect the leading edge of wind turbine blades sector.

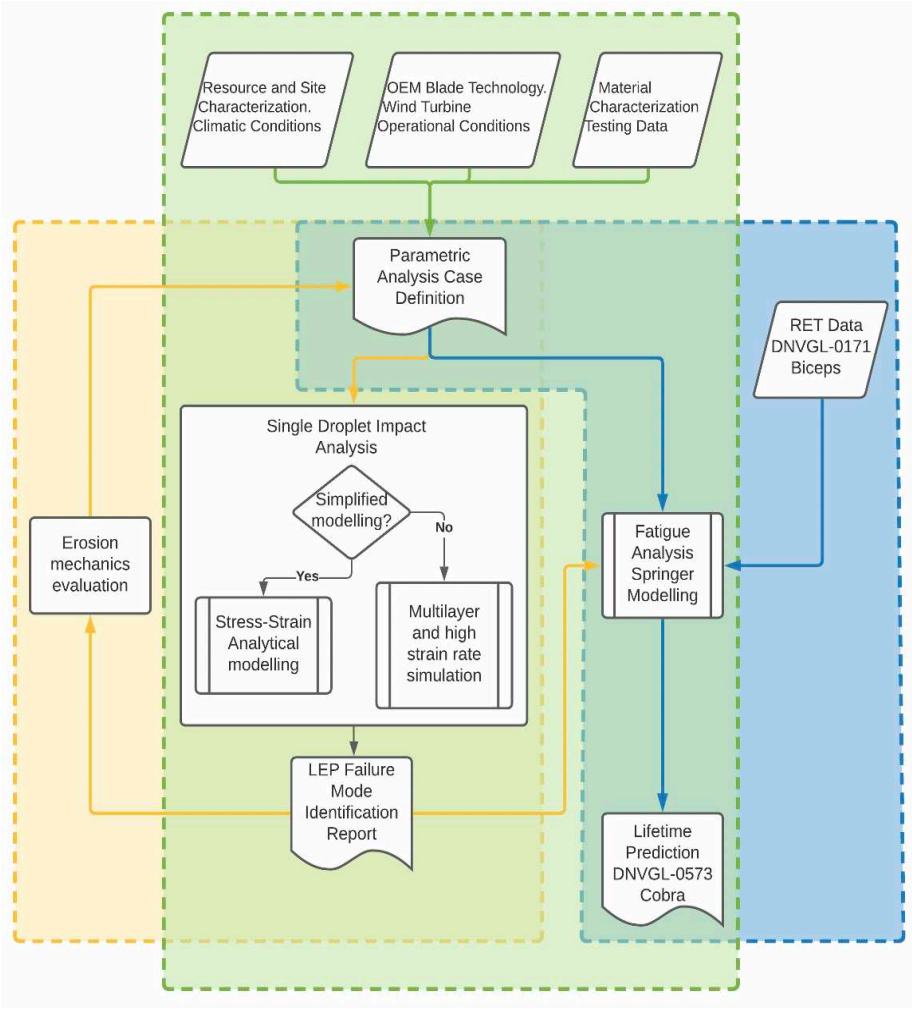

Figure 4. Process diagram of the computational tool of the BEETool project. In this work the fatigue analysis based on Springer modelling is obtained and aplied for coating thickness variation studies.

  doi:10.5075/epfl-298799_978-2-9701614-0-0

The modelling approach has then been applied to an industrial coating to determine its lifetime and the influence of the coating material configuration and testing uncertainties. Coating thickness analysis was developed with Ultrasonic measurements as the input material configuration data for the numerical modelling of erosion performance and to identify suitable coating and substrate combinations due to their acoustic matching optimization. This provides guidance in the selection and modulation of coating properties and should reduce the scope of testing to verify the rain erosion resistance of coating systems. In this work the analysis is developed in terms of evaluating the effect of a coating thickness layer variation on the erosion performance. To obtain the model inputs, mechanical tests were also performed along with erosion testing in a whirling arm rain erosion test rig until failure of the coating. The degree of uncertainty in the property measurements and rain erosion testing inputs (droplet size, impact velocity) was recorded. The framework was then used to calculate a range in the lifetime of the coating based on the layer thickness input and to scrutinize the Springer model.

3. Material and operational uncertainty issues. A modelling approach based on sensitivity functions

Figure 2 illustrates a complete map of the input parameters of the used modelling to carry out studies for the optimization of the operational and mechanical parameters that affect the LEP material performance. A complementary approach is developed to consider induced parameter values deviation. The source of these uncertainties are mainly due to inherent statistical accuracy when developing the material characterization and production (density, speed of sound, ultimate strength, poisson coefficient, fatigue slope, etc.), the operational loads (droplet impact velocity, impingement efficiency, rain flow, droplet diameter, etc.), and the pure numerical parameters introduced in the modelling.

Incubation time estimation n_i depends on the appropriate definition of the droplet diameter, d the erosion strength S_{ec}, and the averaged stress on the surface for a single droplet impact σ_o . These direct performance factors are also function of the previously stated input parameters as

$$\left.\begin{array}{rcl} n_i & = & n_i(d, S_{ec}, \sigma_o) \\ S_{ec} & = & S_{ec}(b_c, \sigma_{uc}, \nu_c, k, \psi_{sc}) \\ \sigma_o & = & \sigma_o(V, Z_L, \psi_{sc}, \psi_{Lc}, \gamma) \\ & \vdots & \end{array}\right\} \Longrightarrow n_i = n_i(b_c, \sigma_{uc}, \nu_c, V, C_L, C_c, C_s, \rho_L, \rho_c, \rho_s, h_c, d) \quad (1)$$

Consequently, a variation on the performance has to consider coupled deviation of the parameters contained in the analysis,

$$dn_i = \frac{\partial n_i}{\partial b_c} db_c + \frac{\partial n_i}{\partial \sigma_{uc}} d\sigma_{uc} + \frac{\partial n_i}{\partial \nu_c} d\nu_c + \frac{\partial n_i}{\partial V} dV + \frac{\partial n_i}{\partial C_L} dC_L + \cdots \quad (2)$$

Numerically, small parameters variations are considered as

$$\Delta n_i = \frac{\partial n_i}{\partial b_c} \Delta b_c + \frac{\partial n_i}{\partial \sigma_{uc}} \Delta\sigma_{uc} + \frac{\partial n_i}{\partial \nu_c} \Delta\nu_c + \frac{\partial n_i}{\partial V} \Delta V + \frac{\partial n_i}{\partial C_L} \Delta C_L + \cdots \quad (3)$$

And the uncertainty in the parameters estimations as

$$\varepsilon_{n_i}^2 = \left(\frac{\partial n_i}{\partial b_c}\right)^2 \varepsilon_{b_c}^2 + \left(\frac{\partial n_i}{\partial \sigma_{uc}}\right)^2 \varepsilon_{\sigma_{uc}}^2 + \left(\frac{\partial n_i}{\partial \nu_c}\right)^2 \varepsilon_{\nu_c}^2 + \left(\frac{\partial n_i}{\partial V}\right)^2 \varepsilon_V^2 + \left(\frac{\partial n_i}{\partial C_L}\right)^2 \varepsilon_{C_L}^2 + \cdots \quad (4)$$

  doi:10.5075/epfl-298799_978-2-9701614-0-0

The sensitivity functions may be used to analyse the uncertainty of the aggregated properties variation. The variation on the incubation time due to a variation on the coating thickness, may be computed as

$$\frac{\partial n_i}{\partial h_c} = \left(\frac{\partial n_i}{\partial S_{ec}}\right)\left(\frac{\partial S_{ec}}{\partial \mathrm{h}_c}\right) + \left(\frac{\partial n_i}{\partial \sigma_o}\right)\left(\frac{\partial \sigma_o}{\partial \mathrm{h}_c}\right) = \left(\frac{5.7n_i}{S_{ec}}\right)\left(\left(\frac{\partial S_{ec}}{\partial k}\right)\left(\frac{\partial \mathrm{k}}{\partial \gamma}\right)\left(\frac{\partial \gamma}{\partial \mathrm{h}_c}\right)\right) + \left(\frac{-5.7n_i}{\sigma_o}\right)\left(\left(\frac{\partial \sigma_\mathrm{o}}{\partial \gamma}\right)\left(\frac{\partial \gamma}{\partial \mathrm{h}_c}\right)\right) =$$

$$\left(\frac{5.7n_i}{S_{ec}}\right)\left(\left(-\frac{2|\psi_{\mathrm{sc}}|}{2\mathrm{k}|\psi_{\mathrm{sc}}|+1}\cdot S_{ec}\right)\left(\frac{\mathrm{e}^{-\gamma}}{1-\psi_{\mathrm{Lc}}\psi_{\mathrm{sc}}}\right)\left(-\frac{\gamma}{\mathrm{h_c}}\right)\right) +$$

$$\left(\frac{-5.7n_i}{\sigma_o}\right)\left(\left(\frac{-\sigma_\mathrm{o}\cdot(\mathrm{e}^{\gamma}-\gamma-1)\cdot(\psi_{\mathrm{Lc}}+1)\cdot\psi_{\mathrm{sc}}}{\gamma\cdot(\mathrm{e}^{\gamma}\cdot\psi_{\mathrm{Lc}}\psi_{\mathrm{sc}}-\psi_{\mathrm{Lc}}\psi_{\mathrm{sc}}-\gamma\cdot\psi_{\mathrm{sc}}\cdot\mathrm{e}^{\gamma}+\psi_{\mathrm{sc}}\cdot\mathrm{e}^{\gamma}-\psi_{\mathrm{sc}}-\gamma\cdot\mathrm{e}^{\gamma})}\right)\left(-\frac{\gamma}{\mathrm{h_c}}\right)\right) =$$

$$\left(\left(\frac{5.7n_i\cdot 2|\psi_{\mathrm{sc}}|\gamma\mathrm{e}^{-\gamma}}{\mathrm{h_c}(2\mathrm{k}|\psi_{\mathrm{sc}}|+1)(1-\psi_{\mathrm{Lc}}\psi_{\mathrm{sc}})}\right)\right) + \left(\left(\frac{-5.7n_i(\mathrm{e}^{\gamma}-\gamma-1)(\psi_{\mathrm{Lc}}+1)\psi_{\mathrm{sc}}}{\mathrm{h_c}(\mathrm{e}^{\gamma}\psi_{\mathrm{Lc}}\psi_{\mathrm{sc}}-\psi_{\mathrm{Lc}}\psi_{\mathrm{sc}}-\gamma\psi_{\mathrm{sc}}\mathrm{e}^{\gamma}+\psi_{\mathrm{sc}}\mathrm{e}^{\gamma}-\psi_{\mathrm{sc}}-\gamma\mathrm{e}^{\gamma})}\right)\right) \quad (5)$$

4. Results and validation

In line with the DNV-GL-RP-0171 [5] guideline, the time to end of incubation can be directly related to the number of droplets impacting each point and the local velocity at the impact location. The test specimens were prepared in three configurations: one sample with the LEP coating thickness of 582 µm on average through its length (sample B7), one sample of LEP coating of 390 µm (sample B8) and one sample with 591 µm (sample B9). Figure 5 shows the eroded samples after Rain Erosion Testing. Figure 6 presents the VN incubation curve for the three samples. Erosion progressed along the three samples at similar rates. These results suggest that different layer thicknesses have little impact on the time to incubation damage.

Figure 5. Test samples eroded in the rain erosion test rig

The Springer model assessed in this study estimates the time to incubation and therefore the time to breakthrough considering the coating thickness variation. Figure 7 shows, the lifetime analysis of the variation (from 50% to 150% of its reference value for the coating layer thickness) on the coating thickness hC input values. It includes the uncertainty region given by equation (5) calculated for each of the simulations and considering statistical deviations that may be defined on their testing measurements (in this analysis example, these values were not available, so were introduced ideally, i.e the uncertainty region is usually lower).

  doi:10.5075/epfl-298799_978-2-9701614-0-0

Figure 8 shows the performance analysis due to a variation of the coating thickness as in Figure 7. In this case, the incubation time estimation for each simulated hC value is coupled with the analysis of the induced effect due to a particular material property variation included in equation (5) and defined in the map properties of Figure 2. It is observed how the VN curve agrees with the weak effect of the thickness on the erosion performance compared with other material properties. The tendencies (computed as partial derivatives) of such variations are plotted additionally. It is observed in blue the abrupt effect on the incubation time for a 5% variation of the ultimate strength σ_uc value or the coating Poisson coefficient value, i.e. PoissonC. On the contrary, the effect of increasing the substrate speed of sound value Cs (dotted green) produces a loss in erosion performance for a range of hC values. The same occurs for the coating speed of sound variation Cc.

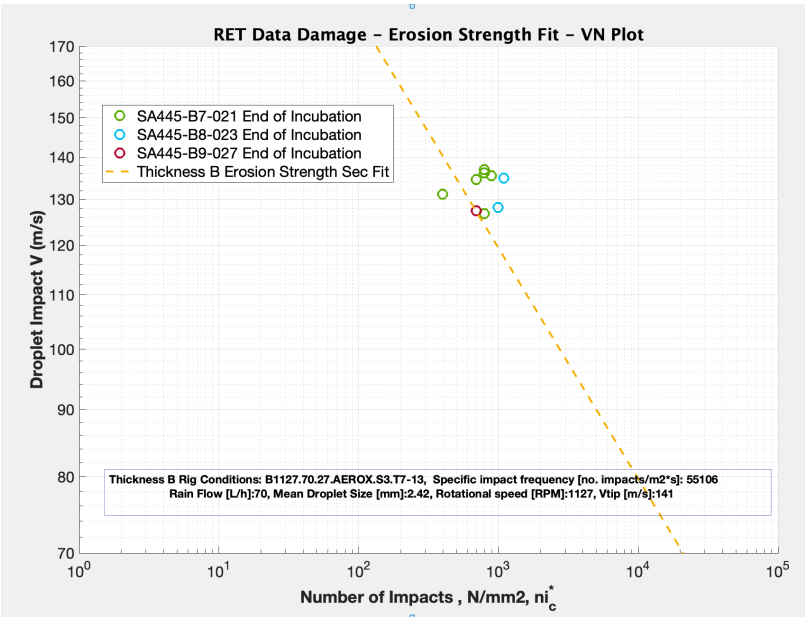

Figure 6. VN Incubation curve for the test specimens, presenting the end of incubation at different local velocities for B7,B8 and B9 samples.

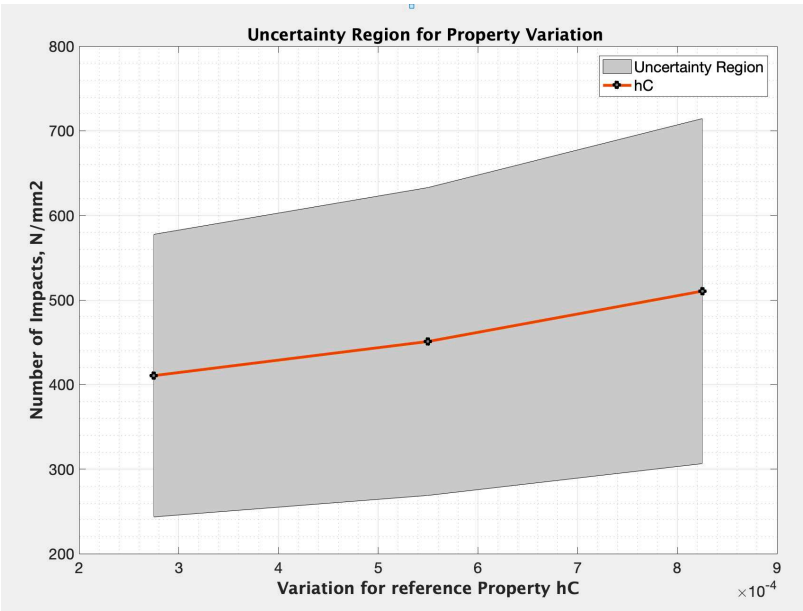

Figure 7. Thickness variation sensitivity analysis for 50%, 100% and 150% of coating thickness hC=550 µm *as reference value.*

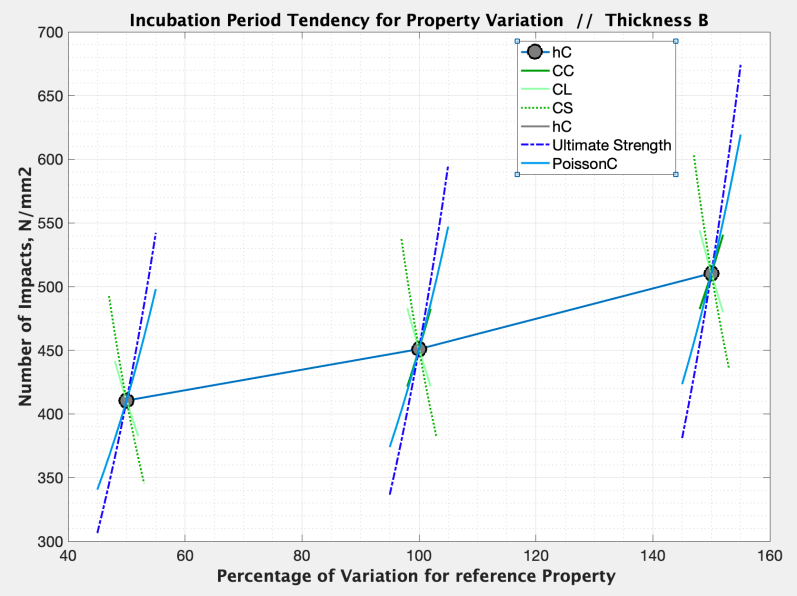

Figure 8. Incubation time estimation due to a variation of the coating thickness hC coupled with the tendency analysis of the induced effect due to a particular material property variation: Coating speed of sound CC, substrate speed of sound Cs, Liquid-water speed of sound CL, coating Ultimate Strength and coating poisson coefficient.

5. Conclusions and future work

The erosion lifetime prediction model developed by Springer has been computationally evaluated and implemented for evaluating the effect of a coating thickness layer variation on the Leading Edge Protection system anti-erosion performance. The computational framework was used to calculate a range in the lifetime of the coating solution based on the layer thickness definition and to identify suitable coating thickness configuration. This methodology provides guidance in the selection and modulation of coating properties and should reduce the scope of testing to verify the rain erosion resistance of coating systems depending on thickness variations.

Acknowledgements

Authors would like to acknowledge financial support the Agencia Valenciana de la Innovación with the project “ROTOR BLADE EROSION EVALUATION TOOL (BEETOOL)”. INNVA1/2021/57. Funded by Agencia Valenciana de Innovación (AVI).

6. References

1. E.Cortés, F.Sánchez, A.O’Carroll, B.Madramany, M.Hardiman,T.M.Young; On the material characterization of wind turbine blade coatings: Effect of the interphase adhesion on rain erosion performance, *Materials; September 2017, Vol 10, 1146, doi:10.3390/ma10101146*.
2. Springer, G.S. Erosion by Liquid Impact; *Scripta Technica Publishing Co.* 1976.

3. Herring, R.; Domenech, L.; Renau, J.; Šakalytė, A.; Ward, C.; Dyer, K.; Sánchez, F. Assessment of a Wind Turbine Blade Erosion Lifetime Prediction Model with Industrial Protection Materials and Testing Methods. Coatings 2021, 11, 767.
4. Domenech, L.; Renau, J.; Šakalytė, A.; Sánchez, F. Top Coating Anti-Erosion Performance Analysis in Wind Turbine Blades Depending on Relative Acoustic Impedance. Part 1: Modelling Approach. *Coatings* **2020**, *10*, 685. doi:10.3390/coatings10070685
5. DNVGL: RP-0171. Testing of Rotor Blade Erosion Protection Systems; Recommended Practice; DNV GL: Oslo, Norway, 2018. Available online: http://www.dnvgl.com (accessed on February 2020).

  doi:10.5075/epfl-298799_978-2-9701614-0-0

INVESTIGATION OF BULK ADHESIVE MATERIAL AND THICK ADHESIVE JOINTS FOR WIND TURBINE APPLICATIONS

Jialiang Fan[a], Javane Karami[b], Ali Kojouri[b], Danny Van Hemelrijck[b], Anastasios Vassilopoulos[c], Veronique Michaud[a].

a: Laboratory for Processing of Advanced Composites (LPAC), Ecole Polytechnique Fédérale de Lausanne (EPFL), Lausanne, Switzerland – jialiang.fan@epfl.ch.
b: Vrije Universiteit Brussel, Brussel, Belgium.
c: Composite Construction Laboratory (CCLab), Ecole Polytechnique Fédérale de Lausanne (EPFL), Lausanne, Switzerland.

Abstract: *Adhesive joints connecting the outer shells of wind turbine blades can reach up to several cm in thickness. This leads to particular requirements in terms of processing and assessment of the mechanical properties and resistance to damage of these joints. In this paper, a commercial epoxy adhesive designed for wind turbine blades, Sikapower®-830, was characterized. Rheological and mechanical properties were assessed on the bulk resin, which were obtained during this study. The yield stress of the uncured adhesive is about 400 Pa, which is required by the manufacturing process. The fracture toughness of the cured resin, K_{IC}, is 2.79 MPa√m. Its Young's modulus is about 2.5 GPa and tensile strength is about 40 MPa. Based on its rheological properties, double cantilever beam (DCB) specimens were produced with thick adhesive layers by adding and removing spacers during production. During the DCB tests, stick-slip and crack-kinking occurred, changing from stable to unstable crack propagation. Defined sample manufacturing methods and commercial epoxy adhesive results are shown in this paper and will be used for the development of novel adhesive formulations.*

Keywords: Adhesives; Thick joints; Fracture; Mode I

1. Introduction

Thick adhesive joints are widely used in wind industry, shipbuilding, and bridge construction [1]. For example, wind turbine blades are usually made with two skins and webs that are connected with a structural adhesive. The length of blades keeps increasing over the last decades to favor power extraction, which also leads to an increase in the adhesive layer thickness [2]. The bond thickness varies along with the shape of the blades, from several millimeters to centimeters. Adhesive formulations for wind turbine blades need to have sufficient viscosity and yield stress to maintain the shape of the layer after being applied to the composite skin surface during manufacturing. During operation, these adhesive joints endure mixed-mode static and fatigue loading [3,4]. As a result, the bulk adhesive should also have excellent mechanical properties, such as high ultimate strength, high E-modulus and high fracture toughness.

Limited research has been focused on the behavior of thick adhesive joints. Lopes Fernandes et al. [5] studied the mode I fracture behavior of DCB joints with varying adhesive thickness, from 0.4 mm to 10.1 mm. The critical mode I strain energy release rate (G_{Ic}) of joints with 10.1 mm thick adhesive layer was much higher than the G_{Ic} of joints with 0.4-2.6 mm thick adhesive layers, by about 46 %. Crack path, fracture surface and the stress field ahead of the crack tip are the

  doi:10.5075/epfl-298799_978-2-9701614-0-0

reasons for this increase. Rosendahl et al. [6] tested DCB joints with 6 mm and 12 mm thick silicone sealant adhesive layers. They suggested that when the joints were thick enough, the G_{Ic} values became independent of adhesive thickness. In this case, they could determine the bulk material fracture toughness from joints with 6 mm and 12 mm thick adhesive layers. Xu et al. [7] carried out fatigue tests with DCB joints with 0.2 mm and 1 mm thick adhesive layers. Thicker ones showed lower fatigue growth rates. So far, thick adhesive joint behavior is not well understood.

This study focuses on the investigation of adhesives for wind turbine blades by conducting bulk material and thick adhesive joint tests, including rheology yield stress, tensile, single edge notch bend (SENB), and DCB joint tests. Sample preparation protocols are defined for these tests with preliminary test results given in this paper.

2. Materials and experimental methods

2.1 Materials

The material used is the epoxy adhesive, Sikapower®-830 (SP830) delivered by Sika Technology AG. It is a two-component epoxy adhesive specifically designed for wind turbine rotor blade connections. The two-component weight mixing ratio is 100:47. The demolding agent for bulk material sample fabrication is Sika liquid wax-815.

Adhesive joints were produced using the SP830 adhesive and glass fiber reinforced epoxy adherends. Unidirectional glass fabric with 425 g/m^2 areal weight from P-D interglas technologies GmbH was used as the reinforcement. EPIKOTE Resin MGS RIMR 135 and EPIKURE Curing Agent MGS RIMH 137 from Hexion Inc were used as two-component infusion epoxy resin to produce the composite adherends.

2.2 Processing Methods

Rheology tests were conducted immediately after mixing the SP830 A and B components in order to explore the yield stress without the influence of epoxy polymerization. As for the other bulk material test specimens for the tensile and the SENB tests, SP830 was mixed and degassed under vacuum for 10 mins in order to reduce void volume. Degassed epoxy was poured and cured within aluminum molds, treated with a demolding agent. After pouring, the epoxy was cured at 70 degrees for 4 hours, according to the datasheet provided by Sika.

Tensile test dog-bone specimens were shaped following the ASTM D638 standard with Type I dimensions [8]. The dimensions of the SENB specimens were 10×20×130 mm. After curing, dog-bone specimen edges were polished with 220 grit SiC sandpaper. The 10 mm pre-crack of the SENB specimens was obtained by cutting the first 8 mm with a circular saw blade of 0.6 mm thickness and the next 2 mm with a thin saw with 0.16 mm blades.

The DCB joint specimen adherends were made by cross-ply composite laminates $[90/0]_{7S}$ fabricated by vacuum assisted resin infusion. The composite was cured at room temperature for 24 h and post-cured at 60 degrees for 9.5 h with a temperature ramp rate of 0.3 degrees per minute and 80 degrees for 6 h.

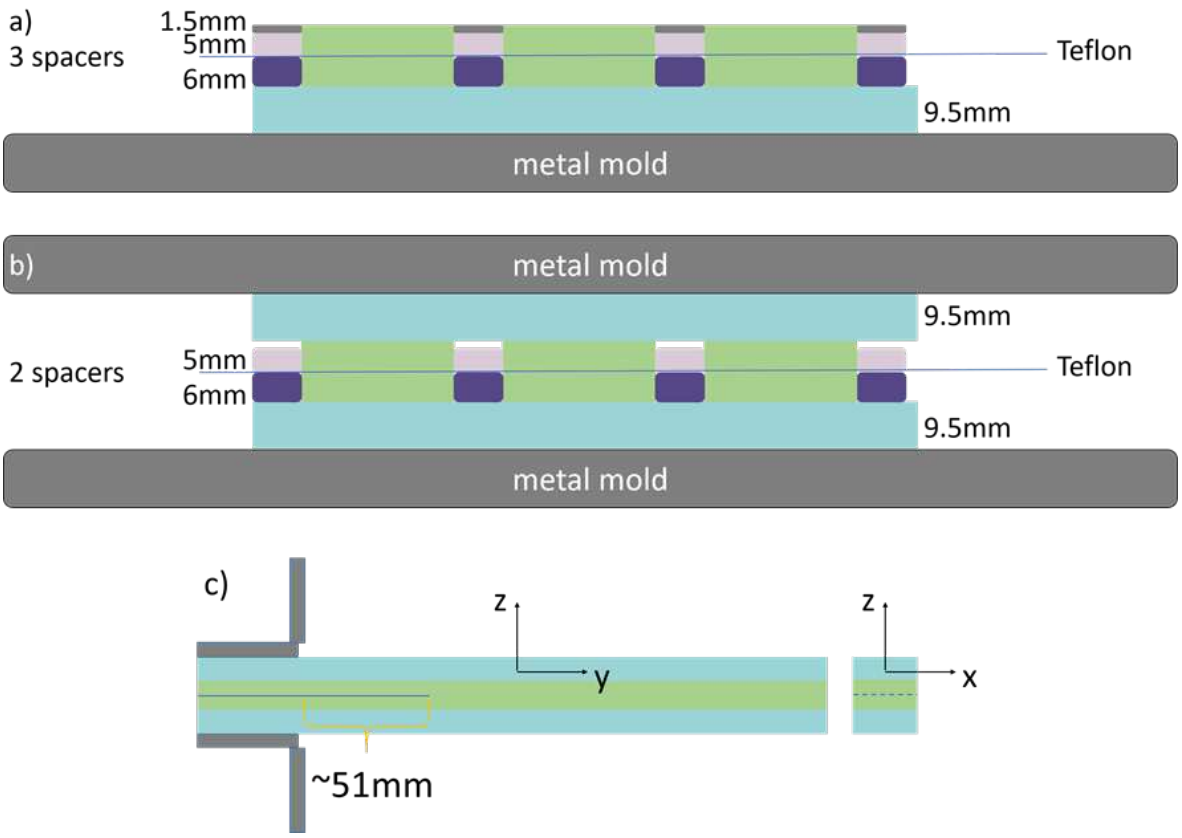

Figure 1 DCB joint production process: a) sketch after placing 3 spacers and controlling epoxy thickness. b) sketch after removing third spacers and placing top adherend and metal mold. c) sketch of DCB adhesive joint with piano hinges.

The thickness of the epoxy adhesive layer was controlled by aluminum spacers. Due to the interaction between the scraper and the high viscosity material, the scraped surface was not flat, excess epoxy was dragged out by the scraper. As a result, the top composite adherend could not touch the entire epoxy surface. In this study, DCB joints were produced successfully using an additional spacer, which was removed in a second stage after scraping to ensure better contact between the adhesive and the composite skins. Figure 1 illustrates the process of making DCB joints with 12 mm thick adhesive layer. First, epoxy was mixed and degassed, 6 mm spacers were placed and epoxy was poured into the cavity. After flattening the surface with a scraper, a Teflon sheet was inserted for pre-crack positioning. Then, the other two spacers were added and further epoxy was poured into the cavity. Afterward, the third spacers were removed, and the top composite and metal mold were placed on the top. The whole mold and joints were cured at 70 degrees for 6 hours and then the DCB joints were cut into 25.4 mm×250 mm dimensions. The specimens were polished with 220 grit SiC sandpaper and painted for the DIC technique. The piano hinges were also glued on the specimens before testing. The fabric direction of the layer in contact with the adhesive was parallel to the x-direction, as shown in Figure 1c.

2.3 Test procedures

A rheometer (Anton Paar, MCR 302e) equipped with 25 mm aluminum plates was employed for the yield stress tests. Experiments started with mixing two components and immediately filling epoxy in between two plates. After setting the gap to 1 mm, there was a relaxation period of 2

mins and 5 s pre-shear with 0.01 s^{-1} shear rate. The shear rate sweep was from 0.01 to 10 s^{-1}. In the end, shear stress at 0.1 s^{-1} was considered as the yield stress.

Tensile tests were performed with a universal testing machine (Walter + Bai AG, LFM-125 kN, Switzerland) using a 10 kN load cell with ±0.5 % accuracy. The test speed was 2 mm/min. Tensile test specimen elongation was measured with a clip-on extensometer.

SENB tests were carried out with a universal testing machine (Instron 4505) equipped with 10 kN load cell having ±0.5 % accuracy and 20 mm diameter support. The loading spam was 80 mm and the test speed was 1 mm/min.

DCB joint tests were conducted with the same machine as that used for the tensile tests. DCB joints were tested with the initial loading and reloading process and the test speed was 2 mm/min. All the tests were executed at room temperature.

3. Results and discussion

3.1 Bulk material test results

Bulk material test results are illustrated in Table 1. SP830 has sufficient yield stress to avoid spontaneous flow of a few cm thick layer. The presence of a silica filler and other ingredients forms a network that resists flow, but this also results in high viscosity for the epoxy adhesive. This high viscosity further causes some problems during specimen manufacturing, such as the presence of porosities and the difficulty of precisely controlling thickness.

Figure 2a shows the obtained stress-strain curves. High ultimate strength and E-modulus are the prerequisites of the envisaged applications. Voids are found on the fracture surface (Figure 2b). The possible source could be the trapped air from mixing and from transferring epoxy to the mold. The adhesive is highly viscous and the degassing procedures during sample preparation still leave lots of trapped air inside.

SENB test curves are presented in Figure 3a. The average max load is around 360 N and the K_{Ic} of epoxy adhesive is 2.79 MPa√m, while the fracture toughness of most nanomaterial toughened epoxy is within 0.5-2 range [9]. Figure 3b presents one SENB fracture surface, the white color surface area is rough and created under stable crack propagation, while the green color area results from the manual fracture after the test.

Table 1: Bulk material test results for SP830.

Rheology test	Viscosity [Pa·s at 10s^{-1}]	71.60
	Yield stress [Pa]	428.27
Tensile test	elongation at break [%]	2.87±0.31
	ultimate strength [MPa]	41.59±1.15
	E-modulus [GPa]	2.57±0.12
SENB test	Max load [N]	362.97±13.41
	K_{Ic}[MPa√m]	2.79±0.07

  doi:10.5075/epfl-298799_978-2-9701614-0-0

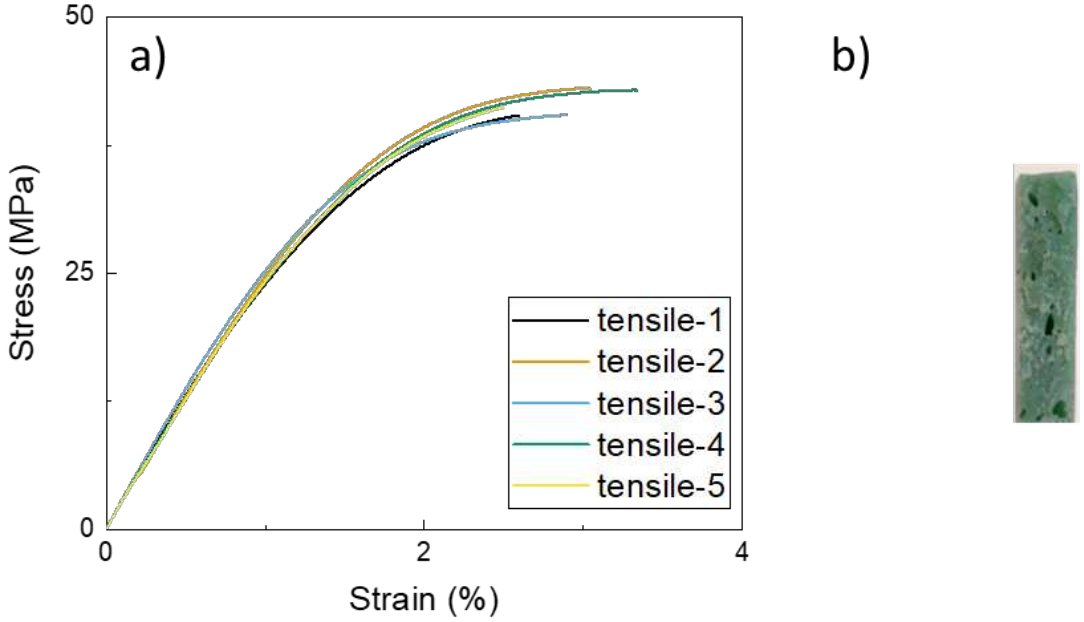

Figure 2 a) Tensile test stress-strain curves for SP830. b) Fracture surface of a tensile test dog-bone specimen.

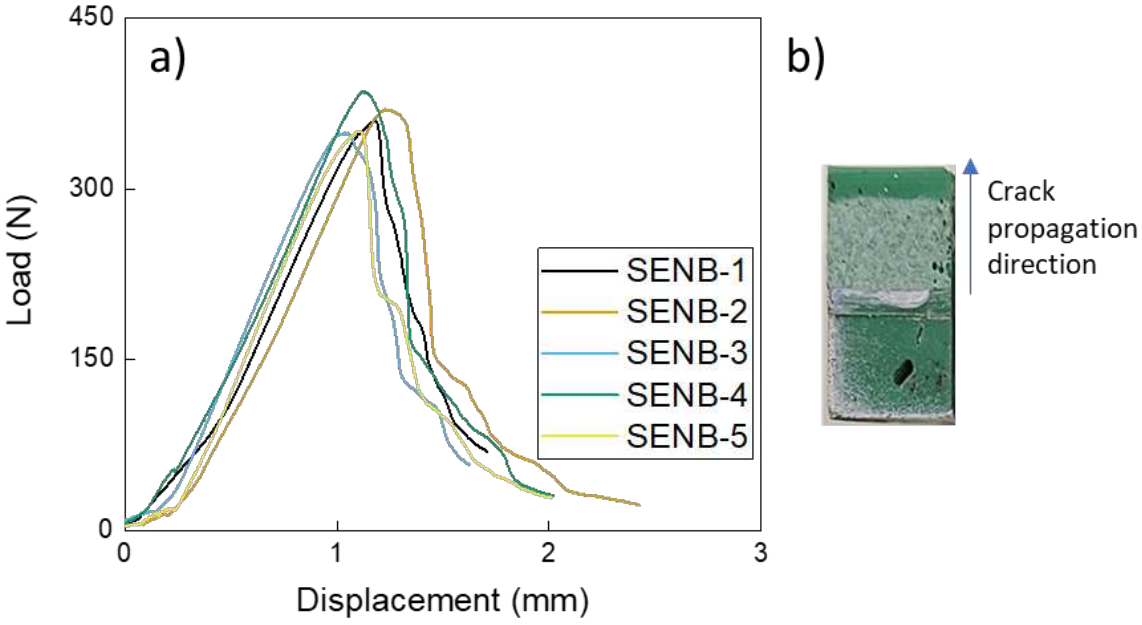

Figure 3 a) SENB test load-displacement curves for SP830. b) Fracture surface of a SENB specimen.

3.2 DCB joint test results

Figure 4a illustrates a typical load-displacement curve obtained during the DCB tests. At first, there was a short stable propagation within the adhesive layer. Afterward, stick-slip and crack kinking occurred during DCB joint tests. The crack was initially arrested within the composite adherend, and then, propagated in between the first and second layers of fabric.

The two propagation regions are also observed from the fracture surface (Figure 4b). The white region, which is very limited in length, corresponds to the stable propagation, and the green region to the stick-slip propagation. As a result, limited relevant data points with the information on crack propagation inside the adhesive layer were obtained.

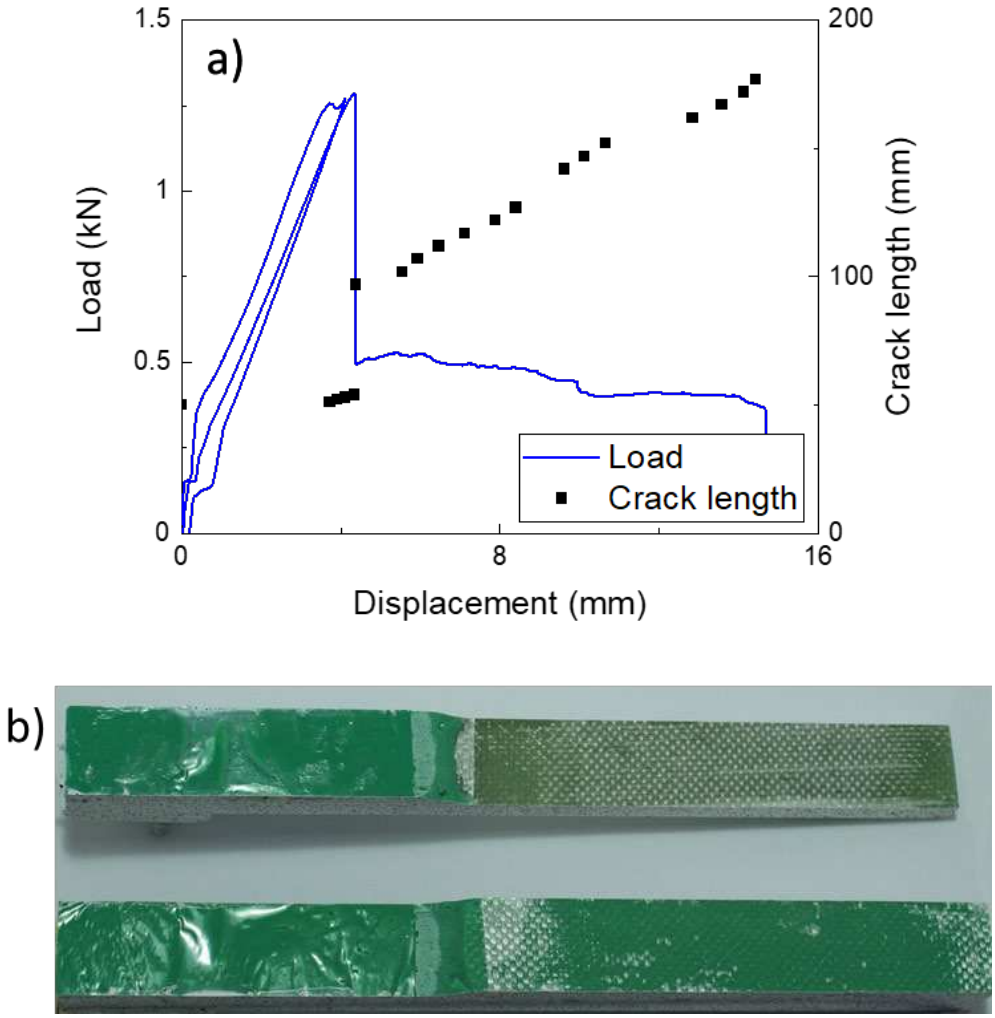

Figure 4 DCB joint with 12mm thick adhesive layer: a) load-displacement curve and b) fracture surface.

Voids are also observed on the DCB fracture surface. This could be one possible explanation of the stick-slip and crack kinking. A thin DCB joint with weak interface, i.e. very low $G_{interface}$ value, could have a similar behavior [10]. Assuming the voids as weak interface and the G_{void} to be zero, the stress field ahead of the crack tip would be influenced when the crack is near or going through the voids. This would further influence the crack propagation direction and when the

void size is large enough, stick-slip occurs. More tests should be designed and conducted to prove this hypothesis.

4. Conclusions

SP830, a commercial epoxy used for wind turbine blade manufacturing has high E-modulus, high ultimate strength, and high fracture toughness. In addition, it has sufficient yield stress for the manufacturing process, which, however, leads to unwanted trapped air inside the bulk adhesive and joints.

DCB joint tests showed stick-slip and crack kinking. One possible explanation is the existence of voids leading to crack deflection. Also, the composite adherend intrinsic toughness seems to be lower than that of the adhesive, which also leads to further crack propagation into the composite. More dedicated procedures for making DCB joints will be proposed to study the influence of voids, and try to guide the propagation towards a more stable path within the adhesive phase. Nonetheless, bulk sample preparation protocols are defined and will be used for new material development.

Acknowledgements

The authors acknowledge funding under the Lead Agency scheme from the Research Foundation - Flanders (FWO Vlaanderen) through the project grant G031020N and the Swiss National Science Foundation (SNF) through the project grant 200021E_18944/1 with the title "Combined numerical and experimental approach for the development, testing and analysis of thick adhesive joints in large wind turbine blades". The authors also acknowledge Sika Technology AG for providing materials and support.

5. References

1. Zuo P, Vassilopoulos AP. Review of fatigue of bulk structural adhesives and thick adhesive joints. Int Mater Rev. 2021 Jul 4;66(5):313–38.

2. Molina MG, Mercado PE. Modelling and Control Design of Pitch-Controlled Variable Speed Wind Turbines [Internet]. Wind Turbines. IntechOpen; 2011 [cited 2022 Mar 28]. Available from: https://www.intechopen.com/chapters/14810

3. Samborsky D, Mandell J, Sears A, Kils O. Static and Fatigue Testing of Thick Adhesive Joints for Wind Turbine Blades. In: 47th AIAA Aerospace Sciences Meeting including The New Horizons Forum and Aerospace Exposition [Internet]. Orlando, Florida: American Institute of Aeronautics and Astronautics; 2009 [cited 2020 Aug 19]. Available from: http://arc.aiaa.org/doi/10.2514/6.2009-1550

4. Ataya S, Ahmed MMZ. Damages of wind turbine blade trailing edge: Forms, location, and root causes. Eng Fail Anal. 2013 Dec 15;35:480–8.

5. Lopes Fernandes R, Teixeira de Freitas S, Budzik MK, Poulis JA, Benedictus R. From thin to extra-thick adhesive layer thicknesses: Fracture of bonded joints under mode I loading conditions. Eng Fract Mech. 2019 Sep 1;218:106607.

  doi:10.5075/epfl-298799_978-2-9701614-0-0

6. Rosendahl PL, Staudt Y, Odenbreit C, Schneider J, Becker W. Measuring mode I fracture properties of thick-layered structural silicone sealants. Int J Adhes Adhes. 2019 Jun 1;91:64–71.

7. Xu XX, Crocombe AD, Smith PA. Fatigue Crack Growth Rates in Adhesive Joints Tested at Different Frequencies. J Adhes. 1996 Jun;58(3–4):191–204.

8. ASTM. Test Method for Tensile Properties of Plastics [Internet]. West Conshohocken (PA): ASTM International; [cited 2021 Jun 10]. Available from: http://www.astm.org/cgi-bin/resolver.cgi?D638-14

9. Domun N, Hadavinia H, Zhang T, Sainsbury T, Liaghat GH, Vahid S. Improving the fracture toughness and the strength of epoxy using nanomaterials – a review of the current status. Nanoscale. 2015;7(23):10294–329.

10. Ranade SR, Guan Y, Moore RB, Dillard JG, Batra RC, Dillard DA. Characterizing fracture performance and the interaction of propagating cracks with locally weakened interfaces in adhesive joints. Int J Adhes Adhes. 2018 Apr;82:196–205.

  doi:10.5075/epfl-298799_978-2-9701614-0-0

EXPERIMENTAL VALIDATION OF A RESIDUAL STRESS HYPOTHESIS FOR BOND LINES IN THICK ADHESIVE JOINTS

Tobias Holst[a], Alexandros Antoniou[a,] Nils Englisch[a]

a: Fraunhofer Institute for Wind Energy Systems, Bremerhaven, 27572, Germany
tobias.holst@iwes.fraunhofer.de

Abstract: *In this work a novel approach for the prediction of cure-induced residual stresses in bond lines of wind turbine blades is validated through an experimental campaign at coupon level. The adhesive strength of the neat material is compared to the adhesive structural strength of a bonded joint. Bonded sandwich and neat adhesive specimens are manufactured under identical boundary conditions. A residual stress hypothesis for the cure-induced residual stress state in the sandwich specimens is raised, considering the manufacturing conditions. The specimen sets are subjected both to static and tension-tension fatigue loads. The sandwich specimens are tested with a load ratio of R=0.1, where the neat adhesive specimens are loaded with the load case resulting from an R=0.1 load ratio with amplified mean stresses, equal to the predicted residual stress state of the adhesive in the sandwich laminate. The results are analyzed statistically and found to be in a good agreement.*

Keywords: Residual stresses; experimental validation; thick bond lines; wind turbine blades

1. Introduction

Structural rotor blade damages are causing considerable costs due to repair measures and downtimes [1, 2]. The repair measures are only an interim solution and do not address the root causes though [3]. The use of optimized design routines, based on advanced and validated material models, is an important approach to address the root causes and improve the reliability of operating wind turbine rotor blades.

Bond lines are of central structural relevance in wind turbine rotor blades and are often the origin of structural damages. The propagation of these damages as tunneling cracks in the surrounding laminate can affect the blades structural integrity [4]. An unwanted driver for the premature crack formation in bond lines are cure-induced residual stresses emerging during the manufacturing process [5]. Here chemical and thermal shrinkage mechanisms in the adhesive are leading to the evolution of residual stress states after adhesive gelation [6]. At the same time however the viscoelastic nature of the adhesive reduces the residual stress magnitude through relaxation effects [7]. The remaining residual stress state affects the mean stress level of the bond line during fatigue exposure and is therefore a driver for crack initiation [8, 9]. The development of advanced and validated material models, focusing on the failure behavior of bond lines by considering the curing-induced residual stresses, provides added value to the reliability of rotor blades.

This work therefore focuses on the experimental validation of a residual stress model for bond lines, manufactured with an industry standard epoxy adhesive, based on Zocher's thermoviscoelastic formulation [10].

  doi:10.5075/epfl-298799_978-2-9701614-0-0

2. Experimental setup

2.1 Manufacturing of the specimen plates

Both specimen configurations (sandwich & neat adhesive specimen) were manufactured under the same boundary conditions to achieve comparable preconditions. Two sets of glass fiber reinforced plates were premanufactured, consisting of 4 layers unidirectional glass fibers (E-glass, 996 g/m^2,) in combination with Hexion's *EPIKOTE MGS RIMR035c* infusion resin and the corresponding *EPIKURE MGS RIMH037* curing agent. The GFRP-plate sets were then bonded to 8 mm thickness using *Hexion's EPIKOTE MGS BPR 135G3* bonding paste in combination with the *EPIKURE BPH 137G hardener*. After adhesive curing in an oven at 80 °C for 4 hours with embedded temperature sensors, one set of GFRP-plates (pretreated with release agent) was removed to extract a comparable neat adhesive plate, see Figure 1.

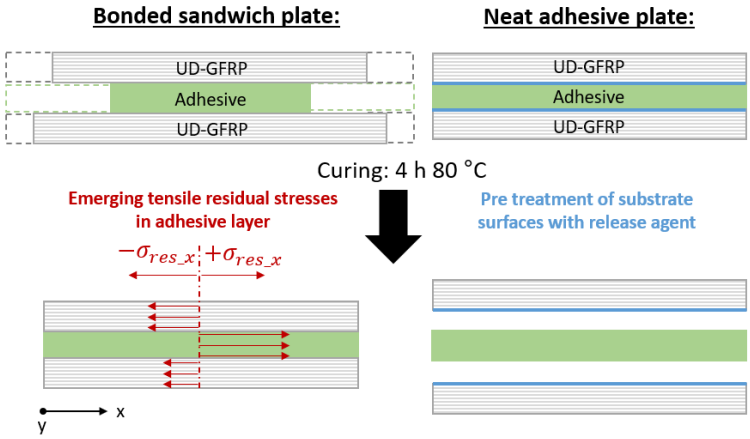

Figure 1. Manufacturing procedure for achieving comparable bonded sandwich and neat adhesive plates by using pretreatment of substrates with release agent (right side)

2.2 Implementation of the cure-induced residual stress hypothesis

By applying Zocher's approach [10] for describing the adhesive's thermoviscoelastic response to chemical and thermal induced strains after gelation, the resulting misfit plane stresses ($\sigma_{mf\,x}$ & $\sigma_{mf\,y}$) in the adhesive layer between the substrate parts were estimated considering the recorded temperature history. Here submodels of curing kinetics, chemical and thermal shrinkage were combined to derive cumulated misfit strain increments $\Delta\varepsilon_{mf}$ in the post gelation phase, Eq. (1). The thermal shrinkage increments were formulated as the difference between adhesive and substrate coefficients of thermal expansion in combination with a temperature delta.

$$\Delta\varepsilon_{mf\,x,y} = \Delta\varepsilon_{chem\,x,y} + \Delta\varepsilon_{therm\,x,y} = \Delta\varepsilon_{chem\,x,y} + \left(\alpha_{neat\,x,y} - \alpha_{subst\,x,y}\right) * \Delta T \quad (1)$$

These strain increments serve as input parameters for the Zocher's formulation in which the adhesive thermoviscoelastic model parameters were determined according to the method described in [7]. Eq. (2) represents a simplified formulation, applied to a one-dimensional stress state, to explain the main relationships. The misfit strain increments $\Delta\varepsilon_{mf}$ are embedded in a function f_{Zocher} which combines them with the relaxation modulus and a term $\Delta\sigma_{relax}$ that considers occurring stress relaxation during the computation step.

$$\Delta\sigma_{mf} = f_{Zocher}(\Delta\varepsilon_{mf} * E_{relax} - \Delta\sigma_{relax}) \quad (2)$$

The hypothesis of the adhesive's plane residual stress state ($\sigma_{res\ x}$ & $\sigma_{res\ y}$) was then derived from the computed misfit stress state by using Eq. (3), taken from [11]. This final step considers the mechanical interaction of the bond line with its compliant substrate parts and the resulting reduction of the stress state in the adhesive. Here t_1 refers to the cumulated substrate thickness and t_2 to the bond line thickness.

$$\sigma_{res\ x,y} = \frac{\sigma_{mf\ x,y}}{1+\frac{E_{2\ x,y}/(1-\nu_2)}{E_{1\ x,y}/(1-\nu_1)}*\frac{t_2}{t_1}} \tag{3}$$

The main assumptions of the applied residual stress hypothesis are listed below.

- Substrates' stiffness properties were estimated with classical laminate theory.
- The substrates' coefficients of thermal expansion in glassy und rubbery state were measured in fiber direction and transversely with thermomechanical analysis.
- The short fiber influenced adhesive properties were assumed orthotropic with directional properties in x- and y-direction.
- The adhesives' directional properties, contributing to the evolution of residual stresses (coefficient of thermal expansion, relaxation modulus), were characterized with a DMA-procedure. These properties were assumed dependent from temperature and independent from conversion.
- The Poisson's ratio of the adhesive was determined with three static tests based on DIN EN ISO 527-2. The transverse Poisson's ratio was derived from the law of elasticity.
- Curing kinetics and chemical shrinkage properties of the adhesive are taken from [12], where the linear induced chemical shrinkage strain was correlated with the directional linear thermal shrinkage strain.
- The adhesive's point of gelation was determined with oscillating rheometer measurements in plate-plate configuration at 0.61 conversion.
- The standard error of the residual stress hypothesis was estimated with probabilistic simulations based on the standard errors of the used submodels.

Table 1: Condensed material properties used, to estimate the residual stresses in sandwich plate with additional rubbery state properties given in brackets

Properties	Adhesive	Substrate
CTE_x [10^6 K^{-1}]	81.9 (210.7)	8.9 (7.8)
CTE_y [10^6 K^{-1}]	44.5 (47.9)	29.8 (63.7)
E_x [MPa]	2973	39686
E_y [MPa]	4224	14177

The residual stress hypothesis yields axial stresses in the bond line of the sandwich plate with a magnitude of 9.8 MPa (1.2 MPa) in x- and 3.9 MPa (0.7 MPa) in y-direction with the estimated standard errors in brackets. Due to the UD-glass fiber reinforced substrate along the x-direction, the corresponding axial residual stresses are significantly higher. Here the larger difference in thermal expansion coefficients between substrate and adhesive induces larger thermal residual strains in the adhesive, which leads to higher residual stresses during the cooling phase.

2.3 Mechanical coupon test setup

Two sets of neat adhesive specimens were cut out from the neat adhesive plate (8 mm thickness) by waterjet with a specimen geometry based on DIN EN ISO 527-2. One set of sandwich specimens was sawn out of the sandwich plate with a geometry similar to DIN EN ISO 527-5. Detailed information of the sandwich specimen geometry are given in Figure 2.

All specimen sets were subjected to static and tension-tension fatigue loads along the x-direction. The sandwich specimens were tested force controlled at a *250 kN* coupon machine. After three static tests, eight fatigue tests with specified levels of load amplitudes ($\sigma^i_{a\_sandw}$) and corresponding mean stresses ($\sigma^i_{m\ sandw}$) were performed at a load ratio of *R*=0.1. A sandwich specimen failure was defined by the appearance of a transverse (tunneling) crack in the adhesive layer, which was documented with photos every 100 cycles during fatigue testing.

The reference fatigue data set of the neat adhesive specimens was tested also force controlled at a *25 kN* coupon machine at the same load ratio (*R*=0.1) as the aforementioned sandwich specimens.

To validate the effect of the residual stress state, the second series of neat adhesive specimens was tested under fatigue loading. The stress levels were resulting from the corresponding *R*=0.1 stress amplitudes of the reference neat adhesive and the corresponding mean stress levels, amplified by the predicted cure-induced residual stresses ($\sigma_{res\ x}$ & $\sigma_{res\ y}$) of the adhesive in the sandwich laminate. By using of Beltrami equivalent stress criterion, Eq. (5), the mean stress levels of the neat adhesive specimens ($\sigma^i_{m\ neat}$) were individually modified.

$$\sigma^i_{a\ neat} = \sigma^i_{a\ sandw} \tag{4}$$

$$\sigma^i_{m\ neat} = \sqrt{\left(\sigma^i_{m\ sandw} + \sigma_{res\ x}\right)^2 + \sigma^2_{res\ y} + 2\nu\left(\left(\sigma^i_{m\ sandw} + \sigma_{res\ x}\right) * \sigma_{res\ y}\right)} \tag{5}$$

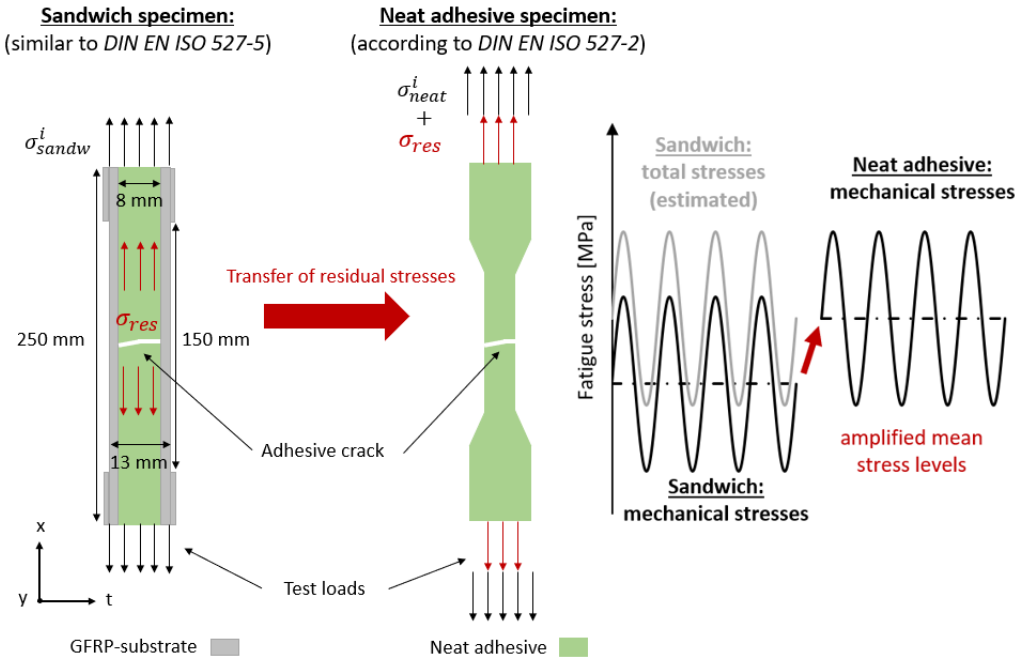

Figure 2. Comparison of the adhesives' neat material strength to the adhesives' structural strength in a bonded joint by artificial amplified mean stress levels

  doi:10.5075/epfl-298799_978-2-9701614-0-0

The assumption made is that the adhesive material in both specimen types is subjected to equivalent total loads during fatigue testing, as illustrated by Figure 2.

2.4 Derivation of test-induced adhesive stresses in the sandwich specimens

The adhesive stresses in the sandwich specimens were derived from the force signal F_{sandw} according to a two-step procedure by assuming that no transverse stresses are induced due to different Poisson's ratios of adhesive layer and substrate. The global stiffness of the sandwich specimens was therefore considered as a parallel connection of adhesive and substrate stiffnesses E_{neat} & E_{subst} in combination with the cross-section areas A_{neat} & A_{subst}. Eq. (6) was first used to derive an individual substrate stiffness value for each tested static sandwich specimen by using its known stress-strain data under consideration of a linear neat adhesive stress-strain behavior, obtained by three performed static neat adhesive tests.

$$\sigma_{subst} = \frac{F_{sandw} - \varepsilon_{sandw} * E_{neat} * A_{neat}}{A_{subst}} \rightarrow E_{subst} \tag{6}$$

Accordingly, the adhesive stresses at all specified test forces were then computed for each sandwich specimen with Eq. (7) by using the average stiffnesses for substrate und adhesive.

$$\sigma_{neat} = \frac{F_{sandw} * E_{neat}}{E_{neat} * A_{neat} + E_{subs} * A_{subs}} \tag{7}$$

3. Experimental results

3.1 Test results of sandwich and neat adhesive specimens

Figure 3 lists the observed mean static tensile strength values of both specimen types based on three static tests each. The observed neat adhesive tensile strength is 37.0 MPa on average. The mechanical degradation of the bond line in the sandwich specimens due to the present cure-induced residual stress state is represented by the lower adhesive tensile strength of 29.4 MPa.

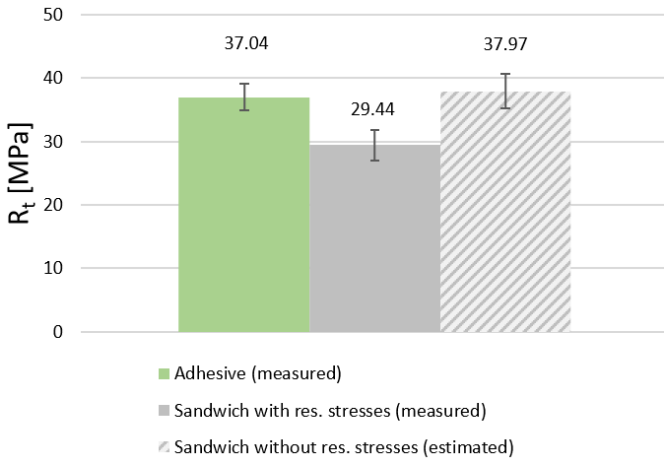

Figure 3. Comparison of the adhesives' neat static tensile strength with its structural static strength in a bonded joint with and without residual stresses

Assuming that the static tensile strength of the adhesive layer in the sandwich specimens ($R_{t_{sandw}}$) is a resulting effect of superimposed mechanical loads and residual stresses, the Beltrami equivalent stress criterion was used to estimate the theoretical tensile strength of the adhesive material between the substrates without present residual stresses (R_t^*), see Eq. (8).

$$R_t^* = \sqrt{\left(R_{t_{sandw}} + \sigma_{res\_x}\right)^2 + \sigma_{res\_y}^2 + 2\nu\left(\left(R_{t_{sandw}} + \sigma_{res\_x}\right) * \sigma_{res\_y}\right)} \quad (8)$$

The comparison of the derived theoretical tensile strength of the adhesive layer without residual stresses (37.97 MPa) with the measured tensile strength of the neat adhesive (37.04 MPa) shows that both tensile strength values are in the same range when uncertainties are considered.

Table 2 presents the applied mechanical load levels during fatigue testing for the comparable fatigue series of sandwich and neat adhesive specimens (amplified mean stresses). Both specimen series were tested with identical amplitudes as described in Section 2.3. The mean stress levels of the neat adhesive specimen were amplified with a representative stress state corresponding to the residual stress hypothesis to subject both specimen types to equal stress levels during fatigue testing. The shifted load ratios of the neat adhesive specimens are a result of the increased mean stress levels.

Table 2: Fatigue test results for comparable specimen types based on amplified load levels.

σ_a^i [MPa]	Sandwich specimen				Neat adhesive specimen			
	ID	Cycles N^i	σ_m^i [MPa]	R	ID	Cycles N^i	σ_m^i [MPa]	R
9.2	S4	2500	11.3	0.1	A4	866	20.1	0.37
8.9	S5	11600	10.9	0.1	A5	7420	19.3	0.39
8.4	S6	21600	10.3	0.1	A6	1860	19.1	0.39
8.0	S7	60600	9.8	0.1	A7	20100	18.6	0.40
7.5	S8	49000	9.2	0.1	A8	21900	18.0	0.42
7.1	S9	62900	8.7	0.1	A9	62200	17.5	0.43
6.4	S10	606000	7.9	0.1	A10	261300	16.7	0.45
6.2	S11	348000	7.6	0.1	A11	436000	16.5	0.6

The fatigue results for all three series are summarized in Figure 4. The three SN-curves were fitted by assuming a Basquin relationship between log(N^i) and log(σ_a^i), see Eq. (9) and Table 3.

$$\log\left(N^i\right) = \log(b) - m * log(\sigma_a^i) \quad (9)$$

To statistically evaluate both specimen series being compared, a 5% and 95% confidence limit was derived for the sandwich fatigue results after the method given in [13]. The confidence limits of the two neat adhesive series are not shown in Figure 4 to maintain a clear overview.

Table 3: Overview of Basquin-fit parameters for all three fatigue test series

Basquin-fit	Neat adhesive reference	Sandwich	Modified neat adhesive
m	11.1	11.4	15.0
$\log(b)$	15.6	14.7	17.5

  doi:10.5075/epfl-298799_978-2-9701614-0-0

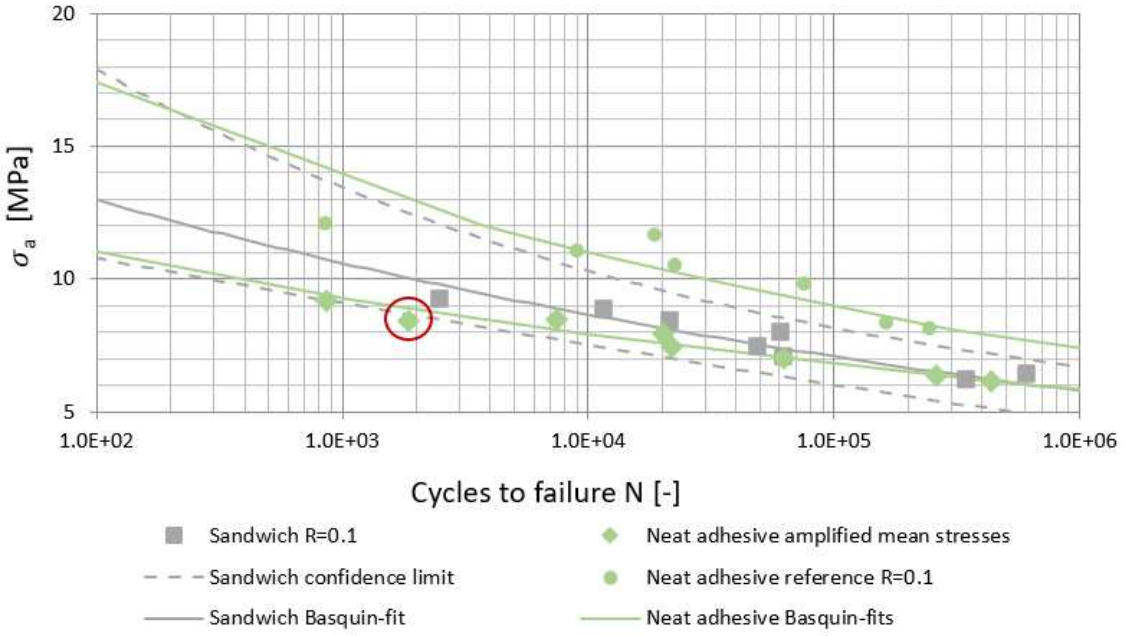

Figure 4. Test results for all three fatigue series with applied Basquin-fit

Figure 4 shows that the data points of the neat adhesive reference series (R=0.1) are clearly above the data points of the two comparable series presented in Table 2. Although mechanically identical loads were applied to the adhesive layer in the sandwich specimens, their mechanical performance is below the reference neat adhesive series. If the raised residual stress hypothesis is correct, the data points of both series from Table 2 should overlap. Here, seven out of eight data points of the corresponding neat adhesive series are within the 5% and 95% confidence limits of the sandwich samples. One data point (red marking) is slightly outside the sandwich specimen's confidence range.

3.2 Discussion of the test results

The observed static neat adhesive tensile strength (37.0 MPa) appears low regarding the value, stated in the adhesives' data sheet (70 MPa) [14]. Due to the manual adhesive application technique during manufacturing, air inclusions were unintentionally introduced, which explains the lower neat tensile strength. This effect might also explain the premature fatigue failure of the marked data point from the neat adhesive series with amplified mean stresses.

The demonstrated procedure has limitations and restrictions, which must be named. The comparative test assumes identical conditions of the adhesive material in both specimen types. Due to deviating curing temperatures, the final curing degree may vary, so that the adhesive strength could be affected. Furthermore, due to the manual adhesive application during manufacturing, the adhesive strength was significantly reduced by induced air inclusions. Since this impairment is present in both specimen types, the method for validating the residual stress hypothesis still works as both types are equally affected. Instead of applying the adhesive by hand, the use of a mixing and metering system can create better boundary conditions through fewer air inclusions in the adhesive material. This can reduce the scatter of test results and increase the accuracy of the validation method in future studies.

All in all, the comparison of tested neat and sandwich series shows that the residual stress hypothesis can be considered as plausible.

3.3 Conclusions

This work has demonstrated the experimental validation of a residual stress hypothesis in adhesive bond lines by coupon tests. In addition, this work reveals that the effects of residual stresses on the fatigue behavior of bond lines can be represented with an amplification of the mean stress levels during fatigue exposure.

Acknowledgements

We acknowledge the support provided by the German Federal Ministry for Economic Affairs and Climate Action (BMWK) within the HANNAH project (0324345C).

4. References

1. Quiévy N. Most frequent blade damages and strategies to mitigate their impact on operational costs. Wind Turbine Blade Manufacturer Cologne. 2021.
2. Katsaprakakis D A, Papadakis N, Ntintakis I. A comprehensive analysis of wind turbine blade damage. Energies 2021; 14:5974.
3. Buliga A. Solution for cracks. Bladena. 2018.
4. Rosemeier M et al. Tunneling crack initiation in trailing-edge bond lines of wind turbine blades. AIAA Journal 2019; 57: 5462-5474.
5. Jørgensen J B, Sørensen B F, Kildegaard C. Tunneling cracks in full scale wind turbine blade joints. Engineering Fracture Mechanics 2018; 189: 361-376
6. Sayer F. Sub-component testing for structural adhesive joint assessment in wind turbine blades. Dissertation Leibniz University Hanover. 2020.
7. Holst T, Sayer F, Antoniou A. A viscoelastic model for residual stress prediction in bond lines of wind turbine blades. Wind Energy Science Conference Hanover. 2021.
8. Antoniou A et al. Life prediction analysis of thick adhesive bond lines under variable amplitude fatigue loading. European Conference on Composite Materials Athens. 2018.
9. Antoniou A et al. Impact of site-specific thermal residual stress on the fatigue of wind-turbine blades. AIAA Journal 2020. 58: 4781-4793.
10. Zocher M A. A thermoviscoelastic finite element formulation for the analysis of composites. Dissertation Texas A & M University. 1995.
11. Jørgensen J B, Sørensen B F, Kildegaard C. The effect of residual stresses on the formation of transverse cracks in adhesive joints for wind turbine blades. International Journal of Solids and Structures 2019; 163: 139-156
12. Holst T, Sayer F, Antoniou A. Modelling of chemical shrinkage evolution with curing degree of a filled epoxy adhesive. IOP Conference Series Material Science and Engineering 2020; 945
13. Schneider C R A, Maddox S J. Best practice guide on statistical analysis of fatigue data. www.twi-global.com. 2002
14. Hexion inc. Technical data sheet Epikote resin MGS BPR135G3 Epikure curing agent MGS BPH1340G-137GF 2021

SUSTAINABLE MANAGEMENT OF MANUFACTURING WASTES AND END-OF-LIFE WIND TURBINE BLADES FROM FULLY RECYCLABLE THERMOPLASTIC COMPOSITES

Pierre GERARD[a], *Jean-François DEVAUX*[b]

a: Arkema France, GRL, 64170 Lacq, France - pierre.gerard@arkema.com
b: Arkema France, CRRA, 69491 Pierre-Bénite, France

Abstract: *The current manufacture of wind turbine blades is based on thermoset composite technology, but is facing new environmental constraints and especially a growing need for recyclability. Thermoplastic matrix composites could offer sustainable solutions. Newly developed acrylic liquid thermoplastic Elium® resin for composite polymerizes in-situ in the mold at room temperature during a vacuum infusion process and reduces manufacturing cycle time, embodied energy and costs due to non-heated tooling. This new generation of thermoplastic composites may offer the possibility to recover raw materials from production wastes and end-of-life parts, which can provide substantial environmental and economic benefits. This study presents a manufacturing and recycling demonstration for a 25-m-long thermoplastic composite wind turbine blade. An original pyrolysis process was applied to both production wastes and grinded blade. It allowed the depolymerisation of the acrylic thermoplastic matrix and recovery of clean fibers and matrix monomer. Distillation is used to purify the monomer from impurities and a recycled acrylic resin is synthesized and could be reused as recycled matrix for the manufacturing of new wind turbine blades with exactly the same use properties and thus meets the criteria for circular economy.*

Keywords: Thermoplastic composites ; Infusion ; Recycling ; Depolymerisation ; Wind blades ;

1. Introduction

The current manufacture of wind turbine blades is based on thermoset composite technology, but is facing to new environmental constraints and especially a growing need for recyclability. Thermoplastic matrix composites could offer some advantages and sustainable solutions. Thermoplastic-based composites are commonly processed by hot-stamping of pre-impregnated reinforcing plies but thermoplastic matrices usually exhibit high viscosity in the molten state that could impair the fiber impregnation. Higher processing temperature generally required and thermoforming issues of large thermoplastic parts have been overcome by developing a new acrylic liquid thermoplastic resin in-situ polymerized in the mold at room temperature during a vacuum infusion process. A further advantage of this process is that the reactive nature of the thermoplastic resin gives a better fiber to matrix bond, which significantly improves fatigue properties [1].

This study was carried out as part of the Effiwind project, supported by ADEME (French Agency for ecological transition) as part of the low-carbon energy sources program. The objective was to 'eco-design', manufacture and test a new generation of wind turbine blades using recyclable acrylic thermoplastic composites. The main goal of this project was to manufacture 25 m-long-blades that are longer than standard ones (23 meters), but which weigh the same, thanks to the

  doi:10.5075/epfl-298799_978-2-9701614-0-0

use of recyclable acrylic resin along with pultruded carbon fibers planks and methacrylic adhesive for the assembly of the two outer shells and shear webs.

Alongside the development of an appropriate resin composition, based on the lessons learned from the trial parts, the infusion manufacturing process was studied, first on a composite coupon and then on a full-scale section of wind blade, studying several areas of the blade. The mechanical performance of the glass fibre/acrylic laminate with PET foam as the core material (sandwich part), and of the glass fibre/acrylic laminate with carbon/epoxy pultruded composite (spar cap part), was demonstrated. An infusion strategy was defined and validated for the manufacturing of thick glass fibre/acrylic laminate (root of the blade), shear webs and shells (figure 1). A 25 m-long blade prototype was produced for full-scale industrial transfer (figure 2). The infusion strategy was validated: no dry zones on the root of the blade, controlled exothermy at the root of the blade and in the sandwich part, no internal draining between the carbon spar caps, pre-consolidation of the spar cap by adhesion before draping, etc.) Bonding strategy for the two outer shells using the methacrylic adhesive was also confirmed [2].

Figure 1. Vacuum assisted Elium® resin infusion of Low Pressure shell

Figure 2. Twenty five-meter thermoplastic composite blade

The 25 m-long blade prototype was tested with success in static and fatigue mode by the IWES Fraunhofer Institute (one of Europe's recognised full-size wind turbine test centres). This test

  doi:10.5075/epfl-298799_978-2-9701614-0-0

campaign included a vibration assessment, static tests in the four directions (Flap +/- and Edge +/-) up to extreme design loads (figure 3), fatigue tests at 1,000,000 cycles in the Flap and Edge directions for a load equivalent to two years of operation (figure 4), and residual static tests in all four directions up to extreme design loads [3].

Figure 3. Static test of the 25 m-long thermoplastic blade

Figure 4. Fatigue test of the 25 m-long thermoplastic blade

The blade's design loads were applied in static and fatigue mode without producing any critical damage to the structure of the blade. These tests helped to remove recent concerns about a full-scale thermoplastic blade in terms of i) the resistance of the root of the blade in static and fatigue mode, ii) the adhesive performance between the carbon/epoxy pultruded composite planks and the Elium® thermoplastic composite skins of the two half-shells of the blade, iii) the performance of the methacrylic adhesive joints in static and fatigue mode, and iv) the performance of the bond at the root of the blade in static and fatigue mode. A good correlation was also demonstrated between the model results, obtained by numerical simulation in accordance with the normative approach, and their coherence with the test results. The deviations observed were conservative and within the safety margins considered for the blade design. The 25 m-long thermoplastic blade was certified with success by the DNV-GL European certification body (C-design assessment).

This blade was then used as a full-scale demonstrator to establish a first proof of concept of the recyclability of continuous fibres reinforced thermoplastic composites [4] in production wastes

and end-of-life products by pyrolysis method [5]. Pyrolysis technique was employed to depolymerise the matrix and recover both the fibres and condensed monomer, which was purified to remanufacture recycle Elium® resin.

2. Materials and testing methods

2.1 Material

A blade manufacturing process involves the use of several thermoplastic consumables (peel-ply, flow medium, tubing, tacky tape, vacuum bagging, …). Bill of materials from the 25 m-long thermoplastic blade were analysed and in-process waste weight represents almost 15% of the weight of the blade (distributed among only one third for the consumables and two third for the fully polymerized resin).

The Elium® 188 XO resin, used for the vacuum assisted infusion of the blade, is a polymer solution of methyl methacrylate (MMA) monomer and of acrylic copolymers, having a viscosity of 100 mPa.s and activated by a benzoyl peroxide (BPO) thermal initiator.

A specific developed grade Elium® 351 SO, co-accelerated with Elium® A20 and initiated by a liquid methylethylketone peroxide (MEKP) was used for repair and over lamination.

A combination of Chomarat UD (960 g/m^2) and Biax (1000 g/m^2 ±45°) fiberglass with specific sizing were used in the blade skins and shear webs. Specific sizing made the use of glass fibre easier and improved the mechanical properties of the composite, particularly after fatigue ageing [6].The carbon/epoxy pultruded planks for the spar-cap were supplied by Epsilon Composites and a combination of 6-mm and 12-mm thick recycled PET foam from Armacell was sandwiched between the fiberglass layers of the blade skins.

A SAF® methacrylic structural adhesive was developed by AEC polymers (Bostik) for bonding operations of the blade. This 2K thixotropic adhesive can be used to fill thick bond line, up to 10 mm, has a pot life of 1 hour and a half and polymerizes quickly at ambient temperature without the need of post-curing.

Infusion wastes of blade subsections include fully polymerized Elium® resin, left in the resin feedlines, used infusion flow media and inlet profile and pad and peel ply that are also impregnated with the same resin. Infusion media is influplex isonet (Diatex), inlet profile is diadrain (Diatex) and peel ply is PA64 (Diatex).

2.2 Testing methods

Depolymerisation of infusion wastes was performed in a 250 cm^3 quartz three-neck flask equipped with a glass condenser. 50 g of material was heated under inert atmosphere with a heating mantle regulated at 460°C. After 1 hour, condensed crude monomer was collected and analysed by gas chromatography on apolar column with FID detection. Purity as methyl methacrylate was evaluated with an internal standard.

Depolymerisation of grinded composite was performed in a one liter stainless steel reactor with mechanical stirring and connected to a single tube & shell condenser. It was heated by a hot plate and electrical tracing and it was insulated by 5 cm of mineral insulation. 100 g of material

  doi:10.5075/epfl-298799_978-2-9701614-0-0

was heated at 410°C under an absolute pressure of 25 kPa for 1 hour. Condensed crude monomer was collected and methyl methacrylate monomer was quantified by gas chromatography. Organic residue on recovered fibres was quantified by calcination under air at 600°C for 3 hours.

3. Recycling of infusion wastes

Infusion waste is depolymerised by heating above 400°C for about 1 hour. The monomer of Elium® resin is formed as a hot gas that is condensed and recovered (see Table 1). Neat cured resin could be almost fully depolymerized and yielded a crude monomer with 83% purity. Depolymerisation of used infusion flow media made of polyethylene (PE) and copolymer (coPE) and used inlet profile and pad, mainly made of PET yielded 65-70% of crude monomer with a 66-70% purity. Depolymerisation of used peel-ply made of polyamide produced a lower amount of crude monomer with a lower purity, likely due to lower resin content in material and secondary reaction with PA during depolymerisation. In these depolymerisation conditions, the major part of PE, coPE, PET or PA is not vaporized and stays in the reactor as solid at ambient temperature. In an industrial recycling plant, these residues would be eliminated by incineration or energy valorisation.

Mixture of crude monomers from these depolymerisation trials was distilled to a colourless monomer having a purity > 99%, that can be used to make Elium® formulation.

In order to improve purity of crude monomer and lower the amount of residues, mixed infusion waste was grinded with a cutting mill with a 4 mm sieve then underwent density separation in brine (26% sodium chloride in water). Upper solid phase was rinsed with deionised water then underwent density separation in deionised water. Light solid phase contained PE and coPE. Lower solid phase was separated from water then dried. It contained mainly polymerised Elium® resin. Depolymerisation of this material was almost as efficient as depolymerisation of neat resin (*Table 1*): there was a very low amount of depolymerisation residue (3%), an excellent yield in crude monomer (92%) and a good purity in methyl methacrylate (81%).

  doi:10.5075/epfl-298799_978-2-9701614-0-0

Table 1: depolymerisation of infusion waste

Material	Depolymerisation residue (kg/kg material)	Crude monomer (kg/kg material)	Purity of crude monomer (wt%)
Cured Elium®	0.016	0.97	83
Used infusion media	0.26	0.70	70
Used inlet profile and pad	0.29	0.65	66
Used peel ply	0.68	0.21	47
Elium® fraction separated by density from mixed infusion waste	0.03	0.92	81

As a conclusion, the preferred process for recycling of infusion waste comprises the following steps: grinding, density separation, depolymerisation, distillation, formulation of recycled Elium®. A second life of PE, CoPE and PA fraction obtained by density separation might then be considered.

4. End of life recycling

4.1 Cutting and grinding a thermoplastic wind blade

The 25 meter-long thermoplastic wind blade was cut into less 2 meter pieces. Circular diamond saw was used for blade root cutting and automated wire saw was used for the rest of the blade (figure 5) [7]. The pieces were injected in a 220 kW pregrinder with a 10 mm sieve, which delaminates composite to large 10-40 mm needles. The material collected out of the pregrinder was treated in a 55 kW granulator with an 8 mm sieve to form needles of 0.5-12 mm length and 0.02-2 mm width, along with round particles of PET foam and adhesive. 2600 kg of regrind were collected.

Figure 5. Cutting of Elium® wind blade with automated wire saw (left)
Outlet of granulator (right)

4.2 Depolymerisation of wind blade regrind

Regrind of windblade was depolymerized in a stirred reactor under partial vacuum at 410°C for 1 hour and 0.206 kg of crude monomer per kg of regrind was collected with a purity of 85%wt. 0.71 kg of brown glass fibres with some carbon fibres per kg of regrind were collected. Their organic content was 7%.

Crude monomer was distilled to yield a 99% purity monomer. It was formulated to Elium® resin and polymerized as a cast sheet. We observed that reactivity in casting and analysis of the polymer by size exclusion chromatography are identical to virgin resin (*Table 2*).

Table 2: comparison of virgin Elium® and recycled Elium®

Monomer used to formulate Elium	Polymerisation peak temperature (min)	Average molecular weight in number (Da)	Polydispersity index Ip
Virgin monomer	44	77,000	3.6
Recycled monomer obtained by depolymerisation of grinded wind blade and distillation	45	84,000	3.5

This recycled Elium® resin could be reused as recycled matrix for the manufacturing of new wind turbine blades with exactly the same use properties and thus meets the criteria for circular economy**.**

5. Conclusion

This study successfully demonstrated the recyclability of a thermoplastic blade manufactured using vacuum assisted resin infusion. The 25 meter long thermoplastic blade constitutes a major technological innovation for the wind energy sector since it helps to i) reduce manufacturing costs (the thermoplastic blade polymerized at room temperature after infusion and did not require any post-cure heating, hence requiring less energy during manufacturing) and ii) increase the recyclability and resale value of the recycled resin compared to existing wind blades that use thermoset composites (figure 6). The three major wind turbine blade waste sources are manufacturing waste (in-process waste, plus defective blades and blades used for testing), service waste (from repairs and blade upgrading) and end-of-life waste (decommissioned blades). Continued work will further scale up recycling process and explore the cost benefit of recycling thermoplastic blades.

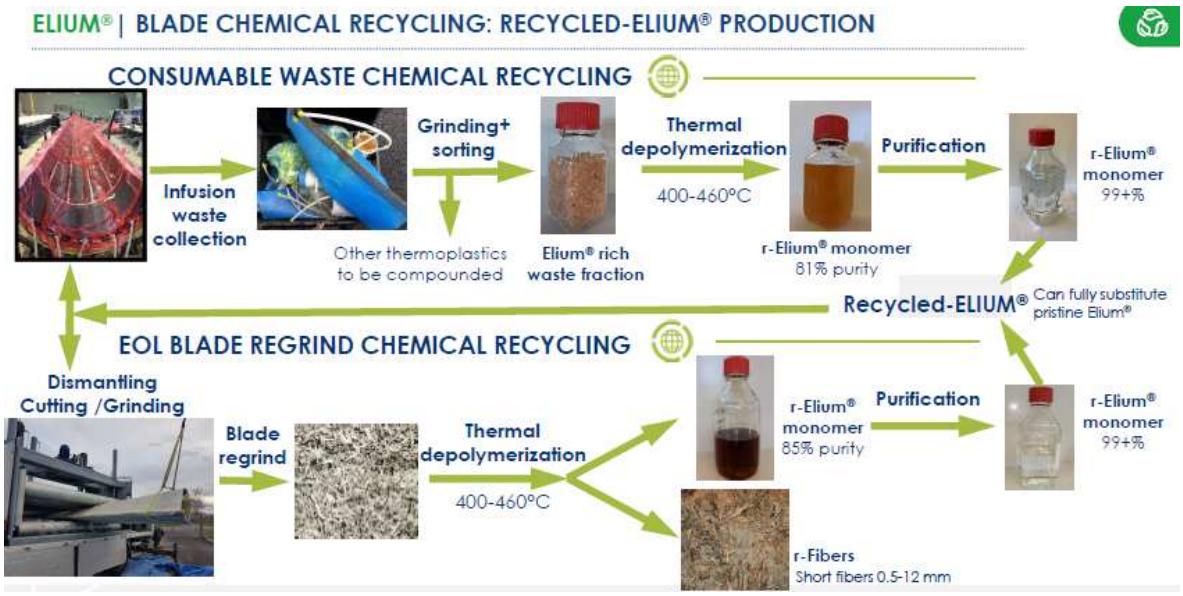

Figure 6. Chemical recycling of infusion consumable wastes and thermoplastic blade by pyrolysis (thermal depolymerisation) process

6. References

1. Davies P, Arhant M, Fatigue behaviour of acrylic matrix composites: influence of seawater. Applied Composites Materials 2018
2. Murray R.E, et *al.*, Manufacturing a 9-meter thermoplastic composite wind turbine blade, in: ASC 32nd Technical Conference. Purdue University, USA, 2017
3. Murray R.E, et *al.*, Structural validation of a thermoplastic composite wind turbine blade with comparison to a thermoset composite blade. Renewable Energy 2021; 164:1100-1107
4. Cousins D, et *al.*, Recycling glass fiber thermoplastic composites from wind turbine blades. Journal of Cleaner Production. 2019; 209:1252-1263
5. Bel Haj Frej H, Léger R, Perrin D, Ienny P, Gérard P, Devaux J.F, Recovery and reuse of carbon fibre and acrylic resin from thermoplastic composites used in marine application. Resources, Conservation & Recycling 2021; 173:105705
6. Boissin E, Effect of temperature on damage mechanisms and mechanical behavior of an acrylic-thermoplastic-matrix and glass-fibre-reinforced composite. Journal of Composite Materials 2020; 0:1-14
7. https://reciclaliacomposite.com/constrictor_/ accessed April 15, 2022.

  doi:10.5075/epfl-298799_978-2-9701614-0-0

DISMANTLING, SHREDDING, SORTING OF ROTOR BLADES FROM WIND TURBINES AND REUSE OF THE WOOD COMPONENTS

Peter Meinlschmidt

Fraunhofer Institute for Wood Research (WKI), Bienroder Weg 54 E 38108 Braunschweig - Germany – peter.meinlschmidt@wki.fraunhofer.de

Abstract: *At the end of a rotor blade's life cycle (estimated at 10 - 20 years), wind turbine blades have to be recycled.*

In various projects, the development of a suitable recycling and recovery process was to separate the excellent material properties of the balsa wood and the foam as purely as possible from the glass and carbon fibers and make them usable for new applications.

The presentation will show the dismantling of a rotor blade of more than 80 m in length using water jet technology and the shredding of essential parts using a shredder.

The further separation of the shredded pieces and the separation of the glass fibers from the balsa wood and the foam will be demonstrated.

At the end, renewed utilization possibilities for the waste wood and the foams will be shown.

The new products from the old rotor blades will be wood fiber insulation mats, wood foam and wood polymer composites.

Keywords: Rotor blade recycling; Recovery; Balsa wood, sorting; waterjet decomposition

1. Introduction

A modern wind turbine consists of over 90% concrete and steel on a mass basis depending on the design, which can essentially be fed into established recycling processes with a high recycling rate.

The rotor blades, which can be up to 100 m long, are much more difficult to recycle. They are largely made of glass fiber composite (GFRP) materials. In larger and newer rotor blades, additional carbon fiber composite (CFRP) materials can be found. At the same time, large quantities of matrix plastics, resin adhesives, and core materials (balsa wood or polymer foams) are used. Currently, most of the blades to be disposed are mechanically processed and used in clinker production for the cement industry. The resin and adhesive components serve as fuel and are recovered for energy. The glass fraction and the ash are used for aggregate substitution. Today, the CFRP fraction from recycled blades is small so far. Typically, the material is mechanically processed and then used as filler or aggregate in the plastics industry. In some cases, further processing into short- or long-fiber-reinforced nonwovens can take place via a pyrolytic processing route. After a service life of about 20 years, end-of-life rotor blades are rarely used anymore for repowering in other wind turbines. The renewed efficient use of rotor blade sections, large parts or materials would be desirable in the sense of a circular economy.

  doi:10.5075/epfl-298799_978-2-9701614-0-0

Resulting research questions and measures include the creation of framework conditions that allow the economic reuse of old rotor blades at the sites beyond the typical service life, as well as the expansion and optimization of standards and guidelines for the ecologically and economically safe dismantling and reprocessing of rotor blades and their technical support. Other necessary measures include product development that includes large pieces of old rotor blades as parts of new products (design for recycling/recovery), accompanied by the development of new concepts and technologies that facilitate rotor blade disassembly and separation of individual materials. These include rotor blade disassembly techniques adapted to the respective recycling plants, the production and use of GRP and CFRP fiber recyclate (taking health aspects into account) in homogeneous quality, product development for wood core materials and foams from rotor blade waste, the recycling of resin systems into new feedstocks (e.g. adhesives or basic chemicals), and the further development of thermoplastic resin, or functionally recyclable thermoset resin for new rotor blade production.

2. Rotor blade design and structure

Essentially, the blade shape of the rotor blades consists of two half-shells which are individually manufactured in sandwich design using vacuum infusion technology. The two shells are then glued together at the leading and trailing edges and at the webs using a two-component adhesive (Figure 1). Rigid foams (e.g. PVC, PET) or balsa end-grain wood are usually used as core materials in the lower and upper shells of the rotor blades. To absorb the bending forces within the blade, either one or more spar webs or a spar box are installed between the half-shells.

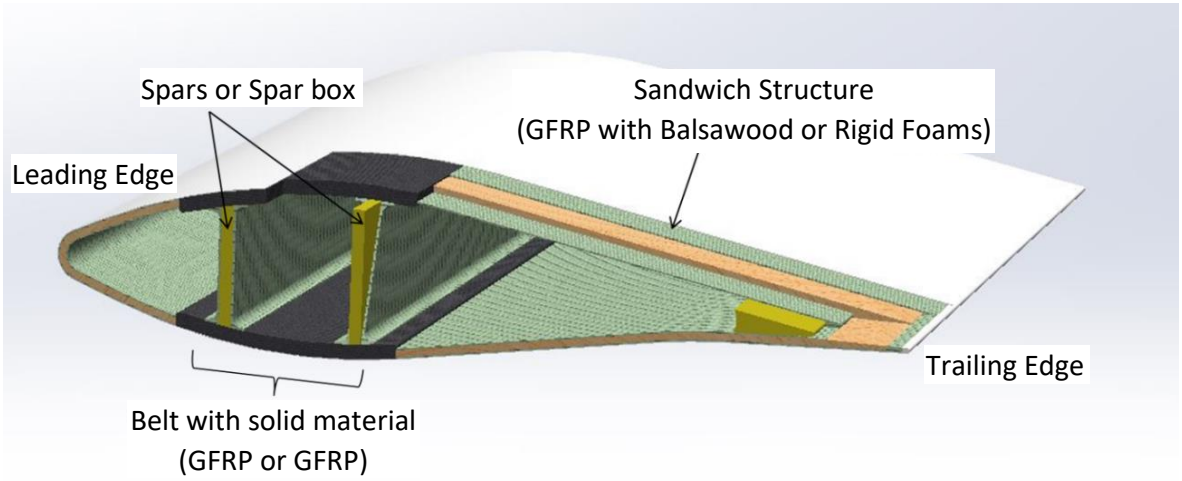

Figure 1: Typical rotor blade structure (Source : Fraunhofer ICT)

2. Deconstruction and Removal

The requirements for a suitable disassembly technology for large-sized rotor blades are sawing the blades into transportable pieces on site at the wind turbine (mobile application) and avoid danger to humans or nature.

A permit-free transport offers several advantages like significant reduction in administrative work and costs, the elimination of restrictions on travel times. In order to emphasize the advantages more precisely, the necessities for the transport of a complete rotor blade will be briefly discussed at this point:

  doi:10.5075/epfl-298799_978-2-9701614-0-0

The evaluation of whether a permit for transport is necessary or not is determined by the dimensions, axle loads or total weights of the vehicles and vehicle combinations. If the following limit values are exceeded, an exception permit is necessary according to §70 StVZO:

- in width 2,55 m (§32 Abs. 1 StVZO)
- in the height 4 m (§32 Abs. 2 StVZO)
- vehicle length for articulated vehicles 16,50 m (§32 Abs. 3Ziffer 2 StVZO)
- Single axle load of 10 t per axle (§34 Abs.4 StVZO)

Figure 2 : Permit-free transport of cut rotor blade segments. Transport of larger parts on a low loader (left) or shorter pieces in a container (right) (Source: Matetec, Teek)

3. Dismantling, shredding and separation

3.1 Dismantling

Usually, the long rotor blades are disassembled with wire saws or excavator saws after dismantling near the wind energy plant.

Within the framework of an “KMU Innovative” Projekt (ReRoBalsa), the technology of water jetting for the cutting of rotor blades was to be tested and optimized. First, at the waterjet manufacturer, the cutting speeds as well as the water quantity and possible additives (special sand) for cutting rotor blades were tested in the laboratory. It turned out that when cutting the pure GFRP as well as the sandwich structure of GFRP and balsa wood, sand as an abrasive additive is not necessary. Nevertheless, high cutting speeds could be achieved. However, the cutting speed of 20 mm GRP specimens is reduced from a feed rate of 60 mm/s to 20 mm/s for 40 mm thick specimens of the same material.

As part of an internal Fraunhofer research project (DeCaBo), a rotor blade is being segmented at the Fraunhofer IWES using waterjet cutting technology (*Figure 3*) and the segments are shredded with a mobile shredder (Figure 4). A test is being carried out to determine which shredding process generates the most suitable material for further processing.

  doi:10.5075/epfl-298799_978-2-9701614-0-0

Figure 3 : Water jet cutting of an 80m long blade on the property of the Fraunhofer IWES. Start of waterjet cutting along the carbon planks on the belt (left) and at the end of the cutting process (right) (Source Fraunhofer WKI, Meinlschmidt)

3.2 Shredding and separation

The shredded material will be used in further processes in the wood and foam processing to produce insulation materials in the first phase. The scientists also want to use other material components, such as carbon fiber belts, for their potential recycling.

Figure 4 : Shredding of the 2.5 m wide and over 10 m long segment of a rotor blade (left). Shredded rotor blade material consisting of GFRP and balsa wood (right) (Source : Fraunhofer WKI, Meinlschmidt)

With the help of a simple float-sink technique, the desired balsa wood or foam could be easily separated from the fiberglass face sheets, because balsa wood/foam floats and GFRP sinks to the bottom.

  doi:10.5075/epfl-298799_978-2-9701614-0-0

Figure 5 : Separating the foam and balsa wood fractions from the sheared GFRP using the float-sink technique (left) and the produced insulation boards made of balsa wood fibers and various adhesives (Source : Fraunhofer WKI, Meinlschmidt / Burgold)

4. Products from recycled Balsa wood and properties

4.1 Products made of recycled balsa wood

As part of the investigations for the master's thesis by Burgold [1], wood fiber insulation boards were manufactured from balsa waste wood (Figure 5, right). Among other things, the extent to which it is possible to optimize the insulation materials in terms of their heat conductivity by varying the parameter board density varying from 50 kg/m³ to 200 kg/m³, adhesive types (PMDI and PUR) and quantities (4%, 7%, 10%) or contamination with glass fibers was tested. For this purpose, the balsa wood with and without glass fiber fabric was first pulped in a Andritz refiner using the TMP process. Then, insulation boards were produced from the fiber material according to the parameters to be investigated using the dry method on a laboratory scale. The heat conductivity of the individual fiberboards was measured with the aid of a heat flow meter in accordance with the standards DIN EN 13171 and DIN EN 12667. The samples were dried for 72 hours at 70 °C, then sealed in a thin polyethylene foil, and the heat conductivity $\lambda_{10,dry}$ was determined at a sample medium temperature of 10 °C. The heat conductivity $\lambda_{10,dry}$ was then determined.

4.2 Properties of the produced insulation boards

In terms of sheet densities, target raw densities of 50 kg/m³, 100 kg/m³, 150 kg/m³ and 200 kg/m³ were targeted. A PMDI and an isocyanate-rich PUR system (prepolymer), which was specially developed for the production of wood fibers insulating materials, were used as adhesives.

Figure 6 shows the dependence of the heat conductivity on the raw density as well as on the type and proportion of adhesive and with and without glass fibers.

A non-linear increase in heat conductivity with increasing bulk density can be seen. However, there is no significant influence on the heat conductivity due to the type and quantity of

  doi:10.5075/epfl-298799_978-2-9701614-0-0

adhesive, nor due to contamination by glass fibers. These results are in good agreement with previous investigations.

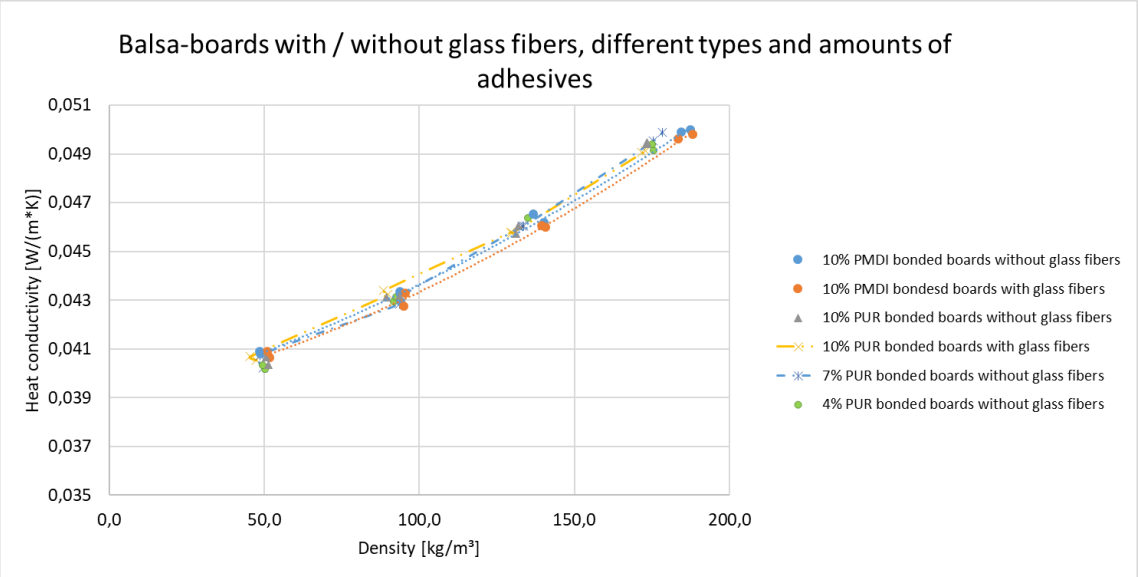

Figure 6 : Heat conductivity $\lambda_{10,\,dry}$ depending on the bulk density, type and proportion of adhesive, with and without glass fibers (Source : Fraunhofer WKI, Burgold)

In further tests, the amount of adhesive was varied from 4% to 7% and up to 10% of the PUR adhesive (I-Bond WFI 4370). Boards with the four different densities were again produced with these three amounts of adhesive and their heat conductivity was determined (Figure 7) in a 2-plate heat flow meter in accordance with the standards DIN EN 13171 and DIN EN 12667.

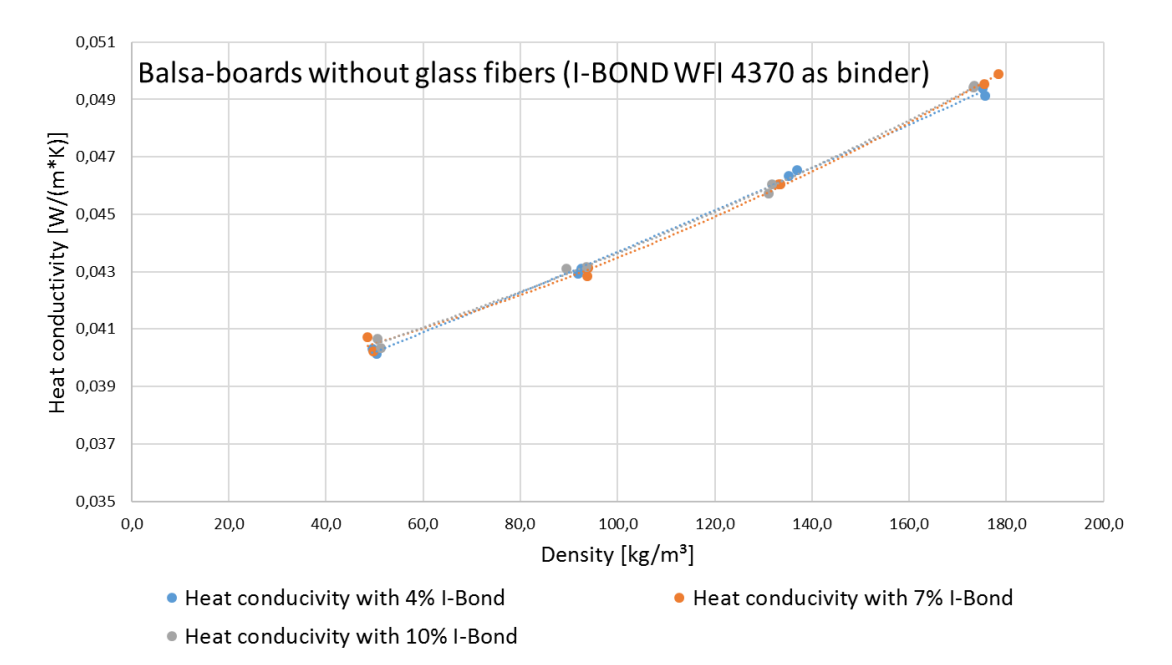

Figure 7 : Heat conductivity of balsa wood panels as a function of the amount of adhesive (Source : Fraunhofer WKI, Burgold)

Figure 7 shows again the direct dependency of the heat conductivity on the bulk density of the wood-based panel produced, but has no dependency on the quantity of adhesive used.

  doi:10.5075/epfl-298799_978-2-9701614-0-0

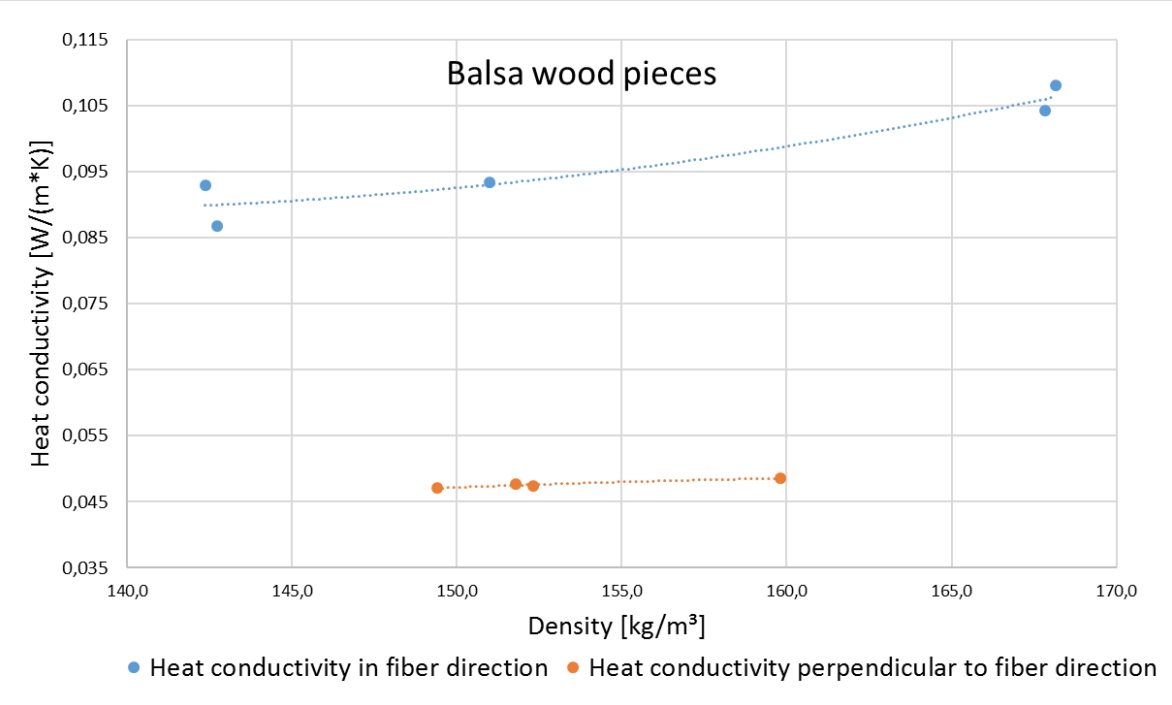

Figure 8 : The heat conductivity of balsa wood with the fiber direction parallel and perpendicular to the direction of the boards. The heat conductivity differs by a factor of 2 along and across the grain (Source : Fraunhofer WKI, Burgold).

4.3 Conclusion of the product properties

The studies described above show that good quality wood fiber insulation mats and panels which can be produced from recycled balsa wood. Due to its low density, however, balsa wood is better suited for insulating materials than many other types of wood. The determined heat conductivity values of the balsa wood insulating materials can certainly be significantly optimized by the alignment of the fibers and a significant reduction in the bulk density. The biggest advantage, however, is that the expensive balsa wood is used again (circular economy) as a material and is not immediately used for energy production that is not very effective (low calorific value).

Acknowledgements

I would like to thank the BMBF for funding the KMU-Innovativ Project ReRoBalsa as well as the Fraunhofer Gesellschaft for supporting the internal Corona-Push Project DeCaBo which made the achieved results possible.

5. References

1. Burgold C. Herstellung und Optimierung der Wärmeleitfähigkeit von Dämmstoffplatten aus recyceltem Balsaholz, Masterthesis Technical University Dresden 2017
2. Meinlschmidt P.: Recycling of Balsawood from Rotorblades for the Production of Building Insulation. Pol-Eco System Messe, 23. October 2018, Posen, Poland

  doi:10.5075/epfl-298799_978-2-9701614-0-0

STRUCTURAL OPTIMIZATION OF LARGE OFFSHORE WIND TURBINE BLADES

Sebastian M. Hermansen[a], Terence Macquart[b], Erik Lund[a]

a: Department of Materials and Production, Aalborg University, Pontoppidanstræde 103, 9220 Aalborg East, Denmark, Email: smhe@mp.aau.dk
b: Bristol Composites Institute (ACCIS), University of Bristol, BS8 1TR, UK

Abstract: *This work will demonstrate structural optimization of large offshore wind turbine blades. Offset in taken in a state-of-the-art commercial wind turbine blade, and the objective is to minimize its mass under critical structural and manufacturing criteria. Finite element models of the root-to-max-chord segment are built taking blade geometry, material layup and loads as input. It is chosen only to model this segment, as the majority of material is placed here. As such, the size of the analysis model is reduced for optimization. The finite element models will demonstrate optimization with both shell and solid-shell elements as well as combinations hereof. The structure is parametrized with layer thicknesses as design variables, which are assigned to patches to reduce the number of design variables. This paper will show preliminary analysis results, and the optimization results will be presented at the conference.*

Keywords: Gradient-based Structural Optimization; Laminated Composites; Wind Turbine Blades

1. Introduction

The energy harvest potential of a wind turbine is proportional to the size of the swept area by its blades. As a result, state-of-the-art commercial offshore wind turbine blades exceed 100m in length, with even larger blades being announced almost yearly. Designing structures of this size is in itself challenging, but for wind turbine blades the challenge is exacerbated by the use of fiber-reinforced laminated composites. By successfully using these materials in design, it is possible to achieve high stiffness- and strength-to-weight ratios, but they also exhibit directional-dependent behavior and complex failure mechanisms due to their fiber-matrix composition. The materials are used by layering them in a non-crimp fabric format, forming a laminate, and it is thus the objective of the designer to choose the number of layers (thickness) and the orientation of the fibers in each layer that ensures structural integrity.

This selection of materials and their thickness is an obvious optimization problem although a large and non-convex one, which is difficult to solve. Recent work in gradient-based structural optimization has however demonstrated, that it is indeed feasible to achieve a solution that significantly improves the design. Relevant work includes [1], where a very large-scale compliance topology optimization problem is solved for an airplane wing, [2] that solves a multi-criteria optimization problem to minimize the mass of a wind turbine blade using beam elements, and [3] that demonstrates multi-criteria thickness optimization of a commercial wind turbine blade to minimize its mass.

This work is based on the latter reference, and as such, the mass of a wind turbine blade will be minimized under multiple structural and manufacturing criteria. To reduce computational cost,

  doi:10.5075/epfl-298799_978-2-9701614-0-0

only the part from root to max chord is modeled, as the majority of material in the blade is placed in this region. The work will demonstrate the use of shell elements, solid-shell elements and combinations hereof. The structure is parametrized using layer thickness as design variables, and a gradient-based approach is used to efficiently solve the optimization problem. The results will demonstrate the potential of the approach.

2. Modeling

The work is based on a commercial offshore wind turbine blade with a length exceeding 100m, and as part of this work, a finite element model of the blade is created. It is desirable to make the model as efficient as possible to be able to perform the optimization, while still being able to capture the local stress behavior with decent accuracy, as it is included in the optimization criteria. In this aspect, the size of the blade is problematic, as the mesh must be sufficiently fine on a global scale, and this makes the model expensive to evaluate.

It has been realized that most material is concentrated in the first section of the blade towards the root. Therefore, the finite element model will be created for the root-to-max-chord section of the blade only. This model is built from the ground up, taking outer shell geometry, shear web geometry, layup file and load file as input. How these are accounted for is described in the following.

2.1 Finite Element Model

This work will make use of both layered shell and solid-shell elements to model the outer shell, and demonstrate their use in an optimization context. Traditionally, wind turbine blades are modeled primarily using shell finite elements, however it has been shown that the applied shell approach inaccurately captures torsional response. This inaccuracy is related to the thickness offset used to displace the layup to the outer shell for simplifying building the model, see [4] and [5].

This discrepancy does not occur for solid-shell elements. Furthermore, they capture out-of-plane stresses better than shell elements with post processing, which is particularly important for modeling the trailing edge of the blade. The solid-shell mesh is generated with only a single element through the thickness, and thus their use does not incur any increased computational cost compared to the commonly used 4-noded shell elements. Additionally, solid-shell elements allow for straightforward coupling to regular solid elements if increased fidelity is desired. However, modeling becomes inconvenient, as a both the in- and outside of the geometry must be known.

2.2 Layup and Materials

A layup, based on that of the original blade, is applied to the model. It consists of uni-directional (UD) glass fiber and carbon fiber reinforced polymers (GFRP and CFRP), biaxial GFRP and CFRP, balsa wood and foam. It is, however, beyond the scope of this paper to describe the layup in detail. The material layout in the blade forms distinct areas in the cross-section, see Figure 1.

  doi:10.5075/epfl-298799_978-2-9701614-0-0

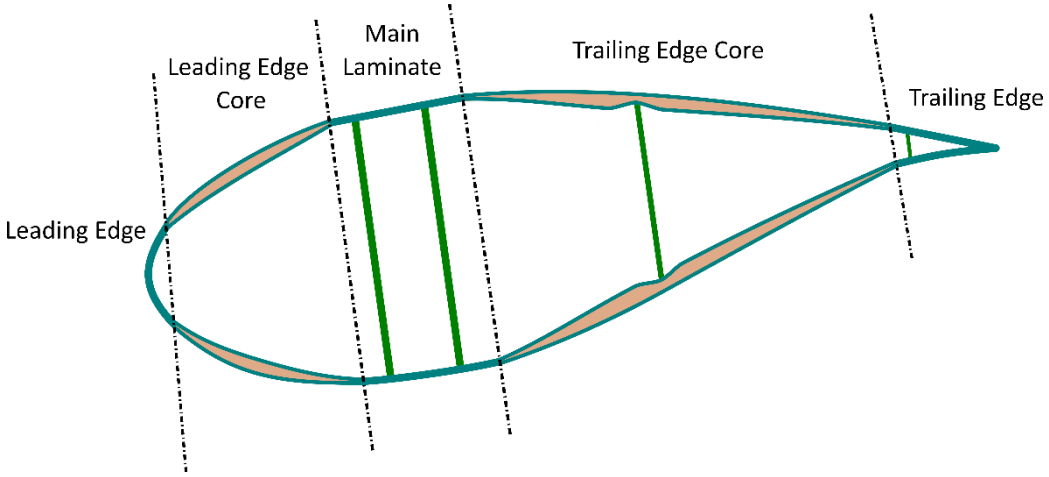

Figure 1. A cross section of the blade demonstrating the distinct areas of layup in the cross section.

For reducing the number of design variables in the optimization, it is assumed that the layup is constant within these distinct cross-sectional regions. The parametrization is discussed further in Section 3.

2.3 Boundary Conditions

The blade is fixed at its root and subject to twelve different load cases. These load cases consist of bending moments applied at different orientations with respect to the blade's longitudinal axis, illustrated in the load envelope in Figure 2 (left). The moments are given for a number of points along the longitudinal direction of the blade for each load case. They are applied to the finite element model at the top and bottom of each shear web as a distributed line load derived through a cubic spline fit, see Figure 2 (right).

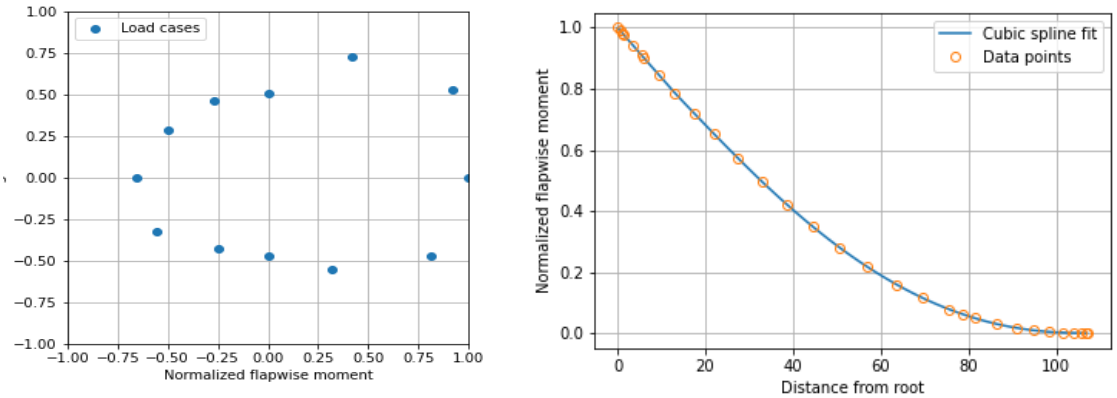

Figure 2. Left: the ratio of flapwise to edgewise bending moments for each load case at the root of the blade. Right: the spline fit to the flapwise bending case along the length of the blade. All values have been normalized with the maximum flapwise moment.

The influence of the removed part of the blade is taken into account by adding section forces to the cross-section at the cut.

  doi:10.5075/epfl-298799_978-2-9701614-0-0

3. Parametrization

The structure is parametrized with layer thicknesses as the design variables. It is common to include fiber orientation design variables in optimization of laminated composites, however this has been neglected for two reasons. Fiber angle optimization problems are parametrized using, for example, continuous fiber angle optimization (CFAO) or the Discrete Material and Optimization (DMO) approach, see [6]. The former is notorious for being highly non convex, thus having many local minima, making it is difficult to find a good solution. Furthermore, much post processing is required, as industry typically uses nominal fiber angles (+-45, 0 and 90) in their layups, and there are no restrictions on this in the CFAO problem formulation. DMO, and its extension DMTO for including thickness [7], is less non-convex, and it is possible to specify the discrete candidates directly, however the amount of design variables and constraints increases significantly, increasing the computational expense. Secondly, the layup in wind turbine blades is dominated by UD fiber material as loads in this study are in bending, and thus the gains should be negligible.

The design variables are assigned to patches, which are regions where the layup is assumed to be constant. These regions have been identified in both the cross-sectional and longitudinal directions, see Figure 3.

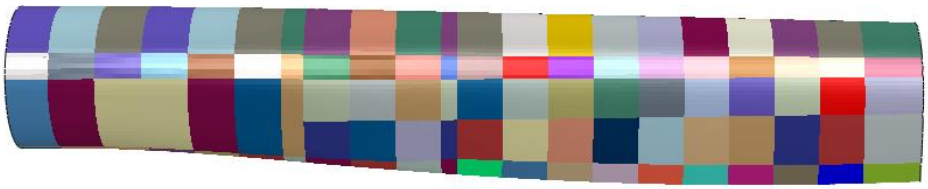

Figure 3. Top view of the patch parametrization of the blade.

Using the patch parametrization reduces the number of design variables, and thereby the computational cost of solving the optimization problem as opposed to element-wise design variable assignment.

Since solid-shell elements are used to model the blade, a change in thickness involves moving the nodes of each element in a patch. Therefore, the thickness optimization, which normally is a sizing optimization, also involves shape sensitivities. To prevent elements from becoming distorted or collapsing, the directions are computed in advance, which differs to the general case. Most often, the offset is normal to the surface with an exception at the shear webs, where the move direction is corrected to follow the shear web. For further details, see [3].

4. Optimization Approach

The objective of the optimization is to reduce the mass of the wind turbine blade subject to a number of structural and manufacturing constraints. The structural criteria included are tip displacement, eigenfrequency, linear buckling, static and fatigue failure. For buckling, it is necessary to include several load factors in the optimization problem in order to avoid issues with mode switching. For simplicity, static failure is included using the max stress approach. Fatigue failure is accounted for using the traditional constant lifetime diagram approach. The load history used for fatigue analysis is randomly generated and quantified using rainflow counting, and it is assumed that proportional loading is applied, such that the rainflow counting only has to be carried out once. Cycles to failure is calculated using double logarithmic S-N curve

  doi:10.5075/epfl-298799_978-2-9701614-0-0

relation (the Basquin expression) and partial damages are accumulated using linear Palmgren-Miner.

As the optimization problem involves criteria for static and fatigue failure, that are computed at the top and bottom for each layer for each element, direct inclusion in the optimization problem will result in many local constraints. With this many constraints, it is difficult to find a solution, that satisfies all constraints. This problem is solved by using a P-norm approximation for the maximum failure index and fatigue damage. A P-norm approximation, f_{PN}, is given as:

$$f_{PN} = \left(\sum_{i=1}^{N} f_i^P\right)^{1/P} \quad (1)$$

Here, N is the number of function values in the aggregation, f_i is a function value and P is a value that governs the accuracy of the approximation, i.e. as $P \to \infty$, $f_{PN} \to \max f_i$. However, a too large P-value makes the problem more non-linear, thereby increasing the difficulty of solving it. To remove the necessity for a large P-value, adaptive constraint scaling [8] is used to perform a scaling between the P-norm approximation and the maximum function value. This method makes use of a max-operator, which makes the problem non-differentiable, however the effect becomes negligible as the scaling factor computed converges with the problem, thereby reducing its influence. It is widely used in stress-based optimization, demonstrating its effectiveness.

To solve the optimization problem, a gradient-based approach is adopted. Gradient-based methods are most efficient for solving optimization problems, and is therefore necessitated by the present large-scale problem. The gradients are computed by an efficient semi-analytical adjoint formulation. The mathematical programming problem is solved using a Sequential Linear Programming with merit function approach, see details in [7]. It is based on and solved using the SNOPT framework, see [9]. The robustness of this approach has been demonstrated in numerous works involving highly non-convex problems with a high number of both design variables and constraints, see e.g. [3,10].

5. Preliminary Results

The displacement from the flapwise bending load case is presented in Figure 4.

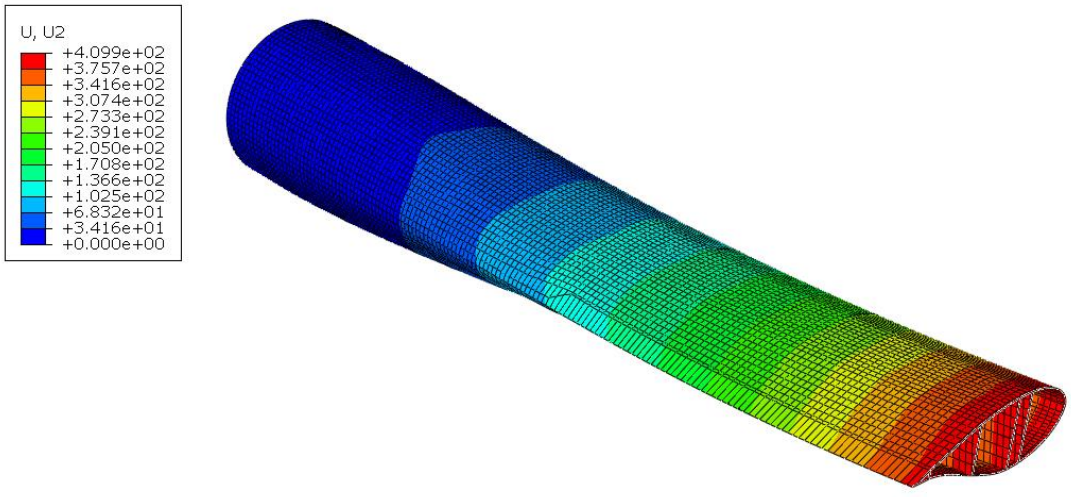

Figure 4. Flapwise displacement distribution.

The distribution of the displacement is comparable to a higher fidelity model containing more sections with additional materials, however the maximum displacement is reduced, as the optimization model has more material to open the design space. Further results, including an optimized design, will be shown at the conference.

6. Concluding Remarks

This paper has outlined an approach for structural optimization of large offshore wind turbine blades. How the blade is modeled, and the parametrization has been shown. The optimization approach is outlined and some preliminary results are presented.

Acknowledgements

The work is supported by the MADEBLADES project funded by the Energy Technology Development and Demonstration Program, Grant No. 64019-0514. This support is gratefully acknowledged.

7. References

1. Aage N., Andreassen E., Lazarov BS, Sigmund, O. Giga-voxel computational morphogenesis for structural design. Nature 2017; 550:84-86.
2. Scott S, Greaves P, Weaver PM, Pirrera A, Macquart T. Efficient structural optimisation of a 20 MW wind turbine blade. J. Phys.: Conf. Ser. 2020; 1618(4):042025.
3. Sjølund J, Lund E. Structural gradient based sizing optimization of wind turbine blades with fixed outer geometry Composite Structures 2018; 203:725–739.
4. Laird DL, Montoya FC, Malcolm DJ. Finite element modeling of wind turbine blades. In: Collection of the 2005 ASME Wind Energy Symposium Technical Papers at the 43rd AIAA Aerospace Sciences Meeting and Exhibit; pp. 9–17.
5. Tavares RP, Bouwman V, Paepegem WV. Finite element analysis of wind turbine blades subjected to torsional loads: Shell vs solid elements. Composite Structures 2022; 280:114905.
6. Stegman J, Lund E. Discrete material optimization of general composite shell structures. Int. J. Numer. Meth. Engng 2005; 62:2009–2027.
7. Sørensen SN, Sørensen R, Lund E. DMTO - a method for Discrete Material and Thickness Optimization of laminated composite structures. Struct Multidiscip Optim 2014; 50(1):25–47.
8. Le C, Norato J, Bruns T, Ha C, Tortorelli D. Stress-based topology optimization for continua. Struct Multidisc Optim 2010; 41:605–620.
9. Gill PE, Murray W, Saunders MA. SNOPT: An SQP Algorithm for Large-Scale Constrained Optimization. SIAM Review 2005; 47(1):99-131.
10. Lund E. Discrete Material and Thickness Optimization of laminated composite structures including failure criteria. Struct Multidisc Optim 2018; 57: 2357–2375.

  doi:10.5075/epfl-298799_978-2-9701614-0-0

SUB-COMPONENT VERSUS FULL WIND TURBINE BLADE STRUCTURE: INFLUENCE OF MANUFACTURE-INDUCED THERMAL RESIDUAL STRESSES ON TUNNELING CRACK INITIATION IN ADHESIVE JOINTS

Malo Rosemeier[a], Thomas Gebauer[b], and Alexandros Antoniou[a]

a: Department of Rotor Blades, Fraunhofer IWES, Fraunhofer Institute for Wind Energy Systems, Am Seedeich 45, 27572 Bremerhaven, Germany,
malo.rosemeier@iwes.fraunhofer.de
b: P. E. Concepts GmbH, Wiener Straße 5, 28359 Bremen, Germany

Abstract: *This work investigates the root causes for tunneling crack initiations in the trailing-edge adhesive joint that were observed on the fleet of more than 100 rotor blades of a single type for 2 MW wind turbines during manufacture and in the field. The highest crack frequency was observed at around 50% blade length. To identify the root causes, a trailing-edge sub-component of the blade was manufactured from the main mold under process conditions comparable to those used in the manufacture of the full blade. Contrary to the observations made for the full blade, no cracks were initiated during the sub-component manufacture. A linear thermal stress analysis by means of a comparable FE blade model revealed that the full blade was subjected to a higher residual stress level than the sub-component, which was in line with observations. This research shows that sub-components do not necessarily represent all aspects of the structural behavior of a full blade. Therefore, caution must be exercised when designing sub-components for design model validation.*

Keywords: bond line; shrinkage; finite element modeling

1. Introduction

Thermal residual stresses have a major impact on the bond line fatigue of wind turbine blades, which can initiate tunneling cracks in the adhesive layer of the trailing edge early in the operational life of the blade [1]. Tunneling cracks can propagate through the bordering fiber reinforced polymer (FRP) laminae into the sandwich panels toward primary structures, e.g., spar caps. Any damage to those can lead to a total loss of a blade. Thermal residual stress was found to have a major impact on the crack initiation in the adhesive layer. This stress develops during cooling after a typical curing cycle of a wind turbine blade manufacturing process [2].

Antoniou et al. [3] have shown that the thermal shrinkage and stress calculation can be conducted as a linear elastic analysis. That is to say, the temperature-dependent material properties, i.e., Young's modulus and the coefficient of thermal expansion (CTE), can be considered to be constant during cooling. A more detailed review of thermal stress analysis methods with a higher fidelity is given in [4].

A finite element (FE) blade model and two probabilistic stress-life models, which considered the multi-axial stress state (Figure 1c) resulting from the manufacture-induced thermal load and the mechanical loads, were validated with crack initiations observed in a full-scale test [5].

  doi:10.5075/epfl-298799_978-2-9701614-0-0

Encouraged by current guidelines and standards for the design of rotor blades [6,7], various sub-component testing concepts have been developed, cf. [8,9,11,12]. It was shown that they can replicate the mechanical stress states of a full blade structure. To the authors' knowledge, there are no relevant publications in the international literature that consider manufacture-induced stress states encountered in a full blade to be replicated on a subcomponent level.

The observations in our work show that tunneling cracks can already be initiated during the manufacture of blades. Therefore, our work investigates the root causes of crack initiations relating to the manufacturing process and its boundary conditions. To this end, a trailing-edge sub-component of a blade (Figure 1b) was manufactured from the main mold under process conditions comparable to those used during the manufacture of the full blade. The experiment was accompanied by FE simulations using a model of a blade type similar to the 2 MW type of blade under investigation.

Section 2 analyses the crack observations made during manufacture and in the field, gives details about the sub-component experiment, and the FE simulations. Section 3 shows the results of the FE simulations. Section 4 discusses the results. Finally, Section 5 summarizes the main findings.

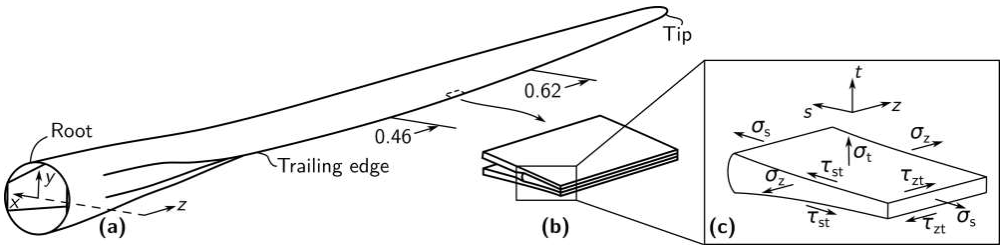

Figure 1. (a) Rotor blade, (b) trailing-edge sub-component cut-out, and (c) zoom-in on adhesive layer.

2. Materials and methods

2.1. Tunneling crack observations

Tunneling cracks at the trailing edge were observed on more than 100 blades of a single type for 2 MW onshore turbines during manufacture and in the field (Figure 2). Statistically, the region around the 50% span-wise position suffered the highest crack frequency (Figure 3). Tunneling cracks were detected after the blade had been demolded and the trailing edge trimmed.

  doi:10.5075/epfl-298799_978-2-9701614-0-0

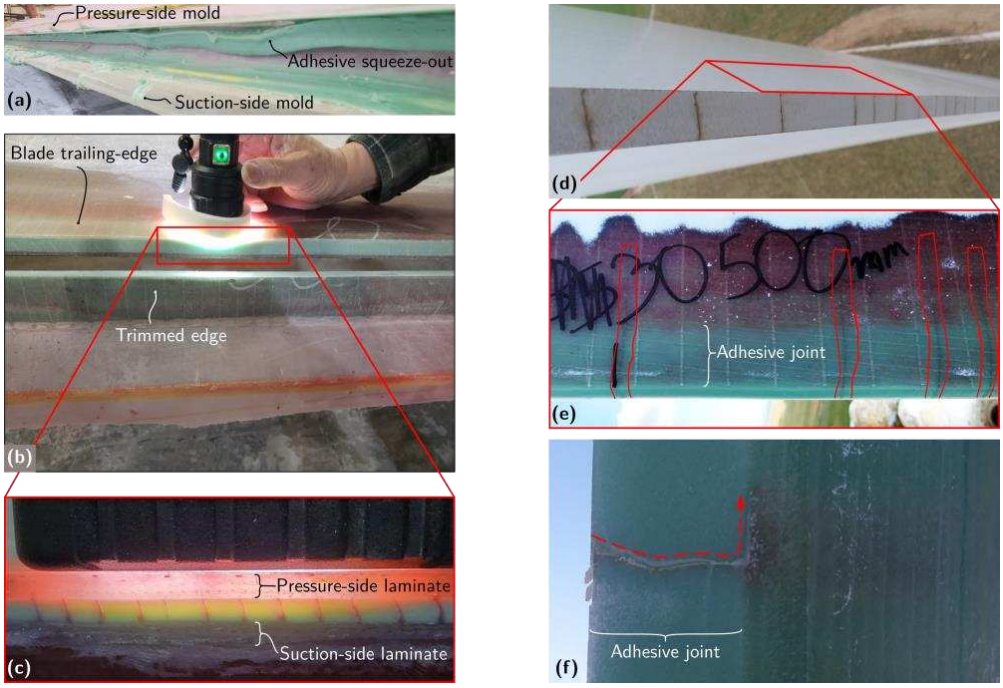

Figure 2. Crack observations: trailing-edge view during manufacture (a) of the closed mold after curing cycle, (b) after demolding and trimming, and (c) of tunneling cracks in the adhesive layer; trailing-edge view of tunneling cracks in the field (d) painted surface, (e) propagation in transverse s−direction (ground-off surface), and (f) propagation in transverse s− and span-wise z-direction.

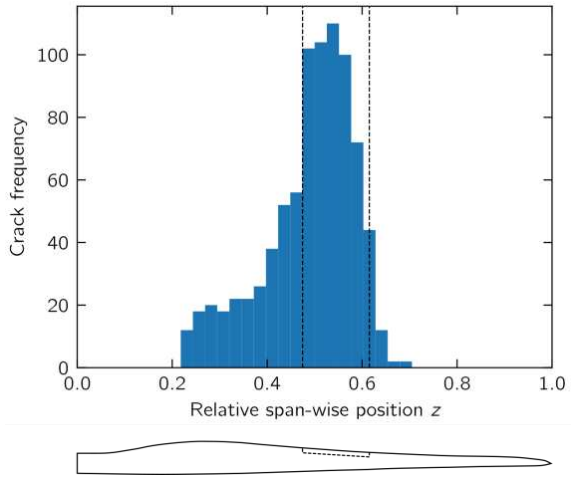

Figure 3. Crack frequency distribution.

2.2. Sub-component experiment

To investigate the root cause in the area of highest crack frequency, a sub-component specimen of the blade trailing-edge region between z=0.46 and z=0.62 (Figure 3) was manufactured from the full blade mold (Figure 4). The same manufacturing process steps and tempering cycles were carried out for the sub-component manufacture as for the manufacture of a full blade on a commercial production line. This allowed for a direct comparison of the sub-component with the full blade.

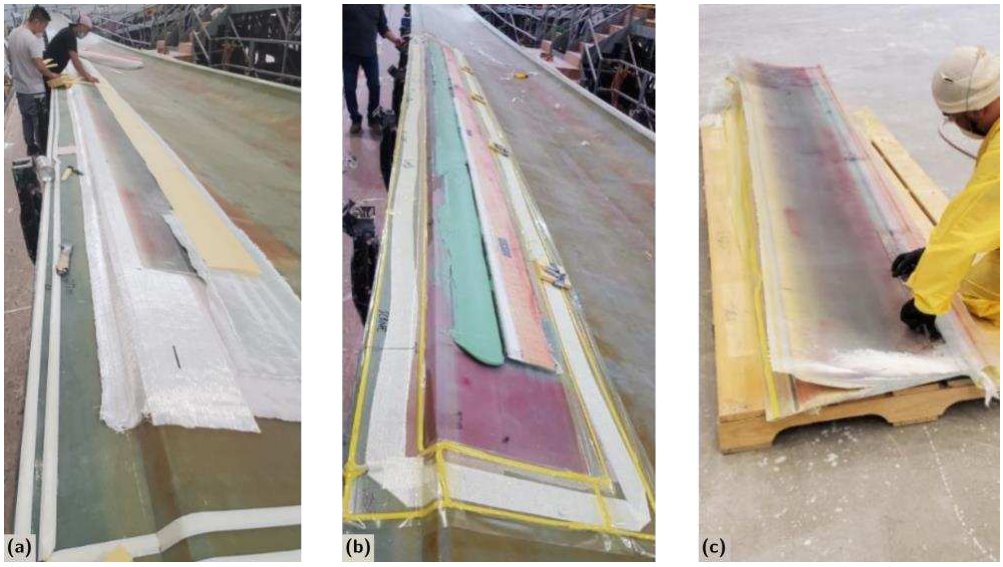

Figure 4. Manufacture of sub-component specimen: (a) layup of suction-side laminate, (b) application of adhesive, and (c) trimming of cured specimen.

2.3. Finite element simulation

The experiment was accompanied by FE simulations. To this end, a model of a commercial blade design similar to the 2 MW type of blade under consideration in this research was set up; cf. [2]. This model was comparable to the blade type under investigation insofar as the cross-sectional topology was similar. However, the blade length of the model was shorter. Both the full blade and the sub-component were modeled with and without squeeze out to investigate the influence of the trimming on the stress state within the adhesive (Figure 5).

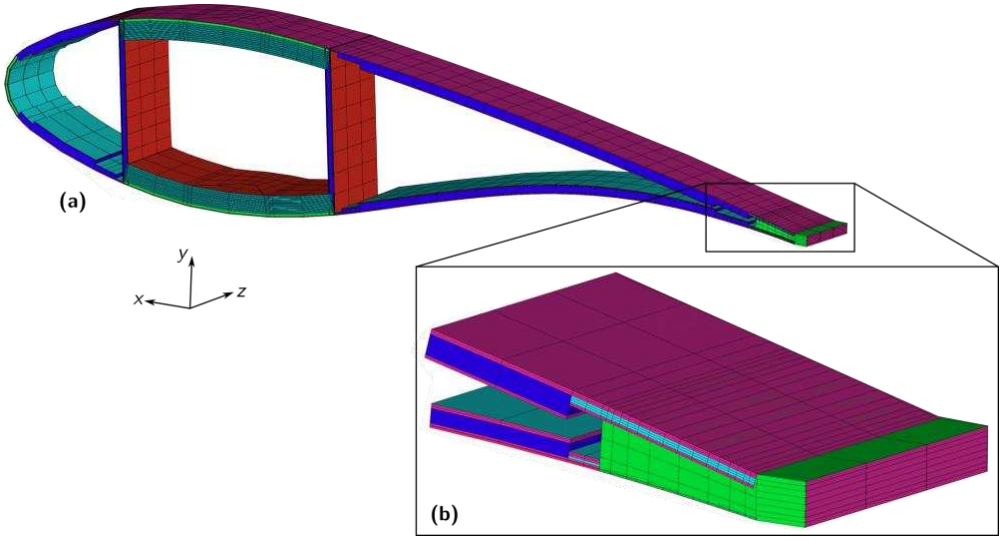

Figure 5. Finite element model showing extruded shell elements of (a) the full blade, and (b) zoom-in on the trailing-edge bond line modeled with solid elements and squeeze out shown as extruded shell elements. Note that in this graphical visualization the extruded shells overlap the solids on the suction side while the solids overlap the extruded shells on the pressure side. Also, the midnodes are shown for the shell elements but not for the solids.

  doi:10.5075/epfl-298799_978-2-9701614-0-0

The CTEs of the bond line FRP materials were calculated on the lamina level on the basis of Krimmer's [13] micro-mechanical Cylinder Fiber Model with hexagonal array (CFMh); cf. [1]. In order to obtain the CTEs of the FRP materials, the laminates were modeled using Classical Laminated Plate Theory. The CTEs of the adhesive and the epoxy matrix were determined experimentally [1].

A linear stress analysis was conducted as described in [2]. A three-dimensional finite element model implemented in ANSYS APDL was developed to determine all six mechanical stress components along the trailing-edge adhesive layer (Figure 1c). The FRP laminae of the bond line were modeled using quadratic shell elements of type SHELL281, while the adhesive layer was modeled using quadratic solid elements of type SOLID186 (Figure 5b). The two element types shared coinciding nodes. This modeling technique is called the "solid/shell share" technique [2]. The squeeze out was modeled using SHELL281 elements and considered adhesive material only. These shell elements also shared coinciding nodes with the solid elements. The adhesive was modeled with three elements through the thickness and 8 elements across the width.

The FE blade models were constrained at one node at the root-ward end in order to simulate the cool down of the full blade and sub-component after demolding. Consequently, the models were not constrained by a mold.

The two models were subjected to a thermal load stemming from the temperature difference ΔT, which indicates the temperature difference between curing T_c and operation T_o:

$$\Delta T = T_c - T_o. \quad (1)$$

At a curing temperature T_c = 70°C, the bond line laminate is considered to be free of thermal residual stress. The operating temperature was selected to be T_o = 23°C.

3. Results

3.1. Cracks

In contrast to the observations made during full blade manufacture, no tunneling cracks were observed in the sub-component specimen after trimming.

3.2. Thermal stress analysis

The linear stress analysis was conducted for both the full blade and the sub-component for the two situations - untrimmed and trimmed. The structure contracted at the trailing edge such that the whole blade bent in the edge-wise direction (Figure 6). The untrimmed situation exhibited a greater deflection than the trimmed situation, whereby the difference was significantly larger for the sub-component than for the full blade (Figure 7a).

The span-wise residual stress component σ_z^R of the trimmed compared to the untrimmed situation was about 31% higher for the full blade and about 43% higher for the subcomponent (Figure 7b), while the overall stress level of σ_z^R was higher for the full blade than for the sub-component.

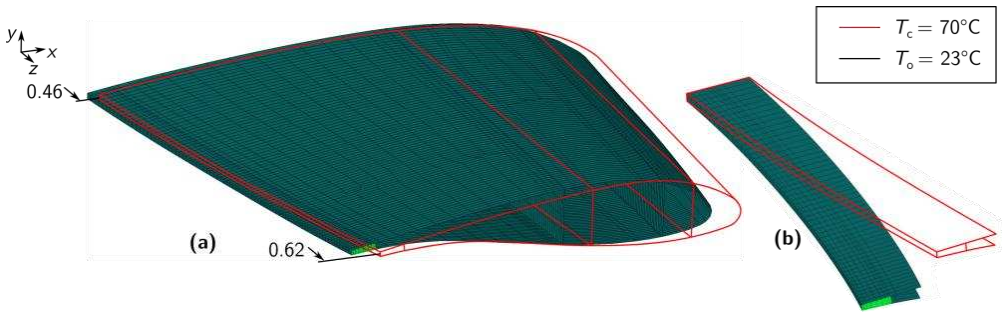

Figure 6. Thermal deformation: (a) full blade and (b) sub-component.

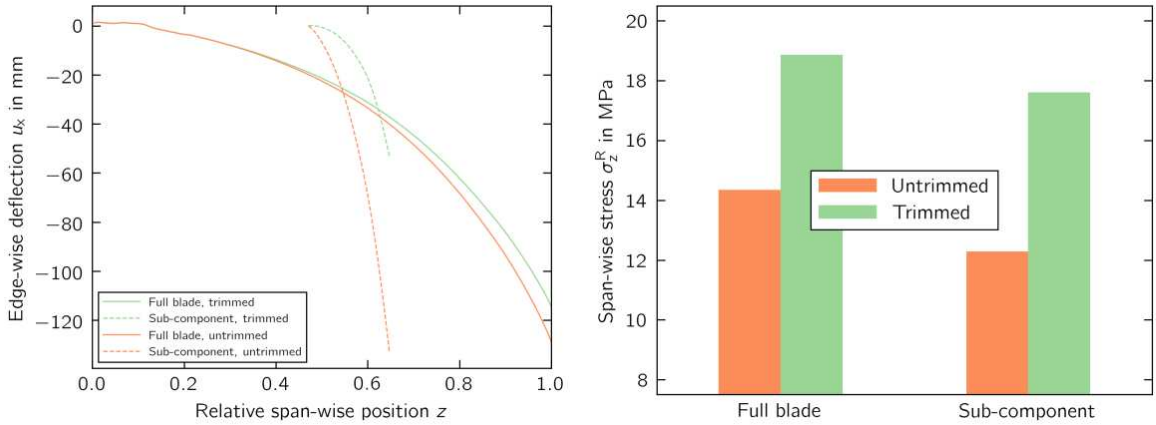

(a) *(b)*

Figure 7. (a) Edge-wise deflection of full blade and sub-component models.
(b) Span-wise residual stress vector component at critical outer edge of adhesive layer at span-wise position z = 0.5.

4. Discussion

4.1. Crack locations

In [5], the crack density of an 81.6-meter-long blade prototype was evaluated after a lead-lag certification test campaign, where no initial cracks due to manufacture were observed before the test, although the FE model predicted a relatively high and mostly constant but not critical residual equivalent stress level along the crack observation area between 28% and 51% blade length. Moreover, the crack density peaked at 30% and 37%, where the mechanical amplitude loading was also highest.

However, the statistical analysis of the blade fleet investigated in this research showed that cracks were observed in an area between 21% and 70% blade length, with a peak at 50%. If an FE model of the 2 MW type of blade were available, a thermal stress analysis would reveal more insights about the differences in stress states along this area.

When comparing the crack locations of the two blades, the area along the 2 MW type of blade with purely residual stress induced cracks extends further toward the tip, as does the peak.

4.2. Effect of trimming

A span-wise stress jump is introduced at the outer adhesive edge when the trailing edge is trimmed (Figure 7b). This is a consequence of the expansion of the trailing edge between the

  doi:10.5075/epfl-298799_978-2-9701614-0-0

untrimmed and trimmed situations (Figure 7a), which can be explained by an increase in strain in the trailing-edge laminate. This results in a larger residual strain difference between the adhesive and the bordering laminae, inducing a larger residual stress in the adhesive.

4.3. Residual stress and edge-wise bending tendency

The full blade was subjected to a higher stress level than the sub-component since the whole blade structure strongly constrained the edge-wise bending tendency, whereas the isolated trailing-edge sub-component could deform relatively freely.

Although the sub-component bent more over its total length than the respective segment in the full blade, i.e., by a factor of 1.6 for the trimmed situation (Figure 7a), the residual stress level in the sub-component was only 7% lower (Figure 7b). This is explained by means of Euler-Bernoulli beam theory. The edge-wise bending stiffness of the full blade was larger, the edge-wise elastic axis was positioned approx. between the two shear webs (Figure 5a), and the cantilever arm from the bending axis to the outer adhesive edge was larger than that of the sub-component, where the edge-wise bending stiffness was lower and the edge-wise elastic axis was positioned at approx. 1/3 of the sub-component width measured from the outer adhesive edge (Figure 5b). Thus, the lower bending stiffness of the sub-component was compensated by the shorter cantilever arm to a larger extent than was the case with the full blade.

4.4. Sub-component testing for model validation

Current guidelines and standards for the design of rotor blades [6,7] encourage the use of sub-components for the design evaluation. This investigation showed that the cross-sectional dimension of the sub-component chosen for this research did not entirely capture the stress response to which the part of interest was subjected to in the full blade. Therefore, we recommend that the cross-sectional and also the length-wise dimension of the sub-component be chosen so as to be large enough to reflect effects stemming from the deformation of the whole blade structure. Consequently, the sub-component will fully represent the behavior of the full blade structure.

Approaches given in [10] can act as a design guide for tailoring a sub-component toward the replication of the full blade behavior.

4.5. Model accuracy

For this research, the model chosen had a similar blade design to the manufactured 2 MW type of blade. Therefore, the results shown can be interpreted only qualitatively. Moreover, the “solid/shell share” technique used in the model is expected to underestimate the actual residual stress since the adhesive layer overlaps with the PS- and SS-laminates and introduces a smaller difference in the coefficients of thermal expansion between the trailing-edge bond line and the adhesive, cf. [2].

Also, the untrimmed edge was modeled using pure adhesive only. In a more realistic model, the whole bond line laminate would need to be reflected for the untrimmed situation.

5. Conclusion

With a 2 MW type of blade, the highest tunneling crack frequency was observed at around 50% blade length both during manufacture and in the field. One root cause for tunneling cracks being

initiated in the trailing-edge adhesive joint during the manufacture of a full blade but not a sub-component was found to be the thermal residual stress.

A linear thermal stress analysis by means of a comparable FE blade model revealed that the full blade was subjected to a higher residual stress level than the sub-component, which was in line with observations. Moreover, trimming the trailing-edge caused a higher stress increase for the sub-component than for the full blade.

Consequently, sub-components do not necessarily represent the structural behavior of a full blade. Therefore, caution must be exercised when designing sub-components for design model validation.

References

1. Rosemeier, M.; Krimmer, A.; Bardenhagen, A.; Antoniou, A. Tunneling Crack Initiation in Trailing-Edge Bond Lines of Wind Turbine Blades. AIAA Journal 2019, 57, 5462–5474.
2. Rosemeier, M.; Krimmer, A.; Antoniou, A. Development of thermal residual stresses during manufacture of wind turbine blades. Journal of Physics: Conference Series 2020, 1452, 012060.
3. Antoniou, A.; Rosemeier, M.; Tazefidan, K.; Krimmer, A.; Wolken-Möhlmann, G. Impact of Site-Specific Thermal Residual Stress on the Fatigue of Wind-Turbine Blades. AIAA Journal 2020, 58, 4781–4793.
4. Rosemeier, M.; Saathoff, M. Impact of manufacture-induced blade shape distortion on turbine loads and energy yield. Journal of Physics: Conference Series 2020, 1618, 052011.
5. Rosemeier, M.; Melcher, D.; Krimmer, A.; Wroblewski, W.; Antoniou, A. Validation of crack initiation model by means of cyclic full-scale blade test. Journal of Physics: Conference Series 2022, 2265, 032045.
6. DNV GL A/S. DNVGL-ST-0376 - Rotor blades for wind turbines; 2015.
7. IEC. IEC 61400-5 - Wind energy generation systems - Part 5: Wind turbine blades, 1 ed.; International Electrotechnical Commission: Geneva, Switzerland, 2020.
8. Branner, K.; Berring, P.; Haselbach, P.U. Subcomponent testing of trailing edge panels in wind turbine blades. In Proceedings of the 17th European Conference on Composite Materials, 2016, pp. 26–30.
9. Lahuerta, F.; de Ruiter, M.J.; Espinosa, L.; Koorn, N.; Smissaert, D. Assessment of wind turbine blade trailing edge failure with sub-component tests. In Proceedings of the Proceedings of 21st International Conference on Composite Materials, 2017.
10. Rosemeier, M.; Antoniou, A.; Chen, X.; Lahuerta, F.; Berring, P.; Branner, K. Trailing edge subcomponent testing for wind turbine blades–Part A: Comparison of concepts. Wind Energy 2019, 22, 487–498.
11. Rosemeier, M.; Antoniou, A.; Lester, C. Sub-components of wind turbine blades: Proof of a novel trailing edge testing concept. In Mechanics of Composite, Hybrid and Multifunctional Materials, Volume 5; Springer, 2019; pp. 267–274.
12. Sayer, F. Sub-Component testing for structural adhesive joint assessment in wind turbine rotor blades; Fraunhofer Verlag, 2020.
13. Krimmer, A. Mikromechanische Modellierung von Fasergelege-Kunststoff-Verbunden auf Basis von Normprüfungen unter Berücksichtigung der in-situ-Eigenschaften der Matrix. Dissertation, TU Berlin University, 2014.

AUTOMATED MODEL GENERATION OF LARGE WIND TURBINE BLADES: SHELL VS SOLID MODELS

R. Tavares[a,b] and W. Van Paepegem[a]

a: Department of Materials, Textiles and Chemical Engineering, Ghent University,
Technologiepark 46, 9052 Zwijnaarde, Belgium
E-mail: Wim.VanPaepegem@UGent.be
b: Solvay, Rue de Ransbeek 310, 1120 Brussels, Belgium

Abstract: *In this work, a novel approach to create FE blade models, which allows both shell, solid and hybrid modelling strategies is presented. The developed modelling approach is implemented as a stand-alone software that handles all the different steps of the model creation process in a matter of seconds. This approach considers the blade to consist of a collection of parametric pre-defined blocks, allowing models consisting of shell or solid elements to be created. By including the tools to accurately partition the OML, create the required offset surfaces and calculate accurate element-wise material orientations, a high level of detail and fidelity can be achieved. The developed software is used to create a high fidelity model of a 43m long glass-fibre epoxy wind turbine blade that is analysed under different static loading conditions. The relevance of using solid element meshes, is demonstrated by a case study on torsional stiffness calculation of large wind turbine blades, where large discrepancies can be observed between conventional shell models and solid models.*

Keywords: wind turbine blade, finite element modelling, torsional stiffness, shell and solid

1. Introduction

Due to market demand the size of wind turbines has been rapidly increasing as a result of the reduction in cost of energy for larger turbines, leading to blades of extreme complexity, both in terms of geometry and materials. The increased structural complexity of larger turbines requires a better understanding of their behaviour, thus higher fidelity numerical models are essential. The behaviour of these structures is usually investigated using Outer Mold Layer (OML) shell models, however different studies have identified significant drawbacks of this approach. Firstly, OML based shell models predict a lower torsional stiffness of the blades when compared to solid element models. The second issue with the shell approach is related to the correct representation of the adhesive joints in the blade, since the inner surfaces that make contact with the adhesive are not directly modelled. Finally, the usage of solid elements allows a better representation of the stress state within the composite materials, which increases its fidelity and is essential when predicting damage progression and failure.

2. Materials and methods

The novel approach is implemented as an object-oriented software tool. This tool is able to generate full 3D FE models of wind turbine blades. It consists of a series of modules that take care of the individual model creation steps. While it is a standalone tool, it was developed in python for fast implementation. To simplify the challenge of creating the models, a divide and conquer approach is used. Instead of considering the blade as a single entity, it is considered in the novel approach as a collection of pre-defined parametric blocks. Each block consists of a

  doi:10.5075/epfl-298799_978-2-9701614-0-0

number of components that each have their geometry and layup. To account for different regions and modelling strategies, a library of block types is available. Each block type has a different configuration and serves a single or two opposing panels (one on the Pressure Side (PS) and one on the Suction Side (SS)). For example, there is both a block type that creates a single face from a panel (that is later meshed with shell elements) and a block type that creates a single cell (that is later meshed with solid elements). More advanced block types create multiple cells and faces through the thickness. In this way there are also block types creating a trailing edge (TE) by modelling the entities representing the laminate on the PS and SS as well as that on the TE side and the adhesive connecting them. The same goes for the shear webs and their flanges. A schematic overview of some different block types can be seen in Figure 1.

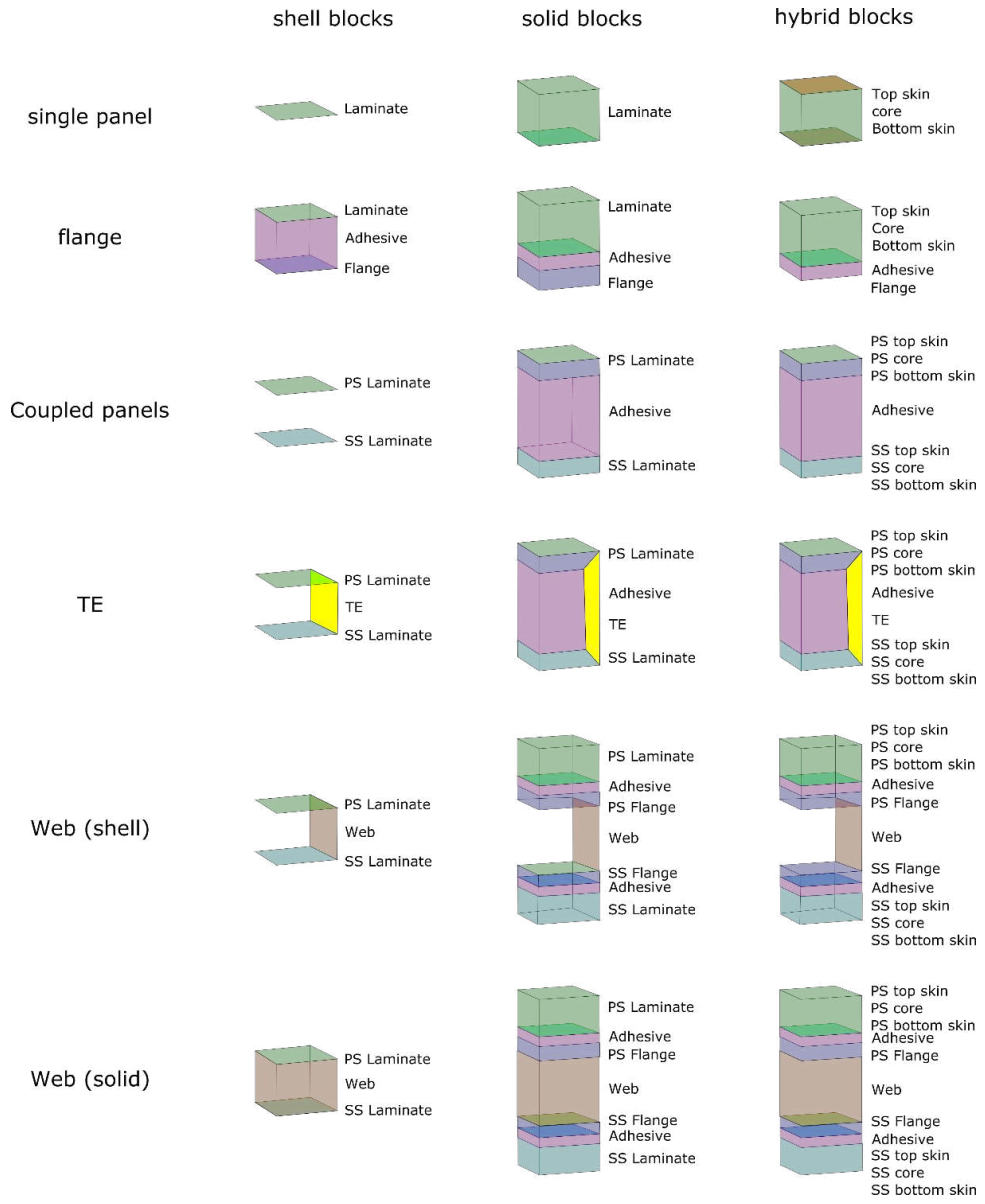

Figure 1: Schematic overview of blade blocks. Three main compatible categories are shown (shell, solid, hybrid). A single panel block is assigned only to a single panel, while other blocks are assigned to a combination of a panel on the SS and a panel on the PS. Various blocks are available to model different features.

Other software tools that are able to create models other than those with shell elements on the OML, typically consider a fixed pre-defined chord-wise topology for the blade. This facilitates the process of creating the mesh features. Other software tools that do not constrain the topology are typically only able to create OML shell models. In contrast, the approach allows very different layouts and is still able to create both OML shell, mid-thickness shell and solid models as well as combinations of those. Figure 2 shows an example of how a collection of blocks can be used to model a blade section.

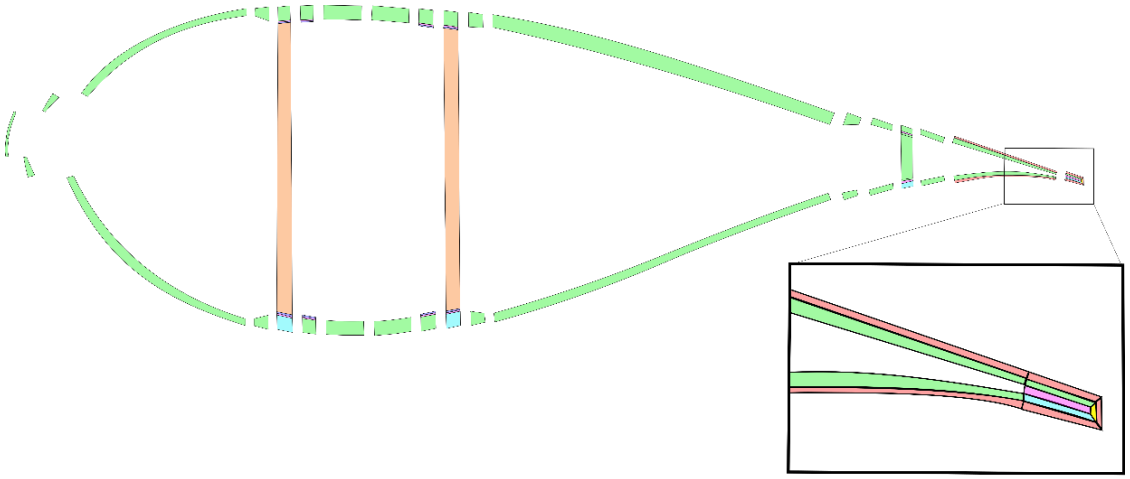

Figure 2: Example of how a number of compatible blocks result in a cross-section of a high fidelity solid model..

The software is broken down in a number of modules able to handle the different tasks. In this paragraph, a brief overview is given. As a first task, a parametric surface is created from the OML shape. As a second task, this surface is partitioned. This is done in a two-step process. The surface is first partitioned by means of functions along the length of the blade and subsequently at a series of span-wise positions. The result is a “map” of the blade. This map represents the topology and consists of vertices, edges and panels. On this map, each ply in the composite layup can be assigned to the correct region. It is worth noting that this intermediate result is independent of the desired output model. Once the topology is clear, blocks can be assigned to the panels. This allows that the actual features such as faces and cells can be created. As final tasks, these features are meshed and material orientations can be calculated. An overview of the different stages in the modelling process can be seen in Figure 3.

More information on the methodology can be found in ref. [1].

  doi:10.5075/epfl-298799_978-2-9701614-0-0

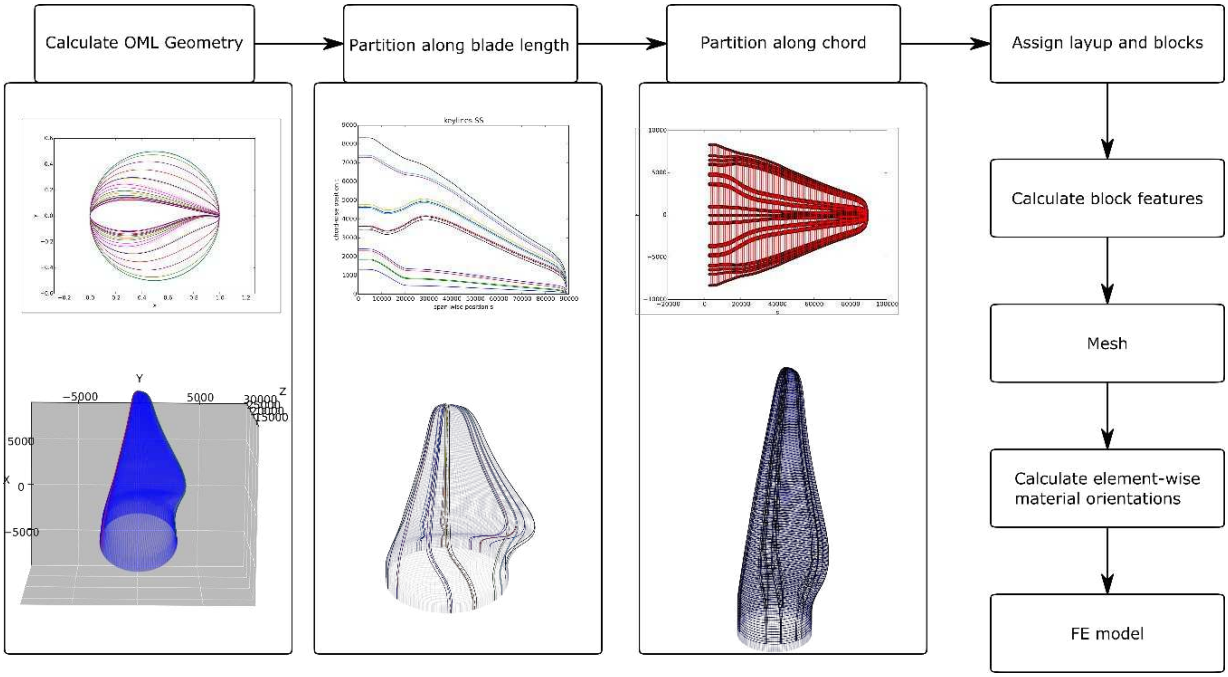

Figure 3: An overview of the different stages of the process of generating a FE model of a wind turbine blade with the proposed approach.

3. Results and Discussion

To obtain a useful model from a collection of pre-defined blocks, the adjacent blocks have to be compatible. This means that the interfaces between adjacent blocks should match, so that a continuous mesh can be formed. Compatibility is on one hand determined by the type of block, in the sense that there are different families of compatible blocks. An example of such a family are shell blocks, since they are compatible with other shell blocks, but not (directly) with solid blocks. In addition, the vertices on the edges that are adjacent to other blocks have to coincide with the vertices of those blocks so that they are stitched together and a single compatible mesh can be formed. This requires that both the offset normal and distance are identical for the adjacent blocks. Therefore, at the map level, the component thicknesses and offset normals are calculated in every corner, based on the values of the adjacent panels. These values are then used by the individual blocks. Examples of resulting meshes can be seen in Figure 4. Both first and second order meshing is available while both structured and transitional meshes can be created. Furthermore, both solid, shell and solid-shell elements can be created.

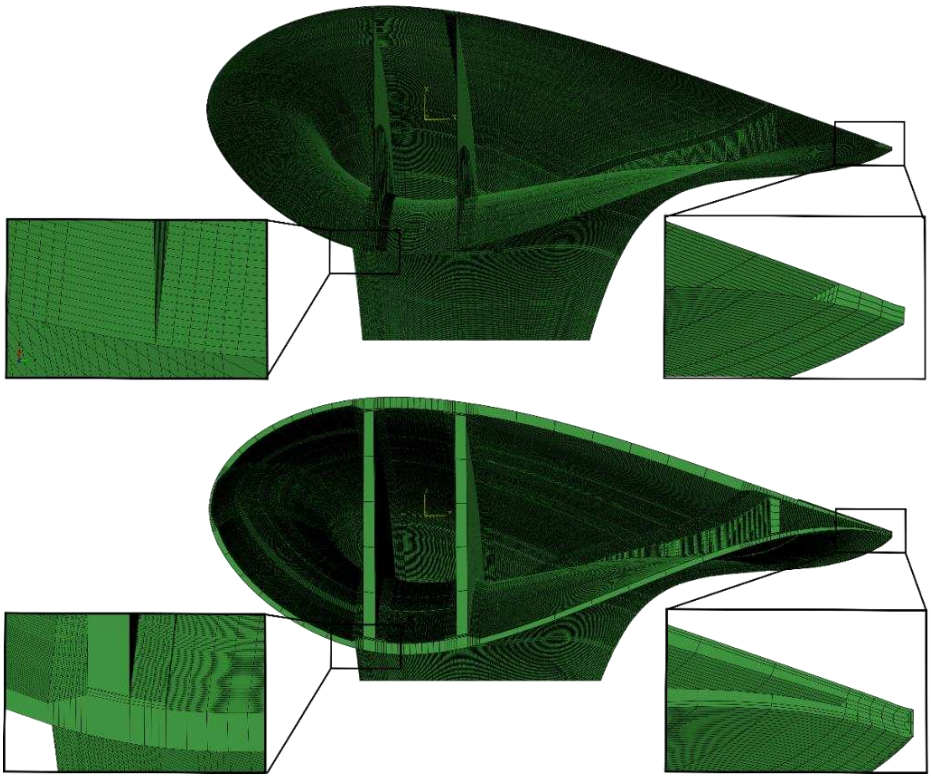

Figure 4: Meshes produced by the software along with details of the trailing edge joint and web-girder connections. (top) Shell output with solid elements to model the adhesive. (bottom) Second order solid output.

3.1 Application examples

At first, the shell and solid element modelling have been compared for a static certification test of a large wind turbine blade [2]. The shell and solid element models were first verified against the available experimental data for reaction forces and moments and global deflections. Next, detailed comparison was made on the available local strain gauge data from 60 different locations on the blade. The agreement was very good for both shell and solid models [2].

In a next application, the shell models were used in fully coupled fluid-structure interaction problems, where the shell finite element model was coupled with a CFD mesh of the air domain in the Fluent software. Those models were used to study the effect of the boundary layer of wind loads, the transient effects of wind gusts and the induced loading on the blade [3,4].

3.2 Case study of torsional stiffness

A particular case study is the prediction of torsional stiffness. There it is shown that the difference between the shell and solid element models is as large as 40%, where the solid model predicts a much higher torsional stiffness and is in line with experimental measurements of torsional stiffness. It is shown that the gap between shell and solid elements prediction can be substantially reduced by suppressing the spurious deformation modes of the shell elements, and having a more accurate cross-sectional representation of the blade lay-out [5].

4. Conclusion

The increasing dimensions of wind turbine blades, cascade effects in the costs of the turbine and current failure ratio's make the use of advanced FE modelling of the blades desirable. Current modelling efforts appear to be limited in detail and fidelity because of the difficulty to obtain them. The newly presented approach divides the modelling process in a number of steps and allows for a variety of models to be created.

The approach allows:

- Creation of the OML shape
- Accurate partitioning of the OML shape
- Creating models by combining pre-defined parametric blocks
- Assigning the layup and blocks at the map level, enabling:
    - Shell models (on the OML, at mid-thickness or on the inside surface)
    - Layered continuum (solid or solid-shell) models with adhesive bonds at the geometrically correct locations
- Simple global-local modelling approaches
- Calculating element-wise material orientations based on keylines

The approach is flexible since it allows different topologies to be modelled. Likewise, different outputs can be created by modifying only the user inputs in the last stage of the model creation process. In addition, the approach is highly extendible. Additional functionality can be created by simply adding a new type of block to the available collection. Furthermore, the tool gives possibilities to investigate the effect of manufacturing flaws. One approach to do this is using the sub-modelling method, for which the presented tool is well suited.

Acknowledgements

The work leading to this publication has been supported by VLAIO (Flemish government agency for Innovation and Entrepeneurship) under the SBO project "OptiWind: Serviceability optimisation of the next generation offshore wind turbines" (project no. 120029) and FWO project G031020N "Combined numerical and experimental approach for the development, testing and analysis of thick adhesive joints in large wind turbine blades".

5. References

[1] Peeters, M., Santo, G., Degroote, J. and Van Paepegem, W. (2018). High-fidelity finite element models of composite wind turbine blades with shell and solid elements. Composite Structures, 200, 521-531.

  doi:10.5075/epfl-298799_978-2-9701614-0-0

[2] Peeters, M., Santo, G., Degroote, J. and Van Paepegem, W. (2018). Comparison of shell and solid finite element models for the static certification tests of a 43m wind turbine blade. Energies, 11(6), Art. 1346.

[3] Santo, G., Peeters, M., Van Paepegem, W. and Degroote, J. (2019). Numerical Investigation of the Effect of Tower Dam and Rotor Misalignment on Performance and Loads of a Large Wind Turbine in the Atmospheric Boundary Layer. Energies, 12(7), Article number 1208.

[4] Santo, G., Peeters, M., Van Paepegem, W. and Degroote, J. (2019). Dynamic load and stress analysis of a large horizontal axis wind turbine using full scale fluid-structure interaction simulation. Renewable Energy, 140, 212-226.

[5] Tavares, R.P., Bouwman, V. and Van Paepegem, W. (2021). Finite element analysis of wind turbine blades subjected to torsional loads: Shell vs solid elements. Composite Structures, 280, article number 114905.

  doi:10.5075/epfl-298799_978-2-9701614-0-0

DYNAMIC MECHANICAL ANALYSIS OF EPOXY-MATRIX CROSS LINKING MEASURED IN-SITU USING AN ELASTOMER CONTAINER

Volker Trappe[a], Patrick Sachs[a]

a: Bundesanstalt für Materialforschung und -prüfung (BAM) – volker.trappe@bam.de

Abstract: *A new patented [1] dynamic mechanical analysis (DMA) is presented, where the tensile, bending- or torsional stiffness of a media can be characterized in-situ during the phase transition from liquid to solid. An epoxy system, e.g. Hexion L285/H287, is filled into an elastomer container, such as a silicone tube. This can be mounted into a conventional DMA and, based on a linear viscoelastic approach, the storage modulus (E';G'), the loss modulus (E'';G'') and the loss angle tan(δ) can be measured at constant temperature as a function of time in order to investigate the liquid to sol-gel to solid transition. With this new method, the stiffness increase as a result of the cure process can be directly measured more precisely thanwith a rheometer in a shear plate set-up, because using an elastomer container gives a defined cross section for calculating the Young's modulus.*

Keywords: dynamic mechanical analysis (DMA), thermoset polymers, cure process, cross linking

1. Introduction

Fiber reinforced plastics made with a thermoset molding technique are often used for high-performance applications including aircraft and wind turbine blades. To optimize the production process of these materials, the manufacturer must know the cure process for the cross-linking of the epoxy matrix system. A sufficient amount of stiffness of the composite structure has to be reached before the component can be removed from the mold and a subsequent post-cure outside of the mold can begin. The production rate of a component is ultimately dependent on the occupancy time in the mold.

Based on a linear viscoelastic approach [2,3], it is state of the art to measure the glass transition temperature (T_g) for polymer materials by measuring the storage modulus (E';G'), the loss modulus (E'';G'') and the loss angle tan(δ) as a function of temperature (typically in the range of -150°C to 250°C, depending on the kind of polymer). For cross-linking thermoset polymers it is common to measure T_g at more or less perfectly cured specimens starting in the solid (glassy) state and moving in the entropy elastic "rubber" state at higher temperatures.

In this study, a patented [1] dynamic mechanical analysis (DMA) is used, where the Young's and shear modulus of a medium can be characterized in-situ during the phase transition from liquid to solid. In a first feasibility experiment, water was filled into an elastomer container, such as a silicone tube. This can be mounted into a conventional DMA and, by cooling down the temperature chamber from room temperature (RT) to -20°C, the phase transition from liquid to solid (ice) and vice versa can be investigated. The wall thickness and diameter of the tube was dimensioned with respect to the capability of the DMA, and the empty tube should have a stiffness of less than 1% of the total specimen stiffness in the solid state. Additionally, the glass transition temperature T_g of the elastomeric tube should be far below the investigated temperature range. In

  doi:10.5075/epfl-298799_978-2-9701614-0-0

this study, the T_g of the silicon tube was about -50°C. Based on the common linear viscoelastic approach [2,3], the storage modulus (E';G'), the loss modulus (E'';G'') and the loss angle tan(δ) was measured at constant temperature as a function of time in order to investigate the liquid to sol-gel to solid transition of an epoxy resin.

2. Experimental

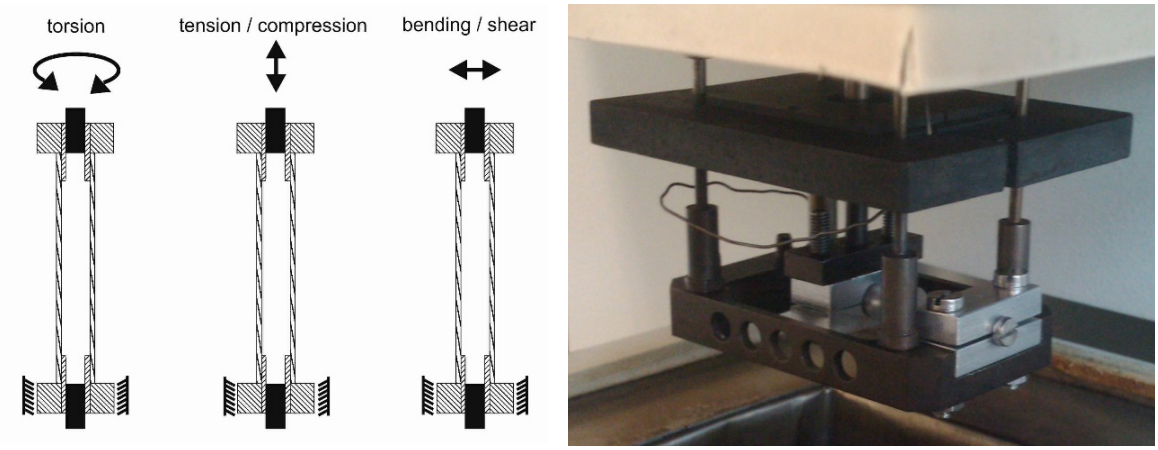

Figure 1. Left – measuring the cure conversion in a DMA in three possible set-ups according to [1]. Right – realized cantilever beam set-up in a Netzsch DMA 242D (bending / shear)

First a 3 mm inner diameter silicone tube, filled with the epoxy resin system Hexion L285/H287 was mounted in a Netzsch DMA type 242 D in a cantilever beam set-up (s. Figure 1). For a proof of concept, the modulus E' was measured at different constant temperatures. A torsional loaded tube with the same dimensions was mounted in a Myrenne DMA ATM3, and a second possible set up was checked successfully. Finally, the tension / compression loading set up should be checked. However, the capability of the Netzsch DMA was not high enough for cyclic loading of the cured epoxy resin. Hence, a polyvinylchloride (PVC) tube of 12 mm inner diameter was mounted in a 10 kN servo-hydraulic tensile testing machine with a temperature chamber. At different temperatures (RT, 40°C, 60°C, 80°C) every 15 minutes, the specimen was subjected to displacement-controlled cyclic loading with 0.01 Hz at a load ratio of R=-1, and hysteresis loops were measured. The dynamic stiffness was calculated according to [4,5]:

$$E_{dyn} = \frac{\sigma(\varepsilon_{max}) - \sigma(\varepsilon_{min})}{\varepsilon_{max} - \varepsilon_{min}} \quad (1)$$

and the dissipated energy according to:

$$W_{diss} = \oint \sigma d\varepsilon \quad (2)$$

was calculated by numerical integration of the hysteresis loops. This procedure enables a deeper understanding, where the phase transition of the Hexion LR285/LH287 epoxy resin system was investigated in the time domain (s. Figure 2) [4,5]. In displacement-controlled mode, hysteresis loops were measured every 15 minutes and the specimen stiffness was calculated from the force

  doi:10.5075/epfl-298799_978-2-9701614-0-0

at the minimum and maximum displacement values (corresponding to Eq. 1). Additionally, the energy dissipation was calculated by numerical integration of the hysteresis loops (corresponding to Eq. 2). Furthermore, the specimen was loaded with rectangular and triangular displacement functions to analyze the constitutive material law beside a linear viscoelastic approach in the different material states of the epoxy system [4,5]. The specimen was held in a temperature chamber to investigate the cross-linking at different temperature-time runs from room temperature up to 80°C, with the possibility of testing up to 150°C.

Figure 1 displays the cure conversion of LR285/LH287 by means of the specimen stiffness increase (kN/mm) corresponding to the storage modulus *E'* and the slope of the dissipated energy (kN*mm) corresponding to the loss modulus *E''* at room temperature [2]. Three hysteresis loops are exemplary displayed after 5 (a),16 (b) and 80 (c) hours cure time. By moving the average calculation, the first derivative of the stiffness-time slope was derived, and the inflection point occurred at the same time as the maximum of the energy dissipation curve at approximately 16 hours.

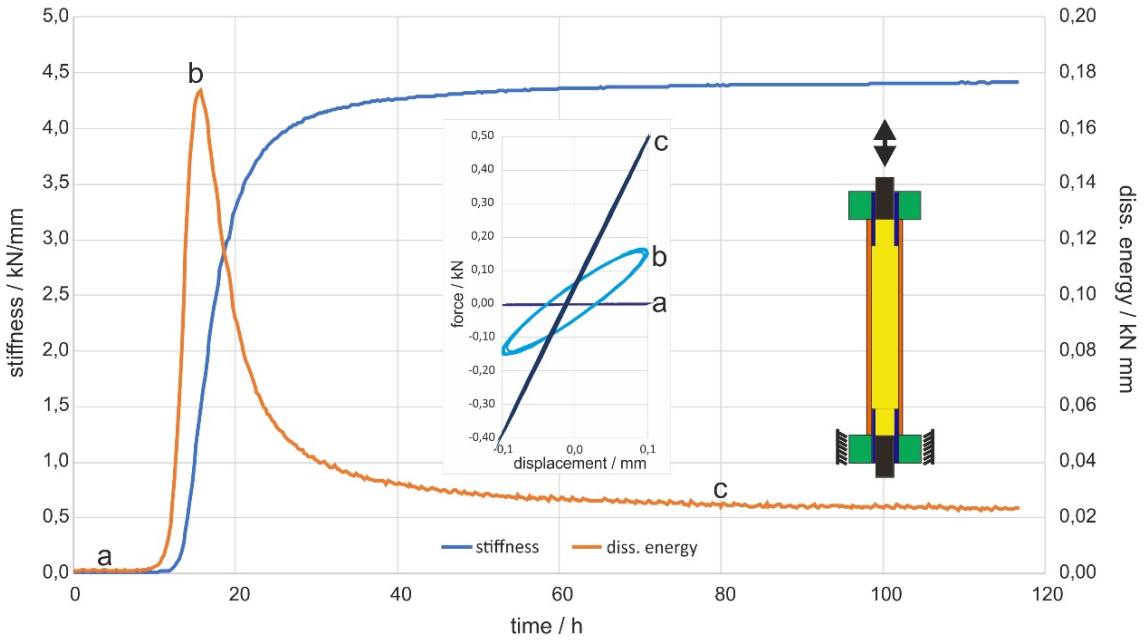

Figure 2: Liquid epoxy resin (LR285/LH287) was filled in an elastomer container, which was mounted into a servo-hydraulic tensile testing machine. Every 15 minutes, a force over displacement hysteresis loop was measured to monitor the cross-linking over time by calculating the dynamic stiffness and energy dissipation. Three hysteresis loops are exemplary displayed at 5 (a),16 (b) and 80 (c) hours cure time.

In the next step, the epoxy resin was cured in addition to RT at 40°C, 60°C and 80°C and the force and displacement were normalized to stress and strain. The results are depicted in Figure 3. By increasing the cure temperature, the crosslinking is accelerated by means of a faster increase of the Young's modulus over time. However, the asymptotic reached maximum values of stiffness decrease systematically with shortened cure time at higher cure temperatures. Finally, it is well known that the Young's modulus of a polymer decreases with temperature even in the glassy

state. Hence, the effective Young's modulus reached with different cure processes are comparative measured at room temperature after each in-situ cure experiment. The results are listed in Table 1. The effect of a lower Young's modulus at higher cure temperature and accelerated cross linking remained quantitatively the same, but the effective stiffnesses are significantly higher than monitored in the in-situ experiment.

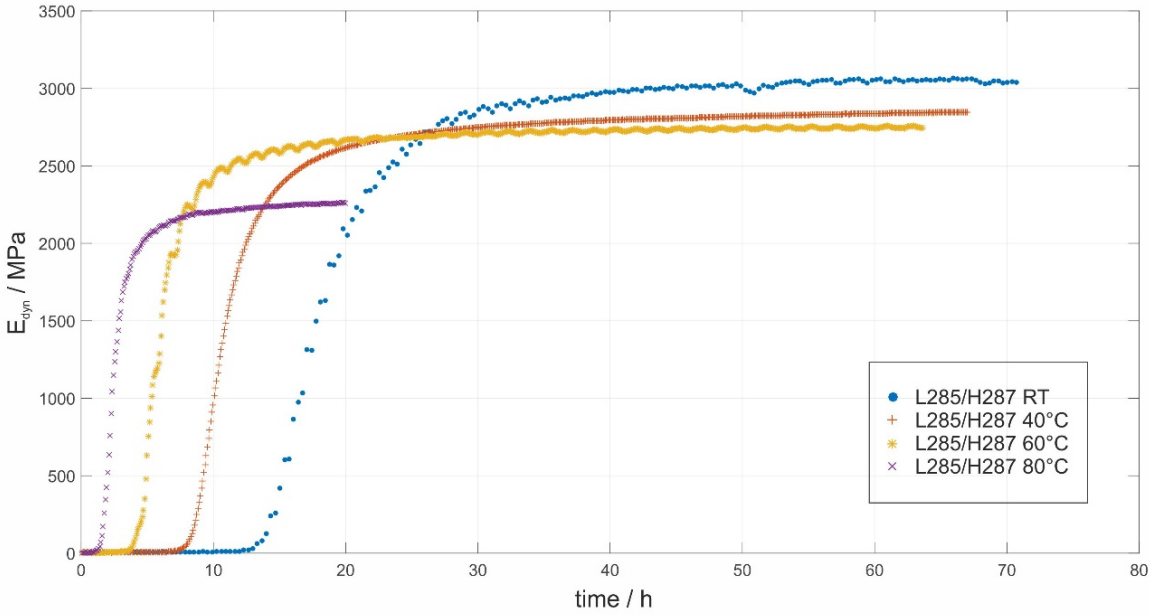

Figure 3: Increase of dynamic Young's Modulus over time at different cure temperatures for LR285/LH287 epoxy resin measured in-situ cure process

Table 1: Cure temperature and dynamic Young's Modulus, measured at RT.

Cure temp. [°C]	E_{dyn} at RT [MPa]
RT	3040
40	2990
60	2940
80	2700

Finally, the in-situ cure conversion monitoring using an elastomer container mounted in a DMA or tensile testing machine should be compared to the capability of a rheometer. Measurements with the same epoxy system were done with a Haake-Mars-III rheometer at room temperature with a plate-plate setup in rotating and cyclic loading. The results are comparatively depicted in Figure 4. Qualitatively, the in-situ measured shear *G*' - and loss modulus *G*'' correspond very well to the in-situ measured Young's modulus (in MPa) and energy dissipation (in J/m³) slop over the cure time. However, the capability of the rheometer is not high enough to measure into the fully crosslinked state. Additionally, the plate-plate setup is not capable of giving precise shear modulus values.

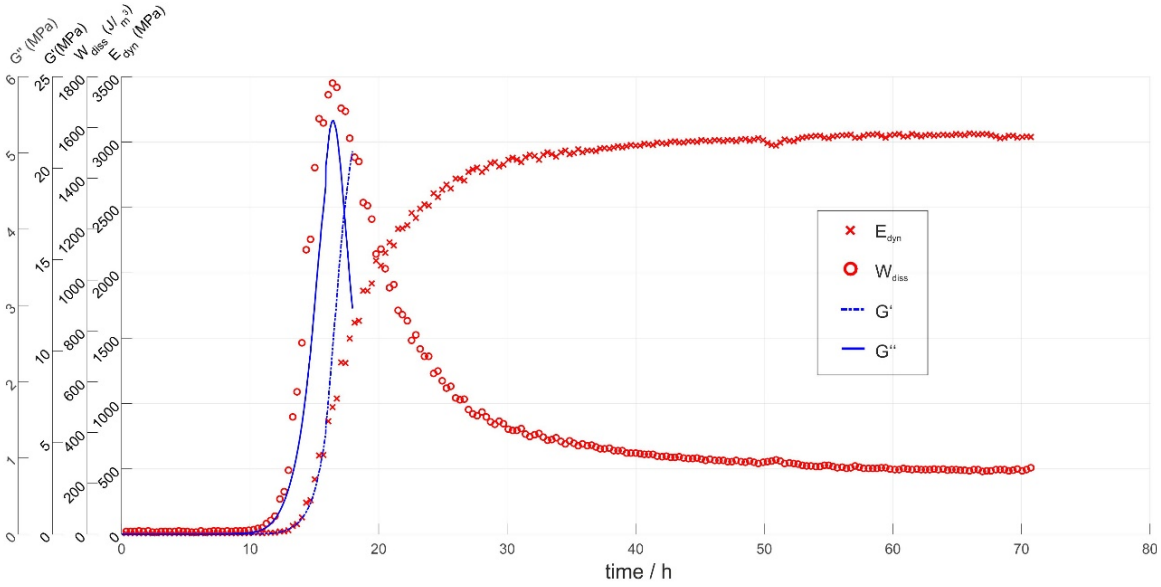

Figure 4: Cure conversion of LH285/LR287 at room temperature monitored comparatively with elastomer container technology and a Haake-Mars-III rheometer in a plate-plate setup.

3. Discussion / Conclusion

With the new described method of filling a epoxy system in a elastomer container and mounting into a DMA or tensile testing machine, the stiffness / Young's modulus increase as a result of the cure process can be directly measured. Using the temperature-time slope, as used in the component production process, a manufacturing optimization can be done. Using an elastomer container gives a defined cross section, and hence the Young's modulus can be calculated more precisely than e.g. with torsional braid analysis [6].

Compared to the viscosity measurement with a conventional rheometer, the resolution of the rheometer is much better at lower degrees of cure conversion in defining the effective pot life for the impregnation process. However, to monitor the Young's or shear modulus at higher degrees of cure conversion, the presented elastomer container technique is superior.

A decreasing Young's modulus at increased cure temperature and an accelerated cross linking was also reported by Ellis [7] and observed in [8]. A higher Young's modulus does not necessarily mean a higher degree of a cross linking density, and this has an impact on the fatigue or crack propagation rate in a cured epoxy polymer [8].

In future work, this method should be compared in greater depth to the outcomes of cure conversion in-situ monitoring using infrared spectroscopy [9] and ultrasound [10]. Preliminary results showed a good accordance with these techniques.

4. Acknowledgements

This investigation was supported by Hexion by providing epoxy resins and hardeners. The authors would also like to acknowledge Stefan Hickmann and Nicolai Schmidt for their support in specimen production, test setup and testing.

5. References

1. Patent DE102014108690A1; Sample holder for dynamic mechanical analysis (DMA) in the field of liquid-solid phase transition and its use for polymer materials, submitted 2014-06-20, granted / published 2017-08-03
2. Plastics - Determination of dynamic mechanical properties - Part 1: General principles (ISO 6721-1:2001)
3. Plastics – Determination of dynamic mechanical properties – Part 2: Torsion-pendulum method (ISO 6721-2:2008)
4. Trappe, V., Harbich, K-W. Intralaminar fatigue behaviour of carbon fibre reinforced plastics. International Journal of Fatigue 28(2006)1187-1196
5. Trappe V. Beschreibung des intralaminaren Ermüdungsverhaltens von CFK mit Hilfe innerer Zustandsvariablen. Reihe 5, Nr. 646, VDI-Verlag: Düsseldorf; 2002.
6. Gillham, J.K. Characterization of thermosetting materials by torsional braid analysis. Polymer Engineering and Science, 1976. **16**(5): p. 353-356.
7. Ellis, B. et al. *Chemistry and technology of epoxy resins*. Springer, 1993.
8. Trappe, V. Günzel, S., Jaunich, M. Correlation between crack propagation rate and cure process of epoxy resins. *Polymer Testing*, 31(5):654 – 659, 2012.
9. Erdmann, M., Trappe, V., Sturm, H., Braun, U., Duemichen, E.Cure conversion of structural epoxies by cure state analysis and in situ cure kinetics using nondestructive NIR spectroscopy. Thermochimica Acta 650 (2017) 8–17
10. Mc Hugh, J. Ultrasound Technique for the Dynamic Mechanical Analysis (DMA) of Polymers. Berlin 2008, BAM Dissertationsreihe (31), urn:nbn:de:kobv:b43-1278

STIFFNESS DEGRADATION OF GLASS-FIBER REINFORCED EPOXY COMPOSITES DUE TO MATRIX CRACKING UNDER QUASI-STATIC LOADING

Merle, Vespermann[a], Alexander, Krimmer[b], Alexandros, Antoniou[a]

a: Department of Rotor Blades, Fraunhofer Institute for Wind Energy Systems (IWES), Am Seedeich 45, 27572 Bremerhaven, Germany – alexandros.antoniou@iwes.fraunhofer.de.
b: TPI Composites Germany GmbH, Falkenberger Str. 146 A/B, 13088 Berlin, Germany.

Abstract: *A micromechanical, empirical quasi-static degradation model for glass-fiber reinforced epoxy laminates is presented, assuming that stiffness degradation begins with the first microcrack and is driven by the matrix damage behavior. A degradation factor is introduced, directly applying to the matrix' Young's modulus upon damage initiation. As input, the model requires fiber and matrix mechanical properties only. Based on micromechanical rules of mixture, ply stresses are transformed into stresses on the matrix level. The matrix stress exposure factor is calculated with a classical strain energy approach and is implemented in a damage onset criterion. Stiffness degradation curves are derived experimentally. As a result, two generic degradation functions for tensile/shear and for compressive loading as a function of the matrix stress exposure factor are proposed, that can be implemented in a layer-wise strength analysis.*

Keywords: degradation; micromechanics; microcracking

1. Introduction

In the calculation of fiber reinforced composites, usually all stresses and strains of a lamina are assumed to be related through linear equations. This applies to load cases in which the laminas' properties are fiber dominated. However, certain laminate structures show a distinct nonlinear stress-strain behavior, which can be observed especially under loading conditions leading to inter fiber failure (IFF), such as tension and compression transverse to the fibers, and transverse or longitudinal shear. Neglecting this behavior in the calculation can lead to an underestimation of strains at failure.

Looking at the different forms of failure modes in fiber reinforced composites, matrix microcracking and IFF often count as tolerable damages, since they do not necessarily lead to a complete failure of the laminate. Instead, the layer loses its load-carrying capacity in the surroundings of the crack, leading to a redistribution of stresses and eventually resulting in further cracks. If the load is further increased, number and length of cracks will grow further [1]. The formation of cracks may not result in a sudden failure, but primarily leads to a noticeable reduction of the stiffness properties [2].

The coherence between the stress-strain behavior and an increase in internal surfaces is shown by Basan in [3] by means of X ray refraction topography on carbon-fiber-reinforced polymers (CFRP) under quasi-static loading. The same observations are described in [4] for fatigue loading. Knops investigated a practically identical degradation behavior of CFRP and glass-fiber-reinforced polymers (GFRP) regarding the Young's modulus in [1], which enables the assumption, that these results are also applicable to GFRP.

  doi:10.5075/epfl-298799_978-2-9701614-0-0

To describe the correlation between damages and laminate's properties evolution, degradation models are used. Numerous methods can be found in the literature. They consist of a characterization of the damage state and a damage growth law [2]. Classical failure criteria, e.g. the widely used Tsai-Wu criterion [5] or the Puck's criteria for fiber and inter-fiber fracture [6], are used to evaluate stress vectors leading to fracture of a single ply or the whole laminate. Correlated to crack density or, in the case of the model proposed by Puck and Knops [1, 7, 8], the laminas' stress exposure factor, degradation is then modeled by phenomenologically reducing the ply's macroscopic properties. The so-called shear-lag analysis, first developed by Cox in 1952 [9], often finds application for the prediction of elastic properties, e.g. in the studies of Quaresimin and Carraro [10], Kashtalyan and Soutis [11] and Barbero and Cortes [12]. Also widely used is a finite element method calculation [13, 14] and the method of continuum damage mechanics [15, 16].

However, microcracking within the matrix, which develops long before the macroscopic IFF, and its role in the degradation process is often neglected. The model presented in this paper assumes that degradation is driven by the matrix damage behavior, and that both microcracking within the matrix and macroscopic IFF equally lead to a loss of stiffness. The process of damage is divided into three stages:

- Stage 1 - Loading of the undamaged lamina: There are no damages in the material caused by mechanical loading and therefore no increase in crack density.
- Stage 2: Loading of the damaged lamina: Damage initiation is the occurrence of a first microcrack within the matrix and the beginning of this phase. The crack density increases until it reaches a maximum (saturation).
- Stage 3: After saturation of matrix cracking, fibers may remain intact and be able to carry a certain amount of load. This stage ends with the complete failure of a lamina, meaning the loss of load carrying capacity.

2. Material Modeling

The presented model describes degradation on a micromechanical level, differentiating between the constituents, fiber and matrix. Since degradation is apparently driven by the matrix damage behavior, the occurrence of the first microcrack in the matrix is equated to the beginning of degradation. A degradation factor is introduced, directly applying to the matrix' Young's modulus upon damage initiation. With an increasing stress level in the matrix, the crack density and therefore the stiffness degradation grows as well. A common linear material model adapted to experimental stress-strain-data. Residual stresses, developed in the manufacturing process, can anticipate this phenomenon but are neglected within this paper. A plain stress state is considered.

  doi:10.5075/epfl-298799_978-2-9701614-0-0

2.1 Linear Material Model

For a linear material model, stresses $\{\sigma\}$ and strains $\{\varepsilon\}$ are assumed to be related by the well-known Hooke's law [17], which is defined for a two-dimensional stress-state as follows:

$$\begin{Bmatrix}\sigma_1\\ \sigma_2\\ \tau_{21}\end{Bmatrix} = [Q]\begin{Bmatrix}\varepsilon_1\\ \varepsilon_2\\ \gamma_{21}\end{Bmatrix} \tag{1}$$

Herein $[Q]$ is the stiffness matrix of the lamina, whose entries are defined by the materials' elastic properties. Within this paper, elastic properties of the lamina are calculated using micromechanical rules of mixture as introduced by Krimmer [18], taking account of the in-situ properties of the matrix. As input, fiber and matrix properties are required. The implemented Young's modulus E, the Poisson's ratio ν, the strength R and the undulation factor f_u are listed in Table 1. These values have been determined with an inverse calculation [18] based on material testing. Further input parameters are the fiber volume fraction φ and the configuration of fibers, for which a regular hexagonal array is assumed.

Table 1: Fiber and matrix properties defined as input for the model

	E in MPa	ν in -	R in MPa	f_u in -
Glass Fiber	81500.0	0.221	2290.0	0.95
Epoxy Resin	3090.0	0.368	73.5	-

2.2 Degradation Model

The linear assumption applies as long as the loading is in Stage 1 and no damage has been initiated in the material. To characterize the current state of stresses in the matrix and therefore the current stage of damage according to the classification above, the matrix' stress exposure factor is used. The micromechanical model by Krimmer [18] enables a distinction between stresses in the lamina and those in the constituents. According to that, ply stresses σ_i and τ_{ij} are transformed into stresses on matrix level $\sigma_{\mathrm{M}i}$ and $\tau_{\mathrm{M}ij}$ as shown in Eq. (2)-(4), in which r_{F} is the fiber radius in a hexagonal array configuration.

$$\sigma_{\mathrm{M1}} = \sigma_1 \frac{E'_{\mathrm{M}\parallel}}{E'_{\parallel}} \tag{2}$$

$$\sigma_{\mathrm{M2}} = \frac{\sigma_2}{E'_{\perp}\left(\frac{r_F}{E_{F\perp}} + \frac{1-r_F}{E'_{M\perp}}\right)} \tag{3}$$

$$\tau_{\mathrm{M21}} = \frac{\tau_{21}}{G'_{\perp\parallel}\left(\frac{r_F}{G_{F\perp\parallel}} + \frac{1-r_F}{G'_{M\perp\parallel}}\right)} \tag{4}$$

  doi:10.5075/epfl-298799_978-2-9701614-0-0

Using a classical strain-energy approach proposed by Beltrami [19], suitably for compressible, isotropic materials, the equivalent tensile stress σ_{MB} in the matrix is calculated through:

$$\sigma_{\mathrm{MB}} = [\sigma_{\mathrm{M1}}^2 + \sigma_{\mathrm{M2}}^2 + \sigma_{\mathrm{M3}}^2 - 2\nu(\sigma_{\mathrm{M1}}\sigma_{\mathrm{M2}} + \sigma_{\mathrm{M2}}\sigma_{\mathrm{M3}} + \sigma_{\mathrm{M3}}\sigma_{\mathrm{M1}} + 2(1+\nu)(\tau_{\mathrm{M31}}^2 + \tau_{\mathrm{M23}}^2 + \tau_{\mathrm{M21}}^2)]^{\frac{1}{2}} \tag{5}$$

A damage initiation criterion is required to define the beginning of non-linear material behavior. The stress exposure factor defines the actual stress state in relation to the stresses leading to failure [1]. In this case, failure means cracking within the matrix, therefore the maximum allowable stress is assumed to be the matrix tensile strength $R_{\mathrm{M}}^{(+)}$. Thus, the matrix stress exposure factor e_{M} is calculated through:

$$e_{\mathrm{M}} = \frac{\sigma_{\mathrm{MB}}}{R_{\mathrm{M}}^{(+)}} \tag{6}$$

Values of $e_{\mathrm{M}} \geq 1$ indicate that the given stress state exceeds the allowable stresses and leads to failure. Therefore, the damage initiation criterion for the matrix is described by:

$$\frac{\sigma_{\mathrm{MB}}}{R_{\mathrm{M}}^{(+)}} = 1 \tag{7}$$

From this point on, the Young's modulus of the matrix E_{M} is reduced by the matrix degradation factor η_{M} (Eq. 8), which represents the amount of stiffness loss at a certain stress state. η_{M} is a function of the matrix stress exposure factor.

$$E_{\mathrm{M}}^{*} = E_{\mathrm{M}} \cdot \eta_{\mathrm{M}}(e_{\mathrm{M}}) \tag{8}$$

The reduction of the matrix Young's modulus by η_{M} requires a recalculation of the lamina's stiffness properties, which results in a new stiffness matrix $[Q]$ and therefore a new relation between stresses and strains described by Hooke's law. To describe the dependency $\eta_{\mathrm{M}}(e_{\mathrm{M}})$, stiffness degradation curves are derived based on experimental stress-strain data. Figure 1 displays experimental stress-strain data for a biaxially orientated laminate loaded under tension, and both calculations of the linear model and the degradation fitting. The degradation factor is shown as a function of the strain value ε_x in Figure 1. The calculations are carried out for biaxially orientated +45° laminates under tensile loading in 0° direction and for unidirectional laminates under compressive loading in 90° direction.

  doi:10.5075/epfl-298799_978-2-9701614-0-0

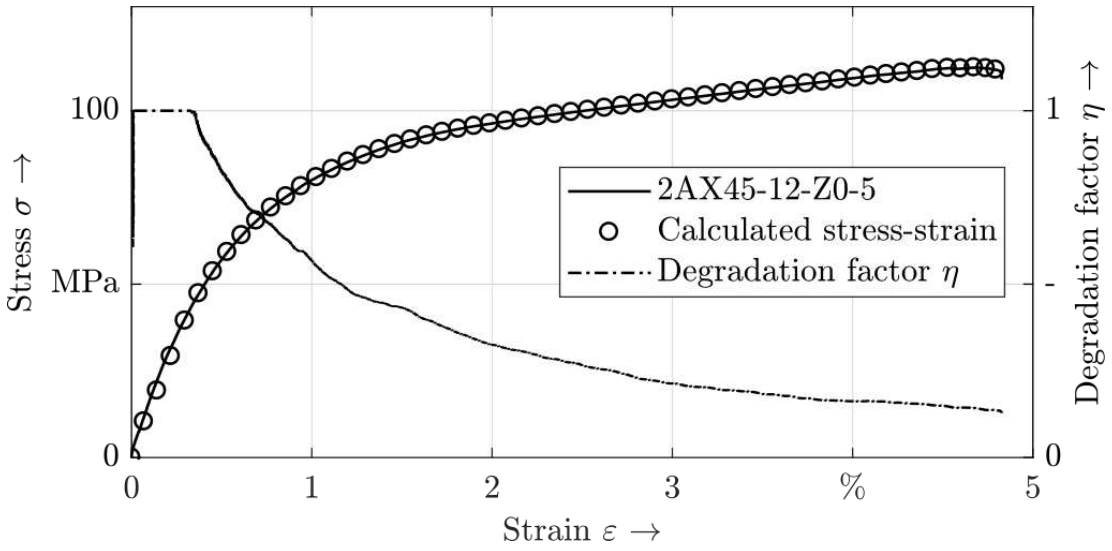

Figure 1. Experimental stress-strain data for tensile loading (2AX45-12-Z0-5), degradation model fitting and the degradation factor as a function of strain

For further considerations the degradation factor is related to the matrix stress exposure factor for each loading step. The results are fitted with mathematical functions.

3. Results

3.1 Degradation functions

The resulting degradation curves for tensile and compressive loading as a function of the matrix stress exposure factor are shown in Figure 2. In both cases the degradation factor remains constant at $\eta_{\mathrm{M}} = 1$, meaning no degradation, until the point of onset of damage at $e_{\mathrm{M}} = 1$. After damage onset, degradation behavior depends on the loading case due to different processes within the material.

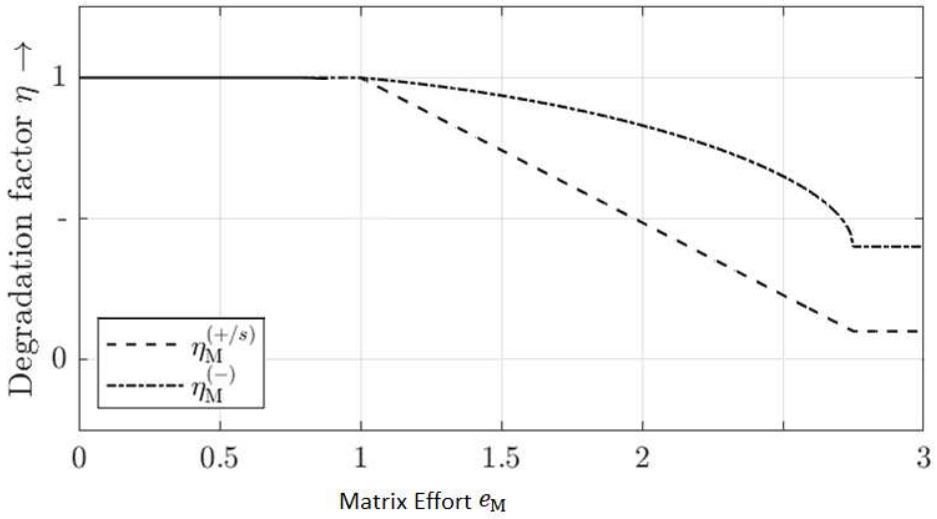

Figure 2. Degradation curves for tensile and compressive loading as a function of the matrix stress exposure factor

  doi:10.5075/epfl-298799_978-2-9701614-0-0

Loaded under tension, crack surfaces open and therefore do not transfer any load. η_{M} is linearly decreasing until it reaches a minimum, which indicates a crack saturation. The matrix effort e_{S} and the degradation factor η_{S} at saturation depend on the material. In this case, the values $e_{\mathrm{S}} = 2.75$ and $\eta_{\mathrm{S}} = 0.1$ have been derived.

Eq. (9) describes the generic degradation function for tensile and shear loading $\eta_{\mathrm{M}}^{(+)}$, taking into consideration the case distinction for the different stages of damage:

$$\eta_{\mathrm{M}}^{(+)} = \begin{cases} 1 & for \quad e_{\mathrm{M}} \leq 1 \\ 1 + \dfrac{\eta_{\mathrm{S}} - 1}{e_{\mathrm{S}} - 1}(e_{\mathrm{M}} - 1) & for \quad 1 < e_{\mathrm{M}} \leq e_{\mathrm{S}} \\ \eta_{\mathrm{S}} & for \quad e_{\mathrm{M}} > e_{\mathrm{S}} \end{cases} \tag{9}$$

Loaded under compression, the curve can be fitted using a segment of an ellipse superimposed on a straight line with slope m_η. The resulting function for the degradation factor under compressive loading $\eta_{\mathrm{M}}^{(-)}$ is shown in Eq. (10). The material dependent values are $m_\eta = -0.09$, $e_{\mathrm{S}} = 2.75$ and $\eta_{\mathrm{S}} = 0.4$.

$$\eta_{\mathrm{M}}^{(-)} = \begin{cases} 1 & for \quad e_{\mathrm{M}} \leq 1 \\ \sqrt{\left[1 - \left(\dfrac{e_{\mathrm{M}} - 1}{e_{\mathrm{S}} - 1}\right)^2\right]\left[1 - \eta_{\mathrm{S}} + m_\eta(e_{\mathrm{S}} - 1)\right]^2 + \eta_{\mathrm{S}} - m_\eta(e_S - e_M)} & for \quad 1 < e_{\mathrm{M}} \leq e_{\mathrm{S}} \\ \eta_{\mathrm{S}} & for \quad e_{\mathrm{M}} > e_{\mathrm{S}} \end{cases} \tag{10}$$

3.2 Discussion

It has been found that the success of the model is dependent on the combination of failure criterion and degradation laws. Assuming that the degradation of the macroscopic elastic properties is driven by the matrix damage behavior, damage initiation and therefore the beginning of degradation is defined as the first crack in the matrix. In contrast to common failure criteria, the presented approach does not distinguish between microscopic and macroscopic cracks. Consequently, damage initiation in the matrix is determined to occur at a much earlier stress state, which represents experimental observations.

Onset and propagation of matrix cracks are described as a function of the matrix stress exposure factor. Therefore, the model is not dependent on the crack density. As a result, the study presents one generic degradation function each for tensile/shear and compressive loading. Using a combination of these functions, each loading condition can be described. They can be implemented in a layer wise strength analysis. Furthermore, using a damage accumulation theory, it can be extended to an assessment of the fatigue effort of the laminae.

4. Summary

The present work studies the stiffness loss of glass-fiber reinforced composites due to failure within the matrix caused by mechanical loading. An analytical material model is described, based on a differentiation between the constituents, fiber and matrix, on a micromechanical level. A degradation factor η_{M} for the matrix as a function of the matrix stress exposure factor e_{M} is introduced. Damage initiation is described as the first microcrack in the matrix and thus

  doi:10.5075/epfl-298799_978-2-9701614-0-0

represents the beginning of degradation. It is calculated using the damage onset failure criterion by Krimmer based on a classical strain-energy approach by Beltrami. As a result, the study presents one degradation function each for tensile and compressive loading. The macroscopic behavior predicted by the degradation of the matrix is found to be in very good agreement with experimental data.

5. References

1. Knops M. Analysis of Failure in Fiber Polymer Laminates, The Theory of Alfred Puck. Springer Verlag. 2008.
2. Gross D, Seelig T. Bruchmechanik. Springer Verlag. 2016.
3. Basan R. Untersuchung der intralaminaren Schubeigenschaften von Faserverbundwerkstoffen mit Epoxidharzmatrix unter Berücksichtigung nichtlinearer Effekte. Technische Universität Berlin. 2011.
4. Trappe V. Beschreibung des intralaminaren Ermüdungsverhaltens von CFK mit Hilfe innerer Zustandsvariablen. Technische Universität Carolo-Wilhelmina zu Braunschweig. 2002.
5. Tsai SW, Wu EM. A general theory of strength for anisotropic materials. Journal of Composite Materials 1971; 5:58-80.
6. Puck A. Festigkeitsanalyse von Faser-Matrix-Laminaten, Modelle für die Praxis. Carl Hanser Verlag. 1996.
7. Puck A. Guidelines for the determination of the parameters in Puck's action plane strength criterion. Composites Science and Technology 2002; 62:371-78.
8. Knops M. Sukzessives Bruchgeschehen in Faserverbundlaminaten. Mainz Verlag. 2003.
9. Cox HL. The Elasticity and Strength of Paper and other Fibrous Materials. British Journal of Applied Physics 1952; 72:72-79.
10. Quaresimin M, Carraro PA. A stiffness degradation model for cracked multidirectional laminates with cracks in multiple layers. International Journal of Solids and Structures 2015; 58:34-51.
11. Kashtalyan M, Soutis C. Stiffness degradation in cross-ply laminates damaged by transverse cracking and splitting. Composites Part A: Applied Science and Manufacturing 2000; 31:335-51.
12. Barbero EJ, Cortes DH. A mechanistic model for transverse damage initiation, evolution and stiffness reduction in laminated composites. Composites Part B: Engineering 2010; 41:124-32.
13. Li S, Singh CV, Talreja R. A representative volume element based on translational symmetries for FE analysis of cracked laminates with two arrays of cracks. International Journal of Solids and Structures 2009; 46:1793-1804.
14. Taubert R. Einfluss von nichtlinearem Materialverhalten auf die Entwicklung und Auswirkung von Zwischenfaserbrüchen in Verbundlaminaten. Technische Universität München. 2017.
15. Talreja R. A continuum mechanics characterization of damage in composite materials. Proceedings of the Royal Society A: Mathematical, Physical 1985; 399:195-216.
16. Li S, Reid R, Soden PD. A continuum damage model for transverse matrix cracking in laminated fibre-reinforced composites. Philosophical Transactions of the Royal Society A 1998; 356:2379-412.
17. Schürmann H. Konstruieren mit Faser-Kunststoff-Verbunden. Springer Verlag. 2007.

  doi:10.5075/epfl-298799_978-2-9701614-0-0

18. Krimmer A. Mikromechanische Modellierung von Fasergelege-Kunststoff-Verbunden auf Basis von Normprüfungen unter Berücksichtigung der in-situ Eigenschaften der Matrix. Technische Universität Berlin. 2014.
19. Beltrami E. Sulle condizioni di resistenza dei corpi elastivi. Nuovo Cim 1885; 12:145–55.

  doi:10.5075/epfl-298799_978-2-9701614-0-0

FULLY-REVERSED FATIGUE BEHAVIOR OF SCARF JOINT REPAIRS FOR WIND TURBINE BLADE SHELL APPLICATIONS

Carineh Ghafafian[a], Volker Trappe[a]

a: Bundesanstalt für Materialforschung und -prüfung (BAM) – carineh.ghafafan@bam.de

Abstract: *To enable a quick and cost-effective return to service for wind turbine blades, localized repairs can be executed by technicians in the field. Scarf repairs, shown to be highly efficient with a smooth load transition across angled joint walls and a restored aerodynamic profile, are the focus of this work. The failure mechanisms of these structures were examined under quasi-static tensile and fully-reversed cyclic loading. While the scarf ratio was held constant at 1:50, the repair layup was varied between large-to-small and small-to-large. The effect of the presence of resin pockets and the fiber orientation mismatch between parent and repair material on the restored strength of BIAX ±45° glass fiber reinforced polymer scarf joint structures was studied.*

Keywords: glass fiber reinforced polymers; scarf repairs; fatigue

1. Introduction

Composite repairs are commonly done as adhesively bonded joints because of the efficiency in comparison to mechanical joints in terms of a large area over which load is distributed. These structures are especially advantageous as joints in fiber reinforced polymers (FRP), since they avoid drilling holes for fasteners or bolts, which could disrupt load-carrying fibers and create stress concentrations [1]. As the focus of this work, scarf repairs have been shown to be the most efficient in terms of property restoration for composites, and are well-suited for smooth aerodynamic surface repair applications. Angled parent walls are removed, upon which repair layers are attached to create a bond in a thin layer over a large joint area, allowing for more uniform stress distribution of the applied loads for an overall efficient repair [3-6].

70-80% of defects in wind turbine blade shells are known from industry experience to be a result of manufacturing imperfections. These lead to maintenance requirements significantly before the 20-year design life [7, 8]. The high loss of earnings due to turbine standstill during blade replacement and repairs fuels the need for effective repair methods for a quick return to service.

The mechanical property restoration of scarf joints has been studied in the context of FRP, including the effect of the scarf ratio and external reinforcement plies [9-13]. A 1:50 scarf ratio has been shown in literature as well as practice to be a good compromise between restored mechanical properties and the size of the repair area [2]. Most work to-date has focused on the quasi-static or cyclic tensile loading effects of the scarf joint structure. Less studied are the fully-reversed cyclic fatigue behavior of the scarf joint structure for FRP. There is also a need for a systematic comparison of a large-to-small versus small-to-large layup. This work therefore aims to characterize the fully-reversed cyclic fatigue behavior of a 1:50 scarf joint structure depending on repair layup using representative glass FRP (GFRP) structures for wind turbine blade shell repair applications.

  doi:10.5075/epfl-298799_978-2-9701614-0-0

Methodology

2.1 Specimen Production

To examine the effect of the layup on the mechanical behavior of scarf joint structures, monolithic GFRP specimens were used in this study to isolate the joint interface region of interest. Representative of a portion of a scarf repair in the outer face sheet of a rotor blade shell, the specimens were produced using E-glass non-crimp fabric (NCF). Using the vacuum-assisted resin infusion (VARI) process with the RIMR135/RIMH137 and LR285/LH287 epoxy resin systems for the parent and repair sides, respectively, specimens were produced following the methodology described in [13]. A wet-to-hard layup was used to create the bi-material joint specimens, representative of wind turbine blade shell repairs in terms of materials and methods. Two repair layups were the focus of this work: large-to-small (LS) and small-to-large (SL). A detailed description of these two layups is given in [13].

Four groups of BIAX ±45° specimens were tested under quasi-static tensile load, as well as fully-reversed cyclic fatigue load under a range of load levels corresponding to the strains endured in-service by the blade shell: $\varepsilon_{\mathrm{x},0} = 0.2\%$ under rated wind and $\varepsilon_{\mathrm{x},0} = 0.5\%$ under 50-year gust loads [14]. Table 1 summarizes the specimen groups, including the terminology for group names used throughout this work, as well as the materials, repair layup, and fatigue load levels tested. The average fiber volume content of the parent material of the specimens was $V_{\mathrm{f}} = 0.46$, while the repair material side was $V_{\mathrm{f}} = 0.45$, determined according to Test Method I of ASTM D 3171-99:2000, Procedure G.

Table 1: Group parameters of tested GFRP coupon specimens.

Group name	Material	Sequence	Repair layup	Load levels tested
Parent reference	778 g/m^2 BIAX E-glass	$[\pm45°]_{4S}$	--	$\varepsilon_{x,0}$=0.2-0.4%
Repair reference	444 g/m^2 BIAX E-glass	$[\pm45°]_{4S}$	--	$\varepsilon_{x,0}$=0.3-0.5%
LS joint	778 g/m^2 BIAX E-glass + 444 g/m^2 BIAX E-glass	$[\pm45°]_{4S}$ + $[\pm45°]_{8S}$	Large-to-small	$\varepsilon_{x,0}$=0.25-0.4%
SL joint	778 g/m^2 BIAX E-glass + 444 g/m^2 BIAX E-glass	$[\pm45°]_{4S}$ + $[\pm45°]_{8S}$	Small-to-large	$\varepsilon_{x,0}$=0.25-0.4%

2.2 Test Parameters

The specimens were subjected to quasi-static tensile load according to DIN 527-1:2012-06 at a crosshead displacement speed of 2 mm/min, as well as fully-reversed (with load ratio $R = \frac{\sigma_{min}}{\sigma_{max}} = -1$) mechanical cyclic load on a 63 kN capacity Schenk PSB servo-hydraulic testing machine with hydraulic grips. Specimens were supported with an anti-buckling support to discourage unwanted displacement in the specimen thickness direction during the compressive component of the cyclic loading. All testing was done at room temperature. The number of cycles to failure was used as a metric to study the effect of the scarf joint layup on the cyclic

  doi:10.5075/epfl-298799_978-2-9701614-0-0

fatigue behavior of the structure, and testing frequency was varied across load levels to account for constant energy dissipation [15, 16]:

$$f = f_{ref}\left(\frac{\varepsilon_{ref}}{\varepsilon}\right)^2 \quad (1)$$

2. Results and Discussion

3.1 Quasi-static Tensile Loading

All groups of specimens were first subjected to quasi-static tensile load to understand the effect of the scarf joint layup on the restored tensile strength of the structure. The average ultimate tensile strength σ_{UTS} of all reference and joint specimens were compared and summarized in Table 2. Here, the restored values were calculated as a comparison of the average σ_{UTS} ultimate tensile strength of the joint group divided by the reference parent group:

$$\sigma_{\mathrm{UTS,restored}} = \frac{\sigma_{\mathrm{UTS,joint}}}{\sigma_{\mathrm{UTS,refence}}} \quad (2)$$

There was an overall high ultimate tensile strength σ_{UTS} restoration of the joint specimens, reaching a minimum of 80% for both layups, consistent with findings in literature for scarf joint structures [6, 17, 18]. In these specimens, the flat angle of the 1:50 scarf ratio connecting the two materials led to a high-quality joint. Both the reference and joint specimens failed due to intralaminar crack propagation through the specimen thickness. There was no significant change in failure mechanism caused by the presence of the LS joint, as discussed in [13], and the effect of the SL joint on the local failure mechanism was not detrimental to the restored strength due to the lack of change in global failure mechanism.

Prior to ultimate failure, the LS joint specimens underwent a period of localized necking in the specimen center before fracture, which had also been observed in ±45° FRP specimens without scarf joints subjected to tensile load. This was likely due to the concentration of IFF already having occurred in this region, making the material less stiff and thereby undergoing more local deformation.

Under quasi-static tensile load, the role of the SL joint on the restored ultimate tensile strength σ_{UTS} of the structure was relatively insignificant. Existing resin pockets in the joint interface served as localized damage initiation sites, which coalesced and led to ultimate failure with an intralaminar failure path. In comparison to the LS joint specimens, however, the fracture surface of the SL joint was larger due to the less localized behavior prior to fracture. The localized yielding of the resin pockets in the SL joint layup had a beneficial effect of breaking the fracture path, seen in Figure 1 with the relatively larger fracture surface in comparison to the LS joint specimen and in Table 2 with the higher restored σ_{UTS}.

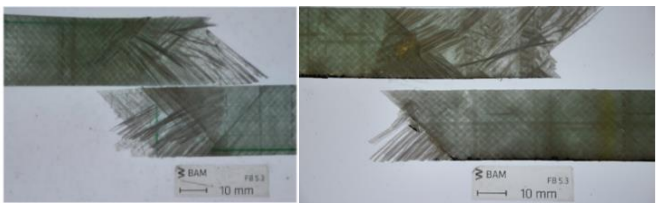

(a) LS joint (b) SL joint

Figure 1. Fractured surfaces of scarf joint specimens under quasi-static tensile load.

  doi:10.5075/epfl-298799_978-2-9701614-0-0

Table 2: Comparison of restored ultimate tensile strength σ_{UTS} between reference and joint specimens.

Group name	$\sigma_{\mathrm{UTS}} \pm S_{\mathrm{UTS}}$ / MPa	Restored σ_{UTS}
Parent reference	125 ±12	--
Repair reference	145 ±12	--
LS joint	100 ±25	0.80
SL joint	136 ±6	1.09

3.2 Cyclic Fatigue Loading

Upon understanding the quasi-static tensile behavior of the two scarf joint layups in comparison to the reference structure, all specimen groups were then subjected to fully-reversed cyclic fatigue loading. Fatigue behavior was summarized by plotting the number of cycles to failure N_{B} versus stress amplitude σ_{a} according to load level following DIN 50100:2016-12 and DIN SPEC 16457:2019-12, fit with the pearl string method as a power law fit derived from the Basquin equation [19]:

$$logN = a + b \cdot \log[\sigma_{\mathrm{a}}(N)] \tag{3}$$

The resulting S-N curve is shown in Figure 2. Fracture was taken as the failure criteria, and run-outs are marked with an outline and arrow. Both joint specimen groups failed in the parent region, speaking with adherend failure for the effectiveness of a 1:50 scarf joint.

Table 3 shows the average cycles to failure $N_{50\%}$of all test groups tested at a load level corresponding to $\varepsilon_{\mathrm{x},0} = 0.4\%$. This load level was chosen for comparison because all specimen groups were tested to failure, with no run-outs. The $N_{50\%}$ value of each joint group was compared to the parent reference group. For this, the restored fatigue strength was defined as:

$$N_{50\%,\mathrm{restored}} = \frac{N_{50\%,\mathrm{joint}}}{N_{50\%,\mathrm{parent}}} \tag{4}$$

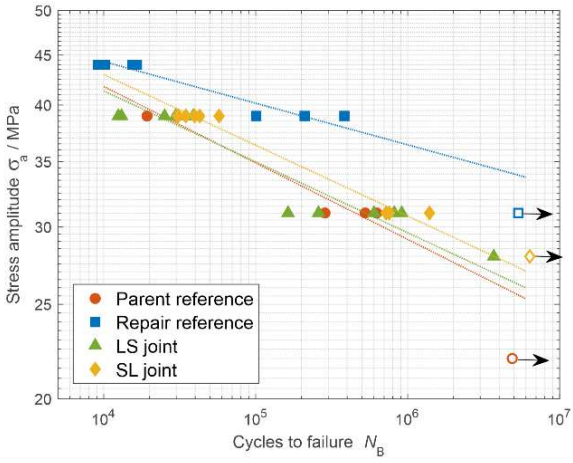

Figure 2. Fatigue behavior of all test groups, shown with a power law fit. Run-outs are marked with an outline and arrow.

The LS joint specimens consistently had a very similar cyclic fatigue strength to the parent reference groups across all tested load levels, as seen for the exemplary $\varepsilon_{x,0} = 0.4\%$ load level in Table 3. The effectiveness of the 1:50 scarf joint ratio allowed for a smooth load transfer between parent and repair adherends. The LS joint applied to a BIAX ±45° laminate, where fiber orientation mismatch insignificant in comparison to the applied load direction [13], was successful enough to not decrease the number of cycles to failure in the structure despite the disruption in continuous fiber reinforcement.

The SL joint specimens consistently had the highest restored fatigue strength across all load levels. As in the LS joint specimens, failure occurred in the parent adherend, speaking for the effectiveness of the scarf joint due to a good load transfer through shear stresses parallel to the scarf and thereby almost parallel to the load direction in the case of a flat angle. The resin pockets which result from the end of the repair layers in the joint interface seemed to act as a disruption to the damage propagation directly along the joint.

Table 3: Average cycles to failure $N_{50\%}$ of all joint specimens compared to reference specimens, tested at a load level corresponding to $\varepsilon_{x,0} = 0.4\%$.

Group name	$N_{50\%}$	$N_{50\%,\mathrm{restored}}$
Parent reference	24167	--
Repair reference	200830	--
LS joint	23396	0.97
SL joint	38361	1.59

4. Conclusions

The failure of large-to-small and small-to-large scarf joint layups was examined under fully-reversed $R = -1$ cyclic load with GFRP coupon specimens. With a constant 1:50 scarf ratio, focus was directed to the influence of the joint interface variables and adherends on the cyclic fatigue behavior of the structure.

The effectiveness of the 1:50 scarf ratio and the low fiber orientation mismatch in a BIAX ±45° structure led to a successful load transfer across the joint in a large-to-small layup, and therefore a restored average cycles to failure $N_{50\%}$ similar to the reference parent structure. The resin pockets in the small-to-large layup did not play a detrimental role to the quasi-static and cyclic fatigue behavior of the scarf joint structure. By disrupting the damage propagation path combined with the fatigue-superior repair material, the SL joint structure had the highest restored average cycles to failure $N_{50\%}$.

Acknowledgements

This research was supported by funding from the Technical University of Berlin Manfred Fricke Foundation. The materials used for the experiments were made possible through the support of Saertex for the glass non-crimp fabrics and Hexion for the epoxy resins and hardeners. The

  doi:10.5075/epfl-298799_978-2-9701614-0-0

authors would also like to acknowledge Stefan Hickmann, Nicolai Schmidt, and Julian Marzik for their support in specimen production and test setup.

5. References

1. Cardrick A and Smith M. An approach to the development of meaningful design rules for fatigue-loaded CFRP components, Composites 1974; 96-100.

2. Lekou D and van Wingerde A. Evaluation of Repair Techniques as Used for Small Specimens. Optimat Blades Technical Report 2006.

3. Oztelcan C, Ochoa O, Martin J, Sem K. Design and analysis of test coupons for composite blade repairs, Composite Structures 1997; 37:185-193.

4. Caminero M, Pavlopoulou S, Lopez-Pedrosa M, Nicolaisson B, Pinna C, Soutis C. Analysis of adhesively bonded repairs in composites: Damage detection and prognosis, Composite Structures 2013; 95:500-517.

5. Jen Y-M. Fatigue life evaluation of adhesively bonded scarf joints, International Journal of Fatigue 2012; 36:30-39.

6. Lekou D and Vionis P. Report on repair techniques for composite parts of wind turbine blades. Optimat Blades Technical Report 2002.

7. Trappe V and Nielow D. Fatigue loading of sandwich shell test specimens with simulated production imperfections and in-situ NDT, in ICFC 7 – The International Conference on Fatigue of Composites 2018.

8. Nielow D. Einfluss fertigungsbedingter Imperfektionen auf die Betriebsfestigkeit von FKV-Schalenstrukturen in Sandwichbauweise, Technische Universität Dresden 2022.

9. Moreira R, De Moura M, Silva F, Ramirez F. Numerical comparison of several composite bonded repairs under fatigue loading, Composite Structures 2020; 243.

10. Ahn S and Springer G. Repair of composite laminates – I: Test results, Journal of Composite Materials 1998; 32:1036-1074.

11. Yoo J-S, Truong V-H, Park M-Y, Choi J-H, Kweon J-H. Parametric study on static and fatigue strength recovery of scarf-patch-repaired composite laminates, Composite Structures 2016; 140:417-432.

12. Wu C, Chen C, He L, Yan W. Comparison on damage tolerance of scarf and stepped-lap bonded composite joints under quasi-static loading, Composites Part B: Engineering 2018; 155:19-30.

13. Ghafafian C, Popiela B, Trappe V. Failure Mechanisms of GFRP Scarf Joints under Static Tensile Load, Materials 2021; 14.

14. Grasse F. Beitrag zur Untersuchung des Betriebsfestigkeitsverhaltens von Rotorblättern für Windenergieanlagen im verkleinerten Maßstab, Technische Universität Berlin 2014.

15. Trappe V. Beschreibung des intralaminaren Ermüdungsverhaltens von CFK mit Hilfe innerer Zustandsvariablen, Technische Universität Carolo-Wilhelmina Braunschweig 2001.

  doi:10.5075/epfl-298799_978-2-9701614-0-0

16. Krause O. Frequency effects on lifetime, DLR Technical Report 2002.

17. Kumari P, Wang J, Sahil. Residual Tensile Strength of the Multi-impacted Scarf-repaired Glass Fiber-reinforced Polymer (GFRP) Composites, Materials 2018; 11.

18. Jen Y-M and Ko C-W. Evaluation of fatigue life of adhesively bonded aluminum single-lap joints using interfacial parameters, International Journal of Fatigue 2009; 32:330-340.

19. Basquin O. The exponential law of endurance tests, in American Society for Testing and Materials Proceedings 1910.

  doi:10.5075/epfl-298799_978-2-9701614-0-0

DAMAGE AND DEGRADATION OF UNIDIRECTIONAL COMPOSITES UNDER QUASI-STATIC AND FATIGUE LOADING – A CONTINUUM DAMAGE MICRO MECHANICS APPROACH

Alexander Krimmer[a], Alexandros Antoniou[b], Merle Vespermann[c]

a: TPI Composites Germany GmbH, Falkenberger Straße 146 A/B, 13055 Berlin, Germany – a.krimmer@tpicomposites.com
b, c: Fraunhofer-Institut für Windenergiesysteme IWES, Großer Westring 2, 27572 Bremerhaven, Germany

Abstract: *This work proposes an analytically based approach to assessment of the fatigue behavior of composites on the micro-mechanical level of constituents fiber and matrix. It implies adequate transferring functions for stresses from ply level to constituent material level. The stress-exposure e of the constituent materials can be assessed utilizing an equivalent stress approach for isotropic materials. Furthermore, a continuum damage description for matrix and fiber that relates constituent moduli to their stress-exposure and damage is of vital importance. Resulting damages are accumulated and lead to further degradation. As a next step, strain-energy based functions for assessment of load carrying capacity of constituents of different plies within the composite are applied and compared to identify the residual load carrying capacity of the laminate in comparison to applied loading in each load cycle. Thereby, not only damage initiation and degradation but as well failure of the laminate can be predicted. The combination of the above modules is referred to as Continuum Damage Micro Mechanics (CDMM) framework.*

Keywords: fatigue; degradation; continuum damage micro mechanics; composites

1. Introduction

Understanding, describing and predicting the fatigue behavior of uni-directionally fiber reinforced polymer matrix composites is a challenging task. This is a result of the complex interaction of fibers and matrix under different loading situations resulting in complex 3D stress states, acting on the constituent materials level. Not only the nature of the loading situation but as well the stiffness degradation behavior of composites vs. load cycle number as described in [1] add to the complexity. State of the art modelling works [2, 3, 4] deal with damage accumulation on a meso scale level. To overcome the challenges to a certain extent by reducing this complexity, a step on the length scale of observation from the meso to the micro level is necessary. Today, this step is usually taken by applying FEA-codes to predict the behavior resulting in extra-ordinary calculation effort.

This work proposes an analytically based approach to assessment of the fatigue behavior of composites on the micro-mechanical level of constituents fiber and matrix. It implies adequate transferring functions for stresses from ply level to constituent material level comparable to [5]. Subsequently, the stress-exposure *e* of the constituent materials can be assessed utilizing an equivalent stress approach [6] if the constituents are isotropic. Furthermore, a continuum damage description for matrix and fiber that relates constituent moduli to their stress-exposure and damage as provided in [7] is of vital importance. Resulting damages are accumulated as per

  doi:10.5075/epfl-298799_978-2-9701614-0-0

[8, 9] and lead to further degradation. As a next step, strain-energy based functions for assessment of load carrying capacity of constituents of different plies within the composite are applied and compared to identify the residual load carrying capacity of the laminate in comparison to applied loading in each load cycle. Thereby, not only damage initiation and degradation but as well failure of the laminate can be predicted.

The combination of the above modules is referred to as Continuum Damage Micro Mechanics (CDMM) framework. The required material input parameters are determined to a wide extent by quasi-static testing [10, 7] and limited fatigue testing of the constituent materials. The proposed method and corresponding formulations are explicitly described within this work. Resulting graphs for e.g. Young's moduli of a Uni-Directional (UD) composite as function of load cycle number are presented. Testing at different R-ratios has been carried out on coupons made of wind rotor blade specific UD and Bi-aXial (BX) NCF in epoxy matrix manufactured in Vacuum assisted Resin Infusion Molding (VaRIM) processing.

2. Micro mechanical modelling

Micro-mechanical approaches for modeling of Fiber Reinforced Polymers (FRP) represent the most traditional approach to describing mechanical behavior of FRP materials. However, the analytical description of damage degradation and failure is usually based on modeling of FRP starting on the lamina level. Therefore, it is difficult to attribute observed behavior to individual constituents fiber and matrix of a lamina or even their interface. Further, the modeling on ply level is complex due to the at least transversely isotropic nature of a ply. Based on established approaches, modeling of the damage, degradation and failure behavior of composites needs individual assessment for different loading directions and loading types.

To overcome the complexity of the modeling, a step from ply level into modeling on constituent level is proposed within this work. This consequently continues and expands the micro-mechanical modeling of the material on to damage initiation, degradation and failure description of composites. Starting from Glass Fiber Reinforced Polymers (GFRP), where fiber and matrix are usually isotropic, a simplified assessment is enabled, since simple strain energy-based approaches such as BELTRAMI [6] can be used for the assessment of the constituents. Now, different degradation behavior throughout the life of a composite as observed by REIFSNIDER [1] can be attributed to the constituents and connected to degradation functions. Throughout this work derivation of micro-mechanically based approaches for prediction of properties of UD composites are based on following assumptions:

- Simplified cross section of the fiber (square, rectangular or circle)
- Regular array of the fibers (square or hexagonal array)
- Two-phase composite consisting of fiber and matrix neglecting voids or inter-phases
- Parallel fibers
- Ideal connection between fibers and matrix
- Transversely isotropic behavior on ply level

2.1 Elasticity and strength of FRP

Micro-mechanical models for elasticity show sufficient correlation with testing results on UD laminates, either carbon and glass fiber reinforced [11, 12, 13, 14]. Nevertheless, micro-mechanically based prediction of strength, damage and failure of composites is not possible on

  doi:10.5075/epfl-298799_978-2-9701614-0-0

the same quality level, today [15]. Therefore, even for modeling of elasticity properties, the approach provided by KRIMMER [10] is applied within this work, to predict the in-situ moduli of the matrix as well. This enables more realistic prediction of stress magnification factors within the constituents fiber and matrix as can be shown in comparison with ADAMS and DONER [16, 17]. Based on these, within this section 3D transferring functions from ply stresses into constituent stresses will be given.

Coordinate Systems

A right-handed Cartesian material Coordinate System (CoS) is introduced. Its first axis is indicated by ∥ and points in fiber direction. The second axis is indicated by ⊥ and is oriented perpendicular to the fiber direction. For a UD lamina the properties are given in a right-handed Cartesian CoS where the 1-axis is parallel to the fiber direction. The 2-axis is perpendicular to the fiber direction in the lamina plane and the 3-axis is perpendicular to the lamina plane.

Elasticity Properties

For the YOUNG's modulus in fiber direction the linear Rule of Mixture (ROM) as per VOIGT [11] is used. Deviating from that the fiber modulus $\tilde{E}_{\mathrm{F}\parallel}$ considers undulation of the fibers in terms of an undulation factor f_{u} and the matrix modulus $E'_{\mathrm{M}\parallel}$ incorporates the in-situ behavior of the matrix meaning POISSON's effects in the matrix due to the embedded fiber. The choice of the index implies that the effect is dependent on the fiber direction of the embedded fiber. The Fiber Volume Fraction (FVF) is given by φ.

For transverse tensile moduli of a UD the expression based on a Cylinder Fiber Model in hexagonal array (CFMh) [5] is applied. Shear moduli in two directions are given, accordingly. In deviation from [5] the effective transverse Poisson's ratio of the matrix as per equation (10) in the reference is now calculated by

$$\nu'_{\mathrm{M}\perp\perp} = \frac{\nu_{\mathrm{M}}\left(1+\varphi\left[\frac{E_{\mathrm{F}\parallel}}{E_{\mathrm{M}}}\left(1+\nu'_{\mathrm{M}\perp}\right)-1\right]\right)}{1+\varphi\left\{\frac{E_{\mathrm{F}\parallel}}{E_{\mathrm{M}}}\left[1+{\nu'_{\mathrm{M}\perp}}^{2}\left(\frac{E_{\mathrm{M}}}{E_{\perp}}-1\right)\right]-1\right\}}. \tag{1}$$

Critical stresses in constituents fiber and matrix

Critical stresses within the constituents can be determined utilizing stress magnification factors as per [5], as well. The stress transferring functions are only given for the matrix since fatigue of FRP is assumed to be mainly driven by matrix dominated effects. In eq. (2) indices L and R indicate load determined and residual stresses, respectively while α_{MT}, α_{MM} and α_{MP} are referring to the linear thermal, moisture and polymer-physical Coefficients of Expansion (CoE). In deviation from [5] an improved consideration of hygro-thermal stresses is taken into account. The formulation in equation (2) assumes loading of a ply mainly in plane. Therefore, matrix dominated stresses in plane (σ_2 and τ_{21}) are considered more critical than out of plane stresses (σ_3 and τ_{31}).

Utilizing these formulae, determining the critical 3D stress state within the constituents of a UD ply is enabled. These can now be fed into a transferring function to calculate equivalent stresses as per BELTRAMI [6].

$$\{\sigma_{\mathrm{M}}\} = \begin{Bmatrix} \sigma_{\mathrm{M1}} \\ \sigma_{\mathrm{M2}} \\ \sigma_{\mathrm{M3}} \\ \tau_{\mathrm{M23}} \\ \tau_{\mathrm{M31}} \\ \tau_{\mathrm{M21}} \end{Bmatrix} = \begin{Bmatrix} \frac{\sigma_{1\mathrm{L}}+\sigma_{1\mathrm{R}}}{E'_{\parallel}} E'_{\mathrm{M}\parallel} \\ \frac{\sigma_{2\mathrm{L}}+\sigma_{2\mathrm{R}}}{E'_{\perp}\left(\frac{\sqrt{2\sqrt{3}\frac{\varphi}{\pi}}}{E_{\mathrm{F}\perp}}+\frac{1-\sqrt{2\sqrt{3}\frac{\varphi}{\pi}}}{E'_{\mathrm{M}\perp}}\right)} \\ \frac{\sigma_{3\mathrm{L}}+\sigma_{3\mathrm{R}}}{E'_{\perp}\left(\frac{\sqrt{2\sqrt{3}\frac{\varphi}{\pi}}}{E_{\mathrm{F}\perp}}+\frac{\sqrt{3}-\sqrt{2\sqrt{3}\frac{\varphi}{\pi}}}{E'_{\mathrm{M}\perp}}\right)} \\ \frac{\tau_{23\mathrm{L}}+\tau_{23\mathrm{R}}}{G'_{\perp\perp}\left(\frac{\sqrt{2\sqrt{3}\frac{\varphi}{\pi}}}{G_{\mathrm{F}\perp\perp}}+\frac{1-\sqrt{2\sqrt{3}\frac{\varphi}{\pi}}}{G'_{\mathrm{M}\perp\perp}}\right)} \\ \frac{\tau_{31\mathrm{L}}+\tau_{31\mathrm{R}}}{G'_{\perp\parallel}\left(\frac{\sqrt{2\sqrt{3}\frac{\varphi}{\pi}}}{G_{\mathrm{F}\perp\parallel}}+\frac{\sqrt{3}-\sqrt{2\sqrt{3}\frac{\varphi}{\pi}}}{G'_{\mathrm{M}\perp\parallel}}\right)} \\ \frac{\tau_{21\mathrm{L}}+\tau_{21\mathrm{R}}}{G'_{\perp\parallel}\left(\frac{\sqrt{2\sqrt{3}(\varphi)}}{G_{\mathrm{F}\perp\parallel}}+\frac{1-\sqrt{2\sqrt{3}(\varphi)}}{G'_{\mathrm{M}\perp\parallel}}\right)} \end{Bmatrix} - \begin{Bmatrix} (\alpha_{\mathrm{MT}}\Delta T + \alpha_{\mathrm{MM}}\Delta M + \alpha_{\mathrm{MP}} - \varepsilon_{\mathrm{R1}})E'_{\mathrm{M}\parallel} \\ \frac{\varepsilon_{\mathrm{R2}}E'_{\perp}-\alpha_{\mathrm{FT}\perp}\Delta T E_{\mathrm{F}\perp}\sqrt{2\sqrt{3}\frac{\varphi}{\pi}}}{1-\sqrt{2\sqrt{3}\frac{\varphi}{\pi}}} \\ \frac{\varepsilon_{\mathrm{R3}}E'_{\perp}-\alpha_{\mathrm{FT}\perp}\Delta T E_{\mathrm{F}\perp}\sqrt{2\sqrt{3}\frac{\varphi}{\pi}}}{\sqrt{3}-\sqrt{2\sqrt{3}\frac{\varphi}{\pi}}} \\ 0 \\ 0 \\ 0 \end{Bmatrix} \quad (2)$$

Damage initiation under quasi-static loading

It is assumed that cracking within the constituents occurs as soon as its equivalent stress exceeds its tensile strength. Therefore, under quasi-static loading the equivalent stress in the constituent fiber or matrix can be related to its tensile strength resulting in an expression for stress-exposure e as provided for the matrix (e_{M}) within equation (3).

$$e_{\mathrm{M}} = \frac{1}{R_{\mathrm{M}}}\left[\begin{matrix}\sigma_{\mathrm{M1}}^2 + \sigma_{\mathrm{M2}}^2 + \sigma_{\mathrm{M3}}^2 - 2\nu_{\mathrm{M}}(\sigma_{\mathrm{M1}}\sigma_{\mathrm{M2}} + \sigma_{\mathrm{M2}}\sigma_{\mathrm{M3}} + \sigma_{\mathrm{M3}}\sigma_{\mathrm{M1}}) \dots \\ +2(1+\nu_{\mathrm{M}})\left(\tau_{\mathrm{M23}}^2 + \tau_{\mathrm{M31}}^2 + \tau_{\mathrm{M21}}^2\right)\end{matrix}\right]^{\frac{1}{2}} \quad (3)$$

If the stress-exposure reaches a value of $e \geq 1$ the matrix will start cracking. The same applies to the fiber. For higher stresses, the constituents are assumed to degrade and CDMM applies.

2.2 Fatigue of UD laminae

To enable description of the fatigue behavior the process is divided into two stages:

- Initiation stage: loading of undamaged lamina, no increase of crack density due to loading up to the point of damage initiation called “damage onset”
- Degradation stage: loading of damaged lamina with increase of crack density due to loading, valid for all load cycles after damage onset up to the point of failure

The second stage comes to an end at laminate failure as soon as the load carrying capacity defined by the load which introduces a strain energy equal to or higher than the residual allowable strain energy of the laminate, is exceeded.

Initiation stage

Under fatigue loading It is assumed that damage accumulation as per PALMGREN and MINER [8, 9] can be applied. Further, since no damages are present within the matrix throughout the initiation stage, a simple symmetric Goodman diagram can be applied for taking mean-stress effects into account. This can be formulated based on matrix stress-exposure. Damage onset

  doi:10.5075/epfl-298799_978-2-9701614-0-0

and the connected damage increments as well as allowable load cycle number up to damage onset are given by

$$D_{p\mathrm{M}} = \sum_i D_{p\mathrm{M}i} \text{ with } D_{p\mathrm{M}i} = \frac{n_i}{N_{p\mathrm{M}i}} \text{ and } N_{p\mathrm{M}i} = \left(\frac{1-e_{p\mathrm{M}i\mathrm{m}}}{e_{p\mathrm{M}i\mathrm{a}}}\right)^{m_{p\mathrm{M}}}. \quad (4)$$

Herein i indicates the load collective while m indicates the stress-exposure from the mean stress vector $\{\sigma_{p\mathrm{M}i\mathrm{m}}\}$ in load collective i while a indicates the amplitude stress-exposure from the amplitude stress vector $\{\sigma_{p\mathrm{M}i\mathrm{a}}\}$. The negative inverse S/N slope is given by $m_{p\mathrm{M}}$. Summation over i results in the matrix damage $D_{p\mathrm{M}i}$. Matrix cracking is initiated if $D_{p\mathrm{M}} \geq 1$ applies.

Degradation stage

After initiation of damage cracks will occur and crack density will grow with increasing load cycle number. From this point on the behavior of the laminate is not linearly elastic anymore. The degradation behavior can be well observed throughout quasi-static testing [7]. Within this work it is assumed that the quasi-static degradation behavior can be mapped on degradation under fatigue loading, as well. The underlying assumption is an isotropic damaging of the matrix that is mainly driving the degradation behavior of FRP laminae. Based thereon the Young's and shear moduli of a damaged matrix can be calculated by

$$E^*_{p\mathrm{M}} = \eta_{p\mathrm{M}} E_{p\mathrm{M}} \text{ and } G^*_{p\mathrm{M}} = \frac{E^*_{p\mathrm{M}}}{2(1+\nu_{p\mathrm{M}})}. \quad (5)$$

Herein $\eta_{p\mathrm{M}}$ is the degradation factor of the matrix as per figure 1. It is a function of damage $D_{p\mathrm{M}}$ of the matrix and its stress state. Further, it is assumed that the matrix behaves isotropic even after damage initiation and the Poisson's ratio does not change during damaging of the material. This adapted set of mechanical properties can now be fed into the micro-mechanical ROM as stated above. Based on the elasticity properties of the lamina the compliance matrix of laminae and laminate are derived and exposed to the stress connected to the subsequent load cycle. Adapting the degradation factor $\eta_{p\mathrm{M}}$ to find the equilibrium between load and deformation is a highly iterative process and needs to be repeated for every load cycle, applied.

2.3 Fatigue and degradation of laminates

Under fatigue loading every load cycle i results in a damage increment $D_{p\mathrm{M}i}$ in the matrix of each ply p that leads to further degradation. Either a combination of an amplitude strain $\{\varepsilon\}_{i\mathrm{a}}$ and a mean strain $\{\varepsilon\}_{i\mathrm{m}}$ or the related stresses $\{\sigma\}_{i\mathrm{a}}$ and $\{\sigma\}_{i\mathrm{m}}$ are applied to the laminate. These must be converted either into upper and lower strain vectors $\{\varepsilon\}_{i\mathrm{u}}$ and $\{\varepsilon\}_{i\mathrm{l}}$ or into upper and lower stress vectors $\{\sigma\}_{i\mathrm{u}}$ and $\{\sigma\}_{i\mathrm{l}}$. Here, only stresses are addressed knowing that the procedure is similar for strains.

$$\{\sigma\}_{i\mathrm{u}} = \{\sigma\}_{i\mathrm{m}} + \{\sigma\}_{i\mathrm{a}} \text{ and } \{\sigma\}_{i\mathrm{l}} = \{\sigma\}_{i\mathrm{m}} - \{\sigma\}_{i\mathrm{a}} \quad (6)$$

This is since degradation in upper and lower turning point of a cycle can be different depending on the overall state of stress being tensile or compressive. For upper and lower turning point the equilibrium between stress and strain must be determined by adapting degradation factors for all plies p within a laminate. This does not necessarily change the laminate stress state but the stress distribution between the laminae. Now, the lamina stresses must be transferred to matrix stresses utilizing eq. (2) and converted back to mean and amplitude stress vectors.

$$\{\sigma_{\mathrm{M}}\}_{pi\mathrm{a}} = \frac{\{\sigma_{\mathrm{M}}\}_{pi\mathrm{u}} - \{\sigma_{\mathrm{M}}\}_{pi\mathrm{l}}}{2} \text{ and } \{\sigma_{\mathrm{M}}\}_{pi\mathrm{m}} = \frac{\{\sigma_{\mathrm{M}}\}_{pi\mathrm{u}} + \{\sigma_{\mathrm{M}}\}_{pi\mathrm{l}}}{2} \quad (7)$$

Feeding those into eq. (3) enables determination of the matrix damage increment due to the applied load cycle

$$D_{p\mathrm{M}i} = \left(\frac{1 - e_{p\mathrm{M}i\mathrm{m}}}{e_{p\mathrm{M}i\mathrm{a}}}\right)^{-m_{p\mathrm{M}}} \text{ summed up to } D_{p\mathrm{M}n} = \sum_i^n D_{p\mathrm{M}i}. \quad (8)$$

Now, the damage as function of load cycle number n is given. Based on the cycle number dependent damages the according degradation factors can be applied. As a consequence, the Young's moduli of the laminate can be plotted as function of load cycle number.

2.4 Failure of laminates

This procedure is ending if the strain energy introduced during the next load cycle is exceeding the capability of the degraded laminate to take up strain energy. Here the allowable strain energies of all constituents in all laminae must be summed up and compared to the strain energy introduced. Details to this procedure will be published within future works.

3. Testing and Results

Within this chapter results of the fatigue degradation calculations and testing are shown and compared based on testing on E-glass UD fabric laminate as per Table 1.

Table 1: 1182 g/m² UD fabric construction applied throughout quasi-static and fatigue testing.

Ply number	Material	Fiber angle	Area mass
1	E-glass (2400 tex)	0°	1134 g/m²
Stitching yarn	PES (110 dtex	Trikot/Franse	12 g/m²
3	E-glass (68 tex)	90°	36 g/m²

Different material testing has been carried out to enable evaluation of the presented calculation method. Initially, tensile testing of a E-glass UD fabric laminate has been carried out according to DIN EN ISO 527-5A at 23°C and 50 % relative humidity and 52.7 % fiber volume fraction (FVF). The testing results finally showed higher values for Young's modulus and strength than predicted by the calculation model. The Poisson's ratio showed the same value for testing and prediction. A comparison is given in Table 2.

Table 2: Material model parameters and comparison of tensile 0° testing results with model prediction (quasi-static), 52.7 % FVF.

Material	Young's modulus	Poisson's ratio	Tensile strength	S/N slope -1/m
E-glass	81.4 GPa	0.283	2.02 GPa	10
Epoxy Resin	3.02 GPa	0.399	79.8 MPa	10
PES Yarn	15.0 GPa	0.280	1.10 GPa	10

UD NCF Testing	42.4 GPa	0.302	1.01 GPa	-
UD NCF Prediction	41.1 GPa	0.302	932 MPa	-
Deviation	+3.00 %	-0.04 %	+7.26 %	-

Figure 1 shows a qualitative comparison of fatigue calculation results vs. testing results. Unfortunately, testing has been carried out relying on displacement measurements of the machine which is why the stiffness has been calculated by

$$S(n) = \frac{\Delta F_i}{\Delta x_i} = \frac{F_{\mathrm{u}i} - F_{\mathrm{l}i}}{x_{\mathrm{u}i} - x_{\mathrm{l}i}}. \tag{8}$$

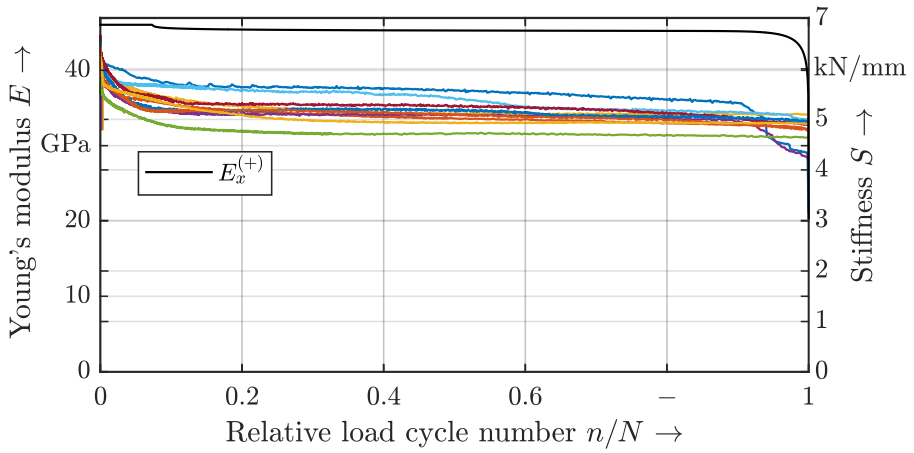

Figure 1. Fatigue degradation of UD under constant amplitude stress fatigue loading, R = 0.1 at 42 % upper stress vs. strength to 1,608,672 cycles compared to testing results

Therefor it is assumed that the higher degradation at the beginning of the testing is a result of slipping grips on the coupons. The effect stabilizes after around 15 % of the total load cycle number. After that, a nearly constant range of load cycles can be observed up to around 95 % of the total load cycle number. In comparison to that the calculation shows a decrease in Young's modulus around 7 % of the total load cycles which is attributed to matrix cracking in the 0° layer of the UD fabric. After that the Young's modulus is nearly constant up to around 95 % of the load cycles. From that point on degradation of the fibers drives the behavior, which is considered in the calculations.

Summary and Outlook

A qualitative comparison of calculated Young's modulus under R = 0.1 cycling shows both, similarities in terms of a long cycle range between 15 % and 95 % of the cycles where the stiffness does not change significantly and an obvious difference at the beginning of testing up to 15 % of the load cycles where the degradation is much higher for the coupons tested than throughout the calculation. Towards the failure of the coupons the degradation dominated by the fiber can be observed in both cases but is much more distinct in the calculation results. Due to a lack of strain data on the fatigue coupons a quantitative comparison is not yet possible. According testing will be carried out in the future and extended to the 90° direction as well as to other R ratios.

  doi:10.5075/epfl-298799_978-2-9701614-0-0

Acknowledgements

This research has been subsidized by the German Federal Ministry for Economic Affairs and Climate Action within the ReliaBlade (0324335A) and the Add2ReliaBlade (0324335G) project.

4. References

1. K. L. Reifsnider, Fatigue of Composite Materials, Elsevier, Amsterdam - Oxford - New York - Tokyo, 2012.
2. J. A. Bhangale, Fatigue analysis of wind turbine blade materials using a continuum damage mechanics framework, Ph.D. thesis, Delft Univer-ity of Technology, 2021. doi:10.4233 / uuid:7ea21785-c7ec-49db-85c4-d2e2f6ce6e9b.
3. A. Puck, Festigkeitsanalyse von Faser-Matrix-Laminaten, Hanser, München, Wien, 1996.
4. M. Knops, Sukzessives Bruchgeschehen in Faserverbundlaminaten, bd. 140 ikv – berichte aus der kunststoffverarbeitung ed., Verlag Mainz, 2003.
5. A. Krimmer, R. Leifheit, A. Bardenhagen, Assessment of quasi-static and fatigue performance of uni-directionally fi bre reinforced polymers on the basis of matrix e ff ort, in: Proceedings of the International Conference of the EASN Association - 6th EASN International Conference on Innovation in European Aeronautics Research, European Aeronautics Science Network - EASN, 2016, pp. 253–264. ISSN 2617-1481.
6. E. Beltrami, Sulle condizioni di resistenza dei corpi elastici, Rendic. R. Istituto Lombardo di Scienze Lettere e Arti 18, No. 2. (1885).
7. M. Vespermann, Stiffness degradation of glass-fiber reinforced epoxy composites due to matrix cracking under quasi-static loading (2022). To be published at ECCM20.
8. A. Palmgren, Lebensdauer von kugellagern, Zeitschrift des Vereins Deutscher Ingenieure 68 (1924) 339–341.
9. M. A. Miner, Cumulative damage in fatigue, Journal of Applied Mechanics 67 (1945) 159–164.
10. A. Krimmer, Mikromechanische Modellierung von Fasergelege-Kunststoff-Verbunden auf Basis von Normprüfungen unter Berücksichtigung der in-situ-Eigenschaften der Matrix, Ph.D. thesis, Technische Universität Berlin, 2014.
11. W. Voigt, Ueber die Beziehung zwischen den beiden Elastizitätsconstanten isotroper körper, Annalen der Physik 274 (1889) 573–587. doi:10.1002 / andp.18892741206.
12. K. Tanaka, T. Mori, Note on volume integrals of the elastic field around an ellipsoidal inclusion, Journal of Elasticity 2 (1972) 199–200.
13. Z. Hashin, B. Rosen, The elastic moduli of fiber-reinforced materials, Journal of applied Mechanics 31 (1964) 223–232.
14. C. C. Chamis, G. P. Sendeckyj, Critique on theories predicting thermo-elastic properties of fibrous composites, J. Composite Materials 2 (1968).
15. H. Schürmann, Konstruieren mit Faser-Kunststoff-Verbunden, Springer-Verlag, Berlin, Heidelberg, New York, 2005.
16. D. F. Adams, D. R. Doner, Transverse normal loading of a unidirectional composite, Journal of Composite Materials 1 (1967) 152–164.
17. D. F. Adams, D. R. Doner, Longitudinal shear loading of a unidirectional composite, Journal of Composite Materials 1 (1967) 4–17.

HOW LITERATURE REVIEWS INFLUENCE THE SELECTION OF FATIGUE ANALYSIS FRAMEWORK

Jaykarna Bhangale[a,b], Rene Alderliesten[a], Rinze Benedictus[a], Harald Bersee[a,b]

a: Faculty of Aerospace Engineering, Technical University, Kluyverweg 1, 2629 HS, Delft, Netherland
b: Suzlon Energy Limited - Netherlands Branch, Jan Tinbergenstraat 290, 7559 ST, Hengelo, Netherlands
Email: abhangale@suzlon.com

Abstract: *Prediction models for fatigue in engineering applications are developed within a fatigue analysis framework, deliberately selected in some cases, but mostly chosen without substantiation. The proposition of this paper is that selecting the most appropriate framework can only be done with the knowledge and a complete overview of existing frameworks and their systematic categorization. In particular for composite materials, where due to the coexistence of different mechanisms and their complex interaction under fatigue loading, only a unified approach can characterize the complete fatigue phenomenon.*

Keywords: Fatigue analysis frameworks; Thermodynamics; Damage mechanics; cyclic inelasticity.

1. Introduction

More than 150 years have passed since humanity encountered the fatigue phenomenon in engineering applications. Over this time, a transition can be observed in how the understanding of the fatigue phenomenon is developed. Initially, the development of fundamental theories outpaced the experimental observations. More recently, facilitated by the development of sophisticated testing capabilities, the experimental observations outpace the development of theories. Hence today, material deformation theories are developed, and experimental results are generated in different fatigue research communities that are not in synchronization. In many cases, oversimplified theories, that are developed on prior art, are fitted to new experimental datasets without awareness of other (often more) theoretical work.

For example, in the case of composite materials of a wind turbine blade, the international standards [1, 2] accept fatigue verification based on a Goodman diagram [3] which is a simplified approach based on the linear influence of mean stresses (or strains) on the fatigue life. Such acceptance leads to generating a massive amount of experimental data only to fulfil the standard requirements. However, in many cases, this data is not synchronized with the underlying governing theories, ultimately creating a gap between experiments and theory.

An overview with a systematic categorization of different fatigue analysis frameworks can increase the awareness of the other methodologies. A most appropriate analysis framework can be identified based on such knowledge that represents the specific experimental dataset and addresses the gap between the governing theory and experiments.

  doi:10.5075/epfl-298799_978-2-9701614-0-0

The construction of a framework based on a unified approach requires several prerequisites and specific steps to be followed. These prerequisites are discussed in the next section first.

2. Prerequisites to fatigue analysis

Any framework used in fatigue analysis is built upon a specific research objective and corresponding methodology. Before adopting a fatigue analysis framework, sufficient attention must be given to its prerequisites, which in sequence, can be written as

- Prior knowledge of how loading conditions relate to damage mechanisms in the structure and its sub-components during operation.
- Selection of length scale at which fatigue analysis needs to be performed.
- Selection of the analysis methodology.

Once these prerequisites are fulfilled, then attention can be given to the identification or construction of a most appropriate analysis framework.

3. Fatigue analysis frameworks

The best way to get acquainted with different analysis frameworks is by systematic categorization of the methodology, and by learning from surveys and critical reviews in respective categories. In this paper, the fatigue analysis frameworks are categorized by their methodology.

3.1Traditional phenomenological framework

Traditionally fatigue data is analyzed within a very simplified framework based on the empirical (phenomenological) methodology. The simplicity in the application of this traditional framework favoured its widespread use in engineering applications to date. Figure 1 gives a schematic representation of different stages followed within this framework.

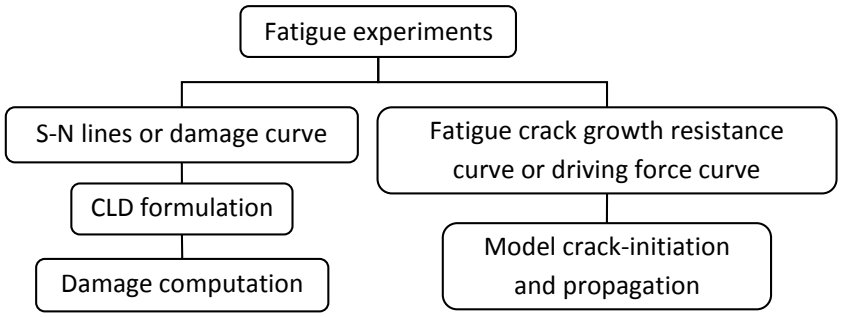

Figure 1 Traditional phenomenological framework of fatigue data analysis

The first stage comprises the execution of fatigue experiments at various stress or strain levels and for various stress or strain ratios. After that, the experimental results are analyzed in different ways, depending on the damage type.

In case a single crack forms the dominant damage mechanism degrading the structure (e.g. ply drop or thickness transitions), its initiation and propagation over time are monitored and studied. The study of crack propagation using methods of solid mechanics is known as fracture mechanics. In this framework, fatigue crack growth rate is studied against either stress intensity factors or strain energy release rates. Such a curve is known as the fatigue crack growth

resistance curve, and it became the input to the simulation of crack propagation in a finite element environment.

When only final failure or gross damage is considered, the number of cycles to failure or any stress or strain ratio is assumed to follow a power-law relationship with the input constraints. To identify any nonlinearity in the power-law relationship, one of the practices followed in the industry is to perform fatigue tests that give failure lives scattered over at least four orders of magnitude in life. In the case of nonlinearity in the data, the SN line formulation needs to be adapted accordingly. The next step in this framework is to construct a constant life diagram (CLD), which represents lines for constant life in mean and alternating stress/strain space. The CLD construction increases the life prediction capability to non-tested stress ratios. The formulation of constant lifelines and their estimated model parameters are input to structural analysis. The constant life lines merge to a single point when alternating stress/strain reaches a value of 0. Physically there is no explanation possible for such a situation where a single point is representing failure life for any number of cycles. Due to practical difficulties in the execution of tests and very few applications that demand validation at the high mean and low alternating loading, the practice of merging constant lifelines to a single point continued.

The analysis in this framework is based on survival probability only; in other words, failed or not failed, hence does not give insight into how much damage a material has sustained over particular life or vice versa. Many attempts were made in the past to get more understanding from the traditional framework by using either a strength or stiffness reduction rule as input [4, 5]. To date, the application of strength and stiffness reduction rules and the formulation of new ones for different materials continued.

The last step in the traditional framework is the calculation of damage accumulation. Various empirical rules for damage accumulation were proposed and reviewed in the past. Out of these, one popular and the extensively applied rule is linear damage which assumes linear dependency of damage on fatigue life. In almost all materials and particularly in composite materials, the damage does not show linear dependency on life. The simplicity of this rule in terms of computing damage makes their application very attractive even to a complicated structure.

Despite a continuous evolution in methodology, achieving a detailed understanding of material behaviour is still a target to achieve for the traditional framework due to the following shortfalls-

- The fatigue life prediction includes only the final damage level and not the intermittent damage level.
- The fatigue life prediction lacks both qualitative and quantitative descriptions of associated different mechanisms and their coupling.

Hence, the use of another framework needs to be explored to achieve a better understanding.

3.2 The framework from the thermodynamic theory of irreversible processes with internal variables

In search of more understanding, many studies adopt a physics-based methodology. The basis for this adoption is in the similarity of the qualitative mechanical behaviour of most of the materials. Due to this similarity, it is possible to generalize the macro-scale behaviour with the help of macro-scale (bulk) mechanisms (elastic behaviour, yielding, inelastic strain, anisotropy

  doi:10.5075/epfl-298799_978-2-9701614-0-0

induced by strain, cyclic inelasticity, damage development) that are similar for these materials. One such possibility is provided by the well-established continuum damage mechanics (CDM) framework. This framework requires input from the thermodynamic theory of continuum and general concepts of thermodynamics of irreversible processes with internal variables. The generalization of material behaviour is made by approximating the irreversible process by a sequence of constrained states that are near equilibrium and that can be characterized locally by a finite set of internal variables. Figure 2 outlines the steps followed in this framework.

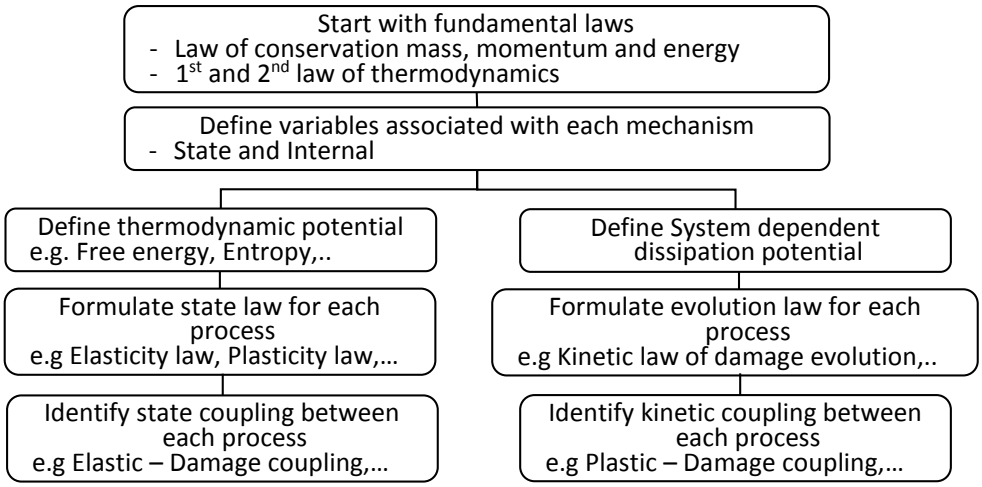

Figure 2 Schematic flow chart followed in the framework of thermodynamics theory

The framework starts with fundamental laws that are central principles of thermodynamics. These laws are general, pervasive and apply to both micro and macro scales of the material as a whole or every element within it. When the material is deformed, its microstructure changes in either a reversible (elastic) or irreversible (inelastic) manner. Here, each change can be characterized as a material's specific property and described by certain parameters known as state variables, because they only depend on the initial and final states of a material. State variables are further divided into observable variables (which can be observed and directly measured) and internal variables (which are not directly observed but derived from observable variables). Maugin [6] gave a critical review on the use of internal variables of state in rational thermodynamics.

During the deformation, the energy involved in any change in state can be linked to its (state) potential. Hence when a state potential is written as a function of the state variable, then it defines the condition of the state and is known as state law. When a change in the state consists of dissipation of input energy in any form, then the process is known as the dissipative process. The description of such a process requires the evolution of such dissipation. Similar to the state potential when the dissipation potential is written as a function of associated variables, then it gives the evolution of dissipation and is known as evolution or complementary law.

The last part of the framework is to identify the coupling between different mechanisms. During the deformation, when two or more different mechanisms simultaneously represent the material's behaviour, then they are considered coupled. In such a coupling, variable(s) associated with one mechanism is modified by the change of the value or the evolution rate of the variable(s) associated with the other mechanism. These couplings can be of direct, indirect, or secondary nature [7]. In the case of direct coupling, the absolute value of one variable

  doi:10.5075/epfl-298799_978-2-9701614-0-0

influences the other variable. In the case of indirect coupling, the absolute value of one variable influences the rate of another one. Whereas in the secondary coupling, a third variable value is influenced by the second one where the first and second variable shows either direct or indirect coupling.

3.3 Continuum Damage Mechanics (CDM) framework

The framework of irreversible thermodynamics plays a fundamental role in constructing CDM models for various damage mechanisms. Damage during deformation in the physical sense means discontinuities in a material at the micro or macro scale. These discontinuities result in strain dissipation. Depending on the nature of discontinuities, they either are represented by single or multiple damage variables and their associated variable strain energy release rate. Here, damage potential as a function of the strain energy release rate gives the evolution of the damage variable, and this functional relationship is called damage evolution law. The discontinuities in the material can be at the micro or macro level, and hence the definition of damage variables also can be given at respective levels. If the damage variable is defined using continuum level material properties, then the damage state can be treated as a continuum.

Similar to the area of fatigue phenomenon, the area of CDM is having an extensive scope and is interlinked to other mechanisms like elasticity, inelasticity, ageing, and thermal effects. Hence to get acquainted with this area, a systematic categorization of the scope of CDM application is needed. This categorization can be done based on damage types like brittle, ductile, creep, fatigue, and their coupling with other mechanisms[9], as shown in Figure 3.

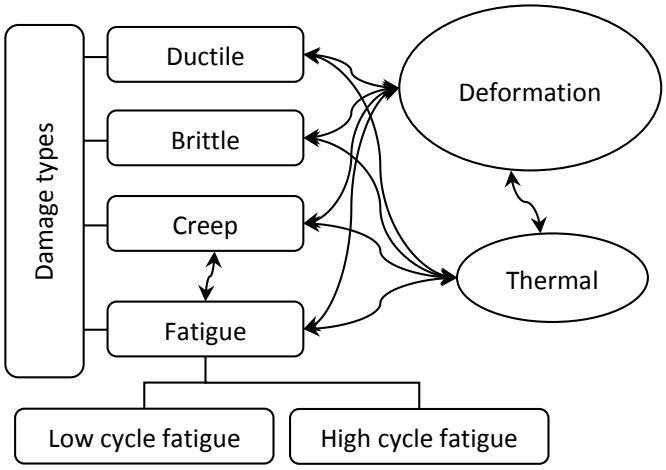

Figure 3 Categorization and coupling of the CDM framework

To date, the CDM framework was applied and matured for various types of damage mechanisms to various materials including metal, rubber, concrete, soil, rock and composite [8]. An extensive amount of literature is available on different damage mechanisms observed in composite materials [10 - 15]. The overall damage development is highly complex, due to the presence of different damage mechanisms with strong unilateral features and their interactions. Hence, characterization of damage at the microscale requires the development of mathematical formulation with anisotropic and unilateral damage evolution. Whereas at the macro scale by ignoring the detailed microstructure, the discontinuity introduced into the displacement field can also be ignored, and the mathematical formulation can be constructed using continuum theory [16].

  doi:10.5075/epfl-298799_978-2-9701614-0-0

One key feature of damage development under fatigue loading is its stochastic nature. During fatigue testing for any two coupons from the same material configuration and under the same test conditions, the damage development is not similar. For composite materials, generating the correct damage mode in the specific areas for all loading situations is still a target to achieve [17 - 26]. For the same reason, the fatigue results analyzed are mostly based on failure near or in the clamp region of the coupon.

The damage evolution law derived using the CDM framework is deterministic, which means there is no uncertainty associated with the value of damage or the rate of damage growth. The thermodynamic principles do not include any spatial variability while defining either state variables or potentials; hence the damage law also does not include this variability. To understand the damage growth either this deterministic law needs to be extended into the probabilistic domain [27], or the stochastic nature needs to be represented by some average non-random function.

3.4 Cyclic inelasticity framework

Under fatigue loading, the material deforms in various ways; hence a framework is also required to describe all these deformation mechanisms. The theory of elasticity addresses the elastic deformation, while the cyclic inelasticity theory addresses the inelastic deformation under fatigue loading.

Inelastic deformation in the physical sense means irreversible changes in microstructure that do not lead to the generation of discontinuity during the deformation process. Under non-zero mean stress cyclic loading, materials show more changes in microstructure than monotonic loading because of the presence of two loading situations. The cyclic amplitude load is superimposed on-to constant minimum stress (except the tension-compression loading). As a result of an additional change in microstructure, the material shows either hardening/softening or no change in response to applied loading in the subsequent cycle. The elastic domain defines the threshold state of material between elastic and inelastic deformations and is represented as a surface in the space of stresses [28 P.28].

The inelastic strain consists of two parts: plastic and viscous component. The plastic strain evolution is associated with certain limited stress intensity, and the mathematical formulation is based on the rate-independent formalism [29, 30]. This theory is known as cyclic plasticity theory. If the viscous component is present in the deformation, then the mathematical formulation needs to be adapted for a rate-dependent base, and this theory is known as cyclic viscoplasticity theory [30, 31]. In both theories, the mathematical formulation consists of the following steps [28, 32] -

- First defining the elastic domain, that gives a boundary to the linear elastic region.
- Formulation of flow rule that describes the relationship between stresses and strains development post elastic region.
- Application of consistency condition to get the direction of stresses.
- Formulation of hardening/softening rule to define change of loading surface during flow.
- Determination of inelastic modulus, and
- Calculation of stresses and inelastic strains.

  doi:10.5075/epfl-298799_978-2-9701614-0-0

In almost all materials, Hook's law characterizes the elastic response and the Ramberg-Osgood law [33] characterizes the plastic response. Hence generalization in the elastic and plastic response is possible for most of the materials and derived using thermodynamic potentials. Unlike the elastic response, the post elastic region (hardening/softening) behaviour for multimillion cycles is different for every material. Hence, the generalization of the hardening rule is not possible. So far, an earlier proposed hardening rule from literature is modified to address the changes and differences from new materials. To the author's knowledge, there exists no hardening/softening rule for high cycle fatigue situations, and the field of cyclic inelasticity is still an active field of research.

4. Conclusion

This paper provides an overview of different frameworks followed in the fatigue analysis of various materials. Such an overview enables the selection of the most appropriate analysis framework required for desired understanding and/or application. In the absence of such an overview, the selected analysis framework can lead to incomplete answers widening the gap between theory and experiments or expenditure of extra resources for identifying missing links.

A framework based on a unified approach that addresses the role played by all relevant mechanisms in the development of the overall phenomenon seems the most appropriate choice. As the theory of the thermodynamics of the irreversible processes is generic, and the CDM framework is based on this theory, many material classes like metals and composites can be analyzed using this framework. Such a framework has similarities up to a certain level, and at the detailed level, it differs by addressing the difference in the contribution of various mechanisms and their coupling associated with different material classes.

5. References

1. Standard DNVGL-ST-0376. Rotor Blades for Wind Turbines. DNV GL AS; Oslo, Norway; 2015
2. International Electrotechnical Commission. Wind energy generation systems – Part 5: Wind turbine blades (IEC 61400-5); 2020.
3. Goodman J. Mechanics applied to engineering, Longman, Green & Company, London; 1899.
4. Degrieck J. Van Paepegem W. Fatigue damage modelling of fibre-reinforced composite materials: Review. Applied Mechanics Reviews. 2001;54(4): 279-300.
5. Philippidis TP. Passipoularidis V. Residual static strength of fibrous composites after fatigue: A literature survey. OPTIMAT BLADE Deliverable (OB_TG5_R001_UP rev. 000). 2003.
6. Maugin GA. The saga of internal variables of state in continuum thermo-mechanics (1893–2013). Mech Res Commun. 2015;69:79–86.
7. Marquis D, Lemaitre J. Constitutive equations for the coupling between elasto-plasticity damage and aging. Revue phys appl. 1988;23(4):615–24.
8. Desmorat R. Damage and fatigue: Continuum damage mechanics modeling for fatigue of materials and structures. Rev fr génie civ. 2006;10(6–7):849–77.
9. Lemaitre J, Desmorat R. Engineering damage mechanics: Ductile, creep, fatigue and brittle failures. Berlin, Germany: Springer; 2010.
10. Hart-Smith LJ. What the textbooks won't teach you about interactive composite failure criteria. In: Composite Structures: Theory and Practice. 100 Barr Harbor Drive, PO Box C700, West Conshohocken, PA 19428-2959: ASTM International; 2008. p. 413-24.
11. Reifsnider KL, Fatigue of Composite Materials. London: Elsevier Science; 1991.

  doi:10.5075/epfl-298799_978-2-9701614-0-0

12. Carvelli V, Lomov S, Fatigue of Textile Composites. Cambridge: Woodhead Publishing; 2015.
13. Talreja RR, Varna J, Modeling damage, fatigue and failure of composite materials. Cambridge: Woodhead Publishing; 2015.
14. Hashin Z, Herakovich CT, Mechanics of composite materials: Recent advances. Elsevier 2013.
15. Gamstedt EK, Sjögren BA. Micromechanisms in tension-compression fatigue of composite laminates containing transverse plies. Compos Sci Technol. 1999;59(2):167-78.
16. Dougill JW. On stable progressively fracturing solids. Z Angew Math Phys. 1976;27(4):423-37.
17. Hojo M, Sawada Y, Miyairi H. Influence of clamping method on tensile properties of unidirectional CFRP in 0° and 90° directions — round robin activity for international standardization in Japan. Composites. 1994;25(8):786–96.
18. Milette J. Static and Fatigue Behaviour of Unidirectional Composites in Compression. Mechanical Engineering Department McGill University Montréal, Québec, Canada; 1995.
19. Sims G Niklewicz J. Size effects in composite materials (Report MATC (A) 74). NPL Materials Centre National Physical Laboratory. 2002.
20. De Baere I, Van Paepegem W, Degrieck J. On the design of end tabs for quasi-static and fatigue testing of fibre-reinforced composites. Polym Compos. 2009;30(4):381–90.
21. Mikkelsen LP. Bech JI. Secondary stress effects during load introduction into unidirectional composite test coupons. In: O. T. Thomsen, B. F. Sørensen, & C. Berggreen, editor. 6th International Conference on Composites Testing and Model Identification. 2013.
22. Bailey PBS, Lafferty AD. Specimen gripping effects in composites fatigue testing –– Concerns from initial investigation. EXPRESS Polym Lett. 2015;9(5):480–8.
23. Tost A. Heinrich F. Ridzewski J. Novel test method for characterization of unidirectional composite fatigue properties. In: ECCM17: 17th European conference on composite materials, Munich, Germany, 26 - 30th June 2016.
24. Luthada P. Tension-Tension Fatigue Testing of Pultruded Carbon Fibre Composite Profiles. School of Engineering, Department of Mechanical Engineering, Aalto University, Espoo, Finland; 2016.
25. Fraisse A. Brøndsted P. Compression fatigue of Wind Turbine Blade composites materials and damage mechanisms. In: 21st International Conference on Composite Materials, China. 2017.
26. Afshar A. Alkhader M. Korach CS. Chiang F. Synergistic effects of fatigue and marine environments on carbon fibre vinyl-ester composites. J Eng Mater Technol. 2015;137(4).
27. Paas M. Continuum damage mechanics with an application to fatigue. 1990.
28. Dunne F, Petrinic N. Introduction to computational plasticity. Oxford; 2005.
29. Flügge S, Encyclopedia of physics - Elasticity and Plasticity. Springer, Heidelberg; 1958.
30. Chaboche JL. Constitutive equations for cyclic plasticity and cyclic viscoplasticity. Int J Plast. 1989;5(3):247–302.
31. Guedes RM, Creep and fatigue in polymer matrix composites. Cambridge: Woodhead Publishing; 2011.
32. Lee Y-L, Barkey ME, Kang H-T. Metal fatigue analysis handbook: Practical problem-solving techniques for computer-aided engineering. Woburn, MA: Butterworth-Heinemann; 2014.
33. Ramberg W. Osgood WR. Description of stress-strain curves by three parameters (NACA-TN-902). NASA Scientific and Technical Information Facility; 1943.

  doi:10.5075/epfl-298799_978-2-9701614-0-0

IN-SITU MEASUREMENTS OF THE LOAD TRANSFERRING SHRINKAGE OF THERMOSETS USED IN COMPOSITE MATERIALS FOR WIND TURBINE BLADES

Lars Pilgaard Mikkelsen

Composites Manufacturing and Testing, DTU Wind Energy,
Technical University of Denmark, DK-4000 Roskilde, Denmark, Email: lapm@dtu.dk

Abstract: *An experimental setup for in-situ measurement of the load transferring shrinkage during the curing process of thermosets is demonstrated. The experimental setup makes it possible to determine the load-transferring point and the resulting cure-induced strain for a specific material system during a specific cure profile. Measurements that make it possible to tailor the cure profile aiming for a low resulting residual stress in a composite material. The accuracy of the measurements of the cue-induced strain is validated through finite element simulations of the deformation of the embedded optical glass fiber containing a Fiber Bragg Grating deformation sensor. The simulations show that a minimum thickness of 2mm and the presence of a minimum of 10 mm embedded optical fibers on both sides of the Fiber Bragg Grating sensor are important for obtaining accurate strain measurements.*

Keywords: Residual stresses; Cure-kinetic; Fiber Bragg Gratings; Finite element model

1. Introduction

Glass and carbon fiber reinforced polymer matrix composites is the key structural element in wind turbine blades. Something due to its excellent mechanical performance regarding low weight, high stiffness, and good fatigue resistance. Nevertheless, the mechanical performance, especially regarding the fatigue resistance [1], is influenced by manufacturing-induced residual stresses. Residual stresses, which can be difficult to quantify during the manufacturing process.

In the presented work, embedded optical glass fibers with Fiber Bragg Grating (FBG) sensors [2] are used for experimental in-situ measurement [3] of the load transferring part of the shrinkage of typical thermosets used in composite materials for wind turbine blades. The measurements are performed in two experimental setups: a neat polymer plate curing during un-constrained shrinkage and a polymer plate constrained by surrounding laminates. From the embedded FBG sensor in the unconstrained polymer plate, the load transferring point and the unconstrained load transferring shrinkage can be measured in-situ during the curing process. In this case, a linear relationship is observed between the total shrinkage and the temperature difference between the temperature where the polymer shrinkage first is transferred to the FBG sensor, and the final de-molding temperature. For the constrained case, a different load transferring shrinkage of the polymer is measured by the embedded FBG sensor. A measurement which is obtained after the constraining layer has been removed. Thereby, it is possible to quantify the amount of viscoelastic relaxation during the curing process.

  doi:10.5075/epfl-298799_978-2-9701614-0-0

Even though optical glass fibers with FBG-sensors are excellent for measuring the load transferring part of the resin shrinkage, the stiffness difference between the two material systems can result in too low strain measures. In the following, a finite element model of a resin system with an embedded FBG-sensor is used with the purpose of quantifying this difference. It has thereby been found that by keeping a minimum of 10 mm embedded optical glass fiber on both sides of the FBG-sensor, a rather small difference below 2-4% is obtained between the two strain values.

2. Methods and models

2.1 Experimental setup

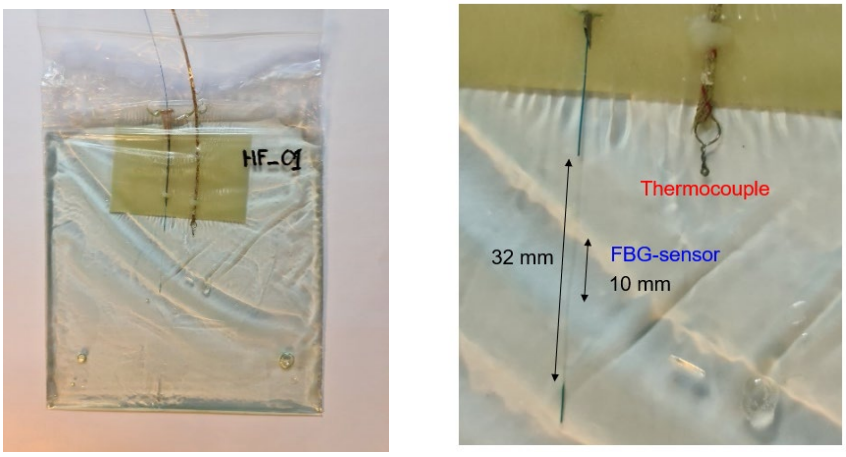

Figure 1. Un-constrained experimental setup with an approximately 160x160x4 mm³ plastic bag containing the curing resin system with an embedded optical glass fiber with an FBG-sensor and an embedded thermocouple.

Fig 1 shows the un-constrained experimental setup used for in-situ measurement of the load-transferring part of the resin shrinkage during a prescribed cure profile. In the experimental setup, the plastic bag is filled with an un-cured resin system and placed under temperature control. Embedded in the resin are an FBG sensor and a thermocouple. The FBG sensor is located over 10 mm of a 250 µm thick optical fiber centrally located along an approximately 32 mm long un-coated optical glass fiber segment, see the zoom-in-picture in Fig. 1.

Fig. 2 shows a typical output from such an in-situ cure experiment performed on a typical epoxy material system used in the composite material in a wind turbine blade. The thin red curve, T_{air}, shows the prescribed temperature profile which here corresponds to a 2-stage cure: 50°C(5h) + 80°C(5h). The thick red curve, T_{resin} , shows the resulting temperature profile measured inside the resin system by the thermocouple. The green curve shows the Degree of Cure (DoC), ξ, predicted from a DSC determined cure-kinetic model determined for the specific material system. The blue curve shows the amount of the shrinkage of the polymer system which are transferred to the embedded FBG-sensor as a linear load transferring strain, ε_{CI}, in the fiber direction. The load transfer point, $()_\sigma$, is on the curves marked with large dots defining the first time, $\varepsilon_{CI} > 0.01\%$. It is found for the un-constrained case that the temperature difference from this point, T_σ , until the final temperature, $T_{room} = 21°C$, determine the resulting cure-induced strain, ε_{CI} , independent on the intermedia post-cure profile. Therefore, the in-situ strain measure can be used for determining the point when the temperature can be raised for the

  doi:10.5075/epfl-298799_978-2-9701614-0-0

higher temperature post-cure part without causing additional cure-induced strains and for measuring the final cure-induced strain. For the specific resin system and cure-profile, the finale load-transferring part of the resin shrinkage is seen to results in a cure induced strain on $\varepsilon_{CI} = -0.63\%$. It should be noted that the load-transferring part of the shrinkage is significant smaller than the approximately volumetric 6% or linear 2% total resin shrinkage.

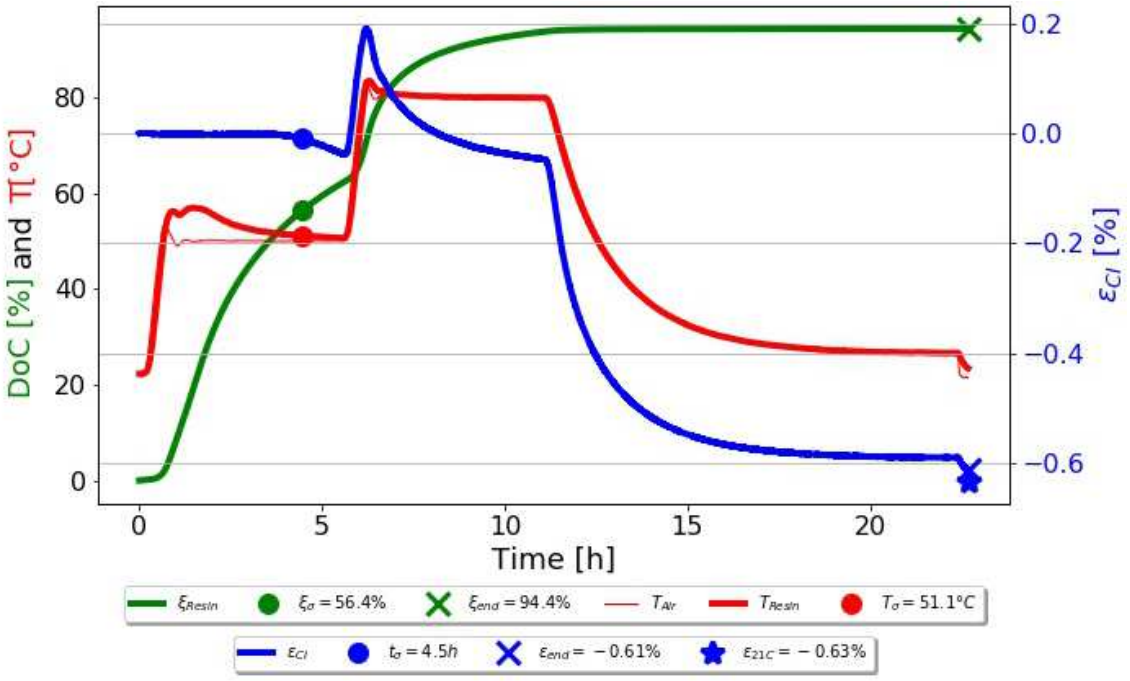

Figure 2. Measurements from a 2-stage cure profile where the blue curve shows the temperature compensated strain measurement in the optical glass fibers where the three big dots indicate the time, temperature and DoC for the load-transferring point.

2.2 Finite element model

The load-transferring shrinkage of the $E_m = 3GPa$ resin system is measured through the deformation of a FBG-sensor located on a $D_{FBG} = 250\mu m$ thick and $E_{FBG} = 70GPa$ stiff optical glass-fiber. To ensure that the presence of the optical fiber does not significantly influence the measured cure-induced strain, a finite element model of the test setup as shown in Fig. 1 is made. Due to symmetry, only ¼ of the curing resin plate is modeled. The model is shown in Fig. 3, including some details around the embedded optical fiber, modeled as ¼ of the fiber. The matrix system and the optical fiber are modeled as two isotropic linear elastic materials using the following stiffness parameters:

$$(E_{FBG}; \nu_{FBG}) = (70GPa; 0.2) \text{ and } (E_m; \nu_m) = (3GPa; 0.4) \quad (1)$$

A perfect bond is assumed between the fiber and resin system. In addition, the thermal expansion coefficient of the optical glass fiber $\alpha_{FBG} = 0.55 \times 10^{-6}/K$ is order of magnitudes smaller than the resin system with $\alpha_{resin} = 50 \times 10^{-6}/K$ so in the finite element model, only the contraction of the resin system is considered.

  doi:10.5075/epfl-298799_978-2-9701614-0-0

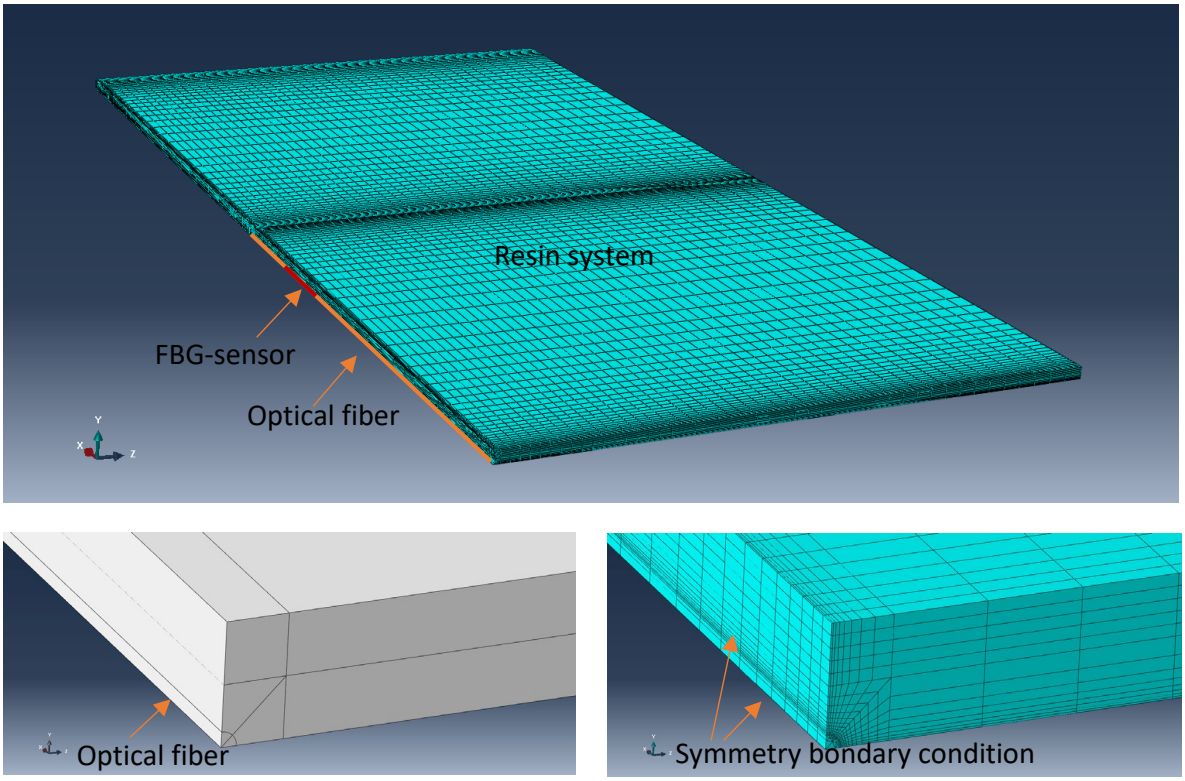

Figure 3. Finite element model ¼ of the resin system with the embedded optical glass fiber

3. Results

Fig. 4 shows the simulated axial strain in the optical fiber for a 4 mm thick resin plate when the resin experiences a load-transferring shrinkage of 0.5% strain corresponding to a volumetric load-transferring shrinkage on $\frac{\Delta V}{V} = 1.5\%$. The strains shown in the figure are extracted from the finite element model along a path following the center of the optical fiber and continuing in the center part of the neat resin in the plate. Except from near the end of the optical fiber and close to the end of the resin plate, the much stiffer fiber is found to follow the shrinkage of the resin system. Nevertheless, from the simulation, the importance of keeping a part with a minimum length of 10 mm of the optical fiber after the FBG-sensor can be seen.

  doi:10.5075/epfl-298799_978-2-9701614-0-0

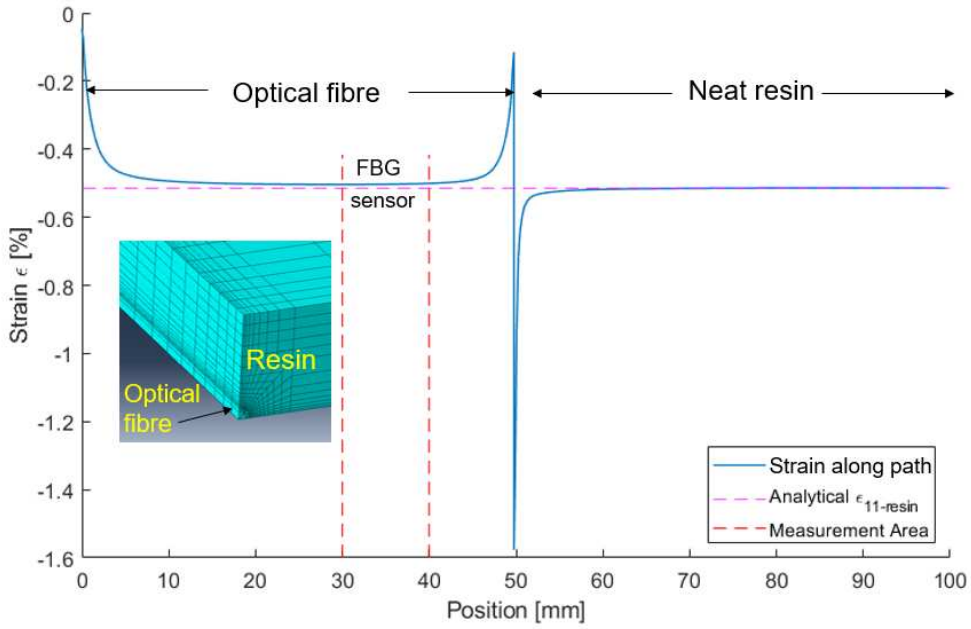

Figure 4. Finite element calculation of the axial strains of the optical glass fibers embedded in a resin system deformed approximately 0.5% strain. The strains are extracted in the center line of the embedded glass fiber and the resin sample.

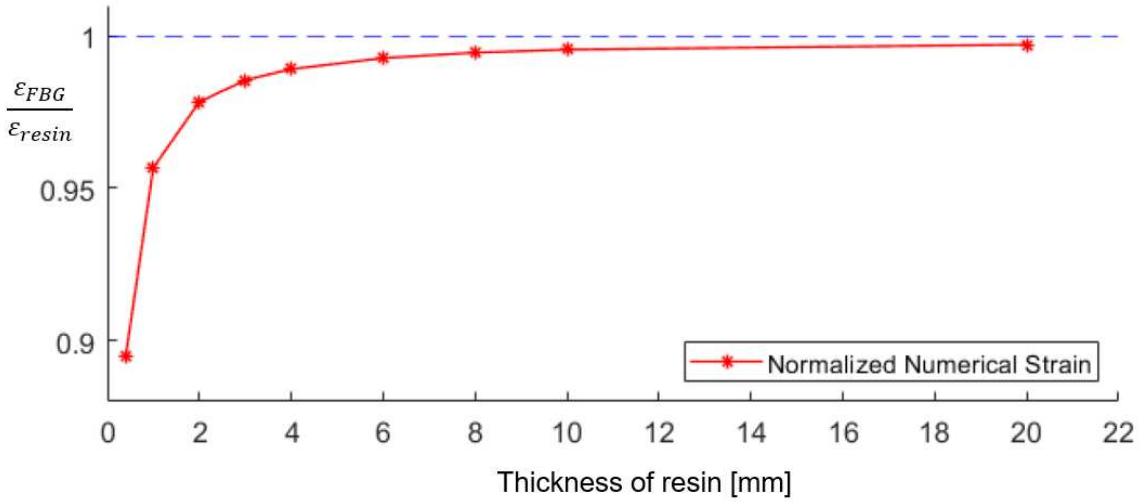

Figure 5. The difference between the mean strain of the FBG sensor and the unaffected strain of the surrounding resin material

Fig. 5 quantifies this difference, and from this, it can be seen that if the resin plate has a thickness of minimum 2 mm, then the difference between the cure-induced strain of the unaffected neat resin and the FBG-sensor is seen to be below 3%. The simulation is performed using a resin stiffness of $E_m = 3GPa$. A value which is the stiffness for the fully cured resin. For a partly cured resin, this stiffness will be lower. Therefore, the in-situ measured load-transferring strains may results in a larger difference. Nevertheless, an accurate measure of the in-situ strain development will in many cases not be as important as the final load-transferring cure-induced strain

The experimental setup is used both in an un-constrained and a constrained version. The constrained version differs from the case analyzed here as the curing resin is located between two 2 mm thick cross-ply laminates. During this, the resin will be constrained for shrinkage in the length and width direction during the shrinkage and the embedded FBG-sensor will therefore only measure a very limited strain. Something which is similar to the curing process happening inside a composite. Nevertheless, different from the cured composite, it is for the constrained cured resin system possible subsequently to remove the constraining laminate whereby, the cure-induced strains can be measured from where the residual stresses during the constrained cure can be determined.

4. Conclusion

A procedure for measuring the in-situ build-up of cure-induced strains is demonstrated. The in-situ procedure makes it possible to determine the load transferring point and thereby the cure-time after when the cure can go from the low-temperature 1st stage to the high-temperature 2nd stage cure sequence. Using such measurement, it is possible to lower the final cure-induced strains and thereby the corresponding residual stresses in a composite cured under the same condition. A finite element simulation shows that the embedded FBG-sensor is capable for measure the final cure-induced strain with high precision as long as the resulting resin plate has a thickness of a minimum of 2 mm and that the FBG sensor is located a minimum of 10 mm from the end of optical fiber and the end of the resin plate.

Acknowledgments

The study is supported by the Danish Energy Agency through the Energy Technology Development and Demonstration Program (EUDP), grant no. 64018-0068. The supported project is RELIABLADE: Improving Blade Reliability through Application of Digital Twins over Entire Life Cycle.

5. References

1. Patel A, Kravchenko O, Manas-Zloczower I. Effect of curing rate on the microstructure and macroscopic properties of epoxy fiberglass composites. Polymers 2018, 10: pp. 125
2. Morey W, Meltz G, Glenn H. Fiber optic Bragg grating sensors. , In: Proceeding SPIE, Fiber Optic and Laser Sensors VII, 1990.
3. Parlevliet PP, Bersee HEN, Beukers A. Measurement of (post-)curing strain development with fibre Bragg gratings. Polymer Testing 2010; 29: 291–301.

  doi:10.5075/epfl-298799_978-2-9701614-0-0

Predicting fibre wrinkling in binder-stabilised preforms during wind turbine blade manufacturing

Peter Hede Broberg[a,b], Christian Krogh[a], Esben Lindgaard[a,b], and Brian Lau Verndal Bak[a,b]

a: Department of Materials and Production, Aalborg University, Fibigerstræde 16, Aalborg Denmark - phb@mp.aau.dk
b: CraCS Research group, Aalborg University, www.CraCS.aau.dk

Abstract: *Binder-stabilised fibre preforms may be used to decrease production costs of large wind turbine blades by increasing throughput. In this context, preforms are stacks of unidirectional glass fibre non-crimp fabrics (UD-NCFs), pre-consolidated with a polymeric binder. The preforms are manufactured separately and subsequently placed in the casting mould. Limitations of the preform deformations may lead to fibre wrinkling during placement in the casting mould. In this paper, we propose a simulation model capable of predicting fibre wrinkling in preforms such that severe wrinkles may be avoided during wind turbine blade manufacturing. The UD-NCFs are modelled at a macroscale using solid finite elements, and the binder interface is modelled with a bilinear traction-separation law. The model shows good agreement with preform coupon specimens of real thickness and can predict final wrinkle geometry and location.*

Keywords: Forming simulation; Binder-stabilised preform; Wrinkles; Cohesive zone modelling

1. Introduction

Wind turbine blades are steadily increasing in length to increase the power output, with the largest blades now exceeding 100 m. The blades are traditionally manufactured by manual placement of glass fibre mats in the blade mould, leading to long processing times [1]. Therefore, there is a great interest in using binder-stabilised preforms to increase process automation and reduce the production cost of large wind turbine blades. Binder-stabilised preforms are stacks of dry unidirectional non-crimp fabric that are manufactured outside of the main blade mould. The preforms are pre-consolidated with a polymeric binder to stabilise it during the subsequent placement in the main blade mould. When the preforms are placed in the main blade mould, out-of-plane fibre waviness (wrinkles) may arise due to the UD-NCFs not being able to move relative to each other [2,3]. Wrinkles cause a severe reduction of wind turbine blade strength [4-6]. To avoid costly repair or discarding of blades, simulation models have proven useful in predicting wrinkling and obtaining knowledge on the mechanisms leading to wrinkles [7,8]. Generally, fabric forming models can be divided into two categories: kinematic and mechanical models [9]. The kinematic models are numerically efficient and may be used to predict final fibre orientation [10]. However, they do not consider the forming process, which makes them unsuited for predicting wrinkles. On the other hand, mechanical models take more deformation modes and process-related boundary conditions into account and may e.g. be used with commercially available finite element software. The bending stiffness of the fabrics plays a significant role in the final wrinkle geometry and should be included in the model to predict wrinkling accurately [11]. Most mechanical models consider the fabric at a macroscale [7,11]. The challenge with macroscale modelling of fibre structures is that relative fibre movement should be considered, which means that the membrane stiffness of the fabric must be decoupled from the bending stiffness. The purpose of the current paper is to present a preform

  doi:10.5075/epfl-298799_978-2-9701614-0-0

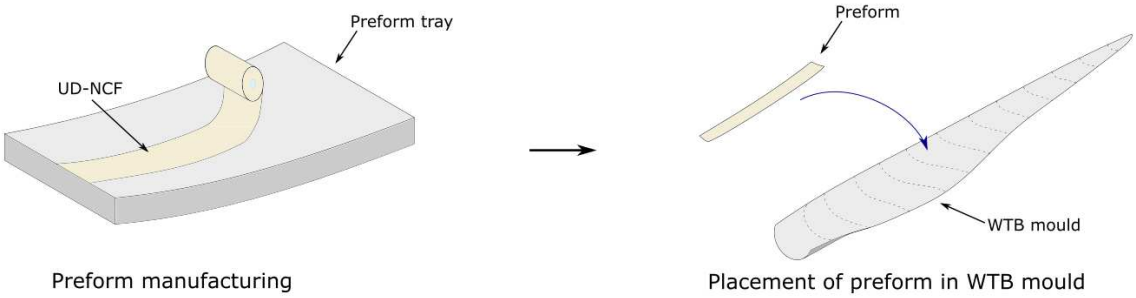

Figure 1. Principle of wind turbine blade manufacturing using binder-stabilised preforms. The preforms are manufactured separately and subsequently placed in the main blade mould.

model made using commercially available software. The preform is modelled using continuum shell elements in ABAQUS with a cohesive interface between each layer.

The rest of the paper is structured as follows: In Sec. 2, the mechanisms leading to fibre wrinkling in preforms are briefly discussed. In Sec. 3, the preform model is presented together with a description of the material characterisation performed. In Sec. 4, the simulation model results are compared to the forming experiments. Sec. 5 contains a discussion on the predictive capabilities of the preform model, and the paper is concluded in Sec. 6.

2. Wrinkling arising during preform forming

Binder-stabilised preforms are manufactured separately and subsequently placed in the main wind turbine blade mould, see Fig. 1. The separation of these two processes makes it possible to increase automation and reduce the cost of produced blades. The preforms considered in this paper consist of stacks of quasi UD-NCF with an areal weight of 1322 g/m^2. The term "quasi" is because the UD rovings are stabilised by a backing layer oriented at $\pm 80°$. The weight percent of the backing fibres is approximately 2wt%, and they are stitched to the UD rovings with a polyester thread in a tricot-chain pattern. The UD-NCF are pre-consolidated at elevated temperatures with a polymeric binder between each layer. Each UD-NCF layer is approximately 1mm, and the preforms consist of 16 layers, which gives it a total thickness of approximately 16mm. The preform considered can be seen in Fig. 2 with the local system of coordinates indicated.

Wrinkling may occur when the preform is formed over geometric transitions, i.e. core material for the sandwich structure in the main blade mould, see Fig. 3. The preform is loaded like a

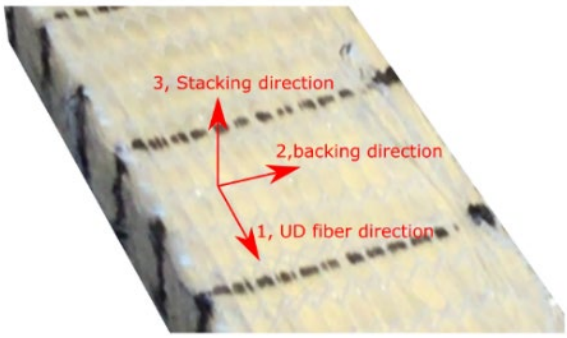

Figure 2. The binder-stabilised preform considered. The preform is made of stacked UD-NCFs with a polymeric binder between each layer [12].

  doi:10.5075/epfl-298799_978-2-9701614-0-0

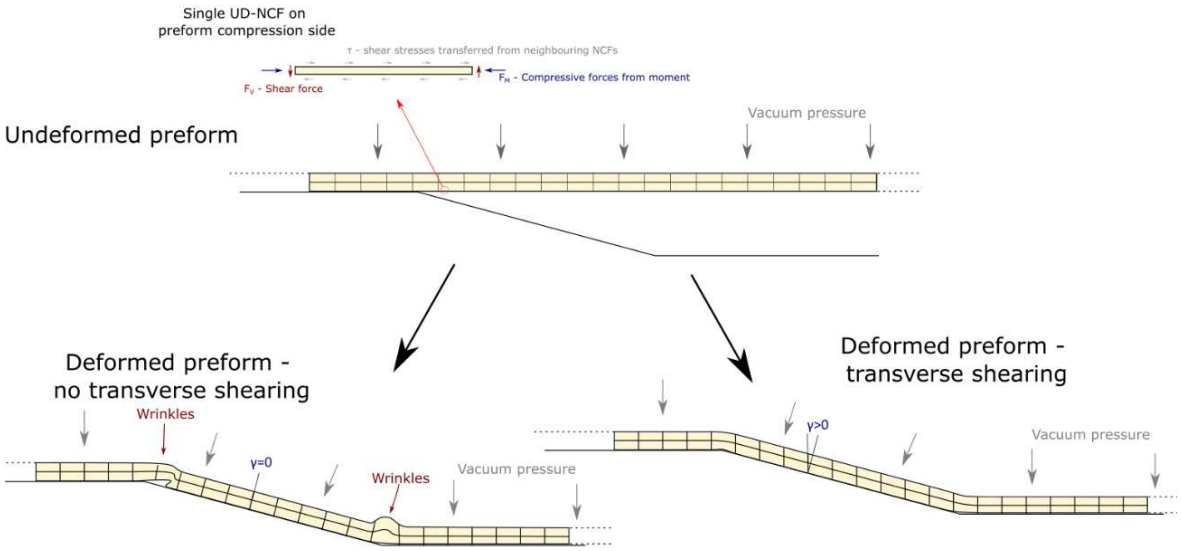

Figure 3. During forming of the preform the NCF layers may either slide relative to each other or buckle out causing fibre wrinkling.

cantilevered beam with a distributed loading during forming over transitions. This results in the individual NCFs experiencing shear stresses transferred from neighbouring mats due to the transverse shear forces and also compression/tension due to the bending moment. As the UD-NCFs have a very high tensile modulus compared to other stiffnesses, it is more likely that the NCFs will buckle or move relative to each other than compress/elongate. There are, thus, two competing mechanisms: fibre sliding and fibre buckling. In one extreme case there will only be fibre sliding due to the transverse shear stresses and no fibre buckling. In another extreme case there is no fibre sliding which makes the UD-NCF buckle leading to fibre wrinkling. During preform forming it is desired to minimise fibre wrinkling and allow the fibres to slide relative to each other. However, the binder material and friction between mats may impede fibre sliding and thereby cause fibre wrinkling. The purpose of the preform model is to predict wrinkling, such that it can be used to find out how wrinkle free-forming can be achieved. The current model considers the preform forming as a 2D problem, i.e. in-plane shearing is not considered.

3. Preform modelling

The preform can be modelled at different scales [12,13]. At the structural scale, the whole preform is considered as a continuum. At the macroscale, each UD-NCF mat is modelled as a continuum and the binder interface is modelled as a homogenous interface. A mesoscale model models the stitching and dispersed binder discretely. The microscale model would make the mesoscale model even more detailed by modelling each fibre individually.

The present model is made at the macroscale to get information on the interface mechanics between each UD-NCF which a structural scale model would not be capable of. The macroscale model is also more computationally efficient than the meso-microscale model.

3.1 Description of the model

The preform is modelled as a 2D structure in the 1-3 plane of the preform, see Fig. 4. The UD-NCF layers are modelled separately using continuum shell elements (SC8R in ABAQUS). Solid elements are used because they improve the contact formulation by describing the interface between individual NCFs with a well-defined geometry (element edges) rather than midline

  doi:10.5075/epfl-298799_978-2-9701614-0-0

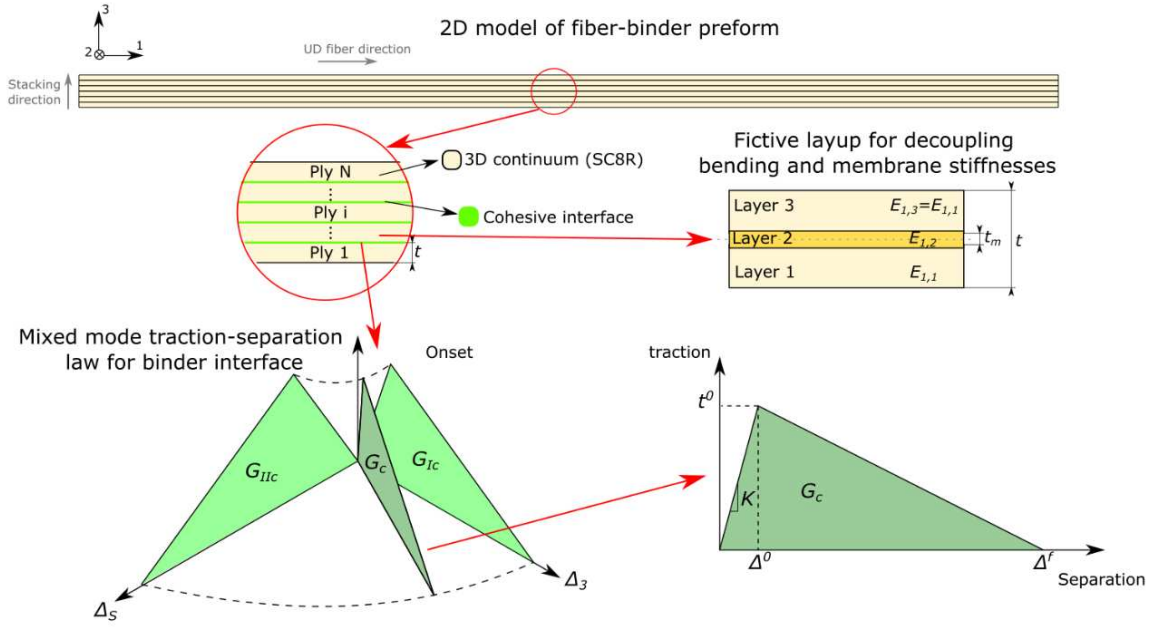

Figure 4. 2D preform model. The individual UD-NCFs are modelled with continuum shell elements with a fictive layup for decoupling membrane and bending stiffnesses. The binder is modelled as a cohesive interface with a mixed mode bilinear traction separation law.

offset as would be the case for shell elements. The model is constrained by plane stress boundary conditions. The bending- and membrane stiffness of the plies have been decoupled using a fictive three-layer laminate layup [14]. The laminate layup consists of a stiff middle layer with stiffness E_2 and thickness t_m and two compliant outer plies with stiffness E_1 and thickness $\frac{t-t_m}{2}$, where t is the total thickness of the fabric. The entries for the axial stiffness, A_{11} , and bending stiffness, D_{11}, in the ABD-matrix of the laminate is given as [15],

$$A_{11} = \sum_k^N (\overline{Q_{11}})_k (z_k - z_{k-1}) \tag{1}$$

$$D_{11} = \frac{1}{3}\sum_k^N (\overline{Q_{11}})_k \left(z_k^3 - z_{k-1}^3\right) \tag{2}$$

Where $\bar{Q}$ is the stiffness of each layer, N is the number of layers, and z_k is the coordinates to the layer edges. By specifying t, t_m, the axial stiffness of the ply, A_{11}, and the bending stiffness of the ply, D_{11}, and inserting in Eq. (1) and (2) a closed-form solution for E_1 and E_2 can be obtained.

The binder interface between the UD-NCFs are modelled as a bilinear mixed mode traction-separation law, see Fig. 4. Damage is initiated once the maximum onset traction is reached,

$$\max\left\{\frac{\langle t_3 \rangle}{t_3^0}, \frac{t_2}{t_2^0}, \frac{t_1}{t_1^0}\right\} = 1 \tag{3}$$

Here t_3 is the tractions normal to the interface, and t_2 and t_1 are the shear stress in both shear directions. The superscript 0 denotes the onset traction. The critical energy release rate is used as the criterion for crack propagation,

$$G = G_I + G_S \geq G_c \tag{4}$$

Where $G_S = G_{II} + G_{III}$, and the critical energy release rate is obtained by interpolation following the Benzeggagh-Kenane criterion [16],

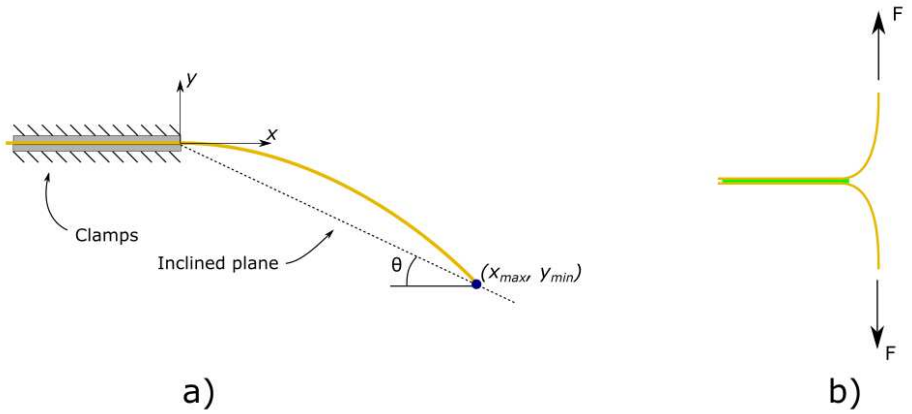

Figure 5. Material characterisation carried out. a) cantilever bending test. b) T-peel test.

$$G_c = G_{Ic} + (G_{IIc} - G_{Ic})B^{\eta},\ B = \frac{G_S}{G_I + G_S} \tag{5}$$

3.2 Material characterisation

Two tests have been carried out to characterise the material properties of the preform: a cantilever bending test, and T-peel test, see Fig. 5.

In the cantilever bending test a linear bending stiffness is estimated from a UD-NCF specimen which is clamped in one end and thus allowed to cantilever under gravity. The dimensions are width $b = 50$mm and length $L = 250$mm. The linear bending stiffness of the fabric can be approximated by Peirce's formula [17,18],

$$D_{11} = \frac{L^3}{8}\frac{\cos\theta/2}{\tan\theta}w,\ \tan\theta = \frac{y_{min}}{x_{max}} \tag{6}$$

Where L is the bent length of the fabric, and θ is the angle of an imagined inclined plane described by the maximum deflection of the fabric (x_{max}, y_{min}). The bending stiffness is estimated to $D_{11} = 0.049$ Nm.

To estimate the mode-I critical energy release rate of the binder interface, a t-peel test has been carried out [19]. From this the critical energy release rate has been estimated by,

$$G_{IC} \approx \frac{2F}{b} \tag{7}$$

where b is the width of the specimen. The mode-I critical energy release rate is measured to 160 J/m^2. A mass (Rayleigh) damping value of 20 is added to the model.

4. Comparison of the model with experimental results

4.1 Experimental forming of preform

The simulation model is compared with forming of full-thickness preform specimens. The full-thickness preforms specimens have a width of 50 mm and length of 1000 mm. The preform specimens are initially straight and are formed over a wedge by vacuum. The wedge dimensions are L = 320 and $\theta_t = 25°$. During the experiment, wrinkles are observed at the wedge transitions, see Fig. 6.

4.2 Comparison

  doi:10.5075/epfl-298799_978-2-9701614-0-0

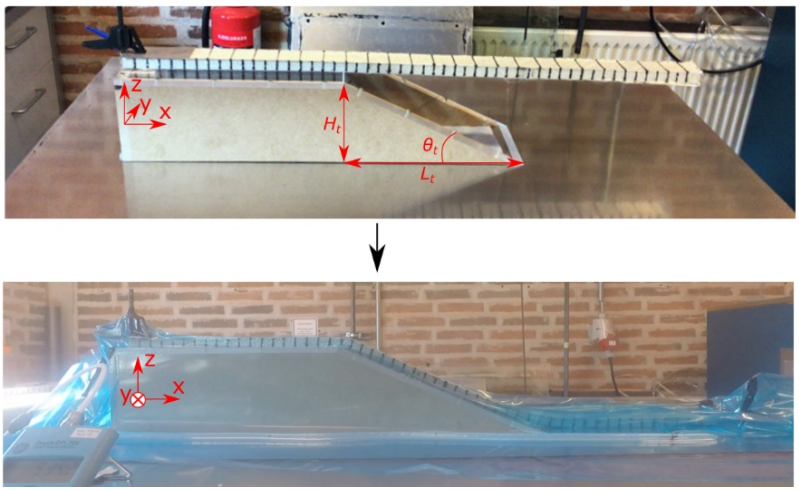

Figure 7. Experimental forming of the preform specimens.

The simulation results compared with the experiments can be seen in Fig. 7. The simulation model predicts wrinkles at the top and bottom transition. It also predicts that there is delamination of the binder material at the wrinkle sites, which is also observed in the experiments. The shapes of the model-predicted wrinkles are the same as observed in the experiments. However, the wrinkles predicted by the model are slightly larger than the wrinkles observed in the experiments, see Fig. 7. At the middle of the transition (termed the shear region in the image), the model predicts shearing of the preform with no delamination of the binder material, which is also observed in the experiments.

5. Discussion

In this paper a binder-stabilised preform simulation model has been proposed. The model can predict the shape and location of wrinkles arising during forming of the preform over geometric transitions. The model predicts binder delamination at the wrinkle sites observed in the experiments. At the middle of the preform (shear region in Fig. 7) the model predicts transverse shearing of the preform with no delamination of the binder. This is in good agreement with the experiments.

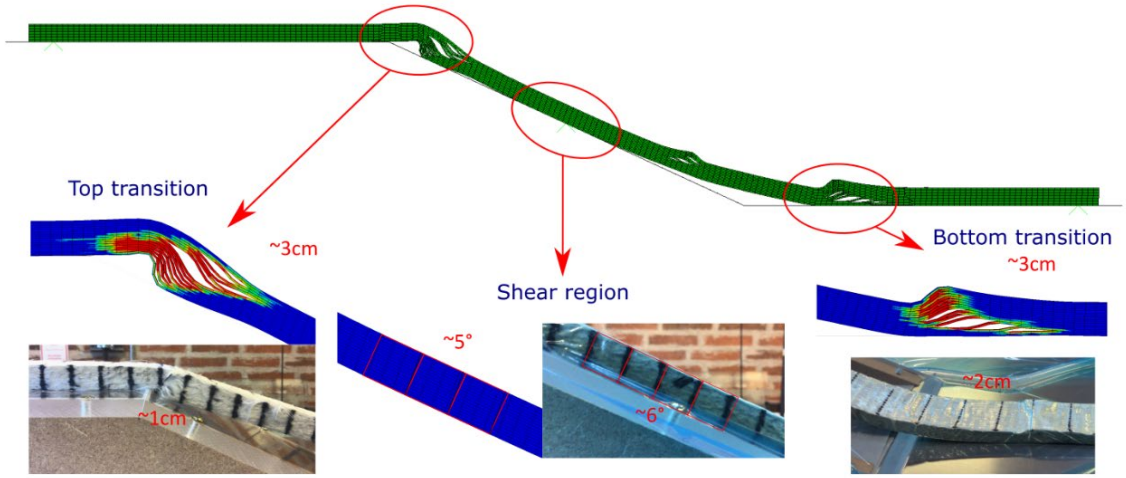

Figure 6. Comparison of the model predictions with the real preform wrinkles. The model predicts the overall shape and location of wrinkles. Red areas indicate delamination of the binder material.

  doi:10.5075/epfl-298799_978-2-9701614-0-0

The wrinkles being predicted by the model are larger than the experimentally observed wrinkles. In the model, the wrinkle at the top transition has a length of approximately 3 cm while the wrinkles in the experiments have a length of approximately 1 cm. At the bottom transition, the model predicts a 3 cm long wrinkle, while the wrinkle in the experiments is approximately 2 cm long, see Fig. 7. This is expected since a linear bending stiffness has been used in the model. The UD-NCFs have a very nonlinear bending stiffness with a high stiffness at low curvatures and low bending stiffness at higher curvatures [18]. The wrinkling at the transitions involves very high curvatures of the fabric resulting in the bending stiffness at these high curvature sites being overpredicted by the model. The wrinkle at the top transition involves higher curvatures than the wrinkle at the bottom transition. Due to this, the difference between model and experimental wrinkle size is larger at the top transition than at the bottom transition.

The transverse shearing of the preform is slightly underpredicted by the model, see Fig. 7. This causes higher compressive loads on the UD-NCF at the wrinkle sites, see Sec. 2, which will result in slightly larger wrinkles predicted by the model. As of now only the mode-I critical energy release rate has been characterised whereas the mode-II value has been fitted to the model. The mode-II critical energy release rate will be higher than the mode-I. A higher mode-II critical energy release rate will make it more difficult for wrinkles to propagate and, therefore, localise the wrinkles.

6. Conclusion

In this paper, a macroscale model for predicting wrinkling during forming of binder-stabilised preforms has been presented. The UD-NCFs are modelled with continuum shell elements, and the binder interface is modelled as a homogenous, cohesive interface. The bending and membrane stiffness of the NCFs are decoupled using a fictive 3-layer laminate layup with a stiff middle layer controlling the membrane stiffness and two compliant outer layers for controlling the bending stiffness. The binder interface is modelled with a bilinear mixed-mode traction separation law. The UD-NCFs linear bending stiffness and the mode-I critical energy release rate of the binder interface have been characterised and inputted in the model. The model is capable of predicting the shape and location of wrinkles. As a linear bending stiffness is used, the size of the wrinkles is slightly overpredicted by the model. In future work, the modelling framework will be extended to include the nonlinear bending stiffness of the NCFs. The enhanced model may be used to accurately predict wrinkles during preform forming such that they can be avoided in wind turbine blade manufacturing.

Acknowledgements

This study was completed as part of the MADEBLADES research project supported by the Energy Technology Development and Demonstration Program, Grant no. 64019-0514

7. References

1. Zangenberg J, Brøndsted P, Koefoed M. Design of fibrous composite preform for wind turbine rotor blades. Materials and Design 2014; 56:635-641.
2. Hallander P, Åkermo M, Mattei C, Petersson M, Nyman T. An experimental study of mechanisms behind wrinkle development during forming of composite laminates. Composites: Part A 2013; 50:54-64.

  doi:10.5075/epfl-298799_978-2-9701614-0-0

3. Yu F, Chen S, Harper LT, Warrior NA. Investigation into the effects of inter-ply sliding during double diaphragm forming for multi-layered biaxial non-crimp fabrics. Composites Part A 2021; 150:106611.
4. Bender JJ, Hallett SR, Lindgaard E. Parametric study of the effect of wrinkle features on the strength of a tapered wind turbine blade sub-structure. Composite Structures 2019; 218:120-129.
5. Bender JJ, Hallett SR, Lindgaard E. Investigation of the effect of wrinkle features on wind turbine blade sub-structure strength. Composite Structures 2019; 218:39-49.
6. Nelson JW, Riddle TW, Cairns DS. Effects of defects in composite wind turbine blades-Part 1: Characterization and mechanical testing. Wind Energy Science 2017; 2(2):641-652.
7. Rashidi A, Belnoue JP-H, Thompson AJ, Hallett SR, Milani AS. Consolidation-driven wrinkling in carbon/epoxy woven fabric prepregs: An experimental and numerical study. Composites Part A 2021; 143:106298.
8. Boisse P, Huang J, Guzman-Maldonado E. Analysis and modeling of wrinkling in composite forming. Journal of Composite Science 2021; 5(3):1-16
9. Sun X, Belnoue JP-H, Thompson A, El Said B, Hallett SR. Dry Textile Forming Simulations: A Benchmarking Exercise. Frontiers in Materials 2022; 9:831820.
10. Krogh C, Bak BLV, Lindgaard E, Olesen AM, Hermansen SM, Broberg PH, Kepler JA, Lund E, Jakobsen J. A simple MATLAB draping code for fiber-reinforced composites with application to optimization of manufacturing process parameters. Structural and Multidisciplinary Optimization 2021; 64:457-471.
11. Boisse P, Colmars J, Hamila N, Naouar N, Steer Q. Bending and wrinkling of composite fiber preforms and prepregs. A review and new developments in the draping simulations. Composites Part B 2018; 141:234-249.
12. Broberg PH, Krogh C, Lindgaard E, Bak BLV. Simulation of wrinkling during forming of binder stabilized UD-NCF preforms in wind turbine blade manufacturing. The 25th International Conference on Material Forming 2022, Braga, Portugal.
13. Bussetta P, Correia N. Numerical forming of continuous fibre reinforced composite material: A review. Composites Part A 2018; 113:12-31.
14. Döbrich O, Gereke T, Diestel O, Krzywinski S, Cherif C. Decoupling the bending behavior and the membrane properties of finite shell elements for a correct description of the mechanical behavior of textiles with a laminate formulation. Journal of Industrial Textiles 2014; 44(1):70-84
15. Jones RM. Mechanics of Composite Materials. Taylor & Francis 1999
16. Benzeggagh ML, Kenane M. Measurement of mixed-mode delamination fracture toughness of unidirectional glass/epoxy composites with mixed-mode bending apparatur. Composites Science and Technology 1996; 56:439-449
17. de Bilbao E, Soulat D, Hivet G. Experimental Study of Bending Behaviour of Reinforcements. Experiments Mechanics 2010; 50(3):333-351
18. Krogh C, Broberg PH, Kepler J, Jakobsen J. Comprehending the bending: A comparison of different test setups for measuring the out-of-plane flexural rigidity of a UD fabric. The 25th International Conference on Material Forming 2022, Braga, Portugal.
19. Schmidt S, Mahrholz T, Kühn A, Wierach P. Powder binders used for the manufacturing of wind turbine rotor blades. Part 1. Characterization of resin-binder interaction and preform properties. Polymer Composites 2018; 53(1):1-12.

  doi:10.5075/epfl-298799_978-2-9701614-0-0

IMPROVEMENT POTENTIAL FOR CFRP PRESSURE VESSELS TO REACH FUTURE REQUIRED GRAVIMETRIC STORAGE DENSITIES

Sebastian Spitzer[a], David Schlegel[ab], Linus Tönnishoff[a], Shiwoo Lee[c], Sang-Eui Lee[c], Maik Gude[a]

a: Institute of Lightweight Engineering and Polymer Technology, Technische Universität Dresden, 01307 Dresden, Germany, sebastian.spitzer@tu-dresden.de; b: Boysen-TU Dresden-Research Training Group, 01187 Dresden, Germany; c: Department of Mechanical Engineering, Inha University, Korea, selee@inha.ac.kr

Abstract: *Hydrogen is becoming increasingly important among the propulsion technologies for the mobility of the future. To achieve the required energy densities of storage systems for gaseous storage, the mass of high-pressure vessels must be reduced while maintaining or increasing the stored amount of hydrogen. This paper provides an overview of the gravimetric storage density of hydrogen pressure vessels available on the market. The mass distribution of those vessels dependent on the weight of the system components. Subsequently, the individual components and their mass savings potential are determined on different scale levels. Physical effects and associated parameters are deduced. The influences of the different parameters in the levels and their potential for further improving the gravimetric storage density are assessed.*

Keywords: Composite pressure vessel; gravimetric storage density; improvement potential

1. Introduction

The US Department of Energy (DoE) calls for an increase of the gravimetric storage density (GSD) of pressure vessels up to 6.5 % [1]. Figure 1 shows the GSD of various hydrogen pressure vessels, their application scenario and the target of GSD demanded by the U.S. Department. Apart from LH_2 vessels in aircraft and space, no storage systems in use meet the required density.

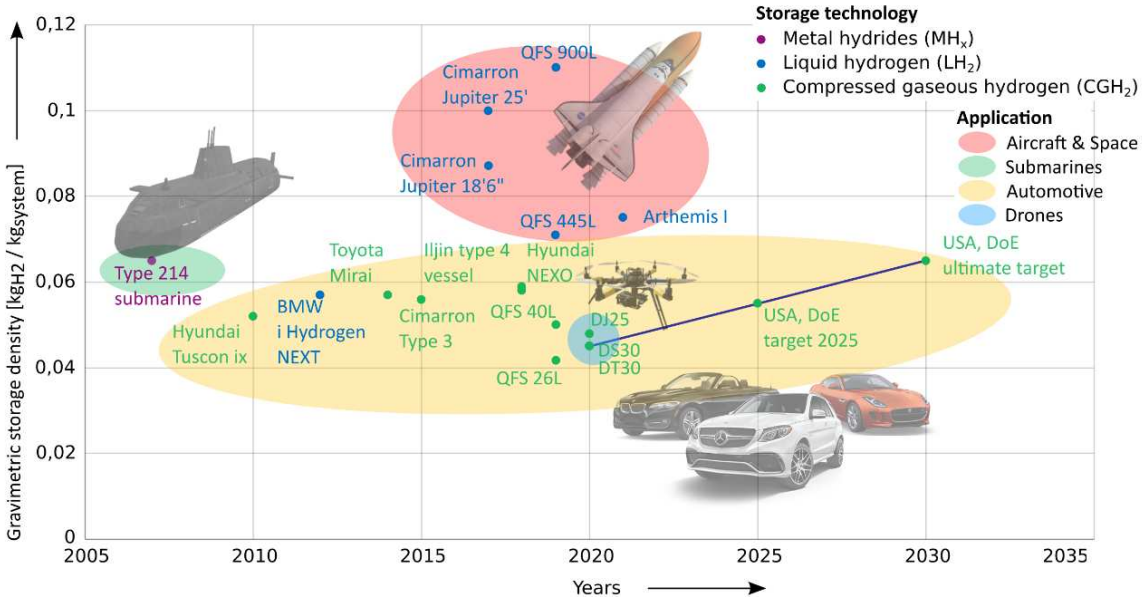

Figure 1. Gravimetric storage density of commercially hydrogen vessels, their application scenario and the storage density postulated by the US Department of Energy [1] (line)

The GSD is defined as the hydrogen mass in relation to the storage system mass:

$$\eta_{gravim} = \frac{m_{H_2}}{m_{H_2}+m_{System}} \quad . \tag{1}$$

2. Storage System and Mass Distribution

The most established storage pressures in industrial applications are 35 MPa and 70 MPa. Figure 2 shows two type 4 tanks with a polymer liner and dome protection. The vessel from Doosan Mobility Innovation (Figure 2, left) is designed for a working pressure of 35 MPa. This vessel is meant for the use in fuel cell driven drones, has aquired European Transportable Pressure Equipment Directive (TPED) certification and was subjected to a drop test from 150 m, penetration, fire and internal pressure test [4]. The vessel from Iljin Hysolus (Figure 2, right) is certified after Korea Gas Safety Corporation (Korea), EC79 certified products & hydrogen applications (Europe), UN Regulation (UNR) for Hydrogen-Fuelled Vehicles of Categories L1, L2, L3, L4 and L5 (UNR134, global) and Japan High Pressure Gas Control Law (KHK, Japan) for 70 MPa working pressure. It is meant for the use in various commercial vehicles, like forklifts, ships and trains as well as passenger cars [5]. In mobile systems, a high volumetric storage density is usually also required. Fundamental investigations to increase the GSD are independent of the working pressure of the vessel. Though the comparison with the targets of the US DOE is only reasonable for the 70 MPa technology, as the targets for the volumetric storage density may not be reached by a 35 MPa vessel.

Figure 2. Commercially available hydrogen high-pressure vessel with 35 MPa storage pressure from Doosan [4] (left) and 70 MPa storage pressure from Iljin [5] (right)

In order to provide hydrogen effective, efficient and safe in mobile applications, a multitude of single components are necessary (cf. Figure 3, left). A type 4 hydrogen storage system consists of the load bearing composite shell, liner, valves, pressure control system, sensors, dome protection and others (cf. Figure 3, right), which contribute to the GSD.

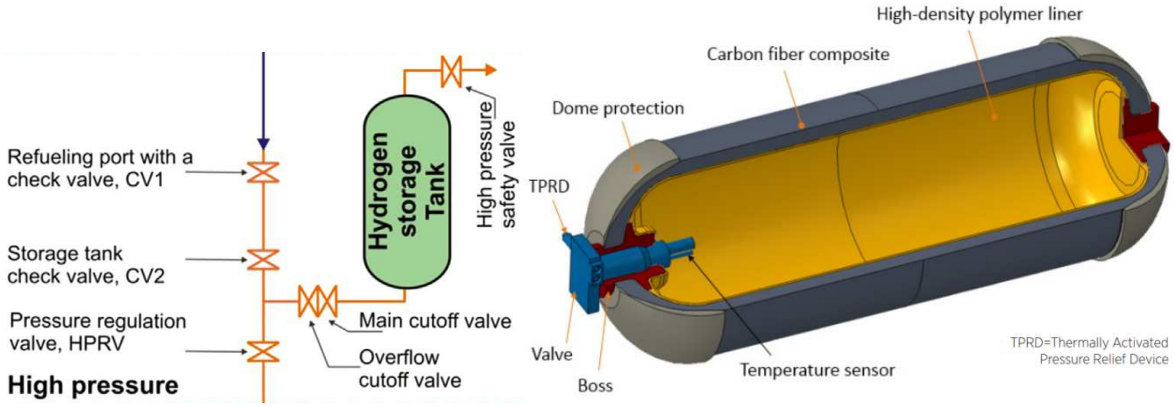

Figure 3. Schematic hydrogen storage system with typical components (left) [3], subsystem of a type 4 pressure vessel with load bearing composite shell, liner and valve (right) [2]

3. Identification of Mass saving Possibilities on different Scales

For the effective development of high-performance composite structures, the building block approach of the Composite Materials Handbook 17 [6] is proposed. Starting from the fundamentals of the material at the coupon level, the entire system can be designed by progressively elaborating and validating the configurations at the levels in between. At each level, the design, manufacturing and material aspects must be considered, following an interactive approach. Figure 4 shows the different elements of the entire high-pressure storage system and the associated functions, starting with the material substances.

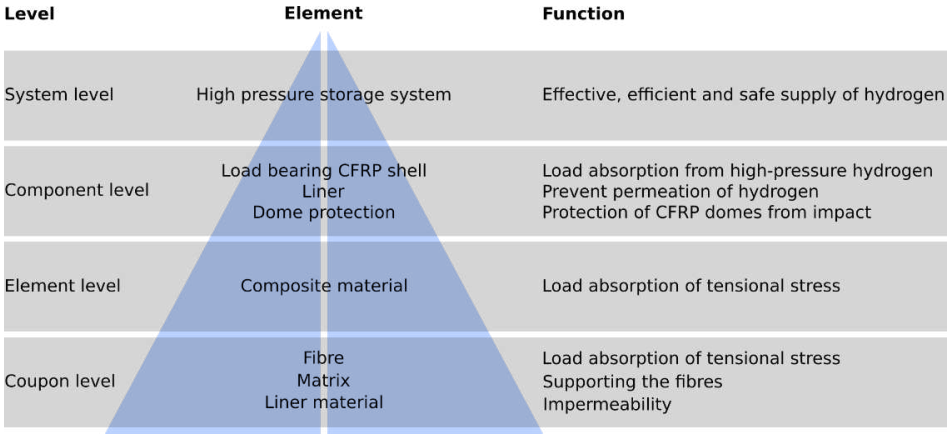

Figure 4. Polymer related levels of the storage system according to the building block approach [6] (left), the associated elements (centre) and its functions (right)

System level: A mass analysis of the single components enables the identification of the decisive parameters for increasing the GSD at system level. Figure 5 shows the weight distribution of two representative composite pressure vessels. The vessel with a working pressure of 35 MPa has an empty system mass of 98.5 kg and a mass of stored hydrogen of 6.0 kg, which leads to a GSD of 5.7 %. The pressure vessel with a working pressure of 70 MPa has an empty mass of 121.6 kg and a mass of stored hydrogen of 5.8 kg, which leads to a GSD of 4.5 %. The complete 70 MPa vessel has a volume of 224.0 l whereas the 35 MPa vessel has a volume of 316.4 l, which shows the advantage of the higher pressure in terms of volumetric storage density.

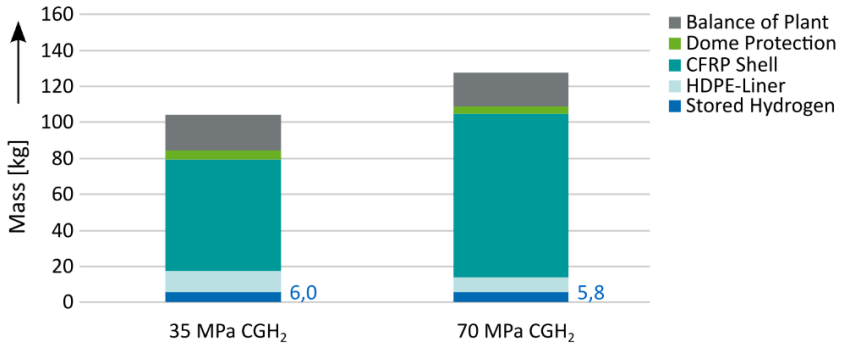

Figure 5. Mass distribution in type 4 vessels for 35 MPa (left) and 70 MPa (right) based on [8]

This analysis shows, that the largest share of the mass of a type 4 vessel is accounted by the load-bearing composite shell, followed by the balance of plant and the liner. The balance of plant includes valves, filters, temperature and pressure transducers, pressure regulators, thermally activated pressure relief devices, mounting hardware and piping [8].

On system-level the influence of the pressure and the geometry are analysed. Equation 1 shows, that the mass of the load bearing CFRP is directly proportional to the burst pressure and to the volume of the vessel. As the density of hydrogen does not behave proportional to the pressure (cf. Figure 6), the GSD is decreasing with increasing pressure. Therefore, a compromise between volumetric and gravimetric storage density must be found.

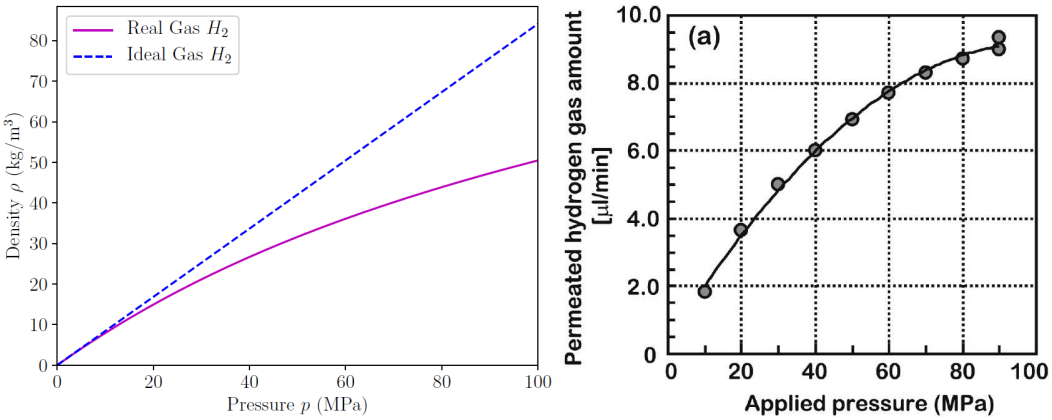

Figure 6. Comparison of the ideal gas equation and the real gas properties of H_2 [12] (left) and the permeation of H_2 gas amount depending on the internal pressure [13] (right)

The ideal composite shell is isotensoid and thus maximally weight efficient. The following equation describes the mass of any ideal pressurized composite shell of revolution m_{CFRP} [7]:

$$m_{CFRP} = 3 * \rho_{CFRP} * \frac{\overline{p} * V}{\overline{\sigma}_1}, \tag{2}$$

with ρ_{CFRP} density of CFRP, $\overline{p}$ internal pressure, V volume and $\overline{\sigma}_1$ tension. The mass of the load-bearing CFRP is directly proportional to the volume of the vessel, which limits the gravimetric storage density. It assumes the perfect isotensoid laminate. This means that geometric investigations must always take place on system level considering technological limitations.

Component level: Geodesic winding (cf. Figure 7, left) is the established technology for composite pressure vessels. The dome contour is defined in a way, that when overwound, the fibres lay in the direction of the principal tension stress. The challenge is the realization of the structurally-required ideal wall thickness in every point, to reach the isotensoid stress state (cf. Figure 7, right).

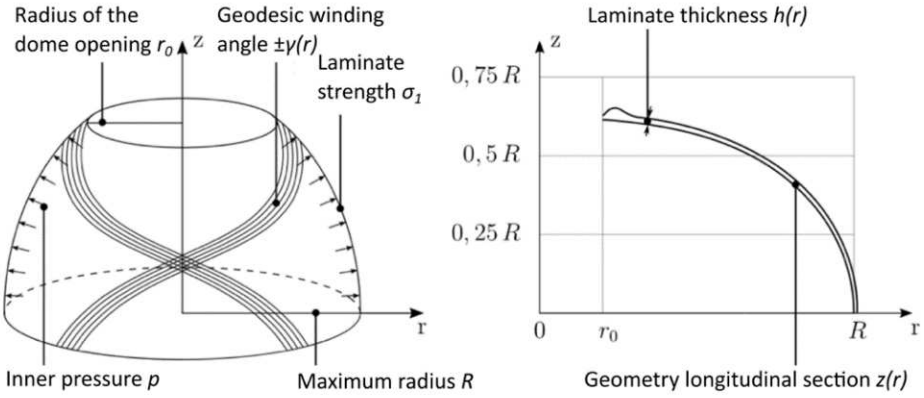

Figure 7. Schematic representation of the input parameters (left) and the output parameters (right) according to VASILIEV's design concept under the condition of geodesic winding

To realize a continuous winding process, the fibre angle needs to be 90° at the opening of the pressure vessel. With this boundary condition and the given dome contour a specific fibre angle results in the cylindrical part of the vessel. To accommodate the circumferential stress in this cylindrical area, additional circumferential windings are necessary. Using this method, the laminate can be adjusted very accurately in the cylindrical area, in terms of stiffness and strength gradients and wall thickness.

The technological necessity of a 90° angle at the dome opening leads to an overlay of all rovings in this area. This material build-up is not structurally necessary, and thus represents an over-dimensioning of the composite laminate. The bigger the vessel diameter gets, the more significant becomes the material lay-up. Therefore, the gravimetric storage density decreases with increasing vessel diameter.

To optimize the dome design for a better gravimetric storage density, while considering the technological implications of the geodesic winding process, a staggering of the turnaround areas is proposed by VASILIEV (cf. Figure 8).

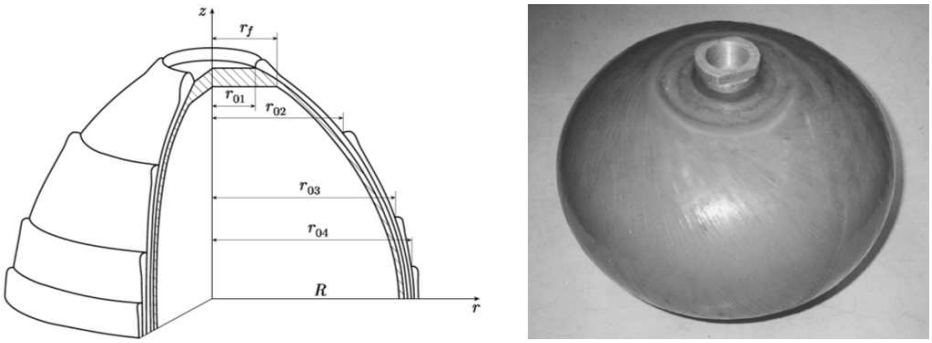

Figure 8. Schematic representation of a staggered turnaround area for a pressure vessel dome (left) and a filament wound pressure vessel using this method (right) [7]

Such an optimization of the winding process leads to a closer representation of the structurally required laminate thickness distribution. The change of the turnaround diameter leads to changed geodesic fibre angles that need to be considered in the design and dimensioning process. This means the pole geometry needs to be adjusted to align the fibres on the principal tension stress through the geodesic winding process.

In the life cycle of composite pressure vessel, it is common that micro cracks appear in the CFRP laminate [7]. As the tensile load in the laminate acts in the direction of the fibres, this has no significant structural implications, but these microcracks allow hydrogen to permeate through the composite shell. To prevent this from happening a liner is used, which makes up typically around 5 - 11 % of the vessel mass [8]. With a low surface to volume ratio, the liner mass relative to the hydrogen mass decreases. Therefore, the ideal geometry for a minimal liner mass is a sphere. The liner thickness is influenced by the pressure. As the permeated hydrogen gas amount increases with increasing pressure (cf. Figure 6, right), the liner must be designed thicker in order to realise a comparable diffusion barrier. Assuming a constant hydrogen mass, the vessel needs to become smaller with increasing internal pressure, leading to a smaller surface area and thus decreasing the liner mass. The sensitivities of these variables depend largely on the geometry of the vessel and therefore the analysis of the liner mass dependency needs to be done for the specific use case.

The integration of the permeation barrier in the CFRP laminate could save mass and thus increase the gravimetric storage density. This type of pressure vessel is called type 5 tank, and is subject to ongoing research. The exclusion of a liner has implications for the manufacturing process, as the liner usually acts as a winding core. The necessary requirements for the matrix material must be discussed on the coupon level (cf. Figure 4).

A further option to save weight is to omit or to substitute the dome protections. Integrated extra glass fibre layers in the CFRP shell might be an option. Therefore, the assembly and operating instructions should be formulated in a way, that the protection would be unnecessary. Although this would have implications on the handling and the qualification of the personnel responsible for the handling.

Element level: The element level includes parameters of the specific (non-generic) sub-areas of the pressure vessel. The laminate consists of generic parameters, that will be discussed on the coupon level, and specific parameters, that are part of the element level.

A specific parameter is the fibre volume content of the curved shell, which is influenced by the viscosity of the resin, the roving type, the roving tensioning in the winding process and the consolidation and hardening process. Through a higher fibre volume content, the tensile strength of the laminate increases, thus reducing the wall thickness necessary to support the pressure induced loads. Another influence on the CFRP strength poses the undulations. As undulations represent deviations from the principal stress direction, they are to be avoided as much as possible. Using a suitable winding pattern, undulations may be avoided almost entirely.

Coupon level: The elongation of the carbon fibre under load, leads to a strain in the matrix of the neighbouring CFRP layers. To prevent an inter fibre failure, the fracture strain of the carbon fibre $\bar{\varepsilon_1}$ needs to be smaller than the fracture strain of the matrix [7]:

$$\bar{\varepsilon_1} < \bar{\varepsilon_2}. \tag{3}$$

Following equation 2 the necessary CFRP mass of the pressure vessel is proportional to the laminate strength in fibre direction. Thus, the fibre strength has a direct influence on the vessel mass. Commonly the T700S fibre is used for composite pressure vessels. With a tensile strength of 4900 MPa it is suited very well for this application [8]. Fibres like the T1100G reach a tensile strength up to 7000 MPa and can contribute to incise the GSD.

To integrate the permeation barrier in the CFRP laminate, as described in Chapter 4.3, the matrix needs to be modified to prevent hydrogen permeating. There are two different kinds of permeation to be considered. The first one is the diffusion of hydrogen through the matrix. This takes place on a molecular level, and may also be prevented through the modification of the resin or is accepted in combination with a sufficient ventilation. The second kind of permeation to be considered is a leakage that may take place through the mechanically induced micro cracks. This may be prevented through an according selection of the matrix system ($\bar{\varepsilon_1} < \bar{\varepsilon_2}$). This is usually done by additives [9].

Gravimetric Density Improvement Potential and corresponding Parameter

The main effect is the internal pressure *p* of the vessel. The resulting loads are to be endured by the load bearing CFRP shell, which makes up the biggest proportion of the total vessel weight. Hydrogen specific effects are the permeation and the embrittlement of materials in a hydrogen

environment. Both effects are considered by a liner. To omit the liner, the corresponding functions as a permeation barrier and a protection against embrittlement need to be incorporated into the composite shell. Without liner, the GSD of the 35 MPa storage system could be increased from 5.7 % to 6.5 %. The GSD of the 70 MPa storage system can be increased from 4.5 % to 4.9 %.

A T1100G laminate with 60 % fibre volume content has a tensile strength of 3460 MPa. This is approx. 21 % higher than the tensile strength of a comparable T700S laminate with a strength of 2860 MPa. This suggests that the mass of the load-bearing CFRP can be reduced by about 17 %, which means that the gravimetric storage density of the 35 MPa storage system can theoretically be increased to 6.4 %. Thus, the gravimetric storage density of the 70 MPa storage system can be increased to 5.2 %.

In the following, the influence of overdimensioning due to production technology restrictions is considered. Based on a fibre volume content of 60 %, the density of a T700S/epoxy resin composite is 1.56 g/cm^3. According to the data sheet, this results in a tensile strength of 2860 MPa. For the approval for the use in automobiles, a safety factor of 2.25 is applied on the nominal working pressure [11]. This results in a design pressure of 157.5 MPa for the 70 MPa vessel. According to Equation 2, the volume of 145.2 l results in a mass of 37.4 kg for the ideal isotensoid load-bearing fibre-plastic composite. Thus, the gravimetric storage density may be increased up to 7.8 %. Considering the same safety factor, the design pressure of the 35 MPa vessel results in 78.75 MPa. With the volume of 250.4 l, Equation 2 gives a mass of 32.3 kg for the ideal isotensoid load-bearing CFRP shell. Thus, the gravimetric storage density may be increased up to 8.0 %.

Table 1 summarises the potential for improvement for the two established storage pressures of 35 MPa (10.3 %) and 70 MPa (9.4 %).

Table 1: Potential improvements of a CFRP pressure vessel on its gravimetric storage density

	Baseline	High strength fibre	Isotensoid CFRP shell	No dome protection	No liner (Type V tank)	Total
35 MPa	5.7 %	6.4 %	8.0 %	6.0 %	6.5 %	10.3 %
70 MPa	4.5 %	5.2 %	7.8 %	4.7 %	4.9 %	9.4 %

Conclusion

The US Department of Energy requires a gravimetric storage density of 6.5 % for mobile pressurised hydrogen storage by 2030. Practically all commercially available systems, except Space, have a storage density between 4 % and 6 % and currently do not meet the requirements set for the future.

The storage density is largely determined by the operating storage pressure. 35 MPa and 70 MPa systems are established on the market, whereby the higher pressure has a negative effect on the gravimetric storage density due to the resulting higher demands on the individual components of the storage system, e.g. CFRP load baring shell, media-tight liner. Basically, 70 MPa systems have a physically justified lower gravimetric storage density compared to 35 MPa

systems. In mobile systems, a high volumetric storage density is usually also required. Therefore, investigations to increase the storage density refer to the more demanding 70 MPa technology. This paper analyses potentials for increasing the storage density on different scales of the system, from the material level (coupon) via the component level to the overall system. At each level, measures are identified that can lead to an increase in storage density. For example, by improving the manufacturing technology for isotensoid deposition of fibre layers without imperfections in relation to the supporting structure (manufacturing approach), the utilisation of the material can be improved. The use of high-strength fibres can also lead to an increase in efficiency (material approach). In addition to these two technological approaches, the storage density can also be achieved by reducing the loads during assembly and use (usage approach).

The target storage density of 6.5 % can be achieved through a combination of improvement measures. The parameters to be improved for this are proposed.

References

1. US Department of Energy (2017): Targets for Onboard Hydrogen Storage Systems for Light-Duty Vehicles.
2. Rivard, Etienne; Trudeau, Michel; Zaghib, Karim (2019): Hydrogen Storage for Mobility: A Review. In: *Materials (Basel, Switzerland)* 12 (12).
3. Salvi, B. L.; Subramanian, K. A. (2015): Sustainable development of road transportation sector using hydrogen energy system. In: *Renewable and Sustainable Energy Reviews* 51, S. 1132–1155.
4. Doosan Mobility Innovation. (14.03.2022); www.doosanmobility.com/en/products/hydrogen-tank/
5. ILJIN Hysolus. (14.03.2022); www.composite.co.kr/eng/product/prd_info.jsp?cd=101215
6. National Institute for Aviation Research (2012): Composite Materials Handbook - Polymer matrix composites - materials usage, design, and analysis. Warrendale, Pa. (SAE-R, SAE-R-424).
7. Vasiliev, V. Composite Pressure Vessels. Moscow: Bull Ridge Publishing, 2009.
8. Stolten, Detlef; Samsun, Remzi C.; Garland, Nancy (2016): Fuel Cells. Data, Facts and Figures: Wiley-VCH Verlag.
9. Newhouse, Norman L. (2016): Development of Improved Composite Pressure Vessels for Hydrogen Storage. US Department of Energy.
10. Hua, Thanh; Rajesh, Ahluwalia; Peng J-K; Kromer, Matt; Lasher, Stephen; McKenney, Kurtis et al. (2010): Technical Assessment of Compressed Hydrogen Storage Tank Systems for Automotive Applications. Argonne National Laboratory. Argonne, Illinois, US.
11. UNECE (2019): Regelung Nr. 134 - Einheitliche Bestimmungen für die Genehmigung von Kraftfahrzeugen und Kraftfahrzeugbauteilen hinsichtlich der sicherheitsrelevanten Eigenschaften von mit Wasserstoff und Brennstoffzellen betriebenen Fahrzeugen (HFCV) [2019/795].
12. Macher, Johannes; Hausberger, Andreas; Macher, Astrid E.; Morak, Matthias; Schrittesser, Bernd (2021): Critical review of models for H2-permeation through polymers with focus on the differential pressure method. In: *International Journal of Hydrogen Energy* 46 (43), S. 22574–22590.
13. Su, Ying; Lv, Hong; Zhou, Wei; Zhang, Cunman (2021): Review of the Hydrogen Permeability of the Liner Material of Type IV On-Board Hydrogen Storage Tank.

COATING OF LFP/GRAPHENE OXIDE ON CARBON FIBRES AS POSITIVE ELECTRODES FOR STRUCTURAL BATTERIES

Johanna Xu[a], Zhenyuan Xia[a,], Jaime S. Sanchez[a], Mrcus Johansen[a], Fang Liu[a], Leif E. Asp[a]

a: Industrial and Materials Science, Chalmers University of Technology, Sweden
johannax@chalmers.se

Abstract: *Structural battery composites are carbon fibre-based materials with the ability to simultaneously carry mechanical load and store electrical energy. This study investigates a method for manufacturing structural positive electrodes via electrophoretic deposition (EPD). Electrostatic forces on different scales are exploited in the EPD process. On the nanoscale, electrostatic interactions are employed for self-assembly of the nanometric components, followed by EPD on the macroscale with carbon fibres immersed in organic solution to attract the nanoscale components. Hereby, we use $LiFePO_4$ as the active material, where electrochemically exfoliated graphene oxide (EGO) is compared with reduced graphene oxide (rGO) as a multifunctional carbon additive.*

Keywords: Carbon fibres; Coating; Multifunctionality; Electrophoretic deposition

1. Introduction

The increased interest in electrical vehicles in the automotive and aeronautical industries has expedited the need to increase energy storage capability in cars and airplanes. The challenge is the need to add large batteries while maintaining a low vehicle weight. Weight reduction is often achieved using lightweight composite materials, typically based on polymers and carbon fibres. Multifunctional composites that can simultaneously store and deliver electrical energy while carrying mechanical loads have been coined as “structural batteries”. The concept is to employ carbon fibres for mechanical performance and as electrodes. A lithium-ion conductive multifunctional polymer electrolyte matrix is used for mechanical load transfer between fibres and for ion transport and electrical insulation between electrodes [1].

Carbon fibres are particularly suitable for this type of multifunctional use, as graphitized carbon is commonly used in high performance composite materials and electrodes in batteries. Research from the past decade shows that carbon fibres can perform on par with ordinary graphite-based commercial electrode materials [2]. The ability for commercially available PAN-based fibres to host lithium is close to that of the theoretical maximum for pure graphite. Jacques et al. studied the effect of intercalation on mechanical properties and concluded that the fibres retain their stiffness after lithium-insertion but suffer a small drop in strength [3]. This decrease in strength has a negligible practical effect since carbon fibre composites are generally not designed for strength. Repeated ion insertion/extraction (charging/discharging) of the fibres did not reveal further degradation of their tensile properties.

Important efforts towards realising structural batteries have been made by improving the ion conductivity while maintaining the stiffness of the structural battery electrolyte (SBE). These two properties in many cases counteract each other, i.e. it is possible to achieve a high ion conduction but then without mechanical rigidity, or vice versa. A two-phase (or bi-continuous)

structural electrolyte containing conventional liquid solvent/Li-salt electrolyte with a bis-phenol-A based methacrylate monomer was demonstrated by Ihrner et al. [1], where a homogenous liquid upon solidification transforms to heterogenous material with two percolating phases, where one phase determines the ion transport and the other mechanical load transfer. Photoinduced free radical polymerization of the monomer system was used to make the fully phase separated SBE with two percolating intermingled phases, obtaining a stiffness of ~500 MPa while simultaneously having ion conductivities in the range of 10^{-4} S cm^{-1}. Schneider et al. [4] later demonstrated a thermally induced polymerization route, more suitable for carbon fibre systems. The thermally cured SBE has a pore size in the range of 50-200 nm, and exhibits similar modulus and ionic conductivities as its UV-cured predecessor. Further, it was demonstrated that the thermal curing could be performed in presence of carbon fibres without any impact on the curing rate, enabling laminated structural battery composites to be realised [5].

Unlike the research done on the negative electrode, to date, only a few studies have been performed to realise structural positive electrodes. While as-received carbon fibres embedded in SBE constitutes a structural negative electrode lamina, carbon fibres intended as positive electrode require functionalization with lithium compounds. Among various active materials available, lithium iron phosphate ($LiFePO_4$, or LFP) is a suitable positive electrode material, due to its high theoretic specific capacity of 170 mAh g^{-1}, non-toxicity and chemical stability. However, its intrinsically low electronic conductivity of about 10^{-11} S m^{-1} prevents sufficient electron transport pathways, which leads to large energy loss in charge/discharge at high cycling rates. By introducing additives to the active material, the issue of poor electronic conductivity is overcome. However, it is a challenge to achieve high practical electrochemical capacity for the synthesized carbon fibre structural positive electrodes. In 2018, Hagberg *et al.* [6] described a path to manufacture structural positive electrodes via electrophoretic deposition (EPD) of LFP, carbon black, and polyvinylidene fluoride (PVDF) binder onto carbon fibres. Electrochemical characterisation of the electrode in a half-cell setup with liquid electrolyte demonstrated a specific capacity of ~ 110 mAh g^{-1}, with good rate performance and high coulombic efficiency. Bouton et al. [7] used a repeated dip-coating process to generate a layer-by-layer assembly of LFP particles as an alternative method to achieve LFP coated carbon fibres with a specific capacity close to 100 mAh g^{-1}. Electrophoretic deposition was also used by Sanchez et al. [8] to produce carbon fibres coated with LFP and exfoliated graphene oxide (EGO), achieving ~ 130 mAh g^{-1}. A full cell was assembled using these coated fibres as positive electrode and pristine fibres as negative electrode in a liquid electrolyte, with an energy density of 222.1 Wh·kg^{-1} and a maximum specific power of 290.9 W·kg^{-1} with excellent long-term cycling stability of 88.1% over 300 cycles.

The present study is an extension of the study by Sanchez et al. [8], where we use the same method for functionalization and coating of the carbon fibres intended as structural positive electrodes. Electrostatic forces on different scales are exploited in the EPD process. On nanoscale electrostatic interactions are employed to assemble LFP particles with 2D nanosheets of graphene. On macroscale electrostatic forces are used to charge the carbon fibres in an organic solution to attract the LFP particles through EPD. The focus is on the comparison between electrochemically exfoliated graphene oxide (EGO) and reduced graphene oxide (rGO) as a multifunctional additive to the active material.

241/716 ©2022 Xu et al. doi:10.5075/epfl-298799_978-2-9701614-0-0 published under CC BY-NC 4.0 license

2. Material and methods

2.1 Materials

Ultra-thin TeXtreme® spread tow UD tapes of T800SC-12k-50C PAN-based carbon fibres with a linear weight of the fibres of 0.52 g/m were supplied by Oxeon AB, Sweden. The as-received fibres were treated by refluxing in chloroform to remove the sizing agents. EGO was prepared using a method based on direct electrochemical exfoliation of graphite flakes, as previously reported by Xia et al. [9]. rGO was supplied by NanoGrafen.
The EPD bath contained $LiFePO_4$ with an average particle size of 3.5 µm, carbon black (CB, Super P), poly diallyldimethylammonium chloride (PDDA), and either EGO or rGO, dispersed in dimethylformamide (DMF) and ethanol, respectively.

2.2 Synthesis of lithium iron phosphate coated carbon fibres

A schematic of the EPD setup is shown in Figure 1. The working electrode (WE) consisted of a 60 mm x 15 mm bundle of desized carbon fibres, and a stainless-steel served as the counter electrode (CE) and was fixed parallel to the carbon fibres at a distance of 40 mm. The carbon fibre tow WE was connected to the negative output and the CE to the positive output with an applied DC voltage of 70 V for 10 min.

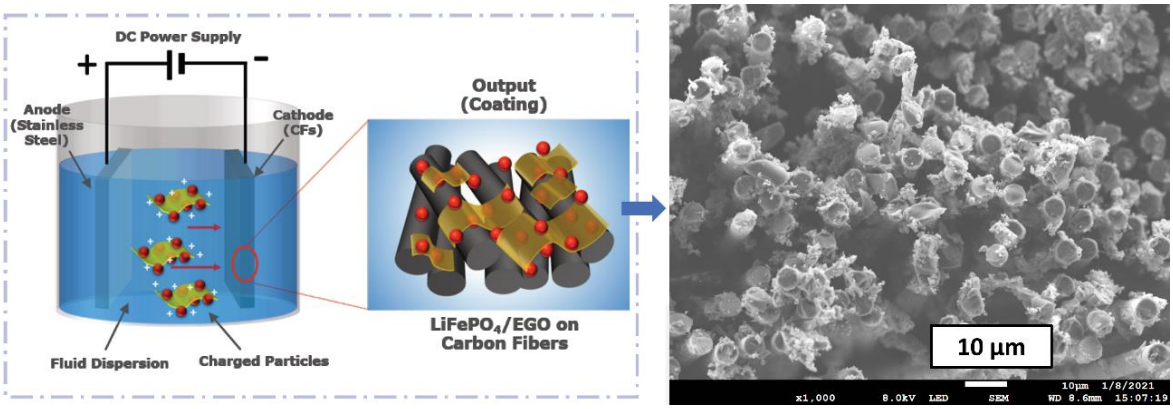

Figure 1. Schematics of the EPD process with EGO and resulting uniformly coated carbon fibres

2.3 Measurement of Electrochemical characteristics

For electrochemical cycling experiments, a pouch cell design was used. A half-cell setup was used with lithium metal as counter electrode, a glass microfiber filter separator (Whatman GF/A, 260 µm thick) was saturated with electrolyte (0.4 M LiBoB and 0.6 M LiTf in EC:PC 1:1 wt/wt.). Galvanostatic cycling at different rates was carried out using a potentiostat (SP-300, BioLogic). All cycling was carried out between 2.6 – 4.2 V.

2.4 Manufacturing of the structural electrode

The bi-continuous structural battery electrolyte (SBE) was prepared by mixing the liquid electrolyte with monomer Bisphenol A ethoxylate dimethacrylate (M_n ~ 540 g mol^{-1}) and initiator 2,2'-azobis(2-methylpropionitrile) (AIBN) 50:50 % wt. The SBE solution was prepared and added to the coated fibres in accordance with the procedure described by Asp et al. [10].

2.5 Characterization of interface for mechanical load transfer

The adhesion of the SBE/coated carbon fibre interface was investigated using scanning electron microscopy (SEM). Each sample was immersed in de-ionised water and then dried to remove the liquid electrolyte phase from the SBE prior to SEM-imaging.
Cross-sections for imaging were generated by broad ion beam (BIB) in a PECS II (precision etch and coating system) from Gatan. To mitigate ion beam-induced damage, the samples were cryogenically cooled to -50 °C. The samples were milled for 4 hours by an Ar^+ beam at 6 kV acceleration voltage. A Zeiss Gemini SEM 450 with field emission gun (FEG) source and accelerating voltage of 10 kV was used to image the BIB-milled cross sections.

3. Results

In Table 1 the performance of the two materials is presented. **Error! Reference source not found.**a shows the cyclic voltammetry (CV) of the EGO and rGO samples at a scan rate of 0.1 mVs^{-1} in a voltage range of 2.6 – 4.2 V vs Li^+/Li. Both samples show typical oxidation/reduction peaks during the anodic/cathodic scan arising from the reversible faradaic redox reaction Fe^{2+}/Fe^{3+} in $LiFePO_4$ particles. The EGO sample shows higher specific currents and stored charge compared to rGO, as the area under the CV curves is directly related to the amount of stored charge. The stability and decay of the two samples under galvanostatic cycling at different C-rates of 0.1 C, 0.2 C, 0.5 C, 1 C, and 2C is shown in **Error! Reference source not found.**b. The performance of both samples decreases with increasing C-rate; however, this process is reversible, and the initial capacity is restored upon returning to 0.1 C. This excludes degradation processes, such as debonding of the active material or detachment of fragments.

Table 1. Comparison of electrochemical performance of $LiFePO_4$ electrodes via EPD.

Sample	Specific capacity (mAh/g) at 0.1 C	Mass loading (mg/cm^2)	Cyclic behaviour 100 cycles at 2 C, (%)
EGO	106.4	5.3	91.5
rGO	111.6	1.5	90.3

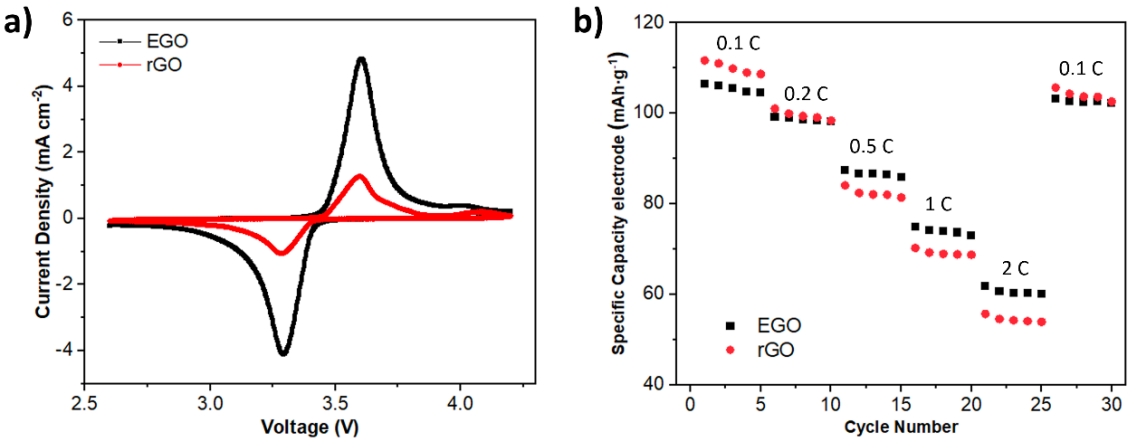

Figure 2. a) Cyclic voltammetry of the EGO and rGO samples at a scan rate of 0.1mV/s in 2.6-4.2 V vs Li^+/Li. b) Specific capacities (normalized over the total electrode mass) of the two samples at various C-rates.

243/716 ©2022 Xu et al. doi:10.5075/epfl-298799_978-2-9701614-0-0 published under CC BY-NC 4.0 license

Studies on fibre-coating-matrix interfaces using SEM, Figure 3, showed that the coating has sufficient porosity to enable impregnation of the SBE and that the necessary phase separation takes place. Further, the porosity of the SBE is the same in the vicinity of the fibre as in the bulk. However, the coating containing EGO (Figure 3a) shows weak interfacial bonding between the fibre and the coating, while in the rGO-sample (Figure 3b) cohesive fractures within the coating are observed. It is not fully understood why the same EPD parameters result in different damage mechanisms for small amounts of different graphene additives. Cracks in the material prevent mechanical load transfer and impede electrochemical processes as certain species transport is shielded. The occurrence of these cracks without prior mechanical load indicates the direction for future work, where the challenge is to find material-and-process parameters that provide coating with a sufficient interface with SBE, in addition to being robust for long-term electrochemical cycling.

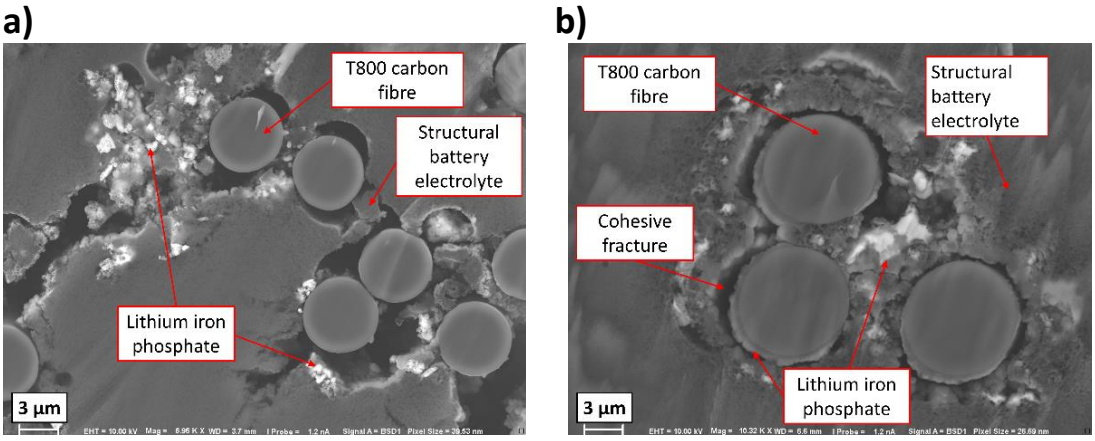

Figure 3. SEM images of the BIB-milled cross-sections of the a) EGO-sample and b) rGO-sample.

4. Conclusion

In this study, electrophoresis is used to produce fibre-reinforced battery electrodes made of $LiFePO_4$, carbon black, and graphene additive. The coated carbon fibres in liquid electrolyte were electrochemically characterized, to allow for comparison between EGO and rGO as additives. The electrochemical evaluation revealed good rate performance and high coulombic efficiency, with the EGO-sample outperforming the rGO-sample by small margins.

For the material in this study to function as positive electrodes in a structural battery, the coated carbon fibres must be combined with pristine carbon fibre negative electrodes and a structural battery electrolyte, to form a full cell. However, initial studies of the fibre-coating-matrix interfaces using SEM showed that the coated carbon fibres when infused with solid battery electrolyte exhibits extensive damage in the form of cracks between coating and fibre for the EGO-sample and cohesive damage in the coating for the rGO-sample. Both types of damage have a detrimental effect on the material's multifunctional performance, as a crack both prevents mechanical load transfer and impedes material transport for electrochemical processes.

244/716 ©2022 Xu et al. doi:10.5075/epfl-298799_978-2-9701614-0-0 published under CC BY-NC 4.0 license

Acknowledgements

We acknowledge the funding provided by 2D TECH VINNOVA competence Center (Ref. 2019-00068), USAF, EOARD Award No. FA8655-21-1-7038 and the Swedish National Space Agency, project no. 2020-00256.

References

[1] N. Ihrner, W. Johannisson, F. Sieland, D. Zenkert, M. Johansson, Structural lithium ion battery electrolytes: Via reaction induced phase-separation, J. Mater. Chem. A. 5 (2017) 25652–25659. doi:10.1039/c7ta04684g.

[2] M.H. Kjell, E. Jacques, D. Zenkert, M. Behm, G. Lindbergh, PAN-Based Carbon Fiber Negative Electrodes for Structural Lithium-Ion Batteries, J. Electrochem. Soc. 158 (2011) A1455. doi:10.1149/2.053112jes.

[3] E. Jacques, M.H.M.H. Kjell, D. Zenkert, G. Lindbergh, M. Behm, M. Willgert, Impact of electrochemical cycling on the tensile properties of carbon fibres for structural lithium-ion composite batteries, Compos. Sci. Technol. 72 (2012). doi:10.1016/j.compscitech.2012.02.006.

[4] L.M. Schneider, N. Ihrner, D. Zenkert, M. Johansson, Bicontinuous Electrolytes via Thermally Initiated Polymerization for Structural Lithium Ion Batteries, ACS Appl. Energy Mater. 2 (2019) acsaem.9b00563. doi:10.1021/acsaem.9b00563.

[5] L.E. Asp, M. Johansson, G. Lindbergh, J. Xu, D. Zenkert, Structural battery composites: a review, Funct. Compos. Struct. 1 (2019) 042001. doi:10.1088/2631-6331/ab5571.

[6] J. Hagberg, H.A. Maples, K.S.P. Alvim, J. Xu, W. Johannisson, A. Bismarck, D. Zenkert, G. Lindbergh, Lithium iron phosphate coated carbon fiber electrodes for structural lithium ion batteries, Compos. Sci. Technol. 162 (2018). doi:10.1016/j.compscitech.2018.04.041.

[7] K. Bouton, B. Chen, D. Zenkert, G. Lindbergh, Structural positive electrodes for multifunctional composite materials, in: Proc. 22nd Int. Conf. Compos. Mater., Melbourne, 2019.

[8] J.S. Sanchez, J. Xu, Z. Xia, J. Sun, L.E. Asp, V. Palermo, Electrophoretic coating of LiFePO 4 / Graphene oxide on carbon fibers as cathode electrodes for structural lithium ion batteries, Compos. Sci. Technol. 208 (2021) 108768. doi:10.1016/j.compscitech.2021.108768.

[9] Z.Y. Xia, M. Christian, C. Arbizzani, V. Morandi, M. Gazzano, V. Quintano, A. Kovtun, V. Palermo, A robust, modular approach to produce graphene-MO X multilayer foams as electrodes for Li-ion batteries, Nanoscale. 11 (2019) 5265–5273. doi:10.1039/c8nr09195a.

[10] L.E. Asp, K. Bouton, D. Carlstedt, S. Duan, R. Harnden, W. Johannisson, M. Johansen, M.K.G. Johansson, G. Lindbergh, F. Liu, K. Peuvot, L.M. Schneider, J. Xu, D. Zenkert, A Structural Battery and its Multifunctional Performance, Adv. Energy Sustain. Res. 2000093 (2021) 2000093. doi:10.1002/aesr.202000093.

Composites Meet Sustainability – Proceedings of the 20th European Conference on Composite Materials,
ECCM20. 26-30 June, 2022, Lausanne, Switzerland

IMPROVED CFRP HYDROGEN TANK PERFORMANCE WITH GRAPHENE OXIDE MATERIALS

Farzin Javanshour[a], Karolina Hopia[a], Pekka Laurikainen[a], Rama Kanta Layek[b], Essi Sarlin[a]

a: Department of Materials Science and Environmental Engineering, Tampere University, Tampere, Finland – essi.sarlin@tuni.fi
b: Department of Separation Science, LUT University, Lahti, Finland

Abstract: *One of the main challenges for linerless, fully composite hydrogen tank structures is the permeability of the material for hydrogen gas (H_2). In this study, a carbon fibre reinforced epoxy composite was modified with graphene oxide (GO) to decrease the H_2 permeation through the laminate with different GO concentrations. The geometric pore size of graphene is small compared to the diameter of hydrogen molecules, and therefore, it is an efficient barrier material. The permeability was tested at 20 °C and 200 bar pressure. Further, the mechanical performance of the CFRP laminates with and without GO modification was evaluated by short-beam and three-point flexural tests.*

Keywords: Carbon fibres; Energy Materials; Nanoparticles; Adhesion; Permeability

1. Introduction

The transition towards more sustainable options in transportation has evoked an interest in lightweight, high-pressure vessel options for hydrogen storage. Especially linerless fully composite hydrogen tank structures are in the interest of the automotive industry. The main challenge of these structures is the permeability of the material for small molecule hydrogen gas.

Incorporation of impermeable fillers, such as graphene oxide (GO) and reduced graphene oxide (rGO), can effectively decrease the hydrogen permeability of polymeric materials [1]. The oxygen-containing functional groups in GO act as spacers between graphene layers and trap the H_2 molecules on the graphene sheets with hydrogen bonds [1]. Also, topological defects developed during the GO synthesis are shown to enhance the H_2 storage capacity of GO [1]. Reduced graphene oxide (rGO) has fewer oxygen groups in its structure compared to GO. Rajaura et al. [1] reported better H_2 uptake capacity (1.9 wt%) for GO compared to rGO (1.34 wt%) at room temperature and 80 bar pressure. Singh et al. [2] reported hydrogen uptake of 3.12 wt% at -196 °C and 30 bar pressure for thermally (300 °C) exfoliated GO flakes. Regardless of extensive studies on the H_2 permeability of GO and rGO sheets and laminates, their application to fibre reinforced hydrogen tank structures is not yet covered. Graphene is considered one of the most effective reinforcement materials for polymers. Significant improvements in mechanical properties (stiffness, strength, ductility) have been shown for GO/polymer nanocomposites, especially with low load [3]. Therefore, finding a synergy between the optimal mechanical performance and hydrogen storage capability of GO modified fibre reinforced pressure vessels is desirable.

In this study, the hydrogen permeability of carbon fibre reinforced epoxy (CFRP) composites with GO nanofillers was investigated by custom-made equipment. The dispersion quality of GO

  doi:10.5075/epfl-298799_978-2-9701614-0-0

in epoxy resin was studied based on optical image analysis. The effect of nanofillers on the viscosity of epoxy resin was analysed by the rheology method. The mechanical performance of composites was assessed based on quasi-static flexural testing.

2. Materials and Methods

The fibre reinforcement in this study was twill 2/2 woven carbon fibre fabrics (Primetex® Hexel, purchased from Kevra Oy, Vantaa, Finland) with an areal density of 200 g/m^2 and 0.2 mm in thickness. Standard bisphenol-A epoxy resin and suitable hardener were used as the polymer matrix system with a 26 wt% hardener to resin ratio, according to supplier's guidelines.

A stable graphene oxide-acetone slurry (10 gr GO/390 mL water/600 mL acetone) was provided by Graphenea (Donostia, Gipuzkoa, Spain). The datasheet provided by the manufacturer reported the GO particles size of 29-33 µm (90th percentile), 14-17 µm (50th percentile), and 6-7 µm (10th percentile). The X-ray photoelectron spectroscopy results provided in the datasheet suggested an elemental composition of 49-50% carbon, 41-50% oxygen, 2-3% sulfur, 0-2% nitrogen, and 1-2% hydrogen for the GO. Three types of epoxy-GO dispersions with GO concentrations of 0.038 wt%, 0.075 wt%, and 0.15 wt% were prepared to find the best combination between hydrogen-barrier properties and mechanical performance of carbon fibre epoxy composites. The GO slurry was dispersed in epoxy resin and stirred for 10 minutes by a mechanical stirrer. The GO-epoxy dispersion was placed in a vacuum oven (40°C, 0.7 bar) for 24 hours to remove acetone and water before mixing it with the hardener. Viscosities of the GO-epoxy dispersions were measured with a rotational rheometer (model MCR 301, Anton Paar GmbH, Graz, Austria) at a constant temperature of 22 °C. Shear rates between 0.1 – 100 s^{-1} were tested using a concentric cylinder system.

The GO dispersion in epoxy was studied with an optical stereomicroscope (model MZ 7.5, LEICA, Heerbrugg, Switzerland). Epoxy resins with three different GO concentrations were cast into circular shape specimens with dimensions of 10 mm × 5 mm epoxy (diameter × thickness). The resins were first degassed in a vacuum chamber (23 °C, 0.7 bar) and then cured at 80 °C (2 hours). The areal coverage of the GO in epoxy was analysed with Image J software (1.52n version, National Institutes of Health, USA). A representative, approx. 30 mm^2 area was considered in the image analysis per series.

Carbon fibre reinforced epoxy composites (CFRP) were manufactured by vacuum-assisted resin infusion (23°C, 0.7 bar). The epoxy resins were degassed in a vacuum chamber before infusion. Each laminate was comprised of seven plies of twill 2/2 woven carbon fibre fabrics with ply dimensions of 200 mm × 200 mm × 0.2 mm (length × width × thickness). Composites were cured at 80 °C (2 hours) and post cured at 120 °C (4 hours) in a hot press. Steel-made spacers were used to control the final thickness of composites. Composite laminates with 2 mm and 1.4 mm thickness values were prepared for hydrogen permeability and flexural testing, respectively.

The quasi-static flexural testing of CFRP composites was carried out with a universal testing machine (model 5967, Instron, MA, USA). The three-point flexural (3PF) testing of CFRP specimens with dimensions of 1.4 mm × 13 mm × 70 mm (thickness × width × length) was performed with a 30 kN load cell, 45 mm span length, and 1 mm/min crosshead movement rate following the ASTM D7264 standard guidelines. The 3PF testing was selected as the loading condition of specimens is similar to the main loading conditions in hydrogen tanks (concurrent compression and tension). Effects of the GO dispersed epoxy resins on the interlaminar shear

  doi:10.5075/epfl-298799_978-2-9701614-0-0

strength of CFRP composites were studied by short beam shear (SBS) testing according to ASTM D2344 with specimen dimensions of 1.4 mm × 2.8 mm × 20 mm (thickness × width × length). The SBS testing was performed with a 500 N load cell, span length of 5.6 mm and 1 mm/min crosshead movement rate. Specimens for the mechanical testing were cut from the CFRP laminates using a band sawing machine (model RBS904, Ryobi, Hiroshima, Japan). Specimen edges were polished to a final finish so that fibres in each ply were clearly observable.

The hydrogen permeability of CFRP laminates was studied at 20 °C and 200 bar hydrogen pressure with custom-made equipment developed by HyCentA (Graz, Austria). The CFRP laminates for the hydrogen permeability testing were water-jet cut into circular-shaped specimens with 150 mm × 2 mm (diameter × thickness) dimensions.

3. Results and discussions

3.1 GO dispersion analysis

Figure 1 shows the optical microscope images of graphene oxide (GO) dispersed epoxy resins. Based on the image analysis, the GO coverage of 0.038 wt% and 0.075 wt% samples were 54% and 71%, respectively. The optical microscopy images of the 0.15 wt% samples were fully black, so the coverage was considered to be 100%. It is clear that already very low GO concentrations ensure good coverage, and an improvement in barrier properties can be achieved.

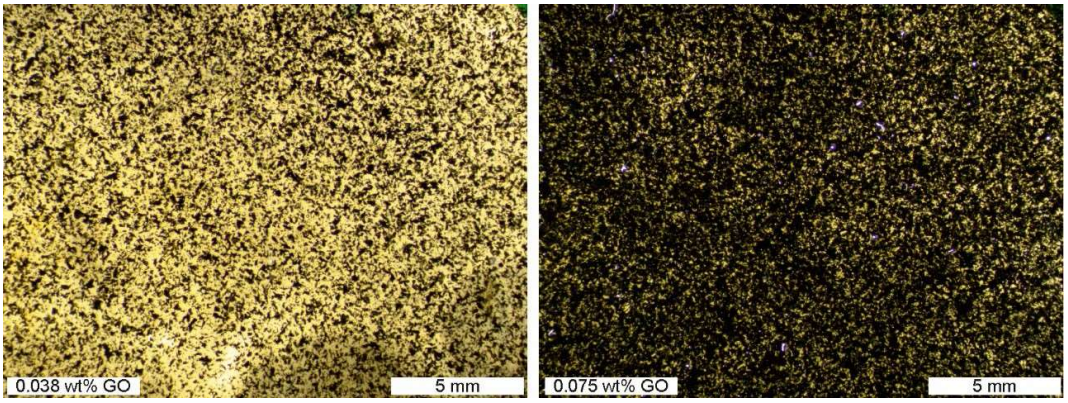

Figure 1. Epoxy films (thickness 5 mm) modified with 0.038 wt% and 0.075 wt% *GO.*

3.2 Rheological studies

To ensure the processability of the GO modified resin, its viscosity should not exceed the values of unmodified resin around the shear rates realistic for filament winding, which is the manufacturing method used for composite tanks. Figure 2 presents the shear rate – viscosity relation of the uncured reference epoxy and 0.15 wt% GO dispersed epoxy. The reference material obeys an expected Newtonian behaviour while the GO dispersed material shows clear shear thinning behaviour which likely evens out into a Newtonian plateau at high shear rates. This phenomenon is known as the apparent yield stress, and it represents the change in dominance from particle interactions to hydrodynamics in the flow behaviour. The lower Newtonian plateau is likely due to the small platelet-like GO particles orienting in the flow direction. Based on the results, the GO addition does not cause issues from the processability point of view, even at the highest GO concentration.

  doi:10.5075/epfl-298799_978-2-9701614-0-0

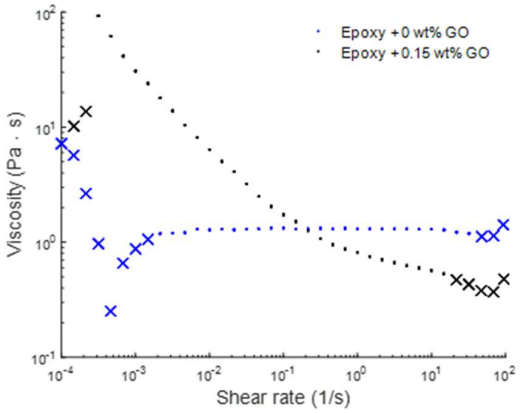

Figure 2. Viscosity- shear rate relations of pure and 0.15 wt% GO dispersed epoxy resins. Crossed out data points indicate unstable measurements within the shear rate range.

3.3 Three-point flexural (3PF) testing of composites

In Figure 3, the typical flexural stress-strain curves of CFRP composites are presented. The chord moduli (E_f^{chord}) of elasticity (within 0.001-0.003 nominal strain range) were in the range of 54 GPa for all CFRP composites. The extent of the resin cure can alter the elastic modulus of composites [4]. Similar E_f^{chord} values of the composites (see Table 1) indicate that the addition of the GO slurry does not hinder the curing state of the epoxy resin. The flexural failure strength (σ_f) values of the reference CFRP composite and CFRP composites with GO concentrations of 0.038 wt% and 0.075 wt% were in the same range considering their error margin. However, the highest GO concentration (0.15 wt%) decreased the σ_f of CFRP composites by 17%, possibly due to the GO agglomeration and stress concentration. Therefore, from the mechanical behaviour point of view, the optimal GO concentration would be below 0.15 wt%.

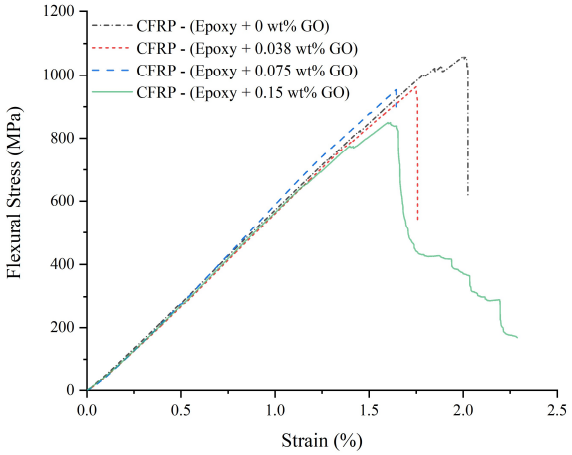

Figure 3. Typical and representative flexural stress-strain curves of CFRP composites.

The GO-dispersed composites had relatively low flexural failure strain values compared to the reference CFRP. However, the highest GO centration (0.15 wt%) altered the brittle failure of CFRP composites to a progressive failure mode which can be ascribed to a lower interlaminar shear strength (ILSS), allowing interlaminar crack propagation before fracture.

Table 1: Results of three-point flexural (3PF) testing of the CFRP composites.

CFRP	E_f^{chord} (GPa)	σ_f [MPa]	ε [%]
Referene	54 ± 2	1000 ± 70	2.02 ± 0.07
0.038 wt% GO	54 ± 1	950 ± 20	1.75 ± 0.09
0.075 wt% GO	55 ± 1	970 ± 70	1.64 ± 0.09
0.15 wt% GO	54 ± 1	830 ± 50	2.28 ± 0.08

3.4 Short-beam shear (SBS) testing of composites

The results of SBS testing of CFRP composites are summarised in Figure 4. The interlaminar shear strength (ILSS) of CFRP composites with 0.038 wt% GO (52 ± 5 MPa) was the same as the reference specimens (53 ± 4 MPa). Further increasing the GO content by one and two folds, respectively, decreases the ILSS values by 11% and 23% compared to the reference CFRP. Lower ILSS values of CFRP composites with GO dispersed content beyond 0.038 wt% GO can be related to the stick-slip friction between GO and epoxy and interfacial sliding inside the GO platelets. For instance, Lu et al. [5] showed that laminated polyurethane (PU) nanocomposites with 0.08 wt% GO possess a 94% higher damping factor in dynamic mechanical analysis than unmodified PU. Similarly, epoxy resins with 0.075 wt% and 0.15 wt% GO concentrations in this study might enhance CFRP composites' damping performance and long-term service life, which needs further studies with dynamic loading conditions.

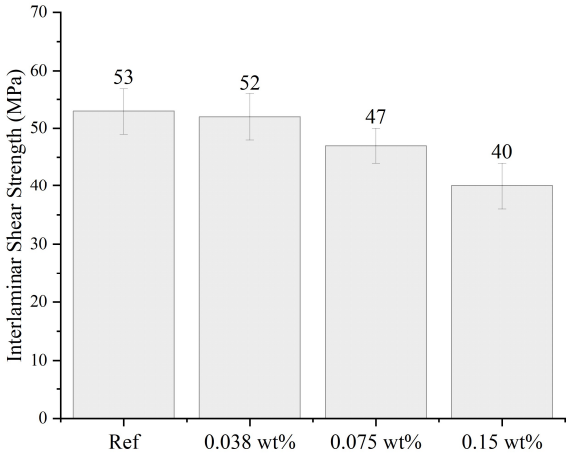

Figure 4. The average ILSS values of CFRP composites.

3.5 Hydrogen permeability

The H_2 permeability of the reference and GO modified (0.038 wt%) laminates was approximately $5 \cdot 10^{-14} \frac{mol}{cm \cdot s \cdot bar}$. Testing of composite specimens with the high pressure test system was challenging due to the relatively thick laminate (2 mm) and a good time-lag curve was not achieved during the measurement. Further, one of the sample surfaces was rough due to the peel ply used during infusion. To avoid H_2 leaking due the rough surface, an additional soft sealing was used. However, the poor time-lag curve was still an issue. Therefore, thinner

  doi:10.5075/epfl-298799_978-2-9701614-0-0

laminates (1 mm) with very smooth surfaces will be used in the test to get more accurate results and the test system will be further developed.

4. Conclusions

Lightweight and linerless carbon fibre reinforced plastic (CFRP) composites as hydrogen storage tanks should be developed to promote sustainable vehicles and transportation. This study aimed to find a synergy between hydrogen (H_2) permeability and the outstanding mechanical performance of CFRP composites. Hydrogen impermeable graphene oxide (GO) flakes were uniformly dispersed in epoxy resin as a polymer matrix for CFRP. The microscopic analysis of GO dispersed epoxy resins showed that well-dispersed and exfoliated graphene oxide flakes at low concentrations of 0.038 wt% and 0.075 wt%, respectively provide 54% and 71% surface coverage. The GO concentration of 0.15 wt% provided a complete surface coverage. Based on the rheological investigation, the GO addition did not cause any issues from the processability point of view, even at the highest GO concentration of 0.15 wt%. Overall, the mechanical performance of unmodified and GO dispersed (0.038 wt% and 0.075 wt%) CFRP composites was in the same range. The flexural strength and interlaminar shear strength of CFRP specimens with the highest GO concentration (0.15 wt%) were respectively 17% and 23% lower than the unmodified CFRP.

Acknowledgements

The authors are grateful for Dipl.-Ing. Thomas Hafner from HyCentA Research GmbH for the permeability tests. The research work was performed within the COMET-modul “Polymers4Hydrogen “(I.D. 21647053) at Tampere University (Department of Engineering Material Science) within the framework of the COMET-program of the Federal Ministry for Climate, Action, Environment, Energy, Mobility, Innovation and Technology and the Federal Ministry for Digital and Economic Affairs with contributions by Polymer Competence Center Leoben, Montanuniversität Leoben (Department Polymer Engineering and Science, Chair of Chemistry of Polymeric Materials, Chair of Materials Science and Testing of Polymers), Technical University of Munich (Department of Mechanical Engineering, Chair of Carbon Composites), Peak Technology and Faurecia Automotive GmbH.

5. References

1. Rajaura RS, Srivastava S, Sharma V, Sharma PK, Lal C, Singh M, et al. Role of interlayer spacing and functional group on the hydrogen storage properties of graphene oxide and reduced graphene oxide. Int J Hydrogen Energy. 2016 Jun 15;41(22):9454–9461. Available from: https://doi.org/10.1016/j.ijhydene.2016.04.115.

2. Singh SB, De M. Thermally exfoliated graphene oxide for hydrogen storage. Mater Chem Phys. 2020 Jan 1;239:122102. Available from: https://doi.org/10.1016/j.matchemphys.2019.122102.

3. Wan C, Chen B. Reinforcement and interphase of polymer/graphene oxide nanocomposites. J. Mater. Chem. 2012 Jan 19;22 (8):3637-3646. Available from: http://dx.doi.org/10.1039/C2JM15062J.

4. Bilge K, Yorulmaz Y, Javanshour F, Ürkmez A, Yılmaz B, Şimşek E, et al. Synergistic role of in-situ crosslinkable electrospun nanofiber/epoxy nanocomposite interlayers for superior laminated composites. Compos Sci Technol. 2017 Oct 20;151:310-316. Available from: https://doi.org/10.1016/j.compscitech.2017.08.029.

5. Lu W, Qin F, Wang Y, Luo Y, Wang H, Scarpa F, et al. Engineering Graphene Wrinkles for Large Enhancement of Interlaminar Friction Enabled Damping Capability. ACS Appl Mater Interfaces. 2019 Aug 21;11(33):30278–89. Available from: https://pubs.acs.org/doi/full/10.1021/acsami.9b09393.

  doi:10.5075/epfl-298799_978-2-9701614-0-0

STRUCTURAL SUPERCAPACITOR COMPOSITE TECHNOLOGY DEMONSTRATOR

David B. Anthony[a,b], Emile S. Greenhalgh[a], Tomas Katafiasz[a], Anthony R. J. Kucernak[b], Peter Linde[c,d], Sang Nguyen[a], Guocheng Qi[a], Seyedalireza Razavi[a], Evgeny Senokos[b], Milo S. P. Shaffer[b], Maria Valkova[b]

a: The Composite Centre, Department of Aeronautics, Imperial College London, UK, snguyen@ic.ac.uk
b: Department of Chemistry, Imperial College London, UK
c: Department of Industrial and Materials Science, Chalmers University of Technology, Gothenburg, Sweden
d: German Aerospace Center (DLR), Bonn, Germany

Abstract: *Structural power composites, a class of multifunctional materials, have significant potential to facilitate lightweighting and accelerate widespread electrification in sustainable transportation. In civil aircraft, a bank of supercapacitors can provide power to open the doors in an emergency. Structural power composite fuselage components near the doors could provide this power and eliminate the mass and volume needed for the supercapacitors. To demonstrate this concept, we designed and manufactured a multifunctional component representative of a fuselage rib, which powered the opening and closing of a desktop scale composite aircraft door. This paper provides information about structural supercapacitor technology demonstrators, discusses the fabrication of this demonstrator and concludes by providing an insight into the future challenges that need to be addressed to realise structural power composite components.*

Keywords: structural; supercapacitor; composite; demonstrator

1. Introduction

Structural power composites (SPCs) [1] can significantly reduce the parasitic mass associated with conventional energy storage devices [2] and facilitate widespread electrification in sustainable transportation [3]. These emerging multifunctional materials can store and deliver electrical energy as well as support mechanical loads. Structural supercapacitors provide lower energy densities but greater power densities than structural batteries and have potential applications for electrical load levelling, buffering and high power delivery. Despite growing interest in structural batteries and supercapacitors, much of the research to date has focused on developing the multifunctional constituents (i.e., the electrodes/reinforcements and/or the structural electrolyte) rather than assembly, scale-up and demonstration through multicell assembly; the latter aspects are the focus of this paper.

The aim of this study was to develop a physical embodiment of structural supercapacitor technology to (a) aid researchers, stakeholders and the general public to readily grasp the concept of energy-storing structural materials; (b) demonstrate the elevation of the technology readiness level of SPCs and (c) gain an improved understanding of the engineering issues associated with scaling up from small lab-scale single-cell devices to larger multi-cell structural components. For these purposes, the structural requirements were chosen to meet those

  doi:10.5075/epfl-298799_978-2-9701614-0-0

needed to ensure durability for handling and transportation, rather than those needed to carry the structural loads for the intended industrial application.

To date, more large-scale structural power demonstrators have been reported for structural supercapacitors than for structural batteries due to the higher level of maturity of the former type of device and the greater complexity associated with battery chemistry and scale-up. The electrical performance requirements have been fairly modest and representative of low power and energy applications such as lighting systems. Structural components for demonstration were selected to be easy identifiable to all target groups and not necessarily on the basis of optimal system weight saving considerations. Other considerations for selection were the ease of access for replacement, similar stiffness demands to those achievable by the SPCs developed in the corresponding research projects and space to allow for thicker laminates and additional wiring. In all of the demonstrators developed so far, the approach has primarily involved direct replacement of the existing structural components. The geometries were kept the same as the original parts and only the thickness of the component differed from the originals. In some cases, finite element modelling was carried out to design the multifunctional component to meet the specific structural requirements of the application. Examples of previous structural supercapacitor demonstrators and their characteristics are shown in Figure 1 and Table 1.

Figure 1 Desktop scale (approximately 30 cm long) structural supercapacitor composite demonstrators in the form of automotive exterior panels able to power LED lights [1]

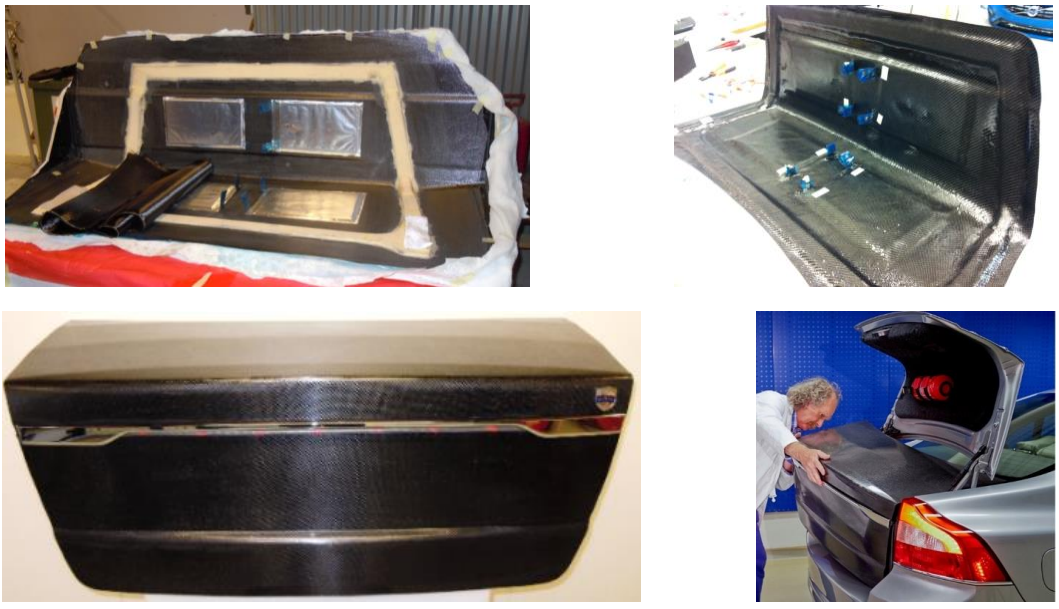

Figure 2 Full scale Volvo S80 boot lid demonstrator with integrated structural supercapacitors to power external lights [1]

  doi:10.5075/epfl-298799_978-2-9701614-0-0

Table 1: Structural supercapacitor technology demonstrators manufactured to date [1,2]

Structural component	Electrical system powered	Cells	Voltage [V]
Small scale car body shell	LED lights	1	3
Small scale Volvo car roof	LED lights	2	6
Aircraft electronics box casing	Power spike buffer	15	30
Volvo S80 boot lid	External rear lighting	16	12

2. Demonstrator

In this study, a demonstrator was fabricated to illustrate the concept of a multifunctional fuselage component which can open aircraft passenger doors in an emergency and eliminate the mass and volume needed for conventional supercapacitors. The structural and electrical components selected were representative of a fuselage C-section rib (Figure 3a) and a bank of conventional supercapacitors (Figure 3b) located on the door (Figure 3c). The supercapacitors produce the torque to open the door as a backup power source. The multifunctional beam (Figure 3d) was to be a representative element which stores energy in the web region (blue) rather than in the whole beam. The potential mass saving if SPCs were used to power all sixteen passenger doors is approximately equal to the mass of sixteen supercapacitor banks. The potential volume saving if SPCs were used for all doors could reach the volume of 16 supercapacitor banks. Both of these benefits are conditional on the SPC being able to completely fulfil both the structural and power requirements provided by the existing ribs and conventional supercapacitor banks without significant changes in mass or volume compared to the original ribs.

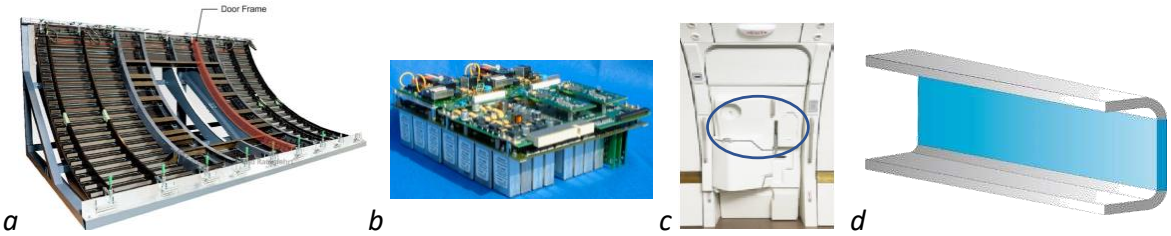

Figure 3 (a) Location of the actual curved fuselage rib shown in red (b) supercapacitor bank and circuit board (c) passenger door showing the location of the supercapacitor bank circled (d) proposed multifunctional web of the C-section beam

An 80 cm long × 20 cm wide × 7 mm thick C-section beam containing two stacks of four 30 cm × 15 cm × 0.5 mm structural supercapacitor cells (Figures 4 and 5) within the web region was manufactured. These structural supercapacitors comprise Oxeon spread tow carbon fibre fabric electrodes reinforced with high surface area carbon aerogel [4] to provide high capacitance and structural rigidity. A polymeric separator was bonded between the electrodes using patterned structural epoxy, and the whole laminate was infused with an electrolyte and packaged with protruding current collector tapes. A computer aided design (CAD) model (Figure 6) of an aircraft fuselage and passenger door assembly (approximately A3 size) was generated and this assembly was manufactured. The majority of the parts were 3D printed using ABS and the fuselage, door

  doi:10.5075/epfl-298799_978-2-9701614-0-0

and floor panel (Figure 7) were made from a low temperature cure prepreg as used for the C-beam structural plies.

Figure 4 Structural supercapacitor composite cells integrated into the 80 cm long beam

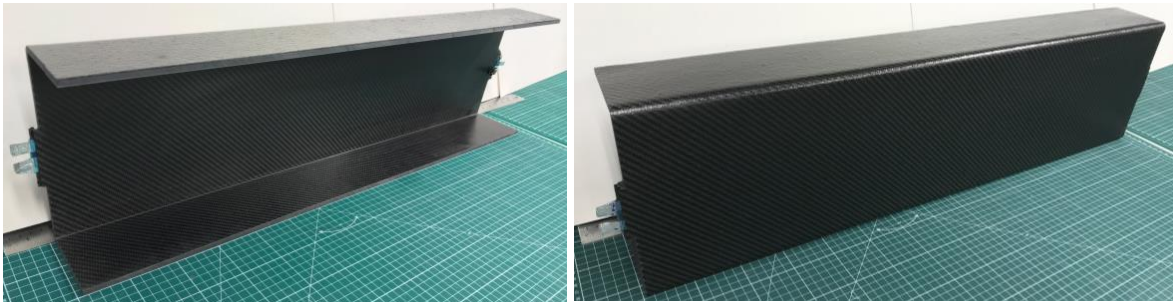

Figure 5 Inner and outer surfaces of structural supercapacitor composite beam

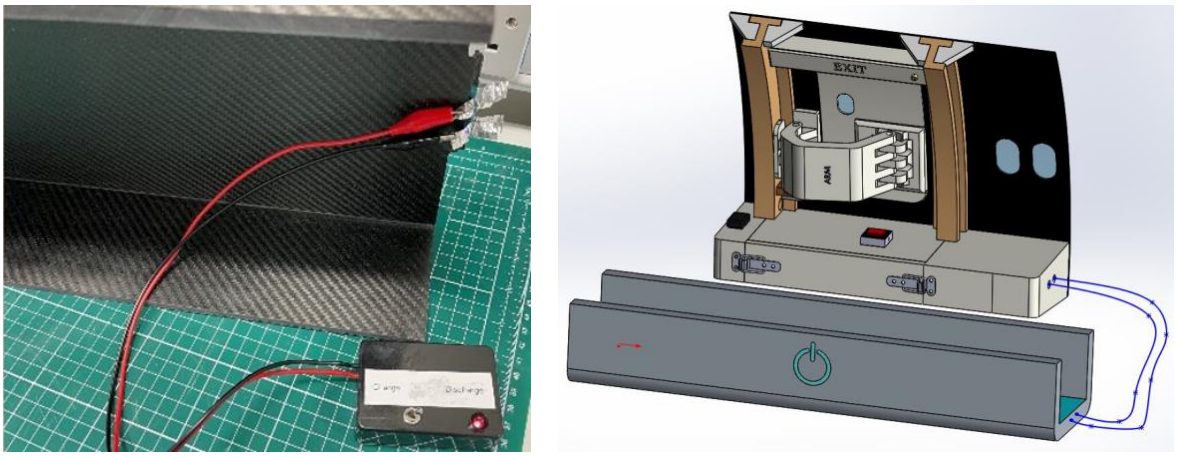

Figure 6 LED indicator to check operation and CAD model showing the scaled fuselage door assembly and structural supercapacitor composite beam

Prior to integrating the cells into the beam, charging four of the structural supercapacitor cells connected in series to 6 V for 10 s could power the door mechanism (Figure 7) to open and close three times. However, after integrating the cells into the beam, some loss in electrochemical performance was observed such that a longer charge time of 30 s was needed to achieve the same door mechanism operating performance. (A video showing the operation can be viewed at https://www.youtube.com/watch?v=yxa-BOpuDIs&t=17s). A major contributor to the loss in performance was considered to be the lack of through-thickness pressure on the structural

  doi:10.5075/epfl-298799_978-2-9701614-0-0

supercapacitors after consolidation and curing. Measurements indicated that greater through-thickness pressure reduced the internal resistance by enhancing the electrical contact between the aluminium tape current collector material and the active electrode material.

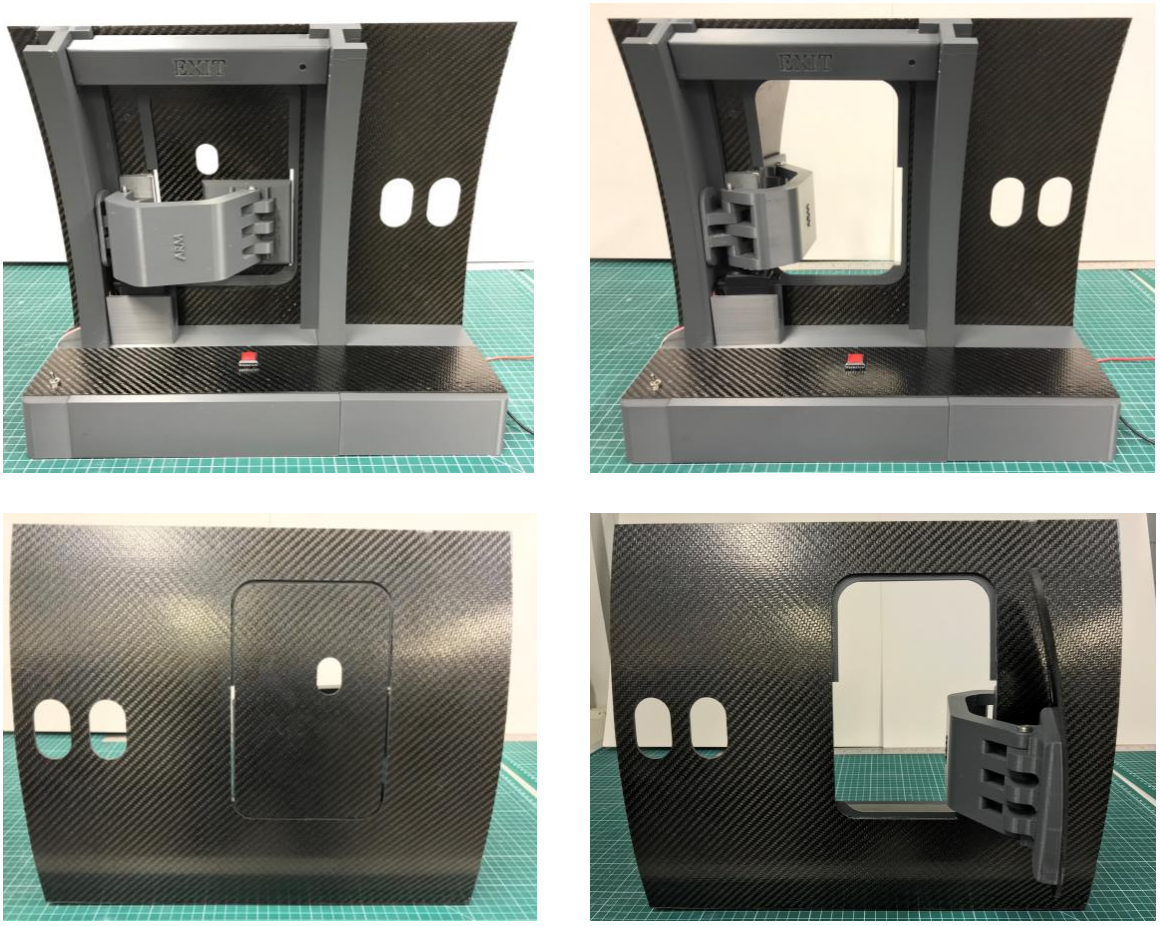

Figure 7 Desktop scale aircraft fuselage and door opening and closing powered by the beam

3. Challenges

A number of challenges arise when manufacturing large scale multifunctional components for demonstrators that are not encountered when manufacturing single-cell lab-scale devices. The key issues are current collection, encapsulation / packaging, reproducible manufacturing and multicell power management. The relatively low electrical conductivity of carbon fibres as compared to metals can lead to large power losses due to internal resistance for thin devices with large areas. One way of addressing this issue has been to use carbon nanotube fibre veils that act as corrosion-resistant current collectors as well as the active electrodes [5]. Another approach has been to incorporate a copper mesh (lightning strike protection) coated with a conductive carbon ink for passivation outside each electrode [6].

A second issue is that most applications require multiple cells to meet the operating voltage requirements. Efficient structural configurations rely on continuous load paths throughout the structure, which is contradictory to the arrangement of most power sources that consist of stacks or cylindrical configurations of small cells. The packaging arrangement for such cells requires greater consideration than that for a single cell to optimise mechanical and electrochemical efficiency and efficacy. Two main configurations have been utilised, and the

  doi:10.5075/epfl-298799_978-2-9701614-0-0

demonstrator reported here used both configurations together. The first configuration involves stacking cells on top of each other and the second is placing cells adjacent to each other in the same plane. Where cells are stacked, the relative proportion of packaging mass (for encapsulation and conventional structural plies) can be reduced as compared to single cell devices. For planar cell arrangements, the space in between cells present potential structural weaknesses as well as regions where defects in composite manufacturing such as ply wrinkles or resin rich regions in the surrounding structural composite plies may manifest.

A third issue that becomes much more pronounced for multicell structural power components is the issue of manufacturing both from a structural perspective and from an electrochemical perspective. The manufacturing process is more difficult than for a conventional composite. The relatively small-scale fabrication processes of structural power materials used to date have typically not ensured a high degree of reproducibility in the performance from one cell to another. This can lead to inherent variability in the capacitance and resistance across a set of cells and an uneven voltage distribution across the cells. Furthermore, high performance electrochemical device materials, especially for the separator, are very thin and it is thus often difficult to handle large sheets manually without introducing wrinkles or other such defects. Manufacturing in a moisture-free environment to permit high voltage operation without electrochemical degradation requires fabrication in a glove box, which adds difficulties associated with the size of the glove box airlock, reduced manual dexterity and being able to use conventional composites manufacturing equipment. For this reason, most demonstrators have instead opted to use vacuum sealing to encapsulate devices immediately after manufacture outside a glovebox.

Translation of structural power composite technology from the lab to larger scale components that are relevant to industry requires further research to address all of these technical hurdles. In particular, there is a need for more studies to investigate scale-up issues and demonstration using multicell assemblies and complex geometry structural components. Solutions to the aforementioned technical challenges would enable structural power composites to revolutionise future structural and electrical engineering applications.

Acknowledgements

We would like to thank Jonathon Cole, Roland Hutchins, Gary Senior and Franco Giammaria for their advice and support with manufacturing of the demonstrator. This research was funded by the EPSRC Future Composites Research Manufacturing Hub (EP/P006701/1), the EPSRC Beyond Structural project (EP/P007465/1), the European Office of Aerospace Research and Development (IOE Grant FA9550-17-1-0251), EU Clean Sky 2 (SORCERER Project #738085) and the Royal Academy of Engineering (Chair in Emerging Technologies).

4. References

1. Greenhalgh ES, Asp LE. STORAGE (Composite Structural Power Storage for Hybrid Vehicles) Final Publishable Summary Report, STORAGE/WP1/ICL/M1-42, 2013. Available online: https://cordis.europa.eu/project/id/234236/reporting [accessed 6/3/22].
2. Nguyen SN, Millereux A, Pouyat A, Greenhalgh ES, Shaffer MSP, Kucernak ARJ, Linde P. Conceptual Multifunctional Design, Feasibility and Requirements for Structural Power in Aircraft Cabins, AIAA Journal of Aircraft 2021; 58 (3).

  doi:10.5075/epfl-298799_978-2-9701614-0-0

3. Karadotcheva E, Nguyen SN, Greenhalgh ES, Shaffer MSP, Kucernak ARJ, Linde P. Structural Power Performance Targets for Future Electric Aircraft, Energies 2021; 14 (19): 6006.
4. Nguyen SN, Anthony DB, Qian H, Yue C, Singh A, Bismarck A, Shaffer MSP, Greenhalgh ES. Mechanical and physical performance of carbon aerogel reinforced carbon fibre hierarchical composites, Composites Science and Technology 2019; 182 (107720).
5. Rana M, Ou Y, Meng C, Sket F, González C, Vilatela JJ. Damage-tolerant, laminated structural supercapacitor composites enabled by integration of carbon nanotube fibres, Multifunctional Materials 2020; 3 (015001).
6. Ankersen J, Mistry M, Nguyen SN, Greenhalgh ES, Kucernak A. Addressing Engineering Issues for a Composite Structural Power Demonstrator, ICCCM19, Montreal, Canada, 28 Jul - 2 Aug 2013.

  doi:10.5075/epfl-298799_978-2-9701614-0-0

DEVELOPMENT OF NOVEL MATRIX MATERIALS FOR TYPE V HYDROGEN GAS PRESSURE VESSELS

Florian, Wanghofer[a], Markus, Wolfahrt[a], Archim, Wolfberger[a], Sandra, Schlögl[a]

a: Polymer Competence Center Leoben GmbH, Roseggerstraße 12, 8700 Leoben, Austria – florian.wanghofer@pccl.at

Abstract: *High-pressure vessels for hydrogen gas storage are an important component for the development and commercialization of hydrogen as a green energy resource. More recent developments are directed to linerless, all composite vessels (Type V), however, finding a material providing sufficient strength, toughness and permeation resistance remains a challenge. To this end, epoxy-functional resins based on ionic liquids (IL) have been synthesized and crosslinked. The IL-resins are cured with multi-functional hardeners to tailor the properties of the cured networks to the requirements applicable for high pressure gas vessels. Through hardener and IL-resin variation, multiple thermosets with glass transition temperatures (T_g) varying between 30 °C and 130 °C have been produced and characterized.*

Keywords: epoxy; gaseous hydrogen; ionic liquid

1. Introduction

With energy efficiency three times higher than petroleum, hydrogen has the potential to solve the steadily rising fuel needs (e.g., fuel cell, hydrogen internal combustion engine – ICE) [1]. However, the development of hydrogen fuel cell systems and the associated hydrogen distribution and dispensing infrastructure will require a multi-materials' approach that utilizes the most effective combination of materials to achieve operational safety and competitiveness of novel technologies (e.g. fuel cells). In trying to achieve this aim, relying on the reliability and lifetime of polymers will finally lead to massive cost reductions.

Therein, the on-board storage of hydrogen is an important factor for success. Compared with liquid hydrogen storage, high pressure compressed hydrogen storage has become the most popular method due to its technical simplicity and the relatively low costs for storage and transportation [2]. Pressure vessels are the key equipment for high pressure storage. However, as a result of the rather small gravimetric and volumetric hydrogen density on carbon, this technique requires large space to store the compressed hydrogen gas (e.g. 5 kg of hydrogen need 390 liters at a pressure of 20 MPa) [3, 4]. In this context, fully wrapped composite vessels (Type IV) with a polymer liner as gas barrier are considered as the leading candidate to store compressed hydrogen up to 70 MPa. Attempts have been made to produce type V pressure vessels, which consist solely of the composite overwrap. Finding a matrix material that combines high strength, toughness and low permeability for the targeted working pressures proves to be challenging, however.

Within the COMET-module "Polymers4Hydrogen" novel epoxy monomers are synthesized and characterized for developing the next generation of thermosets used in type V pressure vessels.

  doi:10.5075/epfl-298799_978-2-9701614-0-0

The synthesized epoxy-functional resins are based on ionic liquids (IL), which are composed of ions, yet liquid over wide temperature ranges. Amongst other interesting features, the ionic centers within the polymer network are expected to provide additional intermolecular bonds and consequently increase the barrier properties due to a tighter packing density. The IL-resins are cured with multifunctional hardeners to tailor the properties of the cured networks to the requirements applicable for high pressure gas vessels.

2. Results

The synthesis of the first investigated epoxy functional IL (IL-1) was performed following a literature procedure [5]. An imidazole ring was alkylated and quaternized by 4-bromo-1-butene followed by anion exchange to bistrifluorosulfonimide. Subsequent epoxidation of the double bonds yielded IL-1 as liquid resin in good yields. IL-2 was synthesized in a similar manner but a different, smaller anion was used. Additionally, IL-3 was synthesized using the bistrifluorosulfonimide anion but more rigid ligands instead of the butene functionalities, to assess the influence of anion and cation structure of the resins on the final properties of the networks.

IL-1 was used to perform the hardener selection. For this, the resin was cured with an aliphatic, cycloaliphatic and aromatic amine, and an anhydride hardener and was thermally and thermo-mechanically characterized [6]. Differential scanning calorimetry (DSC) was performed to confirm complete curing, indicated by the absence of an exothermic peak, and to assess the glass transition temperature (T_g) of the cross-linked materials (Table 1). The aliphatic amine yields a rather soft material with a T_g of 39 °C, which could be increased to 64 °C by using the cycloaliphatic amine hardeners. However, the intended upper service temperature of pressure vessels in the automotive sector is 85 °C or better even 95 °C, rendering the aliphatic hardeners unsuitable for this resin. Satisfactory T_g values of 97 °C and 98 °C could be achieved with the aromatic amine hardener and the anhydride hardener, respectively. This was attributed to the reduction of aliphatic segments in the network for both hardeners. The networks were further characterized regarding their short thermal stability in thermogravimetric analyses (TGA), represented by the temperature at which 5% mass loss occurs ($T_{dec,5}$) (Table 1). The decomposition temperatures of the networks follow the same trend as the glass transition temperature, indicating that the aliphatic segments do not only possess increased mobility but are also more prone to thermal degradation. However, even the aliphatic hardeners give networks with $T_{dec,5}$ of 300 °C and 301 °C compared to approximately 334 °C and 338 °C for the aromatic amine and the anhydride hardener, indicating a good thermal stability of IL-1, as illustrated in Figure 2A.

  doi:10.5075/epfl-298799_978-2-9701614-0-0

Table 1: Thermal and thermo-mechanical properties of IL-1 cured with different hardeners.

Hardener	T_g, DSC, °C[a]	$T_{dec,5}$, °C[b]	T_g, DMA, °C[c]		E' (20 °C), GPa[d]
			Onset	Max tan δ	
Aliphatic amine	39	301	18	28	1.3 (0 °C)*
Alicyclic amine	64	300	44	73	2.0
Aromatic amine	97	334	99	113	1.9
Alicyclic anhydride	98	338	91	107	1.8

[a] Glass transition temperature determined as mid-point in DSC measurements; [b] Temperature at which 5% mass loss was measured in TGA; [c] Glass transition temperature determined in DMA as onset temperature and temperature of maximum tan δ; [d] Storage modulus determined in DMA at 20 °C. *Storage modulus at 0 °C due to the low transition temperature.

Additionally, dynamic mechanical analyses (DMA) were performed to estimate the stiffness of the networks and the T_g values as onset temperature ($T_{g,\,onset}$) and the temperature at maximum tan delta ($T_{g,\,\delta}$). The trend of the T_g values corresponds to the values attained from DSC (Table 1). Interestingly, with 2.0 GPa the network with the cycloaliphatic amine hardener exhibits the highest storage modulus of all samples despite its relatively low T_g. The hardener further leads to a broader transition range, visible also as a shoulder in the loss factor tan δ (Figure 2B). The aliphatic amine hardener produces a rather soft network with a storage modulus of 1.3 GPa. Once again, the aromatic amine hardener and the anhydride hardener have similar properties with 1.9 GPa and 1.8 GPa, respectively, whereas the aromatic amine hardener produces a network with a slightly higher T_g and a sharper transition.

Due to the similar thermal properties, the lower viscosity and consequently easier handling of the liquid anhydride hardener compared to the solid aromatic hardener, the anhydride was chosen as the hardener for further tests.

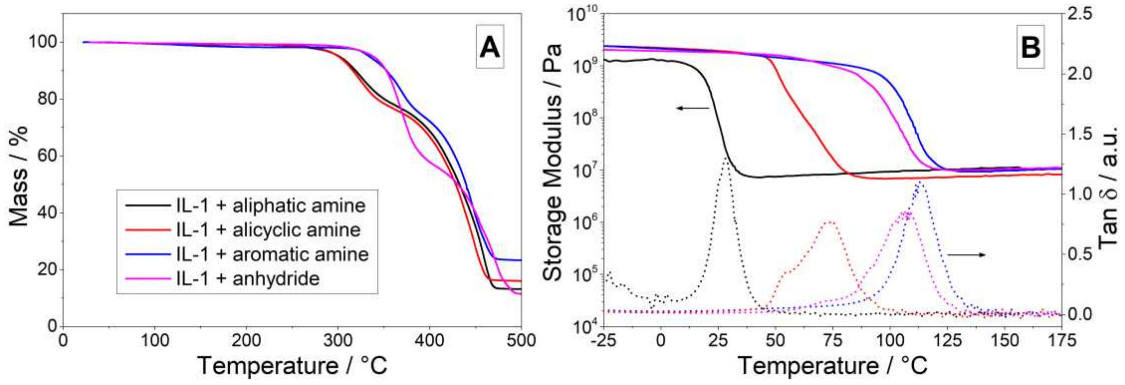

Figure 2: Thermogravimetric analysis (A) and dynamic mechanical analysis (B) of IL-1 epoxy resin cured with different hardeners. Adapted from [6]

  doi:10.5075/epfl-298799_978-2-9701614-0-0

The influence of the anion and cation structure of the resin was assessed by comparing networks of IL-1, IL-2 and IL-3 cured with the anhydride hardener. While both the more rigid ligands of the cation in IL-3 and the smaller anion in IL-2 led to increased T_g values in DSC measurements (Figure 3A) to 109 °C and 119 °C, respectively, the anion exchange had a more significant impact on the transition temperature. The larger anion of IL-1 and IL-3 reduces the chain packing density and acts as a plasticizer, therefore enhancing the chain mobility. Moreover, the smaller anion of IL-2 has an increased hydrogen bonding capability, which further improves the chain packing and the additional intramolecular bonding increases the stiffness of the material, visible in DMA curves (Figure 3C). As a consequence, the storage modulus at of IL-2 at 20 °C amounts to 3.6 GPa, double the amount of IL-1. IL-3 exhibits a modest increase with 2.1 GPa at 20 °C. It has to be noted that due to the significantly lower molecular weight of IL-2 compared to IL-3 and also IL-1, the stoichiometric ratio of the hardener equals a higher weight ratio, which might enhance the effect of the hardener on the final material properties. $T_{dec,5}$ of the networks decreases from 338 °C for IL-1 to 303 °C and 287 °C for IL-2 and IL-3, respectively (Figure 3B).

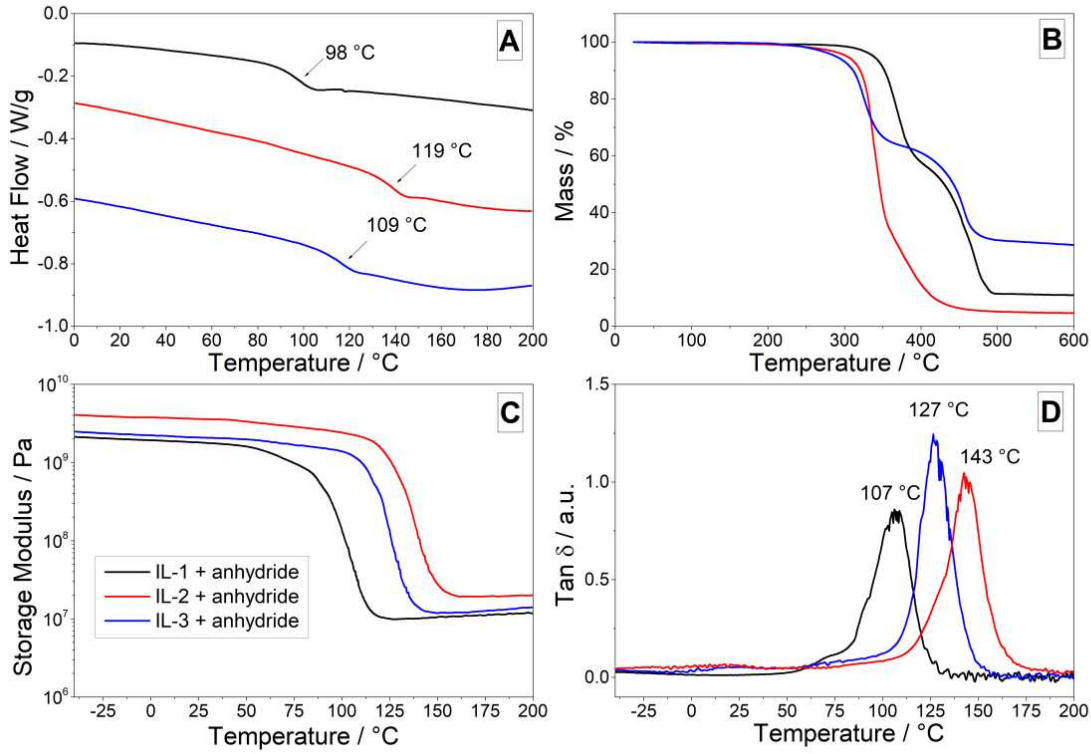

Figure 3: Differential scanning calorimetry (A), thermogravimetric analysis (B) and dynamic mechanical analysis (C + D) of the IL resins cured with an anhydride hardener.

  doi:10.5075/epfl-298799_978-2-9701614-0-0

3. Summary and outlook

Ionic liquid-based epoxy resins have been synthesized and characterized thermally and thermo-mechanically. Through variation of hardener and the chemical structure of the anion and the cation, storage moduli of up to 3.6 GPa and glass transition temperatures of up to 143 °C (DMA, max tan δ) were reached. The three epoxy resins, cured with the same anhydride hardener, are subjected to hydrogen gas permeability measurements to select a resin for an upscaling of the synthesis to the kilogram scale. This resin will then be further characterized mechanically, laminates will be produced and the formulation will be optimized to improve the suitability of the resin for an application in a type V hydrogen pressure vessel. In this process, the response of the fiber reinforced resin to the cyclic thermal and mechanical loading during the service life of a pressure vessel will be of special interest in terms of crack formation and influence on the permeability thereof.

4. Methods

The thermal analysis equipment DSC 4000 (PerkinElmer, Waltham, MA, USA) was used for differential scanning calorimetry (DSC) measurements according to DIN EN ISO 11357. The weight of the samples in the standard aluminium pans (40 µL) was in the range of 12 mg to 14 mg for cured samples and 4 mg to 6 mg for uncured samples. All samples were first heated from -50 °C to 200 °C or 300 °C, for resins containing the aromatic amine hardener, with 20 K/min under nitrogen atmosphere. Afterwards each sample was cooled down to -50 °C. In the second run, all samples were heated up again to the above-mentioned temperatures using the same heating rate and atmosphere. The glass transition temperature was determined as midpoint temperature from the second heating run. The second heating run was chosen for T_g evaluation to remove the influence of the relaxation of residual stresses.

Thermogravimetric analysis (TGA) was performed on a TGA/DSC thermogravimetric analyzer (Mettler-Toledo, Columbus, OH, USA) from 25 °C to 900 °C with a heating rate of 10 K/min under nitrogen in aluminium oxide crucibles with a volume of 70 µL and an approximate sample weight of 30 mg. The measured curves were evaluated with the STARe Evaluation Software (Mettler-Toledo, Columbus, OH, USA)

Dynamic mechanical analysis (DMA) was done on a DMA/SDTA861e instrument (Mettler-Toledo, Columbus, OH, USA) in tensile mode with a clamping length of 9 mm in accordance to DIN EN ISO 6721-5. Rectangular specimens of 20 mm x 2.5 mm x 1 mm were tested in a temperature range of 50 °C up to a maximum temperature of 250 °C or at least 100 °C above the maximum tan delta with a heating rate of 2 K/min under nitrogen. All measurements were performed in the strain-controlled mode with 3 µm deformation, 1 Hz frequency and 150 % off-set.

  doi:10.5075/epfl-298799_978-2-9701614-0-0

Acknowledgements

The research work was performed within the COMET-module “Polymers4Hydrogen“ (project-no.: 21647053) at the Polymer Competence Center Leoben GmbH (PCCL, Austria) within the framework of the COMET-program of the Federal Ministry for Climate, Action, Environment, Energy, Mobility, Innovation and Technology and the Federal Ministry for Digital and Economic Affairs with contributions by Montanuniversitaet Leoben (Department Polymer Engineering and Science, Chair of Chemistry of Polymeric Materials, Chair of Materials Science and Testing of Polymers), Technical University of Munich (Department of Mechanical Engineering, Chair of Carbon Composites), Tampere University (Department of Engineering Material Science), Peak Technology and Faurecia. The PCCL is funded by the Austrian Government and the State Governments of Styria, Lower Austria and Upper Austria.

5. References

1. Barth RR, Simmons KL, San Marchi C. Polymers for Hydrogen Infrastructure and Vehicle Fuel Systems: Applications, Properties, and Gap Analysis. Albuquerque, USA; 2013.
2. Züttel A. Hydrogen storage methods. Naturwissenschaften. 2004;91:157–72. doi:10.1007/s00114-004-0516-x.
3. Takeichi N. “Hybrid hydrogen storage vessel”, a novel high-pressure hydrogen storage vessel combined with hydrogen storage material. International Journal of Hydrogen Energy 2003. doi:10.1016/S0360-3199(02)00216-1.
4. Züttel A. Materials for hydrogen storage. Materials Today. 2003;6:24–33. doi:10.1016/S1369-7021(03)00922-2.
5. McDanel WM, Cowan MG, Carlisle TK, Swanson AK, Noble RD, Gin DL. Cross-linked ionic resins and gels from epoxide-functionalized imidazolium ionic liquid monomers. Polymer. 2014;55:3305–13. doi:10.1016/j.polymer.2014.04.039.
6. Wanghofer F, Wolfberger A, Wolfahrt M, Schlögl S. Cross-Linking and Evaluation of the Thermo-Mechanical Behavior of Epoxy Based Poly(ionic Liquid) Thermosets. Polymers (Basel) 2021. doi:10.3390/polym13223914.

  doi:10.5075/epfl-298799_978-2-9701614-0-0

EVALUATING THE MULTIFUNCTIONAL PERFORMANCE OF STRUCTURAL COMPOSITES FOR THERMAL ENERGY STORAGE

Giulia Fredi, Andrea Dorigato, Luca Fambri, and Alessandro Pegoretti

University of Trento, Department of Industrial Engineering and INSTM Research Unit, Via Sommarive 9, 38123 Trento, Italy - alessandro.pegoretti@unitn.it

Abstract: *The demand for high mechanical properties and thermal energy storage (TES) functions simultaneously can be tackled by including a reinforcing agent and a phase change material (PCM) in a polymer matrix. Although the PCMs usually impair the mechanical properties of the host structural composite, a multifunctional three-phase composite can still allow mass saving compared to two monofunctional components, each of them in charge of either the structural function or the heat management. To quantify possible benefits, this paper proposes an approach to highlight the requirements for mass saving at the system level and ranks some investigated structural TES composites with a parameter called multifunctional efficiency. The presented analysis evidences that the potential mass saving increases when the single phases (reinforcement, PCM) are themselves multifunctional or when the volume fraction of the reinforcement does not decrease upon PCM addition.*

Keywords: multifunctional composites; thermal energy storage; phase change materials; multifunctional efficiency.

1. Introduction

Thermal energy storage (TES) allows the temporary conservation of excess heat that can be released at another time or place, as the demand for thermal energy overcomes its availability [1, 2]. Among the most promising materials for TES one can include the organic solid-liquid phase change materials (PCMs), such as paraffin waxes, which store heat when they melt and release it during crystallization [3, 4]. Organic PCMs store a high amount of latent heat at a nearly constant temperature, and thus they are often used to maintain the temperature in a specific range [5], which makes them suitable for thermal management applications [6-10]. To prevent leakage above the melting temperature, PCMs can be either encapsulated in macro-, micro-, or nano-shells or “shape-stabilized” in organic or inorganic matrices [11-14].

TES systems generally represent a supplementary component added to the main structure of a device, which can increase the volume and weight of the device itself. However, in applications where weight and volume savings are critical design parameters, it would be beneficial to embed heat storage/management functionalities directly into structural or semi-structural materials. In this context, polymer-matrix composites have the potential to be designed as multifunctional materials with both structural and non-structural functions [15-17]. They gather in one material the properties of two or more phases, and their composition can be fine-tuned to obtain the desired combination of properties [18-20]. Lightweight polymer composites combining good mechanical properties and TES capability could be applied in the automotive industry, where the diffusion of lightweight structures could complicate the thermal management of the environment

  doi:10.5075/epfl-298799_978-2-9701614-0-0

in the cockpit, or in the portable electronics field, where the reduction in volumes and masses also limits the space available for the cooling system.

Little has been carried out to deeply investigate their mechanical properties and enhance them with a reinforcing agent. In fact, most of the reported PCM-containing polymers are not suitable for load-bearing applications. Our research group has recently developed many systems consisting of polymer composites containing a PCM, made of continuous or discontinuous reinforcing fibers, thermoplastic or thermosetting matrices, and microencapsulated or shape-stabilized PCMs. [21-35]. These works showed that the introduction of an organic PCM in a fiber-reinforced composite increases its TES capability but generally weakens its mechanical performance. This occurs because the addition of a third phase may decrease the fiber volume fraction, but also because the commercial microencapsulated PCMs are generally not intended as fillers for polymer matrices, and therefore their thermomechanical and surface properties are not optimized for this purpose. Nevertheless, combining structural and TES functions in a composite material may still be advantageous in terms of mass and volume saving, compared to two separated monofunctional units performing the structural and TES functions individually [36].

Therefore, this work aims at developing an approach to quantitatively evaluate the multifunctionality of these structural TES composites. A criterium is discussed to minimize the mass of a component with both thermal energy storage and structural functions, and a multifunctionality parameter is developed that quantifies the mass saving at the system level. This parameter is then applied to evaluate and rank the structural TES composites investigated by our group. This approach allows the development of objective design principles and material selection guidelines, fundamental to maximize the advantages of using multifunctional materials.

2. Case studies of structural TES composites

The research work carried out by our group on composites containing a reinforcing phase and a PCM evidenced that, despite the potential of such materials, the structural and TES properties are hardly ever synergistic: an increase in the MC weight fraction increases the TES capability and the total heat exchanged, but it decreases almost all mechanical properties. This was observed in almost all the composites produced and investigated by our group, which are listed in Table 1 with the specification of their main constituents.

To compare the different composites on the relationship between the mechanical and the TES properties, the elastic modulus (structural parameter) of all composites can be plotted as a function of the melting enthalpy (TES parameter) (Figure 1). It is evident that the elastic modulus generally decreases with increasing melting enthalpy, and so does the mechanical strength (not reported). This is the result of the decreasing fiber volume fraction upon PCM addition and the generally low mechanical properties of the PCM phases.

The ideal case would be a combination of high stiffness (and strength) and high melting enthalpy, which would be represented in the top right corner of Figure 1. However, it is challenging to maximize both properties simultaneously, because the mechanical properties generally increase with the fiber volume fraction and the TES properties with the PCM weight fraction, while the experimental results show that fiber and PCM fractions generally follow opposite trends. The best materials for such composites would be a reinforcement with high stiffness- and strength-to-density ratio and a PCM with a large enthalpy-to-mass ratio, in order to maximize the product between fiber volume fraction and PCM mass fraction. In any case, the property to be maximized

  doi:10.5075/epfl-298799_978-2-9701614-0-0

depends on the specific application, as well as the combination of properties to be considered optimal.

The decrease in mechanical properties with an increase in TES function occurs because, in general, the reinforcement does not contribute to storing heat and the PCM does not perform any load-bearing function. One strategy to make structural and TES properties truly synergistic and not parasitic could be to shift the multifunctionality from the level of the composite to that of the single phase. This was achieved in one of the investigated systems, i.e., the starch/wood/PEG laminate. Here, the beechwood laminae acted both as reinforcement and shape-stabilizing agent for PEG, and PEG not only played the role of the PCM, but also significantly increased the tensile, impact, and dynamic-mechanical properties of the composite.

Table 1. *Multifunctional composites under investigation in this paper with specifications of matrices, reinforcing agents, and PCMs.*

Label	Matrix	Reinforcement	PCM	Reference
PA-ParCNT-GF	Polyamide 12	Bidir. glass fibers	CNT-stabilized paraffin	[21, 23]
PA-MC-GF	Polyamide 12	Bidir. glass fibers	Paraffin microcapsules	[23]
EL-MC-CF	Reactive thermoplastic	Bidir.carbon fibers	Paraffin microcapsules	[30, 31]
Starch/PEG/wood	Thermoplastic starch	Thin beechwood laminae	Poly(ethylene glycol) 600	[33]
EP-ParCNT-CF	Epoxy	Bidir. carbon fibers	CNT-stabilized paraffin	[21, 22]
EP-MC-CFu-A	Epoxy	Unidir. carbon fibers	Paraffin microcapsules	[24]
EP-MCx	Epoxy	-	Paraffin microcapsules	[37]
EP-MCx-CFSy	Epoxy	Milled carbon fibers	Paraffin microcapsules	[29]
PA-MCx	Polyamide 12	-	Paraffin microcapsules	[26]
PA-CFLx	Polyamide 12	Chopped carbon fibers	-	[26]
PA-CFSx	Polyamide 12	Milled carbon fibers	-	[26]
PA-MCx-CFLy	Polyamide 12	Chopped carbon fibers	Paraffin microcapsules	[26]
PA-MCx-CFSy	Polyamide 12	Milled carbon fibers	Paraffin microcapsules	[26]

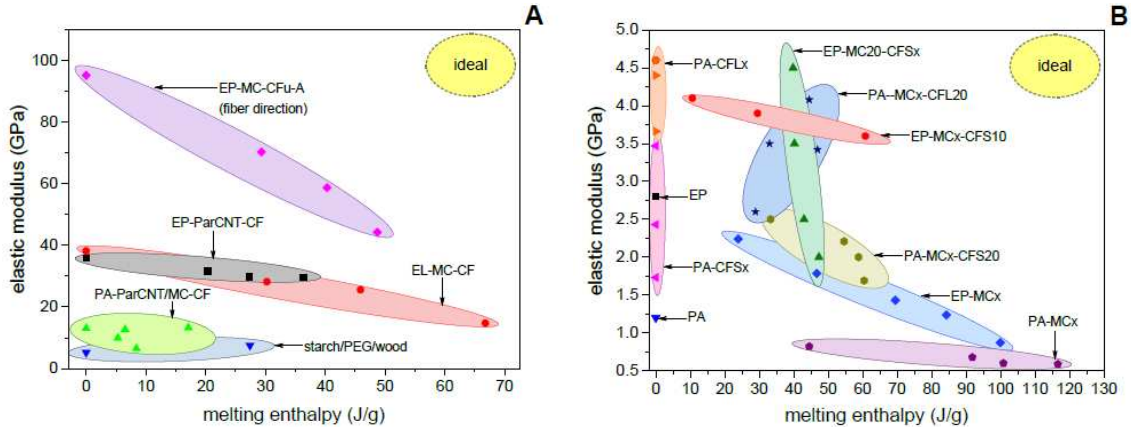

Figure 1. *Relationship between elastic modulus and melting enthalpy of all evaluated composites. The ideal case is found in the top-right corner, with simultaneous maximization of stiffness and melting enthalpy. (**A**) Continuous-fiber composites. The plot reports values of modulus along the fiber axis for unidirectional composites and in the 0–90 direction for bidirectional composites.; (**B**) Discontinuous-fiber composites. [35]*

3. Evaluation of the multifunctional performance

To bring together the competing requirements of structural TES composites, it is important to define objective parameters that capture all their functions. The approach followed in the analysis presented here is derived from that developed by O'Brien et al. [38] for structural capacitors and

used by other authors for analogous systems [25,56,57]. The objective here is to minimize the system mass for a unit presenting both structural and TES requirements.

Conventional systems can be seen as made of two monofunctional units performing the structural and the TES function separately and having masses m_s and m_{TES}, respectively. Therefore, the system (System 1) has a total mass (M) given by the sum of m_s and m_{TES}, as described in Equation (1):

$$M = m_s + m_{TES} \tag{1}$$

The TES unit has a phase change enthalpy per unit mass (ΔH), measured in J/g, and the structural unit has a specific (normalized by density) elastic modulus ($\bar{E}$). If the TES unit does not perform any load-bearing function and the structural unit does not participate in the thermal management function, then the whole system has a total melting enthalpy of ΔH and a total specific modulus of $\bar{E}$. Hence, ΔH and $\bar{E}$ are the parameters describing the performance of the full system.

Let us consider another system, System 2, composed of a multifunctional material, i.e., a structural TES composite with a mass m^*_{mf}. Of course, the total mass of this system (M^*) is now the mass of this structural TES material itself, or, as described by Equation (2),

$$M^* = m^*_{mf} \tag{2}$$

System 2, having a specific enthalpy of ΔH^*_{mf} and specific elastic modulus of $\bar{E}^*_{mf}$, must maintain the same structural and TES performance as those of System 1, in terms of overall elastic modulus (in GPa) and absorbed and released energy (in J). The two conditions, per unit volume, are described by Equations (3) and (4):

$$\Delta H \cdot m_{TES} = \Delta H^*_{mf} \cdot m^*_{mf} \tag{3}$$

$$\bar{E} \cdot m_s = \bar{E}^*_{mf} \cdot m^*_{mf} \tag{4}$$

Hence, an effective mass saving is verified if Equation (5) is met:

$$M - M^* = \frac{\bar{E}^*_{mf}}{\bar{E}} \cdot m^*_{mf} + \frac{\Delta H^*_{mf}}{\Delta H} \cdot m^*_{mf} - m^*_{mf} = \left(\frac{\bar{E}^*_{mf}}{\bar{E}} + \frac{\Delta H^*_{mf}}{\Delta H} - 1 \right) \cdot m^*_{mf} > 0. \tag{5}$$

Or, as expressed in Equation (6),

$$\frac{\bar{E}^*_{mf}}{\bar{E}} + \frac{\Delta H^*_{mf}}{\Delta H} > 1. \tag{6}$$

We can now define a structural efficiency η_s and a TES efficiency η_{TES} as described in Equations (7) and (8):

$$\eta_s = \frac{\bar{E}^*_{mf}}{\bar{E}}, \tag{7}$$

$$\eta_{TES} = \frac{\Delta H^*_{mf}}{\Delta H}, \tag{8}$$

and a multifunctional efficiency η_{mf} as described in Equation (9), as

$$\eta_{mf} = \eta_s + \eta_{TES} \tag{9}$$

  doi:10.5075/epfl-298799_978-2-9701614-0-0

Therefore, the multifunctional material allows an effective mass saving when $\eta_{mf} > 1$.

The presented analysis can be directly applied to assess if some of the prepared systems would allow an effective mass saving. The parameters η_s, η_{TES} and η_{mf} were calculated for all the composites investigated by our group (and listed in Table 1). The monofunctional structural units were represented by the respective composite without PCM, which present an η_s equal to 1 and an η_{TES} equal to zero, while the monofunctional TES units by the respective microencapsulated or shape-stabilized PCMs.

The values of η_s, η_{TES}, and η_{mf} calculated with average data of elastic modulus, density, and phase change enthalpy, are presented in Figure 2A,B. For the composites containing continuous fibers (Figure 2A), a considerable mass saving is obtained for the system starch/wood/PEG, in which not only η_{mf}, but also η_s is greater than 1. This result likely depends on the shift of the multifunctionality to the phase level, as the wood laminae are both the reinforcement and the shape-stabilizing agent and PEG contributes to the mechanical properties of the laminae, thereby further contributing to the specific mechanical and TES performance. However, η_{mf} is greater than 1 also for some other systems, and thus they also allow a certain (although lower) mass saving.

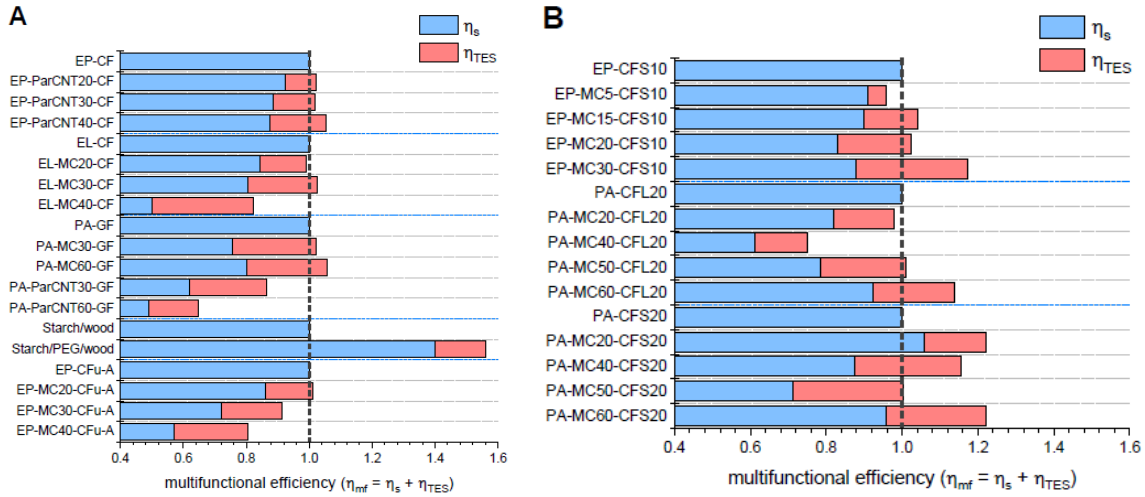

Figure 2. Multifunctional efficiency (η_{mf}) as the sum of structural and TES efficiencies. (A) Continuous-fiber composites; (B) Discontinuous-fiber composites. [35]

For the composites EP-ParCNTx-CF and PA-MCx-GF (Figure 2A), η_{mf} increases with the PCM content. This depends on two factors: (i) the fiber volume fraction was kept constant, and (ii) the processing parameters were mild enough to avoid massive PCM degradation. For the other systems, the maximum η_{mf} is generally found at medium PCM concentrations, as for higher PCM concentrations not only does the PCM decrease the elastic modulus per se, but it also contributes to decreasing the fiber fraction. For the composites containing discontinuous fibers (Figure 2B), the fiber content is generally lower than that of continuous fibers and the introduction of PCMs does not influence the fiber weight fraction, even though it could sometimes slightly decrease the total fiber volume fraction due to a decrease in the density of the non-load-bearing components. For the systems EP-MCx-CFS10 and PA-MCx-CFS20, the multifunctional efficiency is generally higher than 1 and increases with the PCM content, again because the fiber content is nearly constant and the processing conditions preserve most of the PCM from degradation.

  doi:10.5075/epfl-298799_978-2-9701614-0-0

This approach allows identifying, for each system, the composition that maximizes η_{mf}. However, this analysis is only valid if it considers parameters that are the most significant for a specific application, as for other cases it may be more meaningful to perform a volume-saving analysis or to maximize other properties such as the thermal conductivity, fracture toughness, or mechanical strength.

4. Conclusions

This work presented the concept of structural TES composite as a multifunctional material composed of a polymer matrix, a reinforcing agent, and a phase change material. Although the PCMs hardly ever contribute to the mechanical performance, and sometimes it even impairs the mechanical properties, and the reinforcement generally does not participate in the TES function, the combination of reinforcing agents and PCMs in a composite may still bring substantial mass and volume saving compared to two monofunctional units performing the structural and TES functions individually. This advantage can be quantified by calculating the composites' multifunctional efficiency (η_{mf}), defined as the sum of the structural and the TES efficiencies. An effective mass saving is obtained when η_{mf} is greater than 1. The higher value of η_{mf} (1.57) was found for the starch/wood/PEG laminate, as the wood laminae are both the reinforcement and the shape-stabilizing agent for the PCM, and the PCM also increases the mechanical stiffness. However, η_{mf} is greater than 1 also in some other composites, which indicates that these structural TES composites would allow a certain mass saving.

To maximize η_{mf}, two routes are recommended, i.e., (i) shifting the multifunctionality from the level of the composite down to the level of the single-phase, as in the case of the starch/wood/PEG laminate, and (ii) optimizing the material design and selection. For the first route, it could be beneficial to find other reinforcing agents with a porous structure that can also act as shape-stabilizers for the PCMs, or it can be useful to optimize the properties of the PCM microcapsules, in terms of the shell's mechanical stiffness and adhesion with the polymer matrix. For the material design and selection, the results showed that semi-structural composites reinforced with discontinuous fibers have generally higher η_{mf}, thus being a better option when maximizing the phase change enthalpy is more important than reaching very high mechanical properties. For continuous fiber composites, since the PCM tends to weaken and thicken the interlaminar region, an improved design of the stacking sequence could concentrate most of the PCM in the core layers and leave the outer layers richer in the reinforcing phase. A further extension of this concept may consider sandwich structures where all the PCM is concentrated in the core and the mechanical resistance is demanded to the outer skins, thereby shifting the multifunctionality from the material level up to the structure level.

5. References

1. Pielichowska K, Pielichowski K. Phase change materials for thermal energy storage. Progress in materials science. 2014;65:67-123.
2. Cabeza LF. Advances in Thermal Energy Storage Systems: Methods and Applications. 80 High Street, Sawston, Cambridge, CB22 3HJ, UK: Woodhead Publishing; 2014.
3. Ibrahim NI, Al-Sulaiman FA, Rahman S, Yilbas BS, Sahin AZ. Heat transfer enhancement of phase change materials for thermal energy storage applications: A critical review. Renew Sust Energ Rev. 2017;74:26-50.

4. Peng H, Zhang D, Ling X, Li Y, Wang Y, Yu Q, et al. *n*-Alkanes phase change materials and their microencapsulation for thermal energy storage: a critical review. Energy & Fuels. 2018;32(7):7262-93.
5. Huang X, Zhu C, Lin Y, Fang G. Thermal properties and applications of microencapsulated PCM for thermal energy storage: A review. Applied Thermal Engineering. 2019;147:841-55.
6. Kenisarin M, Mahkamov K. Passive thermal control in residential buildings using phase change materials. Renewable and Sustainable Energy Reviews. 2016;55:371-98.
7. Ianniciello L, Biwolé PH, Achard P. Electric vehicles batteries thermal management systems employing phase change materials. Journal of Power Sources. 2018;378:383-403.
8. Tan FL, Tso CP. Cooling of mobile electronic devices using phase change materials. Applied Thermal Engineering. 2004;24(2-3):159-69.
9. Ying BA, Kwok YL, Li Y, Zhu QY, Yeung CY. Assessing the performance of textiles incorporating phase change materials. Polymer Testing. 2004;23(5):541-9.
10. Mondal S. Phase Change Fibers. In: Hu J, Kumar B, Lu J, editors. Handbook of Fibrous Materials, First Edition: Wiley-VCH Verlag GmbH&Co. KGaA; 2020.
11. Jamekhorshid A, Sadrameli SM, Farid M. A review of microencapsulation methods of phase change materials (PCMs) as a thermal energy storage (TES) medium. Renewable and Sustainable Energy Reviews. 2014;31:531-42.
12. Hassan A, Shakeel Laghari M, Rashid Y. Micro-Encapsulated Phase Change Materials: A Review of Encapsulation, Safety and Thermal Characteristics. Sustainability. 2016;8(10):1046/1-/32.
13. Sobolciak P, Abdelrazeq H, Ouederni M, Karkri M, Al-Maadeed MA, Krupa I. The stabilizing effect of expanded graphite on the artificial aging of shape stabilized phase change materials. Polymer Testing. 2015;46:65-71.
14. Luyt AS, Krupa I, Assumption HJ, Ahmad EEM, Mofokeng JP. Blends of polyamide 12 and maleic anhydride grafted paraffin wax as potential phase change materials. Polymer Testing. 2010;29(1):100-6.
15. Ozaki T, Takeya H, Kume M, Sekine K. Multifunctional composite structures for space satellites. Sampe J. 2008;44(2):6-11.
16. Gibson RF. A review of recent research on mechanics of multifunctional composite materials and structures. Composite Structures. 2010;92(12):2793-810.
17. Salonitis K, Pandremenos J, Paralikas J, Chryssolouris G. Multifunctional materials: Engineering applications and processing challenges. International Journal of Advanced Manufacturing Technology. 2010;49(5-8):803-26.
18. Friedrich K. Routes for achieving multifunctionality in reinforced polymers and composite structures. In: Friedrich K, Breuer U, editors. Multifunctionality of Polymer Composites: Challenges and New Solutions. Waltham, MA, US: Elsevier; 2015. p. 3-41.
19. González C, Vilatela JJ, Molina-Aldareguía JM, Lopes CS, Llorca J. Structural composites for multifunctional applications: Current challenges and future trends. Progress in Materials Science. 2017;89:194-251.
20. Polydoropoulou PV, Katsiropoulos CV, Pantelakis SG, Raimondo M, Guadagno L. A critical assessment of multifunctional polymers with regard to their potential use in structural applications. Composites Part B: Engineering. 2019;157:150-62.
21. Fredi G, Dorigato A, Fambri L, Pegoretti A. Wax confinement with carbon nanotubes for phase changing epoxy blends. Polymers. 2017;9(9):405/1-16.
22. Fredi G, Dorigato A, Fambri L, Pegoretti A. Multifunctional epoxy/carbon fiber laminates for thermal energy storage and release. Composites Science and Technology. 2018;158:101-11.
23. Fredi G, Dorigato A, Pegoretti A. Multifunctional glass fiber/polyamide composites with thermal energy storage/release capability. eXPRESS polymer letters. 2018;12(4):349-64.

  doi:10.5075/epfl-298799_978-2-9701614-0-0

24. Fredi G, Dorigato A, Fambri L, Unterberger SH, Pegoretti A. Effect of phase change microcapsules on the thermo-mechanical, fracture and heat storage properties of unidirectional carbon/epoxy laminates. Polymer Testing. 2020;91:106747/1-/16.
25. Dorigato A, Fredi G, Pegoretti A, editors. Novel phase change materials using thermoplastic composites. 9th International Conference on "Times of Polymers and Composites" (TOP) AIP Conference Proceedings 2018.
26. Fredi G, Dorigato A, Unterberger S, Artuso N, Pegoretti A. Discontinuous carbon fiber/polyamide composites with microencapsulated paraffin for thermal energy storage. Journal of applied polymer science. 2019;136(16):47408/1-/14.
27. Fredi G, Dorigato A, Fambri L, Pegoretti A. Multifunctional polymer composites reinforced with discontinuous carbon fibers for thermal energy storage. ECCM 2018 - 18th European Conference on Composite Materials; Megaron Athens International Conference Centre (MAICC), Athens, Greece2020.
28. Dorigato A, Fredi G, Meneghini T, Pegoretti A. Thermo-mechanical behaviour of thermoplastic composite laminates with thermal energy storage/release capability ECCM 2018 - 18th European Conference on Composite Materials; Megaron Athens International Conference Centre (MAICC), Athens, Greece2020.
29. Dorigato A, Fredi G, Pegoretti A. Application of the thermal energy storage concept to novel epoxy/short carbon fiber composites. Journal of applied polymer science. 2019;136(21):47434/1-/9.
30. Fredi G, Dorigato A, Pegoretti A. Novel reactive thermoplastic resin as a matrix for laminates containing phase change microcapsules. Polymer Composites. 2019;40(9):3711-24.
31. Fredi G, Dorigato A, Pegoretti A. Dynamic-mechanical response of carbon fiber laminates with a reactive thermoplastic resin containing phase change microcapsules. Mechanics of Time-Dependent Materials. 2020;24(3):395-418.
32. Galvagnini F, Dorigato A, Fambri L, Fredi G, Pegoretti A. Thermophysical Properties of Multifunctional Syntactic Foams Containing Phase Change Microcapsules for Thermal Energy Storage. Polymers. 2021;13(11):1790.
33. Dorigato A, Fredi G, Negri M, Pegoretti A. Thermo-mechanical behaviour of novel wood laminae-thermoplastic starch biodegradable composites with thermal energy storage/release capability. Frontiers in Materials. 2019;6:1-12.
34. Fredi G, Dorigato A, Fambri L, Pegoretti A, editors. Multifunctional Polymer Composites With Structural Function And Thermal Energy Storage (TES) Capability. IRES Conference - International Renewable Energy Storage; 2018 2018-03-12; Düsseldorf, Germany: Oral presentation.
35. Fredi G, Dorigato A, Fambri L, Pegoretti A. Evaluating the multifunctional performance of structural composites for thermal energy storage. Polymers. 2021;13(18):3108.
36. Wirtz R, Fuchs A, Narla V, Shen Y, Zhao T, Jiang Y, editors. A Multi-functional graphite/epoxy-based thermal energy storage composite for temperature control of sensors and electronics2003 2003; University of Nevada, Reno Reno, Nevada, 89557 USA.
37. Fredi G, Dorigato A, Fambri L, Pegoretti A. Detailed experimental and theoretical investigation of the thermo-mechanical properties of epoxy composites containing paraffin microcapsules for thermal management Polymer Engineering and Science. 2020;60:1202–20.
38. O'Brien DJ, Baechle DM, Wetzel ED. Design and performance of multifunctional structural composite capacitors. J Compos Mater. 2011;45(26):2797-809.

  doi:10.5075/epfl-298799_978-2-9701614-0-0

TAILORING THE STRUCTURAL BEHAVIOUR OF A COMPOSITE GAS-FILLED SPRING DEVICE FOR A SWITCH IN POWER GRIDS

Fabian Folprecht[a], Tim Bätzel[a], Moritz Kuhtz[a], Paul Hoffeins[a], Matthias Gerlich[b], Sebastian Spitzer[a], Maik Gude[a]

a: Technical University Dresden, Institute of Lightweight Engineering and Polymer Technology (ILK), Holbeinstr. 3, 01307 Dresden, fabian.folprecht@tu-dresden.de
b: Siemens AG, T REE ELM MES-DE, Otto-Hahn-Ring 6, 81739 München

Abstract: The shortest possible switching times are required to reduce voltage peaks and thus stabilise the power grids in the event of fluctuating renewable energy generation. Gas-loaded springs made of composite materials represent a promising design solution for this. Due to a complex geometry and anisotropic material behaviour, accompanying numerical analyses are required right at the beginning of the development process. In the present study, the deformation and failure behaviour of a composite spring is analysed by means of a parameter study based on a simplified geometry and load case as well as a combination of different materials and fibre angles. Subsequently, suggestions for the design and further development of the composite gas spring are derived.

Keywords: Composite gas spring, power grids, high-speed switches, tailored structural behaviour

1. Introduction

In AC-, DC- and AC/DC-hybrid-grids and their substations, circuit breakers are required to protect equipment like transformers and converters in case of peak voltages and currents resulting from overload or short-circuit [1,2]. Generally, circuit breakers include the main contacts and the operating mechanism as two main functional parts, where the operating mechanism moves the main contacts to open or close them. Thus, the main demand to this mechanism is to translate the mass posed by the main contacts along the switching distance within a specified switching time. Due to dynamic effects the switching time is massively influenced by the eigenfrequencies and the stored energy of the systems.

For the operating mechanism itself, various types are established: mechanical, hydraulic, pneumatic and combinations of them are most common [3]. Alternative mechanisms based on pyrotechnics and electromagnetics [4] can reach very fast switching times but feature the disadvantage of single use only (pyrotechnics) and need of electrical auxiliary equipment (electromagnetics). Mechanical spring mechanisms are the most common ones as they have the advantage of a simple, robust and cost-effective structure with less sensitivity to changing boundary conditions (e.g. temperature) and less inherent failure causes.

Due to changing grid topologies and growing amount of fluctuating renewable energy, shorter switching times in the range of a few milliseconds are required. This demand for higher energy and eigenfrequencies of the operating mechanism often cannot be fulfilled by purely mechanical spring systems like coil or cup springs. Thereby, the technical challenge of switching devices with

  doi:10.5075/epfl-298799_978-2-9701614-0-0

very short shifting times is to tailor the stiffness both of the mechanical components of the drive unit and the passive components.

The approach of shifting eigenfrequencies to higher values though mass reductions achieved by the application of composite materials was successfully verified for coil springs [5,6] and volute springs [7]. Gas-pressure springs are an attractive alternative to coil and bellow springs. Since they have the potential to achieve a lower mass while maintaining the amount of potential energy. Moreover, this type of springs is readily available as sleeve type air springs. The main application of this design is high strokes that require high compliance, e.g. low wall thickness. However, the minimum wall thickness of the material is influenced by strength requirements, resulting in lower stored energy built up by internal pressure and low natural frequencies.

To increase the eigenfrequency, an encapsulated, leakage-free gas spring was introduced [9], which shows the ability to fulfill these requirements in combination with a simple and robust structure. This spring is based on a bellow structure with a steel sleeve. In order to further improve this type of gas spring, the approach of a composite structure is considered in this study due to excellent mechanical properties of fibre reinforced polymers.

In the study presented here, a numerical model for such springs is introduced based on a composite pressure cylinder. Therefore, an idealised geometry is used to compare different lay-ups and the material properties under combined inner pressure and axial loads. In this way, a deeper understanding of the underlying structural effects can be achieved and favourable configurations for further investigations can be identified. These findings provide an excellent basis for further developments to extend the results to more complex geometries.

2. Design concept

The metallic reference structure is shown in Figure 1 (left). The region of the bellow sleeve is about ca. 85 mm in diameter and 80 mm in active deformed length. This prototype reaches a maximum of 9 mm overall deformation in axial direction and can be operated at 100 bar. In case of switching, the stored energy is transferred to the contact by a conversion to a longer path. For a further development of the reference spring to a composite spring structure, an increase of transferring energy is needed. This can be achieved both by increasing the inner pressure for higher output forces and by increasing the displacement. Though, the mass of the structure is intended to not raise with respect to an increase in the eigenfrequency of the spring.

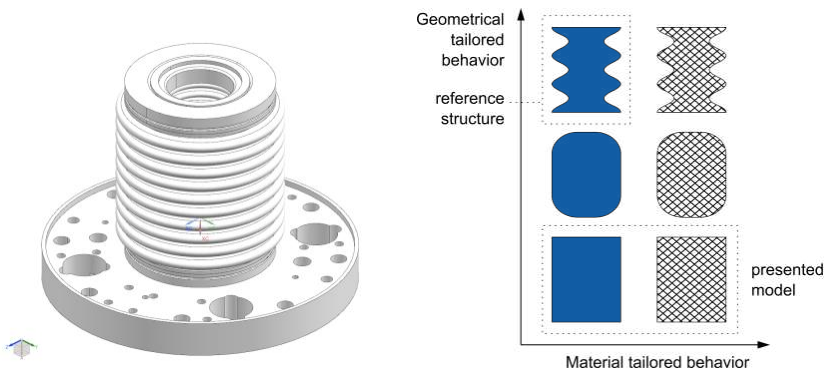

Figure 1: Metallic reference structure of the bellow gas spring (left) and tailored deformation behaviour by the geometric and material design (right)

For composite gas-loaded bellow springs considered in this study there are two basic design elements, which allow a tailored deformation behavior. Adjustments of the relation between pressure resistance and maximum axial stroke are supported by the geometric design of bellow arches and laminate architecture of the bellow material.

The utilisation of fibre-reinforced materials introduces layerwise fibre orientations as additional design parameters and, thus, offers an extended design space. The bellowed design allows for tailored load-dependent stiffness within the gas-spring structure. Through the individual geometry and total number of bellow arches, the structure's axial flexibility can be adjusted as needed for the special application, while maintaining the tangential stability high for internal pressure load capability. Still, those characteristics are interacting with each other.

In a first step, the structural behaviour under internal pressure loading and additional axial stretching as a function of the prevailing fibre orientation is the subject of the numerical investigations. While the numerical studies are focused on a representative cylindrical structure, there are additional geometrical effects to be considered for the application-oriented bellow structure. A detailed investigation of the cylindrical structure will grant a deeper understanding of underlying structural effects.

3. Numerical analysis of the deformation behaviour

The deformation behaviour of the substitute structure is investigated by means of a finite element model. A linear quasi-static model is created using the Siemens Simcenter 3D software. Figure 2 shows the geometric dimensions and the boundary conditions as well as the numerical representation as a substitute model.

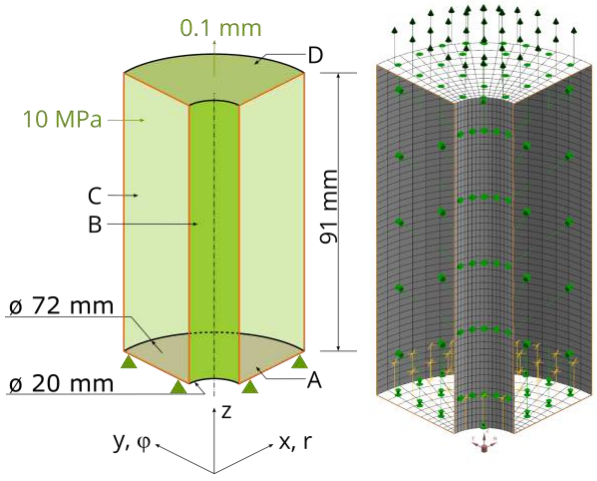

Model information
Simcenter Nastran Structural Linear steady state
1984 4-node shell elements
Base and top surface (A,D): Steel
Shell surfaces (B,C): Laminate

Figure 2: Schematic representation of the dimensions and boundary conditions (left, centre) and key information of the FEA model (right)

The base and top surfaces of the cylinder ring are represented as a 10 mm thick steel shell. The shell surfaces are modelled as a six-layer, balanced and asymmetrical angle ply laminate with lay-up $[\alpha/\text{-}\alpha]_3$. Since the wall thickness is expected to have a significant influence on the stiffness of the subsequent bellows via the Steiner proportion, this is taken from the metallic reference structure. The cylinder is supported at its base surface A in the *z*-direction. The quarter model of the cylinder is supported in the symmetry planes with symmetry boundary conditions. A

  doi:10.5075/epfl-298799_978-2-9701614-0-0

pressure load boundary condition of 10 MPa is applied to the interior of the cylinder ring (surfaces A to D). In addition, the top surface D is displaced up to 0.1 mm in the positive *z*-direction. The deformation is calibrated by an equal model with a steel jacket up to materials yield stress.

In a preliminary investigation, the influence of the symmetry boundary conditions was investigated. Due to the asymmetric layer structure, a coupling between in-plane loads and out-of-plane deformations existed according to classical laminate theory. The difference of the resulting deformations of a full model and a quarter model are very small, which is why the quarter model is chosen as reference model. Secondly, the influence of the solver was investigated by applying a solution in one solution step and in 20 solution steps. The resulting deformations and the corresponding stresses are higher in the model that was solved in one solution step. Since this corresponds to a more conservative design, this solution procedure is chosen as reference.

The failure behaviour is evaluated in post-processing by means of a user-defined material model according to the failure mode concept of Cuntze [8], that enables both a fracture mode-related and a cumulative evaluation of the ply-by-ply failure behaviour. According to the principle of St. Vernant, only the elements located in the undisturbed area of the laminate are used for evaluation.

Two different composite materials are analysed. On the one hand carbon fibre reinforced polymer (CFRP) HexPly8552 (*CF-EP)* and on the other hand glass fibre reinforced polymer GFRP Silenka E-Glass with MY750/HY917/DY063 are investigated. A linear-elastic material behaviour is assumed for both materials. The characteristic values are taken from the ESAComp-Database.

The results for the model with CF-EP material are compiled in Figure 3. For fibre angles of 40° or greater, the model calculates a failure index of less than 1 for all load cases investigated and, thus, testifies a basic suitability of this material for the loading profile.

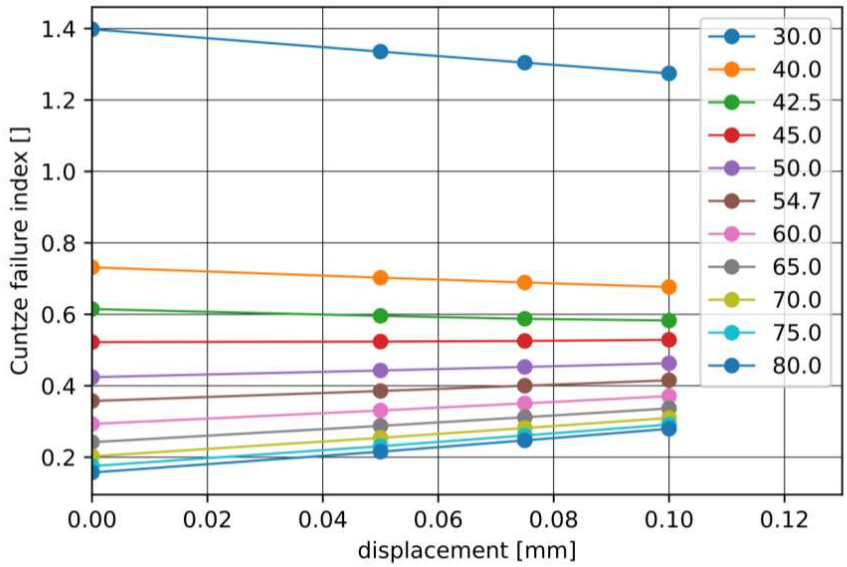

Figure 3: Failure index of the CF-EP Hex8552 dependent of the fibre angle

While ±54.7° fibre angles are optimal for cylindrical areas in conventional pressure tanks, the introduced model exhibits a decreasing failure index with increasing fibre angles for the first loading stage (internal pressure only). This effect is due to the constrained axial displacement at the base and cover plate (cf. A, D in Figure 2), which result in only tangential stresses acting upon the jacket area.

As expected, the application of positive axial strain results in rising Cuntze failure indices for fibre angles of ±50° or above. However, calculations involving fibre angles below ±45° revealed descending failure indices with increasing axial strains. This can be accounted for by the failure envelope's shape in the stress space. Through axial loading, resulting principle stresses are progressively aligned with the fibre axes, leading to decreased failure indices.

The transition between increasing and decreasing failure index due to axial strain occurs at slightly less than ±45°

As illustrated by Figure 4, this structural behaviour was observed for the glass fibre-reinforced cylinder model as well. Compared to the CFRP structure, the material utilisation is significantly higher and none of the calculated layer structures achieves a failure index below 1. This clearly outlines the inferior material strengths of GFRP.

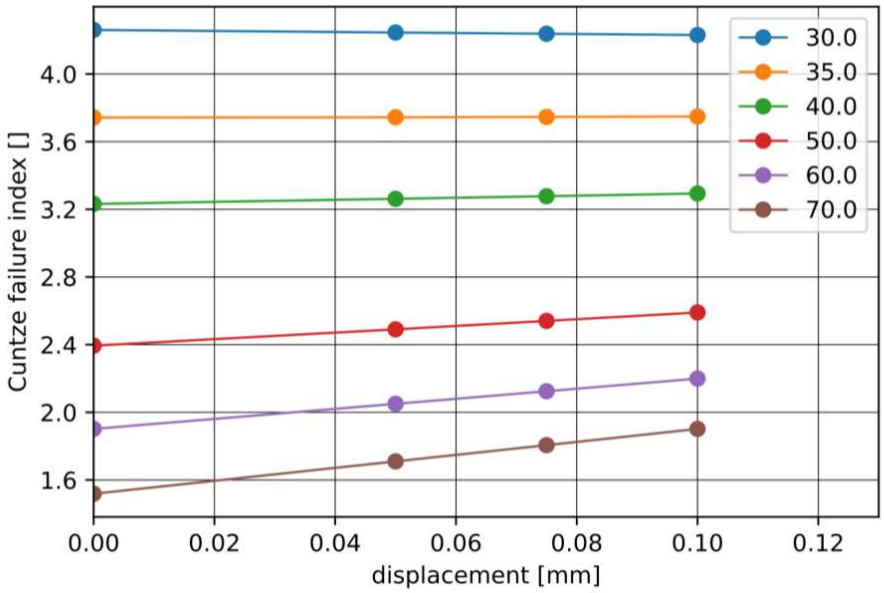

Figure 4: Failure index of E-Glass with MY750/HY917/DY063 dependent of the fibre angle

Corresponding to the calculation with CFRP material, the model exhibits a similar variable behaviour under applied axial strain. The transition from decreasing failure indices (for lower fibre angles) to increasing failure indices (for higher fibre angles) occurs at approximately ±35°, 10° lower than for CFRP material.

4. Interpretation of the results

Due to the axial support of the cylinder model at the end faces, the initially prevailing stress state is decisively characterised by tangential stresses. This is outlined by lower failure indices for higher fibre angles at zero axial strain (Figure 3, Figure 4). The applied axial displacement

causes the build-up of axial stresses in the jacket area. This redistribution of the axial load causes the axes of the principal stresses to shift increasingly in the axial direction.

For the case of a free displaceable top surface, a principal stress ratio of 2:1 (typical ration for internally pressurised hollow bodies) is established in the jacket area and the principal stress axes are oriented at 54.7°. Based on net theory (basic assumption: equilibrium of forces inside single plies), the lowest material utilisation is achieved for the case of aligned principal stress axes and fibre orientations. Based on this approach, the observed failure indices history obtained in the numerical study can be explained through the axial straining. If principal stress axes converge with fibre orientations through the allowance of axial strain, the failure index falls. If both orientations diverge, the failure index increases.

The results for CFRP contain fibre angles that are constantly below a Failure Index 1 in the deformation range considered and exhibit a decreasing failure index for increasing deformation. Compared to the metallic reference, which was used to calculate the maximum axial elongation the numerical study (elongation at which the metallic material's yield stress was reached), these findings suggest a larger possible stroke without structural failure. Suitable non-linear model with higher axial strains are necessary to validate this relationship.

The model presented corresponds to a global view and is not able to consider local effects. This is mainly due to the cylindrical geometry, which does not include the bellows with corresponding local effects. Figure 5 (left) illustrates an exemplary section of the bellow. The effects involving axial and tangential stresses (discussed above) are expected in a similar way for complex bellow structures due to the fundamentally analogous internal pressure load with successively released axial strain. However, this underlying mechanism is likely to be superimposed by further geometry-based effects, as well as dynamic effects. Thus, additional forces and moments act locally on the individual shafts (cf. Figure 5, centre). This is expected to result in local deformations in terms of bending of the single bellows as shown in Figure 5 (right).

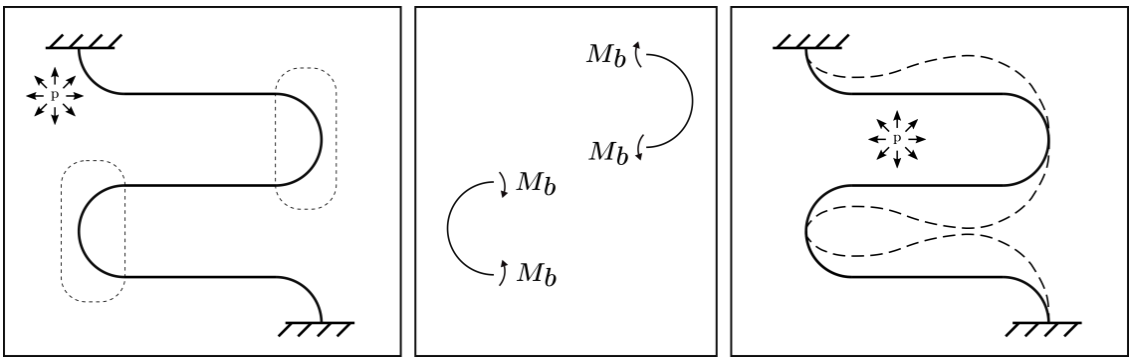

Figure 5: Exemplary bellow structure (left) internal cutting forces in inner and outer bellow (centre) expected local deformation of the bellow structure (right)

Bending deformations in the bellow jacket area are expected to induce tensile and compressive stresses in the composite layup, especially in layers close to both surfaces. Thus, stresses similar to the tension- and compression-loaded cylinder jacket may be the result. Future in-depth investigation is necessary to clarify if it is possible to transfer the effect of decreasing failure indices through increasing axial strain from cylindrical jacket structures to bellowed jacket

structures. At this point, the influence of different laminate thicknesses in correlation with normalized bending strengths are to be considered.

5. Conclusion

Basic investigations for the transformation of an existing gas-filled spring device into a composite spring were presented. A tailored deformation behaviour is crucial to meet given requirements. Exploitable design variables are based on two approaches: the geometric structure and the composite material structure. Within the scope of the paper, the material structure was first investigated. On this behalf, a linear simulation model was developed and the suitability of CFRP and GFRP materials with different fibre angles for a balanced angle ply laminate were investigated. Under constant internal pressure, different axial deflections were considered. The laminate strength was evaluated according to the Cuntze failure criterion.

The CFRP material was found to be particularly suitable for the structure under consideration. For balanced angular composites with fibre orientations of <±45° for CFRP and <±35° for GFRP, the failure index also decreases with increasing axial deflections. Thus, it is expected that the feasible axial deflection is significantly increased compared to the metallic structure. This relationship is to be validated in a non-linear model with large deflections. Finally, the transfer of the results to the bellow structure was discussed. At this point, additional local effects are expected, which must be investigated and validated through the implementation of more comprehensible simulation models.

6. Acknowledgement

The work took place as part of the project "Leichtbautechnologien in lebensphasenübergreifenden Kreislaufprodukten der Energiewende" (LiKE, funding code 03LB2008G). The project is funded as part of the technology transfer program lightweight design of the Bundesministerium für Wirtschaft und Klimaschutz BMWK and supported by Projektträger Jülich.

Supported by:

on the basis of a decision
by the German Bundestag

7. References

1. Jürgen Häfner, Björn Jacobson. Proactive Hybrid HVDC Breakers – A key innovation for reliable HVDC grids. Electric power systems of the future – Integrating supergrids and microgrids. International Symposium in Bolgna, Italy 13-15 September, 2011
2. Marius Langwasser, Giovanni De Carne, Marco Liserre. Requirement Analysis of Circuit Breakers in Future Hybrid AC/DC Grids. PCIM Europe 2019; International Exhibition and

Conference for Power Electronics, Intelligent Motion, Renewable Energy and Energy Management
3. Hiroki Ito. Switching Equipment. International Council on Large Electric Systems (CIGRE) Study Committee A3: High Voltage Equipment. Springer
4. Christian M. Franck. HVDC Circuit Breakers: A Review Identifying Future Research Needs. IEEE Transactions on Power Delivery. Volume: 26, Issue: 2, April 2011
5. DE102011018217A1 – Hufenbach, Lepper, Werner: „Verfahren zur Herstellung von Federelementen aus Faserverbundwerkstoffen“
6. DE102012112937A1 – Lepper, Werner, Köhler, Bartsch, Hufenbach: „Vorrichtung und Verfahren zur Herstellung einer Feder aus Faserverbundwerkstoff“
7. Martin Petrich, Ulft Kletzin, Tom-Luis Weimann, Julius Feld: Carbon-Evolutfeder. Draht Bd 72 (2021), 6, p.38, Bamberg: Meisenbach, 2021.
8. Cuntze, R. G.; Freund, A.: The predictive capability of failure mode concept-based strength criteria for multidirectional laminates. Composites Science and Technology 64 (2004), pp. 343-377.
9. DE102019219728A1 – Ebelsberger, Gerlich, Schacherer: "Elektrische Schalteinrichtung"

  doi:10.5075/epfl-298799_978-2-9701614-0-0

MECHANICAL AND ADSORPTION CHARACTERIZATION OF A GRAPHITE/SAPO-34/S-PEEK COMPOSITE COATINGS FOR WATER VAPOR ADSORPTION HEAT PUMPS

Luigi Calabrese[a,b], Davide Palamara[a], Andrea Frazzica[b] Edoardo Proverbio[a]

a: 1Department of Engineering, University of Messina, Contrada di Dio Sant'Agata, 98166 Messina, Italy; lcalabrese@unime.it ,
b: CNR - ITAE "Nicola Giordano", Via Salita S. Lucia sopra Contesse 5, 98126 Messina, Italy

Abstract: *In this paper, a new composite adsorbent coating on aluminum support, based on SAPO34 and exfoliated graphite fillers embedded into sulfonate polyether ether ketone (S-PEEK) matrix is investigated for adsorption heat pumps (AHP) applications. Composite mixtures at varying adsorbent content (80-95 wt.% SAPO-34 zeolite) and conductive filler (5-10 wt.% exfoliated graphite) have been prepared and coated by drop casting on aluminum substrates. All coatings were mechanically evaluated using pull-off and scratch tests evidencing a good adhesion with the metal substrate. The morphological analysis confirms that the fillers homogenously distributed in the matrix. In order to assess the adsorption/desorption capacity, water vapor adsorption isobars at 11 mbar were measured at equilibrium in the temperature range 30-120 °C, confirming that the matrix not hinder the water vapor mass flow and the zeolite takes part in the adsorption/desorption process, indicating this material potentially suitable per AHP applications.*

Keywords: sulfonate polyether ether ketone; zeolite; adsorption; coating; adhesion

1. Introduction

The adsorbent bed is a component that plays a main role in the high-efficiency design of adsorption heat pump (AHP). The simplest and most economical option is to use an unconsolidated bed in which adsorbent material in the form of granules is placed inside the exchanger fins without a binder. This type of adsorbent bed has a low heat transfer capability due to the punctual contact between the adsorbent grains and the exchanger elements and the low conductivity of the grains themselves [1] but good mass transfer due to the spaces between the grains.

On the other hand, in a consolidated bed the adsorbent material is in direct contact with the metal substrate either due to direct synthesis of the adsorbent material on the substrate [2] [3] [4] or due to the presence of a binder [5] [6] [7]. This option has a higher heat transfer at the coating/metal interface, which reduces cycle time [8], but a lower mass transfer due to the presence of the binder and the low porosity of the coating.

Low mass transfer and heat in the adsorbent bed are the main causes that make it difficult to achieve high performance AHP technologies. These factors lead to an increase in the time required to complete adsorption/desorption cycles. For this reason, it is of key importance to find the proper compromise to achieve maximum adsorbate diffusion between the exchanger fins and maximum heat transfer both at the adsorbent/metal interface and between the adsorbent particles themselves.

  doi:10.5075/epfl-298799_978-2-9701614-0-0

For this reason, in the realization of a binder-based adsorbent composite coating technology, the binder material in addition to have good thermal properties must allow a fast and effective permeation of the adsorbate.

On this concern Calabrese et al. [9] proposed a new adsorbent composite material, constituted by a siloxane macroporous foam as matrix and SAPO-34 zeolite as adsorbent filler. The results evidenced that the permeable polymer matrix not hinder the water vapor diffusion [10] providing high mechanical and adsorption performances [11] [12].

The choice of using a water vapor permeable matrix was similarly proposed in [13] , evidencing suitable mechanical and physicochemical properties of this zeolite/S-PEEK composite coating.

However, considering the low thermal conductivity properties of S-PEEK matrix, in the present paper the effect of exfoliated graphite (EG) addition on the performances of the adsorbent composite coating has been evaluated. For this purpose, a chemical-physical characterization was firstly carried out followed by a mechanical characterization (performed by pull off and scratch tests). Finally, the influence of the recycled polymer on the adsorption performances of the coating has been evaluated.

2. Experimental part

2.1 Materials and sample preparation

The sulfonation of the polyetheretherketone polymer (supplied by Heroflon S.p.A, Italy) has been realized by the same procedure reported in [13]. Briefly, 3 g of the recycled PEEK (preliminarily dried at 100 °C for 12 h) were dissolved in 60 ml of concentrated sulfuric acid (98%) at 25 °C under vigorous stirring for 48 h and poured drop by drop into an ice-cooled demineralized water in order to rapidly arrest sulfonation reaction and precipitate the polymer. The acid polymer in the form of small droplets, after an appropriate washing in distilled water in order to obtain the neutralization, has been dried at 60 °C for 24 h. The time of sulfuric acid treatment (48 h) has been established as a consequence of the results obtained from the previous work [13] as the best compromise between the mechanical properties obtained and not excessive sulfonation times.

2.2 Preparation of composite coatings

S-PEEK particles, previously synthetized, were dissolved in N, N-Dimethylformamide (DMF) solvent. Then, four different amounts of SAPO-34 powder (ranging from 80 wt.% to 95 wt.% of S-PEEK amount) was gradually added to the polymer solution. Subsequently, if required, exfoliated graphite (EG) (supplied by TIMREX C-THERM 002 TIMCAL Ltd. - 5 wt.% of the S-PEEK amount) was added. The resulting composite slurry was poured drop by drop on a metal surface (Aluminum 6061) and dried at 60 °C for 12 h. The thickness of the resulting coatings were lower than 0.50 mm. Composite coatings obtained at varying graphite and SAPO-34 filler content (80 wt.%, 85 wt.%, 90 wt.% and 90 wt.%) were prepared with the purpose to identify the optimal compromise between adsorption and mechanical performances.

The composite coatings of S-PEEK/Zeolite/graphite were coded with a common root “SP-Zxx-Gyy” where xx is a number that denote the dry zeolite content in wt.% and yy is the graphite content employed as fillers in the composite coating. For example, SP-Z80-G05 code is referred

  doi:10.5075/epfl-298799_978-2-9701614-0-0

to a composite coating containing 80 wt.% of SAPO-34 filler and 5 wt.% of graphite in a S-PEEK (sulpfonated recycled PEEK) matrix.

Table 1: Formulation and codes of the composite coating batches

Code	S-Peek (wt.%)	SAPO-34 (wt.%)	Graphite (wt.%)
SP-Z80-G5	15	80	5
SP-Z85-G5	10	85	5
SP-Z90-G5	5	90	5
SP-Z80	20	80	0
SP-Z85	15	85	0
SP-Z90	10	90	0
SP-Z95	5	95	0

2.3 Coating characterization

Pull-off and scratch tests were performed to evaluate the mechanical properties of the coatings. The first one, which allows to evaluate the tensile adhesion strength of the coating on the aluminum substrate, was carried out by using a DeFelsko PosiTest AT-M pull-off tester. The test consists in pulling an aluminum dolly (10 mm in diameter), previously glued on the surface of the coating by means of an appropriate clamping system. The dolly is glued using a cyanoacrylate adhesive and cured at room temperature for 12 hours.

The scratch test, which provides a measure of the scratch resistance of the coating surface (according to EN ISO 1518-1 standard), was performed by using an Elcometer 3000 manual Clement tester. Finally, by means of a thermogravimetric dynamic vapor system (Surface Measurements Systems DVS Vacuum), the isobaric adsorption/desorption performances of the Adsorbent composite coatings were evaluated.

3. Results and discussion

Figure 1 shows pull-off adhesion strength of composite coating at varying filler content. All the composite coatings are characterized by a good adhesion strength. This suggests that a good interaction between metal substrate, fillers and S-PEEK polymer matrix occurs. The pull-off strength progressively decrease at increasing the filler content. Although characterized by lower adhesive properties, composites with 95% filler have quite higher pull-off strength values (between 1.57 and 1.75 MPa) than the values reported in the literature [14]. It is also noted that the substitution of zeolite filler with an exfoliated graphite one leads to a decrease in adhesion, especially at higher values of filler content (for example from values of 1.44 MPa for SP-Z95 to 1.00 MPa for SP-90-G5).

  doi:10.5075/epfl-298799_978-2-9701614-0-0

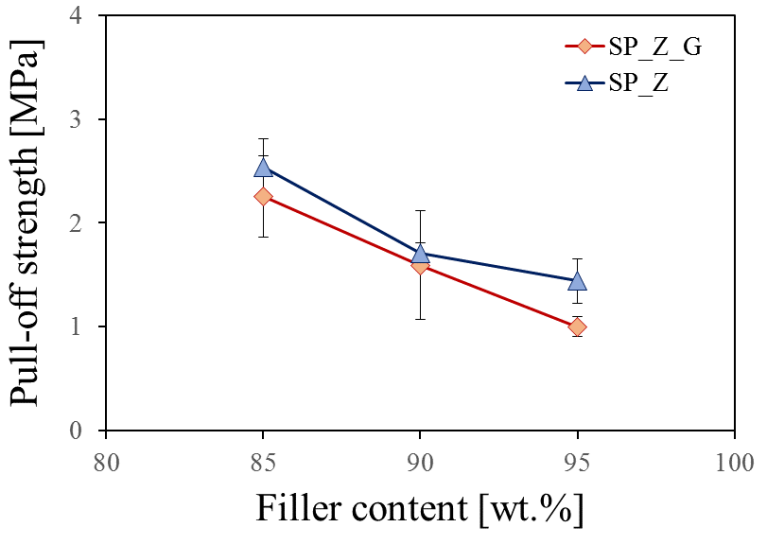

Figure 1: Pull-off adhesion strength of composite coating at varying filler content

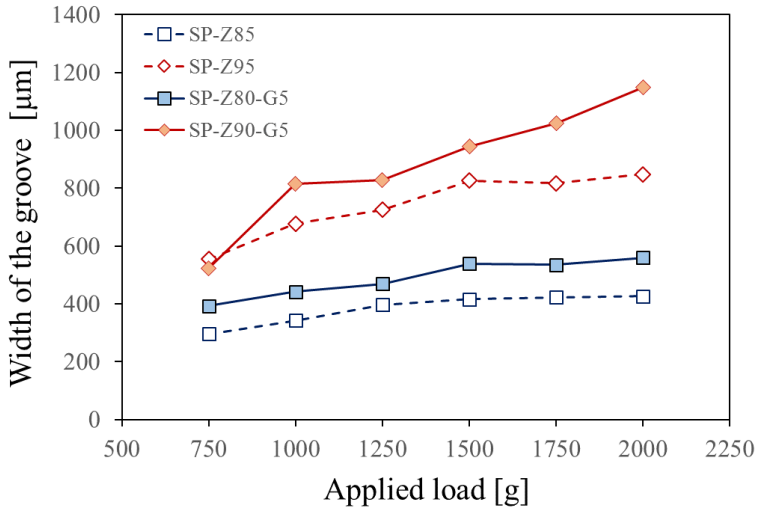

Figure 2: Width of the groove obtained from scratch test at varying applied load for composite coatings with 85 wt.% and 95 wt.% of filler content.

Figure 2 shows the scratch width of the composite coatings realized with 85 wt.% and 95 wt.% of filler content at varying applied load. Identifying a common filler content, e.g. 85 wt.%, two batches without and with exfoliated graphite were compared. The surface scratch width can be related to the coating scratch resistance. The wider this parameter, the lower the scratch resistance is. It can be seen that the best resistance values have been obtained from composite coating without graphite and the lower content of filler (SP-Z85 batch). Substituting the zeolite with the graphite filler (i.e. SP-Z85 toward SP-Z80-G5) a clear increase in the width of the groove can be identified. Analogous consideration can be observed for batches with 95 wt.% of filler content. This behavior is due to the addition of graphite filler that decrease the adhesion properties of the composite coating. The graphite filler is a low density filler, compared to the zeolite one. This indicates that a larger volume of graphite filler is added to the composite

  doi:10.5075/epfl-298799_978-2-9701614-0-0

coating formulation compared to the zeolite one. Furthermore, the zeolite, despite exfoliated graphite, is a porous structure with larger amount of hydroxyl groups able to better interact with the polar groups of the S-PEEK, this leading to a better interfacial adhesion. This provide a composite coating with a lower cohesive force if exfoliated graphite is substituted to zeolite filler.

As attended batches with 85 wt.% of filler exhibited a better scratch resistance than 95 wt.% ones. A higher content of S-PEEK implies that the filler is wrapped in a more homogeneous way in the matrix, allowing a more effective transfer of stress to the interface. Indeed, increasing the amount of zeolite could lead to an increase in defects and voids therefore a decrease in cohesive properties.

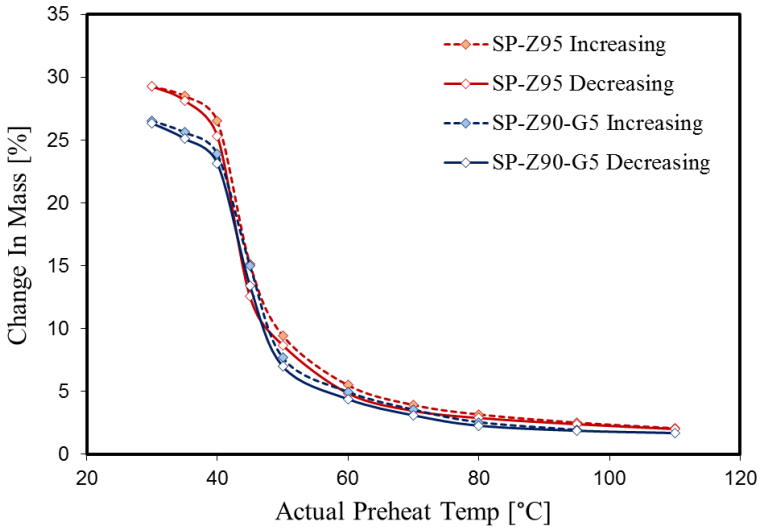

Figure 3: Adsorption (filled marker) and desorption (empty marker) isobars at 11 mbar of water vapor for composite coatings with 95 wt.% of filler content

The water adsorption (filled markers, dotted line) and desorption (empty markers, solid line) isobars of the composite coatings (SP-Z95 and SP-Z90-G5 batches) are reported in Figure 3 in the temperature range of 30–110 °C and at p_{H_2O} of 11 mbar. This water pressure value was chosen since it corresponds to an evaporation temperature Tev of 8 °C that is the usual temperature at which the adsorption chiller works to give an effective cooling effect. The adsorption capacity of the adsorbent composites decreases at decreasing SAPO-34 zeolite content. The adsorption capacity of SP-Z90-G5 composite is always lower than SP-Z95 due a lower content of adsorbent material in the former batch (90 w.t. and 95 wt.%). The highest adsorption value for SP-Z90-G5 batch was equal to 26.34 %. This value is almost compatible with the adsorption behavior of commercial adsorbent materials usually applied in AHPs [15]. This suggests that S-PEEK binder does not have a relevant vapor barrier action. Preferential flow pathways could occur also involving closed and not interconnected cavities and voids in the composite coating. Analogously no detrimental effect on adsorption/desorption capacity of the zeolite filler occurs due to the addition of the conductive filler. These preliminary results indicate that this class of composite adsorbent coating, constituted by exfoliated graphite and SAPO-34 fillers embedded in an S-PEEK polymer matrix can be identified as a promising approach in order to optimize the adsorbent HEX performances and its related maintenance costs.

  doi:10.5075/epfl-298799_978-2-9701614-0-0

4. Conclusions

A SAPO-34/EG/S-PEEK composite coating was investigate coupling mechanical and chemo-physical tests in order to address its applicability in adsorption heat pumps field. The composite material evidenced good perspective in terms of adhesion with substrate and good adsorption performances. In particular, the adsorption/desorption tests evidenced that the composite coatings filled with EG evidenced a maximum water uptake of 26.34% for SP-Z90-G5 batch identifying this coating potential effective applicability in AHP applications. The SP-Z90-G5 batch evidenced acceptable adhesion properties (pull off strength 1.00 MPa) compared to other batches, however, superior to similar composite adsorbent coatings applied for AHPs.

Acknowledgements

This research follows from Project ‘‘NAvi efficienti tramite l’Utilizzo di Soluzioni tecnologiche Innovative e low Carbon (NAUSICA)” (M.I.U.R. – PON 2014/2020), code ARS01_00334 .

5. References

1. Aristov YI. Challenging offers of material science for adsorption heat transformation: A review. Appl Therm Eng 2013; 50:1610–1618.
2. Bauer J, Herrmann R, Mittelbach W, Schwieger W. Zeolite/aluminum composite adsorbents for application in adsorption refrigeration. Int J Energy Res 2009; 33:1233–1249.
3. Bonaccorsi L, Calabrese L, Proverbio E. Low temperature single-step synthesis of zeolite y coatings on aluminium substrates. Microporous Mesoporous Mater 2011; 144:40–45.
4. Schnabel L, Tatlier M, Schmidt F, Erdem-Senatalar A. Adsorption kinetics of zeolite coatings directly crystallized on metal supports for heat pump applications (adsorption kinetics of zeolite coatings). Appl Therm Eng 2010; 30:1409–1416.
5. Freni A, Bonaccorsi L, Calabrese L, Caprì A, Frazzica A, Sapienza A. SAPO-34 coated adsorbent heat exchanger for adsorption chillers. Appl Therm Eng 2015; 82:1–7.
6. Freni A, Frazzica A, Dawoud B, Chmielewski S, Calabrese L, Bonaccorsi L. Adsorbent coatings for heat pumping applications: Verification of hydrothermal and mechanical stabilities. Appl Therm Eng 2013; 50:1658–1663.
7. Kummer H, Fuldner G, Henninger SK. Versatile siloxane based adsorbent coatings for fast water adsorption processes in thermally driven chillers and heat pumps. Appl Therm Eng 2015; 85:1–8.
8. Dias JMS, Costa VAF. Which dimensional model for the analysis of a coated tube adsorber for adsorption heat pumps? Energy 2019; 174:1110–1120.
9. Calabrese L, Bonaccorsi L, Freni A, Proverbio E. Synthesis of SAPO-34 zeolite filled macrocellular foams for adsorption heat pump applications: A preliminary study. Appl Therm Eng 2017; 124:1312–1318.
10. Calabrese L, Bonaccorsi L, Bruzzaniti P, Frazzica A, Freni A, Proverbio E. Adsorption performance and thermodynamic analysis of SAPO-34 silicone composite foams for adsorption heat pump applications. Mater Renew Sustain Energy 2018; 7:1–13.
11. Calabrese L, Bonaccorsi L, Bruzzaniti P, Freni A, Proverbio E. Morphological and functional aspects of zeolite filled siloxane composite foams. J Appl Polym Sci 2018; 135:45683.
12. Calabrese L, Bonaccorsi L, Bruzzaniti P, Gullì G, Freni A, Proverbio E. Zeolite filled

  doi:10.5075/epfl-298799_978-2-9701614-0-0

siloxane composite foams: Compression property. J Appl Polym Sci 2018; 135:46145.
13. Calabrese L, Bruzzaniti P, Palamara D, Freni A, Proverbio E. New SAPO-34-SPEEK composite coatings for adsorption heat pumps: Adsorption performance and thermodynamic analysis. Energy 2020; 203:117814.
14. Calabrese L, Bonaccorsi L, Caprì A, Proverbio E. Adhesion aspects of hydrophobic silane zeolite coatings for corrosion protection of aluminium substrate. Prog Org Coatings 2014; 77:1341–1350.
15. Freni A, Maggio G, Sapienza A, Frazzica A, Restuccia G, Vasta S. Comparative analysis of promising adsorbent/adsorbate pairs for adsorptive heat pumping, air conditioning and refrigeration. Appl Therm Eng 2016; 104:85–95.

  doi:10.5075/epfl-298799_978-2-9701614-0-0

THERMOPLASTIC MULTI-CELL PRESSURE VESSELS FOR HYDROGEN STORAGE – DESIGN, MANUFACTURING AND TESTING

Jan Condé-Wolter[a], Simon Eckardt[a], Dirk Holländer[b], Tobias Lebelt[a], Andreas Gruhl[b], Alexander Rohkamm[c], Michael Ruf[d], Maik Gude[a]

a: Technische Universität Dresden — jan.conde-wolter@tu-dresden.de
b: Leichtbau-Zentrum Sachsen LZS GmbH
c: herone GmbH
d: BMW AG

Abstract:

As hydrogen is a potentially emission free energy source it is a suitable option for clean mobility applications. But as the most mobility applications like cars, trucks and busses are currently still running on combustion engines and as the energy density of conventional fuels is much greater than of pressurized stored hydrogen, new designs and manufacturing methods are necessary to achieve the market requirements in terms of range. Within this paper a multi-cell high-pressure hydrogen storage system based on braided thermoplastic tapes is presented as well as its manufacturing process. Furthermore, a test device for high pressure burst test of pipe section was developed which allows burst test at early development stages. Burst test were taken out on braided thermoplastic pipe sections and the results are shown and discussed. These experimental tests are accompanied by numerical analyses, which are also shown.

Keywords: hydrogen; pressure vessels; thermoplastic, tape-braided; burst test

1. Introduction

As mobility and transport applications are the source of 21.9 % of the European greenhouse gas emissions, it is one of the sectors where climate-neutral alternatives are urgently needed [1]. One solution are battery-electric vehicles (BEV) and with the improvement in battery technology during the past years, they offer a climate-neutral alternative for most use cases. But due to long charging times and still limited energy density and range, BEV show restrictions, when long ranges and short refueling times are needed. For these vehicle applications, such as many commercial vehicles like trucks and busses, hydrogen can be a promising alternative [2].

As the storage of liquid hydrogen offers several disadvantages like the loss of stored energy through blow-offs, a higher system complexity, lower technological maturity and less existing infrastructure, high-pressure storage systems are currently focused. High-pressure hydrogen vessels are available on the market for pressures of 350 and 700 bar and in different types of design. The most common for mobile applications are so-called type-III and type-IV pressure vessels. Both are based on an inner liner which are made out of metal (type-III) or polymer (type-IV) and ensure the leak tightness and a permeation barrier. The liners of both vessel types are supported with a composite structure to withstand the inner pressure. Type-IV vessels offer a lower weight and therefore higher gravimetric energy density as they use low-weight polymers like HDPE or PA6 due to very good permeation barriers [3].

There are many, mostly wet-wound, type-III and type-IV pressure vessels on the market available. Storage capacities range from 2 kg to more than 15 kg of hydrogen. To store these

  doi:10.5075/epfl-298799_978-2-9701614-0-0

amounts of gaseous hydrogen, a large volume is necessary which leads to cylindrical shapes with a diameter starting around 300 mm and length of around 1000 mm and going up to diameters of 700 mm and more than 2 m of length. As a passenger car needs around 4 to 6 kg of hydrogen, up to four smaller but still bulky vessels are integrated in the structure [4]. As most vehicle architectures have few to no empty space left, the integration becomes very difficult and effects the whole vehicle design as it can be seen in *Figure 1* on the left side. Therefore, more flexible high-pressure storage concepts are necessary to address various spaces, improve the volumetric energy density and increase the overall stored mass of hydrogen without affecting the vehicle concept like reducing trunk space.

2. Concept and design of multi-cell high-pressure storage system

2.1 Concept of storage system

Beside many other concepts for space-efficient high-pressure storages, one of particular interest are multi-cell pressure storage systems [5,6]. The reason for this is Barlow's formula, which forms the basis for the design of pressure tanks. For a constant pressure the wall thickness depends linearly only on the mean diameter according to Barlow's formula. This means that a large number of tanks does not have a disadvantage in terms of mass compared to few larger tanks, but these can use the available installation space much more efficiently. *Figure 1* shows an exemplary implementation of the developed concept of the TU Dresden and its partners of the Bryson project of a multi-cell pressure vessel system, illustrated by the integration into an exemplary vehicle.

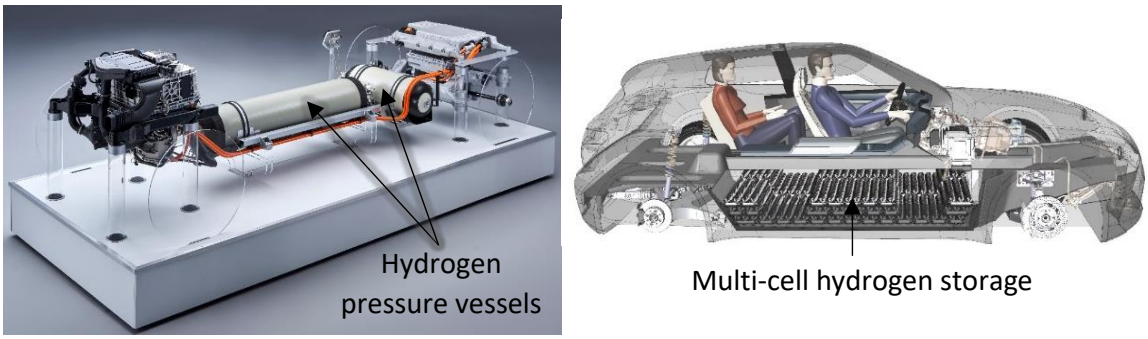

Figure 1. Arrangement of large cylindrical hydrogen pressure vessels in the BMW i Hydrogen concept [7] (left); Concept of the TU Dresden of multi-cell pressure vessels (right)

However, Barlow's formula does not consider the boss area but only the tube area, therefore a slight increase in mass is expected. In addition, the surface area increases, which makes more efficient liner materials necessary. Nevertheless, due to their clear advantages regarding storage density, they are being investigated independently in various projects [6,8]. However, the biggest challenge is the production, as the material input is similar to conventional vessels, but instead of only a few, more than 100 storage cells have to be produced, depending on the configuration. To meet the production targets, the here presented concept uses an efficient and automated tape braiding process. Additionally, the design is optimized for large scale manufacturing for high numbers of units, which is shown in the next section.

  doi:10.5075/epfl-298799_978-2-9701614-0-0

2.1 Design of a single cell

In most cases, composite pressure vessels are manufactured using winding technologies. Hereby, especially the material lay-down at the complex shaped boss-area can be a challenge. With the strongly reduced diameter of each cell, the presented approach proposes a separation of the highly loaded tube section and the end-cap. As small diameters of the individual pipe structures are aimed, these main structures can be manufactured as straight hollow profiles, avoiding necking geometries. This allows the use of the tape-braiding process for the preforming step and enables a continuous, large-scale and cost-efficient production, which has been presented in [9,10]. In addition to the high material lay-down rate, the use of thermoplastic tapes for the braiding process show further benefits. These include short cycle times during consolidation, the need of only few auxiliary materials as well as an improved recyclability compared to thermoset composites.

In former projects, multiple approaches for the integration of fitting elements to tape-braided hollow structures were investigated, which are shown in Figure 2. On the one hand, a hybrid multi-scale contour joint was deeply investigated by Würfel et al., combining an aluminum fitting element with a tape braided structure made out of carbon fiber-reinforced PA6 [11]. Beside the technological feasibility of expanding the tape-braided preform to fill the aluminum contour, this approach demonstrates the increasing mechanical performance by creating a form closure on three different scales. On the other hand, conventional threads can be formed and connected at the inner or outer part of a tube, without needing any additional adhesive. This was demonstrated for a composite strut using PEEK matrix materials.

Figure 2. Fitting concepts for tape-braided hollow structures: Intrinsic hybrid structure of ILK (left); Short fiber reinforced pipe fitting of herone GmbH (right)

These research results, were implemented in the developed end cap concept shown in *Figure 3*. The continuously braided preform is braided with a constant diameter, smaller than the final vessel diameter. This allows to add a short-fiber reinforced outsert (green) based on a compound with a compatible matrix material to the thermoplastic tape. During the bladder-assisted molding consolidation process the braided preform expands to the final diameter and forms a material bond to the short-fiber reinforced outsert. To prevent the open pipe-end from widening due to the inner pressure, the end is reinforced with a metallic fitting. This can be implemented either via a contour connection as shown left in Figure 2 or via a thread. This outer metallic fitting holds the inner metallic fitting, which includes the sealing on the inside and the connectors to other storage cells or the fuel cell.

  doi:10.5075/epfl-298799_978-2-9701614-0-0

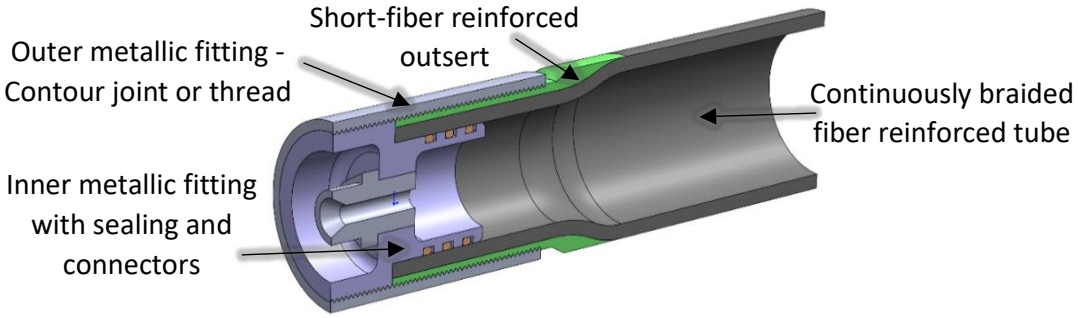

Figure 3. Possible design of the end cap, which allows to use a continuous braiding process

This construction method shows three particular advantages. Firstly, as the design can be manufactured from a straight preform, it allows a continuous production of the fiber composite structure. Secondly, as the consolidated structure is slightly necked at the end cap, the axial force on the thread also decreases, which allows to transmit the forces by contour joints or threads. The third advantage is that the internal pressure supports the sealing and load transfer as it presses the inner fitting and sealing tighter to the composite pipe structure.

3. Experimental Approach

3.1 Development of experimental testing device and test specimen

In order to investigate the performance and feasibility of high-pressure hydrogen vessels based on braided thermoplastic fiber composite structures with small diameters, the two critical areas, the highly stressed tube area and the short-fiber reinforced end-cap area, are investigated separately. This should avoid costly tool rework during design loops. The strength of short -fiber-reinforced threads and the interface to the end cap are tested in separate thread tensile tests. For investigating the highly stressed tube area, a sample geometry and clamping device has been developed to perform high-pressure burst tests, which is shown in detail below.

According to Barlow's pipe formula (1) the inner pressure causes tangential stresses σ_t and axial stresses σ_a of half the size.

$$\sigma_t = \frac{p \cdot d_m}{2 \cdot s} \qquad \sigma_a = \frac{p \cdot d_m}{4 \cdot s} \tag{1}$$

The axial stress is applied to the end plugs which close the open pipe ends. In order to achieve a realistic load condition on a fiber composite pipe, the entire load must be transferred through the fiber composite. Since the focus was on simple and safe experimental analysis of the pipe area under large internal pressures, a simple form-fit connection of the end caps was developed.

The composite pipe specimen, which is shown below in Figure 4, has an outer diameter of 50 mm in the pipe section which expands at the ends to 52 mm and forms a conical shape. A metallic, two-piece cylindrical tool, shown below in brown has the same conical shape on the inside and therefore creates a form-fit, which is supported by the inner pressure and enables to apply high axial loads. The cylindrical part is connected to the end-plug (blue), which holds a patented high-pressure sealing system of Maximator GmbH and an inner cone geometry. This clamps the composite pipe structure and supports the pipe end to avoid buckling as the outer form-fit creates large compression forces.

  doi:10.5075/epfl-298799_978-2-9701614-0-0

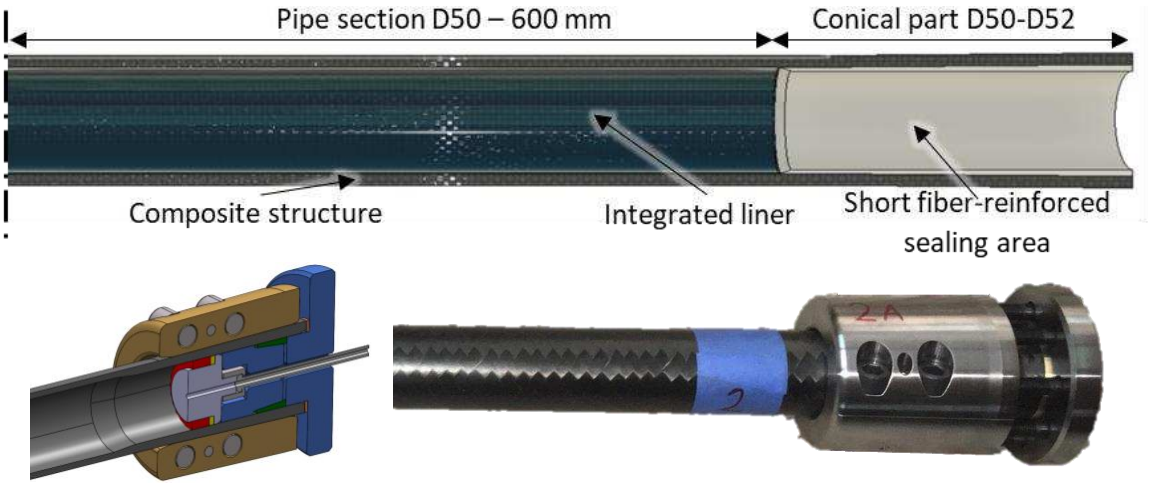

Figure 4. Test specimen: Part concept (Above); Sectional view of test device (Below left); Manufactured specimen with installed end-cap (Below right).

To ensure a leakage-tight sealing a smooth surface is necessary. For this reason, a short fiber-reinforced insert of PA6-GF30 was integrated at the sealing area at both ends of the pipe specimen and machined to the appropriate diameter and surface quality. In addition to this a 400 µm thick film liner was integrated to inhibit leakages through cracks during burst testing.

Numerical structural analysis have been carried out with the finite element code ANSYS Workbench 2021 to analyze the stress in the clamping device and the composite structure at the designed load case of an internal pressure of 1700 bar. The 3d FE-model is meshed with linear and quadratic solid elements. Ansys Composite PrepPost is used to set up the lay-up of fiber reinforced pipe considering linear elastic orthotropic material behavior. The steel clamping parts behave linear elastic and isotropic. Contacts between moveable parts are assumed to be frictional whereby a frictional coefficient of 0.2 is used. Furthermore, bolt pretension loads are defined. The internal pressure is applied to the inner pipe surface and is increased up to 170 MPa. The results are shown in Figure 6. As a reaction to the axial force resulting from internal pressure the outer cylindrical tool moves towards the pipe end and causes large bearing forces. The stresses within the end-plug remain moderate and acceptable for high-alloy steels. The stress distribution within the composite pipe specimen shows clearly that the highest loads do not occur within the clamping mechanism, but in the pipe section with constant diameter. This indicates that burst tests up to 1700 bar can be performed and that the designed specimens tend to fail in the pipe section as required.

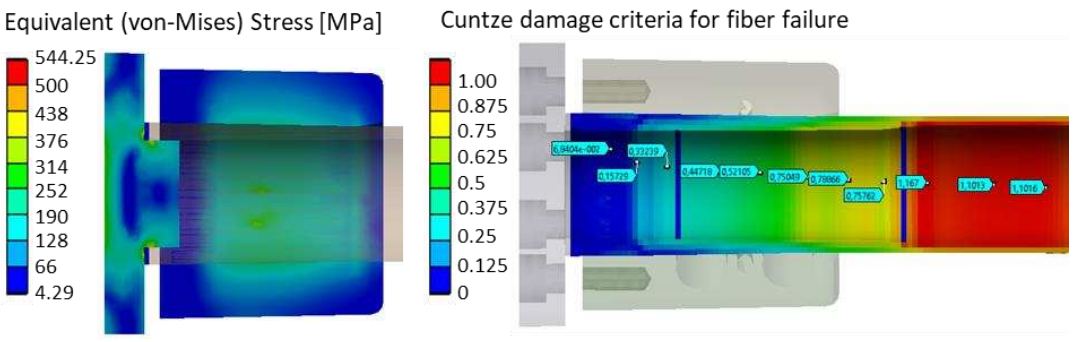

Figure 5. Simulation results at 1700 bar inner pressure: Von-Mises stress of cylindrical tool and end plug (left); Cuntze damage criteria for fiber failure in composite pipe specimen (right)

  doi:10.5075/epfl-298799_978-2-9701614-0-0

3.2 Manufacturing

The burst pressure specimens have a part length of 800 mm and an outer diameter of 50mm in the pipe section, see Figure 4. According to Barlow's formula and classical laminate theory a constant fiber angle of ±54.7° is favorable, which is well suited for the thermoplastic braiding process. The specimens are manufactured out of a CF-PA6 Tape of Celanese (CELSTRAN® CFR-TP PA6 CF60-03) and are designed to a burst pressure of 1400 bar, which leads to a wall thickness of 3.4 mm.

The process chain, which is presented in detail in [9,10], consists out of the continuously working braiding process for preforming which uses thermoplastic tape material as a braiding yarn. For the specimen manufacturing in this investigation an axial braiding machine of type Herzog KFh/48-100 is used. The second step is the consolidation by using the bladder-assisted molding technology. Key characteristics of this process is the expansion of the tape-braided textile preform during molten matrix condition, whereby an internal pressurized membrane forms the preform against an inner tool wall. This leads to an excellent part quality regarding porosity and straight fiber alignment. For the consolidation of the prototypic specimens, process cycle parameters are set to a dwell time of 15 min and a pressure of 6 bar, after a temperature of 230°C is reached. The short fiber-reinforced insert and the liner, which comprises four PA6 film tubes with a thickness of 100 µm, were integrated in the preform before the consolidation process. As all parts are based on the PA6 polymer group, they were molten and fused together during the consolidation process. Afterwards the tubes were cut to length and a smooth surface was machined on the short fiber-reinforced inserts to ensure the sealing.

In total five burst pressure specimens (BPS) have been manufactured, one specimen without an integrated liner, which was used for installation trials of the end plugs and sealing (BPS 1), and four specimens with the same configuration and an integrated liner (BPS 2-5). All specimens were scanned by computed tomography (CT) for quality inspection and to determine fiber angle distribution and overall wall thickness. The results are summarized in table 1.

Table 1: Property analysis of the manufactured specimens.

Sample	Fiber angle [°]	Deviation [°]	Wall thickness [mm]
BPS 1	±56.2	±0.16	3.54
BPS 2	±55.2	±0.23	3.49
BPS 3	±56.0	±1.36	3.44
BPS 4	±53.47	±1.0	3.57
BPS 5	±55.3	±0.44	3.59

3.3 Experimental results

All five BPS were tested at Maximator GmbH, despite the BPS 1 was only designed for installation trials. During the test the inner pressure was applied by a non-compressible fluid and was logged with 100 Hz. The resulting inner pressure during the burst experiments of all specimens are shown in Figure 6.

  doi:10.5075/epfl-298799_978-2-9701614-0-0

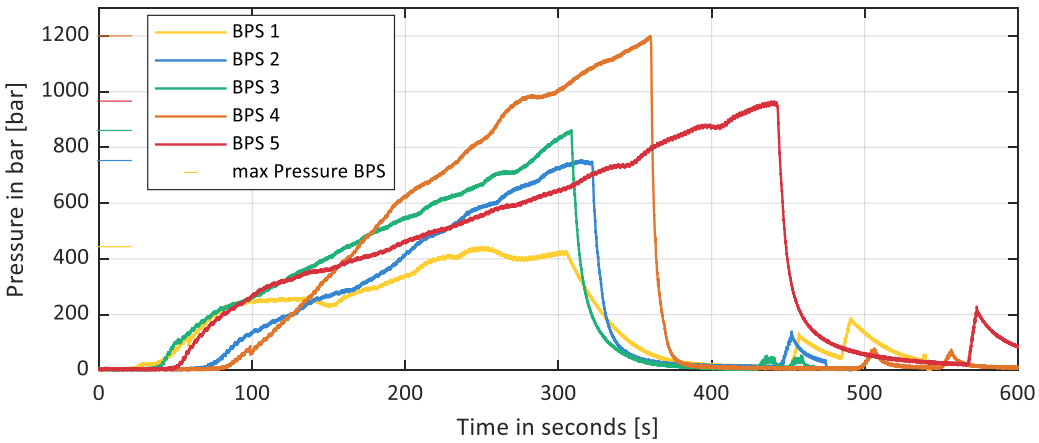

Figure 6. Resulting internal pressure during burst testing

All plots show an increase of the internal pressure up to a maximum, were the pressure drops suddenly. The pressure does not fall to zero immediately, as none of the specimens bursts. All tested samples showed leakages, where fluid sprayed out of single defects. The locations of the leakages were marked and are shown in Figure 7. In a visual inspection after the test, these leakages were invisible and showed no visual defects from outside. The leakages lead to the pressure drop. As all the specimens did not burst, it was tried to apply pressure again. This secondary loading, visible as another rise of pressure at the end of the experiments, was not successful as the leakages were too large.

Figure 7. Burst Pressure Specimen (BPS4) after test with marked leakages of all five specimens

The samples have been designed for a burst pressure of 1400 bar, at which fiber failure should occur, but have not been achieved. As BPS 4 reached pressures up to 1200 bar without burst or fiber failure, it shows the capability of thermoplastic braided pressure vessels. The results also indicate the challenge of leak-proof samples up to the bursting pressure and it shows that the liner issue must be evaluated in detail. BSP 1 showed large leakages already at 440 bar leakages in the pipe section, while all the other specimens reached between 760 bar and 1200 bar and showed leakages in the end-plug area. Therefore, it can be assumed that the general liner concept works for the tube section and is mandatory for the design with little adaptions necessary at the end-plug area.

Figure 8. Liner Integration: End-plug area of BSP 5 (left); Liner delamination of BSP 4 (right)

In Figure 8 the inside surfaces of two samples in the end-plug area are shown. The liner forms a smooth inner surface, and besides small wrinkles due to the deformation of the preform during

  doi:10.5075/epfl-298799_978-2-9701614-0-0

the consolidation process, the liner is flawlessly integrated in the pipe section. As the insert area is machined afterwards, the liner on the inside is removed completely in this section and is damaged at the end of the insert, as the right side of Figure 8 shows. BSP 4 indicates a delamination of the liner in this area, which may have been caused by the machining process.

Figure 9 shows CT scans of the leakage area at the pipe ends. Large cracks are visible within the area of the fitting and sealing. These cracks may result from an unsteadiness in the load distribution along the clamping as the outer metallic ring prevents the deformation. This load peak cannot be seen in the numerical analysis on the right side of Figure 9. It reveals that the damage criteria for fiber matrix failure has its maximum in the tube area and that exceeds the fiber matrix strengths. Therefore, it can be expected that the high inner pressure causes interlaminar fractures across the pipe section which lead to leakages if the liner does not prevent this. This is supported by the results of the liner-less test specimen BSP1 and the leakages of all the other specimen around locations of the damaged liner. Driven by the inner pressure, the pressure fluid can move through these cracks, which leads to leakages and spray-outs. The large cracks around the end-plug may support this, but as BSP 1 showed, even connected interlaminar cracks form leakage paths. According to this inspection one of the main challenges is a damage-free liner integration and not interlaminar damages in the end-plug area primarily influenced by local load peaks. Hence, it can be expected that a non-damaged liner allows to perform successful burst tests and that a redesign of the outer clamping mechanism is not immediately necessary.

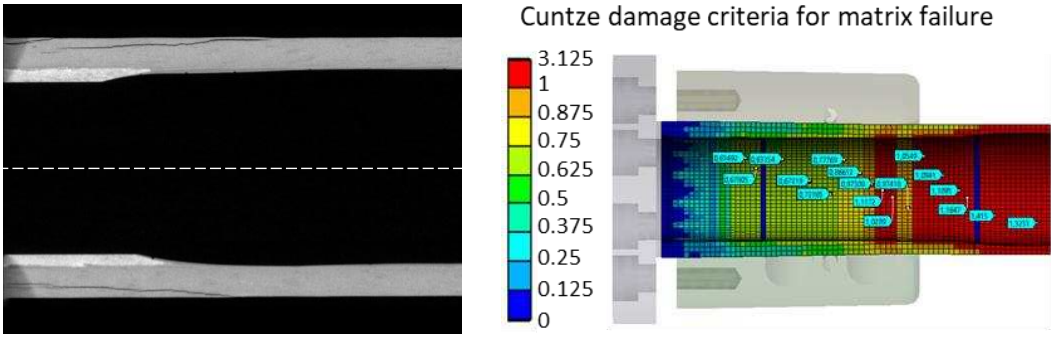

Figure 9. CT-Scan of leakage area of BSP 4 (left); Matrix failure according to Cuntze criteria (right)

4 Conclusion

Driven by the low energy density of pressurised hydrogen storage and the necessary efficient use of space for mobility applications, a concept of a multi-cell storage and the design of the individual cells was presented. The design is strongly based on the manufacturing process, the continuous tape-braiding process and replaces the complex dome geometry of classic pressure vessels with a threaded end-cap.

A test device and sample geometry for testing pipe segments under high pressure up to 1700 bar was designed. Both the test device and the specimen were analysed numerically and experimentally tested. As a result, five pipe samples, designed for burst pressures of 1400 bar, were manufactured and burst tests were carried out.

No samples burst but all samples showed leakages. Those occur around 400 bars for samples without liners and between 750 and 1200 bar for samples with liners. CT-analysis revealed interlaminar damages but also the liner showed delamination and damages due to a machining

  doi:10.5075/epfl-298799_978-2-9701614-0-0

process. In future experiments it must be investigated, whether the end-plug concept leads to premature bursting in the end-plug area. However, the results shown indicate that a burst pressure of 1700 bar is possible with a damage free integrated liner.

As 1200 bar were achieved without bursting, it can be expected that a burst pressure of around the targeted 1400 bar can be achieved. This demonstrates clearly the potential performance of thermoplastic tape materials, the design approach and the manufacturing process. A design to 1700 bar which allows a nominal working pressure of 700 bar, would lead to a wall thickness of around 4.25 mm which is comparable to thermoset composite designs. However, thermoplastic tapes offer a higher productivity compared to a wet winding process and it furthermore offers a wide range of recycling options. Driven by these advantages, the development will be continued on the basis of this concept.

5 Acknowledgements

The authors would like to express appreciation to the Federal Ministry for Economic Affairs and Energy for financial support within the government-funded project “BRYSON”.

6 Sources

1. European Environment Agency. 2021. EEA greenhouse gases. Data viewer. https://www.eea.europa.eu/data-and-maps/data/data-viewers/greenhouse-gases-viewer. Accessed 22 December 2021.
2. Hydrogen Council. 2021. Roadmap towards zero emissions. The complementary role of BEVs and FCEVs
3. Humpenöder, j. 1998. Gas permeation of fibre reinforced plastics. Cryogenics 38, 1, 143–147.
4. Sery, J. and Leduc, P. 2021. Fuel cell behavior and energy balance on board a Hyundai Nexo. International Journal of Engine Research, 146808742110590.
5. Rosen, P. A. 2017. Beitrag zur Optimierung von Wasserstoffdruckbehältern. Dissertation, TU Chemnitz.
6. Ruf, M., Stahl, H.-U., Kunze, K., Zaremba, S., Horoschenkoff, A., Unwerth, T. von, and Drechsler, K. 2020. Neue Bauweisen von Wasserstoffdruckbehältern fuer die Integration in Zukuenftige Fahrzeugarchitekturen. Proceedings ot the Munich Symposium on Lightweight Design 2020
7. BMW AG. 2020. Das Antriebssystem des BMW i Hydrogen NEXT. https://www.press.bmwgroup.com/deutschland/article/detail/T0306930DE/ Accessed 17 March 2022
8. Other Lab LLC, Wexler, J. S., Stone, D. K., and Chandraseker, K. 2019. US2019120432 - Tank Filling System and Method.
9. Garthaus, C.; Barfuß, D.; Witschel, B.; Gude, M. (2016): Tape braiding: high-performance fibrereinforced thermoplastic profile structures. In: JEC Composite Magazine.
10. Eckardt, S.; Barfuß, D.; Condé-Wolter, J.; Gude, M.; Würfel, V.; Böcking, J.: STUDY ON BEND-FORMING BEHAVIOUR OF THERMOPLASTIC TAPE-BRAIDED CFRTP PROFILES. In: Conference Proceedings: SAMPE Europe Conference 2020 Amsterdam 2020.
11. Würfel, V.; Grützner, R.; Hirsch, F.; Barfuß, D.; Gude, M.; Müller, R.; Kästner, M.: Hybrid Fibre Reinforced Thermoplastic Hollow Structures with a Multi-Scale Structured Metal Load Introduction Element. In: Proceedings: Hybrid 2020 - Materials and Structures 2020.

  doi:10.5075/epfl-298799_978-2-9701614-0-0

MULTIFUNCTIONAL CARBON/EPOXY LAMINATES FOR THERMAL ENERGY STORAGE APPLICATIONS

Andrea Dorigato, Giulia Fredi, Luca Fambri, Alessandro Pegoretti

University of Trento (Italy), Department of Industrial Engineering – andrea.dorigato@unitn.it

Abstract: *In this work unidirectional carbon/epoxy laminates with different concentrations of paraffin microcapsules (MC) for thermal energy storage were characterized. The viscosity of the epoxy/MC mixtures increased with the MC amount, enhancing the matrix volume fraction and reducing that of the fibers. Consequently, a decrease in mechanical properties of the laminates at elevated MC amounts was detected. Microcapsules concentration in the interlaminar zone lead to a decrease of the interlaminar shear strength. However, a limited MC loading determined an increase of the interlaminar fracture toughness, because of the generation of new toughening mechanisms. A further increase of the MC content let the crack propagating through the matrix and not at the fiber/matrix interface, reducing thus the toughening effect associated to fiber bridging. The phase change enthalpy increased with the MC content up to 48.7 J/g, indicating thus a good thermal management capability, as proven by thermal imaging tests.*

Keywords: composites; carbon fibers; thermal energy storage; mechanical properties.

1. Introduction

Polymer composites have recently attracted both academic and industrial interest, because they are can be utilized to obtain multifunctional structures, in which the properties of multiple phases can be gathered in one material [1]. Many efforts in multifunctional materials are focused on the development of polymer-matrix structural composites possessing one or more additional non-structural functions. This strategy allows large weight savings at the system level, through the reduction in the number of multiple monofunctional constituents, and it gives better results than the conventional approach of optimizing the weight and geometry of the single subsystems individually. An interesting non-structural feature that could be added to a structural composite is the thermal energy storage (TES) capability, i.e. the ability to store heat that can be released where and when needed. TES technologies have the feature of reducing the gap between thermal energy demand and availability, and are nowadays employed to accumulate excess heat in the solar-thermal power plants, to recover waste industrial heat, to store hot or cold water, but also for thermal management applications such as the indoor thermal regulation in buildings. Thermal energy can be stored and released as sensible heat, latent heat, or through a reversible thermochemical reaction. Nowadays, latent heat TES is the most widely used TES method, especially in the low-medium temperature range (0–100 °C) [2]. Latent heat TES is mostly performed through organic phase change materials (PCMs) such as paraffins, poly(ethylene glycol)s or fatty acids, which store a considerable amount of latent heat at a nearly constant temperature and are chemically inert, inexpensive and easy to handle. They also show small volume variation upon phase transition, congruent melting, negligible supercooling, low density, large availability, and non-corrosiveness. On the other hand, as they are subjected to a solid-liquid phase change, they need to be confined to avoid leakage of material above the melting temperature. Among all available confinement techniques,

  doi:10.5075/epfl-298799_978-2-9701614-0-0

encapsulation in micrometric shells is the most common and effective method, because the shell additionally protects the PCM from the surrounding environment, enhances thermal stability, and contributes to accommodate the core's volume variation during melting and crystallization [3]. It would be advantageous to embed the thermal management function in the structural elements. Therefore, lightweight polymer composites performing structural and TES functions could be employed where it is critical to deal with weight saving and heat management simultaneously, such as in the fields of transportation and portable electronics [4].

Although the literature reports many examples of polymer matrices containing PCMs, little has been done so far to deeply investigate their mechanical properties and to enhance them by adding reinforcing fibers [5]. Our group has recently focused on investigating how the introduction of a PCM impacts the thermo-mechanical properties of several classes of fiber-reinforced polymers [6]. However, a better understanding of how the PCM addition influences the fiber-related and matrix-related properties distinctly can be reached by characterizing a PCM-containing unidirectional laminate, which has never been described in the open scientific literature, to the best of the authors' knowledge. Therefore, this work aims at producing unidirectional carbon/epoxy laminates containing a microencapsulated PCM in different weight fractions, and at characterizing in a comprehensive way the physical, thermal and mechanical properties to assess how they vary with the PCM content.

2. Experimental Part

2.1 Materials

The epoxy base Elan-tech EC157 (density = 1.15 g/cm^3, viscosity at 25 °C = 550 mPa·s) and the hardener Elan-tech W342 (density = 0.95 g/cm^3, viscosity at 25 °C = 50 mPa·s) were kindly provided by Elantas Europe Srl (Collecchio, Italy). Microencapsulated PCM Microtek MPCM43D was supplied by Microtek Laboratories (Dayton, OH, US). The PCM phase consists of a paraffin wax (melting temperature = 43 °C) encapsulated inside a melamine-formaldehyde shell, which constitutes approx. 10–15% of the total mass. The average diameter is 15–30 µm, and the melting enthalpy is 200–210 J/g. Unidirectional carbon fiber fabric UCD-15060, having a nominal areal weight of 150 g/m^2, was kindly provided by Mike Compositi (Milano, Italy).

2.2 Sample preparation

The epoxy base and the hardener were mixed at room temperature at a weight ratio of 100:30, as suggested by the producer, and magnetically stirred at 500 rpm for 5 min. The PCM microcapsules were then added at different weight concentrations, i.e. 20 wt%, 30 wt% or 40 wt%. The resulting mixtures were vigorously stirred manually for 2 min to obtain a homogeneous dispersion of the microcapsules in the resin. These mixtures were used as matrices to prepare laminates via a wet lay-up technique. Eight plies were stacked together, and the resulting unidirectional laminates had an in-plane area of 130 × 200 mm^2. The laminates were vacuum-bagged, left to cure at room temperature for 24 h and post-cured in an oven at 100 °C for 10 h. A carbon fiber/epoxy laminate without MC was prepared with the same procedure for comparison. The same route was followed to produce additional laminates with 16 laminae. In such laminates, a poly(ethylene terephthalate) (PET) film with a thickness of 26 µm was placed in the mid plane to generate a pre-crack for mode I interlaminar fracture toughness tests. The composites were denoted as EP-MCx-CFu, where EP, MC and CFu are the labels for the epoxy resin, PCM microcapsules and unidirectional carbon fibers, respectively, and x represents the

  doi:10.5075/epfl-298799_978-2-9701614-0-0

initial weight percentage of MC on the total mass of the matrix (i.e. 20, 30 and 40 wt%). The laminates labelled "-A" have 8 plies, while those labelled "-B" have 16 plies and the PET film in the mid plane.

2.3 Experimental techniques

The density of the constituents (i.e., carbon fibers, paraffin microcapsules and epoxy resin) was measured through helium pycnometry, performed with a Micromeritics AccuPyc 1330 helium pycnometer (Micromeritics Instrument Corp., Norcross, GA, US) at 23 °C. The microstructure of the prepared laminates was evaluated by obtaining optical microscope (OM) images of polished cross sections at different magnification levels, through a Zeiss Axiophot (Oberkochen, Germany) light optical microscope.

Differential scanning calorimetry (DSC) was performed to investigate the melting and crystallization temperature and enthalpy of the PCM (T_m, T_c, ΔH_m, ΔH_c) and the glass transition temperature of the epoxy resin (T_g). All DSC tests were performed on a Mettler DSC30 instrument (Mettler Toledo, Columbus, OH, US), in the temperature interval 0–120 °C, at a heating/cooling rate of 10 °C/min, under a nitrogen flow of 100 ml/min. All specimens underwent a first heating scan, a cooling scan, and a second heating scan. Thermogravimetric analysis (TGA) was performed through a Mettler TG50 instrument (Mettler Toledo, Columbus, OH, US) at a heating rate of 10 °C/min, up to 700 °C, under a nitrogen flow of 15 ml/min. The tests allowed the determination of the temperatures corresponding to a mass loss of 1 wt%, 3 wt%, 5 wt% ($T_{1\%}$, $T_{3\%}$, $T_{5\%}$), and the degradation temperature (T_d), intended as the temperature at the maximum degradation rate. To check the overall thermal management capacity of the laminates, a simple test was performed with a thermal camera, both on heating and on cooling stages. For the tests on heating ramp, the laminates were inserted in an oven at a temperature of 70 °C, and their surface temperature was recorded through an infrared thermal imaging camera FLIR E60 (FLIR® Systems, Inc., Wilsonville, OR, US), placed at a fixed distance of 30 cm from the laminate surface. For the tests during the cooling stage, the laminates were first heated in an oven at 70 °C, then taken out and left cooling to room temperature, while their surface temperature was measured with the same thermal camera.

Flexural tests were performed at room temperature with a three-point bending configuration, according to the standard ASTM D790, with a universal testing machine Instron 5969 equipped with a 50 kN load cell, on specimens with nominal in-plane dimensions of 10 × 120 mm^2. The span length was 85 mm, the crosshead speed was fixed at 9 mm/min, and at least five specimens were tested for each sample, in the longitudinal direction. The flexural modulus of elasticity (E_f), the flexural strength (σ_{fM}) and the flexural strain at break (ε_{fb}) were thus determined. Short-beam shear (SBS) tests were performed on the laminates Type B to assess the interlaminar shear strength (ILSS), following the standard ASTM D 2344, with an Instron 5969 universal testing machine in a three-point bending configuration, at a crosshead speed of 1 mm/min. Mode I interlaminar fracture toughness was evaluated on the type B laminates according to the standard ASTM D5528, with an Instron 5969 universal testing machine. The tests were performed on pre-cracked Type B specimens with in-plane dimensions of 20 × 130 mm^2, and at least three specimens were tested for each composition. The test was recorded with a LogiTech C920 USB video camera, to correlate each advancement of the crack tip with the corresponding load value. In this way, the values of critical strain energy release rate for crack initiation (G_{Ii}) and for steady-state propagation (G_{IC}) were determined.

3. Results and Discussion

The optical microscope (OM) images of the polished cross sections of the laminates are shown in Fig. 1. The neat EP-CFu laminate shows fibers homogeneously distributed in the laminate thickness, without evident matrix-rich zones. The porosity present in this laminate derives from the hand lay-up technique, and it is evident also in the other compositions. For the laminates containing MC, the micrographs show zones rich in CF and other zones rich in MC, and the PCM phase is preferentially distributed in the interlaminar region and not among the fibers of the same tow. This phenomenon could decrease the interlaminar properties of the laminates and create a preferential path for damage propagation. Moreover, the thickness of the interlaminar region increases with the initial MC fraction in the epoxy/MC mixtures, with a consequent decrease in the relative fiber volume fraction in the laminates.

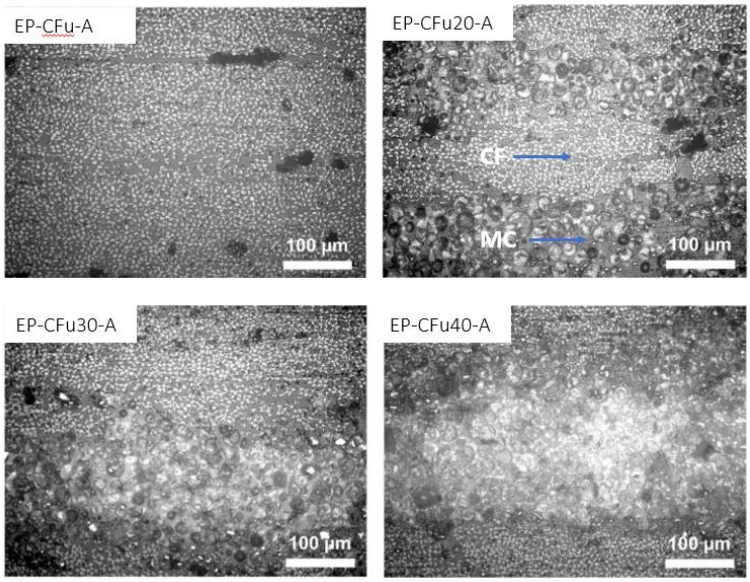

Figure 1. Optical microscope micrographs of the laminates EP-MCx-CFu-A (x=0-40).

The main DSC results for the prepared composites are summarized in Table 1. All samples exhibit glass transition at approx. 90 °C, and the samples containing MC also show endo-/exothermic peaks at the PCM phase change. The endothermic melting peak is observable in the heating scan at 40–60 °C, while the exothermic crystallization peak is appreciable in the cooling scan at 40-15 ◦C, as observed in previous works on the same PCM microcapsules [7]. The glass transition is shifted to slightly higher temperatures with an increase in the MC loading, while the melting and crystallization temperature intervals of the PCM are not considerably affected by the composition of the laminate. The phase change enthalpy increases with the MC loading up to 48.7 J/g for the sample EP-MC40-CFu-A. Since the MC addition increases the viscosity of the EP/MC mixtures considerably, as demonstrated in a previous work on epoxy/MC samples [8], it is reasonable to expect that a high fraction of MC hinders the flowing of the matrix out of the carbon fabric during vacuum bagging, thereby increasing the final matrix weight fraction. The MC weight fraction in the composites can be calculated from the phase change enthalpy measured with DSC, by dividing the melting enthalpy measured on the laminates by that measured on the neat MC. This can be done by assuming that the MC maintain their energy storage efficiency also after the lamination process, which is reasonable if considering the results of previous works on epoxy composites containing the same microcapsules used in this work

[9]. The values of experimental MC weight fraction (%MC) are reported in Table 1. The MC weight fraction increases with the initial MC loading in the epoxy mixture and ranges from 13.2 wt% to 22.0 wt%.

Table 1: Results of the DSC tests on the laminates EP-MCx-CFu-A (first heating and cooling scan).

Sample	T_g [°C]	T_m [°C]	T_c [°C]	ΔH_m [J/g]	ΔH_c [J/g]	MC% [wt%]
MC	-	47.0	27.2	221.7	221.6	100.0
EP-CFu-A	87.0	-	-	-	-	0.0
EP-CFu20-A	89.0	45.4	27.0	29.1	29.8	13.2
EP-CFu30-A	96.8	47.8	25.5	39.7	40.2	18.2
EP-CFu40-A	93.4	48.2	24.9	48.2	48.7	22.0

The effective fiber weight fraction in the laminates was then investigated through TGA, which was also useful to assess their thermal stability. The residual mass after the test allowed the calculation of the fiber weight fraction (w_f), which was computed by considering the residual mass of the EP/MC systems determined in a previous work [8] and that of the employed carbon fibers, that resulted as 96.0 wt%. w_f decreases with an increase in the MC loading, which indicates that the flow of the matrix out of the CF fabric is hindered by the viscosity increase determined by the MC addition. w_f ranges from 71.5 wt% of the sample EP-CFu-A up to 50.0 wt% for the sample EP-MC40-CFu-A, and the decrease does not follow a linear trend with the MC content. The lower fiber content, and the consequent higher epoxy and MC weight fraction, is probably at the basis of the reduced thermal stability of the laminates with the highest MC loading, as can be appreciated from the shift of $T_{1\%}$, $T_{3\%}$, and $T_{5\%}$ to lower temperatures. On the other hand, the degradation interval is not remarkably affected by the composition of the laminate, and the lowest T_d is 387.6 ◦C, which is 14 °C lower than that of the laminate EP-CFu-A. In all cases, the thermal degradation is far above the operative temperature interval for which these materials are intended. From DSC and TGA data, it was possible to determine the weight fractions of MC and CF in the laminates, respectively. These data allowed the calculation of the theoretical density (ρ_{th}) of the laminates, by knowing the density of the microcapsules (0.923 g/cm^3), of the CFu (1.633 g/cm^3) and of the EP phase (1.158 g/cm^3), all measured via helium pycnometry. The same helium pycnometry technique was employed to measure the experimental density (ρ_{exp}) of the prepared laminates. The comparison between ρ_{th} and ρ_{exp} allowed the calculation of the porosity, and then of the volume fraction of the fibers, of the microcapsules and of the EP phase. As already reported in previous works [9], the fiber volume fraction and the MC volume fraction follow opposite trends. This is mainly due to the viscosity increase of the EP/MC mixtures, which reduces the matrix flowing out of the carbon fabric during the vacuum bag process. Additionally, it can be observed that the experimental MC weight fraction in the matrix is generally higher than the initial nominal one, equal to 0 wt%, 20 wt%, 30 wt% or 40 wt%. This implies that during vacuum bagging the EP phase flows out of the carbon fabric more easily than the microcapsules, thereby increasing the resulting MC concentration in the matrix. Finally, the porosity increases with the MC concentration (from 2.3 up to 8.5 vol%), which is once again linked to the increased matrix viscosity.

  doi:10.5075/epfl-298799_978-2-9701614-0-0

In order to study the thermal management properties of the prepared laminates on a slightly bigger scale, a simple test was performed with thermal imaging techniques. Fig. 2 reports the values of the surface temperature of the laminates as a function of time during both the heating and the cooling stages. The temperature trend shows plateau-like regions, caused by the latent heat absorbed during melting and released during crystallization of the PCM, and this phenomenon causes a remarkable increase in the time needed to reach the temperature of the surrounding environment. On the heating phase, the neat EP-CFu-A laminate reaches the temperature of 60 °C in 2.3 min, while the same temperature is reached by the laminate EP-MC40-CFu-A in 8.2 min. In the same way, in the experiment on cooling, the two laminates reach the temperature of 30 °C in 3.4 min and 15.8 min, respectively. The observed plateau-like trends are a clear sign of the variation in the thermal behavior of the laminates (and therefore of the thermal management capability) as a function of the MC content.

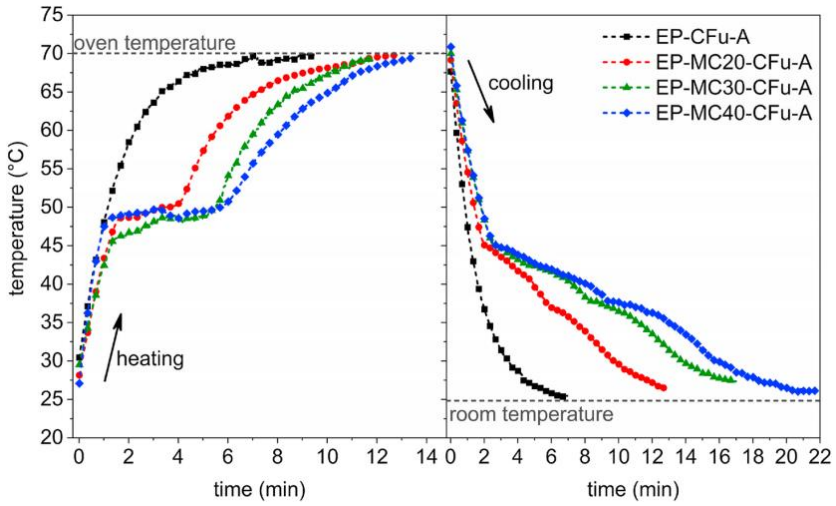

Figure 2. Surface temperature as a function of the testing time for the laminates EP-MCx-CFu-A

The results of the three-point bending tests and short-beam shear strength tests are shown in Fig. 3. The load-displacement curves of all samples present an initial linear zone, but the behavior after the maximum load of the neat EP-CFu laminate is different from that of the MC-containing laminates. The neat laminate is subjected to a catastrophic failure, which always started from the tensile-stressed mid-lower region of the specimen. Such failure mode is often associated to a good interlaminar adhesion [10]. On the other hand, the PCM-containing laminates are subjected to a progressive failure and present a drop-plateau sequence, which indicates a dissipation of mechanical energy also during damage propagation. The damage was observed starting either in the mid-upper zone, subjected to compression, or in the interlaminar zone. This failure mode has been described as typical of materials having a tensile in-plane strength considerably higher than the interlaminar shear strength, which is the case for the MC-containing laminates reported in this work. The elastic modulus is seen decreasing with an increase in the MC content, which is due to the reduction in the fiber volume fraction. However, also the flexural strength decreases, and this is probably related to the introduction of new damaging mechanisms such as the delamination and interlaminar fracturing. The same phenomena are also at the basis of the observed reduction of the ILSS.

  doi:10.5075/epfl-298799_978-2-9701614-0-0

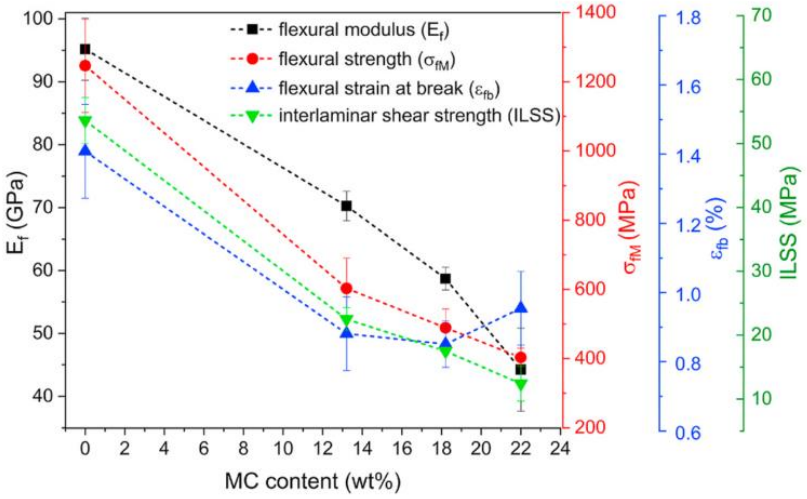

Figure 3. Results of flexural and ILSS tests on the EP-MCx-CFu-A laminates.

For as concerns mode I interlaminar fracture toughness tests, Table 2 collects the mode I critical strain energy release rates for crack initiation (G_{Ii}) and steady-state propagation (G_{Ic}). The G_{Ii} is determined at the initial delamination of the specimen, when the pre-crack starts to grow. For the laminate EP-MC20-CFu-B, both G_{Ii} and G_{Ic} are higher than those of the neat EP-CFu-B, which implies that the introduction of a modest amount of MC activates different toughening mechanisms, like particle debonding, crack pinning, crack deflection and micro-cracking. On the other hand, above a certain MC concentration, both G_{Ii} and G_{Ic} decrease with increasing MC content, which can be due to an excessive thickening and decrease in the mechanical properties of the interlaminar region, in turn caused by a poor capsule/matrix adhesion and by the intrinsic low mechanical properties of the MC. From a visual observation of the specimens during the test, the samples EP-CFu-B and EP-MC20-CFu-B show fiber bridging, while this phenomenon can not be observed for the laminates with a higher MC concentration, for which the crack propagates mostly through the matrix.

Table 2: Mode I critical strain energy release rate for crack initiation (G_{Ii}) and steady state propagation (G_{Ic}) for the laminates EP-MCx-CFu-B.

Sample	G_{Ii} [kJ/m^2]	G_{Ic} [kJ/m^2]
EP-CFu-B	0.15 ± 0.03	0.27 ± 0.01
EP-CFu20-B	0.34 ± 0.02	0.40 ± 0.01
EP-CFu30-B	0.27 ± 0.02	0.32 ± 0.01
EP-CFu40-B	0.24 ± 0.02	0.30 ± 0.02

4. Conclusions

This work presented the thermo-mechanical characterization of unidirectional carbon/epoxy composites containing paraffin microcapsules. The MC phase increased the viscosity of the epoxy matrix, which limited the flow of the epoxy/MC mixtures out of the fiber fabric, thereby

  doi:10.5075/epfl-298799_978-2-9701614-0-0

increasing the matrix volume fraction and reducing that of the fibers. The MC phase was preferentially distributed in the interlaminar region, which led to a decrease in matrix related properties, such as the interlaminar shear strength. On the other hand, a modest MC fraction led to an increase in the mode I interlaminar fracture toughness, probably due to the introduction of new toughening mechanisms, such as the debonding, crack deflection, and microcracking. For the thermal properties, the melting enthalpy increased with the MC fraction and reached a value of 48.7 J/g. Therefore, the TES and thermal management capability of the prepared laminates increased with the MC fraction, as also demonstrated by thermal imaging tests.

Acknowledgements

Mr. Nicola Eccher is gratefully acknowledged for his support to the experimental activity.

5. References

1. Zhao S, Chang H, Chen S, Cui J, Yan Y. High-performance and multifunctional epoxy composites filled with epoxide-functionalized graphene. European Polymer Journal 2016; 84: 300–312.
2. Xi P, Duan Y, Fei P, Xia L, Liu R, Cheng B. Synthesis and thermal energy storage properties of the polyurethane solid–solid phase change materials with a novel tetrahydroxy compound. European Polymer Journal 2012; 48(7): 1295–1303.
3. Khadiran T, Hussein MZ, Zainal Z, Rusli R. Encapsulation techniques for organic phase change materials as thermal energy storage medium: a review. Solar Energy Materials and Solar Cells 2015; 143: 78–98.
4. Yuan W, Yang X, Zhang G, Li X. A thermal conductive composite phase change material with enhanced volume resistivity by introducing silicon carbide for battery thermal management. Applied Thermal Engineering 2018; 144: 551–557.
5. Yoo S, Kandare E, Mahendrarajah G, Al-Maadeed MA, Khatibi AA. Mechanical and thermal characterisation of multifunctional composites incorporating phase change materials. Journal of Composite Materials 2017; 51(18): 2631–2642.
6. Fredi G, Dorigato A, Fambri L, Pegoretti A. Wax confinement with carbon nanotubes for phase changing epoxy blends. Polymers 2017; 9(9): 405/1–405/16.
7. Dorigato A, Fredi G, Pegoretti A. Application of the thermal energy storage concept to novel epoxy/short carbon fiber composites. Journal of Applied Polymer Science 2019; 136(21): 47434/1–47434/9.
8. Fredi G, Dorigato A, Fambri L, Pegoretti A. Detailed experimental and theoretical investigation of the thermo-mechanical properties of epoxy composites containing paraffin microcapsules for thermal management. Polymer Engineering and Science 2020; 60: 1202–1220.
9. Fredi G, Dorigato A, Pegoretti A. Novel reactive thermoplastic resin as a matrix for laminates containing phase change microcapsules. Polymer Composites 2019; 40(9): 3711–3724.
10. Abdel Ghafaar M, Mazen AA, El-Mahallawy NA. Behavior of woven fabric reinforced epoxy composites under bending and compressive loads. Journal of Engineering Sciences 2006; 34(2): 453–469.

  doi:10.5075/epfl-298799_978-2-9701614-0-0

METHODOLOGY FOR THE IDENTIFICATION OF HYDROGEN GAS PERMEATION PATH IN DAMAGED LAMINATES

S.M. Amin Hosseini[a], Bilim Atli-Veltin[a,b], Arjan den Otter[b], John Zevenbergen[b], Clemens Dransfeld[a]

a: Delft University of Technology, Delft, Netherlands, s.m.a.hosseini@tudelft.nl
b: TNO, Delft, Netherlands

Abstract: *The main bottleneck of using composites for cryogenic storage of clean hydrogen fuel is the permeation of gas molecules. In this work, the permeation of hydrogen gas through thermally cycled thermoplastic composite laminates with two different stacking sequence is investigated. The experimental study is based on a methodology of cryogenically cycling the composite specimen and measuring the permeability in a dedicated hydrogen permeation setup. An optical microscope and X-ray computed tomography scanner are employed to investigate the existence of cracks. The results reveal that thermal cycling does not have a profound influence on permeability, while the stacking sequence has a considerable effect. Laminates with dispersed 0° layers resulted in lower permeation values compared to the laminate with grouped 0° layers at the laminate's core. The imaging techniques did not reveal any observable crack which supports the hypothesis that permeation is mostly driven by bulk diffusion in the polymer.*

Keywords: Cryogenic storage; Thermoplastic composite; Hydrogen; Permeation

1. Introduction

Fiber-reinforced thermoplastics (FRTP) and hydrogen play important role in the future of sustainable aviation. FRTPs are proposed over conventional thermoset counterparts due to their superior fracture toughness and recyclability. One technological challenge in this plan is the high cost and weight of the tanks storing liquid hydrogen at cryogenic temperatures close to -253°C. The linerless composite tanks, also known as type V vessels, could lead to the weight saving of up to 30% compared to metallic tanks [1]. A linerless tank concept could potentially be manufactured by a single-step automated tape winding (ATW) process owing to the in-situ consolidation mechanism [2]. This offers the advantage of lower overall manufacturing costs. In the absence of a liner, the tank wall structure should be gas tight, which is a major challenge for composite laminates, especially after cryogenic cycling. Laminates will be subjected to thermal cycles due to the refuelling which would cause the existing cracks to propagate and more hydrogen to leak. The leaked hydrogen not only brings safety risks but also causes economical losses. Therefore, there is a prominent need for research on understanding the permeation of hydrogen gas in the FRTPs to eliminate the leakage.

Permeation of hydrogen molecules through composites is studied by various researchers for both thermosets and thermoplastic composites subjected to different mechanical and thermal loading conditions. Reported experiments make use of different permeating gases such as helium or hydrogen. Gas permeation through composite laminates can be described differently based on the damage state of the laminate. If cracks are present, as depicted in Figure 1, the intersecting microcracks allow the passage of hydrogen molecules, making permeation

  doi:10.5075/epfl-298799_978-2-9701614-0-0

proportional to the area of the intersecting cracks which is dominated by Darcy's law. In contrast, in the absence of the microcracks, hydrogen gas molecules would first travel in the polymer, along with the fiber/resin interface, between the plies and finally reach the other side of the laminate known as near-Fickian diffusion behaviour [3].

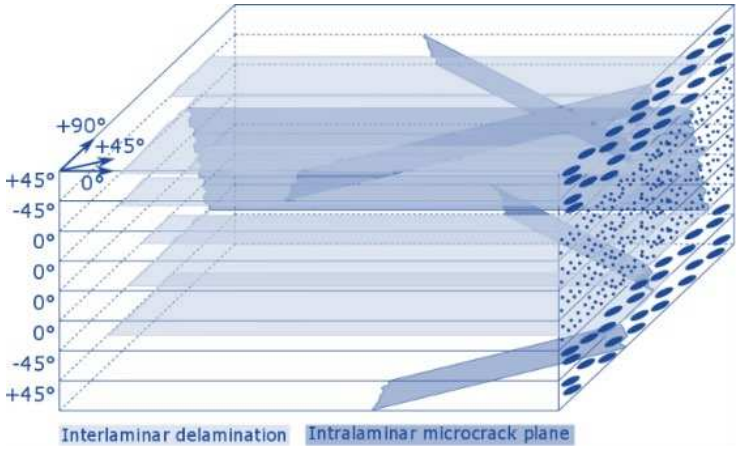

Figure 1. A schematic view of the microcrack network as the permeation path.

There are multiple research papers reporting crack formation on epoxy-based composite laminates after cryogenic cycling. Hamori et al. evaluated the gas permeability of composites made of carbon fiber (CF) and epoxy resin [4]. They performed mechanical tests at -253°C followed by leak tests at 20°C. It was observed that the microcracks were formed by the application of mechanical loads. In another study on the epoxy resin and carbon fiber, 150 thermal cycles were applied between -196°C and room temperature (RT) at the rate of 7°C /min and an X-ray computed tomography (CT) scanner was used to investigate the specimen after cycling [5]. They reported an increase in the microdefects as compared to the as-manufactured sample. In another paper, microcracks were observed in laminates made of graphite/epoxy with a layup of $[0_2/90_2/0_2]$ and thickness of 0.787mm after cryogenic cycling [6].

Thermoplastic composites could be an alternative to thermosets for cryogenic applications providing superior fracture toughness and processability enabling cost-efficient production [7,8]. It was reported that the observable crack network was limited for CF/Polyetheretherketone (CF/PEEK) laminates following thermally cycling the samples (8-layers, 50 thermal cycles between -196°C and 40°C) [9]. Similarly, for unidirectional AS4/PEEK laminate after cryogenic thermal loading between -269°C and ambient temperature, no observable crack was identified [10]. However, it was also reported that relatively thick thermoplastic laminates with 16 and 32 layers show damage, particularly with a quasi-isotropic layup, indicating laminates' thickness affects the permeation performance [9].

Another point of attention is the methodology followed for observing the cracks. The current state-of-the-art for visualization of the cracks is via CT scanning [5,8–12]. CT-scan images provide 3D visualization of the crack's location and orientations. Optical microscopy is also typically used for 2D observation of the cracks for a cross-section of the bulk material. Another parameter that plays a role in the permeation test is the permeant. Most of the reported permeability coefficient is based on helium gas which is the conventional method used by many researchers [3,6,8,9]. Permeation measurements at room temperature using hydrogen results in a higher permeability compared to helium according to Humpenöder [13].

  doi:10.5075/epfl-298799_978-2-9701614-0-0

Based on the aforementioned observations from the literature, the focus of this work is on the thermoplastic material system made of carbon fiber and semi-crystalline low melt Polyaryletherketone resin (CF/LMPAEK). To evaluate the effect of stacking on the permeation two laminates are manufactured with grouped and dispersed layers of 0° fiber orientation. Finally, the effects of thermal cycling on the induced damage and the consequent effect on the permeability behaviour are studied. Optical microscopy and CT scan techniques are used to visualize possible cracks in the material. Permeation tests are performed using hydrogen gas as permeate.

2. Methodology

In this section, information is provided on the tested material, thermal cycling protocol, visualisation technique used for the tested specimen and the working principle of the hydrogen permeation setup.

2.1 Material

The layup used by Flanagan et al. was chosen as a guideline to be able to compare the new results to the ones available in their work [3]. Laminates made of 8 layers of unidirectional plies utilizing CF/LMPAEK with a nominal thickness of 0.14 mm per consolidated ply were manufactured by the press forming process. Disk-shaped samples for the permeation tests with a diameter of 49.9 mm were cut using a water jet. Two layups were considered to evaluate the effect of the grouping versus dispersing the plies as described in Table 1. The laminate with 4 layers of 0° direction stacked together at the core laminate is referred to as “thick”, and the laminate with a more dispersed layup is called “thin” in this study, even though the overall thickness remains the same.

Table 1. Sample definitions.

Permeation barrier layer	Layup
Thick – Grouped 0 layers	$[+45/-45/0/0]_s$
Thin – Dispersed layers	$[+45/0/-45/0]_s$

2.2 Cryogenic thermal cycles

The cryogenic cycling was performed at -196°C using liquid nitrogen (LN_2). Samples were immersed in LN_2 for 3 min and stayed at RT (20 °C) for 8 min followed by warming up by natural convection. The duration of the cooling and heating cycles was based on [3]. Two specimens per layup were subjected to 50 thermal cycles. The samples were positioned in a 3D-printed rack as shown in Figure 2 and submerged in dewar.

  doi:10.5075/epfl-298799_978-2-9701614-0-0

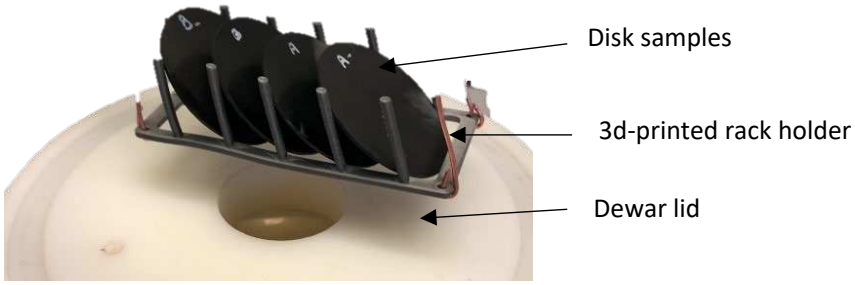

Figure 2. The setup for the cryogenic thermal cycling of the samples.

2.3 Visualization techniques

The optical microscopy and X-ray CT techniques were utilized to visualize the defects in the samples. The visualization was performed on rectangular samples (5mm x 10mm) from each layup cut from the same laminates as the disks for the permeation test and cycled cryogenically in the same manner. The optical microscopy was performed using a Keyence Laser Scanning Confocal Microscope. The CT images were taken by a Phoenix Nanotom® scanner. Images were generated at 160 kV and 28 µA with a voxel size of 3 µm. The volume rendering was completed using VGStudio MAX 2.2 software. The small size of the samples facilitated capturing images of high resolution with a 3µm voxel size which is suitable to identify cracks in the order of the fiber diameter.

2.4 Permeation setup

For the hydrogen permeation tests, the setup developed by TNO, Netherlands, shown in Figure 3 was used. This setup is capable of accommodating temperatures up to 325°C and pressures up to 2000 bars, although not necessary for this study. The working principle of the setup is based on the manometric method. The sample was mounted in the permeation cell to form the barrier between the two chambers. Both chambers were evacuated. Afterwards, one chamber was filled with hydrogen to 10 bars at room temperature. In the other chamber, the pressure increases because of the transmission through the specimen. The area available for permeation was 9.62e-4 m^2.

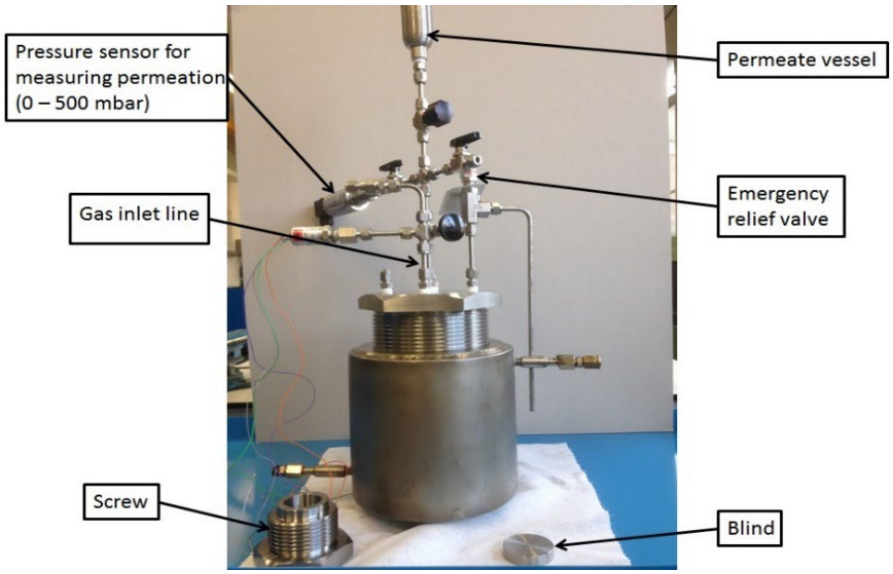

Figure 3. A view of the permeation setup.

3. Results and discussions

In Figure 4 the micrographs of the cross-section of the thick sample before and after 50 thermal cycles are shown. No evidence of cracks, voids and defects is recognized except for some resin-rich areas.

Figure 4. Micrographs of the polished cross-section of the thick laminate before -0 thermal cycles- (top) and after -50 thermal cycles- (bottom).

The CT scan images confirm the microscopic observations as shown in Figure 5 since no delamination or cracks are visible in the bulk of the material. It is of interest to mention the darker areas observed in the slices of the CT scan, indicating a variation in the fibre bundle motion, as observed also by other researchers [14].

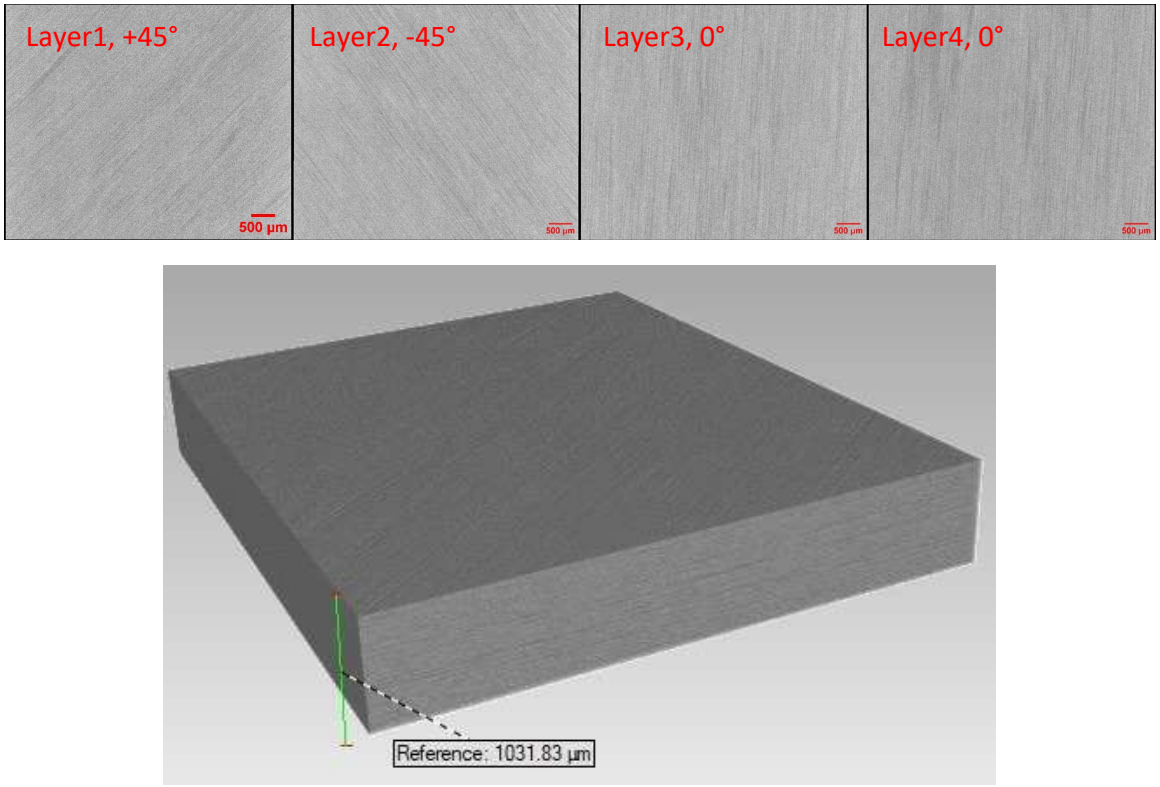

Figure 5. The CT scan images of each ply (top) and the bulk of laminate (bottom).

In Table 2, the permeability coefficients as the average of the two measurements are shown for the tested so-called thin and thick laminates. The permeability of the intact thin laminate with dispersing stacking sequence is 3.4 times higher than the thick laminate with grouped layers (i.e. 1.21e-17 vs. 4.1e-17 mol/(m.s.Pa)). A similar observation is also reported in the literature by

[6,15]. Figure 6 shows the consolidation of the layers of the thin and the thick laminates. In the thick laminate, grouped 0° layers at the centre have no clear boundaries and detecting each ply boundary is difficult, however with the thin laminates, the ply interfaces are more prominent. At the interfaces with non-similar fiber orientations, fibers are occasionally aligned very neatly with local high fiber volume fraction, which could potentially be the reason for the reduced permeability of the thin laminates (with dispersed plies) compared to the thick laminates (with grouped plies), since the aligned fibers are creating a thin physical block against the passage of the hydrogen molecules. This should be evaluated more in future work.

Table 2. Measured values of permeation tests with the unit of e-17xmol/(m.s.Pa). The percentages are the standard deviation of the two samples in the current work.

					Number of thermal cycles				
Reference	Permeant	Fiber	Matrix	Layup	0	1	10	30	50
[3]	He	AS4	PEEK	Thick	4.3 (5%)	4.5 (4%)	4.6 (4%)	5.0 (11%)	
[3]	He	IM7	PEEK	Thick	2.6 (15%)	2.3 (6%)	2.4 (7%)	3.2 (19%)	
[3]	He	AS4	PEEK	Thick	5.5 (1%)	4.9 (7%)	5.2 (6%)	4.9 (6%)	
[3]	He	N/A	PEEK	N/A	56.0				
Current Work	H_2	CF	LMPAEK	Thick	41.0 (2%)				44.6 (12%)
Current Work	H_2	CF	LMPAEK	Thin	12.1 (12%)				18.6 (19%)

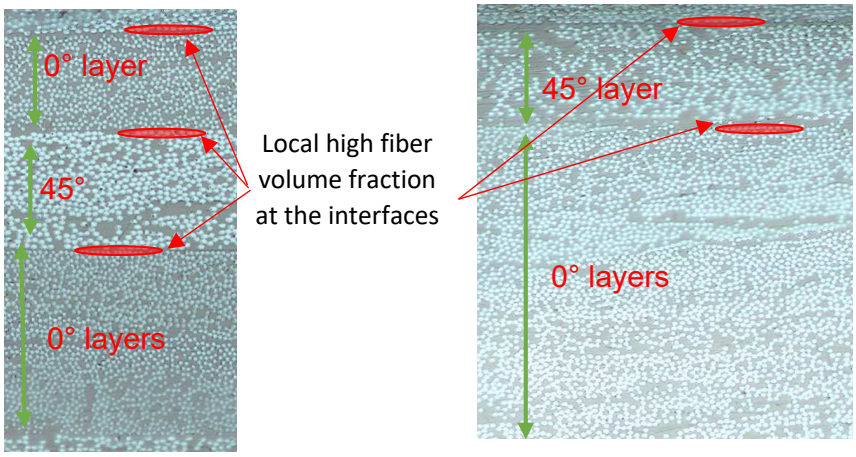

Figure 6. A zoomed view of interfaces for the thin (left) and thick (right) laminate.

Permeation data is also plotted in Figure 7. The effect of thermal cycling on the permeation measurements seems negligible for these materials, which is also observed in [3]. As compared to the literature data, the permeability values from the current work are higher, which could be because of the permeate difference (He vs H_2) or difference in the resin (PEEK vs LMPAEK). According to Humpenöder permeability measurements at room temperature using hydrogen results in a higher permeability compared to helium [13].

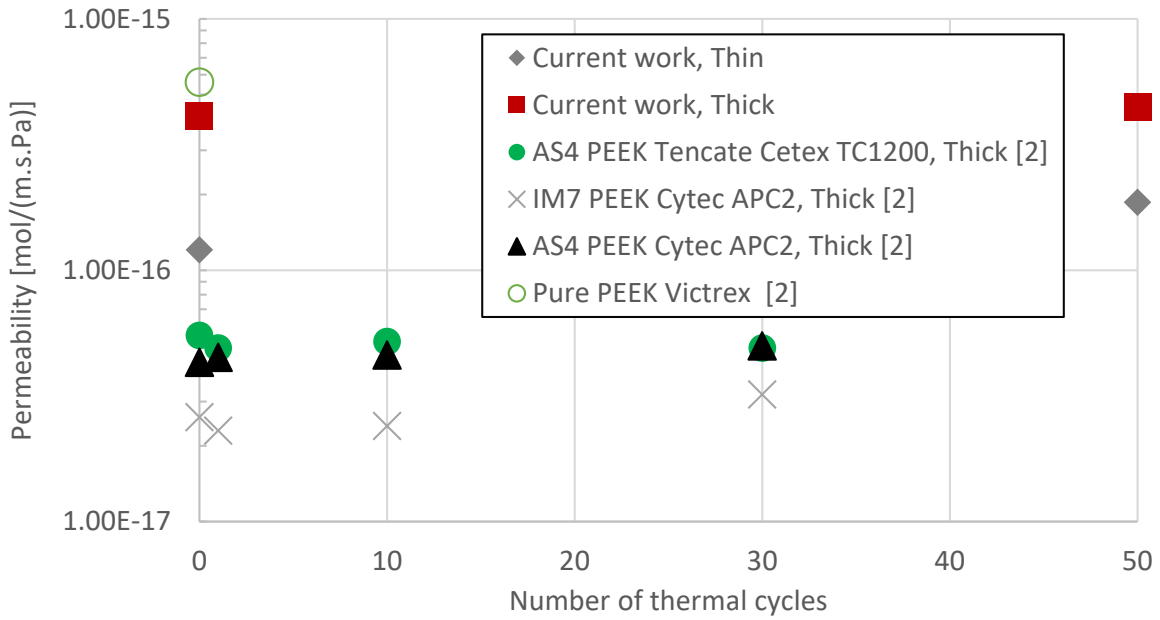

Figure 7. The measured permeation values as compared to the literature data.

4. Conclusions and future works

This work provides the hydrogen gas permeation values through laminates made of carbon fiber and high performance thermoplastic resin LMPAEK. It is encouraging to see that there is no observable crack network which would lead to permeation values that are several magnitudes higher compared to the values that are observed here. This work shed a light on the effect of the number of ply interfaces on the hydrogen permeation. Permeation measurements for "thin" specimens are lower compared to the "thick" specimen, indicating that dispersing the oriented plies through the thickness instead of grouped layers is favourable for lowering the permeation. The results show that for both "thin" and "thick" configurations, subjecting the specimen to a thermal cycle has a negligible effect on the permeation. It is confirmed by the microscopic imaging and the CT scans that there are no visible cracks in these materials. However, images with improved scanning technologies at higher resolution could help to investigate the presence of nano cracks at for instance the fiber/matrix interface. The permeation values are slightly higher compared to the CF/PEEK laminates reported in the literature. The reason could be, among other unknowns and uncertainties, the difference in permeating gas since in this current work hydrogen was used and the results from the literature are based on helium permeation. Therefore, another round of permeation tests with helium gas is suggested. Also, the type of resin is different which could lead to the observed difference. This can be also checked by testing the pure LMPEAK material using both helium and hydrogen gas. The future work may include mechanically induced cracks to represent the load cases similar to the hydrogen tanks.

Acknowledgements

The authors would like to acknowledge Silvia Gomarasca for the nice discussions on imaging and post-processing techniques, Ellen Meijvogel-de Koning from the Laboratory of Geoscience and Engineering, Faculty of Civil Engineering and Geosciences of TU Delft for operating the micro-CT scanner and reconstructing the images.

5. References

1. Boeing all-composite cryogenic fuel tank proves technology readiness. Composite World. 2022.
2. Hosseini SMA, Schäkel M, Baran I, Janssen H, van Drongelen M, Akkerman R. A new global kinematic-optical-thermal process model for laser-assisted tape winding with an application to helical-wound pressure vessel. Materials and Design 2020;193.
3. Flanagan M, Grogan DM, Goggins J, Appel S, Doyle K, Leen SB, et al. Permeability of carbon fibre PEEK composites for cryogenic storage tanks of future space launchers. Composites Part A: Applied Science and Manufacturing 2017;101:173–84.
4. Hamori H, Kumazawa H, Higuchi R, Yokozeki T. Gas permeability of CFRP cross-ply laminates with thin-ply barrier layers under cryogenic and biaxial loading conditions. Composite Structures 2020;245:112326.
5. Meng J, Wang Y, Yang H, Wang P, Lei Q, Shi H, et al. Mechanical properties and internal microdefects evolution of carbon fiber reinforced polymer composites: Cryogenic temperature and thermocycling effects. Composites Science and Technology 2020;191:108083.
6. Choi S, Sankar B V. Gas permeability of various graphite/epoxy composite laminates for cryogenic storage systems. Composites Part B: Engineering 2008;39:782–91.
7. Grogan DM. Damage and permeability in linerless composite cryogenic tanks. National University of Ireland; 2015.
8. Murray BR, Leen SB, Semprimoschnig COA, Brádaigh CMÓ. Helium permeability of polymer materials as liners for composite overwrapped pressure vessels. Journal of Applied Polymer Science 2016;133:1–10.
9. Grogan DM, Leen SB, Semprimoschnig COA, Ó Brádaigh CM. Damage characterisation of cryogenically cycled carbon fibre/PEEK laminates. Composites Part A: Applied Science and Manufacturing 2014;66:237–50.
10. Hohe J, Schober M, Fliegener S, Weiss KP, Appel S. Effect of cryogenic environments on failure of carbon fiber reinforced composites. Composites Science and Technology 2021;212:108850.
11. Grogan DM, Ó Brádaigh CM, Leen SB. A combined XFEM and cohesive zone model for composite laminate microcracking and permeability. Composite Structures 2015;120:246–61.
12. Yu B, Bradley RS, Soutis C, Withers PJ. A comparison of different approaches for imaging cracks in composites by X-ray microtomography. Philosophical Transactions of the Royal Society A: Mathematical, Physical and Engineering Sciences 2016;374:20160037.
13. Humpenöder J. Gas permeation of fibre reinforced plastics. Cryogenics 1998;38:143–7.
14. Gomarasca S, Peeters DMJ, Atli-Veltin B, Dransfeld C. Characterising microstructural organisation in unidirectional composites. Composites Science and Technology 2021;215:109030.
15. Kumazawa H, Aoki T, Susuki I. Influence of stacking sequence on leakage characteristics through CFRP composite laminates. Composites Science and Technology 2006;66:2107–15.

  doi:10.5075/epfl-298799_978-2-9701614-0-0

INTEGRATED COMPOSITE BIPOLAR PLATE-ELECTRODE DESIGN TO REDUCE CONTACT RESISTANCE IN VANADIUM REDOX FLOW BATTERIES

Kwang Il Jeong[a], Nils Demski[b], Jae-moon Jeong[a], Dirk Oberschmidt[b], Seong Su Kim[a]

a: Department of Mechanical Engineering, Korea Advanced Institute of Science and Technology (KAIST), Daejeon, Republic of Korea – lightone@kaist.ac.kr
b: Department of Micro and Precision Devices, Technische Universität Berlin, Berlin, Germany

Abstract: *Vanadium redox flow batteries (VRFBs) are assembled by stacking various components, which results in increase cell resistance. Herein, we propose bipolar plate-electrode integrated design to reduce contact resistance in VRFBs. By selectively impregnating a part of carbon felt with vinyl ester resin, the integrated structure was fabricated. Integrated structures consist of a hard layer and a soft layer, which act as a bipolar plate and an electrode, respectively. The integrated structure had 15% lower electrical resistance than conventional cell of VRFBs, which contribute to reduce ohmic overpotential in a polarization curve. Under a current density of 100 mA·cm^{-2}, the energy efficiency of the integrated structure was 83.4%, which was 5% higher than that of conventional cell.*

Keywords: Vanadium redox flow battery; Integrated structure; Cell resistance; Polarization curve; Energy efficiency

1. Introduction

A vanadium redox flow battery (VRFB) is one of representative stationary batteries for a large-scale energy storage system (ESS) [1-3]. Owing to its low risk of explosion and durability in a wide range of temperature [4-6], it has been considered as the next-generation ESS. VRFB cells consist of current collectors, bipolar plates (BPs), gaskets, flow frames, membranes and electrodes as shown in figure 1. These configuration of VRFB, where various components were stacked, can increase a cell resistance. Especially, high contact resistance between electrodes and BPs causes to nonuniform redox reactions due to uneven charge transfer [7].

The integration of BPs and electrodes can be a solution to minimize the cell resistance in VRFBs. In previous studies, integrated structures were proposed by attaching BPs to conventional electrodes with a slurry of polymeric binders and conductive particles [8]. The contact resistance between the components was substantially reduced by compression molding. However, previous integrated structures seem to have a defect because of development of new layers.

In this paper, we propose a bipolar plate-electrode integrated design to reduce contact resistance in VRFBs. To significantly lower the contact resistance, electrodes and BPs were integrated with a single sheet of carbon felt (CF), which can offer the interconnected structures with the carbon fibers. By selectively filling the vinyl ester resin into a part of carbon felt, the integrated structure was fabricated. Integrated structures consist of a hard layer and a soft layer, which act as a bipolar plate and an electrode, respectively. After the fabrication, the electrical resistance of integrated structures and BP part was measured, and the electrochemical performances of the samples were analyzed by cyclic voltammetry (CV), polarization curve measurement, and VRFB single-cell tests.

  doi:10.5075/epfl-298799_978-2-9701614-0-0

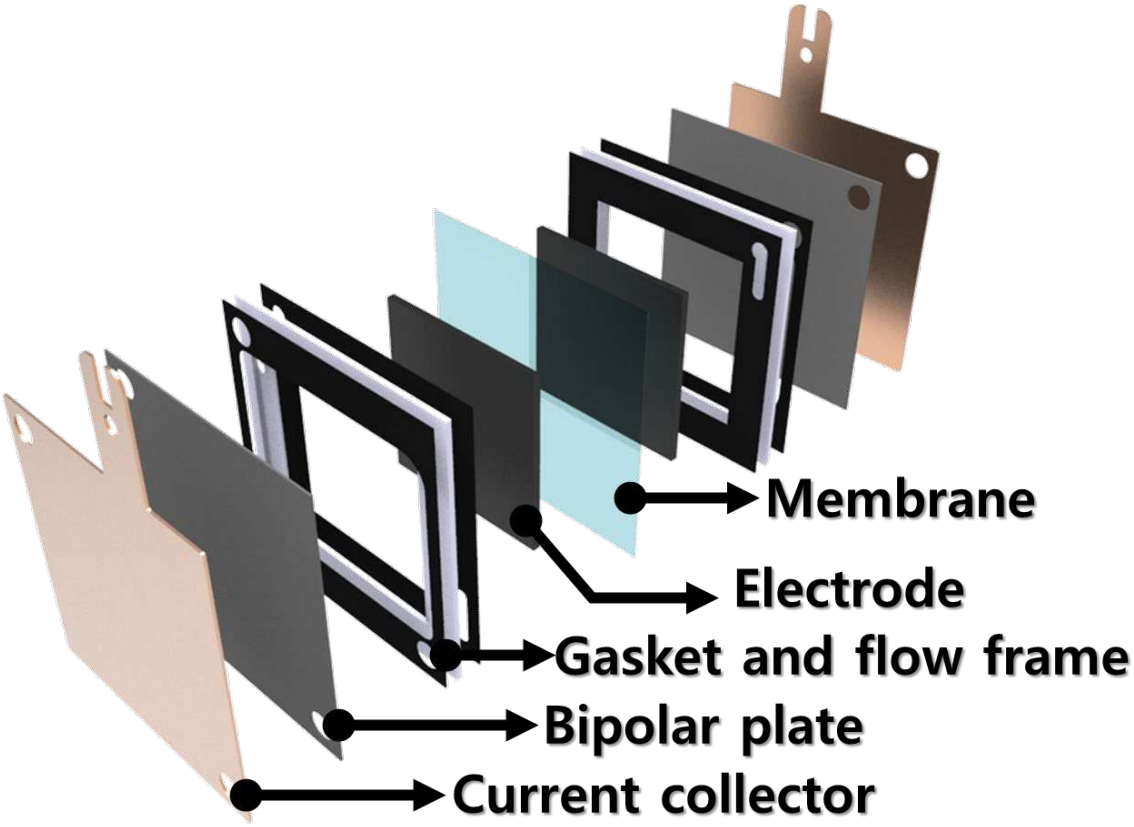

Figure 1. A Schematic of VRFB single cell

2. Experimental section

2.1 Fabrication of integrated structures (IS)

We fabricated an interconnected structure consisting of a BP part and electrode part on a single sheet of CF. The fabrication of the integrated structure (IS) is described in Figure 2. To prepare the BP part, vinyl ester resin and hardener were mixed in a weight ratio of 100:1. The resin mixture was poured to an acryl plate, and uniformly spread out by using spin coating method. A sheet of CF was placed on the acrylic plate where the vinyl ester/hardener mixture was spread. After that, the IS was fabricated by the compression molding, and the thickness ratio of components was adjusted by 3-mm-thick gauge.

2.2 Electrical resistance measurement

The areal specific resistances (ASR) were measured using an LCR meter (E4980A, Keysight, USA). Specimens were placed between two gold-coated copper plates. In addition, BP parts were from integrated structures and ASR of the BP was evaluated.

2.3 Electrochemical measurements

Reactivity change in electrode parts was evaluated by CV using a battery testing system (WBCS3000M2, WonA Tech, Korea). The electrode parts of the specimens were machined to dimensions of 1 cm × 1 cm. A saturated calomel electrode and Pt gauze were used as reference and counter electrodes, respectively. In 0.1 M VO^{2+} and 2 M H_2SO_4 solutions, the current density

  doi:10.5075/epfl-298799_978-2-9701614-0-0

was acquired with respect to the potential at a scan rate of 5 $mV \cdot s^{-1}$. According to the CV test results, the peak current and potential at the peak position of the electrode were analyzed.

The polarization curves of the specimens were obtained using a battery testing system with a VRFB single-cell. A conventional cell was prepared by stacking current collectors, BPs, gaskets, flow frames, membranes, and carbon felt electrodes. In case of IS, BPs and electrode was replaced by integrated structures. The polarization curves of samples were investigated in an electrolyte of 1.6 M $V^{3.5+}$ + 4.0 M H_2SO_4. To analyze the I-V characteristics of the samples at the constant state of charge (SOC), single cells were charged by applying a constant voltage of 1.6 V while the current density of cell was below 1 $mA \cdot cm^{-2}$. After that, current was applied to measure the response of voltage for 30 seconds. The magnitude of current was changed with respect to steps. After each step, single-cell was recharged to make SOC of cell to be constant.

The energy efficiency and discharging capacity of the samples were analyzed by using a single-cell test. Single-cell test was conducted with cut-off method, and cut-off voltages for charging and discharging were 1.6V and 1.0V, respectively. The single-cell test was carried out for 60 cycles under the current density of 100 mA/cm^2.

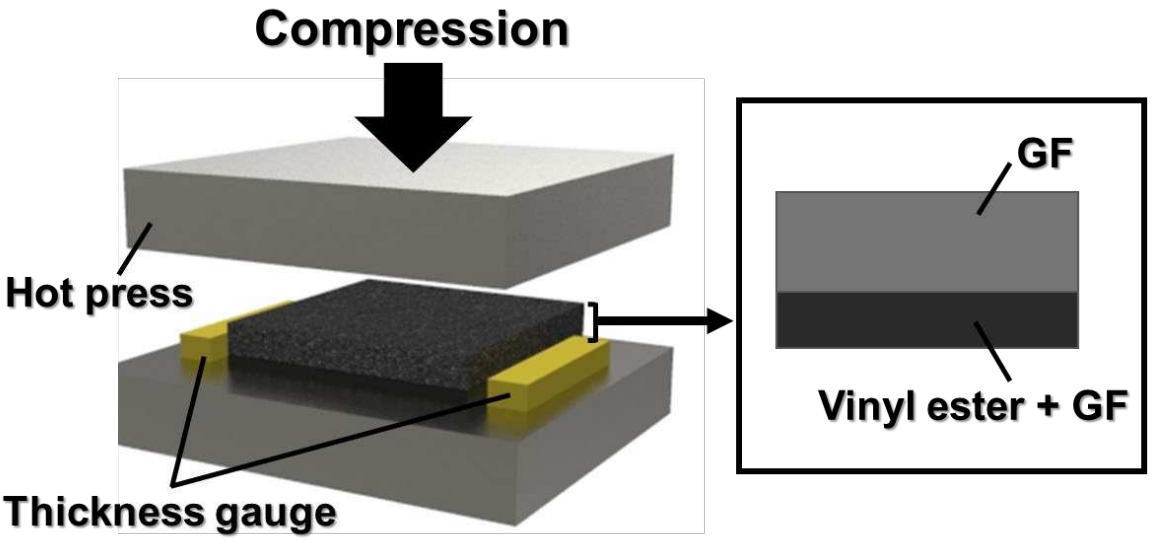

Figure 2. Schematics of the fabrication of IS

3. Results and discussion

Figure 3 shows the ASR of the samples and the BP parts. The ASR of IS was 0.632 $\Omega \cdot cm^2$, which is lower than that of conventional cell (0.740 $\Omega \cdot cm^2$). It was thought that the reduction in ASR was led by the interconnected components with the carbon fibers. In case of IS, the ASR of the BP part was 0.439 $\Omega \cdot cm^2$, which is higher than that of conventional cell (0.368 $\Omega \cdot cm^2$).

Figure 4 indicates the I-V curves in CV test, which can analyze the reactivity of the electrode parts. In the I-V curves, peaks represented at the same voltage in samples, which confirms that the surface compositions of samples were equal. IS had about 10% higher the intensity of the peak current density (12 $mA \cdot cm^{-2}$) than conventional electrode (11 $mA \cdot cm^{-2}$).

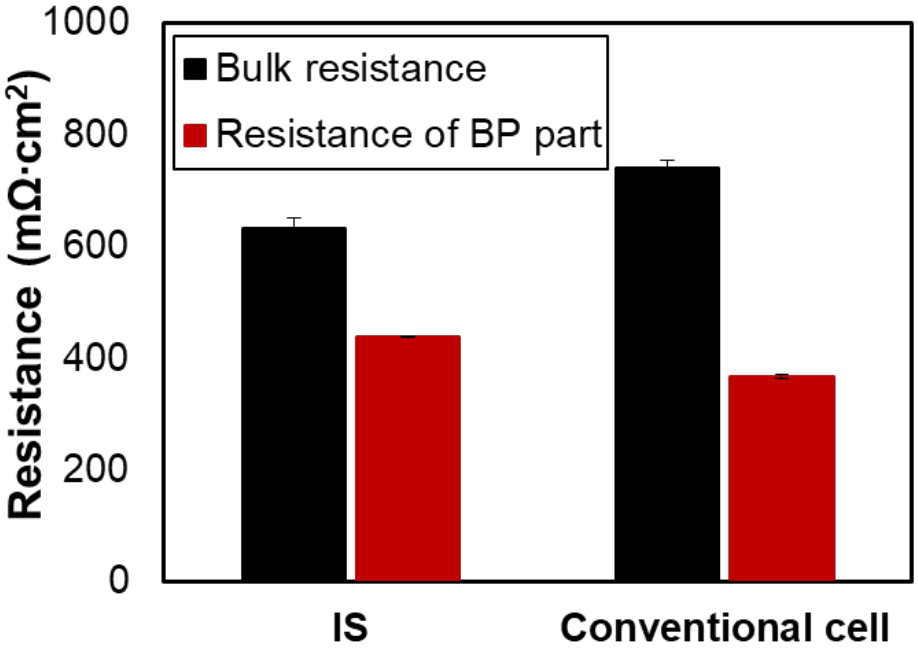

Figure 3. Areal specific resistance of the BP-electrode assembly and the BP parts

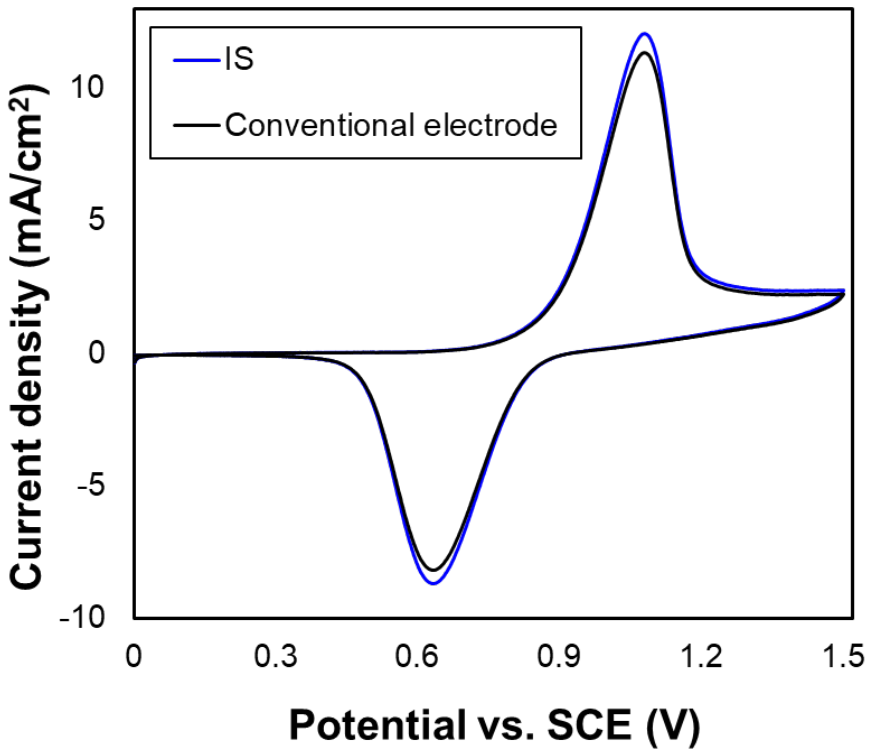

Figure 4. I-V curves in CV test

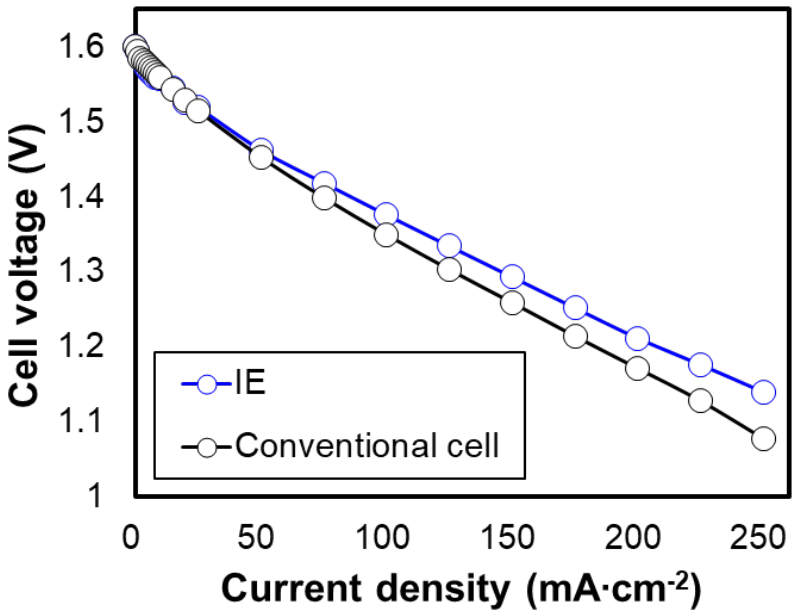

Figure 5. Polarization curves of samples

Figure 5 shows the I–V characteristics of the samples. In the current density range of 50 to 200 mA·cm^{-2}, the voltage drop was linearly increased, which indicates that the Ohmic drop mainly led decrease in the voltage with respect to the current density. In the current density range, the voltage change can be estimated by multiply of the current density and ASR of the VRFB cell. The magnitude of the slope in the current density range was 1.874 Ω·cm^2 for the conventional cell and 1.670 Ω·cm^2 for IS.

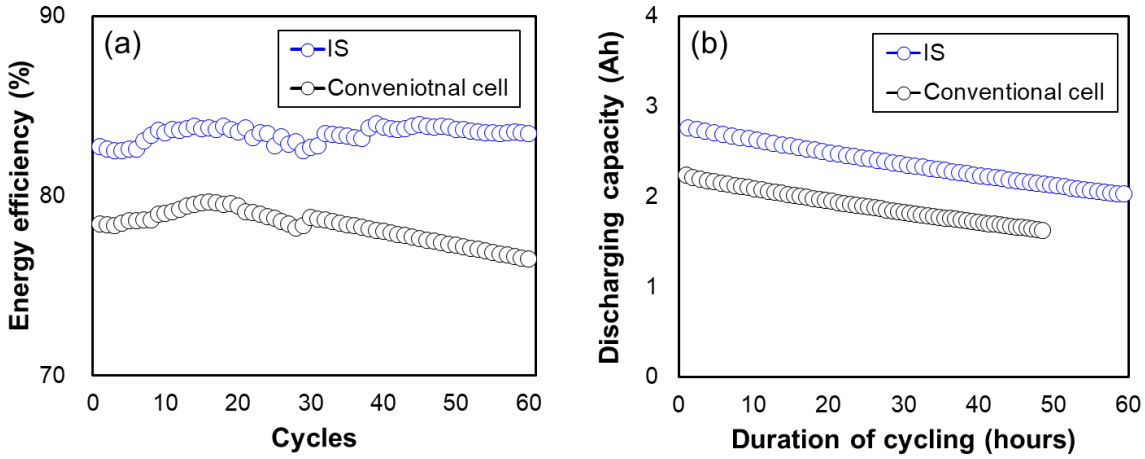

Figure 6. VRFB single-cell test results : (a) EE, (b) DC

Figure 6 shows the VRFB single-cell test results including energy efficiency (EE) and discharging capacity (DC) with a current density of 100 mA·cm^{-2} during 60 cycles. In Figure 6(a), EE of IS was 83.4%, which is higher than that of conventional stack (78.3%). According to the measurement of ASR and polarization curve, the low ASR of IS reduced the Ohmic overpotential, which enhanced the EE of IS.

Additionally, the low ASR of the IS contributed to improve the utilization of electrolyte in the same cut-off voltage (1.0–1.6 V), as shown in Figure 6(b). It can be seen that it improved the DC

of IS (2.34 Ah), which was higher than that of the conventional cell (1.89 Ah). The EEs of the samples during 60 cycles were not changed, while the DCs of the samples decreased with repetitive cycle. In the VRFB system, the reduction in DC can be caused by the degradation of components and parasitic phenomena. Based on the EE results, the electrode and BP degradations were negligible. Therefore, it seems that the side reaction in the electrolyte dominantly led the reduction in DC. In spite of fading in DC, DC of IS at the 60th cycle was (2.27 Ah) at the 60th cycle, which is higher than that of conventional cell (1.63 Ah).

4. Conclusion

In this study, we proposed integrated electrode and BP structures to lower the interfacial contact resistance. The components were internally connected with the carbon fibers because Integrated structures were fabricated with a single sheet of CF. Through electrical resistance measurement and polarization curve, it was confirmed that the ASR of IS was decreased significantly, which contribute to lower Ohmic overpotential. Finally, In a VRFB single-cell test, the energy efficiency of the integrated was 83.4%, which was 5% higher than that of conventional cell.

Acknowledgements

This research was supported by the MOTIE (Ministry of Trade, Industry, and Energy) in Korea, under the Fostering Global Talents for Innovative Growth Program (P0017307) supervised by the Korea Institute for Advancement of Technology (KIAT).

References

1. Jeong J-M, Jeong KI, Oh JH, Chung YS, Kim SS. Stacked carbon paper electrodes with pseudo-channel effect to improve flow characteristics of electrolyte in vanadium redox flow batteries. Applied Materials Today. 2021;24:101139.
2. Jeong KI, Song SA, Kim SS. Glucose-based carbon-coating layer on carbon felt electrodes of vanadium redox flow batteries. Composites Part B: Engineering. 2019;175:107072.
3. Jeong KI, Jeong J-M, Oh J, Lim JW, Kim SS. An integrated composite structure with reduced electrode/bipolar plate contact resistance for vanadium redox flow battery. Composites Part B: Engineering. 2022:109657.
4. Xi J, Xiao S, Yu L, Wu L, Liu L, Qiu X. Broad temperature adaptability of vanadium redox flow battery—Part 2: Cell research. Electrochimica Acta. 2016;191:695-704.
5. Xiao S, Yu L, Wu L, Liu L, Qiu X, Xi J. Broad temperature adaptability of vanadium redox flow battery—Part 1: Electrolyte research. Electrochimica Acta. 2016;187:525-34.
6. Yang Y, Zhang Y, Liu T, Huang J. Improved broad temperature adaptability and energy density of vanadium redox flow battery based on sulfate-chloride mixed acid by optimizing the concentration of electrolyte. Journal of Power Sources. 2019;415:62-8.
7. Peng L, Shao H, Qiu D, Yi P, Lai X. Investigation of the non-uniform distribution of current density in commercial-size proton exchange membrane fuel cells. Journal of Power Sources. 2020;453:227836.
8. Dongjiang Y, Jingyuan L, Litao K. High-temperature conductive binder for an integrated electrode bipolar plate and its application in vanadium redox flow battery. International Journal of Energy Research. 2020;44(3):1920-9.

  doi:10.5075/epfl-298799_978-2-9701614-0-0

EFFECT OF LITHIUM INSERTION ON MECHANICAL PROPERTIES OF INDIVIDUAL COMMERCIAL PAN CARBON FIBRES FOR MULTIFUNCTIONAL COMPOSITES

Marcus, Johansen[a], Johanna, Xu[a], Pui Lam, Tam[a], Leif E., Asp[a], Fang, Liu[a],

a: Department of Industrial and Materials Science, Chalmers University of Technology, 412 96, Gothenburg, Sweden – marcus.johansen@chalmers.se

Abstract: *Carbon fibres can act simultaneously as structural reinforcement and battery electrode. Such multifunctionality is utilised in structural batteries where energy storing capabilities are integrated into load-carrying components, thus creating "mass-less energy storage". Lightweight energy storage is desirable for various applications, particularly electric vehicles, whose driving range is heavily inhibited by the weight of conventional lithium-ion battery packs.*

Structural batteries rely on the ability of carbon fibres to host lithium-ions in their microstructure. Currently, there is a lack in knowledge of how lithium atoms distribute in carbon fibres and what the effects on individual fibres are. Here, with AES and XPS, we elucidate the element distribution in pristine and lithiated T800 PAN-based carbon fibres. Furthermore, mechanical properties are investigated with single filament tensile tests and fractography. It gives an increased understanding of the effect of lithiation on mechanical performance of carbon fibres.

Keywords: Carbon fibre; Multifunctional composites; Energy storage; Lithium insertion; Single filament tensile testing

1. Introduction

In the drive for sustainability, society is moving away from the consumption of finite fuel sources and towards renewable energy that is most commonly stored as electric energy. This pushes the transport sector into an age of electrification. However, electric vehicles have limited driving range compared to traditional internal combustion engine propulsion systems, due to the low energy capacity of the batteries. To battle this disadvantage, the energy consumption can be decreased. The energy consumption of a vehicle is connected to the total weight and can be lowered by reducing the weight, but at the same time all functionalities must remain. Multifunctional composite materials such as the structural battery composite decrease the mass on a systems level by integrating the energy storing capabilities of traditional lithium-ion batteries into the structural components of carbon fibre reinforced composites [1,2]. Here the carbon fibre functions as both reinforcement and storer of electrochemical energy by allowing lithium ions to be inserted into the microstructure, to later be released for energy supply. This puts new demands on the carbon fibres that traditionally are only meant to be structural.

Lithiated carbon fibres, carbon fibres with lithium inserted into the microstructure, have been investigated to a limited degree, and there is still much to learn. During lithiation, carbon fibres expand [3,4]. It has been shown with tensile tests on bundles of carbon fibres that the ultimate tensile load decreases after lithiation [5]. However, testing bundles of thousands of fibres may

  doi:10.5075/epfl-298799_978-2-9701614-0-0

obscure the behaviour of individual fibres. The mechanical properties of individual lithiated carbon fibres have not yet been investigated. Furthermore, the way lithium atoms distribute in carbon fibres may profoundly influence the mechanical properties, but nor has it been investigated.

In this paper, we present results from single filament tensile tests and fractography for pristine and lithiated polyacrylonitrile (PAN)-based carbon fibres of type T800. In addition, we use Auger electron spectroscopy (AES) and X-ray photoelectron spectroscopy (XPS) to unveil the distribution of inserted lithium in carbon fibres and the chemical changes that inserted lithium atoms induce.

2. Material and Method

2.1 Material

Ultra-thin TeXtreme® spread tow unidirectional tapes of T800SC-12k-50C PAN-based carbon fibres with a linear weight of 0.52 g/m were supplied by Oxeon AB, Sweden. The carbon fibres were used as received and attached to a copper current collector with conductive silver paint. A pouch cell design was used to manufacture an electrochemical battery cell with a piece of lithium metal as counter electrode. A glass microfiber filter separator (Whatman GF/A, 260 µm thick) was saturated with electrolyte (1.0 M $LiPF_6$, ethylene carbonate (EC), and dimethyl carbonate (DMC)). The assembly was carried out in a glove box with dry argon atmosphere. To lithiate the carbon fibres, a Neware CT-4008-5V10mA-164 battery cycler was used to cycle the samples between 0.01 V and 1.5 V versus Li/Li+ for 5 cycles. The applied current corresponds to 0.17 C rate. To narrow down the investigation to focus only on the effect of lithiation (excluding the possible effect of wetting by electrolyte), the here called *pristine* carbon fibres were subjects to the same type of assemble, but never cycled and instead left in electrolyte for the same time as required to finish 5 cycles for the lithiated carbon fibres. Based on e-mail correspondence with S. Duan (Department of Industrial and Materials Science, Chalmers University of Technology) 2021 September 21, the nominal cross-section areas of pristine and lithiated T800 were estimated to 18.7 μm^2 and 20.3 μm^2, respectively [6].

2.2 Spectroscopy

Elemental depth analysis of pristine and lithiated carbon fibres was carried out with the surface characterisation techniques AES and XPS. AES was first conducted to obtain the compositional depth profiles, and then, via XPS, the chemical states of elements at the selected sputtered depths were studied. Pristine and lithiated carbon fibres were transported from the glovebox to the spectroscopy instruments without being exposed to ambient air by a sealable transfer vessel.

AES was conducted in PHI 700 Scanning Auger Nanoprobe equipped with Schottky thermal field electron source and a cylindrical mirror analyser. The emission gun was run under 3 kV and 10 nA for both secondary electron imaging and Auger spectrometric measurements. The analysis area was 50 x 35 μm^2. Thus, multiple fibres (~5 µm in diameter) were scanned with AES. Compositional depth profile was assisted with the in-situ argon (Ar) ion gun sputtering, in which the sputter rate was around 145 Å/min with reference to tantalum oxide (Ta_2O_5) calibration.

  doi:10.5075/epfl-298799_978-2-9701614-0-0

XPS was conducted in PHI 5000 VersaProbe III Scanning X-ray Microprobe. Monochromated AlKα (ℏν = 1486.6 eV) source was used. The binding energy scale of the system was aligned with reference to ISO 15472:2010 standard, in which the main peaks of the sputtered gold ($Au4f_{7/2}$), silver ($Ag3d_{5/2}$) and copper ($Cu2p_{3/2}$) were aligned at 83.96 eV, 368.21 eV and 932.63 eV, respectively. In the chemical state analysis, narrow scan mode was used with the pass energy set at 26.0 eV and the step size 0.10 eV. As with AES, the XPS instrument was equipped with an Ar ion gun for sputtering. Due to the risk of the cylindrical fibre geometry causing shadowing effects, ion sputtering was run with the compucentric Zalar rotation to ensure the whole cylindrical 2D surface was sputtered. The analysis area was approximated to the size of the X-ray beam size of 100 µm in diameter, meaning that, like in AES, multiple fibres were scanned with XPS. MultiPak software was used for peak deconvolution.

2.3 Single filament tensile test

A Kammrath&Weiss MZ0-1 tensile module with a 1 N load cell was used for single filament tensile tests. The test was conducted following ASTM standard C1557 [7]. Individual fibres were isolated and placed on polymer film tabs. Commonly paper tabs are used. However, to avoid permeation by electrolyte into the tab and consequent risk of compromising the integrity of the tab, polypropylene film was used as tab material. Individual carbon fibres with gauge length ~20 mm were adhered to the tabs with ethyl cyanoacrylate. 20 pristine and 20 lithiated carbon fibre samples were produced. The displacement speed was 8 µm/s. All tensile tests were performed in ambient atmosphere.

2.4 Fractography

In order to generate multiple carbon fibre with fracture surface, a Deben UK micro-tensile tester with load cell 2 kN was used to break bundles of fibres inside the glovebox. Specimens were tabbed between glass fibre composites with DeltaPreg AX003 epoxy. During transport from glovebox to the scanning electron microscope (SEM) the fracture surfaces were exposed to ambient air. A Zeiss GeminiSEM 450 with field emission gun (FEG) source and accelerating voltage 10 kV was used to image the fracture surface.

3. Results and Discussion

3.1 Spectroscopy

AES and XPS are surface sensitive techniques that together with the material removing capability enabled by an ion sputter gun allow for chemical analysis of elements at sequential depths. The AES survey spectra (first derivative) of the surface of pristine and lithiated carbon fibres differ significantly, with the pristine sample only producing signals related to carbon (C) and traces of nitrogen (N), whereas the lithiated sample showing no N, but C, oxygen (O), lithium (Li), fluorine (F), and phosphorous (P) (Figure 1a). As the sputter commences, the relative intensity for different elements remains constant for the pristine fibre (Figure 1b), but for the lithiated fibre, the initial sputter sees a tumultuous region of variable intensities before the C signal starts to steadily increase as the signal from the other elements decreases (Figure 1c). On the lithiated fibres, this complex outer layer is at least partly related to solid electrolyte interphase (SEI) formed during cycling. However, the thickness of the outer layer, ~3000 Å (estimated thickness using tantalum oxide (Ta_2O_5) as reference), is presumably too large to only contain SEI, since generally the thicknesses of SEI is in the range up to hundreds of Ångström on graphite

  doi:10.5075/epfl-298799_978-2-9701614-0-0

electrodes [8,9]. The remainder is likely residues from the electrolyte. However, it should be noted that the pristine fibres do not exhibit any such outer layer although they also have been submerged in electrolyte. Thus, the whole outer layer is formed due to electrochemical cycling.

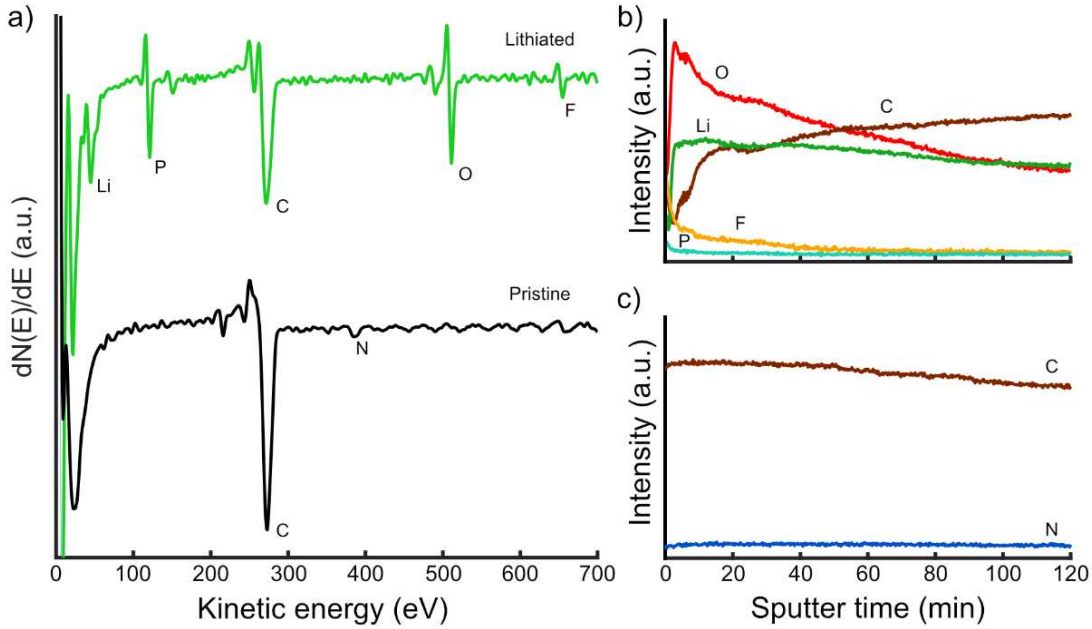

Figure 1. a) AES spectra of the surface of lithiated and pristine fibres. Elemental intensity depth profile for b) lithiated and c) pristine fibres.

In the bulk of the fibres, the differentiated C_{KLL} signal looks distinctly different for pristine and lithiated samples, where, for the lithiated sample, an additional minima is observed at 258 eV (Figure 2a), which can be attributed to carbides [10], and thus a lithium-carbon bond. The ionic nature of intercalated lithium was previously revealed by Wang et. al., using electron energy loss spectroscopy coupled to transmission electron microscopy [11]. Furthermore, the most negative minima, associated to graphite, is located at 276 eV for pristine fibres and 273 eV for lithiated fibres. If a ratio of the carbide/graphite signal is plotted as a function of sputter time, it is seen that the carbide content in the outer layer is relatively low and variable compared to the stable trend inside the fibre (Figure 2b). Towards the deepest part of the analysis, the carbide content shows a weak trend of decreasing. However, with the spatial resolution achieved in this study, Li is shown to be evenly distributed in the carbon fibre along the depth.

The D-parameter (the energy difference between the most positive maxima and the most negative minima in the C_{KLL} signal) indicates the ratio sp^2 and sp^3 hybridisations in a carbon material. For pure diamond, consisting of only sp^3, the D-parameter is ~13 eV, and for pure graphite, consisting of only sp^2, the D-parameter is ~23 eV (12). Throughout the depth the pristine fibre, the D-parameter fluctuates between 22 and 23 eV. The D-parameter for the lithiated fibre instead fluctuates between 21 and 22 eV (Figure 2c). Even though the energy scan step size is relatively coarse (1 eV), the lithiated fibre still seems to have slightly higher content of sp^3.

  doi:10.5075/epfl-298799_978-2-9701614-0-0

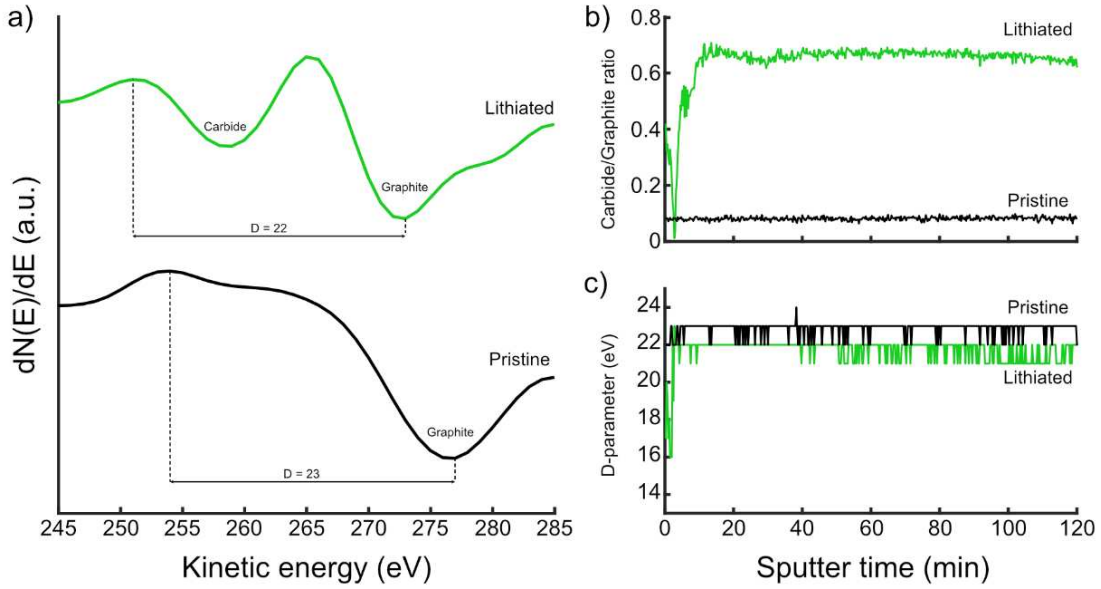

Figure 2. a) Differentiated C_{KLL} signal for lithiated and pristine fibres at sputter depth ~17400 Å, with local minima and D-parameter marked. b) Depth profile of the ratio of carbide and graphite from the C_{KLL} signal in lithiated and pristine fibres. c) The D-parameter depth profile for lithiated and pristine fibres.

At the sputter depth of ~9200 Å, XPS tells a similar story as AES on the bulk of the carbon fibres. The C1s signal around 284 eV can be deconvoluted into two major components for pristine fibres and three major components for lithiated fibres (Figure 3). At 284.4 eV is the signal for sp^2 hybridisation and at 285.6 eV the signal for sp^3 hybridisation [12]. These are found for both samples, but the lithiated fibre has an additional signal at the lower binding energy of 283.2 eV, indicative of a carbide [13–15], a lithium-carbon bond. The ratio between the signals of sp^2 and sp^3 is different for pristine and lithiated fibres, and once again it is suggested that the amount of sp^3 has slightly increased because of the lithiation.

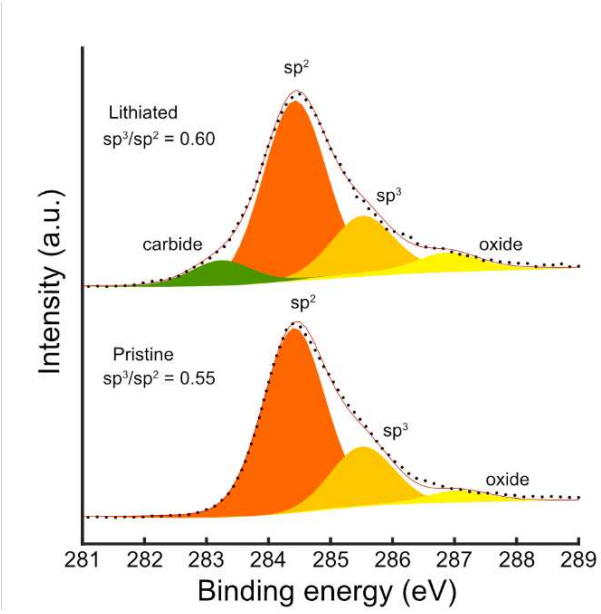

Figure 3. XPS narrow scan of C1s and the deconvoluted signal for lithiated and pristine fibres.

  doi:10.5075/epfl-298799_978-2-9701614-0-0

3.2 Mechanical tests

To determine the effect of the lithiation on mechanical tensile properties, we performed single filament tensile tests of pristine and lithiated carbon fibres. Recently, Duan et.al measured the lithiation induced change in transversal elastic modulus of carbon fibres by compression tests in a corrosion protected environment, and found that the transversal modulus doubled after the first lithation [4]. Note that in the current study, tensile tests were conducted outside the protective argon atmosphere of the glovebox, and thus the lithiated fibres were subject to reactions with oxygen and moisture. The ultimate tensile load, here defined as the largest applied load before failure, proved to be scattered for both pristine and lithiated fibres. Still, the average ultimate tensile load is similar for pristine (95.4 mN) and lithiated fibres (94.2 mN). This is not consistent with previously reported effects of lithiation on ultimate tensile load from tests performed on bundles of carbon fibres [5], where instead the lithiation proved detrimental to ultimate tensile load. This difference can be attributed to several causes, such as different type of tensile testing (bundle vs. single filament), testing condition of the lithiated fibres (protective gas vs. ambient air), and number of fibres tested (average of 2400 fibres vs. 1 fibre).

The scattering in ultimate tensile loads is expected since carbon fibres are brittle materials where failure processes initiate at the weak points of physical defects distributed throughout the material. If these defects are distributed more evenly the mechanical behaviour will be less scattered. Commonly, the distribution of tensile strengths in carbon fibres is presented through the Weibull distribution [16]:

$$P_f = 1 - \exp\left[-L\left(\frac{\sigma_f}{\sigma_0}\right)^{m_f}\right], \quad (1)$$

where a L long carbon fibre exposed to a tensile stress σ_f has the failure probability P_f, the Weibull scale parameter is σ_0, and m_f is the Weibull modulus. A large m_f is a sign of even distribution of physical flaws in the material. The Weibull modulus can be obtained from the slope of the regression line by plotting $ln\left(ln\left[\frac{1}{1-P_f}\right]\right)$ against $ln\,(\sigma_f)$. With the mean rank method, the failure probability is calculated by

$$P_f = \frac{i}{N+1}, \quad (2)$$

where i corresponds to the i-th ranked fibre of N number of fibres. When σ_f is calculated based on the nominal cross-section area of pristine and lithiated T800 carbon fibres, the Weibull modulus is calculated to be 3.3 and 4.5, respectively (Figure 4a). This means that the mechanical behaviour is more uniform for the tested lithiated fibres. However, it should be noted that the exposure of lithiated fibres to ambient air leads to reactions on the surface, which is clearly visible with SEM.

SEM micrographs of the fracture surface of pristine carbon fibres show features of diverging crenulations from an initiation point close to the carbon fibre lateral surface, which are characteristic of tensile failure for PAN-based carbon fibres (Figure 4b). The micrographs of lithiated carbon fibres, on the other hand, look very different (Figure 4c). Here the actual fracture surface is obscured by the reaction products produced post fracture as the newly formed surface is exposed to ambient air. This clearly shows, rather expectedly, that to properly analyse the fracture surface of lithiated carbon fibres, no exposure to ambient air should take

  doi:10.5075/epfl-298799_978-2-9701614-0-0

place. It is possible that these reactions delithiate the fibres, and thus means that the mechanical results from the tensile tests must be confirmed by tests performed in an inert atmosphere. Moreover, a larger quantity of individual fibres must be tested, together with measurement of each fibre's cross-section area.

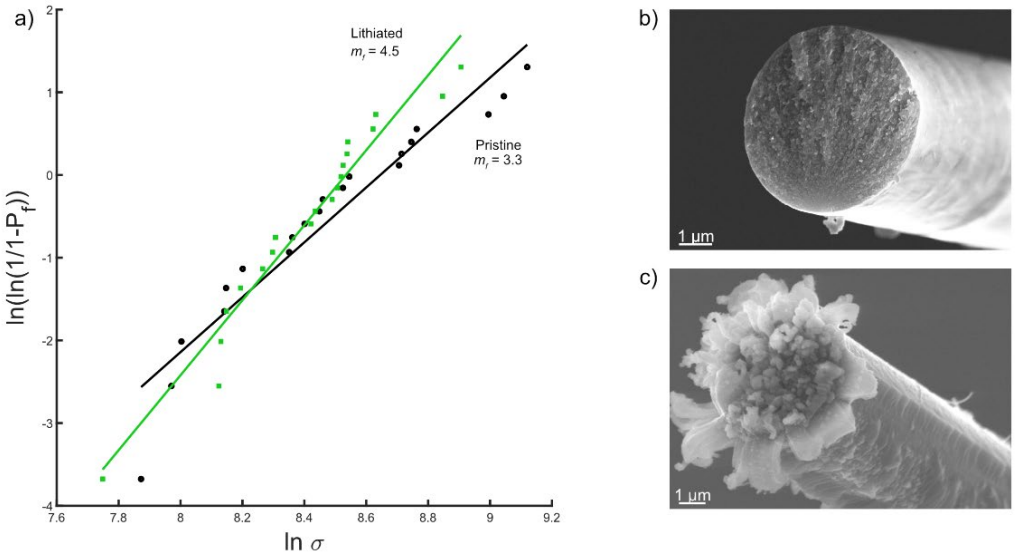

Figure 4. a) Weibull diagram of data from single filament tensile tests of lithiated and pristine. SEM image of the fracture surface of b) a pristine and c) a lithiated fibre after exposure to ambient atmosphere.

4. Conclusion

Pristine and lithiated PAN-based T800 carbon fibres have been analysed with AES, XPS, single filament tensile test, and SEM. AES and XPS identify the formation of lithium-carbon bonds and small increase in the ratio of carbon sp^3 and sp^2 after lithiation. The fibres analysed by AES and XPS are always in protective atmosphere. Ultimate tensile loads are similar for pristine and lithiated fibres, but the Weibull moduli of lithiated carbon fibres is greater. However, the tensile tests were performed in ambient atmosphere, and SEM investigations show clear evidence of side reactions on the lithiated fibres. Thus, the mechanical behaviour of lithiated carbon fibres must be confirmed with tests without exposure to ambient air.

5. References

1. Asp LE, Johansson M, Lindbergh G, Xu J, Zenkert D. Structural battery composites: a review. Funct Compos Struct. 2019;1(4).

2. Asp LE, Bouton K, Carlstedt D, Duan S, Harnden R, Johannisson W, et al. A Structural Battery and its Multifunctional Performance. Adv Energy Sustain Res. 2021;2000093.

3. Jacques E. Expansion of carbon fibres induced by lithium intercalation for structural electrode applications. 2013;9.

4. Duan S, Iyer AHS, Carlstedt D, Rittweger F, Sharits A, Maddox C, et al. Effect of lithiation

  doi:10.5075/epfl-298799_978-2-9701614-0-0

on the elastic moduli of carbon fibres. Carbon N Y [Internet]. 2021;185:234–41. Available from: https://doi.org/10.1016/j.carbon.2021.09.037

5. Jacques E, Kjell MH, Zenkert D, Lindbergh G, Behm M, Willgert M. Impact of electrochemical cycling on the tensile properties of carbon fibres for structural lithium-ion composite batteries. Compos Sci Technol [Internet]. 2012;72(7):792–8. Available from: http://dx.doi.org/10.1016/j.compscitech.2012.02.006

6. S. Duan, Private communication. September 21, 2021.

7. ASTM C1557. Standard Test Method for Tensile Strength and Young's Modulus of Fibers. ASTM Int. 2020. p. 1–5.

8. Edström K, Herstedt M, Abraham DP. A new look at the solid electrolyte interphase on graphite anodes in Li-ion batteries. J Power Sources. 2006;153(2):380–4.

9. Yoshida T, Takahashi M, Morikawa S, Ihara C, Katsukawa H, Shiratsuchi T, et al. Degradation Mechanism and Life Prediction of Lithium-Ion Batteries. J Electrochem Soc. 2006;153(3):A576.

10. Craig S, Harding GL, Payling R. Auger lineshape analysis of carbon bonding in sputtered metal-carbon thin films. 1983;124:591–601.

11. Wang F, Graetz J, Moreno MS, Ma C, Wu L, Volkov V, et al. Chemical distribution and bonding of lithium in intercalated graphite: Identification with optimized electron energy loss spectroscopy. ACS Nano. 2011;5(2):1190–7.

12. Jackson ST, Nuzzo RG. Determining hybridization differences for amorphous carbon from the XPS C 1s envelope. Appl Surf Sci. 1995;90(2):195–203.

13. Galuska AA, Uht JC, Marquez N. Reactive and nonreactive ion mixing of Ti films on carbon substrates. J Vac Sci Technol A Vacuum, Surfaces, Film. 1988;6(1):110–22.

14. Bozack MJ. Single Crystal 6H-SiC(0001) by XPS. Surf Sci Spectra. 1994;3(1):82–5.

15. Håkansson KL, Johansson HIP, Johansson LI. High-resolution core-level study of hexagonal WC(0001). Phys Rev B. 1994;49(3):2035–9.

16. Weibull W. A Statistical Distribution Function of Wide Applicability. J Appl Mech. 1951;Vol. 18:293–7.

  doi:10.5075/epfl-298799_978-2-9701614-0-0

AN EFFICIENT COMPUTATIONAL APPROACH FOR THREE-DIMENSIONAL MODELING AND SIMULATION OF FIBROUS BATTERY ELECTRODES

Mohsen Goudarzi[a], Davide Grazioli[b], Angelo Simone[c]

a: Department of Earth Sciences, Utrecht University, Utrecht, The Netherlands
b: Department of Industrial Engineering, University of Padova, Padua, Italy – davide.grazioli@unipd.it
c: Department of Industrial Engineering, University of Padova, Padua, Italy

Abstract: *Fibrous electrodes are a promising alternative to conventional particle-based lithium-ion battery electrodes. In this contribution we propose an efficient computational approach for the modeling and simulation of electrochemical phenomena taking place in fibrous electrodes during battery charge/discharge processes. Since each fiber is explicitly modeled by means of a dimensionally reduced embedded fiber model, the framework enables simulations in a three-dimensional setting with relatively modest discretization and computational requirements compared to simulations with fully resolved fiber discretization. The approach is applied to electrodes with high volume fractions of high aspect ratio fibers. Various local and global quantities are analyzed and results are compared to those obtained with the standard finite element method and the pseudo-2D model.*

Keywords: Fibrous electrode; nanowire and structural batteries; lithium-ion battery electrodes modeling and simulation; embedded fiber model; finite element method

1. Introduction

One-dimensional electrode architectures, making use of active material in the shape of fibers (Figure 1a), are of interest for a wide range of applications since they show advantages over traditional design (e.g., particle-based electrodes) in terms of surface area to volume ratio, areal and/or specific capacity, and reduced diffusion distance between fibers. Multifunctional fibrous electrodes are suitable candidate for wearable electronics [1] and structural batteries [2–4] thanks to their capability to combine energy storage, mechanical flexibility, and load-bearing functionalities.

Despite the progress in computational battery modeling, the numerical simulation of fibrous electrode architectures has lagged behind that of particle-based battery electrodes for many reasons. Compared to particle-based battery electrodes, fibrous electrodes are more difficult to model in an efficient manner because fibers are elongated objects, and their representation entails several additional design parameters (such as aspect ratio, curvature, spatial orientation, and arrangement). Therefore, simplified models (such as pseudo2D models [5]) cannot easily be extended to simulate electrodes with fibrous active material inclusions. To the best of our knowledge, no simplified models are currently available to model fibrous electrodes. This implies that modeling must follow traditional approaches, using for instance the finite element method (FEM), making simulations like those proposed in this work very costly using conformal mesh techniques [6, 7]. The number of fibers that comprise a full-scale electrode with volume

  doi:10.5075/epfl-298799_978-2-9701614-0-0

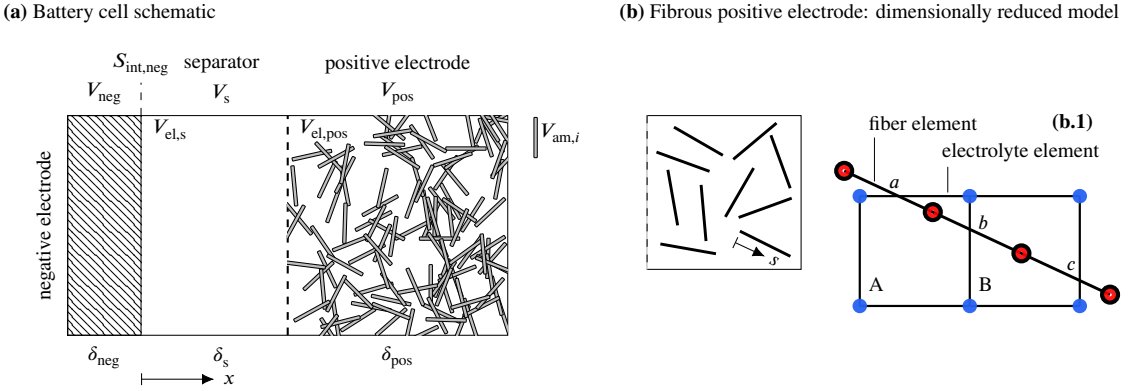

Figure 1 (a) Simplified two-dimensional schematic of a lithium-ion battery half cell with a porous positive electrode containing active material fibers. (b) A fibrous electrode is represented by means of dimensionally reduced fibers. Nodes with the same color share the same set of DOFs (concentration c_{am} and electric potential φ_{am} in the fiber in red, concentration c_{el} and electric potential in the electrolyte φ_{el} in blue, and the exchanged current $i_{BV,am}$ at the active material-electrolyte interface in black). Adapted from [10].

fractions typical of porous electrodes eventually results in very large systems of equations that require dedicated computer resources.

To perform numerical simulations of fibrous electrodes avoiding excessive computational costs, we propose a FE-based dimensionally reduced fiber model ('dimensionally reduced model' from now on) in which the fiber-shaped active material is represented by means of line elements. The approach is inspired by the embedded reinforcement model [8, 9] employed to numerically characterize the mechanical response of fiber-reinforced composite materials. The proposed strategy results in a greatly simplified discretization procedure compared to a traditional fully resolved FE model ('fully resolved model' from now on) as the discretization of one-dimensional active material domains is detached from the three-dimensional discretization of the hosting electrode domain. This is demonstrated in Section 3 where we describe the simulations performed on a three-dimensional fibrous electrode with volume fraction of active material up to 70% (25000 fibers). The results indicate that the accuracy of the dimensionally reduced model is consistent with that of the pseudo-2D model [5].

2. Dimensionally reduced model

Figure 1a shows a schematic representation of the battery cell. The active material fibers in the positive electrode is hereafter referred to as 'active material'. Henceforth, subscripts 'am', 'el', 'neg', 'pos' and 's' indicate active material, electrolyte, negative and positive electrode, and separator, respectively. The active material domain is the union of the fibers in the positive electrode. The problem is formulated in terms of molar concentration c (number of moles per unit volume) and electric potential ϕ in the negative electrode, electrolyte, and active material of the positive electrode. The charge transfer across the interface is denoted with i_{BV}. Details about governing equations, boundary and initial conditions are provided in Goudarzi et al. [10].

We represent active fibers as one-dimensional objects (Figure 1b). The proposed approach shows analogies with the treatment of the pore-filling electrolyte typical of porous electrode theory [11]. A crucial difference however exists: in our dimensionally reduced model the interaction between each fiber and the electrolyte is explicitly accounted for. This feature is

  doi:10.5075/epfl-298799_978-2-9701614-0-0

relevant to the modeling of battery electrodes in which the characteristic length of the active material inclusion is not negligible compared to the characteristic size of the electrode. The representation of a fiber as a one-dimensional object rests upon the following assumption: field variables are uniform on a cross section. Therefore, a single value of ϕ_{am}, c_{am}, and $i_{BV,am}$ is associated at coordinate s along the fiber axis. The dimensionally reduced approach is tailored for fibrous electrode modeling, and approximations are introduced to promote its numerical efficiency. A thorough numerical study is performed in Goudarzi et al. [10] to assess the simplifications introduced and the impact they have on the accuracy of the dimensionally reduced model.

The geometrical representations of electrolyte domain and fibers (and their discretizations) are not conforming. Figure 1b.1 shows the case of two electrolyte elements (A and B) crossed by a dimensionally reduced fiber discretized with three linear elements (*a*, *b*, and *c*). The independence of the two discretizations is evident: the nodes of the fiber elements (in red) do not coincide with the intersection points between fiber axis and electrolyte element edges (the nodes of the electrolyte elements are drawn in blue). There are no limitations on the number of fibers that can cross an electrolyte element. Details about the numerical implementation are provided in Ref. [10].

3. Numerical example

In this section, we aim to show the capability of the proposed approach in dealing with fibrous electrodes when a large number of fibers are involved. Since no reference solution exists about local field distributions for battery electrodes with arbitrary arrangement of fibers, a (qualitative) comparison is performed considering a particle-based system and selecting the work by Doyle et al. [5] as reference. The reader is referred to Goudarzi et al. [10] for numerical simulations details, where a larger set of results is also presented and commented. In the investigation performed by Doyle et al. [5], spherical active particles of diameter d_p = 2 µm occupy 70% of the positive electrode volume. We replace the particles with fibers of diameter d_f = 2/3 d_p = 1.3 µm and length l_f = 20 µm. A distribution of about 25000 fibers is considered. We consider galvanostatic processes with applied current I = 5, 7, and 10 Am^{-2}. Numerical simulations are performed with uniform mesh discretizations: 10 equally sized segments for each fiber and $n_{msh} \times n_{msh} \times n_{msh}$ eight-node hexahedral elements for the electrolyte domain.

Contour plots of the positive electrode are reported in Figure 2 for the numerical simulations performed with I = 10 Am^{-2}. Panel (a) shows the fiber utilization at three stages of the discharge process. The progression of the utilization front is basically one-dimensional. At the beginning of the discharge process lithium insertion into fibers occurs mainly at the leftmost edge of the electrode. As the process continues, fibers near the separator fill up and the reaction front shifts towards the body of the electrode.

Data shown in Figure 3 have been sampled along the axial line of the half cell in the separator and electrode domain. The evolution patterns of the concentration profile are similar for I = 5 Am^{-2} (a) and 10 Am^{-2} (b). When I = 5 Am^{-2} the concentration gradient is modest and the depletion of the electrolyte is attained in about 20% of the positive electrode thickness by the end of the process (SOC= 0.98). A pronounced concentration gradient develops with I = 10 Am^{-2}, causing the depletion of the electrolyte in roughly 50% of the electrode thickness at SOC= 0.45.

  doi:10.5075/epfl-298799_978-2-9701614-0-0

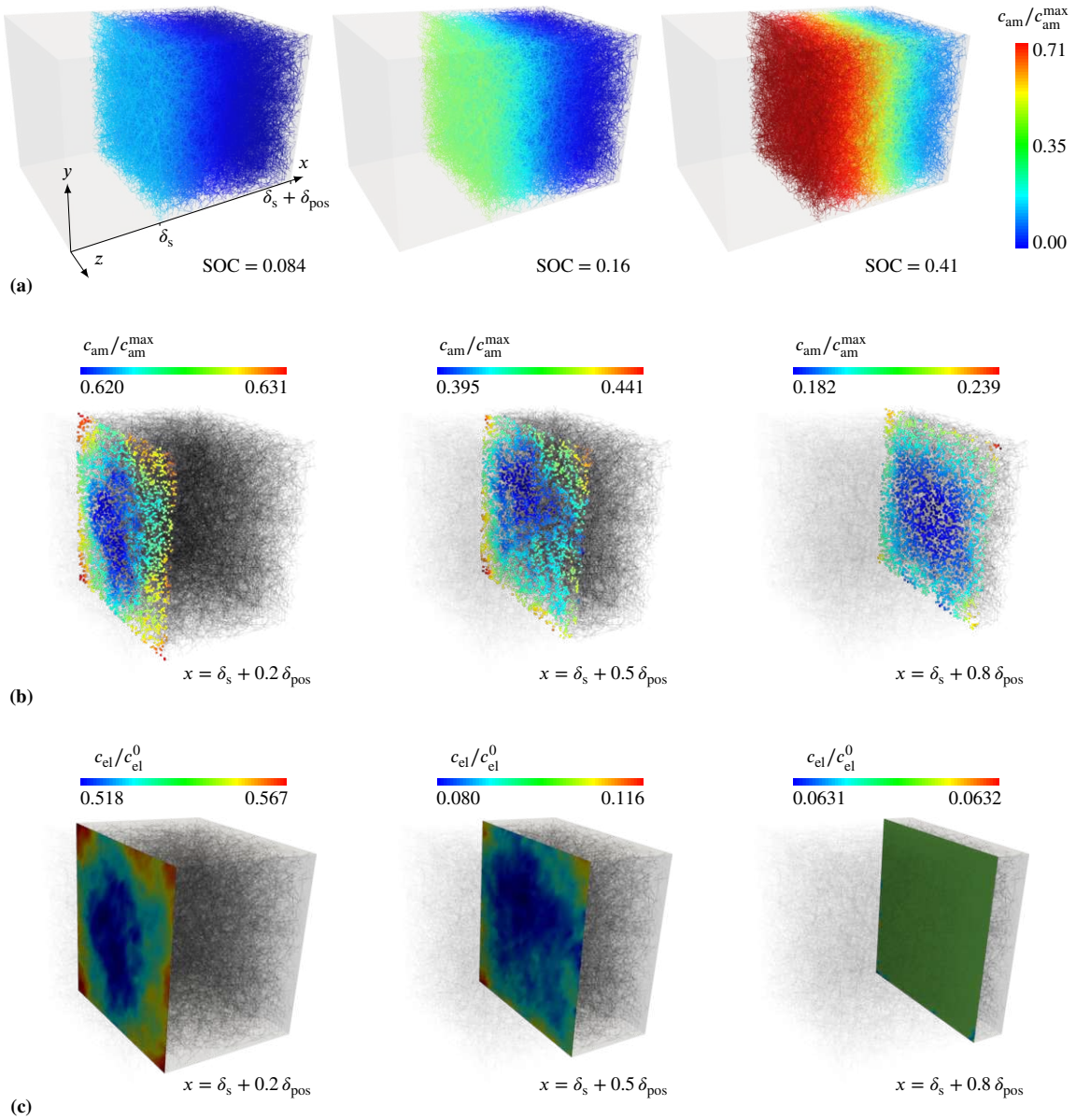

Figure 2 Contour plots of the positive electrode for I = 10 Am^{-2} *discharge. (a) Concentration in the active fibers at SOC = 0.084, 0.16, and 0.41. Concentration distributions on three yz-planes in the positive electrode: (b) on the active fibers intersected by the planes, and (c) in the electrolyte. Each point in panel (b) represents a fiber cross-section. All the contour plots in panels (b) and (c) refer to SOC = 0.41. Reproduced from [10].*

In Figure 3b we report the results by Doyle et al. [5] for comparison. A good agreement is evident in the initial simulation steps; the concentration dip at the separator-positive electrode boundary is clearly captured. Concentration gradients and electrolyte depletion are more pronounced in the fibrous electrode at SOC > 0.006. The main difference between the fibrous and particle-based electrode simulations is that the first one stops at SOC = 0.45, while the second proceeds up to about SOC = 0.83.

  doi:10.5075/epfl-298799_978-2-9701614-0-0

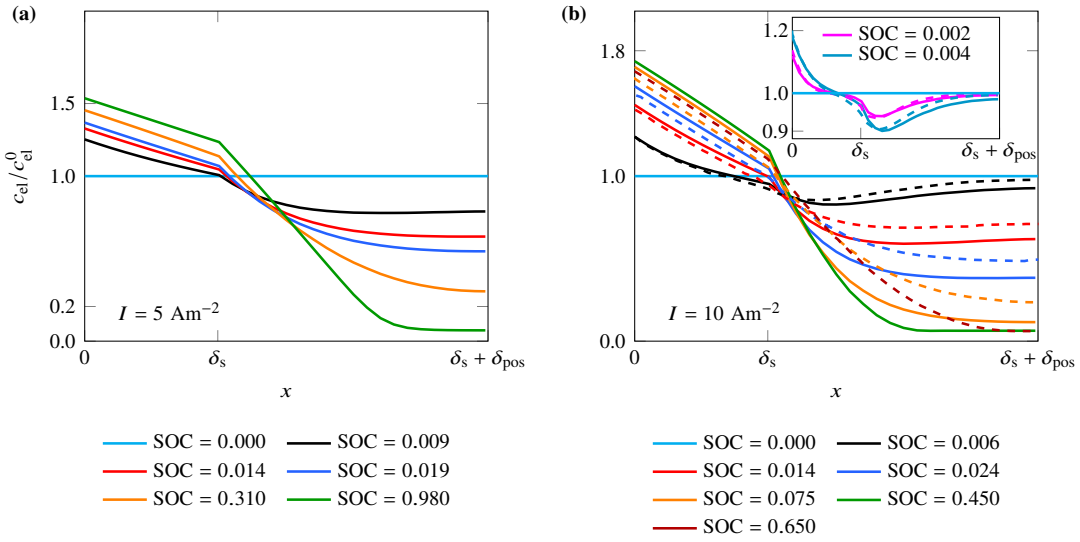

Figure 3 Concentration profiles within the electrolyte in the separator and positive electrode at various SOC with electric current densities (a) I = 5 Am^{-2} *and (b) I = 10* Am^{-2} *(results refer to* n_{msh} *= 30). The results by Doyle et al. [5] are reported with dashed lines in panel (b). The same color is used for our results and those of the reference when the SOC coincides. Reproduced from [10].*

Figure 4 shows the cell potential as a function of the SOC for I = 5, 7, and 10 Am^{-2} and for discretizations n_{msh} = 12, 21, and 30. The active material utilization progressively reduces as the discharge rate increases, in agreement with the results by Doyle et al. [5]. Panel (a) shows that there are no appreciable differences between the results obtained with different meshes when I = 5 Am^{-2} is applied, suggesting that the converged solution is obtained with the coarsest mesh (n_{msh} = 12). Similar arguments apply to the results obtained with I = 7 Am^{-2}. With I = 10 Am^{-2}, the results obtained with different n_{msh} overlap, but the maximum achievable SOC increases with n_{msh}. Since a steeper concentration gradient develops in the electrolyte at higher rates a proper representation of the cell response requires a finer mesh.

The results by Doyle et al. [5] for I = 5 and 10 Am^{-2} are reported in panel (b) for comparison. The cell potential of the particle-based electrode exceeds that of the fibrous electrode with both I = 5 and 10 A m^{-2}. Indeed, fibers near the separator are filled more quickly than particles and, at the same time, shortage of lithium at the rightmost edge of the cell occurs earlier in the fibrous electrode (Figure 3). These circumstances concur to the accelerated reduction of the cell potential of the fibrous electrode that ultimately results in a reduction of the active material utilization compared to the particle-based electrode. At I = 10 A m^{-2}, the ultimate SOC reduces from 0.83 to 0.45 switching from particle-based to fibrous electrode.

  doi:10.5075/epfl-298799_978-2-9701614-0-0

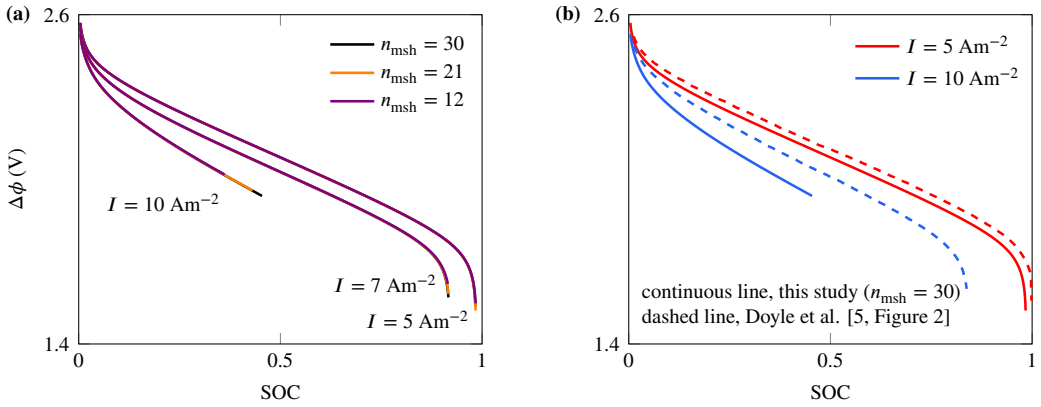

Figure 4 Discharge curve for galvanostatic discharge processes. (a) Mesh refinement study at I = 5, 7, and 10 Am^{-2}*; simulations have been performed with structured hexahedral element meshes with* n_{msh} *= 12, 21, and 30. (b) Comparison with the results by Doyle et al. [5]. Reproduced from [10].*

Figure 4 shows that the fibrous electrode curve for I = 10 Am^{-2} is truncated at SOC = 0.45 and Δϕ = 1.93 V. A similar behavior is reported by Doyle et al. [5], but at a higher discharge rate. We conclude that the time evolution of the field variables predicted with the dimensionally reduced model is consistent with the results reported by Doyle et al. [5], but the insurgence of steep gradients within the positive electrode occurs at lower SOC. For example, Doyle et al. [5] determine electrolyte depletion in 10% of the particle-based electrode thickness at SOC = 0.65, while the dimensionally reduced model predicts electrolyte depletion in 50% of the fibrous electrode thickness at SOC = 0.45 (Figure 3b). Based on the comparisons performed we believe that the approach is sound and applicable with electrodes containing high volume fraction of fibers.

4. Concluding remarks

Structural batteries [2–4] inspired this work. A comprehensive modeling approach for such a multifunctional composite would require a coupled electrochemical-mechanical constitutive model. In this work we focused on the electrochemical modeling and simulation of electrochemical processes in fibrous electrodes, neglecting mechanics and its coupling to electrochemistry. The focus is on the efficient modeling of the fibrous microstructure through a dimensionally reduced embedded fiber model and the corresponding constitutive model. We consider this a necessary first step towards the previously mentioned comprehensive modeling.

The proposed dimensionally reduced model ensures efficiency without sacrificing accuracy. The results reported here and in Goudarzi et al. [10] demonstrate that the accuracy of the dimensionally reduced model is comparable to that of the fully resolved model over a wide range of electrical loading conditions, and the agreement between the outcomes of the two approaches improves as the aspect ratio of the fibers increases. The dimensionally reduced model enables simple geometry discretization procedures and yields a remarkable reduction in the total number of degrees of freedom compared to the fully resolved model. This makes the dimensionally reduced model inherently suitable for three-dimensional numerical simulations of nanowire electrodes that would otherwise be quite costly to perform using conformal

  doi:10.5075/epfl-298799_978-2-9701614-0-0

meshing techniques [6, 7] (in this contribution we have a volume fraction of 70% of active material and 25000 fibers). We further show that the results are consistent with those obtained with the porous-electrode theory if equivalent (in terms of porosity) microstructures are considered. The dimensionally reduced model is, therefore, a valuable alternative to the fully resolved model for the modeling and simulations of battery electrodes comprised of high aspect ratio one-dimensional active materials whose diameter is orders of magnitude smaller than the thickness of the electrode. Nanowire systems and fibrous multifunctional electrodes with high volume fractions of active materials are therefore suitable applications.

Acknowledgements

The research leading to these results has received funding from the European Research Council under the European Union's Seventh Framework Programme (FP7/2007-2013) / ERC Grant agreement n◦ 617972.

References

1. 1. T. Lv, Y. Yao, N. Li, and T. Chen. Wearable fiber-shaped energy conversion and storage devices based on aligned carbon nanotubes. Nano Today, 11(5):644–660, 2016.
2. P. Liu, E. Sherman, and A. Jacobsen. Design and fabrication of multifunctional structural batteries. Journal of Power Sources, 189(1):646–650, 2009.
3. L. E Asp, K. Bouton, D. Carlstedt, S. Duan, R. Harnden, W. Johannisson, M. Johansen, M. K. G. Johansson, G. Lindbergh, F. Liu, K. Peuvot, L. M. Schneider, J. Xu, and D. Zenkert. A structural battery and its multifunctional performance. Advanced Energy and Sustainability Research, 2:2000093, 2021.
4. D. Carlstedt, K. Runesson, F. Larsson, J. Xu, and L. E. Asp. Electro-chemo-mechanically coupled computational modelling of structural batteries. Multifunctional Materials, 3(4):045002, 2020.
5. M. Doyle, T. F. Fuller, and J. Newman. Modeling of galvanostatic charge and discharge of the lithium/polymer/insertion cell. Journal of The Electrochemical Society, 140(6):1526–1533, 1993.
6. B. Liang, A. Nagarajan, and S. Soghrati. Scalable parallel implementation of CISAMR: a non-iterative mesh generation algorithm. Computational Mechanics, 64(1):173–195, 2018.
7. S. A. Roberts, H. Mendoza, V. E. Brunini, and D. R. Noble. A verified conformal decomposition finite element method for implicit, many-material geometries. Journal of Computational Physics, 375:352–367, 2018.
8. S. Balakrishnan and D. W. Murray. Finite element prediction of reinforced concrete behavior. Technical Report Structural Engineering Report No. 138, Department of Civil Engineering, The University of Alberta, Edmonton, Alberta, Canada, July 1986.
9. M. Goudarzi and A. Simone. Fiber neutrality in fiber-reinforced composites: Evidence from a computational study. International Journal of Solids and Structures, 156–157:14–28, 2019.
10. M. Goudarzi, D. Grazioli, and A. Simone. An efficient computational approach for three-dimensional modeling and simulation of fibrous battery electrodes. International Journal for Numerical Methods in Engineering, 123(7):1513–1546, February 2022.
11. J. Newman and W. Tiedemann. Porous-electrode theory with battery applications. AIChE Journal, 21(1):25–41, 1975.

DEVELOPMENT OF A MANUFACTURING PROCESS FOR A CUBOIDAL PRESSURE VESSEL WITH TENSION STRUTS

Elisabeth Gleis[a], Jongwon Kim[a], Swen Zaremba[a], Klaus Drechsler[a]

a: Technical University of Munich, TUM School of Engineering and Design, Department of Aerospace and Geodesy, Chair of Carbon Composites, Boltzmannstr. 15, 85748 Garching, Germany – elisabeth.gleis@tum.de

Abstract: *This article presents a manufacturing concept for an installation-space conformable, box-shaped pressure vessel. As cuboid structures underlie high bending stresses under internal pressure, reinforcing struts are integrated into the tank volume. The incorporation of these reinforcements poses various challenges: The connection of the tension struts to the outer walls of the pressure vessel is of great importance, as this is where most of the forces that counteract the internal pressure are transmitted. For the technological realization of the strut connection, continuous-fiber-reinforced thermoplastic struts are positioned in a winding core.* A CFRP-laminate is generated using filament winding*, with the struts piercing the deposited carbon fiber rovings and protruding beyond the outer surface of the tank. The strut ends are anchored in the vessel wall by thermal bending and the application of additional outer CFRP layers. The main objective of this work is to present the novel manufacturing concept and verify its feasibility.*

Keywords: hydrogen storage; pressure vessel; conformable pressure vessel; process development; filament winding

1. Motivation

As a climate-neutral energy carrier, green hydrogen offers great potential for meeting the challenges of the energy transition, especially for mobile applications [1, 2]. However, due to their higher market maturity, battery electric vehicles (BEVs) are currently the predominant alternative to internal combustion engine vehicles (ICEVs) for passenger cars [3, 4]. Yet, fuel cell electric vehicles (FCEVs) offer a promising alternative especially for long driving ranges exceeding 500 km [3], and include advantages such as short refueling times [3, 5–7] and decreased seasonal range reduction [5]. On this basis, it is considered reasonable in literature to further advance both technologies in parallel [2, 4, 6, 8].

A major disadvantage of FCEVs is the lower production volume compared to BEVs, resulting in higher prices for consumers [2, 9, 10]. One promising way to achieve a cost reduction through economies of scale is to use common vehicle architectures for battery electric and fuel cell vehicles [11–13]. In this case, a flat installation space in the vehicle underbody is available for the hydrogen storage system [12, 13].

Currently, hydrogen in passenger cars is typically stored in gaseous form at 700 bar in cylindrical type-IV pressure vessels consisting of a thermoplastic liner (permeation barrier) and a thermoset fiber-reinforced tank wall [7, 14, 15]. However, these vessels are not ideal for integration into design spaces in cars [7, 16]. Especially for the flat installation space in the vehicle underbody, cylindrical pressure vessels are only suitable to a limited extent. Cuboidal tanks adapted to the

  doi:10.5075/epfl-298799_978-2-9701614-0-0

installation space offer great potential for optimal utilization of the volume for hydrogen storage and thus for achieving extended driving ranges [12].

In this work, a promising manufacturing concept for a conformable carbon-composite pressure vessel is presented. The feasibility of the concept is verified by a process demonstrator. While the proof-of-concept indicates the potential of the manufacturing process, it also reveals some challenges and, therefore, the potential for optimization.

2. Existing Concepts for Conformable Pressure Vessels

While the wall elements in cylindrical and spherical vessels act under pure tension, vessels with deviating geometries are subjected to high bending forces [17]. To counteract these, either a system of subunits of mechanically more stable geometries such as spheres or cylinders is required, or additional reinforcing structures such as plates or struts have to be incorporated. Different design approaches from literature to achieve installation-space conformability of pressure vessels are shown in figure 1:

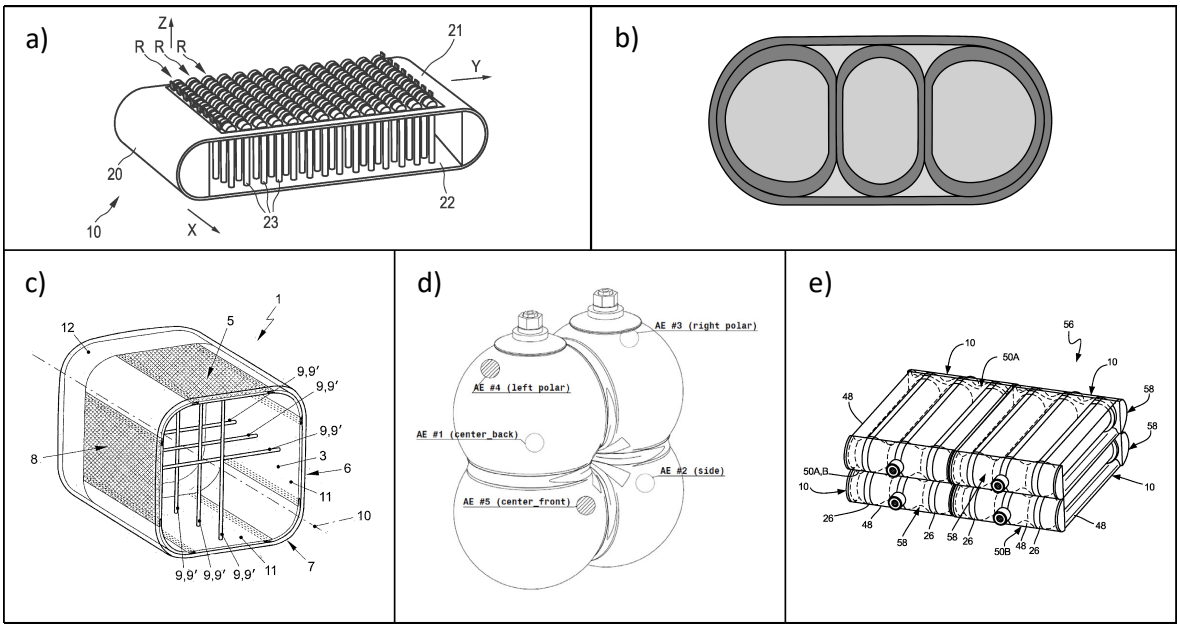

Figure 1. Alternative vessel geometries for improved installation-space conformability. a) Cuboidal vessel with struts implemented by tufting [18]; b) Multi-cell approach [19]; c) Cuboidal tank with reinforcing struts [20]; d) Multi-sphere vessel [21]; e) Multi-cylinder vessel [22].

Concepts using inner reinforcement struts, as shown in figure 1 a) and c), yield a higher conformability within a box-shaped design space, than multi-sphere (d) or multi-cylinder (e) concepts. Ruf et al. [12] compared a multi-cylinder approach with a cuboidal vessel with tension struts and found an approximately 25 % higher driving-range potential for the latter.

Despite the great potential of conformable vessels with inner tension struts, there are only few publications reporting feasible concepts. Aceves et al. [17] examined a box-shaped pressure vessel with metallic struts and optimized the walls to minimize bending stresses. The vessel walls were manufactured using rapid prototyping. Furthermore, a filament-wound conformable pressure vessels with segments in a “pillow-shape” were manufactured and tested. The end

  doi:10.5075/epfl-298799_978-2-9701614-0-0

segments that would be necessary for the full system were not realized. Another concept for a conformable pressure vessel with carbon-fiber-epoxy tension struts was investigated by Farines et al. [23]. In this concept, the CFRP-struts are joined with metallic connector parts using adhesives. The struts are inserted into a metallic liner which is subsequently reinforced using filament winding to create a type-III vessel. Öztas et al. [13, 24] use numerical approaches to investigate a full-steel pressure vessel (type-I) and a similar vessel with an additional composite overwrap (type-II) and propose 3D-printing as a possible technology to manufacture the metallic tank structure with tension struts. A manufacturing approach for a polymer-composite pressure vessel (type-IV) with tension struts was recently presented by Ruf et al. and Horoschenkoff et al. [12, 25]. The concept involves filament winding to generate the vessel walls and a tufting process to insert aramid rovings as inner reinforcements. The struts are anchored on the outside of the vessel wall by inserting a rod into the loop tunnel that is formed in the tufting process.

Up to now, there are no conformable hydrogen storage systems that find practical application in vehicles. One of the biggest challenges for vessels with inner reinforcement structures is the manufacturability and, in particular, the connection of the tension struts or ribs to the vessel wall [17, 24]. To overcome this, novel approaches that incorporate established processes suitable for series production are needed. Another challenge is the increased weight of conformable tanks compared to cylindrical systems [13]. Due to this, it is important to focus on lightweight polymer-composite designs. Lastly, regulations for the certification of tank systems currently only consider cylindrical geometries. Thus, an adaption would be necessary to enable the use of conformable pressure vessels in vehicles [12].

3. New Concept for a Manufacturing Process of a Cuboidal Pressure Vessel with Tension Struts

The proposed concept for the fabrication of a conformable pressure vessel consists of four main steps, which are shown in figure 2. During the development of the concept, the focus was on using processes suitable for series production, such as filament winding, to facilitate subsequent upscaling. The new concept is suitable for the production of tanks with and without a thermoplastic liner (type-IV and type-V). Novel material systems, such as ionic liquid modified epoxy resins, offer great potential to improve hydrogen barrier properties and thus could in the future eliminate the need for thermoplastic liners [26, 27]. For this reason, a linerless embodiment is considered in this work. It should be noted, however, that for type-V tanks, microcracking is also a critical aspect that has to be considered [28].

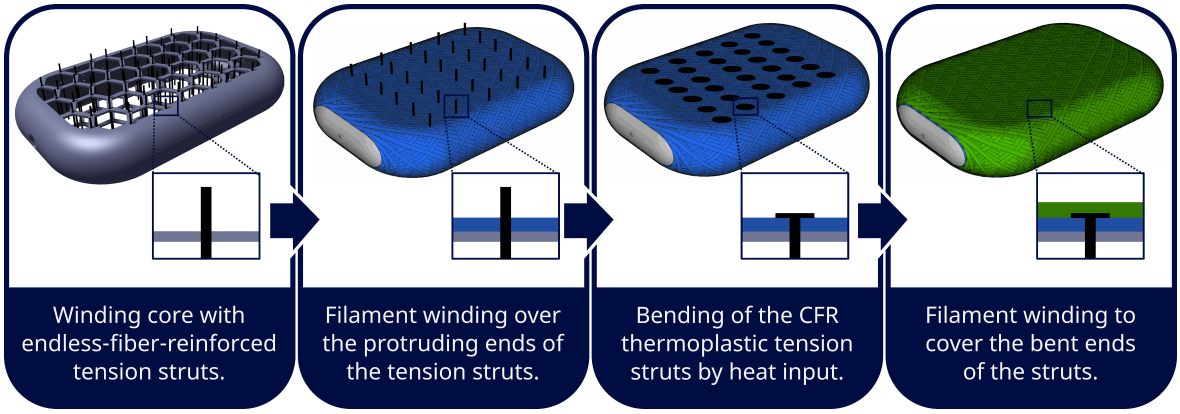

Figure 2. Main steps for the manufacturing of a pressure vessel with the presented method.

  doi:10.5075/epfl-298799_978-2-9701614-0-0

To manufacture a conformable pressure vessel using the proposed method, endless-fiber-reinforced struts are positioned in a winding core with the strut ends protruding beyond the outer surface of the core structure. In the considered embodiment, the winding core consists of a thermoplastic skeleton structure. This offers great potential for the integration of the struts during the fabrication of the modular skeleton structure in a single process step using the "MAI-Skelett" method [29]. When manufacturing type-IV tanks, a thermoplastic liner can be used as the core structure. The concept allows the matrix material of the CFRP struts and the thermoplastic liner to be the same, which can minimize problems with sealing.

The wall of the conformable pressure vessel is manufactured in a two-step wet filament winding process. In the first winding step, the strut ends pierce the carbon fiber rovings as they are deposited on the core structure, resulting in an intermediate state in which the straight strut ends protrude through the composite laminate. After full or partial curing of the laminate, the end parts of the struts are bent using heat to plasticize their thermoplastic matrix. Different geometric options exist for the bending step, examples are shown in figure 3. In a second filament-winding step, the outer CFRP laminate is produced so that the bent ends of the struts are anchored between the wound layers of the tank wall.

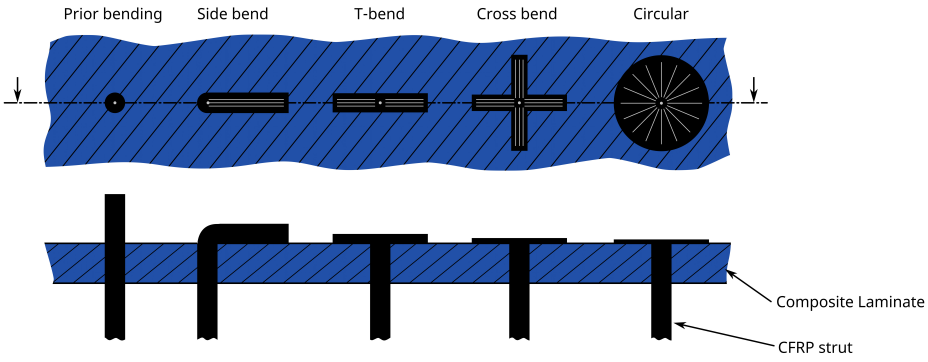

Figure 3. Geometrical options for bending the CFRP struts to achieve connection to the composite laminate of the vessel wall. Fiber directions are indicated in grey.

4. Proof-of-Concept and Discussion

To verify the feasibility of the described manufacturing concept, a process demonstrator (dimensions 450 x 290 x 80 mm) was built. For this purpose, a skeleton structure was produced using 3D-printing and endless-fiber-reinforced struts with a PA-6 matrix were attached with adhesives. Filament winding was performed on a 5-axis winding machine using carbon fiber rovings and epoxy resin. figure 4 a) shows the demonstrator before the first winding step and b) shows the laminate with the protruding strut ends.

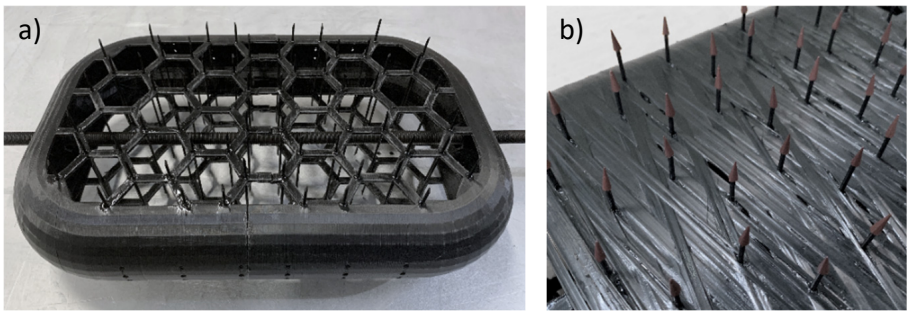

Figure 4. a) Skeleton structure before winding. b) Laminate with protruding strut ends.

To avoid fiber damage when the struts pierce the roving, pointed caps were used as a manufacturing aid during filament winding and were removed before bending of the struts. Figure 5 shows the strut ends with (b) and without (a) the manufacturing aid before bending, as well as the bending process (c).

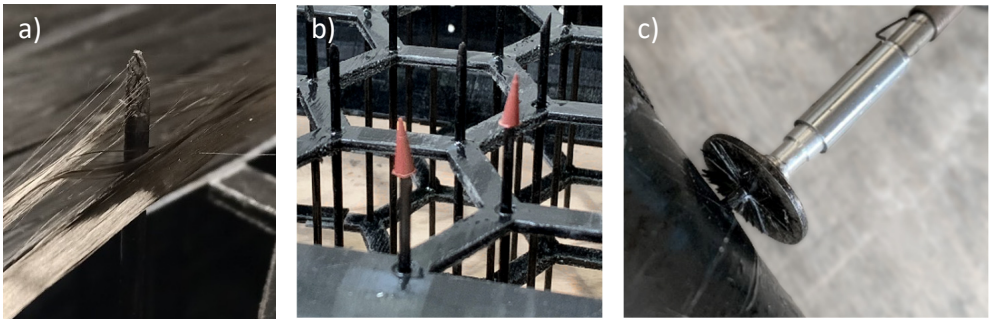

Figure 5. a) When winding over the strut ends, filaments got trapped, resulting in fiber damage. b) To counteract this, pointed caps were used as a manufacturing aid. c) Thermal bending of the strut ends.

Figure 6 a) shows the final demonstrator. Due to difficulties with the generation of winding paths for the non-rotationally symmetric geometry, the structure was not fully covered by the laminate. For investigation, the demonstrator was cut and sectional images of the areas where the struts are connected to the vessel wall were made.

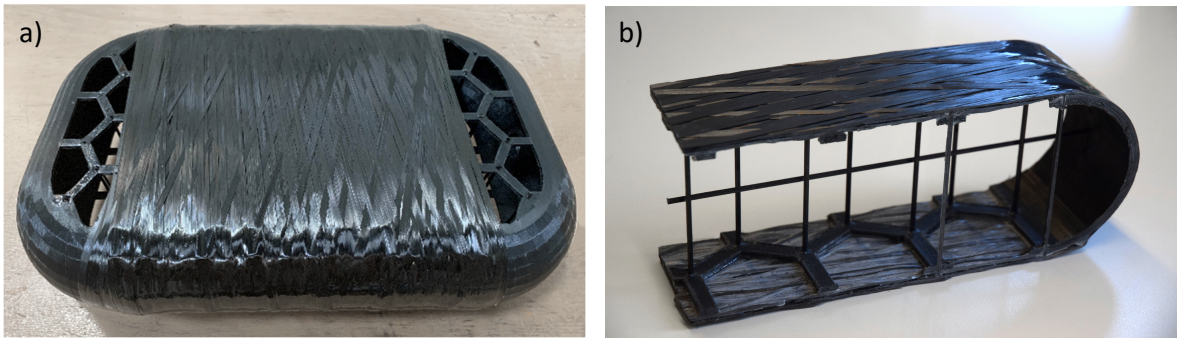

Figure 6. a) Final process demonstrator. b) Section of the demonstrator to allow examination of the interior condition.

The examination of the demonstrator revealed that the connection between the CFRP layers from the two winding steps, as well as the connection between the inner laminate and the bent sections of the tension struts, is insufficient. Figure 7 shows a sectional image of a strut-wall connection and a schematic representation of the problem.

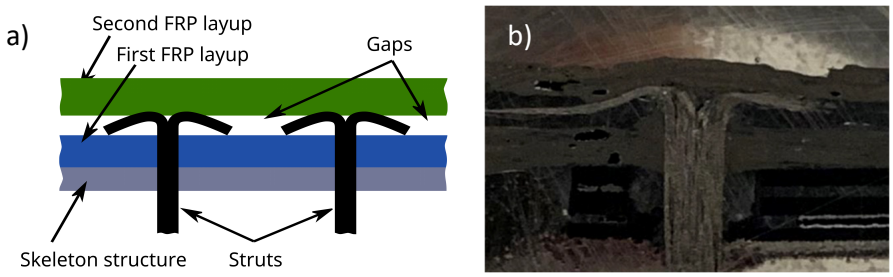

Figure 7. a) Final process demonstrator. b) Section of the demonstrator to allow examination of the interior condition.

  doi:10.5075/epfl-298799_978-2-9701614-0-0

The gap between the bent struts and the laminate occurs because the struts are not perfectly deflected during bending. For future work, a defined bending radius by deflecting the strut onto an underlying ring structure could potentially solve this problem. It is assumed that there is an optimum for the bending radius and the material properties of the ring structure to achieve the maximum mechanical performance of the connection.

The gap between the CFRP-layers from the two winding steps occurs because the rovings deposited in the second step lie on top of the bent strut ends. A possible solution could be to only partially cure the inner laminate and to perform the second winding step under inner pressure. This could reduce or even eliminate the gap. Another approach to achieving a good connection between the layers could be the use of adhesives. For the further development of the manufacturing concept, it is crucial to optimize the anchoring point of the strut to the vessel wall. Therefore, a test method for the mechanical characterization of the connection is of great importance.

5. Conclusion and Outlook

This paper presents a manufacturing concept for a conformable pressure vessel with inner tension struts for the possible integration in the underbody of a vehicle for hydrogen storage. The process involves positioning endless-fiber-reinforced struts with thermoplastic matrix material in a winding core. A CFRP-laminate is generated using filament winding, with the struts piercing through the deposited rovings, so that the strut ends protrude beyond the outer surface of the laminate. In a further step, the struts are bent using heat to plasticize the thermoplastic matrix. Further CFRP layers are wound over the bent ends of the struts to anchor them between two layers of the laminate. A process demonstrator was built to test the feasibility of the concept. The investigation of the demonstrator shows the potential and also reveals some critical aspects where further optimization is needed. The focus of future research in this project will be on the optimization of the connection between the tension struts and the vessel wall. Both, simulative and experimental approaches will be pursued for this purpose. For the mechanical characterization of the interface between the bent strut end and the vessel wall, a setup for a tensile testing machine developed for the specific use case is considered. This allows the qualitative validation of simulative results, and thus, an optimization of the overall system.

Acknowledgements

This research work was performed within the COMET-module “Polymers4Hydrogen” (I.D. 21647053) in the framework of the COMET-program of the Austrian Federal Ministry for Climate, Action, Environment, Energy, Mobility, Innovation and Technology and the Austrian Federal Ministry for Digital and Economic Affairs. The authors thank the involved partners Polymer Competence Center Leoben GmbH (PCCL, Austria), Montanuniversitaet Leoben (Department Polymer Engineering and Science, Chair of Chemistry of Polymeric Materials, Chair of Materials Science and Testing of Polymers), Tampere University (Department of Engineering Material Science), Peak Technology and Faurecia for their contributions to this research work.

  doi:10.5075/epfl-298799_978-2-9701614-0-0

6. References

1. D. Candelaresi, A. Valente, D. Iribarren, J. Dufour, and G. Spazzafumo, International Journal of Hydrogen Energy **46**, 72 (2021).
2. Hydrogen Council, *Roadmap towards zero emissions: The complementary role of BEVs and FCEVs* (2021).
3. G. Schuh, L. Schenk, and P. Scholz, MTZ Worldw **83**, 2-3 (2022).
4. A. Wanitschke and S. Hoffmann, Environmental Innovation and Societal Transitions **35** (2020).
5. M. Henning, A. Smyth, and A. Thomas, *An Analysis of the Association between Changes in Ambient Temperature, Fuel Economy, and Vehicle Range for Battery Electric and Fuel Cell Electric Buses* (2019).
6. M. Baumann, T. Domnik, M. Haase, C. Wulf, P. Emmerich, C. Rösch, P. Zapp, T. Naegler, and M. Weil, Technological Forecasting and Social Change **165** (2021).
7. E. Rivard, M. Trudeau, and K. Zaghib, Materials **12**, 12 (2019).
8. G. Anandarajah, W. McDowall, and P. Ekins, International Journal of Hydrogen Energy **38**, 8 (2013).
9. D. Apostolou and S. N. Welcher, International Journal of Hydrogen Energy **46**, 9 (2021).
10. A. G. Olabi, T. Wilberforce, and M. A. Abdelkareem, Energy **214** (2021).
11. M. Klell, H. Eichlseder, and A. Trattner, *ATZ/MTZ-Fachbuch*: *Wasserstoff in der Fahrzeugtechnik: Erzeugung, Speicherung, Anwendung* (Springer Vieweg, Wiesbaden, 2018) [ger].
12. M. Ruf, H.-U. Stahl, K. Kunze, S. Zaremba, A. Horoschenkoff, T. von Unwerth, and K. Drechsler, in *PROCEEDINGS OF THE MUNICH SYMPOSIUM ON LIGHTWEIGHT DESIGN 2020/ TAGUNGSBAND*, Ed. by S. Pfingstl, A. Horoschenkoff, P. Höfer, and M. Zimmermann, 74–85 (MORGAN KAUFMANN, [S.l.], 2021).
13. K. A. Öztas, K. Kunze, K. Jois, J. Sackmann, S. Zaremba, and M. G. Ruf, International Journal of Hydrogen Energy (2021).
14. Norbert Schramm, Mario D. Naumann, Lars Ulke-Winter, Sebastian Nendel, Marcel Meyer, Lothar Kroll, in *22nd International Conference on Composite Materials* (2019).
15. M. Nebe, *Springer eBook Collection*: *In Situ Characterization Methodology for the Design and Analysis of Composite Pressure Vessels* (Springer Fachmedien Wiesbaden; Imprint Springer Vieweg, Wiesbaden, 2022) [eng].
16. O. Bethoux, Energies **13**, 21 (2020).
17. S. M. Aceves, G. D. Berry, A. H. Weisberg, F. Espinosa-Loza, and S. A. Perfect, in *16th World Hydrogen Energy Conference*, Ed. by International Association for Hydrogen Energy (2006).
18. A. Hupfeld, *Verfahren zum Ausbilden von Verbindungen aus einer Verstärkungsfaser oder Verstärkungsfasern und Verfahren zum Herstellen eines Druckbehälters: Internationales Ver0ffentlichung* (2020), WO 2021/239565 A1.
19. P. A. Rosen, in *AutoUni - Schriftenreihe*, Band 113: *Beitrag zur Optimierung von Wasserstoffdruckbehältern*, Ed. by P. A. Rosen, 49–88 (Springer Fachmedien Wiesbaden, Wiesbaden, 2018).
20. O. Alkan, *Druckbehälter zur Speicherung von fluiden Medien, insbesondere zum Einbau in ein Fahrzeug* (2011), DE102009057170A1.
21. I. Tapeinos, *Multi-Spherical Composite-Overwrapped Cryogenic Fuel Tanks for Hypersonic Aircrafts* (2019).

  doi:10.5075/epfl-298799_978-2-9701614-0-0

22. N. L. Newhouse, *Conformable composite pressure vessel* (Google Patents, 2019), US10465848B1.
23. L. Farines, F. Thiebaud, D. Perreux, in *ECCM15-15th European conference on composite materials* (University. Department of Management and Engineering, Padova, 2012).
24. K. A. Öztas, R. A.J. Weerts, and M. G. Ruf, International Journal of Pressure Vessels and Piping **192** (2021).
25. A. Horoschenkoff, M. Huber, and A. Hupfeld, in *Proceedings of the Munich Symposium on Lightweight Design 2020*, Ed. by S. Pfingstl, A. Horoschenkoff, P. Höfer, and M. Zimmermann, 86–89 (Springer Berlin Heidelberg, Berlin, Heidelberg, 2021).
26. R. N. Grugel, Kaukler, W.F.,Paley, M.S., C. R. Henry, C. T. Canaday, W. C. Hastings, and E. Rabenberg, *National Space & Missile Materials Symposium 2014*: *Development of ionic liquid based epoxies for carbon fiber composite cryogenic tanks* (Huntsville, AL, 2014).
27. F. Wanghofer, A. Wolfberger, M. Wolfahrt, and S. Schlögl, *Polymers*, Vol. 13: *Cross-Linking and Evaluation of the Thermo-Mechanical Behavior of Epoxy Based Poly(ionic Liquid) Thermosets* (2021).
28. K. Mallick, J. Cronin, P. Fabian, and M. Tupper, in *Ceramic transactions*, Vol. 224: *Materials challenges in alternative and renewable energy*: *A collection of papers presented at the Materials Challenges in Alternative and Renewable Energy Conference February 21-24, 2010, Cocoa Beach, Florida*, Ed. by G. G. Wicks, 91–98 (American Ceramic Society, Hoboken, NJ, Westerville, Ohio, 2011).
29. Bayerische Motoren Werke, *Abschlussbericht MAI Skelett für alle Projektpartner : Berichtszeitraum: 01.02.2014-30.06.2015* (BMW AG, München, 2015) [de].

  doi:10.5075/epfl-298799_978-2-9701614-0-0

THERMAL ENERGY STORAGE WITH POLYMER COMPOSITES: TAILORING THE SURFACE PROPERTIES OF PHASE CHANGE MICROCAPSULES WITH POLYDOPAMINE

Giulia Fredi[a], Cordelia Zimmerer[b], Christina Scheffler[b], and Alessandro Pegoretti[a]

[a] University of Trento, Department of Industrial Engineering and INSTM Research Unit, Via Sommarive 9, 38123 Trento, Italy - giulia.fredi@unitn.it
[b] Leibniz-Institut für Polymerforschung, Hohe Str. 6, D01069 Dresden, Germany

Abstract: *This work reports on flexible epoxy (EP) composites containing neat and polydopamine(PDA)-coated paraffin microcapsules (MC) as a phase change material (PCM), with a PCM content of up to 40 wt%. The surface of PDA-coated capsules (MC-PDA) is rougher and has a higher interfacial interaction with the surrounding epoxy matrix compared to neat MC. PDA deposition parameters have been successfully tuned to obtain a thin (53 ± 8 nm) PDA layer, and the total PDA mass in MC-PDA is as low as 2.2 wt%. Therefore, the phase change enthalpy of MC-PDA is only slightly lower than that of neat MC. DSC tests show that the phase change enthalpy of the composites increases with the capsule content (up to 87.8 J/g) and the PDA modification does not significantly affect the resulting TES performance. All mechanical properties increase with the PCM content, in terms of elastic modulus (up to +195 %), tensile strength (up to +42 %), Shore D hardness (up to +36 %), and creep compliance (down to –54 % at 60 min). These effects are more evident for composites containing MC-PDA due to enhanced interfacial adhesion.*

Keywords: polydopamine; paraffin microcapsules; thermal management; flexible epoxy; thermal properties.

1. Introduction

Phase change materials (PCMs) are attracting increasing attention for thermal energy storage (TES) and thermal management applications thanks to their ability to store and release a large amount of thermal energy [1, 2]. The most common PCM working in the temperature range 0-100 °C are organic solid-liquid PCMs such as paraffin waxes, as they feature large latent heat of phase transition, narrow phase change temperature interval, congruent melting, negligible supercooling, and low cost [2]. Their need to be confined to avoid leakage above the melting temperature is generally addressed via micro/nano-encapsulation [3, 4].

Thanks to their narrow working temperature range, organic PCMs are widely used for thermal management applications aimed at maintaining temperature in a well-defined range or below a certain threshold. For example, they can be used to prevent overheating of electronic components [5, 6], which is becoming a very difficult task given their increasing miniaturization, power, and integration [7, 8]. Hence, PCMs are an appealing alternative to bulky equipment such as natural or forced convection systems [9]. To effectively manage not only the temperature but also the weight and volume of the component, it can be beneficial to embed the PCM in an existing part of the electronic device (e.g., the case, the structural components, or the supports).

  doi:10.5075/epfl-298799_978-2-9701614-0-0

In this perspective, polymeric materials are widely used in electronics to build packaging, substrates, boards, sealing materials, but also crucial components such as thermal interface materials (TIM), due to their lightness, flexibility, easy processing, excellent chemical stability, and durability [8]. To improve their heat dissipation properties, other than increasing their thermal conductivity with conductive nanofillers, a way could be [7, 8] to add PCMs, so to increase the total absorbed heat and avoid excessive temperature rise.

Most of the commercial PCM microcapsules have a melamine-urea-formaldehyde (MUF) or melamine-formaldehyde (MF) shell. Previous research [10] highlighted a non-optimal adhesion between MF microcapsules and polymers such as epoxy resins, acrylic resins, and polyamides, due to the lack of reactive sites on a fully cured MF surface. This is an issue that must be addressed to obtain composites with satisfactory mechanical properties. A possible solution is represented by the deposition of polydopamine (PDA), a bioinspired polymer able to adhere to a wide variety of substrates [11]. PDA, produced by the oxidative self-polymerization of dopamine, can be deposited as continuous films exposing a noticeable variety of reactive functional groups, thus considerably increasing the surface activity of the substrate.

This work aims at producing and characterizing flexible epoxy composites containing different amounts of neat and PDA-modified PCM microcapsules. Taking off from the results of our previous work [12], the PDA deposition parameters have been tuned to obtain a thinner PDA layer. The produced composites, containing up to 40 wt% of neat and modified microcapsules, have been characterized microstructurally, thermally, and mechanically.

2. Materials and methods

2.1 Materials and sample preparation

Microencapsulated PCM Microtek MPCM43D (MC) was purchased from Microtek Laboratories (Dayton, OH, USA). Bi-component epoxy system Elan-tech® EC251/W242 NF was kindly provided by Elantas Europe S.r.l. (Collecchio, Italy). Dopamine hydrochloride (DH) and amino-2-(hydroxymethyl)propane-1,3-diol (TRIS buffer, Trizma®) were purchased by Sigma-Aldrich (Steinheim, Germany).

The coating of the microcapsules with PDA was carried out in a similar way to what is reported in a previous paper of our group [12, 13]. To prepare epoxy/PCM composites, the epoxy base and hardener were poured into a glass beaker in a weight ratio of 100:40. Neat or PDA-coated microcapsules were added to the beaker in different weight fractions. The mixture was stirred, degassed, cast in silicone molds, and cured for 24 hours at room temperature and 15 hours at 60 °C. Samples are labeled as EP (neat epoxy), EP-MCx for epoxy/neat MC composites, and EP-MCx-PDA for epoxy/MC-PDA composites, where x represents the weight percentage of PCM and is equal to 20, 30, or 40 wt%.

2.3 Characterization

Scanning electron microscopy (SEM) micrographs of the PDA-modified microcapsules and the tensile fracture surfaces of the composites were acquired with an FE-SEM Zeiss Supra 40 after Pt-Pd sputtering. Differential scanning calorimetry (DSC) was performed on neat and PDA-coated microcapsules and the cured composites with a Mettler DSC 30 calorimeter at 10 °C/min, in the temperature interval -30/80 °C, under an N_2 flow of 100 ml/min, with a heating-cooling-

  doi:10.5075/epfl-298799_978-2-9701614-0-0

heating cycle. The test allowed measuring the glass transition temperature (T_g) of epoxy and the melting/crystallization temperatures (T_m, T_c) and enthalpies (ΔH_m, ΔH_c) of the PCM. Quasi-static tensile tests were performed at room temperature with the universal electromechanical dynamometer Instron 5969 on as-cast specimens with ISO 527-2-1BA geometry. For each composition, four specimens were tested at a crosshead speed of 0.25 mm/min with a resistance extensometer Instron 2620 (gauge length of 12.5 mm), and the elastic modulus (E) was measured as the secant modulus on the stress-strain curve between strain values of 0.05 % and 0.25 %. Four additional specimens were tested at 10 mm/min to determine the stress and strain at break (σ_b, ε_b). The stress at break was always coinciding with the maximum stress and was thus regarded as the ultimate tensile strength (UTS). Shore D hardness was measured according to ASTM D2240 with a Hildebrand Durometer Operating Stand Model OS-2. Ten measurements were acquired per sample.

3. Results and discussion

3.1 Microstructural and thermal properties

Figure 1 shows SEM micrographs of neat and PDA-coated microcapsules. Neat microcapsules appear spherical and with a smooth surface, while the surface of MC-PDA is rougher and with a globular appearance. A similar surface state has already been observed in our previous work [12], but the deposition parameters applied here (i.e., lower DH concentration and reaction time) resulted in a more homogeneous and less rough PDA coating. Since the main adhesion mechanism between PDA and epoxy has been identified in the chemical reaction between the complex surface chemistry of the PDA layer and the epoxy's oxirane groups with the formation of covalent bonds, the decrease in the surface roughness should not constitute a considerable problem, as this adhesion mechanism is expected also with a thinner and smoother PDA layer.

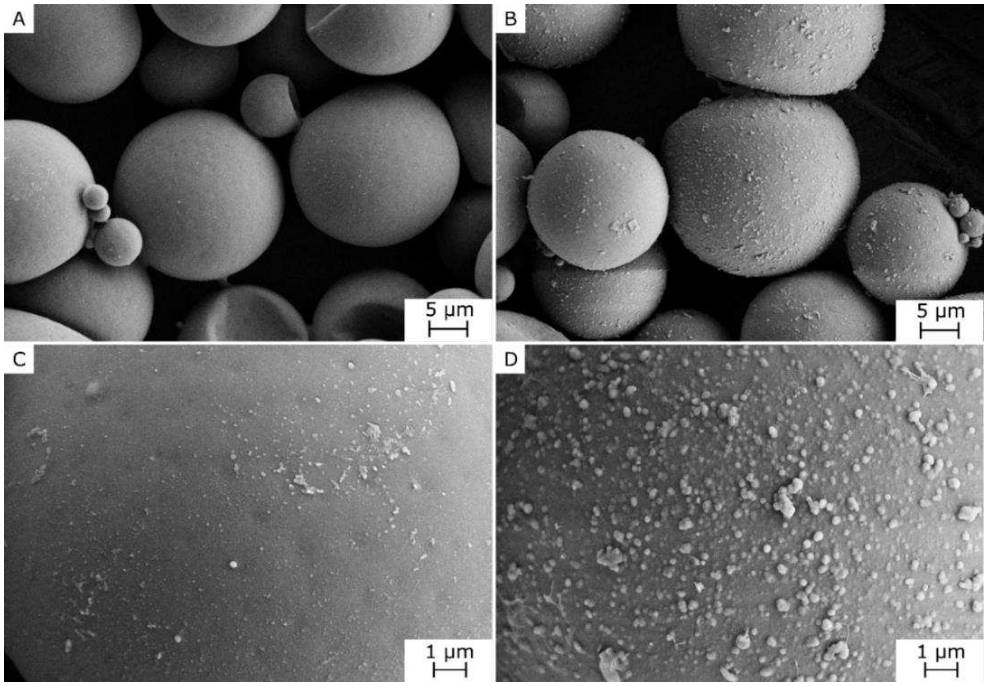

Figure 1. *SEM micrographs of neat (a, c) and PDA-coated (b, d) microcapsules [13]*

Figure 2 shows SEM micrographs of the tensile fracture surface of the composites with a capsule weight fraction of 10 wt%. Most of the microcapsules are broken, indicating that the fracture propagates across the microcapsules and not at the capsule-matrix interface. The microcapsules are homogeneously distributed in the matrix, which suggests that this filler can be well dispersed in this epoxy matrix both with and without PDA coating. As will be illustrated with tensile tests results, the fracture occurs at large deformations (from 20 % to 55 %), but the fracture surface does not show signs of plasticization. These large ε_b values are accompanied by evident microcapsule fracture and debonding, for both the neat and PDA-coated capsules (Figure 2(c-f)). However, the interfacial gap is generally smaller for composites with MC-PDA, which indicates a greater interphase strength, associated with generally higher values of ε_b. From micrographs at higher magnification (Figure 2(g-h)), the PDA coating thickness was estimated as 53 ± 8 nm. Assuming a PDA density of 1.52 g/cm^3 [14] and spherical microcapsules with a mean diameter of 20 µm and density of 0.9 g/cm^3 (from the producer's datasheet), the mass fraction of PDA in PDA-coated capsules can be estimated to be 2.6 ± 0.4 wt %.

Figure 3(a-b) shows the DSC thermograms (first heating scan) of neat and PDA-coated microcapsules and prepared composites, while Table 1 summarizes the main DSC results. The shaded region corresponds to a temperature interval reported with a magnified scale, added to highlight the glass transition of the epoxy resin at approx. 10 °C. Table 1 shows that the glass transition temperature (T_g) is not remarkably affected either by the PCM content or by the PDA modification.

Both PCMs, i.e., MC and MC-PDA, show an endothermic melting peak at approx. 45 °C and the corresponding exothermic peak of the crystallization transition in the cooling scan (not reported) at approx. 29 °C. The DSC thermogram of MC-PDA is similar to that of MC, and the phase change enthalpy of MC-PDA is (97.8 ± 0.7)% of that of MC (calculated on ΔH_m, ΔH_c, and ΔH_{m_2}, Table 1). Assumed that the phase change enthalpy is proportional to the content of microcapsules (more specifically, to the content of core), this percentage also represents the total MC mass in the MC-PDA sample, and therefore the total PDA mass in the MC-PDA sample is approx. 2.2 wt%, in good agreement with SEM results. Therefore, the enthalpy of the EP-MCx-PDA composites is also only slightly lower than that of the EP-MCx composites (Table 1). Moreover, all composites exhibit the same endo/exothermic peaks of PCM phase transition, which are found in approx. the same temperature range.

To assess if the phase change enthalpy of the composites is close to the theoretical one, a relative melting enthalpy (ΔH_m^{rel}) was calculated through Equation (1), as

$$\Delta H_m^{rel} = \frac{\Delta H_m}{\omega_{PCM} \cdot \Delta H_m^{PCM}} \cdot 100, \qquad \textbf{(1)}$$

where ΔH_m is the melting enthalpy of the composites, ω_{PCM} is the nominal weight fraction of MC or MC-PDA, and ΔH_m^{PCM} is the melting enthalpy of MC or MC-PDA. Since the relative enthalpy values (Table 1) are close to 100 %, the PCM weight fraction in the composites after processing is close to the nominal (initial) fraction. On average, the relative enthalpy of the composites containing neat MC is (99.2 ± 2.9) %, not significantly different from that of the composites loaded with MC-PDA ((98.4 ± 1.3) %). This confirms that the PDA-coated microcapsules are not damaged by the production process of these composites, exactly as the neat microcapsules.

  doi:10.5075/epfl-298799_978-2-9701614-0-0

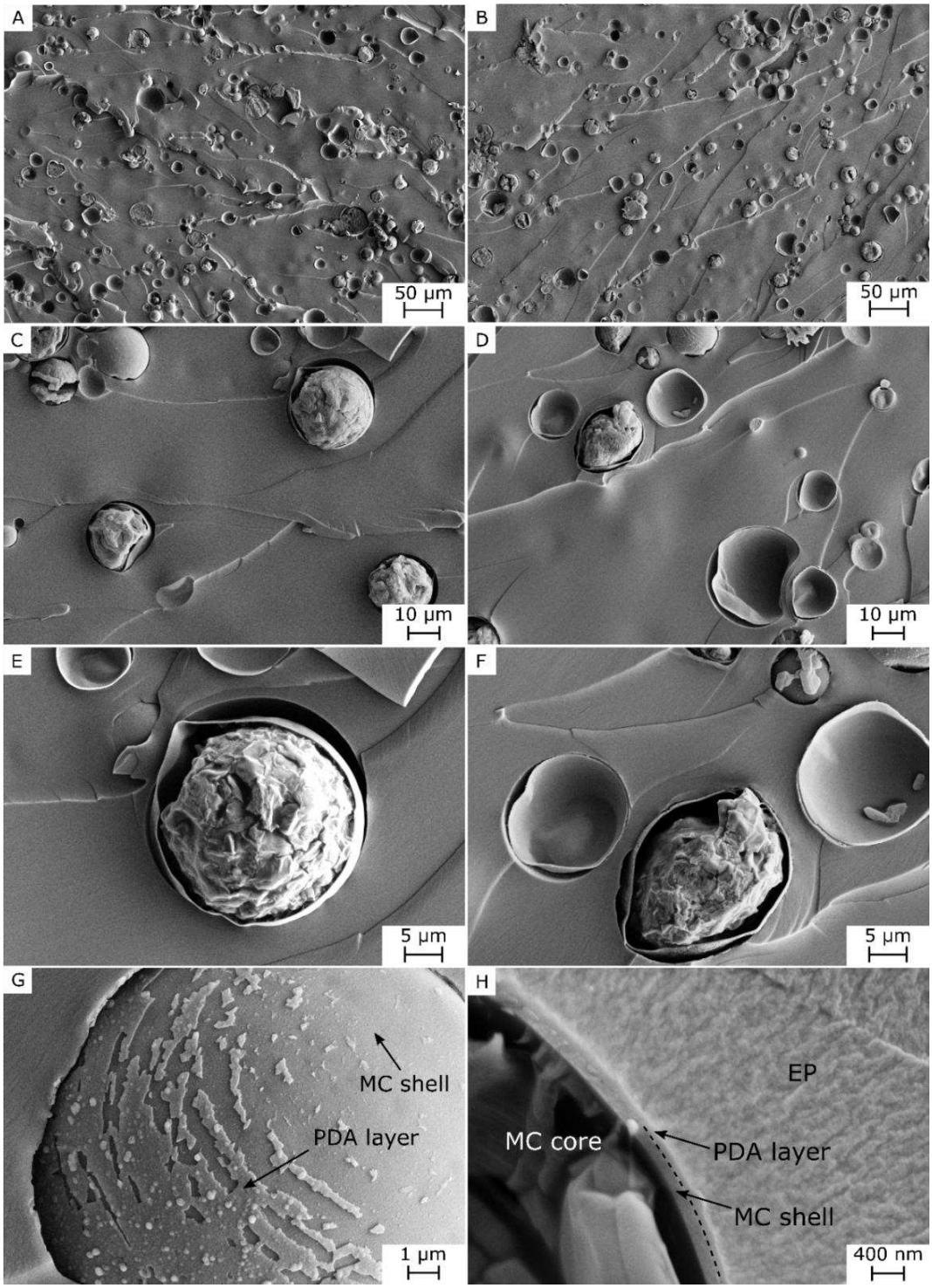

Figure 2. *SEM micrographs of the tensile fracture surface of the prepared composites. (a, c, e) EP-MC10; (b, d, f, g, h) EP-MC10-PDA [13].*

3.3 Mechanical properties

Figure 4(a-b) shows representative tensile stress-strain curves and the main results of tensile and hardness tests. The stress-strain curve of EP and PCM-containing composites exhibits an initial steep region followed by a slope change at a strain of approx. 5 % and the second part of the curve is less steep and nearly linear until fracture. The fracture occurs at large deformation values (20 %-55 %). The introduction of microcapsules increases the stiffness and strength (E

  doi:10.5075/epfl-298799_978-2-9701614-0-0

and UTS) of the composites and impairs their ductility (ε_b). Considering the same PCM fraction, the composites containing PDA-coated capsules show higher elastic modulus and stress and strain at break compared to the composites with uncoated capsules. The same trend can be observed for the Shore D hardness value. Hence, the PDA coating positively contributes to the stiffness of the composites and helps to retain the pristine deformability, and this likely stems from an increased interfacial adhesion.

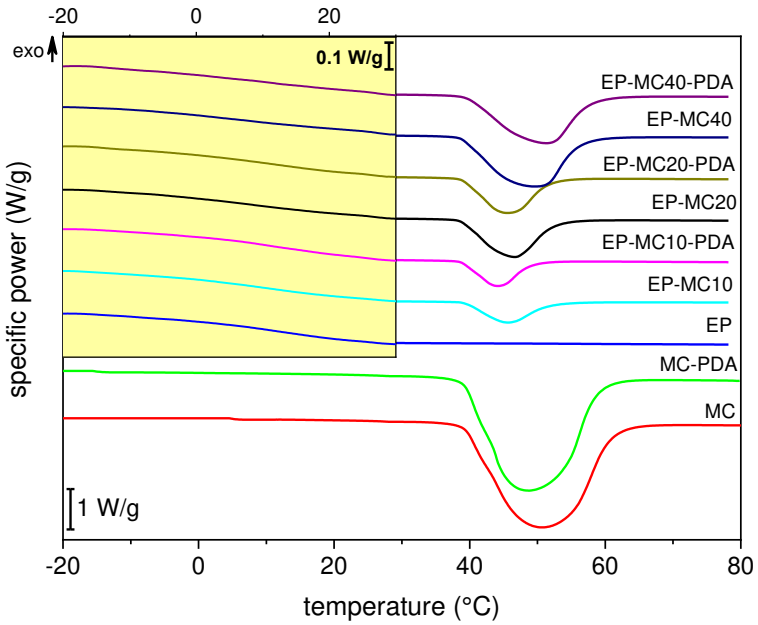

Figure 3. *Results of DSC tests on neat and PDA-coated microcapsules and prepared composites. First heating scan. The shaded box reports the thermograms with a magnified y-scale to highlight the glass transition of the EP matrix [13].*

Table 1. *Main results of DSC tests on the neat and PDA-coated microcapsules and the prepared composites [13].*

Sample	T_{g_1} (°C)	T_{m_1} (°C)	ΔH_{m_1} (J/g)	ΔH_m^{rel} (%)	T_c (°C)	ΔH_c (J/g)	T_{g_2} (°C)	T_{m_2} (°C)	ΔH_{m_2} (J/g)
MC	-	44.7	227.7	100	29.0	224.2	-	44.4	226.1
MC-PDA	-	45.7	221.1	100	29.3	220.8	-	45.5	220.9
EP	11.1	-	-	-	-	-	9.3	-	-
EP-MC10	11.3	44.0	22.6	99.2	32.8	22.9	7.8	44.0	23.4
EP-MC10-PDA	10.7	43.1	21.8	98.6	32.9	21.7	8.8	43.1	21.7
EP-MC20	7.5	44.6	46.6	102.2	32.6	46.5	8.2	44.5	46.1
EP-MC20-PDA	11.1	44.2	44.0	99.6	31.8	43.8	9.9	44.0	43.8
EP-MC40	8.6	47.0	87.8	96.4	28.9	88.8	9.1	46.5	87.3
EP-MC40-PDA	10.7	49.6	85.8	97.1	26.6	85.4	9.9	49.5	85.6

T_{g_1}= glass transition temperature (first heating scan); T_{m_1}= melting temperature (first heating scan); ΔH_{m_1} = melting enthalpy (first heating scan); ΔH_m^{rel} = relative melting enthalpy, compared to the enthalpy of MC or MC-PDA; T_c= crystallization temperature; ΔH_c = crystallization enthalpy; T_{g_2}= glass transition temperature (second heating scan); T_{m_2}= melting temperature (second heating scan); ΔH_{m_2} = melting enthalpy (second heating scan).

  doi:10.5075/epfl-298799_978-2-9701614-0-0

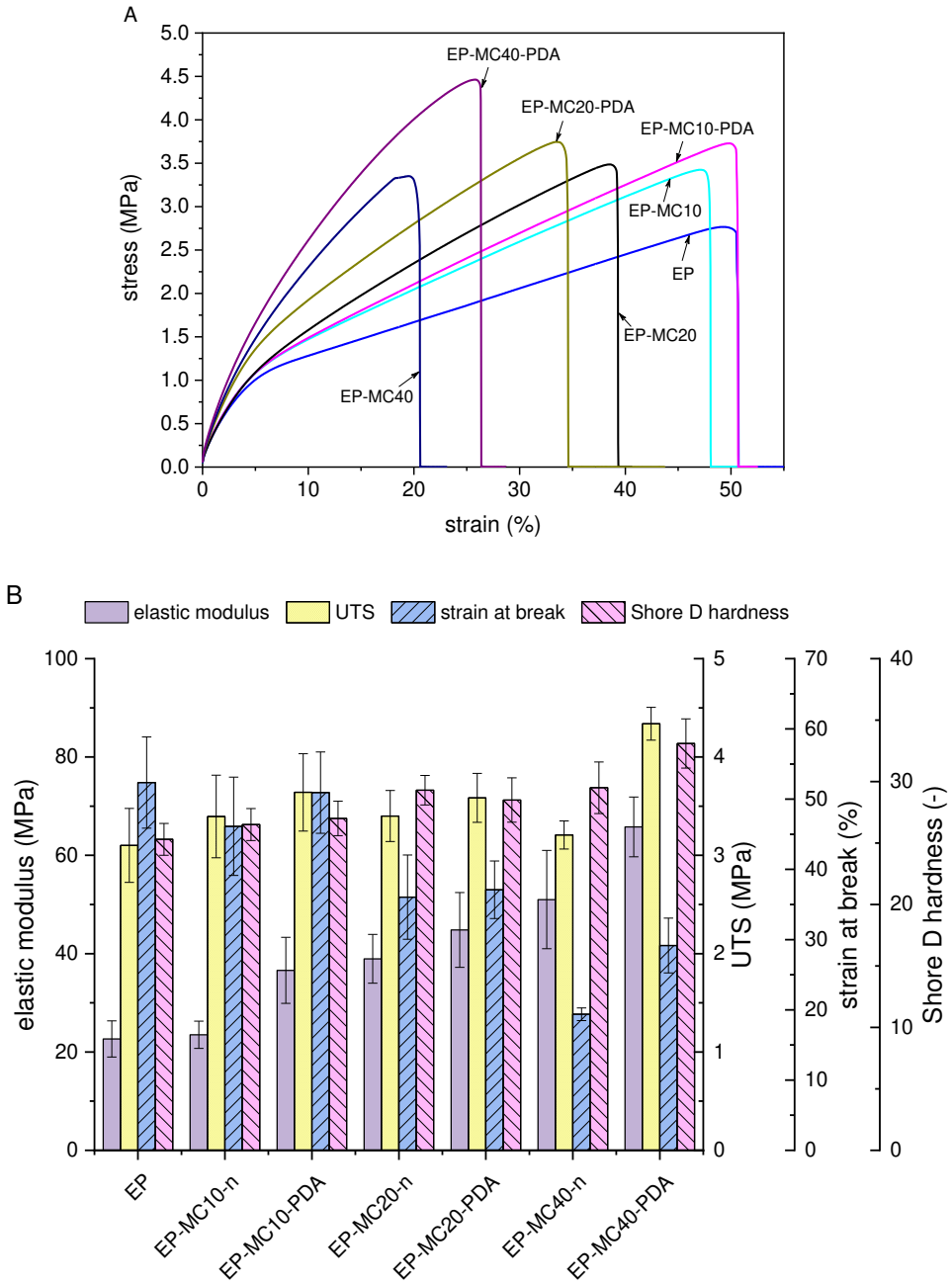

Figure 4. *Results of tensile and Shore D hardness tests on the prepared composites. (a) representative tensile stress-strain curves; (b) elastic modulus, ultimate tensile strength (UTS), strain at break, and Shore D hardness for the prepared composites (mean ± std. dev.).*

4. Conclusions

In this work, a thin polydopamine (PDA) coating on PCM microcapsules was proven effective in increasing the interfacial adhesion with an epoxy matrix, with a consequent increase in the mechanical properties of the final composites, without significantly affecting the total phase change enthalpy. The PDA deposition parameters have been successfully tuned to obtain a thin (53 ± 8 nm) PDA layer with a total PDA mass of only 2.2 wt%. Therefore, the phase change enthalpy of MC-PDA was only slightly lower than that of the neat MC, being 221.1 and 227.7 J/g, respectively. DSC tests also highlighted that the phase change enthalpy increased with the PCM

  doi:10.5075/epfl-298799_978-2-9701614-0-0

content (up to 87.8 J/g for the composite EP-MC40) and that the enthalpy of the composites containing PDA-coated microcapsules was not remarkably lower than that of the EP-MCx composites. The contribution of the PCM was remarkable also for the mechanical properties of the host EP matrix, as they promote an increase in elastic modulus (up to +195 %), tensile strength (up to +42 %), and Shore D hardness (up to +36 %), and this effect was more evident for composites containing PDA-coated microcapsules due to the enhanced interfacial adhesion.

5. References

1. Pielichowska K, Pielichowski K. Phase change materials for thermal energy storage. Progress in materials science. 2014;65:67-123.
2. Fleischer AS. Thermal Energy Storage using Phase Change Materials - Fundamentals and Applications. Kulacki FA, editor. Heidelberg, Germany: Series SpringerBriefs in Thermal Engineering and Applied Science. Springer; 2015.
3. Khadiran T, Hussein MZ, Zainal Z, Rusli R. Encapsulation techniques for organic phase change materials as thermal energy storage medium: A review. Sol Energy Mater Sol Cells. 2015;143:78-98.
4. Fredi G, Dirè S, Callone E, Ceccato R, Mondadori F, Pegoretti A. Docosane-organosilica microcapsules for structural composites with thermal energy storage/release capability. Materials. 2019;12:1286/1-/26.
5. Fok SC, Shen W, Tan FL. Cooling of portable hand-held electronic devices using phase change materials in finned heat sinks. International Journal of Thermal Sciences. 2010;49(1):109-17.
6. Lazrak A, Fourmigué J-F, Robin J-F. An innovative practical battery thermal management system based on phase change materials: Numerical and experimental investigations. Applied Thermal Engineering. 2018;128:20-32.
7. Ji C, Wang Y, Ye Z, Tan L, Mao D, Zhao W, et al. Ice-Templated MXene/Ag-Epoxy Nanocomposites as High-Performance Thermal Management Materials. ACS Appl Mater Interfaces. 2020;12(21):24298-307.
8. Xiao C, Guo Y, Tang Y, Ding J, Zhang X, Zheng K, et al. Epoxy composite with significantly improved thermal conductivity by constructing a vertically aligned three-dimensional network of silicon carbide nanowires/ boron nitride nanosheets. Composites Part B: Engineering. 2020;187:107855.
9. Kandasamy R, Wang X-Q, Mujumdar AS. Application of phase change materials in thermal management of electronics. Applied Thermal Engineering. 2007;27(17-18):2822-32.
10. Dorigato A, Fredi G, Pegoretti A. Application of the thermal energy storage concept to novel epoxy/short carbon fiber composites. Journal of applied polymer science. 2019;136(21):47434/1-/9.
11. Lynge ME, Van Der Westen R, Postmab A, Stadler B. Polydopamine—a nature-inspired polymer coating for biomedical science. Nanoscale. 2011;3:4916-28.
12. Fredi G, Simon F, Sychev D, Melnyk I, Janke A, Scheffler C, et al. Bioinspired Polydopamine Coating as an Adhesion Enhancer Between Paraffin Microcapsules and an Epoxy Matrix. ACS Omega. 2020;5:19639−53.
13. Fredi G, Zimmerer C, Scheffler C, Pegoretti A. Polydopamine-Coated Paraffin Microcapsules as a Multifunctional Filler Enhancing Thermal and Mechanical Performance of a Flexible Epoxy Resin. Journal of Composites Science. 2020;4(4):174.
14. Nishizawa N, Kawamura A, Kohri M, Nakamura Y, Fujii S. Polydopamine particle as a particulate emulsifier. Polymers (Basel). 2016;8(3).

OVERVIEW OF GROUND-BASED TESTING OF COMPONENTS MADE FROM ELECTRICALLY-CONDUCTING DOPED PEEK FOR SPACE APPLICATIONS

Leo Nyman[a], Kirsi Kukko[a], Antti Kestilä[b], Vesa Myllymäki[c], Jarkko Lohilahti[d], Joni Kumpulainen[d], Marko Vehkamäki[e], Mika Salmi[a], Ugo Lafont[f], Esa Kallio[a]

a: Aalto University, FI-00076 Aalto, Finland. Email: leo.nyman@aalto.fi
b: Finnish Meteorological Institute, Finland.
c: Carbodeon Ltd, Finland.
d: Maker3D Ltd, Finland.
e: University of Helsinki, Finland.
f: European Space Research and Technology Centre, Netherlands.

Abstract: *Additive manufacturing (AM) has shown to be a promising method for creating high-performance plastic components. In space, harsh environmental conditions such as vacuum ultraviolet radiation and significant temperature changes cause the degradation of polymers and static electricity buildup on the surface of non-conductive components.*

This study explores geostationary orbit communication-satellite parts additively manufactured using doped polyether ether ketone (PEEK). Several spacecraft parts were selected for detailed redesign and additive manufacturing. These parts are commonly used in communication satellites and belong to secondary structures that need not withstand heavy forces.

The effects of the space environment on the doped PEEK material and its properties were studied in ground-based laboratories. The printed parts were mechanically and functionally tested. Low-mass space-grade components can be made with this method and material combination while conforming with the stiffness requirements for secondary spacecraft structures. This manufacturing method aims to achieve mass savings of 50% compared to metallic baselines.

The analysis showed that that printing parameters used in the fused filament fabrication (FFF) process significantly affect the mechanical performance of the parts. Moreover, the high strength and stiffness of the FFF-printed carbon-fibre doped PEEK brackets was found to make them ideal for joints used in spacecraft honeycomb panel structures, enabling up to 25–50% savings in bracket mass. Overall, the used FFF manufacturing method enables fast, and cost-effective low batch-size production runs.

Keywords: PEEK; Additive manufacturing; thermoplastic composites; spacecraft; material extrusion

1. Introduction

Spacecraft secondary structures must withstand loads that are atypical for terrestrial use cases. One of the most important aspects to consider here is the stiffness of the assemblies that make up the secondary (and primary) structures in a spacecraft. This requirement arises from the vibration-induced acceleration loads during a launch. Most rockets have a vibration-spectrum that favors having as-stiff-as-possible structures to eliminate low resonant frequencies, leading

  doi:10.5075/epfl-298799_978-2-9701614-0-0

to high mechanical loads. By designing high-stiffness structures, their mass can be kept as low as possible – an important aspect when considering the high cost of mass to orbit.

The design of high-stiffness structures from plastics is challenging, but the solution possibly resides in the use of dopants, topology optimization [1] and additive manufacturing [2]. The dopants could also help in solving other major challenges facing the use of plastics in space, such as surface charging and their susceptibility to vacuum ultraviolet (UV) light, radiation, and atomic oxygen. The surface charging issue can be decreased by increasing the electrical conductance of the material. Currently, UV-resistant plastics are common in terrestrial applications and are manufactured using dopants.

Many fields, including the aerospace industry, have shown increased interest in the use of plastics to lower the mass of systems [3, p. 336]. However, the reasons listed above make the use of plastics challenging for space missions. Therefore, a wide array of testing is typically required to certify novel types of plastic components and structures used in spacecraft. If these challenges can be overcome, secondary spacecraft structures three-dimensionally (3D) printed from doped plastics could offer mass savings in the range of 25–50% for some spacecraft components.

Regarding the specific additive manufacturing (AM) method that has viability for the manufacture of plastics designed for harsh space environments, material extrusion is the method used in this work. Specifically, we focus on fused filament fabrication (FFF) since it is a widespread and low-cost process [4,5]. We foresee extensive use of FFF in future for both terrestrial and in-space manufacturing [6]. The apparent benefit of FFF for in-space manufacturing is that it is well suited for use in a microgravity environment, where powder-based and other AM processes require complex devices. The combination of FFF and atomic layer deposition, for instance, was recently studied by the author [7].

Traditionally, complex-shaped brackets and fittings for spacecraft have been machined from a solid block of high-strength metal. Scrap rates can be up to 80–90% [8]. As part of this work, a clean-sheet design based on AM techniques was utilized to manufacture thermoplastic composite 90° corner brackets with minimal scrap rates. Such brackets can be used to attach subsystems to honeycomb panels in spacecraft. In this work, we report on ground-based testing of corner brackets and some other common GEO satellite parts that we consider could be FFF printed from thermoplastic composites, potentially replacing their metallic baselines.

The paper is organized as follow. First, the 'Materials and methods' chapter describes details on the selected part types and manufacturing. Second, the 'Testing' section explains the methods used for the tests conducted during the work. Finally, we present the results and conclusions.

2. Materials and methods

2.1 The space environment and spacecraft interaction

Space is a challenging environment for man-made devices [9,10,11] posing many difficulties also to polymers. The thermal environment in space changes cyclically due to external conditions, such as an eclipse caused by a planetary body or the attitude taken by the spacecraft. Depending on its mission and location, the operating temperature of different parts of a spacecraft can vary drastically. Some instruments might require cold temperatures close to the cosmic background

  doi:10.5075/epfl-298799_978-2-9701614-0-0

radiation. For example, spacecraft closer to the Sun experience a high thermal influx and might heat up considerably. The heat dumping from a hot polymer part can be helped if the part can conduct heat into thermal sinks. The sunlight, particularly vacuum UV, has a significant impact on a polymer part's structural and surface conditions. Light radiation from the Sun or a planetary albedo is the primary way a spacecraft receives heat. Its internal power usage is another primary source of heating.

The electromagnetic environment poses a challenge by electrostatically charging surfaces exposed to the Sun (see, e.g. [12], and references therein). In the case of polymer parts, this charging can potentially lead to electric discharges, resulting in damage or interference with operation of the spacecraft. The non-light radiation environment (alpha and beta radiation) affects more sensitive components, such as electronics.

The radiation-protection capability of polymers differs from metals, and this needs to be considered when selecting materials. The vacuum environment varies significantly depending on the operational orbit of the spacecraft. However, fairly early in the upper atmosphere, low atmospheric pressure can cause material outgassing. The outgassed material deposits on the spacecraft surface can degrade instrument and sensor performance, with higher material temperatures exacerbating the outgassing of materials.

The printed polymer parts will have to withstand mechanical stresses during the spacecraft mission. Irrespective of the use cases of the polymer parts, arguably the most mechanically stressful part of the mission will be the launch. Specifically, engine-induced vibrations and shocks related to stage separation can damage fragile components. The spacecraft's orbit affects the environment it must withstand. For example, in low-Earth orbits, the thin regions of the atmosphere can degrade polymer parts [13].

2.2 Enhancing the electrical conductivity of filament materials

Whilst enhancing the electrical conductivity of thermoplastics used in FFF, great emphasis must be put on not impairing the compound mechanical properties at the same time. An additional prerequisite on compound design is to allow material printability, preferably with further enhanced printing quality. Mono-functionalized nanodiamond additives allow tailoring of the compound thermal and mechanical properties with minimal material additions. Moreover, such carefully designed compositions allow better printability and, generally, higher quality of the printed item.

2.3 3D printing of test articles

A survey of potential applications was undertaken to understand which polymer parts could potentially replace metal parts inside spacecraft. A trade-off was made by dividing spacecraft parts into different application families and evaluating the amount of potential mass savings, their conductive functions, reduced procurement and logistic efforts, customization, and the specific environmental conditions that the part is expected to endure.

The chosen test articles were: 1) An onboard computer (OBC) electronics enclosure, 2) 90° corner brackets, 3) a radio frequency (RF) circuit housing, and 4) an optical sensor enclosure (Fig. 7).

  doi:10.5075/epfl-298799_978-2-9701614-0-0

The chosen OBC electronics housing was a pre-existing antenna-deployment system housing, which included a hardware mechanical-support frame box with four support frames for circuit boards. The size of the housing was 250 x 148 x 194 mm.

The chosen bracket design was a 90° corner bracket (Fig. 1). It was designed as a generic bracket for providing an attachment point to honeycomb panels. The bracket size was 70 x 35 x 35 mm. The brackets were printed using four different print-layer orientations (*flat, tower*, *porous-face-down,* and *porous-face-up*) as shown in Fig. 2, in order to evaluate the effect of the orientation on the strength of the brackets during testing. Two different mesh types were selected, a diamond and a gyroid mesh. A mesh chosen from these two was used to fill the brackets' interior volume, except for the side faces defined as 4 mm thick solid material. The surface with the largest area was not closed solid. Instead, the mesh was left exposed here. M4 screw holes and openings to insert the screws complement the bracket design. The design accommodates button head screws, for example, Wurth® M4 type 0060 004 16.

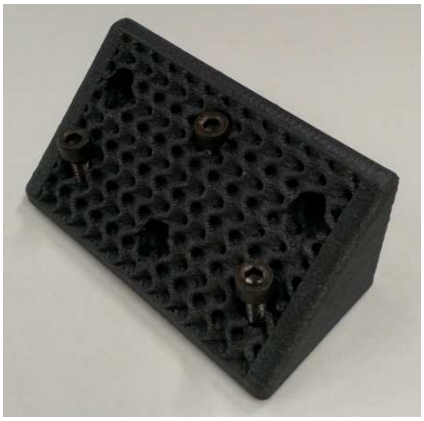

Figure 1. An FFF-printed thermoplastic composite corner bracket. The screw-type was later upgraded to a button-head screw, resulting in better stress distribution within the polymeric material. The bracket features six mounting holes, three for each of the two mounting faces. The additive manufacturing method enables small-batch production of high-stiffness custom-sized and custom-shaped thermoplastic composite brackets.

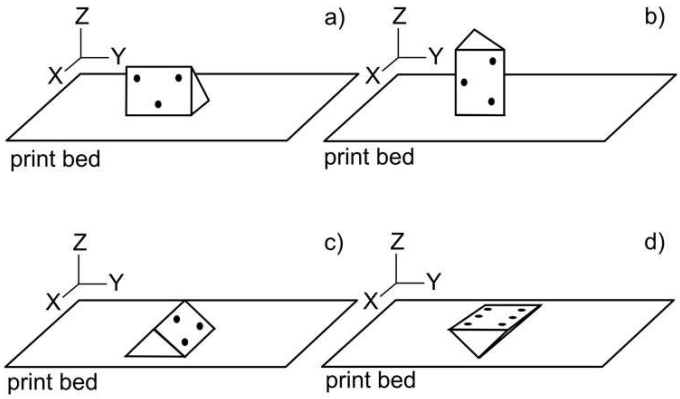

Figure 2. Four possible print-layer orientations for printing the 90° corner brackets used in this work: a) flat, b) tower, c) porous-face-down, and d) porous-face-up.

The chosen radio frequency (RF) circuit housing was a pre-existing RF signal-wire housing. The original housing was machined from aluminium and consisted of two parts, a frame and a lid. The size of the housing was 140 x 67 x 8 mm.

The final test article was an optical sensor enclosure consisting of two parts, a frame, and a dome for an optical sensor. The size of this enclosure was 160 x 165 x 105 mm.

3. Testing

A review of the critical test suite used to qualify space-grade components was conducted at the beginning of the research. Due to the requirements set by the space environment and targeted research outcomes, the following tests were shortlisted: 1) Basic material properties (e.g., tensile strength, Poisson's ratio, density, etc.), 2) thermal cycling, 3) thermal vacuum outgassing, 4) effects of vacuum UV light, 5) vibration test, and 6) manufacturing quality assurance. The following sections contain details of these tests.

3.1 Basic material properties

To enable computer-based loads analysis and finite-element models (FEMs), the basic properties of the material in question need to be investigated when dealing with new materials. In our research, adding dopants into polyether ether ketone (PEEK) necessarily creates a new material with unknown properties. Depending on the level of detail required for the computer-based models, some, or all the properties of the material under study need to be determined. These are well understood at present, and only a few test setups that might be of interest are explained next.

The tensile strength and Poisson's ratio of the new material are derived using a temperature-controlled chamber with a provision to run a tensile load test while an FFF-printed test article is inside the chamber (Fig. 3). The use of liquid nitrogen and heaters allow testing in a temperature range wide enough to qualify components for use in spacecraft.

Figure 3. The chamber used for tensile testing in low and high temperatures at 1 atm.

  doi:10.5075/epfl-298799_978-2-9701614-0-0

For the test of electrical surface conductivity, a special test stand was built (Fig. 4). This stand accepts test articles with the geometry defined by the ISO 527 type 1b standard. The stand has four electrical connections and is built from polycarbonate and Teflon, enabling the use of the stand inside the thermal-vacuum chamber and in 1 atm. The electrical connectors are wired into a Keithley 2701 data acquisition unit which measures the surface conductivity of the test article using the 4-wire resistance measurement method. The unit enables logging of the resistance at set time intervals, allowing the study of how the conductivity changes as a function of ambient pressure and temperature.

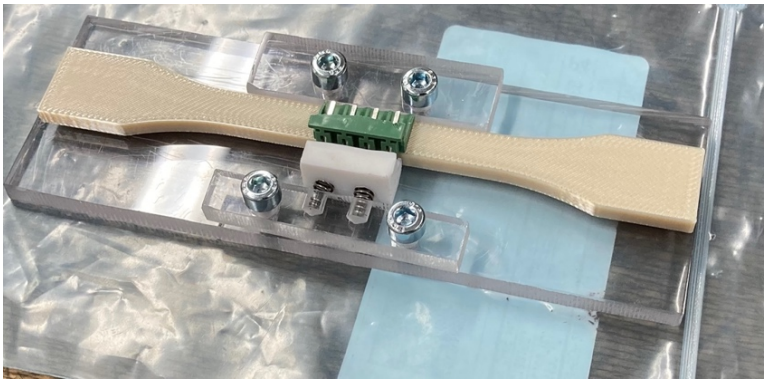

Figure 4. The test stand for performing the 4-wire resistance measurement.

3.2 Thermal cycling

Spacecraft in Earth orbits commonly move in and out of shadow, causing temperature changes due to uneven heating by the Sun. These changes are often cyclical and can be simulated in ground-based testing using environmental chambers (Fig. 5). The thermal cycling test should be conducted in a vacuum for obvious reasons. However, there is always uncertainty regarding the contamination risk of supposedly 'clean' vacuum chambers used for space hardware testing when testing new materials. To manage this risk, the testing was phased so that the new material was first evaluated in the thermal vacuum outgassing test, followed by a thermal cycling test at 1 atm. Based on the analysis of these two tests, the new material under study can be considered safe (or not) for thermal cycling in the vacuum test that follows.

Figure 5. The Espec® chamber for temperature cycling in 1 atm. (left picture), and electrical and data connectors available inside the Aalto Spacelab's thermal vacuum chamber (right picture).

  doi:10.5075/epfl-298799_978-2-9701614-0-0

3.3 Thermal vacuum outgassing

Many materials are unsuitable for use in spacecraft for various reasons, one such reason being the excessive outgassing of volatile material that evacuates the part under vacuum conditions. This outgassing can be further accelerated by heat, commonly generated by the Sun and spacecraft equipment. The reliability of outgassing testing has been questioned in the past. However, processes and instrumentation have improved noticeably in this area. The micro-VCM facility in ESTEC was selected for testing the outgassing behavior of the new material under study.

3.4 Effects of vacuum UV light

Commercial service providers are plentiful for testing materials exposed to UV-A and UV-B light. This is not the case however with regard to the UV-C band due to the requirement of testing in a vacuum [14]. For example, it has been reported that far-ultraviolet (122–200 nm) exposure is a necessary test for assessing the in-space performance of polymer materials [15]. The term "vacuum UV" (VUV) is used extensively in this type of UV testing.

VUV testing of new materials has an inherent risk of contamination. For this reason, a custom-built vacuum chamber (Fig. 6) was selected and modified to incorporate a deuterium lamp. This lamp produces photons in all UV bands and in the visible spectrum, with the peak of the spectrum residing in the UV-C band.

The fact that practically all the UV-C radiation emitted by the Sun is absorbed by the stratospheric ozone allows us to determine the required vacuum level for this test. The atmospheric pressure at 70 km altitude is approximately 5e-2 mb = 5 Pa [16, p. 422], and this was the upper-pressure limit imposed on the vacuum chamber. A typical turbomolecular pump can easily attain this vacuum level. Considering the UV-C attenuation, the amount of air molecules that absorb UV-C still present in the chamber is negligible. The exposure time calculation is based on the acceleration factors (if any) and the requirements set by the space mission in question.

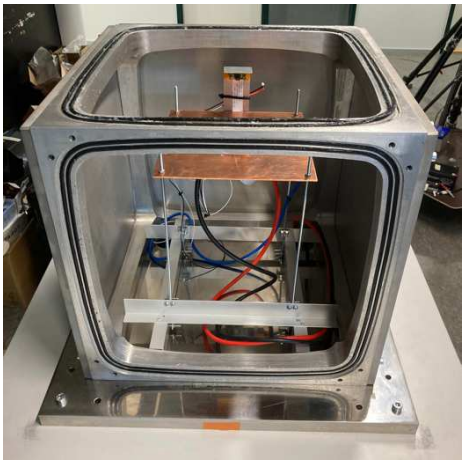

Figure 6. The custom-built "Terrella Cubica" vacuum chamber with one side and the top steel plate removed. The top plate features an opening and a flange for a deuterium lamp. The temperature of samples can be increased by using the resistor-heater attached to the sample holder (copper plate). A camera is installed inside the chamber for monitoring the samples during test runs.

  doi:10.5075/epfl-298799_978-2-9701614-0-0

3.5 Vibration test

The vibration test, also known as the electrodynamic shaker test, seems like a simple verification test. However, this test provides valuable data for the engineers when adequately designed. The natural frequency of parts and assemblies is commonly derived using FEM. The vibration test shows how accurate the FEM is in practice. However, the natural frequencies may differ significantly between the FEM and the actual test. In that case, hardware redesign might be needed to ensure that the natural frequencies of parts and assemblies remain above safe limits during a launch.

Typical vibration tests also include several gentle “sweeps” that produce signature output signals, recorded and later used in the analysis. Any internal damage to the part caused by the high-energy shaking (used to verify the tri-axial launch loads with margins) can be challenging to notice. Conveniently, the signature output measured at the end of the test can be used to detect such failures easily.

Finally, a low-frequency vibration test can be used to create quasi-static loads, enabling a compliance check against static load requirements. The benefit of this approach is that a separate static-load test stand is often not needed. For example, *Ariane 5* load limits are as follows: lateral +/- 2.0 g, axial +4.5 g [17] while in *SpaceX Falcon 9* the values are lateral +/- 2.0 g, axial +6.0 g [18]. The European Cooperation for Space Standardization (ECSS) ECSS-E-ST-32-10C standard defines a factor of 1.25 for the qualification testing of satellite components [19].

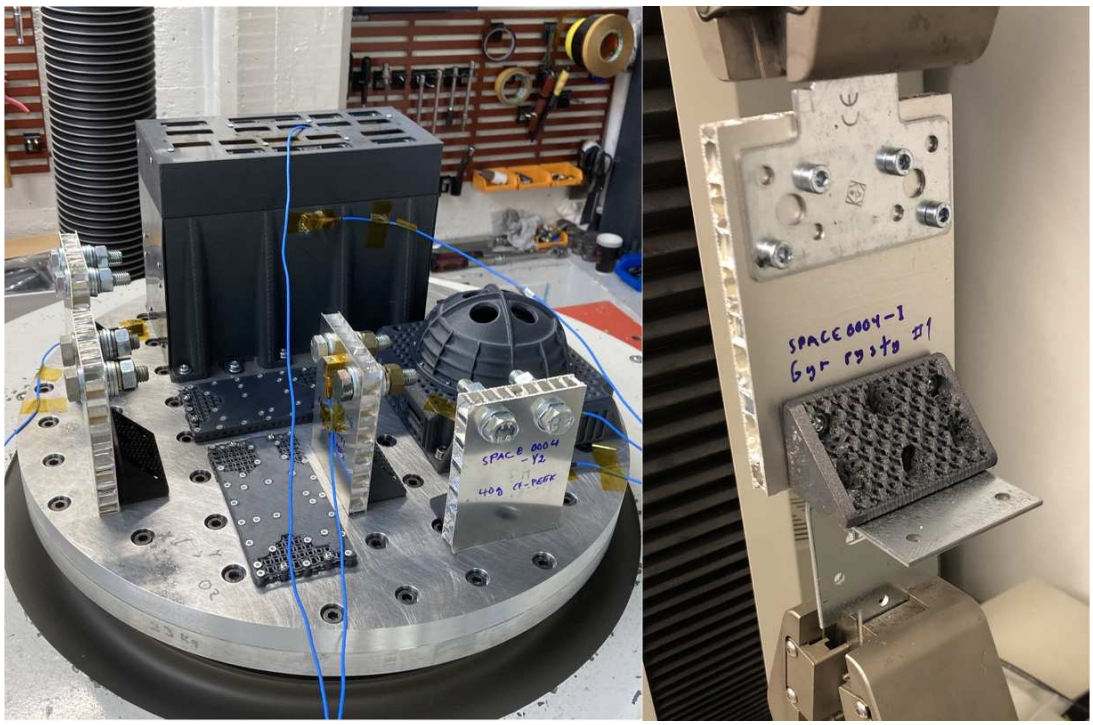

Figure 7. Electrodynamic shaker testing of 3D-printed samples (left). Load testing simulating steady-state acceleration loads was conducted using a tensile load cell. One face of the brackets was attached to a typical aluminium honeycomb panel. The perpendicular face was attached to a steel fixture (right).

  doi:10.5075/epfl-298799_978-2-9701614-0-0

3.6 Corner-brackets load testing

A bracket pull-out test was used to determine the stiffness properties of the corner brackets. The aim was to derive k-values, derived as $k = \Delta F/\Delta l$, where F represents a tensile force (N) and l represents displacement or travel (m). The test was conducted using various bracket designs and materials, including thermoplastics, thermoplastic composites, and aluminium.

3.7 Manufacturing quality assurance

This research determined the quality of FFF-printed parts during and after the manufacturing step. A record of process temperatures, filament-chamber relative humidity and print parameters was stored in a logfile. Deviations from desired values were monitored. Post-manufacturing, the mass and external dimensions of the parts were measured using a microbalance and a vernier caliber. This data was used to plot the x-R charts (Shewhart chart) used in the analysis.

4. Results and discussion

Here, we first describe the design and manufacturing of samples, followed by the test results. The size of the OBC enclosure design created challenges when the design was modified to take advantage of 3D printing while respecting print-chamber size limitations. The OBC enclosure underwent several significant design changes during the iteration process. After trials with the bracket design, two mesh designs (gyroid and diamond) were chosen based on their properties and printability. With these bracket designs, the printing direction affects the strength and durability of the bracket. The brackets printed flat had low strength. The tower and porous-face-down print orientations provided the best results. Strength test results showing brackets made from polylactide (PLA), carbon-fibre doped PEEK and aluminium are shown in Fig. 8. The strength figure-of-merit for the brackets was defined as force divided by bracket mass, where the tensile force (F) is in newtons (N) and applied to the bracket-honeycomb panel joint along one axis as in Fig. 7 (right). The stiffness of the brackets was derived as $k = \Delta F/\Delta l$, where the force (F) is in newtons (N) and the travel (l) is in millimetres (mm). Combining these two parameters to create a plot (Fig. 9) allows the study of the mass-saving enabled by the thermoplastic composite corner brackets.

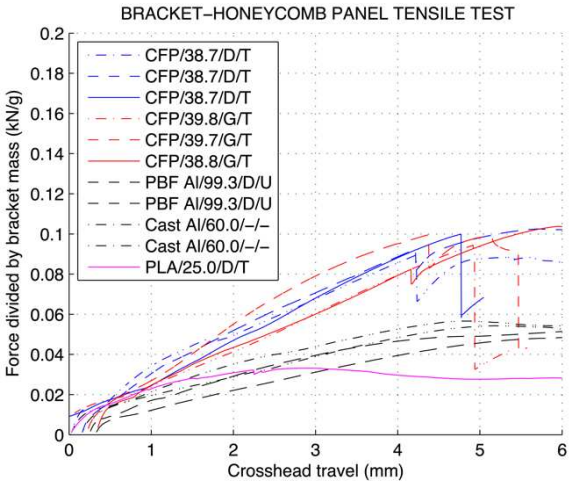

Figure 8. A figure-of-merit (force divided by bracket mass, Y-axis) was used to compare the 90° corner brackets using a tensile load test. The force is in kilonewtons (kN) and the mass in grams

(g). The X-axis shows the travel of the tensile load cell upper grip, while the lower grip remained stationary. The test article descriptions are as follows. PLA (polylactide thermoplastic using FFF), CFP (carbon-fibre doped PEEK using FFF), PBF AlSi10Mg (aluminium using powder bed fusion), and Cast Al (commercial cast aluminium brackets). Next, bracket mass in grams followed by the mesh type used in the brackets' interior volume ("D" for diamond and "G" for gyroid), and finally the print-layer orientation ("T" for tower, "D" for porous-face-down, and "U" for porous-face-up). The brackets made from carbon-fibre doped PEEK showed good performance.

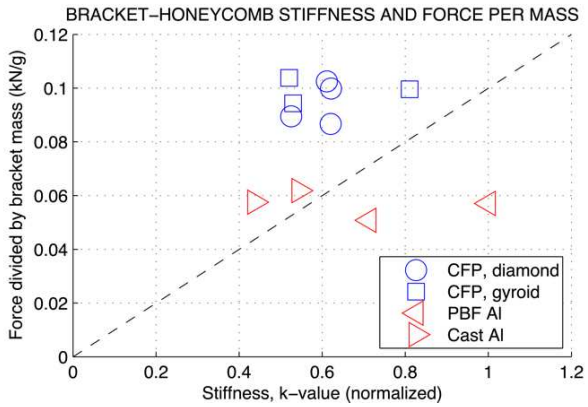

Figure 9. Bracket stiffness (k-value, X-axis) plotted against the force divided by bracket mass figure-of-merit (Y-axis), showing the thermoplastic composite brackets and the powder-bed-fusion (PBF) printed aluminium (AlSi10Mg) baseline bracket. CF-PEEK brackets were FFF-printed using carbon-fibre doped PEEK. The gyroid and diamond refer to the mesh type used in the bracket. A dashed diagonal line shows improved bracket performance when moving right and up.

The RF-housing was redesigned with different meshes to reduce the weight. If the screw positions could be changed from the metallic baseline, further AM-derived mass reduction would be possible. The sensor enclosure was redesigned based on a metallic baseline unit to create new possibilities for similar optical sensor enclosures. The 90-degree corner brackets manufactured using FFF with appropriate settings were demonstrated to have high stiffness and be lightweight, both being highly desirable qualities of a space-grade component. A high k-value corresponds with a structure having a high degree of stiffness.

Doped UV-resistant and AO-resistant plastics are a more robust solution than plastics with a metal oxide coating. That is because coatings are susceptible to pin hole defects, and they lack flexibility.

4.1 Vibration test results

The test articles (Fig. 6) were tested using an electrodynamic shaker in all three axes. The results showed that properly designed structures could fulfill the qualification-level acceleration load requirements commonly applied to spacecraft design. For example, according to these test results, the optical sensor housing would survive a typical launch environment of *SpaceX Falcon 9* and *Ariane 5* rockets.

The natural frequencies of the enclosures were measured and found to be acceptable. The OBC housing enclosure exhibited resonance of the top cover, probably caused by the lack of

attachment screws in the middle of the cover and the thin shell thickness in that same area. Such shortcomings can be easily overcome by redesigning this part of the enclosure. At the time of writing, a new design has been made and demonstrated with FFF but has yet to be stress-tested.

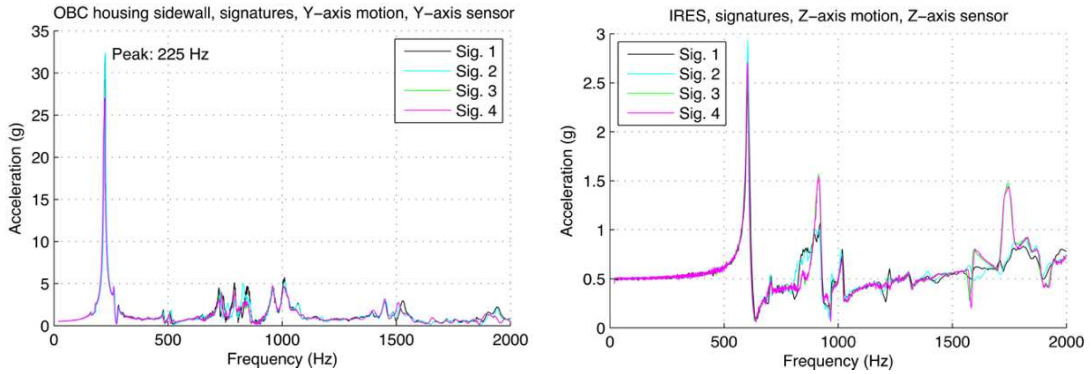

Figure 10. Signature sweep output signals from the OBC housing (left) and optical sensor housing (right), collected during the vibration testing. "Sig. 1–4" refer to four sweeps taken at different phases of testing (before tests, two intermediates, and after tests). These axes had the lowest modal frequencies for these housings. The homogeneity of the signals give proof to the fact that the housing survived the rigors of the test. The highest peak (~225 Hz for the OBC housing and ~600 Hz for the optical sensor housing) shows the natural frequency of the FFF-printed housing. The requirement set for the OBC housing (at least 161 Hz) was fulfilled. Similar requirement for the optical housing was unknown to the authors but was likely met with a good margin. Other axes had higher natural frequencies and are not shown here.

During the research, it became evident that the FEM of the corner bracket and the honeycomb panel joint were more rigid compared to the actual joint based on rivet nuts and screws. This is an excellent example of a case where over-simplification of FEM can lead to problems. On the other hand, detailed FEM of multiple rivet nuts and screws is not feasible due to the severe computing overhead of the simulations (when using desktop computers).

4.2 Results from other tests

Thermal cycling in 1 atm. was completed for three FFF-printed samples, having the shape defined by ISO 527 type 1b and made from nanodiamond doped PEEK (not electrically conducting). The samples were exposed to seven temperature cycles. During these cycles the sample temperatures ranged from -52°C to +144°C. The tensile load test was conducted in room temperature (22°C) in 1 atm. The average tensile strength was 93.98 MPa (SD 0.39 MPa), while the value derived for the tensile modulus was 3.67 GPa (SD 0.05 GPa). Corresponding values for the reference samples (no thermal cycling) were 93.37 MPa (SD 0.12 MPa) and 3.62 GPa (SD 0.02 GPa). At the time of writing, thermal cycling in a vacuum is yet to be done. Regarding the quality assurance, the plotting of Shewhart chart shows promise. However, the data in the charts is highly sensitive to the post processing of FFF-printed parts (cutting and cleaning). The results from the tensile tests in low and high temperatures and from UV-C testing will be published in separate papers. During this work, electrically conducting doped PEEK compound showed a

degree of conductivity to be classified as 'moderately conductive' according to the ECSS-E-ST-32-10C standard [19]. This material has not yet been FFF-printed.

5. Conclusions

This work showed that the printing parameters used in the FFF process (for example, layer orientation) significantly affect the mechanical performance of the parts. Therefore, that aspect needs to be considered carefully in the design and testing phases.

At present, no clear guidelines exist for the qualification of FFF-printed plastic components for spacecraft [6]. This work fills some of the gaps in this field.

The analysis showed that the FFF-printed carbon-fibre doped PEEK brackets' high strength and stiffness make them ideal for joints used in spacecraft honeycomb panel structures, enabling up to 25–50% savings in bracket mass. The large number of brackets employed in spacecraft structures supports the adoption of this technology. It should also be noted that the material used could also be recycled later when in-orbit FFF-printing becomes standard practice. Furthermore, the used manufacturing method (FFF) enables fast, and cost-effective low batch-size production runs.

Acknowledgements

The authors would like to thank Mr Tomi Kärkkäinen for the design and fabrication of the custom-built "Terrella Cubica" vacuum chamber used in this work.

References

1. Bendsøe MP. Optimal shape design as a material distribution problem. *Structural optimization*. 1989 Dec;1(4):193-202.
2. Zanjanijam AR, Major I, Lyons JG, Lafont U, Devine DM. Fused filament fabrication of peek: A review of process-structure-property relationships. *Polymers*. 2020 Aug;12(8):1665.
3. Kutz M, editor. *Handbook of materials selection*. John Wiley & Sons; 2002.
4. Ait-Mansour I, Kretzschmar N, Chekurov S, Salmi M, Rech J. Design-dependent shrinkage compensation modeling and mechanical property targeting of metal FFF. *Progress in Additive Manufacturing*. 2020 Mar;5(1):51-7.
5. Leach N. 3D printing in space. *Architectural Design*. 2014 Nov;84(6):108-13.
6. Lafont U, Costa M, Rampini, R. Thermoplastics and additive manufacturing: from ground to out-of-earth applications. *In Proceedings of the 2021 European Conference on Spacecraft Structures, Materials and Environmental Testing, ECSSMET 2021, 23–25 March 2021, Virtual.* 2021.
7. Nyman L, Kestilä A, Porri P, Pudas M, Salmi M, Silander R, Miikkulainen V, Kaipio M, Kallio E, Ritala M. Constructing spacecraft components using additive manufacturing and atomic layer deposition: First steps for integrated electric circuitry. *Journal of Aerospace Engineering.* 2021 Sep 1;34(5):04021049. Available from: https://doi.org/10.1061/(ASCE)AS.1943-5525.0001298.
8. Rawal S, Brantley J, Karabudak N. Additive manufacturing of Ti-6Al-4V alloy components for spacecraft applications. *In 2013 6th international conference on recent advances in space technologies*, *RAST 2013, 12–14 Jun 2013, Istanbul, Turkey.* IEEE; 2013. pp. 5-11.

9. Hastings D, Garrett H. *Spacecraft-Environment Interactions*. Cambridge University Press; 2009. Available from: https://doi.org/10.1017/CBO9780511525032.
10. Garrett HB, Whittlesey AC. *Guide to mitigating spacecraft charging effects*. John Wiley & Sons; ISBN: 9781118241332; 2012.
11. Tribble AC. *The Space Environment: Implications for Spacecraft Design - Revised and Expanded Edition*. Princeton University Press; ISBN: 9780691213071; 2020.
12. Ganushkina NY, Swiger B, Dubyagin S, Matéo-Vélez JC, Liemohn MW, Sicard A, Payan D. Worst-Case Severe Environments for Surface Charging Observed at LANL Satellites as Dependent on Solar Wind and Geomagnetic Conditions. *Space Weather*. 2021 Sep; 19(9):e2021SW002732. Available from: https://doi.org/10.1029/2021SW002732.
13. De Groh KK, Banks BA. The MISSE-9 Polymers and Composites Experiment Being Flown on the MISSE-Flight Facility. *In International Space Station Research and Development Conference, ISSR&D 2017, 17–20 Jul 2017, Washington, DC, U.S.A*. 2017 Jul.
14. Johnson RH, Montierth LD, Dennison JR, Dyer JS, Lindstrom ER. Small-scale simulation chamber for space environment survivability testing. *IEEE Transactions on Plasma Science*. 2013 Sep 25;41(12):3453-8.
15. Dever J, Pietromica A, Stueber T, Sechkar E, Messer R. Simulated space vacuum ultraviolet (VUV) exposure testing for polymer films. *In 39th Aerospace Sciences Meeting and Exhibit, 08–11 Jan 2001, Reno, NV, U.S.A*. 2001 Jan. p. 1054. Available from: https://arc.aiaa.org/doi/book/10.2514/MASM01.
16. Chamberlain JW, Hunten DM. Theory of planetary atmospheres, second edition. *Academic Press*; 1987. ISBN: 978-0121672522.
17. Arianespace. *Ariane 5 user's manual issue 5 revision 3*. Arianespace. 2020. Available from: https://www.arianespace.com/wp-content/uploads/2016/10/Ariane5-users-manual-Jun2020.pdf.
18. SpaceX. *Falcon Users Guide September 2021*. SpaceX. 2021. Available from: https://www.spacex.com/media/falcon-users-guide-2021-09.pdf.
19. ECSS (European Coordination for Space Standardization). *European coordination for space standardization*. 2022. Available from: https://www.ecss.nl.

LONG LATENCY VITRIMER FORMULATION FOR CARBON FIBRES PREPREGS COMPOSITES

Quentin-Arthur POUTREL[a], Maelys LAHORE[b], Mickaël POMES-HADDA[a], Ugo LAFONT[c], Olivier DAMIANO[b,], François TOURNILHAC[a,*]*

[a] Molecular, Macromolecular Chemistry, and Materials, ESPCI Paris PSL, CNRS, France;

[b] Thales Alenia Space, 5 allée des Gabians, 06156 Cannes la Bocca, France;

[c] ESTEC, European SpaceAgency, Keplerlaan 1, Noordwijk, The Netherlands.

Abstract: *Vitrimers are currently investigated for their potential to produce strong, healable, recyclable and reprocessable matrices. Nonetheless their uses at industrial scale still present new challenges to be addressed. In the present work, we investigate the suitability of vitrimer based carbon fibre reinforced polymers for space application. Especially, we aimed at proving that formulation of catalysed epoxy vitrimer resin can be adapted to form prepregs carbon fibres that have good storage and handling properties. For this purpose, we focused our efforts to develop a vitrimer resin comprised of an epoxide and a crystalline hardener that shows long latency and satisfying viscosity for being stored and laminated in an industrial environment. Spectroscopy and rheology confirmed those requirements before production of a carbon fibres laminates with Thales Alenia Space (TAS). Furthermore, after curing, the vitrimer properties were used to bond laminates without adhesive (exhibiting cohesive fracture after breaking) and separate carbon fibres via depolymerisation.*

Keywords: Composites; Carbon fibres; Vitrimer; Aerospace; Prepregs

1. Introduction

In less than a century, polymers have radically changed our world, becoming a part of almost every aspect in human life. Variety of chemistry and processing techniques combined with affordable primary resources, made polymers indispensable in many applications such as electronics, construction, medical devices, automobile, kitchen utensils etc. [1,2]. Nonetheless, one area that benefits and invests the most for polymers development is the aerospace industry [3,4]. Lightweight, strong, and complex structures are key requirements, improving safety and travelling distance while decreasing costs (*e.g.* fuel consumption). Particulary, carbon fibres composites reinforced polymers (CFRP) have seen increasing development and uses in this industry [5]. Those composites allow to combine fibres strength with processing techniques of polymers to form flat, tubular or more complex shapes. High performance requirements of the aerospace field means that thermosets - especially epoxies - are a preferred choice for matrix in CFRP [4,6]. Despite the variety of advantages brought by those, they also come with their share of drawbacks such as structures hardly repairable, reprocessable or recyclable [7].

Vitrimers, a newer kind of polymer networks, combine the properties of thermosets (insoluble and resistant) with the flow property of thermoplastics, through thermally stimulated covalent bond exchange [8–11]. Many chemistries were developed over the past decade and despite tangible potential for their uses in CFRP applications, their adaptation to classical processes remains barely explored. Techniques, such as resin infusion and resin transfer moulding have been experimented with vitrimers [12], however in high performance CFRP (aerospace, space

automotive, *etc.*), the prepregs technology is usually favoured as it allows to produce higher fibre/resin ratio, and has yet to be performed with vitrimer. Storage and handling steps are key requirements to meet for prepregs production, and the use of catalyst - in vitrimer made from commercially available monomers - can be seen as a limiting factor as it could trigger cure before layup is performed.

Herein, we report a vitrimer formulation compatible with prepregs preparation in an industrial environment. Comprised of a novolac epoxy type resin, a crystalline dicarboxylic acid hardener with high melting temperature and a Zn(II) transesterification catalyst; those reactants shown in Table 1 give a formulation allowing storage up to one month at ambient temperature. Rheological behaviour satisfies viscosity requirement for carbon fibres impregnation at 100°C while remaining tacky at room temperature for laminates layup. Once cured, this resin displays reparability and adhesive behaviour upon heating and can be successfully depolymerised to recover and separate laminates, opening possibility to form CFRP composites with improved sustainability at industrial scale.

Table 1 Reactants information

Monomers	Epoxy	Hardener	Catalyst
Name	Novolac based epoxy Epalloy 8330	Cyclohexane-1,4-dicarboxylic acid CHDA	Zinc acetyl acetonate ZnAcac
Formula	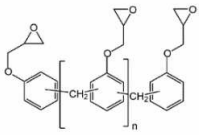		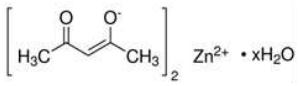
Properties	Epoxy eq. wt. 171-183 (g/eq) Viscosity 20 - 30 Pa.s @ 52°C	Mol wt. 172.18 g/mol Melting T°: 164 - 167°C	Mol wt. 263.59g.mol^{-1} Melting T°: 135-138°C
Suppliers	Huntsman Ltd.	Abcr	Abcr

2. Results

Resin development latency and curing — Resin to impregnate fibres requires a set of simple, yet, altogether complex properties to obtain:

I. A low viscosity for impregnation (< 100 Pa.s, preferably < 10 Pa.s) and latency at impregnation temperature (several hours)
II. Latency at ambient temperature (≥ 7 days)
III. Tackiness at ambient temperature for layup preparation.

The impregnation capacity of the resin (I) was defined using rheology and DSC measurements. Temperature was set between 100°C and 110°C (above the resin T_g, and well below the melting point of the other monomers), rheology measurements made on the novolac epoxy-CHDA mixture (without catalyst), are presented in Figure 1 a) and b) respectively. Due to the crystalline nature of CHDA, at 100°C, the system has little to no reactivity, hence, the measurement does not give particular information except that the gel point is not reached in 24h. At 110°C, conversion of epoxides and carboxylic acids happens leading to the crosslink of the network and the gel point is reached within ~758 min (12 h 38 min). Before that time, the viscosity of the system is comprised between 18-40 Pa.s satisfying the requirement for a 1-2h

fibres impregnation process. The question then arises if the catalysed version of this resin has similar reactivity time in this temperature range. However, the uncanny behaviour of the system (induced by the crystalline hardener constantly dissolving and recrystallising before the gel point) induces noisy rheological measurements, therefore, the activation energies E_a of the epoxy ring opening addition (for catalysed and non-catalysed system) was measured using the Kissinger di Benetto method [13] based on the assumption that the exothermic peak coincides with the maximum reaction rate as described by equation 1:

$$\ln\left(\frac{\emptyset}{T_p^2}\right) = \ln\left(\frac{k_0 R}{E_a}\right) - \left(\frac{E_a}{RT_p}\right) \quad (1)$$

With $\emptyset$, the heating rate, T_p the peak of the exothermal reaction and R the ideal gas constant. E_a was thus obtained from the slope of $\ln(\emptyset/T_p^2)$ as a function of $1/T_p$ (Figure 1 c). The catalysed mixture gives an activation energy of E_a = 63 kJ.mol^{-1}, while the non-catalysed system gives E_a = 51 kJ.mol^{-1}. This fact shows that the chosen catalyst (ZnAcac) does not decrease the energy barriers involved in the (exothermic) ring opening reactions. In such a system comprised of novolac epoxy resin - with an average number of epoxy group per chain higher than 2, gelation occurs at early stage of conversion, without necessary involvement of transesterification [14]. As a result, the rheological evolution of this system is not critically dependant on the rate of transesterification. ZnAcac will therefore catalyse the transesterification reactions of the final cured vitrimer but not influence much the course of curing. Moreover, the slightly higher value of the apparent activation energy in the catalysed system means potentially better thermolatency than the uncatalysed one, which would only improve the required resin properties for prepregs handling and storage.

One of the primary objective of the resin development is to obtain at least several days of latency at room temperature (II). Indeed, the impregnated fibres should give the possibility to have enough time to layup fibres for a composite structure before the impregnated fibres start to show signs of gelation and become difficult to process. The latency of the novolac epoxy / CHDA system, catalysed with ZnAcac was evaluated via ATR-IR spectroscopy over 25 days at room temperature (Figure 1 d). After this period, there was no noticeable changes in the IR spectrum, indicating no significant conversion on this time scale. This confirms good latency for the formulation which has virtually no reactivity at room temperature due to the stability of CHDA crystals in epoxy at this temperature. The last point (III) is the tackiness of the system at ambient temperature. For this matter, as the system remains in its initial state, stickiness is governed by the inherent properties of the novolac resin producing a system of stable tackiness at ambient temperature, allowing easy layup process. Once these preliminary measurements were obtained, the next step was to develop procedures to prepare prepregs. This brings new considerations regarding the base system. Indeed the crystallinity of the CHDA with high melting temperature gives a satisfactory latency for storing, and handling prepreg plates at room temperature or below. On the other hand, the novolac resin gives satisfying viscosity for impregnation at 100°C and tackiness at ambient temperature. However, the raw mix is a dispersion of small solid particles in a viscous liquid, which brings challenges to obtain homogenous samples: a fast curing at high temperature leads to samples with bubbles and high quantity of unreacted CHDA crystals. Meanwhile, a too low temperature leads to a high level of sedimentation of CHDA and phase separation, with epoxy on a side and CHDA on the other side, potentially inducing unwanted homopolymerisation of the epoxy resin.

  doi:10.5075/epfl-298799_978-2-9701614-0-0

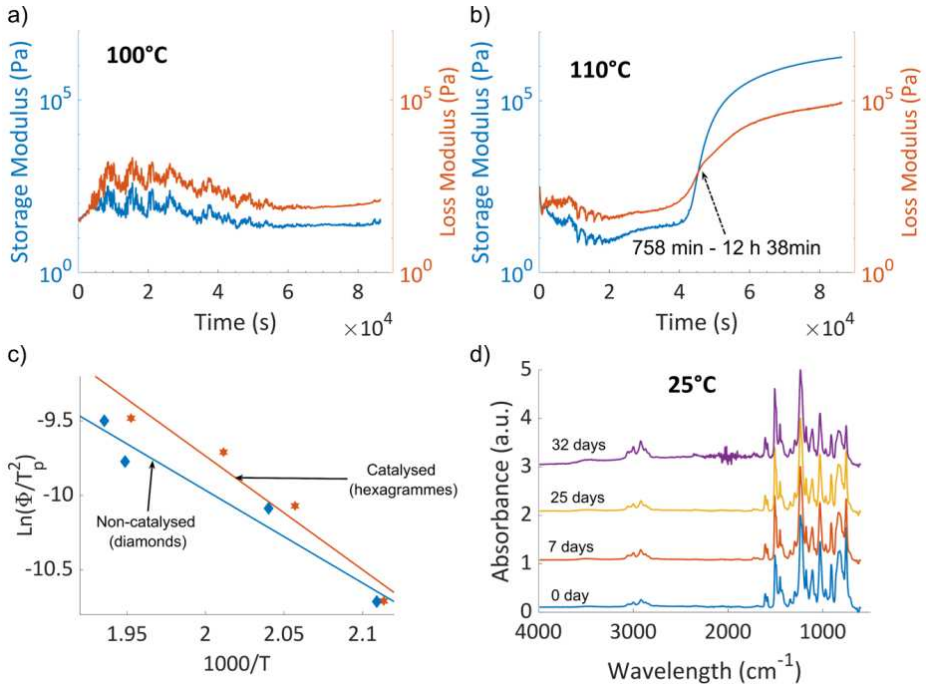

Figure 1 a-b) Rheology measurement: storage and loss modulus of the mix novolac epoxy-CHDA without catalyst at 100°C and 110°C respectively, c) Arrhenius plot of epoxy conversion for catalysed (orange curve) and non-catalysed (blue curve), d) Latency of the catalysed system over 25 days.

In both cases, this would be detrimental to the vitrimer properties and solution to homogenise the system before curing is required. Therefore, CHDA crystals need to be dissolved within the epoxy following procedures developed with similar systems [15,16]. The resin was then pre-cured 1h at 130°C, before starting the curing stage. Although disappearance of CHDA crystals is easily seen by eyes (with the resin becoming transparent), ATR-IR spectroscopy enables to analyse the composition of the reactive mixture throughout the curing process. In this step, our main areas of interest are:

1. The epoxy signal, (asymmetric deformation vibration of the ring) detected at ~917cm^{-1}. Its decrease informs us about the epoxy consumption while reacting with the hardener.
2. The C=O stretching vibration of the β-hydroxylester, **3** formed by epoxy-acid addition, detected at ~1730 cm^{-1}.
3. The C=O stretching vibration of the carboxylic acid, split into two different signals :
   a. $\nu_{C=O}$ of the *oxo*-H-bonded form, **2**a is detected at ~1705 cm^{-1} (Figure 2a)
   b. $\nu_{C=O}$ of the *oxo*-H-bonded form, **2**b is detected at ~1738 cm^{-1} (Figure 2b)

The infrared spectrum of the reactive mixture focussing on the -COOH vibration band region at the beginning and at the end of the precure are presented in Figure 2c. The signal of the carboxylic acid hardener is not detected at the beginning of the curing stage. To explain this, it must be reminded that, in the ATR technique utilised here, the region scanned by the infrared radiation is not deeper than the depth of the evanescent wave D_p. Practically, D_p is of the order of a few microns, or less. In case of a two-phase sample, the heterogeneous distribution of the constituents in the vicinity of the interface may cause one of them to disappear. This is what is happening here. Due to the size of CHDA crystals, there is depletion of this component along the interface as long as it remains in the solid form. Conversely, once the medium becomes homogeneous, all the molecules in presence can access the interface and give rise to

detectable IR absorption signals (Figure 2c). As for the epoxy signal (not represented here), it barely changes between the start and the end of post-curing, showing little reaction at this temperature. This is all the more true since the observed decrease is partly due the dilution brought by the melting of CHDA crystals as shown by the transparency of the reactive mixture after the pre-curing stage (Figure 2d).

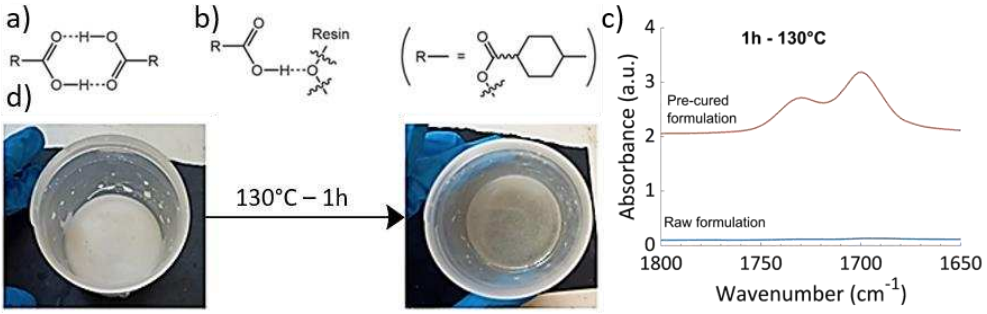

Figure 2 The CHDA crystals dissolution in epoxy: a) oxo-H-bonded acid, b) oxy-H-bonded acid, c) ATR-IR of COOH area before and after the curing stage.

Determining the curing temperature and time was then the next step to insure manufacturing of CFRP composites with satisfying properties. Further analysis of these monitoring was performed by integrating the 3 signals defined earlier over a 24h period at different temperatures: 100°C, 110°C, 130°C and 145°C. At 100°C, after 24h, the characteristic signals of acids and epoxy (Figure 3 a and b respectively) barely evolved indicating that the mixture has little reactivity and thus confirming time to perform impregnation. At 110°C, after 24h, both signals evolved slightly and the characteristic ester's vibration appears (Figure 3c), indicating that the polymerisation started but was not completed (as revealed by the decreasing epoxy signal after 24h (Figure 3b). At 130°C (Figure 5c), both signatures (carboxylic acids and epoxides) completely disappear within 24 h and a clear ester vibration is seen indicating that the polymerisation reaction was fully achieved on the ATR-IR cell. However, at 130°C, the system takes ~500-600 min (*i.e.* > 10h) to reach a plateau, then the conversion slows down for the rest of the measurement. This indicates that most chemical moieties reacted through polymerisation and once most of reactants are consumed (~80%), the reaction slows down. Another classical reason for slackening is the vicinity between the cure temperature and the so-called T_∞ (*i.e* T_g of the fully cured network, reported to be located between 110°C and 130°C for similar network [15]). At 145°C, the plateau is reached within ≈ 420 min (7h). Therefore, to optimise the time of impregnation and curing, the process was finally set as follow: (i) mixing of components, (ii) fibres impregnation at 100°C, (iii) layup at ambient temperature, (iv) precuring stage at 130°C for 1h, (v) curing stage at 145°C for 8h and, (vi) postcuring stage at 180°C for 6h insure a maximal conversion of remaining reactive functions.

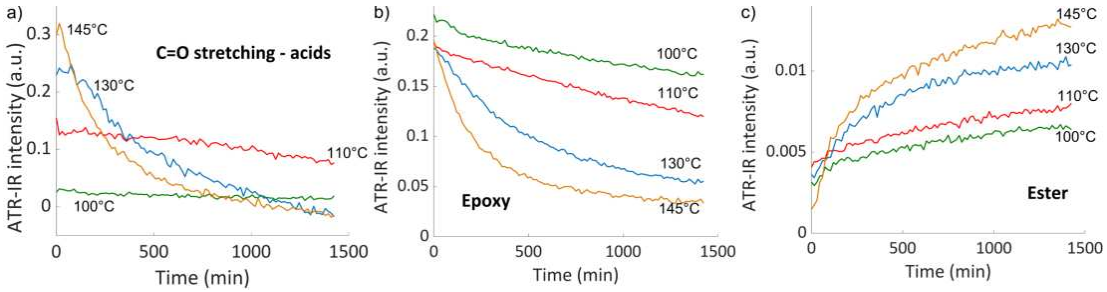

Figure 3 Time dependence of infra-red characteristic signals over a 24h period of time for the pre-cured version of the resin: a) oxy H-bonded acid signal, b) epoxy signal and c) ester signal.

CFRP manufacture and testing — subsequently to the determination of prepregs preparation, the suitability to manufacture large size panels in an industrial environment was verified. TAS and Kalliste composites took upon impregnating a large carbon fibre (1m^2) manually as represented in Figure 4. The fibre was then cut in 30cm^2 size sheets and layed up in a 0/60/-60/0/90/-30/ manner. This panel was then cured under vacuum following procedure determined earlier.

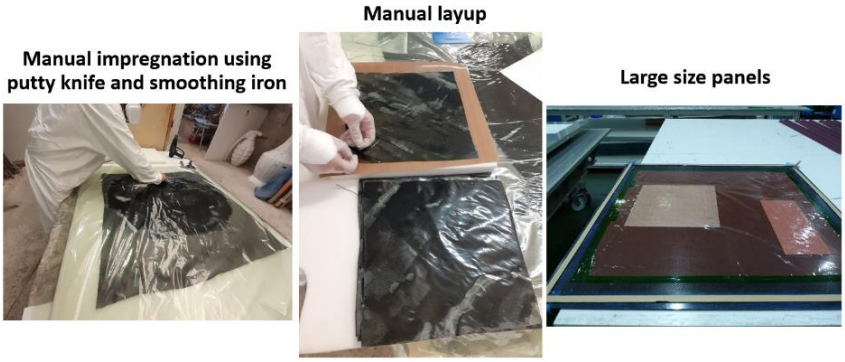

Figure 4 Manufacture of large vitrimer prepreg, layup and curing of 30 cm^2 panels

Subsequently, the panel was then cut in small samples of 10 x 2 cm to proceed of vitrimer properties exploration. As a proper protocol is yet to be determined in order to measure relaxation of CFRP vitrimer and reshaping is rather limited by the fibres [12], our focus went on showing interest of such CFRP vitrimer for sustainable aerospace applications: capacity of cracks healing, adhesion without the use of glue or bolts, and recovery of fibres at the end of the composites life cycle. Firstly, we chose a damaged sample showing signs of delamination during the cutting step. This sample was pressed at 180°C for 1h under 0.5 bar. It can be seen that after the procedure (Figure 5), the fibres successfully adhered to the matrix, reducing the damages induced either during manufacturing or handling of CFRP panel. Other sample pieces were then prepared for adhesion tests. 6 samples were flattened in a hot press for 1h at 180°C under 0.5 bar pressure, 2.5 cm^2 surfaces were sanded and cleaned before being pressed against each other by pairs, as to form three lap-shear joints with an overlap area of 2.5 cm^2. The lap shear specimens were placed for 1h30 at 180°C in a clamp comprising two M5 screws tightened with a torque of 1.7 N.m, thus ensuring a force of approximately 4000 N over the total area of 7.5 cm^2. After the clamp was removed, the samples adhered to each other. To measure the strength of the adhesion, lap-shear tests were performed, the sample was pulled 4 times to 1 kN pulling force (≈ 4 MPa) without break, showing shear strength equivalent to classical epoxy glue. On the 5th pulling, the sample broke at the interface, exhibiting cohesive

fracture (figure 5), indicating that adhesion of the two CFRP pieces was achieved through effective welding of the matrix, permitted by the vitrimer bond exchanges mechanism. Finally, one of the main issues of thermoset CFRP is their end of life. Not only this led to potential environmental wastes but carbon fibres are expensive, and methods to recover them usually imply destruction of fibres length but also high temperature. Here, we took a small sample (2cm x 1cm), and plunged it into an ethanol/acetone solution (50:50). The sample was then heated for 4h at 180°C in a pressurized reactor to trigger vitrimer depolymerisation. After removal and cooling, the fibre sheets were separated with the help of a spatula and recovered as shown in Figure 5. Despite small damage induced by the separation process, it is clear that the depolymerisation allows to separates laminates in the size of the initial sample without the use of high temperature or harsh chemical usually used to remove classical thermoset epoxy resin.

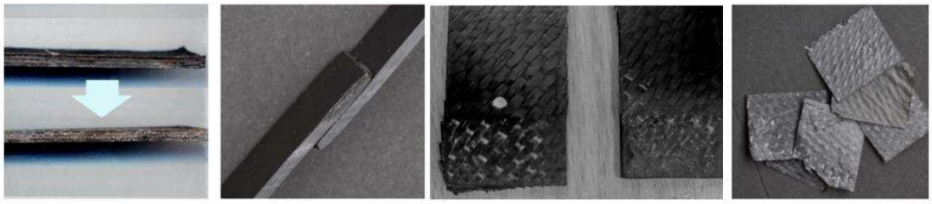

Figure 5 Use of vitrimer properties for crack healing, self-adhesion and CFRP fibres recovery

3. Conclusions and outcomes

The novolac epoxy and crystalline CHDA reactive mixture shows potential for long latency to form prepreg. Combining high melting temperature of the hardener and flow properties of resin at ambient or impregnation temperatures allows to obtain a mixture able to easily impregnate carbon fibres while performing well for storage and handling of CFRP prepregs. The methodology developed at the ESPCI Paris was used at Kallista composites (TAS industrial partner) and led to manufacture of CFRP panels within 3 days of work. Damages that occurred during the manufacturing or cutting of the composites have been repaired. A simple heating under pressure for 1h led to voids and delamination removal, an interesting point which could find practical echo at several stages of composite implementation: (i) improvement of panels after manufacture leading to lower waste on the manufacturing lines. (ii) Repair of damages induces by handling at the pose of composites or even later through their life. Moreover, adhesion tests of CFRP made from vitrimer prepregs show that composite thus produced could be put together in larger scale without the use of adhesive or bolts, reducing weight of structure but also materials costs for production and assembly. It is also envision that this kind of material is relatively suitable for space exploration, CFRP vitrimer prepregs could serve a structure for spacecraft, then disassemble by heat upon arrival to be reassembled as life structure. Finally the CFRP samples have also a greater environmental sustainability, as the fibres can be recovered using soft solvent at relatively low temperature (< 200°C).

Although, results for preparing vitrimer prepregs and their testing with the CHDA formulation are encouraging, many points remained to be determined. Firstly the ratio fibres/matrix obtained through this technique is to be controlled as the main advantages of prepregs samples is to obtain a high fibres proportion relative to the matrix. For this, it is necessary to

  doi:10.5075/epfl-298799_978-2-9701614-0-0

verify that the crystallinity of the CHDA does not limit fibres impregnation with automated machines to obtain a constant fibres/resin ratio difficult to obtain by manual impregnation. On the composites properties sides, rheological behaviour, degassing properties and mechanical properties (compression, tensile, bending, etc.) at ambient and above the polymer T_g have to be performed for comparing with a traditional thermoset resin to validate the use of such resin in demanding environments. Those points are currently under investigation with TAS and the European Space Agency, nonetheless, vitrimer networks have ticked a new box at their potential for adoption in industrial uses to replace or complement traditional thermoset resin.

4. References

1. Scoble MJ. Comprehensive Polymer Science. Syst. Entomol. 2005;30:497–8.
2. Chen H, Ginzburg V V., Yang J, Yang Y, Liu W, Huang Y, et al. Thermal conductivity of polymer-based composites: Fundamentals and applications. Prog. Polym. Sci. 2015;59:41–85.
3. Galos J. Thin-ply composite laminates: a review. Compos. Struct. 2020;236.
4. Bello SA, Agunsoye JO, Hassan SB, Kana MGZ, Raheem IA. Epoxy resin based composites, mechanical and tribological properties: A review. Tribol. Ind. 2015;37:500–24.
5. Cantoni S, De Nicola F, Mercurio U, Quaranta V. The role of polymer based composites materials in modern and future aerospace structures. 2014;10:10–3.
6. Hadden CM, Klimek-McDonald DR, Pineda EJ, King JA, Reichanadter AM, Miskioglu I, et al. Mechanical properties of graphene nanoplatelet/carbon fiber/epoxy hybrid composites: Multiscale modeling and experiments. Carbon 2015;95:100–12.
7. Hia IL, Vahedi V, Pasbakhsh P. Self-Healing Polymer Composites: Prospects, Challenges, and Applications. Polym. Rev. 2016;56:225–61.
8. Montarnal D, Capelot M, Tounilhac F, Leibler L. Silica-Like Malleable Materials from permanent organic network. Science 2011;334:965–8.
9. Denissen W, Winne JM, Du Prez FE. Vitrimers: permanent organic networks with glass-like fluidity. Chem. Sci. 2015;7:30–8.
10. Obadia MM, Mudraboyina BP, Serghei A, Montarnal D, Drockenmuller E. Reprocessing and Recycling of Highly Cross-Linked Ion-Conducting Networks through Transalkylation Exchanges of C–N Bonds. J. Am. Chem. Soc. 2015;137:6078–83.
11. Liu Z, Zhang C, Shi Z, Yin J, Tian M. Tailoring vinylogous urethane chemistry for the cross-linked polybutadiene: Wide freedom design, multiple recycling methods, good shape memory behavior. Polymer 2018;148:202–10.
12. Chabert E, Vial J, Cauchois J-P, Mihaluta M, Tournilhac F. Multiple welding of long fiber epoxy vitrimer composites. Soft Matter 2016;12:4838–45.
13. Jourdain A, Obadia MM, Duchet-Rumeau J, Bernard J, Serghei A, Tournilhac F, Pascault JP, Drockenmuller E. Comparison of Poly(ethylene glycol)-based Networks Obtained by Cationic Ring Opening Polymerization of Neutral and 1,2,3–Triazolium Diepoxy Monomers. Polym. Chem. 2020, 11, 1894
14. Vidil T, Tournilhac F, Musso S, Robisson A, Leibler L. Control of reactions and network structures of epoxy thermosets. Prog. Polym. Sci. 2016;62:126–79.
15. Poutrel QA, Blaker JJ, Soutis C, Tournilhac F, Gresil M. Dicarboxylic acid-epoxy vitrimers: Influence of the off-stoichiometric acid content on cure reactions and thermo-mechanical properties. Polym. Chem. 2020;11:5327–38.
16. Tangthana-umrung K, Poutrel QA, Gresil M. Epoxy Homopolymerization as a Tool to Tune the Thermo-Mechanical Properties and Fracture Toughness of Vitrimers. Macromolecules 2021; 54, 18, 8393–8406

GENERALIZED SOLUTIONS TO THE NON-GEODESIC WINDING PATH EQUATIONS FOR AXISYMMETRIC FILAMENT-WOUND COMPOSITE STRUCTURES

Abderrahmane, RHARDANE[a,b], Damien, HALM[b], Mikaël, GUEGUEN[b], Kévin, MATHIS[a], Philippe, SAFFRE[c]

a: CNES – 52, rue Jacques Hillairet – FR 75012 Paris Cedex, France
b: PPrime Institute, CNRS, ENSMA, Université de Poitiers, BP 40109, F-86961 Futuroscope-Chasseneuil, France
c: SYMME, Université Savoie Mont Blanc, FR 74000 Annecy, France

Abstract: *Fiber-reinforced composites have become an essential component in the range of materials used in the aircraft and aerospace industries, thanks primarily to their high strength, lightweight design, and the automated nature of the manufacturing process. Typically, carbon fibers pre-impregnated in thermosetting resin are continually stretched over a mandrel surface, making the rocket's motor case. Layer after layer, the multi-sequence lay-ups cover both the cylindrical and the dome parts of the vessel, in a way to provide a suitable distribution of fiber reinforcements to resist to high pressures. An adequate simulation of the mechanical behavior of such structures must take into consideration the structure's geometry and mesh singularities which are caused by overlap and bridging. The present article proposes generalized approaches to deal with fiber trajectories bridging over concave surfaces, with low winding angle leading to overlap, and irregular meshing around resin pouches and gaps.*

Keywords: filament winding; composite structures; dome geometry; bridging

1. Introduction

In the energy and aerospace industries, the enhanced performance provided by carbon fiber-reinforced epoxy matrix composite shells has been demonstrated in their increasing application to replace thick metallic hulls [1]. With wound composite structures, the fiber tow's trajectory can be reoriented to counter the effect of the internal pressure and localized loads in different directions, providing the manufacturer with a workability advantage to enhance the structure. For this reason, composite pressure vessels are characterized by a superior strength or stiffness to weight ratio, which is an important asset that should meet the stringent requirements of storage capacities, especially in the case of propellant tanks. The use of composite vessels can affect fuel savings up to 75%, compared to metallic counterparts [2].

An important aspect of the filament winding process is the precise and automated lay-up of fiber reinforcements over a depositing surface. In axisymmetric pressure vessels and propellant tanks with a mandrel surface assembled from a cylindrical part and two dome shapes, multiple layers with different fiber orientations have to be deposited to provide the structure with the adequate stiffness. There are a number of ways in which such structures can be optimized: by modifying the mandrel surface geometry (geometrical optimization) or by modifying the composite lay-up (structural optimization). Since the winding process allows for a number of degrees of freedom in terms of winding angle, layer thickness, number of hoop and helical layers, etc., the composite

  doi:10.5075/epfl-298799_978-2-9701614-0-0

shell can be refined without changing the shape and the size of the tank. If and when such an enhancement is called for, the structural optimization cannot be done by experimentally testing every possible composite lay-up. In this case, numerical optimization provides a better method to deal with such a complex problem. If the tank geometry is properly reproduced by a numerical tool and the mechanical behavior is correctly predicted in modeling, then the overall structure can be further improved.

The first step of the wound composite tank modeling is the generation of a reliable geometry of the structure. Many numerical models have been proposed in the literature (see Leh et al. [3] for a summary). In such models, the composite shell is generated layer by layer. Special attention is given to identify the winding angle evolution in the dome part, as the fiber trajectory naturally deviates from the meridian line, as shown in Figure 1, until it reaches 90°. The fiber then stops at the turn-around radius, or r_{turn}, and changes direction. The turn-around radius is an important variable as it defines the limit of a layer in the dome part. Once the depositing surface is defined for the current layer, its thickness must be determined. Due to the accumulation and intersection of fiber tows in the dome region, thickness build-up always appears at the end of the layer, causing a complex depositing geometry to appear which complicates the trajectory for the next layer. Other points of concern are the integration of slippage in the equations, as well as the curvature of the depositing layer and the fiber tangency at the polar opening. While such methods proposed in the literature help to expand the spectrum of fiber trajectories that can be reproduced and tested in modeling, they are not without limitations.

The current article will first present the theoretical basics of simulating an axisymmetric wound composite structure, such as high pressure vessels (HPVs) and propellant tanks. Secondly, a few upgrades found in the literature are discussed, as well as some of their limits in replicating the geometry. Third, the generalized solutions to the non-geodesic path in the presence of surface irregularities are detailed. These solutions deal particularly with the bridging problem.

2. Theoretical basics

2.1 general methodology

When simulating the mechanical behavior of an axisymmetric wound composite structure, most studies [3-6] use the meso-level (that of individual layers) in order to create the geometry. This provides a compromise, since reproducing each ply at the micro-level is too burdensome, and representing the overall shell at the macro-level offers too little for a more detailed study of the composite. At this meso-level, the composite shell geometry and mesh are generated layer by layer, starting at the liner surface of the tank. The classical methodology, as proposed by Leh et al. [3] and modified by Bizet et al. [7], consists of:

- Reading the depositing surface's geometry (cylinder and dome) as well as the winding sequence parameters (initially, the depositing surface is the liner),
- Defining the *z* and *r* coordinates of the geometry after discretization,
- Calculating the first and second derivatives of the current geometry line,
- Solving the winding angle evolution equation and determining the turn-around radius,
- Computing the layer's thickness using the method proposed by Wang et al. [8],
- Constructing the current layer's profile using normal vectors at each point,
- Smoothing the layer's profile which constitutes the next layer's depositing surface,

- Looping over all the previous steps until the end of the multi-layer sequence.

Two important steps, the determination of the winding angle evolution and of the layer's over-thickness, require further explanation.

2.2 winding angle evolution

The fiber tow starts with an initial angle α_{ini} at the dome-cylinder connection. This value remains constant over the cylinder part. However, it gradually increases in the dome part until reaching 90°. The fiber tow's trajectory is governed by a differential equation that describes both geodesic and non-geodesic paths, and takes into account slippage on the supporting surface (cf. Koussios [9] for more details):

$$\frac{d\alpha}{dz} = \lambda\left[\frac{\sin\alpha\tan\alpha}{r} - \frac{r''\cos\alpha}{1+r'^2}\right] - \frac{r'}{r}\tan\alpha \quad (1)$$

where α(z) is the evolving angle (< 90°), and *r*, *r'* and *r''* represent the radial coordinate and its derivatives. The slippage coefficient λ controls the trajectory of the fiber and the turn-around radius. To ensure continuity at the dome-cylinder connection (*r* = *R*), λ follows the equation [7]:

$$\lambda(r) = \lambda_{max}\left[\frac{\pi}{2}\frac{r-r_{turn}}{R-r_{turn}}\right] \quad (2)$$

where $\lambda_{max} < \lambda_{lim}$ (slippage limit coefficient that depends on practical winding parameters).

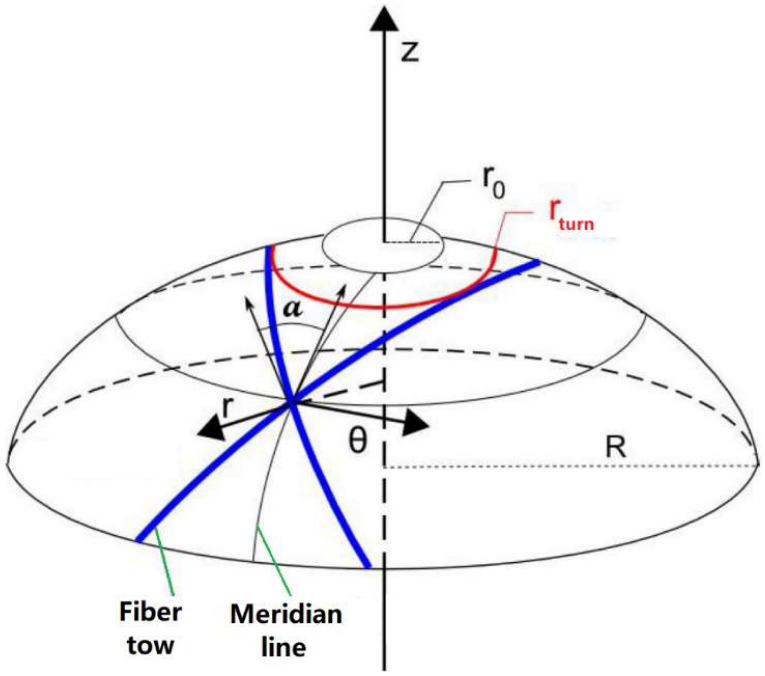

Figure 1. Evolution of the winding angle in the dome part [3].

2.3 layer thickness evolution

After determining the turn-around radius and the winding angle evolution, the thickness must then be calculated. The formulation that shows the best comparison results is that proposed by Wang et al. [8]. The main idea is that, due to the accumulation of plies in the dome part, each point will exhibit an overlay of plies stacked on top of each other, therefore adding to the total thickness at that point. The double formulation proposed by Wang et al. is given such as [7]:

$$t(r) = \frac{n_R m_R t_p}{\pi}\left[\arccos\left(\frac{r_{turn}}{r}\right) - \arccos\left(\frac{r_b}{r}\right)\right] \qquad r_{2b} \le r \le R \tag{3}$$

$$t(r) = A + Br + Cr^2 + Dr^3 \qquad r_{turn} \le r \le r_{2b} \tag{4}$$

Eq. (3) describes thickness far from the turn-around radius, with n_R and m_R representing the number of pseudo-plies (±α) and their quantity at the dome-cylinder connection, t_p the thickness of a single fiber tow, and r_b and r_{2b} the radius at one and two-tape distances, respectively. Due to thickness buildup, Eq. (4) corrects the thickness near the turn-around radius. Coefficient *A*, *B*, *C* and *D* are determined using 4 continuity equations presented in [8].

2.3 model limitations

In Bizet et al. [7], a number of limitations have been identified and addressed. These include the proposition of the robust LSODA algorithm [10], which is more appropriate than Runge-Kutta algorithms in dealing with stiff equations (such as the equation governing the winding angle evolution in Eq. 1), as well as a correcting method to deal with layers overlapping the barrel of the metallic boss. A particularly difficult issue is that of composite layers overlapping previously covered surfaces. Bizet et al. have dealt with this problem by introducing a smoothing function so that the layer's profile in the dome section can be mapped using a unique function *r(z)*, where *r* and *z* are the radial and axial coordinates, respectively (cf. Figure 2(a)). If instabilities emerge due to presence of convex zones, as seen in Figure 2(b), then a special function erases them before continuing to the next layer.

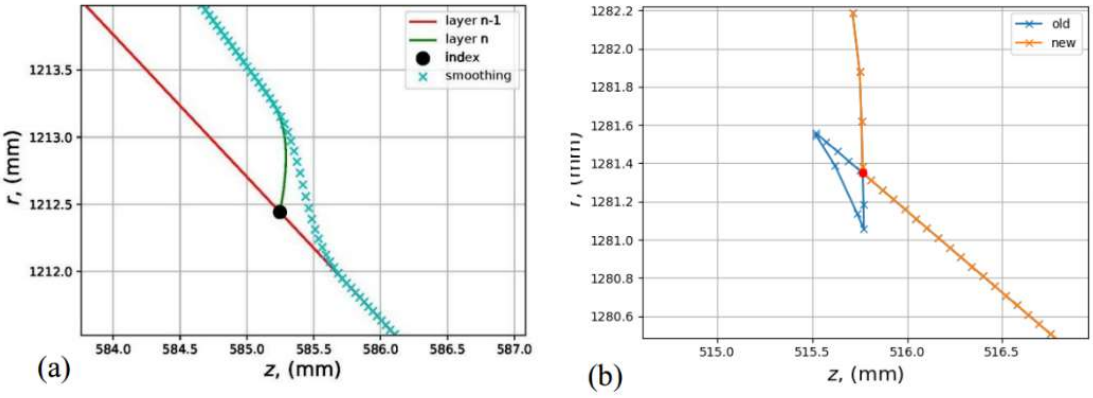

Figure 2. Correction methods proposed by Bizet et al. [7]: (a) redefinition of the layer's profile using a smoothing function, (b) elimination of loop irregularities due to convex zones.

While such corrections deal with the issue at hand from a numerical point of view, and make it possible to construct multi-sequence composite layers with increasing and/or decreasing initial winding angles, the final geometry can be inaccurately depicted in some cases, especially around the polar boss. Using the methodology proposed above and applying the correction methods on a test example with the following multi-layer composite sequence [30°, 35°, 40°$_2$, 90°, 40°, 55°, 40°, 20°, 10°, 90°], the resulting geometry is shown in Figure 3.

As can be observed in the overall composite shell shape, the smoothing function tends to create sharp edges at the end layers with the same initial angle, as is the case with the first 3 layers of 40°. On another note, the fourth 40° layer is stretched near the polar boss end, even though the layer's turn radius must end near the previous layers. This numerical extension overestimates

the amount of the composite near a critical area, adding more axial stiffness than experimentally found. In fact the exact trajectory of the fiber must lead to bridging, which is when the fiber line extends beyond the supporting surface and hangs freely, due to the tension of the fiber, as is shown in Figure 4. The subsequent trajectory of the fiber depends on parameters such as the angle reached before bridging and the curvature inside the concave circle (Figure 4(b)).

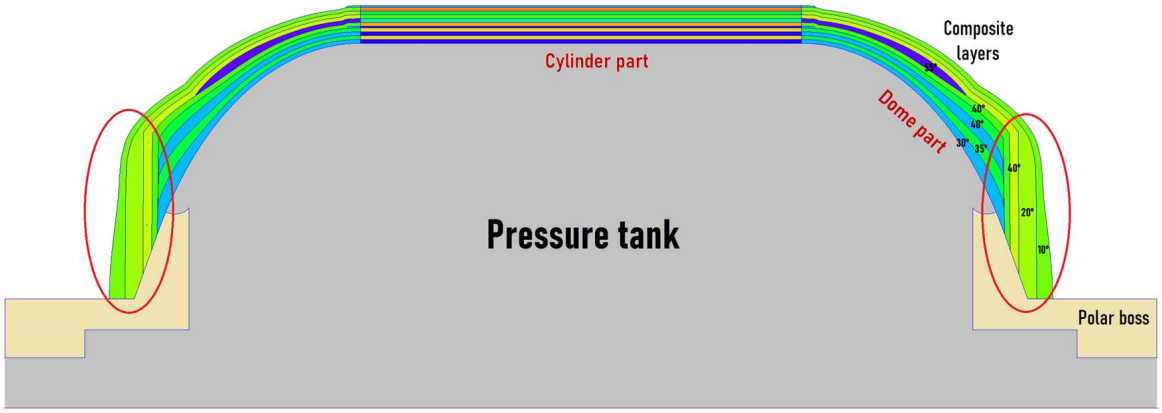

Figure 3. Composite shell of a pressure tank using a test sequence.

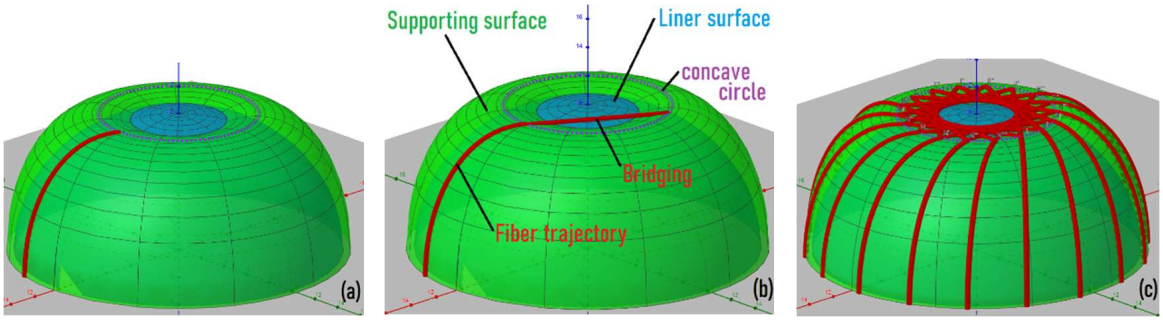

Figure 4. Fiber bridging: when the trajectory reaches the edge of a concave surface (a), bridging occurs between two points on the supporting surface (b) and forms a "virtual" supporting surface for the current layer (c).

3. Bridging solutions

In order to identify the points where any potential bridging happens, the supporting surface (or line in case of axisymmetric modeling) must be segmented into concave and convex parts. Using the equations provided above, and starting at the dome-cylinder connection, the layer's makeup is solved for the first segment which is always convex (if the entire supporting line is convex, no bridging exists). If at the end of a convex segment a concave surface exists, then 3 parameters must be determined in terms of the concave circle: 1) the radius of the concave circle r_c, 2) the angle found at the concave circle α_C, and 3) the flat-drop radius r_D. This last parameter is defined as the radius of the circle on the remaining supporting surface inside the concave zone, having the same z coordinate as the concave circle (if no circle is found, then r_D is equal to r_{boss} which is the radius at the end of the polar boss). This means that $r_D < r_C$ and $z_D=z_C$ always hold true. There are 2 main cases to be distinguished in bridging, depending on the value of α in relation to the critical value $\alpha_{C,lim}$:

$$\alpha_{c,lim} = \arcsin\left(\frac{r_D}{rC}\right) \quad (5)$$

3.1 Flat bridging

If 90° > α_C > $\alpha_{C,lim}$, this suggests that the angle is too big for the fiber line to fall another time on the remaining supporting surface. Since the fiber is taut by the winding machine, the trajectory will follow a strength line until falling on another point on the other side of the concave circle, as shown in Figure 4(a). Numerically, this translates into a *virtual* supporting line which extends beyond the real surface. For the flat bridging case, the turn-around radius and the winding angle evolution can be easily calculated following:

$$r_{turn} = r_C \times \sin \alpha_C \tag{6}$$

$$\alpha(r) = \arcsin\left(\frac{r_C}{r} \sin \alpha_C\right) \tag{7}$$

In this case, Wang's model can be used to compute thickness and the current layer's geometry is completely determined. The algorithm must then proceed to the next layer.

3.2 tilted bridging

If $\alpha_C < \alpha_{C,lim}$, a flat bridge cannot be constructed, as the remaining supporting surface hinders the straight line trajectory. In this case, the fiber must be slightly tilted with a slope that depends on the point at which the fiber rejoins the supporting surface, called the *falling edge* in Figure 5(a). On the other hand, and due to the tilt, the bridge line will start earlier than the concave edge, at the point called the *rising edge*. The main issue remains in determining the two edges.

There are no analytical solutions for this complex trajectory. Instead, a numerical approximation can be found. For this construction, we assume that the bridge, which remains straight between the two edges, belongs to a plane *which remains parallel to the axis of revolution*. This makes it possible to determine the exact geometry but induces slight deviations from the exact solution. The deviation, which can be corrected, is inversely related to the value of α_C and the flatness of the dome surface, but remains below 10% for moderate and high angles (> 10°).

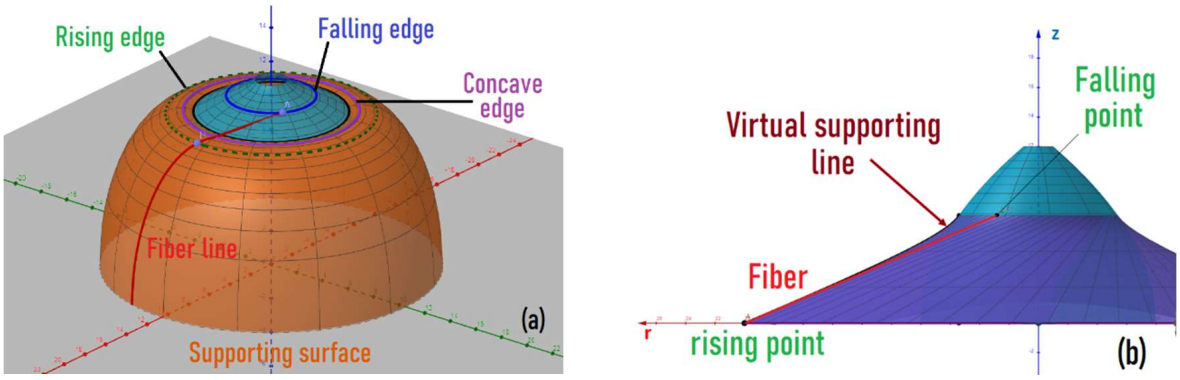

Figure 5. Tilted bridging exists when the angle falls below a critical value (a) and the subsequent virtual supporting line is curved (b)

First, we assume that the bridge starts at the concave circle. Using a parametric definition of the axisymmetric supporting surface and the trajectory of the fiber at the concave edge, we obtain the following differential equation:

$$\mathrm{K}(u) = \frac{dz}{du}(u) \times (u - u_C) - z(u) = 0 \tag{8}$$

with *u* the falling edge's radial position on the trajectory plane's intersection with the supporting surface, which is related to the axisymmetric radial coordinate *r* such as:

$$r = \sqrt{u^2 + (r_C - u)^2 \tan^2 \alpha_C} \tag{9}$$

Eq. (7) has 2 solutions for r = r_D, labelled u_{D1} and u_{D2}, which correspond to the trajectory plane's intersection with the supporting surface at the concave circle. By defining $u_{Ds} = (u_{D1} + u_{D2})/2$, any solution in the [$u_{D1}$, u_{Ds}] interval can be discarded as a potential position for the falling edge since the fiber trajectory must not intersect with the supporting surface. Since the function *K(u)* in Eq. (8) is continuous and differentiable, and by verifying that $K(u_{Ds}) < 0$ and $K(u_{D2}) > 0$, the LSODA algorithm guarantees a solution for Eq. (8). So, by determining the correct position *u*, the falling edge's position is found (blue circle in Figure 5(a)). However, the assumption that the rising point corresponds to r_C must be reevaluated due to the tilted bridge. Since the rising point's position (green circle in Figure 5(a)) must be found between the extremities of the convex segment, then the LSODA algorithm is repeated in a nested loop so that the bridge's tilt at the falling edge must correspond to the supporting surface's curvature. Once the coordinates (z_R, r_R) and (z_F, r_F) of the rising and falling edges are found, the *virtual* supporting line follows the equation:

$$r(z) = \sqrt{r_R^2 + r_{red}^2 \left(\frac{z - z_R}{z_F - z_R}\right)^2 - 2 r_R r_{red} \left(\frac{z - z_R}{z_F - z_R}\right) \cos \alpha_R} \tag{10}$$

with the reduced radius $r_{red} = r_R \cos \alpha_R - \sqrt{r_F^2 - r_R^2 \sin^2 \alpha_R}$. This equation translates the fact that the virtual supporting surface is naturally curved due to the tilt, as shown in Figure 5(b). Once the supporting surface is completely determined, the winding angle can be calculated. The direction vector of the taut fiber remains the same. However, as the winding angle is calculated between the fiber and meridian line (see Figure 1) which changes along the bridging line. In this case, the direction vector of the meridian line depends on the curvature of the bridge, i.e. the partial derivative of Eq. (10). Once the two vectors are computed, the angle is defined as:

$$\alpha(r) = \operatorname{acos}\left(\frac{\vec{V}_{merid}(r)\, \vec{V}_{fiber}}{\|\vec{V}_{merid}(r)\| \|\vec{V}_{fiber}\|}\right) \tag{11}$$

As it is the case for the flat bridging, Wang's model can be used to compute the thickness for the bridging part. However, since the winding angle has not reached 90°, the turn-around radius must still be determined. Eq. (1) will be solved on the remaining part of the new convex segment, with λ set to 0 at the falling edge. If the turn-around radius is not found before the next concave circle, then a new bridge forms.

Figure 6 shows the results of bridging over the complex geometry of the test tank presented in Figure 3. As can be observed in this case, gaps are present due to bridging taken into account. For the first 3 layers, the supporting surface is always convex and the increasing winding angle leads to no bridging. Moreover, layers with the same winding angle (40°) have almost the same turn-around radius, thus avoiding the numerical errors imposed by the smoothing function as proposed in other models. On the other hand, we observe small flat bridges near the concave surface. In addition to that, when the winding angle drops to 20°, the new layers covers almost the entire composite with a flat bridge, creating a gap which naturally forms due to the taut fiber tow. As the angle decrease to a very low value (10°), the last layer covers the entire dome with a tilted bridge. This method leads to better estimation of the composite thickness near the end

  doi:10.5075/epfl-298799_978-2-9701614-0-0

of the polar boss. The gaps formed can either be left empty or meshed to simulate resin-filled pouches, which occasionally occur in the winding process.

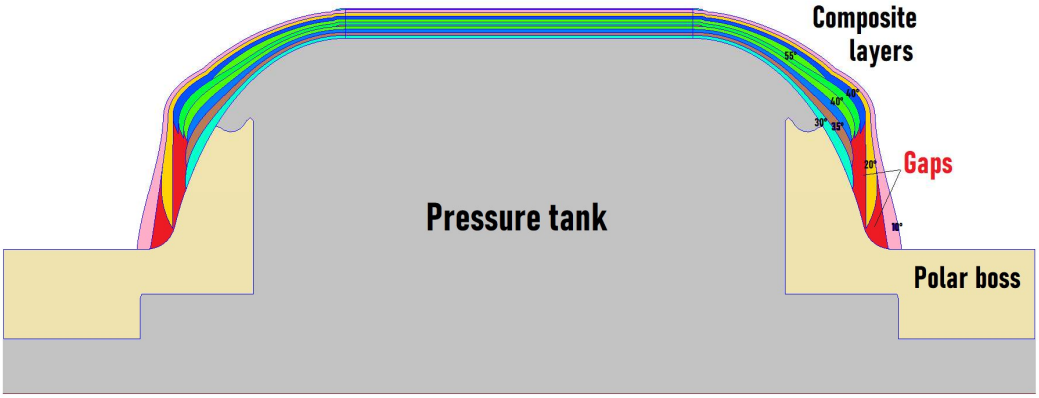

Figure 6. Multi-sequence composite lay-up with bridging over a complex geometry.

4. Acknowledgments

This research is supported by the French Space Agency (CNES).

5. References

1. Liu N, Ma , Liu F, Huang W, Xu B, Qu L. Progress in research on composite cryogenic propellant tank for large aerospace vehicles. *Composites Part A: Applied Science and Manufacturing* 2021; 143.
2. Azeem M, Haji Ya H, Azad Alam M, Kumar M, Stabla P, Smolnicki M, Lokman G, Khan R, Ahmed T, Ma Q, Sadique MR, Mokhtar AA, Mustapha M. Application of Filament Winding Technology in Composite Pressure Vessels and Challenges: A Review. *Journal of Energy Storage 2022;* 49.
3. Leh D, Saffré P, Francescato P et Arrieux R, Multi-sequence dome lay-up simulations of hydrogen hyper-bar composite pressure vessels. *Composites: Part A.* 2013; 53:106-117.
4. Berro Ramírez JP. 700 bar type IV high pressure hydrogen storage vessel burst Simulation and experimental validation. *International Journal of Hydrogen Energy.* 2015; 40:13183-13192
5. Almeida Jr JHS, St-Pierre L, Wang Z, Ribeiro ML, Tita V, Amico SC, Castro SG. Design, modeling, optimization, manufacturing/testing of variable-angle filament-wound cylinders. *Composites Part B: Engineering*. 2021; 225.
6. Zu L, Xu H, Zhang B, Li D, Zi B. Design of filament-wound composite structures with arch-shaped cross sections considering fiber tension simulation. *Composite Structures*. 2018; 194: 119-125.
7. Bizet L, Saffré P, Mathis K, Halm D, Gueguen M, Francescato P. Design of composite filament wound pressure vessels: management of singularities in multi-sequence dome lay-up simulations. *ECCM18 - 18th European Conference on Composite Materials*, Athens, 2018.
8. Wang R, Jiao W, Liu W et Yang F. A new method for predicting dome thickness of composite pressure vessels. *Journal of Reinforced Plastics & Composites.* 2010; 3345-3352.
9. Koussios S. Filament Winding: a Unified Approach, Delft University, 2004.
10. Brown PN, Hindmarsh AC, Reduced storage matrix methods in stiff ODE systems. *Applied Mathematics and Computation. 1989;* 31:40-91.

SELF-HEALING MULTILAYER COMPOSITES AND NANOCOMPOSITES FOR SPACE APPLICATIONS: A STUDY ON DAMAGE RECOVERY PERFORMANCE AFTER SIMULATED SPACE RADIATION EXPOSURE

Laura Pernigoni[a], Greta Wallin[a], Gabriele Magugliani[b], Eros Mossini[b], Ugo Lafont[c], Antonio Mattia Grande[a]

a: Department of Aerospace Science and Technology, Politecnico di Milano, via La Masa 34, 20156 Milan, Italy – laura.pernigoni@polimi.it, antoniomattia.grande@polimi.it
b: Department of Energy, Politecnico di Milano, via La Masa 34, 201556 Milan, Italy
c: European Space Research and Technology Centre, European Space Agency, Keplerlaan 1, PO Box 299, 2200 AG Noordwijk, The Netherlands

Abstract

In recent decades, the possibility of integrating self-healing materials into inflatable and deployable space structures has drawn the attention of the scientific community. This solution would make human activity in space safer and increase spacecraft operational life and autonomy. Nevertheless, the action of space environment may deteriorate these materials.

The presented work analyzes the autonomous repair ability of candidate self-healing polymers, used as nanocomposite matrices or coupled with an elastomer or aramid fabric into a multilayer. Self-healing is evaluated through in-situ flow rate measurements after puncture damage. In the multilayer case, the tests are then repeated on gamma-ray irradiated samples to study the variation of self-repairing and functional properties after exposure to simulated space radiation.

Results show higher repair ability in systems with lower viscous response, and decreased healing performance in the irradiated samples, hence requiring a further analysis of the effects of space environment on the presented materials.

Keywords: self-healing polymers; multilayer; nanocomposites; space radiation; multifunctionality

1. Introduction

Inflatable and deployable structures have recently been considered for space applications, as they would ensure reduced mass and launch cost due to their light weight and high packing efficiency. Nevertheless, their structural integrity might be compromised by environmental factors such as vacuum, atomic oxygen, radiation, and micrometeoroids and orbital debris (MMOD). In particular, impacts with MMOD could generate punctures and cuts leading to depressurization of these structures, which would be a significant issue for long-term crewed missions. The integration of self-healing polymers into inflatable structures seems a promising solution to enhance the duration and safety of spacecraft for future missions, but these materials could themselves significantly change their properties under the action of space environment. As an example, they could undergo degradation due to their exposure to ionizing radiation from Galactic Cosmic Rays (GCR), Solar Particle Events (SPE) and Van Allen Belts (1). These aspects must hence be considered to design and characterize novel solutions for future space missions (2,3).

  doi:10.5075/epfl-298799_978-2-9701614-0-0

The aim of the here presented work is to experimentally characterize the self-healing performance of polyurea-urethanes and a supramolecular polymer with intrinsic autonomic self-healing properties, and to assess their possible applicability to space. This research focuses on puncture tests, as they best represent MMOD impacts, analyzing their effect on different specimen configurations (4). Multilayer and nanocomposite samples are investigated alongside reference neat polymer specimens. After the initial puncture tests, some of the promising specimens are exposed to 100 Gy radiation doses before being tested again. A comparison is then made between pre and post irradiation results, to assess the possible changes of healing performance after exposure to radiation.

2. Materials and experimental setup

2.1 Self-healing polymers

Four poly(urea-urethane)s (PUUs) with similar formulation and fixed disulphide content but different crosslinking densities are analyzed (Table 1). They are obtained from different combinations of trifunctional and difunctional isocyanate-terminated pre-polymers PU-6000 and PU-4000, organized into networks connected by aromatic disulphides linkages and containing urea related H-bonds (5). These pre-polymers can be synthesized trough interaction of poly(propylene glycol) (PPG) and isophorone diisocyanate (IPDI) in the presence of the dibutyltin dilaurate (DBTDL) catalyst (6).

Table 1 : PUUs formulations and basic properties (5).

Sample	Composition [wt%]			ν [10^{-4} mol/cm^3]	T_g [°C]
	PU-6000	PU-4000	Linker		
PUU 100	93.8	0	6.2	2.35	-58.8
PUU 90	84.4	9.4	6.2	2.05	-59
PUU 80	75.1	18.7	6.2	1.77	-59.4
PUU 70	65.7	28.1	6.2	1.50	-60.1

Reverlink® HR contains both covalent bonds and supramolecular hydrogen-bonding crosslinks (50:50 mol%). It is obtained from the combination of supramolecular pre-polymer SP-50, diglycidyl ether of bisphenol A (DGEBA) resin and 2-Methyl Imidazole (2-MI) catalyst, with nominal proportions reported in Table 2 (7,8). The non-cured material is heated to 90 °C, poured into a Teflon® mold and then cured at temperatures in the 120-150 °C range. Its glass transition temperature is between 5 °C and 15 °C (9,10).

Table 2 : Self-healing element nominal components (7).

Component	SP-50	DGEBA	2-MI
Mass [g]	23.900	6.020	0.004

2.2 Nanocomposites and multilayers

Nanocomposites are considered as they could reduce the dose of incoming radiation reaching the interiors of a spacecraft. The used nanofiller is Nanocyl® NC7000™ consisting of multiwalled

  doi:10.5075/epfl-298799_978-2-9701614-0-0

carbon nanotubes (MWCNTs) obtained through catalytic chemical vapor deposition (11). Configurations with Reverlink® matrix and CNT concentrations from 0.1% to 1% are studied to look for a trade-off between radiation shielding and self-healing behavior of the material, as the insertion of these fillers usually decreases the healing performance.

Multilayer specimens are investigated to assess the effect of coupling the polymers with another layer on the self-healing performance. The polymer is coupled either with aramid fabric or a 1.6 mm-thick silicone elastomer. In the aramid-Reverlink® case the resin is poured on top of the aramid fibers, while for the remaining configurations the already cured polymers are re-heated and coupled with the elastomer by applying pressure on the layers. For the sake of clarity, the elastomer-Reverlink® multilayer configuration will be here indicated with the ME label.

2.3 Puncture tests

The Reverlink® specimens have a nominal diameter of 60 mm and variable thickness, while the PUU samples have a nominal diameter of 20 mm. In the multilayer case with PUU, 1 mm-thick polymeric layers are used. Examples of specimens are shown in Figure 1.

(a) (b) (c) (d)

Figure 1 : Specimens examples - (a) Neat polymer, (b) nanocomposite and (c)(d) multilayers.

After undergoing a 24-hour drying cycle to remove humidity all samples are placed between two polyamide films and mounted on an experimental system for the evaluation of the self-healing performance through acquisition of the resulting leakage flow rate (Figure 2). The samples are fixed on the central cylindrical part of the device and pressurized to 30 kPa relative pressure with continuous air supply to reproduce the conditions inside a space suit, used as a reference. A vertical sinusoidal motion is imposed to the puncheon, setting 9.62 mm amplitude and 0.14 Hz frequency to obtain a velocity of 8.467 mm/s when the puncheon penetrates the specimen, coherently with the ASTM F1342/F1342M-05 standard. Each specimen is tested three times, and maximum and minimum flow rates, the time between them and the air volume lost in a reference time are collected as self-healing performance indicators.

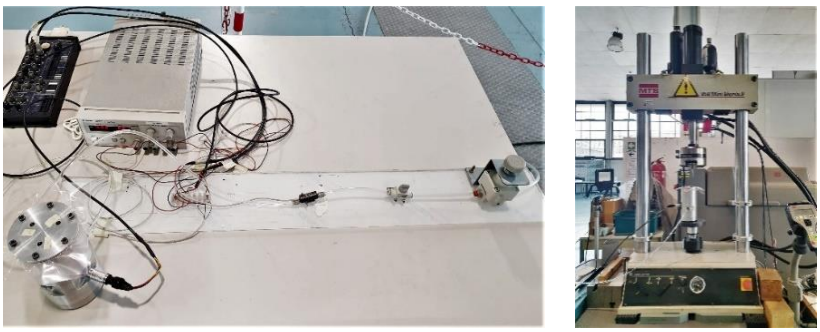

(a) (b)

Figure 2: (a) Testing system; (b) MTS 858 Mini Bionix® II machine for puncture tests.

2.4 Experimental setup for irradiation

The neat PUU samples are exposed to 100 Gy radiation doses emitted at 11.1 Gy/min rate by a Cobalt-60 source placed at a distance of 60.96 cm from the target. The irradiation process is performed in air, and the samples are subsequently stored in a cold room to preserve chemical bonds deterioration generated by exposure to gamma rays.

3. Experimental results and discussion

3.1 Puncture tests on non-irradiated samples

Results obtained for the nanocomposites class containing up to 1% CNTs (Figure 3) show that the self-healing ability is mainly related to the specimen's thickness rather than to the concentration of CNTs. Furthermore, complete healing is not reached, and practical issues were also encountered when trying to increase the amount of nanotubes, making this solution less appealing than the multilayer one. In particular, it is observed that coupling the analyzed polymers with the elastomeric layer increases the self-healing performance, while the aramid fabric does not provide a comparable improvement. This is justified by the elastomer's springback behavior, which accelerates the self-healing process by promoting hole closure in the punctured region (Figure 4, Figure 5). In these terms, the multilayer configuration containing the PUU 90 polymer is characterized by the highest average performance (Table 3). This is in contrast with what is found when considering the neat polymers, as in that case the PUU 100 has a slightly better behavior than PUU 90. This might be due to repeatability issues in the experiments and needs to be further investigated.

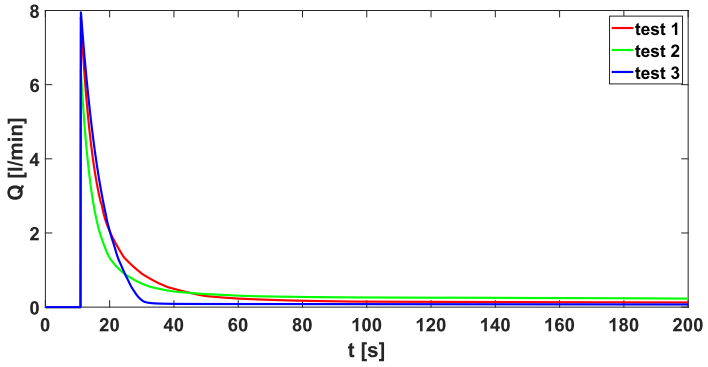

Figure 3: Puncture test results for the CNT nanocomposite.

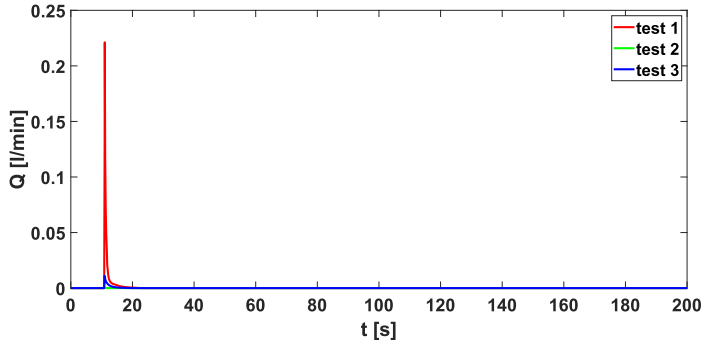

Figure 4: Puncture test results for the ME configuration (Reverlink®-elastomer multilayer).

  doi:10.5075/epfl-298799_978-2-9701614-0-0

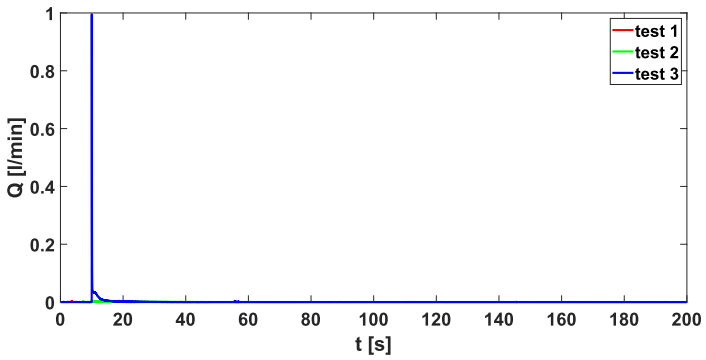

Figure 5: Puncture test results for the PUU 100-elastomer multilayer.

Table 3 : Average results obtained for elastomeric multilayer and nanocomposite specimens.

		Multilayer with elastomer				Nanocomposite
Data	ME	PUU 70	PUU 80	PUU 90	PUU 100	1% CNT
Max. flow rate [l/min]	0.0777	0.4017	0.1860	0.0411	0.3352	7.3830
Min. flow rate [l/min]	0	0	0	0	0	0.1423
Δt to min. flow rate [s]	7.96	99.62	11.44	9.08	10.47	200.00
Leaked volume [l]	0.0005	0.0059	0.0020	0.0004	0.0012	1.2519

The average performance parameters related to ME and PUU 90 multilayers are then compared with results from previous studies (4,12) (Table 4). A space suit bladder with a thickness of 0.289 mm is also considered as a reference. Overall, the best results are related to the PUU 90-elastomer multilayer, but the difference with the ME configuration is small. In both cases, the minimum flow rate is null in all repetitions and the average time to get to it is lower than 10 s, significantly below the healing times of the other materials. The average volume of leaked fluid is two to four orders of magnitude below the other specimens, indicating coupling with a silicone elastomer as a promising solution.

Table 4 : Comparison with results from previous studies (4,12).

Material	Max. flow rate [l/min]	Min. flow rate [l/min]	Time to min. flow rate [s]	Leaked volume [l]
ME average	0.0777	0	7.96	0.0005
PUU 90 multilayer avg.	0.0411	0	9.08	0.0004
Reverlink® + aramid (4)	1.589	0.092	307.13	0.3377
Bladder	2.401	1.032	300.50	3.8968
Sylgard® 30 mil	0.208	0.054	110.00	0.2273
Conathane® 30 mil	1.727	0.249	222.25	0.9960
Rucothane® 15 mil	3.866	1.497	349.70	5.773
TyrLyner® 30 mil	4.523	0.085	153.75	0.524

  doi:10.5075/epfl-298799_978-2-9701614-0-0

3.2 Puncture tests on irradiated samples

Comparison of average results related to irradiated and non-irradiated specimens of the same thickness shows that a dose of 100 Gy already significantly deteriorates the healing performance (Table 5, Figure 6). In general, stronger degradation is observed in materials with a higher content of difunctional units. Overall, the best performing polymer is PUU 100, as its strong springback response ensures short healing times and a reduced air leakage after perforation.

Table 5 : Puncture tests results for irradiated and non-irradiated neat PUU 100 samples.

Irradiated	Max. flow rate [l/min]	Min. flow rate [l/min]	Time to min. flow rate [s]	Leaked volume [l]
1	2.8231	0.0281	189.69	0.1453
2	3	0.0171	189.57	0.1003
3	2.6221	0.0503	188.61	0.2861
Non irradiated				
1	1.2549	0	5.66	0.0025
2	1.7352	0.0147	189.80	0.1057
3	1.5489	0	4.84	0.0017

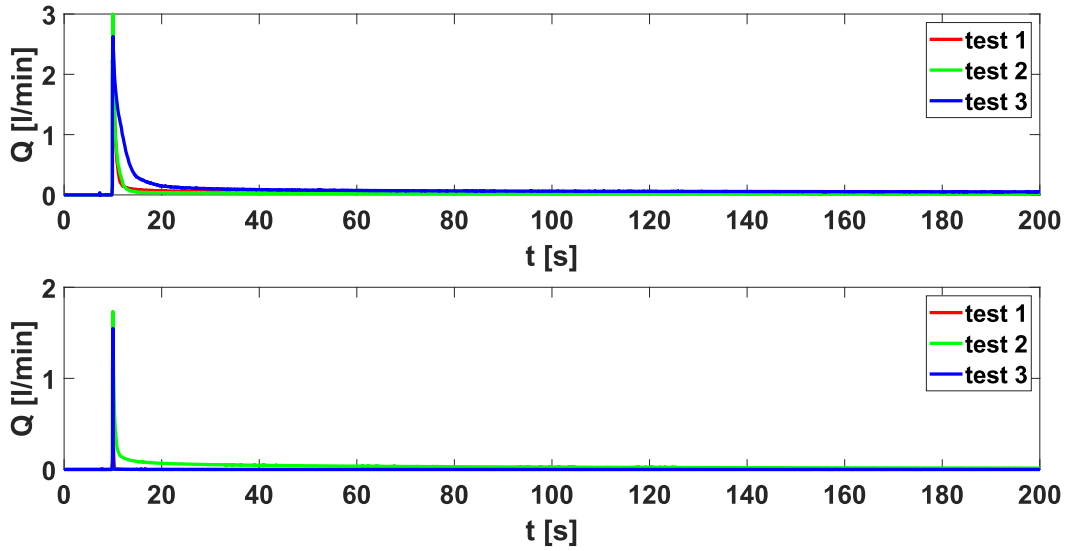

Figure 6: Puncture tests comparison for irradiated and non-irradiated neat PUU 100 samples.

4. Conclusions

4.1 Final considerations

Results obtained through coupling with the elastomeric layer show significant improvements with respect to previous studies. This type of configuration can be optimized through a trade-off between thickness reduction and preservation of the self-healing properties.

  doi:10.5075/epfl-298799_978-2-9701614-0-0

Furthermore, polymers containing a higher content of difunctional moieties present a higher viscoelastic response and a better healing efficiency, while specimens with higher cross-linking density are characterized by a larger elastic and subsequent springback response. An optimal healing performance is hence ensured by a good trade-off between elastic and viscous behavior, as the former allows fast contact between the edges of a damaged area, and the latter is necessary for sealing. Overall, the most promising solution is the multilayer configuration coupling the elastomer with PUU 90. In addition, results are highly influenced by local thickness, while humidity is crucial only when considering Reverlink®.

Concerning the effects of space radiation, it can be stated that even a limited dose such as 100 Gy is sufficient to deteriorate the materials' healing performance.

As a general conclusion, a self-healing layer could indeed significantly increase safety, reliability, and lifetime of spacecraft for future missions. However, further studies must be carried out to succeed in implementing this solution.

4.2 Future work

To achieve more accurate and repeatable experimental results, the tests could be performed in a controlled environment, for example by including the test apparatus in a vacuum chamber. As a matter of fact, self-healing polymers are in general sensitive to factors such as temperature and humidity. The variability of the results, which is partially due to the non-uniformity in the samples' thickness, could be limited through more accurate manufacturing techniques.

Specimens could be subjected to higher radiation doses and dose rates to better evaluate how radiation affects self-healing. To prevent material oxidization and analyze the evolution of radicals, irradiation could be performed in an inert environment, such as in liquid nitrogen. In general, further characterization will be performed to assess and better understand the effects of space environment on the self-healing ability of the analyzed materials. In these terms, the samples will also be exposed to UV irradiation, thermal cycling, atomic oxygen.

Acknowledgements

This research was supported by ESA, contract No. 4000132669/20/NL/MH/ic. The authors are grateful to Arkema for supplying Reverlink®, and to Prof. Mario Mariani and the Radiochemistry and Radiation Chemistry Laboratory at Politecnico di Milano for the help with the irradiation tests.

5. References

1. Rask J, Vercoutere W, Navarro BJ, Krause A. Space faring: the radiation challenge, an interdisciplinary guide on radiation and human space flight. 2008.

2. Ghosh SK, editor. Self-healing materials-Fundamentals, design strategies, and applications. Wiley-VCH; 2009.

3. Pernigoni L, Lafont U, Grande AM. Self-healing materials for space applications: overview of present development and major limitations. CEAS Sp J. 2021;(0123456789).

4. Pernigoni L, Grande AM. Development of a supramolecular polymer based self-healing multilayer system for inflatable structures. Acta Astronaut [Internet]. 2020;177(April):697–706. Available from:

https://doi.org/10.1016/j.actaastro.2020.08.025

5. Grande AM, Martin R, Odriozola I, van der Zwaag S, Garcia SJ. Effect of the polymer structure on the viscoelastic and interfacial healing behaviour of poly(urea-urethane) networks containing aromatic disulphides. Eur Polym J. 2017;97.

6. Rekondo A, Martin R, Ruiz de Luzuriaga A, Cabañero G, Grande HJ, Odriozola I. Catalyst-free room-temperature self-healing elastomers based on aromatic disulfide metathesis. Mater Horiz [Internet]. 2014;1(2):237–40. Available from: http://xlink.rsc.org/?DOI=C3MH00061C

7. Montarnal D, Tournilhac F, Hidalgo M, Leibler L. Epoxy-based networks combining chemical and supramolecular hydrogen-bonding crosslinks. J Polym Sci Part A Polym Chem [Internet]. 2010;48(5):1133–41. Available from: https://onlinelibrary.wiley.com/doi/full/10.1002/pola.23870

8. Sordo F, Mougnier SJ, Loureiro N, Tournilhac F, Michaud V. Design of Self-Healing Supramolecular Rubbers with a Tunable Number of Chemical Cross-Links. Macromolecules. 2015;48(13):4394–402.

9. Sordo F, Michaud V. Processing and damage recovery of intrinsic self-healing glass fiber reinforced composites. Smart Mater Struct [Internet]. 2016 Aug 1;25(8):084012. Available from: https://iopscience.iop.org/article/10.1088/0964-1726/25/8/084012

10. Arkema. Reverlink supramolecular technology. p. 1–8.

11. Nanocyl. NC7000™–Technical Data Sheet. 2021.

12. Fredrickson TH. NASA research announcement final report for space suit survivability enhancement. 1998.

VON ROLL HOLISTIC APPROACH TO SUSTAINABLE COMPOSITES DEMONSTRATED WITH NEW SOLUTIONS FOR THE TRANSPORTATION SECTOR

Fiorenzo Lenzi

a: Von Roll – fiorenzo.lenzi@vonroll.com

Abstract: *The work shows how the sustainability has been the key focus for Von Roll in the development of new composites specifically for the Aerospace and the Automotive market.*

After extensive research, Von Roll presents new epoxy based prepregs for the aerospace interior market that have been developed to substitute phenolic prepregs, in order to reduce the environmental impact of their production process and to reduce the health and safety issue related to their handling. Another example is the use of more sustainable approaches for the development and manufacturing of Mica based products for Li-Ion batteries protection for the e-mobility and Automotive applications.

Keywords: prepreg; epoxy; Mica; battery protection

1. Epoxy prepreg for cabin interiors

Today, most of the prepreg chemistry used in Aerospace for cabin interior parts requires the use of a large amount of solvents when converting the resin into the prepreg. But solvents are harmful for the worker´s health, safety, as well as for the environment since they increase the volatiles emissions. Furthermore, they cause a poor surface quality of the final composite part which would need additional operations before the final assembly. Solvents also have a negative impact on the glass transition temperature of the cured composite and the mechanical performance at high temperature. Traditionally, phenolics were used in the prepreg for cabin due to their excellent FST (Fire, Smoke and Toxicity) properties. But they release phenol and formaldehyde when they cure, and without proper precautions, this also leads to health issues.

For next generation cabin interior materials, the industry targets healthier, cost-efficient, greener and more sustainable products all over the value chain. And this is where it started: Von Roll aim was to create a 100% solvent, phenol and formaldehyde -free range of prepregs with low heat release rate and FST values, which would satisfy the challenging fire protection and retardancy requirements requested by the certification regulation while delivering a better mechanical performance also in terms of toughness and impact requirements for structural applications like floor panels.

Thus, Von Roll developed the cost-efficient range of EP200 prepreg series with fire-retardant epoxy-based systems. Prepreg can be cured in vacuum bag only on in press at a temperature of 140-150°C for 30 minutes.

  doi:10.5075/epfl-298799_978-2-9701614-0-0

The prepreg are based on resin systems, that clearly are overcoming the traditional limitation of phenolic based products, provide very high shelf-life, possibility for storage at ambient conditions and allow to use impregnation processes that are more than two times faster than the ones based on vertical towers, thus translating into 50% lower production cost and a 200% higher productivity on the new Von Roll production line in Breitenbach, Switzerland.

For tradition prepreg processes targeted to cabin interior, using resin systems diluted in solvent in a quantity up to 50% by weight, the process requires the removal of the solvent in a drying heated section of the prepreg machine. This process in the case of using acetone, MEK or similar, requires these solvents to be removed from the prepreg and burned with resulting high emission of CO2. In addition, in the case of phenolic process, additional emissions are generated because of the need to reduce the amount of other volatiles (phenol and water) that can be already released from the resin chemistry, to a value lower that 5% by weight of the prepreg. The Von Roll process eliminates such need, providing then no need for burning – no CO2 emission, cost reduction and a more sustainable production comparing to tradition prepreg processes

Used in various aircraft cabin interiors applications, the prepreg series includes different variants today: EP200 designed for cargo and cabin floor applications, EP210 designed for air ducting applications, EP220 and EP230 designed for cabin interior segments where low heat release values are required such as ceiling panels, lavatories, walls and seat components (see figure 1).

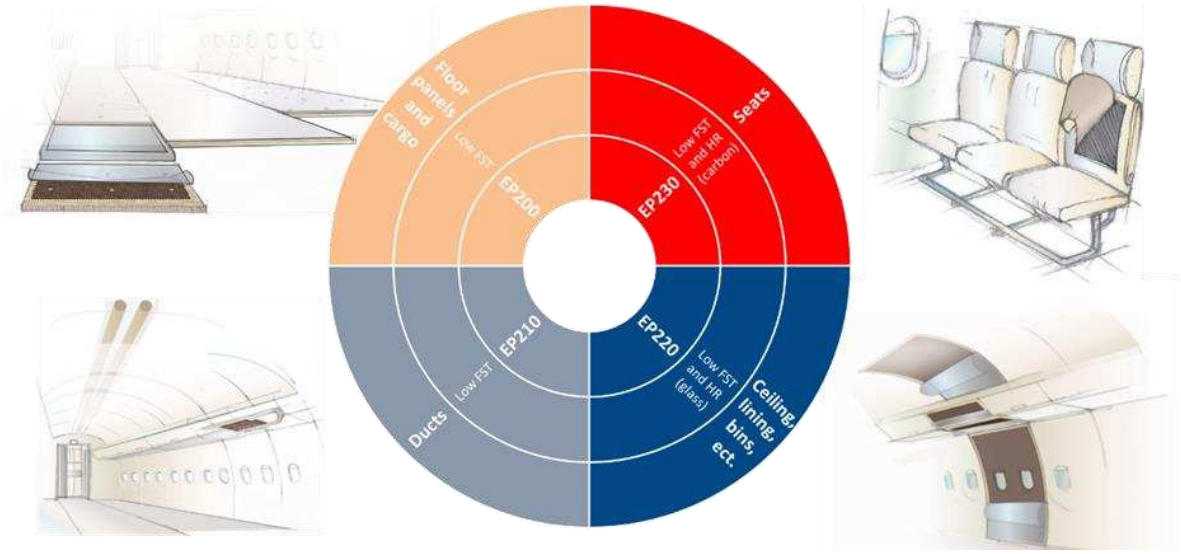

***Figure 1**. Applications of epoxy prepreg for various aircraft interior applications.*

The EP200 prepreg suitable for sandwich construction shows flame time after vertical burning, smoke and toxicity values that are minimized by 70% compared to the maximum allowed by the industry standards and an excellent bonding to the honeycomb core with a measured climbing drum peel value of more than 250 N/75mm when tested on a sandwich with two top and bottom composite skins according to EN 2243-3 test standard.

One of the prepregs (EP210) is a system destined for ducts manufacturing with improved fire properties, and low smoke values which satisfies the regulation of up to 2 mm thick parts. A

measured value of smoke density emission of about 80 Ds was measured when a part of 1,7 mm was measured in flaming mode according to 14 CFR 25, Appendix F, Part V. The combination of high tack and resin flow allows the product to be used effectively for air-conditioning ducting construction, without the use of autoclave or high pressure.

Used in various aircraft cabin interiors applications, EP220 and EP230 generate a 60% improvement in the interlaminar shear strength performance and 20% in the sandwich flexural strength comparing to phenolics, which allows for designing interior parts with less weight (see figure 2).

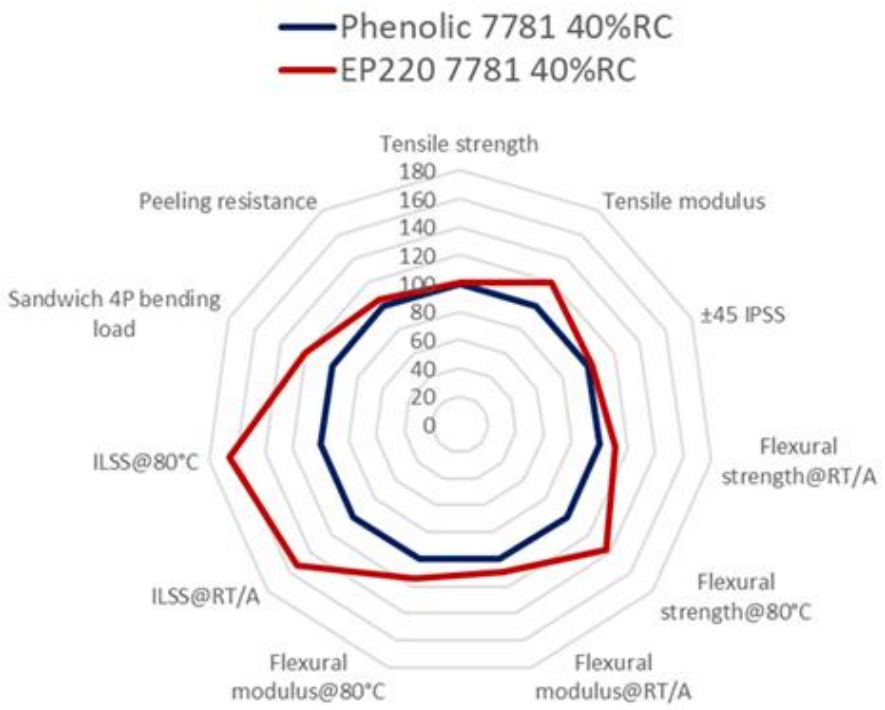

***Figure 2**. Comparative chart between the properties of EP220 reinforced with 7781 US style standard modulus glass fabric at 40% of resin content in weight and a similar product manufactured with the standard phenolic resin.*

On selected critical lay-ups, a composite manufactured with EP220 epoxy resin and 7781 US style glass fabric reinforcement showed a peak heat release rate value which is lower than 45 KW/m^2 and a heat release integral value during 2 minutes which is lower than 45 KW min/m^2, generated when the material is tested in accordance to the heat release rate (OSU) test for 14 CFR 25, Appendix F, Part IV. These values are almost an order of magnitude lower comparing to standard epoxy resins, demonstrating that a significant benefit is achieved in the flammability performance for this new epoxy based materials In addition such materials satisfy all the other stringent FST requirements for cabin interior applications (see table 1).

  doi:10.5075/epfl-298799_978-2-9701614-0-0

***Table 1**. FST and Heat release values for sandwich construction with 2 plies per side EP220 reinforced with 7781 US style, core 3.2 – 48 kg/m3 9.4 mm NOMEX honeycomb.*

Properties	**Test norm**	**Unit**	**Value**	**Standard industry requirement**
Flammability, 12 s vertical - burn length	AITM 2.0002A	mm	50	< 200
Flammability, 12 s vertical - after flame time		s	2	< 15
Flammability, 12 s vertical - drip flame time		s	0	0
Smoke density - flaming mode 4 min	AITM 2.0007	D_s	60	< 200
Toxicity - HCN	AITM 3.0005	ppm	2	< 150
Toxicity – CO		ppm	120	< 1000
Toxicity - NO_x		ppm	20	< 100
Toxicity - SO_2/H_2S		ppm	0	< 100
Toxicity – HF		ppm	0	< 100
Toxicity – HCl		ppm	0	< 150
Heat release rate: maximum in 5 minutes	AITM 2-0006	kW/m^2	45	< 65
Heat release - within 2 minutes		$kW.min/m^2$	45	< 65

Using the Von Roll new prepregs allows to save up to 30% of the total part manufacturing costs because they can be stored longer at ambient conditions and because no pinhole defects on the surface are occurring, thus saving extensive labor cost associated with re-working on those parts to achieve the high surface quality requirements for cabin interior parts. Finally, the use of these prepregs for seat applications or railway market will open possibilities for larger adoption of composites with improved sustainability and a weight reduction of 30% for components traditionally manufactured with metals.

2. Mica based composites for thermal protection applications

Another example of sustainable use of raw materials is related to the use of Mica material for the manufacturing of products with high fire barrier and thermal protection applications.

Mica are a group of minerals whose outstanding physical characteristic is that individual mica crystals can easily be split into extremely thin elastic plates. This characteristic is described as perfect basal cleavage. Mica is common in igneous and metamorphic rock and is occasionally found as small flakes in sedimentary rock. Previous studies have been carried out to describes the compositions of the rock-forming Micas in the, correlating them to their physical and chemical properties [1-2]. The most common types of Mica minerals are Phlogopite and Muscovites: both show exceptional flame-resistance properties, and can easily accommodate peak temperatures of up to 1,000 °C.

  doi:10.5075/epfl-298799_978-2-9701614-0-0

Mica is extracted from mines and after extraction and collection, Von Roll processes the material for manufacturing a mica paper with a grammage from 25gsm to 380gsm held together by surface (Van der Waals) forces only. This complex process relies on controlling important parameters: composition of chemical pulping used for treating the Mica flakes, the grammage of the paper and the mica distribution.

Then prepreg materials comprising of 90 % mica impregnated with a specific high-temperature-resistant binder are manufactured; when this prepreg is exposed to high temperatures, its resin content breaks down, without impairing the high-temperature fire barrier and insulating properties of mica. The resulting products has found application such as for burn-through insulation element for blankets for aviation or for battery protection. Moreover, the mica paper is chemically neutral, non-toxic and entirely halogen-free. It shows excellent resistance to water, acids (excluding sulphuric acid), bases, mineral oils and solvents.

The pictures below showed the process of getting from a rock to a final insulation material.

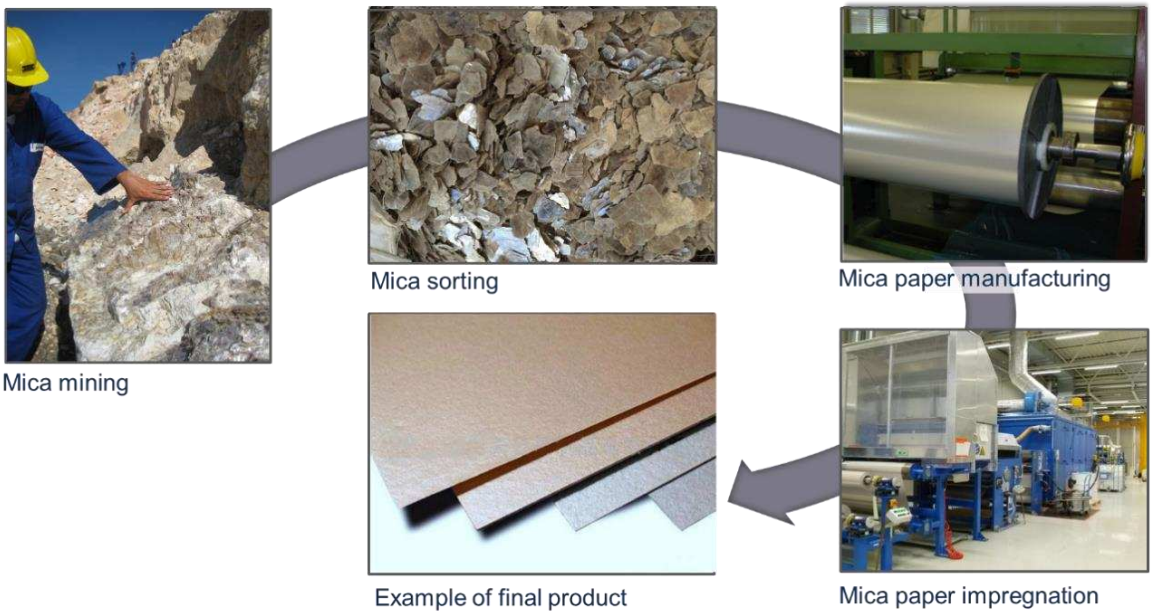

***Figure 3**. Mica processes from extraction to conversion in final Von Roll products.*

The use of such technology translates into the possibility for manufacturing key protective elements for battery applications, such as battery and module cover and cell spacer insulating materials. New Von Roll rigid Mica plates where developed using Muscovite Mica from Brazilian mines and were tested for checking flame resistance over a time of 15min. No burn-through can be observed if a flame with a temperature over 1000°C is placed under a Mica based composite of about 1mm thickness, with a stream of ablative particles (figure 4). The Von Roll test is simulating the condition where a thermal event is generated because of failure of a battery cell or module in an electrical vehicle.

The plates where manufactured by pressing several sheets of silicone based Mica reinforced prepreg. The test results showed the effect of high grammage of Muscovite papers used for

  doi:10.5075/epfl-298799_978-2-9701614-0-0

manufacturing and how they contribute to act as fire barrier and to resist to the steam of the hot ablative particles.

Figure 4. Von Roll Automotive set-up to test burn-through resistance of Mica panels subjected to simulated thermal event with flame temperature above 1000°C.

3. Conclusion

New Von Roll epoxy prepreg products would provide significant benefits in comparison to state-of-the art phenolics for aircraft application and would allow for less HSE issue, less CO2 emission, reduced manufacturing costs and improved sustainability. Other example of sustainability is the use of a g Mineral such as Mica, as reinforcement of composites for the protection of key elements such as batteries in electrical vehicles. This remains part of the company strategy to support the transportation industry to achieve their sustainability goals, in reducing the CO2 emissions for a better compliance with environmental goals, and to satisfy market needs for long-durable solutions for constantly improved passenger safety and comfort.

Acknowledgements

Composites team, Von Roll Schweiz AG, Passwangstrasse 20, CH 4226 Breitenbach, Switzerland.

4. References

1. P.M.Huang, M.K.Wang, MINERALS, PRIMARY, Encyclopedia of Soils in the Environment 2005
2. W. A. Deer, FRS; R. A. Howie; J. Zussman, An Introduction to the Rock-Forming Minerals, DOI: https://doi.org/10.1180/DHZ

DESIGN FOR INNOVATIVE AND COST-EFFICIENT MANUFACTURING OF COMPOSITE SANDWICH STRUCTURES WITH FOAM MOLDED CORES FOR HIGH-RATE PRODUCTION OF WING MOVEABLES

Roland M., Hinterhölzl[a], Karim, Shehata[a], Franz M., Sendner[b], Markus, Wolfahrt[c], Gernot, Schneiderbauer[b], Jonathan, Glinz[a] ,Karl H., Semlitsch[d], Michel, Thor[a]

a: University of Applied Sciences Upper Austria – roland.hinterhoelzl@fh-wels.at
b: FACC Operations GmbH
c: PCCL Polymer Competence Center Leoben GmbH
d: LiteCon GmbH

Abstract: *In sandwich structures, aramid paper or aluminum honeycomb cores are commonly used in the field of the aerospace industry. However, production methods for those, especially the autoclave process, often require many consecutive process steps and therefore do not meet desired requirements given cycle time and costs. The vacuum infusion process can significantly reduce those costs even more when employed in one shot. A requirement for this process is the usage of a core with closed cells to prevent unwanted penetration of resin into honeycomb cells. A polymethacrylimid (PMI) foam core represents a promising solution. Usually, the final geometry is machined out of a core block. In this research, the potential of a particle foam that can be foamed into a general geometry in mold (Rohacell® Triple F) is investigated by employing two different design approaches.*

Keywords: Sandwich; foam core; optimization; X-ray computed tomography; Aerospace

1. Introduction

The demand for new aircrafts has been heavily increasing before the Covid pandemic. A demand for up to 38.000 new aircrafts has been expected for the next 20 years, of which 26.700 aircrafts (70%) are in the single-aisle sector, i.e., short- and medium-haul. To meet this demand for new aircrafts and the strongly increasing number of units, new processes, and design concepts must be developed. Composite materials are well established in the aircraft industry for many years due to their high lightweight potential and their functional properties and are gaining more and more importance. Today´s production methods for composite parts often require too many single process steps and therefore do not meet future requirements given cycle time and costs.

The main goal of this research project is to develop a cost-efficient design and manufacturing method that allows a considerable reduction of the production time (up to 60 %) and the production steps while maintaining the mechanically very efficient lightweight design of a sandwich construction for secondary structures of an aircraft. For this purpose, it is necessary to develop a one-shot technology that does not require an autoclave, since this represents a high-cost factor and a bottleneck in the production of high unit numbers. For this reason, the vacuum infusion process MARI (Membrane Assisted Resin Infusion) is selected. This process requires the usage of a foam core made of polymethacrylimide (PMI) since honeycomb cores would get filled with resin or would need to be covered with separate material causing a

  doi:10.5075/epfl-298799_978-2-9701614-0-0

significant weight penalty. Structurally relevant PMI foam cores that are close to airworthiness certification and enable good production results are still too heavy considering a density of 70 kg/m³ or higher.

The goal is to develop a design and manufacturing approach that allows foaming e.g., three-dimensional grid structures, directly from the tool as a ready-to-use foam core without additional machining. The core will be used either as a modular element or as a single large core in the sandwich structure. The developed design and production technology will be validated based on a demonstrator part in form of a single-aisle spoiler, which has a very high production rate.

2. Polymer rigid foam core

The material behavior of polymer rigid foam cores such as PMI is determined primarily by the properties of the base material and the cell structure, and less by the gas trapped in the cell walls. In this sense, a distinction can be made between a macro level (consideration of the foam as a continuum), a meso level (consideration of the geometry of the cell structure), and a micro-level (consideration of the polymer chains in the base material), see fig.1.

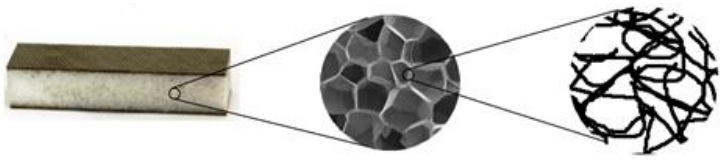

Figure 1. Multiple scales of rigid polymer foams [1]

In terms of manufacturing costs while retaining the advantages of the mechanically and weight-efficient sandwich construction, foam cores represent a very interesting alternative.

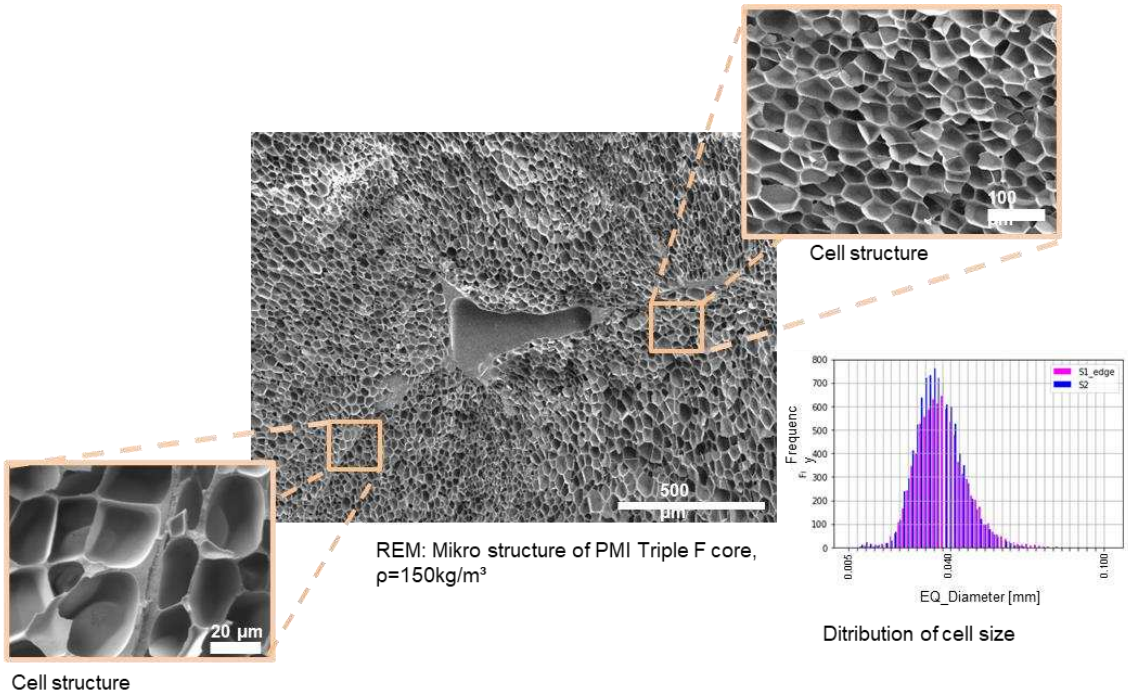

Figure 2. Typical morphology of used PMI Triple F core of LiteCon

  doi:10.5075/epfl-298799_978-2-9701614-0-0

For sufficient mechanical performance, the use of high-strength structural foams is required. For example, the particle foam polymethacrylimide (PMI), known under the trade name Rohacell® from the manufacturer Evonik or LiteCon, is already used in some aerospace applications. This offers several advantages over the honeycomb core as such a core is suitable for a resin infiltration process such as RTM and resin infusion. Regarding the pore structure, the closed cells offer the advantage that the resin only penetrates into the cells on the surface that were opened during the machining of the core. However, a challenge is that today qualified foams are all sheet materials. Three-dimensional components, if they cannot be thermoformed, must be milled at great expense, so the use is mostly for components with low complexity. In this process, up to 80% of the total material becomes waste that can no longer be used. The process is thus very time-consuming and cost-intensive, and by far not all desired geometries can be designed and are suitable for milling. This is where the Rohacell Triple F foam core technology from LiteCon comes in, which makes it possible to foam structures directly from a mold. In this way, full 3D geometries can be realized directly and without machining in a single step in an automated production process. The typical morphology of the core used in this study, the PMI Triple F core of LiteCon, is shown in fig.2. For foaming in a 3D shape, a minimum wall thickness of 5 mm was applied.

3. Design Approaches

The challenge is to compensate for the high foam density, compared to usually used honeycomb cores reaching a similar mechanical performance, via a weight-optimized core structure. Within this work as a demonstrator, **a generic single-aisle-spoiler** is studied. This spoiler is a sandwich part with a Nomex honeycomb core.

Two different design approaches are investigated to obtain a lightweight foam structure, see fig. 3. The first utilizes regions with optimized foam grid structures, to replace sections of full-depth foam core.

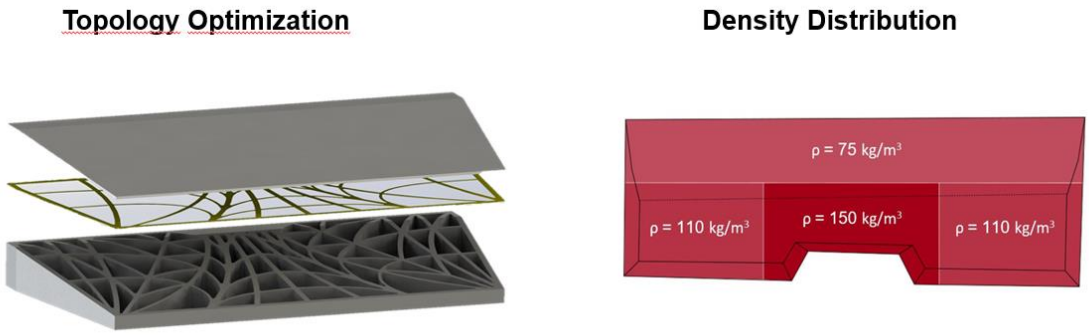

Figure 3. Two design approaches, grid core (left) and core density distribution (right)

The core height is limited for the studied demonstrator part in the thickest area to 25 mm. Considering a minimum wall thickness of 5 mm just a limited area of the spoiler could be used for developing a grid structure (see fig 4). Considering these constraints, a topology optimization employing the software Abaqus was done. Based on these results different types of grid structures were developed (see fig.5) allowing a weight reduction in the best case of 9% compared to a full-depth core for the total spoiler.

  doi:10.5075/epfl-298799_978-2-9701614-0-0

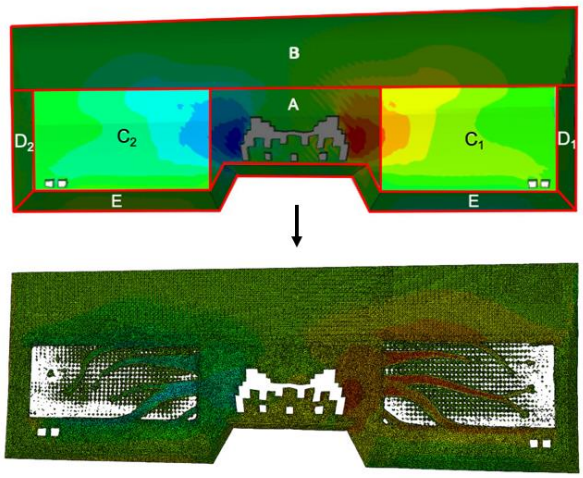

Figure 4. Limited Areas to apply core grid structure C1 & C2 (top) and topology optimization (bottom)

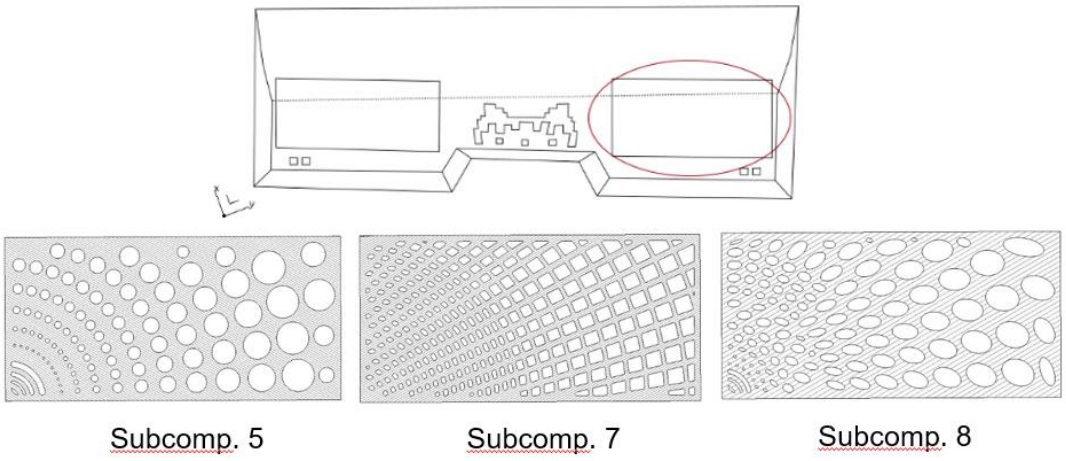

Figure 5. Different grid structures in areas C1 & C2 (fig.4)

To evaluate the mechanical performance of the foam grid structure, subcomponents for three-point bending tests are developed via simulation to represent the stress level of a full-scale spoiler.

In the **second design approach**, regions with full depth foam core but different core densities are optimized, depending on local mechanical loads and stresses (Fig.1b). Here the potential of the in-mold foaming is fully exploited since general “organic formed” optimized geometries can be foamed. Several iterations led to the final design iteration 6, depicted in fig. 6 right bottom. This approach yielded a weight increase of 4% compared to the Nomex core in the reference demonstrator part. This approach yielded thereby a higher weight benefit compared to the grid structure studied before with 9%. Additionally, to that, this design is more robust in manufacturing as will be shown in the next chapter.

  doi:10.5075/epfl-298799_978-2-9701614-0-0

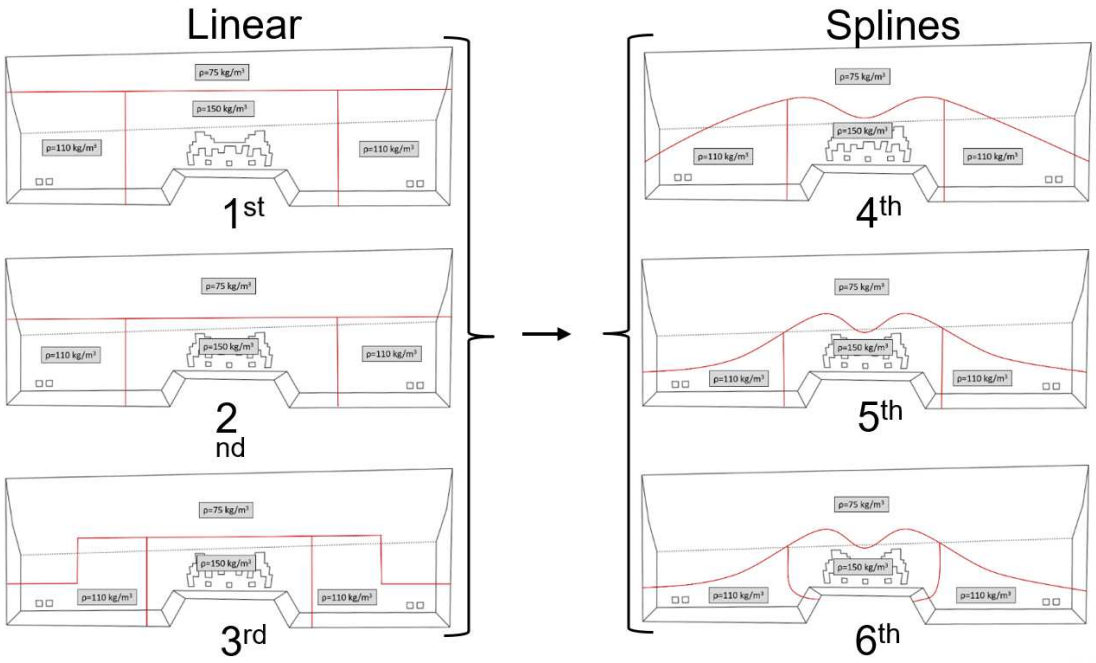

Figure 6. Iterations for developing an efficient density distribution of the PMI core

4. Infusion Process

During the infusion process, it must be ensured for the foam grid structure that the resin cannot penetrate either through the intercellular pore spaces or through the adhesive layer since resin accumulations in foam cells lead to exothermic reactions and the foam may restart foaming. The complex three-dimensional cell structure of the closed-cell foam and its impermeability is investigated via X-ray computed tomography (XCT) as an imaging technique. For the infusion process, different contrast liquids have been investigated to replace the epoxy resin to enhance the level of recognition while still miming the viscosity of epoxy. Finally, a solution of 25% Caesium iodide (CsI) was used. XCT scans of vacuum-infused PMI foam specimens show that the contrast medium is penetrating into the cavities of the lattice structure if the wall thickness is getting too small. To achieve a tight foam grid structure, investigations were carried out in a second step with a finer raw granulate (FG) with a grain diameter of approx. 0.5 - 1 mm, which is significantly smaller than the previous standard granulate (SG) with approx. 1 - 4 mm. Channels leading to contrast penetration into the hollow structure are very likely to be present, but they are very fine and not always well resolvable on CT (fig. 7, 8). It is possible that the contrast agent penetrates directly through the foam surface, e.g., along the grain boundaries. This could also explain the stronger penetration in foam made of fine material, since there are more grain boundaries, i.e. potential resin channels, here. The glue line (see fig. 8 left) is also a potential penetration site. Since contrast medium and adhesive film have the same properties in the CT scan, this could not be investigated.

For an envisaged minimum wall thicknesses of 5-7mm, no tightness could be shown. A higher wall thickness is not meaningful considering a spoiler height of the reference part of 25 mm. However, for thicker sandwich parts a grid foam structure in combination with an infusion process may become feasible.

  doi:10.5075/epfl-298799_978-2-9701614-0-0

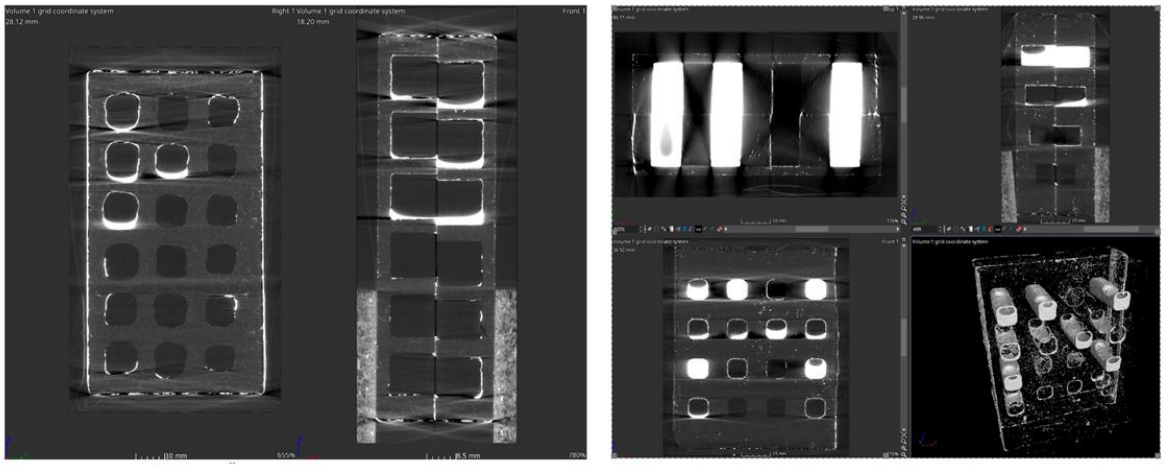

Figure 7. CT scans, core material standard grain, infusion with CsI solution

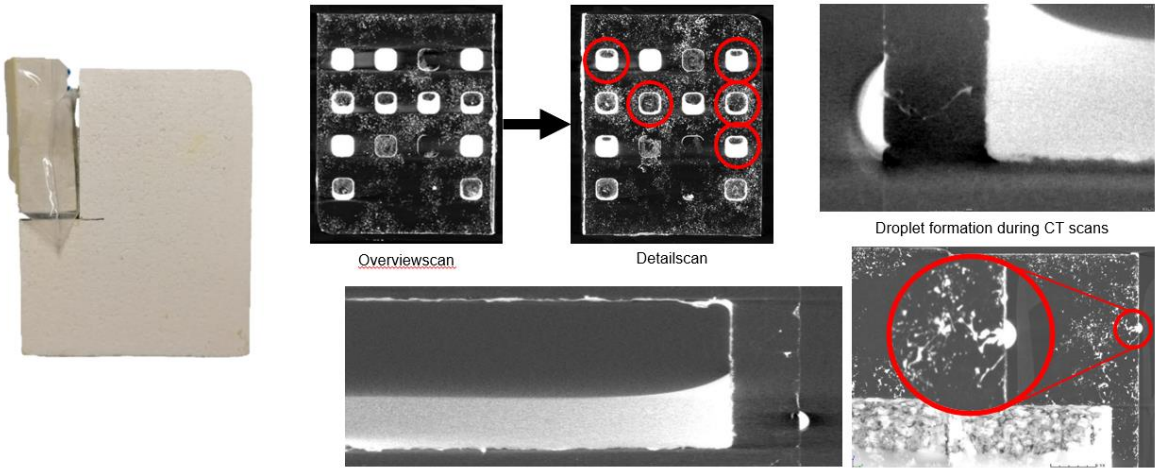

Figure 8. CT scans, core material fine grain, infusion with CsI solution

5. Manufacturing of the demonstrator part

Based on the simulation optimized design depicted in fig. 6, iteration 6, four full-scale demonstrator parts have been manufactured and inspected.

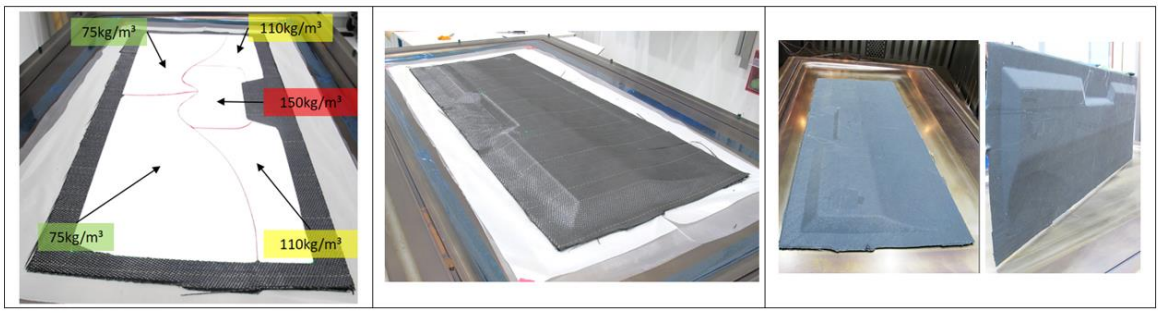

Figure 8. Layup of dry plies and core segments (core foamed directly in 3D shape) - left, the final part before machining - right

  doi:10.5075/epfl-298799_978-2-9701614-0-0

Cost analysis shows a saving potential of up to 30-40% in personnel costs due to the new design. On the one hand, the use of dry materials eliminates compacting times during the lay-up process, which has a significant influence on labor costs. On the other hand, the contour foaming of the cores instead of plate production and subsequent milling shows a further cost advantage of approx. up to 60%. However, this saving can only be reached at a usual production rate of a single-aisle machine (approx. 50 pcs. per month) since the acquisition costs of the tools for in-contour foaming are high. The points mentioned lead to a reduction in the production time of up to 60%. In addition to the personnel and material costs mentioned, a further cost advantage can be derived from the use of an oven instead of an autoclave, since this is less expensive and requires less energy consumption. In summary, the design and manufacturing process of the demonstrator component shows a very interesting overall cost advantage.

6. Conclusion and outlook

The overall objective, to develop a manufacturing method and design approach that allows a significant reduction of the production time, production steps, and recurring costs of sandwich components, has been achieved. The goal to develop a one-shot design was reached. To achieve this goal despite the density challenge of a foam core, two paths, grid/lattice structure and, as an alternative, density variation of the foam core, were studied. For the foam grid structure, to achieve a resin-tight foam, investigations were carried out employing CT scans with a finer and a standard raw granulate. Sufficient tightness could not be shown within this research. For the second approach, which was considered in parallel, a variation in density over the entire spoiler foam core has been investigated. This design shows very high weight potential and a very high process robustness.

As an outlook, both approaches, density distribution, and grid/lattice structure can also be combined to reach an even higher weight-saving potential.

Acknowledgements

The Austrian Research Promotion Agency (FFG) is gratefully acknowledged for funding this research in the TakeOff program (Project IKARUS; Grant No. 861047).

References

1. Rinker M., Zahlen P.C., Schäuble, R. Damage and failure progression in CFRP foam-core sandwich structures. In 8th International Conference on Sandwich Structures. Porto, Portugal.2008

  doi:10.5075/epfl-298799_978-2-9701614-0-0

RESISTANCE WELDING OF LOW-MELT POLYARYLETHERKETONE: PROCESS DEFINITION AND OPTIMIZATION

Manuel Endrass[a], Anton Thomé[a], Victor Gadletz[b], Simon Bauer[a], Stefan Jarka[a], Philipp Gänswürger[a], Frederic Fischer[a], Stefan Ferstl[b], Lars Larsen[a] and Michael Kupke[a]

a: Institute of Structures and Design (IBT), Center for Lightweight Production Technology (ZLP), German Aerospace Center (DLR), Am Technologiezentrum 4,
D - 86159 Augsburg – manuel.endrass@dlr.de
b: Premium AEROTEC GmbH, Haunstetter Str. 225, D - 86179 Augsburg

Abstract: *Within the European Clean Sky 2 Program thermoplastic composites are readied for future single aisle application and validated by the full-scale demonstration of the so-called Multifunctional Fuselage Demonstrator (MFFD). DLR together with Premium AEROTEC, AERNnova and AIRBUS will deliver the upper half shell for this 8 m long barrel made of carbon fiber-reinforced low-melt Polyaryletherketone (LM-PAEK). Resistance welding was chosen to join the C-frames with up to 19 attached flanges of varying length to the fuselage skin. For process definition, the welding parameters of LM-PAEK were investigated using a customized weld module. The main processing parameters affecting the quality of the weld, were defined as input parameters for a Design of Experiments (DoE). The DoE was conducted on the basis of a glass-insulated welding element. The bondline quality of each parameter set (design point) was assessed by water-coupled ultrasonic investigations, the fracture load values defined by single lap shear testing and microscopic fracture surface analyses. Thus, a numerical parameter optimization was performed in order to define the weld parameters for frame integration. Within a second evolution stage of the welding elements, replacing the glassfiber insulation of the welding elements to pure resin films, the potentials for a mechanical performance increase could be demonstrated.*

Keywords: Clean Sky 2, Resistance Welding, LM-PAEK, Design of Experiments, Non-Destructive- & Destructive-Testing

1. Introduction

State-of-the-art aircraft assembly is a mainly sequential process, where the installation of systems and cabin interior monuments is strictly separated from the prior structure assembly. The possibility for re-organizing the aircraft assembly sequence with pre-equipped modules (already containing cabin and systems installations) due to dustless joining technologies for carbon fiber-reinforced high-performance thermoplastics (CFR-TP`s) can be named as game changing opportunity on the reduction of lead time for the aircraft manufacturing. The German Aerospace Center`s (DLR) Center for Lightweight Production Technology (ZLP) Augsburg, together with Premium AEROTEC (PAG), Airbus and AERNnova are responsible for the component manufacturing and assembly of the Multifunctional Fuselage Demonstrators (MFFD) eight-meter long upper shell structure made from Toray Advanced Composites TC 1225 LM-PAEK within the framework of Clean Sky 2.

  doi:10.5075/epfl-298799_978-2-9701614-0-0

In-Situ tape placement (skin manufacturing), continuous ultrasonic (stringer integration) and resistance welding (frame, frame-coupling and cleat integration) are matured, modified and adapted towards a safe and sound process execution within the upper shell structure manufacturing. This paper focusses on the process definition and optimization of resistance welding of LM-PAEK as intermediate project milestone, based on the use case: welding of an attached flange of an integral C-frame onto a thermoplastic skin laminate.

Resistance welding uses joule heating of an electrically conductive implant or welding conductor caused by a flow of an electrical current. The welding element consisting of the welding conductor and additional electrical insulation sheets is placed in between the welding components and generates the heat at the interface. The temperature is increased towards the processing temperature (T_p), while a weld pressure of at least 0.5 MPa assures adequate consolidation of the bondline. Since the heating rate, target temperature level and cooling rate can be adjusted by the power input, the possibility for a multi-stage welding guidance is given and can be used for an optimization of the joint strength.

2. Weld process definition and optimization procedure

2.1 Resistance welding setup and functionality

A weld module (see Figure 1) - comparable to those later used on the full-scale welding tool for attached flange joining - was designed and validated on our resistance welding test bench in order to optimize the processing parameters. The weld module itself consists of the following main components: pneumatic cylinder (1) for applying weld pressure and contact pressure, lever arm (2) with a transmission ratio of 1:4 (piston pressure to welding pressure), disk spring package (3) to ensure a relative movement between welding pressure piece (4) and the copper contacting blocks (5). The process sequence was defined within the software TopControl, which was used to control the power supply (Regatron TopCon Quattro).

The corresponding measurement data of welding pressure, current and voltage levels as well as the bondline temperature were recorded and merged via an in-house developed quality assurance software.

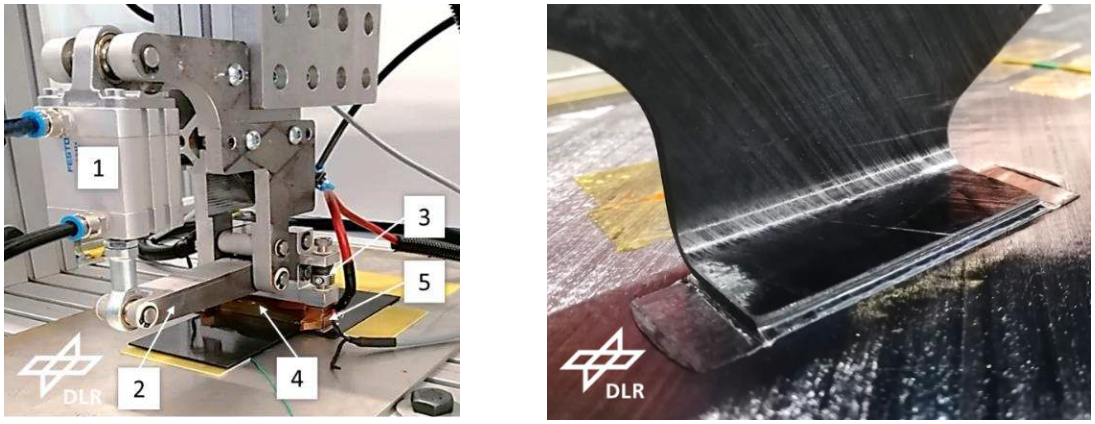

Figure 1 Weld module (left) for performance validation and process parameter definition/ optimization. Full-scale process verification of a resistance-welded C-frame cutout on an in-situ T-AFP skin laminate (right).

Figure 1 (left) shows the weld module used for process parameter identification and optimization. The right-hand side picture highlights a cutout of the later use case, a welded attached flange of an integral C-frame.

  doi:10.5075/epfl-298799_978-2-9701614-0-0

For process definition 2.76 mm thick, flat, press-consolidated laminates of the stacking sequence [45°,135°,90°,0°,135°,45°,45°,90°,135°,45°,135°,0°,90°,135°,45°] were welded with an overall weld length of 84 mm and an overlap of 22 mm in single lap shear (SLS) configuration. This stacking sequence is attributed to the later use case. The organosheets 0°-axis was aligned with the axis of force application. Within this study two different types of welding elements, configuration A with pre-consolidated glassfiber (GF)/LM-PAEK insulation (Toray 4HS, EC5 E-glass prepreg, 105gsm) and configuration B with a 100 µm LM-PAEK film insulation (Victrex APTIV AE™ Film 6013-AEG-100), were used. Toray`s pre-consolidated 5HS, T300JB carbon woven prepreg, 277gsm was chosen as welding conductor. A thermocouple type K placed in the center of the bondline between bottom organosheet and welding element provided temperature feedback during the weld process.

2.2 Water-coupled ultrasonic inspection

Resistance welding technology, based on a carbonfiber welding element, offers the possibility of applying non-destructive testing (NDT) methods, which are conventionally deployed for testing integral structures, since a mono-material composite is produced during assembly. In order to check for non-conformance indications and bondline homogeneity, the standard NDT method water-coupled ultrasonic scanning (WUS) according to AITM6-4010 was chosen. An OLYMPUS OmniScan® SX phased array flaw detector with 5L64-NW1 probe and SNW1-OL-IHC wedge were used to measure the ultrasonic data. Here, the probe was mounted on a 2-axis GLIDER X-Y scanner to allow insightful evaluation of the A-, B- and C- Scans.

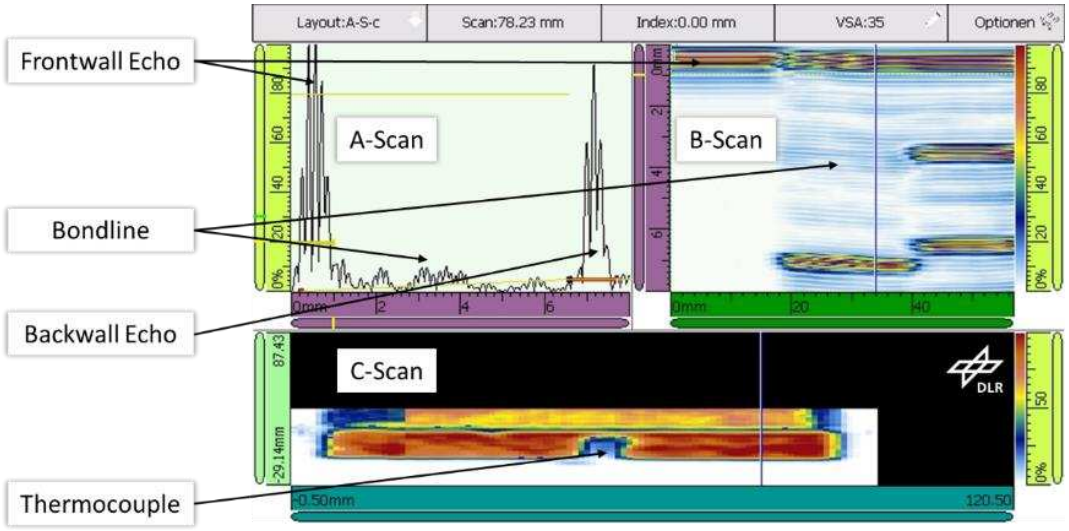

Figure 2 Representative water-coupled ultrasonic scan result of a resistance welded coupon in SLS configuration

The capability of producing completely closed and homogeneous welds by resistance welding is represented within the scan of Figure 2. Here, an 84 mm x 22 mm bondline corresponding to the above described weld setup was achieved. A-, B- and C-Scans highlight a perfect weld quality over the entire bondline indicated by the damping of the amplitude color-coded in red, comparable to an integral composite structure. The damping losses in the center of the bondline marked in blue are attributed to the thermocouple and its Polyimide insulation. Results of the WUS were used for a quantitative comparison of the welding quality and definition of the later DoE input parameter boundaries.

  doi:10.5075/epfl-298799_978-2-9701614-0-0

2.3 Coupon preparation and destructive testing

Each welded specimen was cut into three 25.4 mm wide SLS coupons by a waterjet cutter. In comparison to the standard-compliant tests (according to DIN-EN 2243-1/ AITM1-0019) of an overlap length of 12.5 mm, the entire welding width of 22 mm was used for testing without further preparation, like notching, well knowing that the increased joint overlap would result in a superimposed tensile peel load. The reason was the need to gain knowledge about the bearable fracture load of the entire welded joint. In particular, since it was expected that the effects of lower welding temperature values would especially affect the joint strength at the edges. The mechanical testing of the coupons was performed at PAG`s aerospace certified structural lab. Aluminum tabs were used to compensate for the eccentricity of the coupons at clamping in the tensile testing machine (Zwick BTC Z100 & Pulser P40). The testing was performed at a test speed of 3500 N/min, clamping length according to AITM1-00019 (112,5 - 127) mm at 24.5 °C and 33.7 % rel. humidity. [1]

2.4 Microscopic fracture surface analyses

Following the SLS test, a comprehensive fracture surface analysis was performed to gain insight into the dependence on process control during welding and its influence on the fracture pattern. For this purpose, the fracture surfaces were imaged in reflected light microscopy using a Keyence VHX-5000 microscope. Four fracture zones (ID_1 and ID_2a-c) were defined to allow an exact assignment of the fracture surface fractions to failure location (see Table 1).

Table 1 Schematic and physical fracture classification [2]

Fracture ID_1	Fracture ID_2a	Fracture ID_2b	Fracture ID_2c
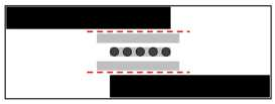	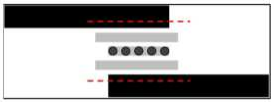	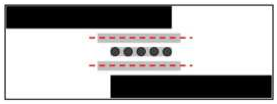	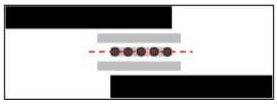
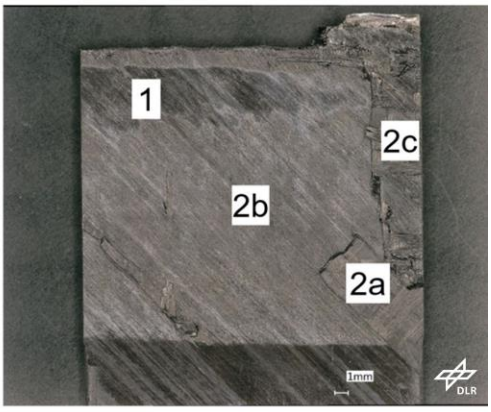	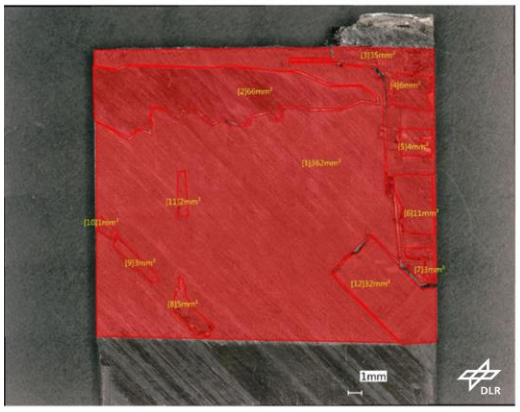		

The respective fracture fractions were characterized optically under the digital microscope and measured geometrically using the polygonal tension function. Fracture ID_1 is characterizing a bondline separation between the welding elements insulation and the organosheet and indicates a too low weld temperature level. At Fracture ID_2a-c the crack propagates through one of the semi-finished products organosheet (ID_2a), welding element insulation (ID_2b) or the electrical conductor (ID_2c).

  doi:10.5075/epfl-298799_978-2-9701614-0-0

3. Design of Experiments

3.1 Model description

Design Expert®, a DoE software was used to plan and evaluate the test series. In order to reduce the overall welding and testing effort and still demonstrate the multifactorial interactions a Face-Centered Central Composite Design (FCCCD) was used. The FCCCD is a response surface method and spans its experimental space as a combination of cube and star. This allows to detect up to quadratic terms. In order to obtain a sufficient statistical validation of the test results, the center point was repeated six times, and the corner and star points of the test room were repeated twice. At each of the test points at least two specimens were welded, containing the described number of three coupons.

3.2 Input parameters, constants and responses

In this study, the influence of the joining parameters on the fracture load as well as the fracture behavior were investigated in detail. The process was designed in two distinct phases. In the first phase, the welding element should be heated first above the melting temperature of the thermoplastic matrix to the final T_P. In the second phase, the voltage and thus the temperature is reduced to allow post-crystallization at about 220 °C. The main influence on the responses were expected in the dwell time above the crystallite melting temperature (represented by the combination of Phase_1 Weld Voltage and Phase_1 Weld Duration), as well as the cooling rate during post-crystallization (represented by the combination of Phase_2 Weld Voltage and Phase_2 Weld Duration). These factors were set as input parameters for the DoE and varied in between the boundaries. The welds were performed in constant voltage mode.

Table 2 Input parameters and their variable ranges within the scope of the performed DoE

Factors/ Input Parameters	Design Points	Unit
Phase_1 Weld Voltage	23 | 25 | 27	V
Phase_1 Weld Duration	20 | 25 | 30	s
Phase_2 Weld Voltage	18 | 19 | 20	V
Phase_2 Weld Duration	5 | 10 | 20	s

The design points shown in Table 2 were determined during preliminary tests [3], [2]. In Phase_1, the voltage-time combinations were designed for a targeted processing temperature range between 305 °C (T_m) and 400 °C. Since the T_P-range of LM-PAEK is at (340-385) °C [4] the upper temperature limit was defined not to extraordinary exceed these limits and to remain below the degradation temperature (T_{d_PEEK} = 520 °C) [5]. During preliminary welding experiments a temperature drop of about 36°C/s, linear approximated from voltage shut down at 360 °C to 220 °C (temperature of maximized crystallization rate) was investigated. In comparison with Differential Scanning Calometry (DSC) measurements from literature [5], [6], the necessity for lower cooling rates was confirmed in order to increase the crystallinity content. For this purpose, the welding Phase_2 was implemented into the process cycle. The Phase_2 Voltage levels were selected to meet a bondline target temperature range of (220-270) °C.

  doi:10.5075/epfl-298799_978-2-9701614-0-0

Besides the described DoE variables, the remaining process parameters like contact pressure, weld pressure and the kind of contact preparation were kept constant on a pre-investigated optimum during this trial series. The parameters fracture load [N], failure mode (ID_1, 2a-c), fracture surface (according to fracture ID as %-value of the overall weld surface) and the maximum processing temperature [°C] were defined as responses of the DoE.

4. Results, interpretation and optimization

4.1 Stage one welding element (GF-based insulation)

The Analysis of Variance (ANOVA) within Design Expert® showed statistically significant influences of the parameters Phase_1 Weld Voltage and Phase_1 Weld Duration on the fracture load. Figure 3 shows the influences of the Phase_1 input parameters on the fracture load, highlighting a major impact due to a voltage increase compared to an extension of the weld duration. This indicates the stronger dependence of the processing temperature as compared to the dwell time.

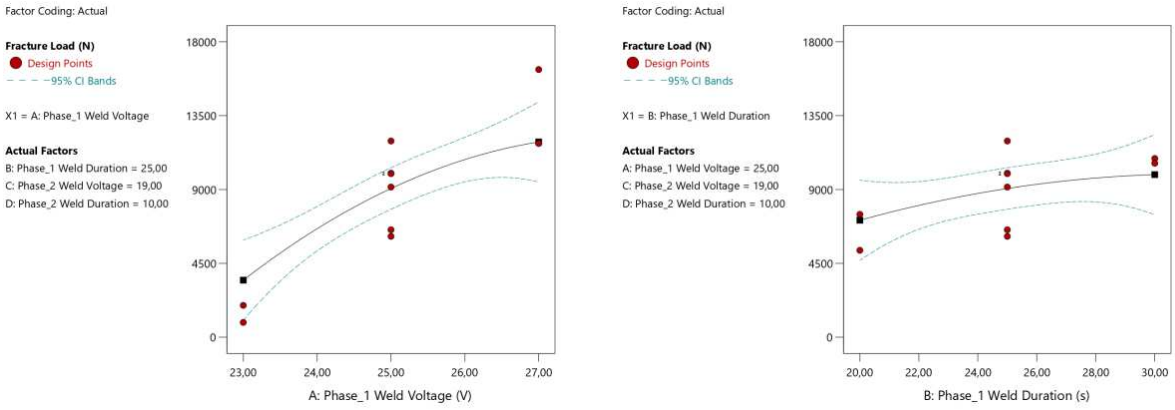

Figure 3 Influence of Phase_1 Weld Voltage (left) and Phase_1 Weld Duration (right) on the bearable fracture load

Fracture surface analyses post to destructive testing exhibited a mixed-mode failure of each specimen with the highest fracture surface percentage in failure mode ID_2b (85.15 %), followed by the failure modes ID_2a (12.23 %), ID_1 (2.46 %) and ID_2c_0.16 %. Since in between the failure modes 2a-c, no valuable impact on the fracture load level was observed, those three ID`s have been summarized to an overall ID_2. In the further course the evaluation, the responses failure mode and fracture surface have been combined to the response percentage of area in failure ID_2, due its higher expressiveness. Here, the occurrence of failure mode ID_1 was exclusively attributed to Phase_1 Weld Voltage levels lower than 24.1 V, leading to weld temperature levels below 330 °C and is thus outside the processing specification.

A comparison of the responses fracture load (Figure 3) and the percentage of area in failure ID_2 (Figure 4), clearly shows that the increase in fracture load is caused by an increase in the welded area due to an elevated maximum processing temperature and is not majorly influenced by a prolonged Phase_1 Weld Duration. Furthermore, an extension of the Phase_1 Weld Duration did not show any significant influence on the shift of the fracture type from ID_1 to ID_2.

  doi:10.5075/epfl-298799_978-2-9701614-0-0

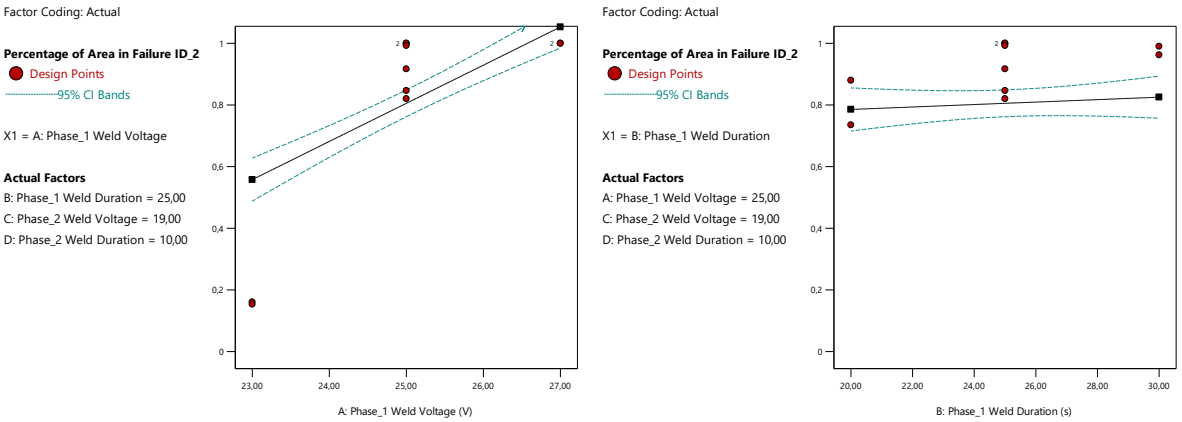

Figure 4 Influence of Phase_1 Weld Voltage (left) and Phase_1 Weld Duration (right) on the percentage of area in failure ID_2

The impact of the second weld phase which should reduce the cooling rate and thus increase the crystallinity content highlights, compared to first weld phase, a minor impact on the overall fracture load (see Figure 5) within the investigated design space. Since the bearable fracture load increases towards the edge of the design space for the first weld phase (longer weld duration at higher voltage levels) it cannot be assured, that the fracture load optimum is located within the chosen design space. However, the design space meets the superordinate criterion on process robustness and reliability. Related to the second weld phase it can be concluded, that a minor increase in the fracture load can be achieved by an increased Phase_2 Weld Duration in combination with a low Phase_2 Weld Voltage level.

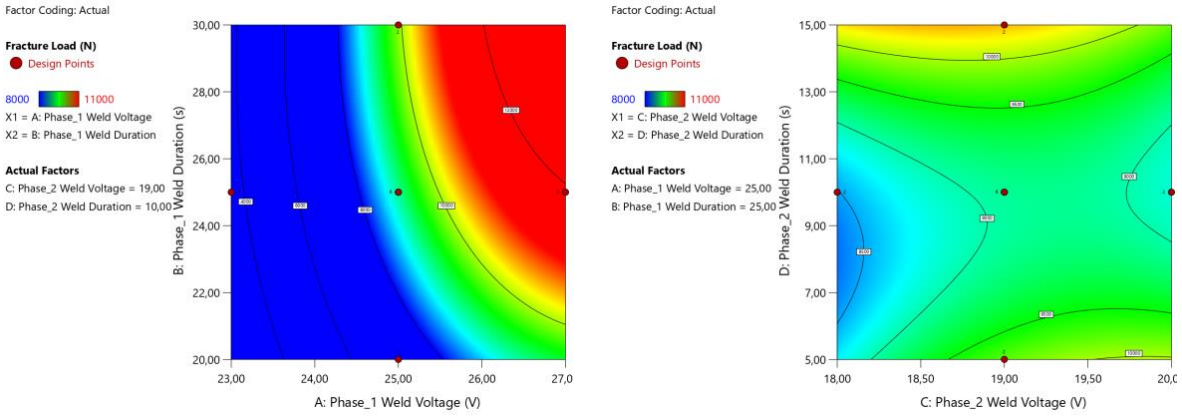

Figure 5 Comparison of the impact of the first (left) and second (right) weld phase on the fracture load.

In order to define a valuable set of input parameter combinations for the described use case (frame integration) a parameter optimization was performed. A maximization of the fracture load (importance: ++++) and percentage of failure area in ID_2 (importance +++), as well as target maximum temperature level within the scope range of T_P (340-385) °C were defined as boundary conditions. The results of the most desirable numerical optimization are plotted within Figure 6, confirming the above concluded suggestion on defining the first welding phase towards the upper right corner and the second phase towards the upper left corner (compare Figure 5) of the design space, i.e. applying maximum voltage of 27 V for 30 s in the first weld phase, whilst in Phase_2 the voltage level is reduced to 19 V for a dwell time of 15 s.

  doi:10.5075/epfl-298799_978-2-9701614-0-0

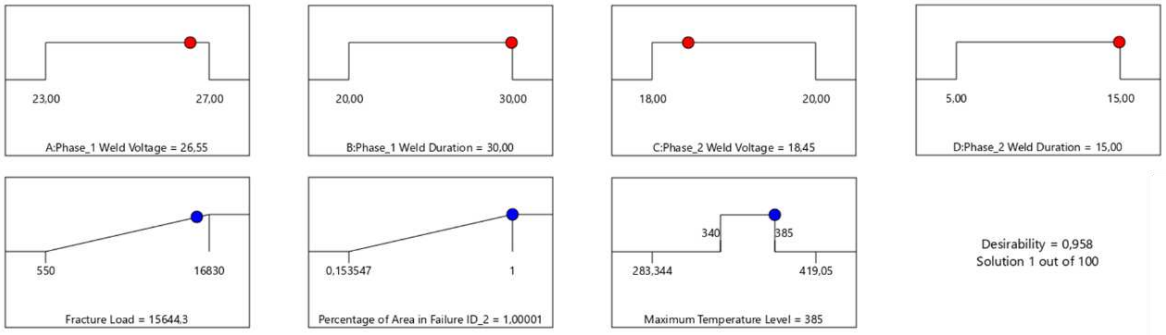

Figure 6 Results of the numerical optimization of the welding parameters for CF/LM-PAEK.

The numerical optimization predicts under assignment of the suggested input parameter combination a resulting fracture load of 15664.3 N at a percentage of area in failure ID_2 of 100 % and a maximum temperature of 385 °C in the bondline.

The proposed parameter combination of 26.6 V for 30 s in the first and 18.5 V for 15 s in the second welding stage was subsequently validated on eight tested specimen and showed with a fracture load of (15795 ± 1089) N a highly precise conformance on the predicted value.

4.2 Stage two welding element (APTIV-based insulation)

A further optimization towards higher fracture loads was made by replacing the GF/LM-PAEK insulation by a pure matrix film. Since the tests were carried out in parallel with the mechanical testing of the specimens from the DoE, the optimized parameter set could not be used here. Furthermore, the possibility of a two-stage weld pressure application (low pressure of 1.2 bar during Phase_1; high pressure of 8.1 bar applied at Phase_1 Voltage shutdown) was implemented in order to reduce the conductor squeeze out during the heating phase and prevent from local overheating and current leakage.

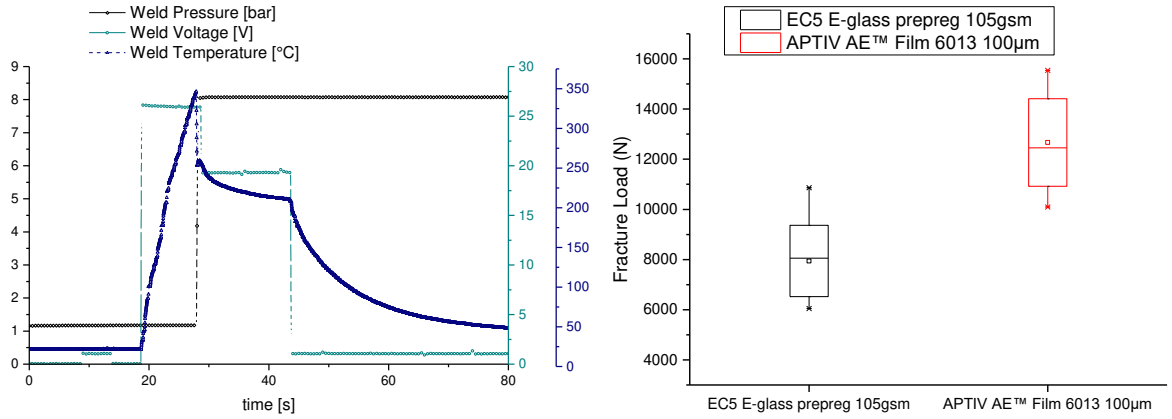

Figure 7 Adapted, non-optimized welding process for increased process robustness at reduced conductor squeeze out (left). Potential increase of fracture load due to replacement of the GF-based insulation by a neat resin film (right).

Figure 7 (left) shows the processing parameters over time for a 27 V/10 s first weld phase and a 20 V/15 s second weld phase process sequence and additional possibility of increasing the weld performance. Since the potential for an increase in mechanical performance could already be shown for a non-optimized parameter set, further investigations are currently being carried out to determine the absolute fracture load increase, based on the optimized weld parameter set.

  doi:10.5075/epfl-298799_978-2-9701614-0-0

5. Summary and Conclusion

Within this paper we present our research activities on the resistance welding technology maturation within the scope of the MFFD upper shell development. For the final all-thermoplastic composite fuselage C-frames shall be welded to the in-situ consolidated skin. The conducted experimental investigations are based on pre-consolidated TC 1225 LM-PAEK laminates provided by TORAY. A custom-made weld module comparable to the final application was used for coupon welding of single lap shear specimen at varying weld parameters defined by design of experiment. The resulting sample quality was determined by WUS inspection, SLS testing and fracture surface analysis. By statistical analysis of the FCCCD an optimum for welding was found with a first stage heating the weld element by applying a voltage of 26.6 V for 30 s. In the second stage, the cooling rate is reduced by applying a voltage of 18.5 V for 15 s so that re-crystallization is promoted at temperatures above 220 °C. The validation of the welding input parameters, provided by the numerical optimization showed good conformance with the validated fracture load values.

Recent investigations have indicated that resistance welding, based on a welding element with a carbonfiber conductor and without glass insulation but a neat resin film may also be a viable opportunity, further reducing the amount of foreign material in the weld seams.

Acknowledgements

This project has received funding from the Clean Sky 2 Joint Undertaking (JU) under grant agreement No 945583. The JU receives support from the European Union's Horizon 2020 research and innovation program and the Clean Sky 2 JU members other than the Union.

Disclaimer

The results, opinions, conclusions, etc. presented in this work are those of the author(s) only and do not necessarily represent the position of the JU; the JU is not responsible for any use made of the information contained herein.

  doi:10.5075/epfl-298799_978-2-9701614-0-0

6. References

[1] V. Gadletz, T. Lehl, and G. Knopp, “TP-WL1413-MFFD SLS DLR_V3 Test Protocol,” Premium Aerotec GmbH, May 2021.

[2] A. Thomé, “Ermittlung und Validierung der Prozessgrößen beim elektrischen Widerstandsschweißen von faserverstärkten Hochleistungsthermoplasten und deren Einfluss auf die Verbindungsqualität,” Institute of Structures and Design (IBT), German Aerospace Center (DLR), Augsburg, Sep. 2021.

[3] M. Endrass, M. Engelschall, S. Jarka, S. Bauer, and F. Fischer, “Deliverable D2.1.8-55 (DEK), Optimization of welding parameters of LM PAEK,” Clean Sky 2, D2.1.8-55, Dec. 2020.

[4] Toray, “Toray Cetex TC1225,” Toray Advanced Composites, G. van der Muelenweg 2 7443 RE Nijverdal, The Netherlands, 2020.

[5] J. Audoit, L. Rivière, J. Dandurand, A. Lonjon, E. Dantras, and C. Lacabanne, “Thermal, mechanical and dielectric behaviour of poly(aryl ether ketone) with low melting temperature,” *Journal of Thermal Analysis and Calorimetry*, vol. 135, no. 4, pp. 2147–2157, Apr. 2018.

[6] I. Schiel, L. Raps, A. R. Chadwick, I. Schmidt, M. Simone, and S. Nowotny, “An investigation of in-situ AFP process parameters using CF/LM-PAEK,” *Advanced Manufacturing: Polymer & Composites Science*, vol. 6, no. 4, pp. 191–197, Oct. 2020.

  doi:10.5075/epfl-298799_978-2-9701614-0-0

NUMERICAL SIMULATION OF EDDY CURRENT GENERATION IN UNI-DIRECTIONAL THERMOPLASTIC COMPOSITES

A.J. de Wit[a], N. van Hoorn[a], B.R. Nahuis[a] and W.J. Vankan[a]

a: Royal Netherlands Aerospace Centre - NLR
Bert.de.Wit@nlr.nl

Abstract: *In this work the generation of eddy currents in uni-directional (UD) plies of thermoplastic carbon fiber reinforced polymer (CFRP) laminates is investigated. The focus is on developing a numerical electromagnetic simulation model that captures the main processes involved in eddy current generation, in particular in the UD plies interface areas. To simulate this eddy current generation an interface model is introduced that represents the mixed electrical properties in the ply interface areas and a measurement technique is presented to measure the necessary material properties. Finally, the effects on the eddy current generation of the positioning of plies with different orientation within the stacking order is shown. Adjacent, different oriented plies increase the eddy current density through the laminate thickness.*

Keywords: eddy currents; thermoplastic composites; numerical simulation; electro-magnetic

1. Introduction

In the Large Passenger Aircraft Platform 2 of the European R&D program Clean Sky 2, a Multifunctional Fuselage Demonstrator (MFFD) for single aisle aircraft is developed that serves as a platform for examining the full potential of Thermoplastic (TP) composites. This TP composite MFFD shall demonstrate the benefits of integrating various functionalities and help future European airliner production to become faster, greener, and more competitive. Significant weight reduction and thus environmental improvements of aircraft are expected as a result of innovative manufacturing, assembly, and installation processes. These innovations in turn will drive down costs and improve product competitiveness to European aeronautics. The TP composite MFFD consists of an assembly of multi-functional building blocks for the next generation fuselage and cabin. Development of advanced joining technologies and effective use of materials is necessary to enable a competitive assembly.

One example of such advanced joining techniques is induction welding. TP composites can be re-melted allowing them to be joined via welding. At present, the inductive heating of woven fabric composites is well documented and understood (Yousefpour, et al., 2004). Several heating mechanisms take place in the induction heating of TP carbon fiber reinforced polymer (CFRP). The extent in which each mechanism contributes to the heating process, depends on the material that is heated and the process parameters that are applied. However, a Uni-Directional (UD) CFRP material is more difficult to heat than a weave CFRP material. According to literature (Ahmed, et al., 2006) this could be due to the absence of a current returning path that is naturally embedded in the weave.

The objective of this work is to develop 3D electromagnetic simulation models that can provide insight into the influence of ply interfaces on the eddy currents that are generated inside a UD CFRP laminate when placed inside an electromagnetic field that is induced by a coil. First, basic

  doi:10.5075/epfl-298799_978-2-9701614-0-0

steps involving eddy current generation in a CFRP laminate are introduced. Second, a numerical simulation model based on electromagnetic Finite Element (FE) analysis is introduced. This model is extended with an updated version of an interface model (Wit, et al., 2021) previously developed by the authors. The updated interface model is constructed analogous to a surface implementation (Cheng, et al., 2021) but is extended to a volumetric implementation in this work. Third, the effect of 0/90 cross-ply interfaces on a laminate stacking is shown. Finally, the main conclusions and steps for further research are presented.

2. Electromagnetic modelling

For IW of TP CFRP, the electromagnetic properties of the plies and the laminate layup are of key importance for the behavior of the electromagnetic eddy currents that emerge in the CFRP composite laminate. Besides the magnetic permeability and magnetic permittivity, the electric conductivity of the material is a key determinant for the eddy current density distribution in the laminate. Although these properties depend on temperature and frequency, in the current study these properties are kept constant.

2.1 Cross-ply laminates and ply interfaces

In cross-ply laminates there are specific areas of increased eddy current density that are located at the interfaces of the cross-plies (Ahmed, et al., 2006) (O'Shaughnessey, et al., 2016) (Yousefpour, et al., 2004). Therefore, these cross-ply interfaces play an important role in the eddy current density distribution in the laminate under inductive electromagnetic loading. The background of this phenomenon is the increased occurrence of contacts between fibers in this interface layer and the opportunity for current to form a closed circuit. This is shown in Figure 1.

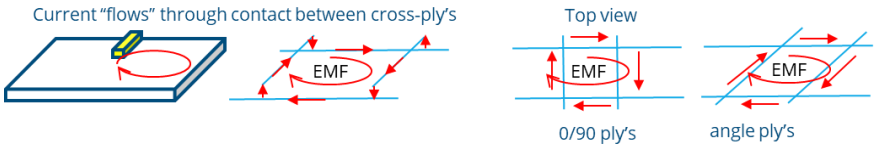

Figure 1 Cross-plies form a closed loop such that current can 'flow' through the plies. EMF stands for electro magnetic field.

These cross-fiber contacts result in a more isotropic in-plane conductivity and increased out-of-plane conductivity in this interface layer. To incorporate this important effect, the augmented electric conductivity properties in the cross-ply interfaces must be included in the FE model.

2.2 Cross-ply interface definition

In this work we develop an approach for solid FE modelling of electromagnetic eddy currents in cross-ply laminates including their cross-ply interfaces. To develop the interface concept, we consider a small two-ply laminate sample with arbitrary thickness, width and length. Furthermore, two interface cases are considered. The first consists of a [0,0] UD laminate and the second of a [0,90] cross-ply laminate. The cross-section is sketched in Figure 2.

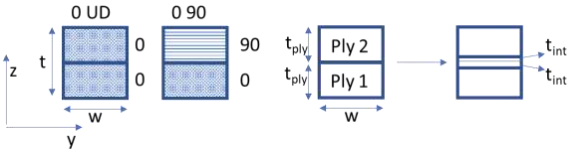

Figure 2 Front view of the small 2-ply laminate sample. A [0,0] and a [0,90] cross-ply laminate. The 0 fibers are oriented in x-direction. The cross-ply interface layer of arbitrary finite thickness t_{int} per ply is considered in between the ply. Hence, interface layer thickness is $2t_{int}$.

In the region around the interface between the plies, a cross-ply interface layer of arbitrary but finite thickness t_{int} per ply is introduced, see Figure 2. This interface layer is considered to have the augmented an-isotropic electric conductivity properties. Furthermore, these properties are taken homogeneous throughout the whole interface. The in-plane conductivities in the interface layer are assumed to result from the combination or mixture of the conductivities of the two plies. The out-of-plane conductivity in the interface layer is taken equal to the out-of-plane conductivity (or resistivity) of the considered cross-ply.

2.3 Electric resistances of plies and interface

The an-isotropic resistance tensor for each of the two plies (ply1 and ply2) in the small laminate sample (recall Figure 2) contains the resistances of each of the two plies in the three directions x,y,z, see Figure 3.

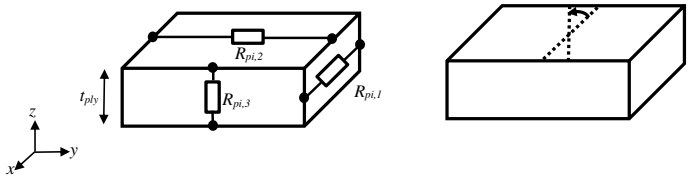

Figure 3 illustration of the an-isotropic resistances (left) and fiber orientation expressed by ply angle (right) for a single ply in the small laminate sample.

Hence, the resistances are written as:

$$\boldsymbol{R}_{pi} = [R_{pi,1}, R_{pi,2}, R_{pi,3}]\ ;\ i\ =\ 1{,}2; \tag{2}$$

In Eq. (2), i is de ply index and each ply can have arbitrary ply orientation, expressed by a ply angle ϕ_i. The resistances of a ply in the small laminate sample at an arbitrary ply angle ϕ_i can be determined by assuming a linear relation between the resistance in fibre direction (R_11) and the resistance in transverse direction (R_22) of a single ply, see (Cheng, et al., 2021).

Since the interface layer has finite thickness (recall Figure 2 right), the total resistance in each direction x,y,z of the small two-ply laminate sample must be equal to the total resistance of the sample without the interface layer (Figure 2 left). This yields that the resistance of the whole interface is equal to the combined resistance of its components. Hence, the lower half of the interface that contains the Ply1 properties and the upper half of the interface that contains the Ply2 properties.

Consequently, the in-plane resistances of the interface, i.e. in x,y directions, are composed from the parallel resistances of the interface components:

$$R_{i,j} = \frac{R_{i1,j}R_{i2,j}}{R_{i1,j}+R_{i2,j}} \text{ ; j} = 1,2 \text{ ;} \quad (5)$$

Here $R_{i,j}$ is the resistance of the whole interface in direction j, and $R_{i1,j}$ is the lower interface component resistance and $R_{i2,j}$ is the upper interface component resistance, in direction j, with j=1,2,3 that refers to the x,y,z directions.

The out-of-plane resistance of the interface, i.e.in z direction, is composed from the serial interface component resistances, and an additional ply-contact resistance. In (Xu, et al., 2018) this ply-contact resistivity ρ_c is determined experimentally for two-ply laminate samples.

3. Electrical characterization of (UD) CFRP

Although material data sheets include recognized standards for mechanical and thermal material properties, electrical properties are less common to be included. For UD material, an additional property involving the cross-ply electrical properties is application specific.

3.1 UD ply electrical conductivity measurements

The anisotropic electrical conductivity of a single ply is characterized by measuring the resistance. This includes a measurement in the longitudinal, transverse, and through-thickness direction.

Experimental setup. Unconsolidated strips of UD tape material with a thickness of 0.21 [mm] are clamped between electrodes. Minimising the contact area is essential to assure maximum contact between fibres/resin and the electrode. In addition, to increase the measurement accuracy a low resistance should be avoided. Therefore, for the resistance measurements in longitudinal direction (i.e., fibre direction) a 6.35[mm] wide and 1000 [mm] long specimen is used, see Figure 4. For the resistance measurement in the transverse and through-thickness direction specimens shorter specimens of 20 [mm] are used and the clamping devices are adjusted, see Figure 4.

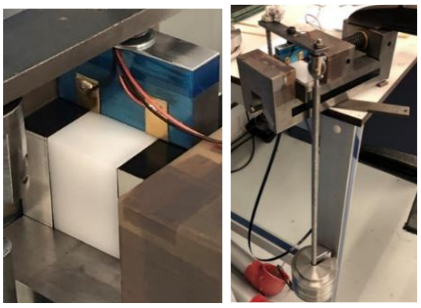
(a)
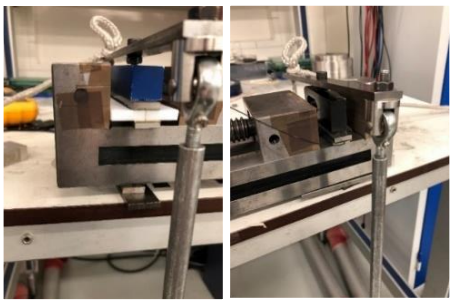
(b)

Figure 4 (a) Illustration of the test setup for the resistance measurement in longitudinal direction. (b) Illustration of the test setup for the resistance measurement in transverse and through thickness direction.

Measurement results. Five samples are used for each measurement and the Direct-Current (DC) resistance, as well as, the Alternating-Current (AC) impedance. The impedance is measured at several frequencies, that is: 50 [Hz], 25 [kHz], 50 [kHz], 75 [kHz], and 100 [kHz]. Each specimen is measured at two instances to exclude the influence of the test setup and clamping procedure. By using the specimen dimensions the resistance in Ohm is transformed to conductivity in [S/m].

The AC conductivity measurements are extrapolated to the frequency of the induction welding simulation (for this measurement, 384 [kHz]). The results are given in Table 1.

Table 1 Measured anisotropic UD ply electrical conductivity.

σ_{11} [S/m]	31307 ± 581	σ_{22} [S/m]	0.865 ± 0.260	σ_{33} [S/m]	0.055 ± 0.018

3.2 Cross-ply electrical conductivity measurements

For the interface modelling conductivity properties have to be assigned to the interface elements. Such values can be determined via a similar measuring approach as described in the previous section. The specimen dimensions and test-setup are identical to the measurements in Section 3.1. Unfortunately, there was little consistency in the measured electrical conductivity properties. A possible cause could be delamination or fiber breakage of the specimens but this has not been further investigated. It is the intention of the authors to repeat the measurements on new specimens in future works.

4. Numerical simulation model

The electromagnetic simulations are carried out in the Finite element package Abaqus (Simulia, 2021). The theoretical manual provides a complete derivation of the underlying equations. In this work we address the relevant steps to build the analysis model.

4.1 Model geometry and boundary conditions

The FEA Model is constructed according to the information provided in (Grouve, et al., 2020). The model consists of a three circular coil, a laminate and a volume of air surrounding the coil and laminate. In Figure *5* the geometry is shown. By making use of symmetry conditions only quart of the geometry is modelled.

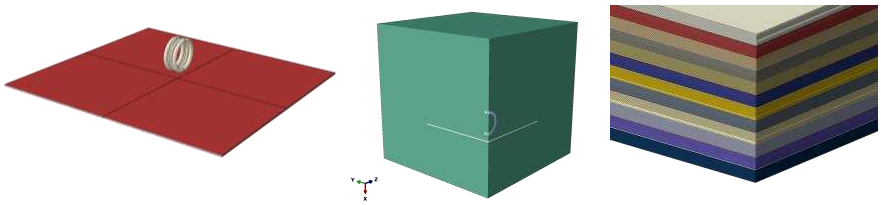

Figure 5 Model geometry. (left) the laminate and coil. (middle) quarter model of the coil, laminate and air surrounding the workpiece. (right) The laminate stacking highlighted with coloring.

The one quarter model consists of a composite laminate with dimensions 145[mm]x145[mm] and 12 plies, see Figure 5. Each ply has a thickness of 0.137[mm]. Hence, the laminate thickness equals 1.644[mm]. The coil consists of three circles with a pitch of 6.1[mm] of which one quarter is modelled. The distance between coil and laminate is 10[mm]. The coil cross section has a radius of 2.4[mm] and the coil turn has a radius of 18.6[mm]. Hence, the coil outer radius is 41.1[mm]. The coil is assumed to have homogenous material properties. A current of 350[A] is applied in circumferential direction of the coil at a frequency of 275kHz. The composite material is C/PEKK corresponding to (Grouve, et al., 2020). For completeness, the material properties that are used in the present model for the air, coil and laminate are listed in Table 2.

Table 2 Material properties taken from (Grouve, et al., 2020) *for the air, coil and plies.*

	Electric conductivity	Magnetic permeability	Magnetic permittivity
Air, Coil	1 [S/m]	$4\pi/1E7$ [H/m]	8.85E-12 [F/m]
Laminate $[0]_{12}$	In-plane 23e3 [S/m] Transverse in-plane 3.4 [S/m] Through thickness 0.6 [S/m]	$4\pi/1E7$ [H/m]	8.85E-12 [F/m]
0/90 interface	In-plane and transverse 11451 [S/m] Through thickness 0.2694 [S/m]	$4\pi/1E7$ [H/m]	8.85E-12 [F/m]

A boundary condition is set on the external domain where the magnetic flux is set to equal zero. Dirichlet boundary conditions and Neumann boundary conditions are set on the symmetry and anti-symmetry surfaces respectively.

The air surrounding the coil and laminate is a box of 275 [mm]x275 [mm]x275 [mm]. Each ply is modeled separately and considered an homogenous anisotropic sheet. For meshing 20 elements are used in thickness direction for each ply. The whole model comprises 460.183 EMC3D8 elements which proved sufficient for this case. The interfaces between plies are taken as 10% of ply thickness. Hence, the interfaces consume 2 elements in thickness direction from each ply except for top and bottom ply that only assign one element to the interface.

4.2 Number and position of interfaces within the laminate stacking

To show the effect of adding ply interfaces, several non-standard stackings are considered to emphasize the difference in induced current density. Hence, a uniform zero stacking is considered and as opposite a uniform $[0/90]_6$ stacking that most closely resembles a weave. To obtain an idea of how interfaces improve the eddy current generation through the thickness both the number of cross-ply interfaces is changed as well as the position of the cross-ply interface. In Table 3 the different stackings considered are summarized.

Table 3 Cross-ply orientations considered in the modelling. Each stacking consists of 12 plies.

Ply stacking	0/90 interfaces	Ply stacking	0/90 interfaces	Ply stacking	0/90 interfaces
$[0]_{12}$	0	$[0_{11}/90]$	1	$[0_2/90_2]_3$	5
		$[90/0_{11}]$	1	$[0/90]_6$	11

5. Results for different stacking sequences

UD ply interfaces are considered to be the main mechanism to allow eddy currents to form in a UD laminate. A laminate that has no UD ply interfaces is a 0_{12} layup where all plies are oriented in the direction of the coil. Since the plies in the simulation model are assumed to perfectly align, the only means of generating an induced current is in thickness and out-of-plane direction. The computed current densities are an order of magnitude lower in the 0_{12} layup as compared to the $[0/90]_6$ layup, see Figure 8.

Abaqus uses the absolute value of the magnitude of the EMCD vector to calculate the Joule Heating. Hence, when plotting the complex magnitude of the EMCD in through the thickness direction an idea of how the heat generation is taking place in the laminate is obtained. Hence, for a 0_{12} laminate the induced heating will mainly occur at the surface, see purple line Figure 9.

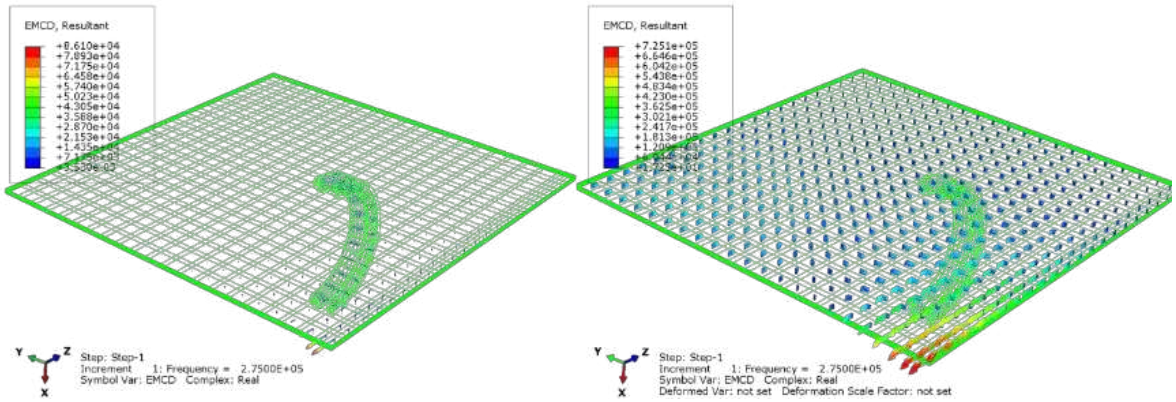

Figure 8 Real part of the eddy current density vector in the laminate Left is the eddy current generated in the 0_{12}.laminate and right is the eddy generated in the $[0/90]_6$ laminate.

Figure 9 shows that increasing the number of UD ply interfaces has the effect of increased current density. Hence, the peak values are higher as well as the part of the thickness in which the high currents are generated. Furthermore, the results show that the current density is not the highest at the top surface. Hence, inside the laminate the heating can be higher than at the surface depending on the stacking. However, this is not further investigated in this study.

Increasing the number of cross plies has the effect that multiple current returning paths are present in the laminate. Hence, the calculated eddy current increases through the thickness. This is shown for a $[0_290_2]3$ (five cross ply interfaces) and a $[0_190_1]_6$ (eleven cross ply interfaces) stacking. The resulting EMCD through the thickness is shown in Figure 9.

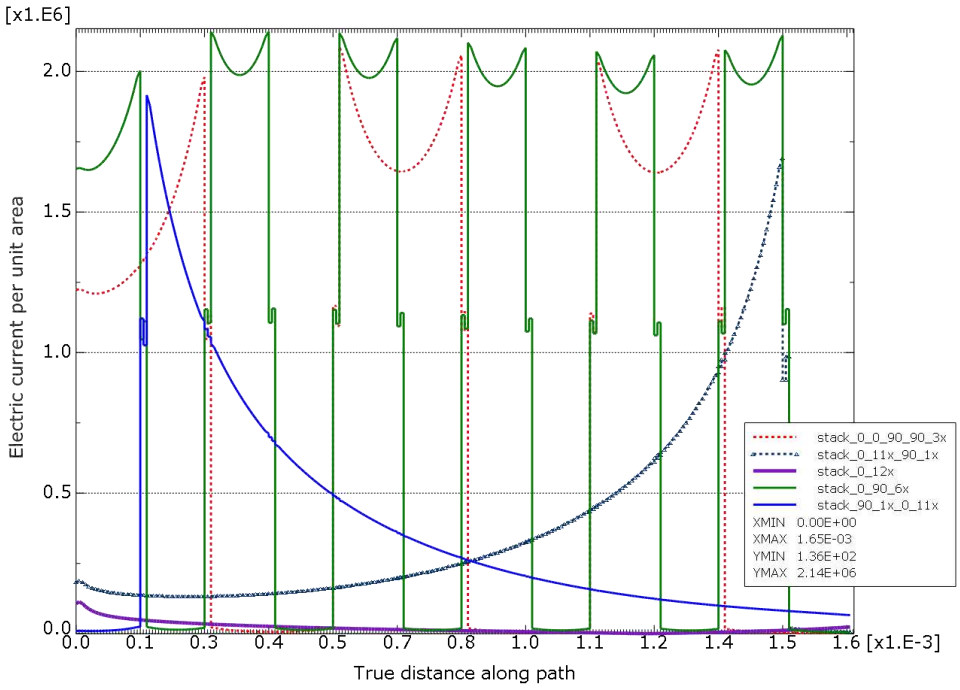

Figure 9 EMCD through the thickness for different ply stackings. Adding ply interfaces to the stacking increases the EMCD value calculated. Furthermore, a ply interface closer to the surface below the coil increases the current density through the laminate thickness.

6. Conclusions and further work

An increased number of cross-ply interfaces inside a UD CFRP laminate has a positive effect on the current density distribution inside the laminate which is important for inductive heating of UD CFRP. The measurement of anisotropic electric material properties was successful in determining electrical properties of the plies with respect to values recorded in literature. In future work we will examine the effect of cross-ply interfaces on thermal behavior of the inductive heating both via numerical simulation as well as thermal imaging of an inductive heating setup with UD CFRP laminate.

Acknowledgements

This project has received funding from the Clean Sky 2 Joint Undertaking (JU) under grant agreement No 945583. The JU receives support from the European Union's Horizon 2020 research and innovation programme and the Clean Sky 2 JU members other than the Union.

Disclaimer

The results, opinions, conclusions, etc. presented in this work are those of the author(s) only and do not necessarily represent the position of the JU; the JU is not responsible for anv use made of the information contained herein.

7. References

1. Ahmed, T., Stavrov, D., Bersee, H. & Beukers, A., 2006. Induction welding of thermoplastic composites - an overview. Composites Part A: applied science and manufacturing, pp. 1638--1651.
2. Cheng, J., Jinhao, Q., Hongli, J., Takagi, T., Uchimoto, T., Hu, N., 2014. Role of interlaminar interface on bulk conductivity and electrical. NDT&E International, Volume 68, pp. 1-12.
3. Cheng, J., Wang, B., Xu, D., Qiu, J., Takagi, T., 2021. Resistive loss considerations in the finite element analysis of eddy current attenuation in anisotropic conductive composites. NDT and E International, Issue 119.
4. Grouve, W., Vruggink, E., Sacchetti, F. & Akkerman, R., 2020. Induction heating of UD C/PEKK cross-ply laminates, Proceedings of 23rd International Conference on Material Forming.
5. O'Shaughnessey, P. G., Dubé, M. & Villegas, I. F., 2016. Modeling and experimental investigation of induction welding of thermoplastic composites and comparison with other welding processes. Journal of composite materials, 50(21), pp. 2895--2910.
6. Wit, A.J. de, Hoorn, N. van, Nahuis, R. & Vankan, W., 2021. Prediction of thermo-mechanic effects through numerical simulation of induction heating of thermoplastic composites, Amsterdam: Royal Netherlands Aerospace Centre – NLR, NLR-TP-2021-491.
7. Xu, X. et al., 2018. Interlaminar contact resistivity and its influence on eddy currents in carbon fiber reinforced polymer laminates. NDT and E International, pp. 79-91.
8. Yousefpour, A., Hojjati, M. & Immarigeon, J.-P., 2004. Fusion Bonding/Welding of Thermoplastic Composites. Journal of thermoplastic composite materials, Volume 17, p. 303.

  doi:10.5075/epfl-298799_978-2-9701614-0-0

STRUCTURAL TESTING OF LOCAL BUCKLING FOR THE DESIGN OF SANDWICH AIRCRAFT STRUCTURES

Ginot Malo[a,b], Castanié Bruno[a], Bouvet Christophe[a], Mahuet Nicolas[a]

a: Institut Clément Ader, Université de Toulouse, INSA – ISAE-SUPAERO – UPS – IMT Mines Albi, 3 rue Caroline Aigle, Toulouse 31400, France
b: Elixir Aircraft, Rue du Jura, 17000 La Rochelle, France

Abstract: *The design of light aircraft sandwich structures is often driven by a local buckling phenomenon named "wrinkling" which can be the primary cause of failure of such structures. Structural tests using the VERTEX Methodology were performed to access the wrinkling behaviour of technological sandwich specimens representative of the technology of Elixir Aircraft. The operating principle of the VERTEX machine is the use of four hydraulic actuators to load a rectangular box structure and therefore, sandwich panels were tested under compressive and shear loading. Wrinkling is observed thanks to Digital Image Correlation (DIC) and a high-speed camera. At this level of the test pyramid for certification of aeronautic structures, the observation of wrinkling on sandwich panels remains rare in literature and may lead to interesting future investigations on the experimental VS numerical finite elements model's dialogue.*

Keywords: Local buckling; Wrinkling; Sandwich structures; Structural testing; Light aircraft

1. Introduction

Thanks to their high specific bending stiffness, sandwich structures have been widely used in aviation for more than a hundred years (1). Recently, they are increasingly used for primary structures for lightweight aviation (like the Elixir from Elixir Aircraft®, certified by the EASA in June 2020). Local buckling phenomenon named "wrinkling" can be the primary cause of failure of such structure (1). An effective methodology for wrinkling sizing is still under discussion (2), and experimental studies could discriminate between existing models. However, experimental tests on the wrinkling phenomenon in the literature are still scarce. Previous works have shown, at beam scale (most experimental studies in literature), the high sensitivity of the phenomenon to boundary conditions and initial geometrical defects leads to difficulties in correlating experiments and models (3)(4)(5). An interesting approach consist in studying the upper-stage of the "pyramid of tests" called "technological", in other words, switching from beam scale to panels. This, to characterize the true behaviour of a structure and reduce the influence of boundary conditions. Therefore, this paper aims to offer protocols/methods with results and analysis of sandwich panels, tested under compressive and shear loading, where wrinkling type failure is observed. For this purpose, the VERTEX test bench (Figure 1) developed by Castanié *et al.* and first used by Serra *et al.* (6)(7)(8) was used. The operating principle of the VERTEX machine consists of four hydraulic actuators used to load a rectangular box structure. The tested panel closes the upper part of the central box. Actuators 1&2 can push or pull symmetrically to bend the box structure of the bench, thus the tested panel is locally loaded in tension or compression. Similarly, actuators 3&4 can push to twist the centre of the box structure, thus the tested panel is locally loaded in shear.

  doi:10.5075/epfl-298799_978-2-9701614-0-0

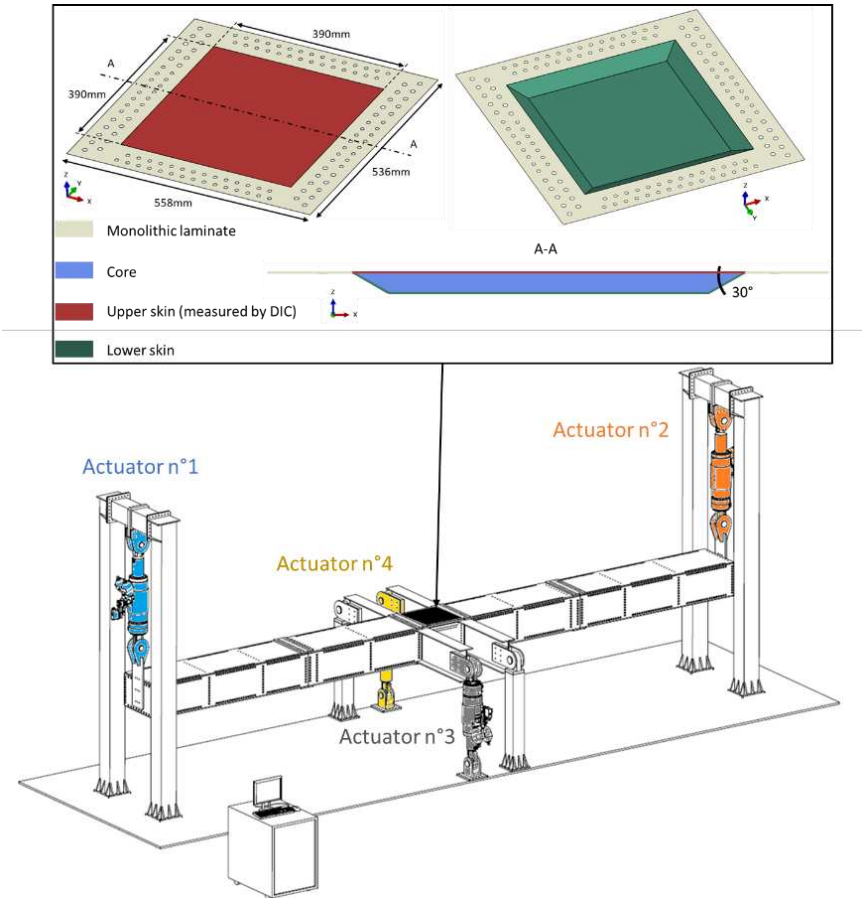

Figure 1: Vertex test rig and sandwich plate specimen

2. Materials and methods

The specimens are sandwich plates with a tapered area to close the sandwich at the centre. As a result, edges are monolithic and can be drilled to bolt the specimen to the VERTEX test bench. The specimen is positioned as shown in Figure 1 and bolted on its 4 sides with 128 screws. The external dimensions are 558x536mm², and the sandwich area with the tapered regions is 390x390mm² and 21 mm thick.

2.1 Specimen design

2.1.1 Geometry: The lower skin of the sandwich plate is not accessible as it faces the test bench box structure (Figure 1). The observable surface is the upper skin, it is thus imperative to localise the wrinkling mode on it. In the case of compressive loading, the tapered asymmetric geometry of the plate allows the upper skin to be more loaded than the lower skin and therefore to buckle. This mismatch between the load introduction axis and the mean geometric plane of the sandwich structure leads to a local bending moment, which induces an additional compressive load in the upper skin and a tensile load in the lower skin (blue arrows in **Erreur ! Source du renvoi introuvable.**). This phenomenon was already explored in asymmetric sandwich structures by Castanié *et al* (9).

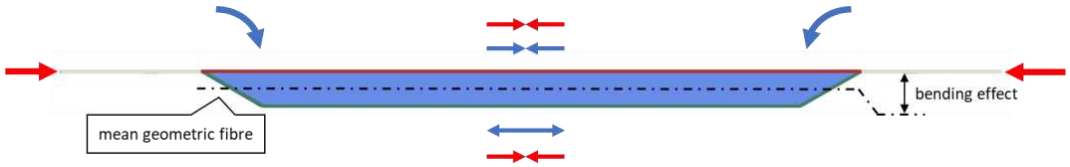

Figure 2: Bending effect on asymmetric sandwich structures.

2.1.2 Materials and process: The materials used for the specimens are ROHACELL HERO® 51 kg/m^3 foam for the core and prepreg epoxy/carbon woven fabric for the skin. An autoclave following a "one-shot/co-cured" process is used. The trimming and drilling are carried out using a CNC (computer numerically controlled) machine.

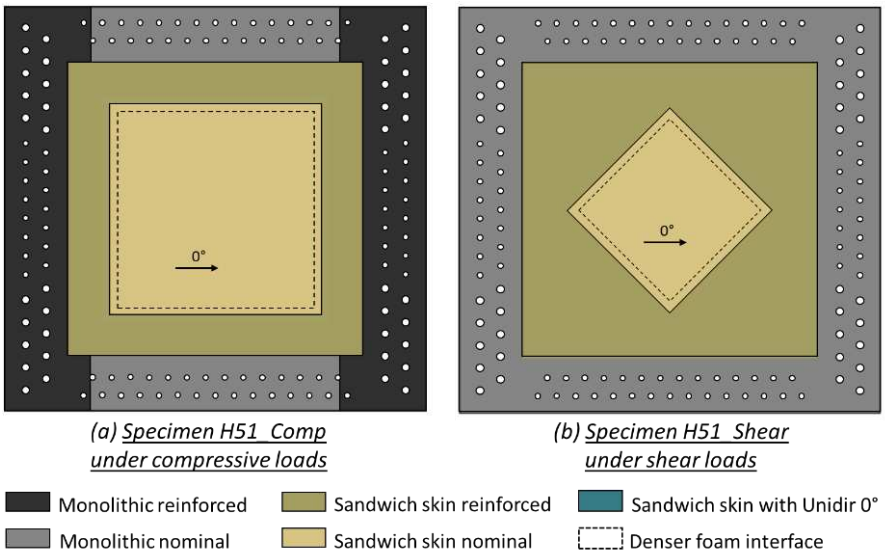

Figure 3: Skin definition

To localise the wrinkling in the centre of the plate, a high-density foam frame is used to reinforce the tapered area of the sandwich where local stresses could be relatively high. For the specimen under compressive loads (H51_Comp), the nominal area is 260x260 mm (dotted frame in *Figure 3*(a)). For the specimen under shear loads (H51_shear), the nominal area (dotted frame in *Figure 3*(b)) is lozenge-shaped of 172x172 mm to have perpendicular edges to the main stresses at 45°. For the same reasons, skins in the tapered area are reinforced (deep brown area in *Figure 3*). For the specimen under compressive loads, the monolithic is reinforced in the specimen height (dark area in *Figure 3*(a)), to avoid bolt bearing. In the width, the monolithic is left with a relatively thin laminate (grey area in *Figure 3*(a)) so that this area does not carry all the loads at the expense of the sandwich zone. For the specimen under shear load, the nominal skin (light brown area in *Figure 3*(b)) is lozenge-shaped. It should be noted that skin reinforcement and core reinforcement are not in the same areas. We call nominal area (where wrinkling is expected) the area where the upper skin stacking sequence corresponds to two +/- 45° ply woven fabrics for H51-Shear specimen and a +/-45° and 0°/90° ply for H51_Comp.

2.2 Instrumentation

Because of numerous structural redundancies in the VERTEX test bench, nowadays, there is still no direct transfer function that links actuator forces with stress flows entering the specimen. An in-situ strains measurement method had to be used to calculate the stresses entering the specimen. Digital Image Correlation (DIC) has been shown to be a very reliable method, and

already been used on previous VERTEX tests (7)(8)(10). Moreover, stereo-DIC allows to measure out-of-plane displacements and reconstruct the 3D shape evolution. This is particularly useful for the wrinkling observation which manifests as short out of plane waves in the skins. To achieve this DIC, a speckled pattern is made on the upper faces of the specimens. A high-speed camera (7000fps) is then used to observe a potential explosive failure. In lower skin, "Rosette" gauges are used.

3. Results

3.1 Deformation fields: stereo-correlation

Figure 4 shows in-plane deformation fields obtained by DIC of the specimen's upper faces, just before failure. In the nominal area, the deformations are mainly uniform and follow typical expectations. For specimen H51_Comp, shear is observed at the corners, but is nearly zero in the central nominal area (see $\boldsymbol{\varepsilon_{xy}}$'s field of H51_Comp). For specimen H51_shear, the average principal compressive strain direction is about 38° from the x-axis. Some traction is shown by the non-null xcomponents (see positive $\boldsymbol{\varepsilon_{xx}}$'s field of H51_Shear), a consequence of an inherent machine behaviour when operated for this solicitation. Local gradients (see $\boldsymbol{\varepsilon_{xx}}$'s field of H51_Comp and $\boldsymbol{\varepsilon_{xy}}$'s field of H51_Shear) at the edge of the nominal area indicate local bending induces by wrinkling waves.

  doi:10.5075/epfl-298799_978-2-9701614-0-0

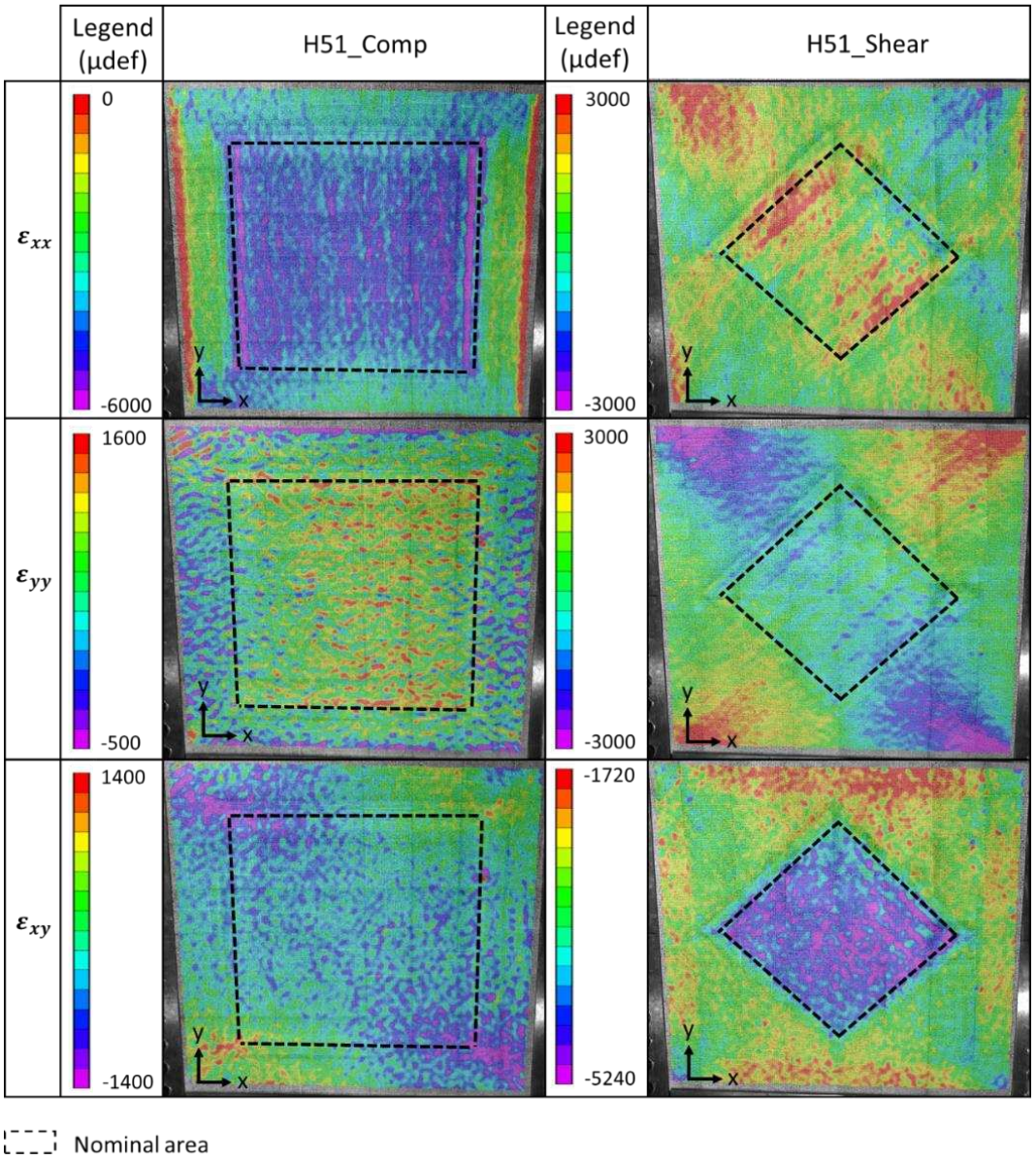

Figure 4: Deformation fields obtained by stereo-correlation.

3.2 Failure scenario

For both specimens, the failure behaviour is similar (*Figure 5*). The specimens fail by wrinkling the upper skin, which validates the design of the specimens. The wrinkling wave appears at the interface between the nominal HERO 51 foam and the denser foam. The core is crushed, and the wave then spreads over the width. Finally, the core fails in tension and the wave moves on a large part of the nominal area. This lasts about 2 milliseconds. For specimen H51_shear the wrinkling wave appears at -45° direction, induced by the compression along the +45° direction associated with shear loading. Skin static failure is observed from the edge of the specimen after the wrinkling event. Note that failure scenarios could be accurately reconstructed thanks to the high-speed camera.

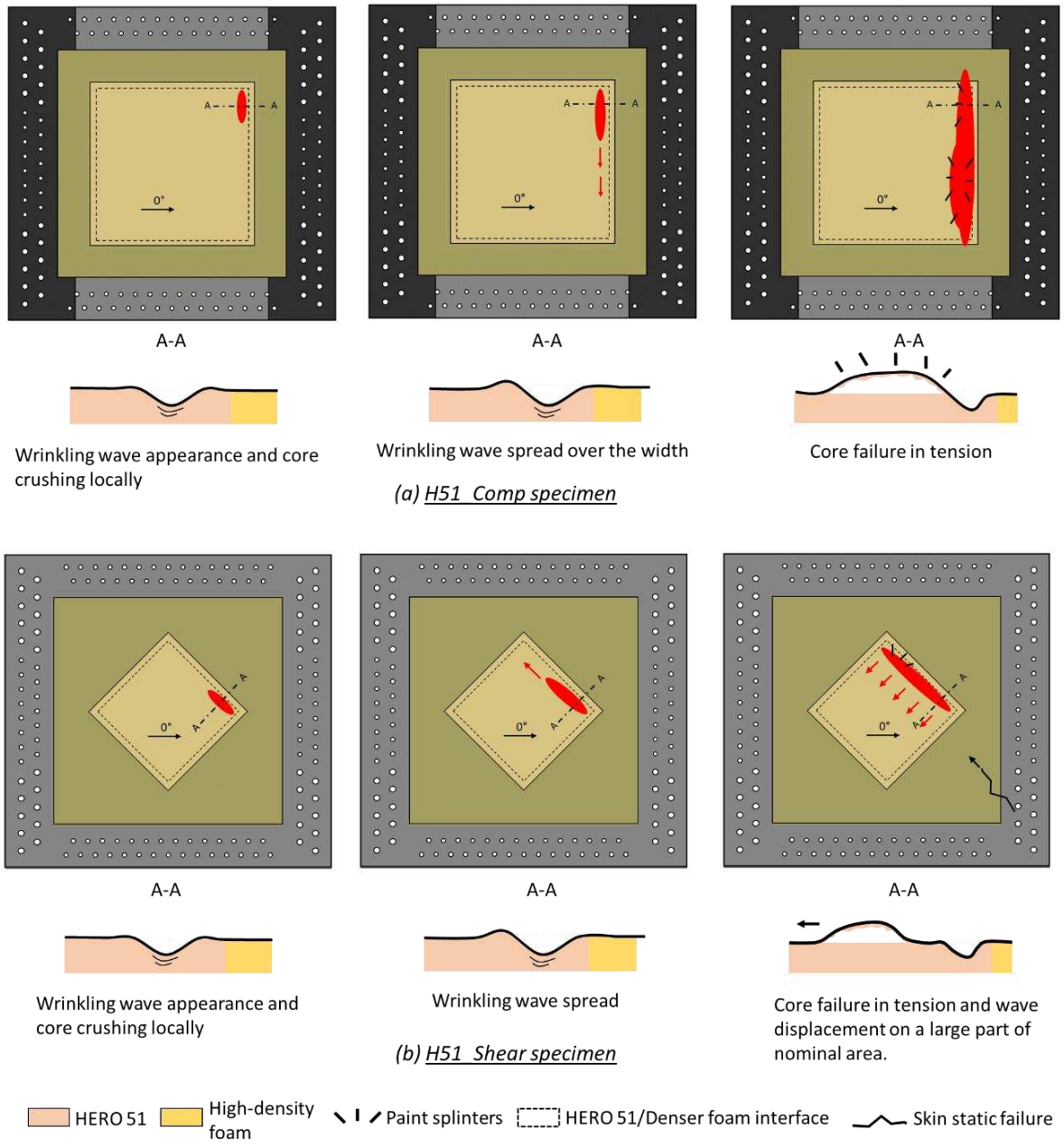

Figure 5: Failure scenario schemes

3.2 Out of plane behaviour

H51_Comp: The specimen plate bend globally (*Figure 6* (a)), a consequence of the tapered asymmetric geometry. $\boldsymbol{\varepsilon_{xx}}$ at the center of both skins highlight the non-linear bending behaviour of the tested plate, with the upper skin showing higher loading (*Figure 6* (b)).

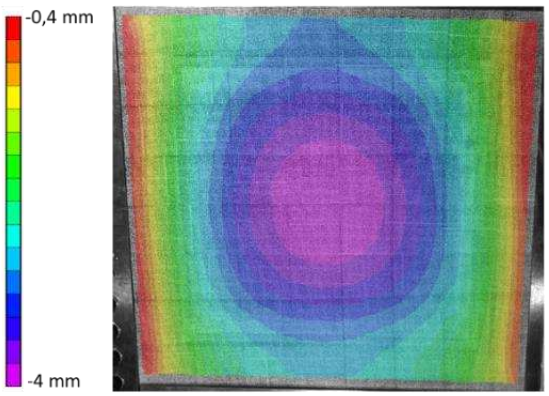

(a) Out of plane displacement field of the upper skin just before failure

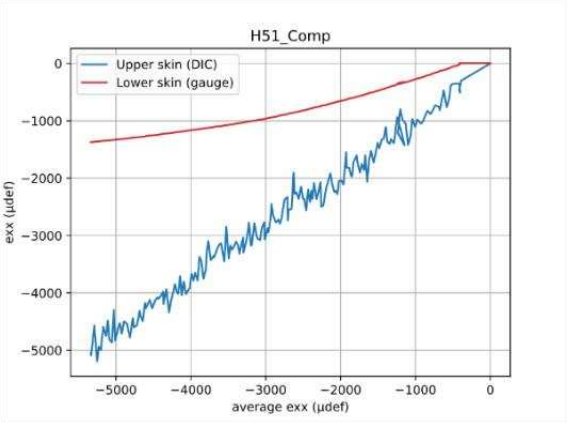

(b) $\boldsymbol{\varepsilon_{xx}}$ of upper and lower skin against average strain

Figure 6: Specimen H51_Comp out of plane behaviour

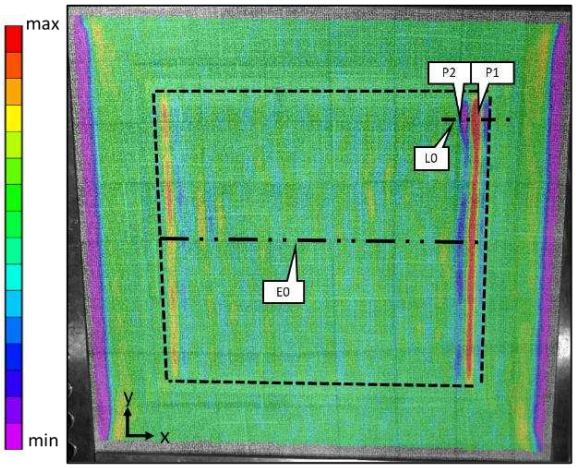

Nominal area — Inspect line for average deformation E0 — Inspect line for out of plane displacement W

(a) Inspect points and lines on curvature evolution field just before failure.

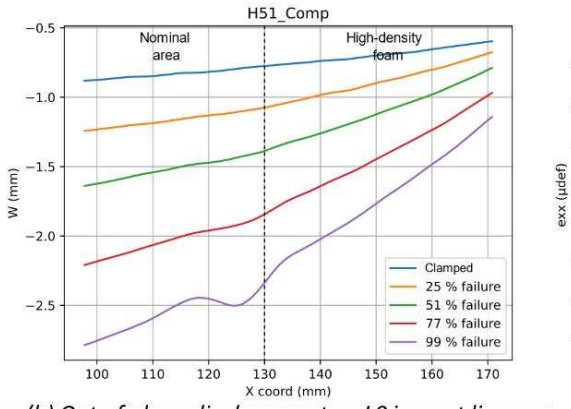

(b) Out of plane displacement on L0 inspect line for various loading rates

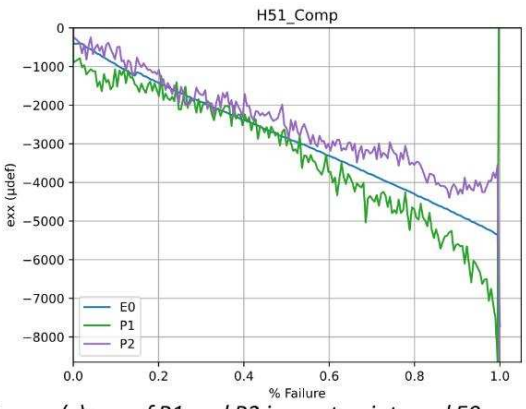

(c) $\boldsymbol{\varepsilon_{xx}}$ of P1 and P2 inspect points and E0 average strain against % of failure

Figure 7: Specimen H51_Comp local behaviour

A wrinkling wave is observed at the interface between the nominal HERO 51 foam and the high-density foam (*Figure 7*(a) and (b)). It appears at the end (>80%) of the test (*Figure 7*(b)). This can be confirmed by looking at in-plane deformation curves (*Figure 7*(c)). $\boldsymbol{\varepsilon_{xx}}$ at P1 and P2 first

decreases linearly with load, until the apparition of the wrinkling wave (around 80% load). It then becomes non-linear, a consequence of a local bending due to the wrinkling wave. The slopes at P1 and P2 differ from the one of the average deformation E0. This is a consequence of the out-of-plane effects of the initial conditions. Since geometrical defects localise wrinkling, it has occurred near the interface with the densified foam, where an initial slight skin depression was observed thanks to DIC. This phenomenon is local, thus the non-linearity does not influence the average deformation E0 which remains linear until failure.

H51_Shear: In this specimen, the global bending behaviour presented previously is not present because the tension and compression at 45° compensate for each other. Wrinkling waves are observed in a major part of the nominal area. The maximum wave's amplitudes are observed at the interface between the nominal HERO 51 foam and the denser foam (*Figure 8*(a) and (b)), where an initial slight skin depression was observed thanks to DIC.

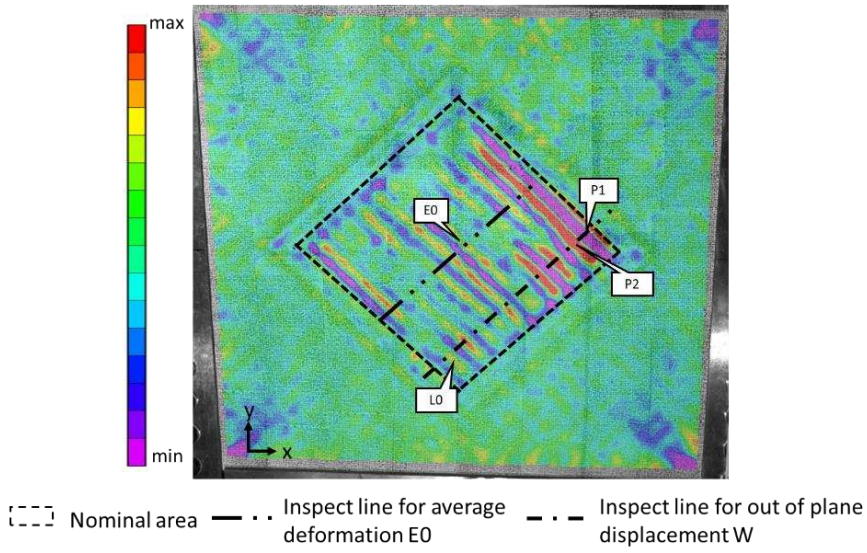

(a) Inspect points and lines on curvature evolution field just before failure.

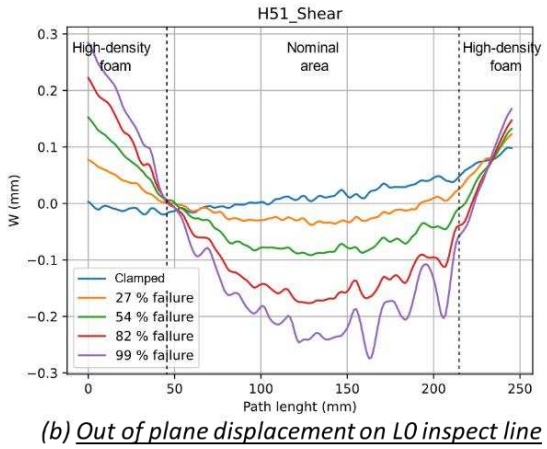

(b) Out of plane displacement on L0 inspect line for various loading rates

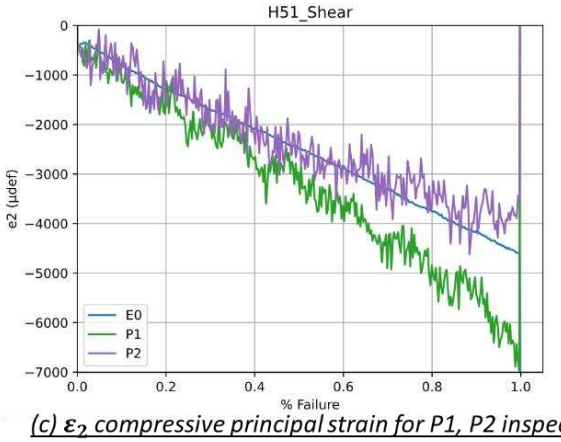

(c) ε_2 compressive principal strain for P1, P2 inspect points and E0 average strain against % of failure

Figure 8: Specimen H51_shear local behaviour

Similar to the compressive test, $\boldsymbol{\varepsilon_{xx}}$ first follows a linear trend with loading, followed by a non-linear regime at the end of the test for inspect points P1 and P2.Again this can be attributed to the local buckling onset that has happened around 80% load (*Figure 8*(c)).

4. Conclusion

This paper presents the materials and methods with the associated results and analysis, of two sandwich plates bolted on 4 sides, tested respectively in compression and shear using the VERTEX test bench. Wrinkling type failure was observed using both DIC and a high-speed camera. Such specimen geometry, material definition and measurements tools have demonstrated their effectiveness to observe wrinkling and insulate the failure scenario from the influence of the boundary conditions. It's appeared that wrinkling is driven by initial geometrical defects which localise the failure. 3D shapes and local deformations rates have been quantified and should be compared with existing models. This will be the object of future works.

5. References

1. Castanié B, Bouvet C, Ginot M. Review of composite sandwich structure in aeronautic applications. Compos Part C Open Access 2020;1:100004.

2. Ginot M, Ottavio MD, Polit O, Bouvet C, Castanié B. Benchmark of wrinkling formulae and methods for pre-sizing of aircraft lightweight sandwich structures. Compos Struct 2021;273:114387.

3. Hoff NJ, Mautner SE. The Buckling of Sandwich-Type Panels. J Aeronaut Sci. 1945;12(3):285–97.

4. Ley RP, Lin W, Mbanefo U. Facesheet wrinkling in sandwich structures. NASA Contract Reports [Internet]. 1999;CR-1999-20. Available from: http://www.cs.odu.edu/~mln/ltrs-pdfs/NASA-99-cr208994.pdf

5. Koissin V, Shipsha A, Skvortsov V. Effect of physical nonlinearity on local buckling in sandwich beams. J Sandw Struct Mater. 2010;12(4):477–94.

6. ANR VERTEX Program [Internet]. 30 March 2020. Available from: https://www.institut-clement-ader.org/vertex/

7. Serra J, Pierré JE, Passieux JC, Périé JN, Bouvet C, Castanié B, et al. Validation and modeling of aeronautical composite structures subjected to combined loadings: The VERTEX project. Part 2: Load envelopes for the assessment of panels with large notches. Compos Struct. 2017;180:550–67.

8. Serra J, Pierré JE, Passieux JC, Périé JN, Bouvet C, Castanié B. Validation and modeling of aeronautical composite structures subjected to combined loadings: The VERTEX project. Part 1: Experimental setup, FE-DIC instrumentation and procedures. Compos Struct. 2017;179:224–44.

9. Castanié B, Barrau JJ, Jaouen JP. Theoretical and experimental analysis of asymmetric sandwich structures. Compos Struct. 2002;55(3):295–306.

10. Trellu A, Pichon G, Bouvet C, Rivallant S, Castanié B, Serra J, et al. Combined loadings after medium velocity impact on large CFRP laminate plates: Tests and enhanced computation/testing dialogue. Compos Sci Technol. 2020;196:108194.

  doi:10.5075/epfl-298799_978-2-9701614-0-0

A 5M LIGHTWEIGHT COMPOSITE ATMOSPHERIC TOWER FOR EXTREME ENVIRONMENTS

Tristan, Décoppet[a], Florian, Guillaumat[a], Iris, Liechti[a], Romain, van Wassenhove[a], Andrea, Baccarini[b], Julia, Schmale[b], Anastasios P., Vassilopoulos[a]

a: Composite Construction Laboratory (CCLab), École Polytechnique Fédérale de Lausanne, Station 16, Batiment BP, Lausanne, CH / tristan.decoppet@epfl.ch
b: Extreme Environments Reasearch Laboratory, École Polytechnique Fédérale de Lausanne, Sion, CH

This contribution presents a student project based on the conceptualization, designing and manufacturing of a lightweight composite tower for atmospheric measurements in extreme environments. The project was initiated by Asclepios, which aim to achieve analog space missions. Deployed on a celestial body, the measurement tower should resist low temperature, high wind loads and the weight of an astronaut climbing it to intervene on the atmospheric measurement equipment. A triangular truss tower was realized using glass fiber tubes. The connection of the tubes is based on 3D-printed PA-12 plastic connectors and the foundation consist of a sandwich panel. The tower is braced using Kevlar ropes connected with tensioners and carabiners. The entire tower weighs less than 30 kg. After proving the tower stability and structural integrity with full-scale mechanical experiments, it was mounted at the EPFL Sion to conduct field measurements and to monitor the tower's behavior under operational loading conditions.

Keywords: Space mission; Glass fiber; 3D-printed; Easily deployable; Economical.

Introduction

Any new space expedition begins with understanding the environment by establishing scientific outposts. One important aspect of the scientific research on a new planet is the study of its atmosphere, by collecting data such as temperature profiles, pressure, humidity rate, wind velocity, or air composition. These atmospheric measurements are collected using measuring devices fixed on a tower.

Designing such a tower leads to many challenges. The tower must suit the extreme environment of a celestial body, while being easily transported, built, and maintained. These towers are generally made of steel, but this project aimed to use the properties of composite materials to achieve the objective.

This is what this project was all about. The tower was designed in the frame of the Asclepios project, aiming to organize analogue space missions led by students, representing a short-term journey to an extraterrestrial body (like moon or mars). After a year of design phase, a prototype was successfully tested for 5 months (Dec-May) at Sion. Now, the project moves forward as the tower will be part of the 2022 Asclepios mission.

  doi:10.5075/epfl-298799_978-2-9701614-0-0

1. Requirements

The extreme environment and the context of a space mission imposed significant constraints on the conception. Space missions are characterized by a small number of astronauts, equipped with a spacesuit which includes gloves that restrain the mobility and precision. Thus, any screwing or small pieces difficult to handle must be avoided. As spacecraft are extremely tight, weight and compactness are primordial. Thus, it was set that the tower must be lighter than 100kg to be easily transportable.

Still, it is recommended for the Astronauts to be accustomed to the building process because of the extreme conditions in which they will build the tower, and because they could gain some precious time by already knowing the building steps. Therefore, an assembly guide had to be created to fully detail the process of the building of the tower.

The tower's primary function is to make atmospheric measurements. It is essential that the tower can carry the equipment that have an aggregated estimated weight of 40 kg. Besides, temperature and wind are also important loads. The tower should resist cold temperature around -20°C and a wind load of about 120 km/h.

2. Design

2.1 Structural concept

It was chosen to design a climbable truss tower. Three arguments pushed the decision. First, the ability to easily fix and repair all the devices by allowing one astronaut to climb. Thus, one device can be repaired without affecting the other measurements. Second, this shape grants very good stiffness and strength against lateral loads such as wind. Third, the tower can be built horizontally. All the operations can be done on the ground, easily and safely. Then, the frame is stiff enough to be lifted from a horizontal to a vertical position.

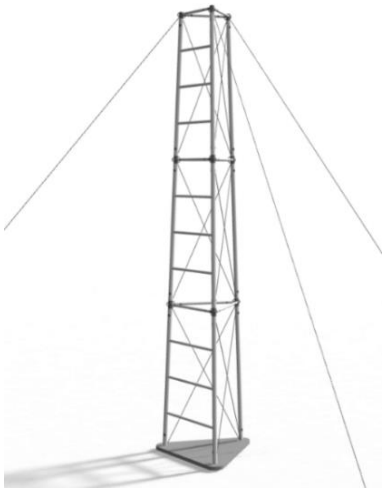

Figure 1. The triangular truss, with a ladder and bracings.

A triangular shape was chosen for its effectiveness. Adding more sides (square, pentagon) would increase the cost of the tower without any benefit on the stability. It was decided to incline the

  doi:10.5075/epfl-298799_978-2-9701614-0-0

columns by 2° degrees inward, to reduce the eccentricity of the vertical loads and enhance the stability. This inclination leads to sides of 80cm at the bottom and 44cm at the top, which is enough to climb. As shown in Figure 1, two intermediate horizontal triangles were added to create a rigid frame. Posts and horizontal bars are connected with 3D printed elements. On one side of the tower horizontal bars were placed to create a ladder and are directly inserted inside the vertical posts which are drilled, to avoid additional connection and facilitate the assembly. To make sure the bars stay in place, two collar clamps maintain the tube in its position. The two other sides of the tower were braced using Kevlar ropes. An external bracing, composed of three ropes anchored in the ground was added to improve the stability of the structure.

2.2 Materials

For transportation reasons, the tower should be lightweight while being 5m high. Besides that, the tower should resist cold conditions, humidity, rain, and snow. Considering this, composite materials were chosen due to their lightness, mechanical properties and durability. Composite tubes of carbon fibers or glass fibers were considered for the tower structure. While glass fiber tubes are five times cheaper than carbon fiber tubes, they have very good mechanical properties, satisfying the design recommendations, and therefore they were chosen for the tower manufacturing.

2.3 Clipping system

The frames were linked with 3D printed connections using Polyamide 12 (PA-12). Each connection is made of a node and four clips screwed in, as shown below in Figure 2. The clips were then inserted in the truss' tubes. The base of the tower was linked with the same clip system inserted into a sandwich panel to ensure the stability of the tower.

Figure 2. 3D-printed connection with a node and clips inserted in the tubes.

The design of these connections was based on a previous work [1]. The adaptation of these connections for this project includes handles for the bracing ropes and local reinforcement at the connections.

2.4 Bracing system

To resist lateral loads, the tower had to be braced. Two bracing systems were considered and appropriately designed in this work:

  doi:10.5075/epfl-298799_978-2-9701614-0-0

• An external bracing fixed on the top of the tower anchored in the ground to prevent any displacements of the top of the tower. It is particularly effective to stiffen the tower when someone is climbing.

• An internal bracing creating a lateral stiffness so that the structure behaves as a frame. This was realized by adding cables in the diagonals of the frame at each storey, for the two sides of the tower (the third one being already stiff with the introduction of ladder steps).

A 4 mm Kevlar rope was chosen as bracing material for its high tensile strength (5.8 kN – according to the product data sheet [2], lightweight and durability properties.

To reduce the number of cables, each one goes through two sides of the tower (see Figure 3) and are connected to the handles of the connections, as shown in Figure 4, mechanical tensioners connected with carabiners were used to easily tighten the system. This system allows one single person to tighten the cables by turning the screws.

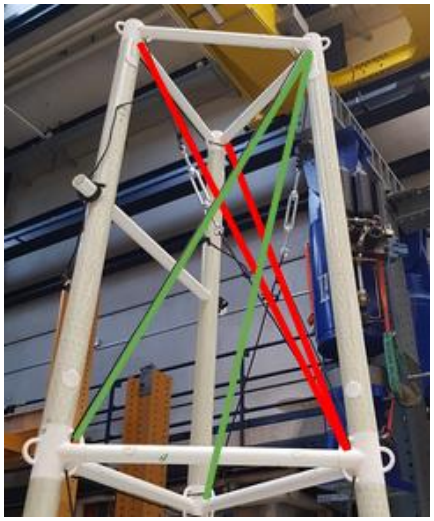

Figure 3. Geometry of the cables

Figure 4. Tensioners connected to the handle

3. Design validation

3.1 Connection test

To have a better understanding of the tower performance, it is important to test the behavior of the connection itself, and especially investigate its rotational stiffness. The idea was to simulate the bending moment created in the connection while an astronaut walks on a ladder step. By doing so, the parameter of rotational stiffness of the connection could be implemented in a numerical model to have a precise definition of the tower's behavior.

A first test was realized by maintaining the connection with the ladder tube (small one) while pushing vertically on the post. The setup is shown on Figure 5. This simulates an instrument hung on the side or the wind pushing on a plate attached to the post. It results in a failure of the clip branch and of the connection simultaneously. As shown in Figure 7, the connection had a linear (elastic) behavior at the beginning of the loading. When the load of 0.2 kN was reached (it corresponds to a 60 km/h wind on a 30cm square plate), the graph continued in a plateau, that

means the deformation becomes plastic. This loading case is not really expected. The only force that could push against the posts is the wind, which is not a point force.

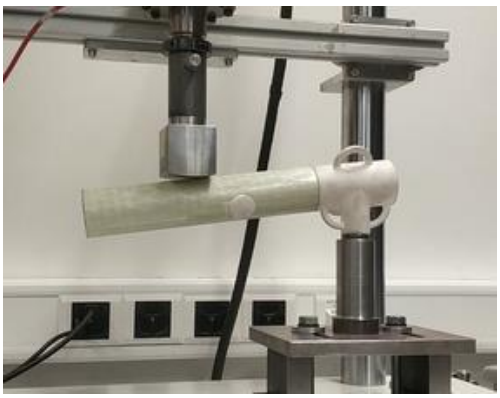

Figure 5: The setup in the post direction

Figure 6: The screwing thread coming out.

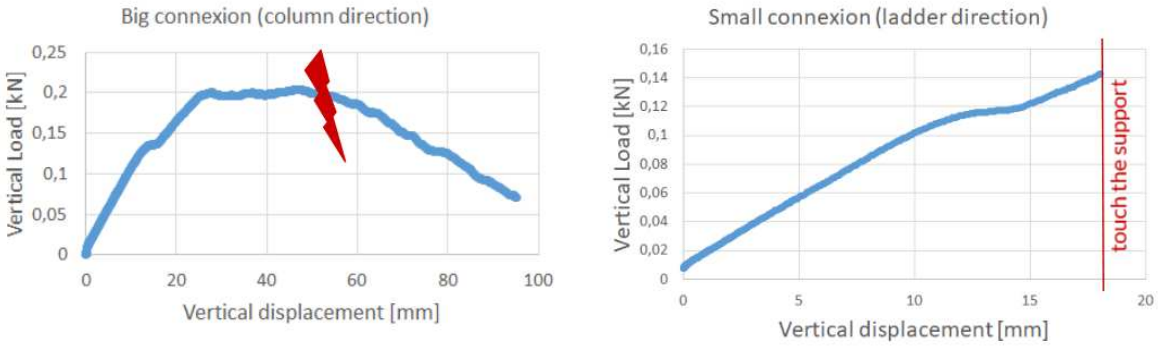

Figure 7: Tests results, in column and ladder direction, showing high connection deformability

The second test in the ladder direction was more representative of a real loading case. By applying a force on the ladder step, it simulates exactly what happens in the connection during the climbing of the astronaut. The behavior of the connection was completely different. As shown in the Figure 6, the screw part slipped little by little from the node. The connection did not carry any stress, but the two parts detached from each other. Unfortunately, the bar touched the support before failure, so the maximal deformation cannot be defined. However, this test led to the conclusion that the maximal deformation was high enough, in both loading cases, even if the forces applied were low. Therefore, the connection is considered as a perfect hinge. In order to increase the stiffness and reduce lateral displacement at the nodes, it could be possible to increase the length of the screw thread.

3.2 Full-scale testing

The aim of the full-scale testing was to simulate a real loading case, i.e., with the equipment fixed on the top and an astronaut climbing on it. This load was estimated to approximately 150kg (120kg for the equipped astronaut and 30kg for the measuring devices). Two tests were realized at the structural engineering platform (GIS-ENAC at the Ecole Polytechnique Fédérale de Lausanne, Switzerland), using a set of 17, 12kg iron bullions for the load application.

  doi:10.5075/epfl-298799_978-2-9701614-0-0

The first test simulated a vertical load centered at the top of the tower, representing the instruments and the astronaut. The setup consists of a belt fixed at one tube on the top supporting a box that can be filled with the iron bullion. The result is shown on Figure 8, with the following main observation: the more the compression in the post, the less the tension in the bracing. Indeed, the dynamometer was fixed to a cable that tend to de-stretch during the loading because the load was not exactly centered. If the dynamometer had been fixed on the opposite cable, a progressive tension would have been measured. Besides the pretension in the bracing cable that was applied manually with the tensioners corresponds to 12 kg, which is satisfying. All these observations ensure that the bracing system works.

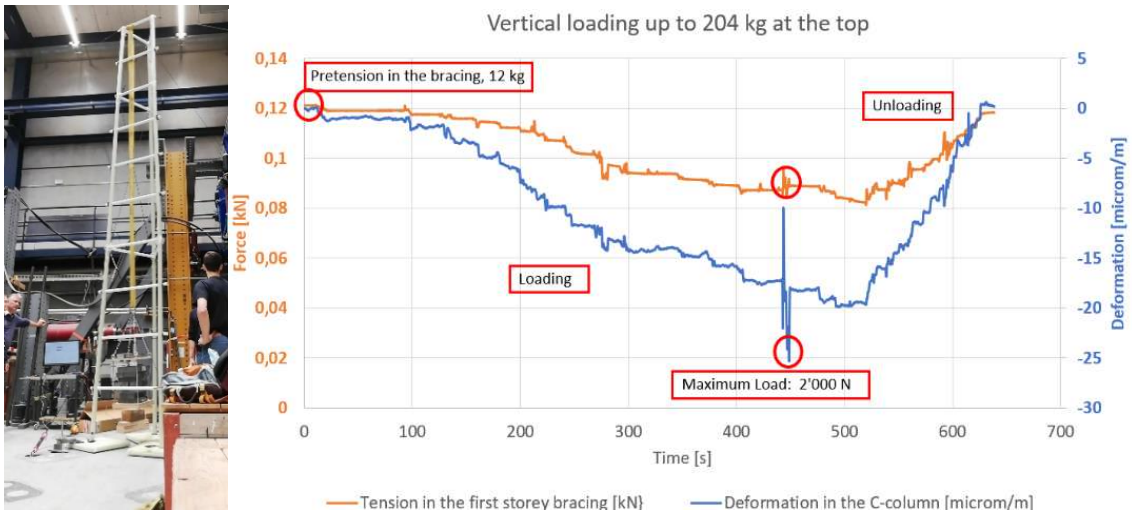

Figure 8. Vertical loading reaching 2'000 N without affecting the tower stability

The tower was loaded until 204 kg and did not show any structural weakness. The only part that was slightly damaged was the horizontal tube that supported the belt. A small deterioration of the tube shell appeared locally close to the node, which does not affect the tower stability. The goal of 150 kg was largely achieved.

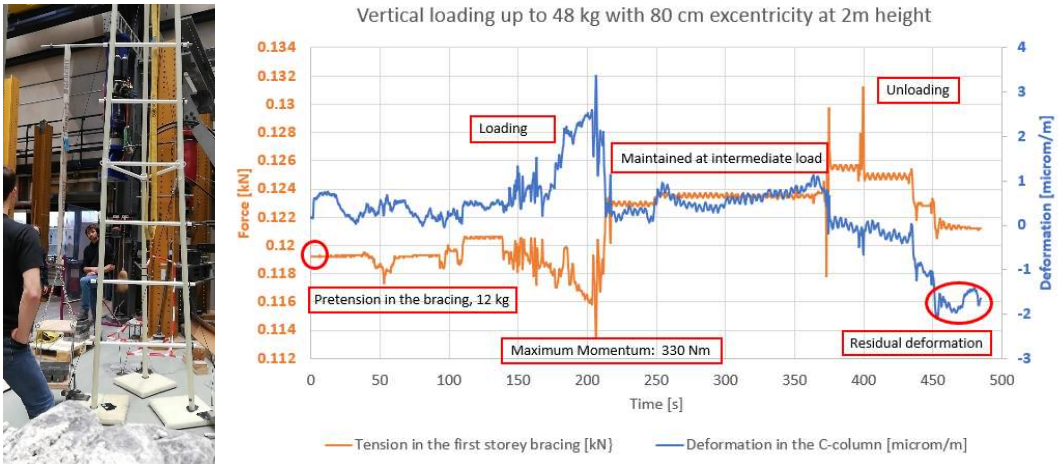

Figure 9. Eccentric vertical loading reaching 330 Nm momentum

The second loading was eccentric to create a moment in the tower, representing equipment fixed on the side. A steel rod was placed into the sixth step (2m high) and the belt was then fixed on it, with an eccentricity of 80cm. The iron bullions were added one by one and then removed.

  doi:10.5075/epfl-298799_978-2-9701614-0-0

On Figure 9, the loading and unloading path can be observed. The noise in the results is probably due to the manipulation of the dynamometers during the experiments and the vibration induced by the loading using bullions.

4. Field testing

After successful tests in the lab, the tower was deployed in real conditions. It was installed the 7th of December 2021 in the garden of the ALPOLE center, Sion, with all the necessary instruments: an anemometer and an optical particle counter. The tower was carried easily by a van as it is very compact when dismantled and weighs less than 30kg. It took one hour for three people to build the tower from scratch. This time includes driving foundation's piles, connecting all the tubes together, bracing the tower, stretching cables, placing instruments, and connecting it to a self-built electrical power box. Then, people could climb the tower easily, that showed great stability, thanks to the addition of internal and external bracings systems.

Figure 10: An astronaut climbing the tower to intervene on the equipment

Monitoring was conducted for 5 months. During this period, the average temperature was -5°, with minimum at -10°C, while wind speed of 45 km/h was recorded. At the end of the winter, the tower did not show any malfunction or damage. Measures were taken without noise or disturbance.

  doi:10.5075/epfl-298799_978-2-9701614-0-0

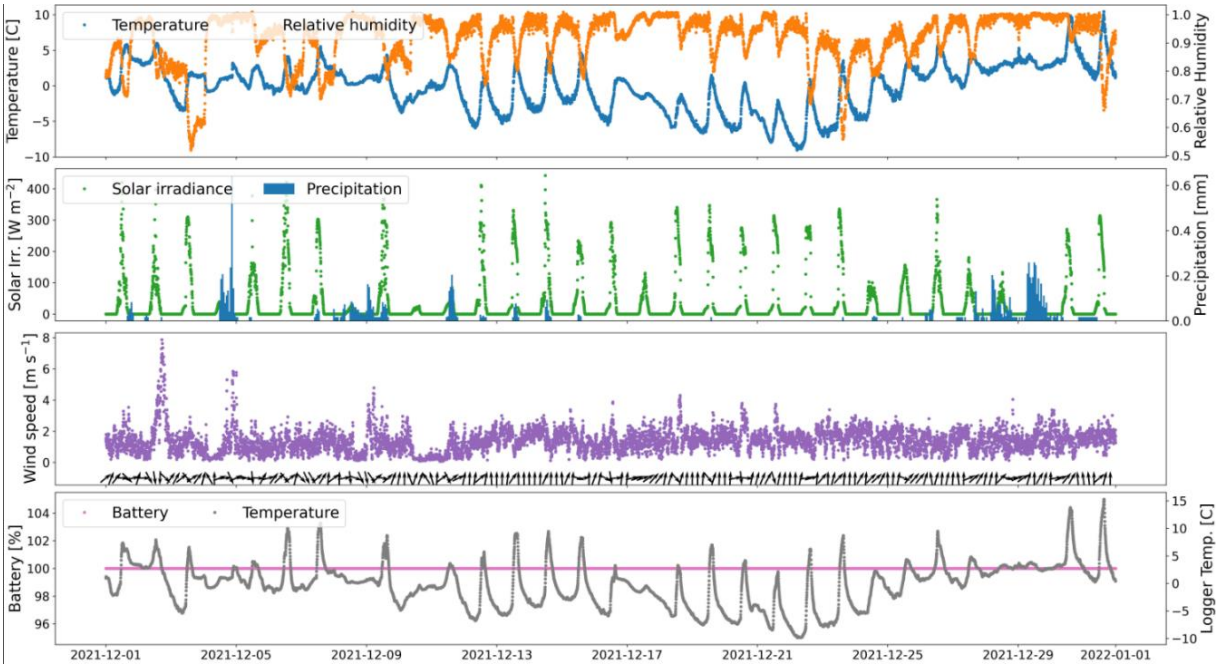

Figure 11 : Weather measurements in December 2021.

Conclusions

This project led to the design of a tower specifically suited to conduct atmospheric measurements in extreme environments. The tower has a low weight to height ratio, is easily buildable by a small crew of astronauts, avoiding any small pieces and the materials are durable. The tower has been easily and quickly built by three people, proving the efficiency of the assembly guide.

The experimental results showed that the tower can carry the atmospheric equipment as well as a man climbing up the ladder. Field testing validated the ability of the tower to operate in extreme environments over a long period (at very low temperatures during 5 months of winter in Sion in Switzerland). The precision of the measurements taken are promising.

To go further, it could be valuable to investigate on the fabrication of the tower to improve the process. Indeed, the tower is a unique prototype and was hand made in the structural engineering Experimental platform (GIS-ENAC at the Ecole Polytechnique Fédérale de Lausanne (EPFL), Switzerland).

References

1. R. van Wassenhove, L. De Laet, A. P. Vassilopoulos. “A 3D printed bio-composite removable connection system for bamboo spatial structures” Composite Structures, 2021;269:114047
2. *Kevlarseil* parabraid. (2021). From kanirope: https://www.kanirope.de/kevlarseil-parabraid-4mm-16-fach-geflochten-kanirope

MULTIPHYSICS SIMULATION OF CONSOLIDATION PROCESS OF HIGH THICKNESS THERMOPLASTIC LAMINATE PARTS

Tuan-Linh Nguyen[a], Yvan Denis[a], Steven Le Corre[a]

a: Nantes Université, CNRS, IRT Jules Verne, Laboratoire de Thermique et Energie de Nantes, UMR 6607, LTeN, F-44000 Nantes, France – tuan-linh.nguyen@irt-jules-verne.fr

Abstract: *In this project, we are interested in the manufacturing of high thickness thermoplastic laminate parts. During this consolidation step, induced stresses or deformation may occur, which can lead to the generation of defects such as delamination or shape distortions. An experiment trial and error approach on the manufacturing of such high-performance materials and thick parts is cost prohibitive and time consuming. Thus, this work aims at reducing the process development cost through the multiphysics simulation of the consolidation processes. The multiphysics model proposed here is based on a coupling approach of the transient heat transfer, crystallization kinetics and elastic models at the macroscopic scale. These simulations can allow studying the consolidation problems such as shape distortion (spring-in) at the cooling phase due to the material shrinkage. Optimal process parameters or a customized mold/part design thus can be considered to minimize the induced defects.*

Keywords: Simulation; Consolidation; Distortion; Composite; Thermoplastic; High thickness

1. Introduction

Nowadays, the aeronautical industry is more and more interested in thermoplastic resin for its capabilities of welding, recycling, corrosion resistance… However, until now, the use of thermoplastic is mostly limited to relative thin parts which are not suitable for structural applications. In this project, we are interested in the manufacturing of high thickness thermoplastic laminate parts. The Automated Fiber Placement (AFP) process is a good candidate which can meet the industrial requirements: robustness, performance, production cost and rate… Nevertheless, it requires a phase of consolidation in an oven or autoclave as the in-situ consolidation is still a challenge, especially for high thickness parts. During this consolidation step, induced stresses or deformation may occur, which can lead to the generation of defects such as delamination or shape distortions. An optimization of the manufacturing strategies (like temperature and pressure cycle) or mold design is required to minimize or avoid these defects. However, an experiment trial and error approach on the manufacturing of such high-performance materials and thick parts is cost prohibitive and time consuming. Beside the thermal and kinetics analysis, mechanical modeling of composite manufacturing processes plays an important role in this case [2]. Thus, this work aims at reducing the process development cost through the multiphysics simulation of the consolidation process.

  doi:10.5075/epfl-298799_978-2-9701614-0-0

2. Shape distortion problem

2.1 Forming processes of high thickness thermoplastic laminate parts

The forming processes used in this project consist of two steps: AFP process and consolidation step. During the AFP step, thermoplastic laminate parts are draped up to 196 plies. The used tapes are made of carbon fiber and high performance semi-crystalline PAEK TP. In the second step, these parts are consolidated in a vacuum oven or in an autoclave with a given pressure/temperature cycle. Figure 1 shows a manufactured "Pylon" (U-shape) part with nearly quasi-isotropic draping scheme. The part is symmetric and the angle between the middle zone and side zones is about 80°.

Figure 1. Manufactured "Pylon" part

2.2 Spring-in - Shape distortion problem of U-shape (angled) composite laminates

Following the mold release,3D scan measurements have been realized. Figure 2 shows the correlation between the 3D scan and the designed (nominal) geometry of the pylon part. Green color indicates where there is less difference while red/violet color indicate zones of large shape distortion. We can see that shape distortion has been observed mainly in the extremities (free edges) of parts (red/violet color). Indeed, after the consolidation, the part tends to be more bended (closed) and the angle between the middle zone and side zones is reduced. This angle deviation is commonly called "spring-in" angle. In the literature, this spring-in phenomenon of angled composite laminates has been studied in many works, both for thermosetting and thermoplastic matrices [1, 7]. This phenomenon leads to the manufacturing of non-conforming parts and thus causes problems in assembly.

An estimation of the angle deviation was derived by Radford [4] which considers both the thermal and chemical shrinkages:

$$\Delta\theta = \Delta\theta_{CTE} + \Delta\theta_{CS} = \theta\left(\frac{(\alpha_l-\alpha_t)\Delta T}{1+\alpha_t\Delta T}\right) + \theta\left(\frac{\varphi_l-\varphi_t}{1+\varphi_t}\right) \quad (1)$$

  doi:10.5075/epfl-298799_978-2-9701614-0-0

where $\Delta\theta$ and θ are the angle deviation and the nominal initial angle, $\Delta\theta_{CTE}$ and $\Delta\theta_{CS}$ are the thermal and crystallization induced angle deviation, α_l and α_t are the in-plane and through-thickness coefficients of thermal expansion, φ_l and φ_t are the in-plane and through-thickness coefficients of crystallization shrinkage. This formula provides a quick estimation of shape distortion. In this case, it overestimates to spring-in angle with respect to 3D scan results. Moreover, it does not consider many process parameters such as: the contact mold/parts, the thickness of part, consolidation cycle, material behavior… A numerical tool and especially finite element (FEM) models are required to be able to predict more precisely the spring-in behavior. In what follows, a multiphysics FEM approach will be presented. Furthermore, it is addressed for high thickness laminates.

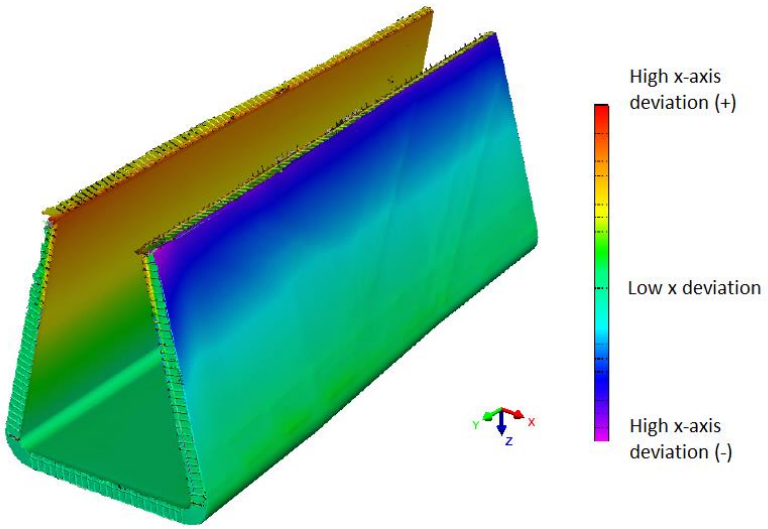

Figure 2. 3D scan result and correlation of shape with respect to designed nominal 'Pylon" part

3. Multiphysics model: coupled heat transfer, crystallization and mechanical models

3.1 Main modelling assumptions

- This work focuses on the consolidation step after AFP step of the forming processes. It is assumed that the parts before the consolidation step are perfectly draped which means: no gap or overlap of AFP, no delamination between layers and no deviation of fibers orientation. No shape distortion or thickness variation is considered after the AFP step. Moreover, the model is developed to predict the distortion after the mold release step. Further steps such as machining where additional distortion is likely to happen are not considered here.

- As the studied parts present many plies (up to 196 plies), a homogenized macroscopic 3D model is proposed in this work where effective properties are used. Indeed, the draping scheme of AFP process leads to a quasi-isotropic planar orientation. Subsequently, the composite part can be considered as a homogeneous transversely isotropic material (where transverse direction along the thickness direction) in this approach.

  doi:10.5075/epfl-298799_978-2-9701614-0-0

3.2 Multiphysics model

The multiphysics model proposed here is thus based on a coupling approach of the transient heat transfer, crystallization kinetics and thermo-elastic models at the macroscopic scale. In a previous study, thermal and thermal-crystallization simulations were carried out to study the influence of thermal contact resistance and mold geometry on thick composite laminates consolidation. The readers can refer to this article [3] for the details of thermal and crystallization models. In the present work, by considering the computed temperature and crystallization fields, a coupled mechanical model based on a simple thermo-elastic approach is introduced. This model aims at providing the evolution of shape distortion during the consolidation process and mold release step.

Let us recall here the corresponding numerical modules used for different physical phenomena occurred during the consolidation of thick laminates.

- Heat transfer: heat transfer module was developed in the FreeFem++ library [4]. FreeFem++ makes it possible to properly consider thermal contact resistance (TCR) by simultaneously solving the transient heat transfer both in the mold and in the part, thus introducing a strong coupling between domains. This heat transfer module allows to simulate the temperature gradient (particularly in the thickness direction for high thickness laminate parts).

- Crystallization kinetics: Based on the temperature result, a coupled thermo-kinetics module was also fully developed in the FreeFEM++ library. It consists of using the classical Nakamura kinetics [5] to simulate the evolution of the crystallization rate.

- Mechanics: The results of temperature and crystallization rate are then transferred to a thermo-elastic model in the Abaqus © (Dassault System) software. A numerical chain has been developed between the FreeFEM++ library and Abaqus. The proposed coupling is an iterative coupling as the data such as meshes, results are transferred at each increment (time step). The impact of thermal and chemical (crystallization) shrinkage is thus updated during the consolidation step.

Figure 3 shows the flow chart of this approach.

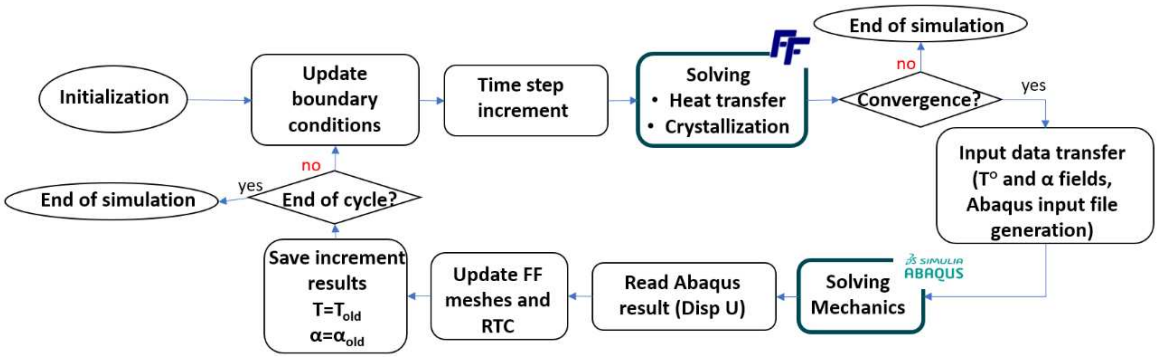

Figure 3. Flow chart of iterative coupling

During the consolidation step, the material evolves between different states: viscous, rubbery and glassy state in function of the temperature and crystallization rate. The material input must be considered with the phase change. Moreover, the material is not isotropic but transversely isotropic. In this work, thermal and crystallization properties were used such as the coefficient of thermal expansion (CTE), specific heat capacity or temperature dependent elastic properties. All of them account for the composite anisotropy, based on the transversely isotropic model.

The study and results presented below essentially target the cooling phase of the consolidation step. For these simulations, the crystallization peak temperature is considered as the stress-free temperature (SFT) which corresponds to the temperature that the stresses begin to develop. SFT means that above this point, it is assumed that no induced stress is generated as the material is in the viscous state. Thus, the contact of the part/mold is assumed perfect before that temperature.

3.3 Numerical model set-up for the consolidation of U shape (pylon) part

Figure 4 (left) shows the full 3D CAD model of the studied pylon (red) part and mold. The part is composed of different zones with variable thicknesses and corresponding nominal angles. In this paper, a representative model is proposed (cf. Fig. 4 on the right) where only a section of the full pylon (colored in white) is considered. This allows to accelerate the computational time and the use of finer meshes.

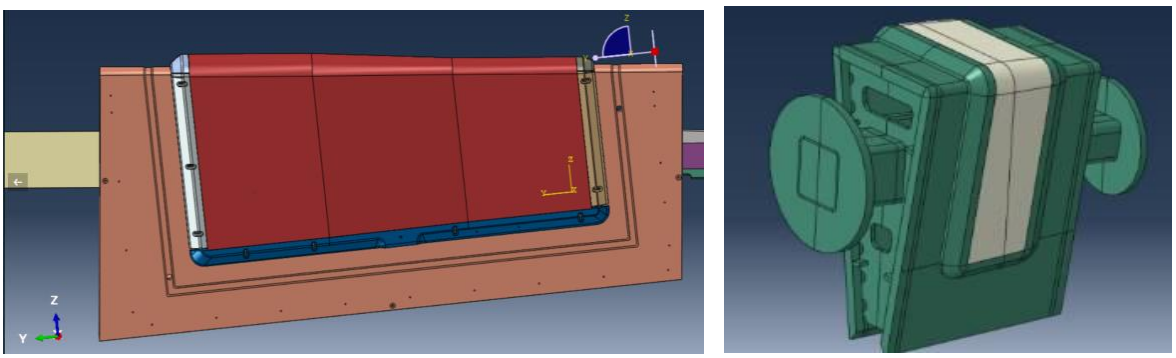

Figure 4. Full CAD (left) and representative model (right)

Figure 5. shows the cooling phase of the consolidation cycle. The material is first cooled down from above the resin fusion temperature (T_f). Then the cooling phase consists of a crystallization plateau (T_c) in order to maximize the crystallization rate. This temperature was chosen in function of the cooling rate regarding to the crystallization kinetics. A second plateau at lower temperature is imposed to homogenize the temperature through the part then part is cooled down to ambient temperature (T_a) at a constant rate. A constant pressure is applied on the part. As mentioned, input data for transversely isotropic material are required such as the thermal properties, crystallization kinetics of composites material, the coefficient of thermal expansion (CTE) at glassy and rubbery state, thermal dependent elastic properties. For the mold, isotropic properties are considered.

  doi:10.5075/epfl-298799_978-2-9701614-0-0

As a transversely isotropic material is considered, Abaqus ORIENT subroutine is used to define the material local coordinate in Abaqus.

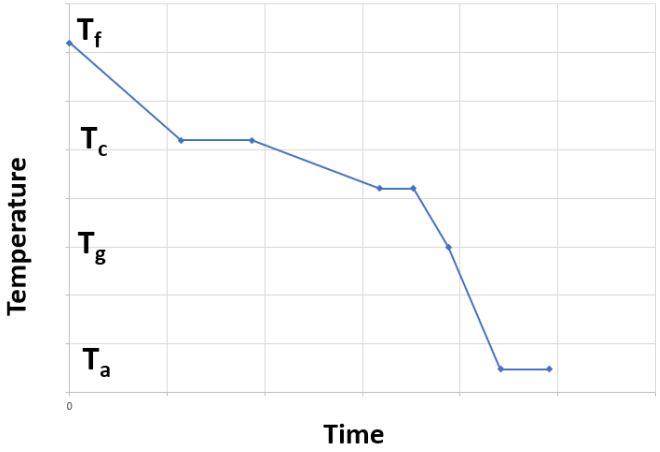

Figure 5. Cooling phase of the used consolidation cycle

4. Results and discussions

Figure 6. shows the results of the temperature and crystallization state at the beginning of the crystallization process. In our case, during the cooling phase, the chamber temperature of autoclave decreases. As the part is thick and there is inertia of mold, the mold is cooled more slowly which creates a gradient of temperature through the thickness of the part. It therefore causes a gradient of crystallization rate (α) through the thickness as well.

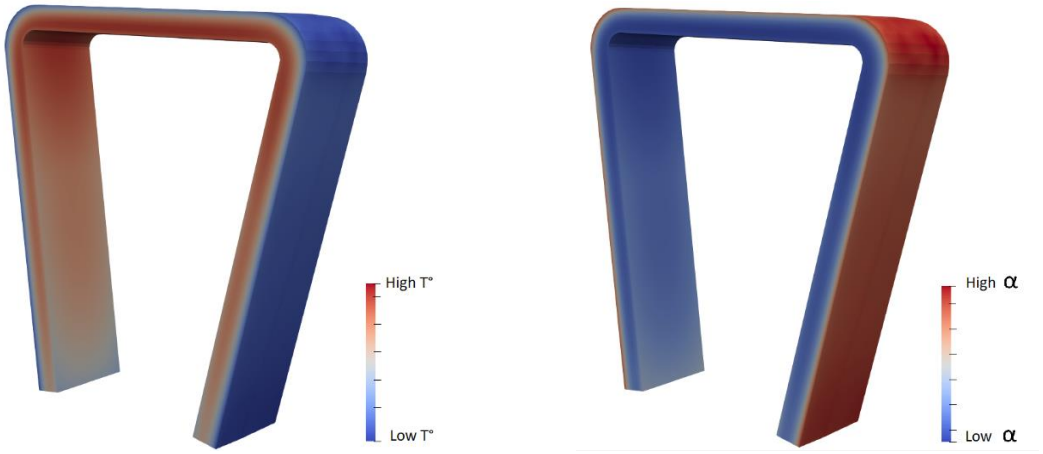

Figure 6. Simulated temperature field (left) and crystallization field (right) at the crystallization temperature during cooling phase

At the end of the cooling step, due to the shrinkages, the part deforms and tends to be more bended. However, it is constrained by the presence of the mold. The part is thus detached a little from its contact with the mold. Figure 7 shows the displacement field of part and mold at the end of consolidation step (view cut at the middle of part). As we can see with a zoom at the corner (Figure 7 right), a contact loss is observed between the part and the mold.

  doi:10.5075/epfl-298799_978-2-9701614-0-0

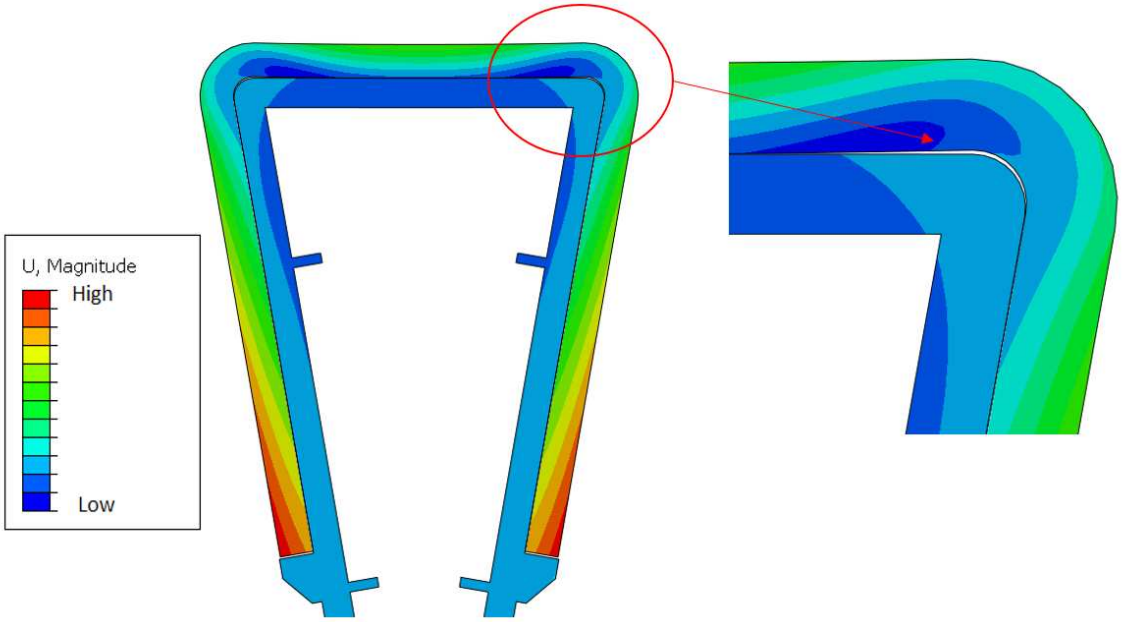

Figure 7. Contact loss between part and mold at the corner due to shrinkages (before mold release)

The angle deviation happens at the step of mold release. Figure 8 shows the displacement field (U) of the part with respect to the initial position at that moment (after mold release step). Indeed, the spring back is caused by the relaxation of the elastic stress. The value of part displacement is maximum at the extremities of the U-shape part. It is in accordance with the experimental results.

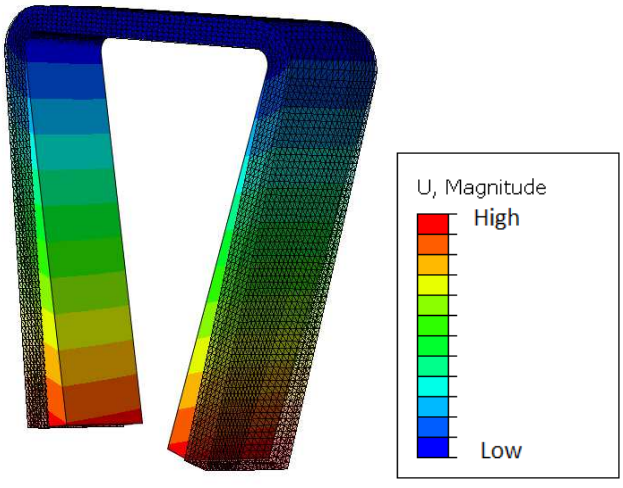

Figure 8. Simulated displacement field of part after mold release step

In our simulation, if the material is fed with isotropic material properties, the deviation is nearly none. It illustrates the origin of spring-in phenomena which is caused by the anisotropic properties.

  doi:10.5075/epfl-298799_978-2-9701614-0-0

5. Conclusion

This work aims at reducing the process development cost through the multiphysics simulation of the consolidation processes to avoid the costly trail-error approach. The multiphysics model proposed here is based on a coupling approach of the transient heat transfer, crystallization kinetics and elastic models at the macroscopic scale. This model can provide the evolution of shape distortion and induced stresses both during the consolidation process and mold release steps. These simulations can allow studying the consolidation problems such as loss of contact between tool and part due to the part shrinkage and its consequence on the heat transfer. Optimal process parameters or a customized mold/part design thus can be considered to minimize the induced defects, such as how to minimize the peak of induced stresses.

Several extensions to this work have been identified. Simulations at the plies scale could give further information about the stress field, such as interlaminar stresses. A proper material characterization of orthotropic properties in the rubbery state is also of paramount importance. Viscoelastic models can also be considered in function of the its impact for a better correlation.

Acknowledgements

This study is part of the MATCH project managed by IRT Jules Verne (French Institute in Research and Technology in Advanced Manufacturing Technologies for Composite, Metallic and Hybrid Structures). The authors wish to associate the industrial and academic partners of this project; Respectively AIRBUS, LOIRETECH, DAHER, LS2N, ENSAM and LTeN laboratory. The authors would like to thank F. Guermeur and A. Levy for their participation on the building of numerical models.

6. References

1. C. Albert, G.Fernlund, Spring-in and warpage of angled composite laminates, Composites Science and Technology, pp 1895-1912, 2002.
2. I. Baran, K. Cinar, N. Ersoy, R. Akkerman and J.H. Hattel “A review on the mechanical modeling of composite manufacturing processes”. Archives of computational methods in engineering, Vol. 24, No. 2, pp 365-395, 2017.
3. Y. Denis; T-L. Nguyen; D. Lecointe; S. Le Corre, A. Levy “Thick thermoplastic composite laminate consolidation: experimental observations and numerical approaches”. Journal of Composites Materials, 2021. (accepted).
4. Hecht F. New development in freefem++. J Numer Math 2012; 20(3-4): 251-265. URL https://freefem.org/.
5. A. Levy “Robust Numerical Resolution of Nakamura Crystallization Kinetics”. International Journal of Theoretical and Applied Mathematics 2017; 3(4): 143.
6. D.W. Radford, R.J. Diefendorfs, Shape Instabilities in Composites Resulting from Laminate Anisotropy, Journal of Reinforced Plastics and Composites, 1993;12(1):58-75.
7. A. Salomi, T. Garstka, K. Potter, A. Greco, A. Maffezzoli, Spring-in angle as molding distortion for thermoplastic matrix composite, Composites Science and Technology, 2008. 68(14):3047-3054.

  doi:10.5075/epfl-298799_978-2-9701614-0-0

MULTI-FIDELITY NONLINEAR STATIC AEROELASTIC OPTIMIZATION OF HIGH-ASPECT RATIO COMPOSITE WINGS

Spyridon, Kilimtzidis[a], Vassilis, Kostopoulos[a]

a: Applied Mechanics Laboratory, Department of Mechanical Engineering and Aeronautics, University of Patras, Patras University Campus, GR-26500 Patras, Greece
– s.kilimtzidis@upnet.gr

Abstract: *Novel high-aspect ratio airframe designs pave the way for a more sustainable aviation. Such configurations enhance the aerodynamic efficiency of an aircraft through induced drag reduction mechanisms. Further performance gains, mainly in terms of structural mass, are accomplished via composite materials airframes. Nevertheless, undesired phenomena such as geometric nonlinearities and aeroelastic couplings due to elevated flexibility may often rise, rendering the design and optimization of such airframes extremely intricate and prohibitive in terms of computational cost. Low-fidelity tools, preferred on the early design stages, accelerate the design process, albeit suffering from reduced accuracy and ability to capture higher-order phenomena. Contrastingly, high-fidelity methods incur excessive computational costs. In our study, variable fidelity analyses are initially conducted in order to shed light on their effect on the structural response of a reference wing. A multi-fidelity optimization framework is then proposed aiming at attaining a minimum mass configuration subject to multidisciplinary design constraints.*

Keywords: Aeroelasticity; composite materials; optimization; numerical analysis; aircraft wings

1. Introduction

In the foreseeable future, the rapid rise in aircraft travel demand will induce several environmental threats. On that front, the European Union envisages decrease in CO_2 and NO_X emissions for future commercial transport aircrafts. Key enabler to this effort is the introduction of novel airframe designs with improved aerodynamic and structural efficiency. Regarding the former, increasing the aspect-ratio of a wing is a well-established practice for increasing the aerodynamic efficiency by reducing the induced drag, thus improving fuel efficiency. For the latter, the introduction of composite materials in the design process results in lighter configurations. Nevertheless, such configurations are prone to undesired phenomena, the most prominent being the elevated flexibility that on one hand induces nonlinear structural behavior and on the other hand aggravates aeroelastic phenomena. Furthermore, accounting for this type of phenomena requires sophisticated computational analyses, which in turn are bound by often prohibitive computational time, hence they are preferred only for the later design stages of an aircraft structure. Aiming to alleviate the aforementioned issues, low fidelity tools are often utilized early on the design stages, albeit suffering from reduced accuracy and inability to capture higher-order phenomena. Early research efforts, confined by modest computational resources, focused on such representations of the structural and aerodynamics disciplines [1-2]. With the advent of computational prowess, high-fidelity computational tools and mostly Computational Fluid Dynamics (CFD) and Finite Element Method (FEM) methods started to emerge. Numerical solutions to the Euler and RANS equations along with coupled Fluid-

  doi:10.5075/epfl-298799_978-2-9701614-0-0

Structure Interaction (FSI) simulations and their subsequent embodiment into efficient optimization frameworks for various aircraft configurations were frequently sought in the literature [3-4]. The quest for improved performance led to the exploration of unconventional aircraft configurations, which highlighted the need for novel computational tools, with such methods being also nowadays subject to extensive scientific studies [5-6]. This research study aims to bridge the various fidelities of the numerical tools and provide an efficient multi-fidelity optimization framework of a high-aspect ratio composite wing. Reference analyses are initially conducted to assess the effect of fidelity of the associated computational tools on the structural response of a reference wing. Regarding the optimization framework, low-fidelity tools are initially tasked with guiding the structural design towards promising regions of the design space. Higher fidelity methods are then employed, aiming at exploring possible further gains in performance. We demonstrate that reasonable gains in structural mass of the test case wing can be realized through this approach.

2. Reference Analyses

2.1 Reference wing geometry

Within the context of this work, the undeflected CRM, namely uCRM13.5, has been chosen as the reference wing model. Constituting a modified, high aspect ratio derivative of the original CRM wing [7], the uCRM13.5 model [8] serves as a benchmark configuration for CFD and aerostructural optimization studies of realistic, future aircraft configurations operating at the transonic regime. The relevant geometric data are summarized in the following Table 1:

Table 1: uCRM-13.5 geometric data.

Wingspan [m]	Root Chord [m]	Tip Chord [m]	Reference Area [m^2]	Aspect Ratio	Quarter Chord Sweep [deg]	MAC [m]	Yehudi Chord [m]
72	11.07	2.06	383.78	13.5	35	5.77	*7.56*

Regarding the internal configuration, two spars located at 10% and 70% of the local chord are present along with 54 evenly distributed ribs. Spar and rib caps are also included along with skin stiffeners, as illustrated in Figure 1.

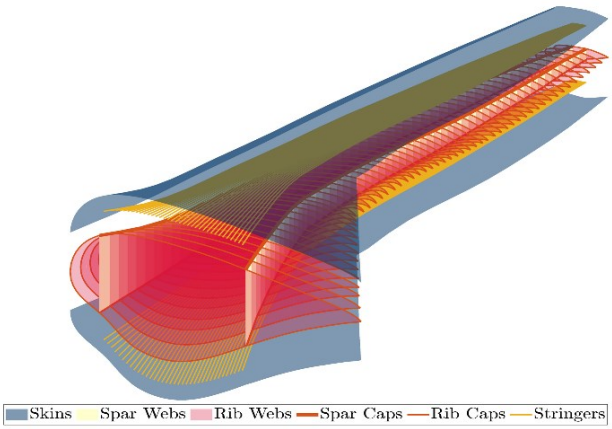

Figure 1. uCRM13.5 wing internal configuration

  doi:10.5075/epfl-298799_978-2-9701614-0-0

2.2 FEM model development

Based on the external geometry and internal configuration of the reference wing, a FEM model has been developed. Specifically, the upper and lower skins along with the spar and rib webs are modeled via 4-noded quadrilateral shell elements, denoted as CQUAD4. On the other hand, the spar and rib caps as well as the skin stiffeners are modeled via CBEAM elements of rectangular cross-section. As a datum design point, a reference balanced and symmetric layup and specifically the $[(45/0\text{-}45/90)_{2s}]_s$ has been considered for all the relevant wing parts. Furthermore, the upper and lower skins are assumed to be manufactured of the Hexcel IM7/8552 UD composite material, while the spars and ribs of the PW Fabric AS4/8552. Regarding the boundary conditions, the wing is assumed to be clamped at its root. External masses (engine & fuel) as well as gravitational loads have also been accounted for. The resulting FEM model of the uCRM13.5 wing is shown in Figure 2.

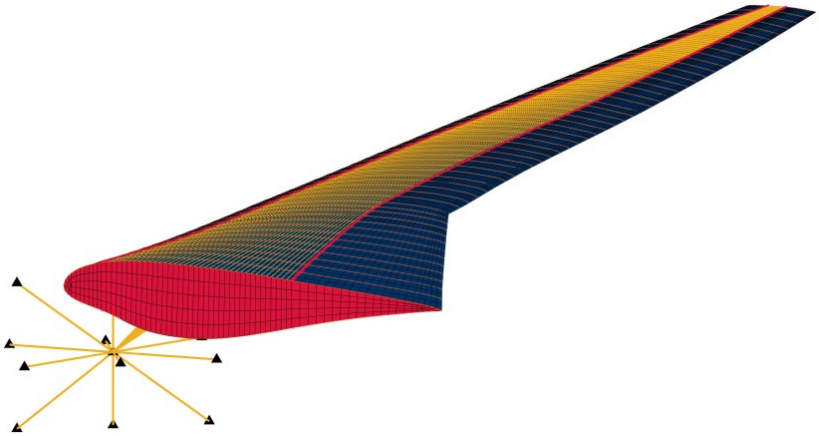

Figure 2. uCRM13.5 wing FEM mesh

2.2 Aerodynamic loading

For the subsequent analyses a 2.5g pull-up maneuver limit load, assumed to be exerted at the conditions indicated in Table 2, is considered as the critical aerodynamic loading scenario. Three types of modeling approaches in terms of aerodynamics have been used in this study, namely high-fidelity RANS CFD, low-fidelity 3D panel methods and the Doublet Lattice Method (DLM) for the generation of the aerodynamic loading, with the angle of attack being modified accordingly at each method in order to obtain the required lift load.

Table 2: Critical aerodynamic loading summary.

Condition	Lift Constraint	Mach	Altitude (m)
2.5 g maneuver	2.5 · MTOW	0.64	0

Where MTOW the Maximum Take-Off Weight of the aircraft, set to $268e^3$ kg.

2.3 Reference analyses

In this section, the effect of the various fidelities involved in the analyses on the structural response of the aforementioned uCRM13.5 wing, in terms of aerodynamics and structures, is investigated. In particular the effect of fidelity in the aerodynamics is investigated via solutions

obtained via CFD RANS, a 3D Panel Method and NASTRAN DLM, with the former enabling steady state aeroelastic calculations also. From a structural point of view, the level of fidelity is dictated by whether the geometric nonlinear behavior of the structural is accounted for. The induced displacement field in terms of deflection and tip torsion angle, the static strength as well as the buckling critical loads for the upper and lower skins constitute the quantities of interest. Regarding the latter, a global-local FEM modeling technique was implemented for the panels of the upper and lower skins. Buckling analyses are executed for each panel, with the first buckling eigenvalue (BE) constituting the quantity of interest. On the static strength front, a First-Ply Failure via the Tsai-Wu criterion is used for the strength prediction in terms of the failure index (FI) of the composite skins, spar, and rib webs. For the rest of the parts, a direct comparison between the maximum stress and the corresponding material strength value is made to obtain the corresponding FI. The constraint aggregation technique of Kreisselmeier-Steinhauser (KS) has been employed for the static strength as well as buckling constraints and are formed separately for the calculated FI of each of the components involved in the static strength as well as for each upper panel buckling critical load evaluation procedure. Results for the reference analyses are summarized in Table 3.

Table 3: Reference analyses results summary.

Value	CFD Linear	CFD Nonlinear	Panels Linear	Panels Nonlinear	DLM Rigid	DLM Elastic
KS, Upper Skin	0.3758	0.3554	0.5315	0.5395	0.4096	0.0869
KS, Lower Skin	0.4398	0.4108	0.6089	0.5897	0.4683	0.1036
KS, Spar Webs	0.1774	0.176	0.2407	0.2421	0.1866	0.0444
KS, Spar Caps	0.2516	0.2447	0.3088	0.3115	0.2638	0.108
KS, Rib Webs	0.5389	0.5182	0.6454	0.6287	0.5578	0.2374
KS, Rib Caps	0.019	0.0366	0.0217	0.0442	0.0209	0.011
KS, Stringers	0.2058	0.2082	0.2449	0.2585	0.2079	0.0901
Maximum Deflection, m	8.861	8.39	11.152	10.794	9.745	4.42
Tip Torsion, ^{0}	6.3441	5.8798	9.6973	9.422	6.2631	0.0247
KS BE, Upper Skin	2.7280	1.8893	2.6316	1.8542	2.754	4.5364
KS BE, Lower Skin	2.4414	1.8506	2.3975	1.8218	2.4798	3.6822

Substantial differences in the results can be observed depending on the level of fidelity of the aerodynamics as well as of the structural representation for this wing configuration. For the former, and despite acquiring similar loading conditions, the 3D panel method seems to be overestimating the maximum deflection and tip torsion induced at the wing, the main culprit being the increased bending moment. Pressure recirculation as well as flow separation near the trailing edge effects are not captured in such methods, resulting into higher pressure difference and eventually higher loads at the outer regions of the wing, which in turn are responsible for such an increase. The similar hold for the stresses and skin buckling eigenvalues. On the contrary, the DLM seems to be more accurately predicting the displacement and stress field when compared to the high-fidelity CFD analysis, as indicated in Figure 3. Of particular interest is the aeroelastic behavior of the uCRM wing, allowing for aerodynamic load redistribution and overall lower displacement and stress fields. From a structural point of view, inclusion of nonlinearities affect the solution and result into lower displacements and stresses as expected

  doi:10.5075/epfl-298799_978-2-9701614-0-0

mainly due to the geometric stiffening of the structure. Other nonlinear phenomena also rise, with one of the most prominent being the tip shortening effect, as illustrated in Figure 4. The presence of Brazier loads drastically alters the stress field in the rib caps, as demonstrated in Table 3, resulting into highly elevated stresses by nearly 50% in comparison with the linear models.

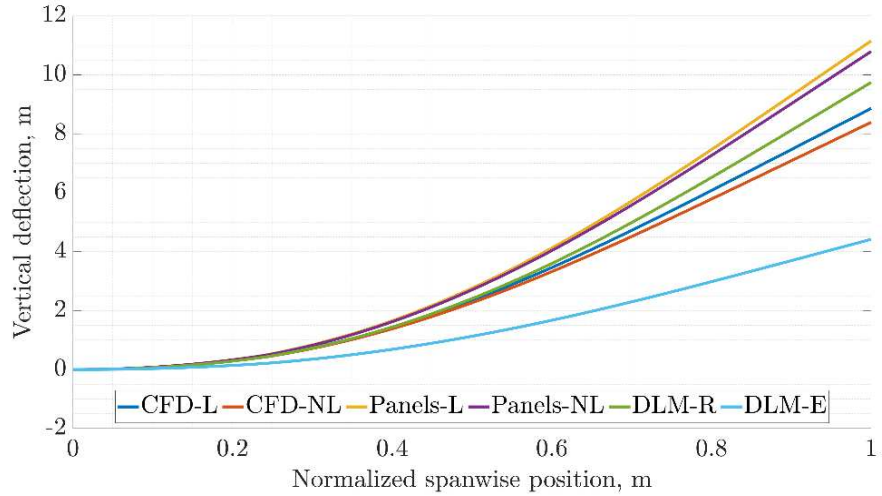

Figure 3. Reference analyses – Vertical deflection

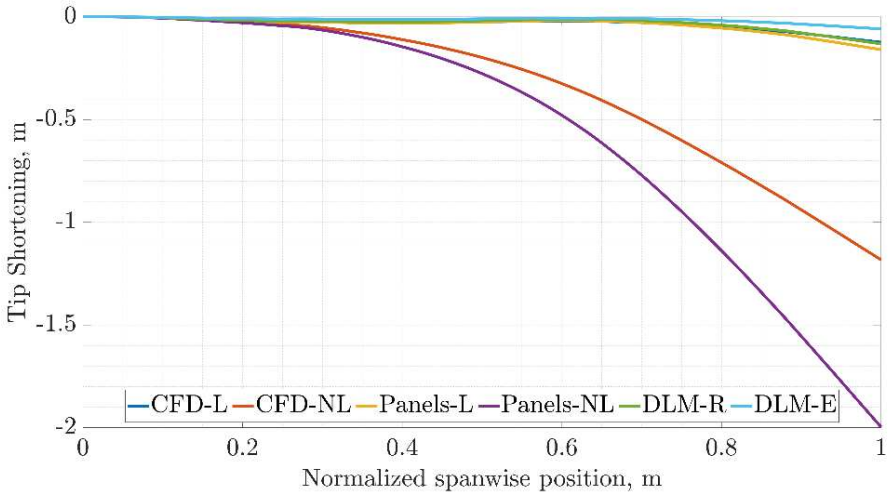

Figure 4. Reference analyses – Tip shortening

3. Optimization Framework

3.1 Variables definition

The ply count of the 0^0, 90^0 and (45^0, -45^0) plies of each laminate and of each wing component, ranging from 2 to 5, constitute the variables of the optimization problem. Allowing for a wider design space as well as increased structural design freedom, the wing is also divided into 8 spanwise and evenly spaced zones. The two materials described earlier are also used as variables and can be assigned during the optimization process to the rib webs and caps, spar webs and caps, upper and lower skin as well as the stringers.

  doi:10.5075/epfl-298799_978-2-9701614-0-0

3.2 Optimization problem

Moving on to the particulars of the optimization problem, the minimization of the mass of the wing represents the objective function. Design constraints in terms of static strength, buckling and flutter velocity, complete the optimization problem, as described in earlier sections. Completing the set of constraints, the dynamic aeroelastic instability by means of flutter velocity of the candidate design solution is also investigated. In particular, the p-k method implemented in NASTRAN SOL 145 is used to identify any possible divergence and flutter instability that might be present. The objective function as well as the constraints are summarized in the following Table 4.

Table 4: Optimization problem setup.

Objective Function	Minimize structural mass
under the constraints	
Constraint Type	Limit Value
KS(FI), Components	≤ 1
KS (BE), Skins	≥ 1
Flutter Speed	≥ 1.2 * V_D

The optimization framework is executed entirely via the MIDACO solver, which utilizes an Ant Colony optimization algorithm along with the ORACLE penalty method for constraint handling. Towards the realization of the multi-fidelity optimization framework, a sequential run approach has been adopted. Particularly, initial runs, carried out by low-fidelity tools, are mainly focused on extensive design space exploration. As the solution advances, the search becomes increasingly local by tweaking accordingly the internal FOCUS parameter that forces the MIDACO solver to focus mostly on the current best solution. In parallel, the constraint satisfaction tolerance is tightened, and high-fidelity modules by means of CFD and nonlinear structural behavior are employed. At each succeeding run, the previous best solution obtained serves as the starting point for the current run. The parameters of the optimization approach are summarized in Table 5.

Table 5: Optimization framework parameters.

Run Nr	Iterations	Tolerance	FOCUS parameter	Starting point	Aerodynamic Fidelity	Structural Fidelity
1	200	0.001	0	scratch	3D Panel	Nonlinear
2	100	0.0001	-100	previous	CFD RANS	Nonlinear

3.3 Optimization results

The optimized mass as well as the values of the constraints are listed in the subsequent Table 6. The obtained thicknesses and ply percentages for each component and zone of the wing are provided in Table 7 and Figure 5 respectively.

  doi:10.5075/epfl-298799_978-2-9701614-0-0

Table 6: Optimization framework results.

	Value
Mass, kg	94152.05
KS(FI), Upper Skin	0.2005
KS(FI), Lower Skin	0.5111
KS(FI), Spar Webs	0.1335
KS(FI), Rib Webs	0.3682
KS(FI), Spar Caps	0.1854
KS(FI), Rib Caps	0.2262
KS(FI), Stringers	0.051
KS (BE), Upper Skin	2.5
KS (BE), Lower Skin	2.3635
Flutter Speed, m/s	1000

Table 7: Optimization framework results-Thickness distribution (m).

Component	Zone 1	Zone 2	Zone 3	Zone 4	Zone 5	Zone 6	Zone 7	Zone 8
Upper Skin	0.019	0.0234	0.019	0.0176	0.0176	0.0219	0.0293	0.0249
Lower Skin	0.0206	0.0206	0.0158	0.0206	0.0238	0.019	0.0222	0.0285
F. Spar Webs	0.0146	0.0205	0.0146	0.0176	0.019	0.0219	0.0176	0.0161
F. Spar Caps	0.0263	0.0278	0.0322	0.0249	0.0205	0.0263	0.0234	0.0249
R. Spar Webs	0.0205	0.0249	0.0146	0.0234	0.0249	0.019	0.0161	0.019
R. Spar Caps	0.0278	0.0322	0.0336	0.0234	0.0263	0.0205	0.0234	0.0176
Rib Webs	0.0205	0.0161	0.0249	0.0249	0.0205	0.0176	0.0146	0.0205
Rib Caps	0.0073	0.0059	0.0088	0.0102	0.0102	0.0102	0.0102	0.0117
Stringers	0.0205	0.0205	0.0205	0.0176	0.0176	0.019	0.019	0.0176

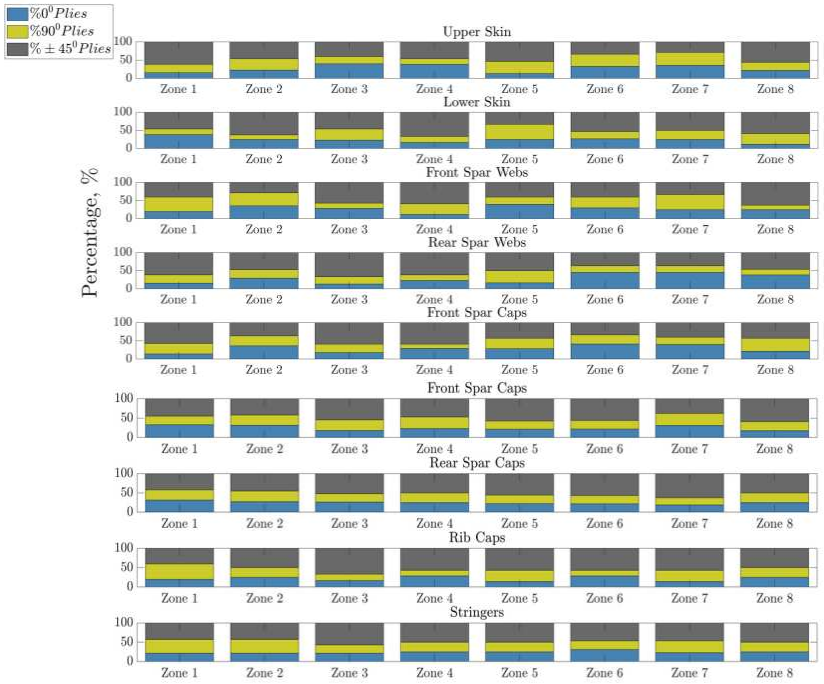

Figure 5. Component-wise layups percentages

  doi:10.5075/epfl-298799_978-2-9701614-0-0

Regarding the thickness distribution, the front and rear spar caps along with the stringers obtain high thickness values since they are critical to buckling. Furthermore, the zones near the yehudi region are accompanied by an increased thickness for nearly all of the components, indicating that this region of the wing is a highly stressed one. Regarding the percentage of plies, there seems to be a retention and even an increase of the initial percentage of $\pm 45^0$ plies in the laminates for the majority of the components, which might be associated with an increase in the induced shear strains and/or the relatively low shear stress allowable of the material under consideration. 0^0 plies also seem to be of great significance, since they are the main contributors to the stiffness and strength of the structure, with the percentage of 90^0 plies counterbalancing the low value of transverse failure stress of the material considered.

4. Conclusion

A multi-fidelity optimization framework for future high-aspect ratio composite aircraft wings, based on the MIDACO algorithm has been presented herein. Variable-fidelity analyses were conducted in order to study their effect on the structural response of the test case. Based on the results, a multi-fidelity optimization framework was developed, guiding the mass of the wing to a minimum, satisfying various design constraints. The present framework could be benefited by the addition of aerodynamic shape as well surrogate-based optimization procedures.

Acknowledgements

The research is co-financed by Greece and the European Union (European Social Fund - ESF) through the Operational Programme << Human Resources Development, Education and Lifelong Learning >> in the context of the project "Strengthening Human Resources Research Potential via Doctorate Research"(MIS-5000432), implemented by the State Scholarships Foundation (IKY).

References

1. Haftka RT. Automated procedure for design of wing structures to satisfy strength and flutter requirements. NASA Technical Report 1973.
2. Triplett WE. Aeroelastic Tailoring Studies in Fighter Aircraft Design. Journal of Aircraft 1980; 17:508-513.
3. Maute K, Nikbay M, Farhat C. Coupled Analytical Sensitivity Analysis and Optimization of Three-Dimensional Nonlinear Aeroelastic Systems. AIAA Journal 2001; 27:2051-2061.
4. Barcelos M, Maute K. Aeroelastic design optimization for laminar and turbulent flows. Computer Methods in Applied Mechanics and Engineering 2008; 197:1813-1832.
5. Smith M, Patil M, Hodges D. CFD-based analysis of nonlinear aeroelastic behavior of high-aspect ratio wings. 19th AIAA Applied Aerodynamics Conference 2001;
6. Howcroft C, Calderon D, Lambert L, Castellani M, Cooper JE, Lowenberg MH, Neild S. Aeroelastic Modeling of Highly Flexible Wings. 15th Dynamics Specialists Conference 2016.
7. Vassberg J, Dehaan M, Rivers M, Wahls R. Development of a Common Research Model for Applied CFD Validation Studies. 26th AIAA Applied Aerodynamics Conference 2008.
8. Brooks TR, Kenway GK, Martins JRRA. Benchmark Aerostructural Models for the Study of Transonic Aircraft Wings. AIAA Journal 2018; 56:2840-2855.

  doi:10.5075/epfl-298799_978-2-9701614-0-0

INTRODUCING DISCONTINUOUS LONG FIBER COMPOSITES IN THE AERO INDUSTRY: A LONG JOURNEY

Nicolas D., Weibel[a], Samuel P., Stutz[b], Sébastien, Kohler[b], Lionel, Germanier[b], Frédéric Perrottet[b]

a: Greene, Tweed & Co. (Suisse) SA – nweibel@gtweed.com
b: Greene, Tweed & Co. (Suisse) SA

Abstract: *Between injection molded complex shaped composites with relatively low stiffness and strength, and panel like shaped parts made from aligned continuous fiber reinforced composites, there is a third type of materials based on a chopped form of continuous fibers tape called DLF (Discontinuous Long Fibers). This paper presents the long journey that Greene, Tweed & Co. (GT) followed to introduce this new material into the aero industry, with a first test flight in 2009, replacing a metallic bumper placed between the engine and the nacelle saving some 78% weight. Since then, over 400 parts have been certified and produced in series with annual volumes ranging from 100 to 10'000 parts per year, introduced in over 10 different commercial airplane models ranging from small single aisle to the largest twin aisle planes. This was only possible thanks to strong and trustworthy relationships with our customers, who estimated that the benefit from the DLF technology outweighed their time, budget and risk related to the introduction of such a novel approach to convert small complex shaped metallic parts to composites.*

Keywords: DLF (Discontinuous Long Fibers); Complex shaped; Thermoplastic composite; Hail impact; Weight reduction

1. Introduction

In modern aircraft over 50% of the structural weight (75% by volume) comes from carbon fiber reinforced composite parts. Most of these composites are panel like shapes such as the wings and the fuselage. Many remaining parts, however, are small and of complex shapes, largely made from machined Aluminum (20%) and Titanium (14%) [1]. The shape complexity of these parts is not adapted for "Advanced Composites" using continuous fiber reinforcement, but the strength and stiffness required is beyond those offered by injection molded reinforced plastics. Greene, Tweed & Co. (GT) has introduced a material called DLF (Discontinues Long Fibers), made from chopped unidirectional thermoplastic composite tape, which can be compression molded into complex shaped parts as shown schematically in Figure 1. DLF offers mechanical properties close to aluminum alloys, yet with a 40% lower density.

The first flight tests with a DLF composite part took place in 2009, and the first production application followed in 2011. 10 years later, in 2019, GT had over 200'000 DLF parts flying in various airplane models, ranging from A220 to A380, including 3 widebody Boeing aircrafts.

Introducing DLF into the aerospace market to replace metallic parts was a long journey. Carbon fiber reinforced PEEK was selected for its excellent smoke and toxicity behavior, its high temperature capabilities, and its chemical resistance. However, while the UD tape properties

  doi:10.5075/epfl-298799_978-2-9701614-0-0

were well understood, the material properties of the chopped form were unknow to the aero industry and a very large testing campaign was needed to build trust within our customer base.

The effort was not in vain, as by compression molding DLF, complex shaped parts can be net-molded with a nearly full conversion of raw material into finished components. As a result, cost-effective solutions have successfully been adopted for replacement of fully machined metallic parts where over 90% waste during machining is common.

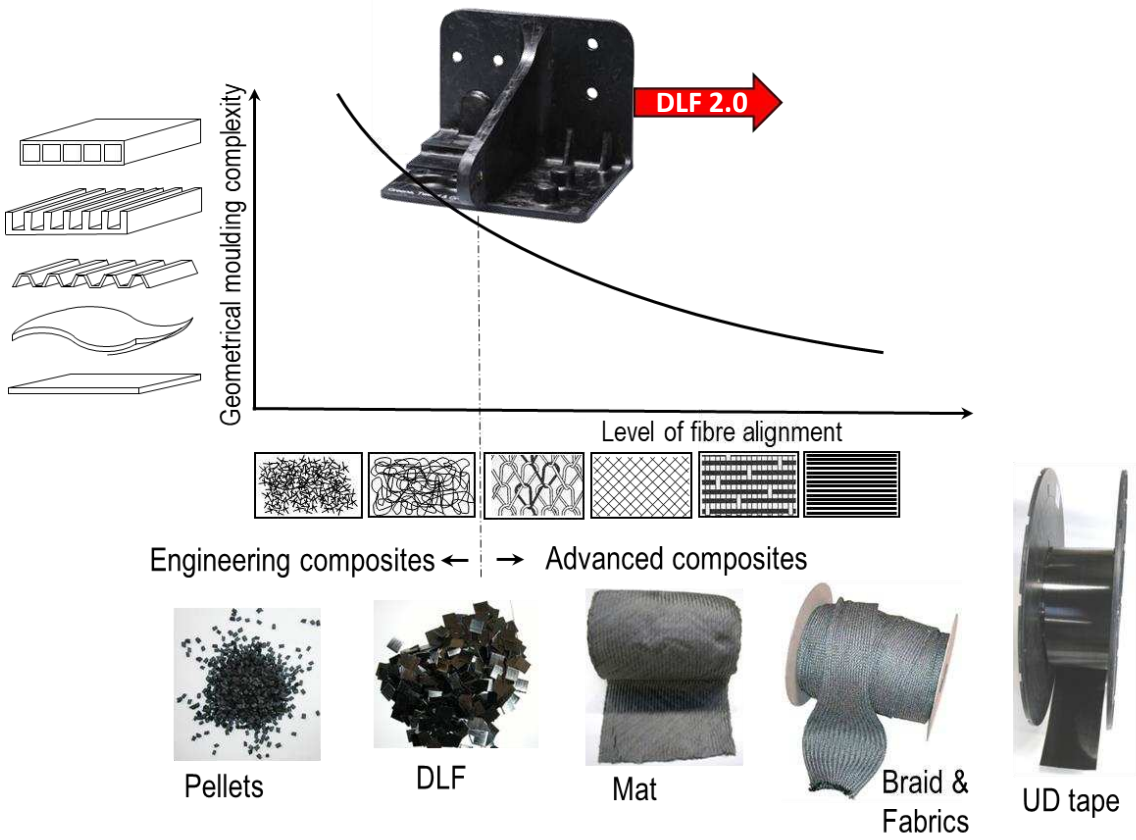

Figure 1. When plastics are reinforced with randomly oriented, short fibers with volume content below 40%, as offered through injection molded pellets, very complex shapes can be made with limited strength and stiffness. Advanced composites are at the other end of the scale with specific properties drastically outperforming the strength and stiffness of metals. In between is DLF, offering a cost-effective solution for complex shaped parts with mechanical properties similar to aluminum alloys. A new form of DLF called DLF 2.0 offers further improvement in DLF performance.

2. C/PEEK DLF Testing required to enter the aero industry

2.1 Quasi-static tests

As the random, discontinuous nature of DLF was new to the aero industry, GT had to create comprehensive allowables data for many conditions. A full test matrix of 21 tests was run for up to 6 different temperatures ranging from -59 to 232°C, in dry and wet conditions, for coupons of up to 4 different thicknesses from 2 to 7.6mm, as well as for multiple batches. Tests include in-plane and interlaminar tension compression and shear strength and modulus (ASTM: D3039, D6641, D7078, D7291, D5379). Open hole tension and compression, filled hole tension as well

  doi:10.5075/epfl-298799_978-2-9701614-0-0

as bearing tension and compression (ASTM D5766, D6742, D6484, D5961). Furthermore, as the mechanical properties are modified when the DLF material flows into a cavity, tension compression and shear properties (axial and transverse) at 4 different temperatures were measured of coupons made with a directional flow. The cost to run all these tests in certified labs was well over $1M.

As an example of extensive testing, Figure 2 below shows the large processing window of C/PEEK DLF, regarding molding pressure, temperature and time. 640 coupons were tested in 64 different combination of pressure temperatures and time. The results indicate that complex molded shapes, where the applied pressure cannot be guaranteed over the entire part due to the high viscosity of the molten PEEK resin and the very high fiber content (60% by volume) will still offer the same homogeneous mechanical properties in every location. Indeed, pressure gradients with over 100 bar within a mold are quite common for the type of complex shaped parts GT produces. Furthermore, whether press heating, oven heating imbedded heating resistance or induction heating is used, different sections of the part will see different temperatures for different durations. This is particularly the case when the cross section varies significantly thought the part. Therefore, knowing that the processing window for C/PEEK DLF is very large, with no adverse implications on strength, is a guarantee that our customers appreciate.

Additionally, to the tensile strength, the porosity of every coupon was measured using the Archimedes density method (ASTM D792). Only condition 1-1-1 (see below) led to a porosity level just above 3%, whereas all other 63 conditions led to a porosity close to zero, and always below 1%.

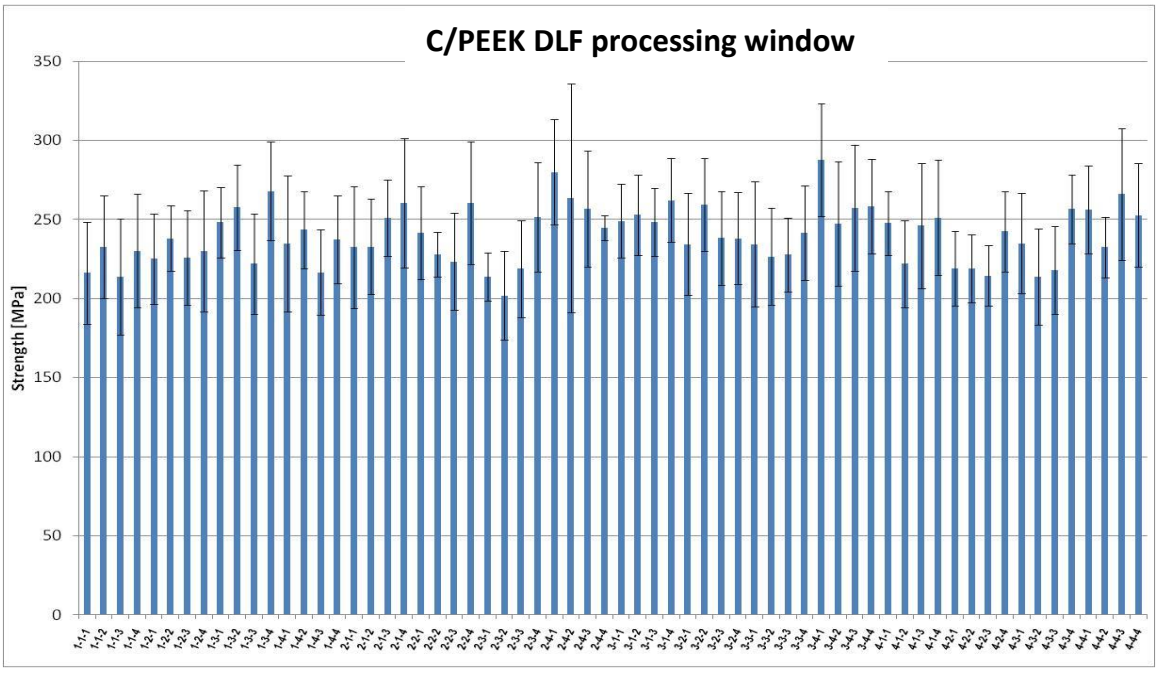

Figure 2. C/PEEK DLF tensile strength as a function of processing parameters. This full factorial processing window has 4 Pressures (10, 40, 100 and 150 bar), 4 Temperatures (360°C. 380°C, 400°C and 450°C) and 4 dwell times (0, 3, 10 ,45min). In the legend, 1-1-1 = 10 bar, 360°C and 0min dwell.

2.2 Dynamic tests

Over 100 creep tests, each of 1000 hours at 8 different temperatures ranging from 93°C to 288°C for random flake orientation as well as oriented (high flow) coupons were conducted to demonstrate the long-term usability of continuously loaded C/PEEK DLF parts at temperatures above the glass transition temperatures (T_g) (ASTM 2990). For example, if DLF is subject to a tensile stress level of 70% of its UTS at 178°C, the expected creep strain after 100'000 hrs (11 years) is 0.72% whereof 0.51% are due to initial elastic deformation [2].

Close to 100 Unnotched and Open hole Tension-Tension and Tenison compression fatigue tests at RT and 121°C up to 10M cycles were performed to demonstrate the remarkably high fatigue limit and notch unsensitivity of parts made from C/PEEK DLF. Indeed, the infinite life, estimated on some 10 tests run for 10M cycles is at a minimum of 45% of the nominal strength [3].

Finally, hundreds of drop weight testes (ASTM D7136), as well as over 100 high velocity impact tests simulating Ø51mm hail impacts at the commercial airplanes cruising speeds (up to 310 m/s) have been performed, showing the viability of C/PEEK DLF composites for parts exposed to the environment found at the front end of the turbofan engine.

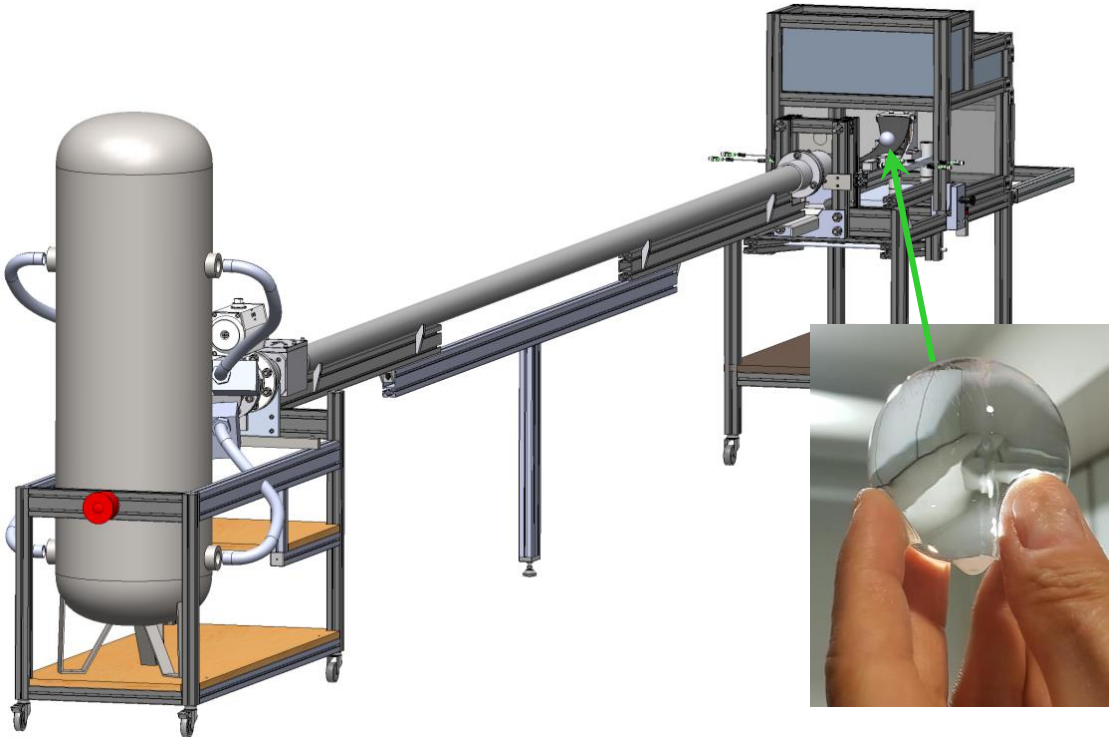

Figure 3. Hail impact testing jig. Compressed air or Helium accelerates the Ø51mm crystal clear hail ball to reach the desired impact speed. Crystal clear ice balls are produced by single Christal germination in a top-down gradient cooling set-up.

3. The weak point of DLF and how to remediate it

C/PEEK DLF, and any other DLF material form, suffers from a relatively low tensile strength due to a high stress concentration at the end of the individual flakes. Indeed, the tensile strength just above 200 MPa is over 3 times lower than the strength of a quasi-isotropic plate made from continuous fibers (for example with a lay-up sequence of $[(0/45/-45/90)_2]_s$) with typical strength values of 750 MPa [4].

  doi:10.5075/epfl-298799_978-2-9701614-0-0

At the end of a flake, where all oriented fibers stop abruptly, there is a region of stress concentration, responsible for the low tensile strength of DLF products. To reduce this local stress concentration, flakes with progressive end have been produced under the name of DLF 2.0. Figure 4 shows how the tensile strength of DLF composites with progressive ends increases by 50%.

This solution to address the weak point of DLF by reducing the stress concentrations at the edge of flake, has been submitted for a patent [5]

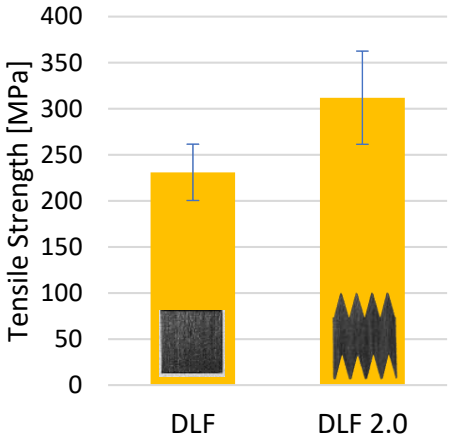

Figure 4. Tensile strength of C/PEEK DLF based on standard flake thickness of 140µm and constant fiber length of 12.7mm but with progressive ends. Plates made with flakes cut with a zigzag end-of-flake, (so called DLF 2.0), show 50% higher tensile strength values compared to a standard straight cut.

As can be seen in figure 5, modifying the flake by creating a progressive end also offered 60% impact strength increase. This significant improvement allowed GT to expand into additional applications where this material is exposed to hail impact such as found at the frontend of a turbofan engine.

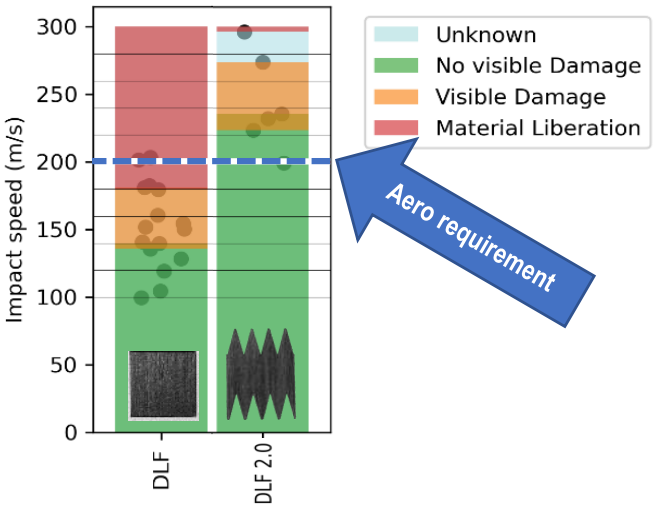

Figure 5. High Velocity Impact resistance of DLF and DLF 2.0 (a flake with progressive ends) as observed on 3.8mm thick plats. Green represents the elastic impact limit, orange indicates the appearance of cracks, and red represents that a fragment of the plate is liberated. Every dot represents a shot at the indicated velocity. The blue line represents a typical aerospace requirement of 200 m/s. These results were obtained using the equipment shown in Figure 3.

  doi:10.5075/epfl-298799_978-2-9701614-0-0

4. Some examples of parts successfully introduced in the aero industry

Figure 6 shows several engine brackets that have successfully replaced the incumbent metallic brackets. The DLF brackets are lighter and offer a part count reduction as the original metallic brackets are made from an assembly. However, before such brackets could be certified a large number of tests have been performed such as creep at temperatures above T_g, high cycle fatigue (up to 10M cycles), thermal cycling, and even a fire test for 15 min at 1000°C on a 2mm panel with no burn through [6].

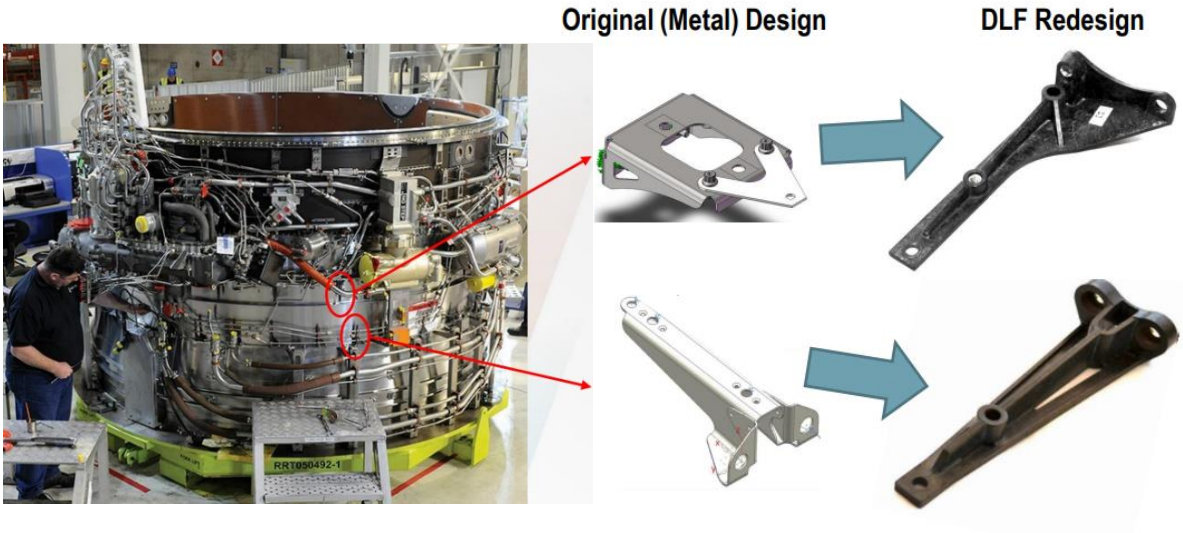

Figure 6. Example of Engine external brackets. Currently 81 DLF brackets for Hydraulic lines and cable support are used per engine in this specific application [7].

The nose landing gear Drag Stay fitting shown in Figure 7, is another example of a highly loaded DLF part developed in collaboration with Latécoère under a CORAC program. For such a critical part, predictive simulations and non-destructive damage analysis based on X-ray tomography was required to correlate predictive results to onset damage at increasing load levels. As a result, GT was certified as TRL5 at Airbus in 2015 [8]

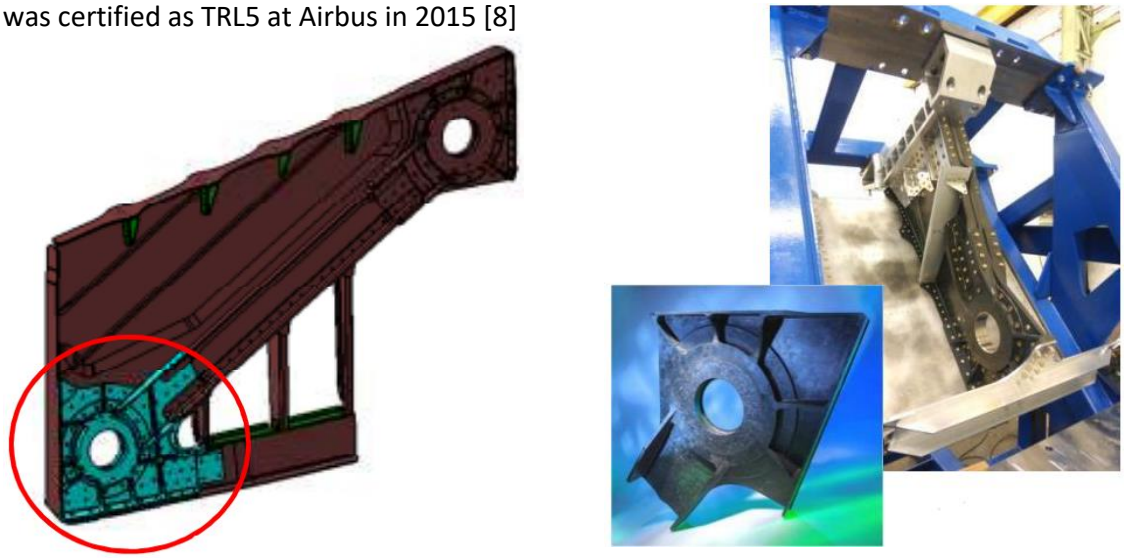

Figure 7. Latécoère Drag Stay Fittings, one of GT's larger, highly loaded DLF parts. On the left the incumbent metallic design is shown. On the right, the testing fixture showing a destructive test of GT's DLF part [8].

  doi:10.5075/epfl-298799_978-2-9701614-0-0

Figure 8 shows a fillet fairing and an extension panel positioned directly behind the Outlet Guide Vanes. These parts were originally made from thermoset composite honeycomb sandwich panels DLF offered weight reduction, parts-consolidation, and improved impact performance. To get parts such as this certified, impact testing is one of the critical selection criteria, specifically the compressive strength retention after impact (CAI). DLF, even if starting off with about half the compressive strength of continuous fiber composites (for example with a lay-up sequence of $[(0/45/-45/90)_2]_s$ and typical strength values of 630 MPa [4]), the incredible notch unsensitivity of DLF led to similar CAI strength, which gave DLF a significant competitive advantage and convinced our customer for large scale adoption.

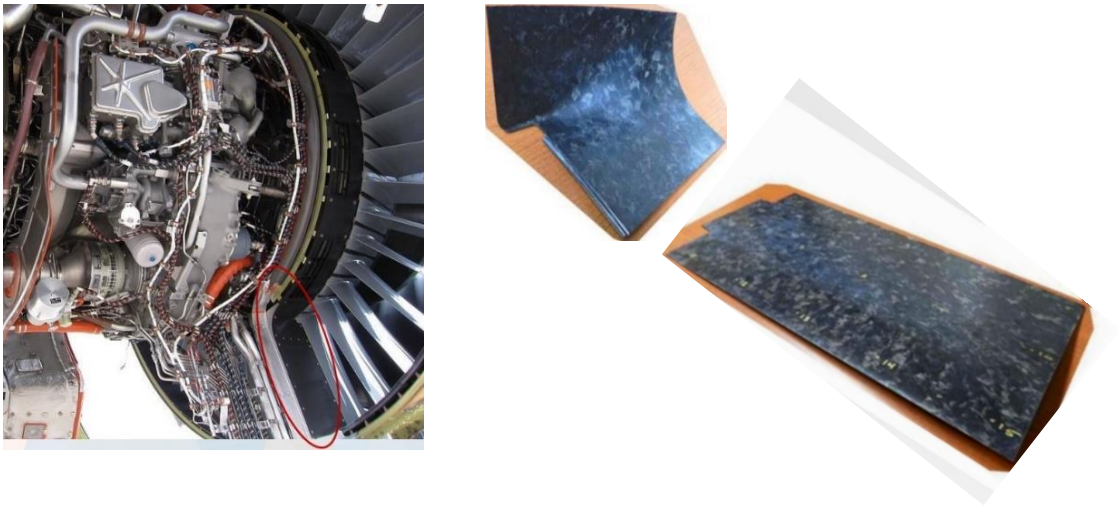

Figure 8. Fillet fairings and Extension panels, selected primarily due to DLF's great compression after impact strength retention, as well as a cost effective weight reducing solution [7].

Figure 9 shows a relatively complex DLF part that replaces an assembly of several metallic components. The part is installed on a business jet's nose landing gear

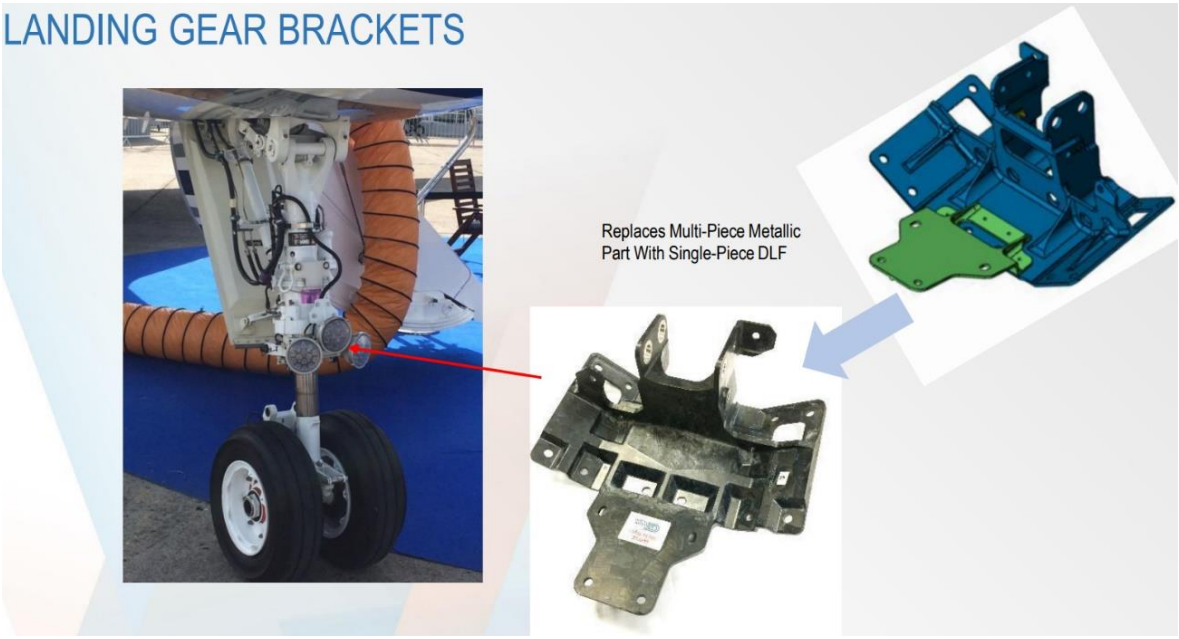

Figure 9. Nose landing gear light support bracket. A single DLF component replacing an assembly of multiple metallic components (upper right image) [7]

In a collaborative development effort between GT and Unison Industries, a wholly owned subsidiary of GE Aviation, structural and functional brackets have been designed, produced, tested and adopted around the Engine and the Nacelle to replace metallic brackets such as the one shown in Figure 10.

Figure 10. Engine build up (EBU) bracket combining structural and functional requirements of hydraulic support. Left: Incumbent metallic design made from machined Inconel with a weight of 1.23kg. Middle: DLF redesign fulfilling the same function with a weight of only 0.18kg (85% weight reduction). Right: one of the numerous structural tests performed on the DLF bracket to demonstrate structural integrity [6]

Closer to the front of the turbofan engine, parts are exposed to high velocity hail impact. Such parts were not originally considered for DLF as the high velocity impact strength measured on standard size plates of 3.8mm thickness did not pass the requirements. Redesign of the support structure geometry based on DLF characteristics enabled successful hail impact performance, as shown on Figure 5. DLF 2.0 demonstrated even further improvements in velocity before incurring damage. DLF offers benefits in reducing the number of manufacturing operations required for parts such as this, offering a cost-effective alternative.

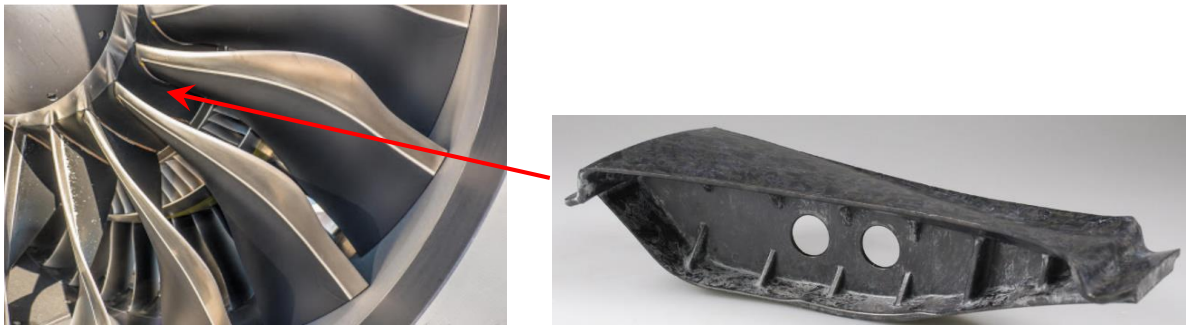

Figure 11. Fan platform demonstrator, capable of passing a Ø51mm hail impact test at over 200 m/s within the elastic range. No cracks were found after the impact test, using X-ray tomography as a means of inspection method

  doi:10.5075/epfl-298799_978-2-9701614-0-0

5. Conclusion

15 years after Greene, Tweed & Co. started its journey with DLF, a very wide range of applications have benefitted, primarily for metal replacement, but also for thermoset composite replacements. With a "zero" waste net-molding approach, DLF offers a cost-effective alternative to machined metallic parts. Today over 200'000 DLF parts fly in multiple Airbus and Boeing commercial aircraft as well as several business jets. With the rising cost of energy and with new programs developing airplanes that do not rely on fossil fuels, the weight of aircraft is becoming even more critical. With a demonstrated average weight reduction of 30% compared to the original metallic parts over GT's whole portfolio, and some examples of 85% weight reduction, DLF has proven its ability to effectively reduce fuel consumption and may be instrumental for the adoptions of alterative air transport systems.

6. References

1. Keith Campbell. "Airbus to start manufacturing parts for new A350 XWB in late '09", Engineering News online, 11 May 2009, https://www.engineeringnews.co.za/article/airbus-to-start-manufacturing-parts-for-new-a350-xwb-in-late-09-2009-05-11
2. Stutz, S. and Weibel, N., "Creep of discontinuous long fiber C / PEEK above Tg," ITHEC 3–5, 2018
3. Internal test data not yet published.
4. Cogswell F.N. Thermoplastic aromatic polymer composite Butterworth-Heinemann Ltd p 257-258, 1992
5. U.S. Provisional Patent Application No. 63/315,022 filed on February 28, 2022
6. Tim L. Greene; Christopher Wonderly, PE; M. Hakan Kilic, Ph.D; Bradley Keller, Complex-shape metallic aircraft engine bracket replacement using compression molded discontinuous long fiber thermoplastic composites, CAMX, Dallas, October 2015
7. Tim Greene, Advances in Aerospace Complex-Shape Metal Replacement using Discontinuous Long-Fiber Thermoplastic Composites, CompositeWorld 28-30 Charleston, SC, USA 2017
8. Tim Greene, James Myers (Greene Tweed) Vincent Labatut (Stelia Aerospace) Philippe Gail (Latécoère) JEC Composites Magazine No. 96, April 2015

  doi:10.5075/epfl-298799_978-2-9701614-0-0

A FRAMEWORK FOR EFFICIENT DESIGN OF MULTIFUNCTIONAL-CFRP FOR FUTURE AIRCRAFT

M Hijaaj Tahir[a], C. E. Jones[a], R.I. Whitfield[b], P. Norman[a], G. Burt[a]*

a: Department of Electronic and Electrical Engineering, University of Strathclyde, Glasgow, UK - [*]Muhammad.tahir@strath.ac.uk
b: Department of Design, Manufacturing and Engineering Management, University of Strathclyde, Glasgow, UK

Abstract: *The development of multifunctional carbon fibre reinforced polymer (MF CFRP) with the combined mechanical, electrical, and thermal functionality offers a route to increased light-weighting for aircraft systems. This paper presents a framework for efficient, early-stage identification of viable solutions for MF CFRP applications with a focus on the detail surrounding the capture of appropriate electrical, mechanical, and thermal requirements of the MF CFRP and defines the limitations and thresholds for the MF CFRP design space. By understanding the key drivers behind the boundaries and the limitations of this design space, future research efforts can be directed at identifying solutions to enable the realisation of MF CFRP which has required functional properties.*

Keywords: aircraft electrical power system; multifunctional materials; carbon fibre reinforced polymer; design space

1 Introduction

Metallic structures on aircraft are multifunctional, providing structural functionality alongside electrical functionality: forming the electrical current return path for the onboard electrical power system (EPS), electromagnetic interference (EMI) shielding, and lightning strike protection. However, most structures on state-of-the-art aircraft are made from carbon fibre reinforced polymer (CFRP) due to their superior lighter weight and mechanical strength properties compared to traditional metallic materials. Due to the poor electrical conductivity of CFRP (e.g. in-fibre direction of UD [0°] CFRP is 30 – 40 kS/m compared to aluminium (35 MS/m) [1], its unadapted structure is not considered to have electrical and structural multifunctionality for electrical power applications. The development of multifunctional CFRP (MF CFRP) with appropriate electrical, structural, and thermal properties offers a route to light-weighting aircraft systems, opening new design spaces and opportunities for the electrification of aircraft. A significant challenge for the development of MF CFRP is the complexity of the design space, and interdependencies between mechanical, electrical and thermal (MET) functionality requirements. There is a need for the development of an efficient design methodology to identify viable design spaces and approaches for materials that meet multifunctional requirements and can be manufactured at scale.

This paper presents a framework (Figure 1) for efficient, early-stage identification of viable candidate approaches for a MF CFRP structural component which also functions as electrically conducting pathways for a more electric aircraft (MEA). The framework is sub-divided into four phases, which step through from the capture of baseline system requirements to the build and test of a hardware prototype. This paper focuses on Phase-1 and Phase-2.

  doi:10.5075/epfl-298799_978-2-9701614-0-0

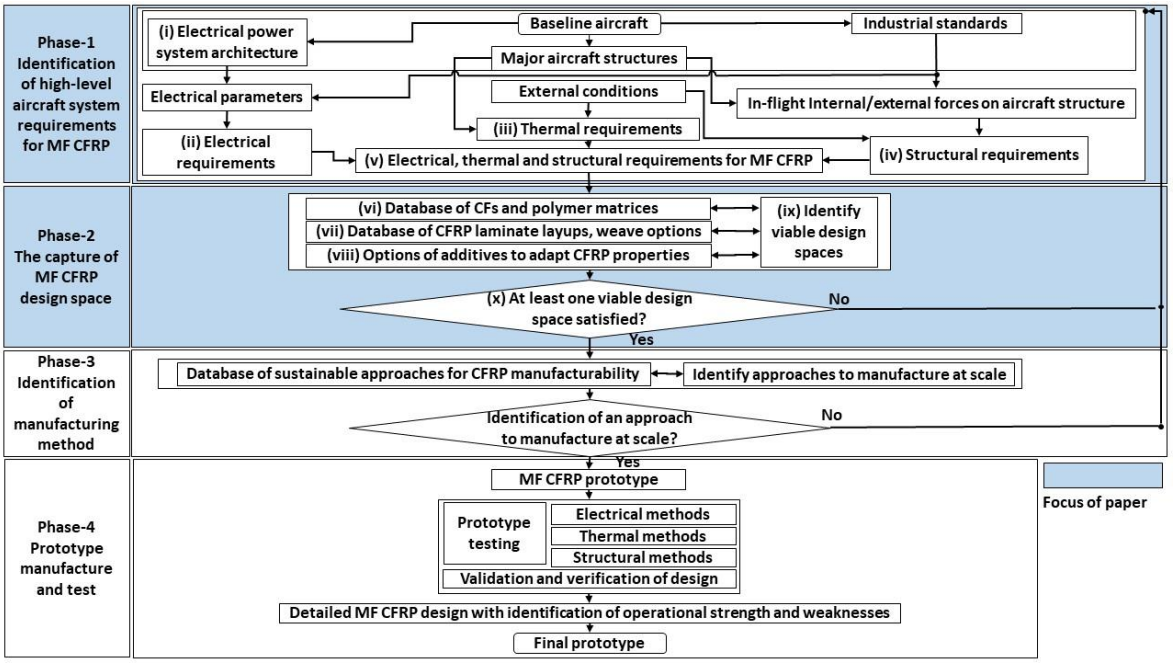

Figure 1. Framework for early-stage identification of viable MF CFRP solutions

2 Identification of high-level aircraft system requirements for MF CFRP

2.1 Aims and objectives of Phase-1

Phase-1 of the framework takes in the baseline electrical and structural requirements associated with a particular aircraft to identify the high-level requirements of the MF CFRP. The processes within Phase-1 from i to v (Figure 1) include consideration of interdependencies between different functionalities and consideration of industrial standards.

2.2 Overview of the state of the art aircraft EPS architecture

An EPS architecture has a significant influence on the electrical and thermal properties required by MF CFRP, and as such is captured in part i (in Phase-1) of the framework in Figure 1. The more-electric aircraft (MEA) concept has been implemented on the current state of the art aircraft, e.g. the Boeing 787. On an MEA, systems which were typically powered by mechanical, hydraulic or pneumatic power are now driven by electrical power. As such, the electrical power rating of an EPS for an MEA is ~1.5 MW. The electrical power is a mixture of alternating current (AC) and direct current (DC), at a range of voltages from 28 V_{dc} up to +/-270 V_{dc} and 230 V_{ph} rms. The majority of electrical power is supplied by gas turbine engine driven generators. Power electronic converters step the power between AC and DC and provide control functionality [2].

2.3 The capture of electrical, thermal and mechanical requirements for MF CFRP

The MF CFRP must have appropriate mechanical, electrical and thermal (MET) properties which are captured in ii - iv in Phase-1 of the framework in Figure 1. These are combined in v of Phase-1 and passed to Phase-2, for the capture of viable design spaces for the MF-CFRP.

2.3.1 Electrical requirements

The electrical requirements of the MF CFRP depend on the function that the MF CFRP is expected to perform. The main considerations are the electrical current, voltage and frequency levels. The focus of the framework is the design of MF CFRP for low frequency (<MHz) electrical current conduction, as part of an EPS. The electrical conductivity of the conducting pathway through the CFRP must be high enough such that, the voltage drop across the conducting path must meet the appropriate industrial standards, and the heat dissipated, due to resistive losses in the conducting pathway (Joule heating), does not cause the glass transition temperature (T_g) of the resin matrix to be reached. Considering a 500mm length of cable within the EPS at $28V_{dc}$ and conducting 10A with a 4% acceptable voltage drop, the required conductivity is ~3 MS/m. For comparison, the conductivity in the in-fibre direction of UD [0^o] CF is 30 – 40 kS/m [1].

2.3.2 Thermal requirements

Alongside assuring that T_g of the CFRP is not reached by Joule heating during electrical conduction, the thermal conductivity of the material must also be considered. This determines the material effectiveness for dissipation of heat that has been induced externally or internally. Hence, thermal conductive properties are crucial to maximise understanding of how heat from Joule heating may dissipate through CFRP. Finally, ideally, the coefficients of thermal expansion (CTE) of the different CFRP components are matched as closely as possible. However, differences in CTE between polymer matrices and CF result in thermal stress between the CF and matrix as the CFRP heats up. This leads to the formation of interlamination cracks, and consequently mechanical strength loss and failure of CFRP [3].

2.3.3 Mechanical requirements

The nature of the strength required for the material of aircraft structural elements varies with stress type. For instance, aircraft wings and stabilisers encounter bending stress under which both tensile and compressive stress act on the material due to gravity and the in-flight air pressure difference between the upper and lower surfaces of the wings [4]. The aircraft fuselage section faces compressive stress owing to external and cabin (inner) pressure differences. Therefore, the key mechanical properties which a CFRP component must possess are high tensile, compression, flexural, and shear strengths.

3 The capture of MF CFRP design space

3.1 A High-level overview of Phase-2 of the framework

During Phase-2 of the framework, from databases of CFRP design elements, system design trades are carried out to identify an appropriate design space for the MF CFRP, to meet the requirements identified in Phase-1. It is possible that a viable design space will not be identified, hence iteration of the requirements from Phase-1 is needed (indicated by the arrow growing from part x of Phase-2 back to Phase-1 in Figure 1. The purpose of developing a design space is to delimit the options of the best available elements (fibre, matrix, layups, additives to adapt properties) to utilise them for MF CFRP, in order to identify approaches to comply with the design requirements of properties passed down from Phase-1.

  doi:10.5075/epfl-298799_978-2-9701614-0-0

3.2 Database of methods to adapt the MET design space

Parts vi – viii of Phase-2 are databases of methods and materials which can then be combined with the MET requirements from Phase-1 to identify viable design spaces for MF CFRP. The three distinct databases are CFs and polymer matrices (part v), different CFRP layup and weave options (part vii) and finally, options for adapting the CFRP properties using additives (part viii). Each of these three areas is discussed below.

3.3 Comparison of different carbon fibres and polymer matrices

Figure 2 and 3 compare the fibre dependent properties of commercially available carbon fibres (CF): Polyacrylonitrile (PAN) and pitch CF. Aluminium alloys are included for comparison, as CFRP is favoured over the use of aluminium for structures on state-of-the-art-aircraft. Data for the figures were collected from available online product databases of manufacturers [5-9]. Figure 2-3 indicate that the selection of one CF over another results in trade between electrical, thermal, and mechanical functionalities of the carbon fibre. Compared to PAN CF, pitch-based CFs have one order higher electrical conductivity (up to ~2 MS/m), 1-6 times better thermal conductivity, and ~1.5 times higher tensile modulus properties (up to 900Gpa). Pitch-based CF has lower strength (3-4 GPa) than PAN-based CF (3-7 GPa). However, Pitch and PAN fibres have considerably higher tensile strength than aluminium alloys [10].

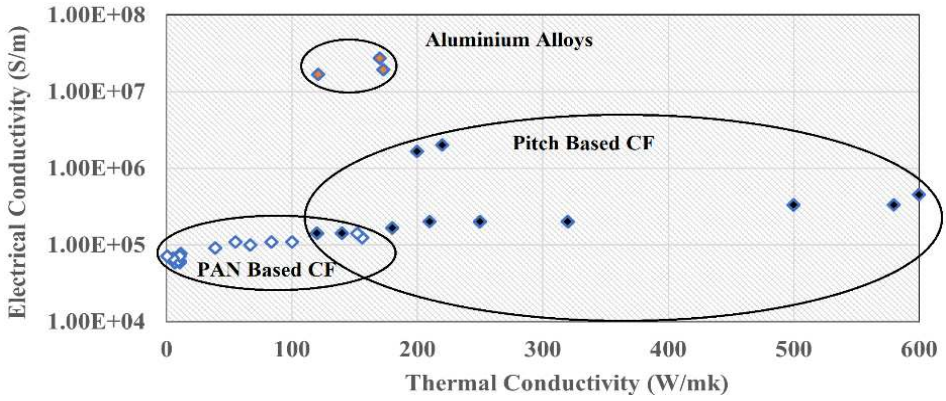

Figure 2. Electrical conductivity vs thermal conductivity of commercially available carbon fibres

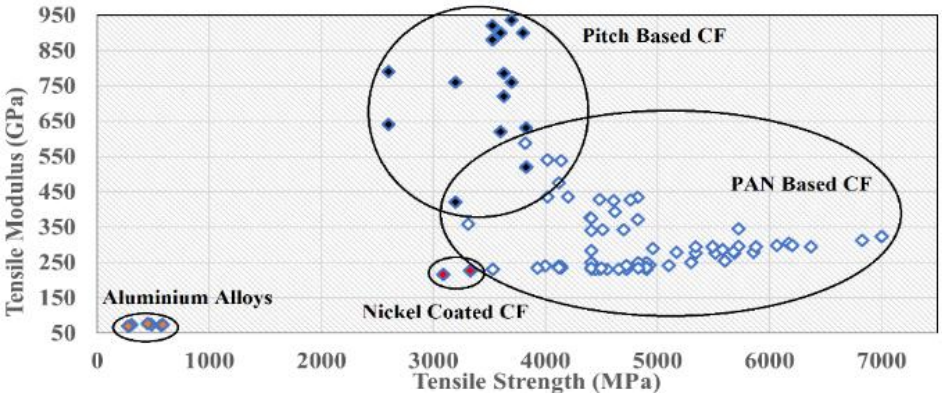

Figure 3. Tensile modulus vs tensile strength of commercially available carbon fibres

A comparison was carried out of matrix-dominant, compressive, flexural and interlaminar shear strength (ILSS) and T_g properties of commercially available CFRP, which have been manufactured

using ten different types of thermoplastic and thermosetting based matrix resins. Figure 4 and 5 represent the comparison of compressive, and flexural strength and ILSS. The choices of resins in Figures 4 and 5 are defined in Table 1.

Inspecting the data showed that epoxy, PEEK and BMI based CFRP have superior mechanical and thermal properties with excellent flexural (1.5 – 2.2 GP) and compressive (1 -1.5 GPa) strength. In terms of T_g (which ranged between 90 to 454°C for all matrices compared) and ILSS, epoxy and PEEK resins show inferior characteristics to BMI-CFRP which has T_g in the range of 320°C and ILSS of 100 MPa. For Epoxy, T_g is around 180°C, while PEEK possesses lower T_g (140°C) and lower ILSS (75 MPa). As T_g and ILSS are important matrix attributes for CFRP to perform well in a high-temperature environment, therefore, BMI can be considered as a suitable resin to be used in MF CFRP with good strength appropriate electrical functionality for an MEA EPS.

Table 1: Matrices used in commercially available prepregs are mentioned in Figure 4 and 5.

Prepreg Serial Number 1-50	Matrix Type
1 → 11	epoxy
12	Polyphenylene Sulfide (PPS) (Thermoplastic Resin)
13 → 20	Polyether ether ketone (PEEK) (Thermoplastic Resin)
21	Polyaryle ether ketone (PAEK)(R)
22 → 32	Cyanate ester
33 → 44	Bismaleimide (BMI)
45 → 47	Phenolic
48	Polyimide (PI)
49	Polyethylene terephthalate (PET) (Thermoplastic Resin)
50	Polycarbonate (PC) (Thermoplastic Resin)

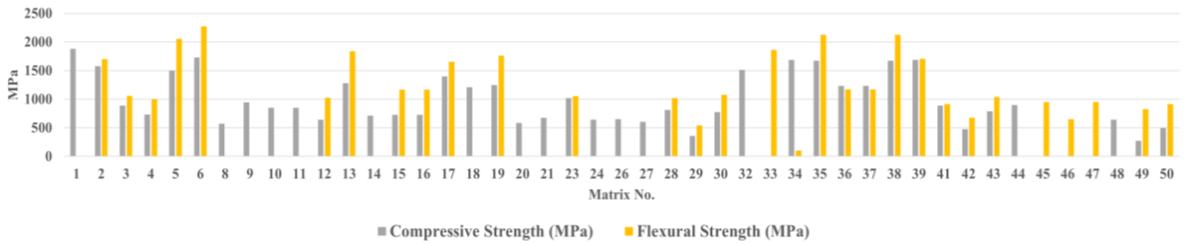

Figure 4. Flexural and compressive strength of available CFRP Prepregs with different matrices

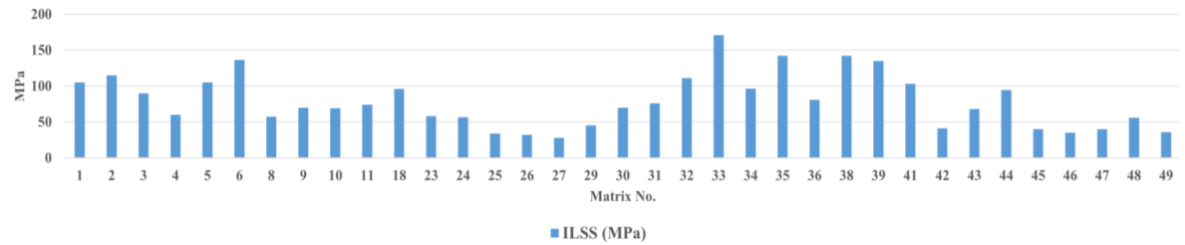

Figure 5. ILSS of commercially available CFRP prepregs with different matrices

3.4 CFRP laminate layups and weave options

The MET properties of a CFRP structure are all sensitive to the layup of the fibres within the structure, which is the focus of the second database in part vii of Phase-2. Table 2 summarizes the mechanical implications of different orientations of carbon fibre plies within a layup mentioned in the literature [11].

Table 2: Selected design considerations for fibre orientation

Design Consideration	Description	Reason
Symmetric orientation	Material symmetric laminate concerning mid-plane.	To eliminate the stretching, shearing, and twisting coupling.
Balance	An equal number of plies of opposing angles	To reduce shear stiffness coupling.
Contiguity	Limited adjacent plies with the same fibre orientation	To prevent crack propagation and ply edge effect
Max. 45^{o} orientation difference between adjacent plies	-	To prevent crack propagation and delamination by reducing ILSS

These design consideration for CF plies layups are based on developing a mechanically robust CFRP. From an electrical perspective, the anisotropic electrical and thermal conductive properties of CFRP are sensitive to layup. For example, along the x-axis, the electrical conductivity of 0 and 90^{o} oriented plies is 22 KS/m and 56.1 S/m respectively [12]. Identification of appropriate design trades between MET properties is required to find a balance between appropriate structural strength and appropriate electrically and thermally conductive CFRP.

3.5 Additives to adapt CFRP properties

The third database of properties in part viii of Phase-2 focuses on methods to adapt the MET properties of CFRP using additives. Different methods have been proposed in the literature to improve the CFRP conductivity in the matrix dominant directions. These methods either modify the fibre surface (e.g., growth of carbon nanotubes (CNT) on fibre to increase conductivity from 0.003 S/m to 0.38 S/m by [13]), modify the matrix by adding conductive additives in it (e.g., enhanced conductivity by adding CNT to a matrix, 10^{-5} (no CNT) to 66.2 S/m (with CNT) [14]) or use the additional layers of conductive elements within CF plies (e.g. silver-plated interleaves increased in-fibre and through-thickness electrical conductivity from 25 kS/m (without interleave) to 50 kS/m (with interleave) and from 12.225 S/m (without interleave) to 500 S/m (with interleave), respectively) [15]).

These methods improve the CFRP conductivity properties but based on the processing technique of incorporating additives in it, these methods can have a detrimental effect on the mechanical properties of CFRP due to decreased interfacial bonding between fibre and matrix because of additive [14]. For example, matrix modification with CNT increases the viscosity of

  doi:10.5075/epfl-298799_978-2-9701614-0-0

the matrix, causing poor wettability of fibres with resin, hence, leading to poor CFRP compression strength (e.g. from 112 MPa (without CNT) to 65 MPa (with CNT) [13]. Similarly, a decrease in flexural strength (e.g. from 584.5 MPa (without bucky paper) to 378.25 MPa (with bucky paper)) has been reported by the addition of bucky paper between CF plies associated with a decrease in fibre volume fraction due to the additional layers [16].

4 Identification of viable design spaces for MF CFRP

In parts ix and x of Phase-2, the databases inform the determination of the viable design spaces for the MF CFRP and the trades between MET properties. In part ix of Phase-2, the process for mapping out the initial design space and then carrying out appropriate system design trades is needed. From the MET requirements identified from Phase-1, approaches to achieving these requirements can be identified from the databases (parts vi – viii). However, the interdependencies between the different MET requirements and the approaches to reaching these must be considered.

A methodology is needed to assess the options for MF CFRP design to meet the design requirements. One methodology may be to determine methods for each of the MET requirements, which will enable requirements to be met, and from that to assess whether a viable design space is available. For example, if the structural requirements are such that a material with high compressive (matrix dependent) strength is required, then pitch carbon fibres may be an option. Layups with pitch fibres that meet the mechanical properties can then be down-selected. Independently to this, approaches to achieve appropriate electrical and thermal conductivity are identified. If no viable design space is identified for each of the MET requirements individually at this stage, part x in Part-2, then the design requirements must be reassessed, as no collective viable design space can exist.

As part of the feedback loop between Phase-2 and Phase-1, the limitations of the design spaces identified in Phase-2, part ix, are fed back to Phase -1, and inform the redesign (e.g. reconsider an aspect of the EPS design to adapt the electrical requirements) and capture of MF CFRP.

If methods can be identified to meet the MET requirements individually, then an assessment must take place to ascertain if there is a common design space where all requirements are met. If not, then appropriate system trades must take place in areas where design flexibility is identified. For example, it may be possible to use pitch rather than PAN fibres and still meet mechanical requirements. Or it may be possible to change the pathway taken by the electrical current through the CFRP by adapting the method of electrical bonding to the component, which may open up available design space. However, if no viable solution space can be found, then the underlying systems in Phase-1 must be adapted, and the MET requirements adjusted.

5 Conclusion

The efficient design and down-selection of MF-CFRP which meets MET requirements is challenging due to the need for adapting CFRP significantly, attaining appropriate combined MET properties, and the interdependencies between these properties. This paper has presented the early stages of a framework to enable the design of MF-CFRP and provide a logical approach to navigating MF CFRP design and the interdependencies with the wider systems (electrical power, structural and thermal) design. The next steps for this work are to develop in more depth the

  doi:10.5075/epfl-298799_978-2-9701614-0-0

interdependencies between the electrical, thermal and structural requirements, and identify the key system design thresholds such that, for example, part of an electrical power system on an aircraft is designed such that its cabling can be formed by a structural, CFRP panel.

Acknowledgement

This work was supported by the Rolls-Royce University Centre for Electrical Power Systems and the National Manufacturing Institute of Scotland (NMIS).

6 References

1. Jones CE, Norman PJ, Burt GM, Hill C, Allegri G, Yon J, et al. A Route to Sustainable Aviation: A Roadmap for the Realization of Aircraft Components with Electrical and Structural Multifunctionality. IEEE Transactions on Transportation Electrification. 2021.
2. Sarlioglu B, Morris CT. More Electric Aircraft: Review, Challenges, and Opportunities for Commercial Transport Aircraft. IEEE Transactions on Transportation Electrification. 2015.
3. Okayasu M, Tsuchiya Y. Mechanical and fatigue properties of long carbon fiber reinforced plastics at low temperature. Journal of Science: Advanced Materials and Devices. 2019.
4. Harakare P, Heblikar VK. Evaluation of Static and Buckling load carrying capability of the Wing box through FEM approach. Intl Journal of Current Engineering and Technology. 2013.
5. Hexcel [Internet]. Available from: https://www.hexcel.com/Resources/DataSheets/.
6. Toray [Internet]. Available from: https://www.cf-composites.toray/resources/data_sheets/.
7. Teijin [Internet]. Available from: https://www.teijincarbon.com/products/.
8. NGF World [Internet]. Available from: https://www.ngfworld.com/en/product/yarn.html.
9. MCCFC [Internet]. Available from: http://mccfc.com/carbon-fiber/.
10. Edwards T. Composite materials revolutionise aerospace engineering. Ingenia. 2008.
11. Daniel IM, Ishai O, Daniel IM, Daniel I. Engineering mechanics of composite materials: Oxford university press New York; 2006.
12. Senis EC, Golosnoy IO, Dulieu-Barton JM, Thomsen OT. Enhancement of the electrical and thermal properties of unidirectional carbon fibre/epoxy laminates through the addition of graphene oxide. Journal of Materials Science. 2019;54(12):8955-70.
13. Lin Y, Gigliotti M, Lafarie-Frenot MC, Bai J, Marchand D, Mellier D. Experimental study to assess the effect of carbon nanotube addition on the through-thickness electrical conductivity of CFRP laminates for aircraft applications. Composites Part B: Engineering. 2015;76:31-7.
14. Zhao ZJ, Zhang BY, Du Y, Hei YW, Yi XS, Shi FH, et al. MWCNT modified structure-conductive composite and its electromagnetic shielding behavior. Composites Part B: Engineering. 2017.
15. Guo M, Yi X, Rudd C, Liu X. Preparation of highly electrically conductive carbon-fiber composites with high interlaminar fracture toughness by using silver-plated interleaves. Composites Science and Technology. 2019;176:29-36.
16. Kumar V, Sharma S, Pathak A, Singh BP, Dhakate SR, Yokozeki T, et al. Interleaved MWCNT buckypaper between CFRP laminates to improve through-thickness electrical conductivity and reducing lightning strike damage. Composite Structures. 2019;210:581-9.

  doi:10.5075/epfl-298799_978-2-9701614-0-0

MANUFACTURING PROCESS SIMULATION FOR COMPRESSION MOULDING OF SHEET MOULDING COMPOUND – AN AUTOMOTIVE CASE STUDY

C. C. Qian[a], A. Deshpande[a], D. Simsek Polat[a], J. Clarke[a], F. Sicard[b], K. N. Kendall[a]*
a: Automotive Composites Research Centre, WMG, University of Warwick, Coventry, United Kingdom, CV4 7AL
b: Jaguar Land Rover, W/11/1 NAIC Building, Abbey Road, Whitley, Coventry, United Kingdom, CV3 4LF
*Corresponding author: connie.qian@warwick.ac.uk

Abstract: *A case study on process simulation for compression moulding of SMC has been conducted using an automotive 'rear header' geometry. Flow simulation has been performed using the commercial package Moldex3D and the results have shown poor correlation with experimental moulding trials in terms of compression forces and filling patterns. A mould tilting analysis has been performed to understand the disagreement in filling patterns between the simulation and the experiment which it has been identified the change in mould parallelism is the main cause. This case study has highlighted the limitations of the existing commercial pression simulation model and calls for the development of an alternative simulation approach.*

Keywords: carbon fibre; sheet moulding compound; compression moulding; process simulation; automotive

1. Introduction

Compression moulding of high fibre content, long discontinuous carbon fibre based Sheet Moulding Compound (SMC) is an attractive solution for high-rate manufacturing of high-performance composite structures, and is the one composites manufacturing process that has the potential to meet future automotive weight saving demands for cost, volume and structural integrity. Unlike continuous fibre based prepreg materials, SMC flows under compression force to fill the mould cavity, allowing complicated geometry to be manufactured such as ribs and variable wall thickness. The manufacturing wastage is also lower than prepreg materials as the initial charge does not need to be net-shaped. Accurate prediction of the fibre orientation distribution in an SMC component offers a significant benefit for the part designers. As in-cavity flow often causes fibres to re-orientate along the preferential flow direction, it is crucial to correctly predict the flow in the first place.

Several commercial simulation software have been developed for compression moulding of SMC including Moldex3D by CoreTech System Co., 3D TIMON by Toray Engineering D Solutions and Moldflow Insight Ultimate by Autodesk. The constitutive material model used in these software is usually adapted from injection moulding process simulation, where the stresses within the material is determined through the shear viscosity of the material. A comprehensive assessment of commercial process simulation software mentioned above was performed by the authors in [1] using two generic case studies: a flat plaque geometry with 1D in-plane flow regime and a ribbed W-profile geometry with 3D, combined in-plane and out-of-plane flow regime. It was reported in [1] that all the commercial software studied failed to correctly predict the compression forces and pressures during the flow process.

  doi:10.5075/epfl-298799_978-2-9701614-0-0

This paper aims to further evaluate the predictive validity of a commercial SMC compression moulding simulation software through an automotive case study. Experimental compression moulding was conducted using an industrial press with instrumented tooling. Partial closures were conducted to investigate the filling pattern. The manufacturing process simulation was performed using Moldex3D and the process conditions were modelled according to the experimental data. The simulation results were validated against experimental data in terms of compression force, in-cavity pressures and filling pattern. A mould tilting analysis was subsequently performed in generic finite element software ABAQUS/standard to understand the disagreement in simulation and experimental filling patterns cause by the change in mould parallelism.

2. Demonstrator geometry

The component studied in this paper, referred as the 'rear header' (Figure 1), was a demonstrator component designed and manufactured during the TUCANA project – a 4-year programme led by Jaguar Land Rover (JLR) to accelerate mainstream use of lightweight electric vehicles. TUCANA aimed to deliver a 30% torsional stiffness uplift and a 35kg saving of a Jaguar I-Pace rear body structure through extensive use of composite materials, whilst achieving high-volume manufacturing for a minimum of 40,000 units per annum at a controlled cost. The application of compression moulded SMC was heavily explored in TUCANA due to the low cost and low cycle time of the material and the process.

The rear header geometry has an overall dimension of 690mm x 340mm x 140mm. The original design of the rear header had two long strips of UD reinforcements to improve the structural stiffness of the part, and an SMC only variation was adopted in this study where the areas for UD reinforcements were filled with SMC. The rear header is located in the upper rear structure of the vehicle, supports the roof panel and enables the assembly of the tailgate. Key manufacturing challenges include large variation in thickness, deep draw at low draft angle and ribs, which makes the rear header an ideal candidate for investigating the Design-for-Manufacture capabilities of SMC.

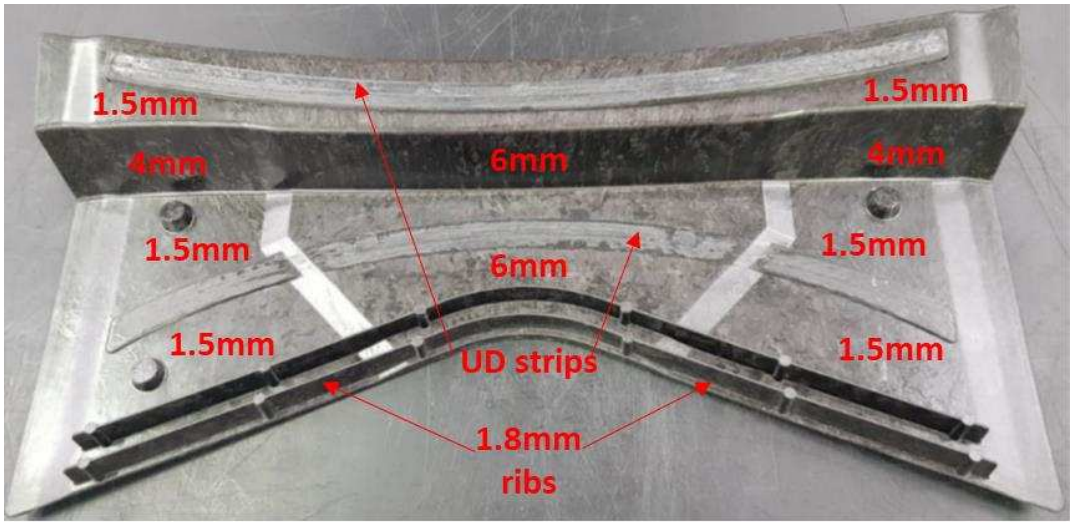

Figure 1: The rear header demonstrator component manufactured using carbon fibre SMC and UD strips. An SMC only version is used in this paper where the cavity for UD reinforcement were filled with SMC

  doi:10.5075/epfl-298799_978-2-9701614-0-0

3. Experimental compression moulding of SMC

The experimental compression moulding was carried out on an Engel V-Duo 1700 tonne press at WMG. The material used in this study was a vinylester based carbon fibre SMC with 25mm fibre length and 57% fibre weight fraction. The initial charge (Figure 2a) measured 370mm x 90mm (approximately 15% coverage) and weighed a total of 1312 g ±2g (16-17 plies). The mould temperatures were 140°C at the top and 145°C at the bottom according to the manufacturer's recommendation, and to prevent jamming of the punch and die due to thermal expansion. The actual instantaneous mould height, closure speed and compression force can be directly exported from the press. The mould closure speed was set to 9mm/s with a switch-over force of 450kN, and a compression force of 4500kN applied once the mould was fully closed. The total cure time was 300 second. Partial closures were performed to investigate the filling pattern. It should be noted that parts moulded using partial closures don't represent the instantaneous fill pattern at the time the mould was closed, because the material would continue to flow further due to inertia. However, partial closures still provide useful information on the progression of flow.

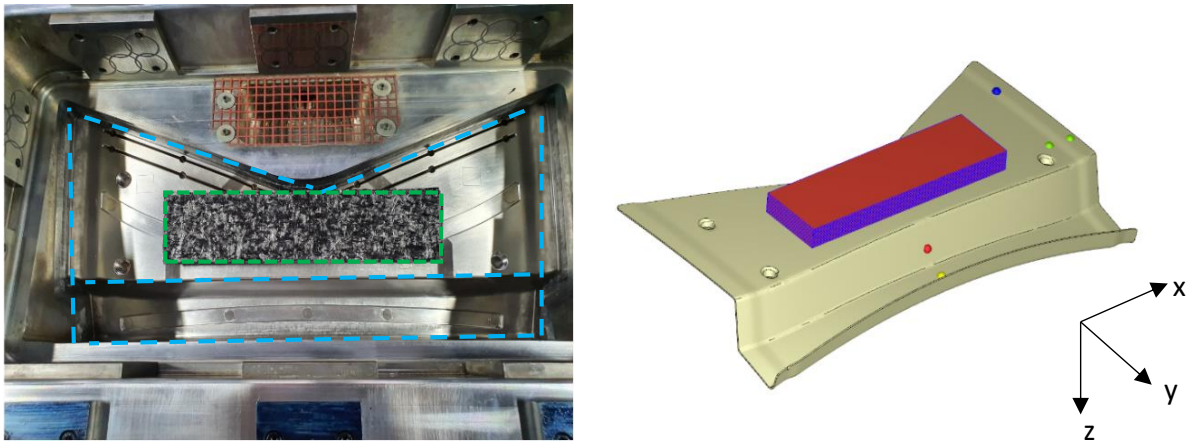

(a) (b)

Figure 2: The charge layout investigated in this report: (a) experimental setup and (b) simulation setup. The blue dashed lines in (a) indicate the boundaries of the mould cavity, and the green dashed lines indicate the boundaries of the charge. The z-direction indicates the compression direction.

4. SMC flow simulation

4.1 Model setup

The compression moulding simulation model was setup in Moldex3D v2017 in accordance with the experimental methodology outlined in Section 3. The charge was modelled as a monolithic block (Figure 2b) with a thickness of 29mm determined based on the total mass of the charge used and the density of the uncured SMC. The mould temperatures were set to 140°C for both top and bottom moulds in the simulation because Moldex3D did not support different mould temperatures. The initial charge temperature was set to 23°C and the charge was preheated for 1 second prior to the start of the compression. The compression process was defined using a displacement based approach. A stepwise speed profile was adopted in this case, where a

constant speed is applied over a given time interval (a step). The stepwise speed is calculated as the total displacement divided the total time for each step.

4.2 Flow simulation results

Figure 3 compares the compression forces as a function of mould height between the simulation and the experiment. Note that the simulation curve and the experimental curve are plotted on difference scale because the magnitude of simulation forces are significantly lowed that that of experimental forces, which has been also reported in the previous study [1]. The maximum difference between the compression forces observed in *Figure 3* is approximately 30 times, which takes place between mould heights of 10mm and 20mm where the majority of the in-cavity flow occurs. There is an 8mm difference in mould height when the compression starts, indicated by the increase in compression force from zero. This is primarily caused by the difference in charge thickness between the experiment and the simulation: in the simulation the charge was modelled as a monolithic block without voids, where in reality the charge contained plies of uneven thickness, increasing the total thickness of the charge by creating loft between plies. Furthermore, raw SMC typically contains voids introduced during the compounding process, which can also increase the overall volume of the charge.

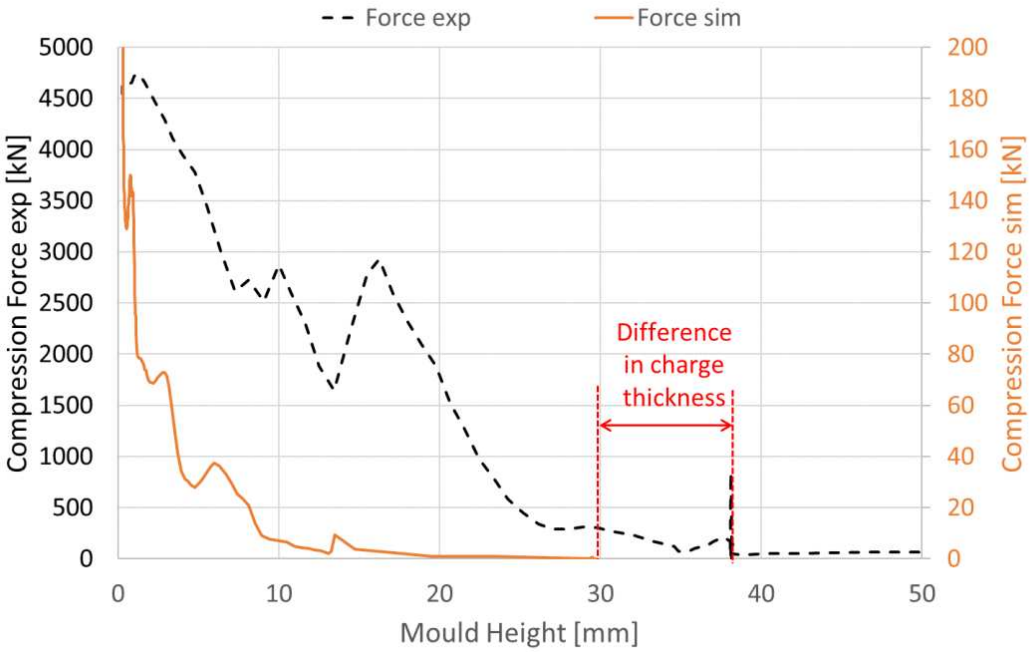

Figure 3: Comparison of compression force vs. mould height relationship between the simulation and the experiment for rear header. Note that the two curves are plotted on different scales due to the large difference in the magnitude of the force between the two sets of results.

Figure 4 compares the filling patterns predicted by the simulation against experimental partial closures of 14mm, 6mm and 1mm. In general, the filling patterns predicted by the simulation show poor agreement with the experiment. The simulation predicts that the 'V' side of the part fills faster, but the experiment shows that the curved side of the part fills faster (see 14mm and 6mm partial closures in *Figure 4*). The most likely cause for such discrepancy in filling patterns is the asymmetric loading on the mould during the compression process. A mould tilting analysis

  doi:10.5075/epfl-298799_978-2-9701614-0-0

will be presented in the next section to further understand this issue. Nevertheless, the simulation correctly predicts the last filling points according to the 1mm partial closure in *Figure 4*.

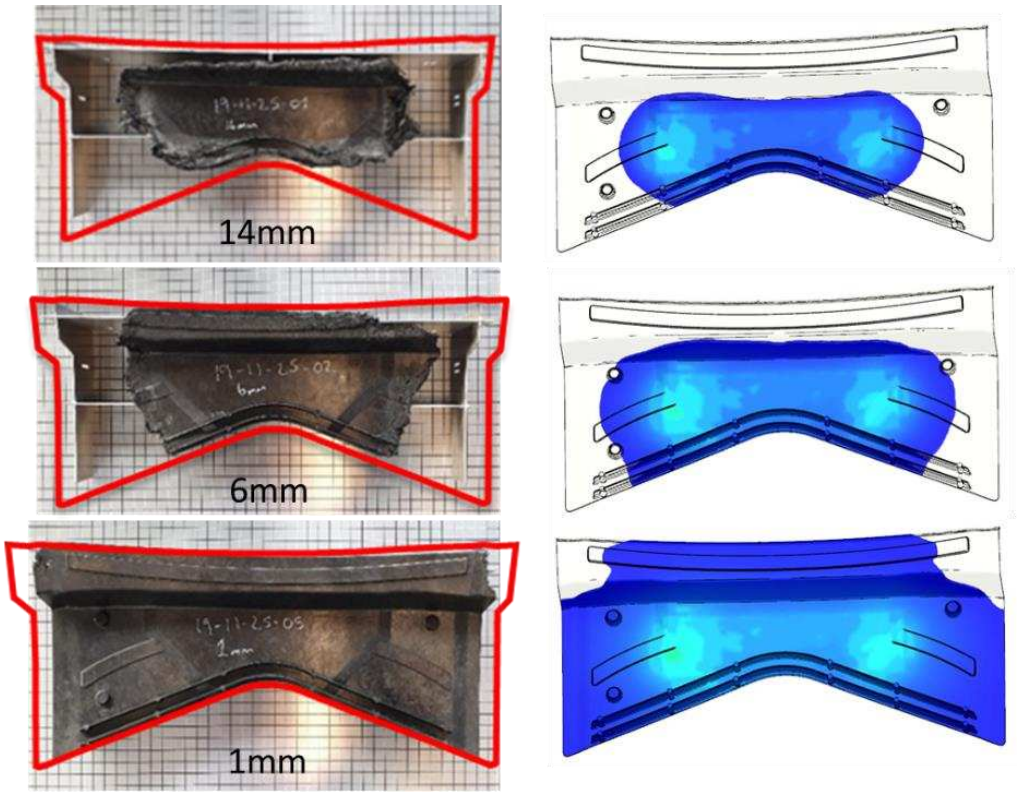

Figure 4: Comparison of the experimental filling patterns from partial closures (14mm, 6mm and 1mm) and the filling patterns predicted by the process simulation. The predicted filling patterns are taken according to the approximate filled areas instead of the partial closure heights.

5. Mould tilting analysis

5.1 Model setup

A mould tilting analysis was performed to understand the difference in filling patterns between the simulation and the experiment caused by the change in mould parallelism. The mould tilting analysis was carried out both experimentally and numerically for the rear header geometry, where the experimental analysis was performed using the tie bar location data recorded by the press, and the numerical analysis was performed using Finite Element Analysis (FEA) in ABAQUS.

Figure 5 illustrates the locations of the four tie bars where the vertical positions of the top platen of the press were recorded, and Figure 6 presents the relative positions of the front and the back tie bars recorded by the press. The red shaded area in Figure 6 indicates the mould height range at which the partial closures were performed. According to Figure 6, the mould is higher than the reference position at locations 1 and 2, but lower than the reference position at locations 3 and 4, which means the actual cavity thickness is larger at the front (curved side) than at the back (V side). Because the material has the tendency to flow faster in a thicker cavity, the curved side fills faster in the experiment. Unfortunately, Moldex3D is not capable of predicting the change in moulds parallelism because the moulds are not physically modelled.

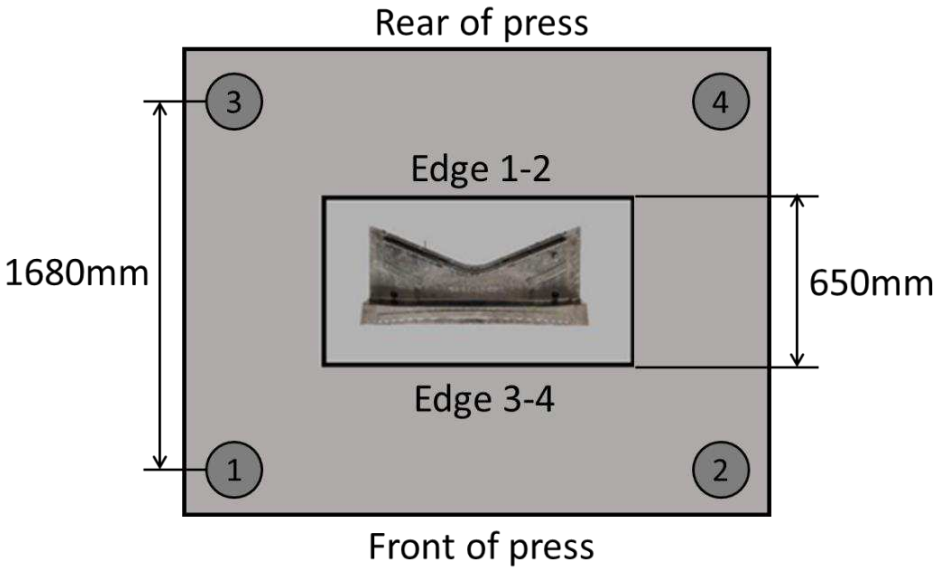

Figure 5: The tie bar locations in relation to the part and the mould.

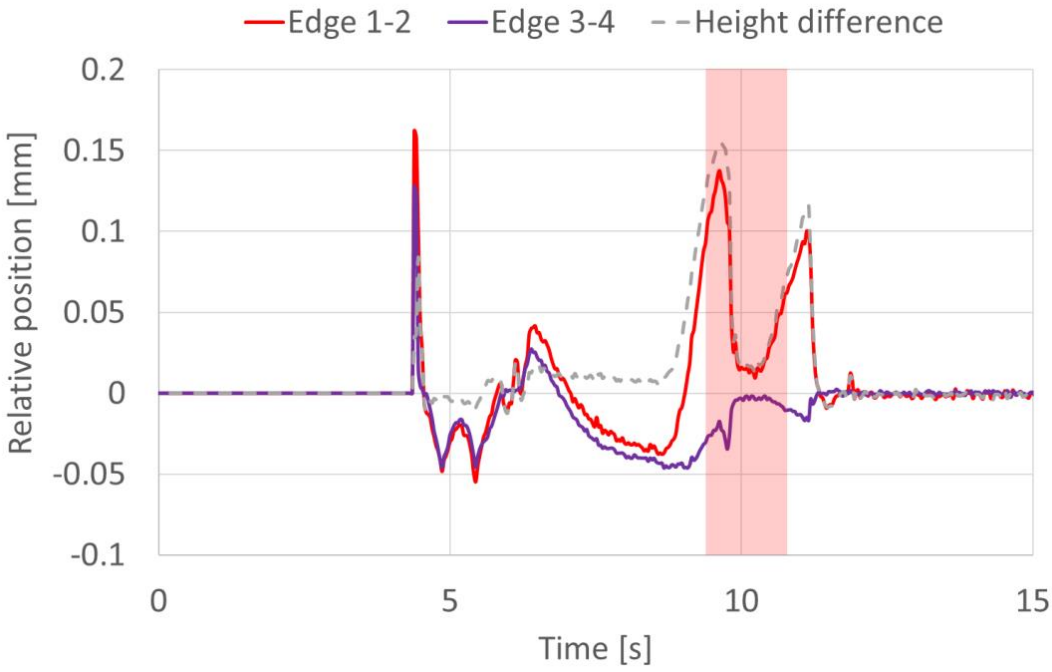

Figure 6: The relative positions of the Edge 1-2 and Edge 3-4 as indicated in Figure 5. The red shaded area indicates the mould height range (1mm – 14mm) where the partial closures in Figure 4 *were performed.*

The numerical model for mould tilting analysis was performed in ABAQUS/standard, and only the mould assembly was modelled (including the male and female mould halves, the guide pins and bushes) to reduce computational efforts. It was assumed that the variation in cavity height was primarily caused by the deformation of the guide pins and bushes, so that the mould halves were modelled as rigid parts. All deformable parts were meshed with 3D continuum linear tetrahedron elements (C3D4) and an isotropic linear elastic material model with a Young's

  doi:10.5075/epfl-298799_978-2-9701614-0-0

modulus of 209GPa and Poisson's ratio of 0.3 was applied. All rigid parts were modelled as 3D discrete shell part and meshed using 3-node triangular elements. The analysis was performed at 50% filling in the simulation in both approaches. A distribution of pressure was applied to the filled region, where the pressure values and the flow front locations were extracted from the Moldex3D simulation result (see Figure 7).

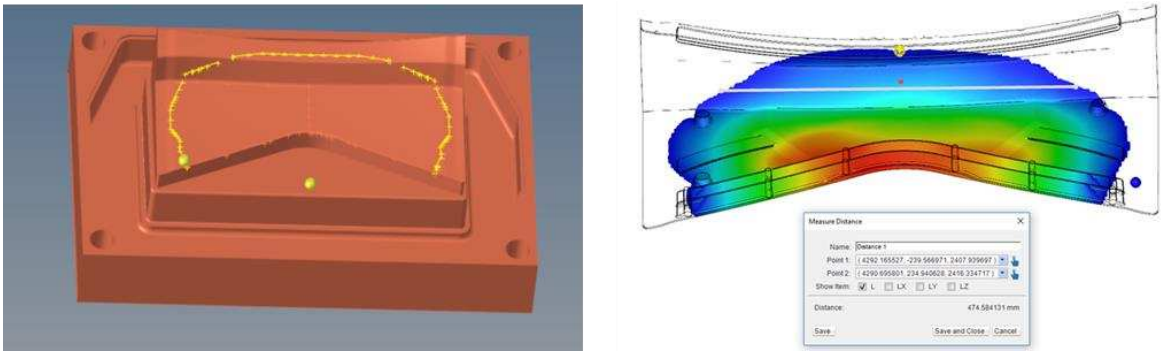

Figure 7: Left: the area where the pressure was applied in the FEA model (indicated by the yellow lines). Right: Pressure distribution and filled region from the Moldex3D simulation at 50% fill.

Figure 8 compares the deflection of the male mould half in the z-direction predicted by the mould tilting analysis. The mould tilting analysis has predicted that cavity has a deflection in the +z direction on the curved side (Edge 1-2 in Figure 5), and a deflection in the -z direction on the "V" side (Edge 3-4 in Figure 5), which means the cavity is expected to be higher in the curved side (Edge 1-2). The FEA results therefore indicate the same tilting direction as the experiment, which explains the reason for the disagreement between the predicted filling pattern and the experimental filling pattern. The maximum height difference predicted by the simulation is 0.43mm between Edge 1-2 and Edge 3-4. Although this value is nearly 2 times higher than the 0.15mm estimated experimentally, several explanations are identified. Firstly, the mould tilting analysis performed in this section only considered the mould assembly, where the stiffness of the press and the tie bar would significantly reduce the level tilting. Secondly, the pressure distribution applied to the model was extrapolated from the process simulation, which was known to have large discrepancy with the experiment in terms of both filled area and the magnitude of the pressures, and would contribute to further cause of errors in the mould tilting analysis. Furthermore, the mould tilting analysis was setup as a steady-state analysis with pressures only applied to the cavity side of the male mould half, where in reality the mould was subjected to pressures from both the material (on the cavity side) and the press (on the opposite side). In reality, the mould did not go through a steady-state motion, but experienced constant acceleration and deceleration, especially during the switch-over process. To accurately model the kinematics of the mould, the mould tilting analysis has to be performed in combination with the flow simulation.

  doi:10.5075/epfl-298799_978-2-9701614-0-0

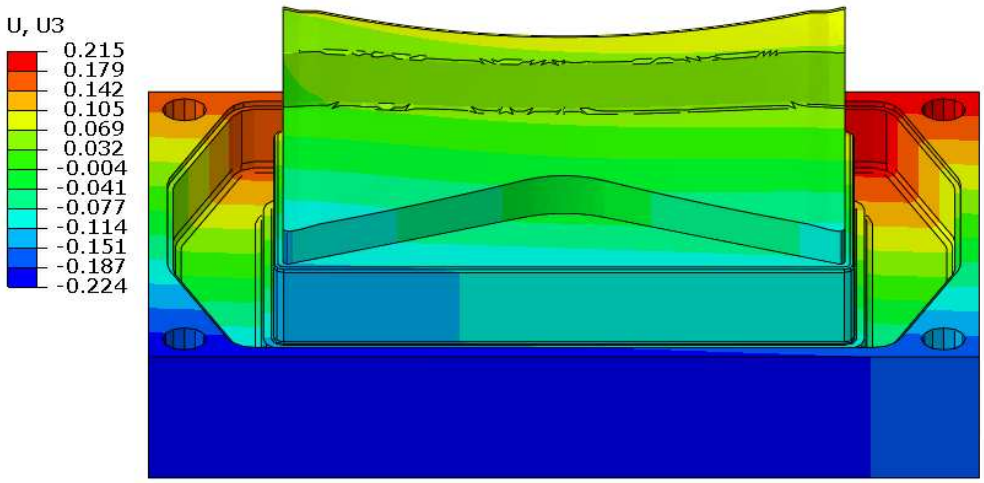

Figure 8: Deflection of the male mould half in the z-direction predicted by the mould tilting analysis

6. Conclusions

The commercial compression moulding process simulation software Moldex3D has been evaluated in this paper through an automotive case study, supported by experimental moulding trials for validating the simulation results. Poor agreement in compression forces has been observed between the flow simulation and the experimental data. The difference in compression force profile also indicates the need for modelling the loft between raw SMC plies with uneven thickness, and the voids within each ply. Poor agreement in filling patterns has also been observed between the simulation and the experiment. A mould tilting analysis has been performed to understand the change in parallelism between the mould halves, which explains the reason for the disagreement in filling patterns. The outcomes from this case study has suggested that an alternative simulation approach needs to be developed in order to accurately model the SMC compression moulding process.

Acknowledgements

This research was delivered through the TUCANA project led by Jaguar Land Rover. The authors would like to acknowledge the financial support provided by the Advanced Propulsion Centre UK.

References

[1] C. Qian, Deshpande, A., Jesri, M., Groves, R., Reynolds, N., & Kendall, K., A Comprehensive Assessment of Commercial Process Simulation Software for Compression Moulding of Sheet Moulding Compound, in: 24th International Conference on Material Forming, Liège, Belgique, 2021.

  doi:10.5075/epfl-298799_978-2-9701614-0-0

POLYMER COATED MATERIAL FOR INNOVATIVE REVERSIBLE DISSIMILAR COMPOSITE-METAL JOINING FOR AUTOMOTIVE APPLICATIONS

Faranak, Bahrami[a], Sadik, Omairey[a], Gareth, Bone[b], Michael, Matthews[b], Chris, Worrall[c], Sofia, Sampethai[c], Neelmanee, Sarin[c], Faisel, Almudaihesh[c], Sophie, Cozien-Cazuc[d], Joaquín, Piccini[e], Nithin, Jayasree[a], Mihalis, Kazilas[a,c]

a: Brunel Composites Centre, Brunel University London – Faranak.Bahrami@brunel.ac.uk
b: Gestamp, UK
c: TWI Ltd, UK
d: Far-UK Ltd, UK
e: Gestamp- Autotech Engineering, Spain

Abstract: *While the cost of composites has dropped over the past decade, the effective joining of these materials to conventional metal parts in the automotive sector remains a significant challenge. Existing joining solutions present several limitations, with major manufacturers inclined to use mechanical fasteners or adhesive bonding. In this study, Polymer Coated Material (PCM) joining process is adapted for thermoplastic composite to metal assembly. This joining method uses induction welding to join a thermoplastic composite to a metallic substrate pre-coated with a compatible thermoplastic polymer film. Compared to mechanical fastening, PCM does not induce stress concentrations in the parts, and as the materials are not pierced, the risk of water damage is reduced. Compared to adhesives, PCM solution is not subject to curing times or shelf-life restrictions. Furthermore, the use of PCM enables easy recyclability of the parts; at the end-of-life, the parts can be disassembled through a reversal heat process.*

Keywords: Induction Welding; Dissimilar Material Joining; Thermoplastic Composite; Disassembly; Automotive

1. Introduction

Compared to metals, fibre-reinforced polymer (FRP) composites offer improved stiffness to weight ratio, thermal/electrical properties, and corrosion resistance. These properties are interesting for advanced industries and applications. For example, the aerospace sector exploits these benefits by replacing metal alloys with composites in primary structures [1, 2]. Similarly, the automotive industry is replacing more conventional materials with lighter and stiffer alternatives that offer higher performance and meet regulating bodies' tighter regulations and restrictions to produce environmentally friendly cars [3-6]. The benefit of light-weighting expands beyond the drive for using composites in electric vehicles (EVs) and fuel cell electric vehicles (FCEVs) where weight reduction is crucial to extend range but also benefits internal combustion engine vehicles (ICEVs) where it is estimated that up to 700 litres of fossil fuel can be saved over the lifetime of an ICEV for every 100kg weight reduction [7]. A state-of-the-art automotive application of thermosetting composites is implemented in BMW's i3 hatchback. However, poor energy absorption, high production cost, long production time, limited recyclability and end of life options of thermosets question their advantages and sustainability with full-body implementations. Hence, although weight reduction is an important aspect, the use of metals remains technically and economically sustainable, especially as metals allow manufacturers to meet the EU's reuse and recycling of ≥ 85 % and reuse and recovery of ≥ 95% (EU Directive 2000/53/EC). As a result, manufacturers seek to increase the stiffness of the vehicle structure at specific locations utilising the available design space. For instance, Jaguar

  doi:10.5075/epfl-298799_978-2-9701614-0-0

Land Rover (JLR) in the Tucana project [8] are replacing the rear section of the body-in-white (BIW) aluminium and steel with composites capable of handling the increased torque generated by high-performance batteries, while improving range efficiency and reducing CO_2 impact. In another example, Hexcel Composites developed thermosetting fibre reinforced patches that can be bonded to aluminium subframes using adhesive to reduce noise, vibration and harshness (NVH) [9]. Nevertheless, these applications do not change the fact that the circular economy for thermosetting composites remains a challenge. Instead, manufacturers are shifting to thermoplastic composites as they offer excellent material options thanks to their weldability, low density, low overall production cost, improved fracture toughness, and recyclability. This is explored in projects such as MAI Skelett [10] (BMW as an end-user partner) to replace the i3's CFRP roof structure with a composite thermoplastic version. Extruded thermoplastics sections combined with overmoulding achieved better overall stiffness responses, and energy absorption in crash load cases outperformed the Carbon fibre reinforced polymer (CFRP), creating a ductile failure mode. Conversely, FlexHYjoin [11] project focused on joining an application-oriented multi-material roof stiffener, namely thermoplastic composite roof crossbar with Cant rail via steel brackets. The project used laser joining to undercuts the steel brackets, then applying pressure and laser beam to initiate induction welding of the thermoplastic to the steel bracket with a primary focus on automation aspects and bond strength via non-destructive testing (NDT).

The above projects demonstrated thermoplastics potential in terms of welding ability. Yet, the scope of the state-of-the-art use of advanced composites is still limited by the number of joining techniques, the areas where these techniques were implemented, commercial feasibility, and disassembly for end-of-life recycling. Therefore, the BRACE project aims to use an advanced joining technique for fibre reinforced thermoplastic composites to lightweight and improve the performance of chassis components while emphasising: 1) the design for disassembly by using polymer-coated materials (PCM) joining technique in which joints can be separated by heat application without damaging any of substrates, 2) the use of thermoplastic patches that are compatible with PCM and offer improved performance and recycling options, and 3) commercial feasibility as PCM process can be integrated with existing manufacturing line and do not require additional time for cure cycle.

2. PCM joining approach

Joining dissimilar materials is challenging as it involves different mechanical properties, surface behaviour and thermal expansion coefficients. Traditional joining technologies for metallic components such as welding, mechanical fastening, and riveting are not directly transferable to fibre reinforced composites because drilling or punching composites with post-manufacture mechanical fasteners or rivets damage the reinforcement [12]. Hence, adhesives are widely adopted for dissimilar joining as they offer several advantages over mechanical fastening, such as uniform stress distribution along the bonded area, sealing and electrical insulation, excellent fatigue strength, damping, and shock absorption, in addition to commercial benefits. However, despite their benefits, the performance of adhesively bonded joints is affected by various types of defects that are hard to inspect and require a high level of quality control. Recently, attention is increasing towards the importance of sustainability and end-of-life recycling by designing products that can be easily disassembled for efficient in-service repair, reuse, and end-of-life recycling. Consequently, using adhesives limits the disassembly opportunity as they are hard to

  doi:10.5075/epfl-298799_978-2-9701614-0-0

separate once set and hard to remove from the substrates without damaging them. Prototypes for developing a disbanding solution for adhesively bonded joints include the use of thermally expandable microspheres to separate joint substrates were investigated. However, separated joints using this approach will still have adhesive remains on joint interfaces, and bond strength is slightly reduced with the introduction of microspheres [13].

On the other hand, BRACE project aims to remove the need for adhesives by utilising the weldability of thermoplastics by adopting an innovative PCM joining approach [14]. PCM involves using thermoplastics as structural adhesives where the final assembly operation is a polymer weld. For example, in the manufacture of a joint between dissimilar materials with one of the substrates being thermoplastic based composite, the non-thermoplastic component is first coated with a compatible thermoplastic before both components are welded together using heat and pressure action. As for disassembly, heat application is repeated until the interface reaches the glass transition temperature and the joint separates efficiently without damaging substrates. A schematic illustration for the PCM joint and Carbon/PEEK to aluminium joint demonstrations can be seen in Figure 1 and Figure 2, respectively.

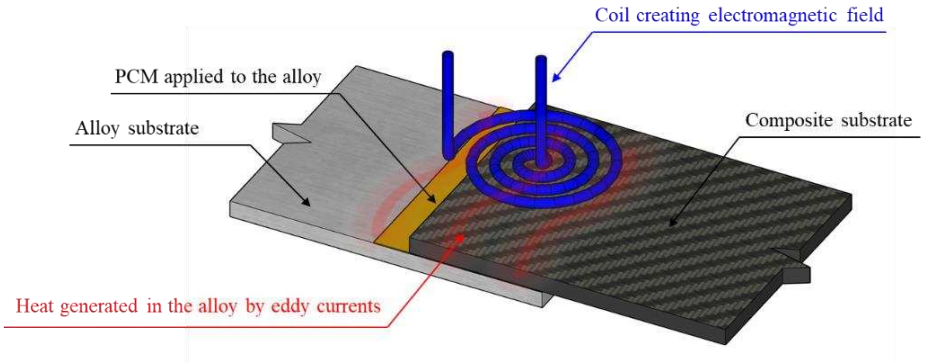

Figure 1 Schematic cross-section through a PCM joint.

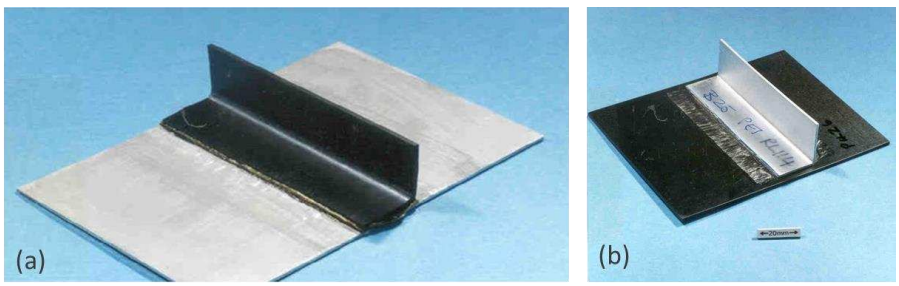

Figure 2 TWI Ltd PCM joining demonstration: a) Carbon/PEEK stiffener joined the PCM aluminium alloy panel. B) PCM Aluminum alloy stiffener joined to carbon/PEEK panel (copyright TWI).

3. Joining and disassembly steps

In this study, five main process steps are followed to achieve an effective PCM joint; these steps are:

1) **Cleaning and decontamination**: In this stage, surface preparation of the metal (laser processing, etching, surface texturing, or abrasion) takes place to prepare the metallic substrate for coating with the polymer material, PCM, see *Figure 3*(a).

  doi:10.5075/epfl-298799_978-2-9701614-0-0

2) **Coat**: a low-viscosity polymer solution is applied to the metal component by either spraying, dipping, or painting. Following effective cleaning and decontamination in the first step, the polymer solution penetrates the micro-features on the surface of the metal as it dries and adheres to the surface through a combination of attachment forces with additional chemical bonding enhancing the strength of the interface, see Figure 4.
3) **Heat**: The thermoplastic composite part is then brought into contact with the PCM applied to the metal part. A work coil is then used to heat the composite and/or metal by electromagnetically inducing eddy currents in the conductive parts of the assembly.
4) **Joint**: Fusion bonding occurs between PCM (applied to the metallic substrate) and composite as the required temperature of the PCM is reached. For effective joints, mechanical pressure is applied along with the induced heat to ensure sufficient contact between the substrates; applying this pressure can vary based on the application.
5) **Disassemble**: At the end-of-life of the product, in the same way as heat is needed to create the joining bonds, the process can also be reversed through the application of heat. The joined parts are easily released and disassembled at end-of-life for recycling, or reuse.

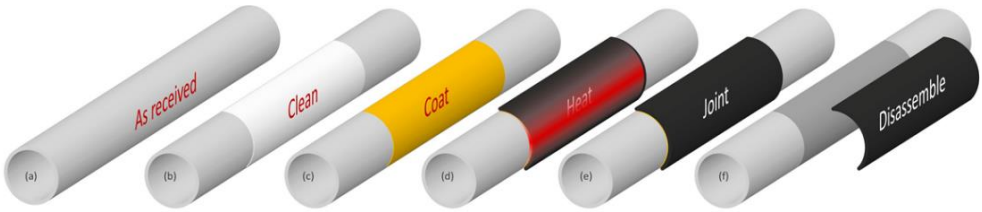

Figure 3 PCM joining (a-e) and end-of-life process (f).

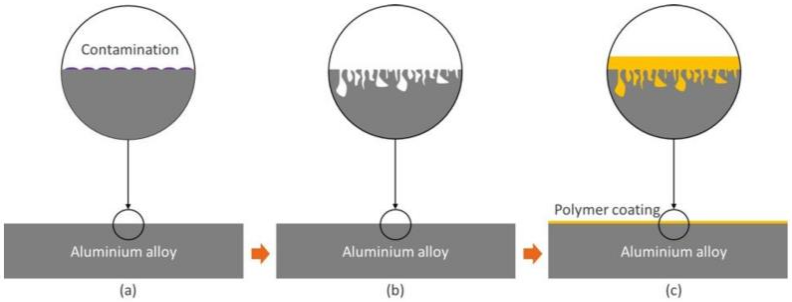

Figure 4 PCM coating process: (a) as received; (b) cleaning, texturing/pre-treatment; (c) polymer coating applied, ready for joining.

4 PCM Automotive Application

In the BRACE project, the consortium further develops the PCM joining process to adapt it for automotive chassis parts. For this purpose, three standard components manufactured by Gestamp Chassis are selected, aluminium and steel (painted and unpainted) lower control arms, see Figure 5. The aim is to apply the patch to these parts to increase their stuffiness, improve NVH for higher-end models, and explore the possibility of downgauging standard parts where economically viable weight reduction is possible. The following sections of this study present the coils developed, coating approach, planned experimental testing and numerical simulation strategy.

Figure 5 The proposed metallic chassis components by Gestamp that will be strengthened with thermoplastic composite patches using PCM joining method.

4.1 Work coils

One of the advantages of thermoplastic over thermoset composites is that they can be melted and reshaped. Hence, they can be joined by welding, also known as fusion bonding. In induction welding, a conducting work coil is used. In this technique, a work coil connected to a high-frequency power supply is placed in close proximity to the joint. As high-frequency electric current passes through the coil, a dynamic magnetic field is generated whose flux couples with the conductive components of the part. Consequently, an electric current is induced, thus heating up the conducting material, which leads to melting of the surrounding thermoplastic. Pressure applied to the joint helps ensure that molten thermoplastic forms a strong bond [15]. In this study, several coils will be used, the first coil used is a pancake coil which mirrors the size of the joint sample. This coil was used to conduct an initial lab-scale joining demonstration, see *Figure 6*.

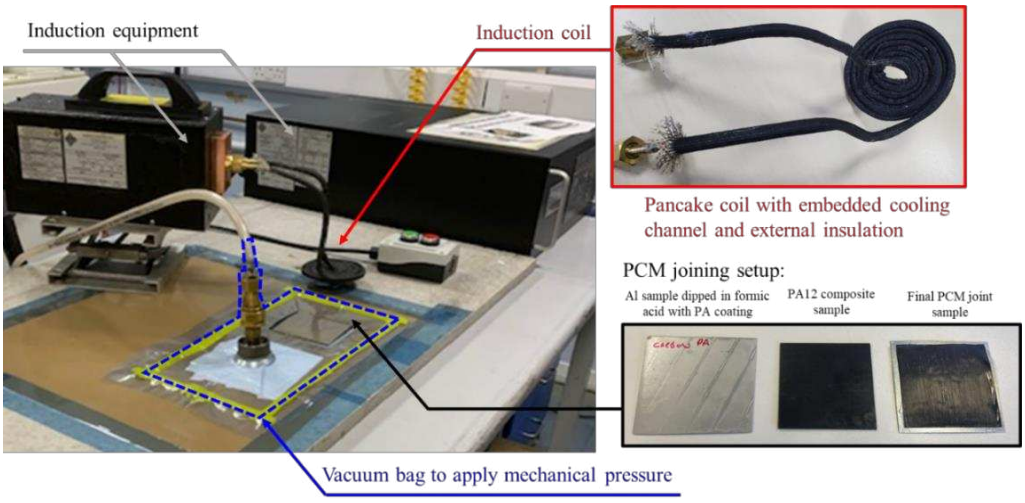

Figure 6 Lab-scale demonstration of dissimilar joining of thermoplastic-metal using PCM technology for BRACE project at TWI Ltd.

A second coil is designed to be used for the single-lap shear (SLS) test coupon samples, see Figure 7. The PCM technology will be first applied on SLS coupons to optimise the process. Then further SLS testing will be conducted to obtain mechanical property parameters, which can be used as input into the finite element analysis (FEA). A third work coil will be designed later in the project

  doi:10.5075/epfl-298799_978-2-9701614-0-0

suitable for the optimised shape composite patch used for chassis parts; the movement of the coil will be automated and integrated within the production line.

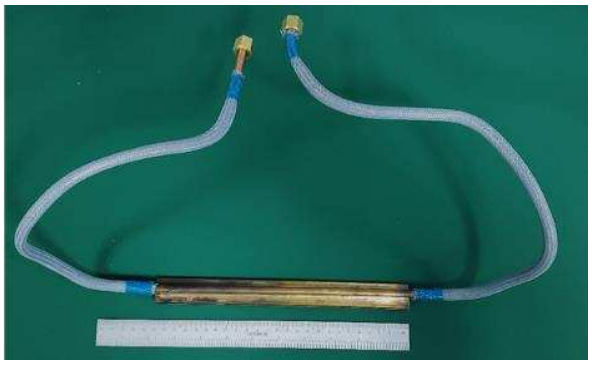

Figure 7 Work coil designed by TWI Ltd to be used in the SLS coupon manufacture using PCM technology.

4.2 Coating process

The metal surface is activated prior to the polymer coating. The surfaces are either grit blasted or mechanical braised and are solvent wiped to remove any contamination. Post deoxidisation of the metal surface is treated with an automotive standard surface Pre-Treatment primer. Once the primer sets in, the surface of the metal is now ready to be coated. The surface can be sprayed or dip-coated with the polymer solution to get a uniformly coated polymer thickness throughout. The final coating method will be aligned with the manufacturing process of the chassis component to ensure maintaining a high production rate.

4.3 Experimental and Numerical Modelling

To design the required patch for the selected automotive parts, there is a need to obtain the mechanical properties of the joint. Hence, in the experimental stage of the study, the SLS test will be completed on both PCM and adhesively bonded coupons. The results will allow characterising the bond for use in the FEA model and comparing the two joining methods. A preliminary FEA model has been generated for the SLS coupons using the commercial FEA software Abaqus. It is assumed that the PCM joint behaves similarly to those of adhesively bonded joints. Hence, a standard solid model was created based on the traction separation method and cohesive zone section property. The cohesive zone parameters will be obtained from the experimental testing of the SLS samples. This model will also be used to optimise PCM's process parameters, i.e. power, time, pressure, coil distance, and PCM coating concentration, to maximise the joint performance. The validated and optimised high-fidelity model of the dissimilar joint section will be analysed under various loading conditions to create a low-fidelity join section that can capture the joint system properties which can then be used in the upscaled case studies.

Simultaneously, a preliminary component scale analysis using was created to assess the buckling behaviour of the chosen demonstration parts with and without the thermoplastic patches. Based on assumed joint parameters, the buckling force needed for both the steel and aluminium was increased by 13.5% and 13.9% after using the thermoplastic patch, respectively as seen in Figure 8. These models will further be calibrated in future work as testing results become available.

  doi:10.5075/epfl-298799_978-2-9701614-0-0

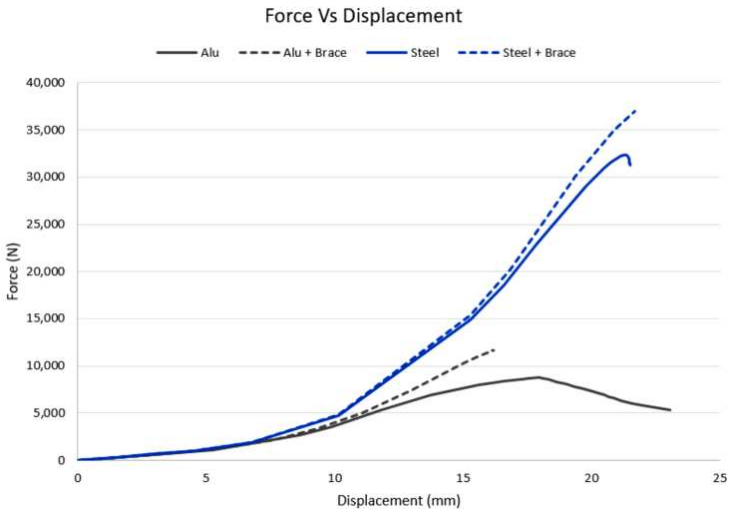

Figure 8 Preliminary simulations by Gestamp show an increase in buckling strength of the LCA after using a thermoplastic patch.

5 Conclusions

Although the cost of composites has dropped over the past decade, there are still significant challenges to effectively join these materials to conventional metal parts. Mechanical fastening and adhesive bonding are amongst the most common joining techniques. Nonetheless, both solutions present several limitations. In this study, PCM joining process is adapted for thermoplastic composite to metal assembly. This joining method uses induction welding to join a thermoplastic composite to a metallic substrate pre-coated with a compatible thermoplastic polymer film. Compared to mechanical fastening, PCM does not induce stress concentrations in the parts, and as the materials are not pierced, the risk of water damage is reduced. Compared to adhesives, PCM solution is not subject to curing times or shelf-life restrictions. Furthermore, the use of PCM enables easy recyclability of the parts; at the end-of-life, the parts can be disassembled through a reversal heat process.

The PCM method is used in conjunction with thermoplastic patches to strengthen automotive chassis parts. In order to assess the performance of PCM joints, experimental and numerical modelling has been utilised. SLS will be used for both PCM and adhesively bonded joints to allow a direct comparison between the two joining techniques. A preliminary FEA model has been completed to evaluate the buckling behaviour of the automotive demonstration parts with and without the thermoplastic patch. The results indicated that thermoplastic patches have led to an approximately 14% increase in the force required to buckle the parts. Further work is ongoing to complete the testing campaign and calibrate the models to optimise the patch geometry accordingly.

Acknowledgements

BRACE has secured funding from Innovate UK under EUREKA collaborative R&D programme 107471. The partners involved are: Gestamp Chassis (Lead partner), Far-UK, TWI Ltd and Brunel University London (participation through the Brunel Composites Centre).

References

1. McIlhagger A., Archer E. and McIlhagger R., (2020). 3 - manufacturing processes for composite materials and components for aerospace applications, pp.59-81. Available at: http://www.sciencedirect.com/science/article/pii/B9780081026793000034
2. Soutis C., (2020). 1 - aerospace engineering requirements in building with composites, pp.3-22. Available at: http://www.sciencedirect.com/science/article/pii/B9780081026793000010
3. Fuchs E.R.H., Field F.R., Roth R. and Kirchain, R.E., (2008). Strategic materials selection in the automobile body: Economic opportunities for polymer composite design, Composites Science and Technology, 68 (9),
4. Pradeep S.A., Iyer R.K., Kazan H. and Pilla S., (2017). 30 - automotive applications of plastics: Past, present, and future, In Kutz M., (Ed.) Applied Plastics Engineering Handbook (Second Edition) William Andrew Publishing, pp. 651-673. Available at: https://www.sciencedirect.com/science/article/pii/B9780323390408000316.
5. Seidlitz H., Kuke F. and Tsombanis N., Advanced joining technology for the production of highly stressable lightweight structures, with fiber-reinforced plastics and metal,
6. Carello M., Amirth N., Airale A.G., Monti M. and Romeo A., (2017). Building Block Approach' for Structural Analysis of Thermoplastic Composite Components for Automotive Applications, Applied Composite Materials, 24 (6), pp.1309-1320.
7. Hinte E. and Beukers A., (2020). Designing Lightness. Netherlands: nai010.
8. Advanced Propulsion Centre. 2022. APC Funding Drives UK Lightweighting - Advanced Propulsion Centre. [online] Available at: <https://www.apcuk.co.uk/apc-funding-drives-uk-lightweighting/> [Accessed 28 March 2022].
9. Hexcel's New Carbon Prepreg Patch Technology Selected as Finalist in JEC Innovation Awards 2019 [online]. Hexcel. 2019 [cited 28 March 2022]. Available from: https://www.hexcel.com/News/News-Releases/2729/hexcels-new-carbon-prepreg-patch-technology-selected-as-finalist-in-jec-innovat
10. More details on MAI Skelett design process [Internet]. Compositesworld. 2019 [cited 28 March 2022]. Available from: https://www.compositesworld.com/articles/more-details-on-mai-skelett-design-process
11. Cordis. 2018. *Flexible production cell for Hybrid Joining*. [online] Available at: https://cordis.europa.eu/project/id/677625 [Accessed 12 April 2022].
12. Omairey S, Jayasree N, Kazilas M. Defects and uncertainties of adhesively bonded composite joints. SN Applied Sciences. 2021;3(9).
13. Rapid Heat Popping Joints could revolutionise use of composites [online]. National Composites Centre. 2022 [cited 28 March 2022]. Available from: https://www.nccuk.com/news/rapid-heat-popping-joints-could-revolutionise-use-of-composites/
14. Wise R.J., Gosai K. Polymer Coated Material (PCM) Joining Technology for Manufacture and Repair of Dissimilar Material Structures [online]. TWI Global. 1999 [cited 28 March 2022]. Available from: https://www.twi-global.com/technical-knowledge/published-papers/polymer-coated-material-pcm-joining-technology-for-manufacture-and-repair-of-dissimilar-material-structures-march-1999
15. Worrall C.M., Wise R.J. Novel Induction Heating Technique for Joining of Carbon Fibre Composites. European Conference on Composite Materials [online]. Seville; 2014 [cited 25 March 2022]. Available from: http://www.escm.eu.org/eccm16/assets/0544.pdf

INVESTIGATION OF LIGHTWEIGHT DESIGN AND ANALYSIS OF HYBRID COMPOSITE BACKREST SEAT

Ali Ulaş Malcıoğlu, Ece Ercin, Emre Gödek, Elif Günister, Göker Mutlu, Ersan Ertürk[a], İrem Topal[b] Elçin Çakal Saraç[c]

a: Assan Hanil Otomotiv Sanayi ve Ticaret A. Ş., Kocaeli, Turkey
ulas.malcioglu@assanhanil.com.tr
b: Karel Kalıp San. A.Ş., İstanbul, Turkey
c: Kordsa Teknik Tekstil A.S., Teknopark Istanbul, 34906, Pendik, Istanbul, Turkey

Abstract: *Based upon the requirements of automotive applications for weight reduction, hybrid composites have gained wide attention as lightweight materials. The enhanced mechanical properties of hybrid composites, in which two or more reinforcing elements are integrated into the matrix, vary due to design and injection parameters. This paper deals with the lightweight design and mechanical characterization of the backrest part as a hybrid composite, instead of the traditional metal backrest on the driver's seat. Based on this, glass fiber reinforced composite material was used in accordance with the overmolding method. By carrying out the design studies for the composite backrest, it is aimed to ensure the lightness of the part compared to the existing metal part. After the design, heterogeneous distributed load paths were determined by applying virtual analysis in line with the ECE R-14 regulation. Within the scope of the analysis, various improvements were made in the related composite design by characterizing the stress, strain and displacement distributions. Accordingly, by modeling the glass fiber reinforced polypropylene raw material on prepreg material, a weight reduction of 30-40% was achieved with appropriate mechanical properties. Besides, mold flow analyzes were carried out and the effect of the process parameters was studied by characterizing the moldability of the part. In addition, the mechanical properties of the final part were determined by applying the ECE R-14 test after the prototype production, and the correlation between virtual analysis and performance test was discussed.*

Keywords: Thermoplastic composite; overmolding; lightweight; finite element analysis

1. Introduction

Global warming has become the most important challenge worldwide in recent years and it affects many sectors directly and indirectly. Especially after the Paris Agreement was signed in 2015, comprehensive efforts to tackle climate gained momentum in order to reduce the emission of greenhouse gases [1-3].

Due to increasing customer demands, the number of mass-produced vehicles is increasing. While customers expect new generation vehicles to outperform their predecessors, this leads to demand for vehicles with enhanced safety and comfort features. The goal of reducing carbon dioxide (CO_2) emissions from automobiles is in direct contradiction to the continued expansion of the automotive industry and, in the case of passenger cars, increased comfort and safety standards leading to weight gain and thus ecological impact. Therefore, a more ecological design

  doi:10.5075/epfl-298799_978-2-9701614-0-0

of vehicles is required to comply with the reduction of CO_2 emissions implemented in many countries [4-5].

Composites are widely used in many application areas due to their superior mechanical properties. The automotive and aerospace industries, which are taken into consideration as key players in the global composite market, carry out development studies for the use of composite materials. Hybrid thermoplastic composite production technology which is a method that replaces metal components used in the automotive industry, is formed by combining fiber-reinforced composites with the plastic injection method. Along with this technology; many structural parts such as battery carriers, bumper carrier systems and seat chassis parts can be produced as composite. In addition, the composite technology must meet the competitive conditions in the automotive sector and be designed to be appropriate for the mass production of parts. Hybrid thermoplastic composite part production technology by applying the overmolding method, which can meet the regulation requirements, has been shown as the most popular composite part production method in recent years [6-8]. The overmolding process is injection molding, in which one material is molded into a plastic material. Regarding overmolding; the processing conditions allow high mechanical properties with good hardness for complex parts [9]. Besides; continuous fiber added thermoplastic prepreg, which is used as a middle product in the production of thermoplastic composites by overmolding, is a material that is expected to be used more in the coming periods because they do not have any special storage conditions, is recyclable and high strength [10].

In case of material or design change, the final product must meet automotive regulations. In terms of the seat; regardless of whether the seat belt attachment points are on the body or seat, physical tests are carried out and approval is obtained for each seat/seat belt under the conditions specified in the regulation. ECE R14 regulation examines the suitability of seat belt fasteners for motor vehicles [11].

The novelty of the present study is to improve the backrest part of the driver seat as a composite by design and FEA analysis considering lightness and mechanical properties. Besides, it's aimed to meet the ECE R14 regulation after prototype production.

2. Experimental studies

Glass fiber reinforced polypropylene matrix prepreg material which was supplied from Kordsa, was used in this study. Prepreg material's technical properties are shown in Table 1.

Table 1: Technical properties of prepreg.

Type	Density	Thickness	Tensile modulus	Tensile Strength
PP	1,4-1,6 g/cm3	3-4 mm	>190 MPa	>380 MPa

40% long glass fiber reinforced polypropylene was used as raw material. In Table 2, technical properties of raw material was given.

  doi:10.5075/epfl-298799_978-2-9701614-0-0

Table 2: Technical properties of raw material.

Density	Tensile Modulus	Tensile Strength	Flexural Modulus	Flexural Strength
1,20-1,25 g/cm^3	>10000 MPa	>120 MPa	>9000 MPa	>190 MPa

The work flowchart of the study was summarized in Table 3. The following steps were conducted in order to enhance the hybrid composite design and to validate the ECE R14 seat belt test.

Table 3: Technical properties of raw material.

CAD design studies
FEA Analysis in compliance with ECE R14 regulations
Moldflow analysis
Overmolding of the prototype
ECE R14 test

Design studies were conducted by using Catia V5 program in particular with the backrest part of the driver seat. Besides, finite element analysis was accomplished by using the Hypermesh program. FEA analyzes were carried out according to the specific loads within the scope of ECE R14 regulation. Regarding the modeling studies, the size of the relevant element was determined as 5 mm, and time and model flatness were taken into account. Also, all the components in the seat structure were modeled using this method, by determining the element properties using P1_shell and QEPH24. FEA analyzes were carried out according to the ECE R14 regulation requirements and the related loads were shown in Figure 1.

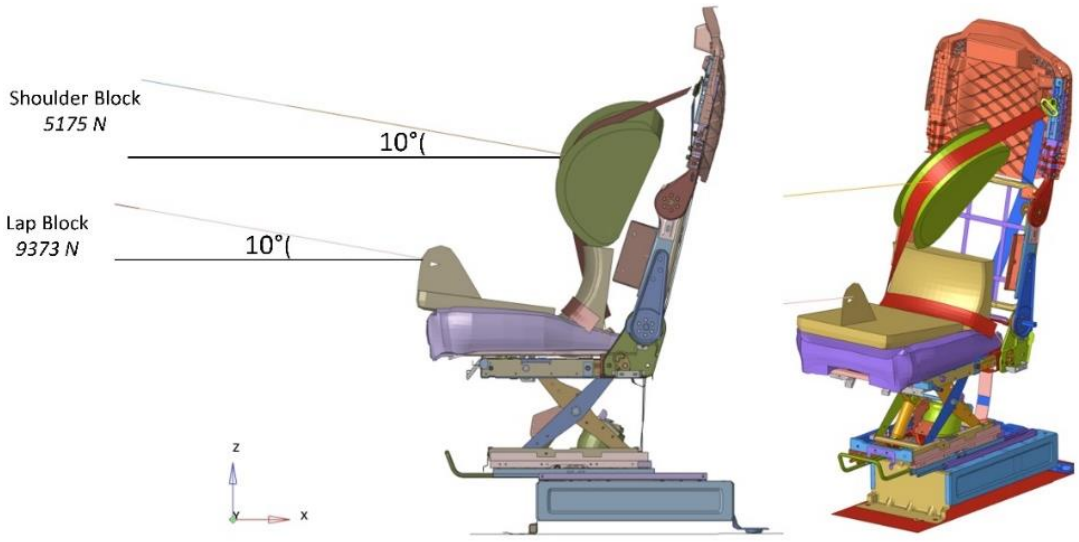

Figure 1. Applied loads according to ECE R14.

ECE R14 regulation tests were performed in Assan Hanil test laboratory in order to associate FEA analysis. The loads to be applied under the test are the same as those introduced during the FEA

analysis. The angle of the backrest frame is adjusted according to the reference position defined by the seat design. All other components should be mounted considering the reference design, by fulfilling the design torque values. The related direction of the tensile force was adjusted to make an angle of 10° with the ground plane.

In order to analyse the moldability of the developed hybrid design, the flow process of the raw material for the plastic injection molding was modelled by performing Autodesk Moldflow software. Regarding Moldflow characterization, flow analysis of the hybrid composite part was carried out.

3. Results and discussion

The current design and FEA analysis of the metal backrest are shown in Figure 2. After the ECE R14 test, it was defined that the tension affects various areas. In this direction, critical points were determined and maximum of 426 MPA stress was defined in the backrest after FEA analysis. The relevant values were taken as a reference in the design studies and the design studies were carried out in which the load was homogeneously distributed.

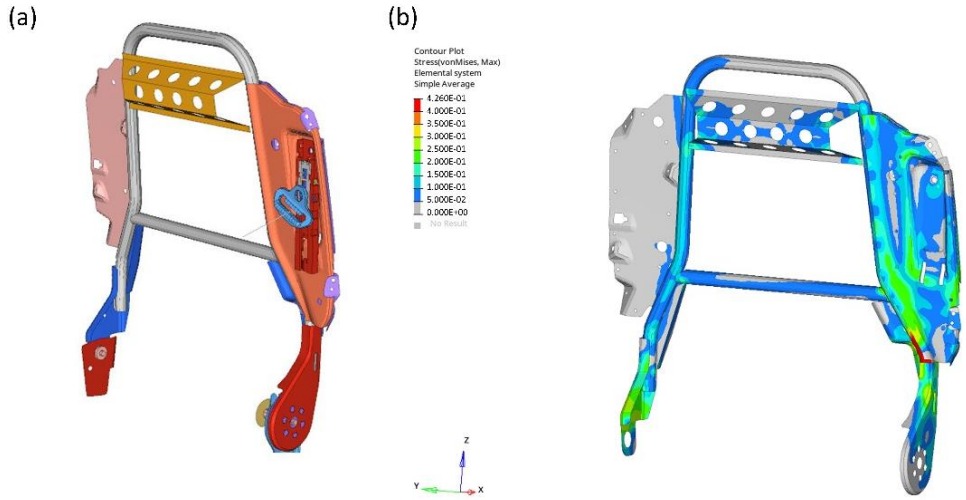

Figure 2. a) Catia model b) FEA analysis of the metal backrest.

In Figure 3, the Revision 1 composite model and the FEA analysis were represented. The prepreg material was positioned in the seat belt area in order to eliminate the high tension. While designing, weight reduction and high strength were taken as a basis and a box profile was added to the design. After the FEA analysis, it was determined that despite the box profile structure, the load could not be distributed to the desired extent and relatively higher stress (maximum 515 MPa) was obtained compared to the metal backrest design.

  doi:10.5075/epfl-298799_978-2-9701614-0-0

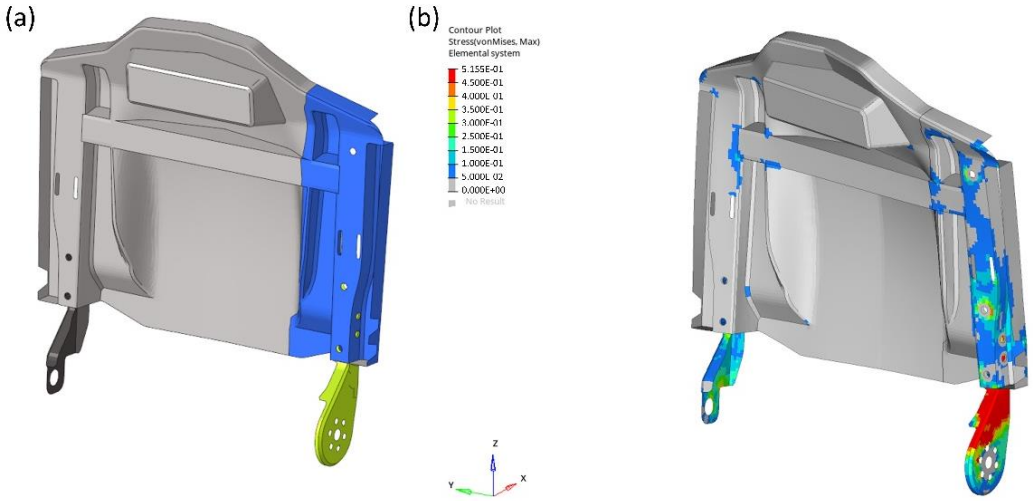

Figure 3. a) Catia model b) FEA analysis of Revision 1 composite model.

In order to increase the strength and eliminate the high tension acting after the Revision 1 model, a secondary box profile was added to the design and is shown in Figure 4 along with the FEA analysis. By increasing the box profile, it is desired to distribute the load more homogeneously in the structure and stress reduction is aimed. After analysis, despite the stress decreased, a design change occurred by the reason of ensuring the desired homogeneity in comparison with the existing design.

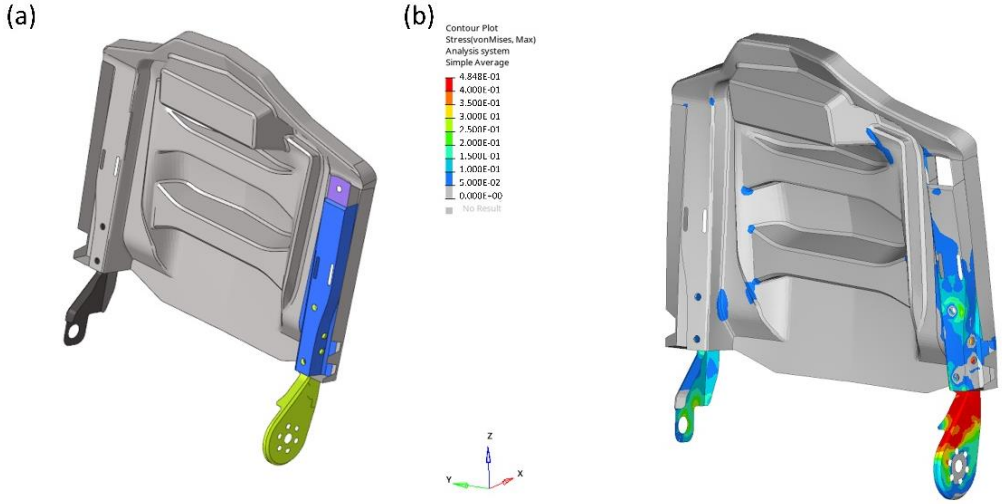

Figure 4. a) Catia model b) FEA analysis of Revision 1 composite model.

The box profile has been removed from the design since the load paths cannot be distributed to the desired extent and relatively lower stress is required when the load is applied. Revision 3 and Revision 4 models were designed by adding the feder structure and are shown in Figure 5 and Figure 6, respectively. In this direction, it is aimed to distribute the load to the entire backrest by adding a one-way rib at Revision 3. Besides, it is desired to compromise the weight at the least amount by using one-way rib instead of two-way. After the analysis, it was determined that the strength of the structure increased as against the box profile. However; although the maximum tension ratio was at a similar level towards the current design since it was aimed to provide better strength than the existing material, a bidirectional rib was added to the design with Revision 4. In addition, considering the adaptation of the realized design to

  doi:10.5075/epfl-298799_978-2-9701614-0-0

plastic injection, a boss structure has been added to the intersection areas of the ribs in order to have a positive effect during molding.

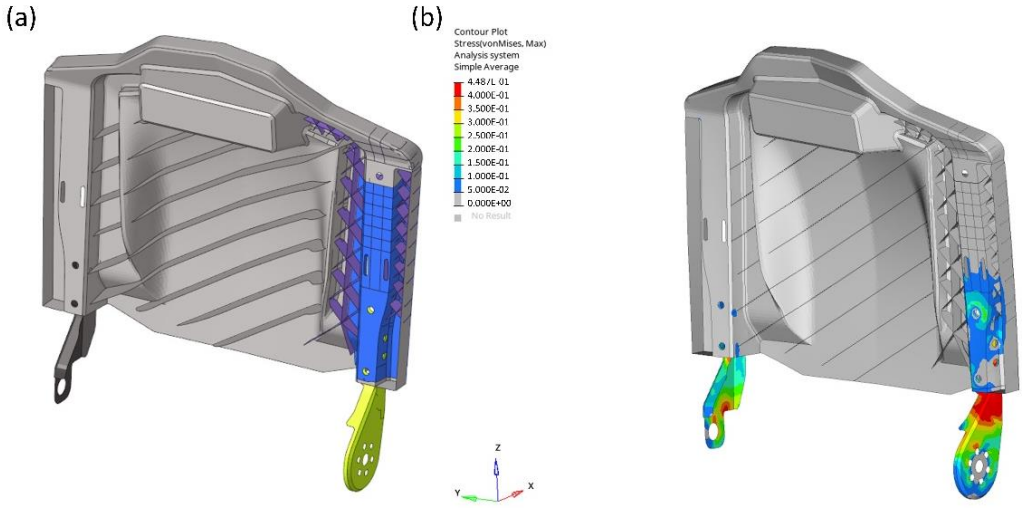

Figure 5. a) Catia model b) FEA analysis of the Revision 3 composite model.

Kim et al. [12] studied the material change in seat frame and investigated the effect of the related material optimization on the mechanical properties considering weight reduction. Based on this, the raw material alteration has revealed the significance of the design studies. Design optimization was carried out considering weight reduction and part validation was analyzed with the CAE analysis and performance tests.

Along with the developed Revision 4 design, the desired mechanical properties were achieved (maximum 422 MPa stress) and the design was frozen. During the design, the strength of the part can be increased by designing high and thick ribs. However, in the parts produced with engineering thermoplastics, related condition causes injection gaps and distortions during production. In addition, excessive rib height causes the rib to deform under the high load. For this reason, these issues were taken into consideration while designing the feder structure.

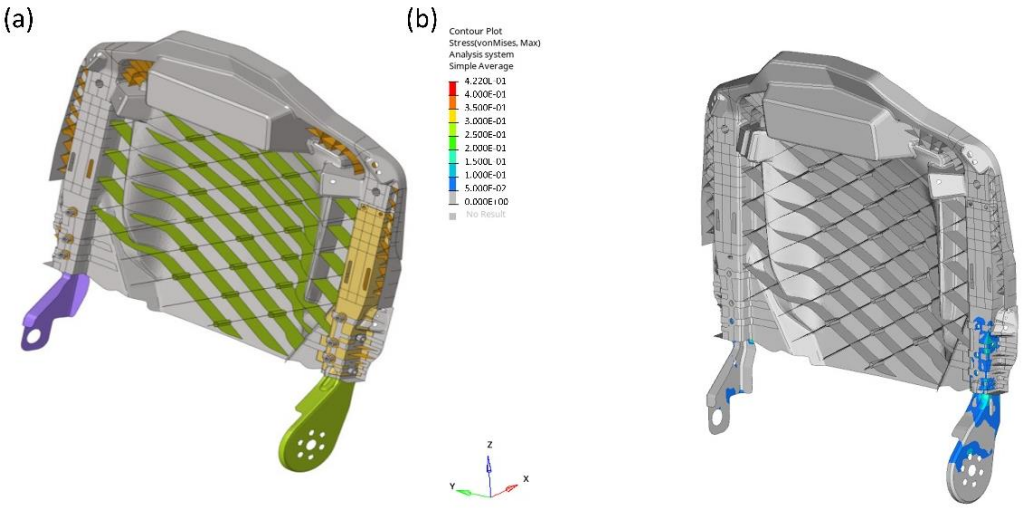

Figure 6. a) Catia model b) FEA analysis of the Revision 4 composite model.

Moldflow analyzes performed to analyze the moldability of the frozen Revision 4 design are given in Figure 7. In the related design, the in-mold filling time was simulated and determined as 2.1 seconds. According to the results of the analysis, it was defined that the in-mold pressure values were obtained before the packing (holding) pressure started (after 98-99% filling of the mold was completed). The related injection pressure was obtained as 41.3 MPa. After the injection filling was completed, the temperature of the part when it completely touched the mold surface has been analyzed as 236°C and has been qualified as appropriate in terms of moldability.

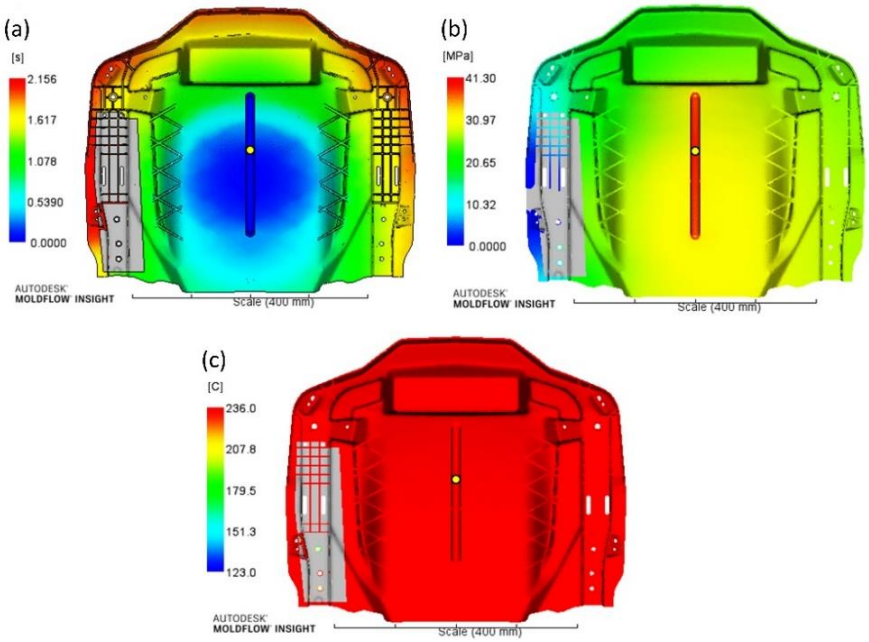

Figure 7. Mold flow analysis (a) Filling time (b) Mold pressure distribution (c) Temp. at flow front.

After the moldability approval, prototype production was carried out and the ECE R14 test was conducted for the seat frame. Figure 8 represents the images of the backrest after ECE R14 testing, along with a load graph. When the results were evaluated, correlation between FEA analysis and physical test was determined. Accordingly, the final design was able to withstand the load of the existing metal design after the applied load and there was no breakage during the test. Besides that, weight reduction of 30-40% was achieved in the developed part.

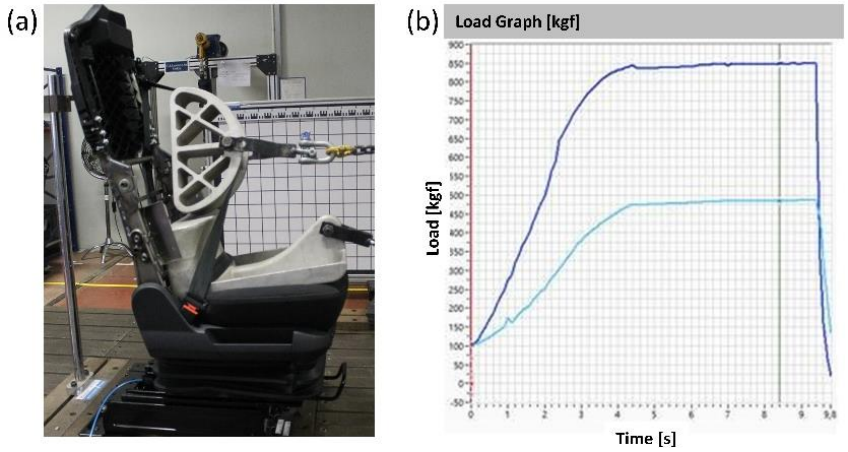

Figure 8. After ECE R-14 testing; (a) Seat image (b) Load graph.

4. Conclusions

The following conclusions can be drawn from the present study:

- Design studies were carried out considering weight reduction and mechanical properties. Various revisions were made in the design by examining the FEA analysis results, and the design was frozen with the Revision 4 design along with 30-40% weight reduction.

- The moldability of Revision 4 was examined by Moldflow analysis and it was determined that the design was appropriate for plastic injection.

- The seat frame, which was produced in order to determine FEA correlation and product validation, was subjected to ECE R14 regulation and as a result of the test, the hybrid design met the maximum load required by the regulation.

5. References

1. Schryvr A, Brakkee K, Goedkoop M, Huijbregts M. characterization factors for global warming in life cycle assessment based on damages to humans and ecosystems. Environ. Sci. Technol. 2009; 43:1689–1695.
2. Herzog T. World greenhouse gas emissions in 2005. 2009.
3. Morimoto S, Cheng Y, Mizukoshi N, Thara K. Methodological Study of Evaluating Future Lightweight Vehicle Scenarios and CO2 Reduction Based on Life Cycle Assessment. Sustainability 2020; 12:5713.
4. Nehuis F, Kleemann S, Vietor T, Herrmann C. Future Trends in the Development of Vehicle Bodies Regarding Lightweight and Cost. Innovative Design, Analysis and Development Practices in Aerospace and Automotive Engineering 2014; 13–21.
5. Danilecki K, Mrozik M, Smurawski P. Changes in the environmental profile of a popular passenger car over the last 30 years - Results of a simplified LCA study. Journal of Cleaner Production 2017; 141:208-218.
6. Ganesarajan D, Simon L, Tamrakar S, Kiziltas A, Mielewski D, Behabtu N, Lenges C. Hybrid composites with engineered polysaccharides for automotive lightweight. Composites Part C: Open Access 2022; 7.
7. Carello M, Amirth N, Airale A, Monti M, Romeo A. Building block approach' for structural analysis of thermoplastic composite components for automotive applications. Applied Composite Materials 2017; 24:1309-1320.
8. Aurrekoetxea J, Castillo G, Cortes F, Sarrionandia M, Urrutibeascoa I. Failure of multimaterial fusion bonding interface generated during over-injection molding/thermoforming hybrid process. Journal of Applied Polymer Science 2006; 261-165.
9. Akkerman R, Bouwman M, Wijskamp S. Analysis of the Thermoplastic Composite Overmolding Process: Interface Strength. Frontiers in Materials 2020; 7.
10. El-Dessouky H, Lawrence C, Ultra-lightweight carbon fibre/thermoplastic composite material using spread tow technology. Composites: Part B 2013; 50:91-97.
11. Hessenberger K. Strength analysis of seat belt anchorage according to ECE R14 and FMVSS. 4th European Ls-Dyna Users Conference. 2003.
12. Kim H. Stress analysis and design strategy for lightweight car seat frame. Key Engineering Materials 2004; 261-263:597-602.

THERMAL AND MECHANICAL INTERFACE BEHAVIOUR OF OVERMOULDED VULCANIZED THERMOPLASTIC ELASTOMERS

Pierre, Le Mouellic[a,b], Nicolas, Boyard[b], Jean-Luc, Bailleul[b], Nicolas, Lefevre[b], Thierry, Gaudry[a], Jean-Marc, Veille[a]

a: Cooper Standard, Route des Eaux, 35503 Vitré, France- pierre.le-mouellic1@etu.univ-nantes.fr
b: Nantes Université, CNRS, Laboratoire de thermique et énergie de Nantes, LTeN, UMR 6607, F-44000 Nantes, France

Abstract: *Vulcanized thermoplastic elastomers (TPV) are widely used in the automotive industry for the manufacturing of weather seals by overmoulding a TPV on an extrudate TPV. This process is assumed to be a fusion bonding in which the quality of the thermal contact is essential to develop the mechanical strength of the assembly. From a thermal point of view, the contact can be quantified by a thermal contact resistance (TCR) which consider the flux lines constriction and their lengthening. From a mechanical point of view, the contact can be qualified by Double Cantilever Beam tests through the calculation of the critical energy restitution rate. The influence of the overmoulding conditions on the contact thermal resistance value and on the critical energy restitution rate is discussed. A correlation was found between these two quantities.*

Keywords: Overmoulding; Vulcanized thermoplastic elastomers; thermal contact resistance; Double Cantilever Beam

1. Introduction

The automotive market uses vulcanized thermoplastic elastomers to produce static sealing solutions. These composite materials consist of a continuous thermoplastic phase in which an elastomeric phase is dispersed, combining the processability of conventional thermoplastics with the mechanical properties of elastomers. The thermoplastic phase is often polypropylene (PP), and the elastomer phase is ethylene-propylene-diene-monomer (EPDM). Static sealing solutions are achieved by overmoulding a melted injected TPV_{inj} onto a cold extruded TPV_{ex} runner. Weng *et al.* [1] described the TPV overmoulding process as the succession of three steps: wetting, polymer chain diffusion and crystallization. The wetting stage refers to the notion of intimate contact, referring to the evolution of the contact, initially imperfect, the consequence of the surface asperities of the extruded TPV_{ex}. The intimate contact increases as the TPV_{ex} asperities squeeze under the application of the pressure and flow of the TPV_{inj}. Once intimate contact is achieved, at the contacting zones, and for a temperature higher than the melting temperature of the TPV, the macromolecules diffuse at the interface to develop the mechanical strength of the assembly. The dynamics of macromolecules is described by the theory of De Gennes [2]: the macromolecules are confined in virtual tubes, defined by the by neighboring chains. Lateral movements are not possible, and the polymer relaxes by monodirectional movements along its tube. They renew their configuration after a characteristic time called reptation time t_{rep} (depending on the temperature and the molar mass of the polymer). The degree of healing is then written [3]:

  doi:10.5075/epfl-298799_978-2-9701614-0-0

$$D_h(t) = \left(\frac{G_c}{G_{c,\infty}}\right)^{1/2} \approx \left(\frac{1}{t_{rep}}\right)^{1/4} \quad (1)$$

Where G_c is the restitution energy rate and $G_{c,\infty}$ is the restitution energy rate of a fully healed interface. G_c is defined as the energy required to propagate a crack per unit area and can be assessed by Double Cantilever Beam (DCB) tests. The latter is based on linear elastic fracture mechanics and measures the loss of stored elastic energy when a crack propagates. The calculation is based on the Irwin-Kies equation [4].

From a thermal point of view, the real contact surface between the extruded TPV_{ex} and the injected TPV_{inj} forms a heterogeneous zone, where the heat transfer are multidirectional. The heat fluxes then cross the interface by two distinct paths. The first one is composed of the contact points generating the constriction of the flux tubes [5]. The second one is related to the heat flux through the interstitial medium. The latter is composed of a entrapped fluid, whose volume evolves with the shrinkage of the polymer. Considering both contributions, the global thermal contact resistance (TCR) is defined as:

$$TCR = \frac{T_{inj,s} - T_{ex,s}}{\varphi} \quad (2)$$

Where $T_{inj,s}$ and $T_{ex,s}$ are the surface temperatures of each TPV and φ is the heat flux density crossing the interface. Levy *et al.* [6] established an analytical relationship between the degree of intimate contact (the ratio of the actual contact area to the total contact area) and the TCR for an interface between two composites. The authors showed that the TCR is related to the actual contact area defined by the geometric surface parameters as well as the conductivity of the interstitial gas at the polymer/mould interface. A decrease of the TCR was shown while increasing the degree of intimate contact. The main difficulty in the TCR calculation lies in the determination of the polymer surface temperature due to the intrusiveness of the sensors. For this reason, inverse methods have been used to calculate the mould temperature and the heat flux through the polymer/mould interface [7].

This document presents the first experimental study establishing a relationship between a thermal approach and a mechanical approach to quantify the contact at a TPV/TPV interface. An experimental mould was thus developed allowing two types of measurements. In its first configuration, the mould allows for calculating the surface temperatures as well as the heat fluxes exchanged at the TPV/TPV interfaces, thus allowing to calculate the thermal contact resistance using the equation 2. The second configuration of the mould allows the fabrication of DCB specimens, under the same moulding conditions as those used for the TCR measurement. The objective is then to establish a correlation between the TCR and the Gc.

2. Experimental methods

2.1 Materials

The materials used in the present study are two polypropylene ethylene propylene diene monomer (PP-EPDM) based vulcanized thermoplastic elastomers (TPV), called TPV_{inj} and TPV_{ex}. TPV_{inj} is an injection moulding grade and TPV_{ex} is an extrusion grade. Because the TPV are soft materials, a 50% glass-fiber reinforced polypropylene was used to ensure elastic deformation of

  doi:10.5075/epfl-298799_978-2-9701614-0-0

the beams during the DCB test. The mechanical properties determined at an appropriate deformation rate in tensile plane stress for the TPV and with a three-point bending test for the PPGF are presented in Table 1. The two TPV are injected in a 40CMD8 steel mould. The specific heat of each TPV was determined by DSC, their conductivity using a home-made guarded hot plate and the specific volume using a home-made PVT device. The thermophysical properties are considered constant in the present study and are presented in Table 1.

Table 1: Mechanical and thermal properties.

Material	Elastic modulus E [MPa]	Yield Stress σ_y [MPa]	λ [W/(m.K)]	C_p [J/(m.K)]	ρ [kg/m^3]
TPV_{inj}	25.5	2.4	0.2	2804	911
TPV_{ex}	16.9	1.2	0.2	2525	970
PPGF	11000	191	-	-	-
Mould 40CMD8		-	36	475	7850

2.2 Experimental mould

The overmoulding developed device has a dual purpose. The first configuration uses heat flux sensors to calculate the surface temperatures and heat flux densities of both TPV, to calculate, in a non-intrusive way, the TCR at their interface. The second configuration consists in moulding Double Cantillever Beam (DCB) specimens, to measure the mechanical strength of the TPV assembly.

2.2.1 TCR measurement methodology and calculation

The first step of the mould development consisted in defining a geometry ensuring unidirectional heat transfer at the TPV_{inj}/TPV_{ex} interface. The validation of the unidirectional heat transfers was performed by comparing two configurations. The first one is a three-dimensional scheme where boundary condition involving TCR was applied over the entire surface in contact with the mould. The second is a unidirectional scheme where the same boundary condition was applied on the upper and lower parts of the overlap area but with an adiabatic condition on the side faces. Temperature simulations for both configurations were performed along a vertical profile in the center of the overlap zone. Unidirectional heat transfer were validated in the center of the overlap area of (50x50) mm² for a maximum duration of 50s.

The overmoulding process consists of two steps. The first step is shown in Figure 1(a) and consists of moulding the TPV_{ex} insert. A metal insert with a known surface roughness is fixed in the fixed part. Three K-type thermocouples (T_{ex1}, T_{ex2} and T_{ex3}) are stretched into the moving part. The TPV_{ex} is then injected. After cooling, the metal insert with the roughness is removed from the fixed part and the produced TPV_{ex} insert is placed in it. Three other thermocouples, T_{inj1}, T_{inj2} and T_{inj3}, are then stretched into the moving part. This is followed by the injection of the TPV_{inj}, as shown in Figure 1 (b). During the whole overmoulding cycle, temperature levels are recorded in both TPVs using thermocouples, which then serve as heat flux sensors. Pressure levels and temperatures in the heat flux sensor placed in the mould cavity are also recorded.

  doi:10.5075/epfl-298799_978-2-9701614-0-0

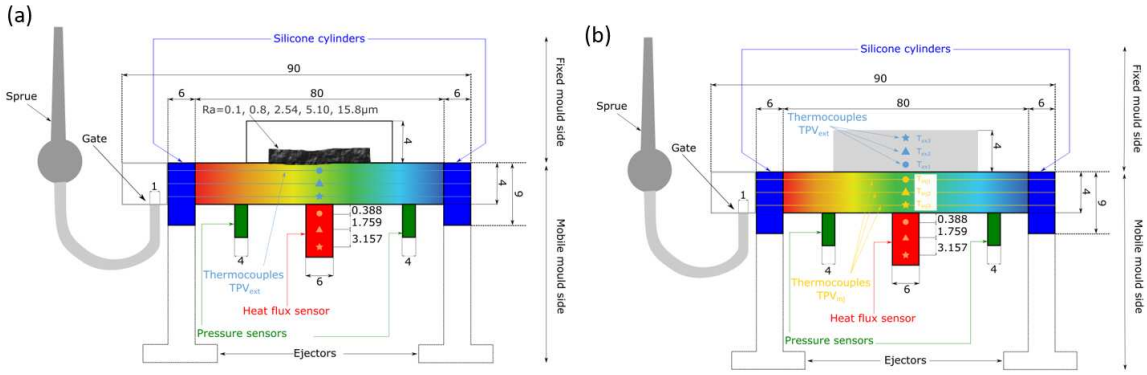

Figure 1: Developed mould in TCR configuration. (a) Injection of the instrumented TPV_{ex} insert with controlled roughness. (b) Injection of the instrumented TPV_{inj} on the TPV_{ex} insert.

During the overmoulding of the TPV_{inj} on the TPV_{ex}, the temperature fields are measured by the thermocouples T_{inj1}, T_{inj2} and T_{inj3} in the TPV_{inj} and T_{ex1}, T_{ex2} and T_{ex3} in the TPV_{ex}, and are presented in Figure 2(a).

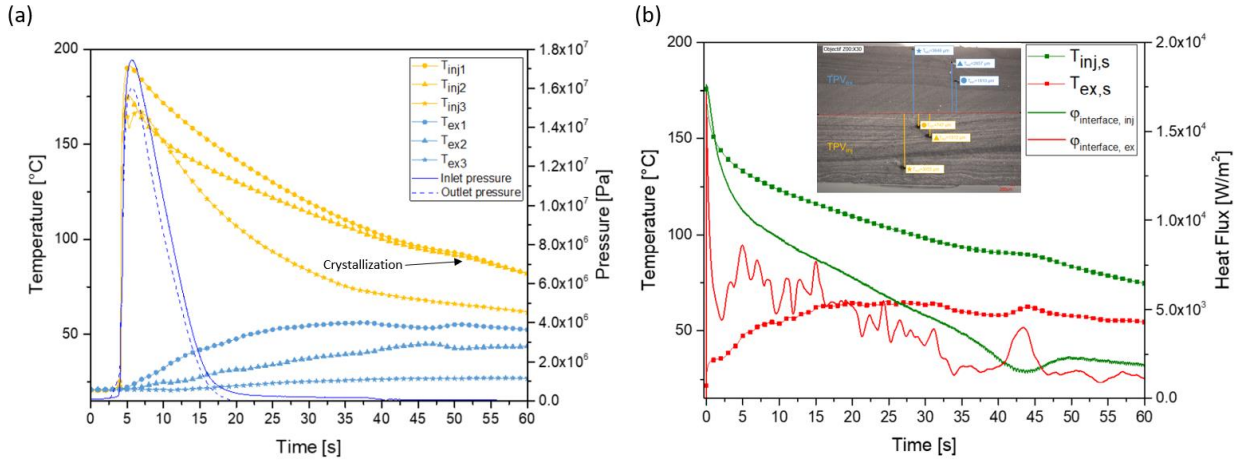

Figure 2: (a) Temperatures recorded in the TPV_{inj} and in the TPV_{ex} and pressure during overmoulding. (b)Surface temperatures for TPV_{inj} and TPV_{ex} and heat flux between TPV_{inj} and TPV_{ex}, calculated from the positions of the thermocouples.

The calculation of heat fluxes and surface temperatures at the two TPV interfaces was performed using Beck's inverse sequential algorithm [8]. The positions of the thermocouples in each of the TPVs are inputs for the algorithm and was obtained by optical microscopy (Keyence VHX-700F). The calculated surface temperatures and heat fluxes are shown in Figure 2 (b). Before injection, the TPV_{ex} is at the temperature of the mould. At t=3.8s, the thermal shock resulting from the encounter of the TPV_{inj} with the TPV_{ex} induces an increase in the temperature of the insert until it reaches a maximum of about 56°C at t=37s. The cooling phase follows the filling phase. As the TPV_{inj} cools, an inflection is observed on the cooling profile at about t=40s. This corresponds to the release of the latent heat of crystallization [9]. The surface temperature of the TPV_{inj} never reaches the surface temperature of the TPV_{ex}. This is the consequence of the imperfect contact between the TPV_{inj} and the TPV_{ex}, quantified by the thermal contact resistance, which can then be calculated during the whole overmoulding cycle by the equation 3.

2.2.2 Gc measurement methodology and calculation

The mechanical strength of TPV_{inj}/TPV_{ex} assemblies was studied by Double Cantillever Beam (DCB) tests. The DCB test is based on linear elastic mechanics. Also, since TPV_{inj} and TPV_{ex} are soft materials, 50% glass-fiber filled PPGF plates (Thermofil HPF911X99), with dimensions (50x80x3)mm^3, was used to stiffen each beam. The PPGF plate was placed in the cavity on the mobile side, and the TPV_{ex} is overmoulded (Figure 3 (a)). Following this step, a second PPGF plate was placed in the cavity on the mobile side, and the plate composed of $PPGF/TPV_{ex}$ was placed in the fixed side of the mould. TPV_{inj} is then overmoulded, as shown in Figure 3 (b). An aluminum foil (thickness 0.04mm) was previously glued on the $PPGF/TPV_{ex}$ composite plate, to ensure a non-welded area of approximatively 30mm length. The resulting specimen is then water jet cut into 5 specimens of 10 mm width (Figure 4 (a)). The measurements are carried out on the two central specimens, at the location of the heat flux sensors used in the TCR configuration.

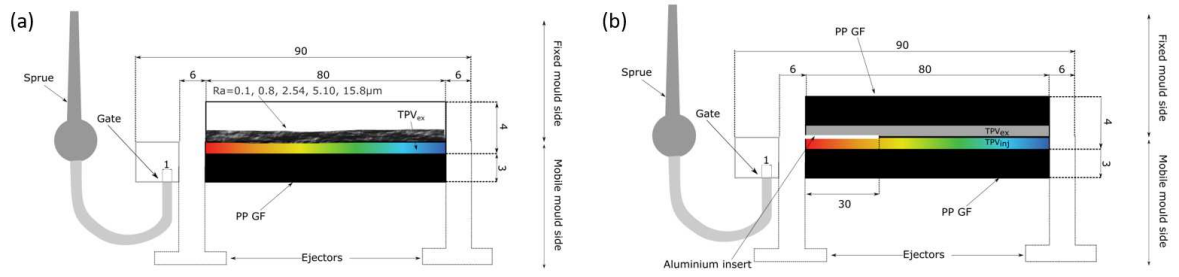

Figure 3: Developed mould in DCB configuration. (a) Injection of the TPV_{ex} on the PPGF. (b) Injection of the TPV_{inj} on the TPV_{ex} /PPGF insert.

The overmoulded specimens were mounted on a 100kN Zwick Roell tensile machine, and homemade jaws were used to fix them to the machine (Figure 4 (b)). The tests were performed at a crosshead speed of 1 mm/min, which corresponds to a quasi-static loading condition. The samples, with a crack length a_0, were loaded once, unloaded at 25mm/min and reloaded with a crack a_1. The initial crack length a_1 was measured before the second loading under a microscope (Keyence VHX-700F). During the test, the force and displacement were recorded continuously. Since TPVs are much softer than PPGF, it was necessary to adapt the geometry of the DCB test mainly used in literature to test adhesion between rigid materials. For each beam, the elastic deformation is provided by the PPGF, making the calculation of G_c relatively straightfowards. However, the resistance to crack propagation G_c is the one of the TPV_{inj}/TPV_{ex} interface. The calculation of the bond energy from the geometric and mechanical properties of the two beams

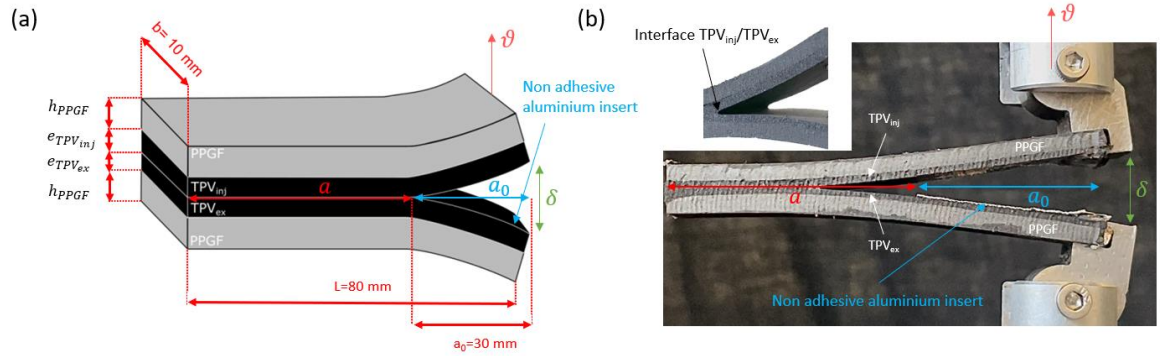

Figure 4: DCB setup. (a) schematic view of the samples geometry. (b)DCB sample under test.

was performed by adapting the Kanninen elastic foundation approach [10] to a sandwich geometry. The calculation of the elastic foundation is based on the adaptation of the Penado

model [11] proposed by Kalb [12]. The restitution energy rate was evaluated with the following expressions:

$$G_c = \frac{3P\delta}{ba} - \frac{6P^2a}{b}\left(\frac{E_{eq,inj}(h_{inj}+e_{inj})^3\beta_{ex}+E_{eq,ex}(h_{ex}+e_{ex})^3\beta_{inj}}{E_{eq,inj}(h_{inj}+e_{inj})^3E_{eq,ex}(h_{ex}+e_{ex})^3}\right) \quad (3)$$

With

$$\beta_i = \frac{1}{\lambda_i} + \frac{2}{a\lambda_i} + \frac{3}{2a^2\lambda_i^3} \quad (4)$$

And

$$\lambda = \sqrt[4]{\frac{6}{h^4} + \frac{8E_{TPV}}{E_{PP}h^3e}} \quad (5)$$

3. Procedure validation

3.1 RTC and Gc validation

Validation of the thermal resistance measurement at the TPV_{inj}/TPV_{ex} interface was carried out by repeating the following moulding condition: T_{TPVinj}=230°C, Ra=5.10µm and T_{mould}=20°C. Figure 5 (a), presents the average TCR value (black line) obtained and temperature deviations from the mean of all measurements. The temperature deviations from the mean TCR plotted are relatively small, reaching 0.0035°C to its maximum. This experiment thus validates the repeatability of the measurement of the TCR, which makes it possible to study the influence of the overmoulding conditions on its value. Since our DCB test does not use video crack tracking, the energy restitution rate G_c is calculated at the crack initiation point, which corresponds to the end of linearity during loading. At this point, the crack length is known and is a_1. To confirm if the G_c value is representative of the sample, incremental tests were performed. They consist in loading the sample for a given crack length, then unloading it as soon as the crack has propagated, which corresponds experimentally to a drop in force. As soon as the crack has propagated from its initial length to its new position, the sample is unloaded at 25mm/min, and the new crack position is measured under a microscope. The sample is then reloaded at 1mm/min and the Gc value for each crack length is calculated. The evolution of Gc as a function of crack length is plotted in Figure 5(b) for an injection temperature of 230°C and a mould temperature of 20°C. The DCB test gives a repeatability of about 20% on the Gc measurement. The measurements obtained by the incremental tests are contained within this margin of error for the different crack lengths.

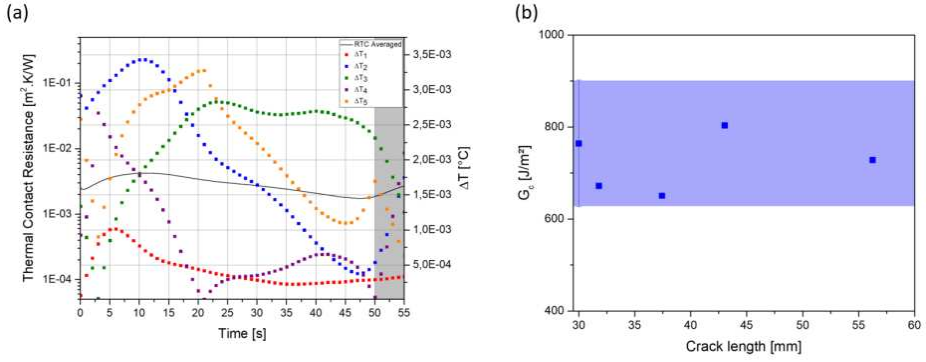

Figure 5: Validation of the tests. (a) TCR. (b) DCB.

4. Results and discussion

The developed mould allowed to quantify separately the contact quality from a thermal point of view, through the TCR, and from a mechanical point of view through DCB tests. The relationship between these two quantities can then be investigated. In the following, the value of TCR is taken at the end of the identified 1D regime, i.e. at t=50s. Figure 6 (a) presents the value of Gc as a function of the TCR for a mould temperature fixed at 20°C, and different injection temperatures for the TPV_{inj}. The energy restitution rate and contact thermal resistance are plotted as a function of the contact temperature, calculated under the assumption of perfect contact from the effusivities of the two TPV in Figure 6 (b). From Figure 6 (a), we can note that a low injection temperature does not favour the development of mechanical strength (Gc≈100 J/m²) nor the heat transfer at TPV interface (TCR≈0.02m².K/W), contrary to high injection temperature, leading to a high mechanical strength (Gc≈2100J/m²) and improved heat transfer (TRC=3.10^{-4}m².K/W). From Figure 6 (b), we can note that increasing the contact temperature results in a decrease in TCR and an increase in Gc, we find here the same trend as for Figure 6(a). Overall, the improvement in mechanical strength and heat transfer with increasing temperature can be explained by the fact that the increase in contact temperature implies a lower viscosity of the TPV_{inj}, allowing the decrease of the air gap formed at the TPV_{inj}/TPV_{ex} interface. In the same way, the increase of the contact temperature allows a decrease of the relaxation time of the chains, allowing an increase of polymer chain diffusion. A plateau is obtained for Gc and TCR for contact temperatures above 150°C. This temperature corresponds to the melting temperature of TPV_{ex}. It is also important to note that in Figure 6(b), the increase of the injection temperature has a greater impact on the mechanical strength than the increase of the mould temperature. Indeed, for a contact temperature of 140°C, the mechanical strength is higher (Gc≈1800 J/m²) for an injection temperature of 260°C and a mould temperature of 20°C, than for an injection temperature of 230°C and a mould at 50°C (Gc≈1000 J/m²).

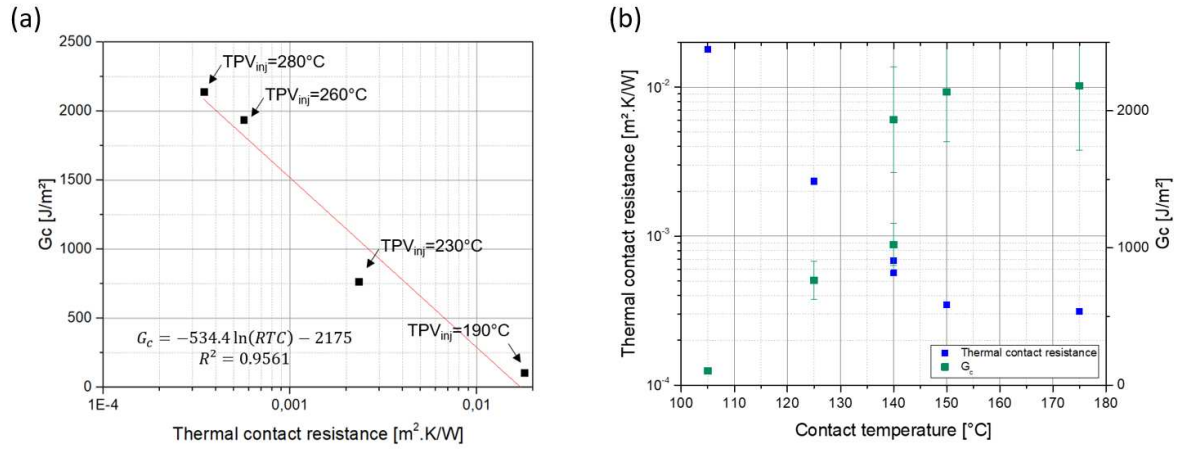

Figure 6: (a) Gc as a function of RTC. (b)Gc and TCR as a function of contact temperature.

4. Conclusion

This paper presents the first experimental study quantifying adhesion from a thermal and mechanical point of view during TPV overmoulding. For this purpose, an original experimental device has been developed to perform thermal and mechanical measurements. This instrumented experimental device allowed to calculate indirectly the surface temperatures and the heat flux densities during the overmoulding, leading to the calculation of the thermal contact

  doi:10.5075/epfl-298799_978-2-9701614-0-0

resistance at the TPV/TPV interface. The device also allowed the fabrication of DCB samples, allowing the mechanical quantification of the adhesion. A relationship between thermal and mechanical measurements was then highlighted. It was shown that the injection temperature during overmoulding was the most influential parameter, allowing to improve the quality of the thermal and mechanical contact.

Acknowledgements

The authors thank Cooper Standard Automotive for financial support.

1. References

1. Weng, D., Andries, J., Morin, P., Saunders, K., & Politis, J. (2000). Fundamentals and material development for thermoplastic elastomer (TPE) overmolding. *Journal of injection molding technology*, *4*(1), 22.Sims FA. Applications of resins in bridge and structural engineering. International Journal of Cement Composites and Lightweight Concrete 1985; 7:225-32.
2. De Gennes, P. G., & Leger, L. (1982). Dynamics of entangled polymer chains. *Annual Review of Physical Chemistry*, *33*(1), 49-61.
3. Yang, F., & Pitchumani, R. (2002). Healing of thermoplastic polymers at an interface under nonisothermal conditions. *Macromolecules*, *35*(8), 3213-3224.
4. Irwin, G. R., & Kies, J. A. (1997). Critical energy rate analysis of fracture strength. *Spie Milestone series MS*, *137*(136-141), 29.
5. Loulou, T., & Bardon, J. P. (1997). Premiers instants du refroidissement d'une goutte métallique après son impact sur une paroi. *Revue générale de thermique*, *36*(9), 682-689.
6. Levy, A., Heider, D., Tierney, J., & Gillespie, J. W. (2014). Inter-layer thermal contact resistance evolution with the degree of intimate contact in the processing of thermoplastic composite laminates. *Journal of Composite Materials*, *48*(4), 491-503.
7. Bendada, A., Derdouri, A., Lamontagne, M., & Simard, Y. (2004). Analysis of thermal contact resistance between polymer and mold in injection molding. *Applied thermal engineering*, *24*(14-15), 2029-2040.
8. Beck, J. V., Blackwell, B., & Clair Jr, C. R. S. (1985). *Inverse heat conduction: Ill-posed problems*. James Beck.
9. Delaunay, D., Le Bot, P., Fulchiron, R., Luye, J. F., & Regnier, G. (2000). Nature of contact between polymer and mold in injection molding. Part I: Influence of a non-perfect thermal contact. *Polymer Engineering & Science*, *40*(7), 1682-1691.
10. Kanninen, M. F. (1973). An augmented double cantilever beam model for studying crack propagation and arrest. *International Journal of fracture*, *9*(1), 83-92.
11. Penado, F. E. (1993). A closed form solution for the energy release rate of the double cantilever beam specimen with an adhesive layer. *Journal of composite materials*, *27*(4), 383-407.
12. Kalb, F. (1998). *Adhésion, microstructure et microdéformations à l'interface de polymères semi-cristallins* (Doctoral dissertation, Paris 6).

  doi:10.5075/epfl-298799_978-2-9701614-0-0

COMPOSITE SPRING CAPABLE OF SELF-ENERGY HARVESTING BASED ON TRIBOELECTRICITY FOR EXO-ROBOTS

Hyunsoo Hong[a], Seong Su Kim[b]

a: Korea Advanced Institute of Science and Technology – flud159@kaist.ac.kr

b: Korea Advanced Institute of Science and Technology – seongsukim@kaist.ac.kr

Abstract: *Exoskeleton robots, which are wearable robots that support human movement, have been developed to improve the performance of the human body. In this study, a self-energy harvesting composite structure was fabricated and applied to a lower limb exoskeleton robot as an ankle spring. The sandwich-type self-energy harvesting composite structure is composed of carbon fiber reinforced epoxy conductive skin and aluminum & polytetrafluoroethylene (PTFE) triboelectric core. The two triboelectric cores contact each other as the composite spring deforms by the external load, which drives the flow of electrons. Output voltages of the self-energy harvesting structure according to various frequencies were analyzed using a vibration shaker. Furthermore, self-energy harvesting composite springs were fabricated and mounted on the lower limb exoskeleton robot as ankle springs. Based on the running tests, it was confirmed that the self-energy harvesting composite springs of the lower limb exoskeleton robot could successfully harvest the electrical energy while storing and releasing elastic energy for assisting human movement.*

Keywords: Self-energy harvesting, Composite spring, Multifunctional composite, Triboelectricity, Exoskeleton robot

1. Introduction

Wearable devices have been developed in various fields such as smart-watches, exoskeleton robots, and virtual reality devices for the purpose of checking a person's health status in real-time or assisting human movement [1-3]. As a power source for a wearable device, secondary batteries which have excellent portability are mainly used. However, as wearable devices become smaller in size and higher in performance, the batteries have limitations in terms of usage time. Therefore, in order to overcome these limitations, self-energy harvesting structures that produce electrical energy for wearable devices from human movement have been actively developed.

An exoskeleton robot is a wearable robot to assist the human movement, and has been receiving many attentions in a variety of fields such as rehabilitation, military, industrial, and leisure fields [3-5]. In particular, lower limb exoskeleton robots have been researched and developed for the purpose of improving human running performance [5, 6]. Human's running performance can be further improved by assisting the muscle-tendon, which stores and releases elastic energy by

  doi:10.5075/epfl-298799_978-2-9701614-0-0

contracting and relaxing. Thus, several studies tried to improve human running performance by mounting ankle springs to lower limb exoskeleton robots [7-9].

The ankle spring of the lower limb exoskeleton robot undergoes a certain deformation according to the human running while storing and releasing elastic energy. If electrical energy is harvested from the certain deformation of the ankle spring caused by human running, the harvested energy can be used to increase the overall system efficiency of the robot. Therefore, in this study, a carbon fiber-reinforced composite spring was fabricated in order to improve the robot's system efficiency by storing and releasing the elastic energy for assisting in running while performing self-energy harvesting based on triboelectricity (Figure 1).

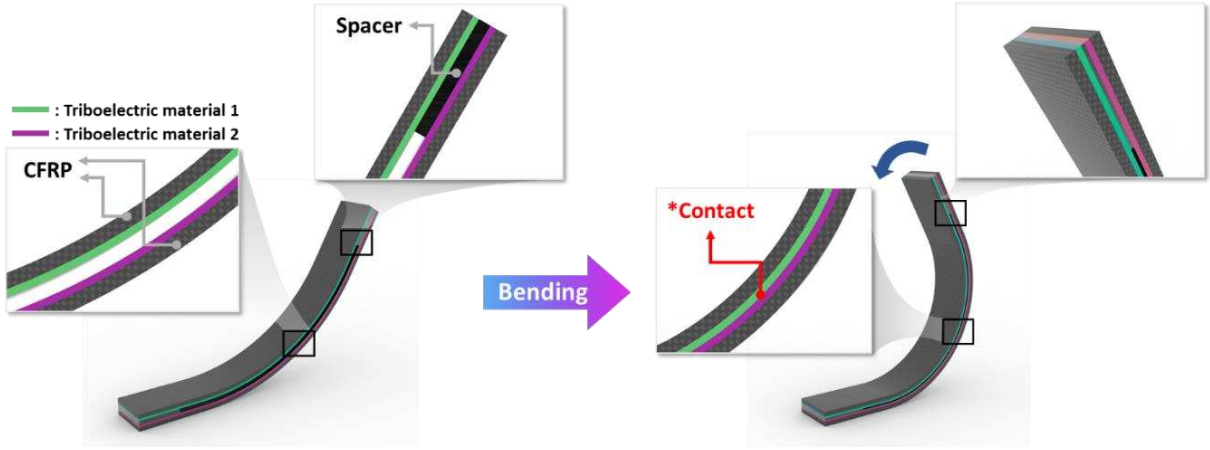

Figure 1. Schematic of self-energy harvesting composite spring

2. Experiments

2.1 Fabrication of the self-energy harvesting composite spring

Figure 2 shows the fabrication process of the self-energy harvesting composite spring. First of all, carbon fiber reinforced epoxy prepregs (USN150, SK Chemicals, Korea) were cut into a certain size and laminated on a curved mold. The curved shape composite laminates were cured by using the vacuum bag molding in an autoclave under the manufacturer recommended cure cycle. Two different triboelectric materials (Aluminum and *polytetrafluoroethylene (PTFE)*) was attached to the fabricated carbon fiber-reinforced plastic (CFRP) structures. Finally, by assembling with placing the spacers between the two CFRP composites, a sandwich-type self-energy harvesting composite spring with a space between the opposing triboelectric materials was fabricated.

  doi:10.5075/epfl-298799_978-2-9701614-0-0

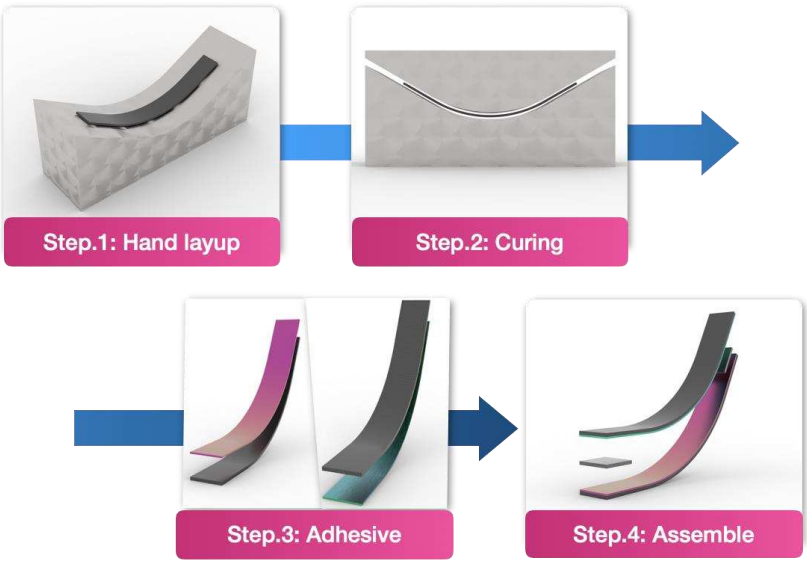

Figure 2. Fabrication process of the self-energy harvesting composite spring

2.2 Vibration tests with the self- energy harvesting composite specimen

Vibration tests were performed using a vibration shaker (DYN-PM-20, DynaLabs, USA) to analyze voltage outputs of the self-energy harvesting composite structure. As shown in Figure 3, voltage outs were measured by a data acquisition board (NI 9201, National Instruments, USA) while applying vibrations of several frequencies (10, 13, and 15 Hz) to the self-energy harvesting composite specimen by the vibration shaker.

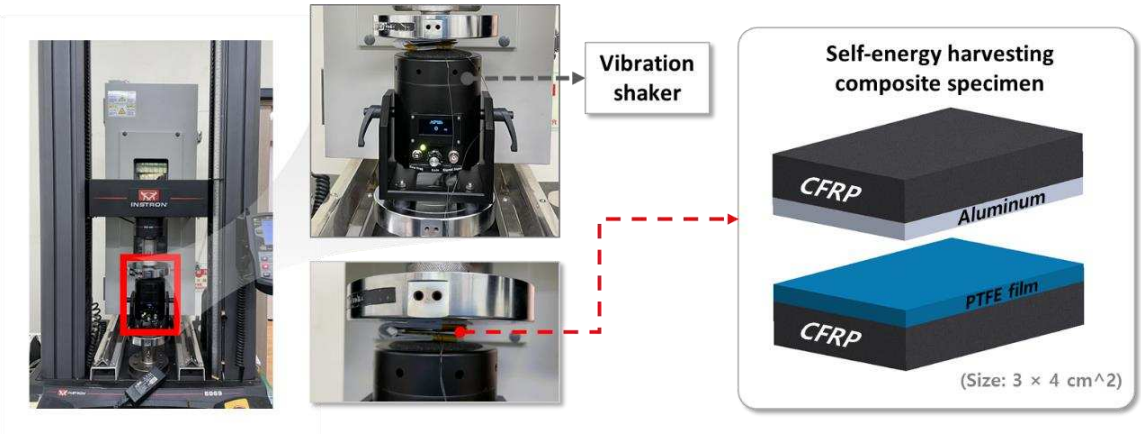

Figure 3. Vibration tests of the self-energy harvesting composite specimen

2.3 Self-energy harvesting composite springs for the lower limb exoskeleton robot

Self-energy harvesting composite springs were mounted to the lower limb exoskeleton robot as ankle springs. Voltage outputs of the self-energy harvesting composite spring while walking and jumping were analyzed. In the same manner as the previous experiment, voltage outs were measured by a data acquisition board (NI 9201, National Instruments, USA)

  doi:10.5075/epfl-298799_978-2-9701614-0-0

3. Results and Discussion

Figure 4 shows the results of the vibration test with a self-sensing composite specimen using the vibration shaker. It was confirmed that self-energy harvesting was working well even when CFRPs were used as electrodes and aluminum & PTFE were used as triboelectric materials. Voltage outputs of harvested electrical energy were different depending on the frequency of vibration. The highest voltage could be harvested at the highest frequency of 15 Hz vibration. Because it is based on triboelectricity, the flow of electrons in electrodes is significantly affected by vibration frequency.

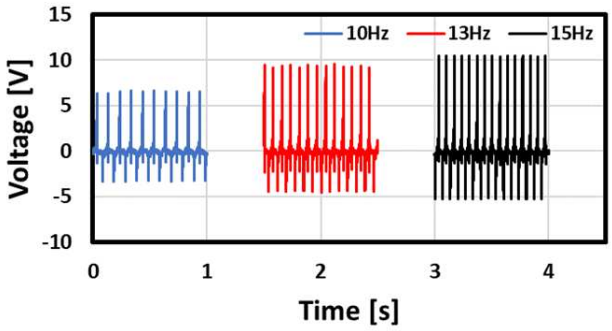

Figure 4. Voltage outputs of harvested energy from the composite specimen with various frequencies

Figure 5 are voltage output results when walking or jumping with self-energy harvesting composite springs mounted on the lower limb exoskeleton robot. As the wearer of the exoskeleton robot walked or jumped, the triboelectric materials of the self-energy harvesting composite spring come into contact with each other. At this time, electrons in electrodes moved, and electrical energy was generated based on triboelectricity. When walking, the maximum output voltage was about 5V, and when jumping, the maximum output voltage was about 10V. Therefore, by using the self-energy harvesting composite spring as the ankle spring of the lower limb exoskeleton robot, it was confirmed that electrical energy can be self-harvested while storing and releasing the elastic energy for assisting human movement.

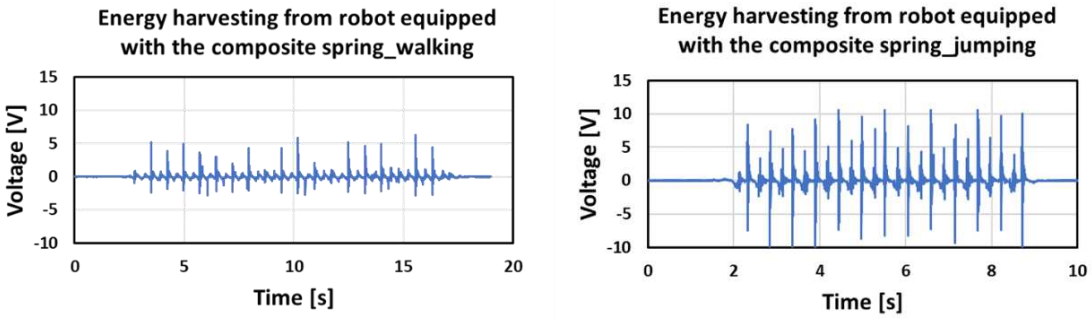

Figure 5. Voltage outputs of the self-energy harvesting composite spring mounted to the lower limb exoskeleton robot

  doi:10.5075/epfl-298799_978-2-9701614-0-0

4. Conclusions

In this study, the self-energy harvesting composite ankle spring for the lower limb exoskeleton robot was fabricated to assist the running movement by storing and releasing the elastic energy as well as to harvest the electrical energy. Based on experiments, the following results were obtained:

(1) Through vibration tests, it was confirmed that self-energy harvesting was achieved by using CFRPs as electrodes and aluminum & PTFE as triboelectric materials, and that the higher the frequency of vibration, the greater the electrical energy harvested.

(2) By fabricating the self-energy harvesting composite spring and applying it to the lower limb exoskeleton robot, self-energy harvesting was also achieved according to the human movement.

(3) The electric energy of voltage outputs of maximum 5V and 10V could be harvested through walking and jumping, respectively, and it was identified that more electrical energy can be harvested especially for fast movement because it is based on triboelectricity.

Acknowledgements

This work was supported by “Human Resources Program in Energy Technology” of the Korea Institute of Energy Technology Evaluation and Planning (KETEP), granted financial resource from the Ministry of Trade, Industry & Energy, Republic of Korea. (No.20204030200050). This work was also supported by the National Research Foundation of Korea (NRF) grant funded by the Korea government (MSIT) (No. 2020R1A2C201096512).

5. References

1. M Chuah SH, Rauschnabel PA, Krey N, Nguyen B, Ramayah T, Lade S. Wearable technologies: The role of usefulness and visibility in smartwatch adoption. Computers in Human Behavior 2016; 65:276-84.
2. Choi I, Hawkes EW, Christensen DL, Ploch CJ, Follmer S. Wolverine: A wearable haptic interface for grasping in virtual reality. In2016 IEEE/RSJ International Conference on Intelligent Robots and Systems (IROS) 2016; pp. 986-993.
3. Veneman JF, Kruidhof R, Hekman EE, Ekkelenkamp R, Van Asseldonk EH, Van Der Kooij H. Design and evaluation of the LOPES exoskeleton robot for interactive gait rehabilitation. IEEE Transactions on Neural Systems and Rehabilitation Engineering 2007; 15(3):379-86.
4. Bogue R. Exoskeletons–a review of industrial applications. Industrial Robot: An International Journal. 2018.
5. awicki GS, Beck ON, Kang I, Young AJ. The exoskeleton expansion: improving walking and running economy. Journal of neuroengineering and rehabilitation. 2020; 17(1):1-9.

  doi:10.5075/epfl-298799_978-2-9701614-0-0

6. Cherry MS, Kota S, Ferris DP. An elastic exoskeleton for assisting human running. InInternational Design Engineering Technical Conferences and Computers and Information in Engineering Conference 2009; Vol. 49040, pp. 727-738.
7. Yandell MB, Quinlivan BT, Popov D, Walsh C, Zelik KE. Physical interface dynamics alter how robotic exosuits augment human movement: implications for optimizing wearable assistive devices. Journal of neuroengineering and rehabilitation. 2017; 14(1):1-1.
8. Zhang J, Fiers P, Witte KA, Jackson RW, Poggensee KL, Atkeson CG, Collins SH. Human-in-the-loop optimization of exoskeleton assistance during walking. Science. 2017; 356(6344):1280-4.
9. Collins SH, Wiggin MB, Sawicki GS. Reducing the energy cost of human walking using an unpowered exoskeleton. Nature. 2015; 522(7555):212-5.

  doi:10.5075/epfl-298799_978-2-9701614-0-0

REPAIRABILITY OF CARBON FIBER REINFORCED 3R AND MODIFIED 3R EPOXY LAMINATES

Kyriaki Tsirka[a], Arrate Huegun[b], Maria Elisavet Kouli[a], Amaia Llorente[b], Aggelos Ntaflos[a], Alaitz Rekondo[b], Georgios Foteinidis[a], Maria Kosarli[a], Konstantinos Anagnostou[a], Alkiviadis Paipetis[a]

a: Department of Materials Science & Engineering, University of Ioannina, GR-45110 Ioannina, Greece – ktsirka@uoi.gr
b: Polymers and Composites, CIDETEC, Paseo Miramón 196, 20014 Donostia-San Sebastián, Spain

Abstract: *The current study evaluated the repairability of a vitrimer epoxy system, called 3R resin, when used as a matrix in carbon fibre reinforced composites. Two types of composite specimens were manufactured using UD prepreg tapes with either the 3R resin or a formulation of carbon black modified 3R resin. Their quality was evaluated non-destructively by phased array c-scan and IR-thermography. Then, the laminates were damaged by applying different levels of impact energy, repaired and damaged again to evaluate their repair capacity. After each step (damage, repair and second damage) the same non-destructive tests (NDTs) were repeated. In this way, the repair capacity of micro-cracks and/or delaminations commonly caused by an impact were evaluated. Finally, the repair efficiency of both types of laminates was evaluated by comparing their mechanical performance against impact before and after repair. The results are very promising for the further exploitation of the novel 3R system.*

Keywords: 3R epoxy resin; repairing efficiency; impact testing; non-destructive evaluation

1. Introduction

Thermosetting resin systems are commonly used as matrices in carbon fiber reinforced polymer (CFRP) composites. They are the constituent that acts as a glue to hold the reinforcing fibres together, protect them from mechanical and environmental damage and they also facilitate the stress transfer between the fibres. During curing thermosetting resins undergo chemical reactions that lead to the crosslinking of the polymer chains in a three-dimensional network. This network is responsible for the rigidity, the thermal stability, and the resistance to creep; properties that characterize the thermosetting matrices and render them an ideal candidate when combined with reinforcing carbon fibres for load bearing applications in advanced fields like the aeronautics.

However, the same 3D network is also responsible for the poor post-formability and repairing ability of high-performance thermoset composite materials when they are damaged. This characteristic often leads to the complete replacement of high-cost parts when delaminations and cracks appear in their structure during service. To overcome this problem, the scientific community has turned its focus on alternative resin formulations that can form a rigid 3D network by crosslinking but can also undergo thermally activated bond exchange reactions that lead to changes of their topology [1]. Consequently, such resin systems, that are named vitrimers, present increased repairing ability and open new possibilities in the use of epoxy resins in high performance structural parts.

  doi:10.5075/epfl-298799_978-2-9701614-0-0

Another popular trend in the scientific community is the modification of epoxy resins to achieve enhanced mechanical properties as well as additional functionalities, i.e. enhanced thermal and electrical properties [2]. However, the modification with nanoparticles increases the viscosity of the resin and can cause filtration issues during the manufacturing of composites. Significant research efforts have been attributed to overcome those issues [3].

This study proposes the use of the 3R technology (Repairability, reprocessability, recyclability), developed by Cidetec [4], to enable the possibillity to repair damage such as delaminations and/or micro-cracks in 3R epoxy resins by simply applying heat and pressure to the damaged area, thanks to its reversible chemistry provided by dynamic bonds [5]. The study evaluates the effects of the modification of the matrix with carbon black (CB) on the impact properties on the 3R laminates and their repair efficiency.

2. Materials and methods

2.1 Manufacturing of prepreg

Two formulations of prepreg were produced by University of Ioannina (UoI) comprising of unidirectional (UD) stitched T700 carbon fibre (CF) (by Toray) fabric and the 3R epoxy resin or the same resin after nanomodification. The 3R epoxy resin was developed and modified by Cidetec (CID) with 1.5 wt.% CB via mechanical stirring using 5 wt.% CB masterbatch as the starting material manufactured by Nanocyl (NCYL). An additional prepreg formulation was manufactured using a UD glass fiber (GF) fabric and the 3R epoxy resin. The CF fabric had an aerial weight of 312.5 g/m^2, while the glass fiber fabric had an aerial weight of 429.2 g/m^2.

2.2 Manufacturing of laminates

Two categories of 100 mm x 150 mm laminates were manufactured by hand lay-up and hot pressing for low velocity impact testing according to ASTM D7136. The first one consisted of 3R resin CF prepreg and 3R resin GF prepreg (H1), while the second one consisted of modified 3R resin CF prepreg and 3R resin GF prepreg (H33). The selection of the lamination sequence was based on the demonstrator part for HARVEST project and is indicated in Table 1. These laminates were used to study the repairing efficiency of 3R and nanomodified 3R epoxy CF composites.

Table 1: Summary of the studied impact specimens and manufacturing details.

Code name	Impact energy	Resin type	Lamination sequence
H1-01	5 J	3R epoxy	(0/90/0/90/45/135/135/45/90/0/90/0) the outer 0^o and 90^o plies are GF prepreg the rest 8 plies are CF prepreg
H1-03			
H33-01		3R nanomodified epoxy	
H33-02			
H1-02	10 J	3R epoxy	
H1-04			
H33-03		3R nanomodified epoxy	
H33-04			

  doi:10.5075/epfl-298799_978-2-9701614-0-0

Four specimens from each of the H1 and the H33 formulations were manufactured. CF and GF prepregs were laid up onto a heated plate at 80 °C and then vacuum was applied for 10 min before inserting them to the hot press. The curing cycle was 1 h at 130°C and 2 hours at 150°C. A two-step manufacturing process was followed for these plates, whereby the two outer GF prepreg plies along with the 8 CF plies were cured during the first curing cycle. Then, the other two glass fiber prepreg plies were laid up onto the finished part (on the opposite side from the two initial GF plies) and were cured again for another curing cycle. Indicative laminates are shown in Figure 1.

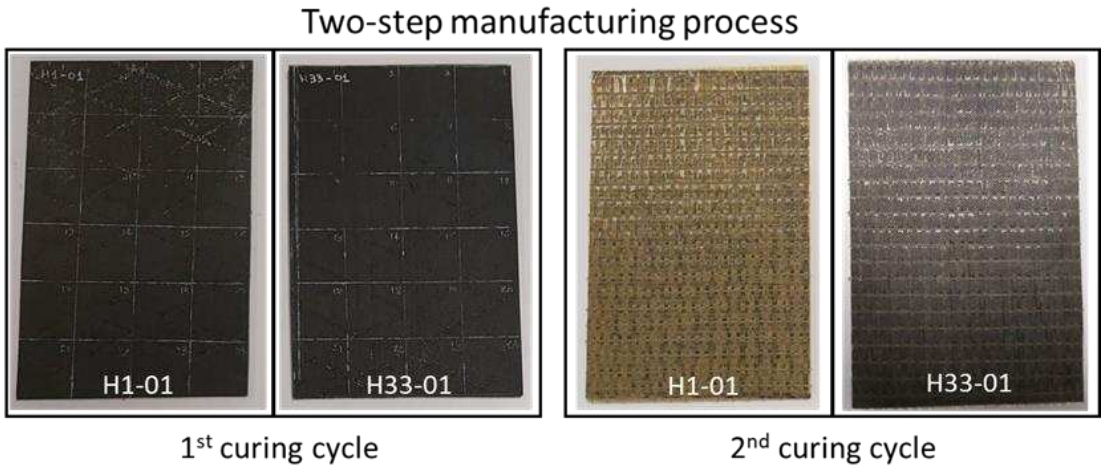

Figure 1. Indicative photos of the laminates manufactured by the two-step curing process.

2.3 Mechanical testing of laminates

All the manufactured laminates were impacted at an Instron Ceast 9340 Drop Tower equipped with a 45 kN loadcell and a 16mm hemispherical impactor. Two 3R H1 and two 3R H33 plates were tested at 5 J impact energy, and the rest two H1 and two H33 plates were tested at 10 J impact energy. The load vs time and load vs displacement values were recorded, and the latter were used to calculate the absorbed energy from the area under the plot of each specimen.

2.4 Repairing process of the impacted laminates

The selection of pressure, temperature and cycle time for the repair process was based on a preliminary study of ILSS composite samples, which due to their small size permitted for several specimens to be manufactured to optimise the selected conditions. In the case of the impact laminates a higher pressure was required as they were 75 times larger than the ILSS samples. The application of such a high pressure in the impact zone was essential as under pressure the laminate could lose its dimensions, so the use of a mold was required for the repair.

The laminates, in the mold, were placed in between the hot press plates at 210°C for 1 hour under 100 bars of pressure, as can be seen in Figure 2. For the first 15 min the laminates were thermostatised at 210°C and, once the press was closed pressure up to 100 bar was gradually applied. Then, the pressure was maintained at 210°C for 1 hour. To promote stress relaxation and flowability of the 3R resin, the plates were kept under pressure, while the temperature was slowly lowered. Once room temperature was reached, the repair process was completed.

Figure 2. A damaged laminate placed in the mould and at the hot press for repair.

2.5 Non-destructive evaluation of laminates

The manufacturing quality of the laminates was evaluated by phased array ultrasonic imaging and Infrared Thermography after production. The same non-destructive tests (NDTs) were repeated after each testing stage (damage, repair and second damage).

For the acquisition of the thermal response of the 3R and nanomodified 3R laminates a FLIR A6750 MWIR camera was utilized, with a resolution of 640 x 512 pixels and an 125Hz frame rate. Two 1000W IR lamps were used as the heating source, triggered by a Tektronix AFG3052C signal generator, for the pulsed thermography method. The ramp pulse had a duration of 7s and the peak-to peak voltage was 7V. The distance between the specimen and the lamp was 1 m, as well as the distance between the specimen and the camera.

The inspection of the composites was performed using a Dolphicam2 phased array ultrasonic imaging platform. The frequency range was from 0.5 to 15MHz while the transducer electrode was 128×128 mm with 16384 elements. The gates were selected to be from 0.9 mm to 3.5 mm to avoid the reflection of the surface and inspect the whole specimen thickness. A stitching technique was used as provided by the software for capturing larger images than the size of the transducer.

2.6 Evaluation of repairing efficiency

The repair efficiency of the 3R (H1) and the nanomodified 3R (H33) laminates was evaluated based on the average maximum load sustained by the plates during the impact process, as well as on the average absorbed energy for each specimen. The average absorbed energy was calculated from the area under the load vs displacement plot.

The following equations were used for the calculation of the two repair efficiencies.

$$n_l\% = \left(\frac{\text{Max load repaired}}{\text{Max load initial}}\right) \times 100\% \quad (1)$$

and

$$n_e\% = \left(\frac{\text{Max absorbed energy repaired}}{\text{Max absorbed energy initial}}\right) \times 100\% \quad (2)$$

2.7 Description of experimental method

The following sequence was used to carry out all the experiments for this study.

  doi:10.5075/epfl-298799_978-2-9701614-0-0

- Manufacturing of laminates
- Non-destructive evaluation of manufacturing quality
- Impact testing
- Non-destructive evaluation of impacted laminates
- Repairing process of impacted laminates
- Non-destructive evaluation of repaired laminates
- 2nd impact test on the repaired laminates
- Non-destructive evaluation of impacted laminates

3. Results and discussion

3.1 Manufacturing quality of impacted laminates

The manufacturing quality of both the 3R and the nanomodified 3R laminates after the first and the second curing cycle are presented in Figure 3. The left images represent measurements from the surface of the specimens to evaluate the quality of the carbon fiber composites before integrating the glass fiber plies on the second side of the laminates. As can be seen from the C-scan images, the plates are not of best quality. The blue color that would be seen in the case of a perfect plate would represent the bottom of the composite. In this case, the laminates were mostly red and yellow, with only a few green spots indicating that the ultrasonic waves encountered defects shortly after they were sent into the material. These defects could be entrapped air that were mainly located near the stitching material as can be seen by the diagonal patterns in the IR-T images. The same is true for the right images which are measurements from the final specimens with the GF plies. Although gates were used to avoid the surface reflections the noise was still present in the images and the attenuation of the ultrasonic signal was again high. In this case, the IR-T images reflect the integration of the GF prepreg as the upper surface of the laminates (through its different stitching pattern) which has covered up the diagonal stitching pattern.

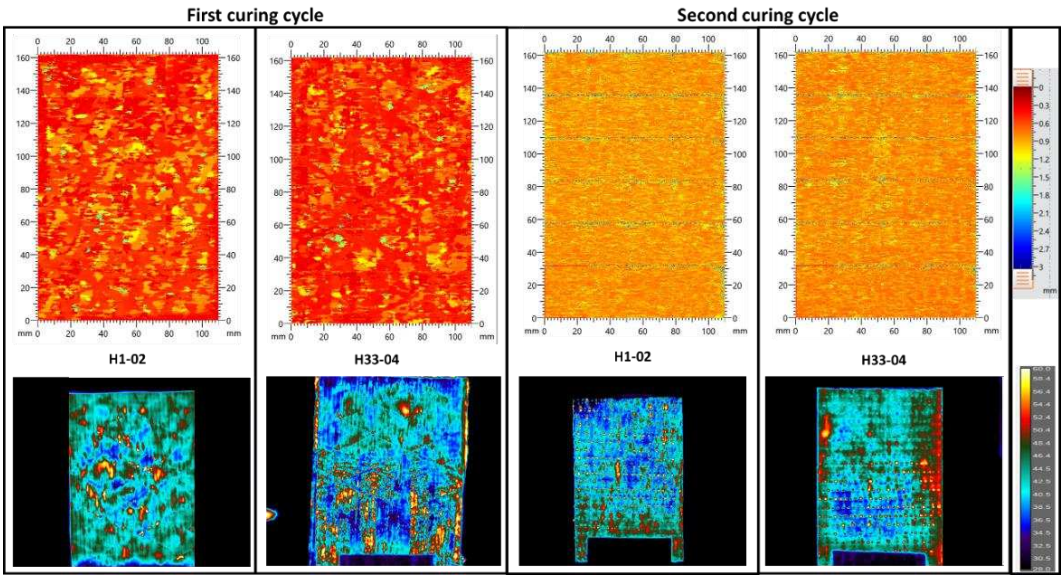

Figure 3. Indicative C-scan stitched images (top) and IR-T images (bottom) of the 3R (H1-01) and nanomodified 3R (H33-01) laminates after the first and the second curing cycle.

3.2 Impact of initial and repaired laminates and evaluation of repair efficiency

The values of maximum load and calculated absorbed energy for the first and the second impact tests are summarised in Table 2. The plates that were impacted at 10 J exhibited significantly higher loads than the ones impacted at 5 J, as expected. The nanomodification of the matrix did not affect the response of the laminates to low velocity impact as expected by other studies [6]. The repair process led to almost a complete recovery of the maximum load, and a small enhancement in the absorbed energy after impact for all the laminates.

Table 2: Max load, absorbed energy for the two impact and repair efficiencies of the laminates.

	1st impact		2nd impact (repaired)		Repair efficiency	
Specimen	Average Max Load (kN)	Average Absorbed Energy (J)	Average Max Load (kN)	Average Absorbed Energy (J)	Max Load n_l %	Absorbed Energy n_e%
H1-5J	2.60 ± 0.04	3.74 ±0.39	2.60 ± 0.10	4.07 ± 0.30	99.76 ± 2.51	108.94 ± 3.51
H33-5J	2.58 ± 0.11	3.71 ± 0.33	2.59 ± 0.12	4.14 ± 0.15	96.55 ± 6.80	104.73 ± 0.02
H1-10J	3.68 ± 0.09	9.16 ± 0.14	3.55 ± 0.16	9.60 ± 0.15	100.61 ± 0.37	112.08 ± 5.92
H33-10J	3.63 ± 0.03	9.23 ± 0.00	3.55 ± 0.26	9.88 ± 0.17	97.84 ± 7.80	107.03 ± 1.85

The repair efficiency based on maximum load during impact of all the studied specimens was in the range of 96.6 to 100.6 %. The differences in n_l % among the H1, the H33 specimens are not considered significant taking into account the standard deviation of the values.

Enhanced repair efficiency values were calculated based on the absorbed energy in comparison to the values based on the maximum load during impact. The n_e% were in the range of 104.7 % to 112.1 % indicating a complete recovery of the energy absorbing capability of the laminates after repair. This was caused by the repair of the extensive damage caused by the 1st impact.

3.3 Non-destructive evaluation of the impacted, repaired, and re-impacted laminates

Indicative C-scan images of the 3R and the nanomodified 3R laminates after the first impact, after the repair process and post second impact are shown in Figure 4. After the 1st impact all laminates presented a similar quality in the c-scan images, with high attenuation of the ultrasonic signal that did not permit the impact imprint to be seen. Similarly, the IR-T images did not provide sufficient evidence of the impact for the 3R laminates. On the other hand, some signs of impact could be identified from the IR-T images of the nanomodified 3R specimens, which are depicted by the combination of yellow and red spots in the middle of the laminates.

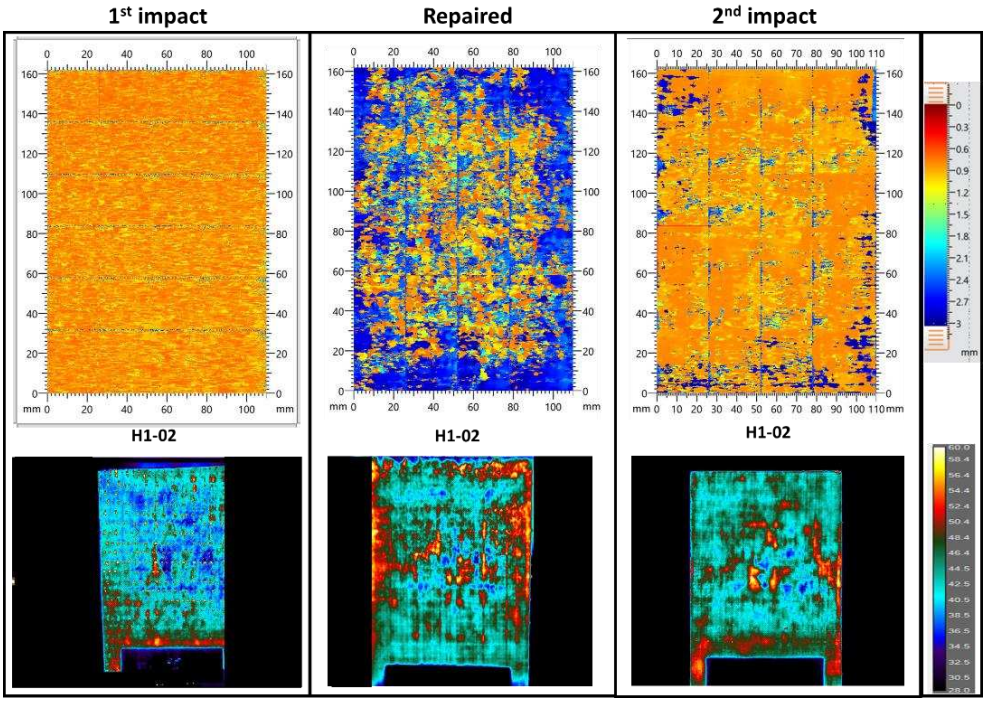

Figure 4. Indicative C-scan stitched images (top) and IR-T images (bottom) of the 3R laminates after the first and the 1st impact, the repair, and the 2nd impact.

The quality of the laminates was clearly improved due to the repair process, as increased pressure and temperature were applied to them into the hot press. This is indicated by the appearance of blue color in the stitched C-scan images of Figure 4 (middle), compared to their color after production (Figure 3) or after the first impact (Figure 4 left). The second impact points were again not visible from the stitched c-scan images of the laminates (Figure 4 and Figure 5 top right). On the other hand, the impact imprints were clearly visible in the IR-T images of the samples by the light-colored imprints in the middle of each image (Figures 4 and 5 bottom right).

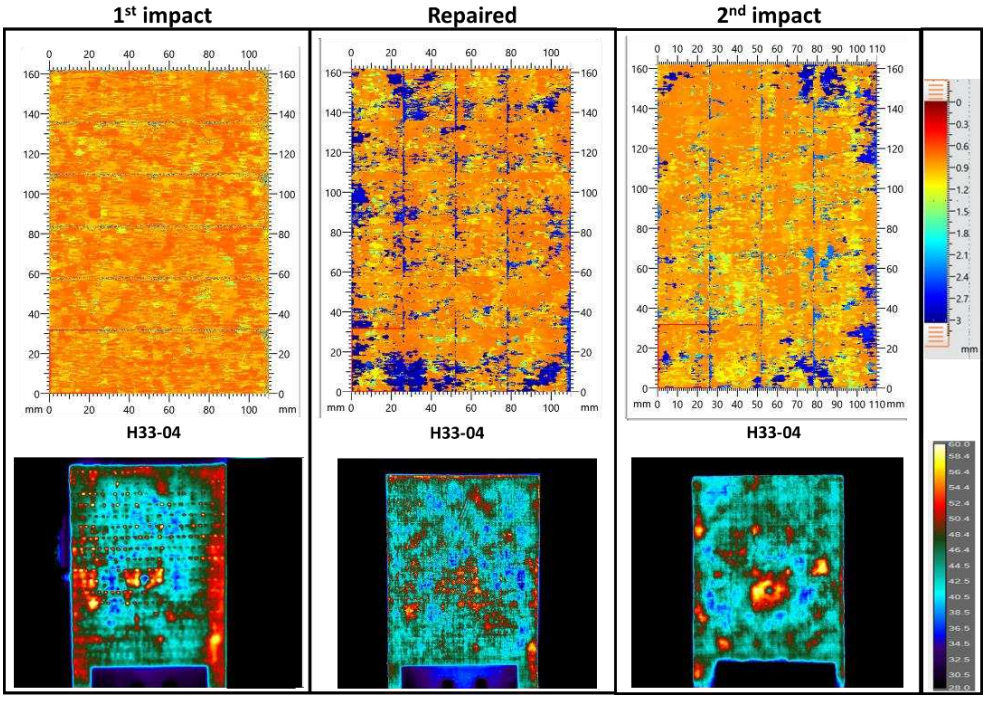

Figure 5. Indicative C-scan stitched images (top) and IR-T images (bottom) of the nanomodified 3R laminates after the first and the 1st impact, the repair, and the 2nd impact.

4. Conclusions

The response to low velocity impact and the repair efficiency of 3R and nanomodified 3R carbon fibre reinforced laminates were evaluated mechanically and by non-destructive methods. The repair process led to the recovery of the maximum load, and a small enhancement in the absorbed energy after impact for all the laminates. The IR-T images were able to depict clearly the impact damage and its repair which was quantified by the mechanical results to be in the order of 100%. The C-scan images were not as helpful since the manufacturing quality of the initial laminates was not adequate for this method to discriminate between pre-existing damage and damage caused by impact. The manufacturing quality of the laminates is the subject of a following study.

Acknowledgements

The research leading to these results has been part of the activities carried out for the European H2020-MG-2017 program under the Grant Agreement n◦ 769140 (HARVEST).

5. References

1. Yang Y, Xu Y, Ji Y, Wei Y. Functional epoxy vitrimers and composites. Prog Mater Sci [Internet]. 2021;120(February 2020):100710. Available from: https://doi.org/10.1016/j.pmatsci.2020.100710

2. Gibson RF. A review of recent research on mechanics of multifunctional composite materials and structures. Compos Struct [Internet]. 2010;92(12):2793–810. Available from: http://dx.doi.org/10.1016/j.compstruct.2010.05.003

3. Foteinidis G, Tsirka K, Tzounis L, Baltzis D, Paipetis AS. The role of synergies of MWCNTs and Carbon Black in the enhancement of the electrical and mechanical response of modified epoxy resins. Appl Sci. 2019;9(18).

4. Ruiz De Luzuriaga A, Martin R, Markaide N, Rekondo A, Cabañero G, Rodríguez J, et al. Epoxy resin with exchangeable disulfide crosslinks to obtain reprocessable, repairable and recyclable fiber-reinforced thermoset composites. Mater Horizons. 2016;3(3):241–7.

5. Matxain JM, Asua JM, Ruipérez F. Design of new disulfide-based organic compounds for the improvement of self-healing materials. Phys Chem Chem Phys. 2016;18(3):1758–70.

6. Kostopoulos V, Baltopoulos A, Karapappas P, Vavouliotis A, Paipetis A. Impact and after-impact properties of carbon fibre reinforced composites enhanced with multi-wall carbon nanotubes. Compos Sci Technol [Internet]. 2010;70(4):553–63.

  doi:10.5075/epfl-298799_978-2-9701614-0-0

EXPERIMENTAL STUDY ON THE FLEXURAL BEHAVIOR OF RC BEAMS STRENGTHENED WITH PRESTRESSED BFRP LAMINATES

Changyuan, Liu[a], Xin Wang[b], Zhishen Wu[c]

a: Key Laboratory of C & PC Structures Ministry of Education, Southeast University, Nanjing 210096, China – changyuanliu@seu.edu.cn
b: Key Laboratory of C & PC Structures Ministry of Education, Southeast University, Nanjing 210096, China – xinwang@seu.edu.cn
b: Key Laboratory of C & PC Structures Ministry of Education, Southeast University, Nanjing 210096, China – zswu@seu.edu.cn

Abstract: *In this study, the flexural behavior of RC beams strengthened with prestressed basalt FRP (BFRP) laminates was investigated. Compared with the conventional carbon FRP (CFRP) laminate, BFRP exhibits a larger failure strain but lower modulus, in addition to its high strength and prominent creep rupture behavior; this makes BFRP a suitable option for cost-effective strengthening of existing beams. Four specimens were prepared to investigate the effects of the FRP type on the flexural behavior of RC beams. The results demonstrated that specimen strengthened with BFRP laminate could achieve 85% of the loading capacity of the specimen strengthened with CFRP laminate under the same laminate section, but ensured a superior crack control effect and ductility when compared with the CFRP laminate. Meanwhile, BFRP laminate with similar stiffness ensured a higher bearing capacity, a better crack control effect, and superior ductility for the specimen.*

Keywords: Prestressed BFRP laminate; externally bonded reinforcement; flexural behavior; strength utilization ratio; FRP type

1. Introduction

Bridge rehabilitation is one of the major challenges faced by the construction industry, and the bonding steel plate method is the earliest method to retrofit structures. But its wider application is restricted by steel corrosion and inconveniences in construction due to the heaviness of the steel material [1,2]. Fiber-reinforced polymers (FRPs) have been widely used as alternatives to steel plates in retrofitting reinforced concrete (RC) structures, due to their high strength-to-weight ratio, excellent fatigue performance, and superior durability in adverse environments [2-5]. Prestressed FRP with special end-anchorages offers advantages such as reducing deflection and crack widths, delaying cracking initiation, providing superior fatigue resistance, increasing the utilization efficiency of the FRP material, overcoming premature debonding failure, and significantly improving the bearing capacity and shear capacity [7].

Carbon FRP (CFRP), with a high creep rupture stress, is the most widely used FRP material and has been extensively utilized in the prestressed FRP strengthening approach [1,6]. However, the high cost and brittle behavior of CFRPs limit their large-scale application in the field of civil engineering [4,8]. Aramid FRP (AFRP) and Glass FRP (GFRP) are not suitable as prestressing materials: the former is expensive and has a large relaxation rate, and the latter has a low creep rupture stress, which is less than 30% of the tensile strength [4]. Basalt FRP (BFRP) is a new type

  doi:10.5075/epfl-298799_978-2-9701614-0-0

of environment-friendly and cost-efficient material. It is a competitive substitute for CFRP and a promising prospect for the following reasons: (1) BFRP is a favorable prestressed material with a high creep fracture stress of 52% f_u [9], low creep rate, and tensile strength more than 1300 MPa; (2) BFRP is insensitive to prestress loss as its elastic modulus is about 1/3 of CFRP; (3) structures strengthened with BFRP are expected to obtain a higher deformation capacity as a result of their higher ultimate elongation compared with CFRP; (4) basalt fiber is more cost-effective, being 9 times lower in price; and (5) BFRP works compatibly with concrete under temperature variation compared with CFRP which differs greatly from concrete in terms of its coefficient of thermal expansion. Therefore, the outlook is promising for the combination of the prestressing method and BFRP materials to obtain a practical prestressing technology. BFRP tendons and basalt fabrics has been introduced as strengthening materials and results show that the overall flexural behavior of the beams has effectively improved[4,10-12]. However, investigations of RC beams strengthened with prestressed BFRP laminates have not been performed. From the aforementioned review, it can be concluded that applying BFRP laminates as prestressing materials can effectively improve the bearing capacities of the strengthened specimens and can provide better ductility.

This study carried out experiments on a series of full-scale RC beams with T-shaped sections strengthened by prestressed BFRP laminates. Epoxy and friction-based anchorages provided by Nanjing Mankate Science & Technology Co., Ltd., China, were applied. The effects of the FRP laminate type on the flexural behavior of the strengthened RC beams were considered. The differences in failure modes, L-D curves, cracking behavior, and strain development of concrete, steel reinforcement, and FRP laminates were analyzed.

2. Experimental program

2.1 Material properties

Table 1: Material characterization.

Matrial	Section dimension	Elastic modulus [GPa]	Yield strength [MPa]	Tensile strength [MPa]	Ultimate strain [%]
CFRP laminate	50mm×2mm	168 (1.51%)[a]	--	3212 (1.71%)	1.91
BFRP laminate	50mm×2mm	53 (1.22%)	--	1339 (2.04%)	2.56
	50mm×5mm	56 (0.81%)	--	1367 (0.60%)	2.42
Steel reinforcement	ϕ10	204 (6.21%)	495 (0.65%)	562 (0.53%)	--
	ϕ20	197 (2.53%)	433 (1.21%)	571 (0.57%)	--
Epoxy adhesive	--	2.76	--	42.2	1.8

[a]Average value (Coefficient of variation)

  doi:10.5075/epfl-298799_978-2-9701614-0-0

BFRP laminates were pultruded with unidirectional basalt fiber impregnated by epoxy vinyl ester resin, provided by Jiangsu GMV Co., Ltd., China. CFRP laminates, the epoxy adhesive used to bond FRP laminates to the subsurface of RC beams, and the anchorages used to fix the prestressed FRP laminates were provided by Nanjing Mankate Science & Technology Co., Ltd., China. The mechanical properties of the materials are listed in Table 1.

2.2 Specimen geometry and configuration

An experiment with five T-section RC beams was conducted to study the flexural behavior of RC beams strengthened with prestressed BFRP laminates. The design parameter of the specimens was FRP laminate type. Details of the specimens are provided in Table 2. The specimen geometry is illustrated in Figure 1. All the specimens were the same size with a total length of 5.2 m and a pure flexural section of 1.1 m.

Table 2: Overview of performed experiments.

Serial No.	Specimen No.	FRP type	Section dimension
1	CON	--	--
2	C2	CFRP	50 mm × 2 mm
3	B2	BFRP	50 mm × 2 mm
4	B5	BFRP	50 mm × 5 mm

Note: Expect for the control specimen (CON), all specimens are labeled with a generic designation: ZT, where Z is the type the FRP laminate (C=CFRP or B=BFRP); T is the thickness of the FRP laminate in millimeters (2 or 5).

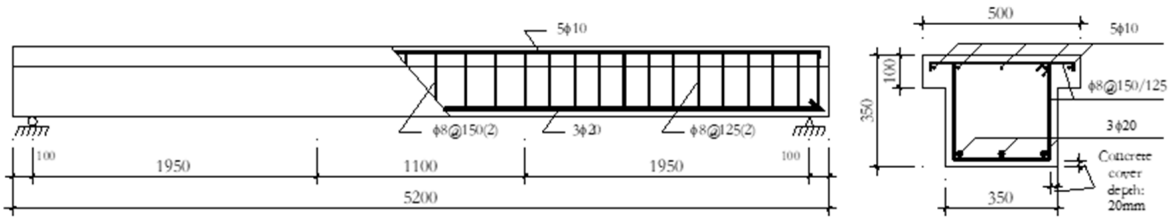

Figure 1. Geometry and reinforcements of the RC beams [Unit: mm]

2.3 Test setup

As shown in Figure 2, all specimens were supported by a pin support and a roller support and loaded in four-point bending with a net span of 5 000 mm and a pure bending span of 1 100 mm. All specimens were loaded using the water + bai Servo-Actuator Type AH 500/250 which was a fatigue testing machine produced by walter+bai ag Testing Machines Co. Ltd. in Switzerland. The load was applied under displacement control at a constant displacement rate of 0.9 mm/min at the beginning of the elastic stage and 6 mm/min after the yielding of steel reinforcements. During the loading process, it's time to end the tests when any of the following criterion met: (1) Compressive concrete crushed; (2) Anchoring system failed; and (3) The deflection was too large to carry the load.

  doi:10.5075/epfl-298799_978-2-9701614-0-0

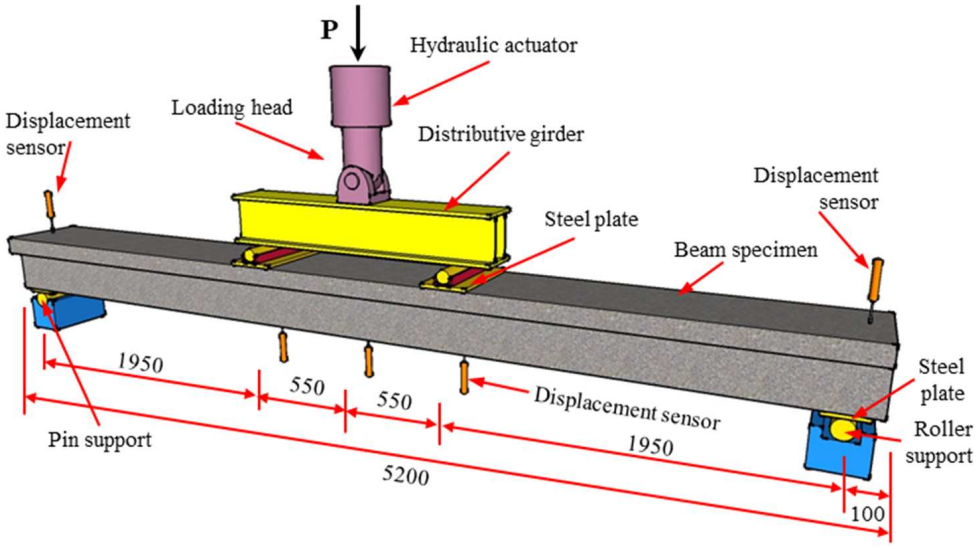

Figure 2. The loading setup [Unit: mm]

3. Results and discussion

3.1 General results

A summary of significant parameters characterizing the behavior of the specimens is provided in Table 3, where P_{cr} is the cracking load; P_y is the yielding load; P_u is the ultimate load; Δ_y means the yielding deflection; and Δ_u indicates the ultimate deflection. The ductility of the specimens was evaluated using the Performance Factor (PF) [13], which is defined as the product of the Deformability Factor (DF) and the Strength Factor (SF). The DF is defined as the ratio of the ultimate deflection (Δ_u) to the yield deflection (Δ_y), and the SF is defined as the ratio of the ultimate load (P_u) to the yielding load (P_y).

Table 3: A summary of results of the specimens.

Serial No.	Specimen No.	P_{cr} [kN]	P_y [kN]	P_u [kN]	Δ_y [mm]	Δ_u [mm]	Failure modes	DF	SF	PF
1	CON	12	104.4	120.9	30.85	166.7	RYCC	5.4	1.2	6.3
2	C2	48	162.5	174.7	40.47	51.18	LS-RYCC	1.3	1.1	1.4
3	B2	32	139.0	155.5	36.94	150.68	LPF-RYCC	4.1	1.1	4.6
4	B5	50	161.3	179.2	40.11	129.72	LPF-RYCC	3.2	1.1	3.6

Note: RYCC = conventional flexural failure due to yielding of steel reinforcements followed by concrete crushing; LS = FRP laminate slipped out of the anchor; LPF = partial fracture of the FRP laminate.

  doi:10.5075/epfl-298799_978-2-9701614-0-0

It can be seen from Table 3 that the overall flexural behavior of the specimens strengthened with prestressed FRP laminates was significantly enhanced compared with that of the control specimen (CON). Meanwhile, it can also be observed that the ductility of the strengthened specimens was generally lower than that of the control specimen (CON). Among all the prestressed specimens, specimen B2 exhibited the best ductility as it had the highest Deformation Factor of 4.1 and Performance Factor of 4.6. As expected, the stiffness of the specimen was increased by strengthening, and as a result, the deflection was decreased accordingly.

3.2 Load versus mid-span deflection curves

Load versus mid-span deflection curves are presented in Figure 3. The L-D curves of the strengthened specimens exhibited several load drops after the steel reinforcement yielding. Based on observations during the test, the behavior was related to the debonding initiation and corresponded to FRP laminate rapture or slippage [14].

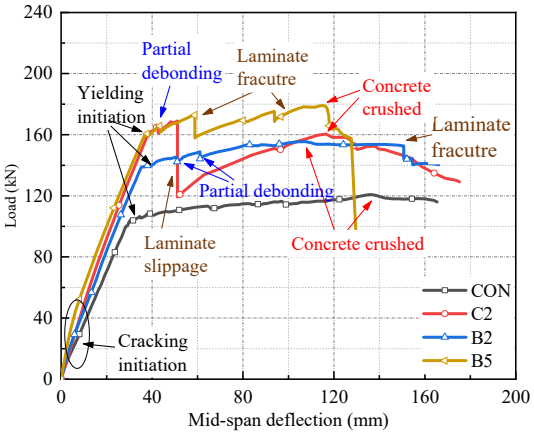

Figure 3. Load versus mid-span deflection curves

Due to the high stiffness of the CFRP laminate, a large shear stress was contained in the adhesive layer, and early debonding was observed for the CFRP strengthened specimen. As the specimen failed by laminate slippage, the bearing capacity showed a sharp drop with relatively low ultimate load and ductility.

Although the prestressing force and the elastic modulus for BFRP laminate with a section of 50 mm × 2 mm were far lower than that of the CFRP laminate, the specimen strengthened with BFRP laminate showed almost the same stiffness in the elastic stage and more than 85% of yielding load compared with the CFRP laminate strengthened specimen, as shown in Table 3 and Figure 3. At the same time, delayed partial debonding and less load fluctuation were observed for the same reason. When it comes to BFRP laminate strengthened specimen B5, which had a similar stiffness to the CFRP laminate strengthened specimen, the L-D curve showed that its performance was better in the elastic and yielding initiation stage and it had a higher ultimate load and ductility compared with the CFRP laminate strengthened specimen. The higher ductility can be explained by the lower modulus and larger failure elongation of the BFRPs [4].

3.3 Crack patterns of specimens

  doi:10.5075/epfl-298799_978-2-9701614-0-0

The crack distribution is shown in Figure 4. Because sufficient stirrups had been arranged in the shear flexural section, there was almost no diagonal crack in the control specimen. Figure 4 shows that all the strengthened specimens exhibited more cracks with a smaller crack width, smaller crack spacing, and more distributed cracking, compared with the control specimen (CON). A more uniform crack distribution was observed for the specimens strengthened with prestressed BFRP laminates. It was observed that the crack width was directly proportional to the load during the elastic stage, as shown in Figure 4 and Figure 5. When it comes to laminate with similar stiffness, BFRP laminate ensured a higher bearing capacity, a better crack control effect, and superior ductility for the specimen.

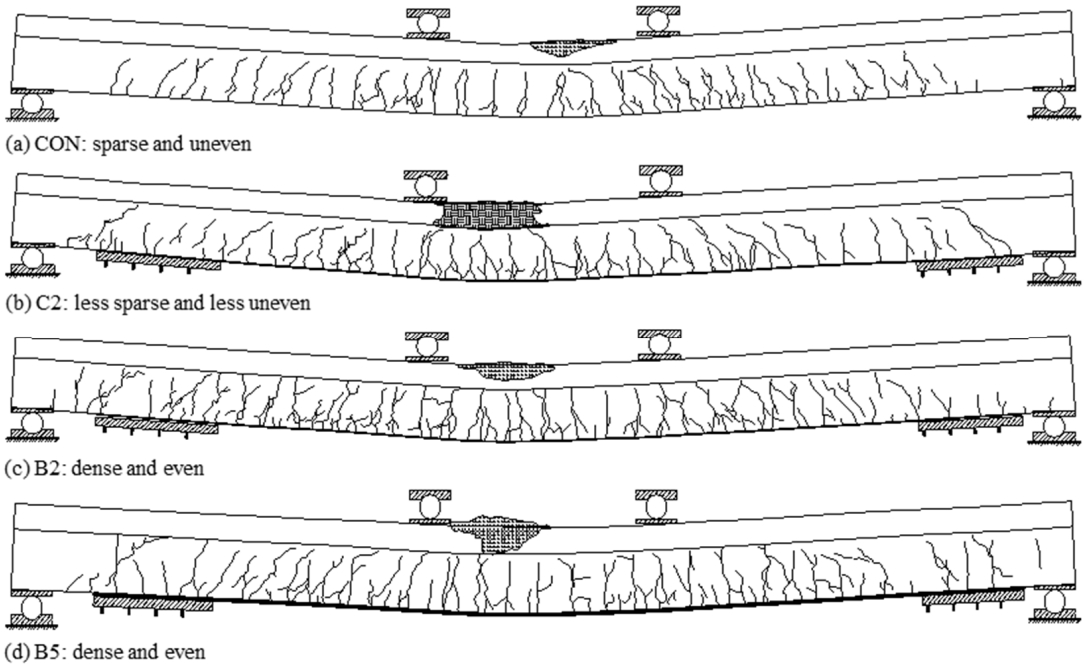

Figure 4. Crack distribution

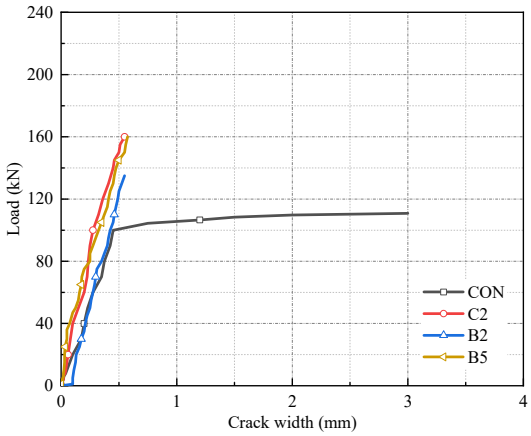

Figure 5. Load versus crack width curves

3.4 Load versus strain curves

The actual tension control stresses of the prestressed FRP laminates measured using strain gauges after the prestressing process is shown in Table 4. The actual tension control stresses were generally 5% higher than the theoretic values for the consideration of prestress loss.

Load versus strain curves of FRP laminates, concrete, and steel reinforcements of the specimens are presented in Figure 6, and it can be seen that all the load versus strain curves show three-stage trends with two inflection points similar to the L-D curves shown in Figure 3. It can be observed that the specimen with CFRP laminate showed a slightly lower concrete, steel reinforcement, and FRP laminate strength utilization ratio compared with the BFRP laminate strengthened specimen.

Table 4: The tension control stress of prestressed FRP laminates.

Serial No.	Specimen No.	Theoretic tension control stress [MPa]	Actual tension control stress [MPa]
1	C2	1080	1135
2	B2	517.5	566
3	B5	517.5	560

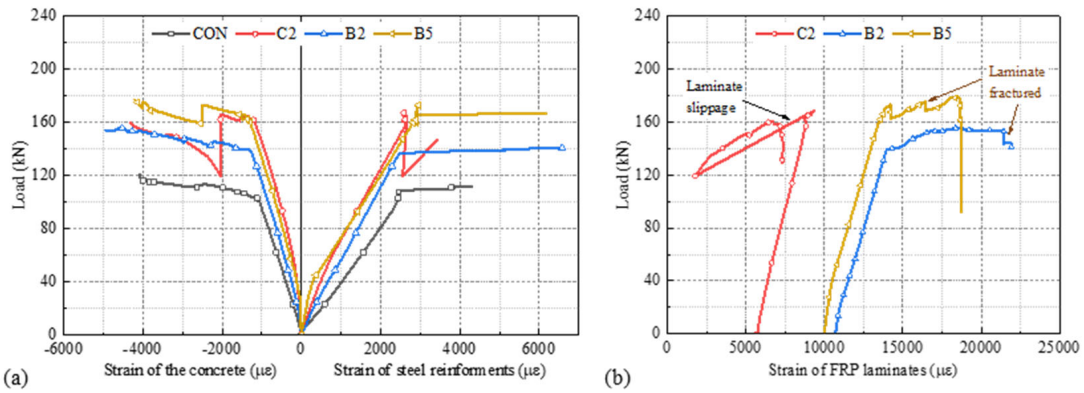

Figure 6. Load versus concrete, steel reinforcements, and FRP laminates strain curves

4. Conclusions

Experiments with four T-section RC beams were conducted to study the flexural behavior of RC beams strengthened with prestressed BFRP laminates. The effect of FRP type on the flexural behavior such as cracking load, yielding load, ultimate load, stiffness, and ductility of strengthened beams was analyzed. The main conclusions are presented below.

- A significant enhancement of the cracking, yielding, and ultimate loads were achieved by applying BFRP laminates as prestressed materials.
- Specimen strengthened with BFRP laminate could achieve 85% of the loading capacity of the specimen strengthened with CFRP laminate under the same laminate section.
- Compared with the CFRP laminate, BFRP laminate with similar stiffness ensured a higher bearing capacity, a better crack control effect, and superior ductility for the specimen.

  doi:10.5075/epfl-298799_978-2-9701614-0-0

Acknowledgements

This work was supported by the National Key Research and Development Program of China [grant numbers No. 2017YFC0703000]; the National Science Foundation of China [grant number No. 51678139]. The authors appreciate the contribution of Nanjing Mankate Science & Technology Co., Ltd., China, which kindly provided the strengthening material.

5. References

1. Garden HN, Hollaway LC. An experimental study of the failure modes of reinforced concrete beams strengthened with prestressed carbon composite plates. Compos Part B-Eng. 1998; 29(4):411-24.
2. Bakis CE, Bank LC, Brown VL, Cosenza E, Davalos JF, Lesko JJ, et al. Fiber-reinforced polymer composites for construction-state-of-the-art review. J Compos Constr. 2002; 6(2):73-87.
3. You YC, Choi KS, Kim J. An experimental investigation on flexural behavior of RC beams strengthened with prestressed CFRP strips using a durable anchorage system. Compos Part B-Eng. 2012; 43(8):3026-36.
4. Wang X, Shi JZ, Wu G, Yang L, Wu ZS. Effectiveness of basalt FRP tendons for strengthening of RC beams through the external prestressing technique. Eng Struct. 2015; 101:34-44.
5. Shi JW, Cao WH, Chen L, Li AL. Durability of wet lay-up BFRP single-lap joints subjected to freeze–thaw cycling. Constr Build Mater. 2020; 238:117664.
6. Wight RG, Green MF, Erki MA. Prestressed FRP sheets for poststrengthening reinforced concrete beams. J Compos Constr. 2001; 5(4):214-20.
7. El‐Hacha R, Wight R, Green M. Prestressed fibre‐reinforced polymer laminates for strengthening structures. Prog Struct Eng Mat. 2001; 3(2):111-21.
8. Garcez MR, Silva Filho G, Meier U. Post-strengthening of reinforced concrete beams with prestressed CFRP strips. Part 1: analysis under static loading. Revista IBRACON de Estruturas e Materiais. 2012; 5(3):343-61.
9. Wang X, Shi J, Liu J, Yang L, Wu Z. Creep behavior of basalt fiber reinforced polymer tendons for prestressing application. Mater Design. 2014; 59:558-64.
10. Duic J, Kenno S, Das S. Flexural rehabilitation and strengthening of concrete beams with BFRP composite. J Compos Constr. 2018; 22(4):04018016.
11. Chen WS, Pham TM, Sichembe H, Chen L, Hao H. Experimental study of flexural behaviour of RC beams strengthened by longitudinal and U-shaped basalt FRP sheet. Compos Part B-Eng. 2018; 134:114-26.
12. Joyklad P, Suparp S, Hussain Q. Flexural response of JFRP and BFRP strengthened RC beams. Int J Eng Sci. 2019; 11(3).
13. Spadea G, Bencardino F, Swamy RN. Optimizing the performance characteristics of beams strengthened with bonded CFRP laminates. Mater Struct. 2000; 33(226):119-26.
14. Correia L, Teixeira T, Michels J, Almeida JAPP, Sena-Cruz J. Flexural behaviour of RC slabs strengthened with prestressed CFRP strips using different anchorage systems. Compos Part B-Eng. 2015; 81:158-70.

  doi:10.5075/epfl-298799_978-2-9701614-0-0

REAL DELAMINATION IN LAMINATED CARBON FIBER REINFORCED POLYMER PRODUCED BY LASER SHOCK FOR AERONAUTIC STRUCTURAL CONTROL

Marine Scius-Bertrand[a], Laurent Videau[b,c], Romain Ecault[d], Yann Rouchausse[e], Laurent Berthe[e]

a: Rescoll, 8 All. Geoffroy Saint-Hilaire, 33600 Pessac – marine.scius-bertrand@rescoll.fr
b: CEA-DAM-DIF, 91297 Arpajon
c: Laboratoire Matière sous Conditions Extrêmes, Université Paris-Saclay, Bruyères-le-Châtel, 91680
d: Airbus Operation Toulouse, France
e: PIMM, UMR8006 ENSAM, CNRS, CNAM, 151 bd de l'Hôpital, 75013 Paris

Abstract: *Composite materials are widely used in the aeronautic industry in order to reduce the total weight of the aircraft and thus the fuel consumption. To be qualified to fly, the material integrity needs to be assessed by the mean of Non-Destructive Testing (NDT). The material control during its utilization can be done using Structure Health Monitoring (SHM). It consists in implementing an automatic damage identification strategy in the airplane [1]. Both NDT and SHM require reference standards with representative defects such as delamination. As of now, there is no way of creating real delamination inside a laminated composite material without destroying its skin. The use of laser-induced shock waves is a promising method. LASer Adhesion Test (LASAT) has indeed proven its capacity to generate a calibrated mechanical stress to a given location inside composite materials [1,2]. The laser loading applied on the target through the laser matter interaction has been characterized in a previous work [3]. We study here laser shock used in symmetrical configuration. Our aim is to create delamination (millimetric to centimetric range) inside the material without damaging its skin. We focus 7 ns Gaussian laser pulses on each surface of the composite sample and study the influence of the different laser parameters (energies, delay between the beams, and position of the beam…) on the induced delamination (shape and position). In particular, we compare different methods to propagate the delamination. In addition, we show how a delay between the two laser beams can change the defect location into the sample. Finally, we show the process capability though the creation of a centimetric delamination into several depths of the composite made with 79 different laser impacts.*

Keywords: Laser Shock; CFRP laminated materials; delamination; NDT

Introduction

The research and development in aerospace industry is working on the reduction of the CO_2 emission by making the aircraft lighter. For that purpose, the use of Carbon Fiber Reinforced Polymer (CFRP) composite is increasing [4]. For instance, 53 % in weight of the A350's fuselage is CFRP [5] which, for the A350-100, leads to of a fuel consumption 25% smaller than the other aircraft of its size [6]. Each flying component has to be inspected with non-destructive testing in order to qualify its integrity. Those inspections are made with tools that are calibrated on reference standards including defects of known size and position. The increasing use of laminated composite materials requires the evolution of the reference standards to include defects representing the one appearing in such materials, as the delamination. As for today,

  doi:10.5075/epfl-298799_978-2-9701614-0-0

there is no way of creating a real and controlled delamination inside a laminated composite material without destroying its skin. The LASer Adhesion Test (LASAT) has already proven its capacity to generate a calibrated mechanical stress to a given location inside composite materials [1,2], that is why we propose here to use it to create on-demand delamination.

The focalization of high-power laser into the surface of a material will generate a plasma. The expansion of this plasma in one direction will induce a reaction force in the opposite direction equivalent to an ablation pressure, that will lead to the propagation of shock waves into the sample [7, 8, 9]. To obtain the desired pressure, a confinement medium which will slow down the plasma expansion, is applied on the sample's surface [10, 11, 12]. Figure 1 schematizes this configuration, with two laser beams, each one focused on one side of the sample.

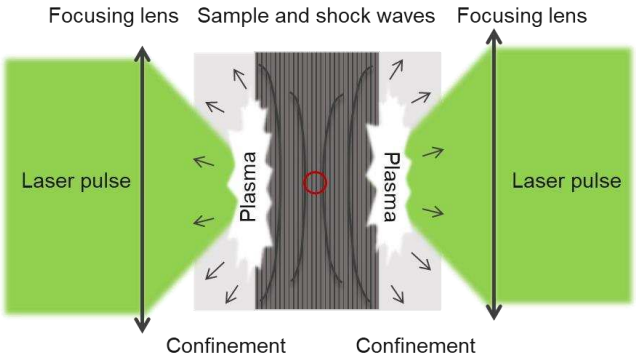

Figure 1 Scheme of the laser shock in symmetrical configuration with solid confinement medium

To predict the propagation of the shock wave trough the sample's depth, space-time (also called X-t) diagrams are used. They are based on an 1D-hydrodynamic approach and consider the shock waves to be mono-dimensional and to propagate at the velocity speed of the sound in the materials, which does not vary with the applied pressure. Under those assumptions, the shock waves are represented with black lines and the release waves with doted lines, as in Figure 2. When the shock wave reaches the back face of the sample, it is reflected as a release wave. The crossing of two release waves induces the localized tensile stress we want to use to create delamination into the sample. The highest value of tensile stress is identified in Figure 2 by a red circle and is localized in a depth e in the sample of total length L. When we use symmetrical laser shock with two beams that are temporally synchronized, this depth e is located in the middle of the sample (Figure 2 (a)). In order to shift it, we can add a delay Δt between the laser beam of pulse τ (Figure 2 (b)).

  doi:10.5075/epfl-298799_978-2-9701614-0-0

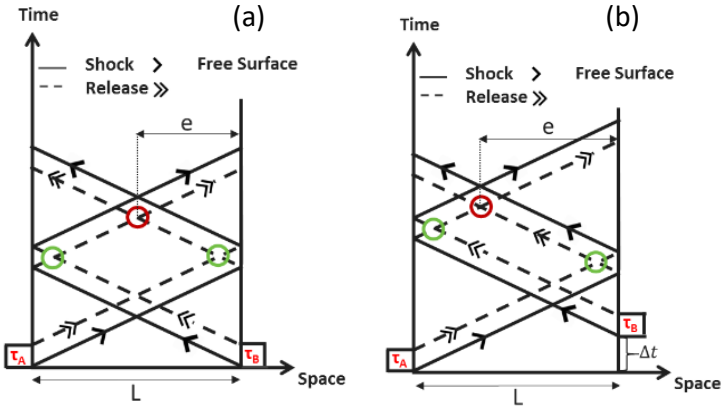

Figure 2 Space time diagram of the shock propagation for symmetrical configuration (a) with both beam synchronized and (b) with a delay Δt. The tensile stresses location are identified with circles.

This work will use this configuration in order to show the laser shock process capability to create on demand delamination into a CFRP laminated composite. The first section will present the experimental set-up and the material characterization under laser shock. Then, the results of delamination displacement and process reproducibility will be presented. Finally, a short conclusion will sum up.

1. Materials and method

1.1 Experimental set-up

The experiments were carried in the Hephaïstos facility, located in the PIMM lab, in Paris. It uses a Thales Gaïa High Power laser that is composed of two Nd:YAG lasers emitting at 532 nm and which beam differ from their polarization. They deliver Gaussian pulses of 7 ns at Full Width at Half Maximum (FWHM) with an energy up to 7 J each. The two laser beams, called A and B, are separated at the entrance of the lab using a polarizer and are directed to impact the target horizontally: beam A from the right and B from the left (Figure 3 (a)). For the purpose of the study, two identical lenses leading to 4.7 mm focal spot were used. The homogenization of the spatial energy distribution was achieved with diffractive object elements (DOE) added at the end of the optical paths. As example, Figure 3 (b) and (c) display the resulting focal spot of beam A and the corresponding the gray values following the white dotted line, showing the top-hat energy distribution.

  doi:10.5075/epfl-298799_978-2-9701614-0-0

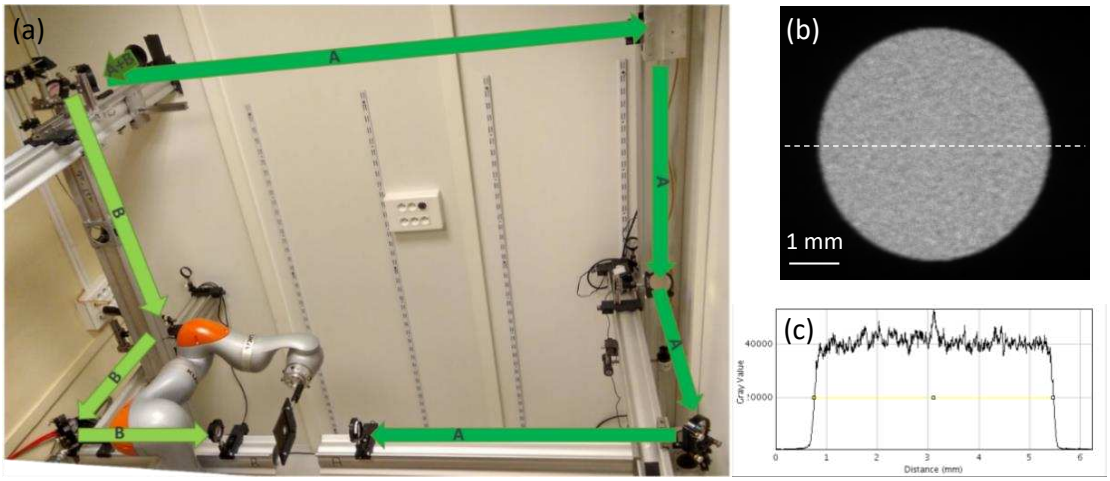

Figure 3 (a) Laser lab 1 in Héphaistos facility for symmetrical shots (b) camera image of a 4.7 mm focal spot (c) grey value top-hat repartition of the focal spot following the dotted line in (b)

The induced on target laser intensity was in between 0.8 and 3.9 GW/cm² per beam. In order to better control the laser mater-interaction and to protect the composite from the ablation, we applied aluminum tape on both sides of the sample. On the top of it, polymer confinement was used [12].

1.2 Materials properties and characterization

The samples studied in this work are laminated CFRP made of 16 layers [0/90] of Hexcel IMA/M21E epoxy resin bought by Airbus and manufactured by Rescoll. Each ply measures about 150 µm and the inter-ply 30 µm, leading a total thickness of 3 mm. The density ρ of the samples is equal to 1580 kg/m^3 and the shock wave propagation velocity in their transversal direction C_0 is equal to 3000 m/s.

The creation of NDT reference standards including delamination with known position and sizes require the ability to create a controlled amount of delamination. For this purpose, we need to characterize the delamination threshold of the composite under symmetrical laser shocks as a function of the irradiation parameters. An experimental campaign of shots was conducted with several laser parameters. As results, Figure 4 displays the delamination area divided by the focal spot area as a function of the laser intensity of each laser beam. The measurement uncertainties, estimated at 10 and 15 % respectively for the defect area and the laser intensity are represented by the black lines. The size of the delamination increases with the laser intensity. To be more precise, this graph highlights three ranges of laser intensity leading to: no ($I < 1$ GW/cm²), one ($1.05 \leq I \leq 1.41$ GW/cm²) or several delamination ($I \geq 1.71$ GW/cm²). In order to obtain one delamination in the reference standard with the irradiation parameters described in section 1.1, one has to select an incident laser intensity in between 1 and 1.5 GW/cm².

  doi:10.5075/epfl-298799_978-2-9701614-0-0

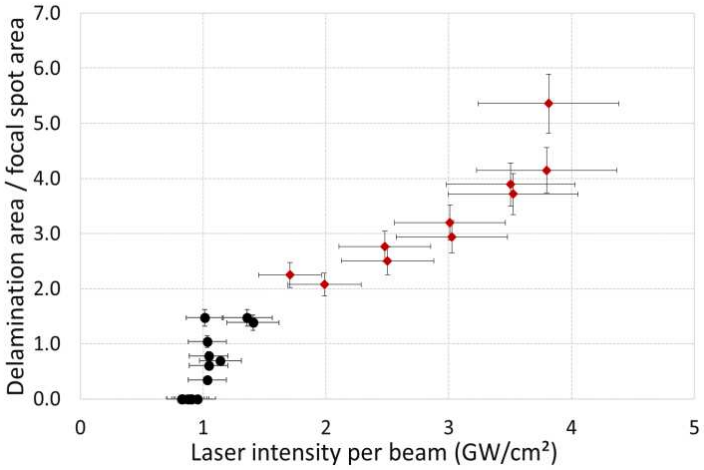

Figure 4 Delamination area/focal spot area as a function of the incident laser power density for CFRP composite of 3 mm

2. Results

2.1 Displacement of the delamination

The depths e of the induced delamination can be moved from Δe, by applying a delay Δt between the two laser beams following the acoustic approximation: $\Delta e = \frac{\Delta t.C_0}{2}$ where C_0 is the shock wave velocity. We shot our samples with delays Δt from 0 to 590 ns. The laser intensity per beam was set to 2 GW/cm², thus leading to secondary delamination on the side of the sample. However, this does not impact our study since we are here interested in the central delamination, induced by the crossing of the two reflected release waves, that are the widest and longest delamination. We measured their position from the surface with three different diagnostics: Computed micro-Tomography (CT) performed at the Soleil synchrotron, cross section observations under microscope and ultrasonic testing (US). The results are gathered in Figure 5, in which we can observe a good agreement between the acoustic model and the experimental results. The discrepancy between the acoustic prevision and the experimental results, and more especially the plateau from 200 and 300 ns, comes from the fact that the delamination appears between two plies. In the case of the sample studied here, the delamination can occur every 150 or 310 µm and not linearly as the model. However, if we take in account the possible position of the delamination, the acoustic approximation enables us to predict which inter-ply will be delaminated as function of the delay of the laser beam.

  doi:10.5075/epfl-298799_978-2-9701614-0-0

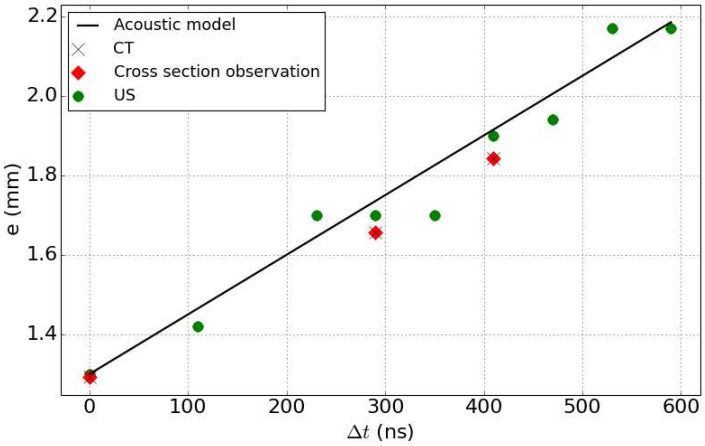

Figure 5 Depth e (mm) of the delamination as function of the delay between the laser beam Δt (ns) measured by three experimental methods, compared with the acoustic prediction (black line)

2.2 Process reproducibility

The previous paragraph showed our capacity to master the laser parameters to create a single delamination in a controlled location through the sample's depth. In order to show the reproducibility of the process, a high number of shots leading to the same results are required. For this purpose, we chose to induce an airplane-shaped delamination in a 10 x 10 cm² sample. We decided to delaminate the fuselage in one depth of the sample and the engines in another. We used the same focal spot, sacrificial layer and confinement medium as for the previous work. From the results of Figure 3Figure 4 and Figure 5, we set the laser intensity to 1.4 GW/cm² and the delay between the beam to 0 ns for the fuselage and 410 ns for the engines. The propagation of the delamination with the use of a laser intensity higher than 1.5 GW/cm² leading to several delamination, we chose to induce the delamination shape with a series of 79 contiguous shots. After the shots, the sample (Figure 6 (a)) was inspected with ultrasonic testing in immersion mode at Airbus, resulting in cartographies of the waves' time of flight (Figure 3Figure 6 (b)) and amplitude (Figure 6 (c)).

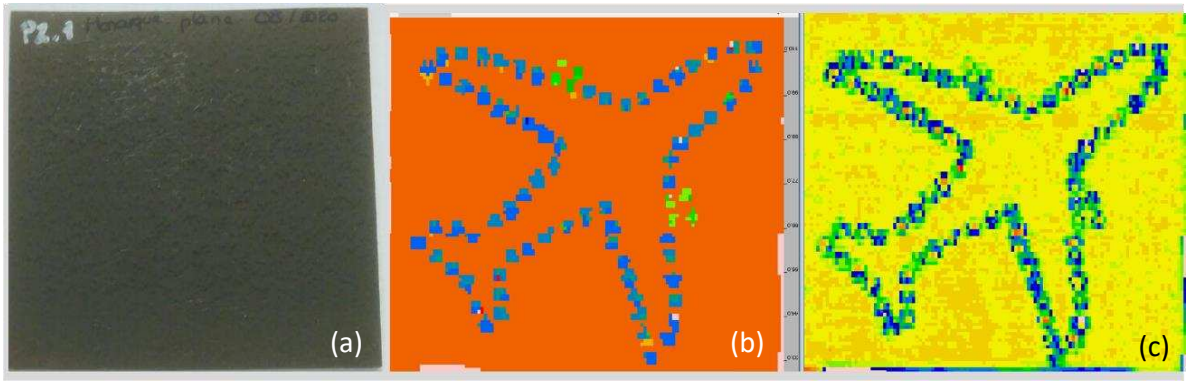

Figure 6 (a) Exterior aspect of the sample after the laser shots. US cartographies of the waves' (b) time of flight and (c) amplitude

From this figure, it is clear that the thermal protection of the composite is efficient: the exterior surface of the sample is spotless. The delamination created with the desired airplane shape is revealed by the US. The time-of-flight and amplitude cartographies are respectively directly proportional to the depth of the defect and its size. The presence of two colors in Figure 6 (b) is

  doi:10.5075/epfl-298799_978-2-9701614-0-0

thus indicating the presence of defects in two locations in the depth. However, the cartography in amplitude shows an even size for the 79 defects (Figure 6 (c)). The process reliability is assessed by the repeatability of the laser shots but also by the consistency of the measurement method. From the A-scan, we systematically measured the amplitude and the time of flight of each US wave reveling a defect and we checked the number of delamination. In total, we extracted 234 measurements for the fuselage and 34 for the engines. We gathered the results in Figure 7. For each shot, only one delamination was detected. The 71 first shots, drawing the fuselage, are detected with US echo's time of flight close to 0.8 µs, corresponding to a defect 1.25 mm from the surface. For the 8 shots creating to the engines, some discrepancies are visible: the US' time of flight varies from 1.2 to 1.1 µs corresponding to delamination 1.88 and 1.72 mm from the surface. A delay of 410 ns between the laser beam, led to the delamination shift of 0.6 mm, as predicted by Figure 5. The creation of a centimetric delamination in two depths of the sample with consistent results for 79 shots shows the capacity of the laser shock to induce on demand delamination.

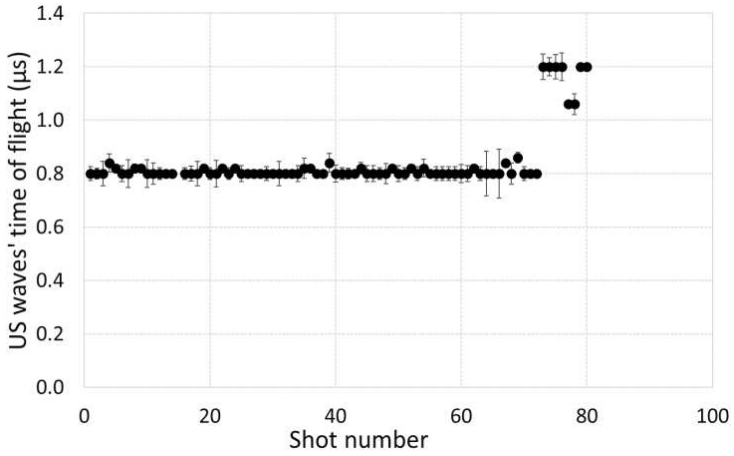

Figure 7 Measurements of ultrasonic waves' time of flight and their standard deviation for each laser shot of Figure 6

Conclusion

In this paper, we showed the mastering of the laser parameter to create real delamination inside a CFRP material. We studied the influence of the incident laser intensity on the number and size of delamination and we identified the range of intensities to be used to induce a single delamination in the composite. The experimental results confirmed a simple acoustic model for the prediction of the delamination displacement accordingly to the delay between the laser beam, permitting the selection of the inter-ply to delaminate. The process demonstration was finally achieved with the creation of a centimetric airplane shaped delamination made of 79 consistent laser shocks, with the fuselage and the engines separated from 0.6 mm in the depth. Each of the laser shot produced one and only one delamination, as required for a reference standard.

Further work should now focus on the realization of delamination with different shapes, positions and their feasibility in sample thicker than 3 mm or made of different materials. The acoustic model we proposed and the understanding of the waves' propagation is very simple and should be completed by numerical simulation.

  doi:10.5075/epfl-298799_978-2-9701614-0-0

Acknowledgements

Those researches were financially supported by the FUI Monarque project.

3 References

1. Ghrib M, Berthe L, Mechbal N., Rébillat M, Guskov M, Ecault R, & Bedreddine N. Generation of controlled delaminations in composites using symmetrical laser shock configuration. Composite Structures, 171, 286-297. 2017.
2. Sagnard M, Ecault R, Touchard F, Boustie M, & Berthe L. Development of the symmetrical laser shock test for weak bond inspection. Optics & Laser Technology, 111, 644-652. 2019.
3. Scius-Bertrand M, Videau L, Rondepierre A, Lescoute E, Rouchausse Y, Kaufman J, ... & Berthe L. Laser induced plasma characterization in direct and water confined regimes: new advances in experimental studies and numerical modelling. Journal of Physics D: Applied Physics, 54(5), 055204. 2021.
4. Xu Y, Zhu J, Wu Z, Cao Y, Zhao Y & Zhang W. A review on the design of laminated composite structures: constant and variable stiffness design and topology optimization. Advanced Composites and Hybrid Materials, vol. 1, 09. 2018.
5. Airbus. A350 xwb family. https ://www.airbus.com/aircraft/passenger-aircraft/a350xwbfamily/a350-1000.html, accessed : 10/2021.
6. Airbus. Airbus to showcase, the a350 1000 for the first time in russia during the maks 2021 international aerospace show. https ://www.airbus.com/newsroom/pressreleases/en/2021/07/airbus-to-showcase-the-a3501000-for-the-first-time-in-russia-during-themaks-2021-international-aerospace-show.html, accessed : 10/2021.
7. Askaryon G A & Morez E. Use of laser generated shocks to improve metals and alloys. JETP LETT, vol. 16, p. 1638. 1963.
8. Mora P. Theoretical model of absorption of laser light by a plasma. Physics of Fluids, vol. 25, no. 6, p. 1051–1056. 1982.
9. Ambartsumyan R, Basov N, Boiko V, Zuev V, Krokhin O, Kryukov P, Senat-Skii Y & Stoilov Y. Heating of Matter by Focused Laser Radiation. Soviet Journal of Experimental and Theoretical Physics, vol. 21, no. February, p. 1061. 1965.
10. Fabbro R, Fournier J, Ballard P, Devaux D & Virmont J. Physical study of laser-produced plasma in confined geometry. Journal of Applied Physics, vol. 68, no. 2. 1990.
11. Sollier A. Etude des plasmas générés par interaction laser-matière en régime confiné : application au traitement des matériaux par choc laser. Phd. 2002
12. Le Bras C, Rondepierre A, Seddik R, Scius-Bertrand M, Rouchausse Y, Videau L, … & Berthe L. Laser shock peening : toward the use of pliable polid polymers for confinement. Metals, vol. 9, no. 7. 2019.

  doi:10.5075/epfl-298799_978-2-9701614-0-0

PRESSURE RESISTANCE CHARACTERISATION OF MICRO-VASCULAR NETWORKS EMBEDDED IN CARBON COMPOSITES FOR HIGH ENERGY PHYSICS APPLICATIONS

Matheo Dias[a,b], Diego Alvarez Feito[b], François Boyer[b], Andrea Catinaccio[b], Corrado Gargiulo [b], Philippe Olivier[a]

a: Institut Clément Ader (ICA), Université de Toulouse, CNRS, France
b: Detector Technologies Group, European Organization for Nuclear Research (CERN), Switzerland

Abstract: *In state-of-the-art trackers such as those installed in the experiments at CERN's Large Hadron Collider, lightweight composite structures provide the main heat path between the silicon modules and a network of metallic or plastic pipes containing a cooling fluid. However, the performance targets of future High Energy Physics (HEP) experiments call for even lighter and more efficient technologies. In this respect, the use of sacrificial materials to create micro-vascular networks in the composite laminates represents a very appealing solution to integrate the cooling circuit in the support structure. Yet, despite the potential advantages in material budget, thermal performance and mechanical stability, the difficulties to predict the pressure resistance and long-term leak tightness of the embedded networks hinder their application in detector areas where reliability is paramount. In this work, both experimental and numerical methods have been used to investigate the pressure resistance of channels embedded in carbon composite laminates.*

Keywords: Tracking detector; Lightweight support; Micro-channels; Cooling; Pressure resistance

1. Introduction

Carbon composite materials are ideal candidates for High Energy Physics (HEP) applications due to their low density, high stiffness-to-weight ratio, and excellent thermal properties. They are widely used in the support structures of tracking detectors, where they play a key role in the thermal management of the silicon sensors and readout electronics [1][2]. In state-of-the-art trackers such as those installed in the experiments at CERN's Large Hadron Collider, lightweight composite structures provide the main heat path between the silicon modules and a network of metallic or plastic pipes containing a cooling fluid. However, despite the good results obtained with this approach, the performance targets of future HEP experiments call for even lighter and more efficient technologies. In this respect, the use of sacrificial materials to create micro-vascular networks in the composite laminates represents a very appealing solution to integrate the cooling circuit in the support structure. Yet, despite the potential advantages in material budget, thermal performance and mechanical stability, the difficulties to predict the pressure resistance and long-term leak tightness of the embedded networks hinder their application in detector areas where reliability is paramount.

In this work, both experimental and numerical methods have been used to investigate the pressure resistance of channels embedded in carbon composite laminates. Modified poly(lactic) acid (PLA) preforms have been combined with a post-cure vaporization technique to

  doi:10.5075/epfl-298799_978-2-9701614-0-0

manufacture plates with longitudinal channels [3]. Destructive tests have been carried out to determine the burst pressure of the plates as a function of the layup and the cross-section geometry of the channels. The deformation of the composite plates during the tests has been monitored using Digital Image Correlation (DIC).

In parallel, a finite element model has been developed to predict the resistance of the plates, relying on cohesive elements to simulate the failure of the channels subject to internal pressure. Experimental delamination results obtained with mode I double cantilever beam (DCB) test specimens have been used to determine the input parameters for the numerical model.

2. Experimental

2.1 Manufacturing of the different samples

Among the different processes used in literature [3][4][5] to produce embedded channels inside carbon composite materials, the Vaporization of Sacrificial Component (VaSC) has been used in this study. Contrary to other disturbing material methods [5] and to have a large flexibility in networks design, the choice was made to use the removal of a modified poly(lactic) acid (PLA) preform material (fibres or thin plates). This modified PLA vaporizes at a temperature of 200°C in a vacuum oven.

The following manufacturing process has been used to produce the embedded channels:

- A first lamination step where PLA preform was placed in between prepreg plies. Depending on the configuration, the stack-up can be defined as [3 or 4 plies / PLA / 3 or 4 plies] with an orientation of plies of 0° and 90°.
- Then a polymerization step of the laminate occurred in an autoclave with the cycle pressure up to 4 bar, 30min at 80°C and 3 hours at 135°C with a 2°C/min heating rate.
- The final step was the vaporization of PLA preform in a vacuum oven at 200°C for 15 hours and the cleaning of generated channel with dry air injection.

The laminate specimens were produced from T800/ER450 unidirectional prepreg provided by CIT composite material and the modified PLA preforms were provided by CU Aerospace company [6]. Before the vaporization step, a thermogravimetry analysis has been performed to verify the vaporization temperature of the modified PLA. Figure 1a shows the changes in the PLA mass as a function of the temperature. At 200°C, the PLA sample has lost 95% of its mass which is also the recommended vaporization temperature specified by the company.

To allow designing structures with embedded channels, a systematic test campaign has been leaded to characterize the pressure resistance of the channels in function of the channel size, the shape, and the specimen stack-up. The samples were made with a mould to produce symmetric plates of 300mm long and 60mm width. The plates produced were cut in two test samples of 130mm. Samples with three different channel shapes produced with 1.75mm PLA fibres and three different stack-up has been tested. Channel geometries were generated by an assembly of two or three fibres (see Figure 1b). All the configurations are summarized in Table 1. X-rays microtomography analysis has been performed on each carbon plate after the PLA vaporization step to observe the geometry and verify that all the channels are open and clean (see Figure 1c).

  doi:10.5075/epfl-298799_978-2-9701614-0-0

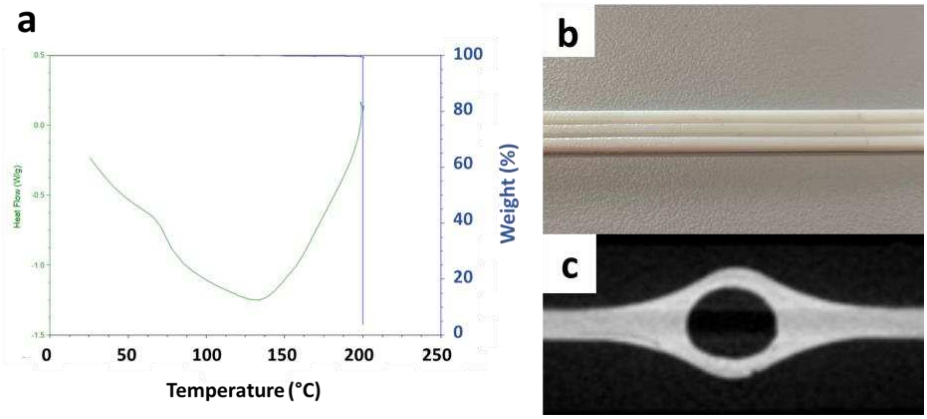

Figure 1. (a) Thermogravimetry of modified PLA material provided by CU Aerospace. (b) Assembly of three PLA fibres of 1.75mm diameter each. (c) X-ray tomography view of the cross section of $[0,90,0]_s$ laminate with a single 1.75mm diameter channel.

Table 1. Samples configurations used for the pressure characterization and designation defined for this article.

Layup \ PLA fibres	●	●●	●●●
$[\mathbf{0},\mathbf{90},\mathbf{0}]_s$	A1	A2	A3
$[\mathbf{90},\mathbf{0},\mathbf{90}]_s$	B1	B2	B3
$[\mathbf{0},\mathbf{90},\mathbf{90},\mathbf{0}]_s$	C1	C2	C3

2.2 Testing setup

Connecting the produced samples to the pressure test system (see Figure 2a) was a challenge. This will be even more challenging to find a solution for a use inside the futures detectors. The solution selected was a use of stainless-steel needles glued on the composite samples in one side and in a PEEK tube in the other side (see Figure 4b). The PEEK tube was then connected to pressure test system with a ferule mechanism. The PEEK tube is supposed to resist up to 276 bar (27.6 MPa). While they were put under an internal pressure, the out of plane displacements of the laminates (perpendicular to surface) were measured owing to a Digital Image Correlation (DIC) system (see Figure 3c). A manual pump was used to put samples under water pressure while recording pressure versus time curves.

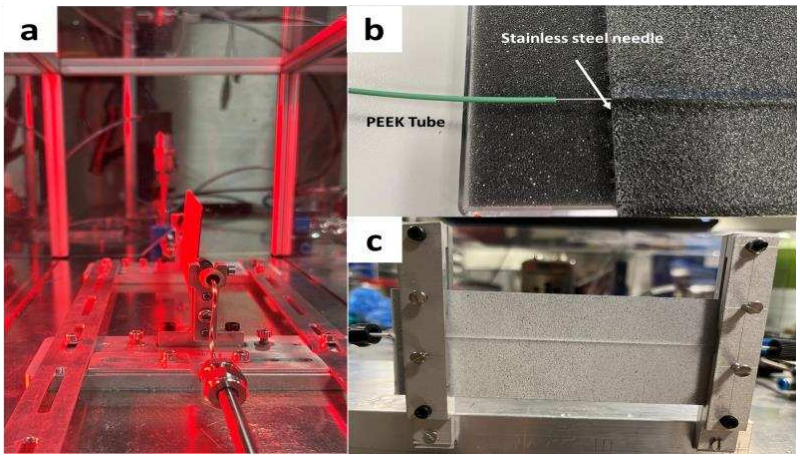

Figure 4. (a) Pressure characterization setup. (b) Parts of fluidic connector before gluing. (c) Support to maintain samples for Digital Image Correlation.

3. Numerical studies

3.1 Finite element. Model and assumptions

A numerical model has been developed with Abaqus to simulate the fracture of the composite material induced by the internal pressure inside the micro-channel. Cohesive elements have been used to simulate numerically the fracture process. Effectively, it is assumed that the internal pressure applied in micro-channels will induce a delamination of the laminate mid plane. In addition, another assumption was made about the microstructure of the laminate near the micro-channel. Effectively in the case of a 90°/90° interface it is hypothesized that an unreinforced resin area appears around the laminate mid-plane (see Figure 8b). This means that the micro-channel axis forms a 90° angle with the reinforcement fibres of the two 90° plies located around the micro-channel. Consequently, the assumption made was the laminate break first begins in the resin pockets. Thus, the cohesive zone elements were then placed on the middle of the laminate section (as shown in Figure 5). Samples are breaking when the first cohesive layer is fully damaged.

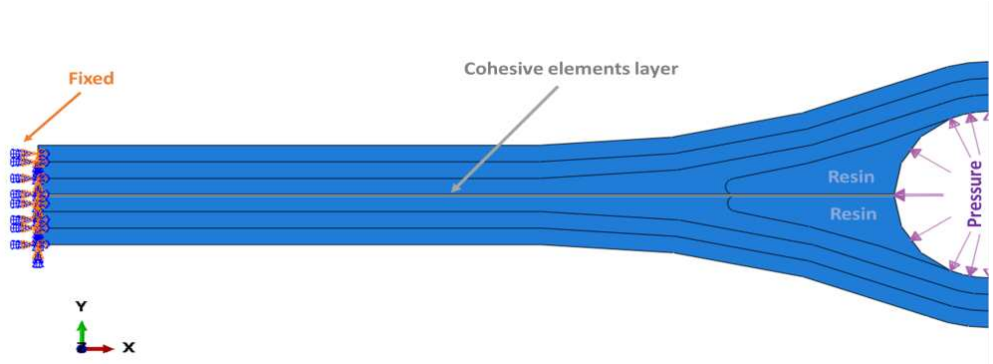

Figure 5. Abaqus half-model of a 1.75mm diameter channel embedded in a $[0,90,0]_s$ *laminate showing boundary conditions, loading, and cohesive elements layer.*

3.2 F.E.M. calibration

The cohesive elements properties have been determined owing to a mechanical characterization of the T800/ER450 prepreg. A Double Cantilever Beam (DCB) tests campaign has been carried out on samples with 0°/0° interfaces according to ISO 15024. Results of the tests are given on Figure 6 and provide the mode I interlaminar fracture toughness (G_{Ic}) of 455 J/m².

Then a mechanical test campaign has been carried out to assess the mechanical properties of T800/ER450 laminates. Tensile tests were performed on unidirectional samples of $[0°]_8$ and $[90°]_{16}$ according to NF EN 2561 and NF EN 2597. $[45°]_{16}$ samples have been tested according to ISO 14129. Table 2 summarizes the obtained results.

  doi:10.5075/epfl-298799_978-2-9701614-0-0

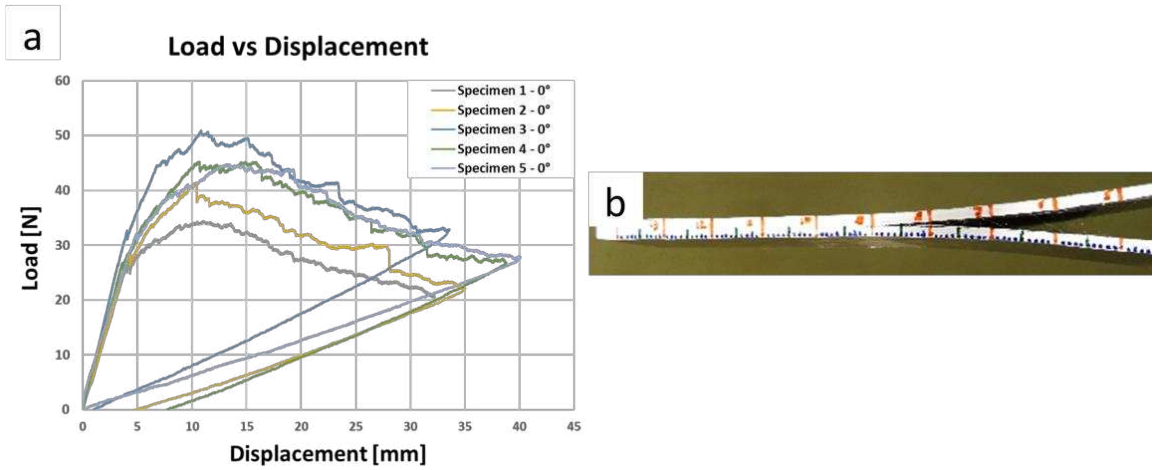

Figure 6. (a) Results of the Double Cantilever Beam (DCB) test campaign with 0°/0° interface (b) DCB specimen being tested.

Table 2. Mechanical properties obtained for a T800/ER450 laminates.

Fiber orientation	Properties	Value
45°	Maximal load [N]	3953 ± 140
	In-plane shear strength [MPa]	36.5 ± 1.6
	In-plane shear modulus [GPa]	3.5 ± 0.1
90°	Tensile strength [MPa]	46.8 ± 3.8
	Elastic modulus [GPa]	7.4 ± 0.7
0°	Tensile strength [MPa]	1188 ± 4.5
	Elastic modulus [PGPa]	64.21 ± 0.7

The cohesive law has been then calibrated with a DCB simulation and compared to experimental and analytical results to assess stiffness and maximal stress of the cohesive elements (*Table 3*).

Table 3. Material properties used to define cohesive elements bilinear law in Abaqus

Abaqus property	Value
Max Stress Damage [MPa]	6
Fracture energy [mJ/mm²]	0.5
Normal stiffness Enn [MPa]	18.5E+6
Shear stiffness Ess [MPa]	15E+6
Tangential stiffness Ett [MPa]	15E+6

Results obtained from mechanical properties and DCB characterization were then applied to the model described in Section 3.1. As an example, numerical results of the cohesive elements damage for configuration A1 is given in Figure 7 and evaluated scalar stiffness degradation of the cohesive element (SDEG). When the value reach 1, the element is fully damaged.

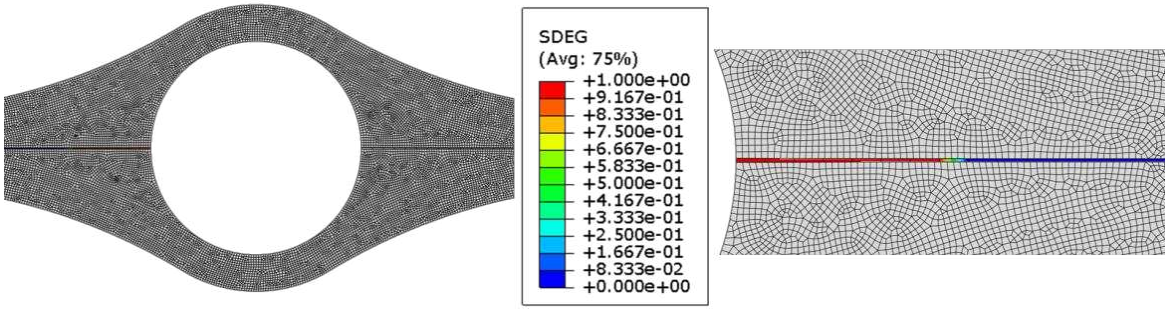

Figure 7. Abaqus numerical results of the cohesive element damage for configuration A1 (left) and a focus on the cohesive elements layer (right).

4. Results and discussions

Microscope images were made on specimens with different channel shapes to analyse the laminate microstructure near the channel (see Figure 8). For a 0°/0° interface around the PLA fibres, it was noticed that the fibres migrate in the supposed resin pockets (Figure 8a). As expected, for a 90°/90° interface the region near the channel is full of resin (see Figure 8b).

In the case of the 0°/0° interface the migration of fibres was not expected, and it is important to consider this phenomenon and implement it in the numerical model. In fact, this presence of fibres should have an influence on the numerical model because the DCB test campaign results are not applicable in this situation where the interface is composed of a specific fibre/matrix ratio. Work is ongoing to determine this ratio with microscope analysis and a modified DCB test is being developed to characterize this specific interface.

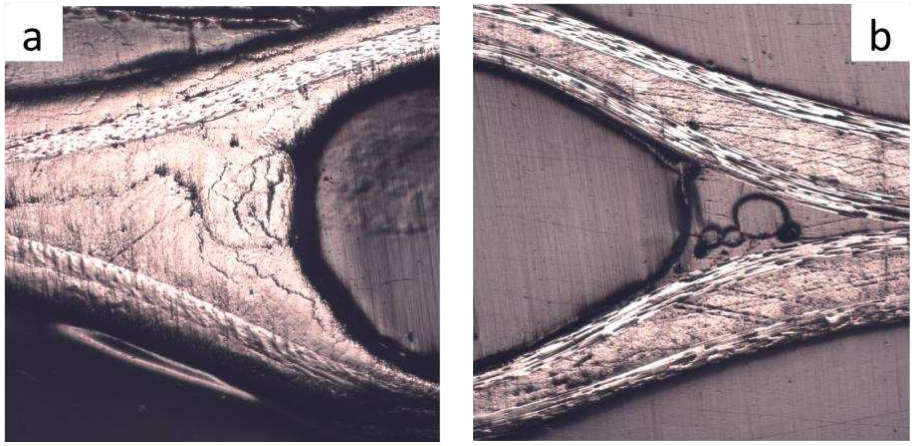

Figure 8. (a) Microscope views of the cross section of $[0,90,0]_s$ *laminate with 1.75mm diameter channel. (b) Same view of a* $[90,0,90]_s$ *laminate.*

Pressure tests campaign provided some tendances curves for different channel shapes, dimensions and stack-up. Results of tests campaign are gathered in Figure 9 . In this figure, the pressure recorded at the onset of the very first recorded leak for configuration A1 to C3 is plotted as a function of micro-channel width. Configuration B1 (Table 1) reached a maximal value of pressure drop around 90 bar (0.9 MPa) and was the most pressure resistant between the different configurations. The 90°/90° interface around the micro-channel seems to provide a better fracture resistance even if the 0°/0° interface contains fibres in the eyes located around laminates mid-plane at micro-channel vicinity. Configuration C is also more pressure resistant

than configuration A. This is coherent because both have the same interface, but configuration C has more plies (8 plies instead of 6 for configurations A1 to B3).

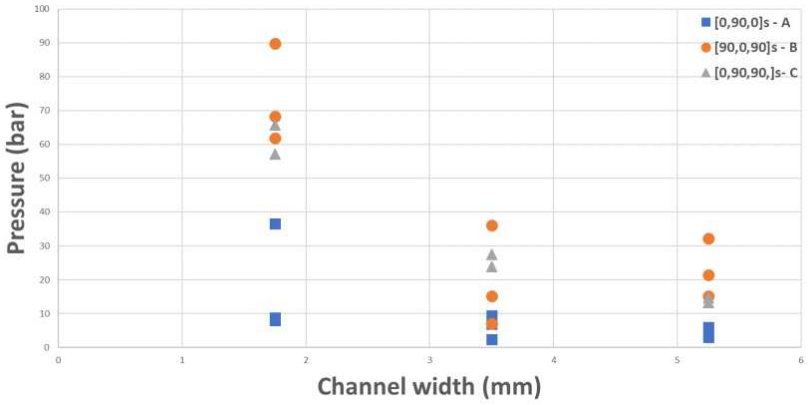

Figure 9. Results of pressure test campaign for channels produced by assembling one, two or three 1.75mm diameter PLA fibres.

The monitoring of the pressure tests with DIC allowed to access the displacement of the samples during the test phase (see Figure 10a and Figure 10b) and the failure location (see Figure 10b to Figure 10d).

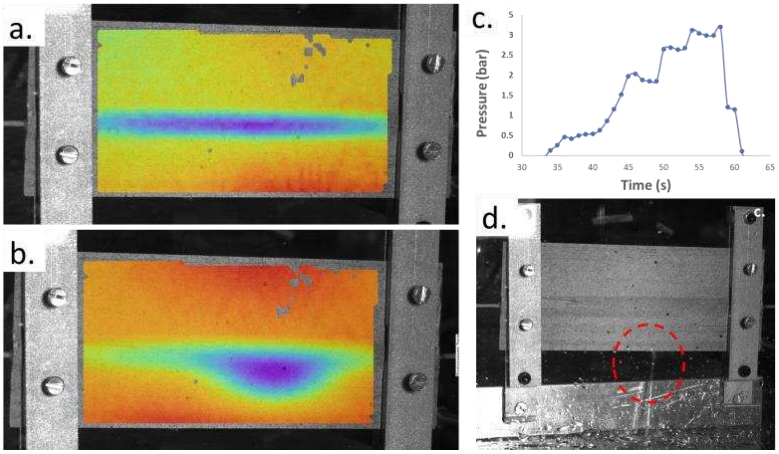

Figure 10. (a) DIC results –out-of-plane displacement – for configuration A1 just before failure. (b) Same DIC result at failure. (c) Corresponding Pressure versus Time curve for configuration A1. (d) Image of the A1 configurations sample at failure showing water jet.

The numerical model developed with cohesive elements seems to be relevant for assessing the channels failure. Results from simulation tend to confirm the better pressure resistance of 90°/90° interface (see Figure 11a). Configuration B is the closest from the numerical model results and is also fitting the best the numerical model assumptions. Indeed, we experimentally observed the presence of resin pockets for these samples (see Figure 8b), thus the material characterisations are well adapted. Compared to the DIC results the model is underestimating the displacement at failure of the channel (see Figure 11b). It can be noticed that if the 90°/90° interface tend to be more pressure resistant, displacement at failure seems to be higher too.

This numerical model developed provides a good estimation of the pressure resistance. Some improvements will be done on better boundary conditions and on a new fracture energy that takes in account the fibres/matrix ratio in the pocket region for 0°/0° interface.

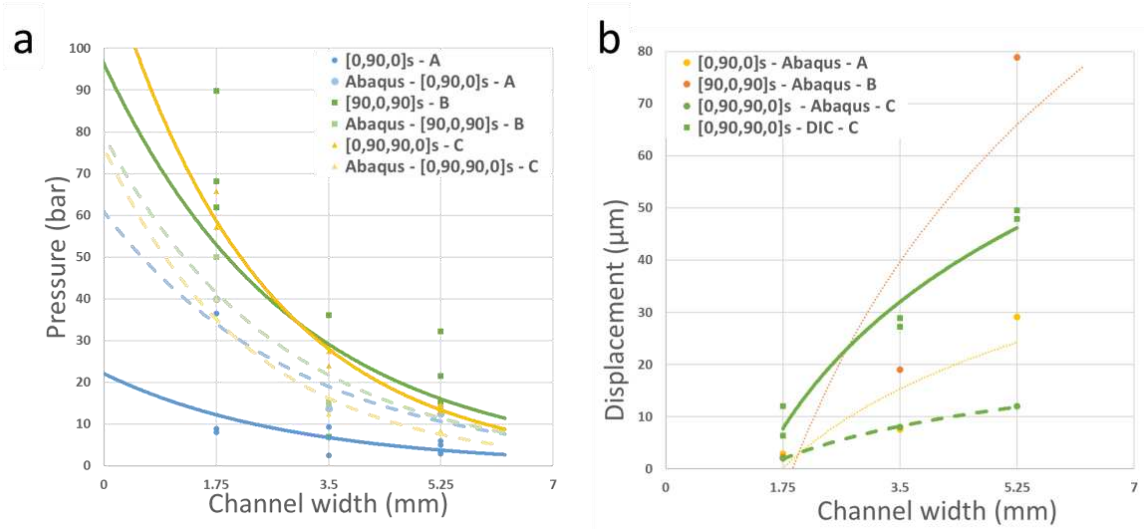

Figure 11. (a) Pressure tests results on channels made with 1.75mm fibres compared with Abaqus simulations. (b) DIC experimental result for $[0,90,90,0]_s$ *stack-up samples compared with Abaqus simulations.*

5. Conclusions

In this study, pressure characterization of manufactured laminates with embedded channels has been experimentally performed. The results obtained in addition with the DIC monitoring allow a comparison with a numerical model made with cohesive elements. If the manufacturing process of samples and the numerical model needs improvements, the methodology of characterization seems promising. More tests will be performed with different channel shapes.

In respect with the current results obtained, meet the 250 bar pressure resistance needed for a use in HEP while minimizing the material budget will require some near channel reinforcements. Some technological solutions are already envisaged.

6. References

[1] The ATLAS collaboration, CERN, 2017. Technical Design Report for the ATLAS Inner Tracker Strip Detector, 1 avril 2017.

[2] Detector technologies Group (EP-DT), 2019, Annual report 2019, Juillet 2020.

[3] Stephen J. Pety, Marcus Hwai Yik Tan, Ahmad R. Najafi, Philip R. Barnett, Philippe H. Geubelle, Scott R. White. Carbon fibre composites with 2D microvascular networks for battery cooling. International Journal of Heat and Mass Transfer, Volume 115, Part

[4] McElroy M. W., Lawrie A., Bond I. P. (2015), Optimisation of an air film cooled CFRP panel with an embedded vascular network, NASA Langley Research Center & University of Bristol.

[5] M. Demiral, H. Tanabi, B. Sabuncuoglu, Experimental and numerical investigation of transverse shear behavior of glass-fibre composites with embedded vascular channel, Composite Structures, Volume 252, 2020, 112697, ISSN 0263-8223, https://doi.org/10.10

[6] CU Aerospace, 2021. VASCTECH [en ligne]. [Consulté le 29 juin 2021]. Disponible à l'adresse : http://www.vasctech.us/Products

THE PERFORMANCE OF FLAX REINFORCED COMPOSITES FOR WIRELESS AND SPORT APPLICATIONS: NATURAL ADDITIVES AND SANDWICH CONCEPTS

Pauli, Hakala[a], Farzin, Javanshour[a], Juha, Jordan[b], Päivi, Laaksonen[b], Lauri, Jutila[c], Jan, Järveläinen[d], Mikko, Kanerva[a]

a: Tampere University, Faculty of Engineering and Natural Sciences,
Materials Science and Environmental Engineering, Finland
Corresponding author: M.K. (mikko.kanerva@tuni.fi)
b: Häme University of applied sciences, Finland
c: CSI - Composite Solutions and Innovations Oy, Finland
d: Premix Group, Finland

Abstract:

In this study, flax reinforced composites are studied for their long-term performance in terms of electromagnetic signal attenuation and mechanical performance. The use of flax fibres and rosin are studied for applications of natural fibre reinforced composites with antimicrobial features. The thermoplastic matrix used is polylactic acid (PLA) and the thermoset matrix used is a partly biobased epoxy. Laminates are prepared for accelerated algae growth (AG) studies (42 days, Klebsormidium flaccidum) and rain-ultraviolet (340 nm, rain, 18 days) ageing conditioning. The signal attenuation at the range of ultra-high frequencies (2.5 GHz) is measured using the split-disk dielectric resonator (SPDR) method. The results indicate that the flax reinforcement is the main source of degradation whether attenuation or mechanical performance is considered.

Keywords: flax; pine rosin; soil burial; algae; signal attenuation

1. Introduction

1.1 Natural components in advanced fibrous composites

Natural fibre reinforced composites (NFRC) are applied in ever wider application areas. Therefore, the functionalities, e.g., attenuation to electromagnetic signals in wireless applications [1,2] along with bonding characteristics in sandwich concepts are important. For this, the design and processing methods require in-depth studies. Especially the long-term mechanical durability combined with functional performance are not known well. Moreover, the use of polymer composites often requires additives to be used. The reason for using additives can be to improve fire resistance or dimensional stability as well as to minimize microbial and ultraviolet (UV) degradation within long-term environmental conditions. For NFRC, these targets are ever more important. Especially moisture can be detrimental to NFRC where the reinforcement is typically hydrophilic and fibre treatments should modify the compatibility with moisture and wetting by polymeric resins [3]. Moisture can result in changes in the ligno-cellulosic structure of natural fibres in composites [4]. It is important to note that there are fungal species inside fibres, e.g., flax – inherent because of the dew-retting process, and these fungi can affect the degradation of flax in composite materials [5].

  doi:10.5075/epfl-298799_978-2-9701614-0-0

NFRCs are preferred materials for lightweight structural components where vibration-damping behaviour is of importance [6]. Currently, these components are typical in the industry sectors of infrastructure construction, transportation, and sports gear [7, 8]. In general, NFRCs are seen as ecological alternatives to traditional carbon and glass fibre reinforced composites. To reach truly environmentally friendly but operational efficient products, it is essential to research the long-term durability of NFRCs further.

1.2 Rosins

Pine rosin (RO) is a product of the forest industry and its application to composites, instead of toxic rivals, can prove to be especially advantageous. Rosin is a complex mixture of numerous compounds, and its exact composition depends on the annual variation and plant. It is mainly an amorphous system of rosin acids, lipophilic compounds and phenol extracts. The rosins from conifer trees (e.g., *Pinus pinaster* and *P. sylvestris*) are probably the most typical ingredients studied for antimicrobial applications. The antimicrobial effects of RO are well-known over several fields and products. For medical applications, rosin has been applied in the forms of polymer-blended fibres [9], nano-fibres [10], food packaging films [11] and various tissue applications of medicine [12]. RO has been reported to be a relatively efficient antimicrobial against viruses and bacteria strains, such as *Escherichia coli*, *Streptococcus pneumoniae* and *Salmonella enterica* [13]. In addition, unlike many of the synthetic counterparts, RO can give long-term and weather-resistant effects against human health-endangering bacteria [14] and also resistance against fungi [15]. Animals and insects use rosin in various ways; ants use rosin in their nests, and it has been found to improve the health of the nest [16] – rosin could perhaps be used to adjust fungal-bacterial degradation of natural fibres in human-made structures.

2. Experimentation

2.1 Laminate preparation

The raw materials of this work included components for 1) thermosetting and 2) thermoplastic matrix composite laminates. The reinforcing fibres were flax fibres in the form of fabric (2×2 twill) (200 g/m^2, Biotex). Flax-reinforced composite laminates were prepared by using ≈30% biobased epoxy (Super Sap, Entropy Resins) and vacuum-assisted resin infusion. In details, Super Sap CLR (with CLS hardener) and Super Sap INH, to adjust the viscosity, were used for infusion processing. The laminates were made with a stacking sequence of [0/45]SE. The reinforcement was dehydrated before infusion carefully (80 °C, 1 hour, following 100 °C for 1 hour). The mould had a glass surface and a vacuum bag (Δp = 0.5 bar) was applied over it. The cured laminates were post-cured (80 °C, 2 hours).

Rosin was blended with poly lactic acid (PLA) (2003D, Ingeo, Nature Works) at 200 °C with gum rosin (pine gum rosin, acid value of 167 mg KOH/g, Forchem) by using a twin-screw extruder (TSE 25E, Brabender). For the mixing, the crashed RO-particulates were simultaneously mixed with PLA granulate (≈5% mass/mass rosin). A hot press was used to prepare actual laminates. PLA without and with rosin was used (granulated after extrusion). A metal frame was used to confine PLA (and RO) during pressing at an exact volume. Flax-reinforced PLA laminates were pressed by stacking (pre-pressed) PLA and flax layers (lay-up [0/45]SE) and pressing (180 °C, 100 bar, 5±1 minutes for single layer, 8±0.1 minutes for final layer stack). When RO-blended PLA

  doi:10.5075/epfl-298799_978-2-9701614-0-0

was sued, press temperature was lowered to 160 °C. The flax was dehydrated before the compression moulding (90 °C, 2 hours).

2.2 Soil burial

In this work, applied soil burial conditioning was applied by using a commercial garden composter (220eco, Biolan). For observing the conditions during the burial, the compost was instrumented with two outside measurement points (recording temperature and relative humidity) and two internal sensors (temperature). The compost was built into four sections by using stainless steel (AISI 304) mesh. These sections divided the volume into mechanically separated zones but allowed essentially free flow of moisture and heat. Also, the sectioning allowed to keep rosin-containing samples separated (i.e., no bare specimens below that would be contaminated by possible rosin secretion downwards) but still conditioning by the same microbial medium and conditions. The soil medium was a mixture of low-nutrition commercial garden peat (Biolan) (nitrogen 15 mg/l, phosphorus 100 mg/l, potassium 500 mg/l) and forest humus, leaves, small branches (200/50 (volume/volume) ratio). In addition, 4.8 % (volume/volume) of moisture was applied in steps (water temperature ≈37 °C). The microbial process was boosted by using commercial compost activators mixed within the medium (Multikraft Produktions und Handels) and in water (Neko). It should be noted that rather mild microbial process (and temperature) was targeted to simulate typical household composting process. During the burial, a temperature change of $\Delta T \approx 10$ °C (maximum temperature 16 °C) was recorded.

2.3 Rain and ultraviolet irradiation conditioning

The harsh effects of ultraviolet (UV) irradiation and sequentially applied water (rain) were studied for the NFRC specimens by using a UV-rain chamber Xe-3 (Q-SUN). The applied test sequence of two steps used for cycling are given in Table 1. The total conditioning time was 432 hours (18 days, 2-hour cycles) (see standard ISO 4892-2-2013 for additional information). The size of each laminate piece was 60 mm × 60 mm (nominal thickness 2.6 mm). After the UV-rain conditioning, the dehydrated specimens were transported in plastic bags for attenuation measurements (see Section 2.6).

Table 1: Steps of rain-UV irradiation condition for cyclic environmental conditioning for 18 days

Phase	UV irradiation (340 nm)	Duration	Chamber condition
1	0.39 W/m^2, black panel temperature 63 °C	108 minutes	(≈38 °C, ≈50% RH)
2	(No UV)	12 minutes	Dark, water spray

2.4 Algae growth cabinet

The effects of rosin in the laminates were studied on accelerated algae growth (AG). AG studies covered in total 42 days, using *Klebsormidium flaccidum*, at 90% RH, 25 °C. A small amount of algae was dosed on the laminated specimens, which were then placed inside a specialized conditioning cabinet. The specimens were kept aligned (20°) during the conditioning. Nutrient solution was sprayed on the specimens for 7 seconds at a time (0,3 l/minute) every 3 hours. Carbon dioxide was purged into the cabinet for 5 seconds (8 l/minute) every (1) hour. The red-

  doi:10.5075/epfl-298799_978-2-9701614-0-0

green light was applied for 12 hours in 24-hour cycles. After the algae growth studies, the specimens were transported in plastic storage bags for measurements (see Section 2.6).

2.5 Interlaminar shear strength testing

This work focused on testing laminates under flexural loading using the three-point bending condition (short-beam three-point bending according to ASTM D 2344) to determine interlaminar shear strength (ILSS). The specimens' planar size was 8 mm × 20 mm (nominal thickness 2.6 mm). The target was to emphasize the shearing component of load and to aim at interlaminar failure. A universal testing machine was used to generate the load (electrical 5967, Instron). The ILSS testing was applied for specimens in the reference condition (ambient conditions) and after the soil burial condition. For epoxy (matrix), a support pin span of 9 mm was used. For PLA, a support pin span of 11 mm was used (per recommendations in the standard procedure). A constant displacement rate of 1.0 mm/minute was used for testing.

2.6 Signal attenuation measurements

Signal attenuation at frequencies typical of various 5G applications [1,2] was studied for the different composites before and after AG. Here, the method of split-disk dielectric resonator (SPDR) was used. The SPDR here was used at 2.45 GHz signal generator (QWED) with a Microwave Frequency Q-Meter (QWED). The sample size was 60 mm × 60 mm (thickness 2.5-3.0 mm). The measurements were made at a constant signal frequency of 2.45 GHz for all specimens and sample-specific thickness was measured to determine attenuation (permittivity, loss factor). Measurements were made in ambient room conditions (21 °C, 50% RH).

3. Results and analysis

3.1 ILSS performance of flax reinforced composites after soil burial

The ILSS determined for the reference specimens and after the soil burial (SB) conditions are given in Table 2. Before SB, the composites without rosin have a similar level of ILSS. The composites with RO blended into PLA have 44.5% lower ILSS compared to the reference that might be due to the lower mechanical properties of RO itself. After SB, the loss in the ILSS value of FX-PLA (-10%) is more pronounced compared to the FX-EPX (-3%). The ILSS value of FX-PLA is relatively stable after a period of soil burial which is promising for the long-term performance of composites. The loss in ILSS values for both composite systems after SB can be due to the intrinsic porosity of flax fibres (e.g., lumen) acting as a channel for moisture diffusion and microbial degradation [17]. The drastic decrease (-58%) in the ILSS value of the FX-PLA-RO after the SB period could be due to the porous morphology of specimens.

Table 2: Flexural behaviour in terms of ILSS for flax reinforced composites before and after SB

Series	ILSS before SB (ref)	ILSS after SB (14 days)	Δ ILSS
FX-EPX	18.6 MPa	18.0 MPa	-3.3 %
FX-PLA	18.4 MPa	16.6 MPa	-10.1 %
FX-PLA-RO	10.2 MPa	4.2 MPa	-58.3 %

  doi:10.5075/epfl-298799_978-2-9701614-0-0

3.2 Growth of algae on specimen surfaces

The algae coverage after the AG period of 42 days on the specimen surfaces was essentially similar for the different laminates. It should be noted that surface roughness can affect the algae observed on the surfaces for this type of test arrangement. However, the algae observed on the non-reinforced PLA-RO (smooth surfaces) was similar compared to the reinforced laminates.

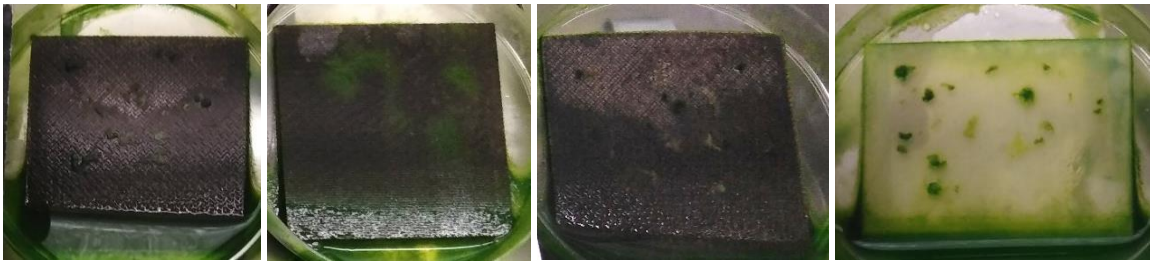

Figure 1. Photographs of laminates applied to AG studies (left to right): series FX-EPX, FX-PLA, FX-PLA-RO, PLA-RO)

3.3 Determined signal attenuation after AG and rain-UV conditioning

The measurement results of attenuation are shown for specimens after the algae growth conditioning (AG) and rain-UV conditioning in Table 3 and Table 4, respectively.

Table 3: Measured permittivity and loss factor before and after algae conditioning.

Series, condition	Permittivity	Δ (vs. ref.)	Loss factor	Δ (vs. ref.)
FX-EPX, ref	3.10	-	0.0871	-
FX-PLA, ref	3.02	-	0.0364	-
PLA-RO, ref	2.73	-	0.0052	-
FX-PLA-RO, ref	2.98	-	0.0351	-
FX-EPX, wet	n/a	n/a	n/a	n/a
FX-PLA, wet	n/a	n/a	n/a	n/a
PLA-RO, wet	6.20	+127%	0.0933	+1707%
FX-PLA-RO, wet	n/a	n/a	n/a	n/a
FX-EPX, dried	3.23	+4%	0.1188	+36%
FX-PLA, dried	3.12	+3%	0.0485	+33%
PLA-RO, dried	2.77	+1%	0.0061	+18%
FX-PLA-RO, dried	3.08	+4%	0.0540	+54%

In Table 3, it can be seen that the addition of the flax reinforcement led to an increase of the value of permittivity and loss factor. These parameters of attenuation were lowest for the non-reinforced PLA-RO series – similarly before AG (reference state) as well as after AG (and

  doi:10.5075/epfl-298799_978-2-9701614-0-0

dehydration) (i.e., dried specimens). The results indicate that algae growth and possible ageing effects permanently affected the loss factor but not the measured permittivity.

The attenuation measurements after the rain-UV conditioning of 432 hours (18 days) are shown in Table 4. Based on the results, it can be seen that the changes (for the dehydrated specimens) are similar to those after the algae growth and conditioning when it comes to the determined level or permittivity. Interestingly, the changes in the loss factor are relatively small except the results for the flax-reinforced rosin-PLA (series FX-PLA-RO), which gained multitudes of more attenuation-affecting ageing during the conditioning (+ ×10). A similar trend among the tested series related to the algae growth and conditioning was seen (+ ×2) in Table 3. Interestingly, the increase in loss factor for the non-reinforced PLA-RO series was low. It seems that the combination of rosin and flax results in electro-mechanical changes due to conditioning by algae or moisture and UV.

Table 4: Measured permittivity and loss after rain-UV conditioning of 18 days.

Series, condition	Permittivity	Δ (vs. ref. in Table 3)	Loss factor	Δ (vs. ref. in Table 3)
FX-EPX, 18 days	3.01	-3%	0.0838	-4%
FX-PLA, 18 days	3.06	-1%	0.0340	+9%
PLA-RO, 18 days	2.70	-1%	0.0054	+7%
FX-PLA-RO, 18 days	2.95	+1%	0.0485	+38%

3.3 Bonding of NFRC laminates to form sandwich panels

Pre-manufactured NFRC laminates can be combined with different core materials to form sandwich panels – these are used to enhance structural properties without increasing weight too much. A practical way of joining laminate skins to core materials also depends on the matrix type in use (see Fig. 2). The pre-manufactured (cured) FX-EPX laminates (with thermoset epoxy resin) need to be joined by using the adhesive bonding method. In this process, the thickness of the panel is controlled with side supports (or alternatively a mould) and a vacuum line can be used to remove trapped air (voids) from the adhesive layer. When using thermoplastic-matrices in skins, i.e., FX-PLA laminates, the laminates were heated in an oven up to a temperature exceeding the softening point (of the matrix) but to stay away from the decomposition temperature of flax (around 200 °C). Following the bonding phase, the panel is next placed in a cooled mould to let the panel cool down evenly and to prevent significant deformation due to residual stresses.

a) 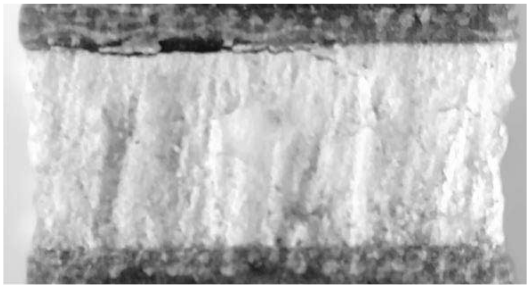 b) 

c) 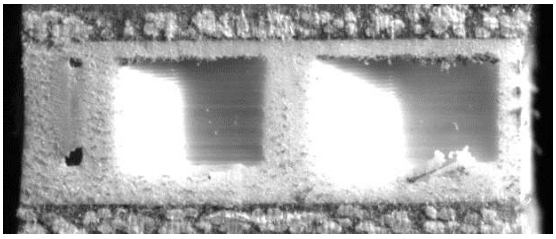 d) 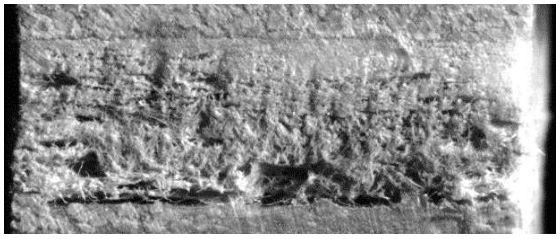

Figure 2. Bonding concepts of NFRCs: a) NFRC bonded to expanded polystyrene (EPS) foam by adhesive bonding under vacuum; b) NFRC to expanded polystyrene (EPS) foam by infusing dry flax fibers directly to core; c) NFRC bonded to PLA 3D-printed honeycomb core by hot-pressing; d) NFRC bonded to foamed cellulose [18] by adhesive bonding under vacuum.

4. Conclusions

This work aimed to study the effects of pine rosin in flax fibre reinforced composites when ageing effects due to soil burial, algae growth and rain-UV are considered. Changes in ultra-high frequency signal attenuation and mechanical performance were determined and reported. The combination of rosin and flax results in changes in composites that requires further research. The laminates in this study included thermosetting (epoxy) matrix composites and thermoplastic (PLA) matrix composites. The results in the study indicated the following outcomes:

- ILSS, measured after 14 days of soil burial and subsequent dehydration before testing, showed significant decrease in flax composites where rosin was blended with PLA.
- Algae (*Klebsormidium flaccidum*) growth was essentially similar on the surfaces of flax reinforced laminates and non-reinforced rosin-blended PLA.
- Signal attenuation after the study of algae growth and subsequent dehydration before testing showed that the algae accumulation and possible ageing of the composites in moist conditions permanently increased the loss factor but no permittivity. Before dehydration, right after algae growth studies, the attenuation was successfully measured only for the non-reinforced rosin-blended PLA.
- Signal attenuation after cyclic rain-UV conditioning over 18 days and subsequent dehydration before testing indicated that the ageing by combined UV irradiation and rain results in permanent increase in loss factor but not in permittivity.

Acknowledgements

This research was supported and funded by different grants from Business Finland (9310/405, 9310/448, 1763/31/2016). M.K. is grateful for the collaborations with P. Laaksonen (at HAMK).

5. References

1. Di Vito D, Kanerva M, Järveläinen J, Laitinen A, Pärnänen T, et al. Safe and sustainable design of composite smart poles for wireless technologies. Applied Sciences (MDPI Switzerland) 2020; 10: 7594.
2. Bangerter B, Talwar S, Arefi R, Stewart K. Networks and devices for the 5G era. IEEE Communications Magazine 2014; 52: 90-96.

3. Thuault A, Eve S, Blond D, Bréard J, Gomina M. Effects of the hygrothermal environment on the mechanical properties of flax fibres. J Composite Materials 2014; 48(14):1699-1707.
4. Yunhong Jian, Lawrence M, Hussain A, Ansell M, Walker P. Comparative moisture and heat sorption properties of fibre and shiv derived from hemp and flax. Cellulose 2018;16: 823-843.
5. Mohanty A, Misra M, Drzal L. Natural Fibers, Biopolymers, and Bio-composites. Baton Rouge: CRC Press. 2005.
6. Awais H, Nawab Y, Amjad A, Anjang A, Akil H, et al. Environmental benign natural fibre reinforced thermoplastic composites: A review. Composites Part C 2021; 4: 100082.
7. Yuan X, Zhu B, Cai X, Liu J, Qiao K, at al. Optimization of interfacial properties of carbon fiber/epoxy composites via a modified polyacrylate emulsion sizing. Applied Surface Science 2017; 401: 414-23.
8. Pil L, Bensadoun F, Pariset J, Verpoest I. Why are designers fascinated by flax and hemp fibre composites? Composites Part A: Applied Science and Manufacture 2016; 83: 193-205.
9. Kanerva M, Puolakka A, Takala TM, Elert AM, Mylläri V, et al. Antibacterial polymer fibres by rosin compounding and melt-spinning. Materials Today Communications 2019; 20: 100527.
10. Kanerva M, Matrenichev V, Layek R, Takala TM, Laurikainen P, et al. Comparison of rosin and propolis antimicrobials in cellulose acetate fibers against *Staphylococcus aureus*. Bioresources 2020; 15(2): 3756-3773.
11. Sipponen A, Peltola R, Jokinen JJ, Laitinen K, Lohi J, et al. Effects of Norway spruce (Picea abies) resin on cell wall and cell membrane of *Staphylococcus aureus*, Ultrastructural Pathology 2009; 33(3): 128-135.
12. Niu X, Liu Y, Song Y, Han J, Pan H, et al. Rosin modified cellulose nanofiber as a reinforcing and co-antimicrobial agents in polylactic acid /chitosan composite film for food packaging. Carbohydrate Polymers 2018; 183: 102-109.
13. Vainio-Kaila T, Hänninen T, Kyyhkynen A. Effect of volatile organic compounds from Pinus sylvestris and Picea abies on *Staphylococcus aureus*, *Escherichia coli*, *Streptococcus pneumoniae* and *Salmonella enterica serovar typhimurium*. Holzforschung 2017;71: 905-912.
14. Kanerva M, Mensah-Attipoe J, Puolakka A, Takala TM, Hyttinen M, et al. Weathering of antibacterial melt-spun poly filaments modified by pine rosin. Molecules (MDPI Switzerland) 2021; 26: 876.
15. Rautio M, Sipponen A, Lohi J, Lounatmaa K, Koukila-Kähkölä P, et al. In vitro fungistatic effects of natural coniferous resin from Norway spruce (Picea abies). European Journal of Clinical Microbiology & Infectious Diseases 2012; 31(8): 1783-9.
16. Chapuisat M, Oppliger A, Magliano P, Christe P. Wood ants use resin to protect themselves against pathogens. Proceedings of the Royal Society B: Biological Sciences 2007; 274(1621): 2013-2017.
17. Melelli A, Pantaloni D, Balnois E, Arnould O, Jamme F, et al. Investigations by AFM of Ageing Mechanisms in PLA-Flax Fibre Composites during Garden Composting. Polymers (MDPI Switzerland) 2021; 13(14): 2225.
18. Ketoja JA, Paunonen S, Jetsu P, Pääkkönen E. Compression Strength Mechanisms of Low-Density Fibrous Materials. Materials 2019; 12(3): 384.

TREATMENTS OF POLYPROPYLENE BICOMPONENT FIBERS TO OPTIMIZE THEIR INTERLOCKING IN CONCRETE BY MICRO- $CACO_3$ PARTICLE ADDITION

Mihaela-Monica, Popa[a], Andreas, Leuteritz[a], Markus, Stommel[a,c], Viktor, Mechtcherine[b], Christina, Scheffler[a]*

a: Leibniz-Institut für Polymerforschung Dresden e. V. (IPF), Dresden, Germany – popa@ipfdd.de
b: Technische Universität Dresden, Institute of Construction Materials, 01062 Dresden, Germany
c: Technische Universität Dresden, Institute of Materials Science, 01062 Dresden, Germany - scheffler@ipfdd.de

Abstract: *Strain-hardening cement-based composites (SHCC) denote a type of fiber-reinforced concrete that exhibits multiple fine cracks under increasing tensile loading. Reinforcement with short polymer fibers is essential to promote the concrete ductility under dynamic loading, since the fiber and fiber-concrete interaction strongly contribute to the energy absorption. PP fibers are of special interest, because they increase ductility, are inexpensive, widely available and recyclable. The principle feasibility of the manufacturing of bicompontent fibers revealing natural $CaCO_3$ particles in their shell were shown in our previous work. Further studies are now accomplished by melt-spinning using synthetic $CaCO_3$ particles in order to increase the surface roughness. The mechanical fiber performance and particles size distribution along the fiber surface were characterized, as well as the fiber-concrete interaction during single fiber pull-out tests in dynamic mode. The particle addition lead to significant improvement of the fiber-matrix mechanical interlocking compared to a reference commercial monocomponent PP fiber.*

Keywords: bicomponent fibers; PP fibers; melt-spinning; single fiber pull-out; loading rate.

1. Introduction

Strain-hardening cement-based composites (SHCC) are a particular category of fiber-reinforced concretes which generate considerably fine cracks when subjected to rising tensile loading [1]. Common SHCC is constructed employing high-performance poly(-vinyl alcohol) (PVA) fibers, usually up to 2% by volume [2]. However, other polymeric fibers such as high-density polyethylene (HDPE) or aramide fibers are efficacious in supplying ductile failure behavior and high strain capacity, though they induce high prices. Polypropylene (PP)-fibers are among the most extensively utilized polymers for fiber-reinforced concrete applications [3, 4, 5, 6]. The insufficient adhesion of typical high tenacity PP fibers can be described based on their low surface energy (hydrophobic character) and their smooth surface [7]. Nonetheless, they are available at a low cost, stable in a high alkaline environment, and chemically absolutely inert. Even with a low modulus of elasticity, PP fibers can remarkably improve the ultimate flexural

  doi:10.5075/epfl-298799_978-2-9701614-0-0

strength, in distinction to that of the non-reinforced matrix; the strength increase being supplemented by extensibility and impact resistance improvements [8].

Besides using pure polypropylene fibers or PP with different chemical surface modifications, the manufacturing of the bicomponent fibers was found to be a promising new approach to overcome the low mechanical properties and smooth surface roughness of pure PP fibers. Naeimirad et al. reported in his investigations about the manufacturing of bicomponent fibers revealing a fiber core made out of polypropylene and it was adjusted to enhance Young's modulus and tensile strength; the interfacial bond was enhanced by adding nanoparticles, fly ash, and glass beads in addition to the polyethylene in the fiber shell [10]. Also the incorporation of $CaCO_3$ particles has been proven to provide beneficial effects on compressive strength, tensile strength and ductility [9]. Since $CaCO_3$ is known for its good workability in polymer processing it was selected to be incorporated in the outer PP-shell in the current work.

In our earlier investigations [11], the monocomponent PP-fibers properties were adapted regarding draw ratio during fiber manufacturing using lab-scale spinning equipment at IPF, diameter, cross-sectional shape, tensile strength, Young's modulus, and also fiber surface treatment. Micromechanical evaluation on single-fiber composites revealed high energy absorption for PP-fibers with high tensile strength in combination with high surface roughness. The established conclusions derived procedures for a new bicomponent fiber configuration to improve the mechanical interlocking between fiber surface and matrix material.

The current work aims to study the feasability of manufacturing of new developed polymeric bicomponent fibers containing different amounts of natural $CaCO_3$ particles in the fiber shell to enhance mechanical interlocking with the concrete matrix, that will induce plastic surface deformation during fiber pull-out during composite crack-briding.

2. Materials and methods

2.1 Materials

The core-shell bicomponent fiber was spun using a commercially available polypropylene (PP: HG 450 FB, Borealis). In addition, the PP was blended with standard natural calcium carbonate ($CaCO_3$) particles for spinning the fiber shell to obtain a homogeneous mix. The $CaCO_3$ micro-particles (OMYAFIBER 800-OM) with a size of 2 µm were delivered from Omya, Germany.

The single-fiber model composites were prepared to determine fiber-matrix interfacial properties through pull-out tests at the single-fiber level, using a cementitious matrix system designed for research purposes (described in [11, 12, 13]) with no large aggregates, provided by the partners from TU Dresden, Institute of Construction Materials

2.2 Fiber manufacturing

Core-shell polymeric fibers (as schematically displayed in Figure 1) were spun in IPF by an inhouse designed and built laboratory-scale piston spinning device [13].

  doi:10.5075/epfl-298799_978-2-9701614-0-0

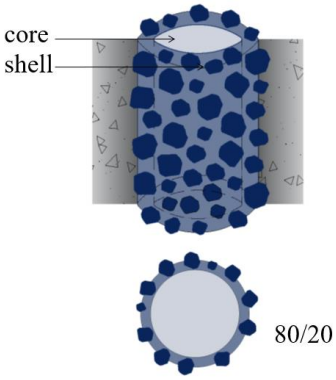

Figure 1. Schematic drawing of a bicomponent fiber with particle shell in concrete matrix and 80/20 core/shell ratio

Various volume percentages of $CaCO_3$ particles were blended with PP operating a microcompounder (DSM Xplore 5&15 Micro Compounder); they blended PP was employed during melt-spinning to create the fiber shell. Before manufacturing the fibers, the blend was pelletized to facilitate the melt-spinning process.

The fiber core and shell polymers were molten in individual screw extruders and spun into a single-hole die with 0.50 mm core - 0.80 mm shell diameters. The materials for core and shell were heated up to 220 °C in the extruder, and then they were passed through a pump and into the spinneret. An 800 m/min take-up velocity was employed to spool the single fibers on a bobbin. Finally, the single fibers were offline drawn to initiate polymer chain orientation and improve the fibers' mechanical properties [11].

Fibers containing 10, 20, and 40 vol.% of $CaCO_3$ in the outer shell were produced. The fibers have been offline drawn using a ratio of three, identified as 'DR=3'.

2.3 Characterization methods

Particles size distribution. The as-received natural $CaCO_3$ particles distribution was analyzed with a laser scanning diffractometer (LSD) to garantee the processability during spinning with regards to the nozzle geometry.

Fiber morphology. The microstructure of single fibers and the $CaCO_3$ particle distribution along the filaments were examined with a scanning electron microscopy (SEM) ULTRA PLUS (Carl Zeiss Microscopy GmbH, Germany), equipped with an SE2 detector. The fiber surface was sputter-coated with a 3 nm thick platin layer to obtain micrographs of the fiber surface.

Mechanical testing of the fibers. Single-fiber tension tests were analyzed with a FAVIMAT+ (Textechno H. Stein GmbH & Co. KG, Germany) equipped with a 610 cN load cell and hard rubber/vulkollan clamps. Single fibers were tested with a gauge length of 10 mm. The linear density of every fiber needed for the evaluation was determined before the tension test using the vibroscopic method according to ASTM D 1577, employing a velocity of 5 mm/min. The force-displacement curves were registered for 30 samples per composition.

Single fiber pull-out test. The effect of the newly developed bicomponent fibers structure on the failure behavior was analyzed by employing devices for sample preparation and pull-out test designed and constructed at IPF, and dynamic pull-out tests were carried out [11].

The single fibers were embedded to a depth of about l_e = 1000 µm at room temperature and controlled climatic conditions in a cementitious matrix prepared with a speed mixer and positioned to a specimen holder. The samples were stored for 28 days in a humid atmosphere until testing. The single fiber composites were mounted in the dynamic SFPO devices, and the upper fiber end was fixed at the mandrel with a cyanoacrylate adhesive at a minimized free fiber length. After adhesive fixing, the fiber's tensile load was adapted to zero to eliminate the stress due to adhesive shrinkage during its curing. Testing was conducted under a displacement rate of about 10 mm/s load conditions; only 300 µm displacement are considered for analysis to set a stable strain rate during the experimental strategy. The force-displacement curves were registered for at least 20 specimens for individual fiber types.

3. Results and discussion

3.1 Particles size distribution

The as-received natural $CaCO_3$ particles distribution was examined to pre-check its feasability during the melt spinning while passing the nozzles.

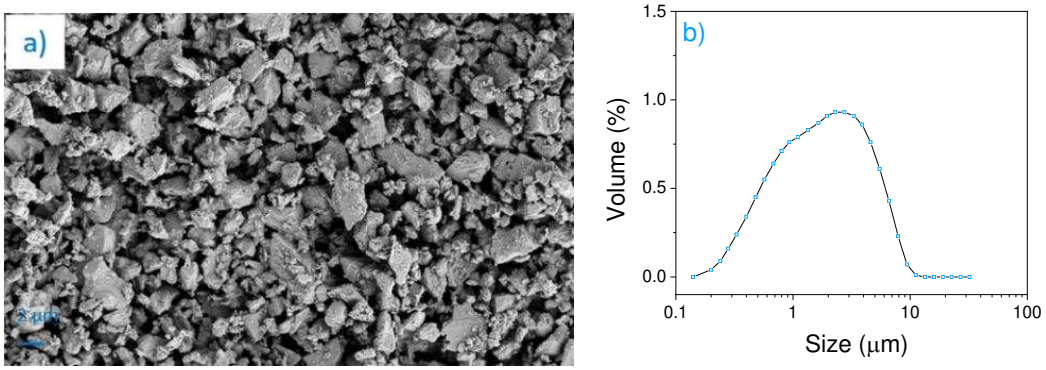

Figure 2. $CaCO_3$ particles represented by a) SEM morphology image, and b) size distribution diagram

The SEM examination displays the particle size that was quantified by the particle size analysis to range from around 0.14 to 10 µm with a maximum value at 2.2 µm. This range was found to be suitable to be used for blending during compounding in order to pass the spinning nozzles for fiber manufacturing. Further, the SEM image reveals the irregular geometry of the particles which is beneficial for the aim to achieve mechanical anchoring in the fiber surface and concrete matrix.

3.2 Surface structure of the bicomponent fibers

The SEM analysis of the single fiber surfaces (see Figure 3) after offline drawing shows that fiber roughness increases with increasing $CaCO_3$ particle amount in the fiber shell; the highest contrast is observed when monocompont PP fibers (Figure 3 a) are compared to the fiber containing 40 vol.% $CaCO_3$ (Figure 3 d). Nevertheless, the last-mentioned one presents a more inhomogeneous surface than the other fibers containing less particles (Figure 3 b, c), where the $CaCO_3$ is well distributed, and the commercial monocomponent PP fiber (see Figure 3 a) presents a nearly smooth structure. It should be noted, that the manufacturing of the fibers containing 40 vol.% $CaCO_3$ was accompanied by fiber breakage and significantly reduced stability of the

spinning process, so that a higher amount of particles could not be incorporated into the fiber shell.

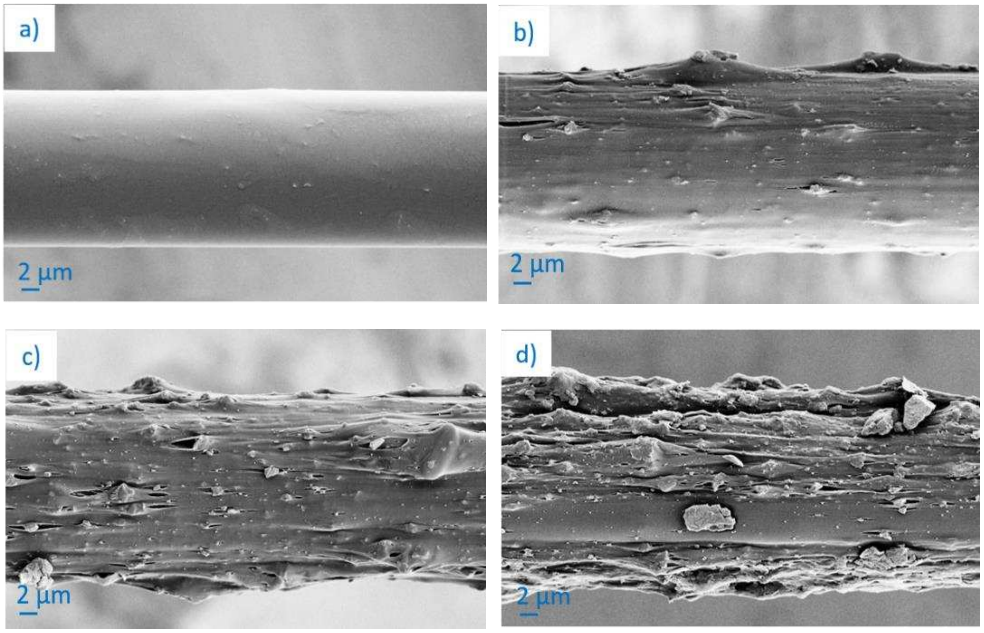

Figure 3. SEM images of a) commercial monocomponent PP fiber compared to offline drawn (DR=3) bicomponent fibers containing b) 10 vol%, c) 20 vol%, d) 40 vol% $CaCO_3$ with increasing surface roughness

3.3 Single-fiber tension tests

After offline drawing of the bicomponent fibers, the mechanical fiber performance was studied. The tensile stress-strain curves displayed in Figure 4 were selected out of thirty as characteristic individual type in order to enable a clear comparison with the commercial monocomponent PP fiber.

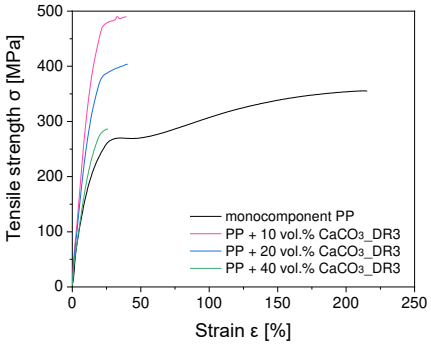

Figure 4. Tensile stress-strain curves of the commercial monocomponent PP fibers and bicomponent fibers (DR=3) with increasing $CaCO_3$ particle content

Table 3: Diameters and mechanical properties of bicomponent fibers

Fiber name / shell composition	Real* [calculated] shell diameter [µm]	Real* [calculated] core diameter [µm]	Tensile strength, σ [MPa]	Strain, ε [%]	Young's modulus, E [GPa]
monocomponent PP	19.8	-	355.0±19.8	212.0±23.6	2.8±0.2
PP + 10 vol.% $CaCO_3$_DR3	23.1±0.4 [22.8]	[16.1]	490.8±18.8	32.7±6.7	4.7±0.4
PP + 20 vol.% $CaCO_3$_DR3	22.7±0.4 [22.8]	[16.1]	403.7±21.5	40.5±5.6	4.2±0.4
PP + 40 vol.% $CaCO_3$_DR3	22.0±1.1 [22.8]	[16.1]	286.8±30.1	25.8±7.3	3.6±0.4

In the case of offline drawn bicomponent fibers, the polymer chains become aligned in the fiber direction of PP fibers, inducing reduced values of elongation as well as high tensile strength and Young's modulus (see Table 3, for absolute values and standard deviations). This tendency is disturbed by the insertion of the particles in the outer shell. Grooves and surface deformations (e.g., holes and stripes) appear on the fiber structure due to drawing that on the one side hinder the orientation of the polymer chains but on the other side enhance surface roughness. Even considering the mentioned issue, commercial monocomponent PP fiber reveal lower mechanical properties (excepting the fiber containing 40 vol% $CaCO_3$ particles in the shell).

3.4 Dynamic single-fiber pull-out

Force-displacement curves of the offline drawn (DR=3) bicomponent fibers acquired during the pull-out tests are displayed in Figure 5 b-d. The fibers are qualitatively compared against commercial monocomponent PP fiber (see Figure 5 a). The low fiber-matrix interaction of the monocomponent PP-fibers becomes obvious by the smallest force level that was found in this study at around 0.05 N. Inside the considered interval of 300 µm of displacement there is only a slight force increase; however, for the most tested samples the force remains constant. The addition of particles in the fiber-matrix-contact zone leads to a pronounced steep increase of the force right from the starting point of displacement. This indicates the mechanical interlocking between the rough surface and the concrete that enables the stresses to be transferred between fiber and matrix. With increasing particle amount the stresses in the fiber even lead increasingly to fiber failure, what is the case for all fibers with 40 vol.% $CaCO_3$. From previous investigations [3, 13] it is known that in the case of smooth monocomponent PP-fibers merely a very small part of the surface is activated during pull-out in terms of polymer deformation. The mechanical interlocking that is achieved by the particle addition induces great deformation of the fiber surface by removing or shifting particles; at the same time, the fiber core is still able to provide tensile strength. The pull-out work up to a displacement of 300 µm (W_{300}) is therefore more or less doubled for samples containing 10 and 20 vol.% of particles. However, the results allow the conclusion that this desired behavior appears only in the case of

a certain particle amount. After reaching an optimum the further increasing particle amount causes premature fiber failure as can be observed for 40 vol.% $CaCO_3$.

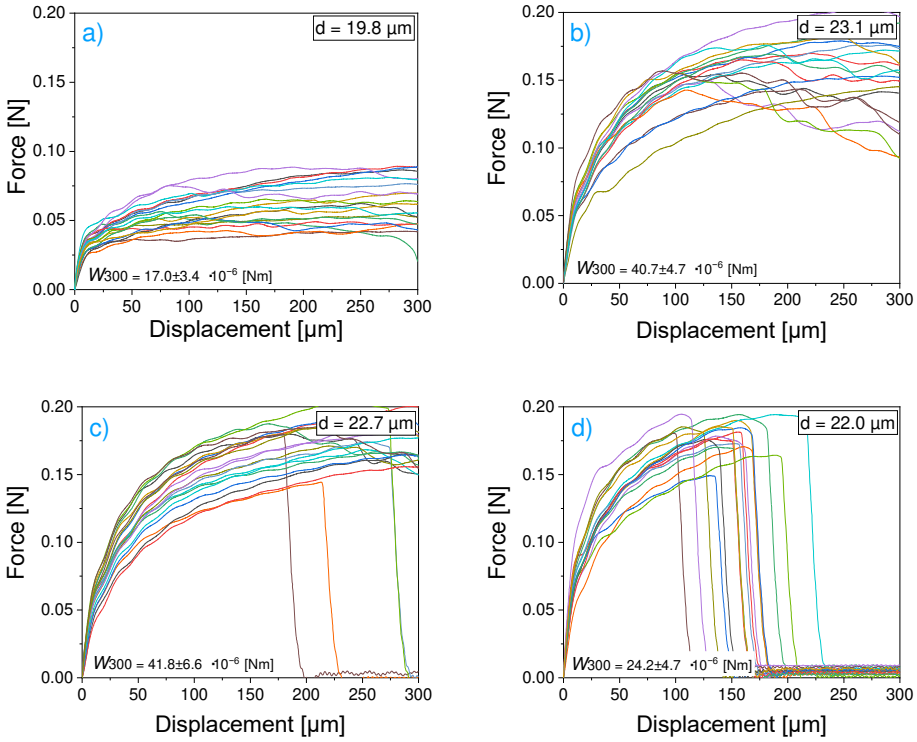

Figure 5. Dynamic SFPO force displacement curves of a) commercial monocomponent PP fiber and offline drawn fibers containing b) 10 vol.% $CaCO_3$, c) 20 vol.% $CaCO_3$ and d) 40 vol.% $CaCO_3$ pulled out of high strength concrete matrix. The curves in each plot represents twenty repeated tests

4. Conclusions

New polymeric bicomponent fibers were developed containing natural $CaCO_3$-particles in the outer shell. The selected particles reveal a size distribution that allows the manufacturing of fibers with up to 40 vol.%.

Tensile strength increased after drawing the bicomponent fibers due to the orientation of the polymer chains in the axial direction. However, this mechanism is hindered by increasing the amount of the particles, making the fiber containing the highest possible particles amount (40 vol.% $CaCO_3$) to present the lowest tensile strength.

Plastic deformation of the polymer fiber surface induced by the particles leads to improved energy absorption during pull-out compared to the less deformed pure polymeric surface of commercial monocomponent PP fiber.

Further work will focus on the optimization of the particles amount for upscaling the fiber manufacturing for macroscopic concrete composite testing in order to enhance the fracture toughness, and energy absorption of SHCC under impact loading.

  doi:10.5075/epfl-298799_978-2-9701614-0-0

Acknowledgements

The authors greatly acknowledge the funding by the Deutsche Forschungsgemeinschaft (DFG - German Research Foundation) in the framework of the Research Training Group GRK 2250/2 “Mineral-bonded composites for enhanced structural impact safety”, project number 287321140.

5. References

1. Li VC. On engineered cementitious composites (ECC) a review of the material and its applications. Journal of advanced concrete technology. 2003;1(3):215-30.
2. Curosu I, Liebscher M, Mechtcherine V, Bellmann C, Michel S. Tensile behavior of high-strength strain-hardening cement-based composites (HS-SHCC) made with high-performance polyethylene, aramid and PBO fibers. Cement and Concrete Research. 2017 Aug 1;98:71-81.
3. Wölfel E, Brünig H, Curosu I, Mechtcherine V, Scheffler C. Dynamic single-fiber pull-out of polypropylene fibers produced with different mechanical and surface properties for concrete reinforcement. Materials. 2021 Jan;14(4):722.
4. Kakooei S, Akil HM, Jamshidi M, Rouhi J. The effects of polypropylene fibers on the properties of reinforced concrete structures. Construction and Building Materials. 2012 Feb 1;27(1):73-7.
5. Combrinck R, Boshoff WP. Typical plastic shrinkage cracking behaviour of concrete. Magazine of Concrete Research. 2013 Apr;65(8):486-93.
6. Banthia N, Gupta R. Influence of polypropylene fiber geometry on plastic shrinkage cracking in concrete. Cement and concrete Research. 2006 Jul 1;36(7):1263-7.
7. de LHONEUX B, Kalbskopf R, Kim P, Li VC, Lin Z, Vidts D, Wang S, Wu HC. Development of high tenacity polypropylene fibers for cementitious composites.
8. Baggott R, Gandhi D. Multiple cracking in aligned polypropylene fibre reinforced cement composites. Journal of materials Science. 1981 Jan;16(1):65-74.
9. Sobolev K. Modern developments related to nanotechnology and nanoengineering of concrete. Frontiers of structural and civil engineering. 2016 Jun;10(2):131-41.
10. Naeimirad M, Zadhoush A, Kotek R, Esmaeely Neisiany R, Nouri Khorasani S, Ramakrishna S. Recent advances in core/shell bicomponent fibers and nanofibers: A review. Journal of Applied Polymer Science. 2018 Jun 5;135(21):46265.
11. Wölfel E, Scheffler C. Interphases in polypropylene and glass fiber reinforced cementitious model composites under dynamic loading. InProceedings of the 10th International Conference on Fracture Mechanics of Concrete and Concrete Structures 2019 Jun.
12. Curosu I, Mechtcherine V, Millon O. Effect of fiber properties and matrix composition on the tensile behavior of strain-hardening cement-based composites (SHCCs) subject to impact loading. Cement and Concrete Research. 2016 Apr 1;82:23-35.
13. Popa MM, Brünig H, Curosu I, Mechtcherine V, Scheffler C. Spinability and Characteristics of Particle-Shell PP-bicomponent Fibers for Crack Bridging in Mineral-Bonded Composites. InRILEM-fib International Symposium on Fibre Reinforced Concrete 2021 Sep 20 (pp. 255-264). Springer, Cham.

  doi:10.5075/epfl-298799_978-2-9701614-0-0

OPTIMISED COMPOSITE CRASH STRUCTURE DEVELOPMENT WITH FOCUS OF LIFE CYCLE ANALYSIS FOR A FUEL CELL ELECTRIC VEHICLE

Nithin Jayasree[a], Sadik Omairey[a], Vasiliki Loukodimou[a], Aidan Bradbury[b] Mark Lidgett[b], Roger Elliott[c], Lucy Bull[c], Chris Page[d], Sofia Sampethai[d], Stuart Lewis[d], Kieran Dennington[e], Richard Coltart[e], MJ Bull[e], Mihalis Kazilas[a]

a: Brunel Composites Centre, Brunel University London, the UK -
Vasiliki.Loukodimou@brunel.ac.uk
b: Far-UK Ltd., the UK
c: Composites Evolution Ltd., the UK
d: TWI Ltd., the UK
e: Riversimple Movement Ltd., the UK

Abstract: *Low-speed accidents see a year-on-year increase. To improve crash performance in these accidents, a crash box is attached between the vehicle bumper structure and the side rail. The determination of the crash box material and geometry is critical to absorb the impact energy to result in safer vehicles and minimised repair costs. As the automotive industry transitions to more sustainable platforms, it is seeking to use lightweight materials including in the crash structure. This study develops an innovative crash box with optimal impact energy-absorption capabilities for a fuel cell electric vehicle. The concept is based on topology optimisation considering the composite structure and crash energy dissipation. In further work, the results from the life cycle analysis are utilised, and a comparative study between carbon fibre reinforced polymers and biocomposites in crash structures is performed. The latter includes an extensive characterisation campaign under static and dynamic conditions.*

Keywords: Composites; crash box; crashworthiness; lightweight; life cycle analysis

1. Introduction

Low-speed (20mph) accidents see a year-on-year increase of 31% [1]; injury increase is broken down as fatal (+79%), serious (+47%), and slight (+42%). A crash box is a thin-walled structure attached between the vehicle bumper structure and the side rail part of the vehicle and aims to improve crash performance in low-speed accidents. Frontal crashes are responsible for more deaths and serious accidents than any other type [2]. The identification of the material and geometry of the crash box plays a key role in the absorbance and dissipation of the impact energy. Hence, having effective crash boxes will result in safer roads and vehicles, along with minimised repair costs.

Conventional crash boxes are manufactured from steel or aluminium. These exhibit high peak force and have no way of controlling the deceleration rate following a crash. However, as the automotive industry is shifting to more sustainable platforms such as fuel cell electric vehicles (FCEVs) and battery electric vehicles (BEVs), weight reduction is essential in designing these vehicles. Hence, there is a shift towards utilising advanced lightweight materials in crash box applications beyond the body in white (BIW). Composite alternatives are excellent candidates for these applications; however, they are limited in use due to unpredictable failure. Multi-material crash boxes' light-weighting, high-specific stiffness and strength, and improved crashworthiness have led to their use in high-end vehicles.

PROTECT project (Modular multi-material crash-box for tailored impact energy absorption during low-speed collision) [3] aims to produce an innovative crash box with improved impact energy absorption capabilities enabling minimal damage to road users, vehicles, vehicle-occupants in low-speed collisions. The challenge lies in designing and developing a multi-material crash-box system that enables tailoring energy absorption and functionality in every millimetre along the component length and smooth energy transition from crash-box to longitudinal. For this purpose, a novel mix of multi-materials (aluminium and carbon fibre reinforced polymers) is utilised, allowing for inter material properties that enable better energy absorption.

The following sections of this paper include a description of the end-user requirements, the architecture of the crash zone, concepts development, and the concept selection process.

2. End-user requirements

To ensure ultimate use and deployment of crash structures being developed in this study, a set of end-user requirements and specifications are defined. These criteria are aligned with the vehicle architectures and business model. This not only assesses the feasibility of the designed solutions but highlights the areas that require further development. Some of the key functional requirements set by the end-user Riversimple [4] are presented in Table 1

Table 1. Examples of End-user's key requirements.

Operating Environment	• Withstand ambient air temperatures from -20°C to +70°C and be able to pass the mandatory crash requirements at those temperature extremes. • Use chemicals and materials within the structure that are chemically unreactive with typical automotive glycol-based coolant. • Withstand direct UV exposure over a period of 20 years and be able to pass the mandatory crash requirements after exposure. • Withstand exposure to water without failing/the structure breaking down. Recommended that the structure meets standards to pass the cyclic damp heat test. • Withstand relative air humidity ranges from 20% to 95% for extended periods of time and be able to pass the mandatory crash requirements after exposure. • The crash structure will be subjected to mechanical vibration and repeated shocks during normal use of the vehicle and must not fail due to this.
Mass	• It is a target that the crash structure developed from this project has a mass of 10.0kg or lower. • Be a bolt-on structure. • Fit within the boundary volume • Target of sitting 50mm or greater below the A-surface of the bonnet for pedestrian impact.
Functional	• Crush in a controlled and predictable manner so that the occupant's head never exceeds 80G for more than 3ms in all mandatory crash tests. • Target peak acceleration to be less than 35G for the European Type Approval test (56km/h frontal impact). • Contain a structural threaded section for a towing eye. This must be able to withstand a force of half the vehicle's mass in the x-direction without plastic deformation occurring (SAE Vehicle Co-ordinate System).

- Towing eye fastening must be of a design that allows it to be attached and removed without removing any of the vehicle's bodywork and without the use of tools. Crash simulations will be conducted without the towing eye fitted.

Crash Tests Scenarios	• Very Low-Speed Impact: 5km/h full-frontal, rigid barrier. Target of no crush of the crash structure. • Low Speed Impact: 32km/h (20mph), recommended to look at full frontal and offset barriers to satisfy the initial project brief. • Medium Speed: 56km/h, offset deformable structure, 40% overlap as per ECE Reg 94 (European type approval regulations).
Performance	• The crash structure must still be able to pass the initial crash performance requirements after 20 years of service on a vehicle. This can be simulated through standard automotive accelerated life testing.
Safety	• Materials used in construction are recommended to not be hazardous to health or the environment. It's advised that the toxicity of the materials chosen is investigated and materials chosen minimise the impact to the environment in the event of an accident.
Sustainability	• Must be designed with a roadmap for recycling in mind at the end of the component's life with a line of sight to closed-loop recycling.
Manufacturing	• Be able to be scaled up to 5000 units manufactured per annum from one set of tooling. • Target of using low energy manufacturing processes where possible.

3. Crash zone architecture and design space

The architecture of Riversimple [4] Rasa vehicle offers a narrow design space for the bumper beam and limited possibility for support above or below it across vehicle's centreline due to packaging constraints created by the cooling system, see Figure 1. As a result, a well-optimised and compact solution is required.

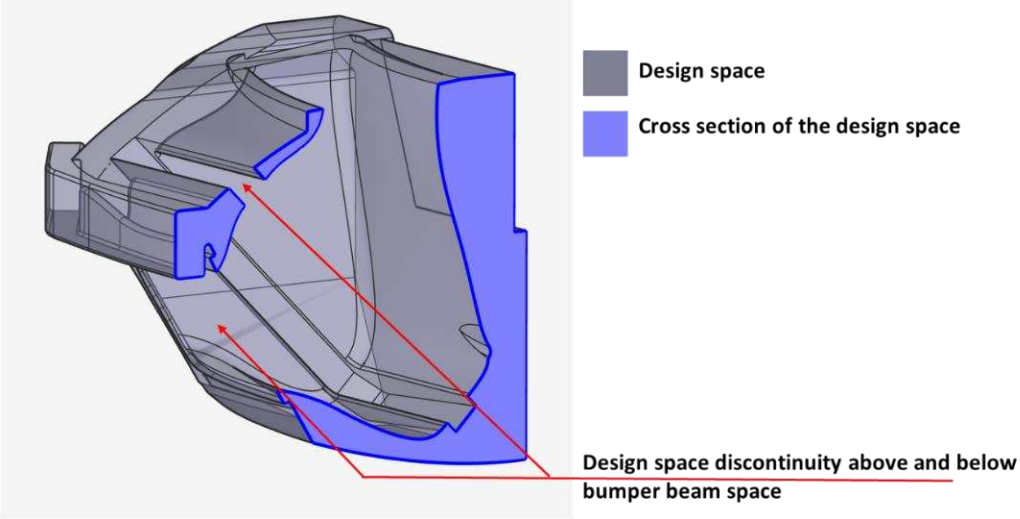

Figure 1. Design space surrounding the bumper beam area.

4. Concepts development and initial crash tests

Following multiple topology optimisation where the surfaces of the cross section were assigned parameters in ANSA which was coupled to LS-OPT [5] where the parameters became design variables. A Design of Experiments (DOE) was created with 50 designs with design variables chosen using the Latin Hypercube Point selection.

Among the 50 initially proposed concepts, a few were shortlisted based on the manufacturability assessment. A quick summary of the shortlisted concepts for further analysis is exhibited in Table 2. The peak force, peak acceleration, mass, absorbed energy and average force were measured. The Specific Energy Absorption (SEA) was measured using the crush mass and the crush tube's displacement. The current study is focused on further shortlisting the concepts based on the crash simulations and the experimental trials. Multiple FE material cards are being generated as part of the project to understand the usability of flax composites, GFRP and CFRP. This was done by performing an extensive static characterisation campaign. Dynamic characterisation was done specifically for the CFRP on multiple strain rates as this material would be the primary candidate for crash structures. The FE material card was written in MAT 58 in LsDyna [6].

Table 2 Sample crash box concepts

Concept		Peak force (N)	SEA (KJ/kg)
Plus box	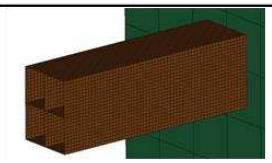	≈ 1E+06	≈70
Crossbox	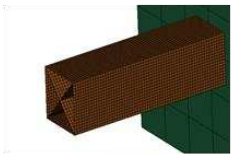	≈ 1E+06	≈50
D-section	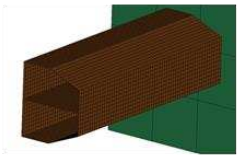	≈7E+05	≈48
Mirrored W section	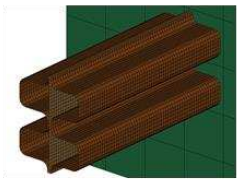	≈1E+06	≈60
W section	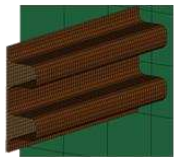	≈9E+05	≈32
Bio inspired [7]	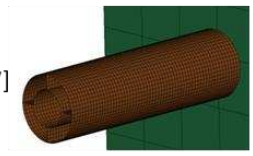	≈ 1E+06	≈90

The structures investigated had the SEA varying from 30KJ/Kg from the mirrored W section to 90 KJ/Kg for the bio inspired [7]. The ideal geometry was expected to have a progressive crush failure mode enabling efficient energy absorption, instead of having a buckling failure mode. The addition of trigger mechanism through the indentation of the geometry was found to reduce the peak force and increase the SEA of the crush tubes. For some concepts that were showing buckling failures, the addition of an indented trigger mechanism has initiated a progressive crush failure, which thereby increased the energy absorption. The most critical consideration is the manufacturability of the concepts which is been explored currently. The best performing concepts will be redesigned for manufacture with composite materials. Based on an initial design for manufacture, some of the concepts are deemed too complex and expensive to be manufactured with composite laminates. The final concept will be selected by CAE that shows the most efficient crush performance.

5. Concepts selection

Similar to any product development process, several concepts are being developed in this study. At the end of the development phase, a single concept should be selected to proceed with.

559/716 ©2022 Jayasree et al. doi:10.5075/epfl-298799_978-2-9701614-0-0 published under CC BY-NC 4.0 license

However, given that the crash structure has several performance requirements with different importance levels, selecting and optimising concepts can be challenging. To address this, a concept selection process is developed to select the optimum concept through achieving the following four key objectives: a) End-user performance requirements indicators are defined along with their relative importance. b) Solution elements are defined in line with what the project aims to achieve and end-user's performance requirements. c) Concepts are developed and optimised to included solutions based on their weighting against end-user performance requirements. d) basing optimum concept selection on measurable indicator that reflects concepts performance against all of the performance requirements set by the end-user. These objectives are implemented in two steps; first using Quality Function Deployment (QFD) to identify and prioritise end-user's expectations quickly and effectively. And second, using Pugh chart to compare design concepts against end-user's criteria to select the final concept. These steps processes are illustrated in Figure 2 and the sections below:

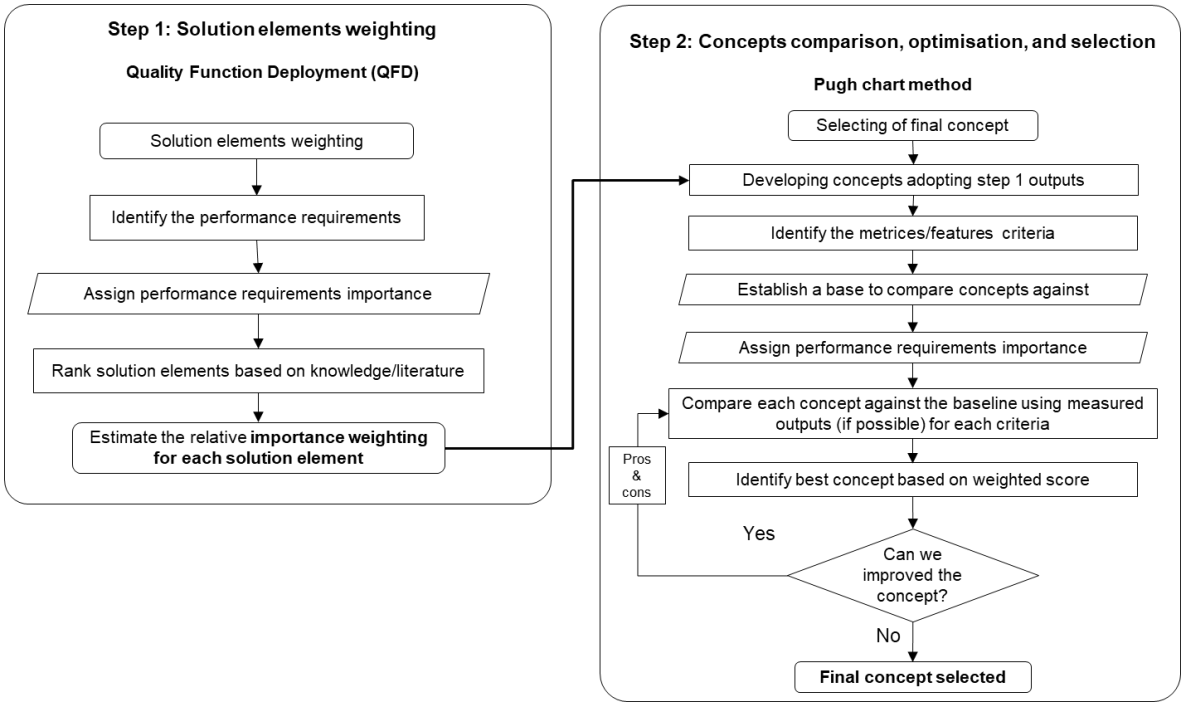

Figure 2. Solution elements weighting and concepts selection process.

4.1 End-user performance requirements indicators

The crash system to be developed in this project aims to offer tailored crash performance, reduce weight, and offer recyclability options. In addition to this, several functional requirements are equally important and should be met, such as cost, modularity, and production rate. Equally important to defining these indicators is their relative importance. Table 3 lists the identified indicators and their significance.

Table 3. End-user performance requirements indicators and their importance (5 very important, 1 less important).

Performance requirements	Description	Relative importance
Sustainability	The indicative contribution of the solutions and concepts towards sustainability in QFD and Pugh chart, respectively.	5
Component Cost	The indicative manufacturing cost for implementing the proposed solution and the overall indirective cost for each concept in QFD and Pugh chart, respectively.	2
Lifetime Cost	Indicates the operational cost associated with implementing a specific solution or the concept in QFD and Pugh chart, respectively.	4
Cycle Time	Indicates the influence of a specific solution or the overall concept on the production rate in QFD and Pugh chart, respectively.	2
Modularity	Indicates the opportunity to have a modular crash structure for a specific solution or the overall concept in QFD and Pugh chart, respectively.	2
Performance	Indicates the effect of solutions on performance in QFD matrix or the overall crash performance of the concept in Pugh chart.	5
Weight	Indicates the influence of solutions on weight in QFD matrix or the overall importance of the concept in Pugh chart.	4

4.2 Solution elements

To meet project's goals, there is an array of solutions that can be employed during concepts development stages such as the use different materials and design philosophies. However, there is a need to link these solutions with end-user performance requirements to produce a satisfactory design that meets end-user's requirements and expectations. Hence, these solutions are listed and defined in Table 4 for use in the QFD matrix to provide the design team with a measurable indicator of which solution(s) have higher relative importance based on their influence on end-user performance requirements indicators (see section 4.1), so that it/they can be implemented in concepts development and optimisation iterations.

Table 4. Proposed key design solutions considered as part of concepts development stage.

Solution elements	Description
Use of biomaterials	The use of biomaterials increases sustainability and can decrease cost compared with the use of carbon fibre. However, the mechanical performance will decrease.
Use of thermoset materials	Manufacturing thermoset composites is a well-established method. Compared with the thermoplastic process, it requires less start-up capital and allows the manufacturing of complex shapes. However, it can be labour intensive, have a limited scaling possibility, and reduce recycling opportunities.
Use of thermoplastic materials	Thermoplastic composites offer higher sustainability compared with thermosets as they can be recycled. However, their overall cost is higher than thermosets. Hence, their use can be limited to smaller sections.
Use of metallic materials	Although metallic materials offer a high level of recyclability, fast production rate, and modularity, their performance to density is lower than composites.
Single-piece solution	Integrated crash concepts, which consist of single-piece attachable, can offer the lowest possible weight and improve the assembly process. However, such solutions can be cost-intensive in manufacturing and operation due to high replacement/repair costs if damaged, hence high insurance costs.
Multi-piece solution	Multi-piece or modular solutions offer less operational cost as they should be repaired or replaced at a lower cost compared with single-piece solutions. However, they generally will have a higher weight due to the number of joints and fasteners needed.

6. Conclusion and future work

Multiple concepts of crash structures have been developed as part of the project through topology optimisation, material homogenisation and manufacturability. These concepts were explored as sampled in Table 2, as the ideal geometry of the crashboxes were further evolved to more manufacturable shapes, and is currently being shortlisted for impact, drop and crash testing scenarios. Based on the initial assessment, the best performing geometry with the best SEA and energy dissipation was the bio-inspired [5], However, this concept was not easily manufacturable based. On the other hand, the addition of a trigger mechanism was investigated, and it was found that the peak force was reduced, and the energy absorption was increased by initiating progressive crushing. This ongoing project is focused on finalising a manufacturable crash box concept, with the ideal material and trigger mechanism to optimise the energy release while considering the lifecycle aspects. Upon defining the final concept, a detailed life cycle analysing study will be conducted to assess the sustainability of the developed crash box.

Acknowledgements

The PROTECT project has received funding from Innovate UK under reference number 68148.

References

1. [Internet]. Assets.publishing.service.gov.uk. 2017 [cited 20 April 2022]. Available from: https://assets.publishing.service.gov.uk/government/uploads/system/uploads/attachment_data/file/635176/dft-annual-report-and-accounts-2016-to-2017-web-version.pdf
2. Offset-Deformable Barrier - ODB | Euro NCAP [Internet]. Euroncap.com. 2022 [cited 20 April 2022]. Available from: https://www.euroncap.com/en/vehicle-safety/the-ratings-explained/adult-occupant-protection/previous-tests/offset-deformable-barrier/
3. PROTECT Project: Improving Vehicle Safety [Internet]. Twi-global.com. 2022 [cited 20 April 2022]. Available from: https://www.twi-global.com/media-and-events/press-releases/2021/protect-project-improving-vehicle-safety
4. Riversimple [Internet]. Riversimple.com. 2022 [cited 20 April 2022]. Available from: https://www.riversimple.com/
5. LS-OPT [Internet]. LS-OPT Support Site. 2022 [cited 20 April 2022]. Available from: https://www.lsoptsupport.com/
6. LS-DYNA | Livermore Software Technology Corp. [Internet]. Lstc.com. 2022 [cited 20 April 2022]. Available from: https://www.lstc.com/products/ls-dyna
7. Ha N, Lu G. A review of recent research on bio-inspired structures and materials for energy absorption applications. Composites Part B: Engineering. 2020;181:107496.

NONMETALIC COMPOSITES AGING IN OIL AND GAS APPLICATION

Wael Badeghaish, Ahmed Wagih, Muhamed seraj, Gilles Lubineau

KAUST (King Abdullah University of Science and Technology), Physical Science and Engineering Division, Mechanical Engineering Program, Laboratory of Mechanics of Composites for Energy and Mobility, Thuwal 23955, Saudi Arabia

*E-mail: wael.badeghaish@kaust.edu.sa

Abstract: *Polymeric composites have been used to replace metals in many onshore and offshore applications due to their corrosion resistance. Transporting petrochemical gases and acids via composite materials at high pressure and temperature represents a challenge because the lack of confidence in such aggressive environments. Therefore, understanding the change in the physical and mechanical properties in polymeric composites under aggressive oil conditions is essential for providing novel designs and materials for these applications. This work presents a short literature review on the challenges facing application of polymeric composites in the oil and gas downhole aggressive corrosion environment. Moreover, it presents preliminary inspection on the integrity of a thermoplastic polymer (PEEK) subjected to HCl (0.8 Ph) at high temperatures (50 and 100 °C) for 14 days. The preliminary results demonstrated the good chemical resistance of PEEK at high temperature. Moreover, there was no effect on the mechanical properties of the PEEK at these conditions.*

Keywords: Composites aging; Nonmetallic in oil and gas; PEEK; Nanoindentation.

1. Introduction

Corrosion in metallic materials is a well-known challenge where engineers and scientists work together to control it. The majority of failures in the oil and gas industry are related to corrosion, which severely affects plant integrity. Downhole is one of the most challenging environments in the industry, as corrosion is always present. Internal corrosion in pipes is influenced by temperature, corrosive gases, Carbon dioxide (CO2) and hydrogen sulfide (H2S), water chemistry, flow velocity, oil or water wetting and composition, sulfate-reducing bacteria, and surface condition of the metallic pipe material [1-3]. The mitigation can be achieved by specific measures such as selecting appropriate materials, coatings, corrosion inhibitors, and internal linings.

In recent years, the Oil and Gas (O&G) industry has shifted its focus increasingly to non-metallic (NM) pipes as a disruptive technology for transporting pressurized fluids from the onshore surface and offshore subsea to downhole operations. The new proposed materials are lightweight, high-strength, and have superior fatigue and corrosion resistance. Economic analysis shows that using NM will yield substantial life-cycle cost savings and increase oil demand [4,5]. NM materials for downhole have been active for many years with limited applications, such as water production/injection and shallower hydrocarbon wells, moderated in temperature rating and have long-term performance reliability. Increasing the deployment of NM composite materials upstream is strategic and aligns with the industry's business needs. The cost savings of utilizing NM material for downhole applications are realized with fewer work-overs, increased tubing and completion life cycle, and faster installation. Figure 1 shows the roadmap for the NM materials in downhole applications. Some of those subsurface applications

  doi:10.5075/epfl-298799_978-2-9701614-0-0

are already replaced or expected to be replaced, with NM composites over the next few years. Several composite tubular designs, such as a reinforced thermosetting resin, thermoplastic composite pipe, and reinforced thermoplastic pipe, are being recognized as suitable and cost effective materials for many onshore and offshore applications [5, 6, and 7]. The substantial properties of those composite materials pave the way to evaluate their performance to replace the conventional steel tubing/casing in the downhole.

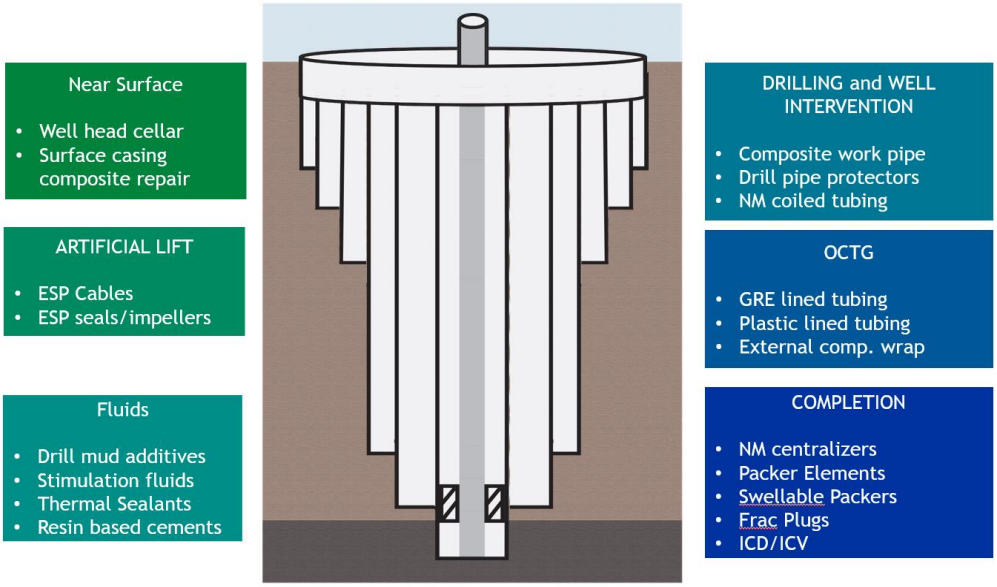

Figure 1: Non-metallic roadmap for downhole applications [5, 6].

As downhole application requires moving progressively to higher pressure and temperature when producing at deeper depth, this poses challenges to the development of high-pressure NM pipes that are suited for continuous use in a harsh environment, especially when the service temperature approaches 150°C and operating pressure from 5,000 to 20,000 psi, commonly in a wet environment [8]. Figure (2) shows the temperature profile vs. depth for two different gas wells in the Middle East. The temperature and pressure gradually increased, reaching almost 150 °C and 7500 PSI, respectively, at 4572m depth [9].

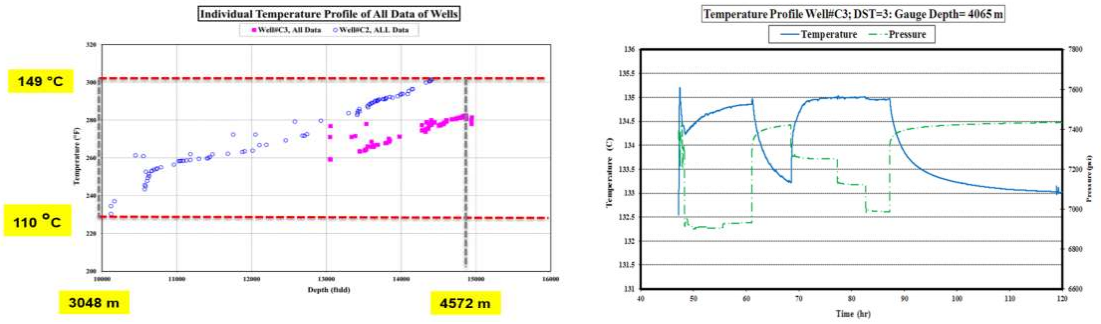

Figure 2: a) Temperature profile of gas wells at different depths, b) temperature and pressure profile at 4065m [9].

Stimulation, enhanced oil recovery, and fracture process are essential processes in downhole, namely (upstream), which require a considerable amount of aggressive acids, fluids, and gases to increase hydrocarbon production. Those conditions could degrade non-metallic equipment

in oil and gas due to the permeation of fluids inside a polymeric pipeline.In downhole application, the environment is harsh in terms of pressure, temperature and working fluids that might affect the polymer properties, when subjected for long time and hence reduces the integrity of the pipelines.

Polyether ether ketone (PEEK) is one of the most known polymers that can sustain high pressure and temperature. With a modulus of around 3.2GPa, and service temperatures of up to 260°C, PEEK is now common within the aerospace and automotive industries [10, 11]. The glass transition temperature (Tg) is 143°C and the crystalline melting temperature is around 336 °C [12]. Its high resistance to chemical and acids degradation [10], making PEEK an ideal candidate for application within aggressive conditions. The importance of heat resistant materials in the aerospace, energy, automotive and electronic industries has become driving force for researchers on high performance applications [11]. Another important advantage of PEEK is its low water absorption, which is less than 0.5% at 23°C compared with 4%–5% for conventional aerospace epoxies [12]. Therefore, PEEK is a suitable material for O&G and particular in aggressive environment such downhole application.

With the aim of understanding the behaviour of PEEK, aging studies, which stand for subjecting polymers to certain environment for certain period, were performed. In the literature, aging and permeability studies are mainly found for limiting applications not related to oil, aiming at studying the influence of aging on polymers. Permeability studies associated with the aging of PEEK bulk and thin-film have not been found in the literature. Nevertheless, permeability studies are essential because the flowing of a fluid, such as acid and hydrocarbon at high pressure and temperature (HPHT) through polymer liner in carbon steel (CS) or composite pipe is considered a critical phenomenon in many sectors, including O &G industry [3]. The thermal stability of PEEK at high temperature was also studied in the literature. For instance, C.Zhu et al. evaluated PEEK thermal stability for nuclear plants [13]. Liuqing Yang et al. investigated the thermal and gamma-ray aging of PEEK and evaluated the thermal and mechanical effects using a wide variety of characterization techniques [14]. Different environmental conditions also could affect the thermal and physical performance of PEEK not been found in the literature.

To ensure the safe and stable operation of polymeric composite in the O&G industry, it is necessary to test the physical and chemical properties of materials before and after aging and investigate multiple effects. Out future work will focus on evaluating the combined impact of HPHT and fluids on PEEK. We will perform aging experiments on PEEK samples for extended periods (> a few months) under HPHT in HCl acids and hydrocarbon. A wide variety of characterization will be performed, such as weight and density change, DSC, FTIR, SEM, and nano-indention to trace the mechanical and thermal changes. In addition, this project aims to characterize the fracture toughness and young modulus of PEEK thin film and to determine how it is affected by thermal and chemical aging. This work will help increase the database and provide O&G operators with more confidence to deploy more NM tubular.

Following the above preliminary literature review, this paper presents preliminary results on the effects of thermal and chemical aging on the mechanical behavior of bulk PEEK using nano-indentation, weight variation and thermal analysis.

  doi:10.5075/epfl-298799_978-2-9701614-0-0

2. Material and methods

Sheet-shaped PEEK samples with a thickness of 5 mm were supplied by (Nanjing Yuwei New Material Co., Ltd, China). Aging of PEEK in HCl with low ph (0.8) was carried out by immersing samples in the bath at 50 °C and 100 °C for 14 days. Aged samples compared with unaged ones in terms of mechanical and thermal analysis. The weight of the samples was measured immediately after they were taken from the bath. The samples weight change due to absorption was calculated right after aged the samples and after ten days according to equation 1 [15]:

$$M(\%)=\frac{Final\ Mass(g)-Intial\ Mass(g)}{Intial\ Mass(g)}*100$$

Nanoindentation is a powerful technique to measure mechanical properties such as Young's modulus and hardness of various materials [16]. This method has been used to evaluate the mechanical response of the aged PEEK samples. The tests were carried out using vintage nano test machine with a Berkovich tip indenter [16]. Before performing the indentation, the PEEK samples were polishing for almost 2 hours using sand papers that varying in grades from 500-4000 with 30N max force and 150 rpm speed of grinding disk.

Scanning electron microscopy (SEM) (model Quattro, Thermofisher, HV: 5 kV), was used to investigate the surface of the samples after aging.

Differential scanning calorimetry (DSC) tests were carried out using A TA Company, Q2000 type. We placed 5 mg of the aged sample in the aluminum crucible and sealed and tested in high purity N2 atmosphere. Then, samples are evaluated according to the following program: 25–400 ℃ with a rate of 20 ℃/min, after 5 min dwell, cooled to 25 ℃ with a rate of 20 ℃/min, and raise the temperature to 400 ℃ with a rate of 20 ℃/min. We took the data from the second temperature rise. The gas flow rate was 20 mL/min.

3. Preliminary results and discussions

Table (1) shows the weight changes of 4 samples after 14 days immersing in HCl (absorption) and after 10 days drying at atmospheric conditions (desorption). It has been demonstrated that there is no significant change in the weight and very minimum acids uptake in PEEK. This is expected at relatively short time and atmospheric conditions due to its crystallinity and good chemical stability.

Table1. PEEK weigh change before and after again

PEEK mass (g) Before Aging	PEEK mass (g) After Aging	Weight change (%)	PEEK mass (g) 10 days later	Weight change (%)
17.0851	17.1305	0.27	17.1186	0.19
16.9166	16.9693	0.31	16.9448	0.17
16.9166	16.9979	0.48	16.9464	0.18
16.8799	16.9551	0.44	16.9104	0.18

Figure (3) shows the load-displacement response of three representative samples of each configuration. The loading portion of the indent is presented from 0 nm to 1500-1600 nm penetration depth at a low load of 15mN, followed by a hold segment (10 s) at the maximum indentation load. The unloading step starts from the entire load and the maximum depth to zero

loads and an unrecoverable indentation depth of the surface. The overall graph shows the same trend for treated and untreated samples, indicating that no plasticization occured on the surface due to aging. Therefore there is no change in measured young modulus (E = 4.65 ± 0.5 GPa) and hardness (H = 0.32 ± 0.1 GPa) of aged PEEK in (HCl) acid at 50 °C &100 °C.

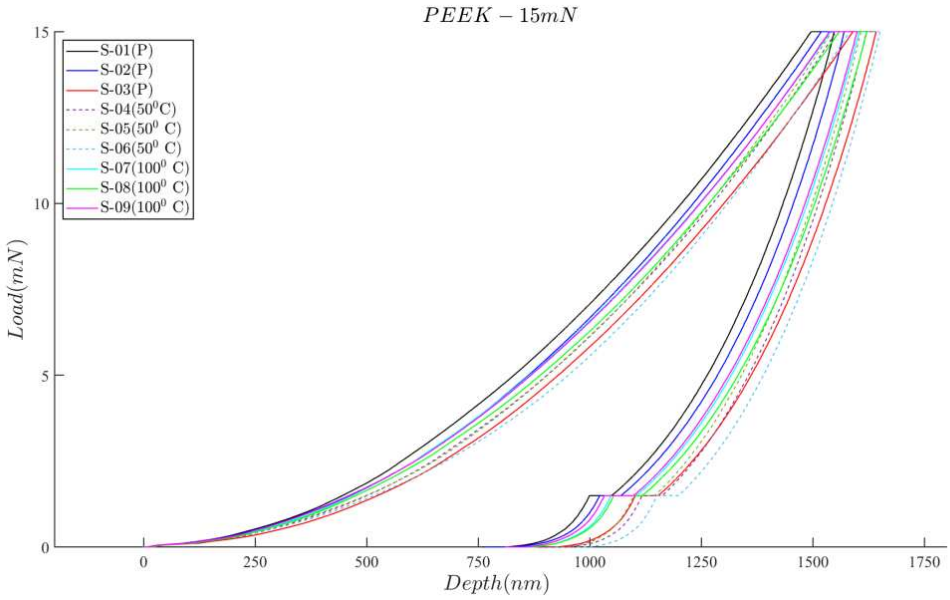

Figure 3: Indentation load–displacement data for the pristine and treated (immersed in hydrochloric acid) semicrystanility PEEK samples at15mN. The treated polymeric samples were immersed for 14 days.

The first heating scan in DSC as shown in Figure (4.a) is mostly used for removal of residual solvents, and erase the thermal history of the polymer. For polymers, the Tg is very distinct in the second heating whereas Tm and Tc show insignificant difference in their respective values between two runs as display in figure (4.b). Table (3) shows insignificant differences for melting Peak temperature (Tm) for first and second scan.

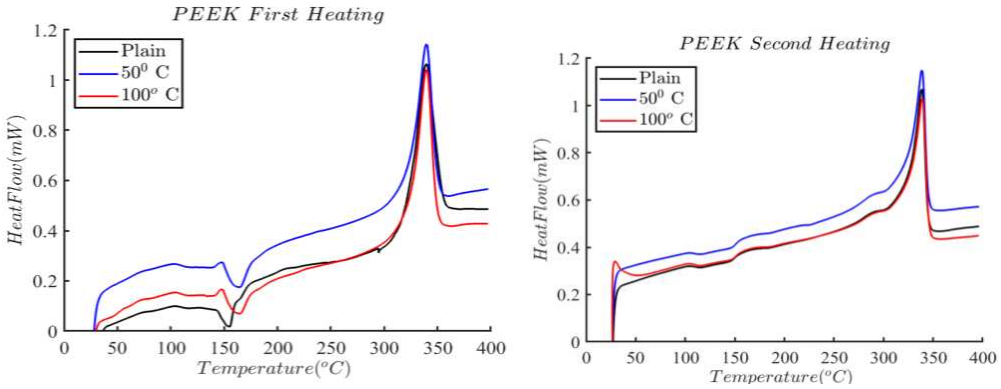

Figure 4: a) PEEK first heating cycle, b) PEEK second heating cycle

Table 3: melting temperature for first and second heating scan

Temp	Tm (First heating Scan)	Tm (Second heating scan)
Preston	339.76	338.52
50℃	339.60	338.58
100℃	339.77	339.05

Figure (5) shows SEM micrographs of the unaged and ages samples at 100 °C. The surface morphology is similar between both samples. Its evidence that the materials removed during the aging process didn't occur in the observed SEM. Surface demonstrated unidirectional scratches coming from the polished process.

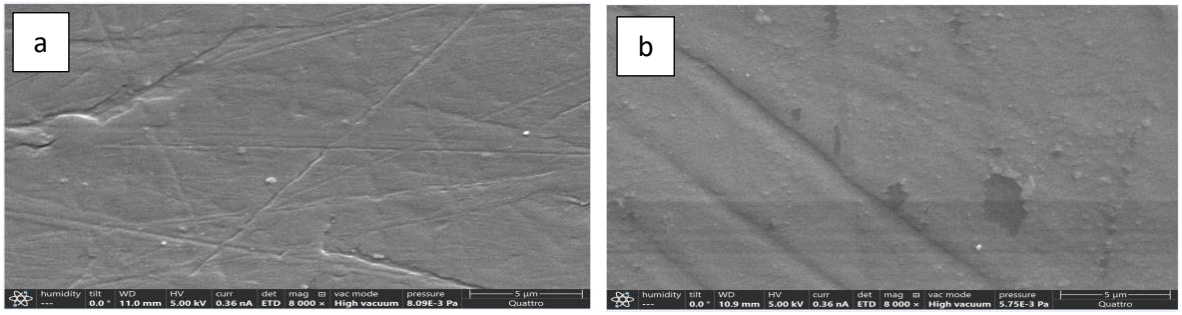

Figure 5: SEM micrographs (8000 mag) of (a) unaged PEEK (b) Aged PEEK in acids @100℃

4. Conclusion

The paper displays an overview of oil corrosion challenges due to the aggressive downhole environments. Potential challenges and the path forward of composites were discussed, highlighting that the aging of thermoplastic composites at harsh environment (high pressure and temperature and acids) was not fully addressed in the literature. Therefore, we focus on this work on aging of PEEK, which is one of the best thermoplastics that possesses good mechanical properties and chemical resistance, at high temperature (100 °C) and immersed in HCl. We used nanoindentaion test to characterize the young's modulus and hardness of PEEK. Moreover, we used DCS to investigate the thermal stability of the aged samples. The results demonstrated that the immersion of PEEK in HCL at 100 °C for 14 days has no influence on the thermal stability and the mechanical properties. As future plans, we will perform the aging of thin-film PEEK sheets to better understand the aging at high temperature and acids of PEEK, that will enable the prediction of the life time and degradation of bulk materials. Moreover, we plan for performing tests at environment that mimics the oil and gas industry atmosphere (high pressure up to70 bar, high temperature up to 100 °C, HCl, and hydrocarbon). Additionally, the same material will be aged in and oil that was collected from a field in the Middle East before any refinement process.

References

1. Ossai, C.I. Advances in Asset Management Techniques: An Overview of Corrosion Mechanisms and Mitigation Strategies for Oil and Gas Pipelines. ISRN Corros. 2012, 2012, 1–

  doi:10.5075/epfl-298799_978-2-9701614-0-0

2. Kermani, M.B.; Morshed, A. Carbon Dioxide Corrosion in Oil and Gas Production—A Compendium. Corrosion 2003, 59, 659–683. doi:10.5006/1.3277596

3. H. U. Khalid, M. C. Ismail and N. Nosbi, "Permeation Damage of Polymer Liner in Oil and Gas Pipelines: A Review", Polymers, 2020, 12, 2307

4. Bukhari, Amer. O., Bashar, Mohammad, Aladawy, Ahmed. S., Goh, Serena. L. M., and Pranjal Sarmah. "Review of Non-Metallic Pipelines in Oil & Gas Applications - Challenges & Way Forward." Paper presented at the International Petroleum Technology Conference, Riyadh, Saudi Arabia, February 2022.

5. Feder, Judy. "Future of Nonmetallic Composite Materials in Downhole Applications." J Pet Technol 72 (2020): 56–57. doi: https://doi.org/10.2118/0720-0056-JPT

6. Badeghaish, Wael , Noui-Mehidi, Mohamed , and Oscar Salazar. "The Future of Nonmetallic Composite Materials in Upstream Applications." Paper presented at the SPE Gas & Oil Technology Showcase and Conference, Dubai, UAE, October 2019. doi: https://doi.org/10.2118/198572-MS

7 . M. Roseman, R. Martin, G. Morgan. Composite materials in offshore oil and gas applications (2016). DOI: 10.1016/B978-1-78242-250-1.00010-7

8. Yusheng, Yuan; Jim, Goodson; “Advanced Composite Downhole Applications and HPHT Environmental Challenges,” NACE-04616, 2004.

9. Kargarpour, M.A .Investigation of reservoir temperature in a gas reservoir in Middle East: case study, August 2016, Journal of Petroleum Exploration and Production Technology 7(2) DOI: 10.1007/s13202-016-0275-1

10.Cogswell, F.N., Thermoplastic Aromatic Polymer Composites. First ed. 1992, Oxford: Butterworth-Heinmann Ltd. 277.

11.Platt, D.K., Engineering and High Performance Plastics. 2003: Rapra Technology Ltd. 198.

12. Mazumdar SK (2002) Composites Manufacturing: Materials, Product and Process. CRC Press

LLC, New York.

13. Zhu, C., Zhang, H. & Li, J. Thermal aging study of PEEK for nuclear power plant containment dome. J Polym Res 29, 5 (2022). https://doi.org/10.1007/s10965-021-02839-w

14.Liuqing Yang, Yoshimichi Ohki, Naoshi Hirai, Shugo Hanada, Aging of poly(ether ether ketone) by heat and gamma rays — Its degradation mechanism and effects on mechanical, dielectric and thermal properties(2017), https://doi.org/10.1016/j.polymdegradstab.2017.06.002.

15.Rocha, M.L., Leite, M.C., Ferreira, E., Melo, J.D., & Barbosa, A.P. (2021). Accelerated aging effects in composites used as repair for pipes in oil industry. *Polymer Composites*.

16.Bhaduri, A. (2018). Hardness. In: Mechanical Properties and Working of Metals and Alloys. Springer Series in Materials Science, vol 264. Springer, Singapore. https://doi.org/10.1007/978-981-10-7209-3_3

POLYETHERETHERKETONE (PEEK) / GRAPHENE BASED NANOCOMPOSITES FOR MULTIFUNCTIONAL BONE IMPLANT APPLICATIONS

Dan, Sun[a], Miaomiao, He[b,] Nan Jiang[c], Peije Tan[c], Li Zhang[b]

a: Advanced Composite Research Group (ACRG), School of Mechanical and Aerospace Engineering, Queen's University Belfast, Belfast, BT9 5AH, UK

b: Analytical & Testing Center, Sichuan University, Chengdu 610065, China

c: State Key Laboratory of Oral Diseases, & National Clinical Research Center for Oral Disease, & West China Hospital of Stomatology, Sichuan University, Chengdu, 610041, China

Abstract: *The use of PEEK has grown exponentially in the biomedical field in recent decades, yet PEEK's bio-inert nature remains a barrier for its applications as bone implants. In recent years, there has been an increasing demand for enhanced treatment efficacy for bone related diseases. This has driven the innovation of PEEK implants, from merely offering supporting mechanical properties, improved bioactivity, to providing multi-modal therapeutic functions. In this paper, the authors will provide an overview of the PEEK based nanocomposites developed in their own laboratories in recent years. We will start with introducing the modification of PEEK using graphene and/or its derivatives graphene oxide, and reveal how such modification can improve the bioactivity and photothermal properties of the resulting composite materials. We will then demonstrate the application of advanced coatings on these implants and show how such implants can be deployed for multimodal bone therapeutics such as bone cancer management and anti-infection applications.*

Keywords: polyetheretherketone (PEEK); nanocomposites; bone implants; 3D printing

1. Introduction

Due to its excellent biocompatibility and mechanical properties, PEEK has attracted great interest in biomedical implant related applications (1) and has been widely used as artificial spine and hip joint replacements (2, 3). Unfortunately, PEEK's bio-inertness often leads to fibrous encapsulation and subsequently loosening and failure of the implants (4). To address this issue, various bioactive nanomaterials have been embedded in PEEK to form nanocomposites that enhance the implants' *in vivo* osteoconductivity.

For instance, Ana et al. (5) added titanium dioxide (TiO_2) to PEI/PEEK composite. The TiO_2 nanoparticles strengthened the polymer matrix, making it suitable for long-term load-bearing implant applications. In addition, the bioactive TiO_2 also provides the implant with excellent bioactivity. Vaezi et al. (6) prepared PEEK/Hyhdroxy apatite (HA) composites. Despite the enhanced bioactivity due to the presence of HA, the mechanical strength of the composite has been greatly reduced with high concentration of HA. Other bioactive ceramics such as ß-TCP (7) and bioglasses have also been deployed to create PEEK based nanocomposites. However, when used as bulk reinforcement, ceramics tend to agglomerate at higher concentration, and hence compromise the resulting composites' mechanical properties (8, 9).

  doi:10.5075/epfl-298799_978-2-9701614-0-0

In recent years, graphene based nanomaterials and its derivatives (such as graphene oxide – GO) have been widely explored in a wide range of biomedical applications (10-12) due to their unique functionality and bioactivity (13). Yan developed graphene nannoplatelet (G) coated PEEK (14) and showed that the G coating promoted Bone marrow mesenchymal stem cells (BMSCs) proliferation and osteogenic differentiation on the implant surface. Arif et al. created 3D printed G reinforced PEEK composites (15). However, their 3D printed composites have not been demonstrated for biomedical applications. GO on the other hand, retained the unique structure and properties of G, but is rich in oxygen rich functional groups (16) which help promote cell adhesion and spreading (17). To date, GO has been used to reinforce various polymeric materials (such as polyamide 6 (18), chitosan (19), PVA (20), etc) for enhancing their mechanical properties. Despite their excellent properties, the use of G and GO in creating PEEK based nanocomposites was less reported for bioimplant applications. Additionally, G and GO possess unique photothermal conversion properties (21), making them ideal materials for providing new functionality for nanocomposite implants.

Our groups recently developed a range of G-PEEK (22) and GO-PEEK (12) nanocomposites through melt processing technique. The resulting nanocomposites were further processed and modified with functional coatings for multi-functional hard tissue implant applications. The unique photothermal property of G and GO has been exploited for bone cancer ablation and anti-microbial applications. In this paper, we summarized the latest research development in our laboratories.

2. Method

G-PEEK preparation: PEEK powder (average particle size = 25 μm) of was dried at 80 ◦C for 12 h before use. Graphene nanoplatelets (G, ~5 layers, radial size = 2 μm) was supplied by the Sixth Element Materials Technology Co., Ltd. PEEK powder with different G content was mixed with absolute ethanol (1 g powder/10 ml ethanol) and magnetically stirred for 30 min at room temperature. The PEEK/G mixture were then extracted by vacuum filtration and dried in a 60 ◦C oven until no further weight loss. G-PEEK composites with different G weight concentrations (0, 0.1, 0.5, 1, 2, 5%) were prepared by injection moulding using SJZS-10A mini conical twin-screw extruder at 367 ℃ and a screw speed of 40 rpm. The GO-PEEK nanocomposites preparation follows the same procedure as G-PEEK.

3D printed G-PEEK implant with hydroxy apatite (HA) coating: G-PEEK scaffold was prepared by 3D printing (Funmat HT, Intamsys, Shanghai, China) using G-PEEK composite filament (10wt%G) propared by melt processing/extension (23). A HA based drug-laden (antibiotics stearyltrimethylammonium chloride (STAC)) coating was then electrophoretically deposited (EPD) onto the scaffold.

The photothermal effect of all samples was tested under an 808 nm near-infrared laser (NIR) irradiation at a laser power density of 0.31 W/cm^2, and the sample's temperature change was monitored using an infrared thermal imaging system (TiS20+, Fluke, USA). The temperature data were analyzed using FLUKE software. Gram-negative *E. coli* (ATCC25922) and Gram-positive *S. aureus* (ATCC25923) were used to evaluate the antibacterial properties of the implants following (24). Bone marrow mesenchymal stem cells (BMSCs) in the third passage from three-day Sprague Dawley rats were chosen to study the osteogenic behaviors of samples. The BMSCs

  doi:10.5075/epfl-298799_978-2-9701614-0-0

were cultured with α-MEM (HyClone, USA) for 1 d. Confocal laser scanning microscopy (CLSM) (OLYMPUS, Japan) and Live/dead staining (Solarbio, China) was used for stained cell observation.

3. Results and Discussions

Figure 1a shows the CLSM images of BMSCs after seeding for 40 h. The results suggest that GO-PEEK composites allow better cell adhesion and spreading than pristine PEEK, with no obvious cytotoxicity. Figure 1 (b) shows that the representative GO-PEEK nanocomposite (0.5wt% GO) demostrates promising photothermal conversion effect. The sample can reach ~ 48 ◦C within 30 s, reaching therapeutic windown for cancer ablation (1).

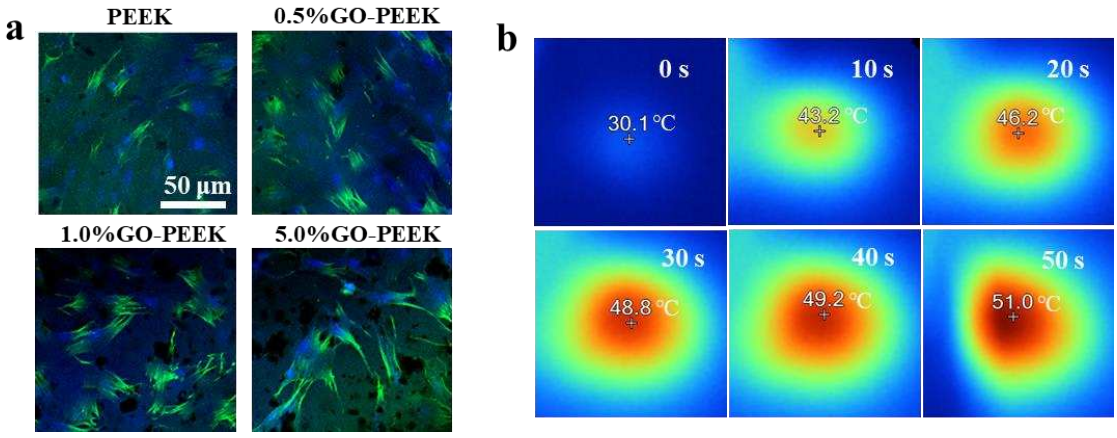

Figure 1. (**a**) CLSM images of BMSCs demostrating bioactivity of the PEEK and GO-PEEK implants *in vitro* and (**b**) photothermal effect of 0.5% GO-PEEK upon laser irradiation (0.31 W/cm^2 for 10 min)

For G-PEEK, the cell adhesion status reflected by cell morphology was illustrated in **Figure 2a**. On the prestine PEEK surface, globular cells exhibit limited spreading in spite of the abundant filopodia found on the cells' leading edge. In contrast, BMSCs on the G-PEEK samples show much better spreading, ellipsoidal with lamellipodia on 0.5% G-PEEK, or featuring polygonal morphologies on 1% G-PEEK and 5% G-PEEK, respectively. Figure 2b shows typical G-PEEK (0.5 wt% G) demostrating photothermal conversion effect, which enabled in vitro tumor cell ablation under NIR irradiation (**Figure 2b**) (23).

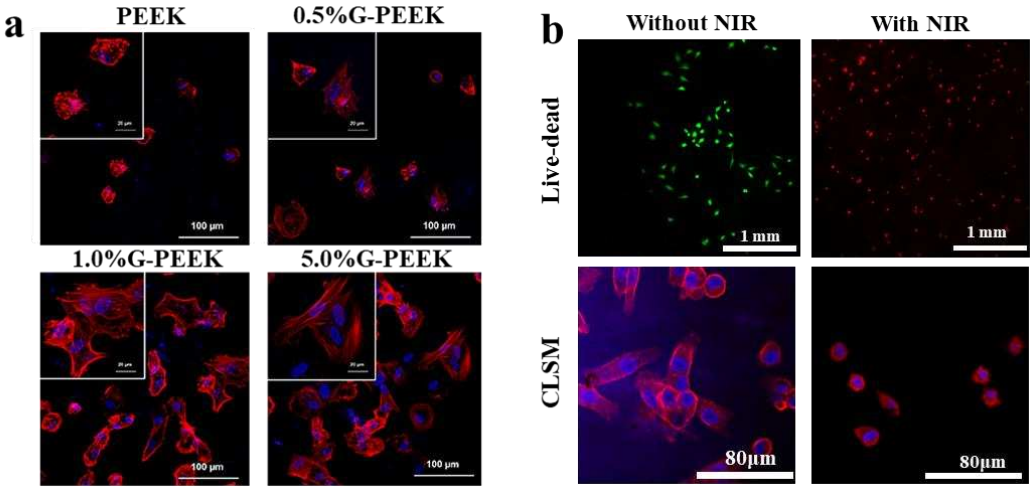

Figure 2. (**a**) CLSM images of BMSCs demostrating bioactivity of the PEEK and GO-PEEK implants *in vitro* and (**b**) Cancer cell (MG-63) ablation deploying photothermal effect of 0.5%G-PEEK (laser irradiation 0.31 W/cm^2 for 10 min)

Figure 3a shows the results for 3D printed G-PEEK scaffold with STAC loaded HA coating. Without laser irradiation, MG63 cells on all samples displayed strong pseudopodia attachment on the surfaces in all directions. Upon laser irradiation (0.31 W/cm^2 for 10 min), cells on G-PEEK and G-PEEK-HA exhibited typical rounded morphology, indicating MG63 growth was significantly inhibited. In this work, we incorporated antibacterial drug STAC into the HA coating to serve as antibacterial agents for broad-spectrum Gram-negative and Gram-positive bacteria. The bacteriostatic rates (BR) of G-PEEK-HA against *S. aureus* and *E. coli* are 99.99 and 56.82%, respectively. With NIR irradiation, the BR for both bacterial strains can reach 99.99%, attaining a bear total bacteria eradication (**Figure 3b**). The much greater BR for G-PEEK-HA is due to combined effect of laser induced heating and the STAC release [23].

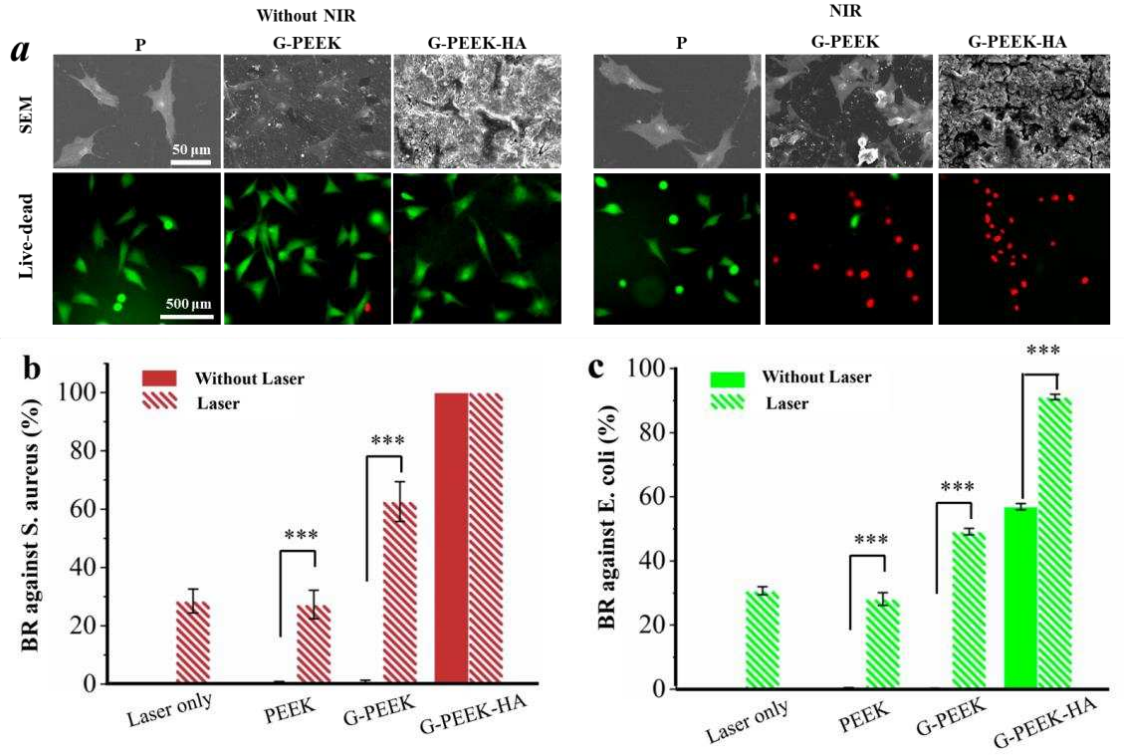

Figure 3. The growth of MG-63 (**a**) and antibacterial property (**b**) of PEEK, G-PEEK and G-PEEK-HA with and without NIR irradiation

Acknowledgements

This work was funded by the National Natural Science Foundation of China (51673131, 81772397 and 81871772) and supported by Sichuan Science and Technology Program (2021YFS0218 and 2021YFH0134). Data can be made available upon reasonable request.

4. References

1. He M, Huang Y, Xu H, Feng G, Liu L, Li Y, et al. Modification of polyetheretherketone implants: From enhancing bone integration to enabling multi-modal therapeutics. Acta biomaterialia. 2021;129:18-32.
2. Almasi D, Lau WJ, Rasaee S, Sharifi R, Mozaffari HR. Fabrication of a novel hydroxyapatite/polyether ether ketone surface nanocomposite via friction stir processing for orthopedic and dental applications. Progress in Biomaterials. 2020;9(1):35-44.
3. Bathala L, Majeti V, Rachuri N, Singh N, Gedela S. The Role of Polyether Ether Ketone (Peek) in Dentistry - A Review. J Med Life. 2019;12(1):5-9.
4. Yuan B, Cheng Q, Zhao R, Zhu X, Yang X, Yang X, et al. Comparison of osteointegration property between PEKK and PEEK: Effects of surface structure and chemistry. Biomaterials. 2018;170:116-26.
5. Díez-Pascual AM, Díez-Vicente AL. Nano-TiO2 Reinforced PEEK/PEI Blends as Biomaterials for Load-Bearing Implant Applications. ACS applied materials & interfaces. 2015;7(9):5561-73.
6. Vaezi M, Black C, Gibbs DM, Oreffo RO, Brady M, Moshrefi-Torbati M, et al. Characterization of New PEEK/HA Composites with 3D HA Network Fabricated by Extrusion Freeforming. Molecules. 2016;21(6):687.
7. Von Wilmonsky C, Lutz R, Meisel U, Srour S, Rupprecht S, Toyoshima T, et al. In Vivo Evaluation of ß-TCP Containing 3D Laser Sintered Poly(ether ether ketone) Composites in Pigs. Journal of Bioactive and Compatible Polymers. 2009;24(2):169-84.
8. von Wilmowsky C, Vairaktaris E, Pohle D, Rechtenwald T, Lutz R, Munstedt H, et al. Effects of bioactive glass and beta-TCP containing three-dimensional laser sintered polyetheretherketone composites on osteoblasts in vitro. Journal of Biomedical Materials Research Part A. 2008;87(4):896-902.
9. Jang HL, Lee K, Kang CS, Lee HK, Ahn H-Y, Jeong H-Y, et al. Biofunctionalized ceramic with self-assembled networks of nanochannels. ACS nano. 2015;9(4):4447-57.
10. Guo Z, Jiang N, Moore J, McCoy CP, Ziminska M, Rafferty C, et al. Nanoscale Hybrid Coating Enables Multifunctional Tissue Scaffold for Potential Multimodal Therapeutic Applications. ACS applied materials & interfaces. 2019;11(30):27269-78.
11. Su Z, Sun D, Zhang L, He M, Jiang Y, Millar B, et al. Chitosan/Silver Nanoparticle/Graphene Oxide Nanocomposites with Multi-Drug Release, Antimicrobial, and Photothermal Conversion Functions. Materials. 2021;14(9).
12. He M, Chen X, Guo Z, Qiu X, Yang Y, Su C, et al. Super tough graphene oxide reinforced polyetheretherketone for potential hard tissue repair applications. Composites Science and Technology. 2019;174:194-201.
13. Newby SD, Masi T, Griffin CD, King WJ, Chipman A, Stephenson S, et al. Functionalized Graphene Nanoparticles Induce Human Mesenchymal Stem Cells to Express Distinct Extracellular Matrix Proteins Mediating Osteogenesis. Int J Nanomedicine. 2020;15:2501-13.
14. Yan JH, Wang CH, Li KW, Zhang Q, Yang M, Di-Wu WL, et al. Enhancement of surface bioactivity on carbon fiber-reinforced polyether ether ketone via graphene modification. Int J Nanomedicine. 2018;13:3425-40.
15. Arif MF, Alhashmi H, Varadarajan KM, Koo JH, Hart AJ, Kumar S. Multifunctional performance of carbon nanotubes and graphene nanoplatelets reinforced PEEK composites enabled via FFF additive manufacturing. Composites Part B: Engineering. 2020;184:107625.
16. Shin SR, Zihlmann C, Akbari M, Assawes P, Cheung L, Zhang K, et al. Reduced Graphene Oxide-GelMA Hybrid Hydrogels as Scaffolds for Cardiac Tissue Engineering. Small. 2016;12(27):3677-89.

17. Peng S, Feng P, Wu P, Huang W, Yang Y, Guo W, et al. Graphene oxide as an interface phase between polyetheretherketone and hydroxyapatite for tissue engineering scaffolds. Scientific reports. 2017;7:46604.
18. Kelnar I, Kratochvíl J, Kaprálková L, Špitálsky Z, Ujčič M, Zhigunov A, et al. Effect of Graphene Oxide on Structure and Properties of Impact-Modified Polyamide 6. Polymer-Plastics Technology and Engineering. 2018;57(9):827-35.
19. Han D, Yan L, Chen W, Li W. Preparation of chitosan/graphene oxide composite film with enhanced mechanical strength in the wet state. Carbohydrate Polymers. 2011;83(2):653-8.
20. Xu Y, Hong W, Bai H, Li C, Shi G. Strong and ductile poly(vinyl alcohol)/graphene oxide composite films with a layered structure. Carbon. 2009;47(15):3538-43.
21. Song P, Xu Z, Wu Y, Cheng Q, Guo Q, Wang H. Super-tough artificial nacre based on graphene oxide via synergistic interface interactions of π-π stacking and hydrogen bonding. Carbon. 2017;111:807-12.
22. Jiang N, Tan P, He M, Zhang J, Sun D, Zhu S. Graphene reinforced polyether ether ketone nanocomposites for bone repair applications. Polymer Testing. 2021;100:107276.
23. He M, Zhu C, Xu H, Sun D, Chen C, Feng G, et al. Conducting Polyetheretherketone Nanocomposites with an Electrophoretically Deposited Bioactive Coating for Bone Tissue Regeneration and Multimodal Therapeutic Applications. ACS applied materials & interfaces. 2020;12(51):56924-34.
24. He M, Hou Y, Jiang Y, Li Y, Zou Q, Chen C, et al. Quaternization on polyetheretherketone and its antimicrobial activity. Materials Letters. 2019;235:242-5.

DESIGN OF FIBRE-COMPOSITE STRUCTURES – EUROPEAN TECHNICAL SPECIFICATION: OVERVIEW AND SCOPE

Luigi Ascione[a], João R. Correia[b], Thomas Keller[c], Jan Knippers[d], Toby Mottram[e], Carlo Paulotto[f], Jose Sena-Cruz[g]

a: University of Salerno – l.ascione@unisa.it
b: University of Lisbon
c: EPFL
d: University of Stuttgart
e: University of Warwick
f: ACCIONA
g: University of Minho

Abstract: *In 2010, the European Community issued the Mandate M/466 to CEN/TC 250 starting the procedure aimed at creating a new generation of structural Eurocodes.*
During the current revision of the first generation of Eurocodes, i.e. the establishment of a second generation, it has been decided to initiate the development of a Eurocode for fibre-polymer composite structures, which were not included in the previous generation.
One of the aims of this paper is to summarize the main steps of the procedure launched by CEN TC 250 [1], as well as the activities so far developed relating to fibre-polymer composite structures.
The document also highlights the scope of application of a Technical Specification drafted up to now, as a preparatory document for the Eurocode, its regulatory characteristics, and an overview of its contents.

Keywords: Materials; Design; Structural Analysis; Eurocodes

1. Introduction

In 2010, the European Community issued the Mandate M/466 to CEN/TC 250 starting the procedure aimed at creating a new generation of structural Eurocodes [1]. The previous one has been in use since 2002.

During the current revision of the first generation of Eurocodes, i.e. the establishment of a second generation, it was decided to start the development of a Eurocode for composite structures, following the classic procedure envisaged by CEN and consisting of three successive phases. Indeed, the first generation did not yet include a Eurocode for fibre-polymer composite structures (referred to as composite structures in the following and known as Fibre-Reinforced Polymer (FRP) structures).

In a first phase, the Scientific and Technical Research Report 'Prospect for New Guidance in the Design of FRP' (EUR 27666) [2] was published by the Working Group WG 4 of CEN/TC250. Based on this report, the development of a CEN Technical Specification (TS) 'Design of Fibre-Polymer Composite Structures' was initiated and a Project Team WG 4.T2 (PT), associated with WG 4, was nominated to prepare this document. The denomination change from FRP to Fibre-Polymer

  doi:10.5075/epfl-298799_978-2-9701614-0-0

Composite Structures was motivated because the former does not correctly reflect the structural roles of the two components, fibres, and polymer, in the composite material. Furthermore, the new denomination is in line with that in other European languages, which all include the term 'composite' or 'composites' in an equivalent translation.

The TS represents the second step of the general procedure established by CEN/TC 250 towards a new generation of Eurocodes. CEN has attributed to TS the identification FprCEN / TS 19101: 2021.

The information provided in this paper corresponds to the most up-to-date state of the procedure, which has undergone a significant acceleration in the last year with the introduction of changes in the text of the TS compared to previous versions [3].

Three subsequent drafts of TS have been subjected to revision by the European National Standards Bodies, and an internal ballot between the members of CEN TC 250 on the conversion of FprCEN / TS 19101 to EN status, the final text of the TS, as revised after the internal ballot, will be submitted in the April 2022 to Formal Vote by the National Members of CEN, who will decide on its approval. Once approved, the TS will be announced and made available at a national level, but conflicting national standards may continue to exist. The conversion of the TS by CEN/TC250, after a period of one to three years for trial use and commenting, into a new Eurocode will be the third and last step.

The document is organized in the same way as the other Eurocodes and comprises twelve Clauses and five Annexes; their main principles and the corresponding background are summarized in the following sections, whose numbering, from 3 to 12, is the same as that of the clauses of the TS.

2. Scope

The scope of the Technical Specification is presented in clause 1. The TS applies to the design of buildings, bridges, and other civil engineering structures, including permanent and temporary structures, made with composite materials or combinations of composite and other structural materials (for hybrid-composite structures). The structural types which are included in the document, even if different types are not excluded, are composite laminates, profiles, sandwich panels (including web-core panels), bolted and bonded joints, composed of glass, carbon, basalt or aramid fibres, thermoset resins and adhesives, and polymeric foam or balsa wood cores. More explicitly, composite cables, concrete rebars, strengthening components and honeycomb cores are not covered by the TS. The main manufacturing processes covered by the document are pultrusion, filament winding, hand layup, resin transfer moulding (RTM), resin infusion moulding (RIM), and vacuum-assisted resin transfer moulding (VARTM).

The TS applies to composite structures in which the temperatures inside members, joints, and components, under service conditions, range from -40°C to T_g - 20°C, where T_g is the lowest glass transition temperature of either the composite, the core, or adhesive materials. T_g is specified as the onset value of the storage modulus decay, obtained from dynamic mechanical analysis (DMA), and should be at least 60°C.

3. Terms, Definitions and Symbols

Terms are introduced in clause 3 relating to the constituent materials, manufacturing, composite components and members, design, failure modes, joints and connections, and defects. In the

  doi:10.5075/epfl-298799_978-2-9701614-0-0

same clause a detailed list of symbols and abbreviations is included, and conventions and member axes are specified.

4. Basis of design

The basis of design is developed in accordance with the general rules given in prEN 1990:2018 [4], supplemented by provisions that are specific to composite structures. According to the rules for limit state design, the design value of resistance, R_d, for a specific design situation should satisfy:

$$R_d = \frac{1}{\gamma_{Rd} \cdot \gamma_m} R\left\{\eta_{c,i} \cdot X_{k,i}; a_d\right\} \quad (1)$$

where

- γ_{Rd} is a partial factor taking into account the uncertainty in the resistance model, and geometrical deviations, if these are not modelled explicitly.
- γ_m is a partial factor taking into account the unfavourable deviations of the representative material or product properties from their characteristic values, and geometrical deviations.
- $R\{\ldots\}$ denotes the output of the resistance model.
- $\eta_{c,i}$ is the total conversion factor, taking into account effects of moisture and temperature, effects of ageing of materials, including the uncertainty of those effects;
- $X_{k,i}$ represents the characteristic values of material or product properties;
- a_d denotes the design values of geometrical parameters.
- i takes into account the i^{th} material.

For the design of creep rupture, fatigue, adhesive connections, and fire, the product $\gamma_{Rd} \cdot \gamma_m$ is replaced by γ_M, which is a single partial material factor considering all the uncertainties and deviations mentioned above.

The partial factor for a material or product property, γ_m, depends only on their coefficient of variation and shall be determined by testing.

For the partial factor for the resistance model, γ_{Rd}, values are given for (i) profiles and laminates (for material failure and global and local buckling); (ii) sandwich panels (for material failure, global and local buckling, laminate wrinkling, core indentation and punching failure); (iii) bolted joints (for net-tension, pin-bearing, shear-out, block shear, and pull-out failure).

Where possible, γ_{Rd} values were derived from detailed statistical analyses of a significant number of resistance models, based on the assumptions of prEN 1990:2018 [4] and ISO 2394:2015 [5]; some of the values were also validated through explicit reliability analyses of design equations based on the Eurocode format.

  doi:10.5075/epfl-298799_978-2-9701614-0-0

The total conversion factor, η_c, is composed of two conversion factors for temperature and moisture effects and can be expressed as $\eta_c = \eta_{ct} \cdot \eta_{cm}$. Nominal values are given for specific composite, core and adhesive materials, and for specific environmental conditions, for a 50-year period (which may be extended, if appropriate maintenance and inspection procedures are implemented). These nominal values were derived from experimental results collected from the literature. As an alternative to the nominal conversion factors, the temperature - and moisture-dependent material properties may be determined by testing in accordance with Annex D in prEN 1990:2018. The same applies for any properties affected by environmental conditions not covered by the nominal factors.

The conversion factor for the temperature, η_{ct}, takes into account changes of material properties due to material temperatures under service conditions, excluding any effects of long-term exposure. Nominal values are provided for the composite materials; these depend on whether the properties are fibre- or matrix-dominated and are functions of T_g. Further values are listed for sandwich foam and balsa wood core materials, with the former also depending on T_g and the latter on density.

The conversion factor for the moisture, η_{cm}, takes into account changes of the material properties due to moisture absorption over time, including ageing effects resulting from long-term exposure. The nominal values were derived for unprotected composite materials and epoxy adhesives, for three exposure classes: class I represents indoor exposure, class II basically concerns outdoor exposure without continuous exposure to water or high relative humidity, while class III basically represents continuous exposure to water or high relative humidity. Also in this case, the nominal values provided were derived from experimental values collected from the literature.

A sub-clause concerning creep effects is further included, complemented by an annex. Both effects of creep on the strength and on the deformations are taken into account. The creep effects on the strength limit the stress levels in composite members and components for the quasi-permanent combinations of actions. Creep effects on the deformations are taken into account by creep coefficients, which reduce the relevant moduli of elasticity of the materials. Values are specified for different moduli for pultruded composite profiles, composite laminates/plies, and core materials, for a 50-year period; they were derived from experimental results collected from the literature. Annex A provides further values for additional periods of design service lives.

5. Materials

Standard test methods are specified to obtain the composite, core and adhesive material properties normally required in the design of composite structures. Preferably, the TS refers to EN ISO standards; alternatively, reference to ASTM standards is made. Instructions for how to extract or manufacture test coupons are also provided, to avoid damaging a composite member and for when the laminates are relatively thick. For a preliminary design, indicative (mean) values of selected material properties are listed in Annex B, which can be applied, provided that appropriate values of the coefficients of variation are assumed to derive characteristic (design) values.

  doi:10.5075/epfl-298799_978-2-9701614-0-0

6. Durability

Clause 6 provides guidance regarding the selection and processing of constituent materials, describes the most relevant environmental conditions and their main effects on material properties over time, and recommends where protective measures should be applied, for both composite members and their connections and joints. The clause considers the environmental conditions of temperature, moisture (humidity, water), chemicals, and ultraviolet (UV) radiation, acting in isolation or in combination.

7. Structural Analysis

Detailed provisions for the structural analysis of composite laminates, profiles, sandwich panels, joints and hybrid composite structures are provided in clause 7. In the case of sandwich panels, panels composed of thin face sheets and homogeneous flexible or rigid cores, or web cores, are explicitly taken into account. Concerning joints, simple, semi-continuous and continuous joints are differentiated.

First-order analysis, based on the initial geometry of the structure, and second-order analysis, taking into account the influence of the deformation of the structure, with consideration of imperfections, are described.

Analytical and finite element modelling approaches for composite laminates, profiles and sandwich panels are subsequently provided.

8. Ultimate Limit States

Ultimate limit state (ULS) verifications for composite laminates, profiles and sandwich panels are described in four sub-clauses and one Annex (Annex C for laminates and profiles). The ULS verification for creep rupture is also provided.

For what concerns the laminates, ULS verifications are provided for balanced symmetrical laminates in the cases of in-plane axial, shear and bending stresses, out-of-plane tensile and bending stresses, interlaminar shear stresses, and combined stresses.

The ULS verifications for profiles concern the typical cases of internal forces and moments, i.e. axial forces, bending, shear, transverse compression, torsion, and combinations of the axial forces and bending, and bending and shear.

Concerning sandwich panels, 20 principal failure modes of the components, i.e. face sheet, core, web in web-core, interface, and the entire panel are included, which should be considered in the ULS verification. In addition to the typical laminate failure modes and core shear failure, the sub-clause includes laminate wrinkling, core indentation and core punching failures. Concerning the face sheet-core interface, interface failure must not occur; failure must occur in the core, which requires testing for verification.

9. Serviceability Limit States

The serviceability criteria considered in the document include deflections, vibrations, and matrix cracking of composite laminates. The latter should be prevented by considering limits of the tensile strain due to the frequent combination of actions, considering the effects of creep in

  doi:10.5075/epfl-298799_978-2-9701614-0-0

permanent and quasi-permanent loads. Corresponding values are provided for composite laminates composed of polyester and epoxy resins.

10. Fatigue

Since fatigue failure normally occurs at locations where geometrical changes in sections or changes in materials generate stress concentrations, a stress-based verification is difficult. Therefore, the fatigue verification, including testing, is conducted at the structural member or joint level (e.g. for a bridge deck or a deck-to-girder joint), based on the action effects, i.e. internal forces and/or moments. Testing at the member and joint level inherently takes into account any geometrical and material imperfections and size effects. A criterion is provided to check whether a fatigue verification is required.

The fatigue verification is performed according to Eq. (1), using a single partial material factor for the fatigue resistance, γ_{Mf}, as mentioned above. The characteristic value of the fatigue resistance of a member or joint is obtained from member or joint testing, at constant amplitude cycles. The conversion factors for static loading are assumed to also be applicable for fatigue. The currently available fatigue data is not sufficient to derive fatigue-specific values; this assumption therefore requires justification by new research.

The partial factor for the fatigue resistance depends on (i) the type of inspection and maintenance and accessibility of the critical details, and (ii) the consequences of failure, i.e. whether or not a member or joint is fail-safe, in accordance with the EUROCOMP guidance [7] and prEN 1990:2018 [4], 8.3.4.4(1), Note 4. Due to the lack of sufficient experimental results, the values listed in the TS were adopted from EUROCOMP, although it was not possible to find their provenance and thus validate them. Plausibility checks were performed, but the values specified in the TS still require further verification.

Qualification and proof testing are specified; the former refers to prEN 1990:2018 [4], D4(1a), and the latter to D4(1e). For bridges, the required number of fatigue tests and fatigue cycles in qualification testing is indicated according to the traffic category, for a 100-year design service life. Proof testing shall be defined case by case in the project-specific quality plan.

11. Detailing

Provisions concerning detailing are provided in clause 11 to minimize any stress concentrations, effects of environmental conditions, and effects of tolerances and imperfections. Profiles, sandwich panels and member laminates, aa well as bolted and adhesive connections are covered. Annex E, which is only informative, shows typical details for bridges, such as bearings, expansion joints, parapets, and crash barrier fixations.

12. Connections and Joints

Clause 12 is devoted to the connections and is subdivided into three sub-clauses, for bolted, adhesive and hybrid bolted-adhesive connections, and joints (whereby a joint is composed of one or more individual connections). Concerning bolted connections under in-plane forces, the resistances in the case of laminate failure modes to be verified are net-tension, pin-bearing, shear-out, and block-shear failure. Subjected to out-of-plane tensile forces, the failure modes at the bolt locations are pull-out failure through the laminate, bolt failure in tension, and failure of the laminate at a bolt location owing to interaction between in- and out-of-plane forces. At the joint level, shear and tying force failures of web cleat joints are considered.

  doi:10.5075/epfl-298799_978-2-9701614-0-0

A composite structure comprising adhesive joints shall be designed as fail-safe, i.e. joint failure shall not result in failure of the structure or critical parts thereof. Failure of an adhesive joint is considered as an accidental situation according to prEN 1990:2018 [4]. The failure mode of adhesive connections shall be either cohesive failure in the adhesive or fibre-tear failure in the adherend; adhesive failure, i.e. failure in the adherend-adhesive interface, shall be prevented by appropriate material selection and surface preparation.

The resistance verification of adhesive connections is performed according to Eq. (1), using a single partial material factor for the adhesive connection resistance, $\gamma_{M,ac}$, as mentioned above. This partial factor depends on (i) the type of inspection and maintenance and accessibility of the adhesive connection, and (ii) the application conditions, either with fully controlled, i.e. reproducible process parameters, or only partially controlled parameters. Owing to insufficient experimental results, the range of values specified is adopted from EUROCOMP [7], 5.1.10, P(4), i.e. from the products of the partial factors $\gamma_{m,1} \cdot \gamma_{m,2}$. The background to these values could not be traced and they thus require further validation. Three methods are described for the design of adhesive joints and connections: (i) design assisted by testing; (ii) design based on stress analysis; (iii) design based on fracture mechanics. Stress-based and fracture mechanics-based failure criteria are provided for the latter two methods and experimental validation is mandatory in both cases.

Provisions are included for the design of hybrid bolted-adhesive connections. Depending on the relative stiffness of the adhesive layer, the individual resistances of the bolted and adhesive connections can be summed or not.

13. Structural Fire Design

Annex D of the document applies to the design of composite structures for the accidental design situation of fire exposure. Composite structures that fulfil a load-bearing function, separating function or both are considered. The structure of this Annex complies with the parts concerning fire of the Eurocodes for other structural materials.

The first sub-clause provides the basis of design, including nominal and physically based fire exposures, actions, design values of material properties, verification methods, member analysis, analysis of parts of structures, global structural analysis, and fire protection measures.

The second sub-clause includes material properties, i.e. thermal properties (emissivity coefficient, thermal conductivity, specific heat, density), and mechanical properties (strength and stiffness, thermal expansion coefficient). For each property, indicative, temperature-dependent values are given for selected composite, foam and balsa core materials, wherever sufficient experimental data was available.

Further sub-clauses comprise tabulated design data, simplified design methods, and advanced design methods.

14. Concluding remarks

Respect to the document published in the first step, i.e. the 'Prospect' [2], towards establishing a structural Eurocode for the design of fibre-polymer composite structures, the following main clauses or sub-clauses were subject to major revision or were added in the TS: (i) Basis of design (regarding partial factors for materials, conversion factors and creep coefficients); (ii) Ultimate

  doi:10.5075/epfl-298799_978-2-9701614-0-0

limit states of sandwich structures; (iii) Creep rupture; (iv) Fatigue; (v) Adhesive joints and connections; (vi) Detailing; (vii) Structural fire design.

Unfortunately, it was not possible to introduce execution rules in the TS as they fall outside the scope of CEN/TC 250. In special cases, CEN/TC 250 may propose to develop implementation rules if no other Technical Committee will undertake the work. The process can be initiated, as desirable, with input from all stakeholders, including constructors. WG 4 will endeavor to promote such an initiative as soon as possible.

The TS will be complemented by a Background Document, which provides background reports for the paragraphs and justifications for the decisions that were taken, and values selected. Furthermore, to support the designer community a document comprising design examples based on the TS clauses will be provided.

15. References

1. CEN/TC 250 Structural Eurocodes: N 1250, Policy Guidelines and Procedures. Version 9.1, 17 March 2020.
2. Ascione L, et al. Prospect for New Guidance in the Design of FRP. EUR 27666, 2016, DOI: 10.2788/22306 (online).
3. Keller T, Correia J R, Knippers J, Mottram T, Paulotto C, Ascione L. *CEN Technical Specification of Fibre_Polymer Composite Structures*. SAMPE Europe Conference 2020 Amsterdam-Netherlands.
4. CEN/TC 250, prEN 1990: 2018, Basis of structural and geotechnical design.
5. CEN, ISO 2394: 2015, General principles on reliability for structures.
6. CEN/TC 250, EN 1991-2: 2003, Actions on structures - Part 2: Traffic loads on bridges.
7. J.L. Clarke (ed.). Structural Design of Polymer Composites: Eurocomp Design Code and Handbook. London: E & FN Spon, 1996.

  doi:10.5075/epfl-298799_978-2-9701614-0-0

DESIGN OF FIBRE-POLYMER COMPOSITE STRUCTURES – EUROPEAN TECHNICAL SPECIFICATION: BASIS OF DESIGN

João R. Correia[a], João Pacheco[a], John D. Sørensen[b], Thomas Keller[c], J. Toby Mottram[d], J. Sena-Cruz[d]

a: CERIS, IST, University of Lisbon, Portugal – joao.ramoa.correia@tecnico.ulisboa.pt
b: Aalborg University, Denmark
c: EPFL, Switzerland
d: University of Warwick, UK
e: University of Minho, Portugal

Abstract: *This paper presents the basis of design of the European Technical Specification (TS) FprCEN/TS 19101 for the ultimate limit state (ULS) design of fibre-polymer composite structures, which follows the philosophy and partial factor format of the Eurocodes. The first part of the paper describes the general format of the design value of resistance adopted in the TS. The second part describes the particularization of such general format for specific types of ULS design, where a differentiation is made between the ULS design of: (i) composite components and members, and bolted connections and joints; and, (ii) creep rupture, fatigue, adhesive connections and fire. The final part of the paper presents a summary of the values of the partial factors included in the TS and provides the rationale for their definition.*

Keywords: Fibre-polymer composites; European Technical Specification; Basis of Design; Partial factors.

1. Introduction

The resistance format defined in the European Technical Specification (TS) FprCEN/TS 19101 [1], *Design of Fibre-Polymer Composite Structures*, follows the philosophy and partial factor format of the Eurocode suite: a semi-probabilistic equation assures that design complies with a target probability of failure or reliability index (β), through partial factors and characteristic values of the parameters of design, as per EN 1990, Annex C [2]. This format implies that a design value of load effects (E_d) is compared with a design value of resistance (R_d).

The first part of the paper (section 2) describes the general format of the design value of resistance, R_d, adopted in the TS. The second part (section 3) describes the particularization of such general format for specific types of ultimate limit state (ULS) design: (i) for fibre-polymer composite components and members, and bolted connections and joints, the resistance format adopted in the TS has two partial factors, one for the resistance model (γ_{Rd}) and one for a representative material property (γ_m); (ii) for creep rupture, fatigue, adhesive connections and fire design, the combinations of γ_m and γ_{Rd} are replaced by single partial factors (γ_M), accounting for uncertainties in the resistance model and material properties, as well as geometrical deviations. The final part of the paper (section 4) presents a summary of the values of partial factors γ_{Rd} and γ_M included in the TS; regarding partial factor γ_{Rd}, for selected failure modes, the estimation of model uncertainties is illustrated, which involved: (i) a large-scale survey of experimental data available in the literature; and, in some cases, (ii) reliability analyses to validate or calibrate the proposed values.

  doi:10.5075/epfl-298799_978-2-9701614-0-0

2. General format of the design value of resistance

The general format of the design value of resistance adopted in the TS is defined according to the provisions of EN 1990 [2]. Each failure mode is associated with a resistance model - $R\{\ldots\}$, and the design value of resistance (R_d) is calculated from that resistance model. For a specific design situation, the design value of resistance (R_d) should be calculated from Eq. (1),

$$R_d = \frac{1}{\gamma_{Rd}} R\left\{ \eta_{c,i} \cdot \frac{X_{k,i}}{\gamma_{m,i}}; a_d; \sum F_{Ed} \right\} \quad (1)$$

where:

- γ_{Rd} is a partial factor accounting for the uncertainty in the resistance model, and for geometrical deviations, if these are not modelled explicitly;
- $R\{\ldots\}$ denotes the output of the resistance model;
- $\eta_{c,i}$ is the conversion factor accounting for effects of temperature and moisture, and effects of ageing of materials;
- $X_{k,i}$ represents the characteristic values of material or product properties (defined as 5% fractiles);
- $\gamma_{m,i}$ is a partial factor for a material or product property accounting for unfavourable deviations of the material or product properties from their characteristic values and the random part of the conversion factor, $\eta_{c,i}$;
- a_d denotes the design values of geometrical parameters;
- F_{Ed} denotes the design values of actions used in the assessment of the design value of the effect of actions, E_d;
- i is for the i^{th} material or product property.

EN 1990 [2] also presents particularizations of this resistance format. The most commonly used one resorts to a partial factor for material properties that includes both the uncertainties in the material or product property and the uncertainties due to resistance modelling and geometric deviations ($\gamma_{M,i}$). This partial factor is obtained from:

$$\gamma_{M,i} = \gamma_{Rd} \cdot \gamma_{m,i} \quad (2)$$

From Eq. (1) follows that the definition of the safety checks of codes requires the assumption of factors for the uncertainties in material properties and resistance modelling. Such factors are representative when they cover the applications (concerning production, specification and design) expected to be found for fibre-polymer composite materials and/or products used in civil engineering. However, unlike other structural materials (e.g. structural steel and reinforced concrete), the uncertainty of material properties found in laminated composites is not bound to a specific range [3]. So, with the exception of design for creep rupture, fatigue, adhesive connections and fire (see section 3), the TS does not replace $\gamma_{m,i}$ and γ_{Rd} with $\gamma_{M,i}$, and it does not present a constant value for $\gamma_{m,i}$. Section 3.1 discusses this issue in further depth.

Another difference of the TS for fibre-polymer composites in comparison to other material-oriented Eurocodes (e.g. EN 1992 and EN 1993) is that in ULS design the stiffness properties of materials are not considered through mean values. Since the ULS design of members with thin-walled sections is often governed by buckling phenomena (because of high strength-to-stiffness

  doi:10.5075/epfl-298799_978-2-9701614-0-0

ratio, as well as due to the importance of material stiffness in buckling failure modes), in ULS resistance formulae, material stiffness is considered with characteristic values. Nonetheless, for both serviceability limit state (SLS) design and to compute the load-effects of ULS design, mean values of material stiffness properties should be considered. The latter is important when finite element methods are used [4] or whenever hyperstatic structures are modelled.

The characteristic value of a material property is determined by: (i) testing according to the appropriate test standard; (ii) using statistical methods to determine the 5% fractile of the data. Subclause D8.2 of Annex D of EN 1990 may be used for this purpose. Similarly, partial factor γ_m is defined based on test result records – see 4.4.5(1-3) of the TS. For the determination of the total conversion factor $\eta_{c,i}$ to be used in a case of design, guidance is given in Subclause 4.4.7 of the TS. Subclause 4.4.6 of the TS concerns γ_{Rd} for different failure modes.

The design value of a geometrical property (a_d) should be considered equal to its nominal value, unless otherwise stated or recommended. Since geometrical variability is not directly accounted for in most formulae of the other Eurocodes and keeping consistency with such codes is intended, the resistance model does not make allowance for explicit consideration of geometrical uncertainty - see Eq. (1), but such uncertainty may be relevant. This was observed for flexural-torsional buckling [5]. In this case, geometrical variability is implicitly accounted for in the design value of resistance, through consideration of geometrical deviations in the calibration of the partial factor γ_{Rd} [3].

The next section particularizes the resistance format of Eq. (1) for specific types of design.

3. Particularization of general format for specific types of ULS design

3.1. ULS design of components and members, bolted connections and joints

For the ULS design of fibre-polymer composite components and members (Clause 8) and bolted connections and joints (subclauses 12.2 and 12.3), the design value of resistance, R_d, should be calculated from Eq. (3),

$$R_d = \frac{1}{\gamma_{Rd} \cdot \gamma_m} R\left\{\eta_{c,i} \cdot X_{k,i}; a_d; \sum F_{Ed}\right\} \tag{3}$$

where γ_m is a partial factor for a material or product property accounting for the unfavourable deviations of the representative material or product properties from their characteristic values and the random part of the conversion factor.

The differences between Eq. (1) and the format for the design value of resistance for the design of components, members, bolted connections and joints of fibre-polymer composites, Eq. (3), are:

- The replacement of individual partial factors for each material property i, $\gamma_{m,i}$, by an overall partial factor (γ_m), determined from a representative material property;
- This representative partial factor γ_m is outside the brackets of the expression of the resistance model $R\{\ldots\}$ – that is, the resistance factor approach [2].

A representative γ_m is used because of the several material properties involved in the resistance models for components and connections. If several partial factors $\gamma_{m,i}$ were used, either design would become overly-conservative (thus, uneconomical), or the partial factors would be below 1,0 – this would occur because the design values of many material properties actually correspond to values closer to the mean than to the 5% fractile (refer to [5] for the definition of

  doi:10.5075/epfl-298799_978-2-9701614-0-0

the design value of a random variable). Furthermore, the reliability index β for different failure modes would be inconsistent if such a format was used because different resistance models include a different number of material properties. Therefore, the TS includes a single representative partial factor γ_m, which is determined from the variability of a representative material property. The representative material property for each failure mode was determined based on mechanical considerations and reliability concepts, and may be regarded as the material property whose uncertainty is the most relevant for the reliability index β of that failure mode. The representative material property is specifically stated in the subclause that refers to each failure mode. The same applies for the conversion factor $\eta_{c,i}$.

Eq. (3) defines the design value of resistance through the resistance factor approach presented in EN 1990 [2] due to practicability. Due to the several possible combinations of γ_R and γ_m (or $\gamma_{m,i}$), alternatives to this format were regarded as unnecessarily confusing and error-prone. Also, placing γ_m outside the brackets of Eq. (3) instead of including it as a factor that reduces the characteristic value of the (representative) material property to a design value - as in Eq (1), has a conceptual advantage, since γ_m is accounting for the "overall effect of material uncertainty", instead of accounting for the effect of the uncertainty of a single material property.

Partial factor γ_m for a given material property can differ among different producers due to differences in constituent materials, fibre reinforcement content, lay-up, and composite manufacturing process. Therefore, the TS defines γ_m based on test results of the specific producer that sources the material (of fibre-polymer composites, core materials or adhesives). The partial factor γ_m may be defined from quality control records, based on the coefficient of variation of experimental data, see Table 1. This table assumes that statistical uncertainty does not influence the coefficient of variation of the material property (V_x), or that a conservative upper bound for V_x is considered, based on the test records of the same producer or on other information based on testing. Whenever this is not the case, γ_m also depends on the number of test records. Guidance for the determination of γ_m is provided in Subclause 4.4.5, which is fully conforming with EN 1990, Annex D [2]. Therefore, the influence of the different combinations of materials and production processes or quality control on material uncertainty is directly accounted for in each specific design case.

Table 1: Material partial factor γ_m as a function of V_x (when V_x is known).

V_x	0,05	0,10	0,15	0,20	0,25	0,30	0,35	0,40	0,45
γ_m	1,07	1,15	1,23	1,32	1,41	1,51	1,61	1,71	1,82

The determination of the material properties of fibre-polymer composites is usually made from a representative data set of coupons extracted from the laminated product. However, in the cases defined in Clause 5 of the TS (such as very thick laminates), laboratory testing may not be practical. Therefore, the TS allows that sub-laminate or ply-level specimens be tested, as long as such specimens are manufactured with the same constituent materials and using the same composite processing method as those of the thicker laminates the specimens seek to represent. In that case, the properties of the full-scale laminate are estimated from sub-laminate or ply data according to the Classical Laminate Theory (CLT) and an appropriate failure criterion in the case of strength.

  doi:10.5075/epfl-298799_978-2-9701614-0-0

The conversion of the material properties determined from sub-laminate or ply specimens to those at the laminate level introduces uncertainty in design, whose quantification has been neglected by research so far. This uncertainty is caused by: (i) the epistemic uncertainty of the analytical methods (e.g. the CLT) and of the failure criterion used; (ii) size effects, including those related to thickness (e.g. [6,7]); (iii) imperfections. This means that partial factor γ_m (which was calibrated for the material properties at the laminate level) needs to be complemented with an additional sub-laminate correction factor, which was defined as 1,2 in the case of strength properties – this value was defined based on guidance available in the EUROCOMP [8] and engineering judgment. For elastic properties, the TS does not stipulate any correction factor since: (i) the estimates of the elastic moduli of laminates from analytical methods are more accurate than their estimates of strength properties [9,10]; (ii) stiffness properties are not so much influenced by localized effects and imperfections, therefore they are less sensitive to size effects than strength properties.

3.2. ULS design of creep rupture, adhesive connections and fire design

For ULS design of creep rupture (Subclause 8.5), fatigue (Clause 10), adhesive connections (Subclause 12.4) and fire (Annex D), the design value of resistance, R_d, should be calculated from Eq. (4):

$$R_d = R\left\{\eta_{c,i}\cdot\frac{X_{k,i}}{\gamma_M};a_d;\sum F_{Ed}\right\} \tag{4}$$

where γ_M is the single partial material factor accounting for the uncertainty in the resistance model, unfavourable deviations of the relevant material or product properties from their characteristic values and the random part of the conversion factor, and geometrical deviations, if these are not modelled explicitly.

This resistance format follows the material factor approach [2], in which a single partial factor, γ_M, reduces a material property. Due to insufficient knowledge and test result data concerning creep rupture, fatigue, adhesive connections and fire resistance behaviour, separate partial factors for resistance (γ_{Rd}) and for material uncertainty (γ_m) could not be determined. Future and necessary research is needed in this respect.

4. Summary of partial factors

4.1. ULS design of composite components and members, bolted connections and joints

The partial factor for the resistance model, γ_{Rd}, for (i) profiles and laminates, (ii) sandwich panels and (iii) bolted connections and joints are given, respectively in Tables 2, 3 and 4. These factors were defined based on: (i) preliminary values of γ_{Rd} using the design value method of EN 1990, Annex C [2], including assumptions; (ii) reliability analyses to validate the preliminary γ_{Rd}; (iii) if deemed justifiable, replacing the preliminary γ_{Rd} by calibrated γ_{Rd} through reliability analyses; (iv) proposal of partial factors for design by rounding the values of each γ_{Rd} to the nearest 0,05.

Table 2: Values of γ_{Rd} for profiles and laminates.

Material failure	Global buckling			Local buckling
	Flexural	Lateral-torsional	Flexural-torsional	
1,40	1,30	1,30	1,55	1,30

Table 3: Values of γ_{Rd} for sandwich panels.

Composite material failure	Core material failure	Global buckling	Local buckling	Face sheet/web wrinkling	Core indentation	Core punching failure
1,40	1,50	1,40	1,30	1,50	1,50	1,50

Table 4: Values of γ_{Rd} for bolted connections.

Net-tension failure	Pin-bearing failure	Shear-out failure	Block-shear failure	Pull-out failure
1,50	1,50	1,50	1,50	1,50

This task included a survey of structural test results to assess the resistance to each failure mode. Databases were assembled with all publications found in which all relevant test parameters were stated and the requirements of standards were complied with. Then, model uncertainties [11] were used to assess the suitability of the resistance models and preliminary values of γ_{Rd} were proposed. The preliminary γ_{Rd} was estimated based on: (i) the statistics of the model uncertainty; (ii) the target reliability index β defined in Annex C of EN 1990 [2] for typical cases of ULS design; (iii) assumptions of EN 1990 [2] concerning the importance of random variables on structural safety. In the case of global buckling, these assumptions were checked through reliability analyses, which also evaluated whether the reliability β values that resulted from design using the resistance models and partial factors proposed in the TS were close to the target reliability index β. When this was not the case, the preliminary γ_{Rd} was replaced with a calibrated one. Fig. 1 shows the closeness of the prediction of the resistance model for flexural buckling to the experimental data (each type of marker corresponds to a different publication – this specific database includes 165 test results from nine publications), while Fig. 2 shows βs for lateral-torsional buckling design before partial factor calibration, which was deemed necessary; the target reliability index of 3.8 is given by the black dashed line. Both failure modes concern global buckling phenomena of thin-walled fibre-polymer composite for either column or beam members.

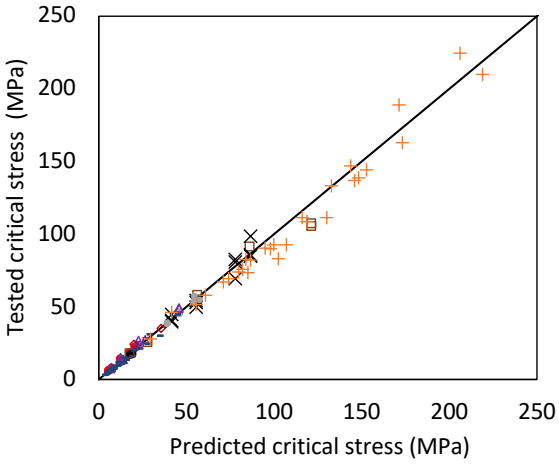

Figure 1. Assessment of model uncertainties from a database several publications (flexural buckling) [12].

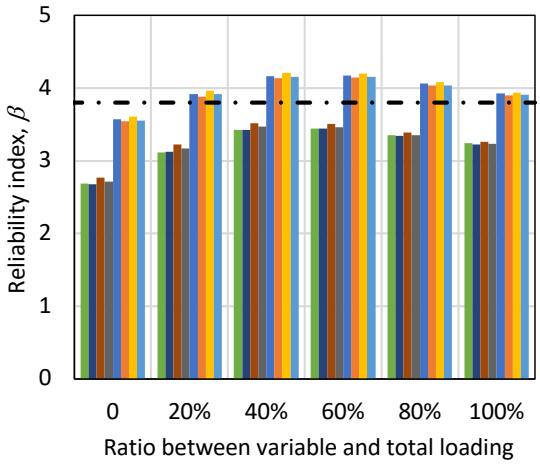

Figure 2. Reliability index β before partial factor calibration for 8 cases of design and six ratios of variable to total loading (lateral-torsional buckling) [5].

4.2. ULS design of creep rupture, fatigue, adhesive connections and fire design

For ULS design of creep rupture, the partial factor is $\gamma_{M,creep}$ = 1,5. This value was defined based on engineering judgement; in fact, only limited test results are available in the literature for the creep rupture of fibre-polymer composites, and such data refers basically to the tensile creep rupture of laminated components with unidirectional fibre reinforcement (for retrofitting or strengthening of existing structures). Future work is needed to validate this hypothesis.

The values for the partial factor for fatigue resistance, γ_{Mf}, are given in Table 5 and they take into account two main aspects: (i) the consequence of fatigue failure, by differentiating between fail-safe and non-fail-safe components; (ii) the ease of inspection and repair of fatigue sensitive components. The values of γ_{Mf} were adopted from the EUROCOMP [8]; however, because it is not possible to trace their provenance they cannot be directly validated. Yet, a plausibility check was performed [3] considering (i) the comparison of partial factors for static resistance and fatigue resistance, (ii) the comparison with provisions included in the guideline for the certification of offshore wind turbines, and (iii) the analysis of fatigue tests for a bridge.

Table 5: Values of γ_{Mf} for fatigue resistance.

Inspection and access	Fail-safe	Non-fail-safe
Member or joint subjected to periodic inspection and maintenance[a]; detail accessible	1,5	2,0
Member or joint subjected to periodic inspection and maintenance[a]; limited accessibility	2,0	2,5
Member or joint not subjected to periodic inspection and maintenance	2,5	3,0
[a] according to maintenance plan.		

Table 6: Values of $\gamma_{M,ac}$ for adhesive connection resistance.

Inspection and access	Fully-controlled application	Partially-controlled application
Connection subjected to periodic inspection and maintenance[a]; adhesive connection accessible	1,5	2,0
Connection subjected to periodic inspection and maintenance[a]; limited accessibility	1,7	2,2
Connection not subjected to periodic inspection and maintenance	2,0	2,5
[a] according to maintenance plan.		

The values for the partial factor for the adhesive connection resistance, $\gamma_{M,ac}$, are given in Table 6. As for the partial factors for fatigue resistance, the values of $\gamma_{M,ac}$ depend on (i) the type (frequency) of inspection and maintenance and accessibility of the adhesive connection, and (ii)

the application conditions, namely if they are either fully-controlled (reproducible process parameters) or only partially controlled. In this case, the partial factors are not graded as a function of the consequence classes [2], because, according to the TS, adhesive connections shall be designed as fail-safe (thus fulfilling the requirements of the highest consequence classes). The range of values adopted for $\gamma_{M,ac}$ (from 1,5 to 2,5) was taken from the EUROCOMP [8], but the background provenance for such values could not be traced and validation is thus required.

For fire design, the partial factor for the relevant mechanical material property for the fire situation, $\gamma_{M,fi}$, is 1,0. This value is similar to that recommended in the fire parts of Eurocodes for different structural materials (e.g. EN 1992-1-2, EN 1993-1-2, EN 1994-1-2, and EN 1995-1-2).

5. Concluding remark

The TS clauses about basis of design are complemented by their corresponding background, comprised in the commentary document [3], which provides the bases and justifications for the decisions taken and values selected.

Acknowledgements

Authors acknowledge funding to WG4.T2 via EC Project M515, and the important and essential scientific and technical support from WG4 to CEN/TC 250 to the drafting of the TS [1] and [3]. The first author also wishes to thank FCT (project Reliable-FRP PTDC/ECI-EGC/3916/2021).

6. References

1. FprCEN/TS 19101: 2021. Design of Fibre-Polymer Composite Structures. European Committee for Standardization, CEN/TC 250, 2021.
2. EN 1990: 2020, Eurocode - Basis of structural and geotechnical design. European Committee for Standardization, CEN/TC 250, 2020.
3. Commentary to FprCEN/TS 19101: 2021. Design of Fibre-Polymer Composite Structures. European Committee for Standardization, CEN/TC 250, March 2022.
4. Gulvanessian H, Calgaro JA, Holicky M. Designers' guide to EN 1990 Eurocode: Basis of structural design, in Designers' Guide to the Eurocodes. Thomas Telford: 2002.
5. Pacheco J, Sá M, Correia JR, Silvestre N, Sørensen JD. Structural safety of pultruded FRP profiles for global buckling. Part 2: Reliability-based calibration of partial factors for resistance models. Composite Structures 2021; 257: 113147.
6. Bazant ZP. Scaling of structural strength. Elsevier. 2005
7. Calahorra FL. Thickness effect in composite laminates in static and fatigue loading. PhD Thesis, TU Delft, 2017.
8. Clarke JL. (ed.). Structural design of polymer composites: EUROCOMP Design code and handbook. E & FN Spon. 1996.
9. Jones RM. Mechanics of Composite Materials. Taylor and Francis. 1999.
10. Barbero EJ. Introduction to Composite Materials Design. Taylor and Francis. 1999.
11. CEB. Bulletin 224: Model uncertainties and concrete barriers for environmental protection. CEB: 1995.
12. Sá M, Pacheco J, Correia JR, Silvestre N, Sørensen JD. Structural safety of pultruded FRP profiles for global buckling. Part 1: approach to material uncertainty, resistance models, and model uncertainties. Composite Structures 2021; 257: 113304.

  doi:10.5075/epfl-298799_978-2-9701614-0-0

DESIGN OF FIBRE-POLYMER COMPOSITE STRUCTURES – EUROPEAN TECHNICAL SPECIFICATION: TEMPERATURE AND MOISTURE EFFECTS

José Sena-Cruz[a], Mário Garrido[b], João R. Correia[b], Thomas Keller[c], João P. Firmo[b], Toby Mottram[c]

a: ISISE/IB-S, University of Minho, Portugal – jsena@civil.uminho.pt
b: CERIS, Instituto Superior Técnico, University of Lisbon, Portugal
c: EPFL, Switzerland
d: The University of Warwick, UK

Abstract: *This paper presents the methodology adopted in the European Technical Specification FprCEN/TS 19101 Design of Fibre-Polymer Composite Structures for the definition of the nominal conversion factors accounting for temperature and moisture effects in the properties of composite materials, sandwich core materials and epoxy adhesives, which is consistent with the partial factor method of the Eurocodes. The values of these factors were calibrated with test results included in databases gathered from the literature. In the case of the temperature conversion factor, the proposed method considers (i) the maximum service temperature experienced by the material and (ii) its glass transition temperature; furthermore, for composite materials, the method also considers the type of mechanical property, namely if it is either fibre- or matrix-dominated. In the case of the moisture conversion factor, the values proposed take into account the type of exposure conditions of the composite structure or material in service conditions.*

Keywords: Fibre-polymer composites; European Technical Specification; Temperature and moisture; Nominal conversion factors

1. Introduction

The short- and long-term mechanical behaviour of fibre-polymer composites are significantly affected by temperature and moisture effects. Therefore, nominal conversion factors that account for the effects of temperature and moisture on material properties were included in the European Technical Specification (TS) FprCEN/TS 19101 [1] *Design of Fibre-Polymer Composite Structures*, for composite materials, sandwich core materials and epoxy adhesives.

This paper provides the rationale for the nominal conversion factors adopted in [1]. In the first part, the format of the design considering temperature and moisture effects is presented. Furthermore, the comparison with recommendations provided in existing guidelines is also provided. The second part of the paper presents the methodology adopted for the definition of the temperature and moisture conversion factors for design purposes, which is consistent with the partial factor method of the Eurocodes. The values of these factors were calibrated based on relevant and reliable experimental data taken from the literature. The temperature conversion factor reflects the short-term changes in (mechanical) material properties compared to a reference temperature (20 °C), considering the maximum service temperature experienced by the material and its glass transition temperature - the effects of long-term exposure are not taken into account. In the case of the moisture conversion factor, the defined values take into

  doi:10.5075/epfl-298799_978-2-9701614-0-0

account the type of exposure conditions of the composite structure or material for a service life of 50 years.

2. Format of the design considering temperature and moisture effects

In the TS, the design of fibre-polymer composite structures takes into account the changes in the mechanical properties of composite materials, sandwich core materials and adhesives, due to temperature and moisture effects through the conversion factor, η_c, given by:

$$\eta_c = \eta_{ct} \cdot \eta_{cm} \quad (1)$$

where, η_{ct} and η_{cm} are the conversion factors for temperature and moisture effects, respectively. While η_{ct} accounts for short-term changes due to temperature effect on the elastic moduli and strengths of composite materials, sandwich core materials and adhesives, η_{cm} accounts for changes of the same material properties due to moisture absorption over time, including ageing effects resulting from long-term exposure, for specific environmental conditions and a 50-year service life.

Eq. (1) assumes that the combined effects of temperature and moisture are given by multiplying the individual effects of temperature and moisture, through the corresponding conversion factors. This assumption was adopted in the absence of a more reliable method of analysis of combined environmental effects and it has been also used in other design guidelines, e.g. [2-5]. It is worth mentioning that, in the TS the time-dependent effects due to creep and fatigue are treated separately, i.e. they are not covered by the conversion factor of Eq. (1).

The TS limits the maximum material temperature in service conditions, T_s, in members, joints and components, to the following range: (i) higher than -40 °C, and (ii) lower than T_g – 20 °C, where T_g is the glass transition temperature of composite, core and adhesive materials determined in accordance with test standard ISO 6721-11 [7], and defined based on the onset of the storage modulus curve (plotted in a logarithmic scale), i.e. following ASTM D7028 [8]. The imposed lower bound temperature of -40 °C is supported by the fact that literature shows limited reductions in different mechanical properties of composite, core and adhesive materials at sub-zero temperatures down to -40 °C. On the other hand, the imposed upper bound temperature of T_g – 20 °C is justified by the relevant reduction in the short-term mechanical properties and the significant increase in viscoelasticity of composites, cores and adhesive materials when temperatures approach the T_g. Other design guidelines also include limits for the upper bound temperature, e.g.: (i) T_g – 22 °C in [3], (ii) T_g – 20 °C in [5], (iii) T_g – 15 °C in [4]. Further background details are given in the commentary document to FprCEN/TS 19101 [8].

For the application of the conversion factor for moisture effects, the TS specifies three different exposure classes, namely: (i) Class I – Indoor exposure; (ii) Class II – Outdoors exposure without continuous exposure to water, or permanent immersion in water, or permanent exposure to a relative humidity higher than 80%, or combined UV-radiation and frequent freeze-thaw cycles; and (iii) Class III – Continuous exposure to water (or seawater), or permanent immersion in water (or seawater), or permanent exposure to a relative humidity higher than 80% (material temperature up to 25 °C).

3. Conversion factors

3.1 Conversion factor for temperature

In the TS, the conversion factor for temperature, η_{ct}, is determined according to the following general equation, considering a reference material temperature of 20 °C:

$$\eta_{ct} = \min\left\{1,0 - \alpha \cdot \frac{T_s - 20\ ^{o}\mathrm{C}}{T_g - 20\ ^{o}\mathrm{C}}; 1,0\right\} \quad (2)$$

where:

- T_s is the maximum material temperature in service conditions, in [°C];
- T_g is the glass transition temperature, in [°C], obtained as previously described;
- For fibre-dominated properties of composite materials with glass, carbon or basalt fibres and thermoset polymer matrix of either unsaturated polyester, vinylester or epoxy, α = **0,25**;
- For matrix-dominated properties of composite materials with glass, carbon or basalt fibres and thermoset polymer matrix of either unsaturated polyester, vinylester or epoxy, α = **0,80**;
- For polymeric foam core materials, namely polyurethane (PUR), polyethylene terephthalate (PET) and polyvinyl chloride (PVC) foams (densities from 40 to 300 kg/m^3), α = **0,46**;
- For epoxy adhesives, α = **0,85**.

In the case of balsa wood core material, the conversion factor for temperature, η_{ct}, is given by:

$$\eta_{ct} = \min\left\{1,0 - \left(\frac{0,2}{\rho} + 0,004\right) \cdot \left(T_s - 20\ ^{o}\mathrm{C}\right); 1,0\right\} \quad (3)$$

where ρ is the density in [kg/m^3].

Composite materials present fibre- and matrix-dominated properties having, respectively, low and high sensitivity to matrix softening as temperature increases towards the T_g. Typically, fibre-dominated properties include tensile strength, tensile modulus and compressive modulus in direction(s) with high ratio of continuous aligned fibres, while matrix-dominated properties include compressive strength, interlaminar shear strength, in-plane shear strength and modulus, and tensile strength and modulus and compressive modulus in direction(s) with low ratio of continuous aligned fibres. Furthermore, for adhesive connections between composite adherends, the resistance to fibre-tear failure is matrix-dominated.

All the proposed conversion factors for temperature of the involved materials (composite materials, sandwich core materials and epoxy adhesives) are based on databases developed from test results available in studies published in the literature, based on the following common requirements [8]:

- The reference material properties at ambient temperature (~20 °C) were obtained from tests conducted according to standard methods;
- The glass transition temperature of the material (T_g) was reported and, in principle, obtained from DMA tests following ISO 6721-11 [6] and defined based on the onset of the storage modulus curve plotted in a logarithmic scale, i.e. in accordance with ASTM D7028 [7];

- At elevated temperature, the failure modes did not change compared to those observed in tests performed at ambient temperature.

Furthermore, for the estimation of the parameter α in Eq. (2), the following two criteria were considered [8]: (i) it would have to provide conservative estimates for more than 90% of experimental test results considered in the analysis; and, (ii) for test results that were overestimated, Eq. (2) would have to provide reasonably low maximum relative differences to test data - a value of 15% specified by the drafters in this respect. Finally, it should be highlighted that the definition of the values of the temperature conversion factors supported on reliability studies, as defined in EN 1990, was not considered due to insufficient amount of experimental data to apply this approach.

In the following paragraphs, a short summary is provided about the assessment of the parameter α in Eq. (2) for the different materials. Detailed information can be found in [8].

3.1.1 Composite materials with glass, carbon or basalt fibres and thermoset polymer matrix of either unsaturated polyester, vinylester or epoxy

The effects of temperatures higher than 20 °C on the mechanical properties of composite materials was based on a database that involved 61 and 24 average test results for fibre- and matrix-dominated properties, respectively, with the following characteristics [8]:

- Type of fibre reinforcement: glass, carbon, basalt;
- Type of polymer-matrix: polyester, vinylester, epoxy, urethane acrylic;
- Fibre-polymer composite shape: profiles (I, C, tubular), flat plates, bars;
- Manufacturing process: pultrusion, hand layup, vacuum infusion;
- T_g: 38 °C to 157 °C;
- Test temperatures: -40 °C to +700 °C;
- Type of loading: tension, compression (coupon and full-section), shear – in-plane (off-axis tension and Iosipescu) and interlaminar;
- Properties: longitudinal tensile strength, longitudinal tensile modulus, longitudinal compressive strength, longitudinal compressive modulus, in-plane shear strength, in-plane shear modulus, interlaminar shear strength.

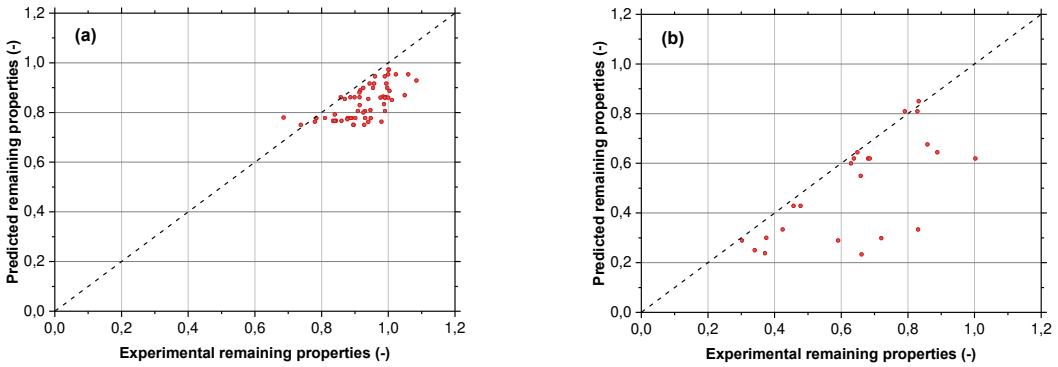

Figure 1. Predicted vs. experimental normalised properties at elevated temperature of composite materials: (a) fibre-dominated; (b) matrix-dominated

The estimation of the parameter α also involved the separation between fibre-dominated and matrix-dominated properties. By using the gathered database and the above-mentioned criteria for the estimation of α, values of **0,25** and **0,80** were found for fibre- and matrix-dominated

properties, respectively. Figure 1 compares experimental ($\eta_{ct,exp}$) and predicted ($\eta_{ct,pre}$) values of normalised remaining properties at elevated temperature using Eq. (2) for fibre- and matrix-dominated properties, respectively, while Table 1 presents statistical parameters of the ratio between $\eta_{ct,exp}$ and $\eta_{ct,pre}$.

Literature about the effects of temperatures lower than 20 °C on composite materials with glass, carbon or basalt fibres and thermoset polymer matrix of either unsaturated polyester, vinylester or epoxy, is very limited and presents inconsistent results. Furthermore, when deleterious effects on mechanical properties are reported, the reductions are relatively low. For these reasons, the conversion factor of temperature for maximum material temperature in service conditions lower than 20 °C was set equal to 1,0 [8].

Table 1: Summary and statistical parameters of the ratio (bias) between experimental and predicted remaining properties at elevated temperature of composite materials.

Type of properties	Test results	Proportion of overestimated test results	Average	Max	Min	CoV
Fibre-dominated	61	4,9%	1,11	1,28	0,88	7,0%
Matrix-dominated	24	8,3%	1,41	2,84	0,98	37,8%

Note: a ratio higher than 1,0 means that Eq. (2) provides conservative estimates of mechanical properties at elevated temperature.

3.1.2 Sandwich core materials and epoxy adhesives

Similarly to composite materials, the effects of temperatures higher than 20 °C on the mechanical properties of polymeric foam core materials were based on a collected database. In total, 140 test results were collected with the following characteristics [8]:

- Polymers: polyurethane (PUR), polyethylene terephthalate (PET), polyvinyl chloride (PVC);
- Densities: PUR: 40 to 68 kg/m^3; PET: 94 to 110 kg/m^3; PVC: 75 to 300 kg/m^3;
- T_g: 64,9 °C to 89,5 °C;
- Test temperatures: -66 °C to 195 °C;
- Type of loading: tension, compression, flexure, shear;
- Properties (z is the through-thickness or out-of-plane direction, and x and y are the in-plane directions): out-of-plane compressive modulus (z), out-of-plane compressive strength (z), out-of-plane tensile modulus (z), in-plane compressive modulus (x or y), in-plane tensile modulus (x or y), shear strength (xz), shear modulus (xz).

According to the method described above for the estimation of α, a value of **0,46** was obtained for polymeric foam core materials.

Figure 2a compares experimental ($\eta_{ct,exp}$) and predicted ($\eta_{ct,pre}$) values of normalised remaining properties of polymeric foam core materials at elevated temperature using Eq. (2), while Table 2 presents statistical parameters of the ratio between $\eta_{ct,exp}$ and $\eta_{ct,pre}$.

The determination of η_{ct} for balsa core materials was based on a limited number of test results available in the literature (five), in which ρ varied from 109 to 285 kg/m^3.

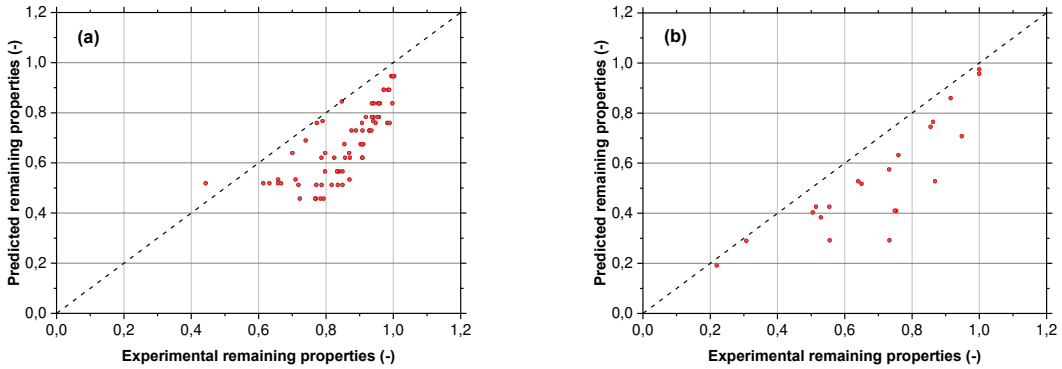

(a) (b)

Figure 2. Predicted vs. experimental normalised properties at elevated temperature of (a) polymeric cores and (b) epoxy adhesives.

Table 2: Summary and statistical parameters of the ratio (bias) between experimental and predicted remaining properties at elevated temperature of polymeric cores and adhesives.

Material	Test results	Proportion of overestimated test results	Average	Max	Min	CoV
Polymeric cores	64	4,7%	1,21	1,47	0,97	11,1%
Epoxy adhesives	21	0,0%	1,37	2,51	1,03	27,2%

In the case of epoxy adhesives, the estimation of the parameter α was based on a total of 47 (average) test results, with the following main characteristics [8]:

- Type of adhesive: epoxy (two-component);
- Manufacturing: mixing at ambient temperature;
- T_g: 47 °C to 87 °C;
- Test temperatures: 20 °C to 120 °C;
- Type of loading: tension, shear;
- Properties: tensile strength, elastic modulus, shear strength, shear modulus.

Figure 2b compares experimental ($\eta_{ct,exp}$) and predicted ($\eta_{ct,pre}$) values of normalised remaining properties of epoxy adhesives at elevated temperature using Eq. (2), while Table 2 presents statistical parameters of the ratio between $\eta_{ct,exp}$ and $\eta_{ct,pre}$, when α = **0,85** (estimated value).

For material temperatures in service conditions below 20 °C, the temperature conversion factor for sandwich core materials and epoxy adhesives was set as 1,0. Therefore, as for composite materials, it is assumed that the changes in the material properties of sandwich core materials and epoxy adhesives is not significant for material temperatures in the range -40 °C to 20 °C [8].

3.2 Conversion factor for moisture

As mentioned in section 2, for the definition of the conversion factor for moisture, three exposure classes are defined in the TS. Therefore, for unprotected composite materials (glass, carbon or basalt reinforcement; thermoset polymer matrix of unsaturated polyester, vinylester or epoxy; fibre volume fraction of at least 35%) and epoxy adhesives, the following conversion factors for moisture, η_{cm}, were adopted:

- Exposure class I: η_{cm} = **1,00**;
- Exposure class II: η_{cm} = **0,85;**
- Exposure class III: η_{cm} = **0,60**.

In the following paragraphs, a short summary is provided about the adopted values in case of exposure classes II and III, since it is assumed that indoor exposure conditions (class I) do not have deleterious effects on the mechanical properties of such materials.

3.2.1 Conversion factor for moisture for natural outdoor weathering (Class II)

The conversion factor for moisture, η_{cm}, of composite materials for Class II was derived from 10 studies (yielding a total of 211 data points – each one is an average value) regarding the effects of natural outdoor weathering on the mechanical properties of laminates or profiles, with the following main characteristics [8]:

- Resins: unsaturated polyester, vinylester;
- Fibre reinforcements: glass;
- Manufacturing processes: pultrusion, vacuum infusion, hand layup;
- Fibre volume content: 33% to 60%;
- Exposure durations: up to 20 years;
- Exposure environments: Alpine (Switzerland), humid continental (Maine, USA), Mediterranean (Lisbon), semi-continental (Milan), temperate oceanic (Rotterdam), temperate (Kyoto), indoor (with relatively high RH, 23 °C, thus included);
- Properties: tensile, flexural, shear, interlaminar shear.

When η_{cm} = **0,85** is adopted, 17,5% of data points of the database gathered present higher degradations than the one accounted for by the conversion factor. However, the average difference between such results and the corresponding estimates is relatively low, around 8%.

Literature about epoxy bulk material is very scarce: only three studies were found for outdoors exposure conditions (equivalent to Exposure Class II) [8]. Based on these test results, the reductions in the mechanical properties of epoxy adhesives seem to be in line with the values reported for composite materials and Exposure Class II. The same value for η_{cm} was therefore adopted.

3.2.2 Conversion factor for moisture for immersion exposure (Class III)

A series of eighteen studies were used for the estimation of the conversion factor for moisture of composite materials for Class III (yielding a total of 516 data points – each one is an average value) regarding the effects of immersion exposure on the mechanical properties of laminates or profiles, with the following main characteristics [8]:

- Resins: polyester, vinylester;
- Fibre reinforcements: glass;
- Manufacturing processes: pultrusion, vacuum infusion, hand layup;
- Fibre volume content: 32% to 62%;
- Exposure durations: up to ~5000 days (~14 years);
- Exposure environments: water, seawater and saline solution (20 °C);
- Properties: tensile, flexural, shear, interlaminar shear.

When η_{cm} = **0,60** is adopted, 1,4% of data points of the database present higher degradation than the one accounted for by the conversion factor. Furthermore, the average difference between such results and the corresponding estimates is relatively low, around 5%.

Similarly to the composite materials, in the case of epoxy adhesive, a database composed of 53 data points with a maximum exposure period of ~2 years [8] was gathered. By adopting η_{cm} = **0,60**, 7,4% of data points present higher degradation than predicted, while the average difference between such results and the corresponding estimates is equal to 7,2% [8].

4. Concluding remarks

The European Technical Specification FprCEN/TS 19101 provides nominal conversion factors that account for the effects of temperature and moisture in the mechanical properties of composite materials, sandwich core materials and epoxy adhesives. The methodology adopted in the definition of the conversion factors is consistent with the partial factor method of the Eurocodes and the values adopted were defined based on experimental test results available in the literature. In spite of this robust effort, additional experimental data is needed to improve the reliability of the estimates of such conversion factors.

Acknowledgements

Authors acknowledge funding to WG4.T2 via EC Project M515, and the important and essential scientific and technical support from WG4 to CEN/TC 250 to the drafting of the TS [1] and [3]. This work is supported by FCT and PIDDAC under the project Durable-FRP PTDC/ECI-EGC/4609/2020 and partly financed by the project POCI-01-0145-FEDER-007633. The second, third and fourth authors also wish to thank FCT (Project FireFloor, no. PTDC/ECI-EGC/30611/2017).

5. References

1. FprCEN/TS 19101: 2021. Design of Fibre-Polymer Composite Structures. European Committee for Standardization, CEN/TC 250, 2021.
2. CNR-DT 205/2007. Guide for the design and construction of structures made of FRP pultruded elements. Italian National Research Council: Advisory Committee on Technical Recommendations for Construction (CNR), 2008.
3. ASCE. Pre-standard for load and resistance factor design (LRFD) of pultruded fiber polymer (FRP) structures (final). American Composites Manufacturer Association, 2010.
4. BUeV-Guideline. Structural Polymer Components for Building and Construction. Draft, Dimensioning and Construction, 2014.
5. CROW-CUR Recommendation 96. Fiber-Reinforced Polymers in Buildings and Civil Engineering Structures. CROW, 2019.
6. ISO 6721-11:2019. Plastics – Determination of dynamic mechanical properties – Part 11: Glass transition temperature. International Organization for Standardization, 2019.
7. ASTM D7028 – 07. Standard Test Method for Glass Transition Temperature (DMA Tg) of Polymer Matrix Composites by Dynamic Mechanical Analysis (DMA). American Society for Testing and Materials, 2015.
8. Commentary to FprCEN/TS 19101: 2021. Design of Fibre-Polymer Composite Structures. European Committee for Standardization, CEN/TC 250, March 2022.

  doi:10.5075/epfl-298799_978-2-9701614-0-0

DESIGN OF FIBRE-POLYMER COMPOSITE STRUCTURES – EUROPEAN TECHNICAL SPECIFICATION: COMBINED STRESSES

J. Toby Mottram[a], Liesbeth Tromp[b], Marko Pavlovic[c], João R. Correia[d], Thomas Keller[e], José Sena-Cruz[f]

a: The University of Warwick, UK – Toby.Mottram@warwick.ac.uk
b: Royal HaskoningDHV, The Netherlands; c: Delft University of Technology, The Netherlands
d: CERIS, University of Lisbon, Portugal; e: EPFL, Switzerland; f: University of Minho, Portugal

Abstract: *It was essential in the European Technical Specification for the Design of Fibre-Polymer Composite Structures (prCEN/TS 19101) to provide an Ultimate Limit State design procedure for a failure criterion for multi-ply laminates subjected to in-plane combined actions, which will give a generically applicable and a simple design procedure. This paper will discuss the rationale for the project team (of Working Group 4 to CEN/TC250) deciding that the resistance formula is to satisfy a linear interaction failure criterion.*

Keywords: Eurocode; combined stresse; laminates; ULS design

1. Introduction

SAMPE conference paper [1] has a helpful introduction to the CEN Technical Specification for the '*Design of Fibre-Polymer Composite Structures*' [2], by presenting its scope, content together with the main principles and their background. FprCEN/TS 19101 [2] was prepared by Project Team (WG4.T2) with essential technical and scientific support from the wider Working Group 4 (WG4: *Fibre-reinforced Polymer Structures*) to the structural Eurocode committee CEN/TC250. Following an inquiry consultation with the National Standards Bodies (NSBs) version FprCEN/TS 19101 [2] of the Technical Specification was submitted to CEN in November 2021 to prepare for a Formal Vote process, commencing in April 2022. A successful outcome of the vote will be for publication of the TS in January 2023, together with a set of worked examples and a comprehensive commentary document [3]. In this paper, the abbreviation TS is used for CEN/TS 19101 [2]. Several of the composite manufacturing processes permitted by the TS are pultrusion, filament winding, hand lay-up, resin transfer moulding, resin infusion moulding, and vacuum-assisted resin transfer moulding. Chapter 4 in [4] has an introduction to composite laminates of fibre-reinforced polymers made by these and other processes.

The basis of design in the TS is developed in accordance with the general rules given in prEN 1990 [5], supplemented by provisions that are specific to fibre-polymer composites. From the rules for limit state design, the design value of resistance, R_{d}, can be calculated from:

$$R_{\mathrm{d}} = \frac{1}{\gamma_{\mathrm{Rd}} \cdot \gamma_{\mathrm{m}}} R\{\eta_{\mathrm{c},i} . X_{\mathrm{k},i}; a_{\mathrm{d}}; \sum F_{\mathrm{Ed}}\} \quad (1)$$

where: γ_{Rd} is a partial factor accounting for the uncertainty in the resistance model, and for geometrical deviations, if these are not modelled explicitly, according to 4.4.6 of the TS; γ_{m} is a partial factor for a material accounting for the unfavourable deviations of the representative material from their characteristic values; $R\{\ldots\}$ denotes the output of the resistance model; $\eta_{\mathrm{c},i}$ is the conversion factor accounting for effects of temperature and moisture, effects of ageing of

  doi:10.5075/epfl-298799_978-2-9701614-0-0

materials, according to 4.4.7 of the TS; $X_{\mathrm{k},i}$ represents the characteristic values of material (defined as 5% fractiles); a_{d} denotes the design values of geometrical parameters; F_{Ed} denotes the design values of actions used in the assessment of the design value of the effect of actions; i is for the i^{th} material property. Note that sub-clauses 4.4.6 and 4.4.7 are not reproduced herein.

Ultimate Limit State (ULS) verifications for laminates, profiles and sandwich panels are described in four sub-clauses in Section 8 *Ultimate limit states* and in formative Annex C *Buckling of orthotropic laminates and profiles*. Relevant to this paper is sub-clause 8.2 *Ultimate limit states of laminates* that provides the necessary ULS verifications for balanced symmetrical laminates in cases of in-plane axial, shear and bending stresses, out-of-plane tensile and bending stresses, interlaminar shear stresses, and, for the topic of this paper, in-plane combined stresses.

2. Rationale for having Formula (8.18) for Combined Stresses

Clearly, the TS has the requirement to include section-level design procedures for known modes of failure for ULSs of composite laminates, which are thin-walled [4] and can be flat or curved. What is proposed in the TS involves also laminate- or ply-level procedures. These are suitable for the evaluation of moulded, laminated structures of monocoque or stiffened shell forms, that owing to the complex stress distributions cannot be designed at the section-level and are therefore designed using finite element outputs and a laminate- or ply-level failure criterion [4].

The first stage towards the publication of a new Eurocode is the preparation of a '*Prospect*' by the Joint Research Council. WG4 to CEN/TC250 drafted a second version of a '*Prospect*' report [6], following a NSBs inquiry consultation of the first version. In [6] sub-clause 6.3.1 presents provisions for ULS verifications at the two levels of ply and laminate, but with a different underlying modelling approach and formulae than for the provisions in sub-clause 8.2 of the TS [2]. A '*Prospect*' approach is however in the more elaborate procedure of Annex B7.7 of the TS.

Based on the findings by leading academic and developers of software/numerical codes associated with the premier World-Wide Failure (WWF) exercises [7], it is recognized that, even today, it is not practical to specify a single formula (or theory) to represent the failure of laminates that are subjected to in-plane combined stresses. The conventional, yet complex approach that designers may apply is to establish the resistances of laminates by employing classical lamination theory or higher-order theory to analyse the stress states inside multi-ply laminates subjected to increasing loads up to their design values. As each analysis proceeds there are continual checks at the ply-level for failure using one of the recognized ply-level failure criteria [4, 7]. The laminate's ULS resistance can be established either by first ply failure or last ply failure (when the laminate has ultimately failed). For background details on the application of finite element analyses to numerically predict resistances of laminated plates and shells subjected to combined stresses you can consult Section 5.2 in [4], with sub-section 5.2.6 covering initial failure and progressive damage of laminates to their ultimate failure.

Appendix I below gives four edited extracts from the TS [2]; note that the commentary [3] has technical and scientific information on these paragraphs. One extract is from the informative Annex B *Indicative values of material properties for preliminary design*. Its sub-clause B.7.7 recommends the application of six well-established failure criteria at the ply-level, namely: Maximum Stress; Maximum Strain; Tsai-Hill; Tsai-Wu; Puck; Hashin. It is noted that paragraph B.7.7(2) defines the closed form formula to the Tsai-Hill failure criterion and B.7.7(3) is similar in presenting the formula to the Tsai-Wu failure criterion. No other ply-level failure criterion

formula is given in the TS. It is recognised that this complex approach aims to predict the failure of multi-ply laminates more precisely and reliably [4, 7]. The choice of which failure criterion to use can be informed by previous structural analysis experience and/or because of the modelling options available in finite element software (e.g. ABAQUS, ANSYS, Altair HyperWorks™, etc.). What today cannot support the decisions made by designers (and thereby code writers) are the gaps in physical test results and in theoretical developments to enable the Project Team to define precisely which modelling approach and/or failure criterion/criteria is/are the most reliable. This can be seen as a relevant on-going finding and weakness from the pioneering contributions comprising the WWF exercises [7], which were started in 1992. It is observed that one of the main challenges, in addition to having a reliable combined stress criterion at ply-level concerns the establishment of degradation models after first ply failure has occurred.

Towards the TS's preparation by Project Team WG4.T2 is noteworthy that in the '*Prospect*' report [6], sub-clause 6.3.1 provided three laminate-level approaches for ULS verification. Paragraph 6.3.1.2(1) recommends an analysis that corresponds to informative Annex B, B.7.7 of the TS [2]. Whereas, for preliminary design of balanced symmetrical laminates having glass reinforcement and uniaxial loading only, paragraph 6.3.1.2(2) offers a design criterion based on direct or shear strain limits. This approach was not deemed acceptable to go into sub-clause 8.2 [2]. Paragraph 6.3.1.2(3) in the '*Prospect*' is for design by testing, which is discussed for fibre-polymer composite laminates and structures in sub-section 5.1.12 in [4].

Following discussions within the Project Team and, also, via consultations with WG4 members it was recognised that the (informative) Annex B design approach (summarized above) does not provide designers with a quick, non-complex and practical procedure to calculate the resistance of laminates subjected to in-plane combined stresses. In the absence of a more general and consensual interaction failure criterion combining both in-plane and out-plane stresses a linear interaction failure criterion is proposed in 8.2.9 [2]. This sub-clause is given in **Appendix I**, which defines terms and cross-links to other paragraphs in clause 8.2 for the determination of eight different design values of resistance that can be required in specific verifications. It is expected that Formula (8.18) in 8.2.9 is providing a safe (conservative) design solution at the laminate-level. To enable the adoption of a more reliable failure criterion (which is likely to be non-linear, e.g., see [8]), targeted research is needed, including the verification and calibration with test results from relevant physical testing of laminates subjected to varying combined stresses.

The combined stress requirement in Formula (8.18) (see **Appendix I**) is for the three stress components from the actions of axial tensions or compression in the x direction, in-plane shearing and axial tension or compression in the y direction. The x direction is defined as the principal load direction, which coincides with the orientation direction of the laminate with the highest direct stiffness and direct strengths; also referred to as the 0° direction [2, 4].

To introduce how to use Formula (8.18), the first linear-interaction term is given next:

$$\left| \frac{\sigma_{\mathrm{x,t,Ed}}}{f_{\mathrm{x,t,d}}} \text{ or } \frac{\sigma_{\mathrm{x,c,Ed}}}{\min\{f_{\mathrm{x,c,d}}, f_{\mathrm{x,cr,d}}\}} \right| \tag{2}$$

In Eq. (2) the numerators are for the calculated stress in the x direction of the laminate, which depending on the effect of actions from the design load cases can be either tension, subscript t, or compression, subscript c,. The denominator is for the required design value, which is $f_{\mathrm{x,t,d}}$ by 8.2.2.1(1), or either $f_{\mathrm{x,c,d}}$ by 8.2.2.2(2) or $f_{\mathrm{x,cr,d}}$ by 8.2.2.2(3) and Annex C.4.

To establish the design value of the tensile strength Eq. (1) is written as:

$$f_{\mathrm{x,t,d}} = \frac{\eta_c}{\gamma_{\mathrm{m}}\gamma_{\mathrm{Rd}}} f_{\mathrm{x,t,k}} \tag{3}$$

where $f_{\mathrm{x,t,d}}$ is the characteristic value of the tensile strength in the x direction of the laminate, which is determined using standard coupon testing (in accordance with EN ISO 527) with the batch results analysed for the characteristic value using the procedure in Annex D of prEN 1990 [5]. For establishing $f_{\mathrm{x,c,d}}$, again Eq. (3) can be used, on this occasion with the characteristic value of the compressive strength, $f_{\mathrm{x,c,k}}$, from testing by EN ISO 14126, replacing $f_{\mathrm{x,t,k}}$.

To determine $f_{\mathrm{x,cr,d}}$ (the design value of the critical buckling compressive stress in the x direction of the laminate under uniform compression) the form of Eq. (1) is now:

$$f_{\mathrm{x,cr,d}} = \frac{1}{\gamma_{\mathrm{m}}\gamma_{\mathrm{Rd}}} \chi_{\mathrm{x,c}} f_{\mathrm{x,cr,k}} \tag{4}$$

where: $f_{\mathrm{x,cr,k}}$ is the characteristic value of the critical buckling compressive stress in the x direction determined analytically using formative Annex C, C.4.2.1 *Compression for flat laminates* (refer to **Appendix I** for extracts from Annex C *Buckling of orthotropic laminates and profiles*), and considering the appropriate values of the conversion factor, η_{c}, for the relevant material properties (defined in 4.4.7 of the TS). Note that characteristics values for the relevant moduli of elasticity (i.e., E_{11}, E_{22} and G_{12}) are the mean values determined using the same ISO standards as for direct strengths. $\chi_{\mathrm{x,c}}$ is the buckling reduction factor for compression in the x direction to consider the effect of imperfections in elastic post-buckling regime. Paragraph 8.2.2.2(4) states that for flat laminates (for which $\chi_{\mathrm{x,c}}$ (or $\chi_{\mathrm{y,c}}$) ≥ 1,0), $\chi_{\mathrm{x,c}}$ or $\chi_{\mathrm{y,c}}$ may be taken as 1,0. Guidance in the TS is that given $\chi_{\mathrm{x,c}}$ (or $\chi_{\mathrm{y,c}}$) is < 1,0 for curved laminates the buckling reduction factor for such laminates can be determined by testing, in accordance with prEN 1990, Annex D [5] and/or by numerical modelling, which should be verified by testing [4].

Although the linear interaction Formula (8.18) has not been, and cannot be verified because of the lack of test data, there is consensus amongst WG4 experts that such a linear interaction failure formula for laminates experiencing in-plane combined stresses should give, on the safe side, a more conservative strength prediction than an interaction formula of higher-order (e.g. a quadratic interaction formulae), such as could be offered by way of the three interaction formulae presented in [8], which have not been verified. Formula (8.18) is therefore offered in 8.2.9 for a quick, non-complex and practical procedure that designers can adopt to carry-out ULS designs of laminates subjected to any combination of in-plane stresses.

3. Application

For the laminate-level failure criterion of Formula (8.18) rectangular fibre-polymer composite plates are to satisfy the conditions of Annex C, C.4.1 (**Appendix I**) and the displacement boundary conditions of a closed form formula (see, e.g., Figure C.1). When subjected to compression stress in either x or y direction or in both directions, and/or an in-plane shear stress a characteristic strength in Formula (8.18) can be for elastic buckling modes of failure (i.e. $f_{\mathrm{x,cr,k}}$ by C.4.2.1, $f_{\mathrm{y,cr,k}}$ by C.4.2.1 or $f_{\mathrm{xy,cr,k}}$ or C.4.2.2). This application of a linear-interaction in a failure criterion is novel, design case specific and owing to lack of test data has not been verified.

To gain an insight into the application of Formula (8.18), let's consider the three effect of actions $\sigma_{\mathrm{x,t,Ed}}$, $\sigma_{\mathrm{y,t,Ed}}$ and $\tau_{\mathrm{xy,Ed}}$, with stress states that ensures elastic buckling is not going to happen. Table B.8 in the TS [2] gives the indicative (characteristic) tensile strengths $f_{\mathrm{x,t,k}}$ and $f_{\mathrm{y,t,k}}$ as 400

MPa for a balanced bidirectional laminate of continuous glass fibre reinforcement (volume fraction of 50%) in an epoxy matrix. Because Table B.8 does not report a characteristic in-plane shear strength we take $f_{xy,v,k}$ = 50 MPa. To simplify the presentation, it is assumed that $\eta_c/(\gamma_m \cdot \gamma_{Rd})$ = 1,0 (unfactored). For this laminate example, Table 1 reports nine different limit combinations of in-plane combined stresses where Formula (8.18) equals 1,0 to signal ULS failure. Practically, these stress combinations translate into a three-dimensional failure envelop, where all combinations bounded within the envelop means the laminate does not fail.

Note that by applying sub-clauses 4.4.5 to 4.4.7 of the TS [2], the value of $\eta_c/(\gamma_m \cdot \gamma_{Rd})$ for material failure of composite laminates is not 1,0, and may be estimated to lie in the bounded range of (0,6·0,6)/(1,23·1,4) = 0,2 (with coefficient of variation V_x known and 0,15 for specifying γ_m) to (1,0/(1,07·1,4) = 0,67 (V_x = 0,05 and known for γ_m). When applying Formula (8.18) in design there will be reductions made to the stress magnitudes, such as to those reported in Table 1.

Table 1: Combinations of $\sigma_{x,Ed}$, $\sigma_{y,Ed}$ and $\tau_{xy,Ed}$ (in MPa) that with Formula (8.18) equal to 1.0 are for ULS failure.

$\sigma_{x,t,Ed}$	$\sigma_{y,t,Ed}$	$\tau_{xy,Ed}$	$\sigma_{x,t,Ed}$	$\sigma_{y,t,Ed}$	$\tau_{xy,Ed}$	$\sigma_{x,t,Ed}$	$\sigma_{y,t,Ed}$	$\tau_{xy,Ed}$
400	0	0	160	160	10	40	40	40
0	400	0	130	130	16,25	83	0	40
200	200	0	80	80	30	0	0	50

4. Acknowledgements

Authors acknowledge funding to WG4.T2 via EC Project M515, and the important and essential scientific and technical support from WG4 to CEN/TC 250 to the drafting of the TS [2] and [3].

5. References

1. Keller T, Correia JR, Knippers J, Mottram JT, Paulo C, Ascione, L. CEN Technical Specification Design of fire-polymer composite structures, Proceedings SAMPE European Conference 2020, Amsterdam. The Netherlands. September 30 - October 1, 2020:1-8.
2. FprCEN/TS 19101. Design of fibre-polymer composite structures. European Committee for Standardization, CEN/TC250, 2021.
3. Commentary to FprCEN/TS 19101. Design of fibre-polymer composite structures. European Committee for Standardization, CEN/TC250, 2021.
4. Mottram, JT, Henderson, J. (Eds). FRP bridges – Guidance for designers. CIRIA C779. London, UK. 2018. (free download at: https://tinyurl.com/yy79wl4b)
5. prEN 1990:2021. Eurocode — Basis of structural and geotechnical design. European Committee for Standardization, CEN/TC250, 2021.
6. Ascione L, Caron J-F, Godonou P, van IJselmuijden K, Knippers J, Mottram T, Oppe M, Gantriis Sorensen M, Taby J, Tromp L. Prospect for new guidance in the design of FRP. European Composite Industry (EuCIA). Brussels, Belgium. 2018.
7. Kaddour AS, Hinton MJ, Li S, Smith PA. The World-wide failure exercises: How can composite design and manufacture communities build their strength. Proceedings of 16th European Conference on Composite Materials (ECCM16). Seville, Spain. 2014:1-14.
8. Weaver, PM, Nemeth, MP, Improved design formulae for buckling of orthotropic plates under combined loading. AIAA Journal 2008; 46(9), 2391-2396.

  doi:10.5075/epfl-298799_978-2-9701614-0-0

Appendix 1. Extracts from Design of Fibre-polymer Composite Structures (CEN/TC 250: FprCEN/TS 19101:2022) [2]

Extracts from the TS are given using Cambria font type with accompanying notes using Calibra font type. NOTES have been removed unless essential. There are four extracts comprising:

- Paragraphs 8.2.9(1) and (2) for design at ULS of laminates subjected to combined stresses.
- Parargraph B.1 on 'use' of Annex B presenting indicative values of material properties for preliminary design; this annex is informative.
- Paragraph B.7.7 on empirical-based failure criteria for plies.
- Annex C and relevant paragraphs, namley C.1(1), C.2(1), C.3(1) and C.3(2), C.4(1) and C.4(2), and C.4.2.1(1) to introducde elastic buckling of orthotropic laminates; for the load case of uniform compression paragraph 8.2.2.2(3) determines $f_{\mathrm{x,cr,d}}$ in Formula (8.118). Extract from C.4.2.1(1) is incomplete because there's not space to reproduce everything.

8.2.9 Combined Stresses

(1) The resistance of laminates subjected to combined stresses may satisfy a linear interaction failure criterion (which represents a conservative approximation for in-plane stresses). For laminates subjected to in-plane stresses the linear interaction failure criterion should be defined as in Formula (8.18):

$$\left|\frac{\sigma_{\mathrm{x,t,Ed}}}{f_{\mathrm{x,t,d}}} \text{ or } \frac{\sigma_{\mathrm{x,c,Ed}}}{\min\{f_{\mathrm{x,c,d}}, f_{\mathrm{x,cr,d}}\}}\right| + \left|\frac{\tau_{\mathrm{xy,Ed}}}{\min\{f_{\mathrm{xy,v,d}}, f_{\mathrm{xy,cr,d}}\}}\right| + \left|\frac{\sigma_{\mathrm{y,t,Ed}}}{f_{\mathrm{y,t,d}}} \text{ or } \frac{\sigma_{\mathrm{y,c,Ed}}}{\min\{f_{\mathrm{y,c,d}}, f_{\mathrm{y,cr,d}}\}}\right| \qquad (8.18)$$

where: $\sigma_{\mathrm{x,t,Ed}}$ is the design value of the axial tensile stress in the x direction of the laminate; $f_{\mathrm{x,t,d}}$ is the design value of the tensile strength in the x direction of the laminate (8.2.2.1); $\sigma_{\mathrm{x,c,Ed}}$ is the design value of the axial compressive stress in the x direction of the laminate; $f_{\mathrm{x,c,d}}$ is the design value of the compressive strength in the x direction of the laminate (8.2.2.2(2)); $f_{\mathrm{x,cr,d}}$ is the design value of the critical buckling compressive stress in the x direction of the laminate under uniform compression (8.2.2.2(3)); $\tau_{\mathrm{xy,Ed}}$ is the design value of the in-plane shear stress of the laminate; $f_{\mathrm{xy,v,d}}$ is the design value of the in-plane shear strength of the laminate (8.2.3(2))); $f_{\mathrm{xy,cr,d}}$ is the design value of the critical buckling shear stress of the laminate under in-plane shear loading (8.2.3(3)); $\sigma_{\mathrm{y,t,Ed}}$ is the design value of the axial tensile stress in the y direction of the laminate; $f_{\mathrm{y,t,d}}$ is the design value of the tensile strength in the y direction of the laminate (8.2.2.1); $\sigma_{\mathrm{y,c,Ed}}$ is the design value of the axial compressive stress in the y direction of the laminate; $f_{\mathrm{y,c,d}}$ is the design value of the compressive strength in the y direction of the laminate (8.2.2.2(2)); $f_{\mathrm{y,cr,d}}$ is the design value of the critical buckling compressive stress in the y direction of the laminate under uniform compression (8.2.2.2(3)).

(2) As an alternative to 8.2.9(1), the resistance of laminates subjected to combined stresses (including in-plane and out-of-plane directions) may be determined by testing, and/or by analytical formulae using the approach given in Annex B, or numerical modelling, both appropriately verified.

Note that there is not space in this paper to priovide the paragraphs, given in brackets (e.g (8.2.2.1) or (8.2.2.2(3)) for the determination of the design values in Formula (8.18).

Annex B (informative) **Indicative values of material properties for preliminary design**

B.1 Use of this annex

(1) This informative Annex provides supplementary guidance to that given in the Note to 4.3.2(1) and Clause 5 for the physical and mechanical properties of fibres, resins, core materials, composite plies and laminates that can be used for the preliminary design of fibre-polymer composite structures.

B.7.7 Failure criteria for plies

(1) Empirical failure criteria, which have been developed to represent experimental data for failure of single plies of composite laminates under plane stress conditions, may be used.

NOTE: Well-established failure criteria for plies of composite laminates include Maximum Stress, Maximum Strain, Tsai-Hill, Tsai-Wu, Puck and Hashin.

Annex C (normative) Buckling of orthotropic laminates and profiles

C.1 Use of this annex

(1) This Normative Annex contains additional provisions to Clause 8 for estimating the elastic buckling resistances of orthotropic laminates and profiles.

C.2 Scope and field of application

(1) This Normative Annex applies to orthotropic laminates and profiles, providing formulae to estimate their elastic buckling resistances. The member types and loading cases covered in this annex are:

— Subclause C.4 is for orthotropic flat laminates with different boundary conditions and under various loading cases.

C.3 General

(1) In general, flexural stiffnesses should be calculated using Classical Laminate Theory (CLT). For orthotropic, symmetric and balanced laminates (e.g., walls of pultruded profiles), when mechanical properties are determined at the laminate level, such stiffnesses should be calculated from Formulae (C.1) to (C.4):

$$D_{11} = \frac{\eta_{\mathrm{c}} \cdot E_{\mathrm{x.c.k}} \cdot t^3}{12\left(1-\upsilon_{\mathrm{xy,k}} \cdot \upsilon_{\mathrm{yx,k}}\right)} \quad \text{(C.1)}; \quad D_{12} = \upsilon_{\mathrm{xy,k}} \cdot D_{11} \quad \text{(C.2)}$$

$$D_{22} = \frac{\eta_{\mathrm{c}} \cdot E_{\mathrm{y.c.k}} \cdot t^3}{12\left(1-\upsilon_{\mathrm{xy,k}} \cdot \upsilon_{\mathrm{yx,k}}\right)} \quad \text{(C.3)}; \quad D_{66} = \frac{\eta_{\mathrm{c}} \cdot G_{\mathrm{xy.k}} \cdot t^3}{12} \quad \text{(C.4)}$$

where: D_{11}, D_{12}, D_{22} and D_{66} are the longitudinal, coupling, transverse and shear flexural stiffness, respectively; t is the wall thickness (laminate, flange or web); $E_{\mathrm{x,c,k}}$ and $E_{\mathrm{y,c,k}}$ are the characteristic values of the elastic moduli in compression in the x and y directions; $G_{\mathrm{xy,k}}$ is the characteristic value of the in-plane shear modulus; $\upsilon_{\mathrm{xy,k}}$ and $\upsilon_{\mathrm{yx,k}}$ are the characteristic values of major and minor Poisson's ratios, respectively.

(2) When the in-plane moduli of a composite laminate in a given direction is significantly different from the flexural moduli in the same direction, the flexural moduli should be considered in Formulae (C.1) to (C.3).

C.4 Elastic buckling of orthotropic laminates

C.4.1 Scope

  doi:10.5075/epfl-298799_978-2-9701614-0-0

(1) Subclause C.4 provides formulae to estimate the critical elastic buckling stresses of flat rectangular laminates that have orthotropic in-plane elastic constants, a balanced symmetrical lamination configuration, width-to-thickness ratio higher than 20 and length-to-width ratio higher than 5, for specific boundary conditions.

NOTE 1: The formulae in subclause C.4 are for elastic critical buckling stresses (bifurcation) of geometrically perfect laminates.

NOTE 3: For flat laminates having width-to-thickness ratio higher than 20 and length-to-width ratio lower than 5, the formulae in subclause C.4 provide conservative estimates of elastic critical buckling stresses.

(2) The critical elastic buckling stresses of laminates (bifurcation) having (i) width-to-thickness ratio lower than 20, or (ii) curvature should be determined by numerical modelling.

C.4.2 Orthotropic symmetrical laminates

C.4.2.1 Compression

(1) The characteristic value of the critical buckling compressive stress of a laminate under in-plane compression loading for the different boundary conditions illustrated in Figure C.1, $f_{i,\mathrm{cr,k}}$, should be calculated from Formulae (C.5) to (C.6):

— Both edges simply supported (SS) (Figure C.1a):

$$f_{i,\mathrm{cr,k}} = \frac{\pi^2}{t \cdot \mathrm{b}^2}\left[2\sqrt{D_{11} \cdot D_{22}} + 2(D_{12} + 2 \cdot D_{66})\right] \quad \text{(C.5)}$$

— One edge simply supported (SS) and one edge clamped (CL) (Figure C.1b):

$$f_{i,\mathrm{cr,k}} = \frac{\pi^2}{t \cdot \mathrm{b}^2}\left[3{,}13\sqrt{D_{11} \cdot D_{22}} + 2{,}33(D_{12} + 2 \cdot D_{66})\right] \quad \text{(C.6)}$$

where: *b* is the width of the laminate (perpendicular to the compressive stress direction)

NOTE: In Formulae (C.5) and (C.6) *i* is either for the x or y direction of the laminate (i.e., longitudinal or perpendicular to the laminate width).

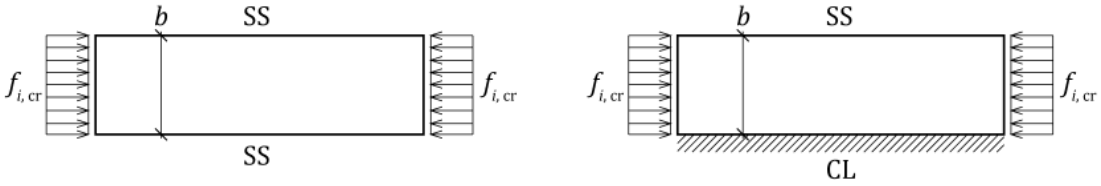

a) Simply-supported (SS) - (SS)

b) Simply-supported (SS) – Clamped (CL)

Figure C.1 — *Orthotropic laminate under in-plane compression with different boundary conditions for the edge(s): Simply Supported (SS), Free (Free) or Clamped (CL).*

To use Annex C, C.4.2.1 with the buckling reduction factor for compression, $\chi_{\mathrm{x,c}}$ or $\chi_{\mathrm{y,c}}$ = 1,0, the designer must be designing with laminates that are flat and of constant thicknesses, and are without geometrical curvature or with significant geometrical or other imperfections. For valid geometries, the rectangular plates will be relatively thin compared to their edge lengths, with the minimum edge length/thickness ratio defined in C.4.1. $f_{\mathrm{x,cr,k}}$, or $f_{\mathrm{y,cr,k}}$, are obtained using the formulae in C.4.2.1 with the relevant longer edges' displacement boundary conditions, see Figure C.1. If the shape of compressed laminates is not rectangular then the designer can determine elastic critical buckling resistances using an appropriate numerical methodolgy.

DESIGN OF FIBRE-POLYMER COMPOSITE STRUCTURES – EUROPEAN TECHNICAL SPECIFICATION: FATIGUE AND DETAILING

Thomas Keller[a], João R. Correia[b], Toby Mottram[c], Jose Sena-Cruz[d]

a: EPFL, Switzerland – thomas.keller@epfl.ch
b: University of Lisbon; Portugal
c: University of Warwick; UK
d: University of Minho, Portugal

Abstract: *The paper gives an overview of the clauses about fatigue and detailing of the new European Technical Specification 'Design of Fibre-Polymer Composite Structures'. A fatigue verification criterion and information about fatigue action models are provided first. The fatigue verification format, including the composition of a single partial factor for the fatigue resistance, are then explained. Subsequently, the specifications about fatigue testing, with a focus on bridge deck applications, are summarized. Finally, the recommendations for the detailing of laminates, profiles, sandwich panels, bolted and bonded joints, and bridge details, are addressed.*

Keywords: Fibre-polymer composites; European Technical Specification; Fatigue; Detailing

1. Introduction

Fibre-polymer composite load-bearing structures are sensitive to fatigue damage, mainly due to (i) the brittleness and anisotropic-layered fibre architecture of composite materials, and (ii) the fact that variable loads normally are high compared to permanent loads, in particular traffic loads in bridge construction.

A composite structural member or joint in bridge and other civil engineering structures can exhibit several different and complex fatigue failure modes. Failure rarely occurs in the basic member components (e.g., in laminates or sandwich cores), but in most cases in component connections and interfaces, i.e., at singularities with stress concentrations in different directions. Rather than basic component fatigue testing (of laminates or cores of sandwich panels), assemblies of components would thus need to be tested (e.g., a web-flange junction). The test set-up of such component assemblies is however complicated, the number of tests required to cover all the possible cases is rather large, and the interpretation of the results is difficult. At these singularities, local stresses normally cannot be obtained easily and reliably. Determining partial factors of fatigue resistance models for such cases seems impossible moreover due to missing data [2].

The fatigue verification method implemented in Clause 10 of the CEN Technical Specification (TS) '*Design of Fibre-Polymer Composite Structures*' [1] is thus performed on the level of the members and their joints, and their internal forces and moments, and not on the level of components and their stresses. This approach also takes into account the effects of geometrical and material imperfections and size effects on the fatigue behaviour.

Stress concentrations can also be minimized by an appropriate detailing of geometrical changes or changes of materials in members, or of member joints and their connections. Recommendations for detailing are thus provided in Clause 11 of the TS and in the informative Annex E for bridge details.

  doi:10.5075/epfl-298799_978-2-9701614-0-0

2. Fatigue verification criterion and action models

A fatigue verification criterion was established as a 95% lower confidence bound of numerous fatigue test results of various composite materials documented in literature [2]. The criterion allows to check whether a fatigue verification is required for a structural member or joint. A verification is required if the following condition is fulfilled:

$$E_d\left(\gamma_{Ff} \cdot Q_{fat}\right) / R_d > 1{,}6 - 0{,}18 \cdot \log N \tag{1}$$

where

$E_d\left(\gamma_{Ff} \cdot Q_{fat}\right)$ is the design value of an action effect in the structural member or joint (an internal force and/or moment), caused by the fatigue action model;

γ_{Ff} is the partial factor for the fatigue action (according to EN 1990, normally =1.0);

Q_{fat} is the relevant constant amplitude fatigue action (see below);

R_d is the design value of the corresponding static resistance of the member or joint;

N is the number of cycles of the fatigue action, i.e. the number of axle loads.

Concerning the above-mentioned action effects, in the case of bridges, a still unsolved problem is that a fatigue action model for traffic loads tailored to composite bridge structures does not yet exist. The current action (or load) models, FLM1-3 of EN 1991-2, which are mainly composed of different truck axle load configurations, were calibrated for steel and concrete bridges, and FLM4 represents a variable amplitude (VA) loading. Applying a VA fatigue verification was however considered to not be reliable and applicable for composites in the framework of this TS since the associated use of the linear Palmgren-Miner's damage rule, in many cases, may significantly over- or underestimate the fatigue life [2, 3]. The fatigue action model for composites should thus be selected and agreed case by case by the relevant parties, until a composite-tailored model will be available. The model should take into account the mean stress level (or the *R*-ratio) exhibited by the actual actions, to which the fatigue behaviour of composites in sensitive [2, 4].

3. Fatigue verification

As introduced above, the fatigue verification implemented in the TS is performed at the structural member or joint level and is based on the design value of an internal force or moment, as follows:

$$E_d\left(\gamma_{Ff} \cdot Q_{fat}\right) \leq \frac{\eta_c}{\gamma_{Mf}} \cdot R_{f,k} \tag{2}$$

where

$R_{f,k}$ is the characteristic value of the fatigue resistance of the member or joint, which should be obtained from member or joint testing, at constant amplitude;

γ_{Mf} is the partial factor for the fatigue resistance, to be selected according to Table 1;

η_c is an environmental conversion factor (see TS, Clause 4 and [2]).

  doi:10.5075/epfl-298799_978-2-9701614-0-0

The characteristic value of the fatigue resistance is obtained from a constant amplitude action model since a variable amplitude verification is not considered to be applicable, as explained above.

A single partial factor for the fatigue resistance is applied, γ_{Mf}, which accounts for both the uncertainty in the resistance model and unfavourable deviations of the relevant material or product properties from their characteristic values. As shown in Table 1, the factor depends on (i) the type of inspection and maintenance and accessibility of the critical details, and (ii) the consequences of failure, i.e., whether a member or joint is fail-safe or not. In fail-safe structural members or joints, local failure of the member or joint should not result in failure of the structure or critical parts thereof. In non-fail-safe members or joints, local failure of the member or joint could lead to failure of the structure or critical parts thereof.

Table 1: Partial factors for fatigue resistance, γ_{Mf}

Inspection and access	Fail-safe	Non-fail-safe
Member or joint subjected to periodic inspection and maintenance, detail accessible	1,5	2,0
Member or joint subjected to periodic inspection and maintenance, limited accessibility	2,0	2,5
Member or joint not subjected to periodic inspection and maintenance	2,5	3,0

The format of Table 1 was adopted from Table 4.19 in EUROCOMP [5], since its composition is in line with prEN 1990, 8.3.5.4(1), which specifies that the partial factor for the fatigue resistance should account for the consequence of fatigue failure and the ease of inspection and repair of fatigue-sensitive members. The values listed in Table 1 were also adopted from EUROCOMP, Table 4.19, although it was not possible to find their origin and thus directly validate them. Based on several plausibility checks, the values were however found to be plausible (details are given in [2]), but they require further verification in the future.

4. Fatigue testing

4.1 General

As indicated in the previous section, the characteristic value of the fatigue resistance should be obtained from testing on the member or joint level, normally under constant amplitude loading. The test should be conceived to reproduce the same design values of the action effects (internal forces and/or moments) as in the structural member under the fatigue action model. The applied fatigue test load should therefore be equal to the design value of the fatigue test load, divided by the conversion factor and multiplied by the partial factor for the fatigue resistance, according to Eq. (2). Furthermore, the fatigue test load should be adjusted, i.e., the maximum and minimum values selected, to represent the same mean stress level (or *R*-ratio) as in the structural member (see above). The selected test frequency should be low enough to not cause inadmissible heating effects.

Testing should be performed for two purposes, for general member qualification and case-by-case proof, in line with EN 1990, D3(1a) and D3(1e), respectively.

4.2 Bridge decks and slab bridges

In the case of composite bridge decks (installed on main girders, normally made of steel) or composite slab bridges (without additional main girders), qualification testing should be applied only once for each new product or design. Additional proof testing may be performed for each new application of the product or design, to verify that the assumed properties are achieved on site and/or to validate project-specific adaptations of the product. Proof testing may be disregarded when agreed by the relevant parties.

Qualification testing to approve a product or design should include:

- at least three static tests to determine the characteristic value of the static resistance; the coefficient of variation of the static resistance should be lower than 0,10;
- a minimum number of fatigue tests, as specified in Table 2;
- after concluding the fatigue loading with the number of cycles specified in Table 2, on each specimen, a post-fatigue static test run to failure under the same conditions as the static tests.

Table 2: Required number of fatigue tests and fatigue cycles in qualification testing for bridges of 50 and 100 years of design service life

Traffic category [a]	Minimum number of fatigue tests	Number of fatigue cycles ($x10^6$)			
		50 years		100 years	
		Local traffic [a]	Long-distance traffic [a]	Local traffic [a]	Long-distance traffic [a]
1	3	10	15	15	50
2	3	2	5	5	10
3 and 4	2	2	2	2	2
[a] according to EN 1991-2					

The required number of cycles for qualification testing was derived from EN 1991-2, assuming, as explained in [2]:

- the four traffic categories and the corresponding N_{obs} (heavy vehicles), acc. to Table 4.5 of EN 1991-2;
- the three traffic types/mixes and five vehicle types and their percentages, acc. to Table 4.7 of EN 1991-2;
- global or local effects, the former caused by the whole vehicle, the latter caused by the individual wheels/axles;
- for local effects, using weighted axle averages from Table 4.7 of EN 1991-2, resulting in 2, 3, 4 axles (rounded values), for local, medium, long-distance traffic, respectively;
- a design service life of 50 or 100 years.

The qualification testing is considered to be successful if:

- the required number of cycles is completed without failure;
- the stiffness reduction is less than 5%, to prevent excessive micro-cracking;
- detectable damage, i.e., macro-cracks, debonding, delamination that could affect durability due to moisture ingress does not occur;

- the result of the post-fatigue static test is within two standard deviations of the mean value of the static resistance achieved in the static tests.

Based on a successful qualification testing, the action effect derived from the characteristic fatigue test load (internal force and/or moment) represents the characteristic value of the fatigue resistance, $R_{f,k}$, in Eq. (2).

Although a VA fatigue verification is not considered in the TS due to the above-mentioned reasons, a VA test load can nevertheless be applied, and the procedure and criteria defined above for a successful qualification testing can be adopted to verify the fatigue resistance.

Further specifications are provided in the TS regarding the test loading device configuration and the consideration of the surfacing layer. In bridge decks, the tyre-deck contact area (i.e., its size and shape) and the contact pressure distribution in this area are complex and depend on several factors, i.e., the tyre geometry and inflation pressure, the surfacing stiffness, and configuration of the deck, i.e., the deck stiffness distribution below the tyre. For instance, the contact area and pressure distribution on the top flange of a cellular deck system and on the top face sheet of a sandwich deck are different due to the different deck component stiffnesses. Furthermore, in the cellular case, significant differences also exist depending on whether the load is applied on a stiff top flange-web joint or on the more flexible top flange between the flange-web joints; more details are given in [2].

Since the fatigue life of deck systems can be very sensitive to the contact area and pressure distribution, particularly in cellular systems where the top flange is subjected to local bending and shear, the loading device configuration applied in testing should simulate the actual contact area and pressure distribution as closely as possible.

Contact pressure measurements on cellular bridge deck systems demonstrated that the pressure decreases to zero at the edges and does not exhibit concentrations as is the case under a steel plate of a loading device [2]. The bending stiffness of a steel plate, as an element of the loading device, should thus not affect the contact pressure distribution, i.e., a softer pad should be placed between the steel plate and deck to prevent a load transfer only at the edges of the device through concentrated local pressure. Finite element analysis can be used to design the soft pad (i.e., its thickness and stiffness) between the steel plate and deck under the fatigue test load.

The consideration of the bridge deck surfacing is also important since it can have two positive effects, depending on the surfacing thickness and stiffness, i.e., (i) a load spreading which results in a larger loaded area on the composite deck's top face (below the surfacing) compared to the tyre-surfacing contact area, and thus a more widely distributed pressure, and (ii) a strain reduction in the composite top laminate or flange caused by the flexural composite action between surfacing and composite top laminate or flange [2].

These positive effects depend however on the surfacing temperature and loading rate. An increasing surfacing temperature, i.e., a possible softening of the surfacing polymer components, can reduce these effects, while a higher loading rate, resulting in a corresponding surfacing stiffening, can increase the effects. If the surfacing layer has a significant stiffness, e.g., in the case of polymer concrete, the surfacing layer may be taken into account in the design and fatigue testing. If this applies, the effects of temperature and loading rate on the surfacing layer stiffness should however be considered.

5. Detailing

The TS also provides recommendations for the detailing of member laminates, profiles, sandwich panels, bolted and bonded joints (in Clause 11), and generic examples of bridge details (in Annex E), such as bearings, expansion joints, parapets, and crash barrier fixations. The goals of these design recommendations are to ensure that stress concentrations are avoided or minimized and that effects of environmental conditions are reduced, e.g., by appropriate protection or dewatering systems. The reduction of stress concentrations also improves the fatigue resistance, see previous sections.

Concerning profiles, it is recommended to use closed sections since outstanding flanges are sensitive to damage, which can be easily caused by local impact. Furthermore, geometrical recommendations are provided for member laminates, such as sandwich panel face sheets, concerning thickness changes (tapering), and angles and overlap lengths of scarf, step-lap or single-strap connections; indications for sandwich core connections and core inserts are also provided.

For bolted joints, recommendations for nominal bolt diameters and bolt hole clearances, end edge distances for single- or multi-row bolted connections, and distances between centres of bolt holes are specified.

Adhesive connections should be designed symmetrical and with minimized eccentricities to reduce peeling stresses, to which the composite adherends normally are sensitive due to their layered fibre architecture. Tapering of the adherends and adhesive fillets can reduce stress peaks in lap-shear connections, the connection resistance may however not be reduced due to a geometrical (statistical) size effect [2]. Recommendations for minimum overlap lengths and adhesive layer thicknesses in lap-shear joints are provided.

6. Concluding remark

The TS clauses about fatigue and detailing are complemented by their corresponding background, comprised in the Commentary document [2], which provides the bases and justifications for the decisions taken and values selected.

Acknowledgements

Authors acknowledge funding to WG4.T2 via EC Project M515, and the important and essential scientific and technical support from WG4 to CEN/TC 250 to the drafting of the TS [1] and [2].

References

1. FprCEN/TS 19101:2021. Design of Fibre-Polymer Composite Structures. European Committee for Standardization, CEN/TC 250, 2021.
2. Commentary to FprCEN/TS 19101:2021. Design of Fibre-Polymer Composite Structures. Submitted to Working Group 4 of CEN/TC 250, April 2022.
3. Broutman LJ, Sahu S. A new theory to predict cumulative fatigue damage in fiberglass reinforced plastics, In: Composite materials: testing and design (2nd Conference), 170-188, ASTM STP 497. Philadelphia: American Society for Testing and Materials, 1972.

4. Roohollah S, Vassilopoulos AP, Keller T. Experimental investigation and modeling of mean load effect on fatigue behavior of adhesively-bonded pultruded GFRP joints. International Journal of Fatigue; 2012, 44: 245-252.
5. Clarke JL (ed.). Structural design of polymer composites: EUROCOMP Design code and handbook. London: E & FN Spon, 1996. ISBN 0 419 19450 9.

  doi:10.5075/epfl-298799_978-2-9701614-0-0

ADHESIVE JOINT DESIGN METHODS AND EXAMPLES

Marko, Pavlovic[a], Angeliki, Christoforidou[b], Thomas, Keller[c]

a, b: Faculty of Civil Engineering and Geosciences, Delft University of Technology, 2628 CN Delft, Netherlands – M.Pavlovic@tudelft.nl
c: EPFL, Switzerland

Abstract: *Challenges of reliable prediction of resistance of bonded joints lie in the complexity of stress concentrations, multiple crack paths, mode-mixity and sudden crack propagation. The new Technical Specification for Design of fibre-polymer composite structures (TS) is bridging this gap by providing comprehensive sets of design recommendations and analyses to be used for the verification of adhesive joints. Two design approaches in the TS, based on stress analysis and fracture mechanics, are summarized and basic design assumptions on allowed failure conditions and partial factors in relation to execution and maintenance are highlighted.*

The application of the design recommendations is shown on the example of determining the design value and the ultimate resistance of a simple double lap joint. FE models built in Abaqus are used to analyse stress concentrations and crack initiation and propagation based on material level experiments. Variability of the material properties are taken into account through partial safety factors. Joint resistances obtained by the stress-based approach and fracture-mechanics approach are compared.

Keywords: adhesive joints; design recommendation; admissible failure modes; stress analysis; fracture mechanics

1. Introduction

Adhesive bonding in fibre-polymer composite structures can be a competitive connection solution over bolting because of slip resistance, no weakening of the cross section of the laminated composite plate, applicability to curved, tapered or non-plated members, etc. More common application of adhesive bonding in load carrying structural details is hinged by the lack of confidence and established design rules to predict resistance of the joints. The new Technical Specification for Design of fibre-polymer composite structures (TS) is bridging this gap by providing comprehensive sets of design recommendations, requirements and framework of analyses and tests on the joint and material level to be used for the verification of adhesive joints.

2. Design of adhesively bonded joints according to Technical Specification

2.1 Design assumptions

The basic principle is that an adhesive joint shall be designed as fail-safe. A joint failure shall not result in failure (progressive collapse) of the whole structure comprising the joint. Failure of an adhesive joint shall be considered as an accidental situation in accordance with EN 1990. For example, the fail-safe condition can be achieved either by providing an alternative (back-up) load carrying mechanism in the joint, e.g. by making hybrid adhesive-bolted joints and/or by providing redundant degrees of freedom in the structure, e.g. by crossed braces in a truss structure.

  doi:10.5075/epfl-298799_978-2-9701614-0-0

The TS defines permissible failure modes of an adhesive connection being either cohesive failure in the adhesive or fibre-tear failure in the adherend. Pure adhesive failure, i.e. complete failure in the adherend-adhesive interface, shall be avoided through appropriate material selection and surface preparation. Validation of the failure mode by tests is required. It is important to consider that the environmental conditions can change the failure mode.

In general, adhesive joints being symmetrical with regard to the load axis are recommended. Eccentricities in the load transfer should be minimized. A minimum thickness of the adhesive layer of 1.0 mm should be specified and properly verified in the production. Measures of tapering the adherents and/or adhesive fillets can be applied to reduce the stress peaks, however care must be taken that the size effects on strength can limit the effectiveness of such improvements.

2.2 Partial safety factors and conversion factors for adhesive connections

A design value of the adhesive connection resistance $R_{ac,Rd} = R_{ac,k} \cdot \eta_c / \gamma_{M,ac}$ is calculated on the basis of the characteristic value of the adhesive connection resistance $R_{ac,k}$ and partial factor $\gamma_{M,ac}$ and conversion factor η_c. The conversion factor η_c is covering aspects of moisture, temperature and ageing on the matrix-dominated property that causes failure, e.g. for fibre-tear or cohesive failure in the adhesive. A single partial factor $\gamma_{M,ac}$ ranging from 1,5 to 2,5 is used to account for uncertainties related to material, resistance model and factors related to inspection, maintenance, accessibility and control in application. The characteristic value of the resistance $R_{ac,k}$ can be determined either from joint experiments with multiple specimens or by FE analysis using either a stress-based or fracture mechanics approach. In both approaches analysis is based on characteristic values of results from material and fracture mechanics tests, and it must be validated in terms of compatible and permissible failure mode by joint experiments.

2.3. Principles of stress-based approach

The design values of out-of-plane (peeling) and in-plane shear stresses $\sigma_{z,t,Ed}$ and $\tau_{xy,Ed}$, respectively, should be obtained in stress analysis using FE models where appropriate mesh is used to obtain consistent stress values in zones of stress concentrations. Homogenized material properties may be and material orthotropy should be considered. A failure criterion to be applied in the failure plane of lap-shear connections exhibiting fibre-tear failure may be defined as:

$$\left(\frac{\sigma_{z,t,Ed}}{f_{z,t,d}}\right)^2 + \left(\frac{\tau_{xy,Ed}}{f_{xy,v,d}}\right)^2 \leq 1{,}0 \qquad (1)$$

The design values of out-of-plane and in-plane shear strengths $f_{z,t,d}$ and $f_{xy,v,d}$ should be determined in material tests with identical failure mode and plane as in joint experiments used for validation, considering statistical size effects governed by the type of stress distribution.

2.4. Principles of fracture-mechanics based approach

A design based on fracture mechanics uses a criterion where design values of the strain energy release rate for Mode I and Mode II obtained in FE models are compared to design values of critical strain energy release rates obtained from fracture mechanics tests, e.g. DCB and ENF tests:

$$\left(\frac{G_{I,Ed}}{G_{Ic,Rd}}\right)^m + \left(\frac{G_{II,Ed}}{G_{IIc,Rd}}\right)^n \leq 1.0 \qquad (2)$$

  doi:10.5075/epfl-298799_978-2-9701614-0-0

Virtual crack closure technique (VCCT) or cohesive zone modelling (CZM) can be used in FE models - the former for crack initiation and the latter for both crack initiation and propagation.

2.5. Limitations

The main limitation of the stress-based approach is the difficulty to account for size effects related to sharp stress peaks. Empirical solutions exist with factors to take those aspects into account for a limited number of overlap geometries, sizes, and material compositions.

VCCT analysis lacks the possibility to account for fibre bridging, requires the definition of a critical zone comprising a pre-crack, and in general is sensitive to pre-crack and mesh size. Analysis using CZM solves the problem of definition of the critical location and in general is less sensitive to mesh size. The main challenge is to define and validate parameters of the traction-separation law from fracture mechanics tests that properly defines the fibre bridging behaviour. The design example shown here compares results of the stress-based fracture mechanics (CZM) approach on a relatively simple joint.

3. Design example of verification of double-lap adhesive joint

The design resistance of a balanced double-lap adhesive joint with pultruded adherends when subjected to axial tension loading is determined by following the procedures described above with the use of Abaqus 2019 software. The geometry of the joint is taken from the experimental work performed in [1] and it is illustrated in Figure 1.

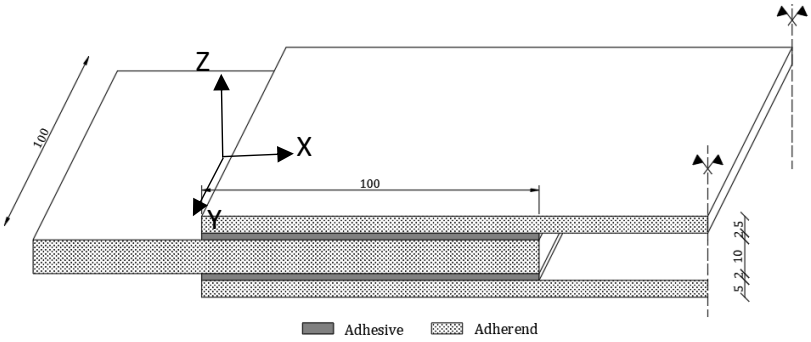

Figure 1. Geometry of half of the double-lap joint

For the given geometry, five experiments were conducted in [1] and fibre-tear failure occurred at 0,5 mm inside the inner adherend at approximately 158 kN load. The crack path was located within the first mat layer (Path I from [2]).

3.1 Joint description

Three symmetry boundary conditions are used, as indicated in Figure 2. Half of the width, half of the thickness, and half of the length of the physical joint are modelled, 1/8 of the complete joint, to reduce the computation time. The two interfaces between the adhesive and the inner and outer adherends are tie constrained.

The adherends are subdivided into six layers and two regions with different elements and sizes are chosen based on a mesh sensitivity analysis, see Figure 3. A relatively fine mesh with an element size of 0,25 mm is chosen at the bonded area, to capture the stress peaks at the end of the bond lines. Eight elements through the thickness of the 2 mm adhesive layer are modelled.

  doi:10.5075/epfl-298799_978-2-9701614-0-0

The three-dimensional 8-node linear brick element with reduced integration, C3D8R, is used for all the parts in the region of the fine mesh. The coarse region is meshed with 2 mm 4-node linear tetrahedron elements, C3D4.

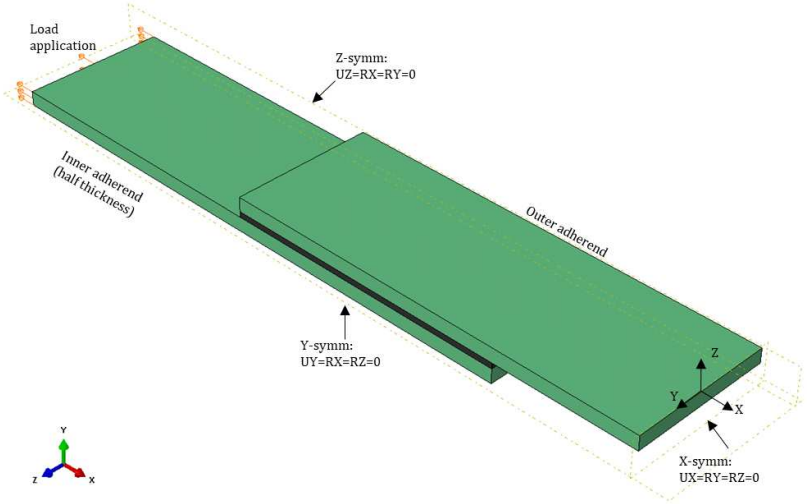

Figure 2. 1/8 model of the double-lap joint

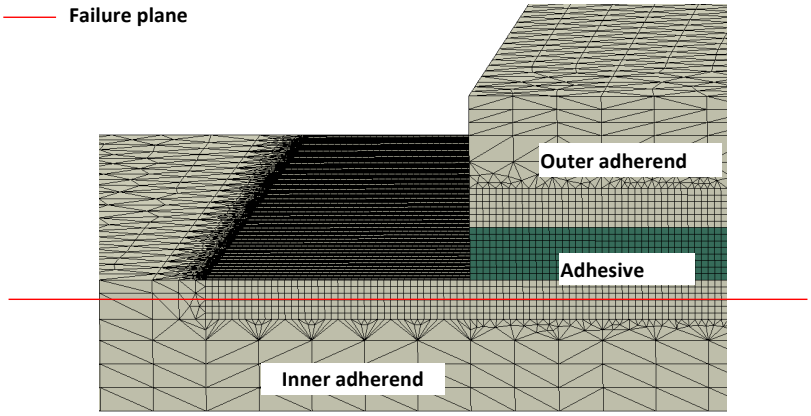

Figure 3. Detail of FE mesh of joint model

3.2 Stress-based approach

3.2.1 Design values of material strength

Average values of 8,0 MPa and 19,3 MPa for the out-of-plane and the shear strength, respectively, at the failure plane embedded 0,5 mm inside the inner laminate were obtained from [2] with 7,92% of coefficient of variation. Therefore, by applying the formula C.15 from prEN 1990 and considering that 10 samples were tested, the characteristic value of the out-of-plane tensile and shear strength is equal to 6,85 MPa and 16,53 MPa, respectively.

The design value of the out-of-plane tensile and shear strength for fibre-tear failure 0,5 mm inside the inner adherend is calculated based on Subclause 12.4.5.3 Paragr. (3). Assuming that the partial factor for the resistance model is $\gamma_{M,ac} = 1{,}7$ and the total conversion factor, η_c, is equal to 1, the design values of material strength in the failure planed embedded 0,5 mm inside the 10 mm thick inner adherend are:

$$f_{\mathrm{z,t,d}} = \frac{\eta_c}{\gamma_{M,ac}} \cdot f_{\mathrm{z,t,k}} = \frac{1}{1{,}7} \cdot 6{,}85 = 4{,}03 \text{ MPa} \quad (3)$$

$$f_{\mathrm{xy,v,d}} = \frac{\eta_c}{\gamma_{M,ac}} \cdot f_{\mathrm{xy,v,k}} = \frac{1}{1{,}7} \cdot 16{,}53 = 9{,}72 \text{ MPa} \quad (4)$$

3.2.2 Homogenized material properties

A summary of the input data for the adherends and adhesive are shown in Table 1, provided as mean values from manufacturer's datasheets, Fiberline and SikaDur, respectively.

Table 1: Homogenized material data for adherends and adhesive.

Pultruded adherends	$E_{x,t,m}$ = 24,0 GPa	$E_{y,t,m}$ = 7,0 GPa	$G_{xy,m}$ = 3,0 GPa	$\nu_{xy,m}$ = 0,07
Adhesive	E_m = 4,6 GPa		G_m = 1,7 GPa	ν_m = 0,37

The stresses in the elements at the failure plane located 0,5 mm inside the inner adherend are read to obtain the design values of the applied action. For example, the S33 stresses, which correspond to the out-of-plane stresses in the adherend, are shown in Figure 4.

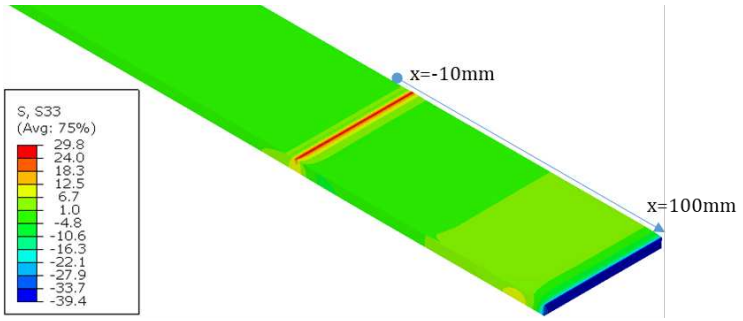

Figure 4. Out-of-plane stresses [MPa] at 0,5 mm inside inner adherend; at 100 kN load level

Due to fairly constant stress distribution along the width of the joint, a line along the middle of the joint (in the symmetry plane, see indication in Figure 4) is used to represent the stress values as a function of the bond length in Figure 5 by solid lines for the homogeneous material data.

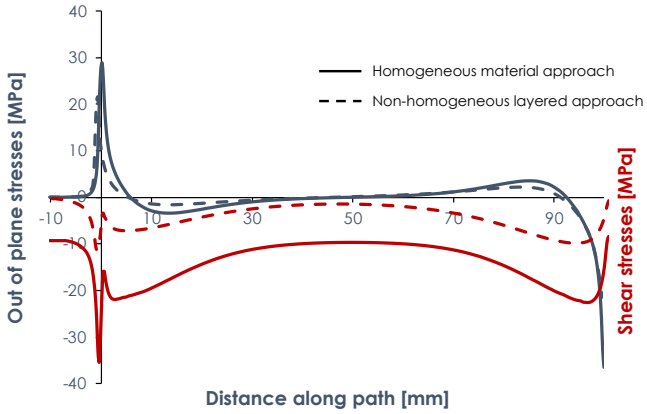

Figure 5. Stresses along bondline 0,5 mm inside inner adherend; at 100 kN load level

The design resistance of the joint for ULS verification is calculated by adjusting the load such that the stress-based quadratic criterion is equal to 1,0. In this specific case, an epoxy adhesive is used for a double-lap joint of 100 mm overlap length which results in sharp stress peaks at the bondline ends. Therefore, according to [2, 3], the two correction factors k_σ = 4,0 and k_τ = 2,0 are selected to take into account the size effect on strength. The maximum ratio of action vs. resistance is found at the location x=0 mm due to the shift in the peak values of the out-of-plane and shear stresses corresponding to the location where the adhesive layer begins. The ratio of action vs. resistance for the critical location is:

  doi:10.5075/epfl-298799_978-2-9701614-0-0

$$\left(\frac{\sigma_{z,t,Ed}}{k_\sigma \cdot f_{z,t,d}}\right)^2 + \left(\frac{\tau_{xy,Ed}}{k_\tau \cdot f_{xy,v,d}}\right)^2 = \left(\frac{27,5}{4 \cdot 4,03}\right)^2 + \left(\frac{17,5}{2 \cdot 9,72}\right)^2 = 2,91 + 0,81 = 3,72 \quad (5)$$

The ULS criterion is not satisfied with the load equal to 100 kN because the criterion given in Eq. (3) is exceeded at the critical location. The values of stresses obtained in the used FE model are linearly dependent on the applied load. Therefore, the design value of resistance for this failure mode can be determined by adjusting the applied load. Since the quadratic mixed-mode criterion is used, the applied load is to be divided by the square root of the obtained ratio of the action vs. resistance. Thus, the design resistance of this joint is equal to:

$$F_{Rd} = \frac{100}{\sqrt{3,72}} = 51,8 \text{ kN} \quad (6)$$

3.2.2.1 Non-homogeneous layered model

The layer-wise material properties of pultruded adherends are tabulated below. The thickness of each layer is listed in Table 2, provided as mean values from literature [4].

Table 1. Input material data for pultruded adherends.

Layer	$E_{x,t}$	$E_{y,t}$	$E_{z,t}$	G_{xy}	G_{yz}	ν_{xy}	ν_{yz}
1st combi-mat (0,5 mm)	12,8 GPa	12,8 GPa	3,2 GPa	6,2 GPa	1,4 GPa	0,27	0,36
2nd combi-mat (1 mm)	15,1 GPa	15,1 GPa	3,2 GPa	6,7 GPa	1,4 GPa	0,27	0,36
UD Roving (remaining)	38,9 GPa	3,2 GPa	3,2 GPa	2,7 GPa	1,4 GPa	0,32	0,27

Figure 5 also shows the calculated out-of-plane (peel) and in-plane shear stress distributions at the load of 100 kN with dashed lines. The values are taken from the same longitudinal path as indicated in Figure 4 i.e., in the middle of the width of the double-lap joint.

Applying the same design values of the out-of-plane tensile and shear strength, the maximum ratio of action vs. resistance at 100 kN load level at the critical location of the bondline end inside the inner adherend is calculated as shown in Eq. (7). Thus, the design resistance of the joint using layer-wise modelling and stress-based approach is given in Eqs. (7) and (8).

$$\left(\frac{\sigma_{z,t,Ed}}{k_\sigma \cdot f_{z,t,d}}\right)^2 + \left(\frac{\tau_{xy,Ed}}{k_\tau \cdot f_{xy,v,d}}\right)^2 = \left(\frac{21,9}{4 \cdot 4,03}\right)^2 + \left(\frac{7,7}{2 \cdot 9,72}\right)^2 = 2,00 \quad (7)$$

$$F_{Rd} = \frac{100}{\sqrt{2,0}} = 70,7 \text{ kN} \quad (8)$$

3.3 Fracture-mechanics approach

The 3D FE model described above is adapted such that it will allow for non-linear progressive failure analysis. In that respect, the quasi-static analysis using explicit dynamic solver with mass-scaling in Abaqus/Explicit is used to assure feasible convergence. CZM interface is applied at the failure plane e.g., 0,5 mm inside the inner adherend. The same material properties as defined in Section 3.2.2.1 are applied for the pultruded profiles and the adhesive layer.

To define the behavior of the CZM, a traction-separation law with design values of critical strain energy release rates at initiation and propagation were introduced as shown in Figure 6. A

  doi:10.5075/epfl-298799_978-2-9701614-0-0

trilinear traction-separation law is used for the CZM to account for the fibre-bridging behavior due to fiber-tear failure. Further subsections show how the CZM parameters are derived.

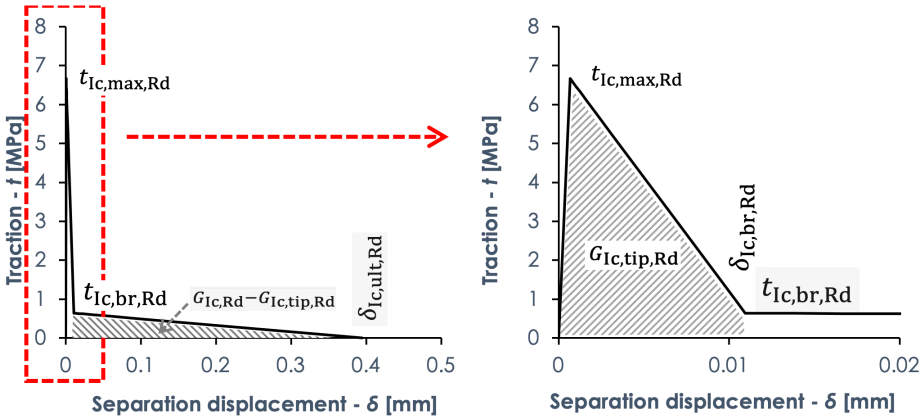

Figure 6. Traction-separation law for CZM with design values of critical parameters

3.3.1 Design values of critical strain energy release rate

Average values of 151 ± 35 J/m^2 and 536 ± 131 J/m^2 of Mode I critical strain energy release rate for crack initiation and propagation, respectively, were obtained from [4]. Therefore, by applying Eq. (C.15) from prEN 1990 and considering the number of tests, the characteristic values of the critical strain energy release rates for initiation and propagation correspond to 67,8 J/m^2 and 276,7 J/m^2.

The design value of the critical strain energy release rates for initiation and propagation of the fiber-tear failure inside the inner adherend is calculated based on Subclause 12.4.5.4 Paragr. (1). Considering the same partial and conversion factor as before, the values obtained are equal to 40 J/m^2 for initiation and 163 J/m^2 for propagation.

3.3.2 Design values of tractions and separations in CZM

The average value for the maximum traction is set equal to 25,2 MPa from [5] whilst 5-10% of that is considered as the fibre-bridging traction thus, 2 MPa. The design values of the tractions based on the proportion between average and design values of critical strain energy release rate are:

$$t_{\mathrm{Ic,max,Rd}} = \frac{G_{\mathrm{Ic,tip,Rd}}}{G_{\mathrm{Ic,tip,m}}} \cdot t_{\mathrm{Ic,max,m}} = \frac{40}{151} \cdot 25{,}2 = 6{,}7 \text{ MPa} \quad (9)$$

$$t_{\mathrm{Ic,br,Rd}} = \frac{G_{\mathrm{Ic,Rd}} - G_{\mathrm{Ic,tip,Rd}}}{G_{\mathrm{Ic,m}} - G_{\mathrm{Ic,tip,m}}} \cdot t_{\mathrm{Ic,max,m}} = \frac{163-40}{536-151} \cdot 2 = 0{,}64 \text{ MPa} \quad (10)$$

This results in the corresponding separations at damage initiation and bridging of the fibre-tear failure inside the inner adherend:

$$\delta_{\mathrm{Ic,br,Rd}} = \frac{2 \cdot G_{\mathrm{Ic,tip,Rd}}}{t_{\mathrm{Ic,max,Rd}}} = \frac{2 \cdot 40/1000}{6{,}7} = 0{,}012 \text{ mm} \quad (11)$$

$$\delta_{\mathrm{Ic,ult,Rd}} = \frac{2 \cdot (G_{\mathrm{Ic,Rd}} - G_{\mathrm{Ic,tip,Rd}})}{t_{\mathrm{Ic,br,Rd}}} = \frac{2 \cdot (163-40)/1000}{0{,}64} = 0{,}384 \text{ mm} \quad (12)$$

3.3.3 Design resistance of the joint and design force at crack initiation

The model ran until failure and therefore the design resistance of the joint is obtained by observing the damage of the interface and the obtained load displacement behavior. The force-

displacement graph resulting from FE analysis of the joint is shown in Figure 7. A slight change of stiffness is noticed at a design load of 32,1 kN corresponding to crack initiation.

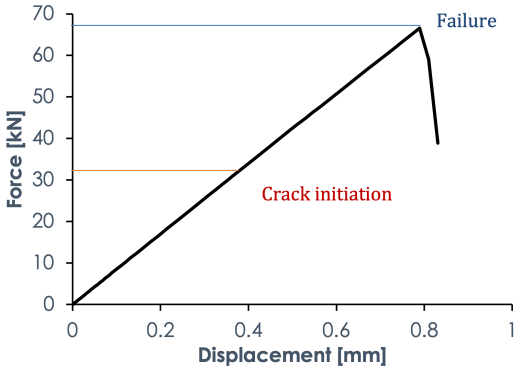

Figure 7. Numerically obtained force displacement graph with application of CZM

3.4 Validation of numerically determined design resistance with experimental data

Based on the available experimental results in [1], the design value of resistance of the given connection is calculated based on a partial factor of 1,7 and the variation of results and number of tests in the joint experiments. More specifically, five experiments were performed for this adhesively bonded joint geometry with a variation of results equal to V_x=13,5%. Thus, the characteristic value of resistance of the joints based on the tests is equal to 114,5 kN. Therefore, the design value of the resistance is given by:

$$F_{\mathrm{d}} = \frac{\eta_c}{\gamma_{M,ac}} \cdot F_k = \frac{1}{1{,}7} \cdot 114{,}5 = 67{,}3 \text{ kN} \quad (13)$$

4. Conclusions

The design value of resistance obtained in joint experiments is 67,3 kN which is 23% higher than the design resistance obtained by the stress-based approach using the design values of homogenized material properties and 5% lower than the corresponding one using the non-homogeneous properties in a layer-wise approach. The layer-wise modelling leads to a higher predicted resistance which however cannot be generalized. Lower stiffness of the material located next to the failure plane in the layer-wise approach leads to a reduction of the stress concentrations and thus increases the predicted joint resistance. The fracture mechanics approach using CZM predicts the design value of resistance corresponding to full crack propagation equal to 66,7 kN which is only 1% higher than the design value of resistance obtained in the joint experiments.

5. References

1. Keller T, Vallee T. Adhesively bonded lap joints from pultruded GFRP profiles. Part I: Stress-strain analysis and failure modes. Composites Part B. 2005, 36(4), 331-340.
2. Keller T, Vallee T. Adhesively bonded lap joints from pultruded GFRP profiles. Part II: joint strength prediction. Composites Part B. 2005, 36(4), 341-350.
3. Vallee T. Adhesively bonded lap joints of pultruded GFRP shapes. EPFL PhD thesis no. 2964, Lausanne, 2004.
4. Shahverdi M, Vassilopoulos AP, Keller T. Mixed-mode quasi-static failure criteria for adhesively-bonded pultruded GFRP joints. Composites Part A. 2014, 59, 45-56.
5. Cameselle-Morales A, et al. Numerical simulation of two-dimensional in-plane crack propagation in FRP laminates. Composite Structures. 2018, 200, 396-407.

  doi:10.5075/epfl-298799_978-2-9701614-0-0

DESIGN APPROACH FOR FIBRE REINFORCED POLYMER STRUCTURES: A WORKED EXAMPLE

Emilie, Lepretre[a], Kévin, Brunellière[b], Samuel, Durand[b], Jean-François, Caron[c], Philippe, Jandin[d] and Anthony, Pruvost[d]

a: Univ Gustave Eiffel, MAST-SMC, F-44344 Bouguenais, France – emilie.lepretre@univ-eiffel.fr
b: MECA Design Office, Nantes, France
c: Ecole des Ponts ParisTech, Laboratoire Navier, Champs-sur-Marne, France
d: Cerema DtecITM, CTOA/DGOI, Sourdun, France

Abstract: *FRP material shows numerous advantages compared to traditional construction materials. It has a high strength to weight ratio, making the final structure lighter, easier to erect and reducing the cost. In order to promote the construction of safe structures with FRP in Europe, it becomes necessary to propose a European standard, providing a common approach for the design. The foundation for this new structural design code is the Technical Specification (CEN/TS) written by Working Group WG4 'Fibre Reinforced Polymers' under CEN Technical Committee 250 (CEN/TC250). The presented paper illustrates through a worked example how the Technical Specification document may be used in practice. In this example, Ultimate Limite State (ULS) verifications are performed for one span of a GFRP footbridge.*

Keywords: Eurocode; codes; standards and design guidelines; design analysis

1. Introduction

The adoption of FRP materials for the construction of buildings and civil engineering structures has increased during the past 20 years. FRP composite bridges show particular advantages such as high strength, lightweight, good corrosion resistance, long-term durability, ease of installation and low-maintenance. Even though having these benefits, the FRP structures have not been widely applied in practice, mainly due to the lack of national design guidelines. To address this challenge, the CEN Technical Committee 250 (CEN/TC250) has initiated the process of development of a new standard regarding the design and verification of composites structures made of FRPs (for both buildings and civil engineering works), since May 2010. The first step was done in July 2016 with the publication of a 'Science and Policy Report' [1]. After agreement of CEN/TC 250, the step 2 has started at the end of 2018 with the aim of producing a first draft of a 'Technical Specification' (TS) in 2020. This future Structural Eurocode will provide common structural design rules for FRP structure and will help engineers to design composite structures. In order to help produce a strong design guideline, the French WG4 (to which the authors belong) decided to propose a case study, which consists of the design of an existing GFRP footbridge. This real footbridge was built in 2015, in France, by Janson Bridging Company (see Figure 1). This footbridge is a sandwich structure with two GFRP (Glass Fibre Reinforced Polymer) skins at the top and bottom of the bridge and a GFRP-reinforced foam core. In this paper, the ULS verifications are performed for only one span of the bridge and following the recommendations of the actual draft of the Technical Specification. Numerical modelling is first used to determine the design values of the action effects at different locations on the structure. Then, the design values of resistance of the material properties for the different constitutive

  doi:10.5075/epfl-298799_978-2-9701614-0-0

parts of the footbridge are determined using the Technical Specification procedure. Finally, the ULS safety verifications are done for the different parts of the bridge.

Figure 1. Pedestrian FRP Bridge, Saint-André de Cubzac, France, ©Photo P. Charbonneau.

2. Description of the Saint-André de Cubzac Bridge

2.1 Geometry and dimensions

The Saint-André de Cubzac Bridge is a two isostatic span pedestrian bridge with a total length of 36 m and a width of 2.4 m. In our case study, we are interested in the verification of only one span of length 21.1m. The bridge was initially designed in compliance with the CUR96 recommendations [2]. It is an integral structure made from GFRP (glass fibre-reinforced polymer) and based on InfraCore Inside-technology (FiberCore construction). An InfraCore Inside structure is a sandwich structure moulded by infusion. The top and bottom skins are structurally most effective (i.e. fibres are concentrated in these skins). For an effective transfer of the shear forces, the FRP webs are connected to the top and the bottom skins. A foam core material is present between each web but it is supposed to be non-structural (only acts as a placeholder during construction). The final structure results in a layered structure with fibres in different directions. Top skin, bottom skin, external webs and flanges have a fibre volume fraction of 50.9% while the internal webs has a fibre volume ratio of 28%. All fibres are E-glass fibres and the matrix is a polyester resin.

The Figure 2 shows the cross-section of the studied GFRP footbridge with its different constitutive parts: top and bottom skins (in blue color), external webs (in green color), flange (in red color) and internal webs (in grey color).

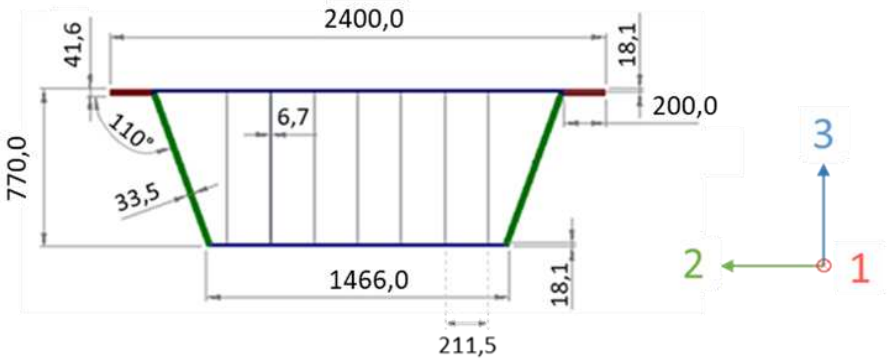

Figure 2. Cross-section of the footbridge (dimensions in mm)

2.2 Material properties

The material properties of each part of the bridge were determined by testing according to the standard test methods. The characteristic values of the material properties (determined according to Annex D of EN 1990, [3]) are given in Table 1. Figure 3 shows the local axes of the different constitutive parts of the bridge.

Table 1: Characteristic values of the material properties for each bridge section.

	Top and bottom skins	Flange	External webs	Internal webs
In-plane tensile modulus in x direction, $E_{x,t,k}$ [MPa]	31 941	25 010	24 700	9 803
In-plane tensile modulus in y direction, $E_{y,t,k}$ [MPa]	17 964	25 010	24 743	9 111
In-plane tensile strength in x direction, $f_{x,t,k}$ [MPa]	150	118	113	77
In-plane tensile strength in y direction, $f_{y,t,k}$ [MPa]	81	118	120	67
In-plane compressive modulus in x direction, $E_{x,c,k}$ [MPa]	31 941	25 010	24 700	9 803
In-plane compressive modulus in y direction, $E_{y,c,k}$ [MPa]	17 964	25 010	24 743	9 111
In-plane compressive strength in x direction, $f_{x,c,k}$ [MPa]	198	155	149	81
In-plane compressive strength in y direction, $f_{y,c,k}$ [MPa]	106	155	157	70
In-plane shear modulus in xy plane, $G_{xy,k}$ [MPa]	3 284	3 284	3 462	3 299
In-plane shear strength in xy plane, $f_{xy,v,k}$ [MPa]	31	31	28	38
In-plane major Poisson's ratio in xy plane, $v_{xy,k}$	0.18	0.13	0.14	0.44
In-plane minor Poisson's ratio in xy plane, $v_{yx,k}$	0.10	0.13	0.14	0.41
Flexural strength in x direction, $f_{x,f,k}$ [MPa]	155	121	123	97
Flexural strength in y direction, $f_{y,f,k}$ [MPa]	96	132	134	108

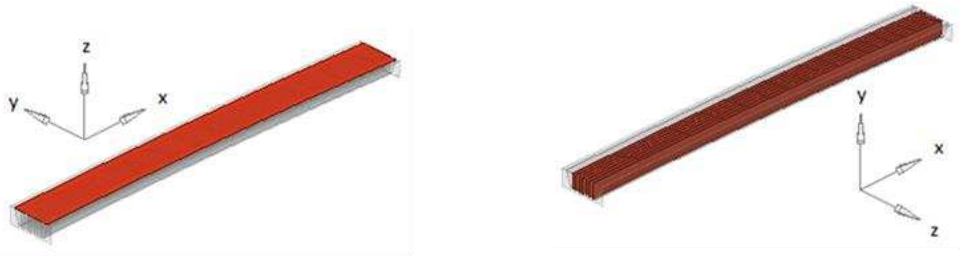

(a) Top skin, bottom skin and flange local axes (b) External and internal webs local axes

Figure 3. Local axes of each constitutive parts of the bridge

3. Numerical modelling

3.1 Description of the Finite Element (FE) model

A 3D numerical modelling was made. Each GFRP part of the footbridge (namely each skin, flange and web) was modelled separately by using appropriate shell finite elements (see Figure 4). Each part was modelled as a single layer with orthotropic elastic properties (the characteristic values are used). Boundary conditions were set to ensure an isostatic behavior of the structure. Displacement and stress level calculations were conducted using linear elastic analysis (small strains and displacements were considered). Structural analysis is conducted using first-order deformation. The present case-study concerns the global design of the footbridge. Local effects, as stress concentrations at the supports, are not addressed here. A specific and local finite-element description could be required if this point has to be checked more precisely.

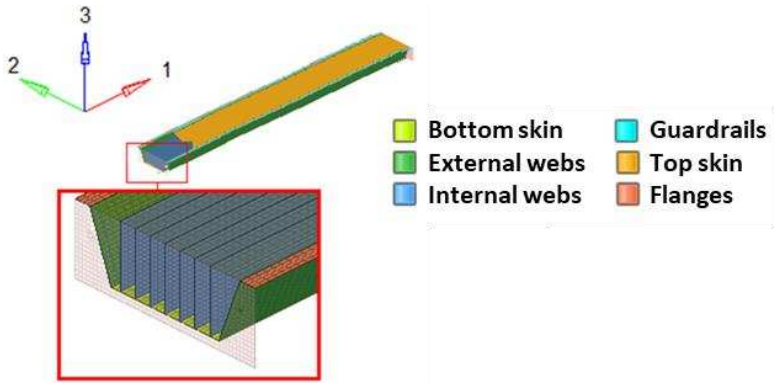

Figure 4. Meshing of the numerical model

3.2 Load combination

The studied load combination considers the self-weight of the structure and four concentrated loads representing a service vehicle (see recommendations of the EN 1991-2 standard, [4]). The permanent loads corresponding to the self-weight of the bridge is taken equal to 423.1 kg/m. Moreover, a horizontal force is considered acting along the bridge deck axis at the pavement level (equal to 10% of the total load corresponding to the uniformly distributed load).

3.3 Design values of the action effects

The design values of the actions were taken at different locations on the footbridge in order to consider the maximum adequate stresses needed for the design verification. The Table 2 summarizes all the maximum values of stresses in each constitutive part of the bridge.

Table 2: Design values of the action effects.

	Type of design value	Value [MPa]
Top skin	Longitudinal (in-plane) compressive stress (x direction)	$\left(\sigma_{\mathrm{x,c,Ed}}\right)_f = -28.8$
Bottom skin	Longitudinal (in-plane) tensile stress (x direction)	$\left(\sigma_{\mathrm{x,t,Ed}}\right)_f = 39.2$
Internal webs	In-plane shear stress	$(\tau_{\mathrm{Ed}})_w = 1.5$
	In-plane bending stress (x direction, tension)	$\left(\sigma_{\mathrm{x,M,Ed}}\right)_w = 11.1$

	In-plane bending stress (x direction, compression)	$\left(\sigma_{\mathrm{x,M,Ed}}\right)_w = -13.7$
	Compressive stress (y direction)	$\left(\sigma_{\mathrm{y,c,Ed}}\right)_w = -0.25$
External webs	In-plane shear stress	$(\tau_{\mathrm{Ed}})_e = 1.3$
	In-plane bending stress (tension)	$\left(\sigma_{\mathrm{x,M,Ed}}\right)_e = 28.9$
	In-plane bending stress (compression)	$\left(\sigma_{\mathrm{x,M,Ed}}\right)_e = -18.6$
	Compressive stress	$\left(\sigma_{\mathrm{y,c,Ed}}\right)_e = -0.02$

4. ULS safety verifications

4.1 Types of verification

According to the draft of the Technical Specification, the principal failure modes of web-core sandwich (without core infill in our case) that should be considered for the ULS verifications, are summarized in the Table 3 for the different bridge parts.

Table 3: Failure modes to considered for web-core sandwich panels (without core infill).

	Type of Verification	Resistance value required
Top and bottom skin	Tensile failure	Design value of the in-plane tensile strength in the x direction ($f_{\mathrm{x,t,d}}$)
	Crushing	Design value of the in-plane compressive strength in the x direction ($f_{\mathrm{x,c,d}}$)
	Local buckling	Design value of the critical buckling compressive stress in the x direction ($f_{\mathrm{x,cr,d}}$)
Internal and external webs	Shear failure	Design value of the in-plane shear strength ($f_{\mathrm{xy,v,d}}$)
	Local buckling due to shear	Design value of the critical buckling shear stress ($f_{\mathrm{xy,cr,d}}$)
	Bending failure	Design value of the tensile strength in the x direction ($f_{\mathrm{x,t,d}}$)
	Local buckling due to in-plane bending	Design value of the critical buckling bending stress in the x direction ($f_{\mathrm{x,b,cr,d}}$)
	Crushing due to transverse compression	Design value of the compressive strength in the y direction ($f_{y,\mathrm{c,d}}$)
	Local buckling due to transverse compression	Design value of the critical local buckling compressive stress in the y direction ($f_{\mathrm{y,cr,d}}$)

4.2 Design values of resistance

The procedure defined in the draft of Technical Specification is adopted to determine the design values of resistance of the material properties of the different constitutive parts of the bridge. The design value of resistance, R_d, is given by Eq. (1):

$$R_d = \frac{1}{\gamma_{Rd}}\left[\eta_c \cdot \frac{X_k}{\gamma_m}\right] \quad (1)$$

With γ_{Rd} the partial factor of the resistance model, η_c the conversion factor, X_k the characteristic value of the material property, and γ_m the material safety factor.

The material safety factor, γ_m, depends on the coefficient of variation of the material property and shall be determined from testing. For laminates, the partial factor for the resistance model, γ_{Rd}, will depend of the type of failure (material failure, global buckling and local buckling). In our case, material failure is considered and γ_{Rd} is taken equal to 1.4. Finally, the conversion factor, η_c, should be calculated from Eq. (2):

$$\eta_c = \eta_{ct} \cdot \eta_{cm} \quad (2)$$

With η_{ct} is the conversion factor for temperature effects (its value depends on the maximum material temperature in service conditions, on the glass transition temperature of the matrix, and on the sensitivity to matrix softening depending on the considered direction of the laminate) and η_{cm} is the conversion factor for moisture effects, for unprotected composite materials, three exposure classes are considered:

- Class I corresponding to indoor exposure;
- Class II corresponding to outdoors exposure without: continuous exposure to water, permanent immersion in water, permanent exposure to a relative humidity higher than 80%, combined UV-radiation and frequent freeze-thaw cycles;
- Class III corresponding to continuous exposure to water (or seawater), or permanent immersion in water (or seawater), or permanent exposure to a relative humidity higher than 80% (material temperature up to 25 °C).

Considering these elements, the design values of resistance were determined for the material properties of the different constitutive parts of the bridge (see Table 4).

Table 4: Design values of resistance for the material properties.

		X_k [MPa]	γ_m [-]	γ_{Rd} [-]	η_c [-]	R_d [MPa]
Top and bottom skin	$f_{x,t,d}$	150	1.15	1.4	0.77	**71.7**
	$f_{x,c,d}$	198	1.19	1.4	0.77	**91.5**
Internal webs	$f_{xy,v,d}$	38	1.09	1.4	0.60	**14.9**
	$f_{x,t,d}$	77	1.25	1.4	0.77	**33.9**
	$f_{y,c,d}$	70	1.38	1.4	0.60	**21.7**
External webs	$f_{xy,v,d}$	28	1.08	1.4	0.60	**11.1**
	$f_{x,t,d}$	113	1.20	1.4	0.77	**51.8**
	$f_{y,c,d}$	157	1.31	1.4	0.60	**51.4**

4.3 Design value of the critical buckling compressive stress in the x direction of the top skin

As mentioned in the Table 3, for local buckling verification, the critical buckling stress should be considered. In order to explain the approach of the Technical Specification, the determination of the design value of the critical buckling compressive stress in the x direction of the top skin is detailed in this part.

First, the flexural stiffnesses of the orthotropic laminate are calculated (see Eq. (3) to (6)):

$$\mathrm{D}_{11} = \frac{\eta_{\mathrm{c}} \cdot E_{\mathrm{x,c,k}} \cdot {t_f}^3}{12 \cdot \left(1 - \nu_{\mathrm{xy,k}} \cdot \nu_{\mathrm{yx,k}}\right)} \tag{3}$$

$$\mathrm{D}_{22} = \frac{\eta_{\mathrm{c}} \cdot E_{\mathrm{y,c,k}} \cdot {t_f}^3}{12 \cdot \left(1 - \nu_{\mathrm{xy,k}} \cdot \nu_{\mathrm{yx,k}}\right)} \tag{4}$$

$$\mathrm{D}_{12} = \nu_{\mathrm{yx,k}} \cdot D_{11} \tag{5}$$

$$\mathrm{D}_{66} = \frac{\eta_{\mathrm{c}} \cdot G_{\mathrm{xy,k}} \cdot {t_f}^3}{12} \tag{6}$$

With t_f the thickness of the top skin.

Then, the characteristic value of the critical buckling compressive stress in the x-direction of the top skin is calculated depending on the connection condition between the top skin and the webs. Here, the top skin is considered sufficiently stiff to be modelled as clamped on the very stiff webs. It could be also verified by the calculation, measuring the evolution of the rotation of the section at the connection between the web and the top skin. Thus, the characteristic value of the critical buckling compressive stress is calculated as follows (Eq. (7)):

$$f_{\mathrm{x,cr,k}} = \frac{\pi^2}{t_f \cdot {b_f}^2} \cdot \left[4{,}53 \cdot \sqrt{D_{11} \cdot D_{22}} + 2{,}44 \cdot (D_{12} + 2 \cdot D_{66})\right] \tag{7}$$

With b_f the maximum width of the top skin (perpendicular to the compressive stress direction) between two webs (see Figure 5).

Figure 5. Value of the maximum width of the top skin between two webs

Finally, the design value of the critical buckling compressive stress in the x direction of the top skin is given by Eq. (8):

$$f_{\mathrm{x,cr,d}} = \frac{1}{\gamma_m \cdot \gamma_{\mathrm{Rd}}} \cdot \chi_{x,c} \cdot f_{\mathrm{x,cr,k}} \tag{8}$$

With γ_m the material partial factor corresponding to $E_{x,c,k}$ and equal to 1.12, γ_{Rd} the partial factor accounting for the uncertainty in the resistance model for local buckling equal to 1.3 and $\chi_{x,c}$ the buckling reduction factor for compression, in the x direction, to take into account imperfections and taken equal to 1 for flat laminates.

The Table 5 gives the design value of each critical buckling stress required in the Table 3.

Table 5: Design value of the critical buckling stresses.

	Type of Verification	Resistance value [MPa]
Top skin	Local buckling	$(f_{\mathrm{x,cr,d}})$ = 133.8
Internal webs	Local buckling due to shear	$(f_{\mathrm{xy,cr,d}})$ = 2.9
	Local buckling due to in-plane bending	$(f_{\mathrm{x,b,cr,d}})$ = 15.5
	Local buckling due to transverse compression	$(f_{\mathrm{y,cr,d}})$ = 1.4
External webs	Local buckling due to shear	$(f_{\mathrm{xy,cr,d}})$ = 129.3
	Local buckling due to in-plane bending	$(f_{\mathrm{x,b,cr,d}})$ = 681.2
	Local buckling due to transverse compression	$(f_{\mathrm{y,cr,d}})$ = 60.2

4.4 ULS verifications

Thanks to the determination of all the resistance values, the ULS safety verifications for each constitutive part of the footbridge can be done by verifying, for each type of verification, the following inequation (Eq. (9)):

$$\frac{E_d}{R_d} \leq 1 \tag{9}$$

With E_d the design value of the action effects (see Table 2) and R_d the design value of resistance (see Tables 4 and 5).

In our case-study, the Eq. (9) was verified for all the types of verifications and for all the constitutive parts of the bridge.

5. Conclusion

The Saint-André de Cubzac Bridge, building in 2015 in France, was considered as a case-study in this paper. The ULS safety verifications, for all the constitutive parts of the bridge were performed, detailing the approach of the actual Technical Specification. However, this study does not consider the global stability and the interactions under combined stresses. These verifications were done but not presented here.

6. References

1. Prospect for New Guidance in the Design of FRP Structures. JRC Science and Policy report. ISSN 1018-5593. 2016.
2. CUR96. Recommendation 96, Fibre-reinforced Polymers in Civil Load Bearing Structures. Dutch Recommendation, Netherlands. 2003.
3. EN 1990. Basis of structural and geotechnical design. European Committee for Standardization, Brussels, Belgium.
4. EN 1991. Actions on structures, part 1-2: General actions. European Committee for Standardization, Brussels, Belgium.

NOVEL MANUFACTURING APPROACHES FOR CAR BODY SHELL APPLICATIONS BASED ON SANDWICH STRUCTURES

L. Mera[a], L. Carral[a], P. Rodriguez[a], A. Gutierrez[a], X. Perez[a], M. Plettig[b] and S. Renner[c]

a: Advanced Materials, AIMEN Technology Centre, Polígono Industrial de Cataboi SUR-PPI-2 (Sector) 2, Parcela 3, Porriño, 36418, Spain - lmera@aimen.es
b: Forster System-Montage-Technik GmbH, Heinrich-Werner-Str. 1a, Forst (Lausitz), D-03149 Germany
c: CG Rail GmbH, Freiberger Straße 33, Dresden, D-01067, Germany

Abstract: *An innovative design of a car body has been developed comprising both novel materials and manufacturing processes for the railway industry. A thorough analysis addressing new smart out of autoclave (OOA) manufacturing processes was performed. Several automated approaches have been studied, such as the robotized lay up of bindered dry fiber as well as laser trimming. Manufacturing was assisted through different monitoring technologies such as resin arrival sensors and thermography in order to ensure high quality components. Additionally, in order to improve the cost efficiency of these structures, a multi-material approach based on 3D printed technologies has been tackled. A thorough analysis of the joint has been performed and different integration approaches have been explored by designing co-cured and co-bonded manufacturing stages. Finally, several demonstrators have been made. In this manner, the most promising technologies were scaled-up and subsequently tested.*

Keywords: railway; automation; cost-efficient; out-of-autoclave; multi-material

1. Introduction

The transport sector has exerted and continue to be the driving force for the development of new materials and lightweight solutions. As such, growing applications are found in structural components within the aeronautical and automotive industries and, to a lesser extent, in the maritime and railway sectors. The present study focuses on the work developed in a recently completed European project (CARBODIN https://carbodin.eu/) where one of the main objectives was to develop innovative and affordable solutions for lightweight car body shells. Composite materials appear to be one of the most promising candidates to attain these ambitious targets given their inherent low weight, but also considering their additional benefits (degradation/corrosion resistance, acoustic insulation, freedom of design, etc.). Ultimately, weight savings up to 50% have been reported with full composite designs as compared as traditional metallic ones [1-3]. In spite of this, industry is still reluctant to adopt these materials and the cost is one of the cornerstones for a plurality of sectors and applications.

In the last years several strategies had emerged to cut back costs on composite applications. Multimaterial concepts have been explored where a rationalized use can be easily attained by using the right material in the right place [4]. Also, process integration where different components are integrated in a single part is a booming line, especially in the aeronautical sector, since it allows reducing manufacturing hours, which are key to achieving production rates and cost reduction [5, 6]. Finally, automation has been pursued by means of robotized

  doi:10.5075/epfl-298799_978-2-9701614-0-0

technologies (DRP, AFP) which are especially advantageous in industries where large parts are manufactured [7, 8].

The work presented in this paper addresses both multimaterial and process integration approaches for the car body shell development, whereas automation has been already covered in a former publication [9]. An assessment has been carried out in order to determine the suitability of the investigated materials to manufacture a technology demonstrator, representing a representative section of a side wall.

2. Case study definition

In order to fully explore the different manufacturing approaches a case study was selected. Given dimensions, geometrical constraints, and weight among other factors the side wall of the car body had been chosen for this study. It should be mentioned that this structure is currently manufactured with traditional metallic materials. The state-of-the-art design comprise also different inserts which are needed for anchoring passenger seats as well as interior panels or luggage racks. Conventionally these grooves are directly extruded together with the aluminium profiles of a metal car body. Ultimately, this leads to a heavy structure with a considerable room of improvement. A trendsetting design was developed to integrate composite C-Grooves to composite sidewalls. Thus, moving from a full metallic structure to a polymer-based one and, on top, avoiding secondary joining operations of metal grooves to composite sidewalls by riveting and bonding. A demonstrator was designed under realistic load scenarios for the anchoring of a seat and 1 passenger. Figure 1 displays a detail of the sidewall designed including also the C-groove insert.

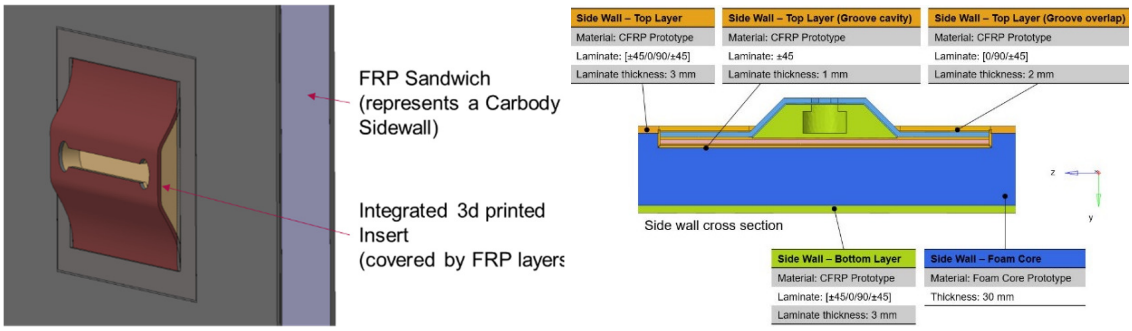

Figure 1. (Left hand side) Integral design with 3D printed insert embedded in CFRP sandwich panel and (right hand side) schematics and stacking sequence of the case study.

Vacuum infusion process (VIP) has been chosen as preferred manufacturing process given mainly cost considerations. On the other hand, material selection has been made considering also mechanical and functional requirements. It should be mentioned that FST requirements are of paramount importance for this very application [10]. At present there are very few resins that comply with this regulation. Besides, the processing difficulties of the highly doped resins and their mechanical properties are also an important topic. This is out of the scope of the present work, but considerations had been taken in this regard in order to stablish the optimal fire resistance strategy. Finally, 3D printed inserts had been chosen to create the raised geometry and fulfill distance requirements efficiently while complying with the lightweight targets. The design implies embedding these inserts by CFRP layers to increase the clamping and pull-out forces which are initiated in the structure by the attached parts. The composite design was

  doi:10.5075/epfl-298799_978-2-9701614-0-0

evaluated by means of FE leading to the final layup. The setup for the resin infusion process was supported by intensively performed process simulations.

3. Methodology

2.1 Material selection

Material screening was performed given the earlier requirements. Thus, a Crestapol 1261 (Scott Bader) urethane acrylate resin was selected. Whereas a 606gsm carbon fiber NCF from Saertex was chosen as the reinforcement. A FST resistance grade PET foam has been selected from 3A Composites (i.e. T90, 210 kg/m3). Finally, due to the novelty of the application, a range of fire resistance filaments were chosen. The Thermax® PPE/PS (3DXTECH) was selected after a through process optimization and subsequent testing of 5 different materials. This study has not been included in the present work, but it should be mentioned that manufacturability aspects together with mechanical performance, ease of bonding and cost constraints were considered.

2.2 Process window adjustment

- 3D printing process

Fused Filament Fabrication (FFF) was selected as the additive manufacturing technology for manufacturing the 3D printed inserts. A 3NTR A2V4 machine has been used for the process window development. Due to the novelty of the technology a standardised manufacturing procedure is still missing and, since every 3D printer is unique, most process parameters depend on the hardware of the equipment used. After optimizing the process window on standardise samples the process was scaled up and the final dimensions inserts were manufactured. Several design iterations have been performed considering manufacturing constraints such as ease of resin flow, among others. The final design is the result of the Design for Manufacturing sessions (DfM). Note that there is an intermediate design for the AM process, where the C-Groove slot is closed. This skin has been added so to prevent resin inlet during VIP (Figure 2). However, after the infusion process is completed, this slot was machined given rise to the final component.

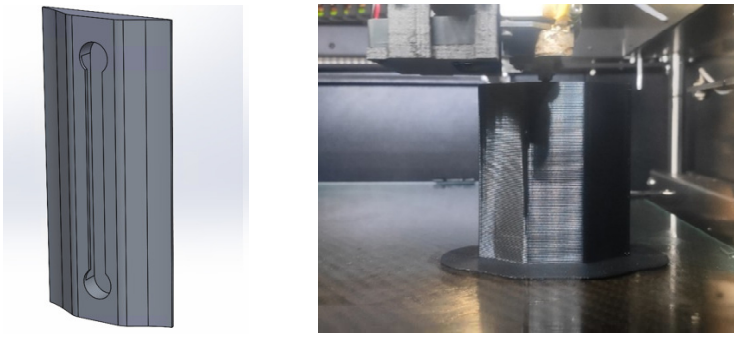

Figure 2. (Left hand side) CAD model corresponding with the C-Groove insert and (right hand side) final iteration of C-Groove insert being 3D printed in PPE-PS.

- Process integration

Resin infusion process (VIP) was optimized according to the levels of integration envisaged. Hence, in this case two levels of integration had been explored: medium and high integration.

  doi:10.5075/epfl-298799_978-2-9701614-0-0

Medium Integration implies that there are pre-manufactured and cured parts which will be integrated in the sidewall manufacturing process (co-bonded). Firstly, the 3D printed insert is covered by the pre-defined dry carbon fiber textiles and resin infused together with the insert (i.e. named as embedded insert). On a second stage, the formerly cured embedded insert is introduced into the CFRP sandwich panel manufacturing process. A second resin infusion process takes place leading to the final structure (Figure 3).

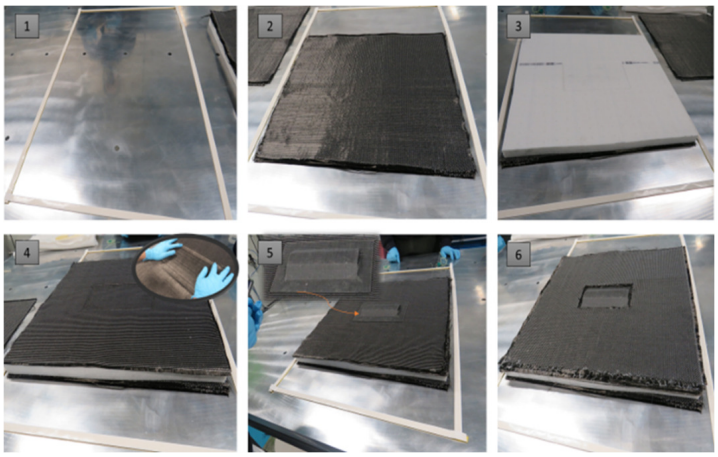

Figure 3. Steps of the demonstrator manufacturing following a medium integration approach.

High integration design describes a one- shot manufacturing process. Hence, all the structure is manufactured in one single infusion process (co-cured). This approach will minimize the number of steps having implications on both cost and productivity (Figure 4).

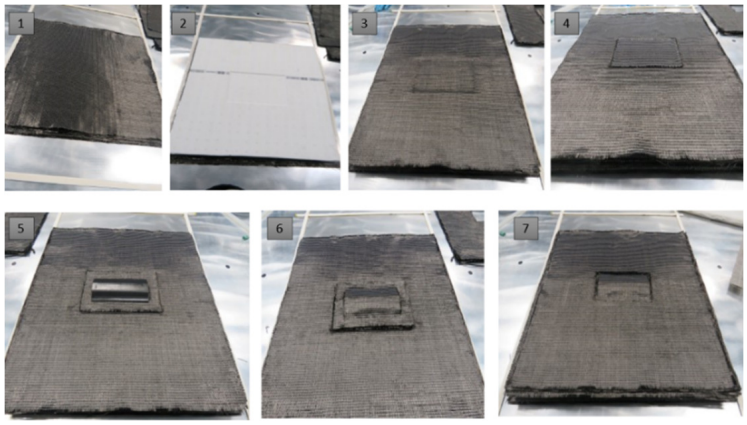

Figure 4. Steps of the demonstrator manufacturing following a high integration approach.

VIP configuration remained similar in both cases and was optimized with FEM. The resin inlet (gate) and vent are positioned opposite to each other with a line configuration. The vacuum is carried out at 0.9 bar for good compaction and optimal process speed. Finally, the catalyzed resin was injected, impregnating the entire structure of the demonstrator. Once the infusion is completed, the resin inlet is closed. Curing and post-curing was performed in a HOBERSAL 4500 CFXL oven. The full cycle consisted of a 3h dwell time a 50 °C followed by a 2h hold at 80°C. The heating ramps were performed at 2°C/min. The component is then cooled down by natural convection to room temperature. When the temperature reaches the set temperature vacuum is switched off and the component was demolded.

2.3 Characterization

As it can be derived, the different levels of integration entail distinct complexity and cost, so it is important to find the right balance. In order to do so the metrics of the process were obtained for each case and a cost estimation was also performed.

- Non-destructive testing

Qualitative and quantitative data of both the different demonstrators made as well as their corresponding manufacturing process have been obtained. Thus, process monitoring with different technologies have been performed in order to get the KPIs of the process, and also to get an insight on the degree of quality of the different components. Measurements have been taken optically by a standard camera at three distinct locations during VIP process. Additionally, fiber content was estimated during manufacturing. Hence, all the components were weighted before and after VIP with a precision balance PS 6000 C from RADWAG in order to get an insight on these values. Additionally, all samples were evaluated visually by means of additional magnification at points of interest. Overall, the irregularities were divided into three categories and rated on a scale from 1 (very poor) to 6 (very good). A grid, see Figure 5, was laid over the samples, thus enabling a rough local resolution. Finally, passive thermal inspection complements the visual evaluation with more details in the defect structure and resolution.

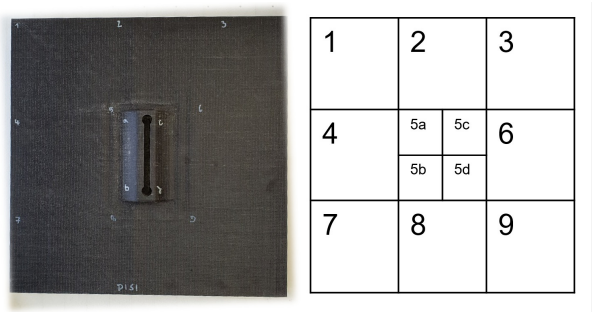

Figure 5: Division of the surface with the help of a grid (high integrated sandwich samples)

- Destructive test

The multi-material groove joint was developed according to an intense FE analysis considering realistic loads and boundary conditions of the study case. The model and load assumption for the calculation is shown in Figure 6.

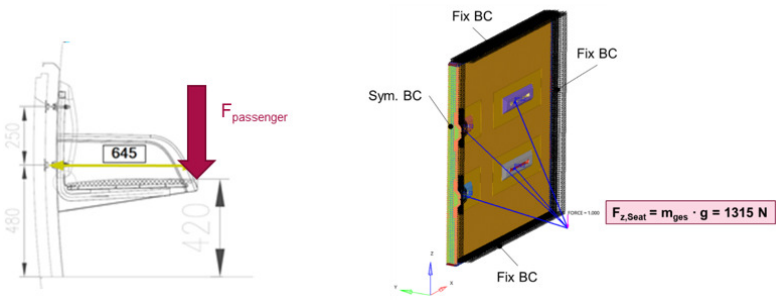

Figure 6. Schematics and FE model with load assumptions for structural FEA of Groove Joint for a 2-passenger seat scenario at sidewall using symmetrical boundaries

The static load of a passenger seat (weight of 14 kg, according reference) and a passenger (weight of 120 kg maximum, as a design load) is transferred with 4 screw connections to the 4 grooves. The 2 grooves in the center are loaded by 2 passenger seats including passengers. Due to space limitations of the testing rig and machine, the team decided to perform pull-out tests of single groove samples only. The force is applied in axial direction to the screws which are fixed with nuts in the insert grooves. The pull-out forces for the load scenario can be determined in axial direction from the FEA results and later compared with the test results. The measured pull-out forces represent the maximum allowable force for the multi-material groove. So, the maximal performance of the pull-out or peel-off as reaction of axial tension load is determined. 3 different types of samples for testing were selected and manufactured. Pull-out tests were performed on a universal testing machine as depicted on Figure 7.

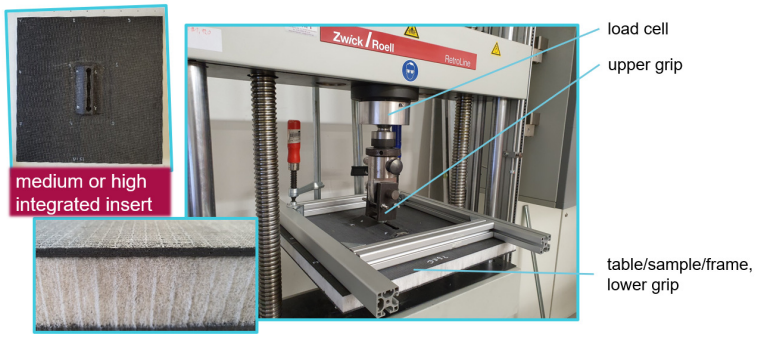

Figure 7. Measurement setup for mechanically testing the demonstrators.

4. Results and discussion

Simulation and experimental results have been found to be in good agreement concerning resin flow fronts. Still some differences concerning the infusion times have shown up. This can be related with minor differences on the configuration and peripherical material (resin flow media, inlet and vent tubing diameters, material and length, among other factors). On the other hand, a comparison of the infusion time was made. Figure 8 displays both the behavior of the high integrated and medium integrated demonstrator. It can be observed that in the former the infusion process takes slightly lesser time. This could be related with the presence of the embedded insert on the latter.

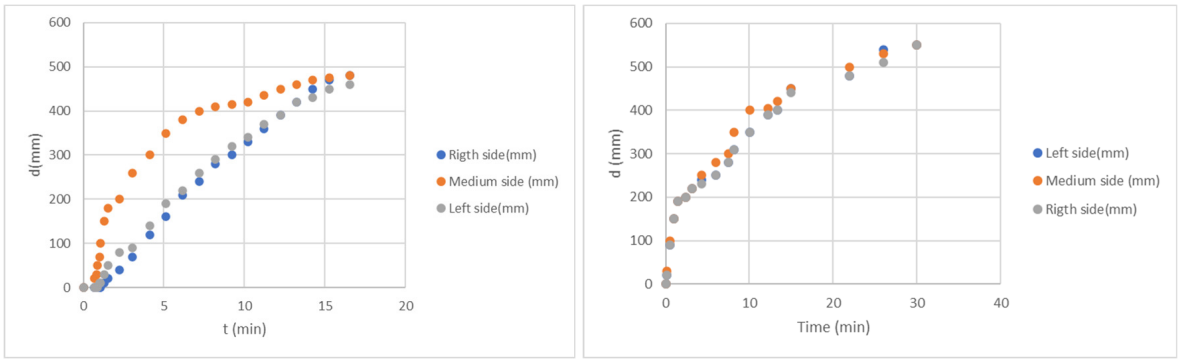

Figure 8. Resin flow displacement (d) as a function of time (t) for the (left hand side) high integration and (right hand side) medium integration approach.

Similar weight ratios were obtained for the different demonstrators. Hence a fiber content of 59-61 wt% was obtained regardless the integration route. Concerning visual and passive thermal inspection indicate that air cavities were the most common occurrences in the different samples. The exact causes are yet to be further investigated, but both the amount and are considered of minor importance.

Figure 9 depicts the loading-displacement curves obtained on both medium and high integrated demonstrators. The average maximum load to failure was 2284 N and 2025N, respectively. The failure is in both cases initiated in the 3D printed insert/CFFP interface as it could be expected.

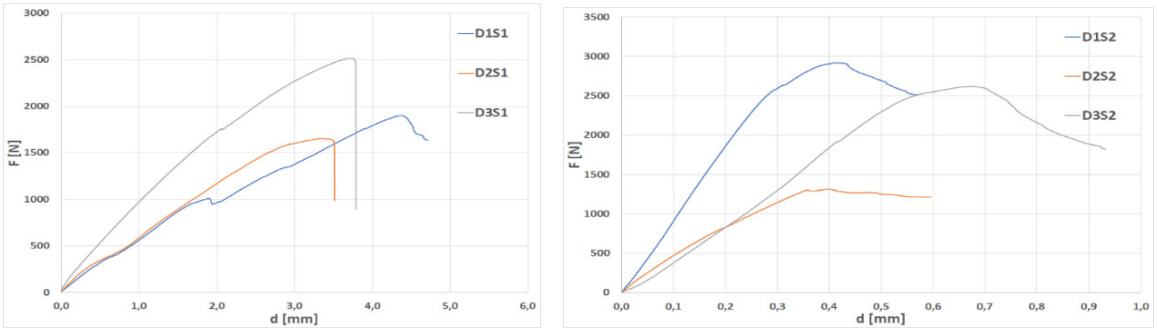

Figure 9. load-path diagram for the (right) high and (left) medium integrated demonstrators.

The mechanical performance of the manufactured and tested coupons was evaluated in comparison with the extracted FE results. The destructive test results show that the pull-out forces are greater than those determined by the FEA. The FE analysis indicates a maximum axial load in y-direction, which represents the pull-out test, of -1061 N. In comparison there is a large reserve between maximum allowable pull-out force from destructive testing and calculated force from the FE analysis according to the weight load of seat including passenger (12kg seat + 120 kg passenger). Besides the reaction forces at the grooves do not fully utilize the material corresponding to the FE calculation. The material utilization according to the composite failure index with safety factor is lower than 50%, which fits well with the experimental results. The FE result, that is worsened by the fact that the model introduces the load from the seat into the groove with a rigid body model without flexibility, is valid. Additionally, the ideal FE modelling assumes the 3D print material as tied bonded with the composite layers and does not consider plastic deformation of the 3D print insert material. With a larger test matrix and more tested samples the pull-out forces could be determined with more accuracy and more safety in the spread.

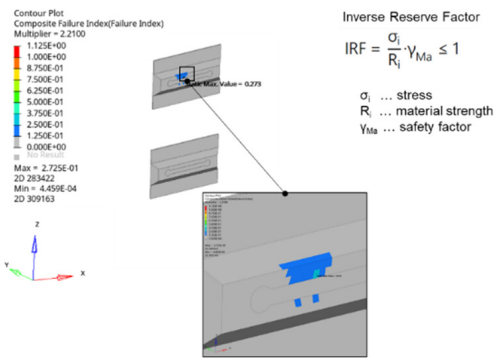

Figure 10. FE analysis with composite failure index and material utilization below 50%

5. Conclusions

A composite-based side wall has been developed and manufactured by different integration approaches. The characterizations performed indicate minimal differences among the components manufactured. However even if the medium integrated components show slightly higher pull-out forces than the high integrated ones both stands the loads for the application. Thus it can be concluded that the integrated groove in a multi-material design seams well-suitable for the application. With some modifications, e.g. the improvement of adhesion in the transition of 3d print material to composite, the pull-out forces of can be increased to be more robust. Finally, one-shot manufacturing has shown savings of 50% in energy consumption and operation, 30% in labor costs and 7% in material.

Acknowledgements

This project has received funding from the European Union's Horizon 2020 research and innovation program under Grant Agreement No 881814.

6. References

1. Ulbricht A, Rail Vehicle in CFRP-intensive Design, Lightweight Design worldwide, Issue 2/2019.
2. Prockat J, Understanding the challenges of composites in rail, AMI, Virtual Summit, 19 - 22 October 2020.
3. Mistry PJ et al., Selection and ranking of rail vehicle components for optimal lightweighting using composite materials, Proc IMechE Part F: J Rail and Rapid Transit 0(0) 1–13, 2020.
4. Mera L et al., Manufacturing process optimization for composite- steel multimaterials design, 18th European Conference on Composite Materials, 2018..
5. Perez Pastor A et al., Superficie sustentadora de gran tamaño, optimizada en coste y peso para altas cadencias de producción, Materiales Compuestos, [S.l.], v. 4, n. 1, p. 73-79, jan. 2020. ISSN 2531-0739.
6. Harismendy I. et al., Desarrollo de procesos de preformado y RTM para estructuras altamente integradas. Materiales Compuestos, [S.l.], v. 2, n. 3, p. 69-74, july 2018. ISSN 2531-0739.
7. Serrano J C, Wind Blade Manufacturing Innovations, Wind Turbine Blade Workshop (Sandia National Laboratories), 2012.
8. Grohmann Y, et al, Development of the direct roving placement technology (DRP), 17th European Conference on Composite Materials, 2016
9. Mera L et al., Novel automated manufacturing solutions for car body shell applications based in CFRP, International Conference on Polymer Science and Composite Materials, 2021.
10. EN45545-2 Railway applications- Fire protection on railway vehicles- Part2: Requirements for fire behavior of materials and components.

  doi:10.5075/epfl-298799_978-2-9701614-0-0

ROBUST AND FLEXIBLE RESISTIVE GRAPHENE AND MWCNT HEATERS - ULTRA-FAST HEATING RESPONSE AND HIGH TEMPERATURE PERFORMANCE

Christos Kostaras[a,b], Christos Pavlou[a,b], George Paterakis[a,b] , Nikolaos Koutroumanis[a,b], George Trakakis[b], Konstantnos Dassios[a], Costas Galiotis[a,b]
a: University of Patras, Caratheodory 1, University Campus, GR 265 04 Patras, Greece – kostaras@uptras.gr
b: FORTH/ICE-HT, Stadiou St, Platani, GR26504 Patras, Greece

Abstract: *This work features the manufacture and use of hybrid buckypapers using multi-walled carbon nanotubes (MWCNT) and 2D graphene-based nanomaterials as free-standing joule heating devices. The hybrid buckypapers tested consist of the following combinations: MWCNT and graphene nano-platelets (GNP), MWCNT and thermally reduced graphene oxide (trGO) and MWCNT and chemically reduced graphene oxide (crGO). Apart from their heating response, the mechanical properties measured from testing under tensile load. Parameters of manufacture depending on the category of tested samples seem to play a role in both their performance as heating elements and their maximum stress (σ_{max}), strain at break (ε_{max}) and elastic modulus (E_{Young}).*

Keywords: buckypaper; MWCNT; GO; hybrid; heaters;

1. Introduction

As possible technological applications of graphene and its related materials are further extended to more areas, the transfer of their impressive properties from the nanoscale to the macroscale becomes an important issue. Such properties are particularly pronounced when it comes to the electrical and thermal conductivities of graphene related materials. Although carbon nanotubes and graphene have been widely combined with polymers in small weight ratios, the dielectric nature of polymeric matrices and interface resistance limit the electrical and thermal conductivity [1] of composites.

On the other hand, for more than two decades, it has been shown that free standing structures consisting solely of the above materials can be achieved mainly through the filtration of stable dispersions. Free-standing paper-like structures which consist solely of CNTs and/or 2D nanomaterials seem to bypass the issue of non-conductive matrix while they can reach good amounts of strength [2], providing in parallel excellent electrical and thermal properties [3].

In this work, CNT and graphene papers that work as Joule heaters are fabricated through simple and accessible techniques. The entanglement between MWCNTs, provides a scaffold for the incorporation of 2d nanomaterials and also ensures compliancy to various shapes, mechanical robustness and reduced or zero binder content. The inherent conductivity of consisting nanomaterials combined with the near or total absence of polymeric materials ensure the low electrical resistance of the papers making them good candidates for flexible joule heaters. Like actual papers they can be folded, applied to irregular surfaces and cut to various shapes with the added benefits of increased electrical conductivity and ultrafast heating response.

  doi:10.5075/epfl-298799_978-2-9701614-0-0

Preparation is based on simple dead-end filtration of inks consisting of CNTs and 2D nanomaterials. The inks contained combinations multi-walled CNTs (MWCNTs) or oxidized MWCNTs (oMWCNTs) and commercially procured graphene nano-platelets (GNP), graphene oxide (GO) or thermally reduced graphene oxide (trGO). Thermal testing was conducted in a stage that allows the direct measurement of the temperature either via a thermal camera or a micron-thick k-type thermocouple. Electrical contacts with direct current source are formed using adhesive copper tape. Current and temperature measurements are collected simultaneously and show a near instantaneous heating response to applied voltage from source. Along with heating rates, maximum temperature and power draw are measured at discrete applied voltage values.

2. Materials and Methods

2.1 Preparation of Graphene Oxide

Graphene oxide is prepared through the chemical oxidation of natural graphite with ~ 500 μm flake size (Naturgraphit, Graphit Kropfmuhl). The first step involves creating graphite oxide (GrO) by imposing a modified Hummer's method [4] on natural graphite of flake size ~500 μm. In the second step, GrO is further reacted to so it can be exfoliated and further modified to GO. The reaction is stopped by adding a small quantity of HCl and GO is left to react until an adequate degree of GrO exfoliation is observed turning the solution colour from golden-green to yellowish brown. In the final step, GO is collected in dialysis bags which are in turn placed in DI H_2O until the pH is stabilized at 6 – 7.

Prepared GO is collected in thick suspensions that contain multi-layered aggregated GO flakes along with the well exfoliated few- (<10) to single layered GO. Consecutive centrifugation steps are used to separate the GO aggregates from the few-layered flakes, as well as controlling the distribution of the lateral size of the latter. Through this process, an extremely stable suspension of well separated GO in H_2O is produced, of concentration 2.5 – 4 mg/ml, with little to none aggregated particles present.

2.2. Thermal reduction of Graphene Oxide

Part of the thick GO slurry collected after production is spread into pans lined with non-stick film. The material is dried through mild heating (~ 60 ^oC) for 48 h, then broken into pieces. The clamps of dried GO are then inserted into a cylindrical CVD reactor capable of working at temperatures over 1000 ^oC. Decomposing functional groups are released in the form of gases. Over the de-composition temperature for oxygen containing species, CO and CO_2 is released causing the violent exfoliation of aggregated of GO flakes that are being simultaneously reduced [5]. This is evident from the approximate 50-fold increase in volume and extremely low density of the resulting powder.

2.2. Preparation of Oxidized MWCNTs

Oxidized MWNCT (oMWCNT) are prepared by reacting with $KMnO_4$ in a 0.5 M sulfuric acid solution (H_2SO_4(aq)). In short, 3 g MWCNT are sonicated in H_2SO_4(aq) for 15 min, while 25 g of $KMnO_4$ dissolve in a separate H_2SO_4 solution. After sonication is completed, the MWCNT solution is transferred in a round flask to be magnetically stirred in a 120 ^oC oil bath while the $KMnO_4$ solution is added dropwise. When fully mixed, the MWCNT react with $KMnO_4$ for a total of 3 h

  doi:10.5075/epfl-298799_978-2-9701614-0-0

under reflux. oMWNCNT are separated from the reaction mixture by dead end filtration and HCl is used to stop the reaction and purify the nanomaterial. oMWCNT are subsequently washed inside the dead-end filtration device using DI H_2O until filtrate reaches a pH value of 6 to 7. Next, H_2O is filtered away and oMWCNT are dried at 60 ^oC under vacuum, overnight.

2.3. Preparation of buckypapers

MWCNT and Graphene based dispersions are prepared in H_2O via tip-sonication. Material that came in powder form (pristine MWCNT, GNP, trGO) or in dried clumps (oMWCNT) is shortly milled using a mortar and pestle while slowly adding small quantities of water so a more even dispersion can occur. Unlike oMWCNT and GO, pristine MWCNT, GNP and trGO required Triton X-100 to form a stable dispersion in water.

After dispersions have been formed, they are filtered through a 0.45 μm pore size filter via vacuum assisted dead-end filtration. The nanomaterial is deposited on the filter membrane and dried via heated air (~80 ^oC). In cases where Triton X-100 is used, it washed away by filtering DI H_2O through the deposited nanomaterial. After drying, buckypapers can be peeled from the filter membrane. Buckypapers fabricated through the above process consist of the following combinations of materials: MWCNT, GNP/MWCNT, trGO/MWCNT, oMWCNT, GO and GO/oMWCNT. Hybrid buckypapers are thus named as follows: MWCNT_GNP, MWCNT_trGO, oMWCNT_GO. As mentioned above MWCNT_GNP and MWCNT_trGO buckypapers were fabricated using Triton X-100 which was expelled by washing with adequate amounts of DI H_2O right before the papers were dried. OMWCNT_GO buckypapers did not require the surfactant.

2.4. Reduction of Graphene oxide-based buckypapers

HI acid is used to chemically reduce GO/oMWCNT buckypapers. Briefly, GO-MWCNT buckypapers are sealed in a glass vessel along with a small amount of HI (2 – 4 ml). The vessel is inserted in an oven for 16 h at 90 ^oC. After the required amount of time has elapsed the reacted papers are washed in acetone until all the HI acid is expelled.

2.5. Spectroscopy and diffractometry techniques

Raman spectroscopy and X-ray diffractometry (XRD) are used to observe the effects of reduction on GO papers. An InVia Raman spectrometer (Renishaw) using a 514 nm laser excitation beam through a 20x lens is used to assess the narrowing of D and G peaks as well as the appearance of the 2D peak in crGO papers. A D8 diffractometer (Bruker) is used to observe the change in interlayer spacing occurring in GO papers after the chemical reduction process.

2.6. Tensile testing

Mechanical tensile load measurements are employed to assess the mechanical performance of all buckypapers. The buckypapers are cut into ~2 mm wide strips and using an epoxy adhesive, are affixed on paper supports with a set gauge length of 25 mm. The samples with paper supports are clamped in a micro-tensile testing device (Deben Inc., UK) to be subjected to tensile loading measurements at 0.2 mm/min crosshead speed.

2.7. Thermal testing

The resistive heating performance of buckypapers is determined by applying direct current through square shaped samples (2.5x2.5 cm^2). To this end, a purpose made stage, constructed

from PTFE is used to hold the samples suspended in air while simultaneously affixed to copper contacts. A PL330QMT (TTi Thurlby Thandar Instruments) is used to drive direct current through the samples. A 34401A multimeter (HP Agilent) is connected in series to measure current (I_{DC}). Temperature (T) readings are recorded via a micron thick thermocouple that lightly touches the samples, to a USB-4718 datalogger (Advantech). Both multimeter and datalogger are connected to a computer so that, using a capture software programmed in Labview, $I_{DC}(t)$ and T(t) data can be recorded simoultaneously. Two types of experiments are conducted to gauge the heating performance of buckypapers. In the first experiment, DC voltage (VDC) is applied on the samples in increments of 1 V. Recording of T and I_{DC} allows to determine heating response for power drawn as

$$P = I_{DC}V \quad (1)$$

The second type of experiment tests the stability of the heating response over 20 on-off cycles.

3. Results & Discussion

3.1. Effects of reduction with HI acid

As GO papers are left to react in HI, covalently attached hydroxyl containing groups are removed possibly via a halogenation substitution reaction [6]. The loss of functional groups allows crGO to chemically resemble that of pure graphene and show an order of magnitude drop in resistance. The change from GO to crGO is also reflected to the appearance of the papers changing from dark brown to gray with a slight metallic lustre (Figure 1a). To allow proper comparison, Raman spectra for GO have been baseline corrected and normalized to the intensity values of crGO (Figure 1c). Otherwise, as seen in Figure 1b, a strong fluorescence is recorded along with spectrum. When examined under the same conditions crGO does not show this kind of behaviour. Interestingly, when comparing the corrected GO and crGO spectra, Raman spectroscopy shows an increase of the I_D/I_G ratio for crGO. This is attributed to damage sustained on flakes of GO during the reduction process. Meanwhile, XRD shows a much clearer image of the effect the reduction process has on the papers. The change of diffraction angle from 11.0° to 24.4° is a clear indication of the change in interlayer spacing from d_{GO} = 0.803 nm to d_{crGO} = 0.373 nm.

a)

b)

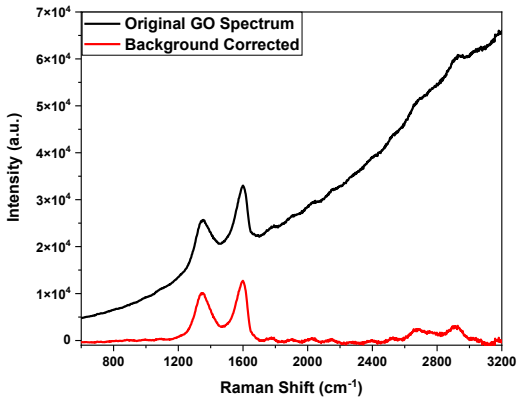

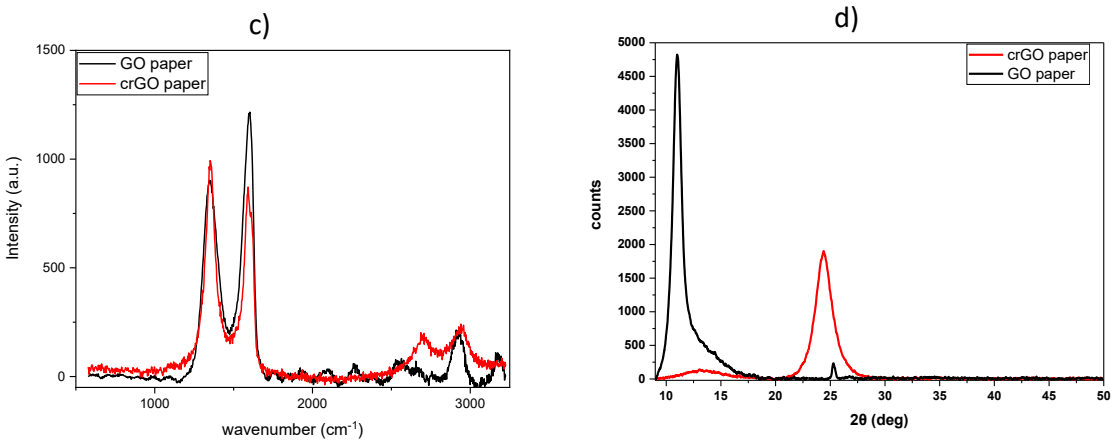

Figure 1 a) Digital photograph of GO and crGO bukypapers. A clear indication of reduction after reaction with HI is the colour change from dark brown to metallic grey. b) Raman spectra of GO before and after baseline correction. As seen here, when examined using the 514 nm excitation frequency, GO shows strong background fluorescence. c) Raman spectra of GO after baseline correction and crGO. b) XRD spectra of GO and crGO. A clear change in interlayer spacing is indicated by the change in diffraction angle.

3.2. Mechanical properties

When maximum stress (σ_{max}) and stiffness (E) are concerned, tensile testing of samples used shows very big differences depending on the type of nanomaterial used for corresponding buckypapers. Specifically, buckypapers that employed pristine MWCNT combined with either as received GNP or trGO showed a noticeable difference of at least ten times less than those that consisted of GO and oMWCNT and their chemically reduced counterparts. Furthermore, GNP containing buckypapers failed to separate from the filter for GNP ratios over 40 wt. % and those containg more than 40 wt. % trGO formed cracks during filtration and drying. On the other hand, buckypapers that were fabricated from oMWCNT and GO could be easily formed with fitration. MWCNT_crGO papers with weight ratios below 40 %wt. could not be retrieved after the chemical reduction process. The MWCNT_crGO buckypapers however maintained most of the mechanical properties of their oMWCNT_GO counterparts and even showed an increase in strain at break (ε_{max}) that follows the increase in crGO weight ratio (Figure 2b). This can be attributed to the interplay between increasing van der Waals interaction between 2D nanomaterials and decreased -OH interaction as a result of chemical modification. Increase of Young's modulus for GNP, trGO and GO containing buckypapers follows the increase of 2D nanomaterials weight ratio (Figure 2c). Oddly enough, such a trend is not observed for crGO containing buckypapers. This happens because MWCNT_crGO will obtain σ_{max} values comparable those of oMWCNT_GO at larger strains. Since stiffness is defined as $E = \sigma/\varepsilon$, the loss of E at higher 2D contents for mwcnt_crGO is thus evident.

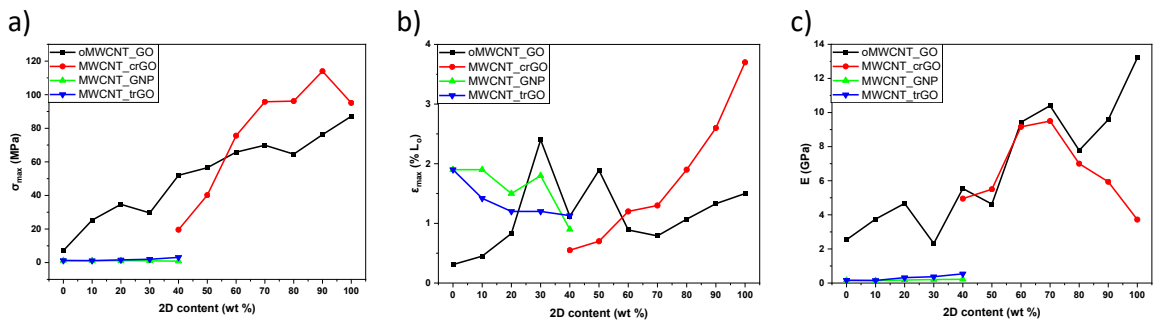

Figure 2 Mechanical testing of buckypapers. a) Ultimate tensile strength measurements. Along with having the ability to form budckypapers for all GO weight ratios, oMWCNT_GO buckypapers and their reduced counterparts show far greater and strength over the pristine MWCNT based buckypapers. b) Strain at break measurements. MWCNT_GNP and MWCNT_trGO buckypapers show decreasing values of ε_{max}, MWCNT_crGO buckypapers show an increase towards higher crGO ratios as a result of reduced -OH containing functionalities. c) Young's modulus (E). In general, as can be expected, increase of graphene-like nanomaterials increases the stiffness of the material. This is more clearly indicated for oMWCNT_GO. Legend: oMWCNT_GO (■),MWCNT_crGO (●),MWCNT_GNP (▲),MWCNT_trGO (▼).

3.3. Resistive heating performance

Joule heating response experiments for increasing V_{DC} show that for applied voltages ranging from 1 V to 8 V temperatures from 40 °C close to 300 °C can be achieved. Figure 3a shows the expected behaviour for chemically reduced buckypaper containing 80 wt. % crGO in response to increasing V_{DC}. The same kind of behaviour is observed for measurements with all kinds of buckypapers. While the graph in Figure 3b demonstrates the cyclic stability of GNP containing buckypapers, which again, is characteristic for all samples tested. The most important aspect of the thermal behaviour of the samples the graphs is the nearly rectangular shape of the data plots in the produced graphs. Fitting on the regions right after the closing of the circuit shows heating rates close to 90 °C/s.

Figure 3c shows the cumulative data for temperature response over the power drawn for each device. As it can be clearly seen, chemically reduced type buckypapers achieve similar temperature response for lower power draw than the GNP and trGO containing buckypapers. A more interesting result is shown in Figure 3d which shows the calculated resistance value for each sample corresponding to temperature. The resistance is calculated from $R=V_{DC}/I_{DC}$. All the samples show a lowering of the resistance at higher temperatures. The lowering of the resistance and its value ranges per sample in 3d as well the non-linear temperature response for increasing power draw in 3c show that lower resistance samples draw more power for the same level of temperature response.

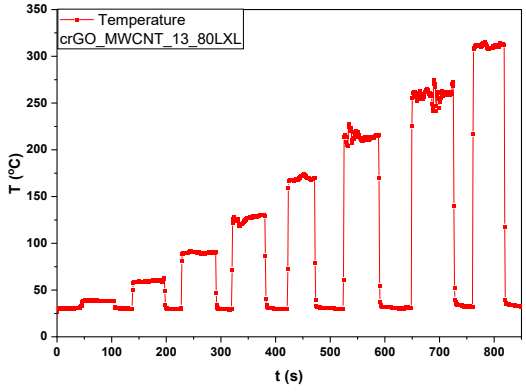

a)

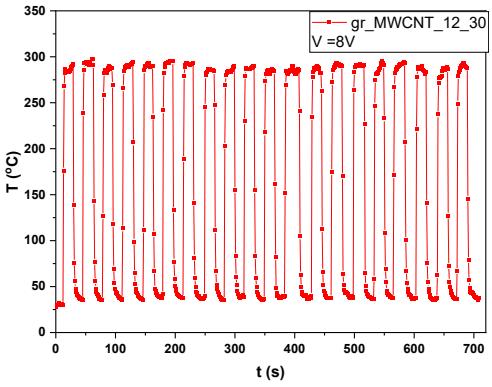

b)

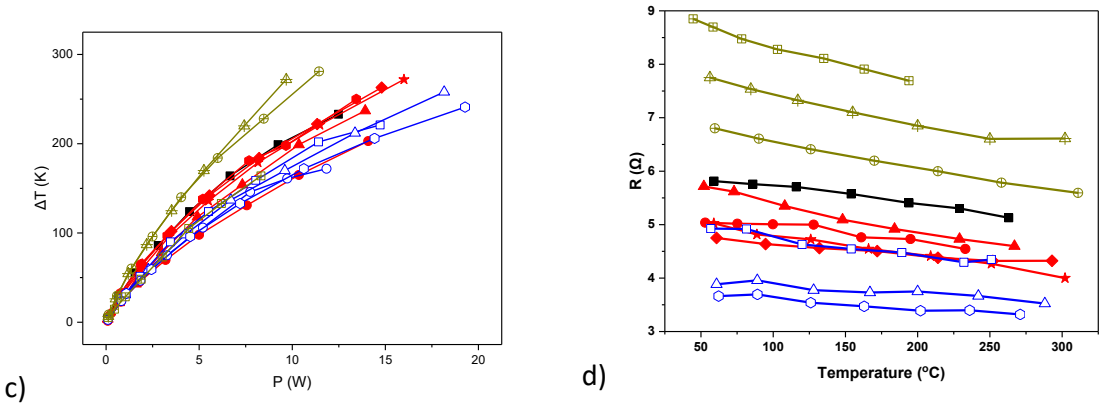

Figure 3 a) Temperature response experiment for crGO_oMWCNT_80. b) Cyclic stability of GNP_MWCNT_30. On-off times were 15s on and 15s off. c) Temperature response over power draw P. d) Resistance values over corresponding temperature. Legend: MWCNT(■), GNP_MWCNT_10(●), GNP_MWCNT_20(▲), GNP_MWCNT_30(◆), GNP_MWCNT_40(⬢), GNP_MWCNT_50(★), trGO_MWCNT_10(□), trGO_MWCNT_20(○), trGO_MWCNT_30(△), trGO_MWCNT_40(⬡), crGO_MWCNT_50(⊞), crGO_MWCNT_80(⊕), crGO_100(⧋)

4. Conclusions

Graphical representation of heating measurements produced near square data plots for all the samples tested. This is a direct consequence of the small mass of the samples (approx. 16 – 20 mg) and as well the fact that the free-standing samples did not interact with any kind of support, allowing for ultra-fast heating rates. On-off behaviour within 20 cycles showed remarkable stability.

Mechanical testing results showed major differences between buckypapers using pristine nanomaterials and buckypapers based on chemically modified nanomaterials. The results reported here suggest that buckypapers fabricated through chemical reduction methods not only showed superior mechanical performance, but also worked slightly more efficiently as Joule Heaters.

Acknowledgements

This project has received funding from the European Union's Horizon 2020 research and innovation programme under grant agreement No 899528.

5. References

1. Lv L, Dai W, Li A, Lin C Te. Graphene-based thermal interface materials: An application-oriented perspective on architecture design. Polymers (Basel). 2018;10(11).

2. Núñez JD, Benito AM, Rouzière S, Launois P, Arenal R, Ajayan PM, et al. Graphene oxide-carbon nanotube hybrid assemblies: Cooperatively strengthened OH···O=C hydrogen bonds and the removal of chemisorbed water. Chem Sci. 2017;8(7):4987–95.

3. Liu Y, Li P, Wang F, Fang W, Xu Z, Gao W, et al. Rapid roll-to-roll production of graphene film using intensive Joule heating. Carbon N Y [Internet]. 2019;155:462–8. Available from: https://doi.org/10.1016/j.carbon.2019.09.021

4. Smith AT, LaChance AM, Zeng S, Liu B, Sun L. Synthesis, properties, and applications of graphene oxide/reduced graphene oxide and their nanocomposites. Nano Mater Sci

  doi:10.5075/epfl-298799_978-2-9701614-0-0

[Internet]. 2019;1(1):31–47. Available from: https://doi.org/10.1016/j.nanoms.2019.02.004

5. Sun T, Fabris S, Baroni S. Surface precursors and reaction mechanisms for the thermal reduction of graphene basal surfaces oxidized by atomic oxygen. J Phys Chem C [Internet]. 2011 Mar 24 [cited 2022 Apr 18];115(11):4730–7. Available from: https://pubs.acs.org/doi/full/10.1021/jp111372k

6. Pei S, Zhao J, Du J, Ren W, Cheng HM. Direct reduction of graphene oxide films into highly conductive and flexible graphene films by hydrohalic acids. Carbon N Y [Internet]. 2010;48(15):4466–74. Available from: http://dx.doi.org/10.1016/j.carbon.2010.08.006

POLYMER-BASED INTERFACE OPTIMIZATION FOR COATED LIGHTWEIGHT COMPOSITES ADDITIVE MANUFACTURING

Alberto Giménez[*a],Manuel Martínez[a],Jordi Renau[a],Víctor García-Peñas[a],Luis Domenech[a],
Manuel Ibañez[a],Antonio Real[a],Enrique Cortés[b],Asta Šakalytė[c],Juan A.García[d],Fernando Sánchez[a]*

a: Research Institute of Design, Innovation and Technology, University CEU Cardenal Herrera, CEU Universities, Avda. Seminario S/N, 46115 Moncada-Valencia, Spain;
Email: *Corresponding author: algisan@uchceu.es
b: Polymer Innovation Force, 46185 Pobla Vallbona-Valencia, Spain
c: AEROX Advanced Polymers, 46185 Pobla Vallbona-Valencia, Spain
d: Departamento de Ingeniería Mecánica y de Materiales, Universidad Politécnica de Valencia, 46022 Valencia, Spain

Abstract: ·*Composite materials of carbon fiber reinforcements with thermoplastic matrices based on additive manufacturing technologies are used today in a large number of highly technological materials, in various applications, such as aeronautics, automotive or the wind sector. These materials are designed to outperform excellent mechanical behavior, although their resistance to atmospheric agents or mechanical and chemical stresses on the surface is limited. To overcome these stresses, the composite materials are usually protected with a polymeric coating that also provides chemical and mechanical resistance to external agents. In the present work a numerical and experimental analysis is presented of how the properties of the interface between polymer matrix and coating affect the mechanical performance of the protection system. The application of research results is then used in the design and manufacture of a remotely piloted aquatic surface vehicle that requires to achieve the optimal performance with the lightest weight composite structures.*

Keywords: Coating protection, composites, additive manufacturing

1. Introduction

Composite materials are the solution adopted to reduce the weight of components in the sustainable transport industry due to the energy eficiency requirements. These materials are designed to outperform excellent mechanical behavior, although their resistance to atmospheric agents or mechanical and chemical stresses on the surface needs optimization, particularly in aquatic or marine applications. To overcome these factors, the composite materials are usually protected with a polymeric coating that also provides chemical and mechanical resistance to external agents. The interface between the polymer matrix of the composite material and the coating crucially determines the durability of the final product [1].

Sustainable mobility demand a renewal of the forming processes in search of the reduction of the weight of the components, as well as the recycling of components and tools. Composite materials are the solution adopted to reduce the weight of components, however, these processes require expensive molds and dies that are not easily reusable or recycled. The proposal of this work aims to explore the Additive Manufacturing (AM) technologies for the

  doi:10.5075/epfl-298799_978-2-9701614-0-0

manufacture of an aquatic surface vehicle parts that allows abandoning the traditional manufacture of composite molds to build them directly by additive manufacturing. In recent years, AM has become the optimal manufacturing method for components with complex geometry for a wide range of applications [2]. . Digital Manufacturing and, particularly, Additive Manufacturing, are perfect technologies to be shared, as evidenced in the guidelines defined in Industry 4.0, which focus on process monitoring, continuous inspection or distributed manufacturing of components [2] [3] [4].

In this research, the authors have developed the design and manufacture of a remotely piloted aquatic surface vehicle with a real-scale 3D printing technology. The main objective is to investigate and analyse the optimum hull geometry and mechanical configuration of the aquatic surface vehicle, as well as the use of advanced materials and manufacturing methods in order to achieve the optimal performance with the lightest weight composite structures. The use of a novel fully functional Additive Manufacturing (AM) system for the development of components in the sustainable mobility industry is explored. The key advantage of this manufacturing process compared to subtractive technologies is the use of the raw material and the possibility of obtaining more efficient products with complex and light geometries thanks to topological optimization. Moreover, in the present work a numerical and experimental analysis is presented of how the properties of the interface between the 3D printed polymer matrix and the surface coating affect the mechanical performance of the protection system. The characterization of various material systems and manufacturing processes are also discussed. The application of research results is then used in an electric vehicle where the performance of different hydrogen fuel cell powerplants (PEMFC) have to be optimized in terms of energy efficiency, see Figure 1.

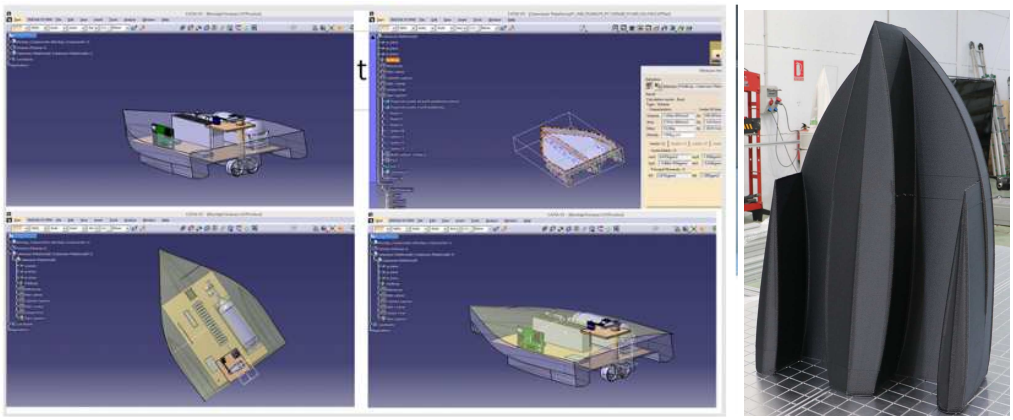

Figure 1. Preliminary 3D printing for Hull geometry design and manufacturing analysis.

2. Materials and Methods

Through carbon fiber printing it is possible to manufacture parts with complex geometries and high structural responsibility. The versatility of Additive Manufacturing by 3D printing allows in the same machine to use different materials, deposition strategies, including process parameters such as temperature, deposition speed or even the fabric's own permeability by controlling the tension of the deposited yarn.

FGF (Fused Grance Fabrication) processing is an additive forming process with great growth expectations for the coming years and has a large number of advantages over classic FDM (Fused Deposition Modelling) systems (ISO/ASTM 52910:2018). Processes dealing with the direct

  doi:10.5075/epfl-298799_978-2-9701614-0-0

extrusion of thermoplastic and composite material from pellets can lead to scale towards larger workspaces that cannot be covered by FDM. The numerical simulation of this forming process is very similar to the plastic injection process, however, today there are very few works carried out in this field, so this topic is one of the most promising research lines for the next years in additive manufacturing. This technology combines the good attributes of injection moulding and 3D printing. The FGF machine is a numerically controlled equipment (CNC) that has three degrees of freedom to position the extrusion head plus a fourth degree of freedom that controls the rate of material deposition. The part is formed on a static building platform and the material is pressed through the nozzle. After each layer, the extrusión nozzle moves up and the next layer is added. A nozzle with an orientation of 45º from the vertical axe could be use in order to avoid supporting structures and create parts with overhangs. Then it is not necessary the part post-processing to removal of support structures. FGF is suitable for medium to large parts, with thick walls and low complexity geometries. The productivity could be up to 10kg/h that is a key factor when it comes to manufacturing large parts, especially if they can be post-processed, e.g. by CNC machining, see Figure 2.

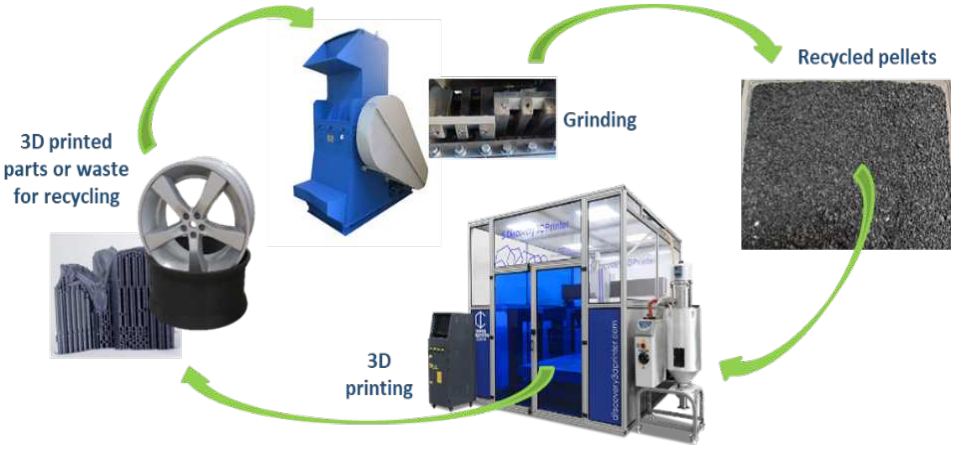

Figure 2. Fully recyclable addittive manufacturing System [Source: CNCBarcenas 5]

As a demonstrator of the technology developed in this paper, a trimaran of one meter in length has been designed and built. This boat must be capable of housing and autonomously transporting all the control equipment, motorization, batteries and a payload of 10kg. For its manufacture, Direct Extrusion of Pellets or Fuse Granular Fabrication (FGF) process has been chosen. This additive manufacturing process consits of deposit thermoplastic granulates on a bed layer by layer to form the 3D-object, as is described in Figure 3. The part has been printed in a Super Discovery 3D printer that is showed in Figure 2.

  doi:10.5075/epfl-298799_978-2-9701614-0-0

Figure 3. Intermediate 3D printing stages of the aquatic surface vehicle hull. The Fuse Granular Fabrication (FGF) technology used ABS reinforcement with Carbon Fiber (CF) materials.

Figure 4 shows the manufacture of the trimaran hull in differentent time steps of the simulation. As can be seen in the figure, the trimaran has been printed with a Skiirt layer of four lines, the first in direct contact with the part surface. The hull has been printed without any infill or supports. Due to the fact that a final machining is necessary to leave the desired final finish, the piece has been printed with two layers of thickness in all its geometry.

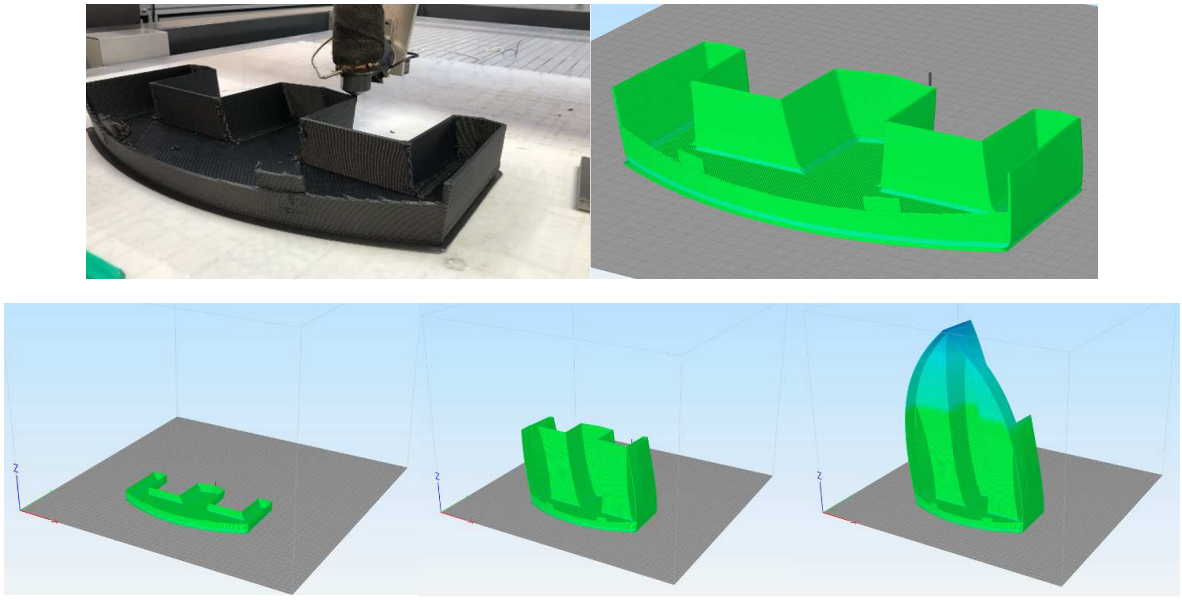

Figure 4. Simulation of the 3D printing manufacturing of the ABS+CF trimaran hull

ABS (Acrylonitrile butadiene styrene) is the second most commonly used filament for Thermoplastic Additive Manufacturing due to it´s moderate strength, flexibility and melt flow characteristics. ABS withstand hot temperatures and has great behavioir in terms of durability. The high-quality ABS material is a right choice for general purpose printing. In this work, an ABS reinforcement with Carbon Fiber (CF) is use for the experiments to improve the general mechanical properties of the plastic base. The material used for this application is LNP™ THERMOCOMP™ AM COMPOUND AC004XXAR1, that is supplied by Sabic [6]. This thermoplastic material is a compound based on Acrylonitrile Butadiene Styrene (ABS) resin containing 20 wt.% carbon fiber for Large Format Additive Manufacturing (LFAM) applications. Added features of this grade include: Higher Stiffness vs. glass fiber, Easy Processing, Low warp and Good Print Surface quality, making them a good candidate material for a broad range of applications and tooling, including thermoforming and vacuum-forming. Further, lower shrinkage during cooling means these materials demonstrate greater dimensional stability and less thermal expansion during part use, see Table 1 that ilustrates the mechanical properties of this material. This material has a specific gravity of 1.14. For a correct extrusion of this material, it is necessary to have a maximum moisture content between 0.05 and 0.1%, then it is necessary to dry the material in the oven (4hours at 80ºC). In Figure 5 is it described the barrel and nozzel temperatures.

Table 1. ABS+CF Material properties

  doi:10.5075/epfl-298799_978-2-9701614-0-0

PROPERTIES	TYPICAL VALUES	TEST METHODS
Tensile Stress		
XZ Orientation	89 MPa	ASTM D638 Modified
ZX Orientation	18 MPa	ASTM D638 Modified
Tensile Strain		
XZ Orientation	1 %	ASTM D638 Modified
ZX Orientation	0.7 %	ASTM D638 Modified
Tensile Stiffness		
XZ Orientation	11.8 GPa	ASTM D638 Modified
ZX Orientation	2.9 GPa	ASTM D638 Modified
Flexural Stress		
XZ Orientation	32 MPa	ASTM D790 Modified
ZX Orientation	125 MPa	ASTM D790 Modified

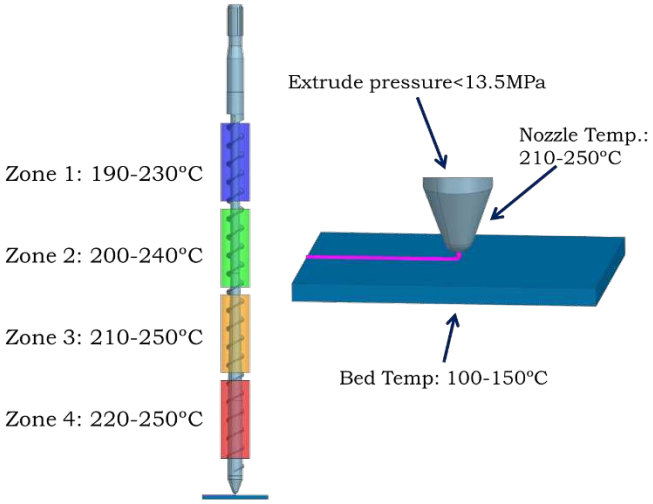

Figure 5. Extrusion barrel and nozzel temperature zones

3. Coating surface protection system

An appropriate material selection, geometric and manufacturing design involves the optimization of the energy consumption of the aquatic vehicle. Moreover, the particular specifications for the surface vehicle will require its protection for the environmental operating conditions (UV protection, humidity, corrosion, surface impacts, waves, etc.), so surface coatings and, in this case, post-3D printing applications of paints will be required in order to ensure the optimal performance during operation in the field tests. In this work different materials based on epoxy and polyurethane technologies are formulated and prepared for characterization and subsequent validation. Two technologies are considered in preparing the materials: in one hand

surface coatings with corresponding fillers applied after the printed part is machined and, in the other hand, adhesive materials, applied in specific areas of the composite shell once it has been completely manufactured in order to join additional components. The adhesives require to complete a curing cycle as joining operation of structural components. Its physico-chemical characterization is developed by performing different tests to determine the chemical structure due to its processing and curing conditions. In addition, its mechanical testing is completed to define also the input data of the variables defined in the different numerical models that are used to validate its capabilities. To determine the characteristic design values for coating materials, test data must be treated statistically to eliminate uncertainties and natural variability in material properties. Moreover, as mentioned above, the resistance of the interface between the surface material layers (coatings, filler, paints) must be measured to identify possible weakness in the system in the face of delamination or debonding damage.

Adhesion between layers in the composite system is a parameter that ensures that loads are transferred between layers. If a premature failure occurs in the material interfaces, this will compromise the capacity of the surface protection system. Adhesion tests will be used in the numerical models developed by the research group under different operational conditions.

Tests are developed for the different application configurations defined and showed in Figure 6 and Table 2 and 3. Appropiate results were obtained so a first prototype coating system was completed and implemented with different coating protection layers, see Figure 7.

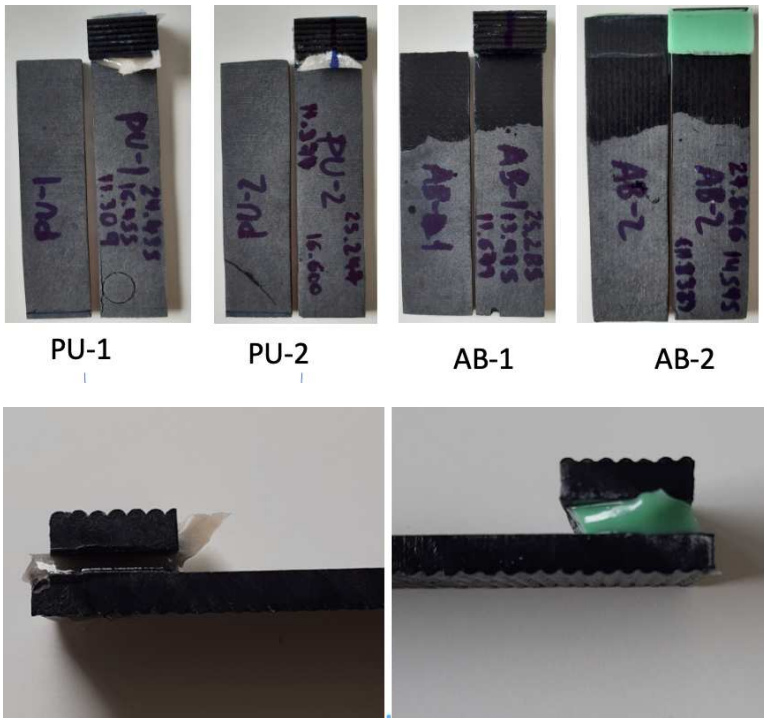

Figure 6. Mechanical characterization of interface. Adhesive shear tests for the Polyurethane PU (left) and Epoxy AB (right) adhesive technologies. In both cases there is a substrate failure.

  doi:10.5075/epfl-298799_978-2-9701614-0-0

Table 2. Mechanical characterization of interface. Pull-off adhesion tests for surface multilayer coating system based on Epoxy technology.

	Material Identification	Pressure σ (MPa)	Failure	Visual Failure Analysis (%)
 Epoxy based coating system: TopCoat 100 µm Primer carboline 100 µm Putty Epoxy Filler 1000 µm Substrate ABS+CF	001_1	2,110	Adhesive failure Primer/Filler	100%
	001_2	1,990	Adhesive failure Primer/Filler	100%
	001_3	2,020	Adhesive failure Primer/Filler	100%
	Average	2,040		
	Standard Deviation	0,062	–	–
	Coefficient of Variation (%)	3,061	–	–
	Minimum	1,990	–	–
	Maximum	2,110	–	–

Table 3. Mechanical characterization of interface. Pull-off adhesion tests for surface multilayer coating system based on Polyurethane technology.

	Material Identification	Pressure σ (MPa)	Failure	Visual Failure Analysis (%)
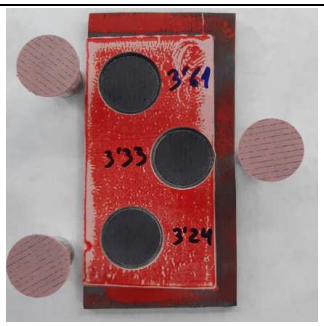 Polyurethane based coating system: TopCoat 100 µm PU Filler 1000 µm Substrate ABS+CF	001_1	2,110	Adhesive failure Primer/Filler	100%
	001_2	1,990	Adhesive failure Primer/Filler	100%
	001_3	2,020	Adhesive failure Primer/Filler	100%
	Average	2,040		
	Standard Deviation	0,062	–	–
	Coefficient of Variation (%)	3,061	–	–
	Minimum	1,990	–	–
	Maximum	2,110	–	–

  doi:10.5075/epfl-298799_978-2-9701614-0-0

Figure 7. Different surface coating layers applied to the 3D printed ABS+CF Hull .

4. Conclusions and future work

The present work has shown the integration of additive manufacturing systems that allow one to design original mechanical components and to achieve its incorporation into the vehicle with optimal functional requirements. The main achievements are: Technical study of different materials and geometrical configurations to achieve optimal performance in composite surface protection systems; the analysis and design of the structure of the hull and structural components with CAD/CAE techniques and 3D prototypes; the manufacturing and material process design of the the aquatic vehicle parts manufacturing and surface coating application.

Acknowledgements

This research has been supported by the project “SISTEMA DE POTENCIA HIBRIDO FLEXIBLE CON PILAS DE COMBUSTIBLE PARA VEHICULOS ELECTRICOS Y FABRICACION AVANZADA DE PLATAFORMA ACUATICA ELECTRICA SUPERFICIAL NO TRIPULADA” with reference RTI2018-096001-B-C33, funded by Ministerio de Ciencia, Innovación y Universidades, and additionaly by the project with reference PID2019-108807RB-I00. Authors would like to acknowledge technological support from the companies AEROX Advanced Polymers and CNC Barcenas.

5. References

1. E.Cortés, F.Sánchez, A.O’Carroll, B.Madramany, M.Hardiman,T.M.Young; On the material characterization of wind turbine blade coatings: Effect of the interphase adhesion on rain erosion performance, *Materials; September 2017, Vol 10, 1146, doi:10.3390/ma10101146*.
2. Ahuett-Garzaa, A, T.Kurfess, T. A brief discussion on the trends of habilitating technologies for Industry 4.0 and Smart manufacturing. Manufacturing Letters. Vo.15, Part B, 2018, 60-63.
3. Airbus_CAI, 2009. International Standard ISO 18352. Carbon-fibre-reinforced plastics Determination of compres-sion-after impact properties at a specified impact-energy level.
4. Mandolla, C; Petruzzelli, A; Percoco, G; Urbinati, A. Building a digital twin for additive manufacturing through the exploitation of blockchain: A case analysis of the aircraft industry. Computers in Industry, Volume 109, August 2019, Pages 134-152.
5. https://cncbarcenas.com/es/inicio/
6. https://www.sabic.com/en/products/specialties/specialty-compounds/lnp-thermocomp-am-compound

MXENES/PAANA BASED SENSORS FOR COMPOSITE STRUCTURES

Olga Bulderberga[a], Evgeni Ovodok[b], Stanislav Stankevich[a], Sergejs Tarasovs[a], Sergey Poznyak[b], Andrey Aniskevich[a]

a: Institute for Mechanics of Materials, University of Latvia – olga.bulderberga@lu.lv
b: Research Institute for Physical-Chemical Problems of the Belarusian State University

Abstract: *Sensor technologies provide huge opportunities in structural health monitoring. Improving sensing of them could lead to wider applications. MXenes-based sensors are under investigation for the last several years, but improvements are always desired. By adding sodium salt of polyacrylic acid (PAANa) to MXenes colloidal solution several issues could be improved. By the work, it was defined that PAANa additive promotes wetting of hydrophobic surfaces of an epoxy matrix of the composite, thus allowing the formation of a uniform conductive layer of MXenes/PAANa. Furthermore, the high conductivity, which is typical for MXenes films, was preserved in MXenes/PAANa. The ability of the MXenes/PAANa thin-film sensor to monitor the structural integrity of the sample was approbated. A trained artificial neural network was developed and applied for the detection and location of damage in the composite plate with a further comparison with the experimental results.*

Keywords: MXenes; Sodium salt of polyacrylic acid; Composite structure; Structural health monitoring

1. Introduction

The development of sensor technologies provides the possibility of more precise control of the structure under exploitation. While MXenes-based sensors, due to the wide range of MXenes application possibilities, could take a separate niche in the existing sensor technologies, some challenges are still actual [1, 2]. For example, the chemical stability of dried MXenes films under exposure to humidity and oxygen in the environment, adhesion of MXenes films to various surfaces, and not least, the high cost of MXenes. Preliminary studies showed that adding sodium salt of polyacrylic acid (PAANa) to MXenes colloidal solution could help deal with these actual problems.

The aim of the study was to evaluate the ability of MXenes/PAANa thin-film sensor to perform Structural Health Monitoring (SHM) of a composite structure.

Non-destructive SHM is an active research field that aims at detecting, locating, and quantifying damage in different structures. Most popular SHM methods are based on measuring the response of the structure on different excitation and identifications of deviations of the response from an undamaged condition. A review of different SHM methods for composite structures can be found in [3, 4]. Electrical conductivity measurements were successfully applied to monitor and identify damage in composite laminates [5-7].

Many SHM methods require the solution of an inverse problem to locate and quantify the damage. A Machine Learning (ML) method, such as artificial neural networks (ANN) has been

  doi:10.5075/epfl-298799_978-2-9701614-0-0

successfully used recently [4] as a powerful tool for the prediction of the damage, where the data for ANN training were collected using numerical simulations.

In this study, an ANN was used to detect and locate damage in a composite plate covered by a conductive MXene coating. The training data for an ANN was obtained through a large set of numerical experiments (ca. 6000 solutions) with randomly located defects of different sizes using the finite element method.

2. Materials and samples

In the present work, Ti_3C_2 MXenes were prepared by etching Ti_3AlC_2 MAX phase powder in LiF + HCl solution. In etching solution, concentration of HCl was 9 M and LiF - 3 M [8]. A colloidal solution of MXenes (5 g/L) was obtained in the process of synthesis, see Figure 1(a). The lateral size of MXene 2*D* particles reaches 3 μm, see Figure 1(b). Sodium salt of polyacrylic acid (PAANa) was added to MXenes colloidal solution in varying amounts for preparation of high quality conductive composite coatings. The PAANa additive promotes wetting of hydrophobic surfaces of an epoxy matrix of the composite, thus allowing the formation of a uniform conductive layer of MXenes/PAANa, isolation of MXenes nanosheets from the surrounding environment, and reduction of used material, see Figure 2.

(a) 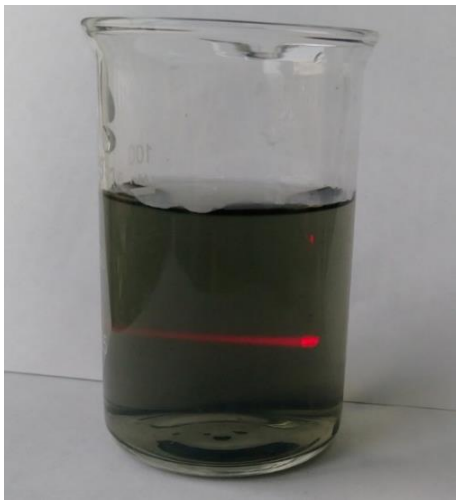 (b) 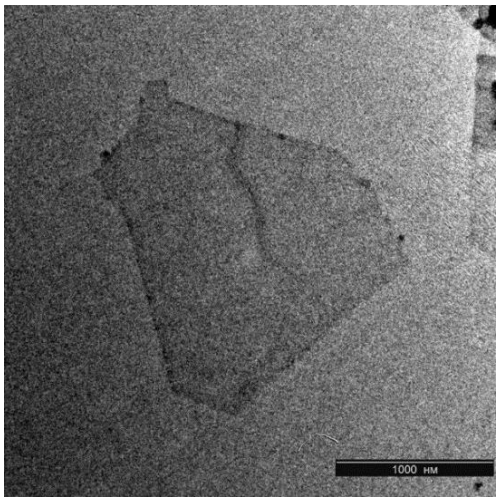

Figure 1. Diluted sol of MXenes after the synthesis (a) and TEM image of MXenes nanosheet (b)

(a) 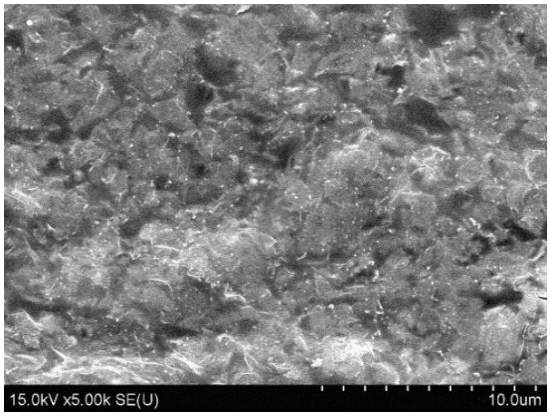

(b) 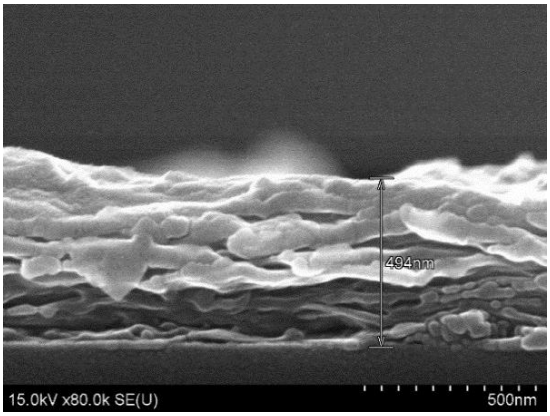

Figure 2. SEM images of MXenes/PAANa (50:50) composite: surface (a) and cross section (b)

For the testing of structural integrity, the composite plate was used. The mixture of MXenes/PAANa in the ratio of 50:50 by weight was uniformly distributed over the surface. The network of contacts was made on the dry surface. The location of contacts and size of the inspected area is presented in Figure 3. The surface was covered with epoxy resin to insulate the MXenes/PAANa surface from water vapour and oxidation in air, while the part of the contacts was left out of the epoxy layer.

Figure 3. Composite plate with the network of contacts

3. Finite element model

To generate a training set for an ANN a finite element model representing the plate with contact points was prepared (Figure 4). Only the outer contact points along the perimeter of the plate were used to train an ANN.

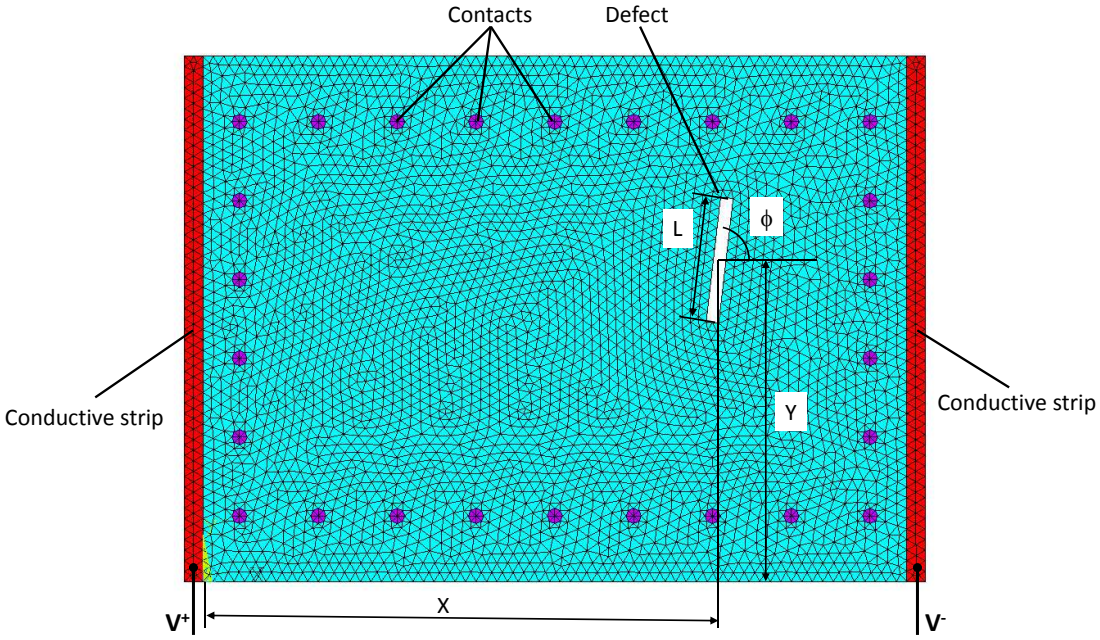

Figure 4. Finite element model of a plate with the defect and geometrical parameters of defects

The resistance of the conductive strips on the left and right edges of the model was several times lower than that of the interior zone, creating a potential field close to the experimentally measured for the undamaged plate. The defect was placed randomly in the interior zone of the plate, varying the position, size, and inclination of the defect. About 6000 simulations were performed and after each simulation, electric potential values at each contact point were recorded, together with geometrical parameters of the defect.

Due to variations of conductivity of the MXene coating in the experimental plate, direct comparison of measured electric potential with numerically simulated is not easy. To address this problem, all data, from numerical simulations and experimentally measured, were normalized using relation

$$\tilde{v}_i = \frac{v_i - \min(v_1,\ldots,v_n)}{\max(v_1,\ldots,v_n) - \min(v_1,\ldots,v_n)} \quad (1)$$

where v_i are the electric potential values measured at contact points and n is the number of contact points (26 in this study). After the normalization procedure, deviation from the undamaged state was calculated as

$$p_i = \tilde{v}_i - \tilde{v}_i^0 \quad (2)$$

where $\tilde{v}_i^0$ is normalized values of electric potential in the undamaged plate. Obtained values p_i were used as input data to train a neural network.

4. Artificial neural network

Multivariate regression with a fully connected neural network was used to predict all four geometrical parameters of the damage, position, size, and inclination, simultaneously. An ML framework Keras was used to define a fully connected ANN with three hidden layers. The ANN has 26 inputs (the number of contact points in the plate) and four output neurons as schematically shown in Figure 5. ReLU activation function was used for all layers except the last one, where no activation function was used. ANN with a different number of neurons in hidden layers, between 13 and 256, were tested, all showing similar results.

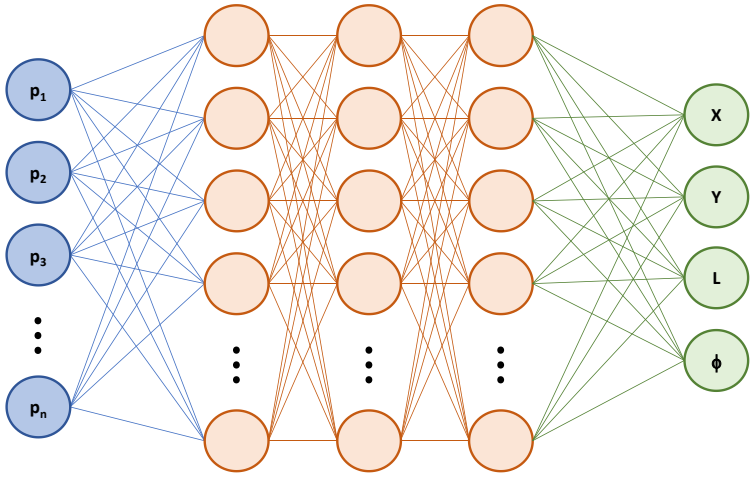

Figure 5. Schematic representation of an artificial neural network with three hidden layers

5. Experiments and results

For characterization of the voltage distribution throughout the surface, a voltage of 1 V was applied between the edges, creating a close to uniform potential field in the interior zone of the sample, and the resistivity on each contact was measured similar to work [9]. Thus, the matrix of resistivity values was obtained. After, the voltage of 1 V was applied in the opposite direction, and data from all contacts were collected again. This resulted in direct and reverse data which theoretically should be the same. The damage was introduced by creating a long narrow cut, see Figure 6(a), in five increments with the length of the cut increasing from 0.45 cm to 3.13 cm. The width of the cut is equal to 0.24 cm. After each cut increment, the deviation of the electric potential field from the undamaged state was measured. To exclude the measurement errors all obtained data were normalized to the max value of the matrix. This was done for all measurement series. The difference of normalized values for the measurement (0) - before the damage and (5) - the biggest damage was calculated. By this, the localization of damage could be defined, see Figure 6(b). Perturbation on damage was defined as a difference between the sum normalized values from all contacts for the first (0) and next measurements, (1),.., (5) ... respectively. The dependence of perturbation on damage length is presented in Figure 7.

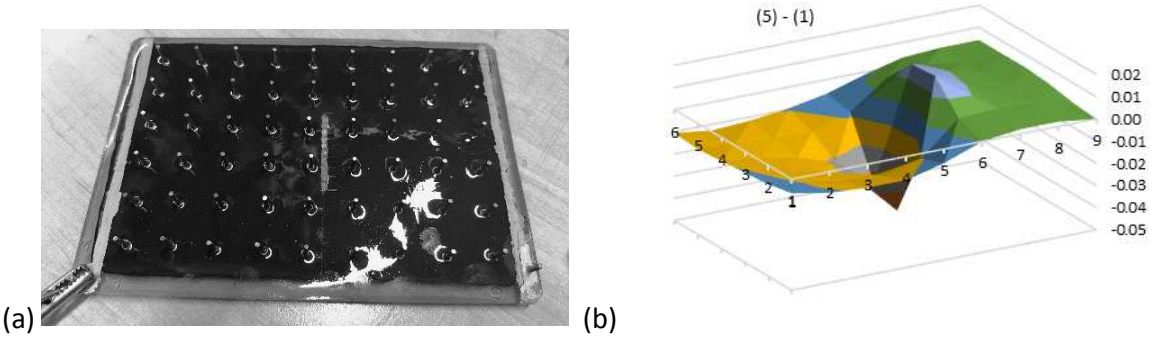

Figure 6. Inspected area with the maximal cut (a) and localization of cut by the resistivity change – damage is located between the 5th and 6th contacts' row in the center (b)

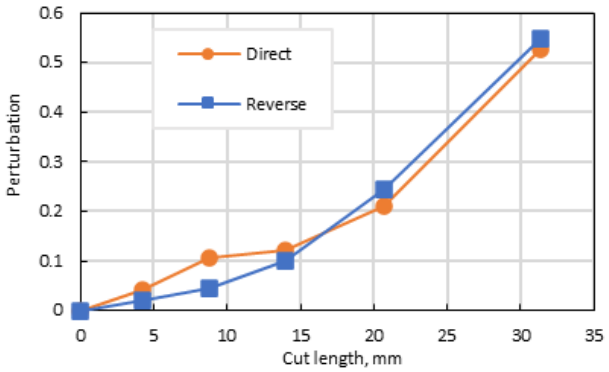

Figure 7. The dependence of perturbation on damage length

To verify the ability of an ANN used in this study to identify the damage parameters, a comparison of the predicted position, size, and inclination of the defect vs. actual data for a small subset of training data, about 240 data samples, is shown in Figure 8.

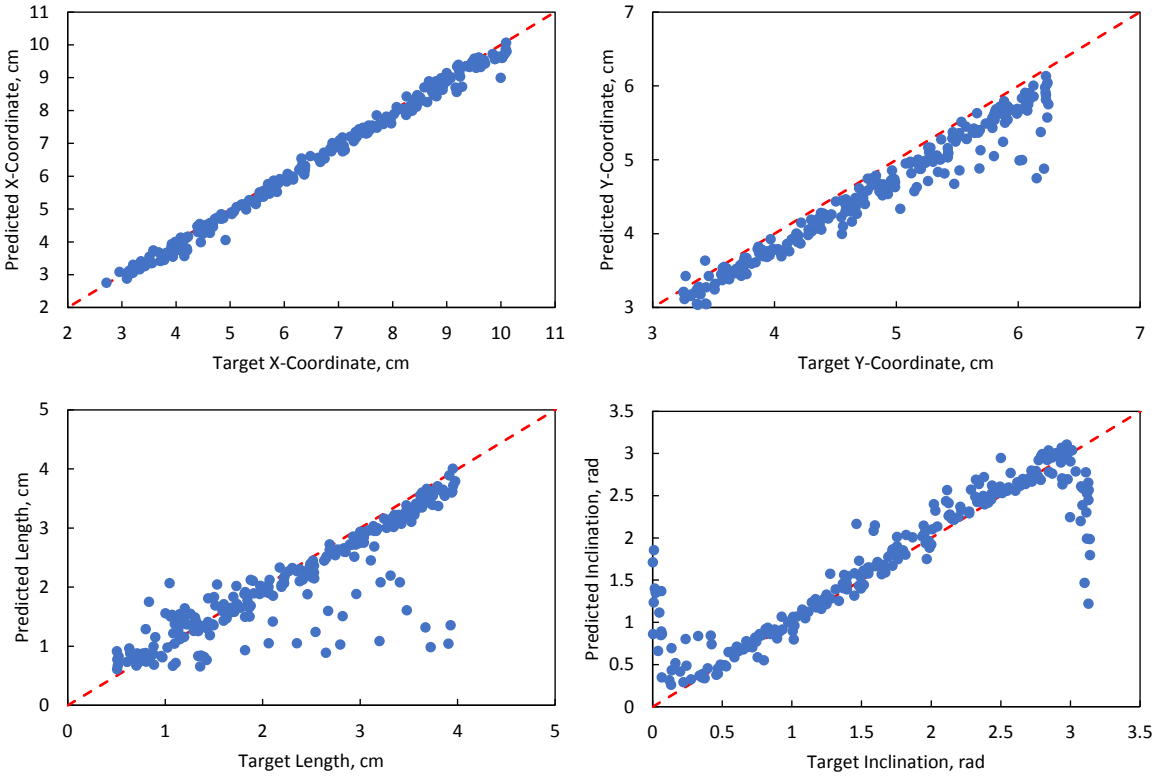

Figure 8. Comparison of the predicted and target values of the damage geometrical parameters for training data

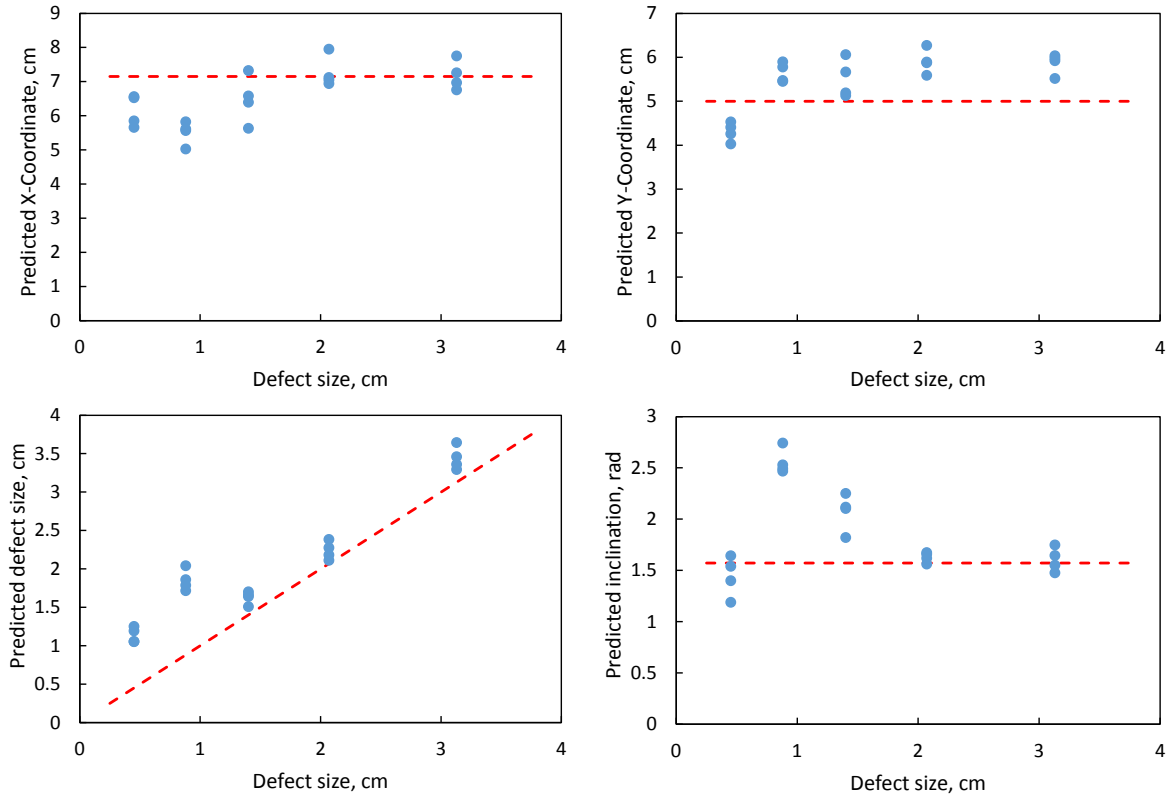

Figure 9. Predicted position, size, and inclination of the cut in the plate (blue dots) and target values (red lines)

  doi:10.5075/epfl-298799_978-2-9701614-0-0

Results show that the proposed method, in general, can predict all geometrical parameters of the defect, however, some discrepancy is seen in the defect size and inclination for several data samples. Detailed examination of points that fall off the target lines has shown that this behaviour was observed for defects with small inclinations. This can be expected for the current configuration of the electric potential field, which is close to uniform and oriented in the X-direction. The proposed method is less sensitive to the defects oriented along the electric current lines. However, it could be noted that even in this case the ANN still can accurately predict the location of the defect.

Results of the predictions with a trained ANN for experimental data are shown in Figure 9 compared with the actual parameters of the cut shown as dashed red lines. Four sets of predictions are shown for four trained neural networks that differ by the number of neurons in hidden layers (three hidden layers were used in all cases). The results show that relatively accurate predictions can be obtained for long cuts with an error of less than 20% in most cases. Accuracy decreases significantly for small defects, as could be expected.

Conclusions

In summary, it was confirmed that the addition of PAANa to MXenes colloids improves epoxy surface wetting, thus uniform MXenes/PAANa thin conductive films could be deposited on surfaces such as a neat and coloured epoxy resin. The results obtained showed that MXenes/PAANa based sensors allow performing SHM - to control the structural integrity of composites. An ANN was successfully applied for detection and location of damage in the composite plate with conductive coating using the deviations of the electric potential field from an undamaged state. A finite element model of a plate with randomly located defects was used to generate data for ANN training. A normalization procedure was applied to numerical and experimentally measured data to reduce the influence of the non-uniformity of the coating that is difficult to address in a numerical solution. Validation of the trained ANN with the experimental data shows a good agreement of the predicted damage parameters with the actual data.

Acknowledgements

This work has received funding from the European Union's H2020-MSCA-RISE-2017 project Nano2Day, "Multifunctional polymer composites doped with novel 2D nanoparticles for advanced applications", grant agreement No 777810 and from Himreagent 2021–2025 № 2.1.04.02. BRFFR grants № Х20СЛКГ-004.

6. References

1. Ho, D.H., et al., *Sensing with MXenes: progress and prospects.* Advanced Materials, 2021. **33**(47): p. 2005846.
2. Grabowski, K., et al., *Recent advances in MXene-based sensors for Structural Health Monitoring applications: A review.* Measurement, 2021: p. 110575.
3. Mitsheal, A., -Daerefa-a, et al., *A Review of Structural Health Monitoring Techniques as Applied to Composite Structures.* Structural Durability \& Health Monitoring, 2017. **11**(2): p. 91--147.

  doi:10.5075/epfl-298799_978-2-9701614-0-0

4. Gomes, G.F., et al., *The use of intelligent computational tools for damage detection and identification with an emphasis on composites – A review.* Composite Structures, 2018. **196**: p. 44-54.
5. Todoroki, A., *The effect of number of electrodes and diagnostic tool for monitoring the delamination of CFRP laminates by changes in electrical resistance.* Composites Science and Technology, 2001. **61**(13): p. 1871-1880.
6. Anderson, T., G. Lemoine, and D. Ambur. *An artificial neural network based damage detection scheme for electrically conductive composite structures*. in *44th AIAA/ASME/ASCE/AHS/ASC Structures, Structural Dynamics, and Materials Conference*. 2003.
7. Yu, M.-H. and H.-S. Kim, *Deep-learning based damage sensing of carbon fiber/polypropylene composite via addressable conducting network.* Composite Structures, 2021. **267**: p. 113871.
8. Alhabeb, M., et al., *Guidelines for Synthesis and Processing of Two-Dimensional Titanium Carbide (Ti3C2Tx MXene).* Chemistry of Materials, 2017. **29**(18): p. 7633-7644.
9. Stankevich, S., et al., *Electrical Conductivity of Glass Fiber-Reinforced Plastic with Nanomodified Matrix for Damage Diagnostic.* Materials, 2021. **14**(16).

  doi:10.5075/epfl-298799_978-2-9701614-0-0

INNOVATIVE USE OF A HIGH FILLED GRAPHENE FILM IN AN AERONAUTICAL COMPOSITE PANEL

Ruggero Volponi[a] Fabrizia Cilento[b,c], Alfonso Martone[c] Giuseppe Giusto[a,e], Cinzia Toscano[a], Michele Giordano[c], Giovanni Barletta[d], Nicola Gallo[d]

A: CIRA, Italian Aerospace Research Centre, Capua (CE) Italy - r.volponi@cira.it
B: Department of Chemical, Materials and Production Engineering, University of Naples Federico II, Napoli, Italy
C: IPCB, Institute of Polymers, Composite and Biomaterials, CNR, Portici, Italy
D: Leonardo S.p.A. – Aerostructure Division – Via per Monteiasi sp.83, 74023 Grottaglie (TA); Italy
e: IMAST S.c.ar.l. - Technological District on Engineering of polymeric and composite Materials, Vico II San Nicola alla dogana, n. 9, 80133 Napoli; Italy

Abstract: *This study proposes as solution to the water uptake the use of a film with a high percentage of graphene (up to 90%wt), as layer to be integrated on the surface of a sandwich composite panel, representative of nacelle landing gear of the ATR aircraft. The very high in-plane orientation of graphene layers in polymer matrix are able to produce a tortuous path in diffusive processes, so the layer works as a barrier structure*

Keywords: Graphene; water uptake; sandwich; film.

1. Introduction

In the last decades the trend has been to expand the use of composite materials also in aircraft and automobile primari~~es~~ structures. Composites have advantages of high specific strength and stiffness over metals. This helps to significantly reduce the weight of the structure, which in turn benefits the industry in terms of cost savings and environmental benefits. For example, it was reported that 1 kg of weight reduction in an aircraft can save over 2900 litres of fuel per year [1].

It is well known that the mechanical properties of fiber-reinforced composites can be very sensitive to environmental parameters, such as temperature, humidity, light or environmental impact phenomena such as rain, lightning or hail. Thus, the durability of composite materials becomes crucial when they are used as structural materials [2].

In an aircraft some primary structures are always subjected to varying temperature and moisture exposures throughout their entire service lifetime. The environmental conditions, especially temperatures ad moisture exposures, varies widely during a flight from the take-off to the landing.

The solution currently used to resist to water adsorption is based on metallic paints, applied trough flame spray, which have some drawbacks, i.e weight, fragility.

An alternative technical solution, proposed in AMICO project [4], is aimed at replacing metallic paints with epoxy layers with a high graphene content. The main expected advantage in using these layers is in terms of manufacturability: they can be easily integrated into the composite panel manufacturing process, thus avoiding the flame-spray process.

  doi:10.5075/epfl-298799_978-2-9701614-0-0

This work shows the results of a testing campaign aimed at the characterization and effectiveness evaluation of the proposed solution in terms of moisture adsorption, applied to composite specimen.

Moisture absorption tests and non-destructive inspection were carried out using an environmental chamber in order to reproduce temperature and relative humidity profiles representative of a real use conditions for a regional aircraft composite part (Ground Air Ground GAG tests [3]).

2. Specimens and Tests

Two kinds of specimens have been produced and tested:

1. epoxy sheets, with an high graphene content.
2. composite sandwich laminates, overlayered with epoxy sheets with high graphene content.

The first kind of samples has been used for the water adsorption evaluation. Moreover they have been characterized in terms of electrical resistance.
The latter has been used for the water uptake measurements, with static tests and GAG tests. A qualitative resistance characterization has been achieved to evaluate superficial damages on the sheets.

2.1 Sheets

Sheets are made of a minimum quantity of polymer, filled with an high quantity of graphene nanoplates, mostly oriented in a planar condition, which act as a reinforcement.
The epoxy simply holds together the various layers of graphene, according to a “brick and mortar” pattern []. The effective in-plane orientation of graphene layers, in the polymer matrix, produces a tortuous path in diffusive processes, so that the layer works as a barrier structure.
Three different kinds of sheet have been produced, with different charge of graphene in weight: 90%, 80% e 70%.

Figure 1 Sheet with different graphene charge

Rectangular samples have been cut from each sheet. On each sample, contacts were made with a conductive adhesive based on silver.

To prevent the samples from breaking during the measurements, they were reinforced with a transparent adhesive tape.

  doi:10.5075/epfl-298799_978-2-9701614-0-0

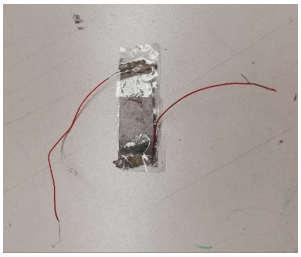

Figure 2 Prepared sheet samples, with electric contacts

2.2 Composite Sandwich Laminates

In order to evaluate the effectiveness of the high graphene content sheets in reducing the water uptake in aeronautical composites, sandwich panel samples have been produced with a honeycomb core inside and a graphene sheet integrated both on the upper and the lower surface.
These panels are representative of an ATR gondola cart panel, and have a size of approximately 17cm x 17cm.
Seven composite plate samples were manufactured:

- Two for each type of sheet (three sheet types with different charge of graphene in weight: 90%, 80%, 70%).
- A reference sample, without overlayered sheets

Figure 3 Composite Sandwhich Samples

2.3 Testing

The test campaign evaluated the increased barrier capacity to moisture absorption in the composites due to the presence of the surface sheets. A first type of static environmental conditioning went on for 42 days. A second type involved conditioning the material through variable cycles of temperature and pressure. Finally, an electrical characterization of the graphene sheets was carried out and the surface electrical resistance of the composite samples was monitored during dynamic conditioning to see any damage suffered by the sheets.

2.3.1 Sandwich Laminates Moisture Uptake Tests

The specimens were set at 70 ° C with a relative humidity of 85% for a period of 42 days using an Angelantoni enviromental chamber CH 2000 which allows a temperature control in a range [-75 ° C; + 180 ° C] and relative humidity in a range of 10% - 98%.

  doi:10.5075/epfl-298799_978-2-9701614-0-0

Figure 4 Enviromental chamber Angelantoni CH 2000

The test consists in monitoring the absorption of moisture by the specimens over time by weighing with a precision balance.

Table 1 Samples

Sample ID	Coating	Skin	Core
P70A	70% GNP/Epoxy	Kevlar/Epoxy	Nomex thickness 13 mm
P70B	70% GNP/Epoxy	Kevlar/Epoxy	Nomex thickness 13 mm
P80A	80% GNP/Epoxy	Kevlar/Epoxy	Nomex thickness 13 mm
P80B	80% GNP/Epoxy	Kevlar/Epoxy	Nomex thickness 13 mm
P90A	90% GNP/Epoxy	Kevlar/Epoxy	Nomex thickness 13 mm
P90B	90% GNP/Epoxy	Kevlar/Epoxy	Nomex thickness 13 mm
P ref	No coating	Kevlar/Epoxy	Nomex thickness 13 mm

Figure 5 Samples placed into the environmental chamber

Weight measurements were done every three days in the first week of conditioning, then once a week.
Unfortunately, due to incorrect information, it was not possible to carry out an initial conditioning of all the samples in the vacuum oven in order to remove the residual moisture.
Only at the end of the conditioning test it was possible to remove all the accumulated humidity and thus to define an initial state with zero humidity.
For that reason, the initial value of humidity are not the same for all the samples.

  doi:10.5075/epfl-298799_978-2-9701614-0-0

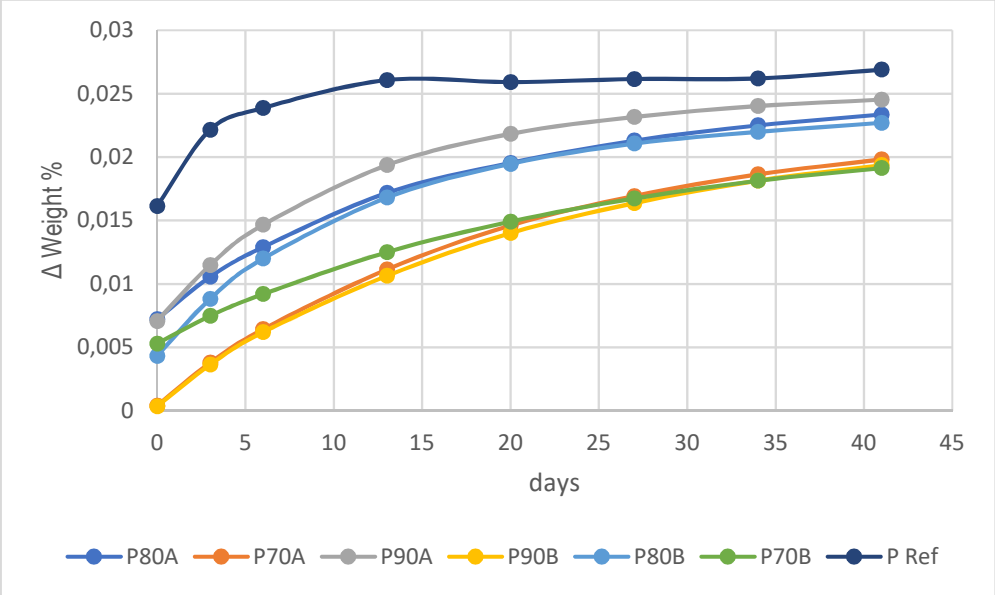

Figure 6 Weight variation of composite samples due to moisture absorption

From the data it can be seen how the graphene surface layer determines a lower permeation of moisture through the composite both in absolute terms and in terms of diffusion speed through it. In fact, it can be observed that the slopes of the curves described by the specimens with the graphene layers are milder in tending to saturation.

2.3.2 **GAG Tests on Sandwich laminates and Sheets**

The dynamic moisture absorption test called GAG test (Ground Air Ground) was performed according to the specification ASTM D5229 [3]. It simulates the stress of the material subjected to sudden drops in temperature down to -54 ° C, in conditions of humidity saturation followed by a subsequent rise in temperature up to 70 ° C. The test was repeated for ten cycles.

The samples were weighted at the start of the test, the after the first cycle and finally at the end of the tenth cycle. In addition to the seven sample of composites, the test were performed also on three different samples of layers of graphene (S 70/30; S 80/20; S 90/10).

Figure 7 Highly loaded Graphene sheets

From measurements it's possible to see Figure 8 how the most sensible sample to the moisture is the reference sample. All the samples of composite with graphene layer on surface, shows an evident retardant effect to the moisture adsorption, and finally, the graphene layers shows an adsorption tendency minimum in the sample with a graphene percentage of 90%.

  doi:10.5075/epfl-298799_978-2-9701614-0-0

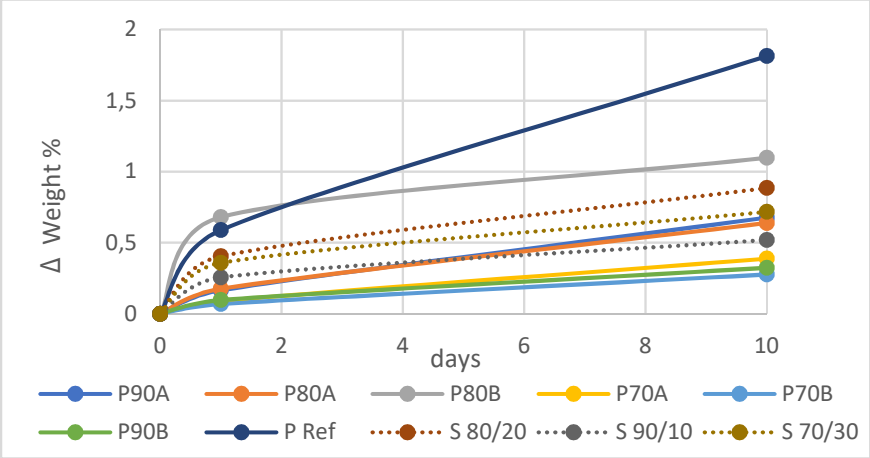

Figure 8 Variation of Weight of Composite Samples and Graphene layers during GAG Test

2.3.3 Electrical Resistance characterization on Sandwhich laminates and Sheets

During the GAG test, the integrity of the graphene layer on the surface was monitored by measuring the electrical conductivity of the layer.

Therefore, two electric wires were fastened with a conductive paste on the diagonal of each specimen and the different specimens were connected in series. The samples were fed with a 100ma current and voltage was recorded across each sample.

Figure 9 Composite Samples connected in a series circuit

The results of the surface resistance measurements of the various specimens during the ground air ground test are summarized in the Figure 10. It's possible to note that in three specimens, respectively P70A, P70B and P80B, the surface resistance increases as the conditioning cycles progress.

A possible explanation of that behavior, could be that these three specimens have some fractures on the layer so the moisture permeates inside it, reducing the electrical conductivity of the layer itself.

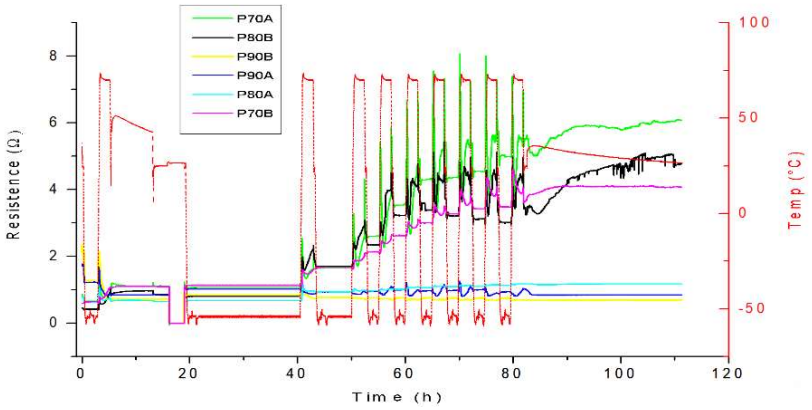

Figure 10 Electrical resistance measurements during GAG test

2.3.3 Electrical Resistance of Graphene Sheet

To evaluate the resistivity of each sample, a volt-amperometric measurement was made, using a KEITHLEY 6221 picoammeter in combination with a Metex M3850D multimeter which acts as a voltmeter**.**

Figure 11 Setup to measure the electrical resistence of graphene layers

By means of the picoammeter different quantities of current were supplied, in a range from 1mA to 100mA and with the voltmeter, the different voltages reached were recorded.

From the measurements carried out on different specimens with different charge of graphene was obtained:

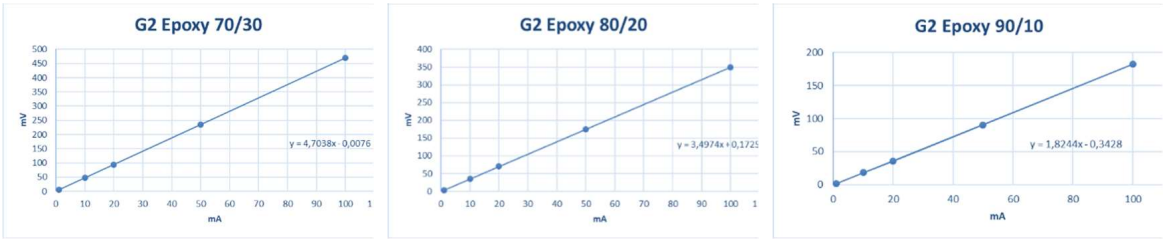

Figure 12 Volt-amperometric measurement on different samples of graphene charged sheets

In all the graphs shown above, a perfectly linear behavior is observed in the measurement range, furthermore the slope of the different lines give the value of the electrical resistance of each specimen.

Finally, considering the dimensions of the specimen, the resistivity value of each formulation can be obtained.

  doi:10.5075/epfl-298799_978-2-9701614-0-0

Table 2 Values of electrical resistivity of the sheets

Specimen	Resistence Ω	Width mm	Length mm	Thicknes µm	Resistivity Ωm
S 90/10	1,82	15,5	40	73	4,96388E-05
S 80/20	3,49	11	57	71	6,75439E-05
S 70/30	4,7	10	55	72	8,54545E-05

It is possible to note that as the graphene charge increases, the resistivity decreases, but the most interesting data is certainly in observing that the resistivity value of the graphene sheet loaded at 90% is only half higher than that of graphite (1.3E-05), which represents the theoretical natural limit for this material.

3. Conclusions

During the manufacturing of the specimens of it was possible to observe how the layers with high graphene content can be easily integrated into the manufacturing processes of a composite panel.
Experimental tests, carried out with the environmental chamber, have shown that the graphene layers are able to reduce significantly the moisture's permeation inside a composite panel as that widely used in aeronautics.
There was an evident delay in the absorption rate into the composite panels due to the presence of the protective layer, so, results motivate their use to protect composites in aeronautical field.

Acknowledgments

This work has been supported by the Research Project AMICO (code ARS01_00758) funded by the Italian Ministry of Education, University and Research.

4. References

1. Soutis C. Carbon fibre reinforced plastics in aircraft construction. Materials Science and Engineering: A. 2005; 412(1-2): 171-176.
2. https://ec.europa.eu/clima/policies/transport/aviation_en
3. ASTM D5229 –Standard Test Method for Moisture Absorption Properties and Equilibrium Conditioning of Polymer Matrix Composite Material.
4. https://www.imast.biz/it/progetti-in-corso/amico
5. Jungmo Kim, Sung Ho Song, Hyeon-Gyun Im, Gabin Yoon, Dongju Lee, Chanyong Choi, Jin Kim, Byeong-Soo Bae, Kisuk Kang, Seokwoo Jeon. Moisture Barrier Composites Made of Non-Oxidized Graphene Flakes. Small 2015; 11 26:3124-3129
6. Sivan Peretz Damari, Lucas Cullari, Roey Nadiv, Yiftach Nir, Dalia Laredo, Jaime Grunlan, Oren Regev. Graphene-induced enhancement of water vapor barrier in polymer nanocomposites. Composites Part B: Engineering 2018; 134: 218-224; ISSN 1359-8368

  doi:10.5075/epfl-298799_978-2-9701614-0-0

ANALYTICAL INVESTIGATION OF PROPAGATING STRAIN REDUCTION IN CFRP COMPOSITE LAMINATE SUBJECTED TO IMPULSIVE LOADING

Sho, Kajihara[a], Ryo, Higuchi[b], Tomohiro, Yokozeki[b], Takahira, Aoki[b]

a: Department of Aeronautics and Astronautics, University of Tokyo, Japan – kajihara@aastr.t.u-tokyo.ac.jp
b: Department of Aeronautics and Astronautics, University of Tokyo, Japan

Abstract: *The projective of this study is to identify the propagating strain in carbon fiber reinforced plastic (CFRP) composite fan blade due to bird strike and to investigate effects of suppressing it. The bird strike analysis of fan blade was simplified to analytical model of rectangular plate considering large deflection and transient response of composite blade impacted impulsive loading was calculated. This model showed detrimental spanwise strain wave propagates to the trailing edge of the blade and chordwise strain wave propagates to tip region. To suppress the peak of the strain, we focused on the lamination configuration which is the characteristics of the composite material. It was suggested that propagating strain can be reduced in the direction to which fiber direction of CFRP is aligned.*

Keywords: Fan Blade; Composite Materials; Structural Analysis; Vibration; Dynamics

1. Introduction

Carbon fiber reinforced plastic (CFRP) is widely used in aerospace structures and composite fan blades have been developed to reduce structural weight of aircraft engine. Fan blades could be subjected to high-speed collisions with foreign objects during flight and the most critical damage will occur due to bird strikes. In general, CFRP has inferior impact resistance in the out-of-plane direction compared to metal, so the leading edge of fan blades, which is the point of impact, is reinforced with a metal sheath. Many researches simulated bird strike phenomenon and have focused on damage and fracture under the impact. On the other hand, there is concern that the stress and strain waves generated by the impact propagate to the tips and trailing edges of the fan blades, resulting in failure in these areas. Siddens et al. performed finite element analysis and the results showed that the high von Mises stress happens in the tip and trailing edge immediately after the bird strike impact in Fig. 1 [1]. This result suggests that not only the damage in the leading edge region but also in the tip and trailing edge regions should be analyzed, but very few studies have examined in detail how impact waves propagate and how to reduce the propagating wave.

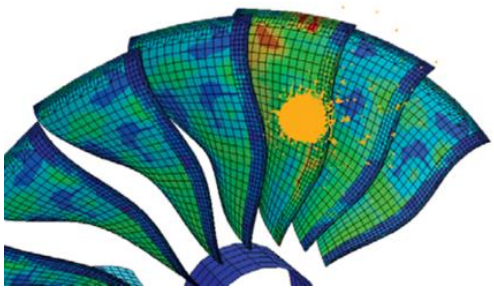

Figure 1. Distribution of von Mises stress caused by bird strike [1]

  doi:10.5075/epfl-298799_978-2-9701614-0-0

In many researches, finite element analyses are now mainly performed with the SPH method in the bird strike simulation, resulting in complex calculations and long computational time. Therefore, we proposed a simplified theoretical model of composite fan blade [2]. In this study, the model is used to calculate the transient analysis of composite fan blade impacted impulsive loading like bird strike. In addition, technological developments such as thinner prepreg layers [3] have made it possible to design structures with a variety of orientation angles. Considering this background and the characteristics of composite materials, the effect of reducing propagating strain by changing orientation angles and the stacking sequence of CFRP layers is discussed as one of the methods to reduce impact waves.

2. Theoretical model

2.1 Overview

In this study, the theoretical analysis was performed on a cantilever rectangular flat plate model with simplified fan blade as shown in Fig. 2. The overall coordinate system is set with the x-axis in the span direction, the y-axis in the chord direction, and the z-axis in the out-of-plane direction. The dimension of this model is referred to the previous research [4], with the span length L = 1000 mm, the chord length b = 500 mm and the thickness h = 20 mm. The leading edge is defined as a side with $y = -b/2$, the trailing edge as a side with $y = b/2$ and the tip as a side with $x = L$. To simulate bird impact loading, the external force $F(t)$ was applied as an impulsive loading in the region $L_b \times W_b$ = 100 mm × 100 mm with reference to the analysis results of Meguid et al. [5], and the coordinate of the center point of load is set as (x_b, y_b). The material properties of the CFRP used in this analysis is the reference value of longitudinal Young's modulus E_1 = 120 GPa, transverse Young's modulus E_2 = 7.9 GPa, In-plane shear modulus G_{12} = 5.5 Gpa, In-plane Poisson's ratio ν_{12} = 0.3, and density ρ = 1580 kg/m^3 [6]. The fiber orientation angle is defined as the angle from the x-axis and the standard lamination configuration is $[0/45/0/-45]_{8s}$, referring to the orientation angles of 0° and ±45° conventionally used in fan blade analysis. For simplicity, this analysis considers the impact response without the rotation effects.

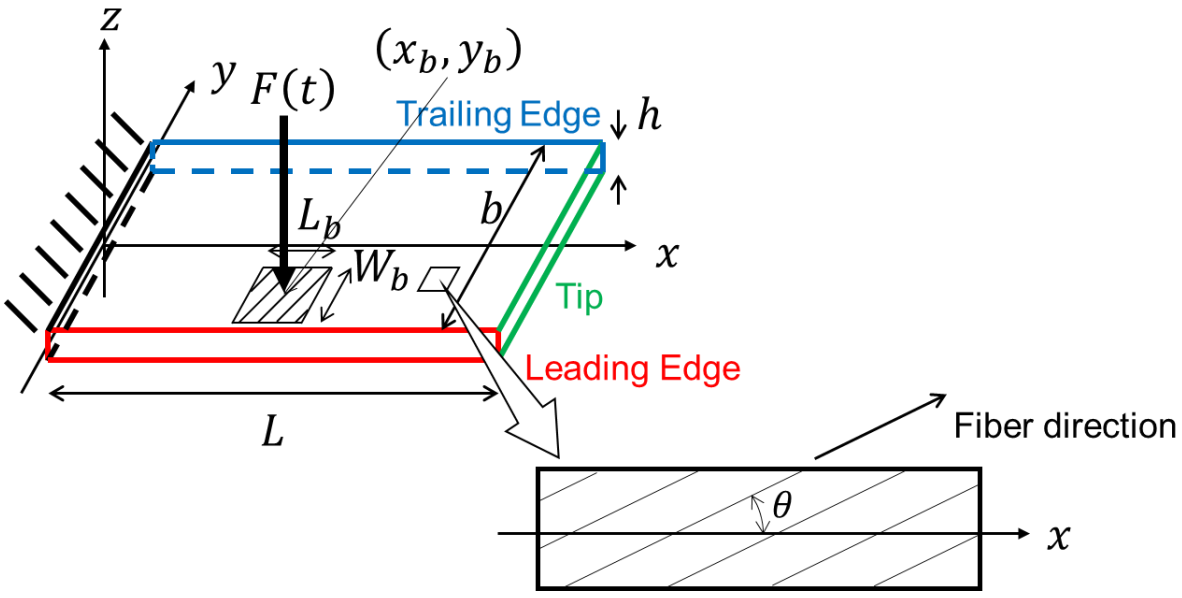

Figure 2. Analytical model of composite plate

2.2 Equation of vibration

Assuming the von Karman plate, the displacement-strain equation was expressed by using the central surface strain $\{\boldsymbol{\varepsilon}_0\}$ and the curvature $\{\boldsymbol{\kappa}\}$ as follows.

$$\begin{Bmatrix}\varepsilon_x\\ \varepsilon_y\\ \gamma_{xy}\end{Bmatrix}=\begin{Bmatrix}\varepsilon_{x_0}\\ \varepsilon_{y_0}\\ \gamma_{xy_0}\end{Bmatrix}+\begin{Bmatrix}\kappa_x\\ \kappa_y\\ \kappa_{xy}\end{Bmatrix}=\begin{Bmatrix}\frac{\partial u_0}{\partial x}+\frac{1}{2}\left(\frac{\partial w_0}{\partial x}\right)^2\\ \frac{\partial v_0}{\partial y}+\frac{1}{2}\left(\frac{\partial w_0}{\partial y}\right)^2\\ \frac{\partial u_0}{\partial y}+\frac{\partial v_0}{\partial x}+\frac{\partial w_0}{\partial x}\frac{\partial w_0}{\partial y}\end{Bmatrix}+\begin{Bmatrix}-\frac{\partial^2 w_0}{\partial x^2}\\ -\frac{\partial^2 w_0}{\partial y^2}\\ -2\frac{\partial^2 w_0}{\partial x\partial y}\end{Bmatrix} \tag{1}$$

Similar to the analysis of Zhao et al [7], the following displacement functions was used, assuming that superposition of linear modes can be used in the nonlinearlity of the large deformations associated with bird strike.

$$u_0(x,y,t)=\sum_m^{N_u} U_m(t)\xi_m(x,y)+\sum_i^{N'}\sum_j^{N'}\Phi_{ij}(t)\phi_{ij}(x,y) \tag{2}$$

$$v_0(x,y,t)=\sum_m^{N_v} V_m(t)\zeta_m(x,y)+\sum_i^{N'}\sum_j^{N'}\Psi_{ij}(t)\psi_{ij}(x,y) \tag{3}$$

$$w_0(x,y,t)=\sum_i^{N}\sum_j^{N} W_{ij}(t)X_i(x)Y_j(y) \tag{4}$$

where X_i and Y_j are the bending vibration mode functions for cantilevered and end-free beams. As for the in-plane vibration modes, it is assumed that they can be expressed by the addition of the in-plane free vibration mode terms U_m and V_m and the terms Φ_{ij} and ψ_{ij} caused by out-of-plane deformation. Thus, ξ_m and ζ_m are the in-plane vibration mode functions of the cantilevered flat plate and ϕ_{ij} and ψ_{ij} are described by X_i and Y_j to satisfy the geometric conditions of displacement. Furthermore, the kinetic energy T, potential energy Π, and external force work Q are expressed as follows.

$$T=\int_V \frac{1}{2}\rho\left\{\left(\frac{\partial u}{\partial t}\right)^2+\left(\frac{\partial v}{\partial t}\right)^2+\left(\frac{\partial w}{\partial t}\right)^2\right\}dV \tag{5}$$

$$\Pi=\int_S \frac{1}{2}\left\{\{\boldsymbol{\varepsilon}_0\}^T[\boldsymbol{A}]\{\boldsymbol{\varepsilon}_0\}+2\{\boldsymbol{\varepsilon}_0\}^T[\boldsymbol{B}]\{\boldsymbol{\kappa}\}+\{\boldsymbol{\kappa}\}^T[\boldsymbol{D}]\{\boldsymbol{\kappa}\}\right\}dA \tag{6}$$

$$Q=\int_S \left(q_x,q_y,q_z\right)\cdot(u,v,w)^{\mathrm{T}}dA \tag{7}$$

$$q_x=-F(t)\frac{\partial w_0}{\partial x},q_x=-F(t)\frac{\partial w_0}{\partial y},q_z=F(t)\left(1+\frac{\partial u_0}{\partial x}+\frac{\partial v_0}{\partial x}\right) \tag{8}$$

From the above equations, using the Hamilton's principle and the Rayleigh-Ritz method, the following nonlinear vibration equations are

$$\left[[\boldsymbol{M}]+[\boldsymbol{\rho I}]\right]\{\ddot{\boldsymbol{q}}\}+([\boldsymbol{K}]+[\boldsymbol{G}_{NL}(\ddot{\boldsymbol{q}},\dot{\boldsymbol{q}},\boldsymbol{q})])\{\boldsymbol{q}\}=\{\boldsymbol{f}(t)\}([\boldsymbol{I}]+[\boldsymbol{F}_{NL}(\boldsymbol{q})])\{\boldsymbol{f}(t)\} \tag{9}$$

Where,

$$\{\boldsymbol{q}\}=\left\{U_1\cdots U_{N_u},V_1\cdots V_{N_v},W_{11}\cdots W_{NN}\right\}^T \tag{10}$$

$[\boldsymbol{M}]$, $[\boldsymbol{\rho I}]$, $[\boldsymbol{K}]$ and $[\boldsymbol{I}]$ are the mass matrix, the rotational inertia matrix, the stiffness matrix, identity matrix, respectively, and $\{\boldsymbol{f}(t)\}$ is the external force vector. $[\boldsymbol{F}_{NL}]$ and $[\boldsymbol{G}_{NL}]$ are matrices that arise from the consideration of nonlinearity due to large deformations in the

  doi:10.5075/epfl-298799_978-2-9701614-0-0

calculation of the external force term and inertia effects, respectively, and depend on the displacement and the other factors. The nonlinear terms were described by using the lower 16 (N'=4) vibration modes with respect to W_{ij}, based on the calculations of Zhao et al [7]. The Newmark-β method was used for the numerical time integration of equation (6) and the value of β was set to 1/4, indicating unconditional stability. However, in order to calculate the nonlinear term, a convergence calculation was performed for the acceleration, and the convergence condition was set to be within 0.1% of the residual. The time step was 10^{-7} s and the analysis was performed up to 10 ms.

3. Results and discussion

3.1 Validation of theoretical model

Assuming a bird strike on the leading edge of the blade, the analysis was performed with the center coordinates of the impulsive loading set to (x_b, y_b) = (500,-200). The strain distributions at the maximum value of ε_x and ε_y in the transient response are shown in Fig. 3. In addition to the fixed edge, large strains are observed around trailing edge and tip, indicating that ε_x and ε_y are the main propagating strains at trailing edge and tip, respectively. Table 1 compares the maximum values of surface strain propagating to trailing edge and tip for different numbers of out-of-plane vibration modes N. Although the values converge as N increases, numerical errors due to higher-order modes can affect the analytical results, and therefore, N = 8 is used in following analyses.

In addition, finite element analysis (FEA) was performed using a nonlinear finite elements analysis software MSC Marc to validate the analytical model. 200 four-node quadrilateral thin shell elements with 20 divisions in the x-direction and 10 in the y-direction are included in the finite element model. The boundary conditions are shown in Fig. 4, with the nodes on x = 0 fixed in all degrees of freedom and the impulsive load applied as the pressure load. The time step was set to 10^{-7} s, the same as in the theoretical analysis, and calculations were performed using the nonlinear dynamic implicit solution. The results of FEA are also shown in Table 3, and this analytical model is considered to be appropriate, with a difference of about 2.5% compared to FEA.

Table 1 also shows the values of the strain ε_{x_0} and ε_{y_0} at the central surface when each surface strain has maximum value, which accounts for about 15% of the maximum surface strain. These are considered to be caused by the presence of $U_m, V_m - W_{ij}$ coupling matrix as components of $[\boldsymbol{F}_{NL}]$ and $[\boldsymbol{G}_{NL}]$ in Eq. (6). The maximum norm ratio of matrix is $|\boldsymbol{G}_{UW_{NL}}|/|\boldsymbol{K}_{WW}| = 6.21\times10^{-6}$, $|\boldsymbol{G}_{VW_{NL}}|/|\boldsymbol{K}_{WW}| = 1.09\times10^{-6}$, $|\boldsymbol{G}_{WW_{NL}}|/|\boldsymbol{K}_{WW}| = 1.78\times10^{-3}$, $|\boldsymbol{I}|/|\boldsymbol{F}_{UW_{NL}}| = 4.64\times10^{-4}$, $|\boldsymbol{I}|/|\boldsymbol{F}_{VW_{NL}}| = 1.35\times10^{-4}$. Due to these terms, the vibration of the central surface was induced by the out-of-plane vibration.

  doi:10.5075/epfl-298799_978-2-9701614-0-0

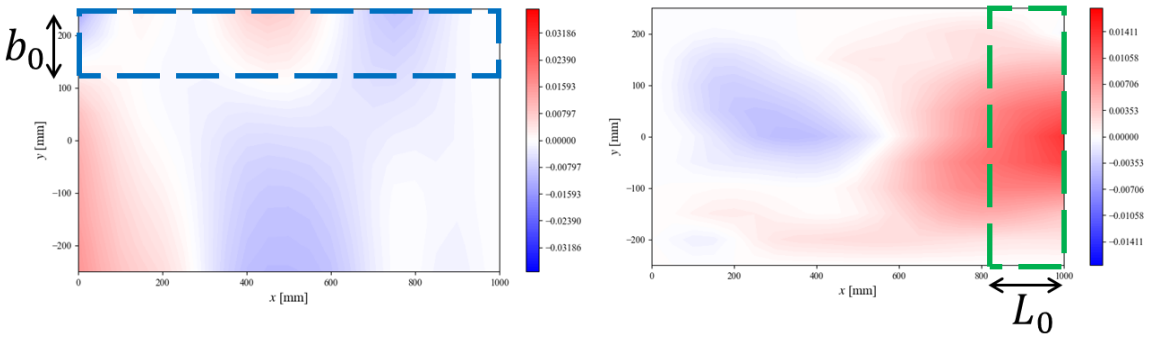

Figure 3. Distribution of the *x*-direction surface strain ε_x (*left*) *and the y*-direction surface strain ε_y (*right*)

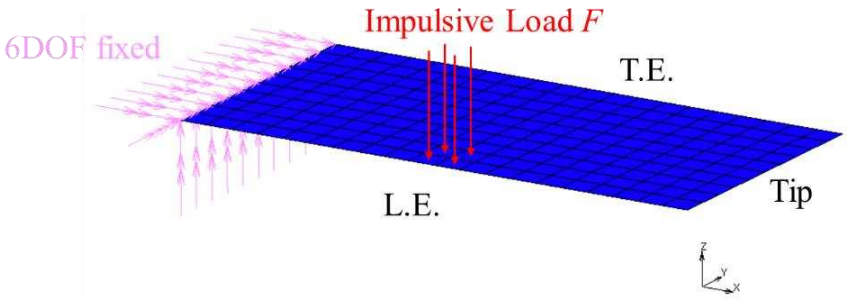

Figure 4. Finite element model of composite plate

Table 1: Strain in the transient response.

Number of modes, N	$\varepsilon_{x\max}$	$\varepsilon_{y\max}$	ε_{x_0}	ε_{y_0}
4	0.0169	0.0209	0.00261	0.00333
6	0.0168	0.0204	0.00250	0.00396
8	0.0165	0.0195	0.00241	0.00405
10	0.0168	0.0202	0.00237	0.00409
FEA	0.0161	0.0196	0.00163	0.00375

3.2 Reduction of strain

In order to suppress the propagation of critical strain to trailing edge and tip, we focused on the utilization of anisotropy, which is a characteristic of CFRP, and partially changed the orientation angle near the high strain generation region. For the protection of trailing edge region, the stacking sequence was changed to $[0/0/0/0]_{8s}$ only in the dashed line region for the length of b_0 from trailing edge shown in Fig. 2. Similarly, for tip region, the stacking configuration was set to $[0/90/0/90]_{8s}$ only in the dashed line area for the length of L_0 from tip shown in Fig. 2.

  doi:10.5075/epfl-298799_978-2-9701614-0-0

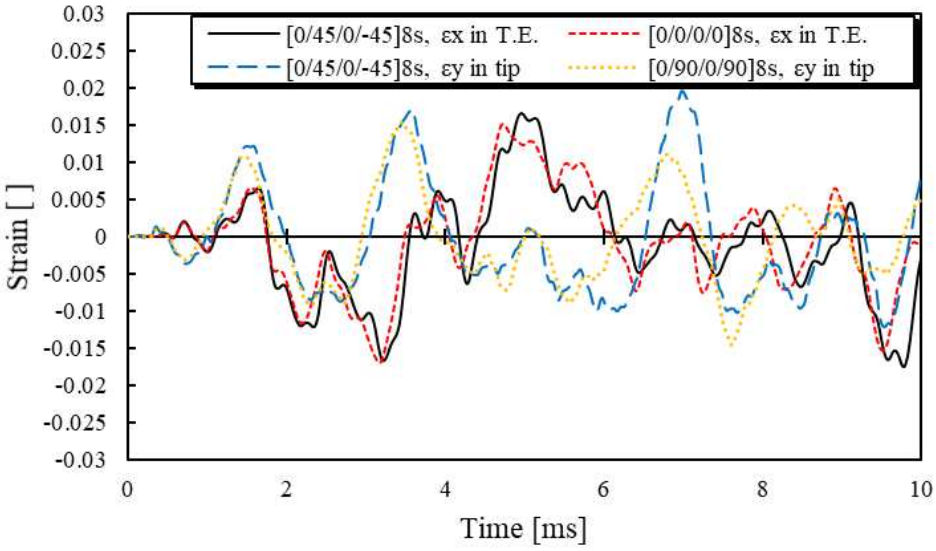

Figure 5. History of propagating strain at the trailing edge and tip of plate

The time history of ε_x at trailing edge when b_0 = 50 mm and the time history of ε_y at tip when L_0 = 50 mm are shown in Fig. 5. The maximum value of ε_x and ε_y was suppressed by increasing 0° and 90° layers, respectively. This is thought to be due to the increased fiber orientation in the x-direction, which increases stiffness in that direction and reduces the component of propagating ε_x wave, and the same can be considered for ε_y. So, these results suggest that the strain propagation of the component in the direction of fiber orientation can be reduced.

4. Conclusion

In this study, a vibration analysis model of composite laminate plate subjected to impulsive loading was performed to assume the bird strike phenomenon of a CFRP fan blade, and it was confirmed that the a large strain wave due to the impact load at leading edge propagates to trailing edge and tip of plate. Furthermore, by using a nonlinear displacement-strain relationship, it was confirmed that in-plane vibration is induced by the out-of-plane deformation. The effect of partially changing the lamination configuration on the strain propagating in the trailing edge and tip was also studied analytically. Strain oriented parallel to the fiber was suggested to be reduced and was confirmed to be dependent on the lamination distribution. This feature is useful for the structural design of composite laminates. Future research will use this model to study the effect of centrifugal force on the in-plane and out-of-plane motions of rotating fan blades, which is closer to the situation of actual fan blades.

Acknowledgements

This work was supported by JST SPRING, Grant Number JPMJSP2108.

5. References

1. A. Siddens, J. Bayandor and M. Celestina, “Detailed Post-Soft Impact Progressive Damage Assessment for Hybrid Structure Jet Engines”, National Aeronautics and Space Administration, Glenn Research Center, 2014.

  doi:10.5075/epfl-298799_978-2-9701614-0-0

2. S. Kajihara, T. Aoki, T. Yokozeki, R. Higuchi, “Impact response analysis of composite plate with different fiber orientation angles”, American Society for Composites 36th Technical Conference, 2021.
3. S. Shin, R. Y. Kim, K. Kawabe and S. W. Tsai, “Experimental studies of thin-ply laminated composites”, Composite Science and Technology, 67 (2007) : 996-1008.
4. S. K. Sinha, “Transient Response of a Multilayered Composite Rotating Airfoil Under Slicing-Impact Loading”, AIAA Journal, Vol. 52, No. 12, 2014.
5. S. A. Meguid et al., Int. J. Impact Eng., Vol. 35, 2008, 487-498. S. A. Meguid, R. H. Mao and T. Y. Ng, “FE analysis of geometry effects of an artificial bird striking an aeroengine fan blade”, International Journal of Impact Engineering 35 (2008) 487-498.
6. Q. Yibo and S. R. Swanson, “A comparison of solution techniques for impact response of composite plates”, Composite structures, 14.3 (1990): 177-192.
7. M. H. Zhao and W. Zhang, “Nonlinear dynamics of composite laminated cantilever rectangular plate subject to third-order piston aerodynamics”, Acta Mechanica, 225.7 (2014): 1985-2004.

  doi:10.5075/epfl-298799_978-2-9701614-0-0

GNP FILMS AS MOISTURE BARRIER IN KEVLAR/EPOXY SANDWICH COMPOSITES

Fabrizia Cilento[a,b], Michele Giordano[b], Giovangiuseppe Giusto[c], Ruggiero Volponi[c], Cinzia Toscano[c], Giovanni Barletta[d], Nicola Gallo[d], Alfonso Martone[b,e]
a: Department of Chemical Materials and Production Engineering, University of Naples Federico II;
b: Institute for Polymers, Composites and Biomaterials, National Research Council of Italy; alfonso.martone@cnr.it
c: CIRA, Italian Aerospace Research Centre;
d: Leonardo S.p.A. – Aerostructure Division;
e: IMAST S.c.ar.l. - Technological District on Engineering of polymeric and composite Materials and Str.

Abstract:

Composite structures are usually subjected to a wide range of environmental conditions whereby they can absorb a substantial amount of moisture from the environment, thus reducing their mechanical, thermal, electrical, and other physical properties and service times. Graphite nanoplatelet (GNP) based materials are a promising nanomaterial in barrier applications thanks to the ability of graphene sheets to block the diffusion of gases or liquids through its plane. In this work, the use GNP rich films with brick-and-mortar architecture at different filler content (up to 90%wt) has been investigated to assess the effectiveness of protection against water uptake. The graphene film has been co-cured onto the panel surfaces as an additional layer. Water uptake tests were carried out in an environmental chamber to reproduce the temperature and relative humidity profiles of a real scale application. The protective layer helped to delay the moisture absorption within the panels, results encourage their use in critical components.

Keywords: GNP; Water uptake; CFRP; barrier properties

1 Introduction

Severe environmental conditions can limit the use of polymeric composites, especially for applications in which high performances are required. In aerospace, one of the most important issues for this type of material is the exposure to humid and low/high temperature environments. Specifically, Kevlar-reinforced composites are prone to moisture uptake, due to the strong hygroscopic nature of both the resin and the fibre. Epoxy resins are strongly sensitive to water absorption because of large amounts of polar OH groups in the networks which facilitate attractive interactions with polar molecules such as water [1,2]. It was found that the maximum moisture absorption for epoxy is 2% at 70°C and for 100% RH [3]. On the other hand, moisture absorption of 6% is reported for Kevlar 49 aramid fibres when they are exposed to a high humidity environment (96% RH) [4].

This turns in possible degradation of the mechanical properties of the material [5–7]. The absorbed moisture in the matrix resin leads to the plasticization phenomenon, decreasing the glass transition temperature and also generating changes in the state of stress in favour of cracking through swelling [8–10]. As a consequence, the stress transfer at the fibre-matrix

  doi:10.5075/epfl-298799_978-2-9701614-0-0

interphase is compromised and the overall behaviour of the composite becomes more brittle: the impact strength and fracture toughness can even drop by 50% [11].
In order to block the water absorption in sandwich panels, barrier coatings can be employed. For aerospace composite applications, paints are used as moisture barrier films. Specifically, metallic coatings are added to the surface of the material also providing protection from electrostatic discharge, using the flame spray technique [12–14]. Although metallic coatings are effective in protecting composites from moisture uptake, they add extra weight to the structure. Among a variety of options, polymer-based films, such as polyvinyl fluoride (PVF) films, are extensively used in aerospace applications thanks to the low permeability for vapours and low ignition time [15,16].
In the last decade, it has been investigated the possibility of using graphite nanoplatelets (GNPs) to improve the barrier properties of polymers [17]. These nanoparticles are a promising nanomaterial in gasor liquid-barrier applications thanks to the ability of perfect graphene sheets to prevent the diffusion of small gases or liquids through its plane.
To fulfil this function, films with special architecture can be employed as protective coatings for composites. In particular, biomimetic materials, with brick and mortar (B&M) architecture are gaining attention due to the possibility of reproducing on large scale the properties of the brick. Films with brick and mortar architecture based on GNPs have been fabricated [18–20]. The hydrophobic nature of GNPs combined with the very high in-plane orientation of nanoplatelets and the low matrix content, create an impervious path for vapour and gases [21,22]. Consequently, the high tortuosity factor leads to high barrier properties and low permeability.
In this work, the authors investigated the possibility of employing GNPs rich films with brick-and-mortar architecture as moisture-proof materials. Graphene films with high filler content have been integrated into Kevlar/Epoxy panels in a one-step manufacturing process. Several panels have been fabricated with protective layers with different filler content (70, 80, 90 wt%). The effectiveness of protection against water uptake has been investigated through a moisture uptake test in an environmental chamber and the level of damage in the panels has been investigated with a non-destructive inspection. Results indicate that graphene films are able to protect the panel from water absorption, with a reduction of the maximum absorption after 40 days of 30%. Also, the easy integration of the films in the manufacturing process of composites, in a co-curing process, ensures a reduction in the processing time and improves energy saving.

2 Materials and methods

Kevlar sandwich panels, employed in the construction of a nacelle engine of an ATR42 aircraft, have been considered in this study. Both panels with and without protection, have been fabricated (Table 2). Samples are faithful to the real configuration of the nacelle, following the lamination lay-up with prepregs skins on the bottom and upper surface and a honeycomb core made of NOMEX with an angle of 18°± 3° (Figure 1).
The total dimension of the samples is 180 x 180 mm^2, with a core footprint of 140 x 140 mm^2 on the lower surface and of 50 x 50 mm^2 on the upper surface.
Figure 2a reports the phases of the manufacturing process, which include lamination lay-up of the lower skin, core positioning and lamination lay-up of the upper skin.
The GNP rich films are integrated on both the lower and upper surfaces of the panel, by stratifying them as superficial layers. The panels are then placed in a vacuum bag (Figure 2b) and

  doi:10.5075/epfl-298799_978-2-9701614-0-0

cured in an oven for 2h at 120°C. Finally, all samples have been trimmed and sealed on the edges. The manufacturing process of coated and uncoated panels follows the same protocols.
The GNP rich films are fabricated following a top-down approach, based on a spray deposition process. These films are preimpregnated with an epoxy resin (Hexcel RTM6) at different contents (70, 80, 90 wt%). Details of the fabrication process are reported in previous work [18]. Films have a thickness of 70±6 µm and a weight of 80-90 g/m^2.
Thermogravimetric analysis (TGA) (TA Instruments Q500) is conducted to evaluate the real composition of GNP/Epoxy films. Measurements are performed in an inert atmosphere, using nitrogen gas, with a temperature ramp of 10°C/min from room temperature to 700 °C. The weight loss is evaluated at 600 °C, temperature at which the percent residue from heating the pure resin is 10.3% [23].

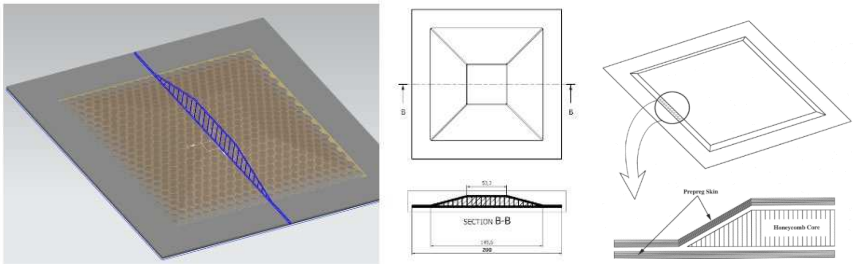

Figure 1. Geometry of the Kevlar sandwich panel

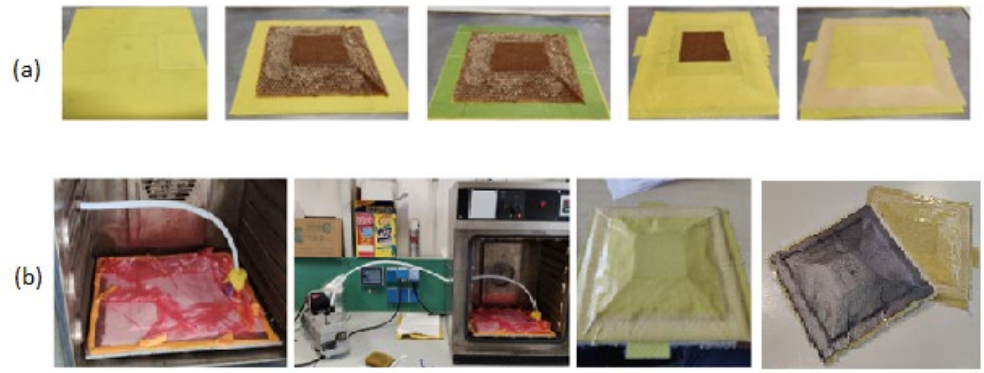

Figure 2. Panel manufacturing: (a) Lamination lay-up; (b) Curing

The moisture uptake test was performed according to [24]. The test consists in monitoring the moisture uptake during the time. All samples, listed in Table 1, are placed in a climatic chamber (Angelantoni CH 2000) at a controlled temperature of 70°C, with a relative humidity of 85% for 40 days. They are fixed on a metallic grid to avoid movements during the test, using four bolts accurately covered with tacky tape, as shown in Figure 3a-c.
The samples have been weighted every 3 days in the first week and then every week as indicated in Table 2. Before weighting the panels, samples have been dried with a paper towel in order to eliminate the excess water. For each sample the measure has been repeated three times.
Non-destructive inspection (NDI) has been conducted to investigate the internal structure of the panels. Analyses have been conducted before and after the test, to assess the potential damage of the panels when placed in a moist environment. Lock-in thermography has been employed and images of the samples at 0.1 Hz and 0.04 Hz have been acquired.

  doi:10.5075/epfl-298799_978-2-9701614-0-0

(a) (b) (c)

Figure 3. (a) Panels positioning on the metallic grid; (b) Uncoated panel; (b) GNP coated panel

Table 1. Weighing schedule for moisture uptake test

Weight	time (days)	time (hr)
W_0	0	0
W_1	3	72
W_2	6	144
W_3	13	312
W_4	20	480
W_5	27	648
W_6	34	816
W_7	41	984

3 Results and discussion

The sorption curves of the Kevlar/epoxy sandwich with and without the protection are shown in Figure 4, where moisture uptake is plotted against the square root of time.
The moisture uptake, *M*, is evaluated according to Eq. (1) [24]:

$$M(t) = \frac{W(t) - W_0}{W_0} \% \tag{1}$$

Where W_0 is the panel weight at time t=0, before conditioning the samples, and W(t) is the weight of the panel at each weighing step.
Results show that the graphene layer improves the resistance to moisture uptake, both in terms of maximum absorbance and diffusion rate. A reduction of 30% of the maximum moisture absorption has been observed in protected samples with respect to the reference Kevlar/epoxy sandwich (Table 4). The graphene layer also modifies the absorption kinetics. In fact, the absorption rate is slower in protected samples, thanks to the tortuous path created by the well-oriented GNP nanoparticles. The inner architecture of graphene films (Figure 5), combined with the hydrophobic nature of GNPs, forces the gas molecules to move in a tortuous path, resulting in a reduction of the diffusion through the protective film.
As the filler content decreases from 90 wt% to 70 wt%, the moisture uptake decreases. This effect is associated with the material's nanoarchitecture. Morphological observations of previous works [18,25] have revealed that the maximum level of compaction in GNP/Epoxy films

is reached at 70 wt%. By increasing the filler content up to 90 wt%, the nanostructure is affected by dry spots and voids, as shown in Figure 5. These areas may be detrimental to the barrier effect since more moisture penetrates and remains trapped. As a consequence, the moisture uptake in panels protected with graphene films with 90 wt% filler content is higher (2.9%) than that of panels coated with graphene film with 70 wt% filler content (2.2%). However, this value is significantly lower than that of the uncoated panel (3.4%).

Table 2. List of tested panels and maximum moisture uptake after 41 days

ID	Coating	Real filler content	M (@41 days)
Panel 001	-	-	3.4%
Panel 002	2 films (70 wt% GNP)	70 wt%	2.2%
Panel 003	2 films (80 wt% GNP)	77 wt%	2.7%
Panel 004	2 films (90 wt% GNP)	91 wt%	2.9%
Panel 005	2 films (70 wt% GNP)	70 wt%	2.3%
Panel 006	2 films (80 wt% GNP)	86 wt%	2.7%

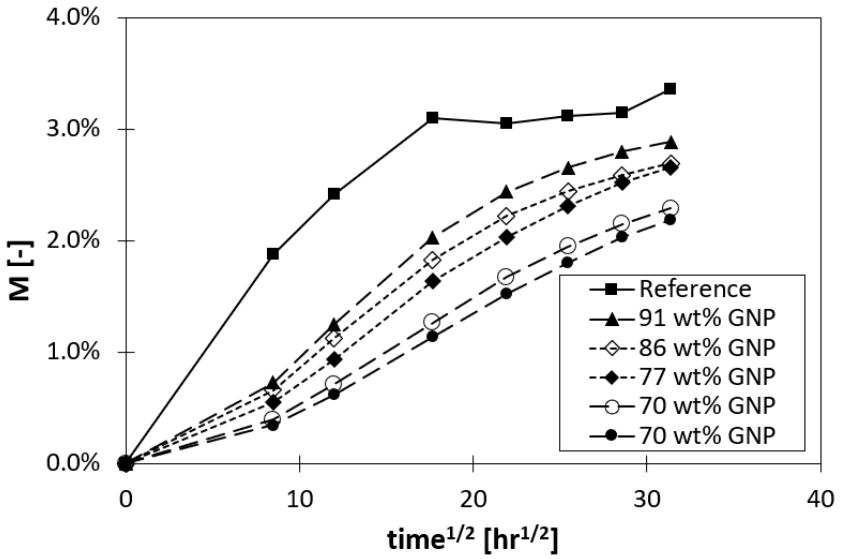

Figure 4. Moisture uptake in percentage for uncoated and coated samples

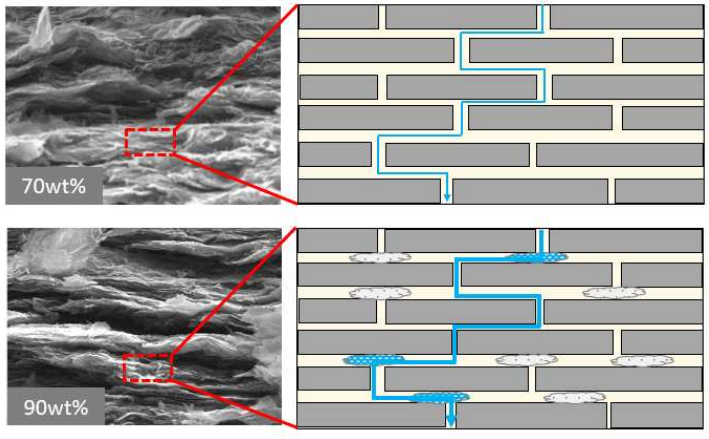

Figure 5. Scheme of brick-and-mortar architecture of graphene films at the various filler content

Figure 6 and Figure 7 show the results of the NDI analysis conducted on the lower surface of the samples at different frequencies of 0.1 Hz and 0.04 Hz. By decreasing the frequency, different depths of the samples are investigated; at 0.04 Hz it is even possible to observe the taper of the inner core. However, by comparing the images of samples before and after the test it appears that the induced stress of the moisture uptake test does not produce any damage.

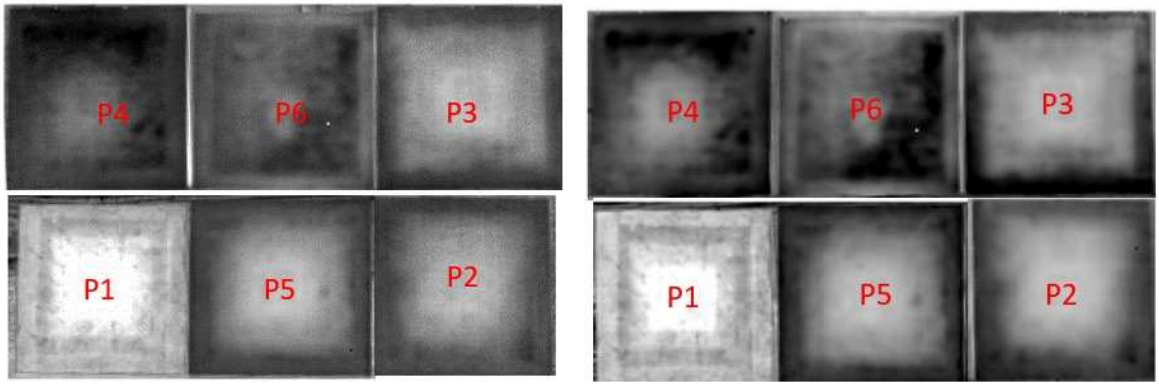

(a) (b)

Figure 6. Thermal images: (a) before the test; (b) after the test at 0.1 Hz

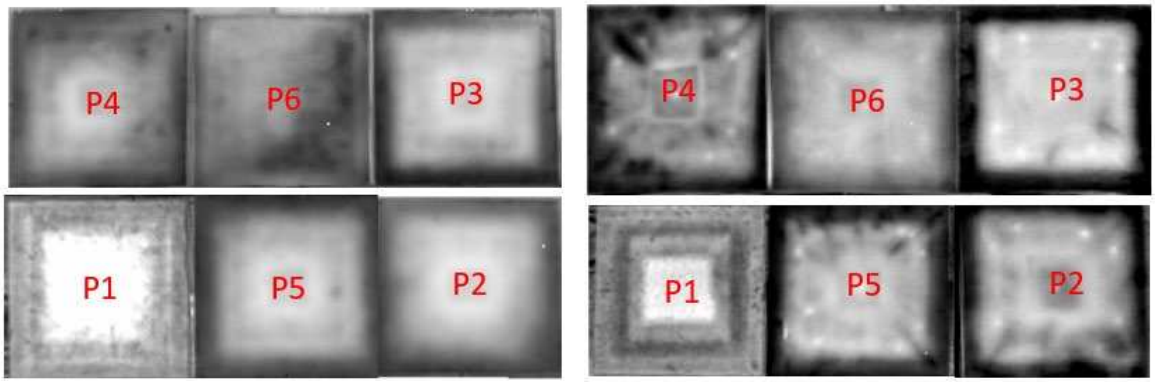

(a) (b)

Figure 7. Thermal images: (a) before the test; (b) after the test at 0.04 Hz

4 Conclusions

The effectiveness of protection against water uptake of graphene rich films has been investigated through a moisture uptake test in an environmental chamber.

It has been demonstrated the ability of graphene films to protect Kevlar/Epoxy panels from water absorption. After 40 days in a humid environment, the maximum sorption of the coated panel is 30% lower than that of the uncoated one. Thanks to the nanoplatelet alignment and their intrinsic hydrophobicity, the film acts as a barrier to moisture. The effect of graphene films architecture has been investigated, showing that the level of compaction of GNPs is crucial for the barrier properties. The use of a film loaded with 90 wt% GNP is not convenient since the nanostructure is affected by voids, which promote absorption. Thus, an optimal GNP content of 70 wt% is found. Finally, NDI analysis with lock-in thermography shows the absence of damage in all panels after the moisture uptake test.

  doi:10.5075/epfl-298799_978-2-9701614-0-0

Acknowledgements

This work has been supported by the Research Project AMICO (code ARS01_00758) funded by the Italian Ministry of Education, University and Research.

References

1. Eckstein, B.H. Moisture Absorption by Epoxy Laminating Resins. In Proceedings of the ABSTRACTS OF PAPERS OF THE AMERICAN CHEMICAL SOCIETY; AMER CHEMICAL SOC 1155 16TH ST, NW, WASHINGTON, DC 20036, 1978; Vol. 175, p. 98.
2. Olmos, D.; López-Morón, R.; González-Benito, J. The Nature of the Glass Fibre Surface and Its Effect in the Water Absorption of Glass Fibre/Epoxy Composites. The Use of Fluorescence to Obtain Information at the Interface. *Compos. Sci. Technol.* **2006**, *66*, 2758–2768, doi:10.1016/j.compscitech.2006.03.004.
3. Verpoest, I.; Springer, G.S. Moisture Absorption Characteristics of Aramid-Epoxy Composites. *J. Reinf. Plast. Compos.* **1988**, *7*, 2–22, doi:10.1177/073168448800700101.
4. Gopalan, R.; Rao, R. m. v. g. k.; Murthy, M.V.V.; Dattaguru, B. Diffusion Studies on Advanced Fibre Hybrid Composites. *J. Reinf. Plast. Compos.* **1986**, *5*, 51–61, doi:10.1177/073168448600500105.
5. Kim, K.S. Hygroscopic Effects in Aramid Fiber / Epoxy Composite. **2017**, *110*, 153–157.
6. Xiao, G.Z.; Shanahan, M.E.R. Water Absorption and Desorption in an Epoxy Resin with Degradation. *J. Polym. Sci. part B Polym. Phys.* **1997**, *35*, 2659–2670.
7. Wan, Y.Z.; Wang, Y.L.; Huang, Y.; Luo, H.L.; He, F.; Chen, G.C. Moisture Absorption in a Three-Dimensional Braided Carbon/Kevlar/Epoxy Hybrid Composite for Orthopaedic Usage and Its Influence on Mechanical Performance. *Compos. Part A Appl. Sci. Manuf.* **2006**, *37*, 1480–1484, doi:10.1016/j.compositesa.2005.09.009.
8. McKague Jr, E.L.; Reynolds, J.D.; Halkias, J.E. Swelling and Glass Transition Relations for Epoxy Matrix Material in Humid Environments. *J. Appl. Polym. Sci.* **1978**, *22*, 1643–1654.
9. Mijović, J.; Lin, K. The Effect of Hygrothermal Fatigue on Physical/Mechanical Properties and Morphology of Neat Epoxy Resin and Graphite/Epoxy Composite. *J. Appl. Polym. Sci.* **1985**, *30*, 2527–2549.
10. Xiao, G.Z.; Shanahan, M.E.R. Swelling of DGEBA/DDA Epoxy Resin during Hygrothermal Ageing. *Polymer (Guildf).* **1998**, *39*, 3253–3260.
11. Yahaya, R.; Sapuan, S.M.; Jawaid, M.; Leman, Z.; Zainudin, E.S. Water Absorption Behaviour and Impact Strength of Kenaf-Kevlar Reinforced Epoxy Hybrid Composites. *Adv. Compos. Lett.* **2016**, *25*, 98–102, doi:10.1177/096369351602500403.
12. Sturgeon, A.; Dunn, B.; Celotto, S.; O'Neill, W. Cold Sprayed Coatings for Polymer Composite Substrate. *ESA SP* **2006**, *616*, 1–5.
13. Edrisy, A.; Perry, T.; Cheng, Y.T.; Alpas, A.T. The Effect of Humidity on the Sliding Wear of Plasma Transfer Wire Arc Thermal Sprayed Low Carbon Steel Coatings. *Surf. Coatings Technol.* **2001**, *146–147*, 571–577, doi:https://doi.org/10.1016/S0257-8972(01)01434-7.
14. Boningari, T.; Inturi, S.N.R.; Suidan, M.; Smirniotis, P.G. Novel One-Step Synthesis of Sulfur Doped-TiO2 by Flame Spray Pyrolysis for Visible Light Photocatalytic Degradation of Acetaldehyde. *Chem. Eng. J.* **2018**, *339*, 249–258, doi:https://doi.org/10.1016/j.cej.2018.01.063.
15. Kececi, E.; Asmatulu, R. Effects of Moisture Ingressions on Mechanical Properties of Honeycomb-Structured Fiber Composites for Aerospace Applications. *Int. J. Adv. Manuf. Technol.* **2017**, *88*, 459–470, doi:10.1007/s00170-016-8744-8.
16. Kececi, E.; Asmatulu, R. Effects of Moisture Ingression on Polymeric Laminate Composites and Its Prevention via Highly Robust Barrier Films. *Int. J. Adv. Manuf. Technol.* **2014**, *73*,

1657–1664, doi:10.1007/s00170-014-5974-5.
17. Cui, Y.; Kundalwal, S.I.; Kumar, S. Gas Barrier Performance of Graphene/Polymer Nanocomposites. *Carbon N. Y.* **2016**, *98*, 313–333, doi:10.1016/j.carbon.2015.11.018.
18. Cilento, F.; Martone, A.; Pastore Carbone, M.G.; Galiotis, C.; Giordano, M. Nacre-like GNP/Epoxy Composites: Reinforcement Efficiency Vis-à-Vis Graphene Content. *Compos. Sci. Technol.* **2021**, *211*, 108873, doi:10.1016/j.compscitech.2021.108873.
19. Wu, H.; Drzal, L.T. Graphene Nanoplatelet Paper as a Light-Weight Composite with Excellent Electrical and Thermal Conductivity and Good Gas Barrier Properties. *Carbon N. Y.* **2012**, *50*, 1135–1145, doi:10.1016/j.carbon.2011.10.026.
20. Li, X.; Manasrah, A.; Al-ostaz, A.; Alkhateb, H.; Lincoln, D.; Rushing, G.; Cheng, A.H. Preparation and Characterization of High Content Graphene Nanoplatelet-Polyetherimide Paper. *J. Nanosci. Nanoeng.* **2015**, *1*, 252–258.
21. Li, J.; Wang, S.; Lai, L.; Liu, P.; Wu, H.; Xu, J.; Severtson, S.J.; Wang, W.-J. Synergistic Enhancement of Gas Barrier and Aging Resistance for Biodegradable Films with Aligned Graphene Nanosheets. *Carbon N. Y.* **2021**, *172*, 31–40, doi:https://doi.org/10.1016/j.carbon.2020.09.071.
22. Leone, C.; Genna, S.; Bertocchi, F.; Giordano, M.; Martone, A. A Procedure to Measure the Emissivity of Ultra-Thin Graphene Based Film in Long Wavelength Infrared (LWIR) Spectrum Region, Optics and Lasers in Engineering. *Opt. Laser Technol.* **2021**, *138*, 106910, doi:10.1016/j.optlastec.2020.106910.
23. Formicola, C. Insight of Thermo-Mechanical and Fire Properties of an Aerospace Epoxy Matrix Loaded with Micro and Nano Fillers . Insight of Thermo-Mechanical and Fire Properties of an Aerospace Epoxy Matrix Loaded with Micro and Nano Fillers ., 2008.
24. ASTM-D5229 Standard Test Method for Moisture Absorption Properties and Equilibrium Conditioning of Polymer Matrix Composite Materials 2020.
25. Cilento, F.; Martone, A.; Cristiano, F.; Fina, A.; Giordano, M. Effect of Matrix Content on Mechanical and Thermal Properties of High Graphene Content Composites. *MATEC Web Conf.* **2019**, *303*, 01002, doi:10.1051/matecconf/201930301002.

GRAPHENE/EPOXY NANOCOMPOSITES FOR THERMOSETS RESISTIVE CURING

Yuheng Huang, Ian Kinloch, Cristina Valles

yuheng.huang-2@postgrad.manchester.ac.uk
Department of Materials and National Graphene Institute, University of Manchester, UK

Abstract:

Epoxy composites reinforced by graphene nanoplatelets (GNPs) have been probed to be successfully cured through resistive heating by a simple Joule heating effect of the electrically conductive network of flakes in the matrix above percolation, which can transform effectively the electric energy into heat. This novel out-of-autoclave curing method holds great potential to replace the conventional oven (or autoclave) curing method and, thus, overcome all the drawbacks associated to oven curing, e.g. huge energy consumption and size limitation. Oven-cured and electrically-cured GNPs/epoxy nanocomposites were prepared in this work by combining the solution mixing and mechanical mixing techniques, followed by curing performed in an oven or, alternatively, through resistive heating of the conductive network of GNPs formed in the epoxy matrix above percolation. Results from DSC revealed that the electrically cured samples led to a complete curing, comparable to that found for the samples cured using the conventional oven. The potential of using this GNPs/epoxy composite mixtures as conductive adhesives to repair CFs/epoxy components through resistive heating is also investigated here.

Keywords: Graphene, Epoxy; Joule heating effect; Carbon Fibres; Composites reparation

1. Introduction

Due to their good physical and chemical properties, such as high strength, low thermal expansion and chemical inertness, thermosetting polymers such as epoxy resins are widely used in the automotive, aerospace and construction sectors. They are characterized because they need a curing process to go from their natural liquid state to a solid polymer or composite material with optimal properties. These curing processes normally involve a heating step, which is typically performed in an oven or autoclave, being this autoclave curing the most widely used method for the fabrication of epoxy-based components (*e.g.* carbon fibres (CFs)/epoxy composites) in industrial sectors such as the aircraft industry. Even though this method is effective and has been used for many years, it has a number of obvious disadvantages, being labour-intensive production, high-energy consumption, complicated quality control, and high cost the most relevant examples [1,2]. Hence, in recent years there has been an increasing interest in developing out-of-autoclave (OoA) methods for thermoset curing, that can replace the use of the conventional autoclave to cure and repair those CFs composites. Resistive curing or Joule heat curing of epoxy composites filled with conductive filler particles emerges as one of the most promising alternatives, showing an enormous potential to replace the use of an autoclave for that purpose.

The addition of electrically conductive carbon nanomaterials into an epoxy matrix above the percolation threshold has recently been probed to provide these nanocomposites with outstanding electrothermal performance [3]. Indeed, the electrically conductive network of these nanoparticles formed in the polymer matrix above percolation shows the ability to act as integrated nanostructured heaters transforming effectively electric current into heat through a

  doi:10.5075/epfl-298799_978-2-9701614-0-0

simple Joule heating effect. This property of conductive epoxy nanocomposite systems will provide a good basis for the development of novel thermoset curing methods based on resistive heating, with great potential to replace the conventional autoclave curing method, which will definitely open the door to novel applications in the aerospace industry. Herein the electrothermal properties of an electrically conductive graphene/epoxy composite system are investigated and its potential as a conductive 'adhesive' to repair CFs/epoxy composites is explored.

2. Experimental Part

2.1 Preparation of GNPs/epoxy nanocomposites

Graphene nanoplatelets (GNPs) M25 from XG Sciences with lateral lengths of ∼25 μm and a thickness of ∼6 nm as quoted by the manufacturer were used as the filler in this work. The epoxy resin (Araldite LY5052) and the hardener (HY5052) were supplied by Huntsman.

GNPs/epoxy nanocomposites with different loadings of GNPs were fabricated following the experimental procedure schematically represented in Figure 1. Initially, the right amount of GNPs powder was added to 400 ml of acetone, followed by bath sonication for 1.5 h in order to get a good dispersion of the GNPs in the solvent. After that time, the epoxy resin was added to the dispersion and mixed using a high shear speed mixer for 1h at 400 rpm. The mixture was then left under mechanical stirring at 60 °C overnight to remove completely the acetone. Once it has been completely removed, the hardener was added to the mixture (epoxy:hardener weight ratio = 100: 38, as suggested by the manufacturer to achieve the optimal mechanical properties) and was mixed manually for several minutes to ensure a homogeneous mixture, which was then degassed under vacuum for 20 mins in order to remove air and avoid the formation of voids. The uncured composite mixtures were then cast into a mould to be cured. The curing process comprised two different steps: (i) initially the epoxy and the GNPs/epoxy nanocomposites were pre-cured for 24 h at room temperature; (ii) the post-curing step was performed at 100 °C for 4 hours. This second curing step, which involved heating, was performed in two different ways: heating the samples using a conventional oven (these samples are labelled as 'oven-cured') and, alternatively, heating them through resistive heating (these samples are labelled as 'electrically-cured'). Pure epoxy and GNPs/epoxy nanocomposites at GNPs loadings from 1 to 11 wt.% were fabricated using the conventional oven curing method, whereas only GNPs/epoxy composites at loadings above percolation threshold were fabricated using the resistive heating curing method. To prepare the resistive cured samples, copper tape ribbons were used as the electrodes to conduct electric current through the thickness direction (z direction), as schematically represented in Figure 2. The cured samples were then demould and cut into specimens with the required shape and dimensions for characterization.

  doi:10.5075/epfl-298799_978-2-9701614-0-0

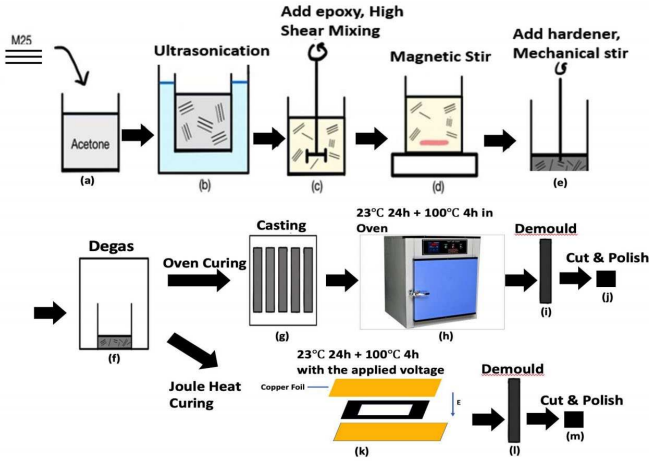

Figure 1. Schematic of the experimental procedure to fabricate oven-cured and resistive cured GNP/epoxy nanocomposites.

Figure 2. Schematic of the set-up employed for the electrically curing step. The red arrow indicates the direction of the applied voltage.

2.2 Characterization of the electrical conductivity of the GNPs/epoxy nanocomposites

The impedance of the oven-cured GNPs/epoxy composites in the range of frequencies 1-10^6 Hz was determined using a PSM 1735 Frequency Response Analyzer from Newtons4th Ltd, connected to an Impedance Analysis Interface (IAI). The specific conductivity (σ) of the nanocomposites was calculated from the impedance using Eq. (1).

$$\sigma = \frac{1}{Z^*} * \frac{t}{A} \quad (1)$$

where Z^* is the complex impedance, and t and A are the thickness and the cross-section area, respectively, of the cured composite samples. The electrical conductivity of the oven-cured samples were determined both in-plane (x direction) and out-of-plane (z direction) as schematically shown in Figure 4a.

Composites with loadings above the percolation threshold found for the oven-cured system were selected to fabricate the electrically-cured composites, and their electrical conductivity was determined both in the direction parallel and perpendicular to the applied voltage (*i.e.* along the directions x, y, according to the schematic shown in Figure 4a).

2.3 Differential Scanning Calorimetry

Differential Scanning Calorimetry (DSC) was used to evaluate the degree of curing of both the oven-cured and the electrically-cured GNPs/epoxy nanocomposites using a DSC Q100 Analyzer

  doi:10.5075/epfl-298799_978-2-9701614-0-0

from TA instruments. A heating ramp of 10 °C/min from room temperature to 200 °C was employed in all the cases.

2.4 Reparation of Carbon fibres (CF)/epoxy laminates through resistive heating of GNPs/epoxy composites

Plain woven Hexcel (USA) HexTow® carbon fibres (CF) were purchased from Sigmatex (UK). The epoxy used to fabricate the CF/epoxy laminates was the same used to fabricate the GNPs/epoxy composites. Six layers of the plain woven CFs were layed up in a stacking sequence of $[0\,°/90\,°]_s$ and the laminates were prepared by liquid resin infusion. They were then cut into small pieces according to the ASTM D1002 standard for single lap-shear test [4] for the reparation process.

The GNP/epoxy nanocomposites were used as an adhesive to repair CFs/epoxy laminates, that is, to connect two parts of them which were initially separated. For that, two copper tape ribbons were used as the electrodes to apply electric current through an uncured electrically conductive GNPs/epoxy composite mixture to cure it through resistive heating, as schematically represented in Figure 3. A FLIR T460 Infrared camera was used to monitor the temperature generated by the GNPs/epoxy composite when an external electric field was applied to it.

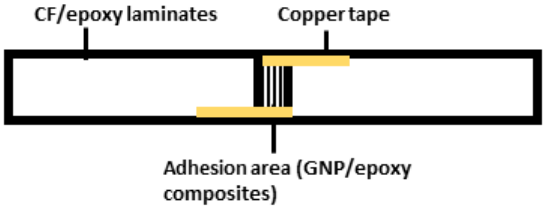

Figure 3. Schematic of the set-up to repair CF/epoxy laminates through resistive heating of a GNPs/epoxy composite used as a conductive adhesive placed in the adhesion area.

3. Results and Discussion

3.1 Electrical properties of the oven-cured GNPs/epoxy composites

In order to evaluate their electrical properties and establish the percolation threshold, the electrical conductivity of the GNPs/epoxy nanocomposites with different loadings of GNPs cured in the oven were determined along two perpendicular directions (x and z, according to the schematic shown in Figure 4a), using the method described in the experimental part. The relationship between the filler loading and the electrical conductivity (in log scale) is shown in Figure 4. From Figure 4 it can be clearly seen that this system behaves as a typical percolated system, where at low loadingds of conductive filler particles the system is not conductive, and as the filler loadings is increased more and more condutive paths of the filler particles are formed in the polymer matrix as the filler particles start connecting to each other. Since it is a percolated system, the classic percolation theory can be applied to determine both the percolation threshold and t (the critical exponent), using Eq. (2):

$$\sigma = \sigma_0 (P - P_c)^t \quad (2)$$

  doi:10.5075/epfl-298799_978-2-9701614-0-0

where σ is the electrical conductivity of the composite, σ_0 is the pre-exponential factor which is related to the conductivity of the epoxy, P_c is the percolation threshold (critical concentration) and *t* is the conductivity exponent, which is related to the dimensionality of the system.

Figure 4b and Figure 4c show the typical behaviour of a percolaed system of the oven-cured GNP/epoxy composites in both studied directions (x and z), with the percolation threshold found ~7 wt.% in both directions. The value of *t* found here was 2.58 (x direction) and 1.45 (z direction), respectively, which suggesting that these composites behave as a 3D conductive system [5]. Finally, it can be seen that very similar values of conductivity were found in the two directions studied, showing clearly an isotropic electrical behaviour. We can, thus, conclude saying that the flakes in the oven-cured samples are randomly oriented.

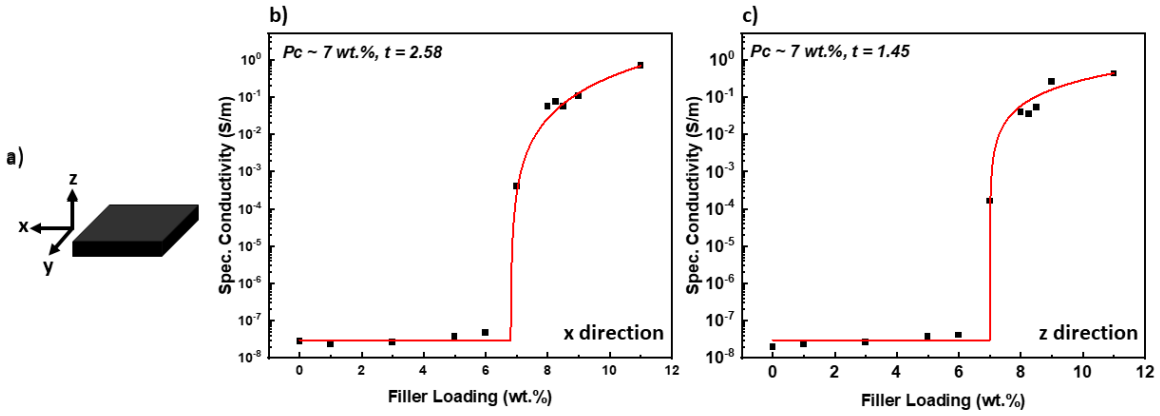

Figure 4. a) Schematic of the oven-cured nanocomposites showing the directions along which the electrical conductivity was measured; Electrical conductivity vs. GNP loading (wt.%) for the oven-cured GNPs/epoxy composites determined along : b) x direction, and c) z direction

3.2. Resistive curing of GNPs/epoxy composites

GNPs/epoxy composites at loadings above the percolation threshold found for the oven-cured system were prepared using the method described in the experimental section. When an electric current was passed through the system, the conductive 3D network of flakes embedded in the polymer matrix were acting as integrated nanoheaters transforming the electric current into heat through a simple Joule heating effect. The generated heat was monitored using an IR camera and could be controlled by controlling the applied voltage to keep it at 100 °C for 4 hours (Figure 5a). Figure 5b shows the DSC curves of the pure epoxy and the GNPs/epoxy composites fabricated by both the oven curing method and the resistive curing method at filler loadings of 8 wt.% and 9 wt.%. The values found for the T_g of the composites were very close to that found for the pure epoxy, revealing that an effective curing process took place for both methods (oven and resistive heating). This clearly gives light to the idea of developing novel out-of-autoclave thermoset curing methods through resistive heating of electrically conductive GNPs/epoxy nanocomposites.

After probing that the heat generated through resistive heating was enough to successfully cure the GNPs/epoxy composite mixtures their electrical conductivities were determined using the same method previously described. A comparison of the electrical conductivities found in the directions parallel (z) and perpendicular (x) to the applied voltage is shown in Figure 6. It can be

  doi:10.5075/epfl-298799_978-2-9701614-0-0 published under CC BY-NC 4.0 license

clearly seen an anisotropic electrical behaviour when the filler loading was ~8-8.25 wt.% (different conductivities were found in the two directions), which might suggest some alignment of the GNPs flakes in the polymer matrix promoted by the electric current passing through the system. The GNPs must get polarized when an electric field is applied and, thus, they tend to rotate in the direction of the electric field due to the generation of a dipole moment between the GNPs, as previously reported for CNTs based systems [6]. As a consequence of this promoted alignment, the electrical conductivity was found to be one order of magnitude higher in the direction of the applied voltage than in the perpendicular direction. However, with the increase of the filler content, the electrical conductivity shows an isotropic electrical behaviour, with the conductivity values being very similar in both directions. This must be related to an increase of the viscosity of the composite mixtures as the filler loading is increased, which must prevent the orientation of the GNPs flakes under an applied electric field that is thought to occur in the less loaded and, thus, less viscous mixtures. Hence, we can conclude that at loadings below 8.5 wt.% the resistive cured composites show anisotropy, whereas at higher filler loadings the composites behave isotropically for both the oven-cured and the resistive cured composites.

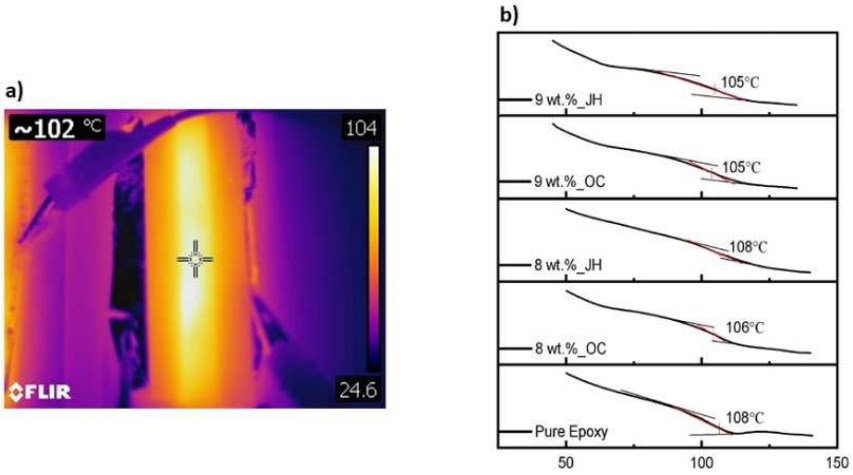

Figure 5. a) Thermographs showing the distribution of the heat generated by Joule heating of the 8 wt.% GNPs/epoxy composites ; b) DSC results of the pure epoxy and GNP/epoxy composites with filler loadings of 8 and 9 wt.% (oven-cured and resistive cured)

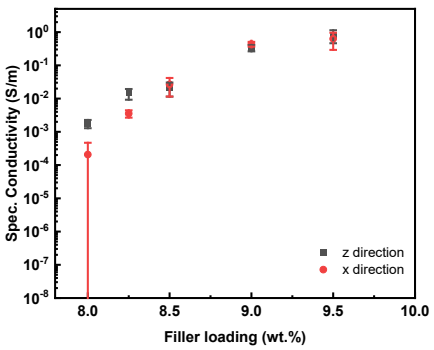

Figure 6. Electrical conductivity vs. GNPs loading of the resistive cured GNPs/epoxy composites found in the direction parallel (z) and perpendicular (x) to the applied voltage.

  doi:10.5075/epfl-298799_978-2-9701614-0-0

3.3 Reparation of CF/epoxy laminates through resistive heating of GNPs/epoxy composites

Since it has been probed in the previous section that the GNPs/epoxy composites can be successfully cured through resistive heating, these GNPs/epoxy composites seem promising to repair other types of composite material. In order to evaluate the potential of the electrically conductive GNPs/epoxy composites as conductive adhesives to repair CF/epoxy laminates through resistive heating, the set-up described in the experimental section (Figure 3) was employed. The performance of GNPs/epoxy composite mixtures with different loadings of GNPs above the percolation threshold determined for the oven-cured composites to be resistive cured and lead successfully to the reparation of CF/epoxy laminates was evaluated. Figure 7 shows the distribution of the heat generated by Joule heating of the conductive adhesive containing 8 wt.% loading of GNPs during resistive curing. By applying an external voltage through the GNPs/epoxy composite mixture a steady increment of the temperature from room temperature to 100 °C was observed using an IR camera. A homogenous distribution of the generated heat in the whole area where the conductive adhesive was applied coud be observed, as shown in Figure 7. It should be noted that the area covered by the copper tape exhibited a higher temperature than the middle area due to the hot spot effect, but that did not influence the curing performance of the GNPs/epoxy composite mixture selected as conductive adhesive.

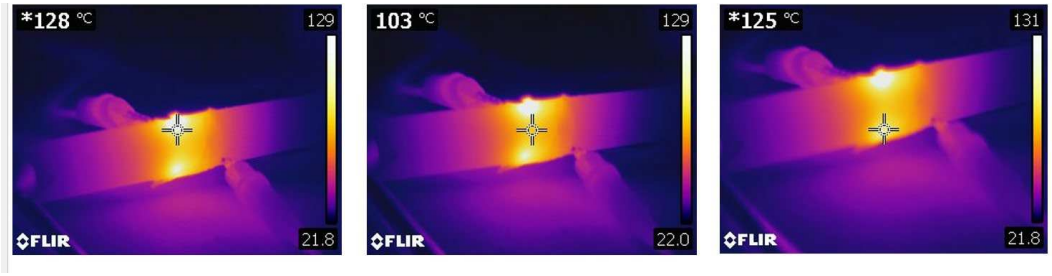

Figure 7. Thermographs showing the thermal distribution of a 8 wt.% GNPs/epoxy composite mixture used as a conductive adhesive to repair CF/epoxy laminates.

The applied voltage was controlled to keep the temperature at 100 °C for 4 hours, after which the composites were fully cured and the CFs/epoxy laminates were successfully repaired. Further work to evaluate how different loadings of GNPs affect the curing degree and to compare their curing performances, as well as the mechanical properties of the laminates repaired using the conventional oven method and using this novel curing method based on resistive heating of electrically conductive nanocomposites is currently under progress.

4. Conclusions

GNPs/epoxy nanocomposites have been prepared successfully using a procedure where the flakes are dispersed into the epoxy matrix by combining solvent method and mechanical mixing to prepare homogeneous mixtures of GNPs and epoxy resin. These mixtures were then cured using the conventional oven-curing method and, alternatively, using a novel resistive curing method through Joule heating of a conductive network of GNPs formed in the polymer matrix above percolation. In addition to a successful resistive curing of the composites, as revealed by DSC, it was also found that at a specific filler loading range (~8 wt.%), the applied external electric field seemed to promote a rotation of the GNPs, leading to a certain alignment, which resulted in an anisotropic electrical behaviour with higher electrical conductivity found in the direction of the applied voltage, whereas an isotropic behaviour was found for the oven-cured

  doi:10.5075/epfl-298799_978-2-9701614-0-0

GNPs/epoxy composites at all studied loadings. Furthermore, we have also probed here that these GNPs/epoxy composite mixtures can be used successfully as conductive adhesives to repair CF/epoxy laminates through resistive heating. Further work to evaluate how different loadings of GNPs affect the curing degree and to compare their curing performances, as well as the mechanical properties of the laminates repaired using the conventional oven method and using this novel curing method based on resistive heating of electrically conductive nanocomposites is currently under progress.

Acknowledgements

The author would like to acknowledge the CDT Graphene NowNano Program. C.V. and I.K. would like to acknowledge the Royal Academy of Engineering, Morgan Advanced Materials and the European Union's Horizon 2020 research and innovation programme EU-Horizon 2020 RIA ("Graphene Core 3" GA: 881603) for funding.

5. References

1. Witik RA, Gaille F, Teuscher R, Ringwald H, Michaud V, Månson JAE. Economic and environmental assessment of alternative production methods for composite aircraft components. J Clean Prod. 2012 Jul 1;29–30:91–102.

2. Liu Y, van Vliet T, Tao Y, Busfield JJC, Peijs T, Bilotti E, et al. Sustainable and self-regulating out-of-oven manufacturing of FRPs with integrated multifunctional capabilities. Compos Sci Technol. 2020 Apr 12;190.

3. Xia T, Zeng D, Li Z, Young RJ, Vallés C, Kinloch IA. Electrically conductive GNP/epoxy composites for out-of-autoclave thermoset curing through Joule heating. Compos Sci Technol. 2018 Aug 18;164:304–12.

4. Method ST. Standard Test Method for Apparent Shear Strength of Single-Lap-Joint Adhesively Bonded Metal Specimens by Tension Loading (Metal-to-. 2019;01(Reapproved):1–5.

5. Dong M, Zhang H, Tzounis L, Santagiuliana G, Bilotti E, Papageorgiou DG. Multifunctional epoxy nanocomposites reinforced by two-dimensional materials: A review. Vol. 185, Carbon. Elsevier Ltd; 2021. p. 57–81.

6. Monti M, Natali M, Torre L, Kenny JM. The alignment of single walled carbon nanotubes in an epoxy resin by applying a DC electric field. Carbon N Y. 2012 Jun;50(7):2453–64.

  doi:10.5075/epfl-298799_978-2-9701614-0-0

WATER ABSORPTION OF EPOXY-AMINE RESIN SYSTEMS AND THE RESPECTIVE EFFECT ON TENSILE STRENGTH AND GLASS TRANSITION TEMPERATURE

Jan-Peter Schümann[a], Alexandros Antoniou[b]

a: Westlake Esslingen GmbH – jan-peter.schuemann@hexion.com
b: Fraunhofer Institut für Windenergiesysteme (IWES), Bremerhaven

Abstract: *Wind turbine blades are exposed to harsh environmental conditions which result in aging effects on the matrix of the composite materials. One of the parameters to affect the mechanical performance of polymers is water absorption. Its effect on well-established epoxy resins is studied in the light of state-of-the-art type approval certification guidelines. An alternative approach to the established method using Fick's law is proposed for the approximation of the water uptake over time. This approach simplifies the water absorption modelling requirements and is found to be in excellent agreement with derived experimental data. The materials are exposed to different conditioning environments, i.e. temperature and relative humidity combinations. Their physical and mechanical properties are summarized, and corresponding degradation approximations are proposed based on real rotor blade data. Recommendations and suggestions are made for the current type approval practices.*

Keywords: water uptake; water saturation; epoxy; amine; rotor blades.

1. Introduction

Materials for wind energy turbine rotor blades have had to undergo a certification process for a long time now. The certification was initially set up with the intention to guarantee that the materials used would withstand external loads which are imposed on them by aerodynamic and handling forces. The state-of-the-art material certification procedures require the material to pass several tests concerning water absorption effects [1], i.e. determination of matrix properties after an arbitrary exposure immersed in water. Some typical examples are the determination of the matrix glass transition temperature (T_G) after 1000 h underwater conditioning according to [2], or quantification of the water uptake of a 50x50x4 mm polymer plate based on [3].

Apart from comparison purposes with reference properties, these values are not used in the design process of a rotor blade. Instead, matrix-dominated properties like the ultimate strength transverse to the fibers and the shear performance of a unidirectional laminate (UD) are required [4]. These are only determined under standard environmental conditions and with an arbitrary amount of water in the samples. To account for the aging effect and the long-term degradation in the design phase, the same guidelines impose a material-dependent safety factor [4]. According to scientific literature, diffusion affects both the fiber-matrix interface as well as the matrix itself [5]. However, most of the published investigations have been performed with submersed specimens, conditioned with temperature to accelerate the water uptake, whereas in reality, rotor blades are not immersed in water but rather their constitutive materials, primarily the composite matrix, absorb water from the environment.

  doi:10.5075/epfl-298799_978-2-9701614-0-0

Soles and Yee have given a possible representation of moisture diffusion in polymers [6]. They describe how water molecules travel through the matrix and find nanoscopic pores to fill. From this representation, it seems possible that the pores close to the surface become filled first. Jacobs and Jones [7, 8] have investigated basic moisture absorption effects for two-phase polymers, using the similarities between thermal conductivity and moisture absorption. They, as well as many other authors [9, 10], accept the assumption that moisture absorption can be described using the one-dimensional case of Fick's second law [11] and that the diffusion coefficients are independent of the moisture content. However, it has been reported that the diffusion value is only constant up to 80% of the saturation [12], which means that the supposed constant is actually a variable. Therefore, Jacobs and Jones [8] recommend optimizing D_a by regression analysis. In doing so, the physical meaning of D_a is lost, and its calculation based on sample geometry becomes unnecessary. Instead, it can be derived from regression analysis directly.

Hence, the goal of the present work is to investigate well-established epoxy matrix systems used in the wind turbine rotor blade industry and differences between water submersion and multiple climate conditions. This study focuses on the effect of moisture absorption on mechanical and thermal performance. The experimental investigations are performed by means of standard test procedures, which characterize the material performance and could potentially substitute actual testing practices for certification purposes.

2. Experimental Methods

Two epoxy material series, Epikote™ Resin MGS® RIMR035c and Epikure™ Curing Agent MGS® RIMH037, referred to as RIM 035c in the following, and the Epikote™ Resin MGS® RIMR1037 and Epikure™ Curing Agent MGS® RIMH 1037, referred to as RIM 1037, were used. Sample plates with 4 mm thickness were manufactured in a metal mold. After curing at 80 °C for 10 h, the plate was cut into pieces and the dogbone specimens were milled from the plate. The specimens were then conditioned in discrete environmental conditions for several time intervals. After specific periods of time, specimens were taken from the conditioning chamber and tested mechanically.

The climate combinations selected are listed below:

- 70 °C at 62 % relative humidity (rH) (as suggested in [13])
- 50 °C at 75 % rH, equilibrium climate achieved with NaCl and water [14]
- 23 °C at 76 % rH, equilibrium climate achieved with NaCl and water [14].

The first of the above climate conditions is suggested in [13], which was written for polyamide. The others can either be achieved by making use of a closed receptacle containing NaCl and water – a set-up suggested by ISO 1110 and widely known as deliquescence relative humidity [14] – or in a climate cabinet. NaCl, more than other salts, provides quite a stable condition over a wide temperature range, is widely available and cost effective. Thus, for the above conditions, all that is required is a heating cabinet in addition to NaCl, a receptacle and distilled water. Making use of deliquescence relative humidity facilitates cost-effective climate conditioning. However, for the following work, the authors resorted to climate cabinets.

The specimens with standard dogbone geometry according to DIN EN ISO 527-2 [15], see Figure 1, were conditioned under the three distinct climates described above. They were removed from the conditioning climate chamber according to a control plan and weighed immediately to

  doi:10.5075/epfl-298799_978-2-9701614-0-0

determine the water uptake. Subsequently, they were left for at least 60 minutes to condition in standard climate conditions i.e. 23 °C / 50 % rH before being quasi-statically tested in tension, see Figure 1.

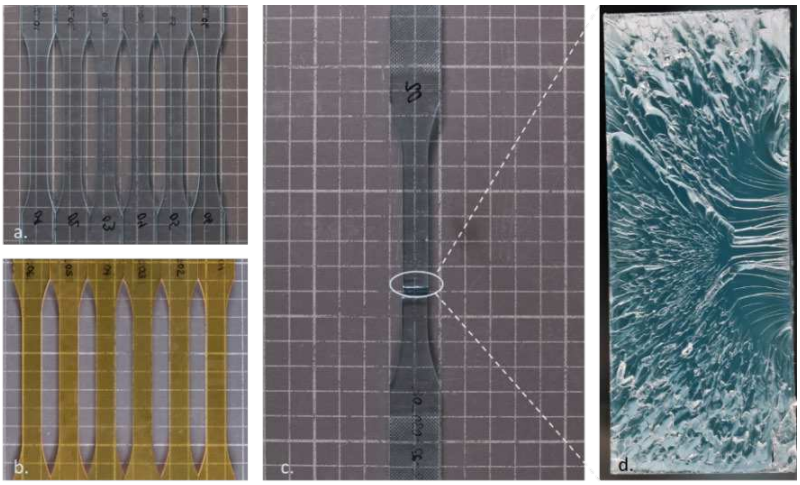

Figure 1: a., b. Specimen geometry, c. typical macroscopic damage and d. damaged surface

After mechanical testing, a small chunk of resin was removed from the cracked surface and tested using differential scanning calorimetry (DSC) [16] to determine the corresponding glass transition temperature, i.e. T_G.

3. Theory

Many approaches exist to describe saturation effects and it is known that in nature, the growth follows an exponential curve up to saturation and is driven by potential differences. From this knowledge, Eq. 1 can be derived by adjusting the known form of the exponential equation and scaling it to the saturation or growth limit as well as to the time to saturation:

$$C(t) = C_{\max}(1 - e^{-tR}). \tag{1}$$

Here, $C(t)$ is the time-dependent saturation, t is the time and R is the growth rate. $C_{\max}$ denotes the saturation limit and acts as a scaling factor, and e is the Euler number. Given the structure of the above equation, $C(t = 0) = 0$ and $C(t = \infty) = C_{\max}$. The growth rate R defines the shape of the curve and must be defined, e. g. it can be found by regression analysis.

Fick's second law [11] is one approach to describe the water diffusion mechanisms, stating that

$$\frac{\partial c}{\partial t} = D_a \frac{\partial^2 c}{\partial x^2}, \tag{2}$$

where c is the concentration of the water diffusing into the substrate, x is the distance through the plate thickness, t is the time and D_a represents the diffusion coefficient in the direction normal to the plate surface. The trivial solution leads to an exponential function as can be found in [7].

Given the cumbersome calculation of D_a via the iterative concept as suggested in [8], i.e. determination of D_a by regression analysis of the measured data, the requirement for prismatic sample cross-sections and the fact that D_a is a variable rather than a constant, the authors propose a more pragmatic approach for the estimation of the diffusion variables. Thus, a

  doi:10.5075/epfl-298799_978-2-9701614-0-0

Weibull distribution function [17] is used, as given in Eq. 3, which has a similar structure to the trivial solution of Eq. 2. However, in this approach, the physical meaning of the diffusion coefficient D_a and the link to Fick's laws is lost, which is also true when D_a is derived by regression analysis.

$$C(t) = C_{\max}\left(1 - e^{-\lambda t^k}\right) \quad (3)$$

Instead of D_a, the parameters λ and k describe the water uptake mechanism as a function of the storage conditions. They change for the different climate conditions and may be seen as parameters which combine the physical diffusion properties of the material and the sample geometry in an undefined manner. Hence, interpolations and predictions for water uptake are limited to the specific sample geometry that has been used to determine λ and k. An additional requirement for a valid interpolation or prediction is the assumption that the final water uptake should be known for a given climate and material. The parameters λ, k and R^2 in this work were found using a least squares analysis which applies a variant of the Levenberg-Marquardt algorithm [18]. $C_{\max}$ was chosen based on knowledge of the maximum water uptake for the respective materials. All relevant parameters for the climate conditions investigated are given in Table 2.

4. Experimental Results

The water absorption of the various polymers over time, conditioned in different environments, are presented along with the modelling results. Moreover, the strength degradation effect is correlated as a function of the same uptake parameter.

The progression of the water absorption over time is illustrated in Figure 2. Not all samples were conditioned to saturation due to time restrictions. The experimental data for the water absorption of RIM 035c under water was published in [12]. These samples were conditioned under water at 50 °C and left to saturate.

Table 1: Interpolation parameters for Eq. 3 and correlation index R^2

Climate	Material	$C_{\max}$ / %	λ / hr^{-1}	k / -	R^2 / %
23 °C 76 % rH	RIM 035c	2.4	7.4590E-3	5.428E-1	99.9
	RIM 1037	3.5	7.2939E-3	5.702E-1	99.9
50 °C 75 % rH	RIM 035c	2.4	1.2479E-1	3.783E-1	99.4
	RIM 1037	3.5	6.5802E-2	4.855E-1	99.3
70 °C 62 % rH	RIM 035c	1.1*	1.9983E-2	8.769E-1	96.3
	RIM 1037	1.86*	2.6278E-2	8.185E-1	99.8
Submersed, 50 °C	RIM 035c	2.4	3.0420E-1	3.557E-1	96.3

*apparent saturation as seen in Figure 2 for this particular climate condition

The interpolation parameters of Eq. 3, which are used for the illustration in Figure 2**,** are listed in Table 1. The correlation index (R^2) indicates very good fit to the test data.

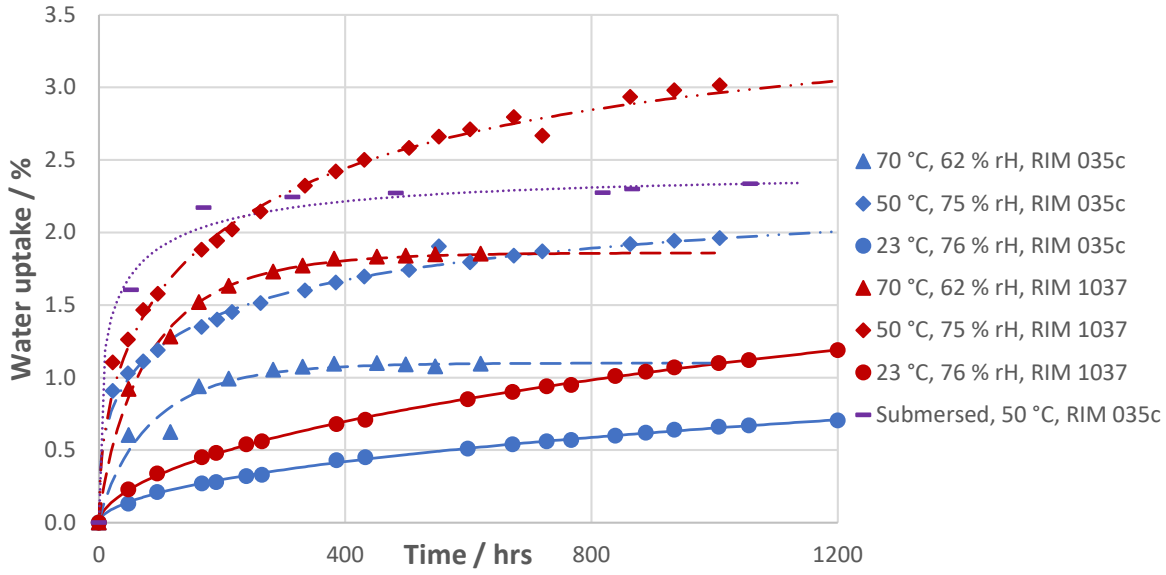

Figure 2: Water absorption for RIM 035c and RIM 1037 under different climate conditions. Symbols for the data points, lines for interpolation. See Table 1 for interpolation parameters.

All mechanical tests were performed successfully, failing in the gauge length area, see Figure 1c. The overview of the tensile strength degradation as a function of the specimen water uptake and the reduced T_G are illustrated in Figure 3 and Figure 4 respectively. Every point on the graph represents the mean value of six specimens. The standard deviation of the strength is very small and can thus not be visually identified in the graphs. For the linear regression fits shown in both graphs, data of each separate material family was considered, irrespective of the conditioning environment. This is a simplification made for comparison purposes, implying that the different temperatures have no effect. The epoxy systems tested here were compared to a reference epoxy system, the Epikote™ Resin MGS® RIMR135 cured with Epikure™ Curing Agent MGS® RIMH137 [4], which is a reference for the wind turbine blade industry. The reference epoxy was conditioned in a water bath at 50 °C. For comparison purposes, each resin data set was fitted using a linear regression method. The corresponding estimations of the quasi-static strength as a function of water uptake and glass transition temperature are listed in Table 2.

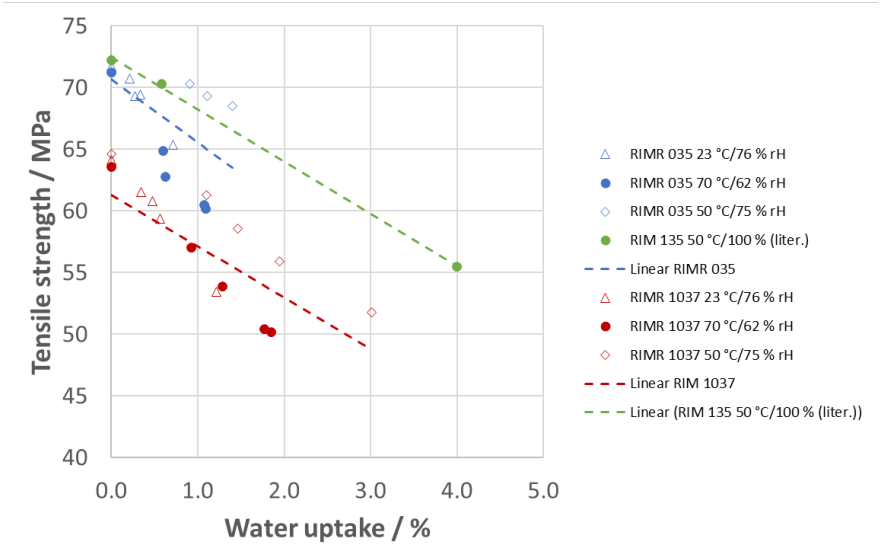

Figure 3: Tensile strength as a function of water uptake

Table 2: Epoxy quasi-static strength (QSS) as a function of physical parameters

Material	*QSS = f (Water uptake)*	*QSS = f (T_G)*
RIM 135	-4.228· *WU* + 72.454	0.8411· T_G - 3.278
RIM 035c	-5.099· *WU* + 70.651	0.7018· T_G + 8.023
RIM 1037	-4.159· *WU* + 61.293	0.7574· T_G - 7.895

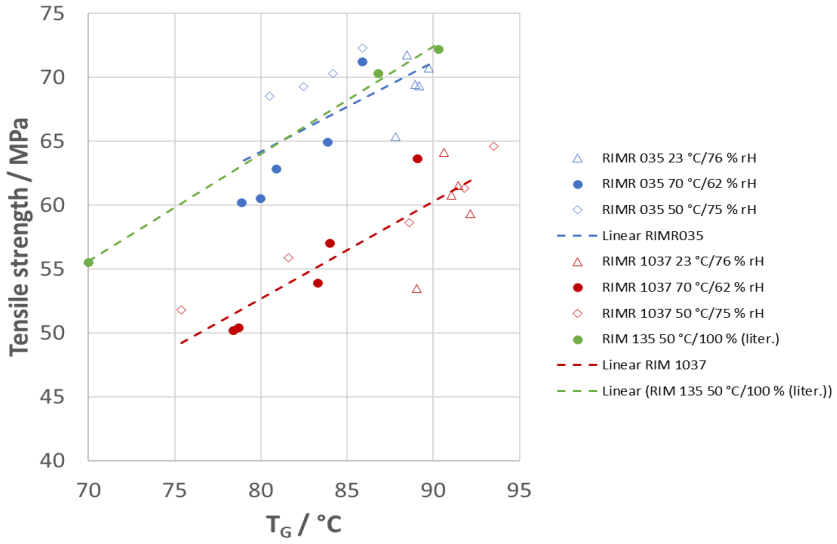

Figure 4: Tensile strength as a function of glass transition temperature (T_G)

5. Discussion

The water uptake data generated is of good quality for all climates with few outliers. The pragmatic Weibull interpolation approach which was chosen proved its suitability by giving a very high correlation index R^2. It is accepted that the water uptake mechanism is described by the parameters λ and k instead of D_a, whose physical meaning is lost as soon as it is optimized by regression analysis. However, if λ and k are a suitable replacement for D_a, it is important that dogbone samples which are subjected to future investigations have consistent geometries – this also applies to the clamping area – as the "free length" can influence the total water uptake.

For the given duration of the experiment, saturation is reached only with the 70 °C climate, apart from the submersed coupons. The absolute water uptake is only just above 1% for RIM 035c and less than 2 % for RIM 1037. For this climate (70 °C, 62 % rH), the samples saturate even though the material has the potential to absorb more water than that, as can be seen for the other two climate conditions. The authors assume that in this case, an equilibrium between water desorption and adsorption is already reached, and the water uptake does not represent the material's full absorption potential [19]. As for the climate at 50 °C and 75% rH, and also at 23 °C and 76 % rH, saturation is not reached after 1200 h. For the latter, a much longer time must be accepted if water uptake saturation is required. Furthermore, it was expected that the water uptake of the submerged samples would be higher: water molecules are readily available in this case, in contrast to climate conditioning. However, saturation merely occurred earlier, while the final value might be similar for both conditions. A starting point for further understanding the

  doi:10.5075/epfl-298799_978-2-9701614-0-0

effects may be that the water molecules travel through free volumes on the molecular level. As suggested in [7, 8], once the volumes close to the surface become filled, it gradually hinders the water molecules to travel further. The water absorption causes a deterioration in strength. The linear regression showed that the average strength degradations of all the epoxy materials compared have similar slopes when compared with respect to the same physical parameters, e.g. water uptake and glass transition temperature. The static tensile strength of the epoxy is reduced by approximately 0.7-0.8 MPa over 1 °C of T_G reduction, while it decreases by around 4-5 MPa for 1 % water absorption. It was observed that Young's modulus deteriorates marginally too. The combination of temperature and humidity appears to affect the material performance, but their impact could not be clearly identified. To this end, more specimens conditioned for a longer duration at various temperatures will be required.

To the authors' knowledge, the only reported water uptake for the laminate of a glass/epoxy wind turbine rotor blade was documented by Sayer et al. [20]. This blade was dismantled after eighteen years of operation in Southern Germany. The absorbed amount in the root laminate was constant through its thickness and thus approximately 0.3 %. Assuming the fiber made up 75 % of the laminate weight, the normalization of the water uptake by the remaining 25 % results in 1.2 % total absorption. This would result in 6 MPa loss of resin strength, which is less than 10 % of the initial strength without absorption. The material partial safety factor imposed in blade design guidelines [4] is 1.2 for the consideration of long-term aging effects.

The work of Sayer et al. [20] showed that after 18 years of service, the composite matrix was not fully saturated under central European climate conditions. The operational climate conditions are of major importance since the absorption will be accelerated under conditions with higher temperature and humidity. To achieve the above absorption level and optimize the test time, tensile test samples should be immersed at e. g. 50 °C for less than 100 hours. The immersion of samples would also make it possible to circumvent adsorption/desorption equilibrium discussions but would lead to full saturation.

6. Summary

The present work investigated the aging effect due to water absorption of two typical epoxy infusion resins which are used for the manufacture of wind turbine blades. When averaging all conditioning results, several epoxies appear to have similar strength degradation, showing a linear deterioration as a function of water uptake or glass transition temperature.

To examine the effects of diffusion on the material degradation, total saturation should be achieved with multiple data points at intermediate saturation levels. However, whether apparent saturation, as indicated by [20], is sufficient for qualification purposes needs to be further investigated. To accelerate the characterization process, it seems appropriate to submerse the samples and to conduct tests for water uptake at elevated temperatures, e. g. 50 °C. It is recommended that the properties of specimens are characterized when saturated. For the infusion resins, a mechanical tensile test according to [15] and DSC test according to [16] are suggested accordingly. In contrast to current practice, this would make it possible to gain a practically relevant impression of the material properties as a function of the water uptake.

Further research should investigate the diffusion effects in detail, e. g. the dependency of water uptake on the geometry, and the temperature on the diffusion depth. The conditions leading to this "apparent saturation" (adsorption/desorption, difference between climate conditions - T_G)

  doi:10.5075/epfl-298799_978-2-9701614-0-0

should be the subject of further investigations, as should the effect of the different combinations of temperature and humidity on the degradation of the mechanical properties.

7. Acknowledgements

The authors would like to acknowledge the assistance and support of Christoph Schädle and Johannes Meunier for funding the research and both IWES and Westlake technicians for conducting the experiments.

8. References

1. DNVGL, Class programme — DNVGL-CP-0089. Edition March 2016 Epoxy resin systems.
2. ISO 75-1:2004, Plastics - Determination of temperature of deflection under load - Part 1: General test method
3. ISO 62:2008, Plastics –Determination of water absorption
4. DNVGL, Standard, DNVGL-ST-0376 – Edition December 2015
5. Rocha I.B.C.M, Raijmaekers S, Nijssen R.P.L, van der Meer F.P, Sluys L.J. Hygrothermal ageing of a glass/epoxy composite used in wind turbine blades. Composite Structures 2017; 174: 110–122.
6. Soles C.L, Yee, A.F. A discussion of the molecular mechanisms of moisture transport in epoxy resins. Journal of Polymer Science Part B: Polymer Physics 2000; 792 - 802.
7. Jacobs P.M, Jones F.R. Part 1: Diffusion of moisture into two-phase polymers. Journal of Material Science 1989; 2331 - 2336.
8. Jacobs P.M, Jones F.R. Part 2: Diffusion of moisture into two-phase polymers. Journal of Material Science 1989; 2343 - 2348.
9. Shen, C.-H., & Springer, G. S. (1 1976). Moisture Absorption and Desorption of Composite Materials. Journal of Composite Materials , 2 - 22.
10. Kailong X.W.C. Chemical, mechanical and morphological investigation on the hygrothermal aging mechanism of a toughened epoxy. Polymer Testing 2022; 110.
11. Fick, A. Ueber Diffusion. Annalen der Physik 1855; 170: 59-86.
12. Ebrahim F. Wasseraufnahme-Einflüsse auf die mechanischen Eigenschaften von Epoxid-basiertem Infusions-und Klebstoffharzsystemen; Master Thesis 2021; Leibniz Universität Hannover Institut für Windenergiesysteme
13. ISO 1110:2019, Plastics — Polyamides — Accelerated conditioning of test specimens
14. Quincot G, Azenha M, Barros J, Faria R. Use of salt solutions for assuring constant relative humidity conditions in contained environments. 2011; Technical report.
15. DIN EN ISO 527-2. Plastics–Determination of Tensile Properties—Part 2: Test Conditions for Moulding and Extrusion Plastics, Deutsches Institut für Normung, Berlin, 2012.
16. ISO 11357-2, Plastics—Differential Scanning Calorimetry (DSC)—Part 2: Determination of Glass Transition Temperature and Glass Transition Step Height, International Organization for Standardization, Geneva, 2013.
17. Weibull W. A statistical distribution function of wide applicability, Journal of Applied Mechanics 1951 ; 18 (3): 293–297
18. Draper N. R, Smith H. (1981). Applied regression analysis. New York : John Wiley and Sons.
19. Pierce C, Smith R. N. The Adsorption–Desorption Hysteresis in Relation to Capillarity of Adsorbents. The Journal of Physical Chemistry 1950 ; 784-794
20. Sayer F, Bürkner F, Buchholz B, Strobel M, van Wingerde A.M, Busmann H. G, Seifert H. Influence of a wind turbine service life on the mechanical properties of the material and the blade. Wind Energy 2013; 16:163–174

  doi:10.5075/epfl-298799_978-2-9701614-0-0

A NUMERICAL MODEL FOR VIBRATION ANALYSES OF AN AIRCRAFT PARTITION WITH PARAMETERIZED INTERFACE PROPERTIES

Philipp Hüttich[a], Emil Heyden[a], Dieter Krause[a]

a: Institute of Product Development and Mechanical Engineering Design (PKT), Hamburg University of Technology (TUHH), Germany – philipp.huettich@tuhh.de

Abstract: *Aircraft structures are subjected to environmental conditions that can cause critical damage. The vibrational behavior of cabin structures can be influenced by adjusting the mechanical properties at the connections. Many possible mechanical properties lead to a large number of necessary investigations. Therefore, a dynamic model of a partition with parameterized interface properties in frequency domain is presented. Physical tests are performed on a vibration test rig to determine the internal damping of the structure. The vibration amplification depending on different interface properties is determined by amplification functions over several resonance frequencies. The resulting behavior is analyzed and its vibration reduction over all interface properties is determined. With the model presented, the possibility of reducing vibrations through adjustable impedance elements can be predicted. Requirements for physical examinations and properties for vibration-optimized connections in aircrafts can be derived from this.*

Keywords: parameterized simulation; dynamic analyses; lightweight structure; environmental conditions; compliant elements

1. Motivation and Introduction

Products in the aviation industry are subjected to a number of environmental conditions, such as static and dynamic loads, pressure changes, temperature and humidity. Among others, vibration loads are of particular importance, as they introduce high amounts of energy into the structure and can cause critical damage when resonance is reached [1]. Cabin structures, such as the partitions of an aircraft, are sensitive to low-frequency vibrations because they consist of panel-like structures whose elasticity is comparatively low due to their small thickness compared to other dimensions. The vibration behavior can be influenced by adjusting the mechanical properties at the connections [2, 3]. The holistic modeling of the test object and its connections are necessary for the optimal selection of suitable mechanical properties. Many possible mechanical properties such as changing stiffness, damping and inertia at each connection, as well as a large number of possible product variants, lead to a large number of necessary investigations [4, 5]. A dynamic FEM model with parameterized interface properties is a suitable option to proceed efficiently in terms of time and costs. This paper presents a numerical model of an aircraft structure with parameterized interface properties. The dynamic model of the partition with detailed material properties and degrees of freedom is modeled in the frequency domain. A particular challenge is the determination of the inner damping of the test object [4], the modeling of the boundary conditions [6], and the systematic evaluation of the large quantities of simulation results.

  doi:10.5075/epfl-298799_978-2-9701614-0-0

2. Methods and development of the model

Numerical models, especially finite element method (FEM) models, can be used to implement complicated geometries, combined load cases, changing boundary conditions, and different material laws [7, 8].

Abaqus brings, in addition to the powerful general-purpose program, advanced theories of nonlinear behavior and a programmable interface, which is why it is most commonly used in research [7]. Abaqus Scripting Interface offers a user-defined extension via the Python programming language with the help of which the possibility exists to create, modify and run models [9]. Due to these given possibilities, the process of creating a large number of models can be automated [9]. This brings a variety of advantages for the system investigation.

- The possibility of parameterization by modifying boundary conditions, materials, geometries, loads, etc. [10].
- Time-efficient creation of a large number of models [11].
- Automated documentation and accompanying evaluation [10], [11].
- Avoidance of failures when defining the respective parameters by the user.

3.1 Definition of the modelled system

Figure 1 a) shows the partition under investigation on the vibration test rig (details in [5]). The dimensions of the test object are defined in figure 1 d). Aircraft partitions are typical lightweight structures with a sandwich structure of GFRP face sheets and a honeycomb core. Due to their large dimensions compared to the thickness, these products are particularly sensitive to low-frequency vibrations. Table 1 shows the composite layers of the partition and each layer thickness. These layer properties can be assigned to the model with the Abaqus composite tool [10]. The material properties of each layer are specified by the manufacturer.

Table 1: Layer structure and thickness of the partition according to manufacturer's specifications.

Ply Name	Material	Thickness [mm]
Face Sheet 1: PHG600-44-50-01	PHG600-44-50-01	0.09
Face Sheet 2: PHG600-68-50-01	PHG600-68-50-01	0.19
Core	WEB48N32	25
Face Sheet 3: PHG600-68-50-01	PHG600-68-50-01	0.19
Face Sheet 4: PHG600-44-50-01	PHG600-44-50-01	0.09

A plane stress state is suitable for a model that is mainly loaded in bending. As long as the sandwich structure is excited in the linear range, shell models offer a suitable computationally efficient alternative [12]. The mesh size in plane direction is chosen to be 10 mm, since at this size it has a negligible effect on the results.

Furthermore, the inserts for adding attachments must be considered in the model. While the real partition has a mass of 9.9 kg, the simulation model without the insert weight has a mass of 5.98 kg. This corresponds to a mass difference of 3.92 kg, this mass is distributed evenly over all 77 inserts on the partition. The partition is connected at four interfaces (shown in figure 1 a, b and c). The partition is rigidly connected to the excitation point in the area of the support and can rotate together centered around this point. Their masses must be taken into account in the

  doi:10.5075/epfl-298799_978-2-9701614-0-0

model ($m_{C1} = 0.89\ \mathrm{kg}; m_{C2} = 0.87\ \mathrm{kg}; m_{C3} = 1.5\ \mathrm{kg}; m_{C4} = 1.35\ \mathrm{kg}$), they are evenly distributed among all connected nodes (highlighted in figure 1 d and e).

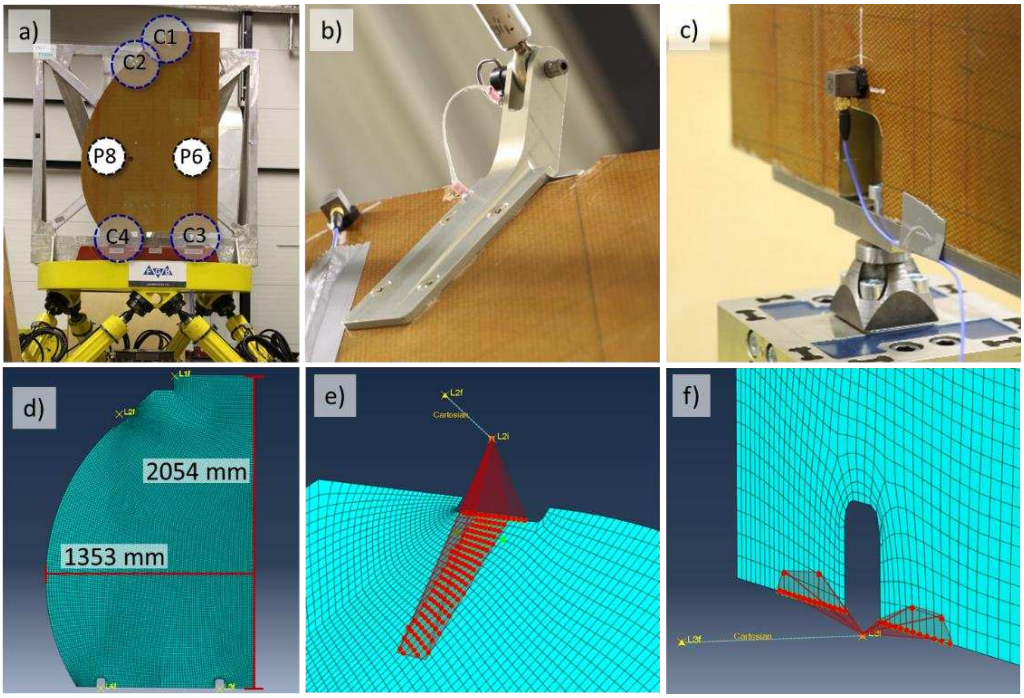

Figure 1. a-c) physical test setup of the partition; d-f) numerical implementation of the partition and its connections.

3.2 Definition of system characteristics

In reality, a wide variety of damping mechanisms occur, which cannot all be transferred separately to the simulation. Abaqus provides the value of the structural damping for this purpose, which must be determined individually for each case. To define the system properties such as the structural damping, a physical test must be carried out.

At the lower connections C3 and C4, the partition is attached to force transducers by a ball bearing (figure 1 c). The ball bearing is the original mounting form in the aircraft and prevents moment transmission in all rotational axes. The connections at the upper connections C1 and C2 to the partition are realized by pendulums with ball joints at each end. They are supported with locking bolts (figure 1 b). Original aluminium adapter plates are attached to the partition by means of screw connections for the two upper connections. To record test results accelerometers (3D 500g 356A02, PCB Piezotronics Inc., Depew NY, USA) are mounted at the test rig itself as well as on several positions of the partition.

A typical and in the aircraft certification process often used form of excitation in vibration analysis is the sweep excitation, in which the frequency of a sinusoidal oscillation increases over time [13, 14]. To be able to compare experimental and simulation data, sweep tests are performed at a constant acceleration amplitude of $3\ m/s^2$ at a constantly rising frequency from 3 to 23 Hz. From the recorded data, the excitation of the different measurement points in the frequency domain is determined using the Fast Fourier Transform and normalized by the reference signal, resulting in the amplification of each point.

In the frequency range from 3-23 Hz two resonance of the partition result. Among others, sensors are placed at points P6 and P8 (figure 1 a), since the movement of these points are

representative for the two occurring resonances. The maximum amplification of the first resonance is 48 at point P6. Point P8 is amplified by a factor of 14 at the first resonance (see Figure 2a). To adapt the simulation model to the experimental data with respect to the amplification factor, the damping coefficient of the simulation model is approximated. The structural damping is set, so that the amplification level at the first resonance of the simulation and experimental data are the same (see Figure 2b below). Resulting, a structural damping coefficient of $s_d = 0.036$ is obtained and used for the further investigations of the partition.

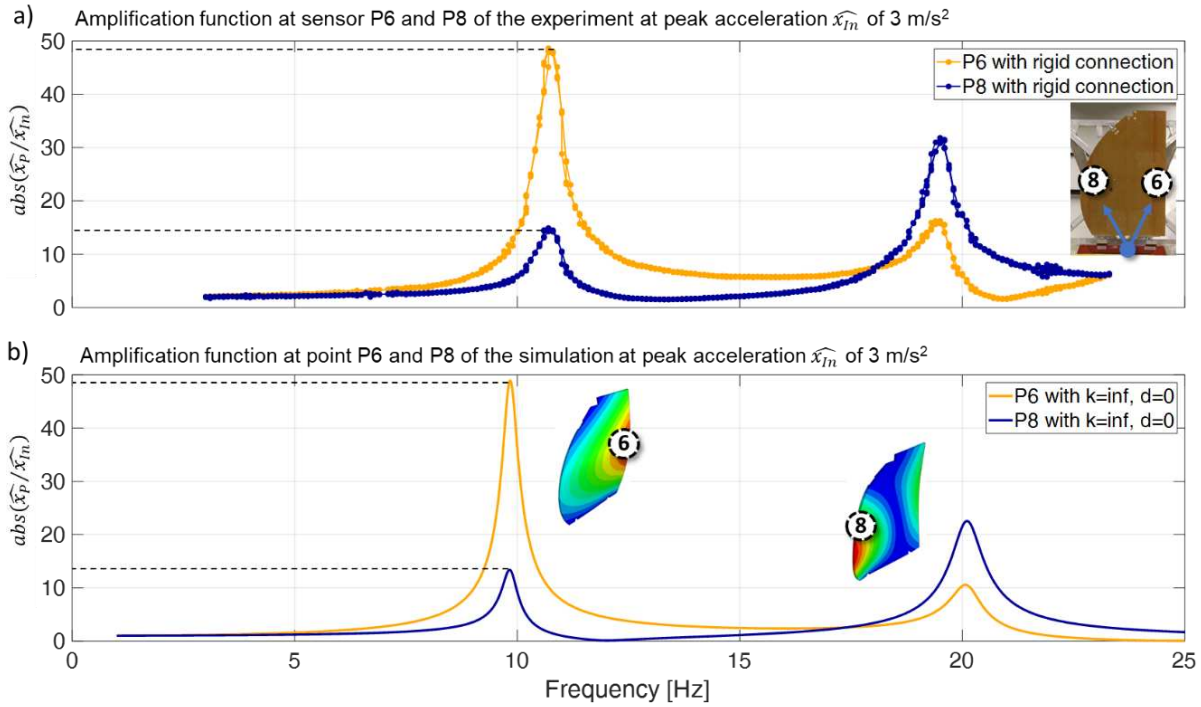

Figure 2. Comparison of the amplification function of the experiment and the simulation model to determine the structural damping.

3.3 Define the excitation and adding parameterized interfaces

The partition is excited by a base motion through its connection elements. For the definition of the base motion in Abaqus it is valid that it acts on the respective blocked degrees of freedom in the given excitation direction of the motion [15]. If the excitations at the bearing points are not all the same, so-called secondary base motions can be defined [15]. The excitation is applied at the four connection points in accordance with the test setup. A sweep movement is applied orthogonal to the partition at the end of the four connections.

Parameterized numerical models are useful when analyzing a large number of factors with many levels to obtain an understanding of the overall system [8]. To investigate the effect of compliant connections on the vibration behavior of the partition, wire connections are added between the center point of the connector and the point of excitation. The mechanical properties stiffness and damping are added to these wire connections [10]. Depending on the simulation case, the properties can be systematically varied and adapted using the Python script.

In the case of rigid connections, the mass of the interface elements themselves is not crucial, since the entire interface follows the defined motion in the model. In the case of compliant interfaces, the movement before and after the connection can differ, therefore it is necessary

  doi:10.5075/epfl-298799_978-2-9701614-0-0

to determine the weight of the connections themselves, as these have an influence on the vibration behavior.

4. Results and Discussion

The amplification resulting from the excitation vibration depends on different interface properties and is determined by amplification functions over several resonance frequencies. It is necessary to distinguish between two objectives, the reduction of the vibration of a given point on the partition and the reduction of the maximum vibrating point on the entire partition.

For the following investigations all four connections have the same properties. A combination among each other does not take place. For the given case of the aircraft partition, a range of 1-500 N/mm was selected for the stiffness and 0.1-5 Ns/mm for the damping.

4.1 Amplification at specific points

By varying the stiffness and damping parameters, the amplification function can be controlled and consequently the maximum amplification can be reduced. Figure 3 shows the resulting amplification function for different values of the stiffness k and damping d.

The vibration behavior of point P6 is shown in figure 3 a) and is particularly affected by the first resonance. At this point a reduction of the amplification from 48 to 19.9 (reduced by 58%) is possible by changing the stiffness from rigid to k = 100 N/mm and the damping to d=1Ns/mm. While the resonant frequency changes only slightly from 9.8 to 9.4. The amplification of point P8 is shown in figure 3 b). The second resonance is more sensitive to the interface adjustment than the behavior at the first resonance. The amplification can be reduced from 22.1 to 2.3 (reduced by 89 %) and the resonnance frequency from 20.1 to 18.35 by adjusting to k = 200 N/mm and d = 4 Ns/mm. An investigation of the vibration behavior with a few settings of the interface is not sufficient to provide an understanding of the overall vibration behavior.

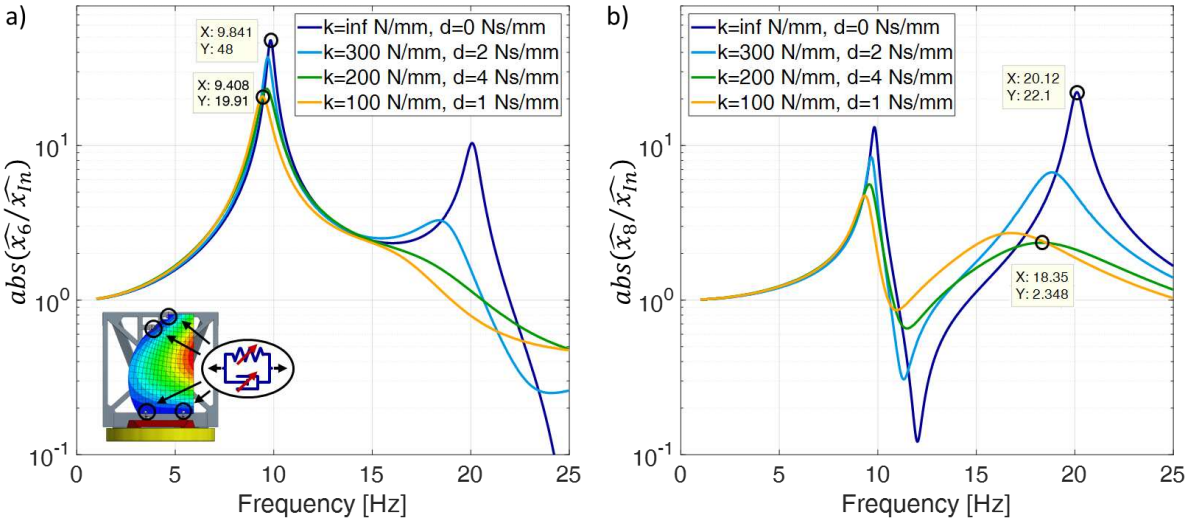

Figure 3. Amplification function of the simulation model with different interface stiffness and damping at Point 6 and 8.

4.2 The maximal amplification over the entire system

An evaluation of the vibration reduction at a specific point is deceptive, since the variation of the interface characteristics can cause the point of maximum gain to drift. To determine the

maximum amplification of the system per interface properties, the movement at all points of the partition $\widehat{x_l}$ is to be determined, and the resulting maximum movement $\widehat{x_m}$ to evaluate. Figure 4 a) shows the resulting amplification at the maximal moving point for different stiffness and damping adjustments. At the kink of the function, the point of maximum amplification jumps from the right side of the partition to the left as shown by the path of the maximal moving point in red. Representable the setting from rigid to k = 200 N/mm and d = 4 Ns/mm leads to a reduction of the amplification from 50.7 to 20.8 (reduced by 59%).

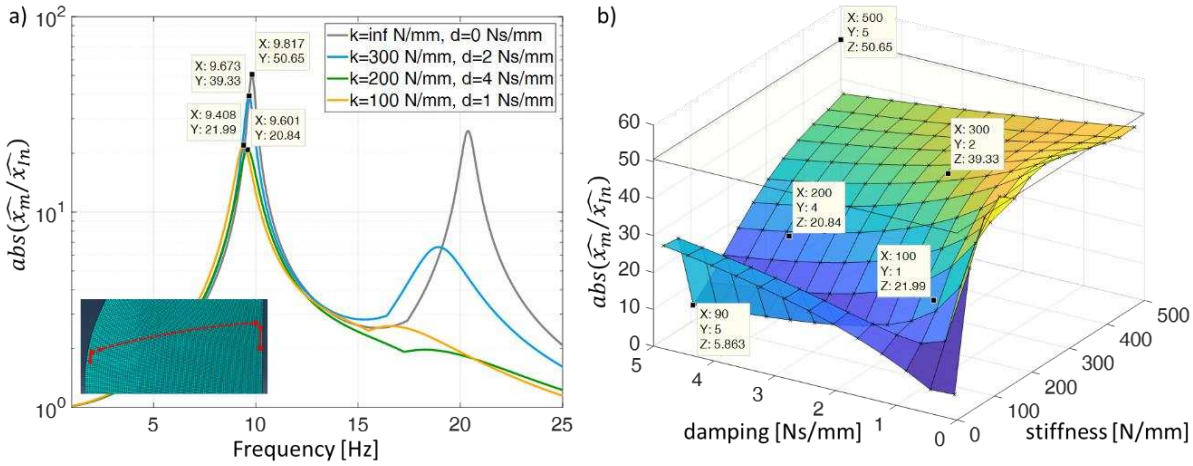

Figure 4. Amplification function of the model at the maximum point of vibration for different stiffness and damping parameters.

Figure 4 b) presents the maximum resonance of the point with the highest movement on the partition over the setting of damping and stiffness of the interfaces. For a stiffness of 90 N/mm and a damping of 5 Ns/mm, the minimum of the curve is obtained. This leads to a reduction of the resonance from the rigid connection at 50.65 to the compliant connection of up to 5.9, which corresponds to a reduction of up to 88%. However, it should be noted that this minimum is very sensitive to a change in its parameters, especially the stiffness. Therefore, this reduction will be challenging to reproduce in physical tests.

4.3 Further findings of the vibration behavior of the partition

Requirements for vibration-optimized connections in aircrafts can be derived from this model. This makes it possible to design cabin structures in aviation in such a way that they themselves need to be less resistant to vibrations and therefore allows lighter structures to be developed.

Adjustable impedance elements are machine elements with separately adjustable stiffness and damping characteristics, which are used as interface elements in vibration testing [16]. The model can be used to derive requirements for these elements to demonstrate the resulting reduction in physical vibration testing. From the numerical model, necessary requirements for interface forces and displacement amplitudes can be derived in addition to the amplification function discussed in this publication.

Depending on the two resonances and corresponding mode shapes investigated, different interface properties can lead to improved vibration reduction. A representative example is provided by the amplification function at point P8 shown in figure 5 a). For the first resonance setting 1 lead to a gain of 5.6 and setting 2 to a gain of 4.7 (reduction from setting 1 to 2 by 16%). For the second resonance, setting 2 leads to a gain of 2.7 and setting 1 to a gain of 2.3 (reduction

  doi:10.5075/epfl-298799_978-2-9701614-0-0

from 2 to 1 by 15%). Dynamically adaptive interface elements could adjust during operation and provide suitable interface characteristics depending on the excitation frequency. This would lead to further vibration reduction over several resonant frequencies.

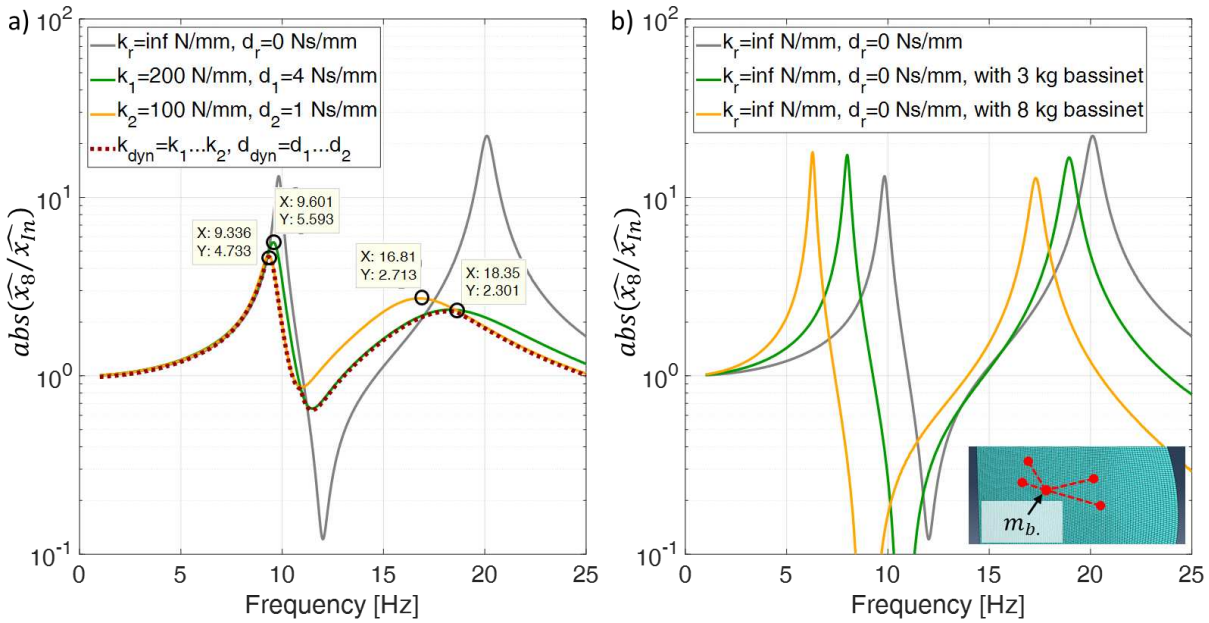

Figure 5. Amplification function at Point P8 a) for stationary adjustable interfaces and dynamical adaptive interfaces and b) for different product variants.

In addition, attachments can change the characteristics of the system during operation. As an example, Figure 5 b) shows the amplification function with an attached baby bassinet (simplified as point mass $m_{b.}$ and ignored change of internal damping). The increase in mass leads to an increase of the first resonance and a reduction of the second resonance. It is expected that dynamically adaptive interface properties lead to a better reduction of vibration per configuration, since they can be optimized for each resulting resonance separately.

5. Conclusion

It can be demonstrated via the numerical model presented that significant vibration reduction of the aircraft partition can be achieved by using compliant boundary conditions. Moreover, the results show that the vibration is sensitive to a change in its interface parameters.

In vibration reduction, it is necessary to examine every point on the object, since the point of maximum motion drifts. This, together with the high number of simulations in a parameter study, leads to a high computational effort and memory consumption and the need for automated algorithms and analysis.

Requirements for adjustable impedance elements can be derived from this model. These are necessary to represent the vibration behavior of test objects with varying boundary conditions in physical tests. In order to achieve different vibration reductions for different vibration modes, dynamically adaptive impedance elements are necessary, that have the ability to adjust during operation.

This publication shows the influence of a parameterization of the interfaces, comparable studies with other environmental conditions are useful to better understand the behavior of the system under investigation.

  doi:10.5075/epfl-298799_978-2-9701614-0-0

Acknowledgements

Special thanks to Ibrahim Kassem, who supported the presented simulation model through many debates and by his student research.

The research results on which this publication is based are part of the project AIProVE that was funded by DFG (Deutsche Forschungsgemeinschaft) and the project CERTEV that is funded by the BMWK (Bundesministerium für Wirtschaft und Klimaschutz). The statements and information in this contribution do not necessarily represent the opinion of BMWK and DFG.

6. References

1. Rasmussen, O.; Krause, D.: Influence of Load Elements on the Dynamic Behaviour of Lightweight. Proceedings of the 6th International Workshop on Aircraft System Technologies, Shaker Verlag, Aachen, 2017.
2. Kim, J. Y. et al.: An Experimental Approach for Structural Dynamic Modification of Fixture in Vibration Test Control. JSME International Journal Series C, Vol. 442, 2001, pp. 334–340. https://doi.org/10.1299/jsmec.44.334
3. Heyden, E. et al.: Approach for Calibrated Measurement of the Frequency Response for Characterization of Compliant Interface Elements on Vibration Test Benches. Applied Sciences, 2021. https://doi.org/10.3390/app11209604
4. Seemann, R. et al.: FE-Modelling Guidelines for the Dimensioning of Aircraft Cabin Interior under Stationary Dynamic Loads. 29th Congress of the International Council of Aeronautical Sciences, 2014.
5. Lindenmann, A. et al.: Adjustable Impedance Elements for Testing and Validation of Aircraft Components and Hand-Held Power Tools. Stuttgarter Symposium für Produktentwicklung, Stuttgart, 2019.
6. Heyden, E. et al.: Transferability of Boundary Conditions in Testing and Validation of Lightweight Structures. Proceedings of the 30th Symposium Design for X, Hamburg, 2019. https://doi.org/10.35199/dfx2019.8
7. Klein, B.: FEM - Grundlagen und Anwendungen der Finite-Element-Methode im Maschinen- und Fahrzeugbau. Springer Vieweg, Lehrbuch, Wiesbaden, 10. Auflage, 2015.
8. Reddy, J. N.: Introduction to the finite element method. McGraw Hill Education, Fourth edition, New York, 2019.
9. Dassault Systèmes Hrsg.: Abaqus Skripting Guide. 2014.
10. Dassault Systèmes Hrsg.: Abaqus Analysis User's Guide. 2014.
11. Puri, G.: Python scripts for Abaqus - Learn by example. Charleston, SC. 1. ed., 2011.
12. Salerno, G. et al.: Reduced Order Modeling of Composite Laminates Through Solid-Shell Coupling. Journal of Aerospace Technology and Management, 2017, 9; pp. 397–403. http://dx.doi.org/10.5028/jatm.v9i3.742
13. Ewins, D. J.: Modal Testing: Theory and Practice. Volume 2, Letchworth, 1986.
14. RTCA, Inc.: RTCA/DO160G – Environmental Conditions and Test Procedures for Airborne Equipment. Washington, 2010.
15. Dassault Systèmes Hrsg.: Abaqus Theory Guide. 2016.
16. Heyden et al.: Adjustable Impedance Elements for Testing and Validation of System Components. Symposium Lightweight Design in Product Development, Zürich, 2018, pp. 45-47. 10.3929/ethz-b-000283432

DISTRIBUTED STRAIN SENSING IN COMPOSITE MATERIALS BY USING A CAPACITIVE SENSOR SHEET WITH CRAKED ELECTRODES.

Hussein Nesser and Gilles Lubineau

King Abdullah University of Science and Technology (KAUST), Physical Sciences and Engineering Division (PSE), Mechanics of Composites For Energy and Mobility Lab, Thuwal 23955-6900, Saudi Arabia

Email: hussein.nesser@kaust.edu.sa

Abstract: *Distributed strain sensing, i.e., the ability to measure strains at different locations, has become especially important for detecting expected damage locations in structures. To date, monitoring distributed strain with high spatial resolution in composite structures is limited due to several technical limitations. Our solution is based on creating multiple sensing regions within the area of a single capacitive sensor body by considering the sensor as an analogical transmission line, reducing the connections to only two wires and simplifying the electronic interface. The proposed distributed sensor is a stretchable parallel-plate capacitor comprising two cracked electrodes separated by a dielectric layer. The piezoresistivity of the electrodes induces the transmission-line behavior in the entire sensor at radio frequencies. The transmission line behavior allows the sensing signal to be attenuated by high-resistance electrodes along the capacitive sensor's length. Different regions of the capacitive sensor can then be moitored by changing the sensing frequency and creating a virtual sensor length. Our system that allows free movements of deformable systems can be an alternative solution to detect local strain in composite materials without affecting their mechanical properties.*

Keywords: Monitoring Large structure, SHM, Distributed strain sensor, Transmission line, Cracked electrodes, Minimizing wiring

1. Introduction

Composite materials-based structures such as aircraft, composite pipes, gas tanks, and wind turbines deteriorate over time, resulting in unexpected failure when exposed to extreme loads. Moreover, lack of follow-up and maintenance can accelerate structural degradation, leading to shortened lifetimes. Consequently, monitoring composite structure is essential because localized degradations due to a high strain can propagate and lead to catastrophic effects [1]. However, composite materials' anisotropy and complex nature result in relatively unpredictable behavior, which makes monitoring composite structures more difficult than monitoring structures based on classical materials such as metal and concrete. Until today, The nondestructive testing tools (NDT) [2] are the most used techniques in the industrial market to analyze composite structures quality like visual inspection, radiography, and ultrasonic testing, but these methods are still very expensive and time-consuming [3]; in addition, they have some limitations in detecting barely visible damage in structures. Some cannot withstand harsh environments and are difficult to deploy over large structures or have a short lifespan.

  doi:10.5075/epfl-298799_978-2-9701614-0-0

Earlier, structural health monitoring (SHM) came to assist in monitoring the structure and taking appropriate action before the catastrophic loss by integrating a real-time system in a decision framework. SHM provides techniques to observe and analyze a system over time to monitor changes to the material, which can be used to identify structural degradation and provide maintenance guidance so that early signs of damage prior to structural failure can be flagged. Several methods have been investigated for SHM applications, including capacitive and resistive strain gauges[4], accelerometers [5], passive acoustic sensors [6], *etc.* Moreover, classical strain monitoring-based methods [3], such as strain gauges, are also frequently used to analyze structures, as they have long demonstrated a high capacity to measure accurate strain in local areas. At a later stage, researchers have developed these electrical strain sensors from wires connected to wireless communications by including the strain gauges in electronic packaging that communicate with the interrogation system without wiring [7]. Some work has gone further by introducing a new model of sensors based on converting the sensor to an RFID tag with passive interaction where no direct power supply is required [8]. Furthermore, fiber Bragg grating (FBG) is a popular technique used in SHM for composite, especially for large-scale [9], but this technique still faces limitations such as intrusivity and the need for wired interrogation systems.

The development of reliable methods to monitor large structures remains one of the main challenges for multi-point and distributed sensing techniques. These methods should be able to detect the damage position even if it is not known with sufficient precision a priori with suitable physical and spatial resolution. Therefore, to effectively detect incidental damage in a structure of industrial complexity, a dense array of sensors distributed over the entire structure is a viable option. However, using traditional wired sensors is difficult due to the cost of deploying and maintaining a dense wired network. It has become preferable to use a network of remote sensors to cover a large area of what is known as wireless sensor networks (WSN) [10]. Over recent years, significant advances in the field WSN have produced innovative and powerful solutions, especially for damage detection in large composite structures [11]. WSNs are attractive because they offer increased robustness through decentralization,however, transferring all the measured information to a central station using wireless sensors is difficult because of power requirements and bandwidth limitations. Wireless data transfer is challenging, particularly if the sensors are embedded in anisotropic and conductive materials such as carbon fiber-reinforced polymer (CFRP). The electromagnetic shielding effect of this kind of material limits the wireless communication between the sensor and its acquisition system[12]. Therefore, to avoid electromagnetic shielding in composite structures, the industry has obligated, in some cases, to integrate a network of analog sensors wired to the central controller. In these systems, wiring sensors to a central node in a large structure is expensive and cumbersome; it may also be detrimental to system reliability as wires may be damaged and severed.

Based on the above remarks, reducing the high cost and complexity of the available methods is an essential requirement. It has become urgent to develop new and innovative methods to monitor large composites structures without losing a large part of the information by shielding or through wires. This paper describes our experience with a new distributed sensing system based on a transmission line model where we replace a network of local sensors with one sensor sheet. We demonstrate a distributed strain-measurement technique using a single-sheet capacitive sensor, which minimizes the quantity and complexity of wiring numbers where we are able with our technology to detect strain in multi-point of a large structure with one sensor

body that operates only with two-wire. Building such a system aims to facilitate the transition to fully distributed SHM applications.

We describe in this paper the mechanism of the transmission line-based sensor and how to benefit from the signal dissipation in a capacitive sensor to localize the strain. We also present the evaluation results and discuss the possibility of using such a sensor to follow the strain location and magnitude. We finish with some perspectives concerning using this technology for the replacement of available distributed sensing methods.

2. Result and discussion

2.1 Strain localization by transmission line model

Our strategy is to use the transmission line model in a parallel plate capacitor (PPC) to replace a network of n local sensors with 2n wires with a one-sheet sensor with only two wires that can detect strain in multi-point, as shown in **Figure 1**.

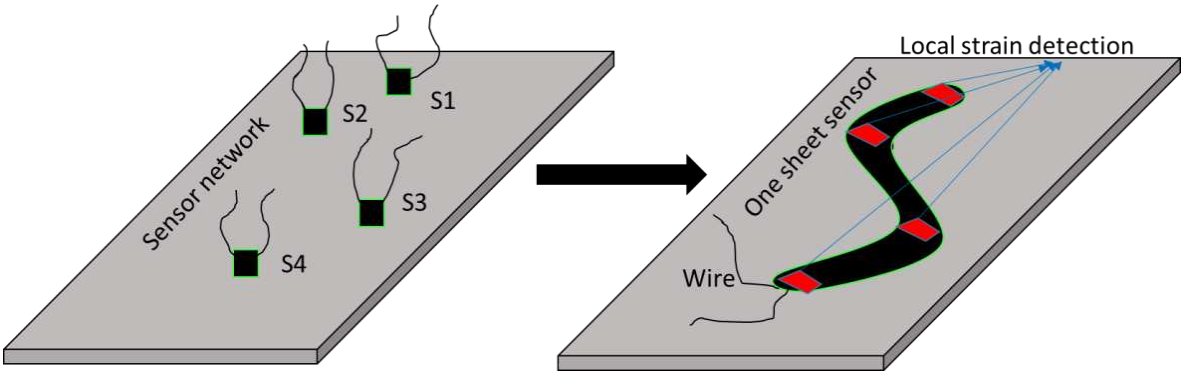

Figure 1. The transition from sensors network system to one sheet sensor While maintaining the same result with a lower number of sensor/wires, the sensor resolution is correlated to the number of red zones.

The transmission line model is frequently used in radio and telecommunications engineering to describe any physical structure that guides electromagnetic waves. A capacitor with relatively resistive electrodes is represented as distributed R–C chains at high frequencies, forming the transmission line model [13]. By creating piezoresistive electrodes in the PPC, we can guide the electromagnetic wave propagation in the PPC, which transforms into a distributed capacitive strain sensor. Some resistance in the electrodes attenuates the electromagnetic wave propagation in the sensor until it disappears before it reaches the end of the sensor. Based on the voltage dissipation mechanism resulting from the electrodes resistance variation, a virtual length (L_V) is created starting from the beginning of the sensor to the point where the signal is totally attenuated [14]. The total electromagnetic signal dissipation happens when the electrodes resistance (R) and/or the interrogation frequency (f) are relatively high [15]; injecting a high-frequency signal allows the whole signal attenuation even with low electrodes resistances. Furthermore, creating local resistance in a one-sheet PPC can drop the signal to the same level where a portion of the sensor is stretched **(Figure 2)**. Thus, the location of the strain can determine by measuring the total capacitance of the PPC and deduce than the level that

reached the signal by the classical capacitance equation that links the geometric of the PPC by the capacitance,C, as follow:

$$L = \frac{Cd}{\varepsilon_0 \varepsilon_r \omega} \tag{1}$$

Where *L* is the length of the PPC that transforms to L_v in the transmission line model, d is the thickness of the dielectric materials and *w* is the width of the PPC , ε_0 and ε_r are the vacuum permittivity and the permittivity of the dielectric materials respectively.

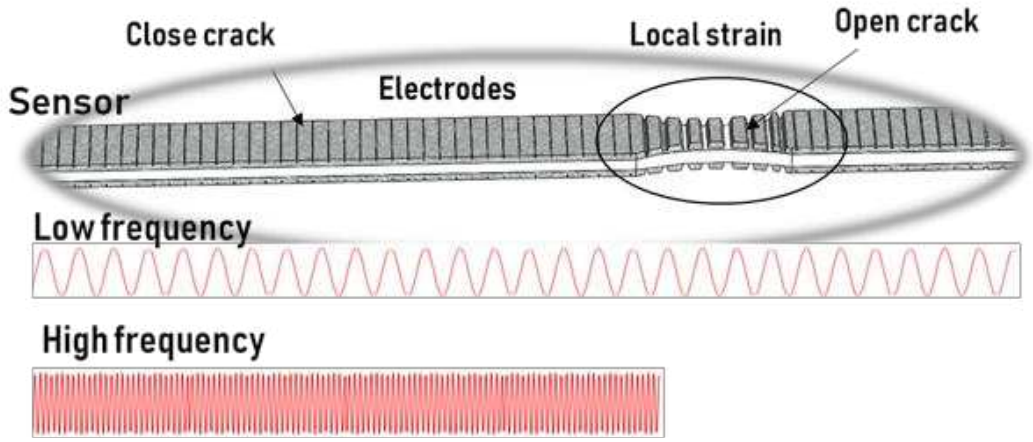

Figure 2: Schematic illustrates the mechanism of the capacitive sensor sheet with variable-resistance electrodes where a new virtual length is created at a high frequency after local deformation that changes the effective capacitance of the sensor.

In order to realize this mechanism, we fabricate a stretchable PPC with piezoresistive electrodes based on PDMS as dielectric materials and cracked carbon nanotube (CNT) paper as electrodes encapsulated on the top and bottom by PDMS layer **(Figure 3,a)**. The Fragmented CNT paper is well known for its excellent piezoresistivity, where we confirm previously an ultra-high resistive gauge factor (GF) of over 4.2×10^4 at 150% strain [16]. The significant change in resistance of the fragmented CNT (from Ω to MΩ) under strain allows PPC to reach the transmission line effect quickly, even for low strain, where we determined a total signal dissipation for 3% strain at 7 MHz [15]. Our 30 mm sensor is divided virtually into 3 zones named Location #1,#2,#3; etch zone of 10 mm length is stretched separately to study the possibilities of positioning, as **Figure 3,b** clarify. Two-wire fixed at the beginning of the top and bottom electrodes are used to inject the electromagnetic signal with variable interrogating frequency in the sensor, where the signal feedback is used to measure the total capacitance of the sensor. The mechanical loading/unloading was applied using a 5944 Instron universal testing frame where the evolution of the capacitance is monitored by an LCR meter (Agilent E4980A).

  doi:10.5075/epfl-298799_978-2-9701614-0-0

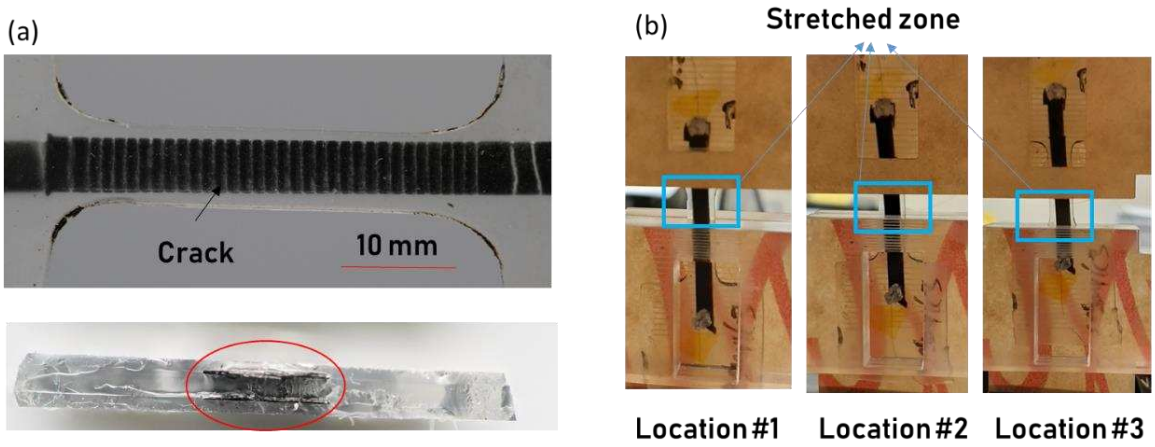

Figure 3: (a) Top view and cross-section of the parallel plate capacitor fabricated by cracked CNT paper and PDMS (b) Experimental process for applying local strain. The local strain is applied by changing the gap between the PMMA grips as only the space between the grips is subjected to strain.

Equation 1 is used to achieve the active length (which represents the distance reached by the electromagnetic signal before attenuation) after measuring capacitance for the different stretched zone. . **Figure 4,a** shows that the active sensor length is 70% of the initial length (L_0) after Applying 10% strain at 600 KHz to location #3. This active length decreases to 42% and 1% when locations #2 and #1 are stretched. The capacitance saturation refers to the signal behavior inside the sensor after applying a local strain (stretching one zone). This signal behavior is illustrated in **Figure 2** where the signal can easily cross the nonstretched zones, as the low electrode resistance ensures no dissipation. However, when the signal reached the high-resistance stretched zone, it dissipated and eventually faded completely. At high *strain* and *frequency*, the signal disappeared within the stretching zone and was absent thereafter; thus, the active sensor length corresponds to the length of all unstretched zones before reaching the area that experiences saturation. Localizing lower strain is possible by increasing the interrogation signal frequency, where we can achieve the attenuation for only 3% strain if we inject 7 MHz signal as mentioned above [15].

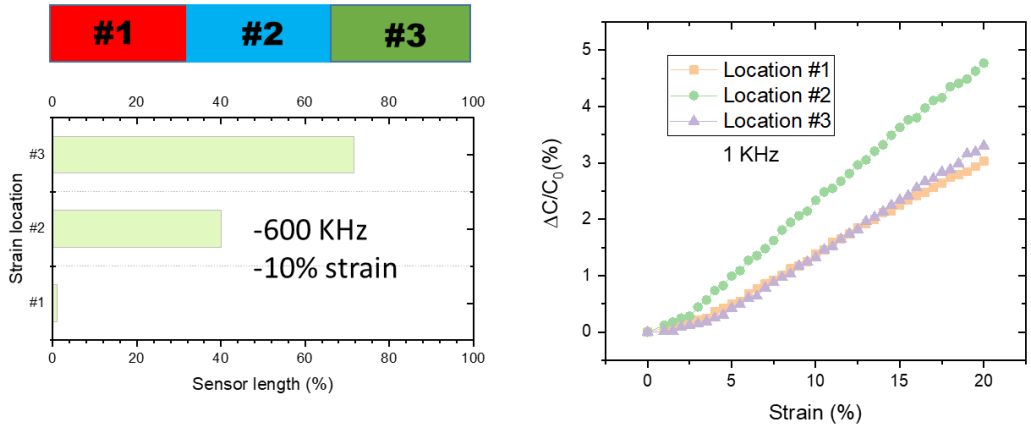

Figure 4: (a) Detection of the strain location applied to a portion of the sensor by following the signal dissipation through the sensor length at 600 kHz interrogation frequency and 12% strain (b) Strain

amplitudes for 3 different portions of the one-sheet sensor by measuring the capacitance variation at low frequency (1 kHz)

2.2 Strain intensity by the geometric effect

On the contrary to the high-frequency case, a complete propagation of the electromagnetic signal is realized for low interrogation frequency even if we have a significant strain; this fact is helpful in discovering the amount of strain applied. At low frequency (some KHz), the capacitance variation is independent of the transmission line model and related only to the geometrical extension of the sensor/PPC length (L) [17]. From equation 1, we can deduce the strain amplitude by measuring the capacitance variation at low frequency. Figure 4,b, where the measurement is made at 1 kHz, shows an increase of the relative capacitance variation as a function of strain with a sensitivity GF of 0.2. The sensitivity was low because the strain was applied to part of the sensor, whereas the capacitance was measured over the entire sensor. The three different strain locations show relatively similar capacitance behavior under strain witch whose sensitivity is related to the stretched length.

The results in **Figure 4** show that our cracked capacitive sensor can simultaneously record the strain magnitude and the strain location simply by measuring the sensor capacitance with interrogation frequency adjustment. This strain measurement and localization method can be applied more widely with much longer sensors and higher spatial resolution. This one sensor sheet is suitable for obtaining accurate strain information on a large scale by minimizing the number of wiring, giving a chance to this technology to replace the available methods such as independent sensor networks and optic fiber. This sensing technology with a reduced number of wires and a simple electronic interface will increase sensing reliability while reducing its cost and complexity.

3. Conclusion

This study presents innovative methods to monitor large-scale composites structures with a minimal number of wires and high spacial resolution that serve as an alternative to limited available technology. Our technology is based on transforming long 2D sensors into a transmission line model by using a stretchable parallel plate capacitor with piezoresistive electrodes and then used as a distributed strain sensor. We selected PDMS and cracked CNT paper as materials to build the sensor. In this work, we demonstrate that by a sensor divided into three virtual zones, our cracked capacitive sensor can simultaneously record strain in each zone by measuring the sensor capacitance at a high frequency. Moreover, we confirm that by changing the frequency from high to low, our sensor is able to measure the local strain amplitudes. Combining the geometrical model with the transmission line mechanism, we confirmed that our sensor detects the strain distribution and amplitudes in deformable systems with a minimal number of individual sensors.

Acknowledgements

The research reported in this publication was financially supported by King Abdullah University of Science and Technology (KAUST), Saudi Arabia, under the award number BAS/1/1315-01-01.

4. References

[1] F. Greco, L. Leonetti, P. Lonetti, and P. Nevone Blasi, "Crack propagation analysis in composite materials by using moving mesh and multiscale techniques," *Computers & Structures*, vol. 153, pp. 201–216, Jun. 2015, doi: 10.1016/j.compstruc.2015.03.002.
[2] B. Wang, S. Zhong, T.-L. Lee, K. S. Fancey, and J. Mi, "Non-destructive testing and evaluation of composite materials/structures: A state-of-the-art review," *Advances in mechanical engineering*, vol. 12, no. 4, p. 1687814020913761, 2020.
[3] S. S. Kessler, S. M. Spearing, and C. Soutis, "Damage detection in composite materials using Lamb wave methods," *Smart materials and structures*, vol. 11, no. 2, p. 269, 2002.
[4] M. Arena and M. Viscardi, "Strain state detection in composite structures: Review and new challenges," *Journal of Composites Science*, vol. 4, no. 2, p. 60, 2020.
[5] G. Loi, N. Uras, M. C. Porcu, and F. Aymerich, "Damage Detection in Composite Materials by Flexural Dynamic Excitation and Accelerometer-Based Acquisition," in *IOP Conference Series: Materials Science and Engineering*, 2022, vol. 1214, no. 1, p. 012007.
[6] M. A. Hamstad, "A review: acoustic emission, a tool for composite-materials studies," *Experimental mechanics*, vol. 26, no. 1, pp. 7–13, 1986.
[7] K. L. Ranganatha *et al.*, "A Wireless, Multi-Channel Printed Capacitive Strain Gauge System for Structural Health Monitoring," in *2021 IEEE Sensors*, pp. 1–4.
[8] C. Occhiuzzi, C. Paggi, and G. Marrocco, "Passive RFID strain-sensor based on meander-line antennas," *IEEE Transactions on Antennas and Propagation*, vol. 59, no. 12, pp. 4836–4840, 2011.
[9] D. Wada, H. Igawa, and T. Kasai, "Vibration monitoring of a helicopter blade model using the optical fiber distributed strain sensing technique," *Applied Optics*, vol. 55, no. 25, pp. 6953–6959, 2016.
[10] J. Yick, B. Mukherjee, and D. Ghosal, "Wireless sensor network survey," *Computer networks*, vol. 52, no. 12, pp. 2292–2330, 2008.
[11] J. P. Lynch and K. J. Loh, "A summary review of wireless sensors and sensor networks for structural health monitoring," *Shock and vibration digest*, vol. 38, no. 2, pp. 91–130, 2006.
[12] J. Hong, P. Xu, H. Xia, Z. Xu, and Q.-Q. Ni, "Electromagnetic interference shielding anisotropy enhanced by CFRP laminated structures," *Composites Science and Technology*, vol. 203, p. 108616, 2021.
[13] M. P. J. Tiggelman *et al.*, "Identifying dielectric and resistive electrode losses in high-density capacitors at radio frequencies," in *2008 IEEE International Conference on Microelectronic Test Structures*, 2008, pp. 190–195.
[14] Hussein Nesser and Lubineau, Gilles, "Minimizing the wiring in distributed strain sensing using a capacitive sensor sheet with variable-resistance electrodes," *Scientific report*, 2020.
[15] H. Nesser and G. Lubineau, "Achieving Super Sensitivity in Capacitive Strain Sensing by Electrode Fragmentation," *ACS Applied Materials & Interfaces*, vol. 13, no. 30, pp. 36062–36070, 2021.
[16] Y. Xin, J. Zhou, X. Xu, and G. Lubineau, "Laser-engraved carbon nanotube paper for instilling high sensitivity, high stretchability, and high linearity in strain sensors," *Nanoscale*, vol. 9, no. 30, pp. 10897–10905, 2017.
[17] H. Nesser and G. Lubineau, "Strain sensing by electrical capacitive variation: From stretchable materials to electronic interfaces," *Advanced Electronic Materials*, vol. 7, no. 10, p. 2100190, 2021.

Composites Meet Sustainability – Proceedings of the 20th European Conference on Composite Materials,
ECCM20. 26-30 June, 2022, Lausanne, Switzerland

QUASI-STATIC AND FATIGUE PERFORMANCE OF NON-TOUGHENED AND TOUGHENED ADHESIVES FOR WIND TURBINE BLADES

Dharun Vadugappatty Srinivasan[a], Anastasios P. Vassilopoulos[a]

a: Composite Construction Laboratory (CCLab), Ecole Polytechnique Fédérale de Lausanne
EPFL, Station 16, CH-1015 Lausanne, Switzerland.
dharun.srinivasan@epfl.ch

Abstract: *Epoxy adhesives used in wind turbine adhesive joints are non-toughened or moderately toughened to meet the loading requirements. Adhesive toughening is not generally cost-effective and such newly modified adhesives need further certification to be used in wind turbine blades. Alternatively, hybrid adhesives with tailored mechanical properties can be attained using commercially available adhesives. In this study, glass fiber and rubber particle-modified adhesives are used to fabricate pristine and a combination of hybrid adhesives through two different manufacturing techniques. The glass transition temperature and quasi-static mechanical properties are insensitive to manufacturing defects. Tensile modulus, tensile strength, shear modulus, shear strength, and fracture toughness are decreased by toughening. Further two different ASTM D638-14 Type I and Type II specimens are considered to determine the influence of size effect on the tensile fatigue performance.*

Keywords: Adhesives; toughening; fatigue; size effect; failure analysis

1. Introduction

Adhesive bonding is widely used in large-scale structures such as aircraft, wind turbine blades and automobiles as it offers nearly uniform stress distribution and less assembly weight as compared with mechanical fasteners. In these applications, non-toughened and toughened epoxy adhesives are typically found due to their inherent mechanical and chemical properties. The non-toughened epoxy adhesive has higher mechanical stiffness, strength and cost-effectiveness as compared with toughened adhesives. But non-toughened adhesives possess poor strain to failure, crack resistance and impact resistance that can be improved by adhesive toughening However, toughening introduces flexible materials and chains inside the rigid epoxies, and it may reduce other mechanical properties such as tensile modulus and tensile strength as well as the temperature-related performance [1]. Implementing the high-cost toughening strategies in these large bond volume applications is not practically feasible. Hence, hybrid adhesives with desirable mechanical properties should be developed using commercially available adhesives. So, further certification of these adhesives is not required and can be readily used by the blade manufacturers. Epoxy base and hardener in paste forms are highly viscous and generally mixed by a mechanical mixer before applying them to the bonding surface. This method is practiced by blade manufacturers to avoid air voids and control the bond quality. In other scenarios such as adhesively bonded local repair processes and academic research, manual mixing is commonly followed. In the manual mixing process, the adhesive and hardener can be poorly mixed, and voids can be introduced while mixing or adhesive deposition process Most of these studies in the literature were focused only on the toughening effect on the DMA, tensile and fracture properties but not on the shear strength. The discussed toughening

methods could not be readily used by wind turbine blade manufacturers. Hence new hybridization strategies reducing the certification process, time and cost need to be developed.

The joints are also subjected to various loadings including static, fatigue [2], impact and environment during the service. Designing the adhesive joints for the above-combined loading conditions is challenging, as the joint performance depends on different parameters such as the joint geometry [3], adherend material, adhesive constituent properties, surface preparation, curing conditions [4–7] and post-curing [8] conditions. Savvilotidou et al. [9,10] studied the effect of moisture on the physical, quasi-static tensile and tensile fatigue life of the epoxy adhesives used in bridges and it can withstand the fatigue stresses higher than 25 % of their static tensile strength for more than 2 million cycles. There is only limited work carried out on the fatigue performance of the structural epoxy adhesives. The effect of hybrid toughening under fatigue loading needs to be investigated as it would aid in tailoring the adhesive properties according to the load levels and fatigue life. The tensile fatigue specimens are tested as recommended by ASTM D638-14 Type I specimen and Type II specimens geometric configuration and they are suggested by ASTM D7791-17, a standard test method for measuring fatigue properties of plastics. These specimens have a width of 13 mm and 6 mm, respectively which may affect the fatigue life. To the best of the author's knowledge, there was no study exploring the size effect of these testing geometries on the fatigue performance of the epoxy adhesives.

In this work, glass fiber and rubber particle-modified adhesives were used to fabricate pristine and hybrid adhesives through two different manufacturing techniques and hybridization strategies. The manufacturing and hybridization effects on the material properties were evaluated by dynamic mechanical analysis (DMA), quasi-static tensile, V-notch shear and single-edge-notch bending (SENB) testing. The hybridization effects on the fatigue performance were evaluated through S-N diagrams. Further, ASTM D638-14 Type I specimen and Type II specimens were tested at different load levels to determine the influence of size effect.

2. Materials and manufacturing

Two different epoxy-based paste adhesives SPABOND™ (SP) 820HTA and SPABOND™ 840HTA provided by Gurit (UK) Ltd were used to fabricate the pristine (BBM1, TTM1, BBM2 and TTM2) and hybrid adhesives (BTM1, TBM1, BTM2 and TBM2). SP 820HTA is a glass fiber-filled, non-toughened adhesive (BB) [13] whereas SP 840HTA is toughened with core-shell rubber particles (TT) [14]. Two different manufacturing methods M1 and M2 are also considered in this study. In the first manufacturing method (M1), the epoxy base and hardener were mixed thoroughly using a mechanical mixer at a weight ratio of 100:33, as practiced by the wind turbine industries. M1 panels were fabricated and provided by Gurit (UK) Ltd. In the manual mixing method (M2), wooden spatulas were used to mix the adhesive materials for 5 to 7 minutes and degassed at 0.95 bar of vacuum for 5 to 10 minutes. After degassing, the adhesive was spread inside the aluminum mold cavity (4 mm) layer by layer. The mixed adhesive system was cured at the ambient temperature for 120 minutes which includes the adhesive mixing and degassing processes, to mimic the time taken by the blade manufacturers for applying adhesive on the long wind turbine blades. Lately, the adhesive was heated to 70°C at a rate of 2 °C⁄min and cured for 120 minutes.

In this study, two different hybridization strategies are considered to develop the new hybrid adhesives. As illustrated in Figure 1a, the hardener of non-toughened and toughened adhesives was swapped in the first strategy. BTM1 hybrid adhesive was prepared by mixing SP 820HTA base and SP 840HTA hardener and vice-versa for TBM1 hybrid adhesive. The above strategy is cost-effective, as any one of the hardener and base materials was used for tailoring the material properties. The second hybridization strategy is mixing the non-toughened adhesive (base with hardener) and toughened adhesive (base with hardener) at certain weight proportions. Figure 1b shows that the hybrid adhesives, BTM2 and TBM2 were prepared by mixing the toughened adhesive with non-toughened adhesive at 25 wt% and 50 wt%, respectively. Specimens fabricated through M2 technique only were used in fatigue testing.

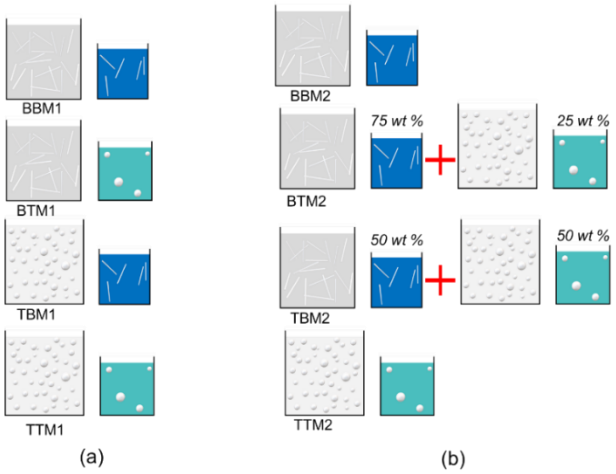

Figure 1. Schematic diagram of adhesive material composition: (a) M1, machine mixing method and (b) M2, manual mixing method.

3. Test methods

3.1 Dynamical mechanical analysis

DMA specimens were tested under single cantilever mode using TA® Q800 series machine as stipulated by ASTM D7028-07 (2015). Liquid nitrogen was supplied to the test machine for capturing the DMA properties at a lower temperature (-50℃). The specimen was aligned well into the fixture using a torque of 1.47 Nm and heated from -50℃ to 150℃ at a rate of 5 ℃/min. The oscillating frequency was set to 1 Hz with an amplitude of 20 µm.

3.2 Quasi-static tensile and V-notch shear testing

The uniaxial tensile experiment was conducted using MTS® 810 Landmark servo-hydraulic machine with a calibrated load cell capacity of 5 kN and applied force accuracy of ±5%. The ASTM D638-14 Type I specimen was tested under displacement control, at a crosshead rate of 1 mm/min. All the tests were performed at the ambient temperature of 22 ± 3°C and relative humidity of 40 ± 10%.

The v-notch shear specimens were prepared as recommended in ASTM D5379-19. Walter + bai (w + b) test machine equipped with a load cell capacity of 50 kN and Iosipescu shear fixture was used to perform the shear tests. The top punch was displacement-controlled at a rate of 1 mm/min.

3.3 Single-edge-notch bending (SENB)

MTS® Acumen equipped with a 3 kN load cell and a three-point bending fixture was used in the plane strain fracture toughness testing. The specimen was adjusted in the fixture such that the initial notch and the contact point of the top roller were on the same loading axis. The top roller was loaded at a displacement rate of 0.25 mm/min to have a stable fracture. During the testing, 2D DIC images were captured from which the mid-span deflection was calculated. To have an effective $\mathrm{K_{IC}}$, the load $\mathrm{P_Q}$ was selected as mentioned in ASTM D5045-14.

3.4 Tensile-Tensile fatigue testing

The fatigue experiments were conducted using the same MTS® machine and the specimens were force-controlled with a stress ratio R of $\sigma_{min}/\sigma_{max} = 0.1$. The selected R ratio prevents compressive stress in the specimen and buckling instability hence, the test results can be compared with the literature values. True sinusoidal loads were applied with a frequency of 10 Hz.

4. Results and discussion

4.1 Hybridization and manufacturing effect on DMA properties

Glass transition temperature, peak $tan\,\delta$ and E' at 25℃ of the M1 adhesives are given in Table 1. Within the experimental scatter, T_g of all the adhesives lies between 71.4℃ to 76.9℃ and there was no significant effect of the first hybridization strategy on T_g. The non-toughened adhesive (BBM1) has a higher E' and lower $tan\,\delta$ than the hybrid (BTM1 and TBM1) and toughened (TTM1) adhesives. Due to higher toughening content, the storage modulus of TBM1 adhesive was 23% lesser than BTM1 adhesive. T_g was not significantly affected by the second hybridization strategy implicating that these non-toughened and toughened adhesives can be mixed or cured together for developing tailored adhesive joints.

Table 1: DMA properties of M1 and M2 adhesives.

Specimen	T_g (℃)	Peak $tan\,\delta$ (-)	E' at 25℃ (GPa)
BBM1	73.4±0.5	0.623±0.003	3.18±0.17
BTM1	75.4±1.8	0.614±0.014	2.91±0.17
TBM1	74.5±1.6	0.663±0.009	2.36±0.05
TTM1	71.4±0.7	0.723±0.007	2.22±0.15
BBM2	72.6±0.8	0.613±0.005	2.98±0.10
BTM2	76.9±0.4	0.620±0.007	2.63±0.03
TBM2	76.1±2.9	0.648±0.008	2.68±0.13
TTM2	72.8±1.7	0.748±0.003	2.06±0.20

4.2 Hybridization and manufacturing effect on tensile properties

The measured tensile properties of the adhesives are provided in Table 2. The tensile modulus of BBM1 adhesive is 10.4%, 32.7% and 41.6% higher than BTM1, TBM1 and TTM1 adhesives,

respectively. The yield stress of BTM1 adhesive was 6.2% lower than BBM1 adhesive. While considering the first hybridization strategy, TBM1 adhesive showed a distinct elastic-plastic tensile behavior than BTM1 adhesive, hence it can be used in practical applications. Similarly, the average tensile modulus of BBM2 adhesive was 11.4%, 28% and 50% higher than BTM2, TBM2 and TTM2 adhesives, respectively. An increase in M2 adhesive toughening also caused an increase in the scattering of the failure strain.

Table 2. Uniaxial tensile properties of the adhesives.

Specimen	Tensile modulus (E)	0.2% offset Yield stress (σ_y)	Tensile toughness (U_T)	Tensile strength (σ_u)	Failure strain (ε_f)
	GPa	MPa	kJ/m^3	MPa	mm/mm
BBM1	5.1±0.08	51.38±1.89	0.68±0.14	60.16±2.65	0.0179±0.0024
BTM1	4.57±0.22	54.78±1.12	0.69±0.12	61.17±2.18	0.0184±0.0017
TBM1	3.43±0.07	42.20±2.27	1.26±0.17	52.56±0.64	0.0329±0.0027
TTM1	2.98±0.14	38.69±0.89	1.38±0.11	45.36±0.15	0.0391±0.0023
BBM2	5.59±0.39	61.47±1.75	0.71±0.03	69.01±0.51	0.0170±0.0007
BTM2	4.95±0.32	55.65±1.95	0.84±0.10	65.01±2.23	0.0201±0.0010
TBM2	4.02±0.06	47.21±0.39	0.96±0.11	55.98±0.87	0.0248±0.0020
TTM2	2.81±0.16	37.86±0.55	1.45±0.20	44.47±1.26	0.0417±0.0054

4.3 Hybridization and manufacturing effect on shear properties

The shear modulus, strength and failure strain of the adhesives are given in *Table 3*. The shear modulus and strength of the adhesives vary between 0.73 GPa to 2.12 GPa and 36.91 MPa to 51.65 MPa. Based on the required joint stiffness and shear strength in real-time applications, any one of these adhesives can be selected.

Table 3. Shear properties of the adhesives.

Specimen	Shear modulus (G)	Shear strength (τ_u)	Failure shear strain (γ_f)
	GPa	MPa	mm/mm
BBM1	2.12±0.19	51.02±1.79	0.0601±0.0102
BTM1	1.13±0.03	51.50±1.14	0.0695±0.0019
TBM1	0.80±0.04	41.19±0.20	0.1316±0.01
TTM1	0.73±0.06	36.91±1.11	0.1574±0.0431
BBM2	1.90±0.50	51.65±1.70	0.0539±0.0035
BTM2	1.63±0.06	46.54±0.34	0.0399±0.0042
TBM2	1.57±0.05	43.03±0.29	0.0435±0.0013
TTM2	0.91±0.09	38.10±1.31	0.12±0.03

4.4 Hybridization and manufacturing effect on fracture toughness

K_{IC} of the BBM1, BTM1, TBM1 and TTM1 adhesives are 1.84 ± 0.17 $MPa\sqrt{m}$, 2.12 ± 0.18 $MPa\sqrt{m}$, 2.17 ± 0.05 $MPa\sqrt{m}$ and 1.63 ± 0.05 $MPa\sqrt{m}$, respectively. Within the experimental scatter, the K_{IC} of BBM2 (2.64 ± 0.12 $MPa\sqrt{m}$), BTM2 (2.39 ± 0.17 $MPa\sqrt{m}$) and TBM2 (2.43 ± 0.27 $MPa\sqrt{m}$) adhesives were found to be similar. K_{IC} of TTM2 adhesive is 23.86% lower than the BBM2 adhesive. The fracture toughness of BBM2 and TTM2 adhesives are comparable to the technical data sheet values [13,14]. The fracture behavior of TTM1 and TTM2 were similar however BBM1 failed at a lower force than BBM2 adhesive. BBM1 fracture surface shows more fiber debonding than fiber breakages that can be correlated to the orientation of glass fibers at the middle section. Therefore, the tensile and fracture behavior of glass fiber-modified adhesives are influenced by the fiber orientation compared with shear.

4.5 Size effect and hybridization effect on fatigue life

The S-N plots of the adhesives and their corresponding fit based on Basquin's fatigue law using CCLab fatigue software are shown in Figure 2. As illustrated in Figure 2a and 2b, the slope of type II specimens of BBM2 and BTM2 adhesives are 13.45% and 6.82% lesser than that of type I specimens, respectively. The higher width (13 mm) specimens could have more defects as compared with the lower width, type II specimens. Comparing all the adhesives, the slop was not influenced by the adhesive toughening. All the specimens manifested brittle fracture at the end of their life, as there was no increase in displacement or strain during the final failure stage. The stiffness degradation of the adhesives was higher at the high load level than at the lower stress levels.

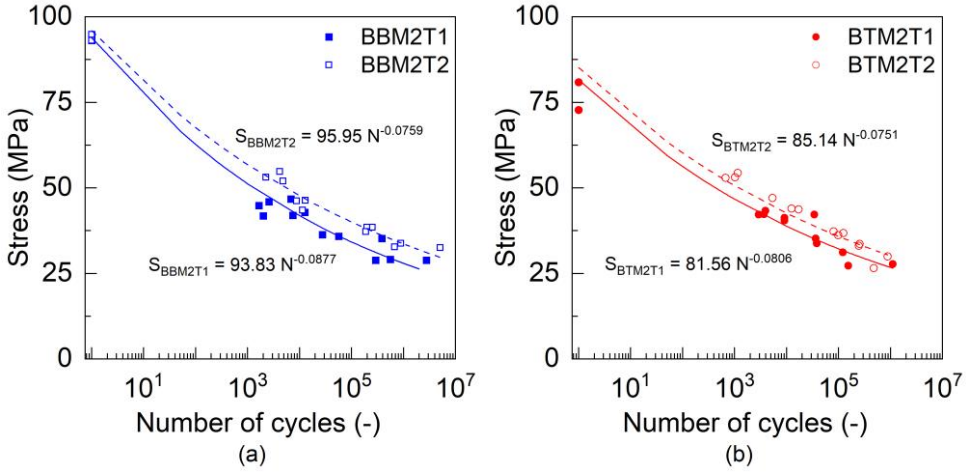

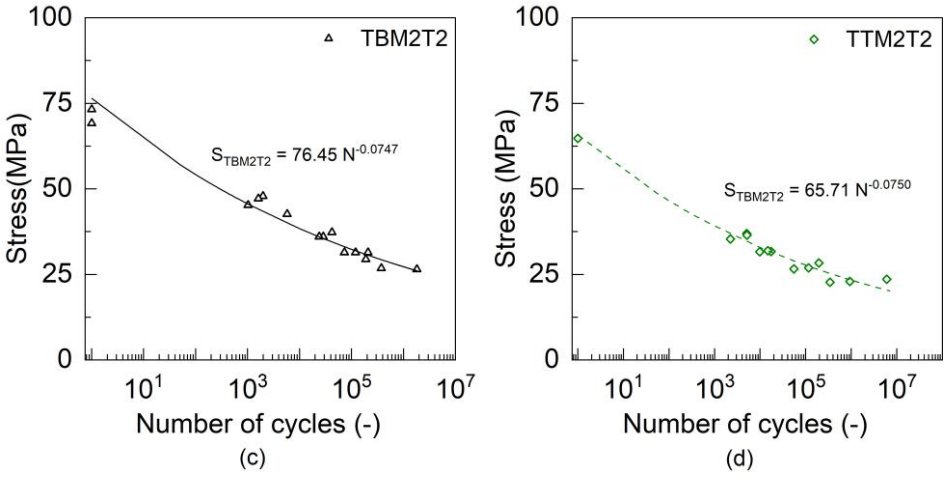

Figure 2. S-N curves of the adhesives: (a) BBM2T1 & BBM2T2, (b) BTM2T1 & BTM2T2, (c)TBM2T2 and (d)TTM2T2.

5. Conclusions

From the experimental study, the following conclusions are made: (a) The tensile modulus, tensile strength, shear modulus, shear strength and critical plane strain fracture toughness were decreased with an increase in toughening. However, the failure strain and tensile toughness were increased with toughening; (b) The tensile strength of the adhesives was decreased more than the shear strength with respect to toughening; (c) Among the developed hybrid adhesives, BTM1 adhesive showed better material properties and this hybridization strategy is recommended in practical applications and (d) Adhesive toughening has a less effect on the slope of S-N curve. On the contrary, the size effect shows a change in the slope of the S-N curves.

Acknowledgments

The authors wish to acknowledge the support and funding of this research by the Swiss National Science Foundation (Grant No. IZCOZ0_189905) under the project, Bonded composite primary structures in engineering applications (BONDS). The authors also acknowledge the experimental assistance provided by the technical team of the structural engineering experimental platform (GIC-ENAC) at the Ecole Polytechnique Fédérale de Lausanne (EPFL), Switzerland. The authors also thank Gurit UK Ltd for providing adhesive materials and for many helpful discussions. The authors thank Marc Edmond for his kind help in CT scan image analysis. This article/publication is based upon work from COST Action CA18120 (CERTBOND - https://certbond.eu/), supported by COST (European Cooperation in Science and Technology).

6. References

1. Kinloch AJ, Lee SH, Taylor AC. Improving the fracture toughness and the cyclic-fatigue resistance of epoxy-polymer blends. Polymer (Guildf). 2014; 55(24):6325–34.

2. Rosemeier M, Krimmer A, Bardenhagen A, Antoniou A. Tunneling crack initiation in trailing-edge bond lines of wind-turbine blades. AIAA Journal. 2019; 57(12):5462–74.
3. Tang JH, Sridhar I, Srikanth N. Static and fatigue failure analysis of adhesively bonded thick composite single lap joints. Composites Science and Technology. 2013; 86:18–25.
4. Czaderski C, Martinelli E, Michels J, Motavalli M. Effect of curing conditions on strength development in an epoxy resin for structural strengthening. Composites Part B: Engineering. 2012; 43(2):398–410.
5. Michels J, Sena Cruz J, Christen R, Czaderski C, Motavalli M. Mechanical performance of cold-curing epoxy adhesives after different mixing and curing procedures. Composites Part B: Engineering. 2016; 98:434–43.
6. Carbas RJC, Marques EAS, da Silva LFM, Lopes AM. Effect of Cure Temperature on the Glass Transition Temperature and Mechanical Properties of Epoxy Adhesives. https://doi.org/101080/002184642013779559. 2013; 90(1):104–19.
7. I. M. Foletti A, Sena Cruz J, Vassilopoulos AP. Fabrication and curing conditions effects on the fatigue behavior of a structural adhesive. International Journal of Fatigue. 2020; 139:105743.
8. Carbas RJC, da Silva LFM, Marques EAS, Lopes AM. Effect of post-cure on the glass transition temperature and mechanical properties of epoxy adhesives. http://dx.doi.org/101080/016942432013790294. 2013; 27(23):2542–57.
9. Savvilotidou M, Keller T, Vassilopoulos AP. Fatigue performance of a cold-curing structural epoxy adhesive subjected to moist environments. International Journal of Fatigue. 2017; 103:405–14.
10. Savvilotidou M, Vassilopoulos AP, Frigione M, Keller T. Effects of aging in dry environment on physical and mechanical properties of a cold-curing structural epoxy adhesive for bridge construction. Construction and Building Materials. 2017; 140:552–61.
11. SPABOND 820HTA™ Fast curing structural epoxy adhesive. Full general datasheet [Internet]. Available from: www.gurit.com.
12. SPABOND™ 840HTA fast-curing structural epoxy adhesive. Full general datasheet [Internet]. Available from: www.gurit.com.

  doi:10.5075/epfl-298799_978-2-9701614-0-0

MODE-I FRACTURE TOUGHNESS OF INTERLAYERED EPOXY ADHESIVES

Dharun, Vadugappatty Srinivasan[a], Anastasios P.Vassilopoulous[a]

a: Composite Construction Laboratory (CCLab), Ecole Polytechnique Fédérale de Lausanne
EPFL, Station 16, CH-1015 Lausanne, Switzerland.
dharun.srinivasan@epfl.ch

Abstract: *Epoxy adhesives are commonly used in the assembly of primary engineering structures such as aircraft, wind turbines, yachts and bridges. Damages in the adhesive bond line can lead to sudden fractures. Crack arresting features (CAFs) like rivets, bolts and other mechanical fasteners are used in these structures at the penalty of additional assembly cost and weight. This paper endeavors to the crack-arresting effect of polyvinylidene fluoride (PVDF) and polyetherimide (PEI) thermoplastic layers under mode-I plane strain fracture. Non-toughened and toughened epoxy adhesives are used to fabricate the reference specimens. The constitutive properties of the adhesives, PVDF and PEI are measured through uniaxial tensile testing. PVDF and PEI layers of 0.5 mm thickness are incorporated in the adhesives and mode-I fracture toughness is determined through single-edge-notched bending (SENB). Experimental test results show that these layers can arrest the cracks effectively at the layer interface***.**

Keywords: Adhesives; fracture toughness; thermoplastic layer; crack shielding.

1. Introduction

Adhesive bonding is used in primary engineering structures however its full potential could not be realized due to its low reliability. Cracks emerging from the inherent defects, in-service damages and high-stress concentrated regions are arrested by mechanical fasteners such as bolts and rivets. Disbond, weak bond and impact damage-induced disbond are the sources of failure initiation in the adhesive joints. The three main requirements of crack arresting features are (i) stopping the disbond at a pre-determined allowable length (b) meeting the desired design loading requirements (c) load-bearing capability that can be determined by reliable and repeatable non-destructive inspection (NDI) methods. One of the three criteria should be met to get certified by the air transportation authorities [1]. In composite materials, delaminations were arrested through-thickness reinforcement such as Z pins. T. Lobel et al. [2] used staple pins with dry fabrics before resin transfer molding and the measured double lap shear strength was 28 % higher than the conventional rivets. Thanks to the axial fixation and no pull-out of the staple pins. Nevertheless, Z pins and staple pins were limited to co-bonding and co-curing. The challenge remains in secondary bonding applications. T. Kruse et al. [3] showed that the cracked lap shear specimen designed with lock bolts of 4 mm to 4.8 mm diameter could offer better fatigue crack growth resistance as compared with the reference specimen. The crack growth was also slowed down by the laser ablation technique in which the carbon fibers of the adherend bond surface were exposed before bonding [4]. Fastener-adhesive hybrid bonding provides a crack-arresting mechanism in three ways (a) closing crack tip by fastener axial stiffness (b) crack friction by fastener preloading and (c) fastener-joint shear stiffness [5]. Selective toughening can be applied to areas that require local toughening, such as free edges, holes and highly stressed regions. Local toughening reduces manufacturing costs or decreases the adverse effect of total

  doi:10.5075/epfl-298799_978-2-9701614-0-0

toughening. In a single-ply interface toughening, unstable crack growth was observed as the crack was propagated from a high fracture toughness to a lower fracture toughness material [6]. A ductile phase thermoplastic was incorporated to arrest the disbond, a fail-safe design methodology to ease the certification requirements. Although the initial crack was unstable and the strain energy release rate was even smaller than the reference value, the crack was stopped as it reached the thermoplastic [1]. The crack was unstable as it penetrated through the PVDF layer. Crack tip blunting is another toughening strategy that was realized by stopping holes in the adhesive joint. Fracture toughness can also be increased up to 120% by incorporating copper (Cu) wire mesh in the adhesive bond line[7].

Several studies reveal that extrinsic toughening through interlayers is a promising technique but there are no clear material design guidelines to aid practical applications and their fracture behavior should be explored. In this study, two thermoplastic layers with 0.5 mm thickness are interlayered with non-toughened and toughened adhesives and their crack-arresting effect was investigated through mode-I plane-strain fracture toughness testing. Additionally, the constituent properties of the adhesives, PVDF and PEI materials are determined through tensile testing.

2. Materials and manufacturing

SPABOND™ (SP) 820HTA and SPABOND™ 840HTA are epoxy paste adhesives, provided by Gurit (UK) Ltd. SP 820HTA is a non-toughened adhesive and primarily modified with glass fibers (BB) whereas SP 840HTA is toughened with core-shell rubber particles (TT). Kynar® PVDF and Ultem® 1000 PEI are high-performance structural thermoplastic interlayers, procured from Emco Industrial Plastics, Inc, USA.

The epoxy base and hardener were mixed at a ratio of 100:33 using a wooden spatula and degassed at 0.95 bar of vacuum for 5 to 10 minutes and filled into a mold cavity. Initially, the adhesive was cured at room temperature (24°C ± 2°C) for 120 minutes and oven-cured for 120 minutes at 70°C. The heating and cooling rate was set to 2°C/min and 5 °C/min. For interlayering, PVDF and PEI layers were sanded with a 60-grit size paper using Bosch sanding tool. The dirt particles were removed by tap water and the layers were conditioned at 40°C for 10 minutes. Meanwhile, 5 g of mixed adhesive was diluted with 25 g of isopropanol as a primer. The primer solution was coated over the layers and dried at room temperature for 30 minutes. The mold cavity was partially filled (15 mm + $\Delta a_{pre\ CAF}$) and the primer-coated layer having a thickness of 0.5 mm (t) was placed before filling the remaining adhesive. $\Delta a_{pre\ CAF}$, a distance between the thermoplastic layer and the initial crack length (see Figure 1) was arbitrarily selected as 6.75 mm to understand the dynamic crack-arresting behavior. Table 1 shows the various material configurations used for fracture toughness testing.

Table 1. Material design details of pristine and interlayered epoxy adhesives.

S.no	Specimen	Adhesive	Interlayer Material	Interlayer Thickness (t) (mm)	Position ($\Delta a_{pre\ CAF}$) (mm)
1	BB	BB	-	-	-
2	TT	TT	-	-	-
3	BBPVDF	BB	PVDF	0.5	6.75
4	BBPEI	BB	PEI	0.5	6.75

Abrasive water-jet machining was used for cutting the thermoplastic layers to the required nominal dimensions for the tensile and SENB testing. The geometrical dimensions S, W and B are 120 mm, 30 mm and 15 mm, respectively (see Figure 1). In the SENB specimens, an initial notch was machined by a rotary saw and further sharpened with an abrasive paste and a razor blade. The initial crack length (a) of prepared specimens was measured through an optical microscope, Dino-Lite AD7013MZT. To use the digital image correlation (DIC) technique, all the tensile and SENB specimens were uniformly coated at least twice with white paint, dried and then sprinkled with the black speckles.

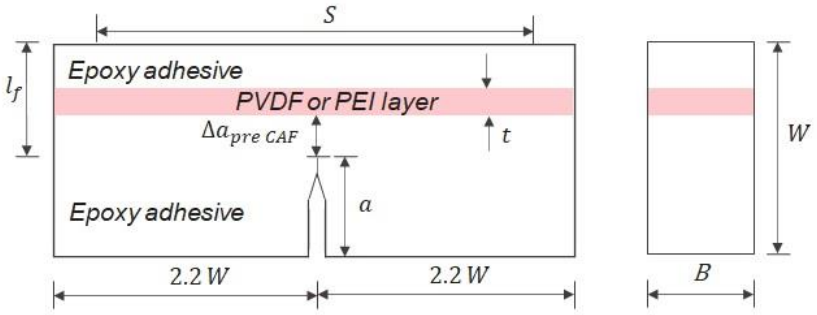

Figure 1. Schematic diagram of thermoplastic interlayered SENB test specimen.

3. Tensile and SENB testing

Uniaxial tensile test was conducted using MTS® 810 Landmark servo-hydraulic machine with a calibrated load cell capacity of 5 kN and applied force accuracy of ±5%. ASTM D638-14 Type II specimens of adhesives and Type I specimens of PVDF and PEI were tested under displacement control, at a crosshead rate of 1 mm/min. All the tests were performed at the ambient temperature of 22 ± 3°C and relative humidity of 40 ± 10%.

Walter + bai (w + b) test machine equipped with a load cell capacity of 50 kN and a three-point bending fixture was used for the plane strain fracture toughness testing. The specimen was adjusted in the fixture such that the initial notch and the contact point of the top roller were on the same loading axis. The top roller was loaded at a displacement rate of 0.25 mm/min to have a stable fracture. During the testing, 2D DIC images were captured from which the mid-span deflection was calculated. To have an effective K_{IC}, the load P_Q was selected as mentioned in ASTM D5045-14.

4. Results and discussion

The true tensile stress versus strain response of the pristine adhesives and interlayered adhesives are shown in Figure 2a. All the specimens showed initial linear-elastic behavior and followed by a non-linear response. Among the tested materials, PVDF showed a very high strain to failure whereas PEI exhibited high tensile strength. The tensile modulus of BB adhesive is higher than the other materials. The longitudinal engineering strain versus lateral engineering strain response of the materials is shown in Figure 2b from which the elastic and plastic Poisson's ratio were calculated. Poisson's ratio of BB adhesive was constant until the final failure. In TT and PVDF, the Poisson's ratio was decreased in the plastic region. Due to PEI softening, there was a slight increase in Poisson's ratio after the linear elastic region.

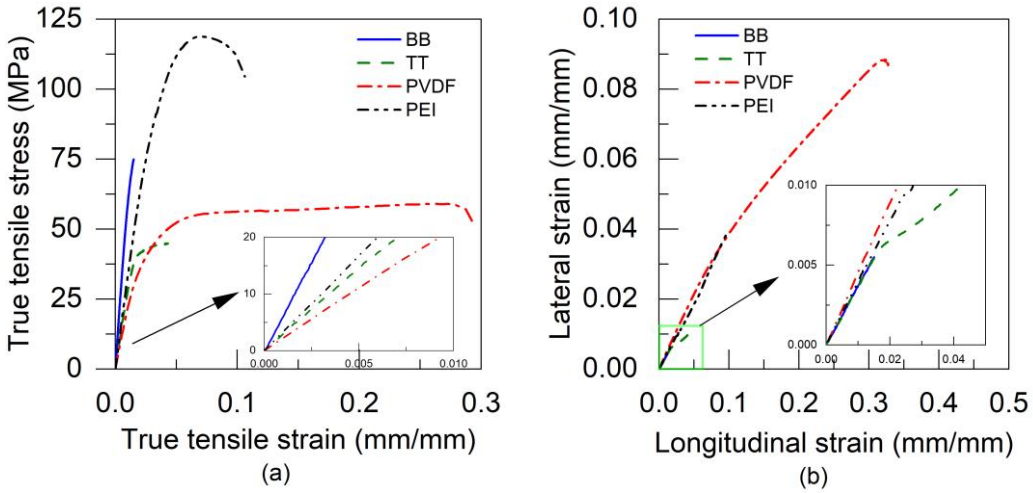

Figure 2. Tensile properties of adhesives, PVDF and PEI: (a) true stress versus strain and (b) longitudinal to lateral strain response.

The tensile properties of the adhesives, PVDF and PEI are shown in Table 2. The tensile modulus of TT and PVDF are comparable. In this case, the yield strength is different which can be referred to as yield strength inhomogeneity.

Table 2. Tensile properties of the epoxy adhesives, PVDF and PEI.

Properties	BB	TT	PVDF	PEI
Tensile modulus (E), GPa	5.59±0.39	2.81±0.16	2.21±0.11	3.44±0.10
0.2% offset Yield stress (σ_y), MPa	61.47±1.75	37.86±0.55	31.09±1.02	67.45±2.99
Tensile strength (σ_u), MPa	69.01±0.51	44.47±1.26	58.03±0.78	117.43±2.13
Failure strain (ε_f), mm/mm	0.0170±0.001	0.0417±0.005	0.238±0.035	0.064±0.008
Tensile toughness (U_T), kJ/m^3	0.71±0.03	1.45±0.20	13.78±1.95	7.35±2.52
Elastic Poisson's ratio	0.374±0.004	0.36±0.002	0.457±0.008	0.337±0.02
Plastic Poisson's ratio	-	0.18±0.018	0.243±0.026	0.43±0.01

Tensile failure images of PVDF and PEI specimens are shown in Figure 3a and 3b, respectively. Whitening due to severe plastic deformation was observed in PVDF whereas the necking phenomenon was noticed in PEI.

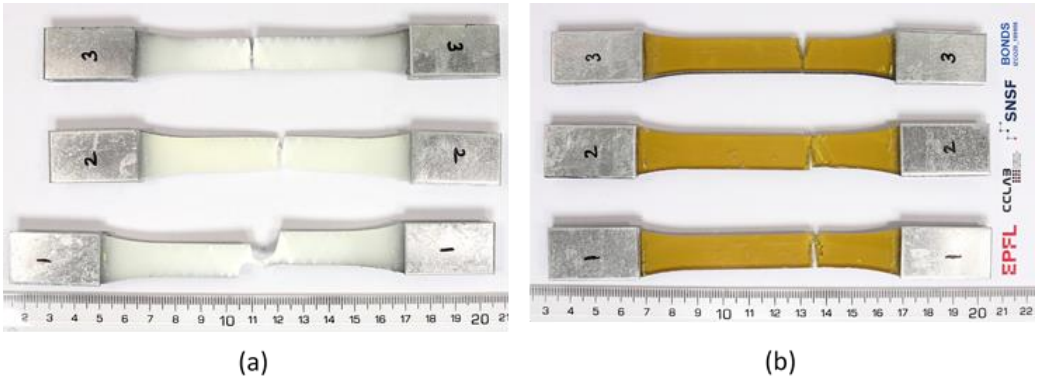

Figure 3. Tensile failure of the thermoplastics: (a) PVDF and (b) PEI.

The force versus deflection response of the pristine and interlayered SENB specimens are compared in Figure 4. After reaching the initial peak load, a very small crack resistance was offered by BB adhesive whereas TT adhesive failed abruptly, exhibiting unstable crack propagation. K_{IC} of BB and TT adhesive were calculated as 2.95±0.19 $Mpa\sqrt{m}$ and 2.17±0.01 $Mpa\sqrt{m}$. In BBPVDF, the crack was stopped by the PVDF layer at a load of 277.05±19.60 N and then it started to grow along with the interface. After reaching the second peak load of 802.53±26.59 N, the crack propagated through the PVDF resulting in an unstable fracture. Similarly, the crack was arrested at 237.58±9.03 in BBPEI specimen and grown at the interface before failing at 734.25±10.08 N. The K_{IC} of BBPVDF and BBPEI are 2.77±0.05 and 2.70±0.05 respectively. The crack arresting load and failure load of PVDF interlayered epoxies are higher than PEI interlayering. However, PEI interlayered epoxies absorbed more fracture energy (3244±63.5 Nmm, area under the curve) than all specimens.

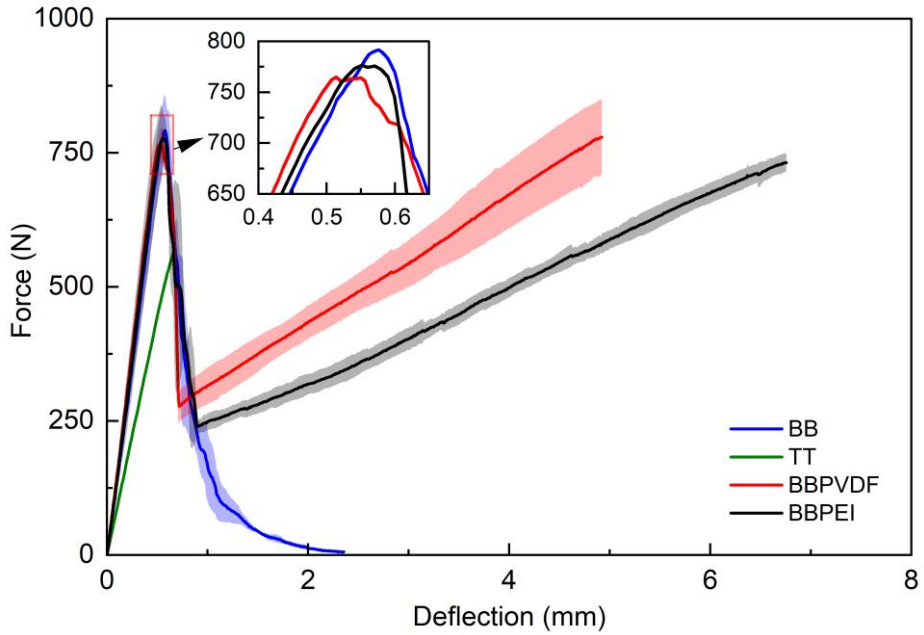

Figure 4. Force versus deflection response of pristine and thermoplastic interlayered adhesives.

Figure 5a and 5b show the crack initiation and propagation at BB specimen, respectively. The crack path slightly deviated from the initial crack plane which can explain the increase in K_{IC} value as compared to the technical data sheet value. Figure 5a reveals the interaction between the crack and PEI interlayer in BBPEI specimen. After the arrest load, the force was increased to another peak as the interface crack started growing.

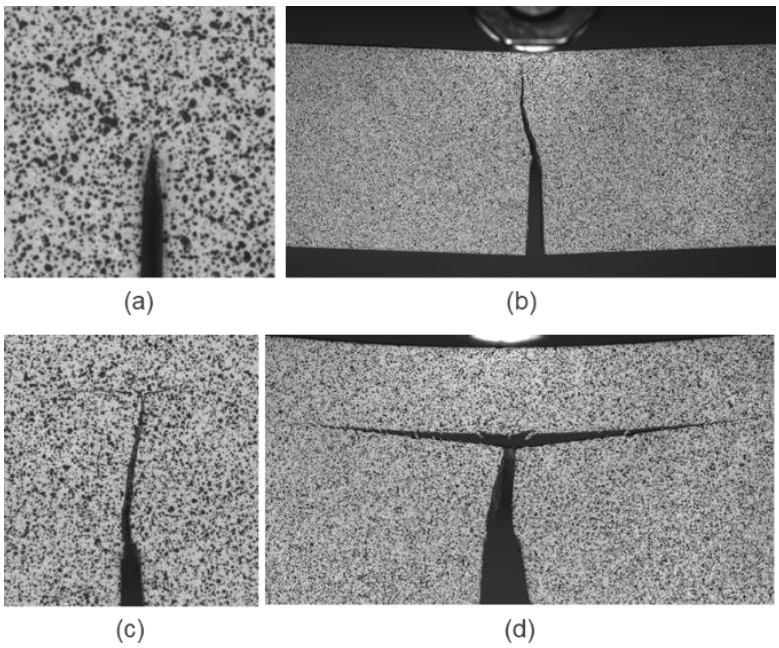

Figure 5. Failure behaviour of the specimens: (a) crack initiation at BB, (b) final failure of BB, (C) crack interacting at PEI layer of BBPEI and (d) interface crack growing before the final failure at BBPEI.

5. Conclusion

The constitutive properties of the adhesives and thermoplastic layers were determined by the uniaxial tensile test. Further incorporating the PVDF or PEI thermoplastic layer, the mode-I crack could be stopped at the layer interface. As compared to PEI, the PVDF layer showed a higher crack arresting and final failure load. In the future, the effect of thermoplastic layer position with respect to the initial crack and layer thickness will be investigated.

Acknowledgments

The authors wish to acknowledge the support and funding of this research by the Swiss National Science Foundation (Grant No. IZCOZ0_189905) under the project, Bonded composite primary structures in engineering applications (BONDS). The authors also acknowledge the experimental assistance provided by the technical team of the structural engineering experimental platform (GIC-ENAC) at the Ecole Polytechnique Fédérale de Lausanne (EPFL), Switzerland. The authors also thank Gurit UK Ltd for providing adhesive materials. This article/publication is based upon work from COST Action CA18120 (CERTBOND - https://certbond.eu/), supported by COST (European Cooperation in Science and Technology).

6. References

1. Löbel T, Holzhüter D, Sinapius M, Hühne C. A hybrid bondline concept for bonded composite joints. International Journal of Adhesion and Adhesives. 2016; 68:229–38.
2. Löbel T, Kolesnikov B, Scheffler S, Stahl A, Hühne C. Enhanced tensile strength of composite joints by using staple-like pins: Working principles and experimental validation. Composite Structures. 2013; 106:453–60.
3. Kruse T, Körwien T, Ruzek R. Fatigue behaviour and damage tolerant design of composite bonded joints for aerospace application. ECCM 2016 - Proceeding of the 17th European Conference on Composite Materials. 2016; 7–9.
4. Kruse T, Körwien T, Heckner S, Geistbeck M. Bonding of CFRP primary aerospace structures - Crackstopping in composite bonded joints under fatigue. ICCM International Conferences on Composite Materials. 2015; 19–24.
5. Richard L, Lin KY. Delamination / Disbond Arrest Features in Aircraft Composite Structures. 2014; 3–6.
6. Malkin R, Trask RS, Bond IP. Control of unstable crack propagation through bio-inspired interface modification. Composites Part A: Applied Science and Manufacturing. 2013; 46(1):122–30.
7. Maloney K, Fleck N. Toughening strategies in adhesive joints. International Journal of Solids and Structures. 2019; 158:66–75.

ECCM
26-30 JUNE
2022
LAUSANNE
SWITZERLAND

ECCM20 - Proceedings

ISBN: 978-2-9701614-0-0
DOI: 10.5075/epfl-298799_978-2-9701614-0-0